



Strongly Coupled Coulomb Systems

Edited by
Gabor J. Kalman
J. Martin Rommel and
Krastan Blagoev

Strongly Coupled Coulomb Systems

This page intentionally left blank

Strongly Coupled Coulomb Systems

Edited by

Gabor J. Kalman
J. Martin Rommel

and

Krastan Blagoev

*Boston College
Chestnut Hill, Massachusetts*

KLUWER ACADEMIC PUBLISHERS
NEW YORK, BOSTON, DORDRECHT, LONDON, MOSCOW

eBook ISBN: 0-306-47086-1
Print ISBN: 0-306-46031-9

©2002 Kluwer Academic Publishers
New York, Boston, Dordrecht, London, Moscow

Print ©1998 Plenum Press
New York

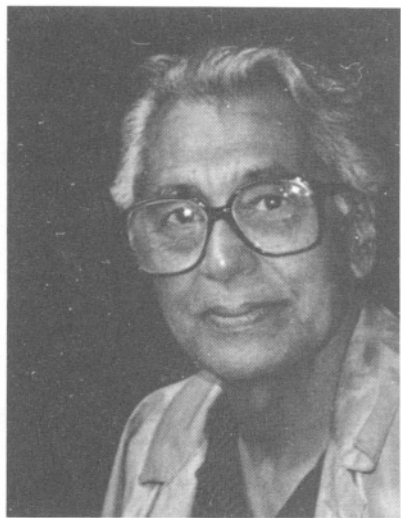
All rights reserved

No part of this eBook may be reproduced or transmitted in any form or by any means, electronic, mechanical, recording, or otherwise, without written consent from the Publisher

Created in the United States of America

Visit Kluwer Online at: <http://kluweronline.com>
and Kluwer's eBookstore at: <http://ebooks.kluweronline.com>

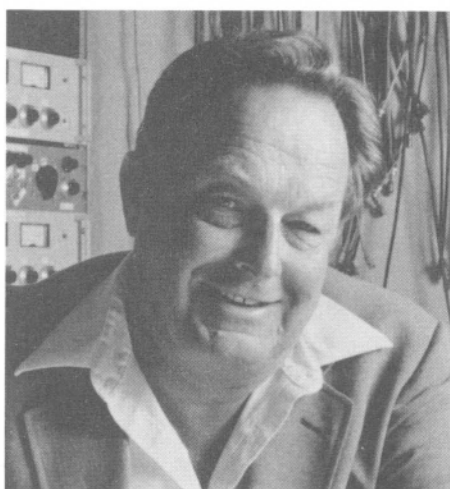
IN MEMORIAM



KUNDAN SINGWI
1919–1990



EUGENE P. GROSS
1926–1991



JOHN MALMBERG
1927–1992

Rien de plus commun et de plus aisé que d'attribuer à la force ce qui procède de la faiblesse.
Paul Valéry

Local Organizing Committee

Gabor J. Kalman *Boston College*
Pradip Bakshi *Boston College*
Kevin Bedell *Boston College*
Krastan Blagoev *Boston College*
Tom T. Chang *M.I.T.*
Kenneth Golden *University of Vermont*
Harvey Gould *Clark University*
John Jasperse *Phillips Laboratory*
Udayan Mohanty *Boston College*
Irwin Oppenheim *M.I.T.*
Martin Rommel *Boston College*
Vladimir Valtchinov *Boston College*

International Advisory Board

Angel Alastuey *Ecole Normale Sup. de Lyon*
Neil Ashcroft *Cornell University*
John Bollinger *NIST*
David Ceperley *Univ. of Illinois, Urbana*
Junzo Chihara *JAERI*
Claude Deutsch *Universite de Paris XI*
Hugh DeWitt *Lawrence Livermore Labs.*
Dan Dubin *Univ. of California, San Diego*
James Dufty *University of Florida*
Werner Ebeling *Humboldt University*
Michael E. Fisher *University of Maryland*
Vladimir Fortov *IVTAN*
Kenneth Golden *University of Vermont*
Satoshi Hamaguchi *IBM*
Jean-Pierre Hansen *Ecole Normale Sup Lyon*
Friedrich Hensel *Philipps-Univ. Marburg*
William B. Hubbard *University of Arizona*
Bernard Jancovici *Univ. de Paris*
Gabor J. Kalman *Boston College*
Walter Kohn *Univ. of Calif., Santa Barbara*
Wolf D. Kraeft *Ernst-Moritz-Arndt Univ.*
Dietrich Kremp *Universitaet Rostock*
Norman March *Oxford University*
David Neilson *Univ. of New South Wales*
Guenri Norman *Moscow Physical Society*
Thomas O'Neil *Univ. of Calif., San Diego*
Rajeev K. Pathak *University of Pune*
Gerd Röpke *Universitaet Rostock*
Yasha Rosenfeld *Nuclear Res. Ctr.-Negev*
Gaetano Senatore *Univ. di Trieste*
Mario Tosi *SNS Studi Teoric*
Hiroo Totsuji *Okayama University*
Hugh M. Van Horn *University of Rochester*

This page intentionally left blank

PREFACE

The International Conference on Strongly Coupled Coulomb Systems was held on the campus of Boston College in Newton, Massachusetts, August 3–10, 1997.

Although this conference was the first under a new name, it was the continuation of a series of international meetings on strongly coupled plasmas and other Coulomb systems that started with the NATO Summer Institute on Strongly Coupled Plasmas, almost exactly twenty years prior to this conference, in July of 1977 in Orleans la Source, France. Over the intervening period the field of strongly coupled plasmas has developed vigorously. In the 1977 meeting the emphasis was on computer (Monte Carlo and molecular dynamics) simulations which provided, for the first time, insight into the rich and new physics of strongly coupled fully ionized plasmas. While theorists scrambled to provide a theoretical underpinning for these results, there was also a dearth of real experimental input to reinforce the computer simulations. Over the past few years this situation has changed drastically and a variety of direct experiments on classical, pure, strongly correlated plasma systems (charged particle traps, dusty plasmas, electrons on the surface of liquid helium, etc.) have become available. Even more importantly, entire new area of experimental interest in condensed matter physics have opened up through developments in nano-technology and the fabrication of low-dimensional systems, where the physical behavior, in many ways, is similar to that in classical plasmas.

Strongly coupled plasma physics has always been an interdisciplinary activity. In fact its roots are in the study of simple condensed matter systems, such as solid and liquid metals, electrolytes, molten salts, etc. The recent burst of activity in the field of dusty plasmas has reinforced the link with charged colloidal systems. Astrophysics has always been the field with some of the most important applications of the theory of strongly coupled plasmas. It is in recognition of this interdisciplinary character of the field that the International Advisory Board decided to change the name of the conference series from “International Conference on Strongly Coupled Plasmas” to “International Conference on Strongly Coupled Coulomb Systems.”

There were 156 participants attending the conference, presenting papers out of which there were 18 Invited Review Papers and 53 Invited Topical Talks, covering a substantial number of different areas. Some of the pioneers who were present 20 years ago and were so instrumental in developing the field into a new discipline were not with us anymore. Eugene Gross was a pioneer not only in strongly coupled plasmas, but in the entire field of plasma physics and became a staunch advocate of maintaining the dialogue between the plasma physics and condensed matter communities. John Malmberg was one of the few visionaries who realized the feasibility of creating strongly coupled plasmas in the laboratory. Kundan Singwi’s name is linked with the STLS approximation, that started out as an approach for the electron gas in metals and has grown into a tremendously successful method in many areas.

There were three sessions during the conference devoted to these colleagues' memory. This volume is dedicated as a further tribute to them and to their work.

This conference would not have been possible without the generous financial support of a large number of government agencies. Thanks are due to AFGL, AFOSR, DOE, NASA, NSF, and ONR for recognizing and supporting the many ramifications of the works presented at the conference. The host institution, Boston College, graciously provided space, facilities, technical support, and manpower without which the conference could not have taken place. Special thanks are due to the offices of the Academic Vice President, of the Dean of the Graduate School, of the Dean of the College of Arts and Sciences, and of the Chair of the Department of Physics for support, financial and otherwise. Out of the many people who were exceptionally helpful, the Organizing Committee is especially indebted to Joan Drane, Shirley Lynch, Giulio Gambarota, and Paul Emery of the Department of Physics and to Ellen MacDonald of the Bureau of Conferences.

The composition of the newly constituted and expanded International Advisory Board also reflects the complementary roles of the various disciplines in the field of strongly coupled Coulomb systems. The roster of the membership of the Board and also of the Organizing Committee appears on the page vii—these are the individuals who are ultimately responsible for the success of the conference.

Gabor J. Kalman
J. Martin Rommel
Krastan Blagoev

CONTENTS

REVIEW PAPERS

Equation of State for Binary Ionic Plasmas, Fluid and Solid Physics	1
H. E. DeWitt and W. L. Slattery	
Density Functional Theory in 1997	9
W. Kohn	
Equation of State of Partially-Ionized Plasmas	15
F. J. Rogers	
Metallization of Fluid Hydrogen at 140 GPa (1.4 Mbar)	25
W. J. Nellis, S. T. Weir, and A. C. Mitchell	
Electrolyte Criticality and Generalized Debye–Hückel Theory	33
M. E. Fisher, B. P. Lee, and S. Bekiranov	
Ordering in Classical Coulombic Systems	43
J. P. Schiffer	
Electron Correlations in Coulomb Systems in 2 and 3 Dimensions	49
A. K. Rajagopal	
Collective Excitations in a Quark–Gluon Plasma	65
M. Le Bellac	
Hohlraum Targets Driven by Cluster Ion Beams for Inertial Confinement Fusion	73
C. Deutsch, N. A. Tahir, O. Geb, and J. A. Maruhn	
Dense Hydrogen at High and Low Temperatures	81
N. W. Ashcroft	
Kinetic Theory of Ionization and Recombination Rates for Dense Quantum Plasmas	95
M. Schlanges and Th. Bornath	
Response Functions for Electron–Ion Strongly Coupled Plasmas	103
G. E. Norman and A. A. Valuev	
Fluctuations in Multicomponent Systems	117
J. L. Lebowitz	

IONIC LIQUIDS

Investigations of Condensed Matter by Inelastic X-Ray Scattering with High Energy Resolution	123
E. Burkel, Ch. Halcoussis, and H. Sinn	
Rubidium from a Liquid Metal to a Plasma	129
J. Chihara and G. Kahl	
Anomalous Phase Diagram in Simplest Plasma Model	135
I. L. Iosilevski and A. Yu. Chigvintsev	
Thermodynamic Properties of the Mixture He–Hg at High Temperatures and Pressures	139
E. Marceca and F. Hensel	
The Atomic–Molecular Transition in Expanded Liquid Rubidium	143
W. C. Pilgrim, M. Ross, L. H. Yang, and F. Hensel	
Ionic Model for Liquid Uranium Dioxide	147
V. K. Gryaznov, I. L. Iosilevski, E. S. Yakub, V. E. Fortov, G. J. Hyland, and C. Ronchi	

MULTICOMPONENT AND ASTROPHYSICAL PLASMAS

Thermodynamic and Structural Properties of Strongly Coupled Plasma Mixtures from the Perturbative HNC Equation	153
H. S. Kang and F. H. Ree	
Statistical Mechanics of Highly Charged Ions in NLTE Plasmas	159
A. Mirone, G. Faussurier, F. Gilleron, and J. Gauthier	
Advances in the Calculation of Virial Expansions for Quantum Plasmas up to Third Order in the Density	165
T. Kahlbaum	

DUSTY PLASMAS

Unified Kinetic Theory for Fluid and Crystal Phases	171
J. W. Dufty and S. P. Das	
Dust Crystals in Plasmas	175
S. Hamaguchi	
Dust Dynamics in Planetary Magnetospheres	179
M. Horányi	
Collective Processes in Strongly Coupled Dusty Plasmas	183
M. Rosenberg	
Lattice Waves in Plasma Crystals	187
H. M. Thomas, J. R. Jokipii, G. E. Morfill, and M. Zuzic	
Structural Transitions in Confined Yukawa System as a Model of Dusty Plasmas and Charge Stabilized Colloidal Suspensions	193
H. Totsuji, T. Kishimoto, and C. Totsuji	

Numerical Simulation of Gravitoelectrodynamics in Dusty Plasmas	199
L. S. Matthews and T. W. Hyde	
Relaxation of Dusty Plasmas	203
Yu. I. Chutov, O. Yu. Kravchenko, R. D. Smirnov, and P. P. J. M. Schram	
Transition from 3-Dimensional Coulomb Crystals to a 2-Dimensional One in a Dusty Plasma	207
Y. Hayashi	
Collective Modes in Strongly Coupled Dusty Plasmas	211
P. K. Kaw and A. Sen	
Expanding Plasma Layers with Dust Particles	215
Yu. I. Chutov, O. Yu. Kravchenko, P. P. J. M. Schram, and V. S. Yakovetsky	
Non-Linear Sheaths with Dust Particles	221
Yu. I. Chutov, O. Yu. Kravchenko, and V. S. Yakovetsky	
From Cold Dusty Plasmas to Hot Microplasmas X-Ray Dust	225
Yu. K. Kurilenkov, M. Skowronek, G. Louvet, and P. Romeas	
On the Lower Limit of Spoke Particle Radii	231
L. A. Bringol-Barge and T. W. Hyde	
MD Simulations of Dusty Plasma Crystal Formation: Preliminary Results	237
J. E. Hammerberg, B. L. Holian, G. Lapenta, M. S. Murillo, W. R. Shanahan, and D. Winske	
Heating and Melting of the Dust Crystal in RF Discharge: Non-Linear Analysis	241
I. V. Schweigert, V. A. Schweigert, A. Melzer, A. Homann, and A. Piel	
Determination of the Effective and Bare Charges in Dusty Plasmas	247
E. A. Allahyarova, P. P. J. M. Schram, and S. A. Trigger	

WHITE DWARFS

Crystallizing White Dwarfs	251
J. Isern, E. García-Berro, M. Hernanz, and R. Mochkovitch	
The Dynamic Effect in the Screening of Nuclear Reactions of Stellar Plasmas	255
G. Shaviv and N. J. Shaviv	
Effect of Dynamical Screening of Charged Particles in Maxwellian Plasmas on Criterion of Plasma Non-Ideality	261
V. P. Krainov, V. A. Rantsev-Kartinov, and E. E. Trofimovich	
The Effects of Exchange and Correlation for Astrophysical Quantities	265
W. Stolzmann and T. Blöcker	

DENSITY FUNCTIONAL THEORY

DFT Calculations for Compressed Aluminum: (I) K-Edge Spectra of Al from Solid to Liquid to Plasma; (II) Energy Relaxation in a Two-Temperature Al-Plasma . . .	271
M. W. C. Dharma-Wardana	
Ensemble Density Functional Approach to Inhomogeneous Quantum Hall Systems . . .	277
O. Heinonen	
Local and Semi-Local Density Functional Approximations for Exchange and Correlation: Why Do They Work, and Do They Work Best at Zero Temperature?	281
J. P. Perdew and S. Kurth	
The Average Atom Model and the Density Functional Theory Using Functional Integrals	287
G. Faussurier	
Density Functional Theory for Strictly Correlated Electrons: An Exact Functional for Spherically Symmetric Two-Electron Systems	293
M. Seidl	

EQUATION OF STATE

Equation of State of Shock Compressed Plasma of Metals	297
V. E. Fortov, V. K. Gryaznov, I. L. Iosilevski, R. F. Trunin, M. V. Zhemokletov, G. Simakov, and L. Trusov	
Disordered Systems with a Virtual Atomic Structure	303
A. A. Likalter	
Dimensional Cross-Over, Close-Packed Configurations, Symmetry Breaking, and Freezing in Density Functional Theory	307
Y. Rosenfeld	
Electrical Conductivity of Dense Copper Plasmas	313
A. W. DeSilva and J. D. Katsouras	
Measuring the EOS of a Dense, Strongly Coupled Plasma: Description of the Technique	319
J. F. Benage, Jr., G. Kyrala, J. Workman, and T. Tierney, IV	
Fission-Fragment Induced Damage of Surfaces: A Quasiclassical Trajectory Calculation	323
K. J. LaGattuta	
The Sun: Strong Constraints on a Weakly-Coupled Plasma	327
W. Däppen and A. Nayfonov	

HYDROGEN

Molecular Dynamics Modeling of Dense Hydrogen	331
J. Kress, L. Collins, T. Lenosky, I. Kwon, and N. Troullier	

Restricted Path Integral Monte Carlo Calculations of Hot, Dense Hydrogen	337
W. R. Magro, B. Militzer, D. M. Ceperley, B. Bernu, and C. Pierleoni	
Wave-Packet Molecular Dynamics Simulation of Hydrogen	341
M. Knaup, D. Klakow, P.-G. Reinhard, and C. Toepffer	
Scattering Cross Sections and Conductivity of Strongly Coupled Hydrogen Plasma . .	347
Kh. T. Nurekenov, F. B. Baimbetov, G. L. Gabdullina, R. Redmer, and G. Röpke	
Monte Carlo Simulation of the Equilibrium Properties of a Strongly Coupled Hydrogen Plasma	353
F. B. Baimbetov, M. A. Bekenov, T. S. Ramazanov, and N. N. Izteleuov	
Fermionic Path Integral Simulation of Dense Hydrogen	357
B. Militzer, W. Magro, and D. Ceperley	
Correlation Functions and the Equation of State of a Strongly Coupled Hydrogen Plasma in HNC Approximation	361
T. S. Ramazanov, N. F. Baimbetov, M. A. Bekenov, R. Redmer, and G. Röpke	
Equation of State and Metal–Nonmetal Transition in Dense Hydrogen Fluid	365
A. Bunker, S. Nagel, R. Redmer, and G. Röpke	
The Dense Hydrogen Plasma: A Comparison between Models	369
J. Clerouin	

SPECTROSCOPY

MD Redistribution Functions of Resonance Radiation in Hot Dense Plasmas	373
A. V. Demura, A. E. Bulyshev, V. S. Lisitsa, A. N. Starostin, A. E. Suvorov, and I.I. Yakunin	
On Plasma Statistics of Microfield Gradients and Line Asymmetries	377
A. V. Demura, D. Gilles, and C. Stehlé	
The Correlation Effect in Spectra of Dense Hydrogen Plasma	381
T. V. Gavrilova, V. P. Averyanov, Y. Vitel, C. Le Guen, L. G. D'yachkov, and Yu. K. Kurilenkov	
Plasma Induced Line Shifts: New Light on an Old Controversy	385
C. F. Hooper, Jr., G. C. Junkel, M. A. Gunderson, D. A. Haynes, Jr., R. C. Mancini, D. Bradley, J. Delettrez, and P. Jaanimagi	
Redistribution Functions of Helium-Like Multicharged Ions in Model Microfield Method	391
A. V. Demura, N. Feautrier, I. N. Kosarev, V. S. Lisitsa, and C. Stehlé	

ELECTROLYTES, COLLOIDAL SUSPENSION

Sticky Charged Spheres in the Mean Spherical Approximation: A Model for Flexible Polyelectrolytes	395
O. Bernard and L. Blum	

Electronic Properties and Mechanism of Superionic Conductivity in Solid Electrolytes	399
H. Kikuchi, H. Iyetomi, and A. Hasegawa	
Polarization of Counterions in a Strongly Coupled Coulombic System: DNA	405
U. Mohanty	
Theory of Colloidal Plasmas	409
P. P. J. M. Schram and S. A. Trigger	
Critique of Electrolyte Theories Using Thermodynamic Bounds	415
M. E. Fisher, D. M. Zuckerman, and B. P. Lee	
Instability of Front Edge of Non-Newtonian Suspension Film	419
S. M. Baturin, G. A. Pavlov, and A. A. Shiryayev	

CHARGED PARTICLE TRAPS, NON-NEUTRAL PLASMAS

Anomalously Low Temperature in Electron Cooled Heavy Ion Beams	423
B. Franzke, K. Beckert, F. Nolden, M. Steck, and T. Winkler	
Formation and Control of Coulomb Crystals in Trapped Ion Plasmas	429
X.-P. Huang, J. J. Bollinger, W. M. Itano, J. N. Tan, B. Jelenković, T. B. Mitchell, and D. J. Wineland	

ELECTRON LIQUID

Quasi-Classical Theory and Simulation of Two-Component Plasmas	433
W. Ebeling, B. Militzer, and F. Schautz	
Screened Interaction Potential and Bound States between Two Negative Charged Particles in the Three- and Two-Dimensional Electron Gas	439
A. Ghazali and A. Gold	
Dynamic Properties of an Electron Gas at $r_s = 3.5$ and $k \gg k_F$ and Application to Deep Inelastic Scattering	445
M. H. Lee, J. Hong, and J. Kim	
Rigorous Bounds to Coulomb Energy Functionals I: Atom-Positron Bound States	449
R. K. Pathak	
Crossover from the Degenerate to the Classical Regime of a Strongly Interacting 2D Hole Layer	455
S. Shapira, U. Sivan, P. M. Solomon, E. Buchstab, M. Tischler, and G. Ben Yoseph	
Exchange-Correlation Potentials in the Electron Gas	461
S. Conti, R. Nifosí, and M. P. Tosi	
Wigner Approach and Generalization Molecular Dynamics Method in Quantum Theory of Strongly Coupled Systems of Particles	467
V. Filinov, Yu. Lozovik, A. Filinov, and I. Zacharov	
Equilibrium Properties of Weakly Coupled Magnetized Plasmas	473
M. Steinberg, J. Ortner, and W. Ebeling	

Modeling of the Electronic Static Local Field Correction	479
I. M. Tkachenko, P. F. de Córdoba, and J. M. Belda	

QUANTUM DOTS, HUBBARD MODEL, SEMICONDUCTOR PLASMAS

Quantum Melting on a Lattice and a Delocalization Transition	483
E. V. Tsiper and A. L. Efros	
Interacting Electrons in Strong Magnetic Fields: A Genuine Example of a Two-Dimensional Non-Fermi-Liquid	487
D. V. Khveshchenko	
Transport through Low Density Quantum Dots	493
R. Berkovits	
Electronic Correlations in Semiconductor Quantum Dots	497
P. Hawrylak	
Collective vs. Individual Dot Response of Quantum Dot Ensembles	503
P. Bakshi and K. Kempa	
Optical Studies of Individual InAs Quantum Dots	509
L. Landin, M. S. Miller, M.-E. Pistol, C. E. Pryor, and L. Samuelson	
Ultrafast Relaxation in Strongly Coupled Coulomb Systems	515
M. Bonitz, N.-H. Kwong, D. Semkat, and D. Kremp	

BILAYERS

Coulomb Drag Measurements of a Double Quantum Well	519
J. T. Nicholls, N. P. R. Hill, E. H. Linfield, M. Pepper, and D. A. Ritchie	
Classical Atomic Bilayers	523
F. M. Peeters, B. Partoens, V. A. Schweigert, and I. V. Schweigert	
Recent Progress on the Phase Diagram of Coupled Electron Layers in Zero Magnetic Field	529
F. Rapisarda and G. Senatore	
Structure and Dynamics of Electronic Bilayer Liquids	533
V. Valtchinov, G. J. Kalman, and K. Golden	

FUSION PLASMAS

Kinetic Approach to the Stopping Power of Dense Plasmas	539
D. O. Gericke, M. Schlanges, and W.-D. Kraeft	
Distribution Function of Charged Particles in a Plasma of Fusion Interest	543
C. Cereceda, M. de Peretti, and M. Sabatier	

DENSE PLASMAS

On Absorbing Power of Dense Plasmas at Weak and Strong Coupling	547
Yu. K. Kurilenkov, G. Maynard, and J. Dufty	

On the Dependence of Continuum Factors on Plasma Parameters	551
M. M. Popović and D. Djordjević	
Observations of the Charged Particle Dynamic Screening Effects and the Plasma Phase Transition in Hot Z-Pinch Plasma	555
V. A. Rantsev-Kartinov and E. E. Trofimovich	
Electrical Conductivity of Strongly Coupled Model and Real Plasmas	561
I. M. Tkachenko and P. F. de Córdoba	
Properties of Strongly Coupled Microplasmas: Experimental Investigations	565
N. Vogel	
Comparison of Collisional and Radiative Plasma Kinetics Model (CRM) and Average Ion Model (AIM) in Dense Plasma	569
P. D. Gasparian, S. A. Belkov, Yu. K. Kotchubey, E. T. Mitrofanov, and V. I. Roslov	
Self-Organization Phenomena in Dense Plasma Focus Experiments	575
A. B. Kukushkin, V. A. Rantsev-Kartinov, and A. R. Terentiev	
Theory of Thermoelectric Field in LTE Plasmas	579
V. P. Krainov, V. A. Rantsev-Kartinov, and E. E. Trofimovich	
Modeling of Strong Discharges in Water	583
I. M. Tkachenko, A. W. DeSilva, and J. L. Iserte	
WEAKLY COUPLED PLASMAS	
Kinetic Equation for Nonideal Spatially Inhomogeneous Plasmas	587
V. V. Belyi, Yu. A. Kukharenko, and J. Wallenborn	
Velocity-Space Drag and Diffusion in Model, Two-Dimensional Plasma	591
M. A. Reynolds, B. D. Fried, and G. J. Morales	
Pair Correlation Function and Nonlinear Kinetic Equation for a Spatially Uniform Polarizable Nonideal Plasma	597
V. V. Belyi, Yu. A. Kukharenko, and J. Wallenborn	
IONIZATION AND BOUND STATES	
Bound States in Strongly Coupled Plasmas	601
D. Kremp, W.-D. Kraeft, and M. Schlanges	
Relevant Ion Time Scales for Electron Impact Processes of Atoms in Dense Plasmas	607
M. S. Murillo	
Stochastic Simulation of Ionization Fronts in Nonideal Plasma	613
D. Beule and A. Förster	
Spectral Properties of Dense Plasmas	617
R. Fehr and W.-D. Kraeft	
Highly Charged Ions in Polyethylene Capillary Discharge Plasma	623
A. Förster, D. Beule, H. Conrads, and W. Ebeling	

Adiabatic Equation of State and Ionization Equilibrium in Strongly Coupled Plasma	629
D. Beule, W. Ebeling, and A. Förster	
Eikonal Cross Section for Elastic Electron–Ion Scattering in Strongly Coupled Plasma	633
Y.-D. Jung and J.-S. Yoon	
Vanishing of Higher Excited Bound States without Lowering of Ionization Potentials in Partially Ionized Strongly Coupled Plasmas	639
A. S. Kaklyugin and G. E. Norman	
Ionization Kinetics in a Dense Carbon Plasma	643
R. Prenzel, T. Bornath, and M. Schlanges	
Nonexponential Temperature Dependence of Reaction Rates in Nonideal Plasmas	647
A. N. Starostin and N. L. Aleksandrov	

RESPONSE FUNCTIONS

Formation of Binary Correlations in Plasma	651
K. Morawetz, V. Spička, and P. Lipavský	
Quadratic Response Solutions for Different Nonlinear Approaches of Static Screening: A Comparative Study	657
I. Nagy, A. Bergara, and P. M. Echenique	
Investigation of the Dynamic Properties of the Electron Gas by Quasi-Classical Simulations	663
J. Ortner, F. Schautz, and W. Ebeling	
The Quadratic Susceptibility in One, Two, and Three Dimensions	669
J. M. Rommel, G. J. Kalman, and R. Genga	
Thermodynamic Functions of Strongly Coupled Plasmas: Local Field Effects	673
W. Stolzmann and M. Rösler	
Dielectric Function and Transport Coefficients in Strongly Coupled Plasmas	679
G. Röpke	
Optical Characteristics of Strongly Coupled Coulomb Systems	683
G. A. Pavlov	
Statistics of Quantum-Electrodynamic Plasmas in External Magnetic Fields	687
L. G. Suttorp	
Extra Loop in Plasmon Dispersion for Strongly Coupled Coulomb Liquids	691
D. Lu	
Effective Transport Coefficients in Low Temperature Multicomponent Plasma	695
G. A. Pavlov	
Electromagnetic Modes in Cold Magnetized Strongly Coupled Plasmas	699
J. Ortner, V. M. Rylyuk, and I. M. Tkachenko	

STATISTICAL PHYSICS

Algebraic Screening and van der Waals Forces in Partially Ionized Gases	705
A. Alastuey, F. Cornu, and P. A. Martin	
Two-Dimensional Logarithmic Interaction on Curved Surfaces	709
B. Jancovici	
A Monte Carlo Finite Size Scaling Study of Charged Hard Sphere Criticality	713
J. M. Caillol, D. Levesque, and J. J. Weis	
Thermal Photonic Screening in a Weakly Relativistic Plasma	717
W. Appel and A. Alastuey	
List of Participants	721
Author Index	725
Subject Index	729

EQUATION OF STATE FOR BINARY IONIC PLASMAS, FLUID AND SOLID PHASES

Hugh E. DeWitt¹ and Wayne L. Slattery²

¹Lawrence Livermore National Laboratory,
Livermore, CA 94551

²Los Alamos National Laboratory,
Los Alamos, NM 87545

This paper gives a summary of the most recent Monte Carlo simulation data for the internal energy, U/NkT , for the the One Component Plasma (OCP) and Binary Ionic Mixtures (HIM) for both fluid and solid phases. The Monte Carlo results are compared with Molecular Dynamics results of nearly the same accuracy. The OCP fluid and solid data are used to give the most accurate available equation of state for both the fluid and the crystalline (bcc) phases of the OCP. For the BIM mixture with 5% charge 2. and 95% charge 1. the deviations from linear mixing are given to the best available accuracy. These results make it possible to obtain the classical contribution to the screening enhancement of thermonuclear reaction rates for white dwarf stars. Current results on deviations from linear mixing are also given for random ionic mixtures for which the two different charges are placed randomly on bcc lattice sites. It is found that the deviation from linear mixing in the crystalline solid is roughly an order of magnitude larger than deviations from linear mixing for BIM fluids. The data supports the conclusion that the phase diagram for a BIM mixture is spindle shaped for carbon and oxygen mixtures found in white dwarf stars.

INTRODUCTION

Numerical simulations of strongly coupled plasmas during the past 30 years using Monte Carlo methods (MC) and Molecular Dynamics (MD) methods have given detailed and accurate results for the equation of state of classical point ions immersed in a rigid uniform neutralizing background. With only one component this mathematical model, the One Component Plasma (OCP), has played a role in strongly coupled plasmas similar to that of the hard sphere system for understanding neutral liquids and solids. With two different charged ions, Z_1 and Z_2 , we will refer to the system as the Binary Ionic Mixture (BIM). This model has extensive uses in the description of very high density matter (10^6 --- 10^9 gm/cc) as found in white dwarf stars and at the still higher densities found in neutron stars. In this extreme situation found in white dwarf interiors the degenerate electrons form the nearly rigid neutralizing background and give the positive pressure that holds the object to a finite size. The deep interior of a white dwarf has Coulombic correlations that are so strong that the ions crystallize in spite of the high temperature, and outside the freezing front there is a strongly coupled Coulomb fluid of ions. The electron Fermi energy is so much larger than

the temperature that the electrons and ions are nearly decoupled. This situation approaches the model BIM with its assumed rigid background.

MC and MD simulations give basically the Coulombic interaction energy of the ions, U/NkT and the ion-ion pair distribution function. One also obtains the Helmholtz free energy, the heat capacity, and the screening function that influences the rate of thermonuclear reactions. The knowledge of the free energies of the fluid and solid phases makes possible the determination of the freezing conditions for the OCP and BIM. Also when the phase diagram of the BIM is sufficiently well known it will be possible to determine the degree of separation of different elements during the freezing process. These processes seriously affect the evolution of white dwarfs over a time of several billion years, and provide motivation for the current work.

The Coulomb crystallization process is also observed in terrestrial laboratories. At NIST in Boulder, CO a cloud of roughly one quarter million Be^+ ions in a Penning trap and cooled by laser cooling to milli kelvins, have been observed to go into the anticipated bcc lattice¹. This experiment opens up the possibility of laboratory studies of Coulomb crystallization. At Livermore in the EBIT program Be^+ and Xe^{+44} are being trapped together so that this and other ionic mixtures can be studied.

The computer simulations require access to very fast computers and a lot of time on them. Both MC and MD use periodic boundary conditions so that the number of particles in the basic cell is conserved. Because of the long range of the Coulomb potential, $1/r$, it is also necessary to replicate the N charges in a 3D cell in every direction to infinity and calculate the Ewald potential^{2,3}. Also to obtain sufficient accuracy one must estimate the N dependence of the simulations, typically $O(1/N)$. With $N \sim 1000$ it is now possible to obtain results for U/NkT to an accuracy of at least one part in 10^5 and perhaps even 10^6 . This kind of accuracy is absolutely necessary in order to define the location of the freezing transition and to obtain the phase diagram of ionic mixtures.

OCP FLUID AND SOLID

The OCP has been extensively studied by MC for three decades and by MD in recent years. The system is conceptually simple since there is only one dimensionless parameter, $\Gamma = (Ze)^2/akT$ with $a = ((4\pi/3)N/V)^{-1/3}$, so that the internal energy is a function of only this quantity; thus $U/NkT = u(\Gamma)$. Since this internal energy is the sum of all pairwise Coulomb interactions of point charges moving in the assumed rigid uniform background, this energy is always negative. The pressure contribution from the Coulomb interactions is given exactly by the virial theorem, and thus is $(1/3)u(\Gamma)$. In a real physical system this negative pressure must be balanced by the positive pressure from the kinetic energy of the ions and the large positive pressure of degenerate electrons as in white dwarf stars. For $\Gamma < .1$ the system is *weakly* coupled and the thermodynamic functions are given by Debye-Huckel theory. For the range $.1 < \Gamma < 1$, the system is in *intermediate* coupling, and quantitatively the thermodynamic functions are given accurately by the Hyper-Netted Chain (HNC) equation. The *strongly* coupled region starts at $\Gamma=1$, and the strongly coupled Coulomb fluid is in the range $1 < \Gamma < 172$ where 172 is the current estimate of the phase transition from fluid to the bcc lattice. Although the HNC equation continues to be remarkably good for Γ much larger than 1, it does fail in accuracy because of the neglect of bridge function^{4,5}. The earlier MC studies of Hansen and Pollock^{2,3} used $N = 128$ and 250 particles and the energies were obtained by averaging over a few million configurations. Later work⁶ increased N up to 686 and energies were obtained by averaging over a few tens of million

configurations. The most accurate currently available results are obtained with $N = 1000$ and averages over a few hundred million configurations⁷.

The strongly coupled MC data for the fluid $u(\Gamma)$ has been fitted to a variety of forms of which the following has proved to be very convenient:

$$u(\Gamma) = a\Gamma + b\Gamma^s + c \quad (1)$$

so that $a, b, c,$ and s are fitting parameters. The value of a which is often referred to as the fluid Madelung constant turns out to be close to $a = -9/10$, and s is close to $1/3$. For the solid phase data for the bcc lattice the basic form is:

$$\begin{aligned} u(\Gamma) &= (U_o + U_{\text{thermal}}) \\ &= a_M\Gamma + 3/2 + A_1/\Gamma + A_2/\Gamma^2 + \dots \end{aligned} \quad (2)$$

where $a_M = -0.859929$ for the bcc lattice and -0.895873 for fcc. The first order anharmonic term has been evaluated exactly using lattice dynamics by Dubin⁷; he obtained $A_1 = 10.84$ for bcc and 12.35 for fcc. A_2 can be found only from sufficiently accurate MC data for the bcc lattice; Dubin's estimate is about 350 . U_o is the static lattice energy, and U_{thermal} is the thermal energy due to lattice vibrations.

The current 'best' fit to the most accurate available 13 MC data point for the OCP fluid are:

$$\begin{aligned} a &= -0.899147 \\ b &= 0.604455 \\ c &= -0.277175 \\ s &= 0.322232 \\ \sigma &= 0.000488 \end{aligned}$$

Note that the value of the fluid Madelung constant, a , less than a_M by $\delta a = a - a_M = -0.003218$. All reasonable fitting functions to the OCP MC data indicate that the value of a is closer to $-9/10$ than to a_M . Rosenfeld⁸ has shown that the asymptotic form of $u(\Gamma)$ from the HNC equation is $-(9/10)\Gamma + B\Gamma^{1/2}$. The lower power of the exponent in the thermal energy of the fluid OCP that is found from the MC data is evidently due to the bridge function. DeWitt and Rosenfeld⁹ using a variational hard sphere approach and the Percus-Yevick hard sphere virial entropy obtained $s = 1/4$. The same approach using the compressibility PY entropy¹⁰ gives $s = 2/5$. The MC fluid data suggest that the thermal energy is dominated by a power law with an exponent s somewhere between $.3$ and $.4$. It should be emphasized, however, that there is no fundamental theory yet for the fluids governed by the $1/r$ potential or other inverse power potentials, $1/r^n$. Thus Eq. 1 should be viewed as only a fitting function.

The MC fluid simulations are done from a random start of the N charges; this corresponds to correlations of $\Gamma = \infty$. The system equilibrates after a few million configurations. If one uses a random start for values of Γ in the solid region, then after equilibration the system will remain in a supercooled fluid state, but will eventually freeze¹¹ usually into an imperfect bcc lattice, but sometimes into a perfect lattice without defects. Freezing was observed with $N = 686$ from a random start for values of Γ ranging from 250 to 700 . One may also start the MC process with all the N charges on bcc lattice sites. When Γ is in the solid region the MC process creates the thermal energy of lattice vibrations as indicated by Eq. 2. However, if Γ is in the fluid region, then the lattice will be superheated and eventually melt. The superheated lattice is reasonably stable in the range from $\Gamma = 145$

to 170. One does not ever see a coexisting two phase region, namely fluid and solid together.

To locate the transition value of Γ the procedure outlined by Pollock and Hansen³ is to find the value where the fluid and solid Helmholtz free energies cross. The fluid Helmholtz free energy is the sum of the ideal gas form (for the ions) plus the temperature integration of Eq. 1 from infinity down to T , which is straightforward with a simple fitting function like Eq. 1. For the solid Helmholtz free energy one integrates from $T = 0$ to T , and takes into account the entropy constant for the OCP obtained by Dubin⁹. The Helmholtz free energy lines do cross, but they are so nearly parallel, that a very small change in the constants in either Eq. 1 or 2 will give a widely different result. Consequently the estimated values of the crossing point have varied from 173 in 1973³ to 178 in the '80's⁶ as the accuracy of the fluid data increased. When Dubin⁹ in 1990 obtained a non-zero value for the coefficient of A_1 for the first anharmonic term in Eq. 2,

the estimate decreased slightly to $\Gamma = 172$. It should be noted that the OCP fluid-lattice transition is not a usual first order phase transition because the volume change is decreed by the model to be zero. There is, however, a change of the internal energy and a change in entropy. A striking feature of phase transition is that the fluid thermal energy at the transition is about 50% larger than the bcc thermal energy. Also the thermal energies of the two states of the OCP at the transition are only one to two percent of the Madelung energy; this fact again shows why great accuracy is required to understand the properties of the OCP.

Farouki and Hamaguchi¹² have done MD simulations of the OCP, also with $N = 1000$, and have essentially reproduced the MC results. In the MD process both the kinetic and the potential energy are computed at the same time by integrating Newton's equations of motion for the N particles. The temperature is defined by the sum of the kinetic energies of the particles and consequently it fluctuates a bit as the equations of motion are time stepped forward. The temperature is rescaled periodically to give a desired value of Γ . In spite of this slight difficulty the MD results are remarkably close. Thus at $\Gamma = 160$ MD gives $u(\Gamma) = -141.036 \pm 0.002$ and MC gives -141.0396 ± 0.00071 . MC may be slightly more accurate when the computer is run longer, but for practical purposes the two simulation methods give the same results for the OCP in both fluid and solid phases.

Likos and Ashcroft¹³ have applied a modified form of density functional theory to the freezing of the OCP taking into account the special feature that $\Delta V = 0$. They obtain the transition at $\Gamma = 176$ for the bcc lattice in good agreement with the result obtained by crossing of free energies. Quantum effects (uncertainty principle) become important even for the C and O ions in a white dwarf star¹⁴ when the thermal deBroglie wavelength is a significant fraction of the interparticle spacing. In the most massive white dwarf stars the freezing temperature is lowered by about 10% which increases the freezing gamma to over 200. Quantum effects also significantly change the form of the thermal energy for the solid and the fluid phase as well. Jones and Ceperley¹⁵ using a quantum path integral Monte Carlo simulation have obtained an approximant phase diagram for the quantum OCP and results for the quantum fluid thermal energies.

BIM FLUID AND SOLID

For the binary ionic mixture MC simulations with $N = N_1 + N_2$ ions of charge Z_1 and Z_2 we need a few extra quantities to specify the system. The neutralizing background is rigid as with the OCP, but the equivalent number of electrons is $N_e = Z_1 N_1 + Z_2 N_2$. The chemical compositions are indicated by:

$$x_1 = N_1/(N_1 + N_2), \quad x_2 = N_2/(N_1 + N_2) = 1 - x_1$$

and the appropriate coupling parameters are:

$$\Gamma_e = e^2/a_e kT, \quad a_e = ((4\pi/3)N_e/V)^{-1/3} \quad (3)$$

$$\Gamma_1 = Z_1^{5/3}\Gamma_e, \quad \Gamma_2 = Z_2^{5/3}\Gamma_e$$

The mixture internal energy is:

$$\begin{aligned} U_{\text{mix}}/NkT &= u_{\text{mix}}(\Gamma_e, Z_2/Z_1, x_2) \\ &= x_1 u_{\text{ocp}}(\Gamma_1) + x_2 u_{\text{ocp}}(\Gamma_2) + \Delta u \end{aligned} \quad (4)$$

where Eq. 4 indicates the linear mixing approximation with the characteristic weighting of ion charges to the 5/3 power. A similar expression gives the linear mixing form for the excess Helmholtz free energy. Δu and Δf refer to the deviations from linear mixing. Particularly for the BIM fluid the values of Δu are so small, typically as low as 0.003, that they nearly disappear into the noise of the MC simulations. Thus to obtain dependable values of Δu it is essential to do *three* MC runs for each mixture, one for the mixture itself and one OCP run for each value of Γ_1 and Γ_2 . Ogata, Iyetomi, Ichimaru, Van Horn¹⁶ (OIHV) did a very thorough study the BIM for both fluid and solid states with MC runs of 1000 charges and averages over a few tens of million configurations. Their solid results are sufficiently accurate, but their fluid BIM estimates of Δu were spuriously negative for small values of the second species of charge, i.e. $x_2 < .05$ as a consequence of using a slightly inaccurate fit for the OCP. DeWitt, Slattery, Chabrier¹⁷ (DSC) did simulations 20 to 50 times longer than the fluid runs of OIHV in order to reduce the MC error by roughly another order of magnitude. These runs were several hundred million configurations. The general conclusions from DSC are:

- i) Linear mixing models the BIM fluids extremely well, and mainly because the fluid Madelung term is confirmed to behave as $u_{0,\text{mix}} = \langle Z^{5/3} \rangle a \Gamma_e$ and $u_{\text{thermal,mix}} \ll u_{0,\text{mix}}$.
- ii) Δu is *always* positive, but small, namely in the range of +0.001 to +0.020
- iii) $\Delta u_{\text{fluid}}(\Gamma)$ is nearly constant for Γ less than about 10, and shows only a slight decrease for larger values of Γ . The $1/\Gamma$ behaviour suggested by OIHV is not indicated in the more accurate fluid data of DSC.

The following Table gives MC BIM fluid results for the mixture $Z_1 = 1, x_1 = .95, Z_2 = 2, x_2 = .05$.

Γ_1	u_{mix}	Δu
1.	- 0.65488 ± .00005	+ .00134 ± .00006
5.	- 4.22167 ± .00014	+ .00134 ± .00019
10.	- 8.94666 ± .00013	+ .00087 ± .00019
20.	- 18.59212 ± .00023	+ .00077 ± .00028
40.	- 38.12452 ± .00031	+ .00109 ± .00037
60.	- 57.77992 ± .00034	+ .00024 ± .00045
80.	- 77.49297 ± .00028	+ .00039 ± .00044
100.	- 97.24303 ± .00052	+ .00056 ± .00061

It should be clear from the size of the values for Δu and the associated error estimates that the determination of deviations from linear mixing is a difficult job. The fitting functions in OIIVH for Δu (their Eq. 12) and Δf (their Eq. 16) do not reproduce the more accurate data for these two quantities given in DSC. Particularly OIIVH have negative values of Δu and hence also for Δf for x_2 which are due to their slightly inaccurate fitting function for the OCP energy data. The size and sign of Δf has a significant effect on the phase diagram for BIM. Thus OIIVH have a tiny azeotropic section in their phase diagrams (their Fig. 7). The density functional estimates of the BIM phase diagrams obtained by Segretain and Chabrier¹⁸ are probably more reliable. They find that the phase diagram for a BIM in the range $1 < Z_2/Z_1 < 1.39$ is spindle shaped, for charged ratios up to 1.72, and greater than 1.72 it is a eutectic.

A BIM with an equal number of charges may have the lowest energy configuration as the CsCl configuration---two intertwined simple cubic lattices. However, in a solidifying white dwarf star which contains unequal numbers of ions of different charge as well as a distribution of higher Z elements, the probability of freezing into any kind of perfect lattice seems remote. More likely a random mixture solid is likely to be preferred. We have done some simulations on

random solid mixtures by placing the $N_1 + N_2 = 1024$ at random on bcc lattice sites at the start of MC runs. This initial state is not an equilibrium situation. As the MC simulation proceeds the larger Z ions push the lower Z ions away so that the random lattice at equilibrium is a distorted lattice. The simulation also sets up the thermal vibrations in the distorted lattice. The consequence is that the deviation from linear mixing for solid BIM is positive and far larger than it is for the relaxed BIM fluid. Typically the Madelung constant for the bcc lattice (-.895929) is larger for the random lattice by an amount roughly +.001 for equal numbers of C and O. The deviation from linear mixing of BIM random solids is dominated by this effect, thus $\Delta u(\Gamma) \cong \delta a_M \Gamma$ where $\delta a_M = a_M - a_{\text{random}}$. The solid mixture MC data of OIIVH for AUBIM agree moderately well with this result.

To summarize the linear mixing approximation is phenomenally accurate for BM fluids and the tiny observed positive deviations are at the level of a constant, not $O(\Gamma)$ or $O(\Gamma^2)$. By contrast the linear mixing approximation for randomly mixed solids is still positive but far larger than in the BIM fluid case. The work left to be done is to generate more BIM data of great accuracy for both fluid and solid phases so as to construct fitting functions for $\Delta u(\Gamma_e, Z_2/Z_1, x_2)$ and $\Delta f(\Gamma_e, Z_2/Z_1, x_2)$. With a sufficiently large data base it will be possible to construct fitting functions for Δf that can lead to more accurate phase diagrams. This project is difficult enough already at the stage of the OCP because the thermal energy of the fluid and solid is only one or two percent of the total energy, thus requiring great accuracy from long computer runs. For the BIM fluids and solids the computational problem is even worse because of the increased number of parameters ($\Gamma_e, Z_1, x_1, Z_2, x_2, \dots$). Also for the BIM random solids it is necessary to carry out several simulations with different random starts. This will be a computer intensive project for some years to come.

YUKAWA PLASMAS

A simple extension of the OCP is the system governed by the exponentially screened potential, the Yukawa potential, $u(r)/kT = (\Gamma/x)\exp(-\kappa x)$, where $x = r/a$ and $\kappa = a/\lambda$ with λ as screening length in units of a . This system is used to model the fluid and solid forms of charged colloidal crystals in electrolytic solutions. Crystals of bcc and fcc are commonly observed¹⁹ at sufficiently high values of Γ . The screening length is the Debye length for the electrolytic solution ions. There has been as much research on the Yukawa system as on the OCP, and too much to detail here. In 1994 Hamaguchi and Farouki²⁰ published

extensive MD results for $N = 1000$ Yukawa charges for the internal energy, $U/NkT = u(\Gamma, \kappa)$ for both fluid and solid phases. Their results for the internal energy are extensions in κ space of their earlier OCP results ($\kappa = 0$), and are correct. Their integration to obtain the excess Helmholtz free energy as functions of κ were inaccurate because of their approximation that the solid phase entropy constant for the bcc lattice had the same value as for the OCP. It was pointed out by Rosenfeld²¹, that this assumption was quantitatively in error and led to incorrect freezing conditions as a function of κ . Meijer and Frenkel²² had previously obtained estimates of the freezing conditions with fewer particles, $N = 250$, that are correct. The error in the entropy constant as a function of κ has recently been corrected by Hamaguchi, Farouki, and Dubin²³ and the freezing value of $\Gamma(\kappa)$ has been obtained; they give $\Gamma = 171.8$ at $\kappa = 0$ and $\Gamma = 217.4$ at $\kappa = 1.0$. More recently they have obtained an accurate result for the triple point for the bcc lattice, fcc lattice, and the fluid state²⁴. Yukawa plasma mixtures have been discussed by Rosenfeld²⁵ who gave an accurate non-linear mixing rule.

ACKNOWLEDGMENT

Work performed under the auspices of the US Dept. of Energy by the Lawrence Livermore National Laboratory under contract number W-7405-ENG-48.

REFERENCES

1. J.N. Tang, J.J. Bollinger, B. Jelenkovic, D.J. Wineland, Phys. Rev. Lett. 75, 4198 (1995)
2. J.P. Hansen, Phys. Rev.A8, 3096 (1973)
3. E.L. Pollock and J.P. Hansen, Phys.Rev. A8, 3110 (1973)
4. P.D. Poll, N.W. Ashcroft, H.E. DeWitt, Phys. Rev. A37, 1672 (1988)
5. Y. Rosenfeld and N.W. Ashcroft, Phys. Rev. A20, 1208 (1979)
6. G.S. Stringfellow, H.E. DeWitt, W.L. Slattery, Phys. Rev. A41, 1105 (1990)
7. D.H.Dubin, Phys. Rev. A42, 4972 (1990)
8. Y. Rosenfeld, Phys. Rev. 33, 2025 (1986)
9. H.E. DeWitt and Y. Rosenfeld, Phys. Lett. A75, 79 (1979)
10. T. Kahlbaum and H. E. DeWitt, Contrib. Plasma Phys. 33, 578 (1993)
11. H. E. DeWitt, W. L. Slattery, J. Yang, Strongly Coupled Plasma Physics, H.M. Van Horn and S. Ichimaru, eds., University of Rochester Press 1993, p.333
12. R. T. Farouki and S. Hamaguchi, Phys. Rev. E47, 4330 (1993).
13. C.N. Likos and N.W. Ashcroft, Phys. Rev. Lett. 69,316 (1992)
14. G. Chabrier, N.W. Ashcroft, H.E. DeWitt, Nature 360, 48, (1992)
15. M.D. Jones and D.M. Ceperley, Phys. Rev. Lett. 76, 4572 (1996)
16. S. Ogata, H. Iyetomi, S. Ichimaru, H.M. VanHorn, Phys.Rev.E48, 1344 (1997)
17. H. DeWitt, W. Slattery, G. Chabrier, Physics B 228, 21 (1996)
18. L. Segretain and G. Chabrier, Astron. Astrophys. 271, L13 (1993)
19. C. A. Murray and R. A. Wenk, Strongly Coupled Plasma Physics, H.M. Van Horn and S. Ichimaru eds., University of Rochester Press, Rochester, 1993
20. S. Hamaguchi and R. T. Farouki, J. Chem. Phys. 101, 9876 (1994)
21. Y. Rosenfeld, J. Chem. Phys. 103, 9800 (1995)
22. E.J. Meijer and D. Frenkel, J. Chem. Phys. 98, 2319 (1993)
23. S. Hamaguchi, R. T. Farouki, D.H.E. Dubin, J. Chem. Phys. 105, 7641, (1996)
24. S. Hamaguchi, R.T. Farouki, D.H.E. Dubin, to be published.
25. Y. Rosenfeld, Phys. Rev. E47, 2676, (1993)

This page intentionally left blank

DENSITY FUNCTIONAL THEORY IN 1997

W. Kohn

Department of Physics
University of California
Santa Barbara, CA
E-mail: kohn@physics.ucsb.edu

This paper offers a brief introduction to Density Functional Theory, an assessment of its strengths and weaknesses and a mention of some current developments. It is meant as an introduction to this session.

QUICK REVIEW OF BASICS

Density Functional Theory (DFT) is primarily a theory applicable to ground states of interacting electrons in given external potentials, $v(r)$, although it has been generalized and extended to many other aspects of electronic and other many body systems. This paper is intended to serve as an introduction to the following papers in this session.

Traditional wave-mechanical methods of ground state electronic structure are couched in terms of the Schroedinger many electron wave function, $\Psi(r_1, r_2, \dots, r_N)$, or — in practice — to approximation of this function. DFT represents a change of viewpoint, in that the central quantity is the much simpler electronic density distribution, $n(r)$. The fact that the theory of an N-electron system can be couched in terms of a real, non-negative, function of three variables, no matter how large the value of $n(r)$, is a consequence of the following lemma due to Hohenberg and Kohn.¹

Let $n(r)$ be the density distribution of the electronic ground state associated with the external potential $v(r)$. Then any other potential, $v'(r) (\neq v(r) + \text{constant})$ necessarily has a ground state with a different density distribution, $n'(r)$. Thus $n(r)$ uniquely determines the Hamiltonian of the system and hence, implicitly, all its properties such as the ground state energy E , the ground state wave function $\Psi(r_1, r_2, \dots, r_N)$, as well as properties of the excited states, density matrices, Greens's functions, etc.

The basic variational principle, in terms of $n(r)$, for the ground state energy E (corresponding to the Rayleigh Ritz variational principle in terms of Ψ) is the following:¹ For a given $v(r)$ we define the Hohenberg Kohn (HK) energy functional

$$E_{v(r)}[n(r)] \equiv \int v(r)n(r)dr + F[n(r)], \quad (1)$$

where the functional $F[n(r)]$ can be formally defined² as

$$F[n(r)] \equiv \min(\Psi_{n(r)}, (T + U)\Psi_{n(r)}), \quad (2)$$

over the set $\Psi_{n(r)}$ comprising all antisymmetric states whose density distribution is $n(r)$, and T and U are the kinetic and interaction energy operators.

Then

$$E \equiv \min_{n(r)} E_{\nu(r)}[n(r)]. \quad (3)$$

In this (exact) formulation approximations for $F[n(r)]$ must be introduced for practical applications, usually starting with the properties of homogeneous electron-gases of densities n .

Another route to practical applications, which has been very fruitful, was taken by Kohn and Sham(KS)³ who, under some assumptions, transformed the HK variational principle into a set of self-consistent equations, now known as the KS equations. They are analogous to the Hartree equations but, in principle, include all many body effects:

$$\left. \begin{aligned} (-\frac{1}{2}\nabla^2 + v_{\text{eff}}(r) - \epsilon_j)\psi_j(r) &= 0, \\ n(r) &= \sum_1^N |\psi_j(r)|^2, \\ v_{\text{eff}}(r) &\equiv v(r) + \int \frac{n(r')}{|r-r'|} dr' + v_{xc}(r), \\ v_{xc}(r) &\equiv \delta E_{xc}[n(r)]/\delta n(r), \end{aligned} \right\} \quad (4)$$

where the sum over j runs over the lowest N eigenvalues ϵ_j ; and $E_{xc}[n(r)]$ is the exchange correlation energy, formally defined as

$$E_{xc}[n(r)] \equiv F[n(r)] - \frac{1}{2} \int \frac{n(r)n(r')}{|r-r'|} dr dr' - T_s[n(r)]; \quad (5)$$

here $T_s[n(r)]$, the non-interacting kinetic energy functional, is defined, in analogy with (2), with $U = 0$, and the Ψ 's limited to single determinants. All many body effects lie in $E_{xc}[n]$.

In the KS formulation of DFT a central issue has been the search for good approximations to $E_{xc}[n(r)]$. The ‘‘mother’’-approximation has been the local density approximation (LDA):³

$$E_{xc}^{LDA}[n(r)] \equiv \int \epsilon_{xc}(n(r))n(r)dr \quad (6)$$

where $\epsilon_{xc}(n)$ is the exchange-correlation energy per particle of a uniform electron gas of density n . This function of one variable is known to an accuracy of better than 1%. In spite of its simplicity, the LDA has, for most purposes, yielded valuable quantitative or at least semi-quantitative results, especially for equilibrium (i.e., minimum energy) structures of molecules and solids.

For binding energies of molecules and solids as well as for barrier heights of chemical reactions generalized gradient approximations (GGA)⁴ have yielded substantial improvements (typically by factors of 3–5) over the LDA. These approximations have the generic form

$$E_{xc}^{GGA} \equiv \int f_{xc}(n(r), |\nabla n(r)|) dr, \quad (7)$$

where the functional form of f_{xc} has been chosen on the basis of various physical considerations (e.g., sum-rules) and/or by fitting empirical data.

A third, so-called hybrid approach,⁵ is to take

$$E_{xc}^{hyb} \equiv \gamma E_x^{exact}[n(r)] + \int f'_{xc}(n(r), |\nabla n(r)|) dr, \quad (8)$$

where E_x^{exact} is the exact exchange energy evaluated with KS orbitals, γ is a constant between 0 and 1, and $f'_{xc}(n, |\nabla n|)$ is an appropriately chosen (different) GGA.

STATUS IN 1997

In this paragraph I try to convey my assessment of the status of DFT at this time.

Strengths

a. A priori theory. The LDA is a wholly parameter-free, *a priori* theory, the only inputs being the positions and charges of the nuclei, R_{μ}, Z_{μ} . It is a very useful benchmark theory. (The GGA's are to a greater or lesser degree parameter free.)

b. Simplicity. Solution of the KS equations in LDA is only insignificantly more demanding, and much better, than solution of the Hartree equations; it is much simpler than solution of the Hartree-Fock equations. It therefore provides a useful, quick orientation for most questions related to the electronic structure of atoms, molecules, clusters, solids etc. Use of the GGA is more computationally intensive, but very often still the simplest method available for a given accuracy of the order a few percent.

c. Excellent results for structures. Experience has shown that, for a given "topology" (e.g., bcs vs. sc), the LDA yields empirical internuclear separation with an accuracy of about 1%. It also generally yields the correct topology unless there is a competing topology within a few meV/atom.

d. Crystals, Defects, and Surfaces. For periodic crystals ($N = \infty$), where Ψ -based many body approximations become either difficult or non-operative, DFT calculations are very simple and "scale" as N^0 . In fact, the LDA has become the standard theoretical method for most of solid state physics. The same is true for crystalline defects and crystalline surfaces with or without adsorbed atoms and molecules.

e. Non-periodic Systems of Very Many Atoms. Traditional, Hartree-Fock based configuration interaction methods scale with the number of atoms as N^{α} , where according to present estimates, $\alpha \approx 7$. They are limited to $N \lesssim 10$ for "chemical accuracy" of 0.1 eV. DFT calculations scale with $\alpha = 1 - 3$ and have been applied to systems with $N \approx 0(10^3)$. There is considerable current activity to develop efficient methods which scale linearly in N .⁶

f. Cohesive and Binding Energies. The LDA typically overbinds by $\sim 20\%$, GGA's have errors of typically $\sim 5\%$. This makes DFT useful for semi-quantitative or quantitative estimates and for studies of trends in sets of related systems. At the present time DFT calculations of molecular binding energies are still short by a factor of 2-3 of the desirable "chemical accuracy" of 0.1 eV, and the accuracy of calculated reaction barrier heights typically falls short by a factor of about 5.

g. Temperature Ensembles. Ground state DFT is readily generalized to one-or multi-component temperature ensembles.⁷ It is a natural tool for the study of the thermodynamic properties of plasmas. While for finite T the LDA is reasonably well known,⁸ GGA's remain to be developed.

h. Chemical Concepts. DFT has shed light on chemical concepts such as the chemical potential, electronegativity and hardness.⁹

i. Static and Dynamic Electric Polarizabilities. DFT has provided good results for static and dynamic polarizabilities, and thus also for asymptotic Van-der-Waals forces.¹⁰ (See also sec. 3.)

Shortcomings

a. Limited accuracy. Of course, any many-body calculation will have finite errors. But while Ψ -based methods, such as the Rayleigh–Ritz variational method, can (given enough computing power), be systematically made arbitrarily accurate, this is (at least at present) not the case for DFT. In principle there exist infinite gradient expansions for E_{xc} , but in practice they generally diverge.

At the present time practical DFT can be roughly characterized as a theory with errors in the 1–10% range. I would be surprised, on the basis of past history and other considerations, if, within the present conceptual framework, this error can be reduced by as much as an order of magnitude.

b. Excited states and scattering. Although the calculation of excited states by DFT is formally possible, and some promising results have been obtained,¹¹ it is my belief that it is intrinsically not as suited for excited states as for ground states or temperature ensembles. (This matter will be elaborated in a future publication). No consistent applications of DFT to scattering of electrons by atoms, molecules etc. are known to me.

SOME ONGOING WORK

Van der Waals energies in DFT

In principle DFT leads to the correct ground state energy E , including long range attractive Van der Waals energies. However, in both the LDA and the GGA-s the interaction energy, between two separated components of a composite system, a distance R apart, fall off asymptotically as $e^{-\gamma R}$, due to density overlap, instead of the correct R^{-6} , due to long range polarization effects.

Recently there has been very good progress in accurately calculating asymptotic Van der Waals coefficients, using approximate theories of the dynamic polarizability $\alpha(\omega)$ of the individual components.¹⁰ In ongoing work with Y. Meir and D. Makarov,¹² we have obtained good results for asymptotic Van der Waals energies and developed a theoretical framework which should allow calculation of the energy $E(R)$ of a composite system as a smooth function of R , from small values to asymptotically large ones.

Electronic edge structure: The Airy Gas.¹³

The LDA and GGA-s take as their starting point the uniform electron gas whose KS functions are oscillatory (corresponding to classical free particles). However any bounded system of atoms has edge regions in which the KS functions evanesce, (corresponding to classically forbidden regions). Thus the LDA and GGA-s for $E_{xc}[n(r)]$ are qualitatively inappropriate in these edge regions.

To correct this deficiency we have put forward the concept of the Airy Gas, designed to play the same paradigmatic role for edge regions as the uniform electron gas does for bulk regions. The Airy gas is defined by

$$v_{\text{eff}}(r) = -Fz \quad z < L \quad (9)$$

$$= +\infty \quad z \geq L \quad (10)$$

$$\epsilon_{\text{max}} = 0 \quad (11)$$

where L describes a mathematical cut-off barrier, which tends to infinity. F , the slope of v_{eff} can be renormalized to 1, so that the KS functions ψ_j , (Eq. 4), become Airy functions of z

multiplied by plane waves in x and y . The half-space $z < 0$ is classically forbidden for all occupied KS energies.

This system captures the essence of the physical edge region, which lies in the interval

$$-\ell \leq z \leq \ell, \quad \ell \equiv (2m/\hbar^2 F)^{1/3}. \quad (12)$$

For $z > \ell$ the local properties of the Airy gas approach those of a uniform electron gas at the local density $n(z)$.

We are currently calculating the single- and many-particle properties of the Airy gas and of some of its refinements. At a later stage we plan to join the edge region smoothly to the bulk region, as described by the LDA or a GGA.

Acknowledgements

This work has been supported by NSF grant No. NSFDMR-96-30452.

REFERENCES

- [1] P. Hohenberg and W. Kohn *Phys. Rev. B* **136**, 864 (1964).
- [2] M. Levy, Proc. Natl. Acad. Sci. USA **T6**, 6062 (1979) and *Physics Rev. A* **26**, 1200 (1982); E. H. Lieb, *Int. J. Quant. Chem.* **24**, 243 (1983)
- [3] W. Kohn and L. J. Sham, *Phys. Rev. A* **140**, 1133 (1965).
- [4] See e.g., A. D. Becke, *Phys. Rev. A* **38**, 3098 (1988); J. Perdew and J. P. Wang, *Phys. Rev. B* **33**, 8800 (1986); C. Lee et al., *Phys. Rev. B* **37**, 785 (1988). New GGA's continue to be developed.
- [5] A. D. Becke, *J. Chem. Phys.* **98**, 5648 (1993); **104**, 1040 (1996).
- [6] See e.g., P. Ordejon et al., *Phys. Rev. B* **53**, R10441 (1996).
- [7] N. D. Mermin, *Phys. Rev.* **137**, A 1441 (1965).
- [8] R. G. Dandree et al., *Phys. Rev. B* **34**, 2097 (1986).
- [9] For a review see W. Kohn et al., *J. Phys. Chem.* **100**, 12974 (1996).
- [10] V. P. Osinga et al., *J. Chem. Phys.* **106**, 5091 (1996).
- [11] H. Petersilka et al., *Phys. Rev. Lett.* **76**, 1212 (1996).
- [12] W. Kohn et al. (to be published).
- [13] W. Kohn, to appear in *Electronic Density Functional Theory — Recent progress and new directions*, J. G. Dobson et al., Eds., Plenum Press (New York) 1988.

This page intentionally left blank

EQUATION OF STATE OF PARTIALLY-IONIZED PLASMAS

Forrest J. Rogers

Lawrence Livermore National Laboratory
P. O. Box 808,
Livermore, CA 94550

The equation of state of partially ionized plasmas is receiving renewed attention due to recent helio- and astero-seismic measurements and laboratory experiments. The new data encompasses a wide range of parameter space, ranging from weakly to strongly coupled. Theoretical methods to treat these plasmas must confront issues concerning plasma screening of bound states, how strong coupling affects ionization balance, and how to include electron degeneracy and diffraction.. Two types of methods are used to treat complicated mixtures, such as occur in stars. Chemical picture methods are based on free energy minimization and must assert the effect the plasma has on bound states. Physical picture methods view the plasma in terms of its fundamental constituents so that plasma screening arises naturally. Herein I give a brief summary of the physical picture method.

INTRODUCTION

The equation of state (EOS) of partially-ionized plasmas has long been of interest in stellar modeling. Stars having masses similar to or greater than the sun are weakly coupled and simple models give results that are adequate for many purposes. However, helioseismology is now able to measure the EOS of the sun, as a function of solar radius, to an accuracy better than 0.1% [1]. This level of accuracy can not be obtained from simple models and efforts to develop more rigorous theories are in progress. The Saha equation [2] is the progenitor of methods to treat partially-ionized plasmas. It solves a set of coupled equations that balance ideal gas chemical potentials across chemical reactions occurring in the plasma. In its original form only the isolated particle ground state of each atomic/ionic component was considered. The next simplest approximation adds the classical Debye-Hückel Coulomb term corrected for electron degeneracy. In spite of its simplicity, this is a particularly good model because the deeply bound states are well represented by isolated (atomic) particles and the Debye-Hückel correction contains most of the excited bound state contribution [3,4]. Helioseismology supports this theoretical result [5]. The EOS calculations should also include a correction for electron exchange, which is large enough to affect comparisons with helioseismic data [6]. In addition there are small quantum diffraction corrections to the Debye-Hückel Coulomb term which are not typically included. For many years it was thought that the next improvement to the Saha equation should be to add excited bound states perturbed by the plasma environment. Since this problem is difficult to treat from fundamental theory, a voluminous literature based on ad hoc approaches was developed. The most commonly used methods to account for

environmental effects assume either bound state energies from screened potentials or the confined atom model. This complicates the calculations and it is now known that EOS based on shifted bound state energies are in significantly worse agreement with helioseismology than those using unshifted bound states [7].

Neither EOS theory now commonly used to model stellar plasmas screens bound states. The MHD method [8,9] is a chemical picture approach where the free energy is assumed to be separable into translational, configurational, and Coulomb interaction components. In the chemical picture it is necessary to assert the effect of the plasma on bound states. Based on the null results of Goldsmith, Griem, and Cohen [10], MHD assumes that the bound state energies are unshifted. Instead, plasma effects enter through an occupation probability formalism that separates the Boltzmann sum into effective bound and continuum state parts. The resulting internal partition function is convergent. For neutrals the bound state occupation probability is obtained from a model based on hard sphere interactions between atomic cores, while for ions the occupation probability is obtained from the dissolution of states due to electric microfield fluctuations. The MHD Coulomb interactions are given by the classical Debye-Hückel term corrected for electron degeneracy, which effectively limits MHD to weakly coupled plasmas. An ad hoc free energy term is added to guarantee pressure ionization. Electron exchange and diffraction corrections are neglected. The ACTEX method [3,4,11,12], is based on a physical picture approach that carries out a many body activity expansion of the grand canonical partition function (GCPF). A conceptual advantage of the physical picture is that it views the system in terms of its fundamental components; i.e., electrons and nuclei. A natural and important consequence of this approach is that low lying bound states are unscreened. ACTEX includes electron degeneracy and the leading quantum diffraction corrections as well as systematic corrections necessary for strongly-coupled regimes.

Other EOS work aimed mostly at dense astrophysical objects has also recently appeared. In the chemical picture: Saumon, Chabrier, and Van Horn [13] generated EOS tables suitable for modeling low-mass stars and giant planets. An important feature of their work is the prediction of a plasma phase transition that may affect models of giant planets. Potekhin [14] has generalized the arguments of MHD so that the occupation probability of charged particles is obtained directly without invoking Stark ionization theory. His method does not require an ad hoc free energy term to produce pressure ionization. Stolzmann and Blocker [15] have given a treatment of fully ionized dense stellar matter. They include exchange and charged particle interaction by Padé approximates as well as relativistic effects. In the physical picture: Perrot and Dharma-wardana [16] have given a density-functional theory (DFT) method; Kraeft et al. [17] have developed a thermodynamic Green's function method; Alustuey and Perez [18] have developed a method based on Feynman-Kac path integrals ; Pierleoni et al. [19] have used the restricted path-integral Monte-Carlo method to study hydrogen; and Penman, Clérouin, and Zerah [20] have used density functional molecular dynamics to also study hydrogen. Due to the extreme accuracy required, it is currently not computationally feasible to apply the simulation methods to helioseismology. Of the remaining methods the quantum diagrammatic physical picture approaches should give the best comparison with helioseismic data. So far however this has not been the case, primarily due to the difficulty of applying these methods in the region of partial ionization. One problem is that the diagrammatic methods involve a dynamic screened potential that significantly affects the bound states. The ACTEX approach follows a similar line but introduces some simplifications that allow it to treat the region of partial-ionization when the deBroglie wavelength, λ , is less than the Debye length, λ_D . Consequently, at the corresponding point in the analysis, ACTEX approximates the dynamic screened potential with a static potential having screened energy levels. However, it can be shown that in the region of partial ionization many additional diagrams must be included to treat composite particles on the same basis as fundamental particles. ACTEX accomplishes this by introducing new activity variables that are built from products of the fundamental particle activities and the Boltzmann factors that control the ionization balance between states. The screening corrections to the isolated atomic states introduced through the screened potential are used to define the composite particle activities. Consequently, only isolated atomic energy levels appear in the renormalized expansion. This is where ACTEX goes beyond the more fundamental approaches. A brief description of the ACTEX methodology is given in Section 2. Comparisons to helioseismic and shock data are given in Section 3.

THE ACTIVITY EXPANSION METHOD FOR PLASMAS (ACTEX)

Quantum diagrammatic methods are quite complex and it is difficult to get beyond asymptotic limits. However, the main affect of quantum mechanics is to remove the short-ranged electron-ion divergence in the bound state sum. When $\lambda < \lambda_D$ it is a good approximation to first develop the classical theory and then replace classical Boltzmann factors with their quantum mechanical analogues. This is the approach taken in ACTEX. At more extreme conditions quantum effects on the distribution of unbound particles become important.

The classical activity expansion of the GCPF of strongly coupled, fully-ionized plasmas involves a many-body analysis of a very large number of both singly connected and multiply connected diagrams. In contrast, only the multiply connected diagrams contribute to a density expansion of the canonical partition function. Abe [21] showed how to carry out an all-orders expansion in the density. The leading terms in the resulting convergent multi-component expression for the non-ideal Helmholtz free energy are

$$\frac{F - F_0}{VkT} \equiv S = S_R + \sum_{ij} S_{ij} + \sum_{ijk} S_{ijk} \dots, \quad (1)$$

where the indices i, j, k etc. range over all components,

$$S_R = \frac{1}{12\pi\lambda_D^3}, \quad (2)$$

is the ring diagram sum,

$$S_{ij} = -n_i n_j [B_{ij}(T, \lambda_D) + 2\pi \int_0^\infty r^2 dr (\beta u_{ij} - \frac{\beta u_{ij}^2}{2})], \quad (3)$$

is closely related to the second virial coefficient, B_{ij} , of the static screened potential

$$u_{ij} = \frac{Z_i Z_j e^2 e^{-r/\lambda_D}}{r}, \quad (4)$$

the n 's number fractions, the Z 's are particle charges and,

$$\lambda_D = \sqrt{\frac{kT}{4\pi e^2 \sum_j n_j Z_j^2}}, \quad (5)$$

is the Debye length. The S_{ijk} , and higher order terms systematically replace the divergent Coulomb virial coefficients with the virial coefficients for the Debye-Hückel potential (equation.(4)). The terms through order n^2 , given by equations. (2-5), show that there are some differences in detail. For example, there appears a term of order $n^{3/2}$, i.e. the Debye-Hückel Coulomb interaction term, coming from the ring diagrams, while terms of order βu_{ij} and $(\beta u_{ij})^2$ are missing from the screened second virial coefficient.

Equation (1) is a complete many-body solution for classical multi-component plasmas. Consequently, even though it is an expansion away from weak coupling, it recovers the Monte-Carlo strong coupling result [12]. It is well known that the grand canonical ensemble (GCE) is the appropriate choice for partially-ionized plasmas. It would be difficult to obtain a classical GCE result similar to the Abe result for the canonical ensemble. The corresponding quantum-mechanical expression, would be even more difficult to develop. The ACTEX method sidesteps both of these problems. The classical GCE result for fully ionized multi-component plasmas is obtained from a procedure that inverts equation (1) in terms of $S(T, n_{ij})$ to obtain an expression for P/kT as a functional

of $S(T, z_{ij})$ The result for a two component plasma of electrons, e , and nuclei, α , of charge Z is

$$\frac{P}{kT} = z_e + z_\alpha + S + \sum_{m=2}^{\infty} \frac{z_e}{m!} \left(\frac{\partial}{\partial z_e} z_e \right)^{m-2} \left(\frac{\partial S}{\partial z_e} \right)^m + \sum_{m=2}^{\infty} \frac{z_\alpha}{m!} \left(\frac{\partial}{\partial z_\alpha} z_\alpha \right)^{m-2} \left(\frac{\partial S}{\partial z_\alpha} \right)^m + \dots \quad (6)$$

where, the ellipsis indicates that cross terms not necessary for the present discussion have been left out and the

$$z_i = (2s_i + 1) \lambda_i^{-3} e^{\mu_i / kT}, \quad i = \{e, \alpha\} \quad (7)$$

are the activities.

As it stands, equation (6) is not very useful, since it involves operations on the function S which is a sum over virial coefficients, whereas, a properly constructed activity expansion of the GCPF should involve cluster coefficients. However, it is a complete result that can be reorganized in terms of cluster coefficients of the screened potential. For a two component plasma of electrons, e , and heavy ions of type, α , the reorganized expression through terms of order $z^{5/2}$ is [12]:

$$\begin{aligned} \frac{P}{kT} = & z_e + z_\alpha + S_R(U^*) + \frac{z_e}{2!} \left(\frac{\partial S_R}{\partial z_e} \right)^2 + \frac{z_\alpha}{2!} \left(\frac{\partial S_R}{\partial z_\alpha} \right)^2 + \dots + z_e^2 c_{ee} + 2z_e z_\alpha c_{e\alpha} + z_\alpha^2 c_{\alpha\alpha} \\ (8) \quad & + z_e \frac{\partial S_R(U^*)}{\partial z_e} \frac{\partial}{\partial z_e} (z_e^2 c_{ee} + 2z_e z_\alpha c_{e\alpha} + z_\alpha^2 c_{\alpha\alpha}) \\ & + z_\alpha \frac{\partial S_R(U^*)}{\partial z_\alpha} \frac{\partial}{\partial z_\alpha} (z_e^2 c_{ee} + 2z_e z_\alpha c_{e\alpha} + z_\alpha^2 c_{\alpha\alpha}) \end{aligned}$$

subject to the conditions,

$$n_e = z_e \frac{\partial}{\partial z_e} \left(\frac{P}{kT} \right), \quad n_\alpha = z_\alpha \frac{\partial}{\partial z_\alpha} \left(\frac{P}{kT} \right). \quad (9)$$

In equation (8),

$$S_R(U^*) = \frac{1}{12\pi\lambda_A^3(U^*)} \quad (10)$$

is the ring diagram sum, similar to equation (2),

$$\lambda_A(U^*) = \sqrt{\frac{kT}{4\pi e^2 U^*}} \quad (11)$$

is the screening length in the GCE, and

$$U^* = z_e + Z^2 z_\alpha \quad (12)$$

is defined for later convenience (the asterisk indicates that U^* is not in final form), the

$$c_{ij} = b_{ij} - b_{ij}^1 - b_{ij}^2 \quad (13)$$

will be referred to as Coulomb cluster coefficients, the b_{ij} are screened second cluster coefficients, b_{ij}^1 and b_{ij}^2 are first and second order perturbation terms corresponding to the linear and square terms in the integral in equation (3), and $i, j = \{e, \alpha\}$. For two body terms

$b_{ij} = -B_{ij}$. The ellipsis in equation (8) indicates that terms of order $z^{5/2}$ not needed in the present discussion are not included.

The second deficiency of equation (6), i.e., the Coulomb short range divergence, can now be removed by replacing classical Boltzmann factors with their quantum analogs. For example, the screened classical second cluster coefficient for the $e-\alpha$ interaction is replaced by

$$b_{e\alpha} = 4\pi\lambda_{e\alpha}^3 \text{Tr} \left(e^{-\beta H_2} - e^{-\beta H_0} \right), \quad (14)$$

where the trace is over the states of the potential

$$u_{e\alpha} = -Ze^2 \frac{e^{-r/\lambda_A}}{r}, \quad \text{and} \quad \lambda_{e\alpha} = \sqrt{\frac{\hbar^2}{2\mu_{e\alpha}kT}}$$

is the thermal deBroglie wavelength. Beth and Uhlenbeck [22] have shown that equation (14) can be expressed in the convenient form

$$b_{e\alpha} = 4\pi^{3/2} [\lambda_{e\alpha}^3 \sum_{nl} (2l+1) e^{-\beta E_{nl}} + \frac{1}{\pi} \sum_l (2l+1) \int_0^\infty \frac{d\delta_l}{dp} e^{-\beta p^2 / 2\mu_{e\alpha}}] \quad (15)$$

where the E_{nl} are bound states and the δ_l are phase shifts. Only the phase shift term contributes to the $e-e$ cluster coefficient, while the $\alpha-\alpha$ second cluster coefficient can be calculated from the classical expression:

$$b_{\alpha\alpha} = 2\pi \int_0^\infty [e^{-\beta u(r, \lambda_A)} - 1] r^2 dr \quad (16)$$

At low temperature the ground state Boltzmann factor in equation (13) completely dominates the sum, indicating that the equilibrium state is largely composed of hydrogenic bound pairs. It is easy to show that in this situation the product $2z_e z_\alpha c_{e\alpha}^{1s}$ in equation (8) is the activity of hydrogenic pairs [12,23]. It follows that in partially-ionized plasmas every occurrence of the product $2z_e z_\alpha c_{e\alpha}$ should be decomposed into linear and quadratic parts. In general, all occurrences of terms involving electron-ion Coulomb cluster coefficients for N particles should be decomposed into N terms of order 1 to N in the activity. In the following we refer to the $1s$ hydrogenic activity as $z_{e\alpha}^*$, dropping the superscript for simplicity, i.e.,

$$z_{e\alpha}^* = 8\pi^{3/2} \lambda_{e\alpha}^3 (2l+1) e^{-\beta E_{1s}(U^*)} z_e z_\alpha. \quad (17)$$

In practice this is not the definition of $z_{e\alpha}^*$ actually used. Compensation [12, 24] between

the bound and scattering state parts of equation (15) replace $e^{\beta E_{1s}}$ with $e^{\beta E_{1s}} - 1 + \beta E_{1s}$. For simplicity this is ignored in the present discussion.

The next step in the ACTEX procedure is to reorganize equation (8) to account for the formation of composite particles as the temperature is lowered. To introduce composite particles on an equal footing with fundamental particles, it is necessary to find terms such that $z_{e\alpha}^*$ appears as a new variable similar to fundamental particles. To lowest order the reorganized expression for the pressure is $P/kT = z_e + z_\alpha + z_{e\alpha}^*$, where the new activity for hydrogenic ions becomes from the term $2z_e z_\alpha c_{e\alpha}$. At the ring sum level (equation (10)) things are already much more complicated. In order to introduce the screening of hydrogenic charges into the Debye length, i.e., replace U^* with $U^* + (Z-1)^2 z_{e\alpha}^*$ it is necessary to find all the terms in the transformation

$$S_R(U^*) \rightarrow S_R(U^* + (Z-1)^2 z_{e\alpha}^*) \quad (18)$$

To start this process note that (see equation (8)), ignoring the term involving $\partial c_{e\alpha} / \partial z_e$,

$$z_e \frac{\partial S_R(U^*)}{\partial z_e} \frac{\partial (2z_e z_{e\alpha} c_{e\alpha})}{\partial z_e} \equiv 2z_e z_{e\alpha} c_{e\alpha} \frac{\partial S_R(U^*)}{\partial z_e} = z_{e\alpha}^* \frac{\partial S_R(U^*)}{\partial z_e}, \quad (19)$$

which is 3/2 order in $z_{e\alpha}^*$, similar to equation (10). Collecting all terms of order $z_{e\alpha}^{*3/2}$ in equation (8) gives

$$S_R(U^*) + z_{e\alpha}^* \frac{\partial S_R(U^*)}{\partial z_e} + z_{e\alpha}^* \frac{\partial S_R(U^*)}{\partial z_{e\alpha}} = S_R(U^*) [1 + (Z^2 + 1) z_{e\alpha}^* \frac{\partial S_R}{\partial U^*}] \quad (20)$$

This is close to what is needed in 1st order to make the transformation (18), except a cross term proportional to Z is absent. A term $\propto Z$ would have to come from $e-\alpha$ interactions and in fact can be found in $z_{e\alpha}^*$.

Consider a perturbation expansion of $E_{nl}(\lambda_A) / kT$:

$$\frac{E_{nl}(\lambda_A)}{kT} = \frac{E_{nl}^0}{kT} + \frac{Ze^2}{kT\lambda_A} - \frac{a_0 e^2}{4kT\lambda_A^2} [3n^2 - l(l+1)] + \dots, \quad (21)$$

where E_{nl}^0 is the unscreened state energy. The linear shift is the same for all states and can be written in the suggestive form

$$\frac{Ze^2}{kT\lambda_A} = 2Z \frac{\partial S_R(U^*)}{\partial U^*} \quad (22)$$

Using this relation we can rewrite equation (21) in terms of the shifted Debye energy levels [25] according to

$$\frac{E_{nl}}{kT} = \frac{E_{nl}^s}{kT} + 2Z \frac{\partial S_R(U^*)}{\partial U^*} \quad (23)$$

Limiting the discussion to just the ground state activity and using (23) in (17) gives

$$z_{e\alpha}^* = 8\pi^{3/2} \lambda_{e\alpha}^3 (2l+1) e^{-\beta E_{1s}^s} e^{-2Z \frac{\partial S_R(U^*)}{\partial U^*}} z_e z_{e\alpha} \quad (24)$$

equation. (24) can be used to define an activity for hydrogenic ions in terms of the shifted Debye energy levels according to

$$z_{e\alpha}^* = e^{-2Z \frac{\partial S_R}{\partial U^*}} z_{e\alpha}, \quad (25)$$

where,

$$z_{e\alpha} = 8\pi^{3/2} \lambda_{e\alpha}^3 (2l+1) e^{-\beta E_{1s}^s} z_e z_{e\alpha}, \quad (26)$$

Next, expanding the exponential term involving $\partial S / \partial U$ gives

$$z_{e\alpha}^* = \left(1 - 2Z \frac{\partial S_R}{\partial U^*} + \dots \right) z_{e\alpha}(U^*) \quad (27)$$

The second term in equation (27) is just what is needed to give the factor $(Z-1)^2$ in equation (20). Repeating the process for higher order terms in the expansion of $S_R(U)$ eventually gives the result

$$S_R(U^*) + (Z-1)^2 z_{e\alpha} \frac{\partial S_R}{\partial U^*} + \dots = S_R(U), \quad (28)$$

where

$$U = z_e + Z^2 z_\alpha + (Z-1)^2 z_{e\alpha} \quad (29)$$

Continuing in this way for higher order terms in the activity gives the transformation

$\frac{P}{kT}(z_e, z_\alpha) \rightarrow \frac{P}{kT}(z_e, z_\alpha, z_{e\alpha})$, plus extra terms. However, these extra terms obey simple relations. For example, the sum of all terms of order $z_{e\alpha}$ have the important property:

$$z_{e\alpha}(U) - U \frac{\partial z_{e\alpha}}{\partial U} + \frac{U^2}{2} \frac{\partial^2 z_{e\alpha}}{\partial U^2} + \dots = z_{e\alpha}(U - U) = z_{e\alpha}(0), \quad (30)$$

Higher order terms display similar properties. The introduction of an augmented set of activities to account for the shifting ionization balance as the temperature and density change, results in an expansion in terms of E_{1s}^0 , i. e. $E_{1s}^s \rightarrow E_{1st}^0$. The result is similar for excited states except near the plasma continuum [3].

The discussion so far has been limited to Boltzmann statistics and weak coupling. This has laid out the essential steps of the method and shows how the addition of diagrams in the region of partial-ionization, which are not included in more fundamental calculations [12], leads to an important result regarding electron bound states. The generalization of the ACTEX method to include the affect of electron degeneracy is accomplished using the method of Cooper and DeWitt [26] The effect of exchange is also added. Quantum diffraction corrections for low order terms are obtained from DeWitt [27]. A method for adding strong ion coupling is given in [12].

COMPARISON WITH SEISMIC AND EXPERIMENTAL DATA

Until recently it was not possible to validate theories of the EOS of partially-ionized plasmas by other means. That situation has changed dramatically. Now there are not only large projects aimed at observing the seismology of the sun to obtain very accurate EOS data, but also laser techniques that measure the shock Hugoniot. There have been a number of interesting comparisons between these observational and experimental projects that can be mentioned only briefly (see the papers by Däppen, Kress et al., and Militzer et al. elsewhere this Volume).

A number of comparisons of the MHD and ACTEX equations of state have been made to helioseismic inversions [28-30]. In general both equations of state are in good agreement with the data, but these studies have found that the ACTEX EOS yields better consistency. Basu and Christensen-Dalsgaard [31] have recently used the newly available LOW L data [32] to compare the difference in $\Gamma_1 = (\partial \ln P / \partial \ln \rho)_s$ between the sun and theories. In this case neither of the calculations stands out as a significantly better match with the data, although ACTEX matches slightly better overall. Analysis of higher-degree data will improve the quality of the inversions near the surface, where the greatest theoretical discrepancies occur. Models using the ACTEX EOS reduced calculated globular cluster ages by about a billion years, in better agreement with cosmology [33]

Gas gun [34] and laser shock measurements [35] of the deuterium Hugoniot present a challenge to theory. Starting from a liquid state with a density $\rho_0 = 0.171$ g/cc these experiments have reached pressures up to 2.1 Mbar (see Fig.(1)). The Hugoniot data displays a large maximum in the compression, a value of six at a pressure of 1.5 Mbar, although for most materials the maximum compression along the Hugoniot generally does not exceed 4.5. The unusually large maximum compression ratio in deuterium is due to

the large internal energy of the diatomic initial state. The shock temperature was not measured, but calculations give a value around 3.5eV at 2 Mbar. Under these conditions deuterium is mostly dissociated and about 15% ionized. There are large discrepancies between the theories and between the theories and experiment. Tight-binding MD calculations [36] give only a slight maximum near $\rho/\rho_0=4$, while quantum MC calculations [9] give a maximum compression ratio around 5 at pressure of 0.7 Mbar. That there are such large discrepancies between the simulations as well as between the simulations and experiment is a puzzle. The SESAME model [37] gives results similar to MD. The Thomas-Fermi-based QEOS model [38] gives a bump at about the same pressure as experiment, but at substantially lower density. Linear mixing model [39] calculations agree well with the experimental data, except at the highest pressures. The ACTEX calculations are in good agreement with the highest pressure data, but they do not include molecules and so do not extend to the low pressure regime.

Comparisons of ACTEX with high density gas gun and nuclear shock data for Be, Al, CH, H₂O, and SiO₂ were recently used to validate [40] the method for Γ up to 9.

DISCUSSION

There are plans to improve the range and the quality of EOS data obtained from helio- and astro-seismic observations as well as laser shock experiments. This will present an increasing challenge to ongoing efforts to model the seismic data from physical picture approaches. The existing discrepancies between MD and MC calculations and experiment are already causing considerable effort to understand the reasons and should lead to improvements in these basic approaches. In the next few years it can be expected that these new experimental and theoretical efforts will expand our understanding of partially-ionized regime.

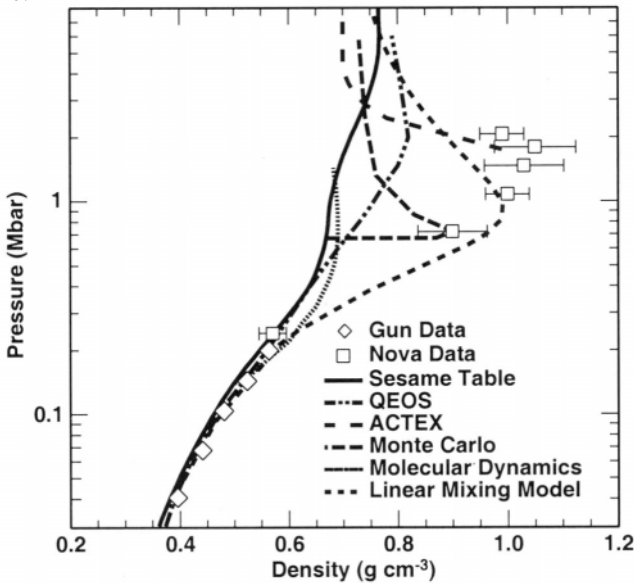


Fig.1 Comparison of theory and experiment for the deuterium Hugoniot.

ACKNOWLEDGMENTS

I wish to thank Burkhard Militzer for providing QMC D2 Hugoniot data and Robert Cauble for providing Figure 1. This work was performed under the auspices of the U. S. Department of Energy by the Lawrence Livermore National Laboratory under Contract W-7405-Eng-48

REFERENCES

1. J. Christensen-Dalsgaard et al., *Science*, 272: 1286 (1996)
2. M. Saha, *Phil. Mag.* 40: 472 (1920)
3. F. J. Rogers, *ApJ.*, 310: 723 (1986)
4. F. J. Rogers, "Equation of State In Astrophysics", eds G. Chabrier and E. Schatzman, Cambridge Univ. Press, Cambridge, (1994)
5. J. Christensen-Dalsgaard and D. Däppen, *A&A. Rev.* 4: 267 (1992)
6. J. A. Guzik and F. J. Swenson, *ApJ* (in press)
7. S. Arndt., W. Däppen, and A. Nayfonov, *ApJ*, (in press)
8. D. G. Hummer and D. Mihalas., *ApJ.*, 331: 794 (1988)
9. D. Mihalas, W.. Däppen, and D. G. Hummer *ApJ*, 331:815 (1988)
10. S Goldsmith, H. E. Griem., and L. Cohen, *Phys. Rev.*, A 30: 2775 (1984)
11. F. J. Rogers, F. J. Swenson., and C. A. Iglesias, *ApJ.*, 456:902 (1996)
12. F. J. Rogers, *Phys. Rev. A*24: 1531 (1981).
13. D. Saumon, G. Chabrier., and H. M. Van Horn. *ApJS*, 99: 713 (1995)
15. W. Stolzmann. and T. Blocker, *A &A*, 314: 365 (1996)
16. F. Perrot and . W. C. Dharma-wardana, *Phys. Rev E.* 52:5352 (1995)
17. D. Kremp, W. D. Kraeft, M. Schlanges, *Contrib. Plasma Phys.*, 33:567 (1993); W. D. Kraeft, et al., *Zeitschr. f. Phys. Chem.* (in Press)
18. A. Alustuey, and A. Perez, *Phys. Rev. E*, 53,:5714 (1996).
19. W. R. Magro, D. M. Ceperley, C. Pierleoni, and B. Bernu, *Phys. Rev. Lett*, 76:1240 (1996); C. Pierleoni, et al. *Phys. Rev. Lett*, 73:2145 (1994)
20. J. I. Penman, J. G. Clérouin, and P. G. Zerah, *Phys Rev. E.*, 51:R5224 (1995)
21. R. Abe, *Prog. Theor. Phys.*, 22:213 (1959)
22. E. Beth and G. E. Uhlenbeck, *Physica*, 3:915 (1937)
23. F. J. Rogers and H. E. DeWitt, *Phys. Rev. A*, 8:1061 (1973)
24. C. Pisano and H. J. McKeller, *Phys. Rev. A*, 40:6597 (1989)
25. J. L. Jackson and L. S. Klein, *Phys. Rev.*, 177:352 (1969)
26. M. S. Cooper and H. E. DeWitt, *Phys. Rev. A*, 8:1910 (1973)
27. H. E. DeWitt, *J. Math. Phys.* 7:161 (1966)
28. W. A. Dziembowski., A. A. Pamyatnykh, and R. Sienkiewicz, *Acta Astr.* 14: 5 (1992)
29. J. Christensen-Dalsgaard et al., *Science*, 272: 1286 (1996)
30. J. N. Bahcall., M. H. Pinsonneault., S. Basu, L. Christensen-Dalsgaard, *Phys. Rev. Lett.*, 78:171(1997)
31. S. Basu. and J. Christensen-Dalsgaard, *J.* 1997, *ApJ* 322, L5
32. Tomczyk, S., Card, K., Elmore, D., Hull, H., and Caccini, A. 1995, *Solar Phys*, 159, 1
33. Salaris, M., Degl'Innocenti, S., and Weiss, A. 1997, *A &A*, 479, 665
34. W. J. Nellis et al., *J. Chem. Phys.*, 79:1480 (1983)
35. DaSilva, L. B, et al. 1992, *Phys. Rev. Lett*, 69, 438
36. T. J. Lenosky, J. L. Kress, and L. A. Collins, *Phys. Rev. B*, 56:5164 (1997)
37. G. I. Kerley, "Molecular-Based Study of Fluids", eds. J. M. Haile and D. A. Mansoori, American Chemical Society, Washington, D. C., (1983)
38. R. M. More, K. H. Warren, D. A. Young, G. B. Zimmerman, *Phys. Fluids*, 31:3059 (1988)
39. M. Ross, *Phys. Rev. E*, (submitted)
40. F. J. Rogers and D. A. Young, *Phys Rev. E*, (in press)

This page intentionally left blank

METALLIZATION OF FLUID HYDROGEN AT 140 GPa (1.4 Mbar)

W. J. Nellis, S. T. Weir, and A. C. Mitchell

Lawrence Livermore National Laboratory
University of California
Livermore, CA 94550

The properties of hydrogen at high pressures and temperatures are important for the interiors of giant planets, such as Jupiter and Saturn, and for Inertial Confinement Fusion. Electrical conductivity measurements indicate that hydrogen becomes a metallic fluid at 140 GPa, ninefold initial liquid-H₂ density, and 2600 K. Metallization density is defined to be that at which the electronic bandgap E_g is reduced by pressure to $E_g \sim k_B T$, at which point E_g is filled in by fluid disorder to produce a metallic density of states with a Fermi surface and the minimum conductivity of a metal. High pressures and temperatures were obtained with a two-stage gun, which accelerates an impactor up to 7 km/s. A strong shock wave is generated on impact with a holder containing liquid hydrogen at 20 K. The impact shock is split into a shock wave reverberating in hydrogen between stiff Al₂O₃ anvils. This dynamic compression heats hydrogen quasi-isentropically to about twice its melting temperature at 100 GPa pressures and lasts ~100 ns, sufficiently long to achieve equilibrium and sufficiently short to preclude loss of hydrogen by mass diffusion and chemical reactions.

The measured electrical conductivity increases four orders of magnitude from 93 to 140 GPa and is constant at 2000 ($\Omega\text{-cm}$)⁻¹ from 140 to 180 GPa. This conductivity is the same as that of Cs and Rb undergoing the same transition from a semiconducting to metallic fluid at 2000 K. This measured value is also within factor of 5 or less of hydrogen conductivities calculated with the following models: (i) minimum conductivity of a metal, (ii) Ziman model of a liquid metal, and (iii) tight-binding molecular dynamics. At metallization this fluid is ~90 at.% H₂ and 10 at.% H with a Fermi energy of ~12 eV. Fluid hydrogen at finite temperature undergoes a Mott transition at $D_m^{1/3} a^* = 0.30$, where D_m is the metallization density and a^* is the Bohr radius of the molecule. Metallization occurs at a lower pressure in the fluid than predicted for the solid probably because crystalline and orientational phase transitions, which occur in the ordered solid and inhibit metallization, do not occur in the fluid.

Tight-binding molecular dynamics calculations by Lenosky et al suggest that fluid metallic hydrogen is a novel state of condensed matter. Protons are paired transiently and exchange on a timescale of a few molecular vibrational periods, ~10-14 s. Also, the kinetic, vibrational, and rotational energies of the dynamically paired protons are comparable. These tight-binding calculations indicate that the measured conductivity is the minimum conductivity of a metal.

INTRODUCTION

Hydrogen has been the prototypical system of the insulator-to-metal transition ever since Wigner and Huntington¹ predicted in 1935 that the insulating molecular solid would transform to a conducting monatomic solid at sufficiently high pressure, P , or density, D , at temperature $T = 0$ K. Substantial pressure is required to do this because solid molecular hydrogen is a wide bandgap insulator ($E_g = 15$ eV) at ambient. The original theoretical estimate of the required pressure was 25 GPa. Since that time, the estimated pressure has ranged up to 2000 GPa² at 0 K. The best recent theoretical estimate is 300 GPa.³ Extrapolation of recent pressure-volume experimental data at static pressures up to 120 GPa in the hcp diatomic solid phase yields a predicted dissociative transition pressure of 620 GPa.⁴ It is also possible that metallization occurs within the diatomic solid, without a transition to the monatomic phase. In this case metallization would be achieved by reduction to zero of the electronic energy gap separating filled valence-band states from empty conduction-band states. However, this metallization pressure is structural dependent⁵⁻⁷ and the structure of solid hydrogen at metallization is not known. Metallization in the solid has not been observed experimentally by optical measurements up to 250 GPa in the diamond anvil cell.⁸⁻¹⁰

Hydrogen is of great importance for planetary science because its cosmological abundance is about 90 at.%. Jupiter and Saturn contain over 400 Earth masses, most of which is hydrogen. Jupiter-size planets now being discovered close to nearby stars¹¹ probably contain massive amounts of hydrogen as well. The interiors of giant planets are at high pressures and high temperatures in the fluid¹² because of the large mass and low thermal conductivity. Jupiter has the largest magnetic field in our solar system. This field varies from 14 G at the north magnetic pole to 11 G at the south magnetic pole, versus 0.5 G on Earth. Magnetic fields of giant planets are produced by the convective motion of electrically conducting hydrogen by dynamo action.

The equation of state of fluid hydrogen is important for inertial confinement fusion. A fuel pellet composed of the hydrogen isotopes deuterium and tritium is placed in a hohlraum and radiated by a multisteped, high-intensity laser pulse.^{13, 14} The first step of the laser pulse produces a ~ 100 GPa shock and the successive compressive pulses comprise a quasi-isentrope to much higher pressures, similar to the compressive process used in our conductivity experiments.

Because of the high kinetic energy of the impactor (0.5 MJ) in our experiment, we are working at a confluence of High Energy and Condensed Matter Physics. This energy is comparable to the total kinetic energy of the proton/antiproton beams in the Tevatron at the Fermi National Accelerator Laboratory. The high kinetic energy enables discovery of novel states of condensed matter, analogous to the discovery of novel states of subnuclear matter.

The reason solid hydrogen has not been observed to metallize at static high pressures is probably caused by phenomena which occur in the ordered solid, including, structural and molecular orientational phase transitions.^{15, 16} Thus, a logical place to look for metallization is in the disordered fluid at temperatures just above melting at high pressures. In this case, metallization is expected when high pressure reduces $E_g \sim k_B T$, where k_B is Boltzmann's constant. When $E_g \sim k_B T$, thermal smearing and fluid disorder fill in the energy gap, a metallic density of states is achieved, and the electronic system has a Fermi surface and the minimum conductivity of a metal.

FINITE TEMPERATURES

It is extremely difficult to produce a stable hydrogen sample at high temperatures. Hydrogen is so mobile that when it is heated statically above 500 K, it rapidly diffuses away into the solid walls of the sample holder.¹⁷ Thus, it is essential that hydrogen be heated for a

very brief time, say ~ 100 ns, which is sufficiently fast that hydrogen cannot be lost by diffusion. Shock compression is ideal because the sample is compressed to high pressures and simultaneously heated adiabatically and uniformly for ~ 100 ns. The calculated temperature is ~ 3000 K, which is larger than the estimated melting temperature of ~ 1500 K at 140 GPa,^{17,18} the observed pressure of metallization. A hydrogen temperature of 3000 K is relatively low because the electronic energy gap is 15 eV at ambient pressure and the zero-point vibrational energy of the molecule is 0.3 eV. The time duration of ~ 100 ns is sufficiently long to obtain both thermal equilibrium and an equilibrated configuration of current flow and sufficiently short to avoid the growth of Rayleigh-Taylor instabilities and loss of hydrogen by mass diffusion.

METALLIZATION EXPERIMENTS

The experimental configuration is illustrated in Fig. 1. A layer of liquid H_2 or D_2 is compressed dynamically by a high-pressure shock wave reverberating between two stiff, electrically-insulating sapphire (single-crystal Al_2O_3) disks, or anvils. The two sapphire anvils are contained between two Al plates, which are part of a cryostat at 20 K. The compression is initiated by a shock wave generated when a metal plate, launched by a two-stage light-gas gun at velocities up to ~ 7 km/s, impacts the Al plate on the left. This shock is amplified when it is transmitted into the first sapphire disk. The first shock pressure in the liquid H_2 is ~ 30 times lower than the shock incident from the sapphire. The shock then reverberates quasi-isentropically between the two anvils until the final hydrogen pressure equals the pressure incident initially from the sapphire. The P-D states achieved by shock reverberation are illustrated in Fig. 2. The loading path consists of an initial weak shock followed by a quasi-isentrope. The final temperature produced by a reverberating shock is about 1/10 what it would be for a single shock to the same pressure.¹⁹ This figure shows that states achieved by shock reverberation are relatively close to the 0 K isotherm and at much higher densities than for the Hugoniot.

Electrical resistance of the hydrogen sample was measured versus time by inserting electrodes through the anvil on the right in Fig. 1. Either H_2 or D_2 samples were used, depending on the final density and temperature desired, H_2 giving lower final temperatures

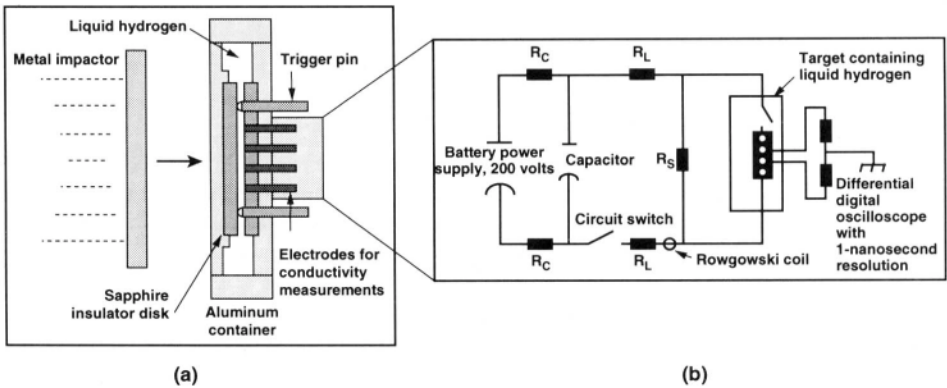


Figure 1. Schematic of electrical conductivity experiments on fluid hydrogen. Metal impactor is launched by 20-m-long two-stage gun. Four electrodes in (a) are connected to circuit in (b). Sapphire disks are 25 mm in diameter; liquid hydrogen layer between sapphire disks is 0.5 mm thick. For conductivities lower than metallic, two probes were used. Trigger pins turn on recording system. All cables are coaxial.

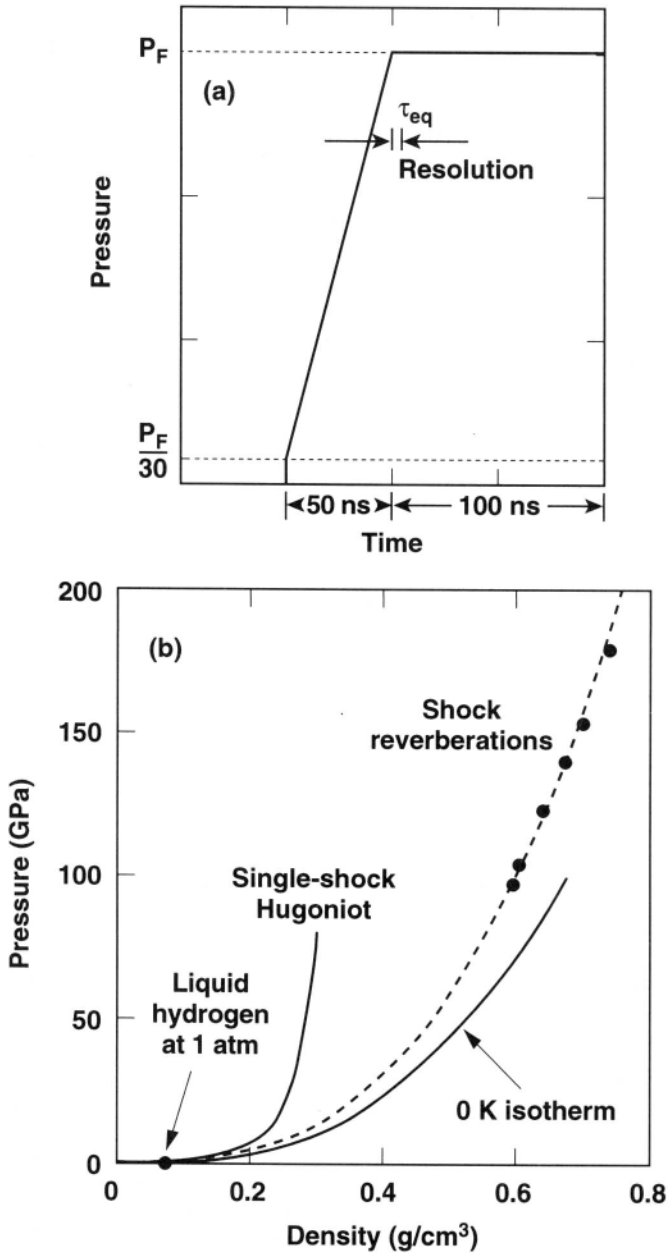


Figure 2. Effect of rise time on pressure-density states. (a) First pressure in hydrogen is $\sim P_F/30$, where P_F is incident shock pressure in Al_2O_3 . Successive reverberations comprise quasi-isentrope up to pressure P_F . This quasi-isentrope is represented by ramp over ~ 50 ns from $P_F/30$ up to P_F . After reverberation is complete, P_F is held for ~ 100 ns. If P_F were achieved in one jump, this state would be on single-shock Hugoniot. (b) Equation-of-state curves plotted as pressures versus densities: 0 K isotherm, points reached by shock reverberations, and single-shock Hugoniot. Initial point is liquid H_2 at 1 atm.

than D_2 . That is, because the initial mass densities of liquid H_2 and D_2 differ by a factor of 2.4, the final shock-compressed densities and temperatures also differ substantially. There is no isotope effect at these densities and temperatures.

At present there is no way to measure hydrogen density and temperature because the high-rate deformations caused by the reverberating shock renders the sapphire anvil opaque. Thus, density and temperature were calculated using two reasonable equations of state of Ross²⁰ and of Kerkey.²¹ The results did not vary significantly. The conservative uncertainties derived from these calculations are 5% in density and 20% in temperature. The experimental data are plotted in Fig. 3 as electrical resistivity versus pressure,²² P_F in Fig. 2a. Electrical resistivities measured under single-shock compression were reported previously.²³

RESULTS

In the semiconducting range, 93-135 GPa, the data were fit to the dependence of a thermally activated semiconductor. The result is $E_g(D) = 1.12 - (54.7)(D - 0.30)$, where $E_g(D)$ is the activation energy in eV and D is in moles/cm³. $E_g(D)$ derived from this fitting procedure and $k_B T$ are equal at a density of 0.32 mol/cm³ (9-fold initial liquid- H_2 density) and a temperature of ~2600 K (0.22 eV). At 0.32 mol/cm³ and 2600 K the calculated pressure is 120 GPa, close to 140 GPa at which the slope changes in the electrical resistivity (Fig. 3). At pressures of 140 to 180 GPa the measured hydrogen resistivity is essentially constant at a metallic value of 500 $\mu\Omega\text{-cm}$. Thus, fluid hydrogen undergoes a continuous transition from a semiconducting to metallic fluid at 140 GPa, 0.32 mol/cm³, and a temperature of ~2600 K.

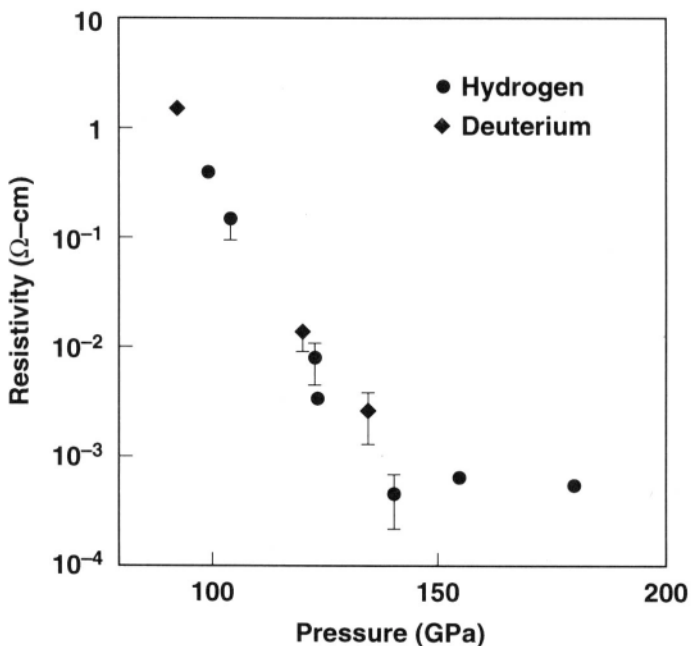


Figure 3. Logarithm of electrical resistivity of H_2 and D_2 samples plotted versus pressure. Slope change at 140 GPa is transition from semiconducting to metallic fluid.

DISCUSSION

This measured metallic value of $500 \mu\Omega\text{-cm}$ is essentially the same resistivity as that of the fluid alkali metals Cs and Rb at 2000 K undergoing the same transition.²⁴ This metallic resistivity of Cs, Rb, and hydrogen is achieved at essentially the same Mott-scaled density of $D_m^{1/3}a^* = 0.30$, where D_m is the density at metallization and a^* is the Bohr radius. Mott's preferred value is 0.25. The Bohr radius is the same for H_2 and H,²⁵ so this relationship cannot distinguish whether hydrogen is in the form of dimers or monomers. Based on Ross' bulk thermodynamic calculations, an estimated 5% of the molecules are dissociated.²² Tight-binding molecular dynamics^{26,27} simulations also show that fluid metallic hydrogen at these temperatures is essentially molecular. Since the size and shape of H_2 and H are very similar, at 3000 K in the fluid the two are probably miscible. Thus, the energy gap we measure is probably that of the mixture of H_2 and H. Neglecting dissociation and assuming one conduction electron per H_2 molecule at metallization density, the free-electron Fermi energy of metallic fluid hydrogen is $E_F \sim 12 \text{ eV}$, as for solid Al. Since at metallization $T/T_F \sim 0.02$, metallic fluid hydrogen is degenerate, highly condensed matter.

The measured value of $500 \mu\Omega\text{-cm}$ is bracketed by simple theoretical models. The minimum electrical conductivity of a metal is given by

$$\sigma = 2\pi e^2/3ha,$$

where e is the charge of an electron, h is Planck's constant, and a is the average distance between particles supplying the electrons.²⁸ In this case $a = D_m^{-1/3}$. This calculated minimum conductivity corresponds to a resistivity of $250 \mu\Omega\text{-cm}$.

The measured metallic conductivity is in reasonable agreement with that calculated for a strong-scattering free-electron system. The Drude conductivity of a metal, σ , is given by:

$$\sigma = n(E_F) e^2 \tau / m,$$

where $n(E_F)$ is the number of electron carriers per unit volume at the Fermi energy E_F , e and m are the charge and mass of the electron, respectively, and

$$\tau = \lambda / v_F$$

is the relaxation time for electron scattering, where λ is the mean free path of an electron and v_F is its Fermi velocity. Since our measured metallic conductivity is the minimum conductivity of a metal, by definition the mean free path, λ , is the distance between particles supplying the electrons or at metallization $\lambda \sim D_m^{-1/3} = 1.7 \text{ \AA}$. The velocity of a conduction electron is the Fermi velocity, $2 \times 10^8 \text{ cm/s}$, of a system with a Fermi energy of 12 eV. The number density of free-electron carriers at the Fermi level is the total electron density, D_m , reduced by the factor $(1.5/E_F)$.²⁹ Thus, the calculated conductivity is $600 (\Omega\text{-cm})^{-1}$, which corresponds to a resistivity of $1700 \mu\Omega\text{-cm}$.

A preliminary calculation of the electrical resistivity of molecular liquid metallic hydrogen in the Ziman model yields a resistivity of $\sim 100 \mu\Omega\text{-cm}$.³⁰

The electrical conductivity of fluid metallic hydrogen has been calculated using tight-binding molecular dynamics.^{26,27} At 140 GPa and temperatures in the range 1500 to 3000 K, the calculated resistivities are 500 to $250 \mu\Omega\text{-cm}$, respectively.

Since all these calculations produce electrical resistivities within a factor of 5 or less of the measured value, our measurement of 500 mW-cm is quite reasonable.

Iodine is another molecular element which metallizes at much lower pressure in the liquid than in the solid, 3 GPa³¹ rather than 16 GPa,³² respectively.

The tight-binding simulations show that protons are paired transiently and exchange on a timescale of a few molecular vibrational periods, $\sim 10^{-14}$ s. When averaged over times long compared to the lifetime of a pair, the system behaves as though there is an equilibrium concentration of molecules and monomers. These MD simulations also show that rotational energies of the transient pairs are comparable to the kinetic and vibrational energies, which complicates calculation of the electrical resistivity. This picture of a fluid in which protons which comprise transient pairs and monomers continually exchange on a dynamical timescale of $\sim 10^{-14}$ s in which characteristic times for collisions, vibrations and rotations are comparable describes a novel state of condensed matter.

ACKNOWLEDGMENTS

We want to acknowledge N. W. Ashcroft, M. Ross, T. W. Barbee III, and A. A. Louis for scientific discussions. This work was performed under the auspices of the U. S. Department of Energy under Contract No. W-7405-ENG-48.

REFERENCES

1. E. Wigner and H. B. Huntington, On the possibility of a metallic modification of hydrogen, *J. Chem. Phys.* **3**:764 (1935).
2. B. J. Alder and R. H. Christian, Destruction of diatomic bonds by pressure, *Phys. Rev. Lett.* **4**:450 (1960).
3. N. W. Ashcroft, Pairing instabilities in dense hydrogen, *Phys. Rev.* **B 41**:10 963 (1990).
4. P. Loubeyre, R. LeToullec, D. Hausermann, M. Hanfland, R. J. Hemley, H. K. Mao, and L. W. Finger, X-ray diffraction and equation of state of hydrogen at megabar pressures, *Nature* **383**:702 (1996).
5. A Garcia, T. W. Barbee, M. L. Cohen, and I. F. Silvera, Band gap closure and metallization of molecular solid hydrogen, *Europhys. Lett.* **13**:355 (1990).
6. H. Chacham and S. G. Louie, Metallization of solid hydrogen at megabar pressures : a first-principles quasiparticle study, *Phys. Rev. Lett.* **66**:64 (1991).
7. E. Kaxiras, J. Broughton, and R. J. Hemley, Onset of metallization and related transitions in solid hydrogen, *Phys. Rev. Lett.* **67**:1138 (1991).
8. H. N. Chen, E. Sterer, and I. F. Silvera, Extended infrared studies of high pressure hydrogen, *Phys. Rev. Lett.* **76**:1663 (1996).
9. R. J. Hemley, H. K. Mao, A. F. Goncharov, M. Hanfland, and V. Struzhkin, Synchrotron infrared spectroscopy to 0.15 eV of H_2 and D_2 at megabar pressures, *Phys. Rev. Lett.* **76**:1667 (1996).
10. A. L. Ruoff, Hydrogen at multimegabar pressures, in "*High Pressure Science and Technology*" W. Trzeciakowski, ed., World Scientific, Singapore (1996).
11. M. Mayor and D. Queloz, A Jupiter-mass companion to a solar-type star, *Nature* **378**:355 (1995).
12. M. Ross, H. C. Graboske, and W. J. Nellis, Equation of state experiments and theory relevant to planetary modelling, *Phil. Trans. R. Soc. Lond.* **A 303**:303 (1981).
13. J. D. Lindl, R. L. McCrory, and E. M. Campbell, Progress toward ignition and burn propagation in inertial confinement fusion, *Physics Today* September:32 (1992).
14. J. Lindl, Development of the indirect-drive approach to inertial confinement fusion and the target physics basis for ignition and gain, *Phys. Plasmas* **2**:3933 (1995).
15. N. W. Ashcroft, Dense hydrogen: the reluctant alkali, *Physics World* **8**:43 (1995).
16. B. Edwards and N. W. Ashcroft, Spontaneous polarization in dense hydrogen, *Nature* **388**:652 (1997).

17. F. Datchi and P. Loubeyre, University of Pierre and Marie Curie, private communication, 1996.
18. V. Diatschenko, C. W. Chu, D. H. Liebenberg, D. A. Young, M. Ross, and R. L. Mills, Melting curves of molecular hydrogen and molecular deuterium under high pressures between 20 and 373 K, *Phys. Rev. B* **32**:381 (1985).
19. K. M. Ogilvie and G. E. Duvall, Shock-induced changes in the electronic spectra of liquid CS_2 , *J. Chem Phys.* **78**:1077 (1983).
20. N. C. Holmes, M. Ross, and W. J. Nellis, Temperature measurements and dissociation of shock-compressed liquid deuterium and hydrogen, *Phys. Rev. B* **52**:15 835 (1995).
21. G. I. Kerley, A model for the calculation of thermodynamic properties of a fluid, in "Molecular-Based Study of Fluids," J. M. Haile and G. A. Mansoori, eds., American Chemical Society, Washington (1983).
22. S. T. Weir, A. C. Mitchell, and W. J. Nellis, Metallization of fluid molecular hydrogen at 140 GPa (1.4 Mbar), *Phys. Rev. Lett.* **76**:1860 (1996).
23. W. J. Nellis, A. C. Mitchell, P. C. McCandless, D. J. Erskine, and S. T. Weir, Electronic energy gap of molecular hydrogen from electrical conductivity measurements at high shock pressures, *Phys. Rev. Lett.* **68**:2937 (1992).
24. F. Hensel and P. Edwards, The changing phase of liquid metals, *Phys. World* April:43 (1996).
25. T. W. Barbee III, LLNL, private communication (1996).
26. T. J. Lenosky, J. D. Kress, L. A. Collins, and I. Kwon, Molecular dynamics modeling of shock-compressed liquid hydrogen, *Phys. Rev. B* **55**:R11 907 (1997).
27. J. Kress, L. Collins, T. Lenosky, I. Kwon, and N. Troullier, Molecular dynamics modeling of dense hydrogen, this proceedings.
28. N. F. Mott and E. A. Davis. "Electronic Processes in Non-Crystalline Materials," Oxford, London (1971), p. 81.
29. N. W. Ashcroft and N. D. Mermin, "Solid State Physics," Holt, Rinehart, and Winston, New York (1976), p. 44.
30. W. J. Nellis, A. A. Louis and N. W. Ashcroft, Metallization of fluid hydrogen, *Phil. Trans. R. Soc. London A* 356:119 (1998).
31. V. V. Brazhkin, S. V. Popova, R. N. Voloshin, and A. G. Umnov, Metallization of liquid iodine under high pressure, *High Pressure Res.* **6**:363 (1992).
32. B. M. Riggelman and H. G. Drickamer, Approach to the metallic state as obtained from optical and electrical measurements, *J. Chem. Phys.* **38**:2721 (1963).

ELECTROLYTE CRITICALITY AND GENERALIZED DEBYE-HÜCKEL THEORY

Michael E. Fisher¹, Benjamin P. Lee², and Stefan Bekiranov¹

¹Institute for Physical Science and Technology,
University of Maryland, College Park, Maryland 20742, U.S.A.

²Polymers Division, National Institute of Standards and Technology,
Gaithersburg, Maryland 20899, U.S.A.

Abstract Recent experiments on electrolyte solutions suggest that the critical behavior of binary fluids in which Coulombic forces dominate may differ from that exhibited by most systems. To attack this problem theoretically, the *full* Debye-Hückel (DH) thermodynamic theory (that recognizes ionic hard cores) was extended by Levin and Fisher to include (+, -) ion pairing and dipolar-pair-ionic-fluid solvation contributions; now DH theory has been generalized to provide, in a natural way, *density* and *charge correlation functions*, both needed to assess critical behavior. The predictions for the various correlation lengths of the RPM, the symmetric, hard-core model, prove *exact* at low densities. The appropriate Ginzburg criterion supports standard (Ising-type) criticality; but that might be modified by the explicitly predicted charge-density *oscillations* that set in near criticality.

I. COULOMBIC CRITICALITY AND CROSSOVER

The *universality* of behavior in the neighborhood of a critical point is now well established on both theoretical and experimental grounds (see e.g. [1]). In a nutshell, the *critical exponents* describing the singular behavior of fluids, alloys, ferromagnets, ferroelectrics, superfluids, etc., near critical points, and many dimensionless ratios and functions depend only on very general features of the physical system in question: foremost is the spatial dimensionality d ; next, although to a quantitatively lesser degree, the tensorial character of the “order parameter” is crucial; the particular forces driving the phase transition and criticality normally play *no* role! But see [1] for a discussion of exceptions when long-range, power-law forces are present: the issue here is “How exceptional are Coulombic forces?” Thus, in typical, nonionic fluids, if ρ is a density (or composition) variable, two phases with densities $\rho_>(T) > \rho_c$ and $\rho_<(T) < \rho_c$ may coexist below the critical

point at (ρ_c, T_c) . Then, asymptotically, as $t \equiv (T - T_c)/T_c \rightarrow 0^-$ one finds

$$\rho_>(T) - \rho_c \approx \rho_c - \rho_<(T) \approx B |t|^\beta, \quad (1)$$

where the critical exponent β takes a universal ($d = 3$, Ising) value $\beta \simeq 0.32_5$ (while the amplitude, B , and, of course, T_c , depend on the details of the system). This widely observed and theoretically rather well understood result [1] contrasts starkly with the “classical,” van der Waals, mean-field, or Landau prediction $\beta = \frac{1}{2}$ (which can usually be valid only when $d > 4$ [1]).

Now many electrolyte solutions do, indeed, obey (1) with $\beta \simeq 0.32$: see the reviews [2, 3, 4]. However, Pitzer [2-5] has reported on a particular system — triethyl-*n*-hexyl ammonium triethyl-*n*-hexyl bromide in diphenyl ether or, for short, $\text{N}_{2226}\text{B}_{2226}$ in Ph_2O — which fits (1) well down to $|t| \gtrsim 10^{-5}$ but with the classical value $\beta \simeq 0.50$. Furthermore, this system was specifically designed to mimic the simplest idealized picture of an electrolyte that is embodied in the so-called *restricted primitive model* (RPM), namely, $N = N^+ + N^- (= \rho V)$ equisized hard spheres of diameter a , one half carrying charges $+q$, the other $-q$, in a medium of dielectric constant D (chosen to represent the solvent). This is just the model treated by Debye and Hückel in 1923 [6].

Further experiments above T_c [2-4] have supported the conclusion that Pitzer’s salt solution obeys a van der Waals (rather than an Ising-type) equation of state [7]! In particular, turbidity measurements (see [2-4]) indicate that the reduced (osmotic) compressibility, $\chi(\rho, T)$, and the associated *density correlation length*, $\xi_N(\rho, T)$ diverge as

$$\chi(\rho_c, T) \approx C^+ / |t|^\gamma, \quad \xi_N(\rho_c, T) \approx \xi_0^+ / |t|^\nu, \quad \text{when } T \rightarrow T_c^+, \quad (2)$$

with exponents $\gamma \simeq 1.0_0$ and $\nu \simeq 0.5_0$ [2, 3, 7] close to the classical values, $\gamma = 2\nu = 1$, in place of the usual Ising values, $\gamma \simeq 1.24 < 2\nu \simeq 1.26$ [1-3].

From a theoretical viewpoint, χ and ξ_N are both derived from the Fourier transform $\widehat{G}_{NN}(\mathbf{k})$ of the density-density correlation function $G_{NN}(\mathbf{r}; \rho, T) = \langle [\rho(\mathbf{r}) - \rho][\rho(\mathbf{0}) - \rho] \rangle$, via

$$\widehat{G}_{NN}(\mathbf{k}) = \rho\chi(\rho, T) / [1 + \xi_N^2 k^2 + \dots], \quad (3)$$

as $k = |\mathbf{k}| \rightarrow 0$. Notice that $\xi_N(\rho, T)$ is quite distinct from the *charge correlation length*, $\xi_Z(\rho, T)$, *alias* the standard Debye screening length, $1/\kappa(\rho, T)$; that, in turn, describes the decay of the charge-charge correlation function, $G_{ZZ}(\mathbf{r}; \rho, T) = \langle [\rho_+(\mathbf{r}) - \rho_-(\mathbf{r})][\rho_+(\mathbf{0}) - \rho_-(\mathbf{0})] \rangle$. Since the density, ρ , is the order parameter for the gas-liquid (or “plasma”) phase transition [8], the correlation function of primary interest in the critical region is $G_{NN}(\mathbf{r})$. However, the behavior of $G_{ZZ}(\mathbf{r})$ near criticality is not reliably known [3(a), 9] and, as will be indicated below, it might play a significant role.

Although the critical behavior of the Pitzer solution seems wholly classical, other electrolytes, notably sodium-ammonia solutions and certain organic salts in solvents of low dielectric constant [2-4] display *crossover*: for temperatures $|t| > t_\times$, i.e., outside the *crossover scale*, t_\times , which depends on the system, classical (effective) exponents ($\beta \simeq \frac{1}{2}$, $\gamma \simeq 1, \dots$) are seen; but for $t \lesssim t_\times$ the behavior crosses over to standard Ising-type behavior, the true asymptotic exponents ($\beta \simeq$

0.32, $\gamma \simeq 1.24 \dots$) appearing for $t \ll t_x$. It is, indeed, possible — perhaps even likely — that the Pitzer solution would, if the observations could be extended, exhibit Ising-type behavior for $|t| \lesssim t_x \simeq 10^{-4.5}$.

The crucial theoretical questions [3] thus become: “What determines the values of t_x in real systems? And, what is the value of t_x in the restricted primitive model?” It is most tempting to speculate that the RPM, with *only* Coulombic and hard-core interactions, has a very small value of t_x , say $\lesssim 10^{-4}$; then the observation of values $t_x \gtrsim 10^{-2}$ [2-4], would most naturally be attributable to the presence of van der Waals forces, hydrogen bonding, etc. The balance of this article reviews briefly the work of the authors and their associates (Yan Levin and Xiao-jun Li) to test this scenario [10-13] focusing, in particular, on a generalization of DH theory [14-16] that yields the charge *and* density correlation functions, in a natural way that proves, furthermore, to give exact, universal results in the low density limit [14, 17] and to satisfy various thermodynamic bounds, in contrast [18] to the predictions of the mean spherical model and its generalizations and extensions (see, e.g., [19, 20]).

II. DEBYE-HÜCKEL THEORY

An exact analysis of the RPM would, clearly, reveal its critical behavior and the value of any crossover scale t_x ! But, in default of that, a renormalization-group (RG) treatment [1] should elucidate the Ising (or other) character of Coulombic criticality; more quantitatively, the implementation of a Ginzburg criterion (for the validity of a classical theory) ought to provide estimates for t_x [10, 15, 19(b)]. As a basis, however, these two latter approaches, require a reliable, ‘first-level’ approximation or mean-field description that captures the essential physical features in the critical region and provides reasonable quantitative accuracy. Such a description is now available for the thermodynamic properties of the RPM in the so-called DHBjDIHC theories of Fisher and Levin [10,11].

To explain these developments it is helpful to recall the basic strategy of Debye and Hückel. Starting with the ideal gas free energy, $F^{ideal}(\rho, T)$, one desires the “excess” contributions arising from the Coulombic interactions: in these days one would usually supplement F^{ideal} by an excluded volume or *hard-core* term, F^{HC} [10, 11]. Then (a) one first aims to compute the mean electrostatic energy, say $u_\sigma(\rho, T)$, of an ion \mathcal{I}_σ of species σ , diameter a , and charge q_σ , in the field of the remaining ions. To this end, (b) one seeks the mean electrostatic potential, $\phi_\sigma(\mathbf{r}; \mathbf{r}')$, induced at \mathbf{r} when \mathcal{I}_σ is held at \mathbf{r}' . From this (c) one may obtain the mean “self-potential”

$$\psi_\sigma(\mathbf{r}') \equiv \lim_{\mathbf{r} \rightarrow \mathbf{r}'} [\phi_\sigma(\mathbf{r}; \mathbf{r}') - q_\sigma / D |\mathbf{r} - \mathbf{r}'|], \quad (4)$$

seen by the charge q_σ (which may be taken at the center of \mathcal{I}_σ). (d) The corresponding species energy density is then just $\rho_\sigma u_\sigma = \rho_\sigma q_\sigma \psi_\sigma(\mathbf{r}')$. (e) Integrating over position and summing on σ yields the total interaction energy. (f) The excess, electrostatic free energy follows by setting $q_\sigma \rightarrow \lambda q_\sigma$ (all σ) and integrating on λ from 0 to 1: this is Debye’s charging process!

Finally, and, crucially, (g) to obtain $\phi_\sigma(\mathbf{r}; \mathbf{r}')$, Debye and Hückel first appeal to electrostatics for Poisson’s equation and then call on statistical mechanics. In

this era we can recognize that there is an exact statistical Poisson’s equation [16, 21, 22]

$$\nabla_{\mathbf{r}}^2 \phi_{\sigma}(\mathbf{r}; \mathbf{r}') = -(4\pi/D) \sum_{\tau} q_{\tau} \rho_{\tau}(\mathbf{r}) g_{\tau\sigma}(\mathbf{r}; \mathbf{r}'), \quad (5)$$

which, in essence, (h) DH approximate for $|\mathbf{r} - \mathbf{r}'| \geq a$ via the natural ansatz

$$g_{\tau\sigma}(\mathbf{r}; \mathbf{r}') \simeq \exp[-q_{\tau} \phi_{\sigma}(\mathbf{r}; \mathbf{r}')], \quad (6)$$

although they impose the exact relation $g_{\tau\sigma}(\mathbf{r}; \mathbf{r}') \equiv 0$, for $|\mathbf{r} - \mathbf{r}'| \leq a$. (j) Linearizing the resulting Poisson-Boltzmann equation then yields the DH equation, namely, $\nabla^2 \phi_{\sigma} = \kappa_D^2 \phi_{\sigma}$ (for $|\mathbf{r} - \mathbf{r}'| \geq a$) where, as usual, the inverse Debye length κ_D is given by

$$\kappa_D^2 = (4\pi/Dk_B T) \sum_{\tau} q_{\tau}^2 \rho_{\tau}. \quad (7)$$

Lastly, (k) solving the DH equation with ϕ_{σ} and $(\partial\phi_{\sigma}/\partial r)$ continuous across $|\mathbf{r} - \mathbf{r}'| = a$ and $\phi_{\sigma} \rightarrow 0$ as $|\mathbf{r} - \mathbf{r}'| \rightarrow \infty$, yields the sought-for potential, $\phi_{\sigma}(\mathbf{r}; \mathbf{r}')$. This, of course, depends on T and on the densities and charges of all the species: it provides the input needed in (4) to obtain what we will call $F^{DH}(\rho, T)$ — the Debye-Hückel approximation for the excess free energy [6, 21].

III. ION-PAIRING AND DIPOLE-IONIC SOLVATION

Now, it was not realized for many years that the “pure” DH theory (with $F \simeq F^{ideal} + F^{DH}$) predicts [3, 20, 11] a critical point at

$$T_c^* \equiv k_B T_c D a / q^2 = \frac{1}{16} = 0.0625, \quad \rho_c^* \equiv \rho_c a^3 = \frac{1}{64\pi} \simeq 0.005, \quad (8)$$

with a corresponding, highly asymmetric coexistence curve. These results change only slightly when a hard-core (HC), excluded volume term, F^{HC} is added using, say, free-volume or Carnahan-Starling approximations [10, 11]. However, as stressed by Bjerrum (Bj) [23], *pairing* of oppositely charged ions must become important at low temperatures say $T^* \lesssim 0.3$. Indeed, the essential role of association into *dipolar ion pairs* can be demonstrated analytically [18] since, when lacking pairing, the DH (and the MSA) free energies, with *or* without HC terms, violate Gillan’s bound (see [18]).

The equilibrium density of ion pairs, say $\rho_2(\rho, T)$, must be determined via a mass-action law with an association constant that (at low temperatures, $T \lesssim T_c$) is optimally chosen in Ebeling’s form (see [10, 11]). Clearly, in creating pairs, the density of *free ions*, $\rho_1 = \rho_+ + \rho_-$, is reduced to $\rho_1 = \rho - 2\rho_2$ and only these contribute to κ_D in (7). Since $(\kappa_D a)_c$ lies close to unity in nearly all the approximate theories, this *depletion* of free ions raises the overall critical density ρ_c^* to around 0.04. This value lies within the range $\rho_c^* = 0.03-0.08$ suggested by Monte Carlo (MC) simulations in the last few years (see [3(b)]); these also indicate $0.056 > T_c^* > 0.048$, with $T_c^* \simeq 0.049$ currently favored [3(b)] — that is only about 20% below the DH value (8)!

However, Fisher and Levin [10, 11] showed that a second, important “missing ingredient” in the total free-energy expression was a dipole-ionic-fluid term, F^{DI} . That is needed to account for the *solvation* (or ‘screening’) of each neutral,

but still electrically active (+,-) ion pair by the fluid of free ions. The required DI contribution can be found [10, 11] simply by *adapting* the basic DH approach, as sketched above, to an *ion pair* \mathcal{I}_{+-} [24].

The resulting DHBjDIHC theories (including some minor variants [11]) predict T_c^* in the range 0.052-0.056, only about 10% higher than the MC values [3(b)]. Note that an overestimate of T_c is to be expected for such classical theories which, in essence, neglect critical fluctuations. (The predicted DHBjDI densities, $\rho_c \simeq 0.024$ -0.028 [11], are lower than current MC estimates but because of the extreme asymmetry of the coexistence curve, these closely correlate with the lower T_c^* values.)

IV. GINZBURG'S CRITERION

By their phenomenological construction, all the DH-based theories (and their MSA counterparts, see [11, 19, 20]) must yield the van der Waals exponents, $\beta = \frac{1}{2}$ and $\gamma = 2\nu = 1$. But that has, of course, no relevance to the *true* nature of criticality in the RPM (or in more realistic models). On the other hand, Ginzburg, followed by others (see [10, 15, 19(b)]), has advanced a criterion for the validity of such classical theories: In the language of (1) and (2), one can construct a "Ginzburg reduced temperature scale"

$$t_G = j_3(C^+)^2/\rho_c^2 B^4(\xi_0^+)^6 \quad (\text{for } d = 3), \quad (9)$$

where j_3 is a somewhat arbitrary numerical coefficient [15, 19(b)]. For $|t| \gg t_G$ the classical theory should be adequate; for $|t| < t_G$ it should fail. If one supposes, as is plausible in light of RG considerations [1], that Ising-type behavior appears for $|t| \ll t_G$, it is reasonable to identify the suspected crossover scale, t_x , with t_G [10, 15, 19(b)]. Accordingly, the speculation of Sec. I, suggests that t_G for the classical RPM theories might prove to be very small.

Now the critical amplitudes C^+ and B in (9) are known, say from DHBjDI theory; but the density correlation length amplitude, ξ_0^+ , which enters to the sixth power, is not! To fill this need, a natural generalization of DH theory has been devised [14, 16] that yields approximations for the correlation functions, $G_{NN}(\mathbf{r})$ and $G_{ZZ}(\mathbf{r})$, that are sensible in the critical region and exact at low densities [14, 17]. The resulting "GDH theories" provide values for ξ_0^+ and, hence, for t_G . (Note that the standard MSA does not generate a density correlation length, $\xi_N(\rho, T)$, that diverges at the critical point.)

V. GENERALIZED DEBYE-HÜCKEL THEORY

To obtain information on correlation functions we aim [14, 16] to obtain a *free energy functional*, $F = k_B T \bar{F}[\{\rho_\sigma(\mathbf{r})\}]$, in which the *spatially varying ionic densities* $\rho_\sigma(\mathbf{r})$ are specified. From such a functional, one can compute the *direct correlation functions* via

$$C_{\sigma\tau}(\mathbf{r}; \mathbf{r}') = \delta^2 \bar{F} / \delta \rho_\sigma(\mathbf{r}) \delta \rho_\tau(\mathbf{r}') |_{\rho_\lambda(\mathbf{r}') = \bar{\rho}_\lambda}, \quad (10)$$

and, thence, using the multicomponent Ornstein-Zernike relations [21, 14, 16] all the correlation functions $G_{\sigma\tau}(\mathbf{r})$ and, so, $G_{NN}(\mathbf{r})$ and $G_{ZZ}(\mathbf{r})$. For the DHBjDI -

based RPM theories one has $\sigma = +, -, 2$, corresponding to free ions and bound pairs; but the approach is quite general [16]. In (10) the $\bar{\rho}_\lambda$ denote the *overall*, uniform equilibrium densities. For computational convenience [14, 16] one may choose the spatial variation

$$\rho_\sigma(\mathbf{r}) = \bar{\rho}_\sigma [1 + \Delta_\sigma \cos(\mathbf{k} \cdot \mathbf{r})]. \quad (11)$$

Expansion of $\bar{F}(\{\Delta_\sigma\})$ to quadratic order in the Δ_σ , then yields $1/\hat{G}_{NN}(\mathbf{k})$ and $1/\hat{G}_{ZZ}(\mathbf{k})$ directly [14, 16].

To obtain the functional $\bar{F}[\{\rho_\sigma(\mathbf{r})\}]$ (approximately!) we follow again the basic DH strategy set out in Sec. II: the only essential difference is that the spatially varying densities, $\rho_\sigma(\mathbf{r})$, must be carried through all steps (a)-(k) [14, 16]. Thus, in (a) and (b), to compute u_σ , we seek $\phi_\sigma(\mathbf{r}; \mathbf{r}' | \{\rho_\tau(\mathbf{r}'')\})$ which leads via (4) to $\psi_\sigma(\mathbf{r}' | \{\rho_\tau(\mathbf{r}'')\})$ and, through steps (d)-(f), to $\bar{F}[T | \{\rho_\sigma(\mathbf{r})\}]$ (or, more conveniently, using (11), to $\bar{F}(T, \rho; \{\Delta_\sigma\})$).

To obtain ϕ_σ we may still appeal to (5) since it remains valid for the inhomogeneous situation [16]. At the next step (h), however, a new insight is required, namely, that any spatially varying charge imbalance entails an overall electrostatic potential $\Phi(\mathbf{r})$ determined by [16]

$$\nabla^2 \Phi(\mathbf{r}) = -4\pi q_0 \rho_Z(\mathbf{r})/D \equiv -(4\pi/D) \sum_\tau q_\tau \rho_\tau(\mathbf{r}), \quad (12)$$

with appropriate boundary conditions (where q_0 is a reference charge). Now $\Phi(\mathbf{r})$ must be separated from $\phi_\sigma(\mathbf{r}; \mathbf{r}')$ to obtain the local induced potential [16, 25]

$$\tilde{\phi}_\sigma(\mathbf{r}; \mathbf{r}') \equiv \phi_\sigma(\mathbf{r}; \mathbf{r}') - \Phi(\mathbf{r}), \quad (13)$$

which decays to zero when $|\mathbf{r} - \mathbf{r}'| \rightarrow \infty$. Accordingly, in the Boltzmann ansatz (6) we should replace ϕ_σ by $\tilde{\phi}_\sigma$. Linearization, (j) then yields the GDH equation [16]

$$\begin{aligned} \nabla_{\mathbf{r}}^2 \tilde{\phi}_\sigma(\mathbf{r}; \mathbf{r}') &= -(4\pi/D) [q_\sigma \delta(\mathbf{r} - \mathbf{r}') - q_0 \rho_Z(\mathbf{r})], & |\mathbf{r} - \mathbf{r}'| \leq a, \\ &= \tilde{\kappa}_D^2(\mathbf{r}) \tilde{\phi}_\sigma(\mathbf{r}; \mathbf{r}'), & |\mathbf{r} - \mathbf{r}'| \geq a, \end{aligned} \quad (14)$$

which replaces the usual DH equation. The new, spatially varying Debye parameter, $\tilde{\kappa}_D(\mathbf{r})$, is defined just as in (7) but with $\rho_\tau(\mathbf{r})$ replacing ρ_τ [26]. Finally, (k) solving (14) with the previous boundary conditions completes the theory.

VI. PREDICTIONS FROM GDH THEORY

GDH theory yields quite novel results for the density correlations of the RPM: Within pure DH theory (neglecting ion pairing) a simple closed form is found for $\xi_N(\rho, T)$ [14]. More generally, when $\rho \rightarrow 0$ the *universal* behavior

$$\xi_N(\rho, T) = (b/48\kappa_D)^{1/2} [1 + \frac{1}{8}\kappa_D b + \dots] \sim 1/(T\rho)^{1/4}, \quad (15)$$

with $b = q^2/k_B T$, is predicted. This is in striking contrast to the variation of the screening length, $\xi_Z(\rho, T) \approx 1/\kappa_D \sim (T/\rho)^{1/2}$, and in strong disagreement with

MSA and GMSA predictions for ξ_N [19]. However, analysis [17] using the Meeron-Mayer -resummation of the cluster expansions for $g_{\sigma\tau}(\mathbf{r})$ [27] proves that (15) is exact! Of course, GDH theory also reproduces the exact thermodynamic limiting laws [21]. But, further, the fourth-moment correlation length [28]

$$\xi_{N,2}(\rho, T) = (b/320\kappa_D^3)^{1/4} [1 + \frac{7}{72}\kappa_D b + \dots] \sim T^{1/8}/\rho^{3/8}, \quad (16)$$

and the density-correlation exponential decay length [15, 16]

$$\xi_{N,\infty}(\rho, T) = \frac{1}{2}\kappa_D^{-1} [1 + 2 \exp(-4/\sqrt{\pi\rho b^3}) - \dots], \quad (17)$$

are likewise predicted correctly to the orders shown [16, 17].

The full charge-charge correlation function, $\widehat{G}_{ZZ}(k)$, can also be found explicitly in GDH theory without pairing [16]. In contrast to the expressions usually ascribed [16] to the DH theory, the GDH form satisfies *both* the Stillinger-Lovett (SL) conditions [29] (which may be expressed as $\widehat{G}_{ZZ}/k^2 \rightarrow \rho/\kappa_D^2$ for $k^2 \rightarrow 0$). More generally, at low densities the charge correlations are predicted to decay as $e^{-\kappa r}/r$ with, as expected, the exact relation $\kappa/\kappa_D \rightarrow 1$ as $\rho \rightarrow 0$. When ion pairing is introduced, following the DHBjDI theories, the first SL condition is still satisfied but the second is obeyed only up to corrections of order $\rho_2 \sim \rho^2$. This observation could, perhaps, point to an improved treatment of the ion-dipole interactions.

Since GDH theory provides a sensible, classical approximation for $\xi_N(\rho, T)$ through the critical region, one may calculate the amplitude ξ_0^+ and, thence, the Ginzburg scale, t_G , within the DHBjDI theories (see (2), (9) and [15]). The results [15] are instructive but, in light of the speculative hopes expressed, disappointing! Calibration of the coefficient j_3 in (9) is necessary. For that, the hard-core square-well (SqW) fluid, which shows *no crossover*, serves well [19(b)]: a reasonable choice of j_3 [19(6)] and a range of approximations gives $t_G^{SqW} \simeq 0.27-2.4$ [15] or, more usefully, $\log_{10} t_G^{SqW} = -0.1 \pm 0.5$.

What transpires for the RPM? The theory predicts values for t_G^{RPM} of the *same* order, or *larger* by a factor of 10, say, $\log_{10} t_G^{RPM} = 0.85 \pm 0.5$ — quite contrary to the proposed smaller values. A similar conclusion has been reached using the GMSA [19(b)]; however, that cannot really be trusted since even the *form* of the low-density behavior (15) is not reproduced. On the other hand, Schröer and Weiss (WS) [30], reach the opposite conclusion, i.e., $t_G^{RPM} \ll 1$; but their analysis is highly suspect since, although the *form* of (15) is now reproduced, the WS coefficient is 5.7 times greater than the exact (GDH) result. Translated directly to the critical region, this error factor would yield $\log_{10} t_G^{RPM} \simeq 1.5$ [30] in consonance with our conclusion [15].

In summary, if the identification of t_G with t_x is valid for the RPM one is driven to conclude that the model should exhibit nothing but Ising-type critical behavior! Indeed, *some*, although not all, recent Monte Carlo studies point in this direction (see [1(b)] and [31, 32]). Such an outcome would certainly *not* serve to rationalize the observations on Pitzer's solution [1-5]; but those, in turn, have come under question [7].

VII. CHARGE-DENSITY OSCILLATIONS

Should one trust the identification of t_G with t_x ? In fact GDH theory can also cast some light on this question. Specifically, the explicit forms for $\widehat{G}_{ZZ}(\mathbf{k})$ (with or without pairing) are readily analyzed to show that *charge oscillations* arise when $x \equiv \kappa_D a$ exceeds $x_K \simeq 1.178$ [16, 33]. Such oscillations in $G_{ZZ}(\mathbf{r})$ have been anticipated in previous treatments [19, 22–29] although with “Kirkwood values,” x_K , higher by 2–6 % [16]. But, as mentioned, the DHBjDI theories all place x_c close to unity (but recall that κ_D is to be computed with the *free ion* density $\rho_1 = \rho_+ + \rho_-$). Consequently, in the critical region charge-density-wave fluctuations may well compete nonlinearly with the basic density fluctuations that ultimately drive the transition. Indeed, in a slightly enlarged parameter space, a multicritical point might appear (see e.g., [3(a)] and [32]). The critical behavior of both the RPM and real systems could be significantly influenced by the presence of such an incipient or hidden multicritical point [3(a), 16, 32]. In these circumstances, furthermore, t_G is unlikely to be a reliable guide to a crossover to Ising criticality at some t_x .

To translate these suggestions into serious calculations, however, seems to demand a renormalization-group treatment [1]. GDH theory may go some way towards providing the necessary starting point; but the way ahead remains misty [32]. In short, the nature of Coulombic criticality is still an open question!

Acknowledgements Interactions with J.-P Hansen, C.W. Outhwaite, and J. Douglas have been much appreciated. Support from the National Science Foundation (through Grants Nos. CHE 93-11729 and CHE 96-14495) and via a National Research Council Research Associateship is gratefully acknowledged.

REFERENCES

1. M.E. Fisher, *Revs. Mod. Phys.* **46**, 597 (1974) and references therein.
2. J.M.H. Levelt Sengers and J.A. Given, *Molec. Phys.* **80**, 989 (1993).
3. M.E. Fisher (a) *J. Stat. Phys.* **75**, 1 (1994); (b) *J. Phys. Cond. Matt.* **8**, 9103 (1996).
4. W. Schröer, *et al.*, *J. Phys. Cond. Matt.* **8**, 9321 (1996) and references therein.
5. K.S. Pitzer, *Accts. Chem. Res.* **23**, 333 (1990).
6. P. W. Debye and E. Hückel, *Phys. Z.* **24**, 185 (1923).
7. But some puzzling recent observations on Pitzer’s solution have, on the contrary, exhibited Ising-type behavior: S. Wiegand *et al.*, *J. Chem. Phys.* **106**, 2777 (1997); W. Schröer, J.M.H. Levelt Sengers and coworkers (private communication, June 1997).
8. G.É. Norman and A.N. Starostin, *Teplofiz. Vys. Temp.* **6**, 410 (1968); **8**, 40 (1970).
9. G. Stell, *J. Stat. Phys.* **78**, 197 (1994).
10. M.E. Fisher and Y. Levin, *Phys. Rev. Lett.* **71**, 3826 (1993).
11. Y. Levin and M.E. Fisher, *Physica A* **225**, 164 (1996). See [18] for errata.
12. X.-J. Li, Y. Levin and M.E. Fisher, *Europhys. Lett.* **26**, 683 (1994).
13. Y. Levin, X.-J. Li, and M.E. Fisher, *Phys. Rev. Lett.* **73**, 2716 (1994).
14. B.P. Lee and M.E. Fisher, *Phys. Rev. Lett.* **76**, 2906 (1996).

15. M.E. Fisher and B.P. Lee, *Phys. Rev. Lett.* **77**, 3561 (1996).
16. B.P. Lee and M.E. Fisher, *Europhys. Lett.* **39** (3) (1997); and to be published.
17. S. Bekiranov and M.E. Fisher, *Bull. Amer. Phys. Soc.* **42** (1) 725 (1997) Q168; and to be published.
18. D.M. Zuckerman, M.E. Fisher and B.P. Lee, *Phys. Rev. E* [in press]: see also M.E. Fisher, D.M. Zuckerman and B.P. Lee in these *Proceedings*.
19. R.J.F. Leote de Carvalho and R. Evans (a) *Molec. Phys.* **83**, 619 (1994); (b) *J. Phys. Cond. Matt.* **7**, L575 (1995).
20. S. Yeh, Y. Zhou, and G. Stell, *J. Phys. Chem.* **100**, 1415 (1996).
21. See, e.g., D.A. McQuarrie, *Statistical Mechanics* (Harper Collins, New York, 1976) Chap. 15.
22. See, e.g., C.W. Outhwaite in *Statistical Mechanics: A Specialist Periodical Report*, Vol. **2**, ed. K. Singer (The Chemical Society, London, 1975).
23. N. Bjerrum, *Kgl. Dan. Vidensk. Selsk. Mat.-fys. Medd.* **7**, 1 (1926).
24. See, e.g., J.G. Kirkwood, *J. Chem. Phys.* **2**, 351 (1934).
25. Compare with E. Trizac and J.-P. Hansen, *J. Phys. Cond. Matt.* **8**, 9191 (1996), Eq. (3.29).
26. Somewhat analogous results appear in the MPB theory [22] of electrical double layers: see S.L. Carnie and G.M. Norrie, *Adv. Chem. Phys.* **56**, 141 (1984) Sec. IV.B and references therein.
27. E. Meeron, *J. Chem. Phys.* **28**, 630, (1958).
28. Defined via

$$\xi_{N,2}^4 = 4!(\partial^4 \widehat{G}_{NN} / \partial k^4)_{k=0} / \rho\chi \propto \int r^4 G_{NN}(\mathbf{r}) d\mathbf{r} / \int G_{NN}(\mathbf{r}) d\mathbf{r}.$$

29. F.H. Stillinger and R. Lovett, *J. Chem. Phys.* **48**, 3858 (1968).
30. V.C. Weiss and W. Schröer, *J. Chem. Phys.* **106**, 1930 (1997); W. Schröer and V.C. Weiss, *J. Chem. Phys.* **106**, 7458 (1997).
31. (a) J.M. Caillol, D. Levesque, and J.J. Weis, *Phys. Rev. Lett.* **77**, 4039 (1996); (b) J.P. Valleau and G.M. Torrie, in preparation, cited in [32].
32. See N.V. Brilliantov, J.P. Valleau, C. Bagnuls, and C. Bervillier (July 1997: to be published).
33. It is also interesting that the GDH result for $\widehat{G}_{ZZ}(\mathbf{k})$ predicts *undamped* charge oscillations, corresponding to “ionic crystallization”, that set in for $x > x_X \simeq 6.652$ with an initial wavelength $\lambda_X \simeq 1.847a$ [16].

This page intentionally left blank

ORDERING IN CLASSICAL COULOMBIC SYSTEMS

John P. Schiffer

Physics Division, Argonne National Laboratory,
9700 S. Cass Avenue, Argonne, IL 60439
and
The University of Chicago,
5720 S. Ellis Avenue, Chicago, IL 60637

The properties of finite one-component plasma clouds at very low temperatures have been investigated—similar to the conditions obtained in laser-cooled ion traps or storage rings. The minimum-energy configurations of few ions in isotropic confinement are discussed, and the features of the shell structure that is characteristic of larger clouds. The eventual transition to infinite-matter behavior is being investigated. Dimensional phase transitions as a function of the external confinement have been studied. Normal modes of these systems has been explored.

It has been well known for some time [1,2] that infinite Coulombic matter will crystallize in body-centered cubic form when the quantity Γ (the dimensionless ratio of the average two-particle Coulomb energy to the kinetic energy per particle) is larger than ~ 175 . But the systems of such particles that have been produced in the laboratory in ion traps, or ion beams, are *finite* with surfaces defined by the boundary conditions that have to be satisfied. This results in ion clouds with sharply defined curved surfaces, and interior structures that show up as a set of concentric layers that are parallel to the outer surface. The ordering does not appear to be cubic, but the charges on each shell exhibit a 'hexatic' pattern of equilateral triangles that is the characteristic of liquid crystals. The curvature of the surfaces prevents the structures on successive shells from interlocking in any simple fashion. This class of structures was first found in simulations [3] and later in experiments [4].

The Molecular Dynamics simulations are straightforward application of Newtonian mechanics with the equations of motion integrated in sufficiently small time steps to approximate the classical trajectories. At each step the interactions between all particles have to be computed anew, thus for an N-particle system $N^2/2$ terms contributing to the net force need to be computed. The method is limited by computer power, but modern parallel computers have been making considerable strides recently.

For small aggregations of ions isotropically confined in a harmonic potential the calculations are almost trivial, yet a number of the minimum-energy configurations have been reported incorrectly until recently [5,6]. This Hamiltonian corresponds to J. J. Thomson's classical pre-quantum-mechanics model of the atom and the configurations are shown in figure 1. Note that the charges are equidistant from the origin up to 12 ions, but the 13th ion

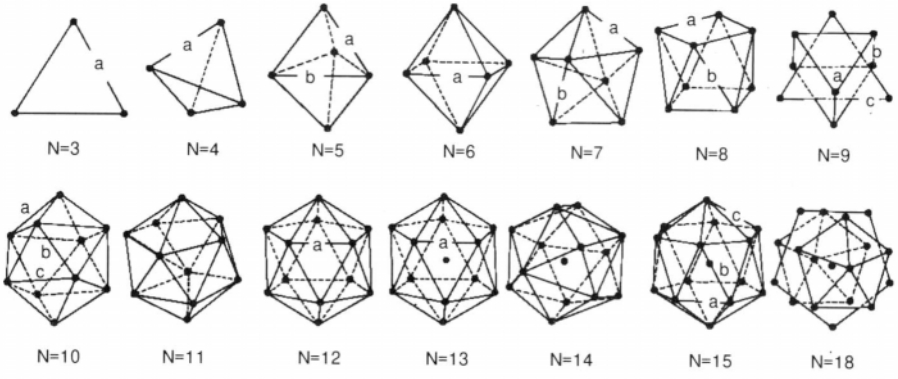


Fig. 1 Minimum energy configurations for few ions in isotropic confinement from ref. 6.

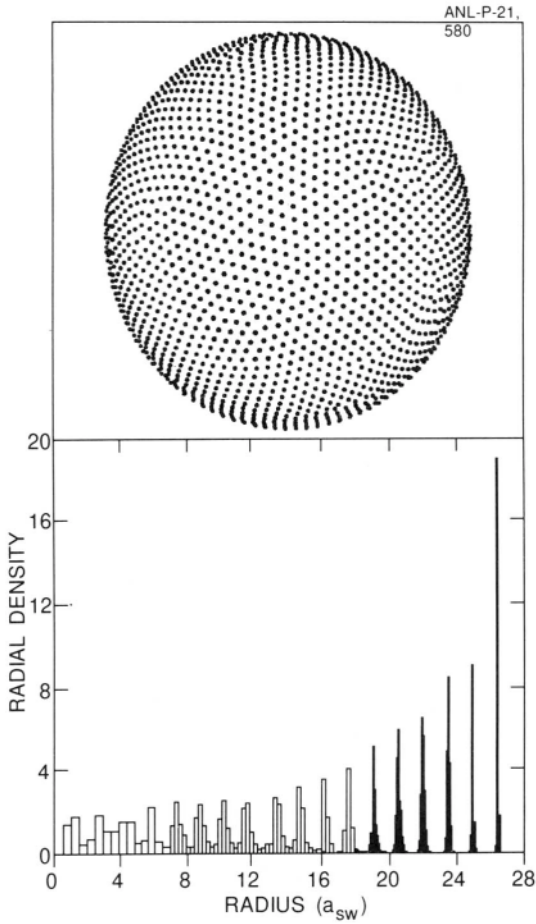


Fig. 2 View of outer surface, and interior radial density distribution of a simulation of 20000 ions in isotropic confinement.

prefers to sit at the origin. This has little to do with the symmetric icosahedron -- it is simply the consequence of 12 being the last integer smaller than 4π . Since the minimum energy configuration requires the ions to be as nearly equidistant as possible, the 13th ion sits at the center. For larger numbers of ions both the outer shell grows further, and slowly more ions join the first one in the interior until for 61 ions the last one again sits at the origin with two shells outside it.

With larger ion clouds the configurations are qualitatively similar: a set of concentric shells with approximate order on each one but no particular order between shells except for constant spacing. The case of 20000 ions in isotropic confinement is shown in figure 2 where 18 concentric shells are discernible in the system. Is there a sharp phase transition as a function of temperature for such systems? The answer is in figure 3 which shows the gradual cooling of a cloud of 1000 ions in isotropic confinement. It seems that an outer crust forms first at the surface of the space-charge limited ion cloud, then the interior layers form gradually, the shells becoming sharper as the temperature is lowered, but the shell widths seem to reach a limit, with the outer shell substantially sharper than the others. No sharp change in the shell structure is found with temperature in the simulations.

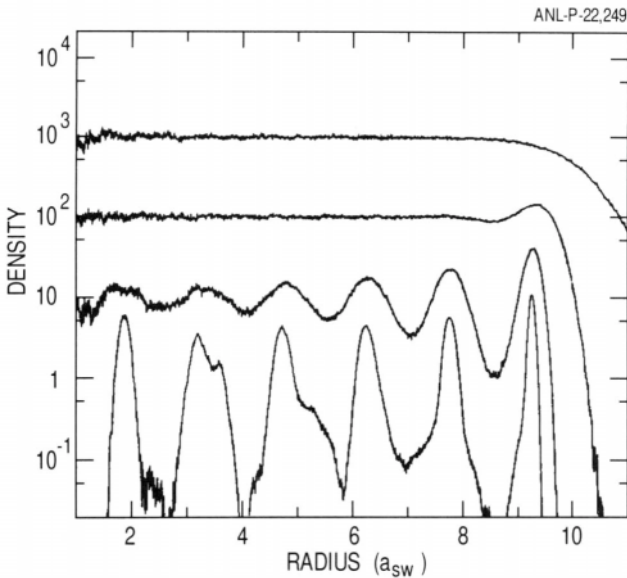


Fig. 3 Radial density profiles of simulations of a 1000 ion cloud in isotropic confinement at various temperatures, corresponding approximately to $\Gamma = 0.1, 10, 100, 10,000$

Now when the ion clouds become anisotropic the cloud takes on a spheroidal shape. But this is not just a matter of concentric spheroids as the consideration of simple systems will show. In the limit, for a relatively very weak restoring force along the z axis, all ions will sit on this axis along a line, though not equally spaced. As this force is increased, there is a distinct point where a two-dimensional configuration is favored, and the ions form a zig-zag pattern, starting at the center. With the force increasing further, another point causes a three-dimensional configuration to be favored. These sharp transitions show all the characteristics of *dimensional phase transitions* [7] and are illustrated for 70 ions in figure 4. In the limit of a relatively very strong force in z the system will again become a two-dimensional pancake at $z = 0$.

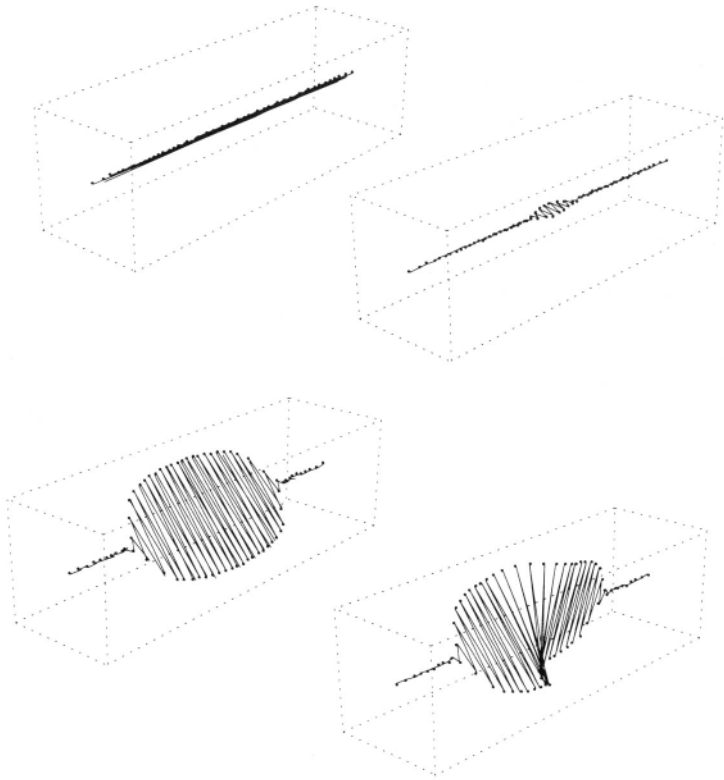


Fig. 4 Simulation of the configurations of seventy ions in anisotropic confinement showing the dimensional transitions as the strength of the confining force in the longitudinal direction is increased, from ref. 7. The transverse dimensions are increased by a factor of ten compared to the longitudinal.

For large systems with anisotropic fields there are many more complicated transitions - and a cloud can have linear tails, and go through the transitions from two to three-dimensional structures moving along its axis. A limiting case of interest is where the restoring force in one direction disappears, but a constant density of charges per unit length is maintained, such as in a beam of ions. In this case, the system is very similar -- with a set of concentric cylindrical shells [8].

How large a cloud is needed before the shells give way to the cubic structure characteristic of infinite systems? Recent experiments reported here with very large ($N > 100000$) ion clouds indicate conclusively that an appreciable fraction of the cloud is in a single body-centered cubic crystals. Simulations have not yet caught up with this, largely because for 100000 ions 10^{10} pairwise interactions must be computed at each time step and this is rather expensive of computer time. Short cuts, such as cutoffs or multipole approximations are dangerous -- since the competition between two symmetries depends on the fine details of the energies.

The simple normal modes of these ion clouds [9] are hydrodynamic multipole modes. One of them, the monopole mode or (for non-magnetic traps) volume oscillation, is a true eigenmode of these systems and proceeds without damping. Others (in non-magnetic confinement the volume-conserving shape oscillations), are illustrated in figure 5 and show damping, and this damping is a result of the mixing of the multipole modes with the true

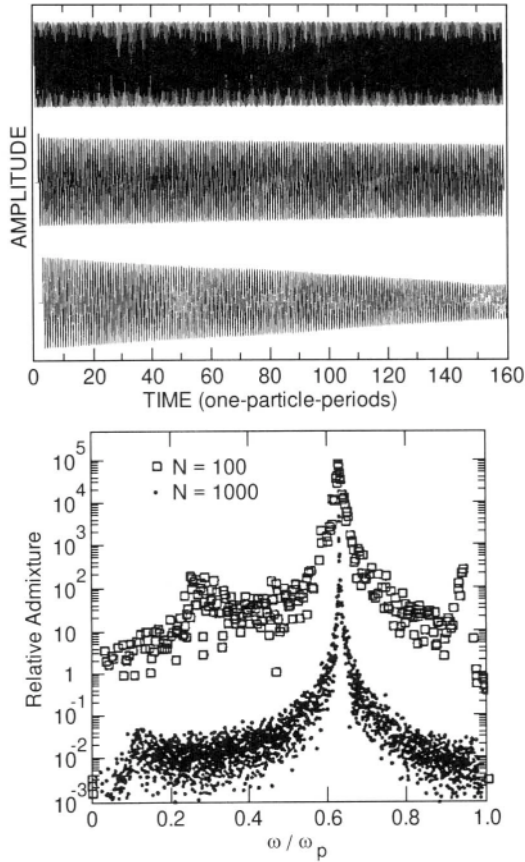


Fig. 5 Various hydrodynamic multipole oscillations induced in the simulation of a 1000 ion cloud. The top figure shows the decay in the amplitude of a monopole, quadrupole and octupole oscillations. The bottom figure shows the decomposition of the quadrupole mode among the true eigenmodes of the system for a 100 and a 1000 ion cloud with the frequencies in units of the plasma frequency, from ref. 9.

eigenmodes of the system. In other words, the multipole modes are those of a charged liquid -- the discrete structure of these clouds only enters into the damping. There are, however, also some (strongly damped) torsional modes that do depend on the discrete ordered structure, since a liquid would not support a shear displacement.

The question of temperature in these systems is an interesting one. In a rotating system, such as a Penning trap, the ion cloud is rapidly rotating and thus in a non-inertial system. The 'temperature' then seems to be the random component of motion in the rotating frame. In the radio-frequency Paul traps the ions are subject to an alternating rf field and the time average of this rf field gives a net confining Hamiltonian. The ions, however, undergo coherent oscillations in this rf field. The question of defining what is meant by a temperature -- from the perspective of the ordering phenomena, for instance, is clearly somewhat fuzzy -- especially since the coherent motion includes shearing movements in different directions between ions and their neighbors. Defining temperatures in these systems is rather delicate -- as a practical matter it is usually done by looking at the velocity spread in the direction that is not affected by the motion (e.g. along the magnetic field in a Penning trap, or perpendicular to the macroscopic motion in rf confinement.)

Quantum effects are not significant in these large clouds. If one were to cool these systems to μK regime it would reach its quantum-mechanical ground state. However the wave functions of the individual ions would extend over a volume that is very small compared to the inter-ionic spacing (typically tens of microns) and so this would be difficult to observe.

This research was supported by the U.S. Department of Energy, Nuclear Physics Division, under Contract W-31-109-Eng-38.

REFERENCES

- [1] S. G. Brush, H. L. Sahlin, and E. Teller, *J. Chem. Phys.* **45**, 2102 (1966)
- [2] E. L. Pollock and J. P. Hansen, *Phys. Rev. A* **8**, 3110 (1973)
- [3] A. Rahman and J. P. Schiffer, *Phys. Rev. Lett.* **57**, 1133 (1986)
- [4] S. L. Gilbert, J. J. Bollinger, and D. J. Wineland, *Phys. Rev. Lett.* **60**, 2022 (1988)
- [5] G. Birkl, S. Kassner, and H. Walther, *Nature* **357**, 310 (1992)
- [6] Robert Rafac, John P. Schiffer, Jeffrey S. Hangst, Daniel H. E. Dubin, and David J. Wales, *Proc. Natl. Acad. Sci.* **88**, 483 (1991)
- [7] J. P. Schiffer, *Phys. Rev. Lett.* **70**, 818-821 (1993)
- [8] R. W. Hasse and J. P. Schiffer, *Annals of Physics* **203**, 441 (1990)
- [9] Daniel H. E. Dubin and J. P. Schiffer, *Phys. Rev. E* **53**, 5249-5267 (1996)

ELECTRON CORRELATIONS IN COULOMB SYSTEMS IN 2 AND 3 DIMENSIONS

A. K. Rajagopal

Naval Research Laboratory,
Washington D. C. 20375 -5320

In this overview, the recent theoretical (and some experimental) works on a variety of physical properties that arise from correlations among electrons interacting via Coulomb interactions in three and two - dimensional systems will be discussed. The subject matter has a long 70 year history which we meander through in this brief presentation, even after exclusion of several important aspects of the problem. The astrophysical and nuclear physics aspects of these problems will not be discussed. The main focus will be concerning issues of condensed matter physics. Also not discussed in this presentation is the important works on the electron correlations based on the Slater-Hubbard model (with a relatively shorter 40-year history) which is central in the recent discussions of strongly coupled systems such as high temperature superconductors and magnetic materials. Excluded also from discussion here is the effects of disorder, which is a separate topic in itself. Included in this talk will be spin-polarization as well as finite temperature effects, in both bulk and semi-infinite situations, and electron-hole plasmas. Interesting physical situations of two-dimensionality occurring in Mosfets, semiconductor heterojunctions, and electrons on cylindrical surfaces as in carbon nanotubules, will be briefly touched upon as they possess rich consequences of correlations. The effects of quantizing magnetic fields and the relativistic situations will only be mentioned in passing. Theoretical techniques used fall basically into five categories in my classification:

- (1) wave function methods - variational and nonvariational,
- (2) phenomenological/intuitive methods subsumed by diagrammatic techniques,
 - (a) collective excitation theory of Bohm-Pines leading to Boson formulation,
 - (b) dielectric formulation of Singwi and coworkers,
 - (c) Fermi liquid theory of Landau, culminating in diagrammatic perturbation theory of Gell-Mann and Brueckner which in various forms contains all these and had important off-shoots,
- (3) Quantum Monte Carlo methods,
- (4) the method of Green functions, and finally,
- (5) density-functional method of Kohn and coworkers.

Each of these had different insights to offer which we will spell out. Very recent work on the single particle Green function will also be discussed because of its implications to several physical properties of the system. A brief discussion of pair correlations and response functions is given as this provides information on collective properties such as plasma and spin wave oscillations, etc.

I. INTRODUCTION

The model of electron gas with mutual Coulomb interactions has been with us ever since the Quantum theory was enunciated as a proto-typical model at the heart of a large number of fields: condensed matter physics (more recently in Chemistry as well via the density functional formalism), astrophysics (Chandrasekhar limit, white dwarfs etc. where relativistic version of the electron gas is employed), physics of one-component plasma, nuclear matter (a different avatara in terms of quark matter), and model field theory. The electron correlations manifest themselves in many ways - originally conceived by Sommerfeld in 1928 [1] as a noninteracting gas obeying the Pauli exclusion principle [2] for explaining properties of metals from its structure to electrical properties. The role of Coulomb interaction and the exclusion principle on the magnetic properties of the electron gas was discussed by Bloch in 1929 [3] based on a discussion of magnetism by Heisenberg earlier in 1928 [4], which in turn was based on the Heitler-London work [5] during 1927-1928 on simple molecules. In 1928, Hartree [6] introduced the famous mean field theory by setting up a many-electron wavefunction without incorporating the Pauli exclusion principle but only invoking electrostatics. This was soon superceded by the proper incorporation of the exclusion principle independently by three different physicists, from different parts of the world, each bringing new methods with their own insights into the problem, all around the same year, 1930: Dirac [7] introduced the density matrix method, showed how the exclusion principle manifests as a new statistics of particles; Slater [8] introduced the antisymmetric (determinantal) wavefunction; and Fock [9] introduced the operator method incorporating the exclusion principle. Slater and Fock introduced also the variational principle and showed how the Hartree result comes about! Dirac and Slater also reported the calculation of the exchange energy of the electron gas. Then came an important contribution from Bloch [10] in 1928 incorporating the periodic arrangement of atoms to describe the real solid, resulting in the idea of band structure for the electrons, thus replacing the simple free electron spectrum used by Sommerfeld. (This Bloch theorem was known to mathematicians as Floquet's theorem.) Wilson [11] in 1931 using just the bands extended the Sommerfeld model to study the electronic properties of semiconductors. In 1934, Wigner [12] showed that at low densities the correlation effects would prevent ferromagnetism of the electron gas found earlier by Bloch [3] but instead would lead to a crystalline antiferromagnetic state. Bardeen [13](1935) introduced the idea of work function associated with surfaces. In 1956, Cooper [14] discovered pairing correlations if the interaction between electrons is attractive and this became the basis for the BCS theory of superconductivity [15], where the attractive interaction comes about because of electron-phonon interaction. Much later, Kohn and Luttinger [16] examined the possibility of Cooper pairing due to the attractive region produced by the screening of the interactions. More recently, in high temperature superconductors, the superconductivity is expected to be arising from electron correlations alone! Overhauser [17] in 1962 showed that in the Hartree-Fock approximation, a broken symmetry solution for the unscreened Coulomb electron gas appears as a ground state in the form of static spiral spin density wave (SOW), with the pitch of the spiral $Q=2k_F$, the diameter of the Fermi sphere. This was shown to be prevented by electron correlations when the Coulomb interactions are screened by Rajagopal [18,19], who besides formulating this in a Green function form, also examined the collective excitations of such a system. It should be remarked, various types of SDW states are now part of the subject matter of magnetic states of metals and alloys (Fawcett, [20]), with the concept of nesting at the Fermi surface as an important ingredient in these problems.

Given this history of the correlation problem blossoming into a "theory of everything" at least as far as condensed matter physics and chemistry was concerned, it is

no surprise this activity has not abated even to this day. Like the knife that has been with the family for generations unknown, with its handle changed several times and the blade a few times, the electron gas correlation problem is now appearing in its two-dimensional form in Mosfets, in superlattice structures, or on the cylindrical surface of a carbon nanotubule or even in three-dimensions in laser produced plasmas, and so on. In the more recent density functional theory of condensed matter due in large part to Professor Walter Kohn and his colleagues, this problem has taken a different turn in that it uses the results of the interacting electron gas in all its forms, be it spin-polarized, relativistic, or at finite temperatures. Thus this problem has resurfaced in many avatars!

In the words of the 12th Century Afghan/Persian poet, Jalaluddin Rumi,

MIND DOES ITS FINE-TUNING HAIR-SPLITTING
BUT NO CRAFT OR ART (SCIENCE?) BEGINS
OR CAN CONTINUE WITHOUT A MASTER
GIVING WISDOM TO IT.

(Tr. Coleman Barks, in *The Essential Rumi*(1995)).

I will here try to summarize the wisdom I have gathered from the masters on the topic of my presentation today.

In sec.II, we describe several theoretical approaches to this problem as pertaining to three dimensional infinite as well as semi-infinite systems to cover the bulk and surface properties. In sec.III, we will give an account of the results obtained for systems manifesting two-dimensionality. In sec.IV, we turn our attention to some new results obtained in the investigations of the one-electron Green function which contains important information about the detailed spectral properties of the system as well as yet another new avatara created by Professor Kohn to take into account correlations near spatially varying situations as near a system surface. In sec.V, we address the problem of linear response to external probes such as neutrons or electromagnetic radiation. This opens up another class of problems of great current interest, because of experimental probes of neutron scattering and photoemission are yielding results to be explained and understood. In the final section contains some concluding remarks. In Table I, the Hamiltonian and the system parameters are defined for the sake of completeness. Table II gives a list of topics not covered in this presentation, as some of them are discussed in this Conference by others.

II. THEORETICAL APPROACHES

- Results for infinite and semi-infinite three dimensional systems

A dramatic improvement in the computational power since the 1980s combined with innovative methods of formulating the problem have contributed to better understand the nature of the electron correlations in real systems. At one level, the model of interacting electron gas provides a bench mark for these methods to check against, and at another level of the density functional formalism, they provide input into the starting of the self-consistent scheme for realistic computation of the actual problems of condensed matter beyond the model stage. We here classify these methods into five broad classes and give a brief description of each, highlighting the insight that each of them provide in its wake. We will intermix historical account in the process of such a description, mainly because the various contributions did not appear in any chronological order. The one thing that stands out is the first seminal work of Bohm and Pines in 1953 [21] which spawned an array of

TABLE I: HAMILTONIAN AND THE SYSTEM PARAMETERS

The Hamiltonian for the system is

$$H = T_e + V_{ie} + V_{ee} + V_{ii} + T_i$$

Here T_e : kinetic energy operator of the electrons, V_{ie}, V_{ee} , and V_{ii} : operators representing the Coulomb interactions between the ions (i) and the electrons (e), and T_i : kinetic energy operator of the ions.

Here we consider $V_{ii} = 0$ and $T_i = 0$, and $V_{ie} \neq 0$ providing a non-responsive neutralizing positive charge background.

This model is characterized by the electron density, n , at zero temperature, $T=0$, parametrized by a dimensionless number (in 3-D) defined by

$$n = \frac{k_F^3}{3\pi^2} = \frac{3}{4\pi\alpha_0^3 r_s^3}; \text{ or, } \alpha r_s k_F a_0 = 1, \alpha = \left(\frac{4}{9\pi}\right)^{1/3} \cong 0.521.$$

Equivalently, in terms of the ratio of Fermi energy,

$$E_F = \frac{1}{2}(\alpha r_s a_0)^2, \text{ to Coulomb energy, } e_0: k_F a_0 = \left(\frac{E_F}{e_0}\right)^{1/2}.$$

$$\text{Plasma frequency, } \omega_p / E_F = \left(16\alpha r_s / 3\pi\right)^{1/2}.$$

The system is characterized by the dimensionless temperature, $t=T/T_F$, T_F being the Fermi temperature. At high temperatures, in classical regimes, the system is characterized by the plasma parameter,

$$\Gamma = e_0 / kT,$$

Spin polarization is parametrized by a dimensionless parameter,

$$\zeta = (n_\uparrow - n_\downarrow) / (n_\uparrow + n_\downarrow), \quad n_\uparrow, n_\downarrow \text{ being the density of up and down spin electrons.}$$

Low temperature ($t \sim 0$), high density parametrized by a single r_s , and high temperature ($t \sim \infty$) and high density (corresponding to Classical Plasmas), similarly parametrized by a single Γ ;

High temperature and low density, and low temperature and low density are parametrized by both t and r_s .

We have no known technique which covers all these regimes in a single scheme. (See however Dandrea et.al. [81], who suggest using the ratio of some average energy, $E_{av}(t)$, in place of Fermi energy, to e_0 , in defining the dimensionless parameter above, $E_{av}(t)$ then goes to E_F for $t=0$, and to kT for $t=\infty$.)

TABLE II: TOPICS NOT COVERED

AREA	PROPERTY OF INTEREST
Classical (High temperature regime)	Classical Plasma
Relativistic	Astrophysics (White Dwarfs); Laser induced plasma; systems with Z larger than 50.
Magnetic Field Effects	Quantum Hall Effects
Impurity / Disorder Effects	Localisation properties
Multicomponent systems	Electron -Positron; Electron - Proton ; Electron - Hole plasma by the action of laser on a semiconductor (Si)
Time-dependent properties	Transport phenomena / explicit time- dep.phenomena
Responsive Background (inclusion of vibrating positive charge background) or attractive fermions	Superconductivity
Slater - Hubbard Model	Strong coupled low density electron systems such as High Temperature Superconductors; Insulators; Ferroelectric systems.

many-body techniques from 1957 onwards, beginning with the pathbreaking publication of Gell-Mann and Brueckner (1957)[22], (henceforth denoted as G-MB) making dramatic changes in the way we perceive the correlation problem. One may refer to the collection of papers on these subjects for a more complete appreciation of these developments by Pines [23] and by Morrison [24]. A summary of the methods and their respective insights are given in Table III.

TABLE III: METHODS WITH THEIR RESPECTIVE INSIGHTS

METHOD	INSIGHT
<p align="center">(1) Wave function methods (a) Variational (Jastrow, Conf.Int.) (b) Nonvariational (Coupled Cluster)</p>	<p align="center">(a) Importance of Pair correlations (b) Two particle electron-electron and electron-hole processes.</p>
<p align="center">(2) Diagrammatic Perturbation Method</p>	<p align="center">Separation of Long- and Short- range parts of interaction</p>
<p align="center">(3) Quantum Monte Carlo method</p>	<p align="center">Computer intensive; use of (1) and (2) above makes this method almost exact.</p>
<p align="center">(4) Method of Green function</p>	<p align="center">Includes (2) above; can incorporate finite temperature extension as well as inclusion of inhomogeneous systems.</p>
<p align="center">(5) Density functional method</p>	<p align="center">Density as a variable - includes self-consistency, inhomogeneous systems as well as electron interactions. Can incorporate finite temperature effects also.</p>

(1) Wave function methods

As stated in the introduction, the Rayleigh-Ritz variational method for calculating the ground state energy of the interacting electron gas began with Slater and Fock in 1930. Besides showing the earlier Hartree's electrostatic self-consistent equations follow, using a simple determinantal wave function consisting of single particle orbitals to take account the antisymmetric property of the wave function of the many-electron system, they obtained the well-known Hartree-Fock-Slater self-consistent equations for the orbitals. In this approximation, Slater already noted the important role played by the pair-correlation function in determining the average energy due to the mutual electron interaction. There followed a large number of calculations of properties of systems with varied degrees difficulty which we shall not discuss here because more sophisticated improvements were forthcoming beginning with the introduction of a symmetric wavefunction of two and more particles multiplying the Slater determinant, D, due to Bijl [25], Dingle [26] in 1949, and Jastrow [27] in 1955.

$$\Psi = D \exp - \sum_{i \langle j} u(r_i - r_j). \quad (1)$$

There is a large literature following this but here we focus on its use for electron gas. This choice of wave function immediately drew attention to the importance of pair correlation function in determining the energy due to the Coulomb interaction as well as the kinetic energy of the system which had a further contribution due to triple-correlation function as well. The phenomenological but collective description of electron correlation theory of Bohm-Pines [21] had already yielded very important insights into the problem: the Coulomb correlations could be separated into a long range part of the Coulomb interaction which is described in terms of the collective plasma oscillations, and a short range part, whose form was determined by them. This played a very important role, it must be emphasized, in the development of this as well as the Monte Carlo method to be discussed later, even though the Bohm-Pines theory itself was superceded later by more sophisticated theories of the electron gas. A successful variational calculation of the ground state energy of the electron gas, including the spin polarization, after incorporating the nature of the short range nature of pair interactions, u , in Eq.(1), observed by Bohm and Pines, was given by Zabolitzky [28]. References to other previous attempts at arriving at the ground state energy may be found in this paper.

A nonvariational coupled cluster expansion method pioneered by Freeman [29], Bishop and Luhrmann [30] for electron gas systems is founded on a method due to Coester and Kummel [31] and Cizek [32] almost 17 years earlier. This method is superficially similar to the Jastrow wave function method, Eq.(1) above but employs an operator form for the exponential. The ground state wave function is thus written in the form, in its lowest order, which suffices for our purposes here, and is called the T_2 approximation,

$$\Psi = \exp T_2 \Phi \quad (2)$$

where Φ represents the antisymmetric Slater state and the exponent T_2 consists of all possible particle-particle, particle-hole, and hole-hole interactions. The coefficients appearing here are determined by requiring the wave function given in Eq.(2) to be the solution of the Schrodinger equation. A further approximation involves choosing a subset of the terms in this equation and solving the resulting integral equation. Freeman [29] solved them numerically while Bishop and Luhrmann [30] solved them analytically. The ground state energy of the electron gas as a function of the electron density, both for paramagnetic (spin unpolarized) and magnetic (spin polarized) cases obtained by Freeman are bench mark results. These extend the first work of Bloch result [3] for electron gas, who had found that the gas is either nonmagnetic or fully magnetic below a certain electron density, but when correlations are included the intermediate values of the magnetization appear and the entire density range is moved to much lower densities. This feature was noticed by Rajagopal et.al.[33] at first for screened Coulomb gas; later, this was found in the correlated electron gas when the spin polrized G-MB without making the high density approximation was studied by von Barth and Hedin [34] and more thoroughly by Rajagopal et.al. [35]. A fairly complete account of the results of the use of variational wave functions used in the electron gas problem may be found in Krotschek [36].

The semi-infinite electron gas problem is a model for studying the electronic properties at surfaces. A variational calculation of the above type was performed by Krotschek et.al.[37], and they found the results of surface energy and work function.

The configuration interaction method involves using not one determinant but a linear combination of several determinants whose orbitals and coefficients are determined by the

variational principle. I do not know if any calculation of the electron gas problem has been reported by this method. As can be seen, these methods are computer intensive.

INSIGHT: Central role of two- and three- particle correlations.

(2) Phenomenological/intuitive methods overtaken by diagrammatic techniques

Soon after the appearance of the work of Bohm and Pines [21], several authors reformulated the problem in terms of the dielectric function or the fourier transform of the dynamical pair correlation function of the system. This led to a clearer understanding of the Bohm-Pines phenomenology which contained certain features of cut-off wave vector beyond which the plasmon collective mode should give place to different excitations. For the early discussion of this see, Pines [23]. Also, the work of Gell-mann and Brueckner [22], who developed a diagrammatic approach to the determination of the correlation energy of the electron gas in the high density limit, had recaptured and obtained a clearer picture of the Bohm-Pines results. The subsequent work of Hubbard and others (see Pines [23]) showed some inadequacies of the G-MB theory, in that while it is exact in the high density limit, it may not be good for lower densities, in particular, the static pair correlation function, which is positive for all interparticle separations, was found to be negative at zero electron pair separations at even moderately high densities. This was rectified by an improved theory of the dielectric formulation of Singwi and coworkers (1968 onwards)[38,39], which took into account in a phenomenological way, further corrections needed to the high density theory of G-MB. The major point of the Singwi method is to introduce a new self-consistent scheme which links the dynamic dielectric function to the pair correlation function in two ways, one by the kinetic equation, and two, by the fluctuation-dissipation theorem. While this corrects the problem of the pair correlation function becoming negative at least for densities of interest in condensed matter, it violates the static compressibility sum rule and the high frequency ω^{-4} sum rule. While the first defect could be remedied [39], the second remains a problem. For a discussion of the possible ways of correcting these, one may refer to the work of Kalman [40] and coworkers. Kalman and coworkers have also generalized the Singwi method in two directions, one, to include higher order dynamic correlations beyond the Singwi's second order, and two, to multicomponent plasmas such as solid state electron-hole plasmas and electron-ion plasmas. As far as the author is aware, the Singwi method has not been generalized to spin-polarized electron systems except by an early attempt by the author with D. K. Ghosh [Phys. Letts.30A, 335 (1969)]. Here we encounter three pair correlation functions corresponding to the singlet and triplet correlations which are then related to the corresponding dynamical susceptibilities. There is a superficial resemblance to the multi-component generalization [40] but the physics is entirely different. This remains an open problem, I believe. It should be pointed out that the coupled cluster theory which appeared a decade later and described under the wave function techniques in (1) above, obtained the correct pair correlation functions because in that theory, the interactions among pair excitations in the system were taken into account more completely than before, thus completing the underlying picture of the phenomenology in terms of particle processes.

It is interesting to point out that the collective excitation theory of Bohm-Pines lead to Boson formulation by Arponen and Pajanne [41] and Pajanne [42]. They developed an entire theory of the electron gas by transforming the problem to boson operators and understood the physics of this problem and other related problems of positron annihilation in electron gas, proton in an electron gas etc.in this language. They also obtained satisfactory results for the pair correlations and the ground state energy of the system.

Yet another important phenomenology was put forward by Landau [43] in 1957, called the Fermi liquid theory which focussed on the properties of the system in the important energy region of the system, namely the fermi energy, the quasi-particles, thus

expressing the physical properties of real systems in terms of the various scattering amplitudes at the Fermi energy. In the hands of Luttinger, Kohn, and Nozieres, this theory was justified for real systems possessing nonspherical Fermi surfaces as well, by elevating the diagrammatic perturbation theory of G-MB which in various forms embraced all these with important off-shoots. The reader is referred to an excellent account of these works and the corresponding references in the book by Nozieres [44].

INSIGHT: Enormous simplification and power of the second quantization methods.

(3) Quantum Monte Carlo methods

The quantum Monte Carlo method was used to examine the electron gas problem notably by Ceperley [45], and Ceperley and Alder [46]. This method is based on newer computational techniques using stochastic methods to obtain a variational bound for the ground state energy of the one component electron plasma. The starting trial function is as in (1), the Bijl-Dingle-Jastrow form and an ensemble of a few suitable number of systems are selected from a variational Monte Carlo calculation. The results are obtained both for nonmagnetic and magnetic electron gas and compares very well with those of Freeman [47] using coupled cluster method. This method has been applied to the semi-infinite electron gas problem by Acioli and Ceperley [48] and they found agreement with the earlier variational results of Krotscheck et. al. [37]. The pair-correlation functions at regions close to the surface exhibit anisotropy of the exchange-correlation hole where there is fast-varying densities.

INSIGHT: Powerful use of computer combining (1) with stochastic methods.

(4) Method of Green functions

There are many other properties of the system that one would like to know besides the ground state energy of the system such as the single particle properties. These are contained in the one particle Green function. The theory of these Green functions was put forward by Galitiskii, Migdal, in 1958 [49, 50]. As can be expected from the work using the wave function methods, the equation for the Green function is quite complicated in view of the various contributions from the interactions among the electrons. Symbolically, this equation is written in the form

$$G^{-1} = G_0^{-1} - \Sigma \quad (3)$$

G_0^{-1} represents the noninteracting part of the Green function and Σ represents the contributions due to the interactions in the system, often called the self-energy of the system. With slight modifications, it is also valid for finite temperatures, which we discuss later in this section. Another important feature is the important result of Luttinger and Ward [51] which states that the free energy (or the ground state energy at T=0K) is a functional of G and is stationary with respect to variations in the Green function. Moreover, G contains all information concerning the one particle aspects of the many-particle system: the expectation value of a one-particle operator, the expectation value of the Hamiltonian of the system, which is the total internal energy at finite temperature and reduces to the average energy at zero temperature, a result due to Galitiskii and Migdal [49]. A good knowledge of the self-energy is therefore of great importance. All types of approximations made are reflected in this self-energy. A very useful approximation scheme suggested by Hedin [52] and is known as the GW approximation continues to be employed to this day. It is a way to include dynamic screening of the interactions in a systematic way. In order to make this applicable to realistic systems with numerical feasibility has only been possible in recent years, mainly due to the efforts of von Barth,

Ambladh and their students, who use this GW scheme with remarkable success. More later on this subject.

Holm [53] and Hindgren [54] have been able to obtain the ground state energy of the electron gas for the nonmagnetic and magnetic cases respectively at the same level of accuracy as the variational and Monte-Carlo results discussed above. The spectrum of the single particle excitations are found to be not as reliable so far, however. The reason for this is the realization that the ground state energy is stationary with respect to the variations in the Green function as was shown long ago by Luttinger and Ward [51] in 1960. Much work needs to be done in this area.

Effects of finite temperature can be determined most elegantly by the Green function method. The extension of the G-MB work to finite temperatures with a view to adoption to the density functional theory was given by Gupta et. al., [55] for nonmagnetic case, by Kanhere et. al. [56] for magnetic case, and more recently by Hong et. al. [57], who improved the earlier work [55, 56] by a self consistent calculation of the chemical potential. One feature of these calculations is that the exchange-correlation energy reduces from its zero-temperature counterpart, because of the smearing of the occupation of the states of the system. No attempts were made to find the transition temperature at which magnetism appears in these calculations.

INSIGHT: Better field theoretic approximations in obtaining information obtainable with difficulty by other methods.

(5) Density-functional method of Kohn and coworkers

Hohenberg and Kohn [58] in 1964 showed in the presence of a local, spin-independent external potentials leading to a nondegenerate ground state of a many-body system is a functional of the particle density.

$$E_v[n] = T[n] + W_{Coul}[n] + \int d^3r v(r)n(r) \quad (4)$$

where the first term is the kinetic energy contribution, the second, the Coulomb interaction energy, are universal functionals of the density $n(r)$, not depending on the external potential $v(r)$ of the last term in Eq.(4).

Many generalizations came soon afterwards and over the last three decades it has become a very practical method of studying the inhomogeneous and interacting electron systems of all conceivable forms. For a review of this subject, one may refer to the book of Dreizler and Gross [59] and a more recent collection of contributions edited by Nalewajski [60] in a four volume comprehensive set, covering almost all aspects of this formalism with applications to many areas of physics and chemistry. The major input into this theory is the interacting electron gas results obtained by the methods outlined above.

Before the Monte Carlo calculations for the semi infinite electron gas mentioned earlier, density functional theory was put forward by Lang and Kohn for nonmagnetic surfaces (see a review article on this subject by Lang [61]) and by Pant et.al. [62] and Kautz et.al. [63] for magnetic case. They had found how the magnetization varies near the surface etc.

Since this topic is most likely covered in more detail by Professor Kohn, I will not dwell on it much more.

INSIGHT: "Density" as a variable, simplifying problems enormously in handling both correlations and inhomogeneities in real systems, which could not be handled by the other methods as easily.

III. SYSTEMS MANIFESTING TWO - DIMENSIONALITY

There are two experimental situations in which one had a two dimensional electron gas. One is the electrons on the surface of liquid Helium (Grimes and Adams, [64]), and the other, the electrons attracted to a silicon-silicon dioxide interface by an electric bias field. One may refer to the review article by Ando et.al.[65]. In the last few months, new experimental findings are reported suggesting an unexpected metal-insulator transition at $T \sim 0$ in 2-D electron system. This is speculated to be due to strong electron correlations. The correlation energy of this system was calculated in the spirit of G-MB, by Rajagopal and Kimball [66], in the Singwi-scheme by Jonson [67], in the coupled cluster method by Freeman [47, 68], and by the Monte-carlo method by Ceperley [45]. These authors also calculated various magnetic ground states, in particular essentially confirmed the earlier work of Rajagopal et. al. [35] who had investigated how the magnetic states change as we go from strictly two-dimensions to quasi-two dimensions by calculating the ground state energies of (a) an ideal 2-D electron gas, (b) a quasi 2-D electron gas resembling electrons trapped on a liquid-helium surface, (c) a quasi 2-D electron system resembling inversion layers of Si(100)-SiO₂ system (MOSFETS), and (d) an ideal 3-D electron gas by numerically evaluating the GMB contributions to the correlation energies for all magnetizations and a wide range of electron densities. In (c) the electrons experience finite thickness of the electron gas due to image forces and the bias field, and the calculations were made for two typical values of the depletion density. The transition from nonmagnetic to ferromagnetic is abrupt in (a) and (b), and gradual in (c) and (d). Ceperley found that his results supported these earlier less sophisticated calculations that the ground state of this system may be spin polarized at intermediate densities.

The plasma oscillations in this system was calculated by Stern [69] who found that it goes to zero as the square root of the wave vector unlike in the three dimensions where it goes to the constant plasma frequency. He also calculated the next term in the dispersion. Rajagopal [70] calculated the longitudinal dielectric function including corrections due to exchange contributions, thus improving Stern's work.

More recently, there are many more types of two dimensional electron systems constructed by experimentalists, using semiconductor heterojunctions. These are at least two-well systems unlike the single-well systems considered in the Silicon-Silicon dioxide MOSFETS, and recently this complication has been included in the calculation of the various possible ground states of this quasi-two dimensional electron gas by Radtke et. al. [71]. Because one has two wells, there are more complicated structures to the plasma mode and the ground states, thus generalizing the earlier work on one-well considerations described above [35].

Electrons on carbon nanotubes offer an interesting two-dimensional system as a many-electron problem. The underlying carbon atoms can appear in several helical forms thereby giving the one-electron states moving in this environment the helical wave character. Lin-Chung and Rajagopal [72] incorporated these features and calculated the magnetoplasma oscillations of this system, when a constant magnetic field was applied along the axis of the tubule. They also considered the case of two concentric tubules and incorporated the corresponding inter- and intra-tubule Coulomb interactions between electrons. They classified the magneto-oscillations in terms of the angular momentum around the tubule axis. A complete summary of the methods, systems investigated, results obtained, and their relevance is given in Table IV.

IV. REMARKS ON SOME NEW RESULTS

Green's function: The Green function is usually expressed as the Hilbert transform of a positive definite spectral weight function as follows:

TABLE IV: CORRELATIONS IN THE ELECTRON GAS WITH NON-RESPONSIVE NEUTRALIZING POSITIVE CHARGE BACKGROUND

SYSTEM	TEMPERATURE (T) AND SPIN POLARIZATION ($0 \leq \zeta \leq 1$)	METHOD USED	RELEVANCE ?
3-D (Infinite Space)	All T and all ζ	Gell-Mann and Brueckner	A lowest order "TOE" of Condensed Matter when combined with the Density Functional Theory.
	T=0 and all ζ T=0 and all ζ	Coupled Cluster; Qu. Monte Carlo;	
	T=0 and $\zeta=0$	Green's function	
3-D (Semi - Infinite)	T=0 and all ζ	Coupled Cluster; Qu. Monte Carlo; DFT	Surface Physics
2-D (Infinite Space)	T=0 and all ζ	Gell-Mann and Brueckner; Coupled Cluster	Electrons on Liquid Helium Four
2-D - like (Infinite Space)	T=0 and all ζ	Gell-Mann and Brueckner; Coupled Cluster; DFT	MOSFETS
	T=0 and all ζ	Gell-Mann and Brueckner -like; DFT	Heterojunctions
	T=0 and $\zeta=0$	Gell-Mann and Brueckner -like & Dielectric Function	Electrons on Carbon Nanotubules

$$\begin{aligned}
G(\vec{r}_1, \vec{r}_2; z) &= \int_{-\infty}^{+\infty} \frac{d\omega}{2\pi} \frac{A(\vec{r}_1, \vec{r}_2; \omega)}{z - \omega}, \\
\int_{-\infty}^{+\infty} \frac{d\omega}{2\pi} A(\vec{r}_1, \vec{r}_2; \omega) &= \delta(\vec{r}_1 - \vec{r}_2); \\
A(\vec{r}_1, \vec{r}_2; \omega) &\text{ is the positive definite spectral} \\
&\text{weight function, } z \text{ is a complex number.}
\end{aligned} \tag{5}$$

The singularities in G give us the physical information about the single particle spectral features of the system. For example, the real part of a complex pole in the Green function tells us about the single particle excitation, the corresponding imaginary part, about its life-time, and the residue at this pole, the strength of the excitation. The GW approximation including self-consistency for investigating G has been recently studied by Shirley [73] as well as von Barth and Holmes [74] for the electron gas. The results of these investigations are that the weight of the quasiparticles increased, reducing that of the plasmon satellite; increased the life-time of the quasi-particles, and the plasmon satellite broadened and shifted towards the Fermi level. The next step is to improve the calculations by incorporating vertex corrections. One of the major problems at the present time is to preserve the positive definiteness of the spectral weight, A , in any reasonable approximation proposed. The reader is referred to a review article on the subject by Aryasetiawan et.al. [75] for more implications of this approximation etc. for condensed matter research.

V. RESPONSE FUNCTIONS

The calculation of response functions are of great interest because of their direct relationship to the experimental cross sections for neutron and electromagnetic scattering. This involves complicated integral equations which have not been studied with the same fervor. Rajagopal [19, 76] developed a variational method for studying these equations and found interesting results such as spin wave dispersion in magnetic electron gas, exchange scattering contributions to the dielectric function, etc. An important point to be made here is that the single-particle electron energies must be consistently used in setting up the vertex equations, otherwise one gets wrong results. In the GW approximation mentioned in the previous section, requires corrections to the vertex appearing in the dielectric function for further improvement. Our method of treating the vertex equation may be of some use in this area of research.

Similar vertex functions were set up by Rajagopal [77] for the study of response functions in the spin density functional theory. In an attempt to better understand the pair correlation functions in the magnetic electron gas, Rajagopal et. al. [78], extended the cusp conditions derived by Kimball [79] for anti-parallel spin correlation function. These conditions have been used by Pickett et. al. [80] in developing variational Monte Carlo method for studying partially polarized electron gas for electron densities in the range found in bulk metals. They confirm the suggestion of Rajagopal et. al. [78] that the correlation energy is more sensitive to the anti-parallel spin correlation function than the parallel spin function, so that special attention should be given to improving the antiparallel correlation factor in the Jastrow function.

There is a lot of work yet to be done in this area.

VI. CONCLUDING COMMENTS

In summary, we note that the model of electron gas is the bench mark problem in assessing any new method of computing many-body properties. The methods such as coupled cluster and Monte Carlo now yield mutually agreeable results on the various properties of this system, with the Green function method joining recently this group in providing results of the same accuracy. The importance of understanding and obtaining accurate results concerning this model lies in its use as the starting point of the self-consistent density-functional formalism.

I have given here a personal summary of a modest fraction of a very large body of work on electron correlations in Coulomb gas, also known as Jellium model, over a period of little over seven decades. The work covers topics where I have myself been personally involved more or less directly. I am sure to have missed important contributions to the areas covered as well as those which are currently becoming important and interesting, such as electron correlations in clusters, quantum dots, wires, etc. The implications of the results of the continuing research in this area to understanding problems of condensed matter physics through the density functional formalism, Green function theory, Monte Carlo methods etc. are staggering. Books and collections of reviews on the subject are appearing in a continuous stream and soon it will be an impossible task for one person to give a comprehensive one hour talk including all these works, let alone write even a mild critical review!

ACKNOWLEDGEMENTS

I thank Professor Gabor Kalman for inviting me to make this presentation here and for fully supporting financially my participation in SCCS97. When I accepted this invitation, I did not realize the enormity of this task but I hope I have presented a modest albeit somewhat personally biased version of this gigantic literature. It is a pleasure for me to place on record my indebtedness to all the people who contributed to my understanding of the electron correlations over many years by calling attention to (a) the papers I have coauthored with them, instead of listing their names, and (b) a few from whom I have learned a great deal, but with whom I have not had the privilege of publishing any papers in collaboration as of now, whose names I give here in alphabetical order: Professors Carl-Olof Almladh, Ferdi Aryasetiawan, Ulf von Earth, Walter Kohn, S. D. Mahanti, Mogus Mochena, and Cyrus Umrigar. The warm hospitality at the Department of Theoretical Physics at Lund University, where most of this article was written, is gratefully appreciated. This work is partially supported by the Office of Naval Research.

REFERENCES

1. A. Sommerfeld, *Ibid.* 47, 1, 47 (1928).
2. W. Pauli, *Z. Phys.* 41, 81 (1927).
3. F. Bloch, *Ibid.* 57, 545 (1929).
4. W. Heisenberg, *Ibid.* 48, 619 (1928).
5. W. Heitler and F. London, *Ibid.* 44, 455 (1927); 46, 47 (1927); 47, 835 (1928).
6. D. R. Hartree, *Proc. Camb. Phil. Soc.* 24, 89, 111 (1928).
7. P. A. M. Dirac, *Ibid.* 26, 376 (1930).
8. J. C. Slater, *Phys. Rev.* 35, 210 (1930).
9. V. A. Fock, *Z. Phys.* 61, 126 (1930).
10. F. Bloch, *Ibid.* 52, 555 (1928).
11. A. H. Wilson, *Proc. Roy. Soc. (London)* A133, 458 (1931).

12. E. P. Wigner, Phys. Rev. 46, 1002 (1934); E. P. Wigner and J. Bardeen, Ibid.48, 84 (1935).
13. J. Bardeen, Ibid. 49, 653 (1936).
14. L. N. Cooper, Ibid. 104, 1189 (1956).
15. J. Bardeen, L. N. Cooper, and J. R. Schrieffer, Ibid. 108, 1175 (1957).
16. W. Kohn and J. M. Luttinger, Phys. Rev. Lett. 15, 524 (1965).
17. A. W. Overhauser, Ibid. 128, 1437 (1962).
18. A. K. Rajagopal, Ibid. 137, A1429 (1965); see also, P. A. Fedders and P. C. Martin, Ibid. 143, 245(1966).
19. A. K. Rajagopal, Ibid. 142, 152 (1966).
20. E. Fawcett, Rev. Mod. Phys. 60, 209 (1988) and references therein. For an earlier review and bibliography, see A. Arrott, *Antiferromagnetism in Metals and Alloys* (1966) Vol.II, Part B, and C. Herring, *Exchange Interactions Among Itinerant Electrons*(1966) Vol.IV, in the Rado-Suhl series on MAGNETISM, Academic Press, New York.
21. D. Bohm and D. Pines, Ibid. 92, 609 (1953).
22. M. Gell-Mann and K. A. Brueckner, Ibid. 106, 364 (1957).
23. D. Pines, *The Many-Body Problem*, W. A. Benjamin, Inc. (New York) (1961).
24. H. L. Morrison, *The Quantum Theory of Many-Particle Systems*, Gordon and Breach, (New York) (1962).
25. A. Bijl, Physica 7, 869 (1940).
26. R. B. Dingle, Phil. Mag. 40, 573 (1949).
27. R. Jastrow, Phys. Rev. 98, 1479 (1955).
28. J. G. Zabolitzky, Phys. Rev. B22, 2353 (1980).
29. D. L. Freeman, Ibid. B15, 5512 (1977).
30. R. F. Bishop and K. H. Luhrmann, Ibid. B17, 3757 (1978).
31. F. Coester and H. Kummel, Nucl. Phys. 17, 477 (1960).
32. J. Cizek, J. Chem. Phys. 45, 4256 (1966).
33. A. K. Rajagopal, H. Brooks, and N. R. Ranganathan, Suppl. Nuovo Cim.(I) 5, 807 (1967).
34. U. von Barth and L. Hedin, J. Phys. C5, 1629 (1972).
35. A. K. Rajagopal, S. P. Singhal, M. Banerjee, and J. C. Kimball, Phys. Rev. B17, 2262 (1978).
36. E. Krotscheck, Ann. Phys. (NY) 155, 1 (1984).
37. E. Krotscheck, W. Kohn, and Guo-Xin Qian, Phys. Rev. 32, 5693 (1985).
38. K. S. Singwi, M. P. Tosi, R. H. Land, and A. Sjolander, Phys. Rev. 176, 589 (1968).
39. K. S. Singwi in *Strongly Coupled Plasmas*, edited by G. Kalman, Plenum Press, (New York)(1978), p.259.
40. G. Kalman in *Strongly Coupled Plasmas*, edited by G. Kalman, Plenum Press, (New York)(1978), p.143.
41. J. Arponen and E. Pajanne, Ann. Phys. (NY) 91, 450 (1975).
42. E. Pajanne, Ph. D. Thesis, Helsinki (1982).
43. L. D. Landau, Soviet Physics JETP, 3, 920 (1957); Ibid. 5, 101 (1957); Ibid. 8, 70 (1959).
44. P. Nozieres, *Theory of Interacting Fermi Systems*, W. A. Benjamin, Inc. (New York) (1964), references therein.
45. D. Ceperley, Phys. Rev. B18, 3126 (1978).
46. D. M. Ceperley and B. J. Alder, Phys. Rev. Lett. 45, 566 (1980).
47. D. L. Freeman, Solid St. Comm. 26, 289 (1978).
48. P. H. Acioli and D. M. Ceperley, Phys. Rev. B54, 17199 (1996).
49. V. Galitiskii and A. Migdal, Sov. Phys. JETP, 7, 96 (1958).
50. V. Galitiskii, Ibid. 7, 104 (1958).
51. J. M. Luttinger and J. C. Ward, Phys. Rev. 118, 1417 (1960).
52. L. Hedin, Phys. Rev. 139, A796 (1965).

53. B. Holm, Ph. D. Thesis, Lund (1997).
54. M. Hindgren, Ph. D. Thesis, Lund (1997).
55. U. Gupta and A. K. Rajagopal, Phys. Repts. 87, 259 (1982) and references therein.
56. D. G. Kanhere, P. V. Panat, A. K. Rajagopal, and J. Callaway, Phys. Rev. A33, 490 (1986).
57. S. Hong and G. D. Mahan, Ibid. B53, 1215 (1996).
58. P. Hohenberg and W. Kohn, Phys. Rev. 136B, 864 (1964).
59. R. M. Dreizler and E. K. U. Gross, *Density Functional Theory*, Springer-Verlag (New York) (1990).
60. Articles in *Topics in Current Chemistry, on Density Functional Theory*, in 4 Volumes, edited by R. F. Nalewajski, Springer-Verlag, (New York), (1996).
61. N. D. Lang, Solid State Physics, 28, 225 (1973), and references therein.
62. M. M. Pant and A. K. Rajagopal, Sol. St. Comm. 10, 1157 (1972).
63. R. L. Kautz and B. B. Schwartz, Phys. Rev. B14, 2017 (1976).
64. C. C. Grimes and G. Adams, Phys. Rev. Lett. 42, 795 (1979).
65. T. Ando, A. B. Fowler, and F. Stern, Rev. Mod. Phys. 54, 437 (1982).
66. A. K. Rajagopal and J. C. Kimball, Phys. Rev. B15, 2819 (1977).
67. M. Jonson, J. Phys. C9, 3055 (1976).
68. D. L. Freeman, J. Phys. C16, 711 (1983).
69. F. Stern, Phys. Rev. Lett. 18, 546 (1967).
70. A. K. Rajagopal, Phys. Rev. B15, 4264 (1977).
71. R. J. Radtke, P. I. Tamborenea, and S. Das Sarma, Ibid. B54, 13832 (1996).
72. P. J. Lin-Chung and A. K. Rajagopal, J. Phys.:Condensed Matter, 6, 3697 (1994); and, P. J. Lin-Chung and A. K. Rajagopal, Phys. Rev. B49, 8454 (1994).
73. E. L. Shirley, Phys. Rev. B54, 7758 (1996).
74. U. von Barth and B. Holm, Ibid. B54, 8411 (1996); erratum Ibid. 55, 10120 (1997).
75. F. Aryasetiawan and O. Gunnarsson, Rep. Prog. Phys. (1997), to appear, references therein. I thank FA for giving me a copy of the early version of this article.
76. A. K. Rajagopal, Phys. Rev. A6, 1239 (1972).
77. A. K. Rajagopal, Ibid. B17, 2980 (1978).
78. A. K. Rajagopal, J. C. Kimball, and M. Banerjee, Ibid. B18, 2339 (1978).
79. J. C. Kimball, Ibid. A7, 1648 (1973); see also, J. Phys. A8, 1513 (1973).
80. W. Pickett and J. Q. Broughton, Phys. Rev. B48, 14859 (1993).
81. R. G. Dandrea, N. W. Ashcroft, and A. E. Carlsson, Ibid. B34, 2097 (1986).

COLLECTIVE EXCITATIONS IN A QUARK–GLUON PLASMA

Michel Le Bellac

Institut Non Linéaire de Nice
1361 Route de Lucioles
06560 Valbonne, France

We use the analogy between ordinary plasmas and the quark–gluon plasma to explain the nature of collective excitations in the latter case. We examine the novel features which are brought by gauge symmetry in the case of collective excitations with fermion or gluon quantum numbers.

INTRODUCTION

The physics of the quark–gluon plasma has been a rapidly expanding subject lately, and it would be impossible to give a general review in a single talk (for a recent review, see e.g., Le Bellac.¹ Thus I have decided to focus the present talk on one specific aspect, the physics of the collective excitations in the quark–gluon plasma. I'll begin with a short introduction, in order to give the physical motivations and to define some basic notions; following common practice in elementary particles physics, I'll use a system of units where $\hbar = c = k_B = 1$.

Quantum Chromodynamics (QCD) is the now accepted theory of strong interactions; in this theory, hadrons (protons, neutrons, pi-mesons...) are made of quarks, which interact by exchanging gauge bosons called gluons, and, most importantly, quarks and gluons carry a new quantum number which has been dubbed color, and which is the analogue of the electric charge in Quantum Electrodynamics (QED). In fact the analogy between QCD and QED is as follows: quarks correspond to electrons, gluons to photons and color to electric charge. The only (but crucial!) difference is that the underlying group is the non-Abelian $SU(3)$ in the case of QCD, while it is the Abelian $U(1)$ in the case of QED. This is the reason why gluons carry color, while photons are electrically neutral.

Hadrons are color neutral (they transform according to the one-dimensional representation of the color group $SU(3)$), while, as explained previously, quarks and gluons are colored objects: they transform according to the representations of dimension 3 and 8 of $SU(3)$ respectively. Confinement means that the only particles which can be observed in nature are color neutral. However, if one heats up a hadronic system at very high temperatures, of the order of 150 MeV, or if one applies to it a strong enough pressure, quarks can be liberated and form, together with gluons, a medium of freely propagating colored particles. The analogy with ordinary plasmas is clear: color neutrality is the analogue of charge neutrality, and freely propagating colored particles in a quark–gluon plasma are the analogue of freely propagating charged particles in an ordinary plasma.

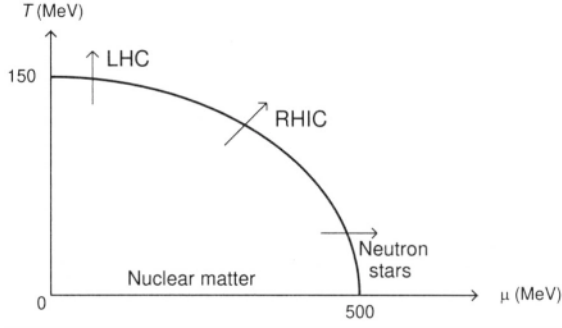


Figure 1. The phase diagram of QCD

The phase diagram of QCD is drawn in figure 1 in the $\mu - T$ plane, where μ is the (baryonic) chemical potential and T the temperature; in this plane, a line separates normal (confined) matter from the deconfined phase. However, although this diagram has been around for more than fifteen years, one must be aware that it is far from being well-established. The only reliable tool for studying the QCD phase transition is lattice simulation, and the non-zero μ part of the phase diagram is out of reach of present lattice simulations, due to the fermion sign problem which was mentioned many times at this Conference. At zero chemical potential, only “pure $SU(3)$,” namely QCD without quarks, is under control in lattice simulations: in that case, one does know that there is a (weakly) first order phase transition (see e.g., Boyd et al.²). However, if one adds quarks, the character of the transition has not yet been established with certainty. Indeed it is quite possible that there is no transition at all, but a smooth cross-over between the confined and plasma phases. The problem is that an order parameter can only be defined in the absence of quarks (the correlator of two Polyakov loops), or in the case of massless quarks (the quark condensate).

ULTRARELATIVISTIC QED PLASMAS

As an introduction to the more complex situations to be treated later on, let me study the case of an ultrarelativistic QED plasma. The particles in the plasma are electrons, positrons and photons, and the electron mass m may be neglected if the temperature is large enough: more precisely one must have $eT \gg m$, where e is the positron charge. For simplicity, I consider only the case of a zero chemical potential, but a non-zero μ could be added without any difficulty. Let me denote by $f(t, \mathbf{x}, \mathbf{k})$ the electron distribution function, for example. It will be convenient to use a four dimensional notation: $x_\mu = (t, \mathbf{x})$, $v_\mu = (1, \mathbf{v})$. The Vlasov equation reads

$$(v \cdot \partial_x) f = -e(\mathbf{E} + \mathbf{v} \times \mathbf{B}) f \quad (1)$$

It is then linearized by writing: $f = f^{(0)} + f^{(1)}$ where $f^{(0)}$ is the equilibrium distribution. Defining an unintegrated electromagnetic current by

$$j_\mu(x, \mathbf{k}) = v_\mu f^{(1)}(x, \mathbf{k}) \quad (2)$$

one obtains from (1) a kinetic equation for $j_\mu(x, \mathbf{k})$

$$(v \cdot \partial_x) j_\mu(x, \mathbf{k}) = -e^2 v_\mu (\mathbf{E} \cdot \hat{\mathbf{k}}) \frac{df^{(0)}}{dk} \quad (3a)$$

From this result one derives the induced electromagnetic current $j_\mu^{\text{ind}}(x)$

$$j_\mu^{\text{ind}}(x) = \int \frac{d^3k}{(2\pi)^3} j_\mu(x, \mathbf{k}) \quad (3b)$$

The last equation (Maxwell equation) is a self-consistency equation, which allows one to compute the electromagnetic field from the external and induced currents

$$\partial^\nu F_{\nu\mu}(x) = j_\mu^{\text{ind}}(x) + j_\mu^{\text{ext}}(x) \quad (3c)$$

where $F_{\nu\mu}$ is the field strength tensor. It is straightforward to write the solution to the kinetic equation (3.b), which can be checked by inspection

$$j_\mu^{\text{ind}}(x) = -e^2 \int \frac{d^3k}{(2\pi)^3} \frac{df^{(0)}}{dk} v_\mu \int_0^\infty d\tau \hat{\mathbf{k}} \cdot \mathbf{E}(x_\mu - v_\mu \tau) e^{-\eta\tau} \quad (4)$$

where the factor $\exp(-\eta\tau)$, $\eta \rightarrow 0^+$ takes care of the adiabatic switching of the external sources. In other words, we are looking for a retarded solution which starts from equilibrium at $t \rightarrow -\infty$. Equation (4) is completely general. Let me now specialize to the ultrarelativistic case: then the velocity v is a unit three-vector $\hat{\mathbf{k}}$, and it is convenient to define a light-like four vector $\hat{K} = (1, \hat{\mathbf{k}})$. In (4) the k and $\Omega_{\mathbf{k}}$ integration decouple, and the k -integration may be performed at once, leading (after summation over electrons and positrons) to

$$j_\mu^{\text{ind}}(x) = 3\omega_p^2 \int \frac{d\Omega_k}{4\pi} \int_0^\infty \hat{K}_\mu \hat{\mathbf{k}} \cdot \mathbf{E}(x - \hat{K}\tau) e^{-\eta\tau} d\tau \quad (5)$$

where $\omega_p = \frac{1}{3}eT$ is the plasma frequency. The retarded photon propagator can be obtained from Kubo's formula

$$\Pi_{\mu\nu}^R(x-y) = \frac{\delta j_\mu^{\text{ind}}(x)}{\delta A^\nu(y)} \quad (6)$$

which leads to the following explicit formula in Fourier space

$$\Pi_{\mu\nu}^R(Q) = 3\omega_p^2 \left(-g_{\mu 0} g_{\nu 0} + q_0 \int \frac{d\Omega}{4\pi} \frac{\hat{K}^\mu \hat{K}^\nu}{Q \cdot \hat{K} + i\eta} \right) \quad (7)$$

This result was obtained long ago by Silin.³

FIELD THEORETICAL FORMULATION

The field theoretical approach to the previous results has been worked out by Blaizot and Iancu.⁴ The main advantage of this approach is that it allows one to generalize the set of equations (3.a,b,c) to the case of fermions and gluons. The strategy consists in finding a consistent approximation scheme to the Schwinger–Dyson (SD) equations of motion. The SD equations are the field-theoretical analogue of the BBGKY hierarchy in classical dynamics: they relate mean fields to two point functions, two-point functions to three point-functions etc. Of course, as in the case of the BBGKY hierarchy, one must truncate the SD equations in order to obtain a manageable scheme. Let me explain the method in the more familiar QED case; the electromagnetic mean field $\langle A_\mu(x) \rangle$ and the fermion mean field $\langle \psi(x) \rangle$ will be denoted by $A_\mu(x)$ and $\psi(x)$. In the Maxwell equation (3.c), the induced current is given by the two-point function $\langle \bar{\psi}(x) \gamma_\mu \psi(x) \rangle_c$, where “c” stands for “connected” and γ_μ is a Dirac matrix. This induced current is related to the momentum integral of a Wigner transform of the electron propagator $S(x,y) = \langle \bar{\psi}(x) \psi(y) \rangle_c$; this Wigner transform depends on a slow variable $X = \frac{1}{2}(x+y)$ and a fast variable $s = x-y$, which is conjugate to the momentum K . Thus the induced current is given by an equation similar to (3.b), where the unintegrated induced current $j_\mu(X, \mathbf{k})$ is now interpreted as a Wigner transform. Finally the SD hierarchy

is truncated by putting to zero the three-point functions and a gradient expansion is performed in the variable X .

The physics behind these approximations relies on the existence of two well separated energy scales in the perturbative limit $e \rightarrow 0$. There are “hard” particles with energy $\sim T$ (the particles of the heat bath) and “soft” collective modes, or mean fields, with typical energy $\sim eT \ll T$. In the gradient expansion which was mentioned previously, $\partial_s \sim T$, while $\partial_X \sim eT$. In the field theoretical approach, the x -derivative in the kinetic equation (3.a) becomes a derivative with respect to X , namely the ordinary derivative ∂_X ; in more complicated cases, kinetic equations will involve the covariant derivative $D_X^\mu = \partial_X^\mu + ieA^\mu$: see eqs (9.a) and (13). One may show that, in an approximation scheme consistent with gauge invariance, both terms of the covariant derivative must be of the same order of magnitude, and this implies that the field A characteristic of collective excitations must be of order T . Now, if one applies on a hard particle a force $eE \sim e \partial_X A \sim e^2 T^2$ during a time interval $\sim 1/eT$ typical of the collective modes, the momentum variation of the hard particle $\Delta p \sim eT \ll T$ so that the hard particle motion remains essentially undisturbed by its interaction with the collective modes. The collective excitations may be treated as classical, while the single particle degrees of freedom remain quantum. Genuine quantum effects, such as pair production and off-shell effects enter at the next-to-leading order, on the same footing as the collision term.

In the general case, the structure of the equations will be similar to that of eqs (3.a,b,c). There will be: (a) a kinetic equation for the unintegrated induced current, (b) an equation giving the induced current from a K -integral and (c) an equation connecting the mean field to the induced current. For example, in the case of electrons, the induced current is given by the mean value of a photon-electron two-point function

$$\eta^{\text{ind}}(x) = e \langle A(x) \psi(x) \rangle_c \quad (8)$$

where $A = \gamma_\mu A^\mu$; defining the two-point function $\Lambda_\nu(x, y) = \langle A_\nu(x) \psi(y) \rangle_c$, its Wigner transform obeys a kinetic equation

$$i(\hat{K} \cdot D_X) \hat{\Lambda}(X, K) = e 2\pi \delta(K^2) [n(k_0) + \tilde{n}(k_0)] \hat{K} \psi(X) \quad (9a)$$

where $n(k_0)$ and $\tilde{n}(k_0)$ are respectively the equilibrium photon and electron distributions. The induced current $\eta^{\text{ind}}(x)$ is given by the AT-integral of $\hat{\Lambda}(X, K)$

$$\eta^{\text{ind}}(X) = \int \frac{d^4 K}{(2\pi)^4} \hat{\Lambda}(X, K) \quad (9b)$$

and the equivalent of Maxwell's equations is

$$iD\psi(X) = \eta^{\text{ext}}(X) + \eta^{\text{ind}}(X) \quad (9c)$$

One should notice the similarity of structure between eqs (3) and (9). However there are two important differences between the two sets of equations. First (9.a) involves the covariant derivative, so that both sides of the equation have the same transformation law under local gauge transformations: then the solution of the kinetic equation depends on the parallel transporter

$$U(X, Y) = \exp\left(-ie \int_Y^X dz^\mu A_\mu(z)\right) \quad (10)$$

and reads, as can be easily checked

$$\eta^{\text{ind}}(X) = -im_f^2 \int \frac{d\Omega}{4\pi} \hat{K} \int_0^\infty d\tau U(X - \hat{K}\tau) \psi(X - \hat{K}\tau) \quad (11)$$

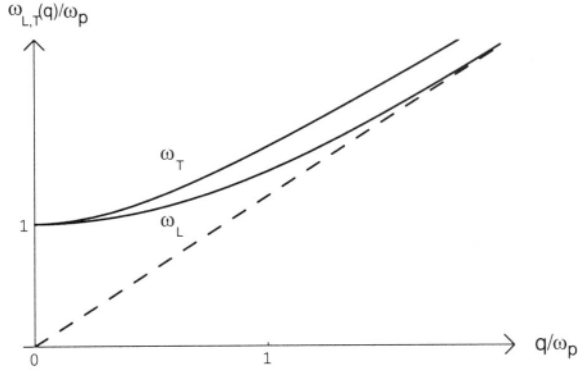


Figure 2. Dispersion law for photons

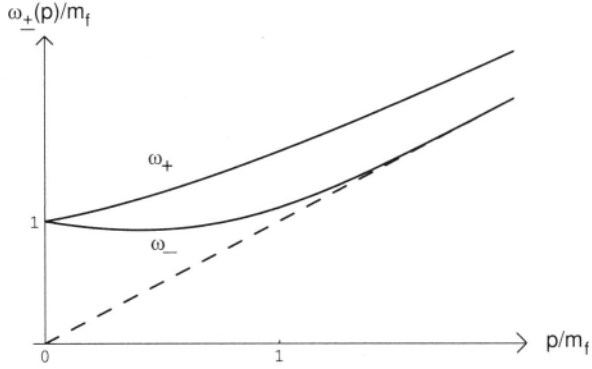


Figure 3. Dispersion law for electrons

where the “electron thermal mass” m_f is given by $m_f^2 = \frac{1}{8}e^2 T^2$. Since U is a non-linear function of A , the induced current will generate, through functional differentiation with respect to ψ and A_μ not only an electron self-energy, but also n -point functions with two electrons and any number of external photons. The explicit expression of the electron self energy is

$$\Sigma(X - Y) = \left. \frac{\delta \eta^{\text{ind}}(X)}{\delta \psi(Y)} \right|_{\psi=A=0} \quad \Sigma(P) = m_f^2 \int \frac{d\Omega}{4\pi} \frac{\hat{K}}{P \cdot \hat{K}} \quad (12)$$

Secondly, (9.a) depends on the electron and photon equilibrium distributions, and not on their derivatives as in (3.a): this means that the interaction of the soft collective modes modifies the quantum number of the hard particles, not their momentum (a hard electron is transformed into a hard photon, or vice-versa), the collective electron excitation providing for the necessary quantum number.

The expressions (7) and (12) of the photon and electron self-energies allow one to compute the dispersion laws of the elementary excitations, which are drawn in figures 2 and 3 respectively. As is well-known, there are two branches in the photon dispersion law, the longitudinal branch and the transverse branch. Much less well-known is the existence of two branches in the electron case; the new branch $\omega_-(p)$ has been sometimes dubbed the “plasmino” branch. It decouples at large momenta, exactly as the longitudinal photon decouples at large momenta; only the vacuum like excitations, namely the transverse photon and the branch $\omega_+(p)$ in the fermionic case, remain coupled at large momenta.

EXCITATIONS IN THE QUARK GLUON PLASMA

After these (lengthy!) preliminaries, I am now ready to write down the results for a non-Abelian gauge theory like QCD; using the notation $A_\mu = \sum_a A_\mu^a T^a$, where the T^a s are color matrices, one can write the kinetic equation obeyed by the unintegrated color current ($K_\mu = (k_0, \mathbf{k})$)

$$\left[K \cdot D_X, J^\mu(X, K) \right] = 2\pi g^2 \delta(K^2) K^\mu K^\nu F_{\nu 0} \frac{d}{dk_0} \left[N n(k_0) + N_f \tilde{n}(k_0) \right] \quad (13)$$

where g is the QCD coupling constant, $N(N_f)$ the number of colors(flavors), $n(k_0)$ ($\tilde{n}(k_0)$) the equilibrium gluon (quark) distribution. The presence of the covariant derivative ensures that (13) is gauge covariant. Since the kinetic equation (13) involves the covariant derivative $D_\mu = \partial_\mu + igA_\mu$, the solution for the induced current $j_\mu^{\text{ind}}(X)$ depends on the parallel transporter $U(X, Y)$

$$j_\mu^{\text{ind}}(X) = 3 \omega_p^2 \int \frac{d\Omega}{4\pi} \hat{K}_\mu \int_0^\infty d\tau U(X, X - \hat{K}\tau) \hat{\mathbf{k}} \cdot \mathbf{E}(X - \hat{K}\tau) U(X - \hat{K}\tau, X) \quad (14)$$

where the plasma frequency is now $\omega_p^2 = \frac{1}{9} g^2 T^2 (N + N_f/2)$. Comparing (5) (6) and (14) one sees that the gluon two-point function is identical, within a numerical factor, with the photon two-point function (7). Thus the dispersion law of collective excitations with gluon quantum numbers will be given again by figure 2. Similarly, the dispersion law of collective excitations with quark quantum numbers will be given by figure 3; one has only to modify the thermal mass, which in the quark case, is $m_f^2 = \frac{1}{8} C_F g^2 T^2$, where $C_F (= 4/3)$ is the Casimir of the quark representation.

However (14) (as well as (11)) depends non linearly on the field A_μ , so that the solution (14) for the induced current generates Green functions with an arbitrary number of external gluons, while the photon four-point function, for example, is identically zero. The remarkable feature of (11) and (14) is that they contain the minimum non-linear effects in the gauge field which are necessary to preserve gauge symmetry.

CONCLUSIONS

The low energy structure and the hierarchy of scales of finite temperature QCD was uncovered before the work of Blaizot and Iancu in a remarkable analysis of Feynman diagrams by Braaten and Pisarski⁵ and independently by Frenkel and Taylor;⁶ this analysis led to the concept of ‘‘Hard Thermal Loops.’’ The main outcome of this analysis is a reorganization of perturbation theory, called the ‘‘effective expansion,’’ which allows one to compute safely many quantities such as transport coefficients, damping rates, production of photons and lepton pairs...,¹ and is able to overcome in almost all cases the difficulties with infrared divergences⁷ and gauge dependence. It seems, however, that difficulties persist in some cases, where the effective expansion does not give the full answer.⁸ Moreover, although asymptotic freedom tells us that QCD becomes certainly perturbative at very high temperatures, in practice T is at most of the order of 3–5 times the critical temperature in heavy ion collisions. Then the QCD coupling constant is not really small ($g \simeq 2$),² so that the hierarchy of scales is not obvious. Nevertheless, one can reasonably hope that the effective expansion gives a good qualitative guide to perturbative hot QCD.

Acknowledgements

I would like to thank Jean-Louis Meunier for his help with LATEX, George Batrouni and Thierry Grandou for their careful reading of the manuscript.

REFERENCES

- [1] M. Le Bellac “Thermal Field Theory,” Cambridge University Press (1996)
- [2] G. Boyd et al. *Nucl. Phys.* B469:419 (1996)
- [3] V. P. Silin *Sov. Phys. JETP* 11:1136 (1960)
- [4] J.-P. Blaizot and E. Iancu *Nucl. Phys.* B390:589 (1993) and B417:608 (1994).
- [5] E. Braaten and R. D. Pisarski *Nucl. Phys.* B337:569 (1990)
- [6] J. Frenkel and J. C. Taylor *Nucl. Phys.* B334:199 (1990)
- [7] J.-P. Blaizot and E. Jancu *Phys. Rev.* D55:973 (1997)
- [8] P. Aurenche et al. *Zeit. Phys.* C75:315 (1997)

This page intentionally left blank

HOHLRAUM TARGETS DRIVEN BY CLUSTER ION BEAMS FOR INERTIAL CONFINEMENT FUSION

Claude Deutsch¹, Naem A. Tahir¹, Otto Geb², Joachim A. Maruhn²

¹LPGP (URA 073 CNRS), Bât. 212, Université Paris XI,
91405 ORSAY, France

²ITP, Postfach 111932, Universität Frankfurt,
60054 FRANKFURT, Germany

Correlated ion stopping of charged debris resulting from the fragmentation of energetic cluster ions focussed on Au foam converters is considered for driving indirectly a thermonuclear capsule. The 1D simulation of converter time evolution demonstrates a very high conversion efficiency of projectile energy into hard X ray photons building up a very hot ($T_r > 300$ eV) thermal bath. Intense and energetic cluster ion beams thus demonstrate considerable potential as a novel driver for inertial confinement fusion.

Presently, in the highly active field of inertial confinement fusion (ICF) driven by intense heavy ion beam (HIB) the so-called indirect drive approach is given a lot of attention¹⁻³. It essentially implies a three steps process. The driver energy is first focussed on purposely laterally located converters on a two-sided hohlraum cavity enclosing a smaller and spherical capsule with the thermonuclear fuel deuterium + tritium (DT) in it (see Fig. 1). Then, the converters get heated up after a few nsec irradiation, up to a few hundreds of eV temperature. They fill the hohlraum cavity with hard X rays for 10-12 nsec.

Table 1. Pulse Parameters

Prepulse Temperature	$T_1 = 100$ eV
Prepulse Power	$P_1 = 10$ TW/cm ²
Maximum Temperature	$T_2 = 300$ eV
Maximum Power	$P_2 = 830$ TW/cm ²
Prepulse Duration	$t_1 = 22$ nsec
Main Pulse Duration	$t_2 = 8$ nsec
Shape Factor	$P_1 = 2.0$
Shape Factor	$P_2 = 20.0$

The corresponding photons then gradually thermalize with a radiative temperature ~ 300 eV, through repeated bouncings on the casing inner surface enclosing the hohlraum and the capsule outer surface. The given heat bath is then able to provide a highly isentropic compression of the inner capsule. To optimize those processes one has to focus kiloamps of

heavy ions ($V \sim c/3$) on a 3 mm radius spot area on converters, in order to get a huge power deposition P_d . The crux of this well established scenario is that one should transport the ion of masse M_i in a lowest charge state Z_i , in order to minimize space charge effects as well as the triggering of electromagnetic instabilities. On the other hand, the much higher projectile charge Z_i in plasma target secures a beam-target coupling $\sim Z_i^2$ through a standard stopping

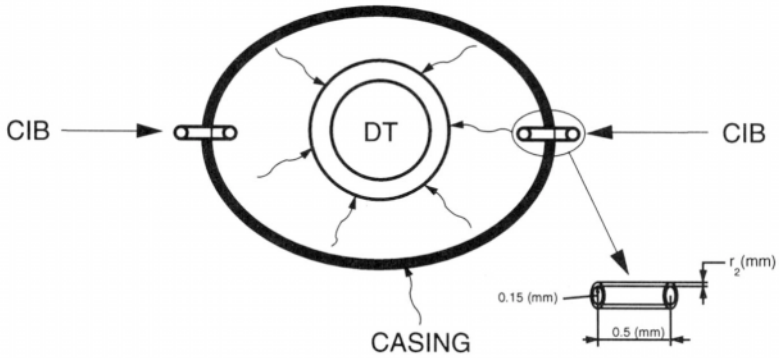


Fig. 1a. Hohlraum design: Target structure with cylindrical Au foam (1g/cc) converters surrounded by a corona (thickness r_2) of solid Au

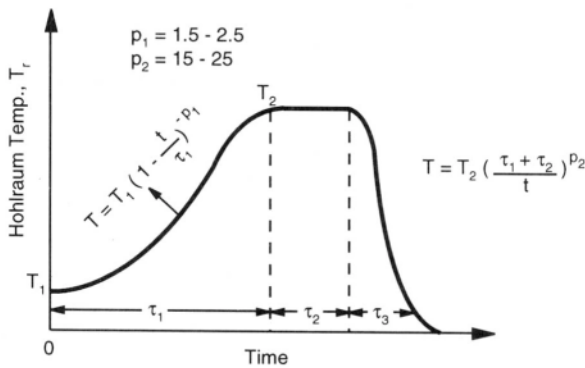


Fig. 1b. Hohlraum design: Pulse shape profile (Table 1)

process in the hot converters. Those rather contradictory requirements on the projectile ion charge could be strongly relaxed or even resolved by considering the focalisation of intense cluster ion beams (CIB). The production, characterization, linear acceleration and even circular storage⁴ of supermolecular arrangements of basic atomic entities is now progressing at a very swift pace^{4,5}. For instance, C_{60}^+ is one of the best known and more robust of them. In contradistinction to atomic ions, there is no M_i limitation for cluster ions. So, one can use them on a much larger $Z_i/M_i \ll 1$ scale, allowing $Z_i > 2$, provided the given structure can sustain linear acceleration or storage⁴. This is indeed the case for C_{60}^{n+} with $-2 \leq n \leq 7$ ⁵.

The CB-converter coupling $\sim (\sum_i Z_i^2)$ features a strongly enhanced and correlated stopping (ECS) arising from inflight and dynamical electrostatic interferences between the ion debris (charge $\sum_i Z_i$) resulting from the initial fragmentation of a cluster ion impacting the target dense electron fluid⁶⁻⁹. The sum over i runs over all those fragments. This

coupling is advantageously contrasted to the usual HIB coupling $\sim (\sum_i Z_i^2)$ corresponding to uncorrelated ion projectiles, in otherwise identical beam-target conditions.

As a result one expects a much shorter penetration in depth. Those specific CIB features have already been used to design highly innovative direct drive scenarios^{6,7}, giving credence to the momentum rich beam concept due to Mashke¹⁰.

Here we intend to unravel their powerful potentialities for the indirect drive approach to ICF.

The much shorter cluster ion ranges makes it possible to envision very thin converter depths accommodating the corresponding very short CIB ranges. A few typical range-energy relationships of related concern are given in Figs. 2 for Au target at various cold matter density. So, in contradistinction to hohlraums¹⁻³ currently designed for heavy ion drivers, a much larger volume is left unoccupied for further isotropization of the thermal photon bath around capsule and converters.

The stopping data displayed in Figs. 2 are then introduced into a 1 D hydrodynamical simulation based¹¹ on the code MULTI to investigating the time evolution of a Au foam cylindrical converter (Fig. 3) 0.15 mm in radius and 0.5 mm long wrapped in a corona (r_2 thick) in solid gold. The latter is expected altogether with a 0.01 g/cc D_2 gas fill in hohlraum to restrict the transverse radial expansion to a few mm only, 10 nsec after the peak CIB illumination has begun according to the pulse shaping featured by Fig. 1b and Table 1.

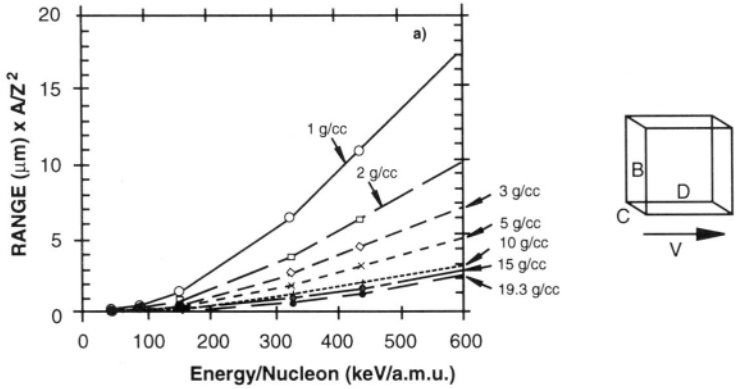


Fig. 2a. Range-Energy relationships for correlated stopping of eight ion debris (charge Z , atomic mass A) on vertices of a 2 atomic unit (a.u.) edge cubic box flowing in foam Au target at several densities with one edge // overall drift velocity.

The specific deposited power P_d is considered in the 10^{18-20} W/g range. Figs. 3 exhibit P_d variations in terms of the coronathickness r_2 parametrized respectively by η , CIB energy conversion efficiency into hard photons and radiative hohlraum temperature T_r . The given converter illumination conditions thus correspond to an energy transfer in the (1-100) MJ range.

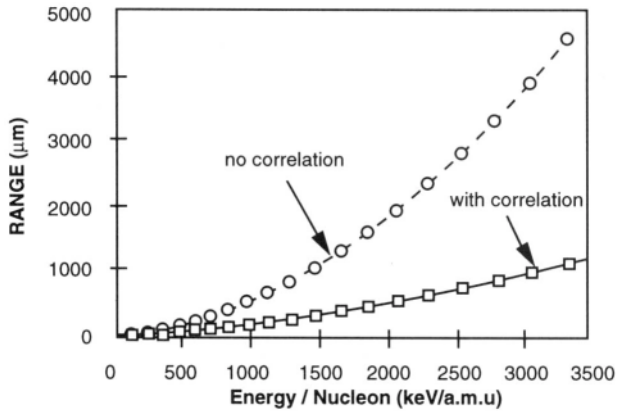


Fig. 2b. As in (a) for $Z = 1$ and gold foam at 1/10 solid density (Table 1)

Envisioning a fullerene (C_{60}) CIB producing ion fragments eightfold correlated in target (Fig. 2), which appears as a reasonable estimate for the fragment distributions available to the presently considered target scenario fixed for instance at 10 MJ irradiation level demands 10 MA of C_{60} on each converter for 8 nsec with a projectile kinetic energy $\cong 1.75 \text{ Mev/a.m.u.}$

The required linear accelerating structures seem to lie within the realm of present technology making use of induction linac facilities provided sufficiently intense cluster ion sources may be developed¹².

Fig. 3a demonstrates that for $r_2 \leq 0.1 \text{ mm}$, η ranges between 0.85 and unity. On the other hand, T_r remains remarkably r_2 -independent for $T \cong 300 \text{ eV}$. It increases rapidly with Pd up to values $> 600 \text{ eV}$.

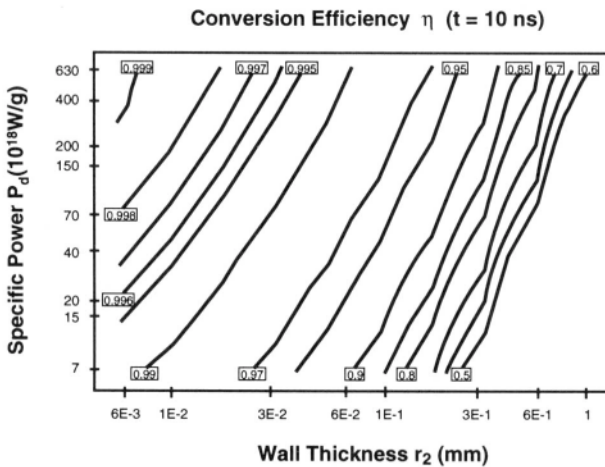


Fig. 3a. 1 D simulation (MULTI) of converters evolution 10 nsec after beginning of peak illumination. Conversion efficiency η of CIB kinetic energy into X rays.

Those results look promising enough to qualify unambiguously CIB as a serious candidate to the indirect drive approach for particle driven fusion.

They also secure a swift thermalization of the produced hard photons in the hohlraum.

The issues of conversion and symmetrization have been also considered at length. It has been shown that in a simple two converters configuration it is not possible to achieve the high level of 98% symmetry in the radiation field.

However, more sophisticated configurations including radiation shields placed at appropriate places in the hohlraum, make it possible to reach this required symmetry level¹³. Then the problem of capsule implosion can be reduced to a 1D problem handled with a three-temperature computer code^{14,15} providing simulation results of compression, ignition and thermonuclear burn of a typical reactor-size target.

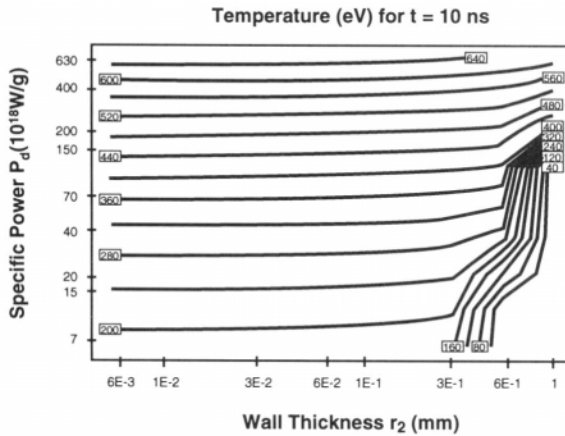


Fig. 3b. 1 D simulation (MULTI) of converters evolution 10 nsec after beginning of peak illumination. Hohlraum radiative temperature T_r .

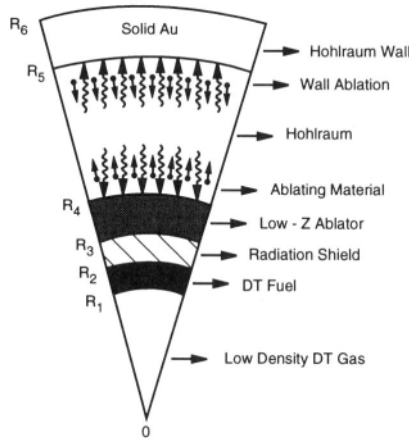


Fig. 4a. 1 D simulation of inner capsule compression. Capsule design (Table 2)

The target initial conditions are shown in Fig. 4a while the target initial parameters are presented in Table 2. The target consists of a fusion capsule that contains 5 mg solid DT shell whose inner radius is 3.02 mm and is filled with a low density DT gas. The fuel shell is followed by a radiation shield made of a low-Z material doped with high-Z atoms. The advantages of using such a radiation shield instead of a pure high-Z radiation shield have already been presented¹⁵. The radiation shield is followed by a carbon ablator shell. The

capsule is enclosed in a solid gold casing and the radius of this hohlraum casing is three times the outer capsule radius. The cavity is filled with a black body radiation characterized with a radiation temperature T_R which varies in time as shown in Fig. 1b. This shaped input pulse is essential to achieve a high target gain^{16,17}. The precise pulse parameters used in this set of calculations are given in Table 1. The heat bath radiation ablates the material from the capsule surface that generates an ablation pressure which is responsible for driving the implosion.

Table 2. Capsule and Target Parameters

Inner Fuel Radius	$R_1 = 3.020$ mm
Outer Fuel Radius	$R_2 = 3.206$ mm
Outer Rad. Shield Radius	$R_3 = 3.248$ mm
Outer Ablator Radius	$R_4 = 3.516$ mm
Hohlraum Radius	$R_5 = 10.510$ mm
Hohlraum Wall Thickness	$R_6 - R_5 = 15.0$ μm
DT Fuel Mass	5.0 mg
DT Fuel Density	0.224 g/cm ³
Rad. Shield Density	2.000 g/cm ³
Rad. Shield Mass	11 mg
Ablator Mass (Solid C)	85 mg
Ablator Density	2.20 g/cm ³
Casing Mass (Solid Au)	396 mg
Casing Density	19.3 g/cm ³

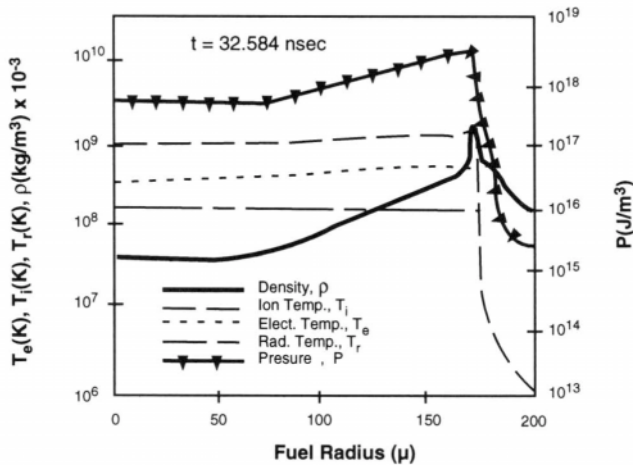


Fig. 4b. 1-D simulation of inner capsule compression. Final compression stage. The ignited hot spot spreads all over the compressed fuel.

In Fig. 4b we plot the electron temperature, T_e , the ion temperature, T_i , the radiation temperature, T_r , the density, ρ and the pressure P vs the capsule radius at $t = 32.584$ ns, when burn has spread into the entire DT fuel. The latter has then absorbed 3.8 MJ radiation energy while about 5.6 MJ radiation energy is lost to the casing, when the target gets 9.4 MJ of CIB kinetic energy. The implosion is shown to yield 965 MJ output energy with a capsule gain $G_C \sim 254$. The overall target gain drops to a still handsome $G_t \cong 100$.

In summary, we have conducted the first investigation of indirectly driven ICF through intense cluster ion beams. Making use of much shorter ion ranges in uniformly irradiated converters, we have been able to demonstrate an unusually high conversion efficiency of projectile kinetic energy into hard X rays altogether with a radiation temperature in the 300-600 eV for a driver energy spanning the [1-100] MJ interval. We expect those encouraging results to foster more investigation on the production and acceleration of intense cluster ion beams.

REFERENCES

1. J.D. Lindl, *Phys. Plasmas* 2: 3933 (1995).
2. J.D. Lindl, R.O. Bangerter, J.W.-K. Mark, and Y.L. Pan, *AIP Conf. Proceed. 152: Heavy Ion Inertial Fusion*, Eds. M. Reiser, T. Godlove, and R. Bangerter (American Institute of Physics, New York (1986), and also
D.-M. Ho, J.D. Lindl, and M. Tabak, *Nucl. Fusion* 34: 1081 (1994).
3. M. Murakami, and J. Meyer ter Vehn, *Nucl. Fus.* 31: 1315 (1991).
4. See for instance, *Science* 271: 877 (1996) also
M. Larsson, *Rep. Prog. Phys.* 58: 1267 (1995).
5. P. Scheier, and T.D. Märk, *Phys. Rev. Lett.* 73: 54 (1994).
6. C. Deutsch, and N.A. Tahir, *Phys. Fluids B* 4: 3735 (1992).
7. S. Eliezer, J.M. Martinez-Val, and C. Deutsch, *Laser Part. Beam* 13: 43 (1995).
8. N.A. Tahir, D.H.H. Hoffmann, J.A. Maruhn, and C. Deutsch, *Nucl. Instr. Meth. B* 88: 127 (1994).
9. C. Deutsch, *Phys. Rev. E* 51: 632 (1995) and also
C. Deutsch, C., and P. Fromy, *Phys. Rev. E* 51: 632 (1995).
10. A.W. Maschke, *Proceeding of HIF 84 International Symposium on Heavy Ion Fusion*, Tokyo (1984) (Institute for Nuclear Study, University of Tokyo (1984), p. 168.
11. R. Ramis, R. Schmalz, and J. Meyer-ter-Vehn, *Comput. Phys. Comm.* 49: 475 (1988).
12. R.O. Bangerter, *Nuo. Cim.* 106 A: 1445 (1993).
13. K.H. Kang, K.-J. Lutz, Tahir, N.A., and J.A. Maruhn, *Nuovo Cimento* 106 A: 1865 (1993).
14. N.A. Tahir, K.A. Long and E.W. Laing, *J. Appl. Phys.* 60: 898 (1986).
15. N.A. Tahir, *et al.*, *Nucl. Fusion*, 32: 581 (1982).
16. R.E. Kidder, *Nucl. Fusion* 19: 223 (1979).
17. S.J. Bodner, *J. Fusion Energy* 1: 219 (1981) .

This page intentionally left blank

DENSE HYDROGEN AT HIGH AND LOW TEMPERATURES*

N. W. Ashcroft

Cornell Materials Science Center and Laboratory of Atomic and Solid State
Physics
Cornell University
Ithaca, NY

Hydrogen, at near 9-fold compression and at low temperatures, conforms to a time-averaged state of crystalline symmetry. By shock methods it can be transiently taken into a state of continuous symmetry which, at approximately the same compression, is at a temperature equivalent to about 0.27 eV. Here it is reported to be significantly conducting, and an appraisal of this state via band-theory suggests that it is not inconsistent either with the electronic character typical of a significantly excited narrow gap semiconductor or, with less certainty, a band-overlap semimetallic state. These states develop from low temperature phases representable by a Landau theory formulated in terms of the order associated with three principal domains, one a crystalline but rotational state, the second a crystalline but highly librating phase, and the third a self-sustaining crystalline assembly of dipoles augmented with significant dynamic polarization.

INTRODUCTION

Some 99 years ago Sir James Dewar succeeded in producing the first *condensed* phase of hydrogen in the laboratory, an insulating liquid state at low temperatures. It is in the same liquid phase, but at high temperatures *and* high densities that a significantly conducting state has been reported. Hydrogen is hardly massive, and quantum effects are not trivial even under the conditions of this measurement. A standard measure is the thermal deBroglie wavelength which for atomic hydrogen is 1.85 Bohrs at room temperature, 5.85 Bohrs at 30K, and importantly for what follows, 0.585 Bohrs at 3000K. Until recently the solid phase structure of dense hydrogen could be summarized by Figure 1a, a largely low temperature and quantum product of many careful crystallographic, Raman and infrared scattering experiments. Up to about 100 Gpa (1 million atmospheres) and for relatively low temperatures hydrogen persists in its common proton-paired or “molecular” conformation, an arrangement where essentially *permanent* pairs appear to be in unfettered rotational states as they go about their vibrational motions, both within the pairs themselves and about the sites of a lattice. This is Phase I, or the low pressure phase. A line separates it from Phase II, or the broken symmetry phase, characterized by the fact that the rotational states of the pairs have evidently become hindered, and they participate in large amplitude librational motion about average directions that are not determined (they may even be disordered). An elegant experiment of Loubeyre *et*

*Work supported by the National Science Foundation.

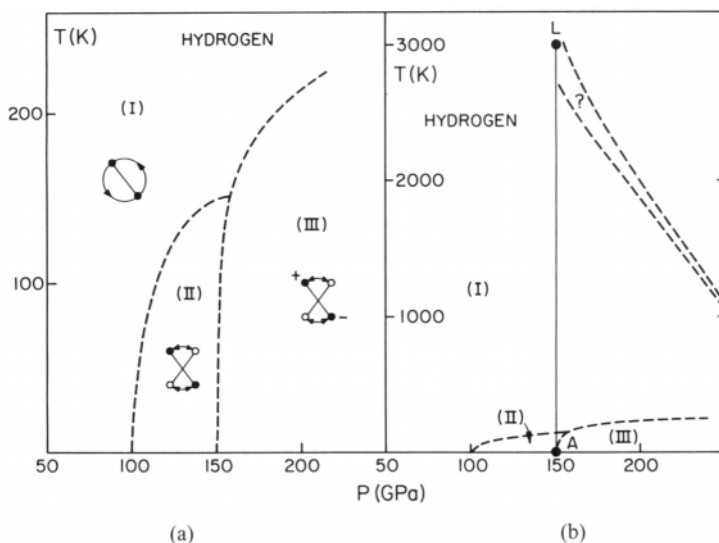


Figure 1. (a) A partial low temperature phase diagram of dense hydrogen showing rotational (Phase I), hindered (Phase II), and hindered and highly infra-red active (Phase III) states. Note that 1 Gpa is equivalent to 10,000 atmospheres, (b) Phase diagram extended to higher temperatures, and showing the point accessed in the experiment of Weir *et al.*⁴ where a conducting state is reported. The dashed region indicates a possible boundary separating conducting from insulating behavior.

*al.*¹ utilizing intense synchrotron x-radiation indicates that the structure itself may be in the hexagonal class, though interpretations in terms of orthorhombic structures are also possible.

Continuing at low temperatures, but moving to higher pressures still, a second line is crossed at 151 Gpa (about 9 fold compression) into a phase of again largely undetermined structure where the proton-pairing is preserved, but the state itself (Phase III, or the HA phase) is significantly different from phase II: the difference is that at a frequency corresponding to the familiar “breathing mode” of the proton pair, Hanfland *et al.*² reported strikingly intense infrared activity, typical of behavior anticipated for permanent distortions of electronic charge, and not expected of the normally quite symmetric arrangements of electron charge usually associated with proton-pairs originating with the molecules we start with at low pressure. The same effect is found in deuterium by Cui *et al.*³ and interestingly enough this infrared activity sets in at the pressure where a noticeable *drop* was earlier found in the Raman shifts; there is little isotope effect at this onset and temperature inexorably drives the infra-red activity away, as recorded in the line separating Phase III from Phase I an observation strongly suggesting that both the development of the infrared activity, and the drop in the vibron, are *collective* properties (they depend on all pairs acting in concert). The experimental situation in the upper reaches of Phase III is not completely clear, something we return to below.

DENSE HYDROGEN: A CONDUCTING PHASE

A quintessential feature of the states represented in Figure 1a is that all are insulating, even though the densities are rising an order of magnitude or more over that of ordinary solid hydrogen and actually into regions of *predicted* metallic behavior. Stated more carefully, all are insulating at the scale of temperatures represented in Figure 1a; for if we fix pressures but proceed towards a much higher scale of temperatures, that is, towards an ostensibly more

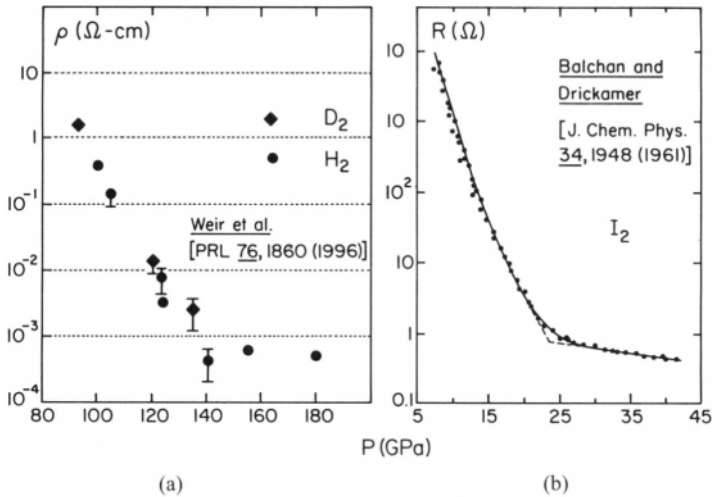


Figure 2. (a) Resistivity of dense hydrogen as a function of pressure as obtained under shock-conditions (temperature is not fixed at different pressures). It is likely that a melting line has been crossed and that the hydrogen is in a fluid state, (b) Resistance of solid iodine as a function of pressure (and at room temperatures). As in Figure 2(a) the evident change in character has been interpreted as an indication of a transition to a metallic state, but actually taking place with pairing preserved.

classical regime (Figure 1b) the experimental situation changes in a very significant way. Recently Weir *et al.*⁴ reported that at 8–9 fold compression, but at some 3000K, hydrogen displays conducting properties. This may at first suggest a line or a band on the phase diagram which, when crossed, could take us into a *metallic-like* region. Standard melting equations indicate that at 3000K this highly compressed form of hydrogen should indeed be in a liquid state. Initial offerings on the character of this liquid are prompted by hydrogen's dual placement in the Periodic Table (both group I and Group VII), that is, fluid states based either on atomic-like particles, or on pairing preferences, as the fundamental elements of a statistical description. These are truly limiting cases, however, and a more reasonable inference is that some intermediate structure is far more likely (e.g monatomic but with strong remnant pairing *correlations*). If this crucial structural issue centering on the degree of permanence of proton pairing can be settled, then in electronic terms an important associated issue concerns the physical nature of the ensuing conducting state. For Weir *et al.* also monitored the resistance and eventually converted it to resistivity; it is shown in Figure 2a as a function of pressure.

In a shock-wave experiment temperature is not constant as pressure increases; nevertheless the changes in resistivity are somewhat reminiscent of those found much earlier in (Group VII) solid iodine (Figure 2b), known to become a metal under increase of density at ordinary temperatures but also known to retain its form as a solid composed of I₂ units. Likewise Weir *et al.* indicate that fluid hydrogen also attains its conducting character with, they report, very little dissociation being recorded. Since hydrogen might also be viewed as a divalent entity its conducting behavior could also be compared with mercury which has also been probed over a wide range of density; again there are qualitative similarities, but also a critical difference for the scattering physics because hydrogen has internal degrees of freedom which can accept energy.

STRUCTURE

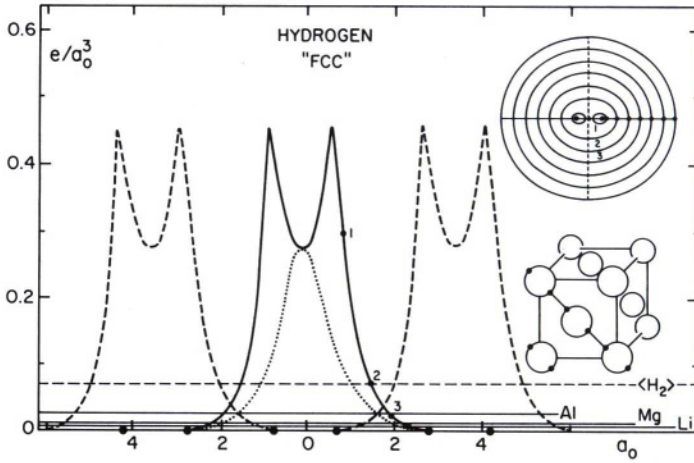
As resistivities go for mercury and many other known liquid metals (usually, it should be stated, at much lower temperatures) the values reported for hydrogen, around $500 \mu\Omega \text{ cm}$ may be considered high. But the conditions of this experiment are intriguing: First, the system becomes extremely dense; typical separations between proton-pairs are comparable to the sizes of the pairs themselves. A common way of representing the density is through the use of the standard parameter r_s , here a linear measure of the average volume available to a proton (for N protons in a volume V we have the defining relation $V/N = (4\pi/3)r_s^3 a_0^3$, where a_0 is Bohr's radius). Thus at one atmosphere and $T = 0$, $r_s = 3.13$; at 9-fold compression $r_s = 1.505$. (Bohr's radii are also the units of Figure 3 which illustrates typical molecular separations in an equivalent crystalline arrangement). Second, the temperature of 3000K, which converts to 0.02 Rydberg units (0.27 eV), is substantial: from equipartition as applied to translational motions the average speed of a proton pair at 3000K is about $6 \times 10^3 \text{ m/s}$; it then takes a mere $3 \times 10^{-14} \text{ s}$ to cross a typical intermolecular separation. Third, an ideal gas at 3000K and with 2.37×10^{23} molecules in a cubic centimeter (corresponding to 9-fold compressed hydrogen) will already be at a pressure of 100,000 atmospheres; the pressures actually achieved are 15 times this reflecting the strength of interactions and associated correlation. Fourth, for kinetic reasons phase transitions, if they exist, can take some time to complete; the experiment is brisk ($\sim 100 \text{ ns}$) and one might well consider the possibility of *mixed* phases should it just transpire that hydrogen has a liquid-liquid phase transition (see below). Fifth, as hinted at above the conditions may be such that the integrity of the molecule itself is not guaranteed. It may opt to dissociate, or the system may even prefer to reconstitute into a phase based on electrons and hydrogen molecular-ions, or other transitory complexes.

Elementary thermodynamics can be brought to bear on molecular integrity: equilibrium between, say, diatomic and monatomic phases would require equality of Gibbs energies per molecule and double the corresponding value per atom, each written as an ideal term augmented by the excess contribution: if $\Delta g_e(p, T)$ is the difference in the latter, then it is straightforward to show that the concentration c of atomic species is approximately

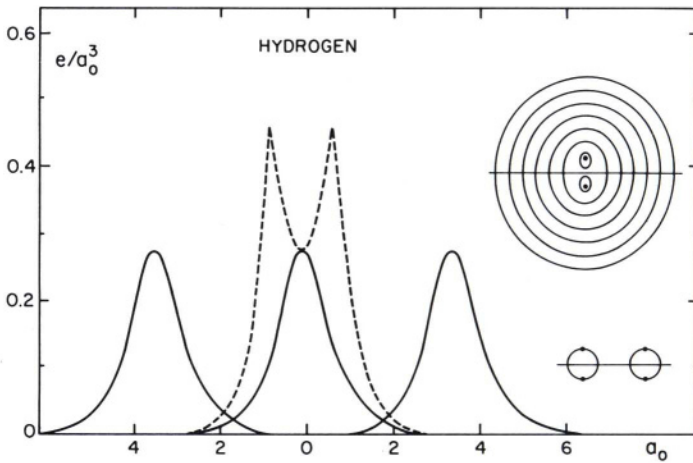
$$c(H) \propto r_s^{3/2} (k_B T)^{3/4} \exp(-\Delta g_e/2k_B T) \quad (1)$$

At quite low densities, Δg_e will just be the dissociation energy of a pair (about 4.8 eV), and even at 3000K the concentration $c(H)$ is small. But the work done in compressing a dense phase of hydrogen by a factor of 9 is substantial, well into the range of an electron volt per proton, and much of it goes into a "weakening of the bond." In a thermodynamic transcription, Δg_e is significantly reduced (it then records the energy of separation but in a dense environment) and (1) then suggests that fragmentation levels can begin to rise very significantly. It provides a basis for the conjecture above on the expected physical character of the high temperature and high density liquid as one in which pairs may be rupturing and reforming constantly, i.e a state intermediate between atomic and paired.

This can also be reinforced by an elementary kinetic argument: In terms of characteristic times an assumption of equipartition (and also of approximate equilibrium) shows that orientational times for the pairs are also about equal to those needed for a pair to transit the intermolecular distances. In other words there must be very considerable entanglement between orientational and translational degrees of freedom. Add to this the fact that the quantum of vibrational excitation energy of a pair rather closely matches the 3000K of the experiment and we see, kinematically, that there is a very favorable situation promoting rapid exchange of energy between pairs. From this the fast exchange mechanisms known to be operative in the notably under-coordinated liquid metallic forms of well studied semiconductors like Si and Ge might also now be the norm for hydrogen. Undercoordination can be a signature of



(a)



(b)

Figure 3. (a) Electronic density in molecules of hydrogen, but arranged on the sites of a fcc-like lattice with a lattice constant chosen to mimic 9-fold compression, the density conditions of the experiment of Weir *et al.*⁴ As can be seen, even under these extreme conditions there is relatively little overlap for the most favorable alignment geometry (indicated in the lower inset). Points 1, 2, 3, *etc.* indicate the values of the contours of density shown in the upper inset (it also shows the cut along the contours). Also given for comparison are the average valence electron densities found in the simple monovalent, divalent and trivalent metals Li, Mg and Al respectively. The line marked $\langle H_2 \rangle$ indicates the *average* electronic density found in hydrogen at 9-fold compression. (b) Electronic density of molecules of hydrogen at the spatial separations of Figure 3(b), but orientationally arranged (lower inset) to *least* favor overlap (the cut along the contours is shown in the upper inset).

the failure of the standard model of simple fluid systems, namely that their configurational energies are comprised mainly of pairwise interactions. Highly covalent systems, with covalency persisting in metallic states, are characterized by very significant three-body and higher interactions. In dense hydrogen, the presence of multi-center interactions are also therefore expected (certainly H_3 is an interesting molecule in its own right).

To get a better idea of average density at 9-fold compression and its consequences, Figure 3 shows the ground-state electron distribution in a single molecule of hydrogen. By placing similar distributions in two relative orientations and at crystalline separations typical of those of the compressions we are dealing with it also makes the point that the changes being wrought by increase of density are literally “in the wings” of the electron distributions. Electron density profiles in crystals are *not* a reliable indicator of non-conducting or conducting behavior; in one-electron terms we need at least a band structure for this in order to establish whether or not an overall energy gap is present. In hydrogen, these abound, but although quite accurate in delivering ground state total energy values for static arrangements, their predictive capabilities for excited states (and hence band gaps) are less satisfactory. Nevertheless, the scale of the gap at 9-fold compression appears to be about an electron volt, depending somewhat on structure.

TRANSPORT

The estimates of band gaps are useful in a beginning assessment of the important role played by thermal effects associated with temperatures which may reach an equivalent of 0.27 eV. A pertinent question is whether dense hydrogen under the conditions of this experiment might be seen as a significantly excited semiconductor (supposing that there *is* a gap, see Figure 4a), or a alternatively as semi-metal, but also one that is significantly excited (supposing there is *not* a gap, see Figure 4c). The question is clearly being posed in the language of independent electrons and for crystalline states; we have to return to the role that correlation plays particularly for disordered states (see below). But for the present, imagine moving along a line such as AL in Figure 1b, where at $A(T = 0)$ the band gap is, let us say from the above, an electron volt, a value not too different from common semiconductors. Persist for the moment with the crystalline phase, but recognize that thermal effects can also affect the band gaps which are themselves, on average, functions of temperature (see below). As temperature increases thermal generation of carriers across these gaps ensues (Figure 4b) and if hydrogen remains crystalline and is of sufficient purity that intrinsic effects dominate (and also that the chemical potential does not wander from the gap region), then the density of either holes or electrons is n_i , where

$$n_i a_0^3 \simeq (1/4)(k_B T / \pi)^{3/2} \exp(-E_g / 2k_B T) \quad (2)$$

Here we are choosing to measure quantities with dimensions of energy (e.g., $k_B T$) in Ry units (13.59 eV) and we are assuming that effective masses are reasonably close to their free electron values. In (1) E_g is an average energy gap under the prescribed thermodynamic conditions, and it is straightforwardly related to the self-consistently determined electron–proton interaction.

Now energy gaps in crystalline semiconductors are well known to depend on temperature, primarily through a reduction originating with a Debye–Waller factor associated with the thermal motion of the ions, here protons. In this case it is determined by *substantial* vibrational and librational motion, and the effects of temperature of the experiment of Weir *et al.* are hardly small, even in a crystalline phase. Given that thermal excitation can also drive libration into full rotational motion (the crossing of the phase line) we see the prospects that E_g can

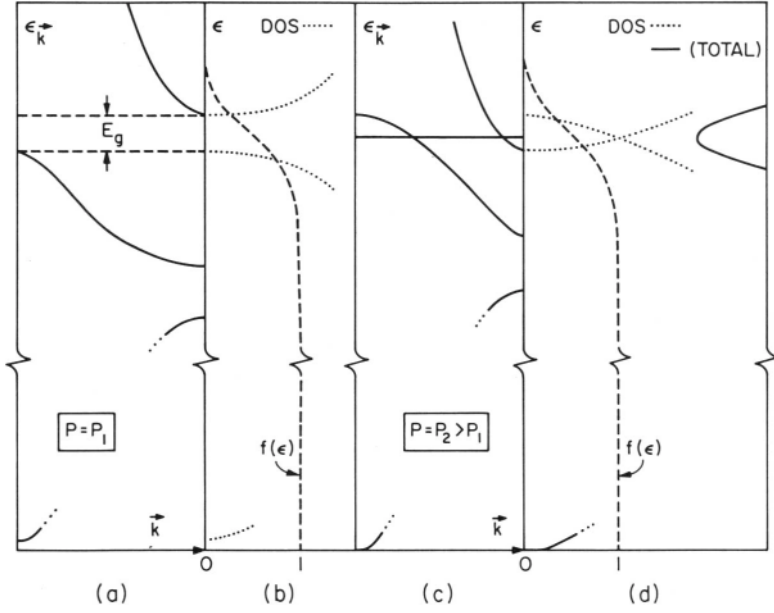


Figure 4. (a) Schematic of energy vs. wavevector (the band-structure at pressure P_1) for a dense proton paired crystalline phase of hydrogen exhibiting a small *overall* but indirect energy gap of about 1/2 eV. (b) Density of states (dotted curve) corresponding to Figure 4a, and (dashed line) the scale of variation (at $T \approx 3000\text{K}$) of the Fermi-Dirac occupation factor. (c) Schematic of energy vs. wavevector (the band-structure at pressure $P_2 > P_1$) for a dense proton-paired crystalline phase of hydrogen in which a band overlap state *has* been attained. (d) Total density of states (full line) corresponding to Figure 4c, and, once again (dashed line) the Fermi-Dirac occupation factor for $T \approx 3000\text{K}$.

quite rapidly diminish.⁵ Since, as noted, $k_B T$ is about 0.25 eV (at 3000K) n_i can quickly become appreciable. If τ is a mean scattering time then the associated resistivity is

$$\rho = \rho_a (\hbar/\tau) (\pi/k_B T)^{3/2} \exp(E_g/2k_B T) \quad (3)$$

where ρ_a is the atomic unit of resistivity ($a_0 \hbar/e^2 \equiv 21.7 \mu\Omega \text{ cm}$) and \hbar/τ is again measured in Ry. Interestingly enough for a gap of just 1/2 eV (corresponding to $2k_B T$ at 3000K) this already gives some $700 \mu\Omega \text{ cm}$ if we merely take for τ a characteristic *ballistic* time for molecules. Here we are invoking the simplest of all physical assumptions namely that transport proceeds by dynamic percolation within an energy band picture similar to the crystalline phase, and therefore that the rate of transference of electrons in the conduction process is dominated by those structural confluences which lead to maximal near-neighbor wave-function overlaps. But these occur at a rate given by the kinematic collision time given above, and it depends on a preference by the protons for a characteristic pairing separation. From inspection of the charge densities associated with a highly paired phase (see Figure 3) the situation is here is obviously quite different from the simple picture of an ionized plasma. To obtain the dependence of resistivity on pressure we clearly require more information from the experiment itself. But using a standard adiabatic law for such a dependence we see that the behavior in Figure 2b is certainly not unexpected. Whether it is a *unique signature* is not, however, so clear.

For example, what of a completely different viewpoint based on a band-overlap state? Again, a crystalline-like picture of energy bands is being invoked and the question implies that a gap *has* closed (see Figure 4c) but that the level of thermal excitation remains very high (see Figure 4b). Now, at low temperatures the system would be typified by a small and

fragmented Fermi surface, S , and the resistivity in such a system is then

$$\rho = \rho_a (\hbar/\tau) (2\pi r_s^3/3) \left/ \int_S \frac{dS}{S_0} \frac{v_{\vec{k}}}{v_0} \right. \quad (4)$$

where S_0 is an equivalent free-electron surface area. In (3) $v_{\vec{k}}$ is a carrier speed and v_0 is again the equivalent free electron value. Using the Schwartz inequality we can rewrite this slightly as

$$\rho > \rho_a (3/8\pi r_s^3) (m^*/m_e) (S_o/S)^2 \quad (5)$$

where m^* is the standard band effective mass. From (3) and (4) (or (5)) it is clear that in order to reach experimental values of ρ in a band-overlap state (if τ is again fixed by percolative physics) the Fermi surface area must be small, in fact so small that the chemical potential must also then be very close to the conduction band minimum. As can be seen from Figure 4d, band overlap can result in a rapidly rising density of states. This indicates a qualitative difference when compared to the previous case possessing an overall band-gap. But (see below) in the presence of strong disorder a *conducting* state is not guaranteed for a given degree of band-overlap.

This crystalline perspective can only be an approximate guide. The experimental situation is one where the electrons face considerable proton disorder; as noted above there is little reason to believe that the proton pairs are endowed with any particular permanence and proton motion is also reasonably violent. If no further phase transitions intervene (see below) it is possible that for a given density the notion of a “gap” may persist but it will now be strongly dependent on the average structure, and in fact is better manifested as a separation between mobility edges, or shoulders, which divide localized from delocalized states. In an adiabatic sense any dense non-crystalline configuration of protons can lead both to non-localized states and to localized states, the latter being slaved in meandering paths to the subsequent motions of the protons. There will be thermal excitation of electrons (from states below the lowest mobility edge and above) into a distribution of states which, by their very definition are far from localized. Their scattering properties are therefore those of quite extended states, and it is straightforward to obtain an estimate of the resistivity from methods similar to those used for ionized gases and again for a gap of about 1/2 eV the result is actually not far from experiment.

But the other case, i.e an equivalent band-overlap situation for significant structural disorder, is also not easy to rule out. In a crystalline environment the “filling in” of the gap would be expected to lead to a conducting state (see Figure 4d), but in a static disordered system, this is not necessarily the case, as was originally shown by Anderson.⁶ With sufficient disorder there is the possibility that electrons will not diffuse, even though the density of states of the highest occupied level is appreciable. To obtain a conducting state it is necessary for this density of states to exceed a certain fraction of the equivalent nearly free electron density of states (about 0.3 according to Mott⁷). However, here the disorder is not at all static; the degree of thermal agitation of this system is considerable and states considered localized in a static environment surely cannot remain so. Instead the concept is more one of dynamic localization where the entangled nature of the fluid state imposes on the electrons just the kind of diffusive motion that typifies the protons themselves: mean free paths would then be expected to fall in the range of intermolecular spacings, and again by this argument it is possible to obtain resistivities on the scale of what is measured in the Weir *et al.* experiment.

For the crystalline phases of dense hydrogen, numerous studies closely link the “gap” to the presence and geometry of proton pairs.⁸ For the high temperature fluid phase the basic units of statistical physics are not enduring proton-pairs but transient objects yet with a lingering preference for a distinct average bond length. Thus, whether or not the “band gap” is closed cannot as yet be established, even within the picture of independent electrons,

though by the arguments given above, it would seem easiest to conclude that it has not even though the state has appreciable conductivity. Adding in the effects of correlation (especially in a state of considerable disorder) is not in the least a trivial matter. One very elementary measure of correlations is embodied in the energy obtained by the simple device of putting 2 electrons as a spin singlet in the same $1s$ orbital, the state responsible for the bulk of the density cusps seen in Figure 3. This is the Hubbard U parameter, and in hydrogen it is large, namely 1.25 Ry. There is much agreement on band widths and at the density of the experiment the paramagnetic band-width W in hydrogen is around 1.4 Ry. These figures are not so far apart, and hence the generally reinforcing effects of disorder and correlation are likely to play an especially important role, even under the conditions of ostensibly high density.

Has a metal been formed in the sense that a Fermi surface exists which, on the scale of widths typical of band overlap, is sharp? That remains to be seen by further experiments, but deciding this question in theoretical terms requires an even deeper understanding of the structure of dense but increasingly energetic phases of hydrogen. The experiment of Weir *et al.* has certainly spurred intensive efforts in this direction, mainly by simulation methods (molecular dynamics, quantum Monte-carlo and the like). Lenosky *et al.*⁹ have approached the problem by using molecular dynamics with the electronic aspects being treated via the tight binding method which in turn provides the required effective pair interactions. At densities somewhat lower than the shock experiments significant dissociation of the proton pairs is found as temperatures climb beyond those of the experiment, and with these they also associate the possibility of significant ionization (akin to 'donor' states in an otherwise semiconductor-like environment). So-called *ab initio* molecular dynamics calculations have been carried out by Pfaffenzeller and Hohl,¹⁰ and they find an even higher dissociation fraction; they also report a resistivity which is about a factor of 6 below experiment. Path-integral Monte Carlo simulations are very close to a first principles approach to this problem; the results of Magro *et al.*¹¹ seem to also support the additional possibility of a plasma-phase-transition, an idea originally introduced by Landau and coworkers where an ionizable system might be induced to undergo a first order transition from a modestly ionized to a significantly ionized state. This indeed might be example of the liquid-liquid phase transition hinted at earlier and if this is in fact an important part of the hydrogen physics then an additional timescale arises namely the time for physical phase separation; this might well be longer than the 100ns of the experiment and since the constituents have very different conductivities the measured conductivity will then be actually determined by the properties of an inhomogeneous medium.

HIGH DENSITIES BUT LOWER TEMPERATURES

Returning now to Figure 1 a the low temperature experimental behavior of dense hydrogen remains puzzling in view of the simplicity of the underlying fundamental description (N electrons, N protons, a volume V , and mutual Coulomb interactions). It is well to be reminded that even at room pressures the average electron density of the low temperature form of solid molecular hydrogen is remarkably high; it corresponds quite closely to the conduction electron density found in calcium, or lithium, or silver. Figure 3 also illustrates that in terms of electron density hydrogen may very much be a special case; the average densities of lithium, magnesium, and aluminum are compared there with the familiar density of the ground state of the hydrogen molecule. They pale in comparison. Yet hydrogen is a tenacious insulator, and as indicated remains so at low temperatures even at the 10 fold or more compressions achievable in ultrahigh pressure diamond cells.

From Figure 1, it is also seen that in crossing from Phase I into Phase II we move into a state where orientational order has begun to develop; crossing the phase II-phase

III boundary adds intense infrared activity to the list of unanticipated but striking physical properties occurring in an otherwise simple system. The symmetry of the strictly isolated free hydrogen molecule forbids such activity, but distortions provided by invasion of charge from neighboring molecules can lift this embargo, albeit weakly for this “induced effect” (as it is called). However, the activity observed in phase III, which is seen to be driven away by increase in temperature, is reported to be orders of magnitude stronger than expected on the basis of any direct induced effect. Hemley *et al.*¹² suggest that the effective charges that might be associated with what, after all, is appearing as partial ionic behavior, may simply be dynamic in origin (though the argument places restrictions on symmetry and cell content). If so one might expect a significant difference between deuterium and hydrogen, something that could be assessed further with current experimental techniques. But it is surely also interesting that all this is happening at densities where the familiar Lorentz–Lorenz factor relating local to total fields present at a molecule should begin to diverge, if we use the average polarizability of a single molecule as a guide.

Following this line of reasoning a little further, if we take the hint from the remarkable infra-red activity that charge is suffering a permanent distortion, then electronic symmetry is being broken in a most unusual way. This is not entirely unanticipated; its likely occurrence can be seen in physical terms with a simple one-dimensional model. Figure 5a shows a row of spherical, polarizable molecules, each with an internal dynamic electronic structure. All of the molecules are coupled by instantaneous dipolar, quadrupolar, etc. interactions. For each molecule taken separately, the instantaneous dipoles \hat{d}_i would follow a principal equation of motion of the type $\ddot{\hat{d}}_i = -\omega_0^2 \hat{d}_i$. But all are coupled (e.g., $\hat{d}_i \cdot \hat{d}_j$) and if for the molecule at i we invoke the molecular field approximation ($\langle \hat{d}_i \rangle = \alpha E_i$ where α is the linear polarizability, and E_i the average local field at i) then to the right hand side of the equation of motion we add a term proportional to αE_i where E_i is proportional to $\sum_j 1/a^3 i^3$. In the same mean field approximation this leads to wave-like solution for the polarization (“polarization waves”) with frequency

$$\omega(k) = \omega_0 \{1 - (4\alpha/a^3)T(k)\}^{1/2} \quad (6)$$

with $T(k) = \sum_i \cos ika/i^3$; a function which peaks at $k = 0$. Because of this, it follows that at $k = 0$, and for increasing values of $(4\alpha/a^3)$ a mode can become “soft” and spontaneous polarization would be developed along the chain. The role of pressure is clear; it is the mechanism by which lattice spacing a is reduced relative to $\alpha^{1/3}$, in fact to the point where the inversion symmetry of the system can be broken. The very same argument obtains for anisotropic molecules as aligned in Figure 5b. But for hydrogen (which has a significant polarizability) a far more interesting prospect arises, and this is illustrated in Figure 5c. Once again conditions on density impel a state of spontaneous broken symmetry, but in this instance a quantized mode of spontaneous polarization becomes “soft” at a zone-boundary wave-vector. From Figure 5c we see that the emerging state is one in which two sublattices develop polarization, but their sum vanishes. The result is an antiferroelectric (the case illustrated by Figure 5b being a ferroelectric), and it is clear that the broken symmetry will now permit coupling to external infrared radiation. The role of the higher multipoles (especially quadrupoles) is not unimportant to this argument since they can also order on their own, and couple to the ordering of the dipoles (see below).

When this argument is carried out in 3 dimensions, the known average value of α for hydrogen predicts¹³ an instability at $r_s = 1.47$ which is very close to the density corresponding to the low temperature onset of intense IR activity. In the Landau theory of phase transitions, antiferroelectrics can be assigned an average order parameter of dipolar origin (say d) in terms of which the Gibbs free-energy, $g(P, T)$ per pair can be developed, i.e., as a classical

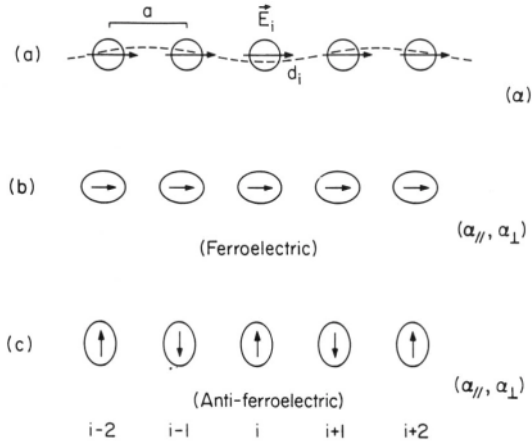


Figure 5. (a) Spherical polarizable molecules with isotropic average linear polarizability α at equal separations a and all coupled by instantaneous dipole–dipole interactions. At each site is a local field E_i resulting from the instantaneous polarization of all other molecules. The system admits of elementary excitations which are quantized waves of electronic polarization (dashed curve) and if a is reduced sufficiently in comparison to the scale of polarizability it is possible for a long wave length mode to become “soft.” This is a Goldstone boson for the system heralding a break in symmetry (and also possibly related to the Dicke phenomenon), (b) The same argument as in Figure 5a but now applied to anisotropic molecules (with principal polarizability components as shown) and again resulting in a long wave length electronic distortion of a ferroelectric character, (c) Once again a similar argument, but here the soft-mode occurs at a zone boundary and results in two opposed sublattices of spontaneous polarization (an anti-ferroelectric arrangement).

guide

$$g(P, T) = g_o(P, T) + \frac{1}{2}a(T - T_o(P))d^2 + \frac{1}{4}bd^4 + \dots \quad (7)$$

Here d could be taken as the average sublattice polarization; if $b < 0$ then we may have a first order transition. It is important to remark that the term quadratic in d includes the energy cost of forming the dipoles; the temperature T_o signals the onset of a transition, but the antiferroelectric phase has a wider stability limit. The coefficient a is dependent on pressure, and again favors formation of the antiferroelectric phase for some $P > P_o$.

Phase II evidently lacks the intense infrared activity associated with Phase III, and we may therefore presume a symmetric disposition of electronic charge (or very nearly so). Phase I is thought to be rotationally symmetric, so in passing from Phase I to Phase II the evident ordering is not associated with any directed quantity; the order parameter is of a higher character, and since hydrogen *does* possess a sizable quadrupole moment, a clue to its form might be sought here. In fact the average order can be given in terms of a quantity

$$S_{\alpha\beta} = S(n_{\alpha}n_{\beta} - \delta_{\alpha\beta}/3)$$

where the n_{α} are components of the unit vector \hat{n} which characterizes the *average* direction of pairs. The scalar S is now a measure of alignment of pairs and will be close to zero in Phase I. Unlike the case where order is associated with polarization, a separate development

of g in powers of S can contain odd powers, the first beginning with, S^3 , i.e., in addition to (7) we now have terms

$$\frac{1}{2}\bar{a}(T - \bar{T}_o(P))S^2 + \frac{1}{3}\bar{e}S^3 + \frac{1}{4}\bar{f}S^4 + \dots$$

and this leads to the possibility of a first-order transition from complete orientational disorder (Phase I) with a corresponding tilt of about 37° in Phase II. This suggests a state of average order in which there is significant libration, and crystal field effects not incorporated in S will also play a role at higher compressions and lower temperatures. The average structure of this phase (Phase II) is now reported by Kohanoff *et al.*¹⁴ to be one which indeed favors alignment of quadrupoles.

As just noted hydrogen has a considerable quadrupole moment, and to a significant degree the form of the order parameter S actually reflects the statistical ordering of quadrupoles. Given this, and a coupling that must necessarily result from quadrupoles and dipoles, we immediately expect one further term in the development of $g(P, T)$, namely a term proportional to Sd , whose role indicates that the ordering of dipoles is *not* independent of the ordering of the quadrupoles, and vice versa. It might well be argued that within current experimental error the Phase II-Phase III boundary (see Figure 1 a) represents a first-order transition, for instance a transition to a new and significantly different crystal structure. Further, an accounting of the intense infra-red activity of Phase III could then be attributed to dynamic polarization now very much larger than in the progenitor phase, and also evidently rising with pressure. As remarked above, such a picture will place significant bounds both on the symmetry and cell content of Phase III; in addition the explanations of other physical characteristics associated with the transition become more troublesome.¹³ But an obvious point is that this issue is decidable by further experimental probing of the nature of the phase boundary itself. Further detailed experimental elucidation of the phase diagram can therefore be expected to lead to some particularly significant insight on the nature of the couplings impelling the transitions. However, these general arguments appear to account for the basic features of the phase diagram of hydrogen at least as recorded in Figure 1a, and in fact, can be given a fully microscopic justification.¹⁵ In particular, Phase III appears consistent with a state of spontaneous polarization, of antiferroelectric character, whose occurrence modestly widens the one-electron gap which had been previously declining with pressure.¹³ It certainly requires additional correction for dynamical polarization, but the main point is that it accounts for the *downward* shift in vibron frequencies at the transition, and the relative insensitivity to mass.

DISCUSSION

Probing the higher reaches of the phase diagram at low temperatures is a currently active enterprise and hints of other structures being favored at even higher pressures (but still preceding the metal) are also now in the literature.¹⁶ Further structural determinations at higher pressures (and densities) will significantly aid in the education of the electronic ordering. Why hydrogen obdurately clings to its Group VII status appears closely linked to the fact that as noted above volume changes per molecule (the manifestation of external physics) can be brought about that are significant fractions of the molecular polarizability (the manifestation of internal molecular physics) and with relative ease. The symmetry of the Wigner–Huntington state which, when broken once to form the paired state, is difficult to reverse. It is traced to hydrogen’s lack of any “inner core” electrons, whose presence in other atoms tend to shield or soften the interaction with the nucleus and to significantly weaken the exchange driven pairing tendencies. As we have seen, hydrogen is a strong scattering system and it is a particularly important one because of hydrogen’s dominance in the universe, and

especially in the giant planets of our own solar system. The understanding of the magnetic field on Jupiter is especially linked to the transport properties that are now emerging. They promise to be extended considerably by laser-shock experiments which are following on the heels of the gas-gun experiments of Weir *et al.*

Acknowledgements

This work has benefitted greatly from discussions with Drs. W. J. Nellis, R. J. Hemley, A. Louis, B. Edwards, and K. Mouloupos.

REFERENCES

- [1] P. Loubeyre, R. Letoullec, D. Hauesermann, M. Hanfland, R. J. Hemley, H. K. Mao, and L. W. Finger, *Nature* **383**, 702 (1996).
- [2] M. Hanfland, R. J. Hemley, and H. K. Mao, *Phys. Rev. Lett.* **70**, 3760 (1993).
- [3] L. Cui, N. H. Chen, and I. Silvera, *Phys. Rev. Lett.* **B 51**, 3048 (1995); see also R. J. Hemley and H. K. Mao in "Elementary Processes in Dense Plasmas," edited by S. Ichimaru and S. Ogata (Addison Wesley, Reading, MA, 1995).
- [4] S. T. Weir, A. C. Mitchell, and W. J. Nellis, *Phys. Rev. Lett.* **76** 1860 (1996).
- [5] W. J. Nellis, A. A. Louis, and N. W. Ashcroft, *Phil. Trans. Roy. Soc.* (to appear).
- [6] P. W. Anderson, *Phys. Rev.* **109**, 1492 (1958).
- [7] N. F. Mott, "Metal-Insulator Transitions," (Taylor and Francis, London, 1990).
- [8] See for example, E. Kaxiras and J. Broughton, *Europhys. Lett.* **17**, 151 (1992); H. Nagara and T. Nakamura, *Phys. Rev. Lett.* **68**, 2468 (1992).
- [9] T. Lenosky, J. D. Kress, L. A. Collins, and I. Kwon, *J. Quant. Spect. Radiat. Trans.* (1997) (to appear).
- [10] O. Pfaffenzeller and D. Hohl, (to be published).
- [11] W. R. Magro, D. M. Ceperley, C. Pierleoni, and B. Bernu, *Phys. Rev. Lett.* **76**, 1860 (1995).
- [12] R. J. Hemley, I.I. Mazin, A. F. Goncharov, and H.-K. Mao, *Europhys. Lett.* **37**, 403 (1997).
- [13] B. Edwards and N. W. Ashcroft, *Nature* **388**, 652 (1997).
- [14] J. Kohanoff, S. Scandolo, G. L. Chiarotti, and E. Tosatti, *Phys. Rev. Lett.* **68**, 2468 (1992).
- [15] B. Edwards and N. W. Ashcroft, (to be published).
- [16] B. Edwards and N. W. Ashcroft, *Europhys. Lett.* (1996).

This page intentionally left blank

KINETIC THEORY OF IONIZATION AND RECOMBINATION RATES FOR DENSE QUANTUM PLASMAS

M. Schlanges¹ and Th. Bornath²

¹Institute of Physics of Greifswald University
D-17487 Greifswald, Germany

²Department of Physics, Rostock University
D-18051 Rostock, Germany

Results are presented which were obtained in the field of quantum kinetic theory to describe reaction processes in dense strongly coupled plasmas. Statistical expressions for ionization and recombination rates are given taking into account plasma density effects such as dynamic screening, self energy, lowering of the ionization energy and Pauli blocking. The influence of these effects on the rate coefficients and on the ionization and population kinetics of dense hydrogen and carbon plasmas is discussed.

INTRODUCTION

The properties of strongly coupled plasmas have obtained a new increasing level of interest. One reason is the progress in the field of laser–matter interaction. Femtosecond laser pulses with intensities of more than 10^{16} W/cm^2 are available now to produce hot dense plasmas in the laboratory.¹ These new developments are a challenge to the theory of strongly coupled plasmas.

The formation and decay of bound states is one of the most important problems in the physics of such dense plasmas. In the laser–plasma experiments mentioned above, dense plasmas are created which are in nonequilibrium.^{2,3} Here, ionization and recombination cannot be modelled by the well-known Saha equation. There are phases in the plasma evolution where one has to start from rate equations instead of the Saha equation and one has to determine the temporal evolution of the number densities of free and bound particles. Usually, these rate equations are based on a phenomenological approach.⁴ Plasma density effects are neglected in the rate coefficients or they are considered from an elementary point of view. However, in dense nonideal plasmas there are strong interparticle correlations and such a level of description cannot be applied.

Recently, calculations of rate coefficients for strongly coupled plasmas were made by several authors based on different theoretical assumptions. We mention papers of Biberman et al.,⁵ Schlanges et al.,^{6,7} Rasolt and Perrot,⁸ Weisheit and Murillo,^{9,10} Gutierrez and Girardeau,¹¹ Leonhardt and Ebeling,¹² Iglesias and Lee¹³ and others. Of course, a systematic approach to calculate rate coefficients for strongly coupled plasmas requires a strict foundation of rate equations on the basis of quantum statistical theory. This leads to explicit expressions for the rates including all the typical plasma density effects such as dynamical

screening, self-energy, lowering of the ionization energy and Pauli blocking.^{7,14} In the present paper we will follow this line and give some results obtained in this field.

LENARD–BALESCU EQUATION FOR BOUND STATES

An appropriate approach to describe the formation and the decay of bound particles in a strongly coupled plasma is quantum kinetic theory.^{15,16} We use Green's function techniques¹⁷ and start from the Bethe–Salpeter equation for the two-particle Green's function g_{ab} defined on the Keldysh time contour \mathcal{C}

$$g_{ab}(1\bar{2}, 1'2') = g_a(1, 1')g_b(2, 2') + i \int_{\mathcal{C}} d\bar{1}d\bar{2}d\bar{1}\bar{2} \times g_a(1, \bar{1})g_b(2, \bar{2})K_{ab}(\bar{1}\bar{2}, \bar{1}\bar{2})g_{ab}(\bar{1}\bar{2}, 1'2'). \quad (1)$$

The g_a are the single-particle Greens functions given by the Dyson equation. K_{ab} is the general effective interaction potential which can be expressed in terms of higher-order Green's functions. To describe ionization and recombination processes in strongly coupled plasmas, a cluster expansion is used for K_{ab} which includes three-particle processes as well as plasma density effects.¹⁸ Using this cluster expansion and positioning the times on the upper and lower branch of the time contour, we get from (1) the following kinetic equation for the two-particle correlation function $g_{ab}^<$

$$i \frac{\partial}{\partial t} g_{ab}^<(\omega, t) - \left[\mathbf{H}_{ab}^{\text{eff}}, g_{ab}^<(\omega, t) \right] = \int \frac{d\omega'}{2\pi} \left\{ g_{ab}^>(\omega', t) \mathbf{W}_S^>(\omega - \omega', t) g_{ab}^<(\omega, t) - g_{ab}^<(\omega', t) \mathbf{W}_S^<(\omega - \omega', t) g_{ab}^>(\omega, t) \right\}. \quad (2)$$

An operator notation is used where t denotes the macroscopic time and ω the energy variable. Equation (2) has a well-known structure. The l.h.s. describes an effective two-particle problem with dynamically screened interaction whereas the r.h.s. represents a collision integral in terms of the screening correlation functions $\mathbf{W}_S^{\gtrless}(\omega, t) = \sum_{cd} V_{cd}^s \gtrless(\omega, t)$. Here, $V_{cd}^s \gtrless$ are the correlation functions of the dynamically screened potential considered in more detail below.

In order to find a kinetic equation for the distribution functions of bound states, we use the bilinear expansion of the two-particle correlation functions

$$i^2 g_{ab}^{\gtrless}(\omega, t) = \sum_K |\Psi_K\rangle \langle \Psi_K | N_K^{\gtrless}(t) 2\pi \delta(\omega - E_K). \quad (3)$$

The sum over K includes all the two-particle states, i.e., the correlation functions g_{ab}^{\gtrless} consist of a bound state part for $K = \mathbf{P}, j$ (total momentum \mathbf{P} , set of internal quantum numbers j) and a scattering contribution for $K = \mathbf{p}_a, \mathbf{p}_b$. The $|\Psi_K\rangle$ are the corresponding eigenstates of the effective hamiltonian $\mathbf{H}_{ab}^{\text{eff}}$ where static screening is assumed to simplify the problem. The occupation numbers are $N_K^<(t) = F_j(\mathbf{P}, t)$ for bound states and $N_K^<(t) = f_a(\mathbf{p}_a, t)f_b(\mathbf{p}_b, t)$ for scattering states with F_j and f_a being the distribution functions of bound and free particles, respectively.

Now, let us return to equation (2). We insert the bilinear expansion (3) and perform the integration over ω what leads to the following kinetic equation for the distribution function of bound particles in the state j ¹⁸

$$\frac{\partial}{\partial t} F_j(\mathbf{P}, t) = I_j^{\text{el}}(\mathbf{P}, t) + I_j^{\text{inel}}(\mathbf{P}, t) + I_j^{\text{react}}(\mathbf{P}, t). \quad (4)$$

There are different collision integrals. The first two terms include elastic and inelastic scattering processes. The last term accounts for collisional ionization and recombination. It is given by

$$I_j^{\text{react}}(\mathbf{P}, t) = \frac{(2\pi)^3}{V} \int \frac{d^3\bar{p}_a}{(2\pi)^3} \frac{d^3\bar{p}_b}{(2\pi)^3} \frac{d^3q}{(2\pi)^3} |\mathcal{P}_{j\mathbf{P}, \bar{p}_a \bar{p}_b}(\mathbf{q})|^2 \times \left\{ \frac{1}{i} V^{S<}(\mathbf{q}, E_{j\mathbf{P}} - \epsilon_a - \epsilon_b) [1 + F_j(\mathbf{P})] f_a(\bar{p}_a) f_b(\bar{p}_b) - \frac{1}{i} V^{S>}(\mathbf{q}, E_{j\mathbf{P}} - \epsilon_a - \epsilon_b) F_j(\mathbf{P}) [1 - f_a(\bar{p}_a)] [1 - f_b(\bar{p}_b)] \right\}. \quad (5)$$

The energies ϵ_a and $E_{j\mathbf{P}}$ are quasiparticle energies which we consider in the so-called ‘‘rigid shift approximation,’’ i.e., thermally averaged shifts are used.¹⁷

For the correlation functions of the dynamically screened potential, a general dissipation-fluctuation theorem can be found. In *random phase approximation* (RPA) it reads

$$V^{S\gtrless}(\mathbf{q}\omega) = \left| \frac{V(q)}{\epsilon^R(\mathbf{q}\omega, t)} \right|^2 \sum_c z_c^2 \int \frac{d^3p}{(2\pi)^2} \delta(\omega - \epsilon_c(\mathbf{p} + \mathbf{q}) + \epsilon_c(\mathbf{p})) f_c^{\gtrless}(\mathbf{p} + \mathbf{q}) f_c^{\lesseqgtr}(\mathbf{p}). \quad (6)$$

Here $V(q) = 4\pi e^2/q^2$ is the Coulomb potential, ϵ^R is the retarded dielectric function in RPA and the abbreviations $f_a^< = f_a$ and $f_a^> = 1 - f_a$ are used.

In RPA, screening is determined by the free particles in the plasma. Of course, a consistent treatment of screening for partially ionized plasmas requires also the inclusion of bound states. Therefore, one has to go beyond the RPA. This was discussed already by Klimontovich¹⁵ based on a pair operator formalism and by Röpke and Der¹⁹ using thermodynamic Green’s function techniques. Recently we have considered the problem for nonequilibrium plasmas starting from the equations of motion for real-time Green’s functions. For the dielectric function then follows¹⁸

$$\epsilon^{R/A}(\mathbf{q}\omega, t) = 1 + \frac{4\pi e^2}{q^2} \sum_a z_a^2 \int \frac{d^3p}{(2\pi)^3} \frac{f_a(\mathbf{p} + \mathbf{q}, t) - f_a(\mathbf{p}, t)}{\omega - \epsilon_a(\mathbf{p} + \mathbf{q}) + \epsilon_a(\mathbf{p}) \pm i0} + \frac{4\pi e^2}{q^2} \sum_K \sum_{K'} |\mathcal{P}_{K, K'}(\mathbf{q})|^2 \frac{N_{K'}^<(t) - N_{K'}^>(t)}{\omega - E_{K'} + E_K \pm i0} \Big|_{\text{connected}}. \quad (7)$$

The first line on the r.h.s. gives the well-known RPA result and the second line presents additional contributions coming from the two-particle bound and scattering states. The atomic form factor can be written as

$$\mathcal{P}_{K, K'}(\mathbf{q}) = \int d^3\mathbf{r}_1 d^3\mathbf{r}_2 \Psi_K^*(\mathbf{r}_1 \mathbf{r}_2) (z_a e^{-i\mathbf{q}\mathbf{r}_1} + z_b e^{-i\mathbf{q}\mathbf{r}_2}) \Psi_{K'}(\mathbf{r}_1 \mathbf{r}_2). \quad (8)$$

An important point is that the wave functions Ψ_K have to be determined from an effective Schrödinger equation. In comparison to the Schrödinger equation of an isolated pair of particles, there are some differences: (i) a dynamic self-energy correction, (ii) Pauli blocking and (iii) a dynamically screened potential. As an important result follows from this equation that the effective ionization energy is mainly determined by the lowering of the continuum. For a more detailed discussion we refer to Ref. [17] and, more recently, Refs. [20] and.²¹

REACTION RATES

Let us now consider the consequences which follow from the kinetic equation (4) in order to describe the ionization and population kinetics in strongly coupled plasmas. Integrating

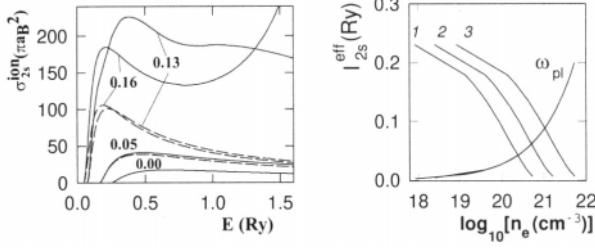


Figure 1. a) Cross section for ionization from the 2s-level versus impact energy for different screening parameters κ/a_B^{-1} . The solid lines refer to dynamic screening in the e-e potential, the dashed curves to static screening, b) Ionization energy I_{2s}^{eff} and plasma frequency versus free electron energy for different temperatures: 1) 10,000 K, 2) 30,000 K, and 3) 100,000 K.

the kinetic equation with respect to the total momentum, we get the following set of rate equations for the number densities n_A^j of bound particles in atomic states $|j\rangle$.^{7,14}

$$\frac{d}{dt}n_A^j = (n_e^2 n_i \beta_j - n_e n_A^j \alpha_j) + \sum_j (n_e n_A^{\bar{j}} K_{j\bar{j}} - n_e n_A^j K_{j\bar{j}}). \quad (9)$$

On the r.h.s. there are the coefficients of three-body recombination β_j , of impact ionization α_j and of excitation (deexcitation) $K_{j\bar{j}}$ for which the theory now gives generalized statistical expressions valid for strongly coupled plasmas. For instance, we get for the coefficient of impact ionization

$$\alpha_j = \frac{1}{n_e} \int \frac{d^3\bar{p}}{(2\pi)^3} d^3q |\mathcal{P}_{j,\bar{p}}(\mathbf{q})|^2 \frac{1}{i} V^{S<} \left(\mathbf{q}, \frac{\bar{p}^2}{2m_{ei}} + I_j^{eff} \right) (1 - f_e(\bar{p})). \quad (10)$$

Similar expressions follow for the recombination, excitation and deexcitation coefficients.

In the following, screening is assumed to be determined mainly by the free plasma particles. Then the RPA expression (6) can be used for the screened potentials $V^{S\lessgtr}$. Furthermore, we consider the case of local equilibrium with respect to the momentum distribution, i.e., the Fermi function can be used for the electrons. It is easy to show that ionization and recombination coefficients are then related by

$$\beta_j = \frac{e\beta\nu_e^{ideal}}{n_e} e^{\beta I_j^{eff}} \alpha_j. \quad (11)$$

The effective ionization energy reads $I_j^{eff} = |E_j| + \Delta_e + \Delta_i - \Delta_j$ where the thermally averaged self-energy shifts of electrons (e), ions (i) and atoms (j), respectively, determine the density and temperature dependent lowering of the ionization energy. At this point we want to mention that the relation (11) cannot be used if the distribution functions are not local equilibrium ones. In this case ionization and recombination rates have to be calculated separately from their statistical expressions.²²

For nondegenerate plasmas the α_j can be written in the usual form⁷ introducing the total ionization cross section

$$\sigma_j^{ion} = \frac{8\pi\hbar^2}{p_e^2 a_B^2} \int \frac{d\Omega_{p_e}}{4\pi} \int_0^{\bar{p}_{max}} d\bar{p} \bar{p}^2 d\Omega_{\bar{p}} \int_{q_{min}}^{q_{max}} dq q \left| \frac{V_{ee}(q)}{\varepsilon(q, \frac{\bar{p}^2}{2m_e} + I_j^{eff})} \mathcal{P}_{j\bar{p}}(q) \right|^2. \quad (12)$$

It is given in terms of the electron-electron potential, screened by the RPA dielectric function, and of the atomic form factor. The latter was calculated using the effective Schrödinger

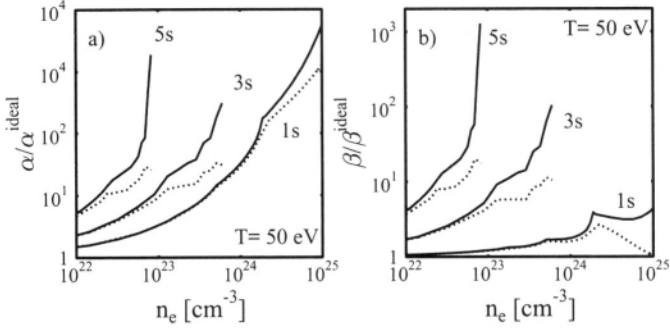


Figure 2. a) Coefficients of ionization of various hydrogen-like carbon ions versus free electron density b) Corresponding recombination coefficients. The solid lines denote the calculation with a dynamically screened potential, the dashed lines those with statically screened potential. Shown is the ratio of the rate coefficients to their ideal values.

equation with statically screened Coulomb potential and with single-particle shifts $\Delta_a = z_a^2 e^2 \kappa / 2$ (κ^2 : inverse screening length).

In Fig. 1a the cross section of ionization from the 2s atomic state of hydrogen is shown in different approximations. The solid lines are the results for dynamic screening in the e-e potential, the dashed curves for pure static screening. Due to plasma density effects there are drastic changes in the behavior of the cross section. With increasing plasma density, the threshold moves down to zero energy which indicates the Mott point. The cross section near the threshold is essentially determined by the screening in the atomic form factor. At high densities we observe an irregular behavior. The cross section calculated with dynamical screening increases with increasing impact energy. This indicates that the usual picture of a scattering process of the atom with one single electron breaks down because of collective effects. Indeed, with lowered effective ionization energy, the energy argument of the dielectric function in (12) can take values near the plasma frequency. This can be seen from Fig. 1 b. We can conclude that there is the special many-body effect of ionization and recombination by absorption and emission of plasmons. This makes the usually defined cross section unsuitable. Therefore, one should start right from the basic statistical expressions for the rate coefficients. For the ionization coefficient we find the following appropriate form^{14, 22}

$$\alpha_j = \frac{1}{n_e} \int \frac{d^3 \vec{p}}{(2\pi)^3} d^3 q |\mathcal{P}_{j, \vec{p}}(\mathbf{q})|^2 V(q) 2\text{Im} \epsilon^{-1} \left(\mathbf{q}, \frac{\vec{p}^2}{2m_{ei}} + I_j^{\text{eff}} \right) n_B \left(\frac{\vec{p}^2}{2m_{ei}} + I_j^{\text{eff}} \right). \quad (13)$$

The expressions derived above make it possible to calculate the rate coefficients studying the influence of many-body effects. There are several papers dealing with this problem. In a simple model, the lowering of the ionization energy was taken into account leading to generalized Arrhenius-like ionization rates.⁶ Statically screened interactions, continuum lowering and Pauli blocking were included in a more systematic way in Ref. [7], see also Ref. [12].

Effects of dynamic screening on ionization rates were first discussed by Murillo and Weisheit¹⁰ and Murillo²³ using an expression similar to that given by (13) and then by Schlanges and Bornath²⁴ on the basis of quantum kinetic theory. A semiclassical approach was recently applied by Jung.²⁵

Let us discuss now some results for rate coefficients obtained from expressions presented in this paper. In Figs. 2a,b the coefficients of ionization and recombination for different states of hydrogen-like carbon ions are given as a function of the free electron density. With increasing density there is a strong density dependence of the rates due to the influence of

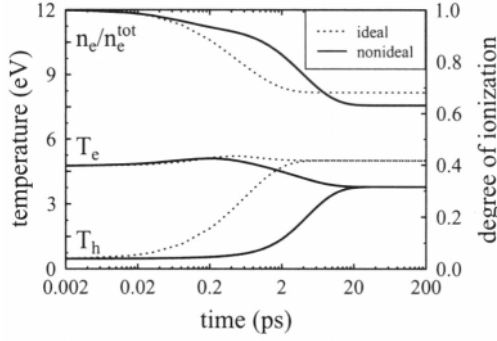


Figure 3. Ionization degree and temperatures of electrons and heavy particles versus time. The initial state is a fully ionized hydrogen plasma with $n^{\text{tot}} = 10^{21} \text{ cm}^{-3}$, $T_e = 50,000\text{K}$, and $T_h = 5,000\text{K}$.

many-body effects. The comparison of dynamic and static screening in Fig. 2 shows higher rates for the case of dynamic screening. This is more drastic for excited states. The step-like behavior of the curves is connected with the shift of higher lying bound states into the scattering continuum.⁷ There they contribute as resonances enhancing thereby the rates. An interesting model to include this effect was recently given also by Iglesias and Lee.¹³

Our calculation have shown a smaller influence of many-body effects on the collisional excitation and deexcitation rates.

DENSITY-TEMPERATURE RELAXATION

In order to study the ionization and population kinetics of a dense spatially homogeneous plasma, we start from the rate equations (9). Balance equations for temperatures of electrons and heavy particles can be derived in usual way from the kinetic equations of free and bound particles. For electrons in a partially ionized hydrogen plasma the equations read²⁶

$$\begin{aligned} & \frac{3}{2}k_B n_e \frac{\partial T_e}{\partial t} - \frac{n_e \Delta_e T_{eh}}{4} \left(\frac{1}{T_e^2} \frac{\partial T_e}{\partial t} + \frac{1}{T_h^2} \frac{\partial T_h}{\partial t} \right) \\ &= \sum_j \left(\frac{3}{2}k_B T_e + I_j^{\text{eff}} - \frac{1}{8} \Delta_e \right) \frac{\partial n_j}{\partial t} + Z_{ei} + Z_{e(i)} \end{aligned} \quad (14)$$

A similar equation follows for the temperature of the heavy particles. The r.h.s. of Eq. (14) describes the energy transfer due to elastic, inelastic and reactive processes including many-body effects. The last two terms stand for the energy transfer following from elastic electron-proton and electron-atom scattering which were calculated in T-matrix approximation.²⁶

In Fig. 3 the temporal evolution of the degree of ionization and the temperatures is shown for a hydrogen plasma which is fully ionized in the initial state.²⁶ The rate coefficients were used in the approximation proposed in earlier papers.⁶ Nonideal plasma effects lead to higher ionization during the relaxation. Furthermore, the equilibration process of electrons and heavy particles takes much longer than in the ideal plasma due to screening.

Figs. 4a and 4b show the population dynamics of a hydrogen-like carbon plasma. The main many-body effect can be seen from the behavior of the population density for the excited level $j = 3$ (j denotes the principal quantum number). The influence of the plasma medium on the reacting particles prevents the population of this state in the first period of relaxation. However, near thermodynamic equilibrium, the state $j = 3$ vanishes again because the Mott point is reached where the bound state moves into the continuum. In this manner

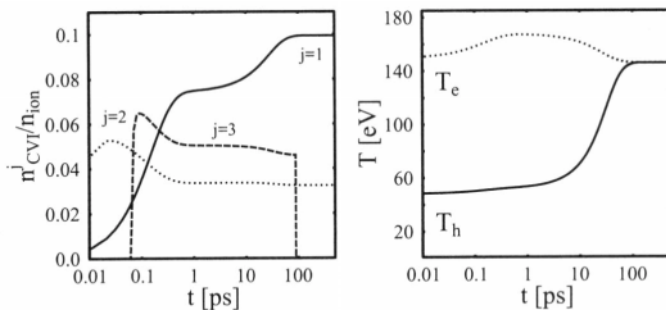


Figure 4. a) Level population and b) temperatures of light and heavy particles versus time for a hydrogen-like carbon plasma. The initial state is a fully ionized plasma with $n^{\text{tot}} = 3.5 \cdot 10^{23} \text{cm}^{-3}$.

the appearance and disappearance of bound states during the relaxation of a strongly coupled plasma is described.^{24, 27} Population dynamics based on a stochastic model was discussed recently by Beule et al.²⁸

In Fig. 3 and Figs. 4a,b examples for the temporal evolution of densities and temperatures are given for the case that the total density remains constant. But for plasmas produced by intense subpicosecond laser pulses impinging on a solid target such an assumption cannot be made. In order to describe the recombination phase after the pulse, the system of equations (9) and (14) has to be modified including an adiabatic expansion model.²⁷

Interesting properties can be studied if ionization and recombination are considered in spatially inhomogeneous plasmas. Now one has to deal with reaction—diffusion equations coupled with the energy balance equations. Besides the reaction rates, the diffusion coefficient and the thermal conductivity must be calculated for the dense partially ionized plasma. An interesting result is that nonideal plasma can lead to well-known nonlinear phenomena such as bistability, phase separation and ionization fronts.^{29–31}

Acknowledgements

This work has been supported by the Deutsche Forschungsgemeinschaft (Sonderforschungsbereich 198: Kinetik partiell ionisierter Plasmen).

REFERENCES

- [1] C. Joshi and P. Corkum, *Phys. Today* **48**, 36 (1995).
- [2] Y. Leng, J. Goldhar, H. R. Griem, and R. W. Lee, *Phys. Rev.* **E52**, 4328 (1995).
- [3] W. Theobald, R. Häßner, C. Wülker, and R. Sauerbrey, *Phys. Rev. Lett.* **77**, 298 (1996).
- [4] L. M. Biberman, V. S. Vorobev, and I. T. Iakubov, *Kinetics of Nonequilibrium Low-temperature Plasmas* (Consultants Bureau, New York, 1987).
- [5] L. M. Biberman, V. S. Vorobev, and I. T. Iakubov, *Sov. Phys. Dokl.* **32**, 752 (1987).
- [6] M. Schlanges, Th. Bornath, and D. Kremp, *Phys. Rev.* **A38**, 2174 (1988).
- [7] M. Schlanges and Th. Bornath, *Physica A* **192**, 262 (1993); Th. Bornath and M. Schlanges, *Physica A* **196**, 427 (1993).
- [8] M. Rasolt and F. Perrot, *Phys. Rev. Lett.* **62**, 2273 (1989).
- [9] J. C. Weisheit, *Advances in Atomic and Molecular Physics* (Academic, New York, 1988), Vol. 25, p. 101.
- [10] M. S. Murillo and J. C. Weisheit, in: H. M. Van Horn and S. Ichimaru, Eds., *Strongly Coupled Plasma Physics* (University of Rochester Press, Rochester, NY, 1993) p. 233.
- [11] F. A. Gutierrez and M. D. Girardeau, *Phys. Rev.* **A42**, 936 (1990).
- [12] U. Leonhardt and W. Ebeling, *Physica A* **192**, 249 (1993).
- [13] C. A. Iglesias and R. W. Lee, *J. Quant. Spectr. Rad. Transf.*, accepted (1997).
- [14] Th. Bornath, M. Schlanges, F. Morales, and R. Prenzel, *J. Quant. Spectr. Rad. Transf.*, accepted (1997).

- [15] Y. L. Klimontovich, *Kinetic theory of nonideal gases and plasmas* (Nauka, Moscow, 1975; Academic Press, New York, 1982).
Y. L. Klimontovich, *Kinetic theory of electrodynamic processes* (Nauka, Moscow, 1980; Springer-Verlag, Berlin, Heidelberg, New York, 1982).
- [16] Y. L. Klimontovich and D. Kremp, *Physica* **109A**, 517 (1981).
- [17] W. D. Kraeft, D. Kremp, W. Ebeling, and G. Röpke, *Quantum Statistics of Charged Particle Systems* (Akademie-Verlag, Berlin, 1986, and Plenum, London, 1986).
- [18] M. Schlanges and Th. Bornath, *Contrib. Plasma Phys.* **37**, 239 (1997).
- [19] G. Röpke and R. Der, *phys. stat. sol.(b)* **92**, 501 (1979).
- [20] J. Seidel, S. Arndt and W. D. Kraeft, *Phys. Rev. E* **52**, 5387 (1995).
- [21] D. Kremp, W. D. Kraeft, and M. Schlanges, (this volume).
- [22] M. Schlanges, Th. Bornath, V. Rietz, and D. Kremp, *Phys. Rev. E* **53**, 2751 (1996).
- [23] M. S. Murillo, in: A. L. Osterheld and W. H. Goldstein, Eds., *Atomic Processes in Plasmas*, (American Institut of Physics, NY, 1996), p. 231.
- [24] M. Schlanges, Th. Bornath, R. Prenzel, and D. Kremp, in: A. L. Osterheld and W. H. Goldstein, Eds., *Atomic Processes in Plasmas*, (American Institut of Physics, NY, 1996), p. 215.
- [25] Y. D. Jung, *Phys. Plasmas* **4**, 21 (1997).
- [26] Th. Ohde, M. Bonitz, Th. Bornath, D. Kremp, and M. Schlanges, *Phys. Plasmas* **3**, 1 (1996).
- [27] R. Prenzel, Th. Bornath, and M. Schlanges, (this volume).
- [28] D. Beule, W. Ebeling, and A. Förster, *Physica* **B228**, 140 (1996).
- [29] W. Ebeling, A. Förster, D. Kremp, and M. Schlanges, *Physica A* **159**, 285 (1989).
- [30] D. Kremp, M. Schlanges, M. Bonitz, and Th. Bornath, *Phys. Fluids B* **5**, 216 (1993).
- [31] D. Beule, W. Ebeling, and A. Förster, (this volume).

RESPONSE FUNCTIONS FOR ELECTRON-ION STRONGLY COUPLED PLASMAS

G. E. Norman and A. A. Valuev

Moscow Physical Society
P. O. Box 110, Moscow 121019, Russia
E-mail: henry@aha.ru

Responses to external perturbations have been treated in many theoretical works for various systems. The same problem has been studied via molecular dynamics (MD). The goal of the review is to compare the results obtained by these three general approaches when they are applied to the same object, namely, strongly coupled electron-ion plasmas.

First, we shall remind of the necessary physical concepts and definitions, then briefly outline theory, discuss MD simulations and consider fluctuations as they follow from theory and simulations. We draw attention to some unexpected features of experimental generations of strongly coupled plasmas (SCP) and proceed to comparison of theory, simulations and experiments. Final remarks concern nonlinear response.

1. GENERAL RELATIONS

Discovery of the connection between equilibrium system fluctuations and dissipative properties of the system at weakly non-equilibrium conditions was an outstanding achievement of statistical physics¹. First relations were of phenomenological kind: the relation between diffusion coefficient and random force amplitude derived from Langevin equation as well as Nyquist relation between conductivity and current fluctuations.

The rigorous proof was carried out in the Green-Kubo linear response theory. The unperturbed Hamiltonian is $H_0(p, q)$ and perturbed one is $H = H_0 + \Delta H(p, q, t)$, perturbation is $\Delta H(t) = B(p, q, t)F(t)$ where $F(t)$ is an external force. The response $A(p, q, t)$ of the system is related to the Hamiltonian by the equation

$$\langle A(t) \rangle = \int_{-\infty}^t \chi(t-t') F(t') dt$$

where generalized susceptibility χ is

$$\chi(t-t') = \langle A(t) B'(t') \rangle$$

$\langle \rangle$ means averaging over equilibrium system. These equations represent a relation between a dissipative coefficient χ and fluctuations of dynamics quantities A and B in the system with a Hamiltonian H_0 . Fourier-transformation results in

$$A(\omega) = \chi(\omega) F(\omega)$$

$$\chi(\omega) = \int e^{i\omega t} \chi(t) dt$$

For constant force F one obtains

$$A = \chi F$$

Later the approach was extended to nonmechanical perturbations, for example to gradients of density, pressure or temperature. Coefficients of diffusion, viscosity and heat conductivity are also related to the corresponding time correlation functions.

The equation for χ is a particular case of the fluctuation-dissipation theorem. The theorem is valid not only for Hamiltonian but for dissipative systems too.

Examples. The conductivity of conductors is related to the current autocorrelation function

$$\sigma = \frac{\Omega_e^2}{4\pi} \int_0^\infty \langle j(0)j(t) \rangle / \langle j(0)^2 \rangle dt$$

The dielectric function $\epsilon(\omega, k)$ of the systems with space dispersion is related to charge density correlation function S_z

$$\epsilon(k, \omega)^{-1} = 1 + T / (ka_e)^2 \chi_z(k, \omega)$$

$$\chi_z(k, \omega) = -T^{-1} \int_{-\infty}^{\infty} \omega' S_z(\omega', k) \left(P \frac{1}{\omega' - \omega} + i\pi \delta(\omega' - \omega) \right) d\omega';$$

P is the principal value.

2. STRONGLY COUPLED (NONIDEAL) PLASMAS^{6,7}

In gas plasmas the electron Debye radius $a_e = (kT/4\pi n_e e^2)^{1/2}$ is much greater than the average intercharge distance $n_e^{-1/3}$, $n_e^{-1/3} \ll a_e$ ⁸⁻¹⁴. T is temperature, n_e is electron number density. Or Debye number $N_D = 4/3 \pi a_e^3 n_e$ is much greater than unity.

As temperature and number density dependencies are different for two radii, it is possible to find out the value of a charge number density for any temperature when this ratio equals to unity. The values for three temperatures are presented in Table 1.

T, 10 ³ K	3	10	20
n=n _e +n _i	3 · 10 ¹⁵	10 ¹⁷	10 ¹⁸

Table 1.

The values are not exotic. So it is possible to generate plasmas which fit the inverse inequalities. The Debye number becomes less than unity for number densities greater than shown in the table and this plasma is non-Debye.

The nonideality parameter $\gamma = e^2 n^{1/3} / kT$, $n = 2n_e$ characterizes the ratio of interaction energy to thermal energy. If γ is about 1 the plasma is nonideal. Virial expansions are no more valid. The Debye number becomes less than 0.1 for $\gamma > 1$. We call both non-Debye and nonideal plasmas strongly coupled plasmas. We consider only non-degenerate plasmas.

Collective phenomena are the basis and essence of any gas plasma theory and it is known that plasma waves are the starting point of the theory⁸⁻¹⁴. It is often assumed⁹ that the range of plasma wave existence is restricted by the following inequalities

$$k < k_0 \approx \alpha \kappa \quad (1)$$

$$\gamma < \gamma_0 < 1 \quad (2)$$

k is the wave number, $\kappa = 1/a_e$. The inequality (1) results from Landau damping, $\alpha \approx 1$. The inequality (2) is due to collision damping. The fact that plasma waves were neglected in^{15,16} may be explained by the violation of (2) in the nonideal plasma region. So there is a barrier between approaches⁸⁻¹⁴ and^{15,16}. Now we know that plasma waves do exist in SCP^{4,7,17-19} and it is possible to develop strongly coupled plasma theory starting with plasma waves just as in gas plasma theory^{5-7,20-25} and thus to incorporate SCP in conventional plasma theories^{6,7}.

In ideal plasmas, the collision damping decrement Γ_c is determined by the Landau collision integral, and its correct form is

$$\Gamma_c / \Omega_e = (1/6) \gamma^{3/2} \ln(\Lambda_1^2 + 1) \quad (3)$$

where $\Omega_e = (4\pi e^2 n_e / m)^{1/2}$, $\Lambda_1 = 1 / [(4\pi)^{1/2} \gamma^{3/2}]$, and the screening length a_e is taken as an upper cut-off distance. Equation (3) takes into account weak long range multiparticle interactions. As γ grows, a_e becomes less than the mean interparticle distance $n^{-1/3}$ and the latter begins to play the role of the screening distance. Then, short range interaction between charged particles is predominant, the collisions become strong and almost binary, and the Landau collision integral should be replaced by the Boltzmann collision integral. In this case, collision damping has the same functional form but with a_e replaced by $n_e^{-1/3}$

$$\Gamma_c / \Omega_e = 1/6 \gamma^{3/2} \ln(\Lambda_2^2 + 1), \quad (4)$$

where $\Lambda_2 = (9/4) \gamma^2$. Thus, at small γ , the quantity Γ_c / Ω_e increases as $\gamma^{3/2}$ according to (3) and at large γ it decreases as $\gamma^{1/2}$. A maximum between these two branches of the damping decrement can be evaluated by matching equations (3) and (4) at $a_e = n_e^{-1/3}$. This estimate gives a value of $(\Gamma_c / \Omega_e)_{max} \approx 0.1$ at $\gamma \approx 1$. The withdrawal of the collision restriction (2) is explained by the fact that a_e becomes less than $n_e^{-1/3}$.

The inequality (1) should also be modified, that is

$$k < q_0 = (6\pi n_e)^{1/3} \quad (5)$$

where q_0 is the Debye wave number. In a Debye plasma, $q_0 \gg \kappa$ and the restriction (1) is stronger than (5). As γ grows, the inequality inverses $q_0 < \kappa$.

Landau damping is determined by the electrons moving with velocity equal to the phase velocity of the wave. In a Debye plasma, this corresponds to the electron thermal velocity. In nonideal plasma, the minimum phase velocity increases so that the number of elec-

trons contributing to Landau damping decreases. They correspond to the tail of the Maxwell distribution. Hence, the maximum value of Landau damping decreases as γ grows.

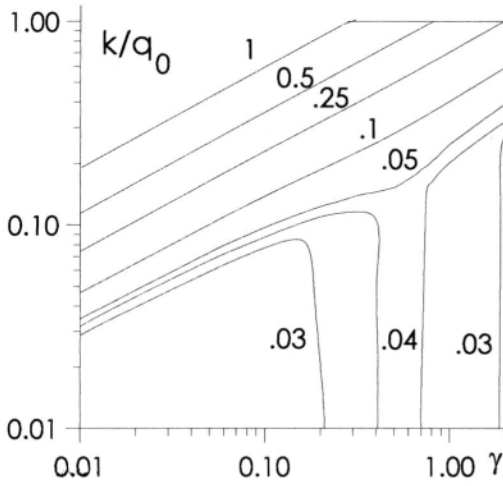


Fig. 1. Range of existence of plasma waves in nonideal plasma. Horizontal line is $k=q_0$, curves are isolines $(\Gamma_c + \Gamma_L)/\omega(k) = \text{const.}$ The values of constant are figured near curves.

The range of plasma waves existence is presented in Fig. 1. Account is taken of the fact that according to ¹³, the Landau damping decrement $\Gamma_L(k_0) = \omega(k_0)$ when $k_0 = 2.34\kappa$ and $\omega(k_0)/\Omega_e = 3.5$.

Two regions can be distinguished in Fig. 1. In the first, where the lines are parallel to the one marked by unity, Landau damping dominates. The region where the isolines are vertical is dominated by collisional damping. And both Landau and collisional damping decrease when γ increases.

From the definition of q_0 , it follows that the fraction of the collective degrees of freedom $s/3n_e = 1/3$ at $\gamma > \gamma_L = 0.3$ ($q_0 = k_0$ for $\gamma = \gamma_L$). The value $1/3$ means that only longitudinal waves are considered.

Thus, the number of collective degrees of freedom in a nonideal plasma is greater than in a Debye plasma, since in that case, they are no longer restricted by Landau damping.

3. OSCILLATION MODES

In order to make use of collective variables in the theory, it is necessary to define them and to carry out a canonical transformation of the Hamiltonian. For gas plasma each collective degree of freedom corresponds to a normal oscillation mode, that is, to an oscillatory motion of a collective variable¹⁴

$$\rho_k(t) = \sum_j^N \exp(-ikx_j(t))$$

with a certain frequency $\omega(k)$. The SCP case is much more complicated, because we deal with a system of interacting oscillators with non-linear coupling.

New collective variables were proposed for SCP in ^{22, 26, 27}. Kaklyugin ²⁷ followed the analogy with phonons in solid state and assumed that every charge (i is its number) in SCP is in a certain equilibrium site x_i^0 . Then its instantaneous position $x_i(t)$ is

$$x_i(t) = x_i^0 + \xi_i(t)$$

where $\xi_i(t)$ is a displacement from equilibrium site. Then new coordinates and momenta are defined by equations

$$\mathbf{X}(\mathbf{r}) = (nm)^{-1/2} \sum_i \xi_i(t) \delta(\mathbf{r}-\mathbf{x}_i^0).$$

$$\mathbf{P}(\mathbf{r}) = (m/n)^{1/2} \sum_i \pi_i(t) \delta(\mathbf{r}-\mathbf{x}_i^0)$$

where $\pi_i(t) = m d\xi_i(t)/dt$. Fourier transformation leads to

$$\Xi_{\mathbf{k}} = (nm)^{-1/2} \sum_i \xi_i(t) \exp(-i\mathbf{x}_i^0 \cdot \mathbf{k}).$$

$$\Pi_{\mathbf{k}} = (n/m)^{1/2} \sum_i \pi_i(t) \exp(-i\mathbf{x}_i^0 \cdot \mathbf{k})$$

In quasilocalized charge approach, Kalman and Golden²² started from $\Xi_{\mathbf{k}}$ and $\Pi_{\mathbf{k}}$ as new collective variables. So the approaches developed in²² and²⁷ were originally identical. However Kalman and Golden²², contrary to Kaklyugin²⁷, completed further transformation. They introduced the equilibrium pair correlation function into their formalism by ensemble averaging over the quasiequilibrium positions of the highly localized charges. Additionally, these authors²² assumed that it is a good approximation to consider variables $\Xi_{\mathbf{k}}$ and $\Pi_{\mathbf{k}}$ as the canonically conjugated dynamics variables.

Kalman and Golden²² obtained a new Hamiltonian, derived equation of motion for $\Xi_{\mathbf{k}}$ and finally obtained the expression for $\epsilon(\omega, \mathbf{k})$. The cost of the approximations was that only the dispersion, but not the damping of the collective modes, can be determined from the theory developed.

To derive the motion equation for collective excitations in SCP and to take into account the damping of the collective modes the authors of^{6, 7} use the smallness of plasma wave damping (cf. Sec. 3) from the very beginning. Then, similarly to¹⁴, the Hamiltonian of the system has the form

$$H = H_{os}(\rho_{\mathbf{k}}) + \Delta H_{kk'} + \Delta H_{os-in} + H_{in}(q, p) \quad (6)$$

where $H_{os}(\rho_{\mathbf{k}})$ is the Hamiltonian of the collective degrees of freedom, $H_{in}(q, p)$ is the energy of the individual degrees of freedom, and $\Delta H_{kk'}$ and ΔH_{os-in} represent relatively small interactions between different collective degrees of freedom and between collective and individual degrees of freedom, respectively.

Differentiating (6) with respect to $\rho_{\mathbf{k}}$, one can obtain the equations of motion of the collective degrees of freedom. Then, following Tatarskii²⁸ who studied a system of coupled oscillators at small evolution times, one can reduce these equations to the Langevin form

$$\ddot{\rho}_{\mathbf{k}} = -\omega_{\mathbf{k}}^2 \rho_{\mathbf{k}} + \Gamma_{eff} \dot{\rho}_{\mathbf{k}} + y \quad (7)$$

where Γ_{eff} is the effective friction coefficient, which includes both collision and Landau damping and y is the δ -correlated random force

$$\langle y(t)y(t') \rangle = 2D_{\rho} \delta(t-t'),$$

D_{ρ} is the diffusion coefficient in ρ space.

The equations (7) are not coupled with respect to different k and can be treated as usual equations for a stochastic oscillator.

4. APPROXIMATE THEORIES

Generalized Langevin equation is a natural bridge to some SCP models. Memory function formalism^{4, 29} uses Laplace transformation of the generalised Langevin equation to relate transforms of density and current correlators to memory function transform. The equation obtained contains static structure factor. The latter should be taken either from MD results or from another independent calculation of pair distribution function.

This or similar models are involved in all SCP theories. Various theoretical treatments can be separated into two groups. Singwi et al (1968) proposed, may be the first model. They, as Singwi³⁰, Kalman and Golden²², Tkachenko and Orner^{21, 25}, Ishimaru³¹ proceed from the most general expressions of statistical physics. For that reason they call sometimes these approaches modelless. However certain transformations then follow which are based on approximations of rather mathematical than physical character. Finally, in order to obtain some numerical results either a model is introduced or data taken from simulation or another theory are used. The principle problem of these theories is how to define physical consequences of the mathematical approximations which were done.

Another treatments are of heuristic nature. Model approximation is a starting point, but its physical meaning is evident, for instance, q_0 -cutting (cf. Sec. 3). Further the approximation can be used both for heuristic model constructions and in analytical approaches.

5. MOLECULAR DYNAMICS SIMULATIONS

We treat non-degenerate plasmas. So Newton equations are used. The principle problem is how to treat short inter-charge distances where classical mechanics is no more valid, in particular, for electron-ion pairs when bound states exist. The situation is just like in solid state theory, where pseudopotential was introduced³² in order to get rid of discrete spectrum. The pseudopotential cuts the Coulomb infinity and replaces it by a shallow well.

The first pseudopotential (or effective pair potential) was introduced for SCP simulation by Zelener, Norman and Filinov³³. It was calculated from the reduced Slater sum, i. e. ignoring contributions of lower ($E_n < -kT$) bound states. The depth of the well was chosen to be equal $-εkT$, where $ε=2-4$. Such pseudopotential satisfies the mechanical similarity condition. For this reason SCP properties occurred to be the functions of one argument, namely, $γ$.

A smooth effective pair potential was introduced independently by Ebeling³⁴. It accounts for layering of results due to various values of quantum parameter.

Having chosen effective pair potentials any MD investigator faces the numerical integration of Newtonian equations. It is not a trivial task for electron-ion SCP. We shall draw attention to the computational peculiarities below, when the MD results are discussed.

MD simulation of electron-ion SCP was performed first by Norman and Valuev¹⁷⁻¹⁹. Only electron dynamics was considered. Ions were moved by Monte Carlo method.

MD of both electrons and protons was simulated by Hansen and McDonald⁴. Their work was very extensive. Its influence has been conserving for many years.

6. ENERGY OF ELECTRIC FIELD FLUCTUATIONS

Fluctuations in uniform equilibrium SCP are the basis for any response theory. This subject is considered in Sec. 7-9.

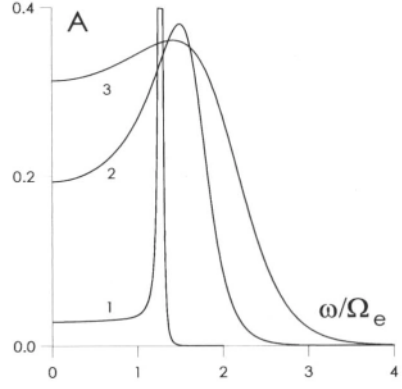
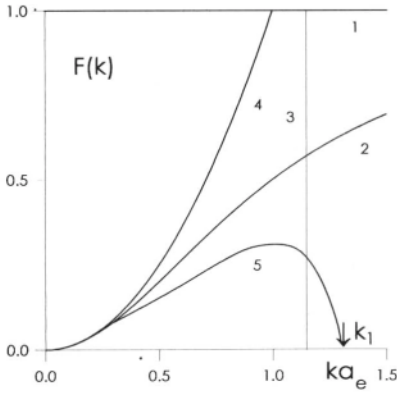


Fig. 2. Energy density $F(k)$ of longitudinal modes. 1 is noncorrelated system of charged particles, 2 is correlated system of charged particles, 3 is $k=q_0$, 4 is collective modes in approximation that neglects damping for $k < \alpha$ ¹³, 5 is collective modes with damping.

Fig. 3. Intensity spectrum $A(\omega, k)$ of longitudinal modes. 1: $ka_e=0.3$, 2: $ka_e=0.7$, 3: $ka_e=1$.

The potential energy of the system of charged particles is proportional to the mean squared intensity of the electric field, including the collective field. However, to obtain thermodynamic functions it is necessary to calculate the difference between the potential energies of the real system and of the system of noncorrelated charged particles (Fig. 2).

The derivation is rather complicated but can be performed analytically using ideal-plasma general formulas. The following expression for internal correlation energy E/nkT (the area between lines 1, 3 and 2 for $k < q_0$) is obtained³⁵:

$$E/nkT = -2 \pi^{-1/2} \gamma^{3/2} \arctg(q_0/\kappa) \quad (8)$$

For $\gamma \ll 1$, equation (8) gives the Debye-Hückel law (the area between lines 1 and 2 for $q_0 \rightarrow \infty$). Further development of the thermodynamics can be performed in the framework of the approaches some of which were considered in^{15, 16}.

The collective field energy is important for evaluation of certain properties of SCP. Its intensity spectrum is related to dielectric function ϵ

$$A(\omega, k) \propto \omega^{-1} \text{Im}[\epsilon^{-1}(k, \omega)].$$

Examples are presented in Fig. 3 for several values of ka_e . The result of numerical integration of $A(\omega, k)$ over ω is given by curve 5 in Fig. 2. Integral over k is the total energy of collective degrees of freedom. It is convenient to reduce it to a dimensionless value ξ , i. e. the fraction of collective degrees of freedom or the ratio of the energy of the collective fluctuations to the electron thermal energy. One can obtain from curve 5

$$\xi = 0.11 \gamma^{3/2}. \quad (9)$$

Curve 4 (Fig. 2) results in¹³

$$\xi = 0.17 \alpha^3 \gamma^{3/2}. \quad (10)$$

The maximum value for a nonideal plasma is $\xi = 1/3$.

Thus, starting up from curve 2 one obtains the negative correlation energy, starting down results in positive energy of plasma waves.

7. DISPERSION RELATIONS

The equation of plasma wave dispersion can be presented in the form⁹

$$\omega^2(k) = \Omega_e^2 + (\partial P / \partial n)_\eta k^2, \quad (11)$$

where P is pressure, $\eta=3$ is a polytrope index. Using (8) to estimate P one obtains curve 2 in Fig. 4. This curve is closer to molecular dynamics results than to the ideal plasma curve 1.

It is necessary to take into account that molecular dynamics data correspond to maximum of function $k^2 A(\omega, k)$. Denote the position of the maximum by $\omega_{max,k}$. Damping of plasma waves reduces the value of $\omega_{max,k}$ comparing with $\omega(k)$. It is demonstrated for ideal plasma by curves 3 and 1 in Fig. 4. The similar effect should be expected for the curve 2, that may improve the agreement with molecular dynamics data^{4, 36}.

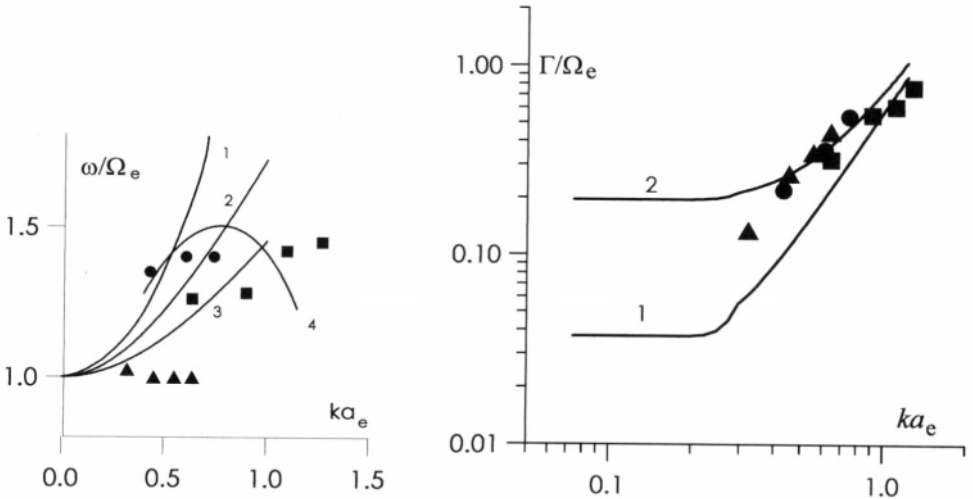


Fig. 4. Dispersion of plasma waves for nonideal plasma. Calculations: 1 is ideal plasma¹³, 2 and 3 are equation (11) using expression (8) for $\gamma=1$ and 1.56, respectively, 4 is $\omega_{max,k}$. Molecular dynamic simulation: squares are⁴ for $\gamma=0$. 39, triangles for $\gamma=1$. 56, circles³⁶ are for $\gamma=1$.

Fig. 5. Dispersion of plasma wave damping decrement for nonideal plasma. 1 and 2 – two estimates corresponding to maximum and minimum choice of the Coulomb logarithm. Molecular dynamic simulation: squares are⁴ for $\gamma=0$. 39, triangles are⁴ for $\gamma=1$. 56, circles are³⁶ for $\gamma=1$.

Damping decrement is presented in Fig. 5. Two curves correspond to maximum and minimum estimates of collision damping. The curves are in agreement with the results of molecular dynamics simulations^{4, 36}, which were obtained for the Landau damping region.

Virial expansions^{16, 37} and response theory consider the same object (SCP) from two points of view. In spite of being very different, two pictures observed should have some inherent proximity. First, the equation of state^{15, 16, 37} incorporating correlation energy (8) can be substituted in (11). Second, short-range quantum correlations studied in^{16, 37} must influence dispersion relations at large k .

The equation of state provides the response theory also with charge number density.

8. INDIVIDUAL DEGREES OF FREEDOM

Differentiating (6) with respect to the coordinates of individual degrees of freedom, one can obtain the motion equations of individual quasiparticles. According to (6), two force terms appear. The first is due to the strong pair interaction of the electrons with other charges at short distances and the second is the action of the collective high frequency electric field.

Each force term results in a corresponding electron “collision” frequency term. Thus, the total effective scattering frequency ν_{eff} can be written in the form

$$\nu_{eff}/\Omega_e = \nu_c/\Omega_e + \xi \quad (12)$$

where ν_c is the electron–charge collision frequency. This estimate agrees with molecular dynamics results^{4, 36} (Fig. 6).

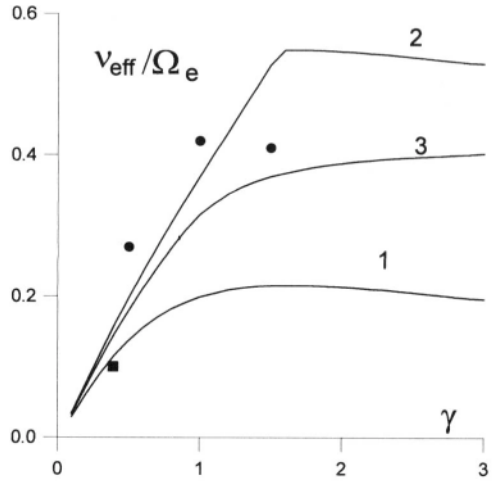


Fig. 6. Effective electron collisional frequency. 1 is collisional contribution, 2 and 3 are total values (12) using ξ according to (10) and (9). Molecular dynamic simulation: points are ³⁶, square is ⁴ (the latter value was obtained for the potential that is more shallow than in³⁶).

9. EXPERIMENTAL SCP ARE FAR FROM EQUILIBRIUM

The most dramatic part of the report is the comparison with experimental results. It is a serious test to theory and simulations.

It is a common place in plasma manuals that the higher is plasma density the closer is plasma state to equilibrium if we consider plasmas at equal temperature. So SCP is used to be considered as an equilibrium plasmas.

Unfortunately for the theory and fortunately for the inquiring theoreticians SCP are generated usually in diverse nonequilibrium states. The general reason is as following. SCP is always generated by impulse methods. Therefore, space inhomogeneity arises. Large density gradients results in charge diffusion. Since diffusions coefficients are different for electrons and ions a region of volume charge appears. The situation is similar to double layer plasma near electrode . There is only one important difference. The thickness of double layer is restricted by several Debye radii. The thickness of volume charge area in impulse experiments is the same as the length of inhomogeneous region. And this region is not necessarily close to any solid surface. The volume charge region may be shock wave front, plasma focuses of various kind³⁸⁻⁴⁰, actual cathode plasmas⁴¹⁻⁴³ etc.

MD simulation^{17-19, 44} showed that breaking of electroneutrality (or presence of a dipole momentum) excites nonequilibrium oscillations in SCP. Separation of charges in non-homogeneous experimental SCP should result in the same effect.

The specific estimates of non-equilibrium plasma wave excitation were made in^{45, 46}. Electrical explosion of caesium wires in high pressure argon atmosphere was considered in⁴⁵. Space gradient creates strong electric field. The field accelerates electron beam from dense almost metallic region. Beam-plasma interaction produces beam instability. The instability excites non-equilibrium plasma wave turbulence. Ion-sound instability caused by plasma density gradient in shock wave front was considered in⁴⁶.

10. RESPONSE FUNCTIONS FOR NON-EQUILIBRIUM SCP

It is necessary to accept the challenge of experimentalists and to modify the theory. Electron velocity autocorrelation function drops exponentially

for equilibrium SCP. It was shown by MD simulations^{4, 36}. However the autocorrelation function of oscillative appearance was obtained by the same method as early as in 1975¹⁷. It was understood later⁴⁴ that the origin of the oscillations which we discovered, was caused by excitation of non-equilibrium plasma waves. We did not calculate dipole momentum that time and, all the more so, did not minimise it. So the oscillations occurred by chance or by accident. It depends on the point of view.

Our simulation results permitted us to present non-equilibrium velocity autocorrelation function in the simplest form as^{6, 47}

$$K(t)/K(0) = \exp(-v_{eff}t) - \xi \sin(\Omega_e t) \exp(-\Gamma t) \tag{13}$$

11. COMPARISON WITH EXPERIMENTAL DATA

Conductivity. SCP conductivity measurements were carried out by many authors (cf.^{20, 48} and references therein). The experimental points are assembled in Fig. 7. The field of the experimental points is rather wide. Scattering of experimental results obtained in

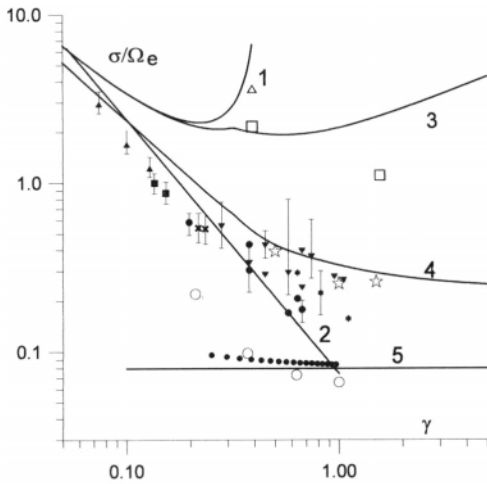


Fig. 7. Electrical conductivity. 1 is Spitzer formula, 2 is Spitzer formula with $\ln A=3$ for $\gamma>0.06$, 3 is Spitzer formula modified according to (4), 4 is estimate corresponding to (12) with equilibrium value of ξ , 5 is estimate corresponding to (12) with $\xi=1$. Open points are MD simulations: squares and triangle are⁴ for two different temperatures, asterisks are³⁶, circles are¹⁷⁻¹⁹. Old points are different experiments (see ref. in²⁰)

different laboratories is a substantial one. However we do not attribute this scattering to experimental errors. We would draw attention to the fact that various installations and methods were used for SCP generation in different laboratories. So the degrees of non-equilibrium plasma wave excitation were also different. Consequently the experimental values of con-

ductivity obtained do not agree with each other. Most of the experimental points lay lower than the equilibrium curve 1, which follows from Eq. (12) with ξ from (10), and higher than the constant value 2, which corresponds to the same Eq. (12) with $\xi=1$.

Spitzer formula (curve 3) and its finite modification (curve 4) which uses correct expression for collision integral are both quite unsatisfactory in this region. Modification⁴⁸ (curve 5) which uses constant value $\ln\Lambda=3$ obtained by fitting to the experimental data at $\gamma = 0.1$ is also unsatisfactory in the region $\gamma = 1$.

MD simulation⁴ results are not better than Spitzer formula. The deviation from experimental results exceeds an order of magnitude. This fact points to a hidden shortcoming inherent in the simulation⁴. We should like to note that the work⁴ is of a very high scientific and computational level. So the hidden defect is able only to emphasise that MD simulation is a very sensitive, sophisticated and subtle method.

Results⁴ were used as a base in many theories discussed in Sec. 5. May be the hidden defect influenced them too.

Equilibrium³⁶ and non-equilibrium^{17, 19} MD simulations are close to the top and bottom bounds of experimental data, just as curve 1 and line 2.

Reflectivity. We use the following expressions

$$R = \left| \frac{\sqrt{\mathcal{E}-1}}{\sqrt{\mathcal{E}+1}} \right|^2$$

$$\mathcal{E} = 1 - \frac{i\omega_p^2}{\omega} \int_0^{\infty} K(t) e^{-i\omega t} dt \quad (14)$$

$$\mathcal{E}^{-1} = 1 + \frac{i\omega_p^2}{\omega} \int_0^{\infty} K(t) e^{-i\omega t} dt \quad (15)$$

The functions $R(\omega)$, corresponding to (14) at $\gamma=1$, $\xi=0$ (plasma waves are not taken into account) and 0.5, as well as corresponding to (15) at $\gamma=1$ ($\xi=0$) and experimental γ values⁴⁹ at $\xi=0.5$ are shown in Fig. 8. Also shown is the curve for ideal plasma. It is seen that expression (15) gives better agreement with experimental data. An account of the plasma waves improves the agreement in comparison with $\xi=0$. Even better agreement is achieved when $\xi > \xi_r$.

Equation of State. This property is not a response function. However it is related to fluctuations. Return to Fig. 2. Non-equilibrium excitation of plasma waves will rise the curve 2 and, consequently, decrease the area between lines 1 and 2 for $k < q_0$, i. e. the absolute value of the correlation energy. So violation of the equilibrium makes SCP closer to ideal gas. The latter statement remind us of the conclusion which Fortov *et al*⁵⁰⁻⁵² derived empirically from the measurements.

It is necessary to remember that here we have a point, where correlation energy should be supplemented by short-range contribution (cf. Sec. 8), modified for non-equilibrium case.

12. NON-LINEAR RESPONSE

Up to now the Maxwell distribution was implied for all particles for the cases of both equilibrium and non-equilibrium excitation of plasma waves. His majesty the experiment put

forward the next challenge for theoreticians. As early as in the measurements^{38, 39} demanded to include deviation from Maxwell distribution for electrons in order to interpret the results for static electrical conductivity and radiation (Fig. 9).

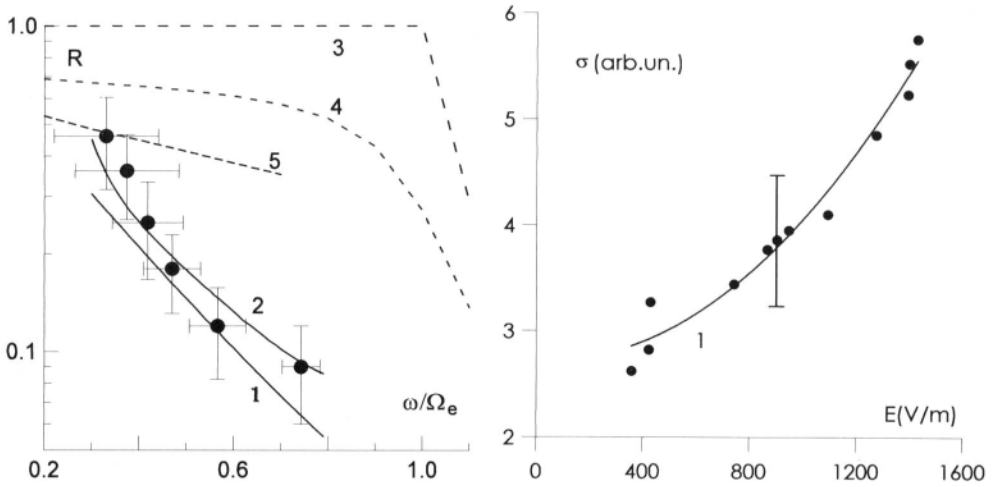


Fig. 8. Reflectivity. Points are the data of⁴⁹. Analytical: 1 is according to (15), $\gamma=1$, $\xi=0$, 2 is according to (15), γ corresponds to the values of experiment⁴⁹, 3 is Drude formula for ideal plasma, 4 is (14) with, $\gamma=1$, $\xi=0$ 5 is (14) with, $\gamma=1$, $\xi=0$.

Fig. 9. Nonlinear response (conductivity) in nonideal plasma. Points are the data of³⁸, 1 is the polynomial-2 fit.

The non-homogeneous plasma was generated in^{38, 39}, but electrical field was relatively small, $E=10^3$ V/cm (cf. the fields in⁵³). So, a very specific effect can be assumed for this case. We think that the electric field is able to arrange plasma waves, which are, in general, chaotically directed. That is why a particular direction of wave vector \mathbf{k} can arise. Landau damping of non-equilibrium plasma waves leads to heating of electrons in the tail of Maxwellian distribution⁵⁴.

The growth of the electric field increases the anisotropy of plasma waves. The latter, in turn, gets stronger pumping of energy to the tail of electron energy distribution. For that reason the non-linear dependence of conductivity on electric field and increase of superradiation should be observed. The effect is possible only for SCP and manifests itself more substantial with increase of γ which was the case in^{38, 39}. Z-dependence of the effect observed in^{38, 39} is required an additional study.

The effect discussed above is a hypothesis. Even when it is seen through to the quantitative results, it will remain an estimate. The rigorous approach to the non-linear response theory has been developing by Kalman, Gu, Tao and Rommel⁵⁵⁻⁵⁷. Initial expressions are generalization of the expressions presented in Sec. 2 for ternary time and space correlation. Quadratic FDT was formulated. The quadratic density response function and the quadratic dynamical structure function were studied and new sum rules were established by Kalman and Rommel⁵⁷. Besides, it was alluded to the intimate relationship between linear and quadratic response functions. It leads to a rather sophisticated improvement in the calculation of the linear response. Results obtained in⁵⁵⁻⁵⁷ have not yet been used in MD simulation.

13. CONCLUSION

The review that was made on response function theory, simulations and experiments for SCP revealed that those three approaches to one problem remain sometimes unnecessarily independent. We found that the approaches were not sometimes seen through to the end where it would be possible to compare the results.

Even if the approaches were seen to the necessary end, it was not easy to compare theory, simulations and experiments. It was not a trivial task to find such characteristics of SCP for which comparison of three approaches is possible. Remember, for instance, theoretical dispersion curve and the value $\omega_{k,max}$ obtained by simulation (Fig. 4). It was not clear earlier that these values are different for large k . So there is a problem of choosing such theoretical values, that are observable in simulations or experiments.

As to the theory, it is necessary to emphasise two main results

- 1.) All integrals in wave vector space for SCP should be cut at the Debye wave number which is well known in solid state theory.
- 2.) It is necessary to apply concepts from both plasma theory and solid state theory to develop SCP theory. Besides the Debye wave number one is able to mention pseudopotentials and phonon-like Kalman&Golden canonical transformation. It was Ebeling who developed SCP theory combining gas and solid approaches most consistently.

MD simulations need caution.

SCP generated experimentally are not mostly in equilibrium state. Nonequilibrium excitation of plasma waves effects SCP properties drastically.

The next step we are going to do is to extend the analytical and MD approaches to plasmas with multiply charged ions.

ACKNOWLEDGEMENT

The authors thank a lot A. S. Kaklyugin for many helpful discussions. The joint paper⁷ was used for Sec. 3, 4, 7, 8 and 9. A. S. Kaklyugin contributed also to the Sec. 3 and 13.

REFERENCES

1. L. D. Landau, \dot{A} . \dot{I} . Lifshitz, *Statisticheskaya fizika*, Moscow, Nauka (1995).
2. D. N. Zubarev, *Neravnovesnaya statisticheskaya Termodinamika*, Nauka, Moscow (1971).
3. P. Martin, *Phys. Rev.*, 161, 143 (1967).
4. J. P. Hansen, I. R. McDonald, *Phys. Rev.*, **A23**, 2041 (1981).
5. H. Zhang, G. Kalman, *Phys. Rev.*, **A45**, 5935 (1992).
6. A. S. Kaklyugin, G. E. Norman and A. A. Valuev, in *Proc. Int. Conf. on Physics of Strongly Coupled Plasmas*, ed. by W. D. Kraeft and M. Schlanges, World Scientific, Singapore (1996), p. 435.
7. A. A. Valuev, A. S. Kaklyugin, G. E. Norman, *Sov. Phys JETP*, **113**, N3 (1998), in press.
8. \dot{A} . \dot{I} . Lifshitz, L. P. Pitayevskii, *Fizicheskaya kinetika*, Nauka, Moscow (1979).
9. L. A. Artzimovich, P. Z. Sagdeev, *Fizika Plasmy dlya Fizikov*, Atomizdat, Moscow (1979).
10. \dot{A} . F. \dot{A} leksandrov, L. S. Bogdankevich, A. A. Rukhadze, *Osnovy Elektrodinamiki Plasmy*, Vysshaya Shkola, Moscow (1978).
11. Yu. L. Klimontovich, *Kineticheskaya Teoriya Neideal'nogo Gaza i Neideal'noi Plasmy*, Nauka, Moscow (1975).
12. L. Spitzer, *Physics of Fully Ionized Plasma*, Interscience, New York (1956).
13. G. Bekefi, *Radiation Processes in Plasmas*, John Willey and Sons, New York-London-Sydney (1966).
14. D. Bohm, *General Theory of Collective Coordinates*, Willey, New York (1959)

15. V. E. Fortov, I. T. Yakubov, *Neideal'naya Plasma*, Energoatomizdat, Moscow (1994).
16. W. Ebeling, A. Forster, V. E. Fortov, V. K. Gryaznov, A. Ya. Polishchuk, *Thermophysical properties of hot dense plasmas. Teubner- Texte zur physik. Bd 25*, ed. by W. Ebeling, A. Forster, R. Radtke, Teubner, Stuttgart (1992).
17. G. E. Norman, A. A. Valuev, in: *Proc. XII IGPIG*, Eindhoven (1975), p. 257.
18. A. A. Valuev, *Teplofizika vysokikh temperatur (High Temp.)*, **15**, 1143 (1977).
19. G. E. Norman, A. A. Valuev, *Plasma Phys*, **21**, 531 (1979).
20. Yu. K. Kurilenkov, A. A. Valuev, *Beitr. Plasmaphys.*, **24**, 529 (1984).
21. V. M. Adamyan, I. M. Tkachenko, *Teplofizika vysokikh temperatur (High Temp.)*, **21**, 417 (1983).
22. G. Kalman, K. I. Golden, *Phys. Rev.*, **A41**, 5516 (1990).
23. K. I. Golden, *Phys. Rev.*, **A35**, 5278 (1987).
24. G. Kalman, in *Physics of nonideal plasmas. Teubner-Texte zur physik. Bd 26*, ed. by W. Ebeling, A. Forster, R. Radtke, Teubner, Stuttgart (1992), p. 167.
25. J. Ortner, I. M. Tkachenko, *Phys. Rev.*, **A46**, 7882 (1992).
26. F. A. Gutierrez, M. A. Girardeau, *Phys. Rev.*, **A42**, 936 (1990).
27. A. S. Kaklugin (1990) unpublished.
28. V. I. Tatarskii, *Sov. Phys. -Uspekhi*, **151**, 273 (1987).
29. J. P. Hansen, L. Sjogren, *Phys. Fluids*, **25**, 617 (1982).
30. Singwi, K. S., Tosi, M. E., Land, R. H., and Sjolander, A., 1968, *Phys. Rev.* **176**: 589.
31. S. Ishimaru, S. Tanaka, *Phys. Rev.*, **A32**, 1790 (1985).
32. W. A. Harrison, *Pseudopotentials in the Theory of Metals*, Benjamin Kummings, Menlo Park, Ca. (1966).
33. B. V. Zelener, G. E. Norman, V. S. Filinov, *Teplofizika vysokikh temperatur (High Temp.)*, **10**, 1160 (1972).
34. W. Ebeling, R. Sandig, *Ann. Phys.*, **28**, 289 (1973).
35. A. S. Kaklyugin, *Teplofizika vysokikh temperatur (High Temp.)*, **23**, 217 (1985).
36. I. V. Morozov, A. A. Valuev (1997) Unpublished.
37. F. Rogers, *Proc. of Int. Conf on Strongly Coupled Systems*, Boston (1997).
38. N. P. Kozlov, G. E. Norman, Yu. S. Protasov, *Phys. Lett.*, **51A**, 443 (1975).
39. N. P. Kozlov, G. E. Norman, Yu. S. Protasov, *Phys. Lett.*, **77A**, 445, (1980).
40. O. N. Krokhin, V. A. Gribkov, *J. Mos. Phys. Soc.*, **4**, 369 (1994).
41. B. Juttner, *Proc. XXIII ICPIG*, Toulouse (1997), Invited Papers.
42. G. A. Mesyats, *Proc. XXIII ICPIG*, Toulouse (1997), Invited Papers.
43. N. Vogel, *J. Phys D: Appl. Phys.*, **26**, 1655 (1993).
44. A. A. Valuev, A. S. Kaklyugin, G. E. Norman, in: *Radiatsionnaya Plasmodinamika*, Ed. Yu. S. Protasov, Energoatomizdat, Moscow (1991), p. 396.
45. V. M. Batenin, M. A. Berkovskii, Yu. K. Kurilenkov, A. A. Valuev, *Teplofizika vysokikh temperatur (High Temp.)*, **25**, 218 and 417 (1987).
46. M. A. Berkovskii, Yu. K. Kurilenkov, *Pis'ma v ZhTF*, **15**, 7 (1989).
47. A. A. Valuev, *Teplofizika vysokikh temperatur (High Temp.)*, **15**, 193 (1978).
48. S. I. Andreev, N. F. Ivasenko, *Osnovy Raschyota impul'snykh ksenonovykh lamp*, Izd. Tomskogo Universiteta, Tomsk (1982), p. 44.
49. V. B. Mintsev, Yu. B. Zaporozhets, *Contrib. Plasma Phys.*, **29**, 493 (1989).
50. B. N. Lomakin, V. E. Fortov, *Sov. Phys. -JETP*, **63**, 92 (1972).
51. V. K. Gryaznov, V. E. Fortov, I. L. Iosilevskii, in *Proc. Int. Conf. on Physics of Strongly Coupled Plasmas*, ed. by W. D. Kraeft and M. Schlanges, World Scientific, Singapore (1996), p. 351.
52. V. K. Gryaznov, V. E. Fortov, I. L. Iosilevskii, *Pis'ma v ZhTF*, **8**, 1376 (1982).
53. Schlanges *et al*, *Phys. Rev.*, **E53**, N3 (1996).
54. V. L. Kovalavskii, V. P. Savinov, *PlasmaPhys. Reports*, **20**, 292 (1994).
55. Z. C. Tao, G. Kalman, *Phys. Rev.*, **A42**, 6201 (1990).
56. X. -Y. Gu, G. Kalman, Z. C. Tao, *J. Stat. Phys.*, **70**, 887 (1993).
57. J. M. Rommel, G. Kalman, *Phys. Rev.*, **E54**, 3518 (1996).

FLUCTUATIONS IN MULTICOMPONENT SYSTEMS*

Joel L. Lebowitz[†]

Departments of Mathematics and Physics
Rutgers University
Piscataway, NJ
E-mail: lebowitz@math.rutgers.edu

I give a brief review of particle and charge fluctuations in multicomponent systems. The long range nature of the Coulomb forces greatly reduce the fluctuations of the net charge Q_Λ in a domain $\Lambda \subset \mathbb{R}^d$. In particular, while the variance of particle numbers in Λ grows like the volume, $\langle Q_\Lambda^2 \rangle$ grows only like the surface area of Λ .

The basic building blocks of matter are charged particles, so the behavior of electric charge fluctuations in space is a problem of some conceptual interest. To be specific I will consider fluctuations in a domain Λ contained inside a very large, spatially homogeneous and overall neutral system in d -dimensions. I shall later take Λ itself to be of macroscopic size but always such that the volume of Λ , denoted by $|\Lambda|$, is very small compared to the size of the whole system. This situation is idealized by taking the system to be infinitely extended from the beginning with Λ some regular domain in \mathbb{R}^d .

The microscopic configuration of the full system is specified by $X = \{\mathbf{x}_i\}, i = 1, 2, 3, \dots$, $\mathbf{x}_i = (\mathbf{r}_i, \sigma_i)$, $\mathbf{r}_i \in \mathbb{R}^d$, representing the coordinates of the particles and $\sigma_i \in \{1, \dots, k\}$ the species of the particle at position \mathbf{r}_i . Statistical properties of relevant observables or functions on the phase space, $f(X)$, will be obtained from a translation invariant (extremal) probability measure $\mu(dX)$. For a classical system in equilibrium, at temperature β^{-1} and uniform densities n_γ , $\gamma = 1, \dots, k$, μ will be an infinite volume Gibbs measure obtained as the thermodynamic limit from some sequence of finite boxes. For an equilibrium quantum system μ will be the infinite volume limit of the diagonal elements of the density matrix $\hat{\mu}$ in the position or X representation.¹ The existence of such a limit measure can be proven under suitable assumptions on the potential; Coulomb interactions require extra care, see [2,3].

To appreciate the “peculiar” behavior of charge fluctuations in equilibrium systems (both classical and quantum), I will first consider fluctuations of particle numbers of the individual species. Let $\rho_\gamma(\mathbf{r}; X)$ be the microscopic particle density of species γ at $\mathbf{r} \in \mathbb{R}^d$

$$\rho_\gamma(\mathbf{r}; X) = \sum_i \delta(\mathbf{r} - \mathbf{r}_i) \delta\sigma_i, \gamma, \quad \gamma = 1, 2, \dots, k. \quad (1)$$

*Dedicated to the Memory of E. P. Gross

[†]Research supported in part by AFOSR Grant 95-0159 and NSF Grant 95-23266

The number of particles of species γ in Λ will then be the integral of the random variables $\rho_\gamma(\mathbf{r}; X)$ over Λ

$$N_\Lambda^{(\gamma)}(X) = \int_\Lambda \rho_\gamma(\mathbf{r}; X) d\mathbf{r}. \quad (2)$$

Their expectations and covariances, with respect to the measure μ , will be given by

$$\langle N_\Lambda^{(\gamma)} \rangle = n_\gamma |\Lambda|, \quad (3)$$

$$B_\Lambda^{(\gamma\delta)} = \langle (N_\Lambda^{(\gamma)} - \langle N_\Lambda^{(\gamma)} \rangle)(N_\Lambda^{(\delta)} - \langle N_\Lambda^{(\delta)} \rangle) \rangle = \int_\Lambda \int_\Lambda d\mathbf{r}_1 d\mathbf{r}_2 \hat{G}_{\gamma\delta}(\mathbf{r}_1 - \mathbf{r}_2) \quad (4)$$

Here $n_\gamma = \langle \rho_\gamma(\mathbf{r}; X) \rangle$ is the density of species γ and

$$\hat{G}_{\gamma\alpha}(\mathbf{r}_1 - \mathbf{r}_2) = \langle \rho_\gamma(\mathbf{r}_1; X) \rho_\alpha(\mathbf{r}_2; X) \rangle - n_\gamma n_\alpha = n_{\gamma\alpha}(\mathbf{r}_1 - \mathbf{r}_2) - n_\gamma n_\alpha + n_\gamma \delta(\mathbf{r}_1 - \mathbf{r}_2) \delta_{\gamma\alpha} \quad (5)$$

where $n_{\gamma\alpha}$ is the usual pair density, see [1,4].

Note that in (3) and (4) we have used the fact that μ is translation invariant. This permits also to rewrite (4) in the form

$$B_\Lambda^{\gamma\delta} = |\Lambda| \int_{\mathbb{R}^d} \hat{G}_{\gamma\delta}(\mathbf{r}) d\mathbf{r} - \int_{\mathbb{R}^d} \hat{G}_{\gamma\delta}(\mathbf{r}) \alpha_\Lambda(\mathbf{r}) d\mathbf{r}, \quad (6)$$

where

$$\alpha_\Lambda(\mathbf{r}) = \int_{\mathbb{R}^d} \chi_\Lambda(\mathbf{r} + \mathbf{r}_1) [1 - \chi_\Lambda(\mathbf{r}_1)] d\mathbf{r}_1, \quad (7)$$

In (7) χ_Λ is the characteristic function of the set $\Lambda \subset \mathbb{R}^d$

$$\chi_\Lambda(\mathbf{y}) = \begin{cases} 1, & \mathbf{y} \in \Lambda \\ 0, & \mathbf{y} \notin \Lambda \end{cases}$$

The existence of the separate integrals in (6) requires that $\hat{G}_{\gamma\delta}(\mathbf{r})$ be integrable, e.g., decay faster than $|r|^{-(d+\epsilon)}$ for some $\epsilon > 0$. This is expected to be the case for pure phases away from critical points. It can generally be proven rigorously only at high temperatures and low densities.^{1,3}

To find out what happens to $B_\Lambda^{\gamma\delta}$ when Λ is large, formally when $|\Lambda| \rightarrow \infty$, we observe⁵⁻⁷ that when $\Lambda \rightarrow \mathbb{R}^d$ in a self-similar way then $\alpha_\Lambda(\mathbf{r})$ will grow like $|\partial\Lambda|$, the $d - 1$ dimensional ‘‘surface area’’ of Λ . ($|\partial\Lambda| \equiv 2$ for $d = 1$.) Averaging $|\partial\Lambda|^{-1} \alpha_\Lambda(\mathbf{r})$ over rotations yields,⁵

$$\lim_{|\Lambda| \rightarrow \infty} |\partial\Lambda|^{-1} \overline{\alpha_\Lambda(\mathbf{r})} = \alpha_d r. \quad (8)$$

with α_d a constant and $r = |\mathbf{r}|$,

$$\alpha_d = \begin{cases} \frac{1}{2}, & d = 1 \\ \pi^{-1}, & d = 2 \\ \frac{1}{4}, & d = 3. \end{cases}$$

Hence, dividing (6) by the volume, the second term on the rhs will vanish when $\Lambda \nearrow \mathbb{R}^d$, to give

$$\lim_{|\Lambda| \rightarrow \infty} |\Lambda|^{-1} B_\Lambda^{\gamma\delta} = b_{\gamma\delta} = \int_{\mathbb{R}^d} \hat{G}_{\gamma\delta}(\mathbf{r}) d\mathbf{r}. \quad (9)$$

For systems in equilibrium the right hand side of (9) can be identified, under general conditions involving equivalence of ensembles, with thermodynamic susceptibilities or compressibilities, that is

$$b_{\gamma\delta} = \frac{\partial n_\gamma}{\partial \lambda_\delta} = \frac{\partial^2 \Pi}{\partial \lambda_\gamma \partial \lambda_\delta}, \quad (10)$$

where λ_δ is the chemical potential of species δ and Π is the Gibbs free energy or grand canonical pressure (each multiplied by β).

The covariance matrix per unit volume, \mathbf{b} , is expected to be *strictly* positive for systems with short range interactions — it was proven by Ginibre for some model classical systems.¹ This implies in particular that if we look at the covariance of the fluctuations in some linear combination of the $N_\Lambda^{(\gamma)}$, say $T_\Lambda = \sum_\gamma c_\gamma N_\Lambda^{(\gamma)}(X)$ with $\sum |c_\gamma| > 0$ then $\langle (T_\Lambda - \langle T_\Lambda \rangle)^2 \rangle / |\Lambda|$ will remain strictly positive as $|\Lambda| \rightarrow \infty$.

We note that $N_\Lambda^{(\gamma)}$ can be thought of as a sum of $|\Lambda|$ random variables, each variable representing the number of particles of species γ in a unit cell inside Λ . When these variables are “approximately” independent, as in systems with short range interactions away from critical points, then the variance will grow like $|\Lambda|$ and the right side of (9) will be bounded away from both zero and infinity. The deviation of $N_\Lambda^{(\gamma)}$ from its average, divided by $\sqrt{|\Lambda|}$, will then also converge to a Gaussian random variable. This is ‘normal’ behavior. At a critical temperature there may be long range positive correlations between the densities in different regions and some of the fluctuations will then grow like $|\Lambda|^\nu$, $\nu > 1$. This represents ‘super-normal’ fluctuations corresponding to infinite susceptibilities. We do not expect to find, in systems with short range interactions, ‘subnormal’ fluctuations or zero susceptibilities.

The situation is however very different when there are free charges in the system, i.e., charged particles which can move about without restraints. These interact with the Coulombic potential,

$$\begin{aligned} \phi(r_i, r_j : \sigma_i, \sigma_j) &= e_{\sigma_i} e_{\sigma_j} \phi_d(r_{ij}), \\ \phi_d(r) &= \begin{cases} -r, & d = 1 \\ -\log r, & d = 2 \\ r^{-1}, & d = 3 \end{cases}, \end{aligned} \quad (11)$$

which are now included explicitly in the Hamiltonian. In such cases, with the system overall neutral, $\sum e_\gamma n_\gamma = 0$, the variance of $Q_\Lambda = \sum e_\gamma N_\Lambda^{(\gamma)}(X)$, the net charge in Λ , is sub-normal, growing more slowly than $|\Lambda|$.⁵ More precisely, while $b_{\gamma\delta}$ is strictly positive, for each γ and δ , $|\Lambda|^{-1} \langle Q_\Lambda^2 \rangle \rightarrow 0$. This is a direct consequence of “complete charge screening”,^{5,8} corresponding to

$$\int_{\mathbb{R}^d} S(\mathbf{r}) d\mathbf{r} = 0 \quad (12)$$

where $S(\mathbf{r})$ is the charge–charge correlation

$$S(\mathbf{r}_1 - \mathbf{r}_2) = \langle q(\mathbf{r}_1; X) q(\mathbf{r}_2; X) \rangle$$

with

$$q(\mathbf{r}; X) = \sum e_\gamma \rho_\gamma(\mathbf{r}; X)$$

What we have instead is that the fluctuations grow only like the surface of Λ

$$\lim_{|\Lambda| \rightarrow \infty} |\partial\Lambda|^{-1} \langle Q_\Lambda^2 \rangle = -\alpha_d \int_{\mathbb{R}^d} r S(r) d\mathbf{r} = \mathcal{K}_d(\beta) \quad (13)$$

with α_d defined in (8). This behavior of $\langle Q_\Lambda^2 \rangle$ implies that the determinant of the matrix \mathbf{b} vanishes, which is consistent with the independence of the thermodynamic pressure from certain components of the chemical potentials.^{2,3}

In writing (13) we have assumed that the infinite system is isotropic and the integral (13) exists, e.g., that $S(r)$ decays faster than $r^{-(d+1+\epsilon)}$. There are also interesting situations corresponding to $(d + 1)$ -dimensional charges (points, lines, $d = 2, 1$) confined to \mathbb{R}^d when $S(\mathbf{r}) \sim r^{-(d+1)}$ in which case $\langle Q_\Lambda^2 \rangle$ grows like $|\partial\Lambda| \log |\Lambda|$. (These have been much studied

for the one component system of ‘charges’ in $d = 1$, where the statistics of the charges corresponds, after suitable scaling, to the distribution of eigenvalues of the Gaussian Orthogonal, Unitary, or Symplectic Random Matrices.⁹⁾

Eq. (12) is the first of an infinite set of moment conditions or sum rules which can be shown to hold for systems with Coulomb interactions under certain assumptions on the decay of correlations; the latter can be proven to hold for classical systems at high temperatures and low densities and for various exactly solvable special cases, see [5,6,8,10] and references there. The sum rule in (12) is expected to always hold for both classical and quantum systems. Hence, starting with the formula analogous to (7)

$$\langle Q_\Lambda^2 \rangle = |\Lambda| \int S(\mathbf{r}) d\mathbf{r} - \int S(\mathbf{r}) \alpha_\Lambda(\mathbf{r}) d\mathbf{r}. \quad (14)$$

and using (12) and (8) leads directly to (13).

Eq. (13) can also be understood and derived by using Gauss’ theorem

$$Q_\Lambda = c_d \int_{\partial\Lambda} \mathbf{E}(\mathbf{s}; X) \cdot d\mathbf{s}, \quad (15)$$

where c_d is the inverse of the area of a unit sphere in \mathbb{R}^d , \mathbf{E} is the electric field and $d\mathbf{s}$ is an element of the surface area of $\partial\Lambda$. The integral in (15) (like that in (2)) can be treated as a sum of $|\partial\Lambda|$ random variables. It is these random variables, rather than the $q(\mathbf{r}; X)$ which turn out to be “approximately” independent so that the variance of their sum grows like $|\partial\Lambda|$.¹¹

A physical interpretation of the charge fluctuations in Λ is that they behave as if the charges in the system were combined into neutral molecules.⁷ To see this consider a two component system with charges $\pm e$ which forms neutral dipoles of length l . Then the charge fluctuation in Λ would be due entirely to the boundary, $\partial\Lambda$, “cutting” some of the dipoles. Assuming further that these dipoles had only short range correlations in position and orientation, we would have $\langle Q_\Lambda^2 \rangle = c n e^2 l |\partial\Lambda|$, where $n = n_1 = n_2$ is the density of dipoles and c is a constant of order unity. This is of course a caricature of what happens in real systems where, at high temperatures, or if we are treating a classical system with hard cores, then at any temperature, we do not expect any permanent very tightly bound neutral structures. The length l should then be identified with the Debye correlation length $l_D = [4\pi\beta \sum e_\gamma^2 n_\gamma]^{-\frac{1}{2}}$. On the other hand, for quantum systems at not too high temperatures, the charges form neutral atoms and molecules and l would then be characteristic of atomic sizes determined by quantum mechanics, e.g., 1 Bohr radius for Hydrogen, unless the dominant contribution to the charge fluctuations comes from the small fraction of ionized charges. What (13) shows is that the fluctuations exhibit similar behavior at all temperatures even when we deal with plasmas or molten salts.

The above interpretation of the charge fluctuations is strengthened by considering not just the variance but the whole probability distribution of Q_Λ . It was shown by Martin and Yalcin⁵ that in dimension $d \geq 2$, $Q_\Lambda / \sqrt{|\partial\Lambda|}$ approaches, as $\Lambda \rightarrow \infty$ a Gaussian random variable with variance \mathcal{K}_d given in (12). This result was extended in [7] to show that the distribution of charges in two disjoint domains, Λ_1 and Λ_2 is again Gaussian with a covariance equal to $-\mathcal{K}_d |\partial\Lambda_1 \cap \partial\Lambda_2|$, i.e., it is proportional to the area of their joint boundary. This is exactly what would be expected from fluctuations due to the surface cutting the dipoles and gives, for two adjacent cubes of volume L^d ,

$$\frac{\langle Q_1 Q_2 \rangle}{2dL^{d-1}} \rightarrow -\mathcal{K}_d. \quad (16)$$

(In one dimension when $|\partial\Lambda|$ doesn’t grow with Λ , the charge fluctuations in a given interval L remains bounded and the probability of finding a charge Q_L in a two species system with charges $\pm e$ can be found exactly.⁶⁾

It would be interesting to know the behavior of the charge fluctuations at the critical point (cp) of the liquid–vapor phase transition in a Coulomb system discussed here by Michael Fisher.¹² While the truncated pair correlation functions corresponding to the particle densities become non-integrable at the cp, it is not clear what happens to the charge correlation function $S(r)$ defined in (12). While there is no apriori reason for $S(r)$ to have power law behavior at the cp, it is surely going to be different in the liquid and vapor phases and hence will have some nonanalytic behavior at the cp. This should carry over to $\mathcal{K}(\beta)$ defined in (13), whose behavior as a function of β is very much an open problem.

Acknowledgements

I thank Francois Cornu, Bernard Jancovici, and Philippe Martin for useful discussions.

REFERENCES

- [1] See, for example, D. Ruelle, *Rigorous Statistical Mechanics*, Benjamin (1969).
- [2] J. L. Lebowitz and E. Lieb, *Physical Review Letters*, **22**:631, 1969; *Advances in Mathematics*, **9**:318–398, 1972.
- [3] *Rigorous Atomic and Molecular Physics*, ed. G. Velo and A. S. Wightman, (Plenum, N. Y. 1981).
- [4] J. L. Lebowitz and J. Percus, *Journal of Mathematical Physics*, **4**:1495, 1963.
- [5] Ch. Gruber, Ch. Lugin, and Ph. A. Martin, *Journal of Statistical Physics*, **22**: 193, 1980.
- [6] Ph. A. Martin and T. Yalcin, *Journal of Statistical Physics*, **22**: 435, 1980.
- [7] J. L. Lebowitz, *Physical Review A*, **27**: 1491, 1983.
- [8] Ch. Gruber, J. L. Lebowitz, and Ph. A. Martin, *Journal of Chemical Physics*, **75**: 994, 1981; L. Blum, Ch. Gruber, J. L. Lebowitz, and Ph. A. Martin, *Physical Review Letters*, **48**:1767, 1982.
- [9] M. L. Mehta, *Random Matrices*, 2nd edition, (Academic Press, 1990); O. Costin and J. L. Lebowitz, *Physical Review Letters*, **75**: 69–72, 1995.
- [10] B. Jancovici, *Physical Review Letters*, **46**: 386, 1981; *Journal of Statistical Physics*, **28**:43, 1982.
- [11] J. L. Lebowitz and Ph. Martin, *Journal of Statistical Physics*, **34**:287, 1984.
- [12] c.f. M. E. Fisher, *Journal of Statistical Physics*, **75**:1, 1994.

This page intentionally left blank

INVESTIGATIONS OF CONDENSED MATTER BY INELASTIC X-RAY SCATTERING WITH HIGH ENERGY RESOLUTION

E. Burkel, Ch. Halcoussis, and H. Sinn

Universität Rostock
D-18051 Rostock, Germany

Synchrotron radiation has opened new possibilities for experimental investigations in condensed matter physics. The high intensities of the emitted X-rays allows scattering experiments with an energy resolution high enough to study ionic excitations and dynamics, directly.¹⁻³

So far, this was only possible by means of inelastic neutron scattering. In that method the probe is coupling to the nuclei in the sample, whereas in case of X-rays the coupling occurs to the electrons. Therefore, X-ray scattering experiments with high resolution in energy and momentum allow to determine the dynamical structure factor $S(Q, \omega)$ which is the fourier transform in time and space of the time dependent electron density-density correlation function. Within the validity of the adiabatic approximation this function is proportional to the ion density-density correlation function

This means, peaks in $S(Q, \omega)$ of a liquid, for example, can be interpreted either as localized density fluctuations around $\omega = 0$ or as propagating sound modes for $\omega \neq 0$. The latter excitations correspond to the well known phonon excitations observable in solids.

Since the coupling of the energy to the momentum transfer is negligible, inelastic X-ray scattering has almost no restrictions in the accessible (Q, ω) -space. Hence this method is extremely attractive for investigations at small Q -values of the coherent part of the dynamical structure factor for liquids and amorphous solids with high sound velocities. In contrast to this, inelastic neutron scattering is strongly limited by the mass of the neutron itself just in this part of the (Q, ω) -space.

Conventional triple axis spectrometer can be optimized for high energy resolution by Bragg scattering from perfect single crystals in extreme backscattering geometry at the monochromator and the analyzer. This technique was used to build the inelastic X-ray spectrometer INELAX^{2,3} at the synchrotron radiation laboratory at DESY, Hamburg and the second generation instrument⁴ at the ESRF in Grenoble. Energy resolution values of 10 meV down to 1 meV can be achieved by using high order reflections from perfect silicon crystals. The energy transfer in an inelastic scattering experiment is established by an energy shift between the monochromator and the analyzer crystals. This is done by thermal tuning of the lattice parameter of the analyzer or the monochromator crystal. Using the (7 7 7) Bragg reflection of silicon with a primary energy of 13.8 keV, a temperature difference of 0.01 K between both crystals corresponds to an energy transfer of 0.35 meV. The resolution function

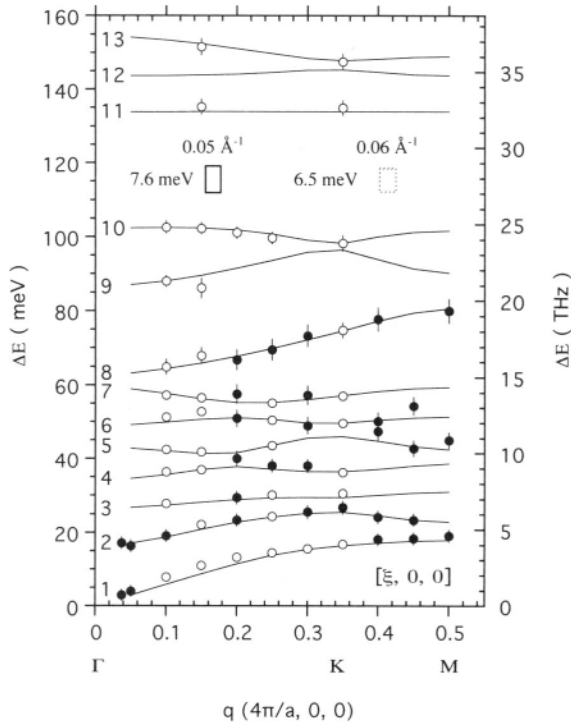


Figure 1. Dispersion scheme of α -quartz along $[\zeta, 0, 0]$ direction. The X-ray data were taken with photon energies of 13.8 keV (open circles) and 17.8 keV (full circles). Open and full squares indicate the instrumental resolution. The lines represent the dispersion according to the shell model of [6,7]. Figure from [5].

of the spectrometer can be directly measured by recording the elastically scattered intensity from fused silica as a function of the energy transfer.

During the development, this new technique was applied to various systems.² The reliability of the method was demonstrated by its application to α -quartz,⁵ lately. It has hexagonal structure and its unit cell contains three SiO_2 units leading to 27 phonon branches. However, along the Γ -K-M direction $[\zeta, 0, 0]$ selection rules reduce these to only 13 visible branches. The investigations with inelastic X-ray scattering were performed along this direction. Figure 1 shows the obtained dispersion scheme for these modes together with dispersion lines according to a shell model^{6,7} based on neutron data. There is excellent agreement between both methods. These results were obtained using a scattering volume of only 0.05 mm^3 at the sample. The analysis of the dynamics of such small samples is one major strength of the new technique.

Investigations of the collective density modes in the liquid metal lithium at $215 \text{ }^\circ\text{C}$ were started at the instrument INELAX with an energy resolution of 30 meV and later of 12 meV.^{2,8} Further data were taken at the inelastic X-ray scattering beamline at the ESRF with a resolution of 11 meV.⁹⁻¹¹ Figure 2 shows the energy resolved X-ray scattering intensities of liquid lithium observed at various momentum transfers as functions of the energy transfer together with the instrumental resolution function.

The quasielastic scattering contribution around zero energy is clearly visible. The inelastic scattering intensities due to energy gain and loss from collective atom excitations called Brillouin lines are well separated and reveal their dispersion already in the raw data. The coherent structure factor $S(\mathbf{Q}, \omega)$ can be described with the model of extended hydrodynamic modes¹² using a central Lorentzian as Rayleigh line and two asymmetrical Lorentzians as

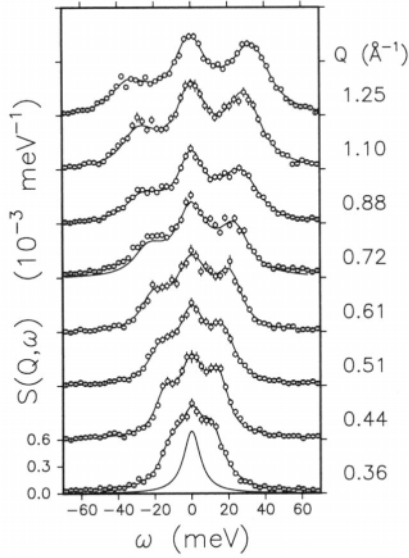


Figure 2. X-ray intensities scattered from liquid lithium at different momentum transfers as functions of the energy transfer. The full lines represent fits according to the extended hydrodynamic modes. The resolution function of the instrument is also given.¹¹

Brillouin lines.

In order to compare the experimental result with a theoretical model, the data can be deconvoluted with the resolution function of the spectrometer, for details see [10]. Figure 3 shows the deconvoluted data with error bars indicating the statistical uncertainty at selected Q values. The full and dashed lines are molecular dynamic calculations performed by [13] using the neutral-pseudo-atom (NPA) potential¹⁴ and the empty-core potential.¹⁵ Obviously, the NPA simulation describes the experimental data better at $Q = 0.72 \text{ \AA}^{-1}$ and $Q = 1.25 \text{ \AA}^{-1}$. At $Q = 3.53 \text{ \AA}^{-1}$ however, it is not possible to distinguish between both models within the experimental error.

The dispersion of the Brillouin lines is shown in Fig. 4 together with results from inelastic neutron scattering¹⁶ and the molecular dynamic calculations. There is good agreement of the experimental data with the NPA model (full line). The empty core potential (dashed line) can not represent the observed dispersion. The discrepancies between the neutron results and the X-ray results are not understood and require further investigations.

Figure 4 also demonstrates the positive dispersion in liquid lithium at small momentum transfers with a slope steeper than the macroscopic sound velocity (dashed-dotted line), known from [17]. This effect is associated with viscoelastic shear relaxations (dotted line).¹⁸

There is another interesting effect looking at the absolute cross section of the X-ray data. The experimentally observed scattering intensity for $Q \leq 1.25 \text{ \AA}^{-1}$ are higher than the NPA simulation predicts. This effect was further investigated by additional small angle scattering experiments with X-rays without energy resolution.¹⁰ The static structure factor of liquid lithium which was derived from the elastic (full circles) and from the inelastic scattering (open circles) experiment is shown in Fig. 5 together with the result from molecular dynamics based on the NPA potential (solid line). The molecular dynamics data can be extrapolated for small Q to values close to the compressibility limit $S(Q = 0)$. But there is significant disagreement between the experimental results and the simulation.

A possible explanation of this extra intensity might lie in incoherent scattering contributions not taken into account, yet. Generally in an X-ray experiment the radiation is scattered

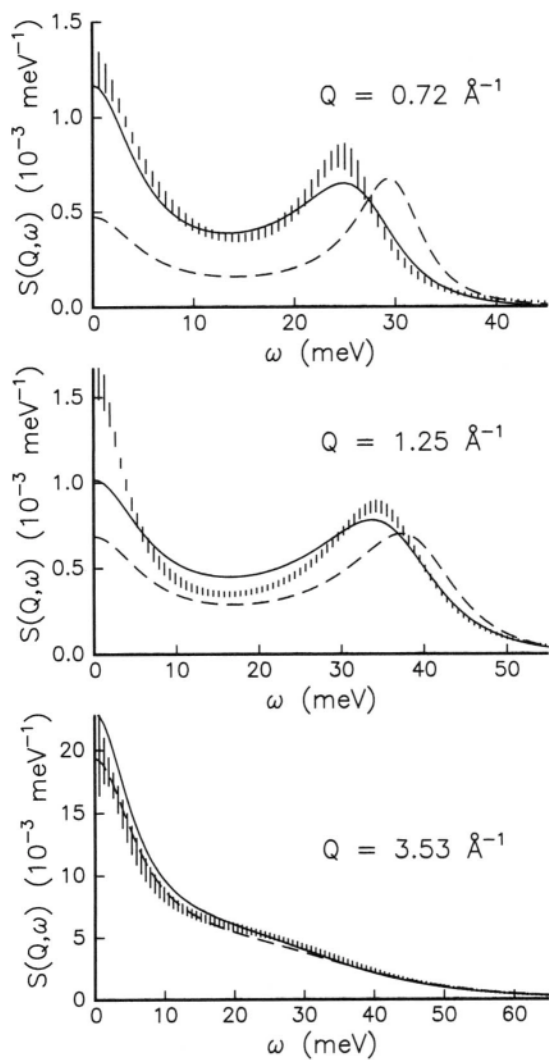


Figure 3. Deconvoluted experimental data (vertical bars) at different momentum transfers in comparison with results from molecular dynamics¹³ with the NPA potential¹⁵ (full line) and the empty core potential¹⁶ (broken line). Figure from [11].

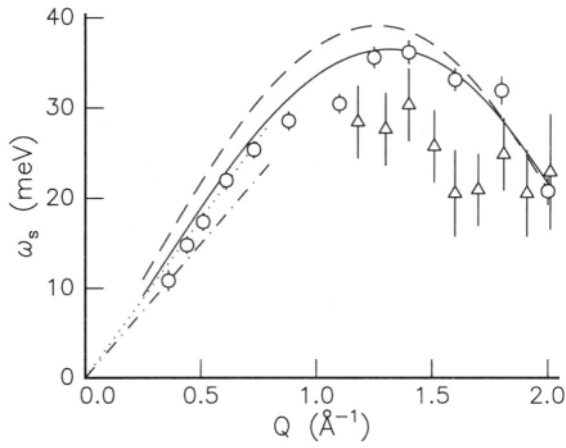


Figure 4. Dispersion of collective modes in liquid lithium. The results from inelastic X-ray scattering (open circles) are shown together with neutron data⁸ (open triangles) and molecular dynamical results¹³ using the NPA (full line) and the empty core (dashed line) potential. The macroscopic sound velocity (dot-dashed line) and the viscoelastic sound velocity (dotted line) are given as well. Figure from [11].

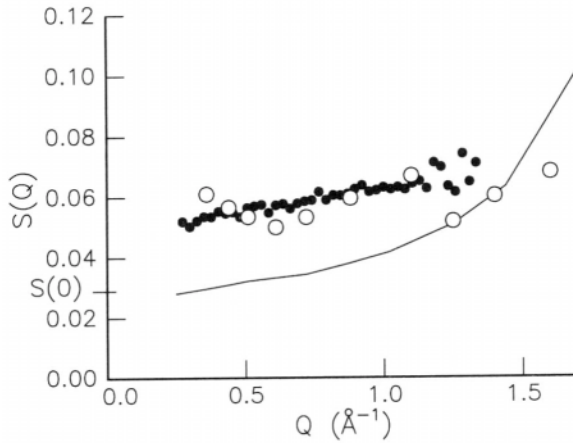


Figure 5. The static structure factor resulting from inelastic X-ray scattering (open circles) and small angle scattering (full circles) and molecular dynamics with the NPA potential (solid line).¹⁰

off of the electron density fluctuations. In the liquid metal, core and valence electrons contribute to the coherent and incoherent scattering.¹⁹ As shown before, the coherent dynamic structure factor describes the collective motions of the ions. The incoherent structure factor is known to be due to excitations of the electron gas that means electron–hole excitations of the core electrons and from Compton scattering. These contributions are not significant at the discussed energy transfers. However, according to calculations for liquid sodium and aluminum from [20], additional correlations of the valence electrons can lead to an additional incoherent contribution as observed. Therefore, it has to be concluded that there are deviations from the adiabatic approximation as it is used normally.

The presented results are a demonstration of the actual capabilities of inelastic scattering of X-rays with meV resolution. Certainly, this new method of spectroscopy is complementary to inelastic neutron scattering. It reveals additional information, which is inaccessible for neutron scattering.

Acknowledgements

This project is supported by the Bundesministerium für Forschung und Technologie and by the European network program.

REFERENCES

- [1] E. Burkel, J. Peisl, and B. Dorner, *Europhys. Letter* **3**, 957 (1987).
- [2] E. Burkel, *Inelastic Scattering of X-rays with Very High Energy Resolution*, Springer Tracts in Modern Physics, Vol. 125, Springer, Berlin (1991).
- [3] E. Burkel, B. Dorner, Th. Illini and J. Peisl *Rev. Sci. Instrum.* **(60)7**, 1671 (1989).
- [4] F. Sette, G. Ruocco, M. Krisch, U. Bergmann, C. Masciovecchio, V. Mazzacurati, G. Signorelli and R. Verbeni, *Phys. Rev. Lett.* **75**, 850 (1995).
- [5] Ch. Halcoussis, thesis, University Rostock, 1997.
- [6] H. Schober, D. Strauch, K. Nützel and B. Dorner, *J. Phys.-Cond. Mat.*, **5**, 6165 (1993).
- [7] H. Schober and B. Dorner, *J. Phys.-Cond. Mat.*, **6**, 5351 (1994).
- [8] E. Burkel and H. Sinn, *J. Phys.-Cond. Mat.*, **6**, A225 (1994).
- [9] E. Burkel and H. Sinn, *Int. J. Thermophys.* **16**, 1135 (1995).
- [10] H. Sinn and E. Burkel, *J. Phys.-Cond. Mat.*, **8**, 9369 (1996).
- [11] H. Sinn, F. Sette, U. Bergmann, Ch. Halcoussis, M. Krisch, R. Verbeni and E. Burkel, *Phys. Rev. Lett* **78**, 1715(1997).
- [12] L. M.de Schepper, P. Verkerk, A. A.van Well and L. A.de Graaf, *Phys. Rev. Lett* **50**, 974 (1983).
- [13] M. Canales, L. E. Gonzales and J. A. Padro, *Phys. Rev. E* **50**, 3656 (1964).
- [14] L. E. Gonzales, D. J. Gonzales, M Silbert and J. A. Alonso, *J. Phys.: Condens. Matter* **5**: 4283 (1993).
- [15] N. W. Ashcroft, *Phys. Lett.* **23**, 48 (1966).
- [16] P. Verkerk and P. H. K. de Jong, *Physica B* **180,181**: 834 (1992).
- [17] T. Bodensteiner, C. Morkel, P. Müller and W. Gläser, *J. Non-Cryst. Solids* **117/118**, 116 (1990).
- [18] J. B. Boon and S. Yip, *Molecular Hydrodynamics* (McGraw-Hill, New York)(1980).
- [19] J. Chihara, *J. Phys. F Met. Phys.* **17**, 295 (1987).
- [20] M. Rasolt, *Phys. Rev. B* **31**, 1615 (1985).

RUBIDIUM FROM A LIQUID METAL TO A PLASMA

Junzo Chihara¹ and Gerhard Kahl²

¹Advanced Photon Research Center, JAERI
Tokai, Ibaraki 319-11, Japan

²Institut für Theoretische Physik and CMS, TU Wien
Wiedner Hauptstraße 8-10, A-1040 Wien, Austria

Usually, a liquid metal is treated as a one-component liquid where the particles interact via a binary effective potential, which is determined within the pseudopotential formalism. However, this quite successful method for a liquid metal cannot be extended to calculate the structure of a plasma, since for such a system this kind of pseudopotential cannot be set up. In previous contributions, we have proposed a method which allows the calculation of the radial distribution functions (RDF's) in an electron-ion mixture on the basis of the density functional (DF) theory; it is called the quantal hypernetted (QHNC) approximation:¹ the QHNC equations are derived from exact expressions for the electron-ion and ion-ion RDF's in an electron-ion mixture. Up to now, we have applied this approach to liquid metallic hydrogen, lithium, sodium, potassium and aluminum, obtaining ion-ion structure factors in excellent agreement with experiments. Recently, we have extended the formalism and have performed a first-principles molecular dynamics simulation based on the QHNC theory for alkali metals near the triple point: in this study those small deviations which were still observed between experimental results and QHNC data for the structure factor disappeared completely.²

In the present study we first show that the QHNC method can provide an accurate description of liquid metals in a wide range of densities and temperatures: we calculate the structure factors of compressed liquid rubidium, which have been studied experimentally at high pressures from 0.2 to 6.1 GPa by Tsuji;³ furthermore we calculate the structure factors of expanded rubidium states which have been studied by Franz *et al.*⁴

Secondly, we show that the QHNC method can be extended to treat a plasma: in such a system, both the ionic valency Z_I and the electron-ion interaction $v_{ei}(r)$ may vary over a wide range as temperature and density are changed. Our method is in particular suited to treat a plasma, since it is able to calculate these quantities in a self-consistent manner using the atomic number of the system as the only input data. In order to treat plasmas, the electron-electron correlation must be determined for arbitrary temperatures. In this work, we show that the QHNC method applied to the electron gas is in fact able to provide the electron correlation at arbitrary temperature. Using then this electron-electron correlation, we study how a liquid metal becomes a plasma for the case of rubidium by increasing the temperature at a fixed density.

We can consider a liquid metal or a plasma as a mixture of electrons and ions interacting

through pair potentials $v_{ij}(r)$ [$i, j = e$ or I]. Since the ion–ion and electron–ion RDF’s, $g_{iI}(r)$ are identical to ion- and electron-density distributions under the external potential caused by a fixed ion at the origin respectively, DF theory provides exact expressions for these functions in terms of direct correlation functions (DCF’s) $C_{ij}(r)$ and bridge functions $B_{iI}(r)$ as follows:¹

$$g_{iI}(r) = n_i^0(r|U_i^{\text{eff}})/n_0^i, \quad (1)$$

$$U_i^{\text{eff}}(r) \equiv v_{iI}(r) - \frac{1}{\beta} \sum_I \int C_{iI}(|\mathbf{r} - \mathbf{r}'|) n_0^I [g_{iI}(r) - 1] d\mathbf{r}' - B_{iI}(r)/\beta. \quad (2)$$

Here, n_0^i is the number density and $n_i^0(r|U_i^{\text{eff}})$ is the density distribution of the noninteracting system. These expressions for $g_{iI}(r)$ can be transformed into a set of integral equations for the one-component model of liquid metals. One of them is a usual integral equation for the DCF $C(r)$ of a one-component fluid:

$$C(r) = \exp[-\beta v_{\text{eff}}(r) + \gamma(r) + B_{II}(r)] - 1 - \gamma(r), \quad (3)$$

with an interaction $\beta v_{\text{eff}}(Q) \equiv \beta v_{II}(Q) - |C_{eI}(Q)|^2 n_0^e \chi_Q^0 / [1 - n_0^e C_{ee}(Q) \chi_Q^0]$ and the other is an equation for the effective interaction $v_{\text{eff}}(r)$, that is expressed in the form of an integral equation for the electron–ion DCF $C_{eI}(r)$:

$$\hat{B}C_{eI}(r) = n_e^0(r|v_{eI} - \Gamma_{eI}/\beta - B_{eI}/\beta)/n_0^e - 1 - \hat{B}\Gamma_{eI}(r), \quad (4)$$

where $n_e^0(r|U_e^{\text{eff}})$ is determined by solving the wave equation for an electron under the external potential $U_e^{\text{eff}}(r)$. Here, χ_Q^0 is the density response function of the noninteracting electrons, n_0^e is the electron density, \hat{B} being an operator to represent some quantum effect and $\gamma(r) \equiv \int C(|\mathbf{r} - \mathbf{r}'|) n_0^I [g_{iI}(r') - 1] d\mathbf{r}'$. The QHNC equation can be obtained from Eqs. (3) and (4) by introducing the following five approximations:¹

1. $B_{eI} \simeq 0$ (the HNC approximation).
2. The bridge function B_{II} of the ion–electron mixture is approximated by that of one-component hard-sphere fluid (Modified HNC approximation⁵).
3. $C_{ee}(Q) \simeq -\beta v_{ee}(Q)[1 - G^{\text{jell}}(Q)]$ in terms of the the local-field correction (LFC) $G^{\text{jell}}(Q)$ of the jellium model.⁶
4. An approximate $v_{eI}(r)$ is obtained by treating a liquid metal as a nucleus–electron mixture⁷ in the form: $v_{eI}(r) = -Z_A e^2/r + \int v_{ee}(|\mathbf{r} - \mathbf{r}'|) n_e^b(r') d\mathbf{r}' + \mu_{XC}(n_e^b(r) + n_0^e) - \mu_{XC}(n_0^e)$, where $n_e^b(r)$ is the bound-electron distribution and $\mu_{XC}(n)$ is the exchange-correlation potential in the local-density approximation.
5. $v_{II}(r)$ is taken as pure Coulombic.

Under these approximations, a set of integral equations can be derived; its solution allows the determination of the electron–ion and ion–ion correlations together with the ionization and the electron bound states. In this contribution, the bridge function required in the MHNC approximation, is the one proposed recently by Rosenfeld.^{8,9} The MHNC equation based on the Rosenfeld bridge function is in fact able to produce accurate data for the structure factors of Rb as shown in Fig. 1: the white and black circles denote the experimental results.

Recently, Tsuji⁵ measured the structure factor of liquid Rb at high pressures: 0.2, 2.5, 3.9 and 6.1 GPa. The corresponding densities are estimated by the author as 1.07, 1.41, 1.56 and 1.95 times the normal density, respectively. We have calculated the structure factors corresponding to these states within the QHNC method. From 0.2 to 6.1 GPa we have

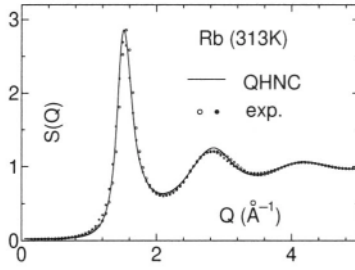


Figure 1. The ion-ion static structure factor $S(Q)$ for liquid Rb at a temperature of 313 K: solid curve, QHNC result; \circ , experiments.¹⁰

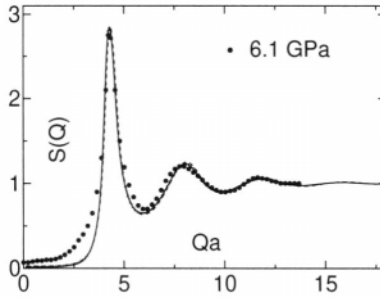


Figure 2. Structure factors for Rb calculated for 0, 0.2, 2.5, 3.9 and 6.1 GPa. All results are scaled in units of a in almost one curve; \bullet , experiment.

found an excellent agreement with experimental results. It should be mentioned here that our method is at high pressures as reliable as for room pressure, since all the approximations in the QHNC method remain valid as the pressure is increased.

The electron-ion RDFs for these five states remain almost unaffected under these pressures variations (if we plot in Angstroms). The effective ion-ion interaction in liquid rubidium is hence practically invariant under pressure variation and no scaling feature is observed in units of the Wigner-Seitz radius a . On the other hand, the structure factors for these five states coincide almost into a single curve when Q is scaled in units of the Wigner-Seitz radius a as shown in Fig. 2.

Next, we briefly consider expanded liquid rubidium, where the structure factors have been measured experimentally by Franz *et al.*⁴

Here, we apply the QHNC method in the same way as we have done for compressed

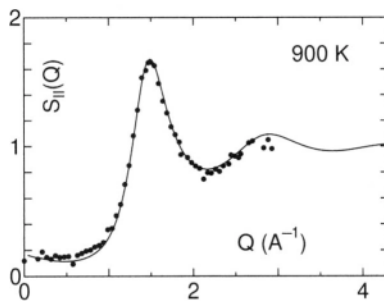


Figure 3. The structure factor $S_{||}(Q)$ for expanded liquid Rb at a temperature of 900 K: solid curve, the QHNC result; \circ , experiment.

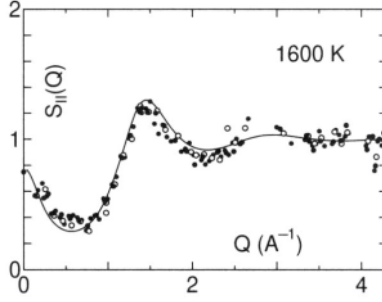


Figure 4. The structure factor $S_{II}(Q)$ for expanded liquid Rb at a temperature of 1600 K: solid curve, the QHNC result; \bullet , \circ , experiment.

liquid Rb. The full curves in Figs. 3 and 4 indicate structure factors at 900 K and 1600 K calculated by the QHNC equation, respectively. The experimental results are shown by circles: the agreement is excellent, in particular for low wave-vectors, a result which could not be obtained when using simple pseudopotentials.¹¹ A similar agreement is observed at 1700 K. As the temperature is increased to 1800 K (which is already quite close to the critical point), the calculated structure factor diverges at the origin stronger than the experimental structure factor.

Up to now we have shown that the QHNC method is able to give accurate results for compressed and expanded liquid Rb; in the following we will demonstrate that this method is able to give results of similar reliability also for a strongly coupled plasma. We now investigate the plasma state of rubidium by increasing the temperature while fixing the density to its value for the normal liquid state. However, when we apply the QHNC method to a plasma, the electron–electron DCF must be evaluated at arbitrary temperature. Here, we apply the QHNC equation to obtain the electron–electron DCF,

$$n_e(r|e) = n_e^0(r|U_{\text{eff}}) = \sum_i f(\epsilon_i) |\psi_i(r)|^2 \quad (5)$$

with $\beta U_{\text{eff}}(r) \equiv \beta v_{ee}(r) - \int C_{ee}(|\mathbf{r} - \mathbf{r}'|) [n_e(r'|e) - n_0] d\mathbf{r}'$, which reduces to the well known HNC equation for the classical electron gas in the high temperature limit. Here, the DCF for the one-component system is defined by $n_0 C_{ee}(Q) = 1/\chi_Q^0 - 1/\chi_Q^{ee} = -\beta v_{ee}(Q)[1 - G(Q)]$. The Fourier transform (denoted by \mathcal{F}) of the density distribution yields the following bootstrap relation for $C_{ee}(Q)$ together with Eqs. (5): $\mathcal{F}_Q[n_e(r|e) - n_0] = 1/[1 - n_0^e C_{ee}(Q)\chi_Q^0] - 1$. The electron–electron correlation, that is, the electron-density distribution around a fixed electron is shown in Fig. 5 calculated for a partially degenerate electron plasma at the density $2.51 \times 10^{22}/\text{cm}^3$ ($r_s = 4$) varying the temperature from 0.05 eV to 30 eV. The degeneracy is denoted by $\Delta = E_F/kT_B$, i.e., the Fermi energy over temperature. For high degeneracy (0.05 eV), the Thomas–Fermi (TF) approximation (denoted by full circles) gives quite a different density distribution from the one calculated by the wave equation. When the temperature is increased to 10 eV, the TF result becomes identical to the result obtained in the wave equation except for small r -values. When the temperature approaches 30 eV, the electron–electron correlation reduces to the classical one.

From these calculations, we can obtain the electron–electron DCF, which determines the plasma properties in terms of the LFC $G(Q)$. Using now the QHNC-LFC $G(Q)$ instead of a Geldart–Vosko⁶ type $G(Q)$, we apply Eqs. (3)–(4) to Rb at the fixed density of the normal liquid metal; the temperature has been varied from 0 to 30 eV in order to investigate how a liquid-metal state changes into a plasma state.

The electron–ion RDF of liquid Rb is plotted in Fig. 6 along with the ion–ion RDF's and the effective ion–ion interactions calculated using both the QHNC- and Geldart–Vosko-

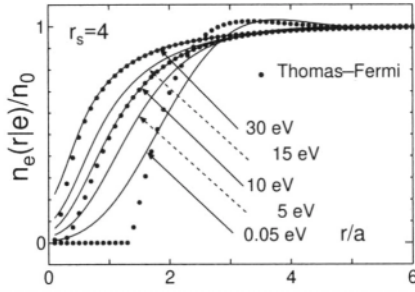


Figure 5. Electron–electron correlations in the electron gas at a density of $r_s = 4$ for temperatures ranging from 0.05 to 30 eV.

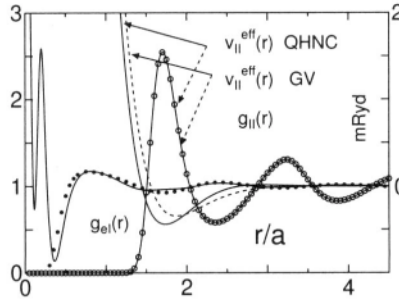


Figure 6. The electron–ion and ion–ion RDF’s with the effective interactions in liquid Rb: solid curve, QHNC result; •, electron–ion RDF derived by using an Ashcroft potential.

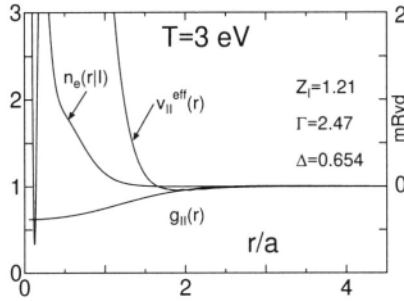


Figure 7. Electron–ion and ion–ion RDF’s together with the effective ion–ion interaction at a temperature of 3 eV.

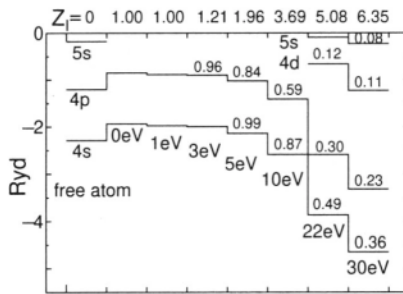


Figure 8. Temperature variation of outer bound levels in the Rb ion in a plasma. Numbers attached to bound levels denote the occupation numbers.

LFC's: the resulting two effective potentials differ, but yield almost the same ion-ion RDF's, as shown by the full curve and the white circles.

In Fig. 6 the electron-ion RDF obtained from the QHNC method has an inner-core structure which is caused by the orthogonality of the free-electron wave function to the core-electron wave functions. On the other hand, it should be noticed that the usual liquid-metal theory based on Ashcroft pseudopotentials yields an electron-ion RDF, which has no inner-core structure (shown by full circles): this cut-off of the inner core structure brings about a simple treatment of liquid metals in the standard liquid-metal theory. At a temperature of 0.05 eV, the electron-ion RDF has a distinct inner-core and outer-core part. Even at a temperature of 1 eV, this clear distinction remains characteristic for a liquid metal: the ionization is practically unity and the ion-ion effective interaction is almost the same as that of liquid metal at the normal condition, although the ion-ion correlation becomes weak. Figure 7 shows that at a temperature of 3 eV the distinction between inner- and outer-core parts has disappeared and that the ionization, now 1.21, has become significant. When the temperature increases to 30 eV, the ionization becomes as large as 6.35. Figure 8 shows the temperature variation of the outer bound levels of an ion in a Rb plasma at the fixed density of the normal liquid metal. The 4s- and 4p-bound levels are plotted there corresponding to a free atom, at 0, 1, 2, 3, 5, 10, 22 and 30 eV, respectively. As the temperature increases, the bound levels become deeper due to the decrease of the number of bound-electrons, which makes the screening effect weak. At 22 and 30 eV new bound levels, 5s and 4d, appear. The occupation number at each level is shown for every level line in Fig. 8. The ionization variation Z_1 is shown at the top of Fig. 8 as the temperature is increased.

GK acknowledges financial support by the Fonds zur Förderung der wissenschaftlichen Forschung under Proj. No. P11194-PHY.

REFERENCES

- [1] J. Chihara, *J. Phys.: Condens. Matter* 3:8715 (1991)
- [2] S. Kambayashi and J. Chihara, *Phys. Rev. E* 53:6253 (1996).
- [3] K. Tsuji, p. 317, in: "Elementary Processes in Dense Plasmas," S. Ichimaru and S. Ogata, ed., Addison-Wesley, New York, (1995)
- [4] G. Franz, W. Freyland, W. Hensel and E. Shneider, *J. Phys. (Paris)* 41 :C8-194 (1980).
- [5] Y. Rosenfeld, *J. Stat. Phys.* 42:437 (1986).
- [6] D. J. W. Geldart and S. H. Vosko, *Can. J. Phys.* 44:2137 (1966).
- [7] J. Chihara, *J. Phys. C: Solid State Phys.* 18:3103 (1985).
- [8] Y. Rosenfeld, *J. Chem. Phys.* 98:8126 (1993).
- [9] G. Kahl, B. Bildstein, and Y. Rosenfeld, *Phys. Rev. E* 54:5391 (1996).
- [10] J. R. D. Copley and S. W. Lovesey, *Int. Phys. Conf. Ser.* 30:575 (1979);
Y. Waseda, "The Structure of Non-Crystalline Materials," McGraw-Hill, New York, (1980).
- [11] G. Kahl and J. Hafner, *Phys. Rev. A* 29:3310 (1984).

ANOMALOUS PHASE DIAGRAM IN SIMPLEST PLASMA MODEL

Igor L. Iosilevski and Alexander Yu. Chigvintsev

Moscow Institute of Physics and Technology, Dolgoprudny 141700, Russia

INTRODUCTION

Problem of Phase Transition (PT) in Strongly Coupled Coulomb Systems (SCCS) is of great interest in plasma theory during very long time¹⁻⁵. Besides the study of hypothetical PT in real plasmas¹⁻³ a complementary approach is developing^{4,5} where the main subject of interest is definitely existing PT in simplified plasma models. In our previous study⁶⁻⁸ we dealt with a phase transition in the set of plasma models with common feature - combination of (i) absence of individual correlations (coupling) between charges of opposite sign, and (ii) total compressibility of system. The simplest example of such a system is One Component Plasma (OCP) on uniform, but *compressible* compensating background (following notation - OCP{c}). The well-known *prototype* model is OCP with a *rigid* background (notation - OCP{r}). This variant of OCP is studied carefully nowadays^{9,10}. The system can not collapse or explode spontaneously. The only phase transition - crystallisation - occurs in OCP{r} without any density change.

Transition to the OCP on uniform and compressible background leads to appearance of a *new* first-order *phase transition* of gas-liquid type⁶. New phase diagram combines previous crystallisation, now with a *finite* density change, with a qualitatively different coexistence curve of the new phase transition. The structure and parameters of this phase diagram strongly depend on exact definition of thermodynamic contribution of background. The simplest variant of OCP{r} is the «**Single OCP**» - the system of classical point charges with a compressible background of ideal fermi-gas of electrons. This variant of OCP was declared repeatedly^{11,12} but the discussed phase transition was out of consideration. Closely similar structure of global phase diagram was obtained in «**Combined OCP**»⁶⁻⁸. This is superposition of two *non-coupled* OCP-s of mass-non-symmetrical charged particles of opposite sign.

PHASE DIAGRAM OF SINGLE OCP{C}

Three qualitatively different situations should be distinguished for the OCP{c} depending on the value of charge number Z :

- 1) Low value of charge number - $Z < Z_1^* \approx 35$
- 2) High value of charge number - $Z > Z_2^* \approx 45$
- 3) Intermediate value of charge number - $Z_1^* < Z < Z_2^*$

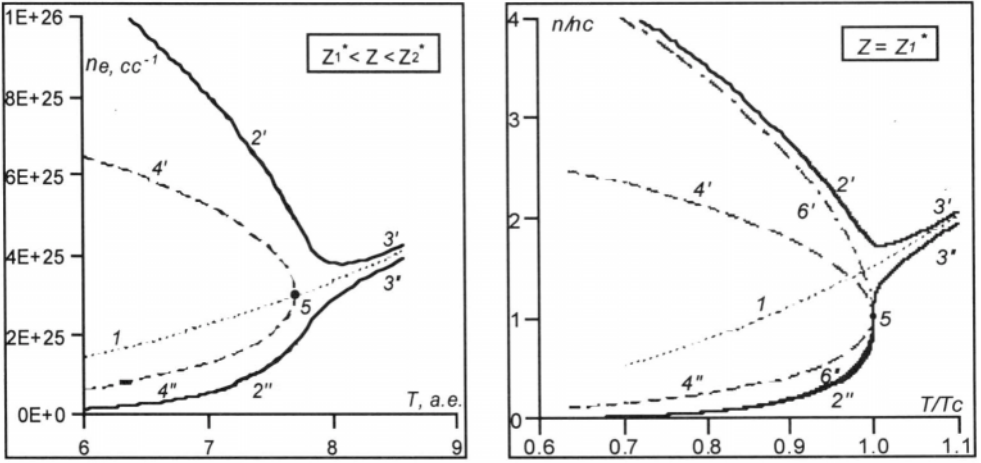


Figure 1. Phase diagram of the Single OCP{c} of classical point charges on uniform compressible background of ideal fermi-gas of electrons at intermediate value of charge number ($Z_1^* < Z < Z_2^*$). Notations: 1- melting line of prototype OCP{r} ($\tilde{A} \sim \tilde{A}_{melt} \approx 178$); 2', 2'', 3', 3''- global crystal-fluid (gas and liquid) coexistence; 2', 2''-sublimation, 3', 3''- melting; 4 - spinodal of metastable liquid-gas coexistence; 5 - its critical point.

Figure 2. The same for the lowest of two boundary values of charge number $Z = Z_1^* \approx 34.6$. Notations: 1-4 - as at Figure 1; 5 - pseudo-critical «termination» point; 6', 6'' - metastable liquid-gas binodal.

Low Values of Charge Number ($Z \sim 1$)

Phase diagram of the model was carefully studied in⁶⁻⁸. The ordinary structure of global phase diagram was obtained in this case: the relative position of critical and triple points, melting «stripe», gas-liquid and gas-crystal coexistence, are totally equivalent to those for normal substances.

High Values of Charge Number ($Z \sim 100$).

Highly anomalous structure of global phase diagram was announced at previous study^{6,7}. The melting «stripe» ($\tilde{A} \approx 178$) crosses gaseous part of coexistence curve of the new phase transition.

- Triple point is placed at gaseous part of two-phase boundary.
- Critical point is placed at crystalline part of two-phase boundary.
- Crystal-crystal coexistence of two dense and expanded crystalline phases of the same structure occurs in OCP{r} at such a high values of charge number Z .

Intermediate Values of Charge Number ($Z_1^* < Z < Z_2^*$)

The most remarkable anomalous phase diagram corresponds to the case when the melting line of prototype OCP{r} ($\tilde{A} \sim \tilde{A}_{melt} \approx 178$) crosses coexistence curve of the new gas-liquid phase transition just closely to its critical point. As a result of this coincidence:

- The only phase transition exists in the model. It corresponds to the global crystal - fluid coexistence – continues superposition of melting and sublimation (see Figure 1).
- There is no true critical point.
- There is no triple point.
- Coexistence curve in $P \leftrightarrow T$ (pressure ↔ temperature) plane is a continues, infinite curve. There is no any break at this curve.

Boundary Values of Intermediate Charge Number Interval ($Z_1^* < Z < Z_2^*$)

Remarkable feature of phase diagram of OCP{c} at $Z = Z_1^*$ or $Z = Z_2^*$ is an existence of *pseudo-critical point* where the well-known standard conditions are fulfilled:

$$(\partial P/\partial V)_T = 0 \quad (\partial^2 P/\partial V^2)_T = 0$$

$Z = Z_1^* \approx 34.6^*$ – on *gaseous part* of crystal-fluid binodal (see Figure 2)

$Z = Z_2^* \approx 45.4^*$ – on *crystalline part* of crystal-fluid binodal.

When we use the same as in⁶⁻⁸ analytical fits for equation of state of both subsystems, OCP{r} and background, we obtain following parameters of the both pseudo-critical points:

Table 1. Parameters of pseudo-critical point in OCP of classical point charges on the uniform and compressible background of ideal fermi-gas of electrons ($Z = Z_1^*$ or Z_2^*)
 $(\bar{A} \equiv Z^2 e^2 / a_s kT; r_s \equiv a_s / a_B; \theta \equiv kT / \epsilon_F \equiv 4 / (9\pi)^{1/3} (n_e \Lambda_e^3)^{2/3}; \Lambda_e^2 \equiv 2\pi \hat{a}^2 / m_e kT; a_s^3 \equiv 4\pi n / 3)$

	Z	T_C , a.u.	$(n_e)_C$, cc ⁻¹	P_C , a.u.	\bar{A}_R	$(r_s)_C$	$(n_e \Lambda_e^3)_C$	$(\theta)_C$
$Z = Z_1^*$	34.6	6.38.	2.24 10 ²⁵	11.4	140	0.416	3.30	2.91
$Z = Z_2^*$	45.4	9.29	3.96 10 ²⁵	28.4	181	0.344	3.26	2.89

CRITICAL EXPONENTS

Remarkable feature of two discussed pseudo-critical points at $Z = Z_1^*$ or $Z = Z_2^*$ is the non-standard values of all critical exponents in comparison with the ordinary (van der Waals like) critical exponents that correspond to the case of OCP{c} with the charge number Z beyond the discussed interval $Z_1^* + Z_2^*$. For example, at the latter case ($Z < Z_1^*$ or $Z > Z_2^*$), the standard **density**↔**temperature** relation is valid

$$(\rho - \rho_C) \sim |T - T_C|^{1/2}$$

For the pseudo-critical points ($Z = Z_1^*$ or $Z = Z_2^*$) the following relation may be proved:

$$(\rho - \rho_C) \sim |T - T_C|^{1/3}$$

Direct calculation gives:

$$|\rho/\rho_C - 1| \equiv 4.57 |T/T_C - 1|^{1/2} \quad (Z = 1)$$

$$|\rho/\rho_C - 1| \equiv 4.07 |T/T_C - 1|^{1/3} \quad (Z = Z_1^* \approx 34.6)$$

SATURATION CURVE

Similar violation is observed for saturation ($P_{sr} \leftrightarrow T_{sr}$) curve. So-called Plank – Gibbs rule (equal slope of saturation curve at $T = T_C - \epsilon$ and critical isohore at $T = T_C + \epsilon$) is valid for an ordinary critical point ($Z < Z_1^*$ or $Z > Z_2^*$),

$$(dP/dT)_{sr} = (\partial P/\partial T)_{v_c}$$

It is not evident (see Figure 3), but it can be proved that this rule is *not valid* for pseudo-critical points ($Z = Z_1^*$ or $Z = Z_2^*$).

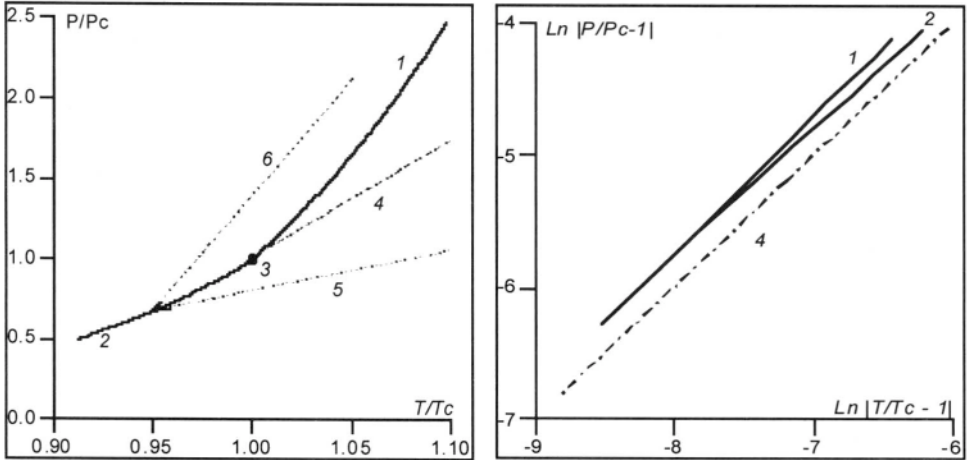


Figure 3. Saturation curve and isohores in reduced coordinates for the Single OCP{c} of classical point charges with uniform compressible background of ideal fermi-gas of electrons at boundary value of charge number $Z = Z_1^* \cong 34.6$. Notations: 1 - sublimation; 2 - melting; 3 - pseudo-critical «**termination**» point; 4 - critical isohore; 5,6 - sub-critical isohores.

Figure 4. The same as on Fig. 3 in $\text{Log} \leftrightarrow \text{Log}$ - coordinates. Notations: 1-4 - as on Fig. 1.

This statement is illustrated on Figure 4. Small deviation in position of binodal (curves 1, 2) and critical isohore (curve 4) corresponds to the small difference in slope of both the curves at pseudo-critical point (Figure 3).

ACKNOWLEDGEMENTS

One of the authors (I.L.I.) thanks M. Fisher, H. DeWitt, J. Perdew, J-M. Caillol, L.Suttorp and Y. Resenfeld for interesting discussions during SCCS'97, and Gabor Kalman for his kind invitation to the Conference.

REFERENCES

1. E. Norman and A. N. Starostin, *Teplofiz. Vysokih. Temp.* 6:410 (1968).
2. Ebeling, W. D. Kraeft and D. Kremp. «**Theory of Bound states and Ionization Equilibrium in Plasmas and Solids,**» Academic-Verlag, Berlin, (1976).
3. Saumon, G. Chabrier, *Phys.Rev.Let.* 62: 2397 (1989).
4. Vorontsov-Veliaminov, V.P. Chasovskih, *Teplofiz. Vysokih. Temp.* 13:1153 (1975)
5. E. Fisher, *J.Stat.Phys.* 75:1 (1994)
6. L. Iosilevski, *High Temperatures.* 23:807 (1985)
7. L. Iosilevski and A. Yu. Chigvintsev in «**Physics of Nonideal Plasmas,**» W. Ebeling, A.Förster and R. Radtke, ed., Teubner Texte, Stuttgart- Leipzig (1992).
8. L. Iosilevski and A. Yu. Chigvintsev in «**Physics of Strongly Coupled Plasmas,**» W.D.Kraeft and M. Schlages, ed., World Scientific, New Jersey-London (1996).
9. Baus and J. P. Hansen, *Phys. Reports*, 59:1 (1980)
10. Ishimaru, H. Yyetomi and S. Tanaka, *Phys. Reports*, 149:91 (1987).
11. L. Pollock and J. P Hansen, *Phys.Rev.* A-8:3110 (1973).
12. Alder, E. Pollock and J. P. Hansen.*Proc.Natl.Acad.Sci.USA.*,77:6272 (1980).

THERMODYNAMIC PROPERTIES OF THE MIXTURE He–Hg AT HIGH TEMPERATURES AND PRESSURES

Ernesto Marceca and Friedrich Hensel

Philipps Universität Marburg
Hans Meerwein Straße, 35043 Marburg, Germany

INTRODUCTION

At low temperature, coexistence of two fluids is possible. Under a wide range of field-variables, a vapor phase characterized by a strong entropic contribution to the free energy is in equilibrium with a denser liquid, in which the configurational internal energy plays a dominant role. As the temperature is increased, the cohesion energy among the particles influences relatively less the free energy content of the system and the liquid and vapor phases abridge their properties; both phases enhance their entropic contribution to the free energy. The critical point is the limiting situation in which the cohesion energy is no longer able to differentiate a second denser phase from the gas. A pure supercritical fluid exhibits therefore an appealing feature, as it is the possibility that their density may be varied in a continuous manner without the occurrence of a liquid–vapor phase transition.

However, as soon as a second component is incorporated to the system, its composition appears as a new density-variable and the occurrence of material instability may force the system to split in two fluid phases. If a sample containing equal volumes of a binary liquid mixture and its equilibrium vapor is heated, and if the pressure is adjusted to maintain the equality of volumes, then the system must come eventually to a critical point at which all the intensive properties of both coexisting phases are the same¹ Moreover, if the sample's composition changes differentially, then a neighboring critical point on the binary critical *line* is reached.

The variety and complexity of phase behavior for mixtures at high pressures and temperatures is large;² even for binary mixtures, the equilibrium region where two fluid phases may coexist is not limited to temperatures lower than the critical temperature of the less volatile component. Poorly attractive and repulsive systems as most simple binary mixtures containing helium as one of their components show an interrupted critical line, one branch of which remains open up to the highest measurable temperatures and pressures. Since a phase separation now occurs at temperatures and pressures above the critical ones of both components one speaks about gas–gas or better fluid–fluid equilibria. The suggestion that fluid–fluid phase separation may occur at astrophysical conditions³ has stimulated intense theoretical research since it has important consequences for forming a conception of the composition and structure of the Jovian planets.

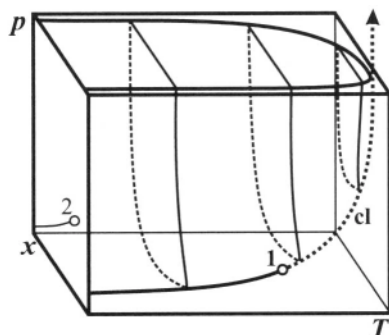


Figure 1. $(p-T-x)$ first-type fluid–fluid phase diagram of a binary mixture. Three isothermal $(p-x)$ sections of the two-phase coexisting surface are shown. 1, 2: critical points of the pure components; cl: critical line of the mixture.

Figure 1 sketches a typical $(p-T-x)$ thermodynamic phase diagram of a binary mixture which shows first-type fluid–fluid equilibrium. Number 1 indicates the critical point of the less volatile component, at the end of the vapor pressure curve, on the front plane of the three-dimensional diagram. Number 2 denotes the critical point of the other substance, on the rear plane. A two-phase coexisting surface appears folded along the vapor pressure curve of component 1 and then along the critical line cl.

Recently, hydrogen has been proven to be a fluid metal at megabar pressures,⁴ a pressure range which is relevant to astrophysical conditions. The existence of a repulsive interaction between helium and the conduction electrons of the metallic phase has often been proposed to be responsible for demixing in the hydrogen–helium planets Jupiter and Saturn. Unfortunately, precise experimental phase diagrams of helium–hydrogen mixtures are only possible up to kilobar pressures,⁵ where hydrogen behaves still as an insulating fluid.

The motivation of the present work is to study the interaction of helium (2) atoms with the conduction electrons present in a model metallic fluid. Expanded supercritical mercury (1) in the density range where its metal–non-metal transition occurs was selected as the model two-electron fluid metal. At sufficiently high density, non-metallic expanded mercury experiences a transition to a metallic state^{6,7} in the same way that hydrogen does at pressures corresponding to those in the interior of the planets. The influence of this change upon helium’s miscibility and its consequences on sensitive thermodynamic properties of the mixture have been investigated here. The control of the density in the supercritical mixture without the occurrence of a phase transition has provided a means of *fine tuning* the present interactions.

RESULTS AND DISCUSSION

The pressure–density–temperature–composition phase diagram of He–Hg mixtures has been measured⁸ using an isochoric synthetic method to temperatures up to 1882 K and pressures up to 3325 bar. The $(p-T-x)$ phase equilibrium surface obtained is qualitatively like the one sketched in figure 1, where the density variable ρ is not shown. The critical line starts at the critical point of pure Hg ($T_1^c = 1751$ K, $p_1^c = 1673$ bar) and runs to higher temperatures and pressures as the helium composition x_2 increases.

Figure 2 shows two isothermal $(\rho-x_2)$ sections of the phase diagram. The two-phase region is located above the He solubility curves of phases (') and (''), on the left and on the right hand side of cl, respectively. Representative tie lines connecting coexisting phases are shown in the figure and the corresponding values of the equilibrium variables are given in

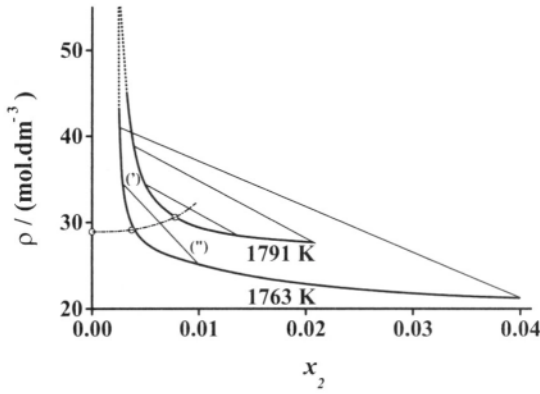


Figure 2. $(\rho-x_2)$ isothermal sections of the He–Hg phase diagram at 1763 K and 1791 K. \circ : critical points; - \bullet -: critical line. Isothermal solubility curves: — experimental; - - - extrapolated to $\rho' = 55 \text{ mol.dm}^{-3}$. Selected tie lines are shown.

Table 1. Critical points and tie lines connecting phases (') and (") on figure 2

isotherm 1763 K					isotherm 1791 K				
p Kbar	x_2'	x_2''	ρ' mol/l	ρ'' mol/l	p Kbar	x_2'	x_2''	ρ' mol/l	ρ'' mol/l
1.78	0.0037	0.0037	29.1	29.1	1.97	0.0078	0.0078	30.6	30.6
1.82	0.0030	0.0101	34.3	25.0	2.01	0.0050	0.0137	34.4	28.5
2.04	0.0026	0.0400	41.0	21.3	2.15	0.0039	0.0209	38.9	27.6

Table 1. Experimental data (thick solid lines) show that He solubility in the denser phase (') decreases monotonically as the density increases along the metal–non-metal transition region of Hg. The ρ' – x_2' data trend has been used to extrapolate the solubility isotherms to $\rho' = 55 \text{ mol.dm}^{-3}$, where most of the properties of Hg are well described by the free electron model.⁷ Here, the solubility of He is low enough to justify the use of an equation of state for pure Hg⁹ to estimate the pressure p .

Derivation of the thermodynamic properties of the mixture was performed by use of a Taylor expanded molar Helmholtz free energy function in powers of $\delta v = v - v^0$ and $\delta x = x_2$, where v^0 is the critical molar volume of the mixture at temperature T

$$\begin{aligned}
 a(x_2, v) = & a^0 + a_x^0 \delta x + a_v^0 \delta v + \frac{1}{2} a_{xx}^0 \delta^2 x + \frac{1}{2} a_{vv}^0 \delta^2 v + a_{xv}^0 \delta x \delta v + \\
 & \frac{1}{6} a_{xxx}^0 \delta^3 x + \frac{1}{6} a_{vvv}^0 \delta^3 v + \frac{1}{2} a_{xxv}^0 \delta^2 x \delta v + \frac{1}{2} a_{xvv}^0 \delta x \delta^2 v + \dots \quad (1)
 \end{aligned}$$

Phase diagram data were employed to fit the parameters a_{ijk}^0 taking into account that $a_v = -p < 0$, $a_{vv} = (v\kappa T_x)^{-1} > 0$, and the phase equilibrium conditions. Important thermodynamic quantities can now be calculated using the parameters a_{ijk}^0 , for example: $(\partial p / \partial x_2)_{TV} = a_{xv}^0 + a_{xvv}^0 \delta v + a_{xxv}^0 \delta x + \dots$. This quantity denotes the rate of change of pressure upon the exchange of solvent by solute molecules at constant (T, V) and it is related to the solvent–solvent (C_{11}) and solvent–solute (C_{12}) direct correlation function integrals in a straightforward way: $(\partial p / \partial x_2)_{TV} = RT\rho(C_{11} - C_{12})$. Large and positive values of $(\partial p / \partial x_2)_{TV}$ are then characteristic of repulsive systems with solvent depletion around the solute.¹⁰

Figure 3 shows the values of $(\partial p / \partial x_2)_{TV}$ for the systems He–Hg and He–Xe as a function of the reduced density $\rho_{\text{red}} = \rho / \rho_1^c$. Although both systems exhibit fluid–fluid phase separation and can be labeled as repulsive systems, the occurrence of a metal–non-metal

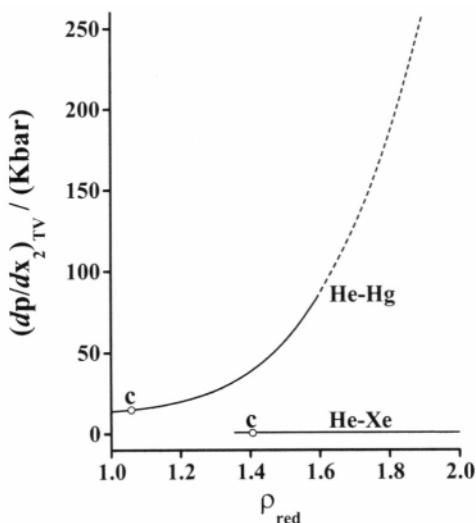


Figure 3. Isothermal isochoric change of pressure upon the exchange of solvent by solute molecules. — experimental; - - - extrapolated to $\rho' = 55 \text{ mol.dm}^{-3}$ (see text). T/T_f^c : 1.023 He-Hg, 1.015 He-Xe. c: critical points on the isotherms. He-Xe values calculated using data from Ref. [11]

transition in the mixture He-Hg dramatically differentiates its behavior from that of the simple mixture He-Xe. Electrical, optical and magnetic evidences⁷ show that a gradual evolution of metallic properties occurs in fluid Hg within the density range $\rho_{\text{red}} = 1.4\text{--}1.9$ (at $\rho_{\text{red}} = 1.9$ most properties are already well described by the nearly free electron model). A clear correlation between the relatively steep increase in the positive figures of $(\partial p / \partial x_2)_{TV}$ and the change in the electronic structure seems to occur demonstrating the interplay between the latter and the helium solubility.

REFERENCES

- [1] J. S. Rowlinson and F. L. Swinton. "Liquids and Liquid Mixtures," Butterworths, London (1982).
- [2] P. H. van Konynenburg and R. L. Scott, *Phil. Trans. R. Soc. London* 298(A):495–540 (1980).
- [3] R. Smoluchowski, *Nature* 215:691–695 (1967).
- [4] S. T. Weir, A. C. Mitchell and W. J. Nellis, *Phys. Rev. Lett.* 76(11):1860–1863 (1996).
- [5] J. A. Schouten, L. C. van den Bergh and N. J. Trappeniers, *Chem. Phys. Lett* 114(4):401–404 (1985).
- [6] N. F. Mott. "Metal-Insulator Transition," Taylor and Francis, London (1974).
- [7] F. Hensel, *J. Phys.: Condens. Matter* 2:SA33–SA45 (1990).
- [8] E. Marceca, G. Schäfer and F. Hensel, *J. Chem. Thermodynamics* 28:647–666 (1996).
- [9] G. Schönherr, R. W. Schmutzler and F. Hensel, *Philosophical Magazine* 40:411–423 (1979).
- [10] I. B. Petsche and P. G. Debenedetti, *J. Phys. Chem.* 95:386–399 (1991).
- [11] J. de Swaan Arons and G. A. M. Diepen, *J. Chem. Phys.* 44:2322–2330 (1966).

THE ATOMIC–MOLECULAR TRANSITION IN EXPANDED LIQUID RUBIDIUM

W. C. Pilgrim,¹ M. Ross,^{1,2} L. H. Yang,² and F. Hensel¹

¹Philipps-University of Marburg
Hans Meerwein Straße, 35043 Marburg, Germany

²Lawrence Livermore National Laboratory
Livermore, CA

INTRODUCTION

Though it is known for long that dilute alkali vapors show significant dimerization¹ it is still an open question to which extend molecular association does also exist at higher densities in the compressed vapor or in the expanded liquid. During the past twenty years the density dependence of the dimer concentration in cesium and rubidium vapors has extensively been investigated. The results from measurements of electrical conductivity,² magnetic susceptibility,³ optical spectroscopy⁴ and from statistical considerations⁵ indicate that in the vicinity of the liquid–vapor critical point a dimer concentration of about 20–30% should be expected and that higher molecular aggregates like trimers and tetramers are also being formed under these conditions. The question that emerges from these findings is, do these molecular aggregates also survive further compression of the fluid into the dense liquid?

Recently, we could investigate this problem in determining the inelastic scattering law $S(Q, \omega)$ for several densities of liquid rubidium between the melting point and the critical point. In a series of experiments we were able to extend our inelastic neutron scattering investigations up to temperatures of 1873 K under conditions close to the vapor pressure curve. This corresponds to about twice the critical density. Measurements of electrical and magnetic properties show that localization of conduction–electrons in the metallic liquid is already significant under these conditions hence interactions between the paramagnetic atoms should be expected.

The liquid was expanded along the liquid–vapor coexistence line towards the critical point ($T_C = 2017$ K, $\rho_C = 0.29$ g/cm³)⁶ by simultaneously increasing temperature and pressure. The results expressed as $S(Q, \omega)$ for $Q = 1.0$ Å⁻¹ and in terms of the longitudinal current correlation function $J_l(Q, \omega) = (\omega^2/Q^2) \cdot S(Q, \omega)$ for $Q = 1.3$ Å⁻¹ are given in figure 1 for some of the experimental conditions investigated hitherto.

As can be seen, neither the scattering law nor the current correlation function shows dramatic changes if the liquid is expanded from high densities at 1073 K to 0.83 g/cm³ at 1673 K which corresponds to about three times the critical density. This indicates that the ion–ion dynamic under these conditions of p and T is still controlled by the electron sea of the metal. The same conclusion can be drawn from comparing our experimental

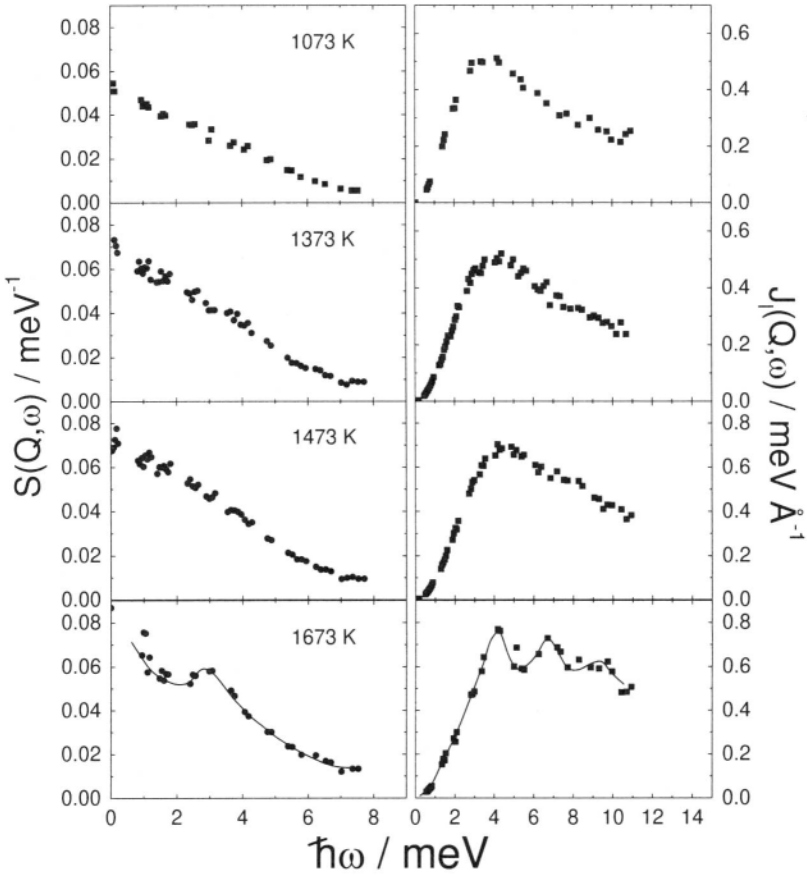


Figure 1. $S(Q, \omega)$ at $Q = 1 \text{ \AA}^{-1}$ and current correlations functions $J_l(Q, \omega)$ at $Q = 1.3 \text{ \AA}^{-1}$ for four different densities measured along the vapor pressure curve: 1073 K, $\rho = 1.13 \text{ g/cm}^3$; 1373 K, $\rho = 0.98 \text{ g/cm}^3$; 1673 K, $\rho = 0.83 \text{ g/cm}^3$; 1873 K, $\rho = 0.61 \text{ g/cm}^3$.

results with theoretical findings of Hoshino et al.⁷ In their work the static structure factor has been calculated in a modified hypernetted chain approximation for 1700 K and a density corresponding to conditions close to the liquid vapor coexistence curve. The resulting $S(Q)$ was then employed to calculate the dynamic scattering law in the viscoelastic approximation.⁸ Although this model is exactly valid only at conditions close to the triple point of a liquid metal, where the nearly free electron approximation applies, the dispersion of the maxima from the longitudinal current correlation functions $J_l(Q, \omega)$ is in accord with our experimental results under similar thermodynamic conditions.⁹ In figure 2 our experimental result at 1723 K is compared with the theoretical finding at 1700 K. The observed consistency between the data again indicates that the dynamic of the liquid at about three times the critical density, is still controlled by the metallic binding between the atoms and the screening from the nearly-free electron-gas. This interpretation is consistent with findings from measurements of electrical conductivity¹⁰ and magnetic susceptibility.³

In decreasing the density further to about twice the critical density drastic changes are observed which are apparent in both, $S(Q, \omega)$ and $J_l(Q, \omega)$. A well defined excitation peak appears in the scattering law. In $S(Q, \omega)$ the peak is centered around 3.2 meV while in $J_l(Q, \omega)$ the peaks can be identified as resulting from excitations at 3.2 meV with higher harmonics around 6.5 and 9.5 meV. In $S(Q, \omega)$ the excitation seems to be most pronounced

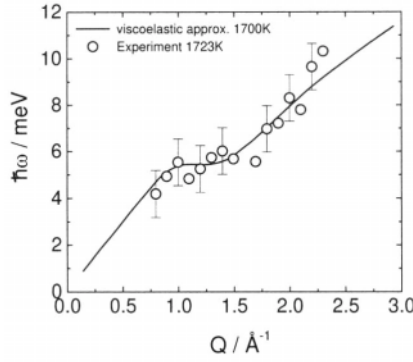


Figure 2. Comparison between the theoretically determined dispersion of the current–current correlation at 1700 K (line) with the corresponding experimental results for 1723 K (open circles).

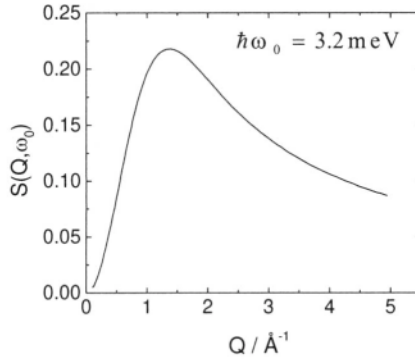


Figure 3. Q -dependence of the intensity of an excitation peak from a particle executing harmonic oscillations about its center of mass for $k_B T > \hbar\omega_0$, with $\hbar\omega_0 = 3.2$ meV,

around 1.0 \AA^{-1} . However, this observation is consistent with a simple model for the scattering law resulting from a system of noninteracting diatomic harmonic oscillators. For $k_B T > \hbar\omega_0$ this model simplifies to [11]:

$$S(Q, \omega) = \sum_{n=-\infty}^{\infty} I_n(y) \cdot e^{-y} \delta(\omega - n\omega_0); \quad y = \frac{\hbar^2 Q^2 k_B T}{M(\hbar\omega_0)^2}$$

Herein $I_n(y)$ are modified Bessel functions of the first kind and n th order, $\hbar\omega_0$ is the energy difference between adjacent energy levels of the oscillating particle and the δ -function under the sum ensures for energy conservation during the interaction between the neutron and the molecule. Inserting the observed value of 3.2 meV and the reduced mass M for a rubidium dimer yields the Q -dependence of the excitation intensity given in figure 3. As can be seen the maximum intensity for such an excitation is indeed centered around 1.0 \AA^{-1} .

In order to get more theoretical support for the existence of molecules in liquid rubidium and to gain an insight into the microscopic properties of such particles we have undertaken exploratory calculations for the total energy of expanded lattices of monatomic Rb and Rb₂-dimers using density functional theory in the local density approximation.¹² The calculations were made for a system of Rb atoms in a body-centered lattice (bcc) and for diatomic molecules in a simple cubic lattice (sc). To create the diatomic solid the two atoms in the bcc unit cell were moved towards one another forming a simple cubic lattice (sc). The lattices were then continuously expanded and the total energy was calculated for several densities. It was found that below a density of 0.9 g/cm^3 the **sc-Rb₂** lattice has the lower energy. The

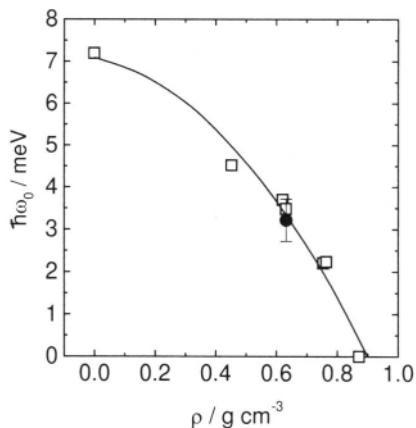


Figure 4. Density-variation of the vibron energy for Rb_2 obtained from theory (open squares). Included is the experimental point (solid circle) at $\rho = 0.61 \text{ g/cm}^3$. The line is a smooth fit to the calculated data.

potential curve of the dimer was obtained by variation of the bond length from its equilibrium value R_0 and calculating the change in energy $E(R - R_0)$. These data were then fitted to a Morse-Potential from which the dissociation energy D_e and excitation energy $\hbar\omega_0$ could be obtained for each density. The latter is given in figure 4 as a function of density.

Also shown is the experimental data point, at $\rho = 0.61 \text{ g/cm}^3$ and $\hbar\omega_0 = 3.2 \text{ meV}$, which is in remarkably good agreement with the calculations. In order to find out whether the concentration of molecules in the liquid is sufficiently high to be observable in a neutron scattering experiment the fraction of molecules present in the liquid was calculated with the mass action equation for an equilibrium mixture of atoms and dimers using the values of $\hbar\omega_0$ and D_e . The vibrational partition function was calculated by summing over all states of the Morse oscillator and the temperature at each density along the liquid-vapor curve was obtained from experimental results.⁶ A value of about 25% dimer concentration is obtained for the experimental conditions. This is in good agreement with other estimates.^{3,5}

REFERENCES

- [1] W. H. Evans, R. Jacobson, T. R. Munson and D. D. Wagman, *J. Res. Natl. Bur. Std.* 55: 83 (1955); C. T. Ewing, J. P. Stone, J. R. Spann, R. R. Miller, *J. Phys. Chem.* 71: 473 (1967).
- [2] A. A. Borzhievskii, V. A. Sechenov, V. I. Khorunzhenko, *Teplofizika Vysokikh Temperatur* 26:722 (1988), translated to English in: *High Temperature* 26:551 (1988).
- [3] W. Freyland, *Phys. Rev.* 20:5104 (1979).
- [4] W. C. Pilgrim, R. Winter and F. Hensel, *J. Phys.: Condens. Matter* 5:B183 (1993); F. Hensel and G. F. Hohl, *The Review of High Pressure Science and Technology* 3:163 (1994).
- [5] R. Redmer and W. W. Warren, *Phys. Rev. B* 48:14892 (1993).
- [6] S. Jünger, B. Knuth and F. Hensel, *Phys. Rev. Lett.* 55:2160 (1985).
- [7] K. Hoshino, H. Ugawa and M. Watabe, *J. Phys. Soc. Japan* 61:2182 (1992).
- [8] J. P. Hansen and I. R. McDonald. "Theory of Simple Liquids," Academic Press, New York, 2nd Ed. (1986).
- [9] W. C. Pilgrim, M. Ross, L. H. Yang, "Proceedings of the International Conference on Neutron Scattering," Toronto 1997, *Physica B* (1998) (to be published).
- [10] R. Winter, F. Noll, T. Bodensteiner, W. Gläser, P. Chieux and F. Hensel, *Z. Physikal. Chem. N. F.* 156:145 (1988).
- [11] S. W. Lovesey. "Theory of Neutron Scattering from Condensed Matter," Vol. 1, Oxford Science Publications, Oxford, (1984).
- [12] W. C. Pilgrim, M. Ross, L. H. Yang, *Phys. Rev. Lett.* 78:3685 (1997).

IONIC MODEL FOR LIQUID URANIUM DIOXIDE

Victor K. Gryaznov¹, Igor L. Iosilevski², Eugene S. Yakub³,
Vladimir E. Fortov¹, Gerald J. Hyland⁴ and Claudio Ronchi⁵

¹Institute of Chemical Physics at Chernogolovka, 142432, Russia

²Moscow Institute of Physics and Technology, Dolgoprudny 141700, Russia

³Odessa State Medical University, Odessa 270026, Ukraine

⁴University of Warwick, United Kingdom

⁵European Commission, Joint Research Centre, Karlsruhe, Germany

INTRODUCTION

Equation of state of gaseous and liquid uranium dioxide is of primary importance for the nuclear safety problem^{1,2}. Solid uranium dioxide is known to be of ionic structure. Liquid uranium dioxide is presumed to keep significant part of ionic bonding on melting³⁻⁵. It is well known that adequate description of ionic systems both of simplified models⁶ and of real ionic liquids⁷ is obtained when bound associations are taken into account explicitly. Study of thermodynamic properties of liquid uranium dioxide within the general approach of INTAS project^{1,2} deals with the assumption that liquid UO_2 may be successfully described in frames of *more than one* "equivalent" models, including *quasi-molecular* model as well as *pure ionic* one^{3,4}. For two such simplified *ionic* models the real calculations were performed^{1,2}. We considered Restricted Ionic Model (RIM-4:2) - electroneutral stoichiometric composition of two ionic species of sort «1» (U^{4+}) and «2» (O^{2-})^{3,4} with *equal hard-sphere diameters* of ions. Within *Restricted Primitive Ionic Model (RPM)* the mixture of ions with *only Coulomb* interaction was studied. An additional short-range attractive interaction of the van der Waals' type was taken into account within *Improved Restricted Ionic Model (IRIM)*.

Equation of State

Inter-ionic interaction assumed to be pair-additive and consisting of two parts: short-range hard-sphere repulsion $\Phi^R(r_{ij})$, and Coulomb long-range interaction $\Phi^C(r_{ij})=Z_\alpha Z_\beta e^2/r$ ($Z_1 = +4$ and $Z_2 = -2$). An additional short-range van der Waals *attraction* $\Phi^A(r_{ij})$ was considered in the Improved Ionic Model.

Free energy of liquid UO_2 was written as the sum of ideal gas contribution $F^{(id)}_{\text{MIX}}$ and three types of interaction corrections corresponding to the Coulomb interactions and to short-range repulsion and attraction,

$$F_{MIX} = F_{MIX}^{(id)} + kT \sum_{\alpha=1}^M N_{\alpha} \left(\frac{\Delta F_{HS}}{RT} + \frac{\Delta F_{vdw}}{RT} + \frac{\Delta F_C}{RT} \right), \quad (1)$$

Partition function of ion U^{4+} , which was included in the ideal gas free energy contribution $F_{MIX}^{(id)}$, was calculated in⁸ with excitation energy levels of ion U^{4+} recommended by IVTAN⁹. Partition function of negative ion O^{2-} was assumed to be equal to that of ion O^- . For the hard-sphere excess free energy contribution we used Carnahan–Starling formula $\Delta F_{HS}/RT \}_{CS} = (4v - 3v^2)/(1 - v)^2$; $v \equiv \sum N_i (\pi d_i^3/6)/V$.

Approximations for Coulomb Contribution

Many of approximations¹⁰ proposed for Coulomb contribution are consistent only in the limit of hot and dilute conditions when diameters of ions d_i are small relatively to Debye radius r_D (weakly non-ideal plasma). For molten salts, on the contrary, the large values of dimensionless parameter $x \equiv d/r_D$ are typical. The most important *assumption* of present study was the specific *one-parametric* form of correction function $\theta(x, v) \equiv \theta(x)$ in the Coulomb contribution, which was represented in the form:

$$\frac{\Delta F_C}{RT} \equiv f(x, v) \equiv \left(\frac{\Delta F_C}{RT} \right)_{DHLL} \theta(x, v) \equiv \left(\frac{\Delta F_C}{RT} \right)_{DHLL} \theta(x) \equiv \frac{\varphi(x)}{72v}; \quad r_D^2 \equiv \frac{4\pi\epsilon^2}{VkT} \sum_{\alpha=1}^2 N_{\alpha} Z_{\alpha}^2 \quad (2)$$

Here $(\Delta F_C/VkT)_{DHLL} \equiv (12\pi r_D^3)^{-1}$ - is the Debye–Hückel Limiting Law¹⁰. It should be noticed that in general case $\theta(v, x)$ is *two-parametric* function, but many of well-known approximations (e.g. Mean Spherical and Debye–Hückel Approximations *etc.*) have the form (2) and this assumption proved to be adequate for the well-known Monte Carlo results of Larsen¹¹ in the limit of dense and cold ionic RPM liquid. A number of approximations for $\theta(x)$ (or $\varphi(x)$) were compared^{1,2} and two of them are presented here:

- Debye–Hückel approximation for charged spheres (from energy equation, DHSE)¹⁰:

$$\theta_{DHSE}(x) = (3/x)[\text{Ln}(1+x) - x + x^2]. \quad (3)$$

- Mean Spherical Approximation (from energy equation, MSAE)¹²:

$$\theta_{MSAE}(x) = [2(1 + 2x)^{3/2} - 3x^2 - 6x - 2]/x^3. \quad (4)$$

Both the approximations give *positive* deviations from the DHLL limiting law, and differ progressively the higher the value of x is. Since we don't know computer simulation for a 4:2 Restricted Primitive Model, we have corrected the form of function $\theta(x)$ for large x values with the aim to describe existing *experimental* data^{13,14} on UO_2 .

RESTRICTED PRIMITIVE IONIC MODEL (RPM)

Flexibility of the RPM is restricted by the hard-sphere diameter and *form* of correction function $\theta(x, v)$. *Two* adjustable parameters were used at present calculations: - hard-sphere diameter, d , and an additional parameter, α , scaling the *modified* DHSE and MSAE correction functions $\theta^*(\alpha, x)$ (3,4).

$$\theta^*_{DHSE}(\alpha, x) = \theta_{DHSE}(\alpha x); \quad \theta^*_{MSAE}(\alpha, x) = \theta_{MSAE}(\alpha x) \quad (5)$$

It should be stressed that we could *not* calibrate these two parameters (d and α), using a procedure of fitting of Gibbs free energy of liquid⁹. It was appropriate in the case of the neutral models of liquid UO_2 ^{1,2}. The problem is the *great uncertainty* in the energies of formation of ions U^{4+} and O^{2-} . Available value of sum of the first four ionisation potentials of uranium vary from $\sim 66.6 \text{ eV}^{15}$ to $\sim 74.3 \text{ eV}^{16}$. The sum of energies needed to attach two electrons $A(\text{O}^{2-}) = E(\text{O}) - E(\text{O}^{2-})$ is also very *uncertain* and was estimated as being within the interval from *zero* to $A(\text{O}^{2-}) \cong 6.5 \text{ eV}^{17}$. Thus, the total uncertainty of energy of formation of one ion U^{4+} and two ions O^{2-} is estimated as $\sim 20 \text{ eV}$ (!). In view of this uncertainty the tabulated⁸ *entropy* value of liquid $\text{UO}_{2.0}$ was used as appropriate fitting parameter, because the entropy *does not depend* on the uncertainty mentioned.

$$S_{\text{UO}_{2.00}}(T=3120 \text{ K, liquid}) \cong 1.18 \text{ kJ/kg K} \quad \{\text{IVTAN-96}^{1,2}\} \quad (6)$$

The second fitting parameter was the density of melting uranium dioxide, from which the pressure in the liquid can be equated to zero:

$$P_{\text{UO}_{2.00}}(T=3120 \text{ K; } \rho = 8.87 \text{ g/cc})_{\text{liquid}} \cong 0 \quad (7)$$

After fixing values of two adjustable parameters of RPM: d and α (3-5), we can achieve an agreement with the tabulated values^{9,1,2} of liquid Gibbs free energy and enthalpy, varying uncertain values of energy of formation of U^{4+} and O^{2-} . For RPM-4:2 the procedure described turned to be successful within the modified DHSE-approximation (3,5), when being combined with the first set of uranium ionization potentials (66.6 eV^{13}) and value $A(\text{O}^{1-}) \sim + 5 \text{ eV}$ for the affinity of O^{1-} . We did not succeed in similar fitting with the modified MSAE-approximation, and it proved to be *obviously impossible* for any variant of *virial* versions of the approximations discussed.

Thermodynamic properties of liquid UO_2 at melting point and its extrapolation up to $T=7000 \text{ K}$ along zero pressure isobar, calculated within RPM, are presented in Table 1 in comparison with known experimental values.

IMPROVED RESTRICTED IONIC MODEL (IRIM)

An additional van der Waals attractive correction was taken into account within the improved variant of ionic model. As well as in the case of ionic model, RPM, considered above, the Coulomb correction in IRIM is still of one-parametric form (2). Its principal feature is special correction term to MSAE formula. The form and parameters of this term, as well as parameters of van der Waals attractive correction, were chosen with the aim to reproduce thermodynamic properties of liquid uranium dioxide at melting temperature: density, ρ , Gibbs free energy, G , enthalpy, H , thermal expansion coefficient, α_p , compressibility, β_T , and heat capacity, C_p . These requirements give rise to the important *compatibility conditions* to which Coulomb correction $\varphi(x)$ (2) and unknown parameters of van der Waals attraction must satisfy.

- 1) Due to identity of equations for *thermal expansion* and *heat capacity* the value of van der Waals attraction parameter a_{vdw} may be calculated directly from measured excess heat capacity, liquid molar volume and thermal coefficients α_p and β_T *independently* of other parameters of the EOS. It gives:

$$a_{vdw}/V_{liq}RT = 1.46 \quad (8)$$

2) Linear dependence of equations for pressure, energy and isothermal compressibility when the Coulomb correction of form $\varphi(x)$ (2) being used, give rise to the equation:

$$z_{HS}(v) + v (\partial z_{HS}/\partial v) = \Delta C_v / R + 2a_{vdw}/V_{liq} RT + V_{liq}/RT \beta_T \quad (9)$$

Using Carnahan-Starling formula we obtain the ion diameter, d , packing fraction, v , and parameter x_0 at melting temperature,

$$v=0.3235, \quad d=2.185 \text{ \AA}, \quad x_0 = 39.0. \quad (10)$$

Being quite reasonable the MSAE and DHSE formulae are incapable to describe experimental data. Thus a correction term was introduced to the MSAE formula in the form

$$\varphi(x)=\varphi_{MSAE}(x)+ \Delta\varphi(x) \quad (11)$$

The correction term $\Delta\varphi(x)$ must reproduce the necessary values of $\varphi(x_0)$, $\varphi'(x_0)$ and $\varphi''(x_0)$, deduced from experiment, and must begin on x^4 - term. The simplest form of $\Delta\varphi(x)$ is the polynomial. More appropriate functional form is the Pade approximant:

$$\Delta\varphi(x) = Ax^4/(1 + Bx + Cx^2) \quad (12)$$

Satisfaction of above requirements gives the following numerical values of coefficients (12): $A = 5.173 \cdot 10^{-4}$; $B = 1.464 \cdot 10^{-2}$; $C = 9.2 \cdot 10^{-6}$. Some results of calculated properties of liquid uranium dioxide are presented below in Table 1.

Table 1. Predicted thermodynamic properties of liquid Uranium Dioxide, calculated within RPM and IRIM using modified DHSE (3,5)^a and MSA (11,12) approximations

T, K	3120 (expt)	3120 MD ³		3120	4000	5000	6000	7000
V_{liq} , cm ³ /mol	30.5	37.5 ^b	RPM ^b	30.5 ^c	33.4	36.7	40.0	43.2
			IRIM ^b	30.5 ^c	33.3	34.8		
S_{liq} , J/g K	1.18^d		RPM	1.183 ^c	1.278	1.361	1.427	1.482
			IRIM	1.034				
$-H_{liq}$, J/g	6360^d		RPM	6343 ^c	6006	5633	5270	4913
			IRIM	6733				
$\beta_T \cdot 10^5$, (MPa) ⁻¹	4.12	8.13	RPM	8.30	8.65	9.11	9.63	10.2
			IRIM	4.89 ^c	4.65	4.35		
$\alpha_p \cdot 10^4$, K ⁻¹	1.05	0.2	RPM	1.15	1.00	0.89	0.81	0.76
			IRIM	1.18 ^c	0.73	0.53		
V_{sound} , m/s	1800		RPM	1260	1300	1333	1360	1380
			IRIM	1750 ^c	1770	1850		
C_v , J/kgK			IRIM	313	270	255		
C_p , J/kgK	440	360	RPM	386	378	368	360	354
			IRIM	413 ^c	324	293		
C_p , (expt ¹⁴)	440			440±60	320	320	356	407±90

^a $\alpha = 0.925$, fitted from experimental S_o , V_o and G_o values, using first set of uranium ionisation potentials data¹⁶ (66.6 eV) and $A(O^{-1}) \sim +5$ eV.

^b Ionic diameters d , 10⁻¹⁰m: MD³ - 2.1; RPM - 1.98; IRIM - 2.185.

^c At this temperature these parameters were fitted.

^d Tabulated values from IVTAN database^{9,2}.

CONCLUSIONS

- Ionic model may be considered as a reasonable basis for development of EOS for liquid UO_2 . It can be successfully used for calculation of gas-liquid phase equilibrium in UO_2 when being combined with separate model for vapours.
- Restricted Primitive Ionic 4:2 Model gives a reasonable agreement for integral thermodynamic properties of liquid UO_2
- It is necessary to take into account both Coulomb *and* van der Waals forces to describe correctly *differential* properties of liquid Urania Dioxide;
- The ionic model provides the simplest way, to date, of reproducing the observed decrease in liquid heat capacity, the decrease being directly related to the Coulomb contribution.
- The predictions of Ionic Model are extremely sensitive upon fine details of ion-ion interaction due to large Coulomb contribution to the free energy. Additional efforts needed to find better expression for this contribution.
- If the assumption of the ionic structure of liquid UO_2 is valid, it is clear that starting from cold and dense mixture of *highly ionized* uranium and oxygen, and moving along the coexistence curve, we have to translate continuously to the cold *neutral* vapors,. The features and location of this translation in uranium dioxide is an open question.

ACKNOWLEDGEMENTS

This work was supported by INTAS (Grant-93-0066). One of the authors (I.L.I.) thanks Norman March, Lesser Blum, John Perdew and Yaakov Resenfeld for illuminating discussions during SCCS'97, and Gabor Kalman for his kind invitation to the Conference.

REFERENCES

1. «Construction of the Equation of State of Uranium Dioxide up to the Critical Point,» Interim Reports Nr. 1,2 on INTAS-93-0066, Karlsruhe (1996).
2. Final Report on INTAS-93-0066, Karlsruhe, (1997).
3. P. Sindringre.and M. J. Gillan, *J.Phys.(Solid State)*. 21: 4017 (1988).
4. L. B. Bhuiyan, N. H. March, *et al.*, *Mol. Phys.* 34: 755 (1977).
5. L. B Bhuiyan,. P. J., Grout, N. H. March, *Phys. Chem. Liquids*. 6:291 (1977).
6. M.E. Fisher., Y. Levin., *Phys.Rev.Lett.* 71:3286 (1993).
7. O. Bernard, L. Blum, *J.Chem.Phys.* 104:4746 (1996).
8. V. K. Gryaznov., I.L. Iosilevski *et al.* «Thermophysical Properties of Substances of the Gas-Core Nuclear Engine,» V. M. Ievlev, ed., ATOMIZDAT, Moscow (1980).
9. L. V Gurvich, I. V. Veyts, V. A. Medvedev *et al.* «Thermodynamic Properties of Individual Substances,» Hemisphere, New-York (1989).
10. W. Ebeling., W. D. Kraeft, D. Kremp. «Theory of Bound States and Ionization Equilibrium in Plasmas and Solids,» Akademie-Verlag, Berlin (1976).
11. B. Larsen, *Chem. Phys. Lett.* 27:41 (1974).
12. E. Waisman, J. L Lebowitz, *J.Chem.Phys.* 56:3086; 3093 (1973).
13. J. K. Fink, M.C. Petri. «Thermophysical Properties of Uranium Dioxide,» Report ANL/RE-97/2 (Argonne Nat. Lab.). Argonne, Illinois (1997).
14. C. Ronchi, J-P. Hiernaut, R. Selfslag, G. J. Hyland. *Nucl. Sci and Eng.* 113:1 (1993).
15. S. L. Thompson, H. S. Lauson, USA Report SC-RR-710713 (Sandia Nat. Lab.)
16. A. M. Emelyanov, Yu.C., Hodeev I. N. Gorohov. *High Temp.* 8:508 (1970)
17. M. Born, M. Göppert-Mayer «Handbuch für Physik,» (1933).

This page intentionally left blank

THERMODYNAMIC AND STRUCTURAL PROPERTIES OF STRONGLY COUPLED PLASMA MIXTURES FROM THE PERTURBATIVE HNC EQUATION

Hong Seok Kang¹ and Francis H. Ree²

¹Department of Chemistry and New Materials
Jeonju University, Chonju, Korea

²University of California
Lawrence Livermore National Laboratory
Livermore, CA

1. INTRODUCTION

Recently, we developed the perturbative hypernetted-chain (PHNC) integral equation which can predict reliable thermodynamic and structural data for a system of particles interacting with either short range or long range (Coulomb) potential.^{1,2} The present work extends this earlier work to mixtures. This is done by employing a reference potential which is designed to satisfy a thermodynamic consistency on the isothermal compressibility as described in the next section.

We test the present theory in Sec. 3 by applying it to plasma mixtures interacting with either an unscreened or a screened Coulomb potential. We made comparisons of results from the present theory with those from the best available theory, *i.e.*, Rosenfeld's density functional theory (DFT).³ The DFT was shown to give internal energy with three to five figure accuracy compared to a wide range of Monte Carlo data.⁴⁻⁶ Meanwhile, small deviations of excess internal energy from the so-called "liner mixing rule" (LMR)^{7,8} are better predicted by a less sophisticated theory like the hypernetted-chain (HNC) equation. This rule relates thermodynamics of an unscreened mixture to those for individual components in a strongly coupled regime where the potential energy of a constituent particle is much larger than its kinetic energy.

We also apply the present theory to a $H_2 + H$ mixture interacting with Morse potentials. For this system, comparison of thermodynamic properties and radial distribution functions from the present theory will be made with those from another successful theory of dense fluid, *i.e.*, the HMSA equation of Zerah and Hansen.^{9,10}

2. FORMULATIONS

The PHNC integral equation for a multi-component mixture employs a closure relation:

$$B_{ij}(r) = B_{ij,0}(r), \quad (1)$$

where $B_{ij}(r)$ and $B_{ij,0}(r)$ denote the bridge function for a system of interest and that for a reference system, respectively. The PHNC chooses the reference system so that the range (λ_{ij}) of the reference potential between species i and j depends on the temperature T and density ρ . For a one-component system $\lambda = \text{Min}(a_{fcc}, r_{ij}^*)$ was shown to give a reliable result, where $a_{fcc}(= 2^{1/6}/\rho^{1/3})$ is the nearest neighbor distance at a given density for the face-centered cubic lattice and r_{ij}^* is the interatomic distance where the potential $V_{ij}(r)$ is the minimum.

For a mixture composed of $N_s (> 1)$ species, we need a more sophisticated choice. Namely, $\lambda_{ii}(i = 1, N_s)$ is chosen so that the partial isothermal compressibility $\partial(\beta P)/\partial\rho_i$ from the compressibility relation,

$$\frac{\partial(\beta P)}{\partial\rho_i} = 1 - \rho \sum_j x_j \int d\mathbf{r} c_{ij}(r), \quad (2)$$

gives the same result as that obtained from the virial equation,

$$\frac{\beta P}{\rho} = 1 - \frac{\beta\rho}{6} \sum_{i,j} x_i x_j \int d\mathbf{r} g_{ij}(r) r \frac{dV_{ij}(r)}{dr}. \quad (3)$$

Here $\beta = 1/kT$, where k is the Boltzmann constant; $c_{ij}(r)$ is the direct correlation function between species i and j , respectively. We choose λ_{ij} ($i \neq j$) to be additive, *i.e.*, $\lambda_{ij} = (\lambda_{ii} + \lambda_{jj})/2$. For a plasma system, Eqs. (2) and (3) need to be modified to include contributions by the compensating background. This is done by replacing $c_{ij}(r)$ and $g_{ij}(r)$ by $c_{ij}(r) + \beta v_{ij}(r)$ and $g_{ij}(r) - 1$, respectively. Other details for choosing the reference potentials are similar to those described in Refs. [1] and ². For example, it is assumed that the perturbation potentials are linear functions of r at $r \leq \lambda_{ij}$ and have continuous first derivatives at λ_{ij} .

Once the reference potentials are defined, $B_{ij,0}(r)$ is determined from the numerical solution of another set of coupled integral equations for the reference systems, using Ballone *et al*'s closure relation¹¹

$$B_{ij,0}(r) = [1 + s\gamma_{ij,0}(r)]^{1/s} - 1 - \gamma_{ij,0}(r), \quad (4)$$

with $s = 15/8$. Here $\gamma_{ij,0}(r) = h_{ij,0}(r) - c_{ij,0}(r)$, where $h_{ij,0}(r) = g_{ij,0}(r) - 1$ is the total correlation function between the species i and j . In summary, Eqs. (1)–(4) constitute a self-consistent cycle.

3. RESULTS AND DISCUSSION

Two-component plasma (TCP) corresponds to a simplest model of plasma mixture where ions with charge (in units of e) Z_1 and Z_2 move in a uniform background. Parameters describing this system are the coupling parameter $\Gamma = e^2/(kTa)$, Z_1 , Z_2 , and the mole fraction x of the species 2, where $a(= 3/4\pi\rho)^{1/3}$ is the ion-sphere radius. Instead of Γ , alternative description is possible in terms of $\Gamma_e = e^2/(kTa_e)$, where $a_e(= 3/4\pi\rho_e)^{1/3}$ is the electron radius and ρ_e is the electron density.

Table 1 compares the excess internal energy U^e for the TCP calculated from the PHNC, computer simulations,⁴⁻⁶ and the DFT.³ Note that $Z_1 = 1$ and $Z_2 > Z_1$. It shows that the PHNC is generally more accurate than the DFT, unless the species 2 is present at a very small mole fraction ($= 0.01$). And yet, more detailed calculation shows that the deviation from the LMR is not accurate enough. Figure 1 shows that the PHNC also gives accurate partial radial distribution functions, which is at least as accurate as the DFT. [See Fig. 5 of Ref. [3].] Next, we briefly mention our results of the PHNC calculation on the Yukawa system, which is a more realistic model for the plasma than the one-component plasma (OCP) or the TCP. For

Table 1. Comparison of the excess internal energy for the TCP: the Monte Carlo data,⁴⁻⁶ the PHNC (this work), and Rosenfeld's DFT.³ Z_2 is the ionic charge of species 2 ($Z_1 = 1$); $\Gamma_e = (e^2/a_e kT)$, where a_e is the electron sphere radius; x is the mole fraction of species 2

Z_2	Γ_e	x	βU^e		
			Exact	PHNC	DFT
3	15	0.05	-15.79068 ± 0.00026	-15.78471	-15.7850
		0.1	-19.265 ± 0.001	-19.26000	-19.252
		0.2	-26.212 ± 0.001	-26.20914	-26.199
		0.5	-47.066 ± 0.002	-47.05487	-47.057
	20	0.01	-17.60188 ± 0.00026	-17.59037	-17.6033
		0.05	-21.31834 ± 0.00019	-21.31049	-21.3100
		0.1	-25.963 ± 0.001	-25.95929	-25.948
		0.2	-35.260 ± 0.002	-35.25469	-35.237
		0.5	-63.145 ± 0.002	-63.13663	-63.126
		5	0.01	-9.20414 ± 0.00015	-9.20216
10	0.05	-14.02753 ± 0.00015	-14.03313	-14.0081	
	0.1	-20.05840 ± 0.00017	-20.06820	-20.0301	
	0.2	-32.12399 ± 0.00023	-32.13566	-32.0974	
	0.5	-68.33913 ± 0.00032	-68.34210	-68.3609	
	8	0.01	-10.75698 ± 0.00018	-10.76172	-10.7466

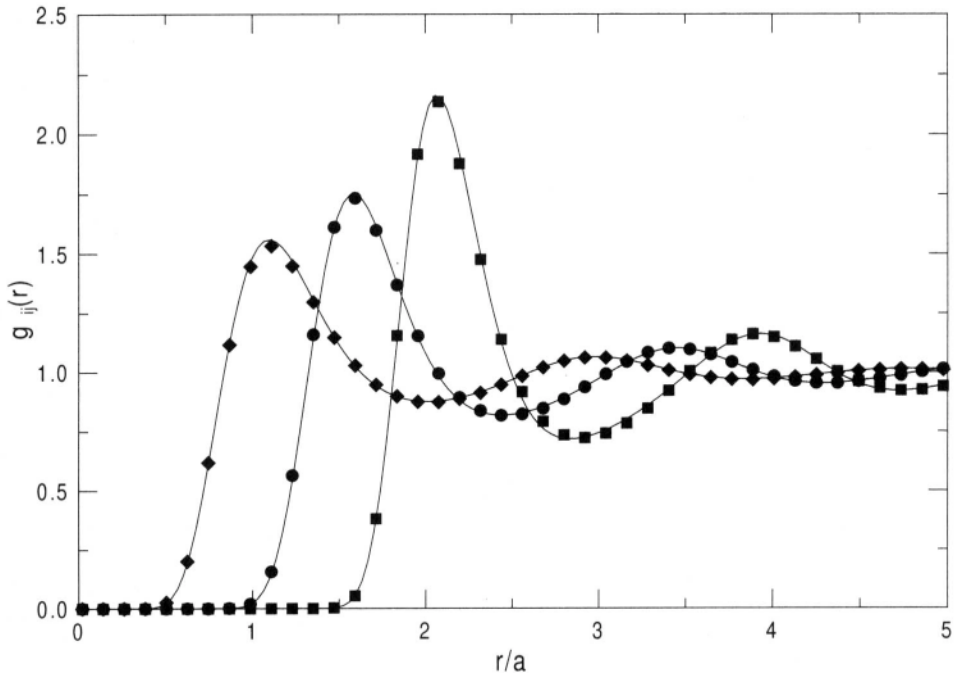


Figure 1. Radial distributions $g_{ij}(r)$ for an equimolar TCP mixture with $Z_1 = 1$ and $Z_2 = 5$ at $\Gamma_e = 10$. Diamonds, circles, and squares represent the Monte Carlo data of DeWitt, Slattery, and Chabrier¹⁴ for the 11, 12, and 22 interactions, respectively. Solid lines correspond to the PHNC.

a two-component Yukawa mixture composed of ions with charges Z_1 and Z_2 , an interaction potential between the ions is represented by $V_{ij}(r) = Z_i Z_j e^2 e^{-\kappa r} / r$. In the linear screening approximation, the screening parameter κ is inversely proportional to the Debye length of background plasma. The potential energy of this system depends on five parameters, *i.e.*, Γ, Z_1, Z_2, x , and κ . Although not shown here, excess internal energy of the one-component Yukawa system calculated from the PHNC is as accurate as those for the OCP in the entire range of $\kappa (< 1)$ investigated. This was confirmed by comparing the PHNC calculations with Monte Carlo data recently presented by Farouki and Hamaguchi.¹² In addition, we have found that λ which satisfies the self-consistency criterion is very close to a_{fcc} at a wide range of density around the freezing point. Typically, the difference between the two is within 5% of the latter for the Yukawa system. This is puzzling in that the weakly screened Yukawa system freezes to the body-centered cubic lattice. Table 2 gives a comparison of the potential energy between Yukawa charges (U^{PP}) calculated from the PHNC and the HNC for the two-component Yukawa system. Also shown are those from the Yukawa mixing rule (YMR)¹³ based on the calculations performed on the one-component Yukawa systems using the PHNC and the HNC. Here U^{PP} is related to the linear response energy $U_{lin.resp.}$ by

$$\beta U_{lin.resp.} = \beta U^{PP} - 3\Gamma \frac{\langle Z \rangle^2}{2\kappa^2} - \frac{\Gamma}{2} \langle Z^2 \rangle \kappa \quad (5)$$

$$= \frac{3\Gamma}{4\pi^2} \sum_{ij} x_i x_j Z_i Z_j \int dk h_{ij}(k) \frac{k^2}{k^2 + \kappa^2} - \frac{\Gamma}{2} \langle Z^2 \rangle \kappa, \quad (6)$$

where distance is in units of the ion-sphere radius a . In terms of $u^{PP} (\equiv \beta U^{PP})$ the YMR can be expressed by

$$u^{PP}(Z_1, Z_2, \Gamma, x, \kappa) = (1-x)u_1^{PP}(\Gamma_1, \kappa_1) + xu_2^{PP}(\Gamma_2, \kappa_2), \quad (7)$$

where u_i^{PP} denotes the potential energy between Yukawa charges in the one-component system of the species i , and

$$\Gamma_i = (Z_i^2 / R_i) \Gamma, \quad \kappa_i = \kappa R_i. \quad (8)$$

Here R_i is obtained from the solution of the coupled algebraic equations

$$R_i^3 = \frac{Z_i Y(\kappa R_i)}{(1-x)Z_1 Y(\kappa R_1) + xZ_2 Y(\kappa R_2)}, \quad (i = 1, 2) \quad (9)$$

and

$$Y(t) = \frac{2t^3}{3[e^t(t-1) + e^{-t}(t+1)]}. \quad (10)$$

Since the simulated data are not available, it is not possible to assess the accuracy of the PHNC. However, the table shows that the YMR holds very well for both of the PHNC and the HNC. We note that deviations of the HNC solution from the YMR are almost constant and positive (≈ 0.008) at all κ values considered in the table. It will be interesting to check this relation at a strong screening condition ($\kappa \gg 1$), where the HNC is generally considered to be inaccurate.

Table 3 shows that the PHNC can predict reliable results for a mixture interacting with potentials for $H + H_2$ mixtures. We note that it gives slightly better results than the HMSA equation of Zerah and Hansen. [The potential parameters used in this work are the same as those in Ref. [10].] This is further supported by the heights of the first peak in the H_2-H_2 radial

Table 2. Potential energy between Yukawa charges U^{PP} calculated from the PHNC and the HNC at various values of the screening parameter κ at $\Gamma = 20, Z_1 = 1, Z_2 = 3$, and $x = 0.5$. Also shown are the results from the Yukawa mixing rule. PHNC-YMR denotes that the data are obtained from the rule based on the solutions of the PHNC for appropriate one-component systems. Similar definition applies to HNC-YMR.

κ	βU^{PP}			
	PHNC	PHNC-YMR	HNC	HNC-YMR
0.4	688.223	688.234	688.695	688.687
0.6	279.2484	279.2531	279.7071	279.6985
0.8	140.2371	140.2366	140.6827	140.6750
1.0	78.7460	78.7468	79.1764	-79.1688

Table 3. Comparison of the compressibility factor $\beta P/\rho$ and the excess internal energy U^e of an equimolar $H + H_2$ mixture: Exact data, the PHNC, and the HMSA.¹⁰ The exact data with standard deviations inside parentheses are obtained in this work using 10^6 to $2 \cdot 10^6$ configurations, while values without standard deviations are taken from Ref.¹⁰

$T(K)$	$\rho(A^{-3})$	$\beta P/\rho$			βU^e		
		Exact	PHNC	HMSA	Exact	PHNC	HMSA
1,000	0.06	3.123	3.124	3.110	0.675	0.674	0.664
	0.20	16.996(6)	17.086	17.053	7.518(4)	7.540	7.538
5,000	1.0	35.31	35.32	35.37	24.07	24.09	24.17
10,000	0.2	3.212	3.212	3.214	1.309	1.308	1.307
	10	18.410(1)	18.429	18.443	12.536(2)	12.548	12.549

distribution function. They are 1.798 ± 0.005 , 1.802, 1.69, and 1.72, for the Monte Carlo data obtained in this work, the PHNC, and the one- and two-parameter HMSA, respectively. In the two-parameter calculation, the HMSA determines two parameters in their “switching functions” from conditions of thermodynamic consistency of two partial compressibilities similarly to the PHNC. [The switching functions are used to mix the soft mean spherical approximation (SMSA) at small r and the HNC closure at large r .] On the one hand, the one-parameter HMSA calculation employs a single switching function and determines its parameter from the consistency in the total compressibility calculated from the virial theorem and the compressibility equation.

Acknowledgements

The work of H. S. Kang was performed by a grant from Jeonju University and Agency for Defence Development. The work of Francis H. Ree was done under the auspices of the U. S. Department of Energy by Lawrence Livermore National Laboratory under Contract No. W-7405-ENG-48.

REFERENCES

- [1] H. S. Kang and F. H. Ree, J. Chem. Phys. **103**, 3629 (1995).

- [2] H. S. Kang and F. H. Ree, *J. Chem. Phys.* **103**, 9377 (1995).
- [3] Y. Rosenfeld, *Phys. Rev. E* **54**, 2827 (1996).
- [4] S. Ogata, H. Iyetomi, S. Ichimaru, and H. M. Van Horn, *Phys. Rev. E* **48**, 1344 (1993).
- [5] “ Strongly Coupled Plasma Physics,” edited by W. Kraeft and M. Schlanges, World Scientific, Singapore (1996).
- [6] H. E. DeWitt, W. L. Slattery, and G. Chabrier, *Physica B* **228**, 21 (1996).
- [7] J. P. Hansen, G. M. Torrie, and P. Vieillefosse, *Phys. Rev. A* **16**, 2153 (1977).
- [8] B. Brami, J. P. Hansen, and F. Joly, *Physica A* **95**, 505 (1979).
- [9] G. Zerah and J. P. Hansen, *J. Chem. Phys.* **84**, 2336 (1986); J. P. Hansen and G. Zerah, *Phys. Lett.* **108A**, 277 (1985). *Physica A* **95**, 505 (1979).
- [10] D. Levesque, J. J. Weis, and G. Chabrier, *J. Chem. Phys.* **94**, 3096 (1991).
- [11] P. Ballone, G. Pastore, G. Galli, and D. Gazzillo, *Mol. Phys.* **59**, 275 (1986).
- [12] R. T. Farouki and S. Hamaguchi, *J. Chem. Phys.* **101**, 9885 (1994).
- [13] Y. Rosenfeld, *Phys. Rev. E* **47**, 2676 (1993).
- [14] H. E. DeWitt (private communication).

STATISTICAL MECHANICS OF HIGHLY CHARGED IONS IN NLTE PLASMAS

A. Mirone,¹ G. Faussurier,² F. Gilleron,¹ and J. C. Gauthier¹

¹Laboratoire pour l'Utilisation des Lasers Intenses
UMR100 du C. N. R. S., Ecole Polytechnique, 91128 Palaiseau Cedex, France

²Commissariat à l'Energie Atomique, Centre de Valenton
94195 Villeneuve Saint-Georges Cedex, France

INTRODUCTION

The properties of hot and dense matter are of great importance in astrophysics or laboratory laser-plasma physics.¹ As the thermodynamic situations encountered can be extremely diverse, their study is often difficult. The number of states (different ionization and excited states) playing a role in the ionization dynamics may be enormous due to the high temperature of the plasma. In addition, soft x-ray radiation transport is very effective in redistributing the absorbed laser energy and the hydrodynamic phenomena are strongly correlated to the emissivity and opacity of the plasma. When LTE conditions fail, the problem to handle shows a great complexity. Since no *a priori* expressions are known for the electronic configuration probabilities, one must resort to find the statistical distribution of the different ionic states by solving the relevant rate equations involving the ions and the photons. Yet, one face rapidly a situation which is very similar to the DCA method for medium- or high-Z element plasmas. The number of many-electron configurations to select can be very large and the data are often lacking, or known only for isolated atoms or ions. Moreover, the NLTE photon distribution has to be coupled self-consistently to the statistical distribution of the ionic states. A widespread solution is to extend to NLTE conditions the LTE average atom model formalism.² By taking into account various microscopic processes that can alter the shell occupations of an electronic configuration, this method consist in going from integer to fractional occupation numbers and in calculating all the transition rates of interest affecting the configuration under study. The shell occupation fractional numbers obey a set of time-dependent non-linear coupled equations which is analogous to the LTE case. The system is closed by using the neutrality condition. This method seems attractive but it suffers of one major drawback: one has no way to estimate NLTE correlations between electrons.

The purpose of this paper is to propose a method to overcome the above difficulty. By using the NLTE average-atom model, an analytic formula of the two-electron correlations (TEC) is obtained. Numerical results are presented and discussed by using a screened hydrogenic model with one-electron configurations treated in the $n - l$ representation³ and analytic transition rates.^{4,5} The variance of ionization, deduced within the framework of our formalism, is compared to the values obtained by extending the LTE formulation to the NLTE

regime, by using the ionization temperature T_Z concept, in which T_Z is the temperature at which an LTE model will give the same average charge $\langle Z \rangle$ as the actual NLTE value.⁶ We have compared our results with full-blown DCA calculations in a germanium plasma at low density (10^{-5} g/cm^3) and an electron temperature between 10 eV and 1 keV.

FORMAL DEVELOPMENT

We develop our formalism in the framework of a one-particle central potential approximation. Each ionic state is determined by the set of occupation numbers m_j of its one-particle bound states j . Each ion embedded in a plasma undergoes collisional and radiative transitions which change by discrete steps the values of its m_j 's. The AA model in NLTE consists in considering the evolution of the first-order moment $\langle m_j \rangle$ (center of mass) of the ionic distribution in the space of the occupation numbers. The fluctuations around the mean value are defined by $\langle m_j m_i \rangle - \langle m_j \rangle \langle m_i \rangle$.

Center of Mass Evolution

The evolution of the center of mass is given by the formal NLTE master equation:

$$\frac{d\langle m_j \rangle}{dt} = \left\langle \sum_{\xi} \tau(\vec{m})_{\xi \rightarrow j} - \tau(\vec{m})_{j \rightarrow \xi} \right\rangle \quad (1)$$

where j runs over bound states. The summation over ξ is made over bound states and the continuum (free states) whereas the transition rates $\tau(\vec{m})$ are functions of the occupation numbers (denoted by vector \vec{m}), the electron temperature, the density and the radiation field. The symbol $\langle \rangle$ denotes the average over the ensemble. The values m_j assume discrete values but their average is continuous. Equation (1) can be simplified by considering the τ 's as functions of continuous parameters. We substitute in Eq. (1) the first-order Taylor expansion, taken at the center of mass. The linear term averages to zero and we get, as in the mean-field model:

$$\frac{d\langle m_j \rangle}{dt} = \sum_{\xi} \tau(\langle \vec{m} \rangle)_{\xi \rightarrow j} - \tau(\langle \vec{m} \rangle)_{j \rightarrow \xi}. \quad (2)$$

Fluctuations

Let us consider an ion initially at position $\vec{m} = x_0$ in the occupation numbers space at $t = t_0$. Let us wait conceptually an infinitesimal time $\delta t = \epsilon$. During this time interval, the ion may undergo a transition and change its coordinates with infinitesimal probability. At $t = t_0 + \epsilon$, the expectation value of $m_i m_j$ is:

$$\begin{aligned} m_i(t_0 + \epsilon) m_j(t_0 + \epsilon) = & \\ & \left(1 - \epsilon \left(\tau_{i \rightarrow j} + \tau_{j \rightarrow i} + \sum_{\nu \neq j} (\tau_{i \rightarrow \nu} + \tau_{\nu \rightarrow i}) \right. \right. \\ & \left. \left. + \sum_{\nu \neq i} (\tau_{j \rightarrow \nu} + \tau_{\nu \rightarrow j}) \right) \right) x_{0i} x_{0j} \\ & + \epsilon \left((x_{0i} - 1)(x_{0j} + 1) \tau_{i \rightarrow j} + (x_{0i} + 1)(x_{0j} - 1) \tau_{j \rightarrow i} \right. \\ & \left. + \sum_{\nu \neq j} ((x_{0i} - 1)x_{0j} \tau_{i \rightarrow \nu} + (x_{0i} + 1)x_{0j} \tau_{\nu \rightarrow i}) + \right. \\ & \left. \sum_{\nu \neq i} (x_{0i}(x_{0j} - 1) \tau_{j \rightarrow \nu} + x_{0i}(x_{0j} + 1) \tau_{\nu \rightarrow j}) \right) \end{aligned}$$

$$+\epsilon\delta_{i,j}\sum_{\nu}(\tau_{i\rightarrow\nu}+\tau_{\nu\rightarrow i}). \quad (3)$$

where the τ 's are the transition rates calculated at \bar{x}_0 and $\delta_{i,j}$ is the Kronecker symbol. We expand to first order the τ 's into Eq. (3) and average over the ensemble. We finally get:

$$\left.\frac{d\langle m_j m_i \rangle}{dt}\right| = \left.\frac{d\langle m_j m_i \rangle}{dt}\right|_{relaxation} + \left.\frac{d\langle m_j m_i \rangle}{dt}\right|_{noise} \quad (4)$$

where the first term in the right hand side of Eq. (4) describes the relaxation towards the AA.

$$\begin{aligned} \left.\frac{d\langle m_j m_i \rangle}{dt}\right|_{relaxation} = & \\ \frac{d}{dt}(\langle m_j \rangle \langle m_i \rangle) & \\ + \sum_{\xi,n} \left(\frac{\partial \tau}{\partial m_n} (\langle \bar{m} \rangle)_{\xi \rightarrow j} - \frac{\partial \tau}{\partial m_n} (\langle \bar{m} \rangle)_{j \rightarrow \xi} \right) (\langle m_n m_i \rangle - \langle m_n \rangle \langle m_i \rangle) & \\ + \sum_{\xi,n} \left(\frac{\partial \tau}{\partial m_n} (\langle \bar{m} \rangle)_{\xi \rightarrow i} - \frac{\partial \tau}{\partial m_n} (\langle \bar{m} \rangle)_{i \rightarrow \xi} \right) (\langle m_j m_n \rangle - \langle m_j \rangle \langle m_n \rangle) & \end{aligned} \quad (5)$$

The second term in the right hand side of Eq. (4) denotes something similar to a ‘‘random noise’’:

$$\left.\frac{d\langle m_j m_i \rangle}{dt}\right|_{noise} = \sum_{\xi,\nu} (\delta_{i,\xi} - \delta_{i,\nu}) (\delta_{j,\xi} - \delta_{j,\nu}) \tau (\langle \bar{m} \rangle)_{\nu \rightarrow \xi} \quad (6)$$

where greek letters runs over both bound and free states.

Equation (4), thanks to its simplicity, is well-suited to be implemented into numerical codes based on AA methods. The fluctuations around the AA configuration depend on the AA configuration only. This equation, with Eq. (5) and (6), can be obtained differently by starting from a general master-equation where the atomic-configuration probabilities appear explicitly.⁷ Because of the analogy with a diffusion process, we coin the name ‘‘Brownian Motion Picture’’ (BMP) to Eq. (4).

NUMERICAL RESULTS

To test our formalism, we have performed calculations with a simple collisional-radiative model based on a screened hydrogenic model³ with $n - l$ splitting. We have performed calculations for Germanium at 10^{-5}g/cm^3 and electronic temperatures between 10 eV and 1 keV. The NLTE calculations were made considering an optically thin media where radiation reabsorption processes were neglected. This assumption breaks microreversibility (spontaneous emission is not balanced by the inverse process). We have calculated the variance σ_Z^2 of the ionic charge $Z^* = Z - \sum_i m_i$: this quantity depends on two-electron correlations as:

$$\sigma_Z^2 = \langle Z^* Z^* \rangle - \langle Z^* \rangle^2 = \sum_{i,j} \langle m_j m_i \rangle - \langle m_j \rangle \langle m_i \rangle \quad (7)$$

In figure 1, we show the ionization variance as a function of temperature. BMP results (heavy line) are compared to DCA calculations, performed with 6×10^3 configurations (thin line). The agreement is excellent where the DCA converges. We did not try to increase the configuration number in the DCA calculations because the computational burden increases rapidly. The rapid decrease of σ_Z^2 for temperatures around and below 1 keV occurs when Z^* is close to 22, a value corresponding to the neon-like ionization stage where both the $n = 1$ and $n = 2$ shells are filled. The dashed and dotted lines are the LTE variances extrapolated to NLTE by using an effective temperature T_{eff} . This temperature can be taken equal to the electron temperature T_e ¹⁰ or to the ionization temperature T_Z .⁶

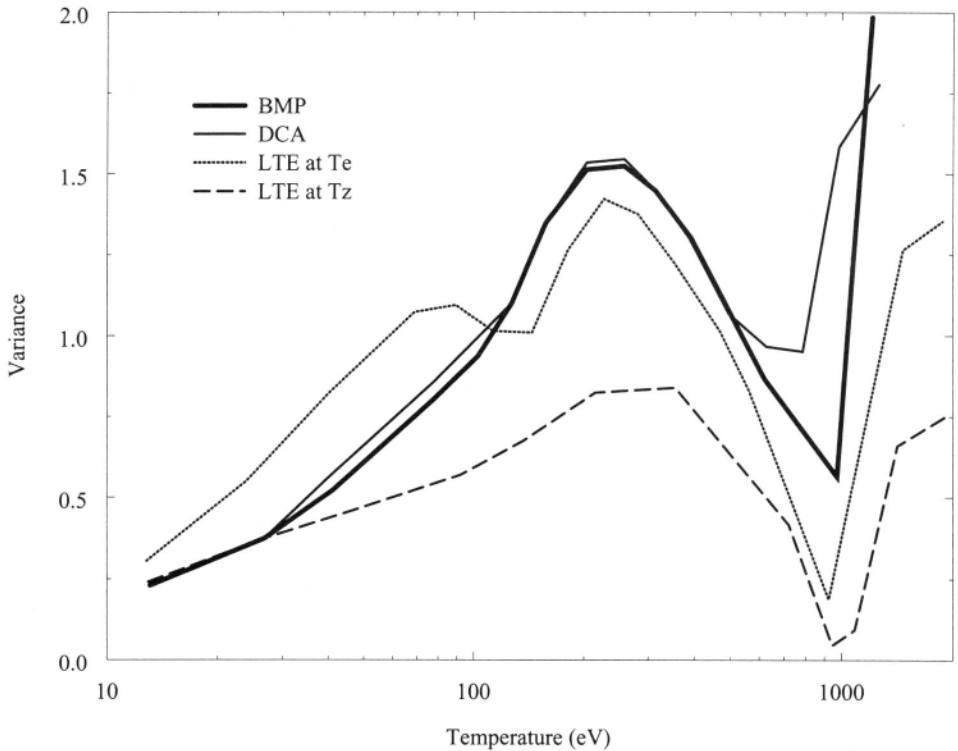


Figure 1. Variance of the ionization as a function of electron temperature for a NLTE optically thin germanium plasma at a density of 10^{-5}g/cm^3 . Heavy solid line: present results, thin solid line: detailed configuration accounting, dotted line: LTE calculation at the ionization temperature, dashed line: LTE calculation at the electron temperature.

CONCLUSIONS

A new description of NLTE statistics of a highly-charged ion plasma has been presented. Two-electron correlations are evaluated by taking into account the “diffusion” of the time-dependent solution of the master equation around the center of mass of the distribution. This method has been tested by calculating the variance of the ionization in a NLTE stationary situation.

Acknowledgements

We acknowledge C. Chenais-Popovics, S. Hüller and C. Blancard for their comments and suggestions. LULI is funded by the Centre National de la Recherche Scientifique and by the European Community under contract CHGECT930046.

REFERENCES

- [1] S. J. Rose, in *Proceedings of the 45th Scottish Universities Summer School in Physics - Laser Plasma Interactions*, edited by M. B. Hooper (Bristol, IOP, 1995).
- [2] R. M. More, Report UCRL-84991, Lawrence Livermore National Laboratory (University of California, Livermore, 1981).
- [3] G. Faussurier, C. Blancard, and A. Decoster, *J. Quant. Spectrosc. Radiat. Transfer* (in press, 1997).
- [4] M. Itoh, T. Yabe, and S. Kiyokawa, *Phys. Rev.* **A35**, 233 (1987).

- [5] A. Rickert and J. Meyer-ter-Vehn, *Laser Part. Beams* **8**, 715 (1990).
- [6] M. Busquet, *Phys. Fluid.* **B5**, 4191 (1993).
- [7] P. Dallot, G. Faussurier, A. Decoster, and A. Mirone, (submitted for publication).
- [8] R. M. More, G. B. Zimmerman, and Z. Zinamon, in *Atomic Processes in Plasmas*, edited by A. Hauer and A. L. Merts, AIP Conf. Proc. No. 168 (AIP, New York, 1998), p. 33.
- [9] L. B. Zhao and S. C. Li, *Phys. Rev.* **A55**, 1039 (1997).
- [10] A. Mirone, J. C. Gauthier, F. Gilleron, and C. Chenais–Popovics, *J. Quant. Spectrosc. Radiat. Transfer* (in press, 1997).
- [11] Frank Gilleron, LULI96 Internal Report, (unpublished, 1997).

This page intentionally left blank

ADVANCES IN THE CALCULATION OF VIRIAL EXPANSIONS FOR QUANTUM PLASMAS UP TO THIRD ORDER IN THE DENSITY

Torsten Kahlbaum

Institut für Physik, Humboldt-Universität zu Berlin
Invalidenstraße 110, D-10115 Berlin, Germany
E-mail: kahlbaum@summa.physik.hu-berlin.de

INTRODUCTION

Since the beginning of the nineties, the renewed interest in the exact calculation of thermodynamic functions for weakly coupled (or, weakly non-ideal), weakly degenerate multicomponent quantum plasmas beyond the Debye–Hückel limiting law has led to a number of profound papers^{1,2} by French, German, and American authors. They derived virial expansions for thermal pressure p and free energy F through the order $n^{5/2}$ in the densities from first principles by using the Feynman–Kac formalism and the method of Green’s functions, respectively. These recent works confirmed and supplemented older results by Haga,³ Friedman,⁴ DeWitt,⁵ and Ebeling⁶ and co-workers from the *Rostock School* dating back to the fifties and sixties, so that now the virial equation of state for Coulomb fluids is generally accepted as completely known up to order $n^{5/2}$.

For the present calculations I employ, like Ebeling, Morita’s effective-potential approach⁷ which allows, starting with a charging procedure, to easily give an expansion for the Helmholtz free energy in terms of the so-called cluster integrals \mathcal{S}_n , $n \geq 2$, that correspond to the screened virial coefficients $B_{a_1 \dots a_n}(\kappa)$. Then, the actual density series follows by expanding \mathcal{S}_n with respect to powers of the reciprocal Debye radius κ , where the involved elimination of the Coulomb divergences requires precise knowledge of the asymptotic behavior of the Slater sums $S_{a_1 \dots a_n}$ for large inter-particle separation. Here I concentrate on all those cluster integrals that contribute to at least the order $n^{5/2}$, namely \mathcal{S}_2 , \mathcal{S}_3 , and \mathcal{S}_4 , and present some new contributions of the orders $n^3 \ln n$ and n^3 arising from \mathcal{S}_2 along with the integral representation of a higher virial function K_1 . Finally, Haga’s constant a_1 that appears in the lowest-order classical term of \mathcal{S}_3 and was known so far only approximately has been evaluated exactly for the first time.

DENSITY EXPANSION OF THE FREE ENERGY UP TO ORDER $n^{5/2}$

The density expansion through the order $n^{5/2}$ for the interaction part F_{int} of the Helmholtz free energy per volume V in units of $k_B T = 1/\beta$ for weakly coupled, weakly degenerate quantum plasmas, i.e., for multi-component fluid mixtures of point-like free electrons, $a = e$,

and bare nuclei, $a = i_1, i_2, \dots$, having masses m_a , charges q_a , and spins s_a at sufficiently low densities n_a and high temperature T , has the compact form

$$\begin{aligned} \frac{\beta F_{\text{int}}}{V} = & -\frac{\kappa^3}{12\pi} + 2\pi \sum_{a,b} n_a n_b \left[(1 - l_{ab}\kappa) \left(\frac{1}{6} l_{ab}^3 \ln(\lambda_{ab}\kappa) - \lambda_{ab}^3 K_0(\xi_{ab}, s_a) \right) \right. \\ & \left. + \frac{1}{6} \left(1 - \ln \frac{4}{3} \right) l_{ab}^4 \kappa \right] - \frac{a_1}{\kappa} \sum_{a,b,c} n_a n_b n_c l_{ab} l_{ac} l_{bc}^2 - \frac{\kappa^3}{24} \sum_a n_a l_{aa} \lambda_{aa}^2 \\ & - \frac{a_2}{\kappa^3} \sum_{a,b,c,d} n_a n_b n_c n_d l_{ab} l_{ac} l_{ad} l_{bc} l_{bd} l_{cd} + \mathcal{O}(n^3 \ln n), \end{aligned} \quad (1)$$

with reciprocal Debye radius $\kappa = \sqrt{4\pi\beta \sum_a n_a q_a^2}$, Landau length $l_{ab} = -\beta q_a q_b$, thermal de Broglie wavelength $\lambda_{ab} = \hbar \sqrt{\beta/2m_{ab}}$, Born interaction parameter $\xi_{ab} = l_{ab}/\lambda_{ab}$, and reduced mass $m_{ab} = m_a m_b / (m_a + m_b)$. a_1 and a_2 are numerical constants, given below.

The different terms in Eq. (1) describe two-particle bound and scattering states, exchange, classical screening, and quantum diffraction where the complete contributions to the orders $n^2 \ln n$, n^2 , and $n^{5/2} \ln n$ were first obtained by Ebeling⁶ while Haga,³ Friedman,⁴ Ebeling,⁶ and Alastuey *et al.*¹ all contributed to F_{int} at the order $n^{5/2}$.

CLUSTER EXPANSION OF THE FREE ENERGY

The basic expressions that are used as starting-point in the present calculations can be readily derived from the charging formula for the excess free energy and summarized as follows: The cluster expansion for F_{int} ,

$$\frac{\beta F_{\text{int}}}{V} = - \left(\frac{\kappa^3}{12\pi} + \sum_{n=2}^{\infty} \mathcal{S}_n \right), \quad (2)$$

is the sum of the Debye–Hückel limiting law, $\propto n^{3/2}$, and all cluster integrals \mathcal{S}_n , e.g.,

$$\mathcal{S}_2 = \sum_{a,b} n_a n_b B_{ab}(\kappa) \quad (3)$$

$$\mathcal{S}_3 = \sum_{a,b,c} n_a n_b n_c B_{abc}(\kappa), \quad (4)$$

which are related to the corresponding screened virial coefficients

$$B_{ab}(\kappa) = \frac{1}{2V} \int d\mathbf{r}_1 d\mathbf{r}_2 \left[\Phi_{ab}(\mathbf{r}_1, \mathbf{r}_2) - \frac{1}{2} g_{ab}^2(\mathbf{r}_1, \mathbf{r}_2) \right] \quad (5)$$

$$\begin{aligned} B_{abc}(\kappa) = & \frac{1}{6V} \int d\mathbf{r}_1 d\mathbf{r}_2 d\mathbf{r}_3 \left[\Phi_{abc}(\mathbf{r}_1, \mathbf{r}_2, \mathbf{r}_3) \right. \\ & \left. + 3g_{ab}(\mathbf{r}_1, \mathbf{r}_2) \Phi_{ac}(\mathbf{r}_1, \mathbf{r}_3) \Phi_{bc}(\mathbf{r}_2, \mathbf{r}_3) \right]. \end{aligned} \quad (6)$$

Here the generalized Mayer functions

$$\Phi_{ab} = S_{ab} \exp(g_{ab} + \beta v_{ab}) - 1 - g_{ab} \quad (7)$$

$$\begin{aligned} \Phi_{abc} = & \Phi_{ab} \Phi_{ac} \Phi_{bc} + (S_{abc} - S_{ab} S_{ac} S_{bc}) \\ & \times \exp(g_{ab} + g_{ac} + g_{bc} + \beta v_{ab} + \beta v_{ac} + \beta v_{bc}) \end{aligned} \quad (8)$$

are written in terms of the two-particle and three-particle Slater sums S_{ab} and S_{abc} , respectively, Debye correlation function $g_{ab}(r) = (l_{ab}/r) \exp(-\kappa r)$, and bare Coulomb potential $v_{ab}(r) = q_a q_b / r$. Note that Eqs. (5) and (6) give closed integral representations for the second and third virial coefficient, B_{ab} and B_{abc} , valid at any value of $\kappa > 0$.

SECOND CLUSTER INTEGRAL

Recently I calculated some new terms⁸ of third order in the density by expanding B_{ab} in powers of κ following the same procedure that was also applied at lower orders. However, as it is explained at the end of Ref. [8], regularization at the order n^3 requires the inclusion of the first quantum correction $\propto \hbar^2$ in the asymptotic expression for S_{ab} at large inter-particle separation. This produces two more terms in comparison with Eq. (35) of the above-mentioned article that are of quantum-diffraction type. Then, the full density expansion of the second cluster integral, Eq. (3), up to order n^3 reads

$$\begin{aligned} \mathfrak{S}_2 = & -2\pi \sum_{a,b} n_a n_b \left\{ \left(1 - l_{ab}\kappa + \frac{1}{2}(l_{ab}\kappa)^2 \right) \left(\frac{1}{6} l_{ab}^3 \ln(\lambda_{ab}\kappa) - \lambda_{ab}^3 K_0(\xi_{ab}, s_a) \right) \right. \\ & + \frac{1}{2} l_{ab} \kappa^2 \left[\left(\frac{1}{24} l_{ab}^4 + \frac{1}{12} l_{ab}^2 \lambda_{ab}^2 \right) \ln(\lambda_{ab}\kappa) - \lambda_{ab}^4 K_1(\xi_{ab}, s_a) \right] \\ & \left. + \frac{1}{6} l_{ab}^3 \left[\left(1 - \ln \frac{4}{3} \right) l_{ab}\kappa - \frac{5}{8} \left(\frac{3}{2} - \ln \frac{5}{3} \right) (l_{ab}\kappa)^2 - \frac{3}{8} (\lambda_{ab}\kappa)^2 \right] \right\}, \end{aligned} \quad (9)$$

with the two quantum virial functions

$$\begin{aligned} K_0(\xi_{ab}, s_a) = & \frac{1}{\lambda_{ab}^3} \lim_{R \rightarrow \infty} \left\{ \int_0^R dr r^2 \left[S_{ab}(r) - 1 - \frac{l_{ab}}{r} - \frac{1}{2} \left(\frac{l_{ab}}{r} \right)^2 \right] \right. \\ & \left. - \frac{1}{6} l_{ab}^3 \left(C_E + \ln \frac{3R}{\lambda_{ab}} \right) \right\} \end{aligned} \quad (10)$$

$$\begin{aligned} K_1(\xi_{ab}, s_a) = & \frac{1}{\lambda_{ab}^4} \lim_{R \rightarrow \infty} \left\{ \int_0^R dr r^3 \left[S_{ab}(r) - 1 - \frac{l_{ab}}{r} - \frac{1}{2} \left(\frac{l_{ab}}{r} \right)^2 - \frac{1}{6} \left(\frac{l_{ab}}{r} \right)^3 \right] \right. \\ & \left. - \frac{1}{24} l_{ab}^4 \left(C_E + \ln \frac{3R}{\lambda_{ab}} \right) - \frac{1}{12} l_{ab}^2 \lambda_{ab}^2 \left(C_E + \ln \frac{R}{\lambda_{ab}} \right) \right\}, \end{aligned} \quad (11)$$

the latter now being the supplemented version of Eq. (34) in Ref. [8]. C_E is the Euler-Mascheroni constant, $C_E = 0.57721566\dots$. K_0 was evaluated by Ebeling⁶ for arbitrary temperatures, whereas the explicit determination of the new K_1 is still lacking.

Similar calculations at the order n^3 have been performed by Czerwon and briefly reported in an unpublished paper.⁹ This author obtained exactly the same result for K_1 as shown in Eq. (10). On the other hand, he has wrong coefficients for the last two terms in Eq. (9), and the second part of the logarithmic term linked to K_1 is missing.

THIRD CLUSTER INTEGRAL

The leading classical term³ coming from the third cluster integral, Eq. (4),

$$\mathfrak{S}_3 = \frac{a_1}{\kappa} \sum_{a,b,c} n_a n_b n_c l_{ab} l_{ac} l_{bc}^2, \quad (12)$$

gives a contribution to the order $e^9 n^{5/2}$ and includes the numerical constant

$$a_1 = \frac{1}{8} \int d\mathbf{x}_1 d\mathbf{x}_2 \left(\frac{e^{-x_1}}{x_1} \right)^2 \frac{e^{-x_{12}}}{x_{12}} \left(\frac{e^{-x_2}}{x_2} \right)^2. \quad (13)$$

Fourier transformation using the convolution theorem leads to the familiar integral³

$$a_1 = 8\pi \int_0^{\pi/2} dx \frac{x^2}{1 + 3 \sin^2 x} \quad (14)$$

that can be computed only numerically, $a_1 \simeq 10.13478 \pm 0.00001$, and is identical¹⁰ to the sum of Eqs. (4.15), (4.16), and (4.20) in the second paper of Ref. [1] with $a_1 = \frac{2}{3} C_1$.

Instead of Eq. (14) I derived another integral by Legendre polynomial expansion,

$$a_1 = 2\pi^2 \int_0^{\infty} \frac{dx}{x} \text{Ei}(-3x) (e^{-3x} - e^{-x}), \quad (15)$$

where $\text{Ei}(x)$ denotes the exponential-integral function, for which an analytical result in terms of Euler's dilogarithm $L_2(x) = \sum_{k=1}^{\infty} x^k/k^2$, $|x| \leq 1$, is easily obtained,

$$a_1 = 2\pi^2 \left[L_2\left(-\frac{1}{3}\right) + \frac{\pi^2}{12} \right] = 10.13477910\dots \quad (16)$$

A quantum diffraction term of the order $n^{5/2}$ also follows from \mathfrak{S}_3 , if the asymptotic forms for the Slater sums S_{ab} and S_{abc} both include their first quantum correction $\propto \hbar^2$.

FOURTH CLUSTER INTEGRAL

The fourth cluster integral yields a classical term^{3,4} of the lowest order $e^9 n^{5/2}$,

$$\mathfrak{S}_4 = \frac{a_2}{\kappa^3} \sum_{a,b,c,d} n_a n_b n_c n_d l_{ab} l_{ac} l_{ad} l_{bc} l_{bd} l_{cd}, \quad (17)$$

with the numerical constant $a_2 = a_{2,\alpha} + a_{2,\omega}$,

$$a_{2,\alpha} = \frac{1}{16} \int d\mathbf{x}_1 d\mathbf{x}_2 d\mathbf{x}_3 \left(\frac{e^{-x_1}}{x_1} \right)^2 \frac{e^{-x_{12}}}{x_{12}} \left(\frac{e^{-x_{23}}}{x_{23}} \right)^2 \frac{e^{-x_3}}{x_3} \quad (18)$$

$$a_{2,\omega} = \frac{1}{24} \int d\mathbf{x}_1 d\mathbf{x}_2 d\mathbf{x}_3 \frac{e^{-x_1}}{x_1} \frac{e^{-x_2}}{x_2} \frac{e^{-x_3}}{x_3} \frac{e^{-x_{12}}}{x_{12}} \frac{e^{-x_{13}}}{x_{13}} \frac{e^{-x_{23}}}{x_{23}}. \quad (19)$$

Here the conventional treatment of Eq. (18) gives an integral⁴ that is similar to Eq. (14),

$$a_{2,\alpha} = 16\pi^2 \int_0^{\pi/2} dx \frac{x^2 \cos^2 x}{(1 + 3 \sin^2 x)^2}, \quad (20)$$

and finally the value $a_{2,\alpha} \simeq 8.052814 \pm 0.000001$. A preliminary estimate for $a_{2,\omega}$ taking into account only the first two terms from the Legendre polynomial expansion of Eq. (19) is $a_{2,\omega} \simeq 1.7376 \pm 0.0001$ while Alastuey *et al.*¹ have $a_{2,\omega} \simeq 1.7699 \pm 0.0001$.

Acknowledgements

Several fruitful discussions with Werner Ebeling, Jens Ortner, Françoise Cornu, Hugh E. DeWitt, and Philippe Martin are gratefully acknowledged.

REFERENCES

- [1] A. Alastuey, F. Cornu, and A. Perez, *Phys. Rev. E* 49:1077 (1994); *ibid.* 51:1725 (1995); A. Alastuey and A. Perez, *Phys. Rev. E* 53:5714 (1996).
- [2] J. Riemann, M. Schlanges, H. E. DeWitt, and W.-D. Kraeft, *Physica A* 219:423 (1995).
- [3] E. Haga, *J. Phys. Soc. Japan* 8:714 (1953).
- [4] H. L. Friedman, "Ionic Solution Theory," Interscience, New York · London (1962), pp. 222–224.
- [5] H. E. DeWitt, *J. Nucl. Energy C* 2:27 (1961); *J. Math. Phys.* 3:1216 (1962); *ibid.* 7:616 (1966).
- [6] W. Ebeling, *Ann. Phys. (Leipzig)* 21:315 (1968); *ibid.* 22:33, 383, 392 (1968/69); *Physica* 38:378 (1968); *ibid.* 40:290 (1968).
- [7] T. Morita, *Progr. Theor. Phys. (Japan)* 22:757 (1959).
- [8] T. Kahlbaum, The second virial coefficient for charged-particle systems, in: "Dynamik, Evolution, Strukturen — Nichtlineare Dynamik und Statistik komplexer Strukturen," J. A. Freund, ed., Verlag Dr. Köster, Berlin (1996), p. 41.
- [9] H.-J. Czerwon, Diploma thesis, Universität Rostock, Rostock (1972).
- [10] T. Kahlbaum, unpublished.

This page intentionally left blank

UNIFIED KINETIC THEORY FOR FLUID AND CRYSTAL PHASES

James W. Dufty¹ and Shankar P. Das²

¹Department of Physics, University of Florida
Gainesville, FL

²School of Physics, Jawaharlal Nehru University
New Delhi 110067, India

INTRODUCTION

The equilibrium and non equilibrium properties of plasmas pose greater experimental problems than those for simple atomic systems. However, the theory for such properties can be applied and tested using closely related systems at the mesoscopic level where experimental control and results are more direct. Dusty plasmas and colloidal suspensions are two such physical systems providing the potential to study the dynamics of freezing, melting, and metastable states of charged particles. For example, charged colloids exhibit a rich phase diagram with fluid and crystal phases easily observed under conditions where the screening length can be varied. More recently, laboratory formation of the crystal phase for dusty plasmas has been accomplished, providing a second system for direct and simple observation of two phase dynamics. The theory for equilibrium properties is well-developed via density functional theory¹ but the dynamics of systems supporting both fluid and crystal phases remains a fundamental challenge. An example of such a challenge is the characterization and description of metastable state dynamics and a possible glass formation. It is believed that such metastable states correspond to local minima of the same density functional that determines the equilibrium states. Thus it is desirable to formulate a dynamical description incorporating the structure of density functional theory to admit stationary solutions corresponding to all phases (including “special” metastable states), and therefore having the capacity to describe the mechanisms for evolution from one phase to the other. Since dense fluids and crystals are strongly coupled the usual perturbative and diagrammatic many-body methods to obtain kinetic equations are not useful for this purpose. Instead, we consider a phenomenological approach based on closure approximations to the second BBGKY hierarchy. The class of acceptable closures are restricted by three requirements: 1) the exact first hierarchy equation must follow from the approximate second hierarchy equation, 2) the exact local conservation laws are preserved, 3) the stationary solutions are the exact equilibrium states, including all phases. One example of such a closure is given in reference 2: A second example, generalizing those results to charged systems is described here.

BBGKY HIERARCHY AND DENSITY FUNCTIONAL THEORY

We consider the simplest model of a dusty plasma or colloid as a one component system of charged particles in the presence of an external force, \mathbf{F}_e . This force represents the confining potential for dusty plasmas (the combined effects of gravity, the electrodes, and the streaming ions) or the effective interaction with the background fluid for colloids. Its detailed form is not important for the present purposes. The construction of an appropriate kinetic equation for the time dependence of the one particle distribution function $f(\mathbf{r}_1, \mathbf{v}_1; t) \equiv f(1; t)$ follows from the exact first two equations of the BBGKY hierarchy

$$[\partial_t + L(1)]f(1; t) = \int d2 \theta(1, 2) f^{(2)}(1, 2; t) \quad (1)$$

$$[\partial_t + L(1) + L(2) - \theta(1, 2)]f^{(2)}(1, 2; t) = \int d3 [\theta(1, 3) + \theta(2, 3)]f^{(3)}(1, 2, 3; t) \quad (2)$$

Here $L(1) = \mathbf{v}_1 \cdot \nabla_{\mathbf{r}_1} + m^{-1} \nabla_{\mathbf{v}_1} \cdot \mathbf{F}_e(1)$, and $\theta(1, 2) = \mathbf{F}(1, 2) \cdot m^{-1} (\nabla_{\mathbf{v}_1} - \nabla_{\mathbf{v}_2})$ where $\mathbf{F}(1, 2)$ is the force between charges 1 and 2 (typically taken to be a screened Coulomb interaction). The equilibrium states are stationary solutions to (1) and (2) with the forms $f_e(1) = n(\mathbf{r}) \phi(\mathbf{v})$ and $f_e^{(s)}(1, 2 \cdots s) = f_e(1) f_e(2) \cdots f_e(s) g_e^{(s)}(\mathbf{r}_1, \mathbf{r}_2 \cdots \mathbf{r}_s | n)$. Here $n(\mathbf{r})$ is the density and f_e is the Maxwell-Boltzmann distribution. The configurational distribution functions $g_e^{(s)}(\mathbf{r}_1, \mathbf{r}_2 \cdots \mathbf{r}_s | n)$ can be generated from the grand potential Ω_e for the Gibbs ensemble by functional differentiation with respect to $u(\mathbf{r}) = \mu - V_e(\mathbf{r})$, where $V_e(\mathbf{r})$ is an external potential. For example,

$$n(\mathbf{r}) = -\frac{\delta \Omega_e}{\delta u(\mathbf{r})}, \quad n(\mathbf{r}_1) n(\mathbf{r}_2) \left[g_e^{(2)}(\mathbf{r}_1, \mathbf{r}_2 | n) - 1 \right] = \frac{\delta^2 \Omega_e}{\delta u(\mathbf{r}_1) \delta u(\mathbf{r}_2)} - n(\mathbf{r}_1) \delta(\mathbf{r}_1 - \mathbf{r}_2) \quad (3)$$

Similarly, $g_e^{(s)}$ is determined from the s^{th} order functional derivative of Ω_e . A fundamental result of density functional theory is that there is a one-to-one functional relationship of $n(\mathbf{r})$ to $u(\mathbf{r})$. Consequently, $\Omega_e = \Omega_e[n]$ and therefore $g_e^{(s)}(\mathbf{r}_1, \mathbf{r}_2 \cdots \mathbf{r}_s | n)$ also are functionals of the density. When the functionals in (1) are evaluated at the equilibrium density, the equilibrium distributions are obtained. The equilibrium density is obtained from the variational condition $\delta \Omega_e[n] / \delta n = 0$, i.e., the topology of $\Omega_e[n]$ determines the most probable density in the Gibbs ensemble.

A closed kinetic equation follows from an approximation expressing the three particle distribution function, $f^{(3)}(1, 2, 3; t)$, as a functional of the one and two particle distributions $f^{(3)}(1, 2, 3; t) \rightarrow \mathcal{F}^{(3)}(1, 2, 3 | f, f^{(2)})$. Accordingly, solution to the corresponding second hierarchy equation with this approximation leads to $f^{(2)}(1, 2; t) \rightarrow \mathcal{F}^{(2)}(1, 2 | f)$. Finally, use of this in the first hierarchy equation gives a closed kinetic equation for f . Many approximate choices for $\mathcal{F}^{(3)}$ have been considered, usually selected on the basis of small parameters such as the density or plasma coupling constant. Here we restrict the class of approximations by requiring that it should reduce to the exact equilibrium functional

$$\mathcal{F}^{(3)}(1, 2, 3 | f_e, f_e^{(2)}) = f_e(1) f_e(2) f_e(3) g_e^{(3)}(\mathbf{r}_1, \mathbf{r}_2, \mathbf{r}_3 | n_e) \quad (4)$$

This is sufficient to assure that $\mathcal{F}^{(2)}(1, 2 | f_e) = f_e(1) f_e(2) g_e^{(2)}(\mathbf{r}_1, \mathbf{r}_2 | n_e)$ as well. Otherwise, for non equilibrium states the functional $\mathcal{F}^{(3)}(1, 2, 3 | f, f^{(2)})$ is unknown.

CLOSURE APPROXIMATION

To motivate an appropriate closure approximation, or equivalently an estimate for $\mathcal{F}^{(3)}$, it is convenient first to represent $f^{(3)}(1, 2, 3; t)$ in terms of two particle correlations, $U(1, 2; t) \equiv$

$f^{(2)}(1,2;t) - f(1;t)f(2;t)$ and the residual three particle correlations defined by $U(1,2,3;t)$,

$$f^{(3)}(1,2,3;t) = f(1;t)f(2;t)f(3;t) + f(1;t)U(2,3;t) + f(2;t)U(1,3;t) \\ + f(3;t)U(1,2;t) + U(1,2,3;t) \quad (5)$$

If $U(1,2,3;t)$ is neglected a weak coupling kinetic equation is obtained which generalizes the Lenard-Balescu equation to all length and time scales. However, it clearly does not satisfy the above constraint (4) and therefore does not lead to the exact equilibrium stationary states. The strong coupling effects contained in $U(1,2,3;t)$ can be accounted for partially by noting that at equilibrium it is a specific functional of $f(1;t)$. Our closure approximation is therefore to replace $U(1,2,3;t)$ by the corresponding equilibrium functional, but evaluated at the non equilibrium state, $U(1,2,3;t) \rightarrow U_e(1,2,3|f)$. More explicitly this is

$$U(1,2,3;t) \rightarrow U_e(1,2,3|n) = f(1;t)f(2;t)f(3;t) \left\{ g_e^{(3)}(\mathbf{r}_1, \mathbf{r}_2, \mathbf{r}_3 | n) \right. \\ \left. - g_e^{(2)}(\mathbf{r}_1, \mathbf{r}_2 | n) - g_e^{(2)}(\mathbf{r}_1, \mathbf{r}_3 | n) - g_e^{(2)}(\mathbf{r}_2, \mathbf{r}_3 | n) + 2 \right\} \quad (6)$$

Note that there is both the explicit functional dependence on f and the implicit dependence through $n(\mathbf{r};t) = \int d\mathbf{v}f(\mathbf{r},\mathbf{v};t)$. The functional dependence of the right side on $n(\mathbf{r},t)$ is known from equilibrium density functional theory. Clearly, (6) gives an approximation that satisfies the equilibrium constraint (4).

The second hierarchy equation is most conveniently expressed in terms of $U(1,2;t)$ rather than $f^{(2)}(1,2;t)$ with the result

$$[\partial_t + \mathcal{L}(1) + \mathcal{L}(2) - \theta(1,2)]U(1,2;t) = [\mathbf{F}_T(1,2) \cdot \nabla_{v_1} + \mathbf{F}_T(2,1) \cdot \nabla_{v_2}]f(1;t)f(2;t) \quad (7)$$

with the definitions

$$\mathcal{L}(1)X(1) = [L(1) + \mathbf{F}_m(1) \cdot \nabla_{v_1}]X(1) - [\nabla_{v_1}f(1;t)] \cdot \int d2\mathbf{F}(1,2)X(2) \quad (8)$$

where $\mathbf{F}_m(1)$ is the usual mean field force

$$\mathbf{F}_m(1) = \int d2n(\mathbf{r}_2;t)\mathbf{F}(1,2) \quad (9)$$

The last term on the right side of (7) is a Vlasov operator that generates dynamic screening effects. Finally, the total force on the right side of (7) includes the effects of three particle correlations necessary for the exact equilibrium states

$$\mathbf{F}_T(1,2) = \mathbf{F}(1,2) + \int d3n(\mathbf{r}_3;t)\mathbf{F}(1,3) \left\{ g_e^{(3)}(\mathbf{r}_1, \mathbf{r}_2, \mathbf{r}_3 | n) - g_e^{(2)}(\mathbf{r}_1, \mathbf{r}_2 | n) \right. \\ \left. - g_e^{(2)}(\mathbf{r}_1, \mathbf{r}_3 | n) - g_e^{(2)}(\mathbf{r}_2, \mathbf{r}_3 | n) + 2 \right\} \quad (10)$$

Equation (7) is the primary result of this work. It has the same form as the ‘‘polarization approximation’’ for a weakly coupled plasma. The latter leads to a generalization of the Lenard-Balescu kinetic equation, valid on all space and times scales and preserving all conservation laws. The generalization here is to extend these properties to strong coupling. This occurs entirely through the total force $\mathbf{F}_T(1,2)$, in place of $\mathbf{F}(1,2)$, on the right side of (7). To interpret this change, consider $\mathbf{F}_T(1,2)$ in the equilibrium fluid state (relevant for linear response). Then only the contribution from $g_e^{(3)}$ survives and (10) can be simplified further using the second BBGKY hierarchy for stationary states to give

$$\mathbf{F}_T(1,2) \rightarrow \beta^{-1} \ln g_e^{(2)}(\mathbf{r}_1, \mathbf{r}_3 | n) \quad (11)$$

This is the mean force representing the interaction between a pair of particles in the presence of correlations with all other particles. Note that Eq. (7) does not simply replace all “bare” forces $\mathbf{F}(1,2)$ by this mean force. Instead, the dynamics is in terms of the bare force while the source of dynamic correlations on the right side is the only place where the mean force occurs. This asymmetry is required by the constraint of energy conservation.

DISCUSSION

The objective here has been to formulate a description of the complex dynamics for systems that can exist in fluid and solid states, and which can transform between them. The dynamics of such systems under dense fluid or solid state conditions is clearly very complex. We have not provided here any solutions to this problem but rather a practical formulation from which to study the problem. To our knowledge there is no other kinetic theory for charged particles capable of describing both the fluid and crystal states. It remains to be seen how accurate this approximation is for quantitative studies. The first test should be an evaluation of the transport coefficients for a one component plasma in the fluid phase at strong coupling. This follows from the corresponding linearized equation and the calculation is in progress. If the results are encouraging, more complex dynamics can be studied, such as a one component plasma in an initial fluid-like state at coupling for which the crystal state is stable. In the longer term, systems such as dusty plasmas with the strong influence of the confining potential can be studied with confidence in both the fluid and crystal phases. Solutions to the kinetic equation under strong coupling, nonlinear conditions will require numerical techniques. There has been remarkable success recently in extending the Bird Monte Carlo simulation method for the Boltzmann equation to dense, strongly coupled neutral systems.³ Corresponding results for screened Coulomb interactions can be anticipated shortly.

Acknowledgements

This research was supported by NSF grants PHY 9722133 and INT 9615767.

REFERENCES

- [1] See, for example, the review by W. Kohn at this Conference.
- [2] Dufty, J. W., 1997, *Contrib. Plasma. Phys.* 37:129.
- [3] Montanero, J. M., and Santos, A., 1997, *Phys. Rev. E* 54:438.

DUST CRYSTALS IN PLASMAS

S. Hamaguchi

IBM Thomas J. Watson Research Center
P. O. Box 218, Yorktown Heights, NY

INTRODUCTION

Small solid particles (i.e., dust particles) in a plasma are usually negatively-charged due to the high mobility of electrons, and they interact through a Yukawa (i.e., screened Coulomb) pair potential.¹⁻⁶ Laboratory experiments have recently shown that, when the interparticle potential energy exceeds the kinetic energy, particulates in plasmas may form crystalline structures (Coulomb crystals).⁷⁻¹⁰ In this paper, we shall employ molecular dynamics (MD) simulations to identify the conditions under which dust particles in a plasma condense into Coulomb crystals.

Consider a system of identical particles with mass m and charge $-Q = -Ze$ ($Z \gg 1$) immersed in a neutralizing background plasma. The interparticle potential is of Yukawa type, given by

$$\phi(r) = \frac{Q^2}{4\pi\epsilon_0 r} \exp(-k_D r),$$

where r denotes the radial distance between two particles and $\lambda_D = k_D^{-1}$ denotes the Debye length, i.e., the electric-field screening length of the background plasma.

Taking the Wigner-Seitz radius $a = (3/4\pi n)^{1/3}$ as the unit of length, where n is the particle number density, we may describe the thermodynamics of the Yukawa system in terms of two dimensionless ratios:

$$\kappa = \frac{a}{\lambda_D} \quad \text{and} \quad \Gamma = \frac{Q^2}{4\pi\epsilon_0 a k T}. \quad (1)$$

In the limit $\kappa \rightarrow 0$, the Yukawa system becomes the classical one-component plasma (OCP) — i.e., a system of mobile charges immersed in a strictly uniform neutralizing background.

MOLECULAR DYNAMICS SIMULATION

In MD simulations, simulation particles are placed in a finite domain. To emulate the infinite physical space, we impose periodic boundary conditions. If the simulation domain is given by a cubical box with side L , the effective pair potential between two simulation

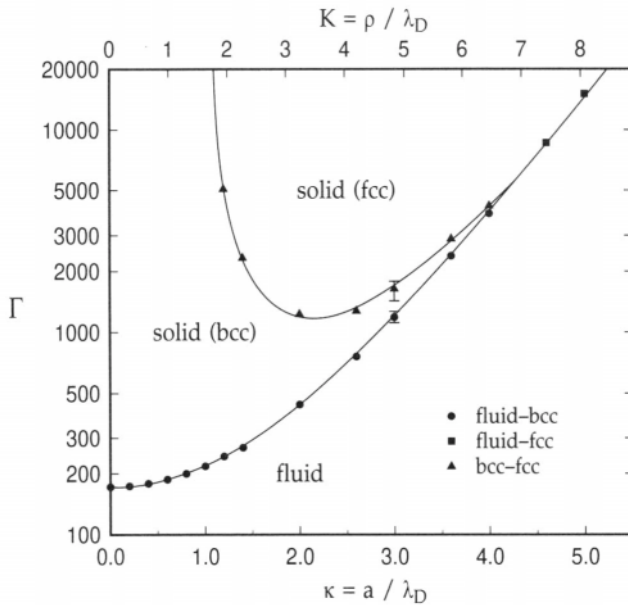


Figure 1. Phase diagram of Yukawa systems in the κ - Γ plane. The circles are fluid–bcc phase boundary points ($\kappa > 4.3$), the squares are fluid–fcc phase boundary points ($\kappa < 4.3$), and the triangles are bcc–fcc phase boundary points. The solid lines are fitting curves.

particles are expressed³ by

$$\Phi(\mathbf{r}) = \phi(|\mathbf{r}|) + \sum_{\mathbf{n} \neq \mathbf{0}} \phi(|\mathbf{r} + \mathbf{nL}|). \quad (2)$$

Here $\Phi(\mathbf{r})$ represents the interaction energy of particle i with particle j (at separation $\mathbf{r} = \mathbf{r}_j - \mathbf{r}_i$) and with all periodic images of the latter. The infinite sum of ϕ over integer vectors $\mathbf{n} = (l, m, n)$ represents the periodic images.¹¹

For a given κ , the intersection of the free energies of Yukawa systems in the fluid and solid phases determines the fluid–solid phase transition (i.e., melting or freezing) Γ value. Similarly the intersection of the bcc and fcc solid free-energies yields Γ values at the bcc–fcc phase transition. These free energies are evaluated by numerically integrating a functional of the potential energy $u(\kappa, \Gamma)$ obtained from MD simulations over the κ - Γ plane.³

MD simulations solve the equations of motion for simulation particles, using the effective pair potential $\Phi(\mathbf{r})$ of Eq. (2). To emulate a constant-temperature system, the velocities of all particles are renormalized periodically to bring the system kinetic energy into agreement with the target Γ value. The numbers of particles used in the simulations reported here were $N = 686$ for a bcc and $N = 500$ for an fcc lattice. These lattices are used as initial conditions, and the system is allowed to equilibrate to the desired Γ .

Figure 1 illustrates the phase diagram of Yukawa systems in the κ - Γ plane, where the curves show the phase boundaries. The representative error bar due to uncertainties in evaluating the free energies is given at $\kappa = 3.0$. The point where the three phases (fluid, bcc and fcc lattices) meet — the triple point — is given as $\kappa = 4.28$ and $\Gamma = 5.6 \times 10^3$. Both the fluid–solid and bcc–fcc phase transitions are of first order as the jump of the entropy per particle is finite at those boundaries.

Some earlier studies^{12–16} have used normalizations different from Eq. (1) to represent the particulate temperature T and the Debye screening length λ_D . For example, one may use $\rho = n^{-1/3}$ instead of the Wigner–Seitz radius a as the length unit, and define $K = \rho / \lambda_D$.

Note then that $K = (4\pi/3)^{1/3}\kappa \approx 1.61199\kappa$. Kremer, Robbins, and Grest¹² normalized the temperature T by the typical phonon energy of the fcc Yukawa lattice according to

$$\mathcal{T} = \frac{kT}{m\omega_E^2\rho^2}, \quad (3)$$

where ω_E is the Einstein frequency for the fcc Yukawa lattice defined by

$$\omega_E^2 = \frac{2k_D^2}{3m} \sum_{i \neq j} \phi(|\mathbf{r}_i - \mathbf{r}_j|)$$

with all particles situated at fcc lattice sites. The triple point ($\kappa = 4.28$ and $\Gamma = 5.6 \times 10^3$) is then given by $K = 6.90$ and $\mathcal{T} = 0.0038$.

In Fig. 2, we recast the phase diagram of Fig. 1 in terms of κ and \mathcal{T} and also plot earlier MD and MC simulation results based on different methods.^{12–16} These earlier MD and MC simulations do not include the infinite sum for periodic boundary conditions—i.e., the second term in Eq. (2)—that we have included in our MD simulations³ and are thus valid only in the large κ regime (i.e., $\kappa \gtrsim 1$). In Fig. 2, the fitting curve is extended to $\kappa = 8.0$. The filled marks and solid lines are the same as those used in Fig. 1. The crosses (\times), together with the error bars, are the fluid–solid phase boundary points obtained by Meijer and Frenkel.¹⁴ The error bars show the statistical errors. The open rectangles (\square), triangles (\triangle), and diamonds (\diamond) indicate stable fluid, bcc, and fcc states, respectively, obtained by Stevens and Robbins.¹⁵ The open circle (\circ), plus ($+$), and nabla (∇) are a fluid–bcc boundary point, a bcc–fcc phase boundary point, and the triple point, respectively, obtained by DuPont *et al.*¹⁶

The fluid–solid phase transition temperatures obtained in our MD simulations are systematically higher (by about 5% in \mathcal{T}) than those obtained by Meijer and Frenkel. The discrepancy may be due to the following reasons. First, the MC simulations by Meijer and Frenkel employed relatively small numbers of particles ($N \leq 256$). Second, Meijer and Frenkel assumed that the solid phase at their data points of $\kappa = 3.30$ ($K = 5.33$) and $\kappa = 4.20$ ($K = 6.77$) is fcc. However, our simulations, as well as those by DuPont *et al.*,¹⁶ indicate that this phase is actually bcc.

The stable fluid phase data presented by Stevens and Robbins,¹⁵ which are considered to give an upper bound of the fluid–solid transition phase, lie more or less on or above our fitted fluid–solid phase boundary, suggesting good agreement with our data. Only two data points given by Stevens and Robbins—those at $\kappa = 2.067$ and 2.597 ($K = 3.332$ and 4.186)—are slightly lower than our fitted phase-transition curve. To determine the stable phase, Stevens and Robbins used the “phenomenological melting test,” i.e., ran MD simulations starting from a two-phase state (equally divided fluid and solid phases) and observed its time evolution. If the difference between the free energies of the two phases is very small, which is the case near the transition point, the evolution of the MD simulation may be sensitively dependent on the shape of the simulation box, number of particles, initial perturbations, and the potential truncation radius. However, it is not clear from Ref. [15] that their phenomenological melting test can distinguish small differences in the free energy near the phase boundary, such as at those data points.

DuPont, Moulinasse, Ryckaert, and Baus¹⁶ used MC simulation and the Frenkel–Ladd lattice coupling method¹⁸ to evaluate solid free energies. The bcc–fcc phase boundary point obtained by DuPont *et al.*¹⁶ [denoted by a plus ($+$) in Fig. 2] is in excellent agreement with the bcc–fcc phase boundary curve estimated in our study.

In summary, we have obtained the phase diagram of Yukawa systems in the range between $\kappa = 0$ and $\kappa = 5$. We have also compared our MD simulation results with earlier MD and MC simulation results obtained by other authors. At larger κ values, for which all the

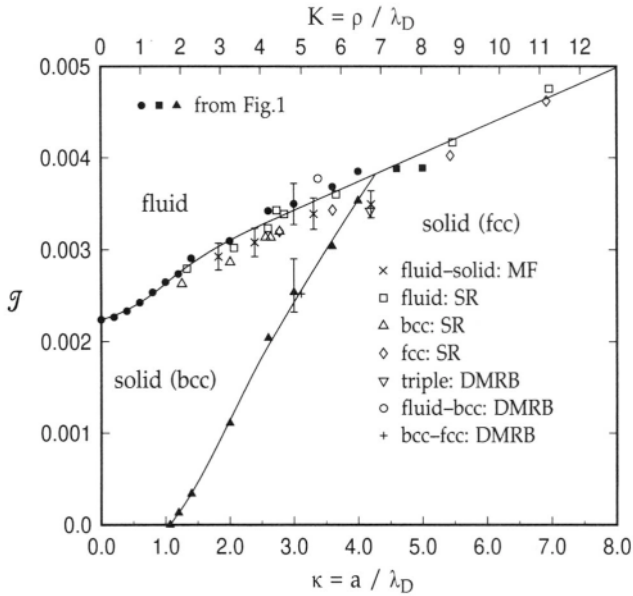


Figure 2. Phase diagram of Yukawa systems in the (κ, Γ) plane.

previous studies are conducted, our simulation results in general show good agreement with earlier results, especially those obtained more recently using more sophisticated techniques. Our MD simulations have identified the triple point — at which the three phases (fluid, bcc and fcc lattices) coexist — as being $\kappa = 4.28$ and $\Gamma = 5.6 \times 10^3$.

Acknowledgements

The author thanks R. T. Farouki for useful discussions on MD simulations and also thanks D. H. E. Dubin for providing values of the harmonic entropy constants, which were used to calculate the free energies of Yukawa systems.

REFERENCES

- [1] S. Hamaguchi, R. T. Farouki, and D. H. E. Dubin, *Phys. Rev. E* **56**, 4671 (1997).
- [2] S. Hamaguchi, R. T. Farouki, and D. H. E. Dubin, *J. Chem. Phys.* **105** 7641 (1996).
- [3] R. T. Farouki and S. Hamaguchi, *J. Chem. Phys.* **101**, 9885 (1994).
- [4] S. Hamaguchi and R. T. Farouki, *J. Chem. Phys.* **101**, 9876 (1994).
- [5] H. Ikezi, *Phys. Fluids* **29**, 1764 (1986).
- [6] R. T. Farouki and S. Hamaguchi, *Appl. Phys. Lett.* **61**, 2973 (1992).
- [7] Y. Hayashi and K. Tachibana, *Jpn. J. App. Phys.* **33**, L804 (1994).
- [8] H. Thomas, G. E. Morfill, V. Demmel, J. Goree, B. Feuerbacher, and D. Möhlmann, *Phys. Rev. Lett.* **73**, 652(1994).
- [9] J. H. Chu and I. Lin, *Phys. Rev. Lett.* **72**, 4009 (1994).
- [10] Th. Trottenberg, A. Melzer, A. Piel, *Plasma Sources Sci. Technol.* **4**, 450 (1995).
- [11] R. T. Farouki and S. Hamaguchi, *J. Comp. Phys.* **115**, 276 (1994).
- [12] K. Kremer, M. O. Robbins, and G. S. Grest, *Phys. Rev. Lett.* **57**, 2694 (1986).
- [13] M. O. Robbins, K. Kremer, and G. S. Grest, *J. Chem. Phys.* **88**, 3286 (1988).
- [14] E. J. Meijer and D. Frenkel, *J. Chem. Phys.* **94**, 2269 (1991).
- [15] M. J. Stevens and M. O. Robbins, *J. Chem. Phys.* **98**, 2319 (1993).
- [16] G. DuPont, S. Moulinasse, J. P. Ryckaert and M. Baus, *Mol. Phys.* **79**, 453 (1993).
- [17] E. J. Meijer, D. Frenkel, R. LaSar, and A. J. C. Ladd, *J. Chem. Phys.* **92**, 7570 (1990).
- [18] D. Frenkel and A. J. C. Ladd, *J. Chem. Phys.* **81**, 3188 (1984).

DUST DYNAMICS IN PLANETARY MAGNETOSPHERES

Mihály Horányi

Laboratory for Atmospheric and Space Physics
University of Colorado
Boulder, CO

INTRODUCTION

Many exciting phenomena were recently recognized that are associated with the interaction of magnetospheric fields and plasmas with the embedded dust grains. Lorentz resonances, gyrophase-drifts due to compositional and/or plasma density and/or plasma temperature gradients, transport due to charge or magnetic field fluctuations, shadow resonance and the coupling between radiation pressure and electrodynamic forces, for example, all contribute to shaping the fine dust distribution in planetary rings. The spokes in Saturn's B-ring, the ring-halo transition at Jupiter or the structure of Saturn's E-ring are examples where the observed radial and vertical structure clearly demonstrates the effect of magnetospheric perturbations.⁸

The extreme cases, where gravitationally dominated particles are perturbed by electrostatic forces (i.e., the charge to mass ratio $Q/m \rightarrow 0$) or when gravity becomes a perturbation on magnetically dominated particles ($Q/m \rightarrow \infty$) are well understood. However, when these forces are of similar amplitudes, dust grains may exhibit unusually complex dynamics: particles can get ejected from or captured into a magnetosphere by swiftly exchanging energy and angular momentum with the electric and magnetic fields. Here we show that dusty plasma effects are responsible producing streams of small grain escaping from Jupiter.

JUPITER

Jupiter was first recognized as a source of dust particles during Ulysses' encounter with the planet in 1992 as high speed intermittent streams of small grains were discovered.⁵ The first estimates put the mass of the stream particles in the range of $1.6 \times 10^{-16} \leq m \leq 1.1 \times 10^{-14}$ g and their velocity in the range of $20 \leq v \leq 56 \text{ kms}^{-1}$. Assuming an average density $\rho = 1 \text{ gcm}^{-3}$, the radii of these grains were estimated in the range of $0.03 \leq a \leq 0.1 \text{ }\mu\text{m}$. However, these estimates remained uncertain since the detector was not calibrated in this size and velocity range. Similar fluxes were seen with the identical dust detector on board the Galileo spacecraft as it first approached Jupiter in 1995.⁵

The suggested mechanism to eject dust particles from within the Jovian magnetosphere matched the size and velocity range of the observed stream particles by recognizing that these

grains become positively charged and can gain energy from the co-rotational electric field.⁷ Dust grains escaping to enter a cold plasma torus where they become negatively charged and all the grains smaller than $\sim 0.03 \mu\text{m}$ in radius remain confined there. Larger grains could visit the outer hot regions of the plasma torus, where they change their sign of charge to positive, due to the switch on of secondary electron production. Once a grain charges positively it will be accelerated by the outward pointing co-rotational electric field. The intermittent nature of the observed dust streams is most likely caused by the changes in the azimuthal component of the solar wind magnetic field, that periodically accelerates these particles toward and away the ecliptic plane.⁶

In fact, the detailed analysis of the propagation of the stream dust particles in the solar wind led to the recognition that they must be much smaller in size and move much faster than it was suggested earlier. The new estimate for the size range of the dust grains seen by Ulysses is $5 \leq a \leq 15 \text{ nm}$ and their velocity $v \geq 100 \text{ km/s}$.¹¹ These seem to be the ranges for the dust particles seen by Galileo as well.¹² This size range was also indicated earlier from the photometry of volcanic plume images.³

DYNAMICS AND CHARGING

In Gaussian units the equation of motion of a dust particle with radius a , mass m and charge Q , in an inertial joventric coordinate system can be written as

$$\ddot{\mathbf{r}} = -GM_J \nabla \left(\frac{1}{r} - \frac{R_J^2}{r^3} J_2 P_2 - \frac{R_J^4}{r^5} J_4 P_4 \right) \quad (1)$$

$$+ \frac{Q}{m} \left(\dot{\mathbf{r}} \times \mathbf{B} + \mathbf{E}_c \right), \quad (2)$$

where \mathbf{r} is the grain's position vector and an over-dot signifies differentiation with respect to time. The first term on the right hand side is the gravitational acceleration due to Jupiter with the gravitational constant $G (= 6.668 \times 10^{-8} \text{ g}^{-1} \text{ s}^{-2} \text{ cm}^3)$, mass of the planet, $M_J (= 1.9 \times 10^{30} \text{ g})$, its radius $R_J (= 71,398 \text{ km})$ and the higher order terms of Jupiter's gravity are expressed in terms of Legendre polynomials P_2, P_4 with coefficients $J_2 (= 0.01474)$ and $J_4 (= -0.00059)$. The last term is the Lorentz acceleration where \mathbf{B} is the local magnetic field and, assuming a rigidly co-rotating magnetosphere (for up to $50 R_J$), $\mathbf{E}_c = (\mathbf{r} \times \boldsymbol{\Omega}_p) \times \mathbf{B}/c$ is the co-rotational electric field, with the rotation rate of Jupiter $\boldsymbol{\Omega}_p (= 1.75 \times 10^{-4} \text{ s}^{-1})$. The magnetic field of Jupiter can be described using the O6 model.² We ignore solar radiation pressure since the light scattering efficiency of the very small grains discussed here is approaching zero. We also ignore plasma, neutral and Poynting–Robertson drags, these are negligible for the short time scales we discuss below.

As grains traverse the various plasma regions their charge will not stay constant. A grain's charge can be followed via the current balance equation

$$\frac{dQ}{dt} = \sum_i I_i, \quad (3)$$

where I_i represent electron and ion thermal currents, and also the secondary and photoelectron emission currents. These are all functions of the plasma parameters, material properties, size, velocity and also the instantaneous charge of a dust particle.¹⁰

To follow the orbits simultaneously with the evolution of the charge we need a particles and fields model of the jovian magnetosphere. We use the most recent interpretation of the Voyager 1 and 2 measurements to describe the plasma parameters in the centrifugal equator, which is the plane of symmetry for the plasma distribution in Jupiter's magnetosphere.¹

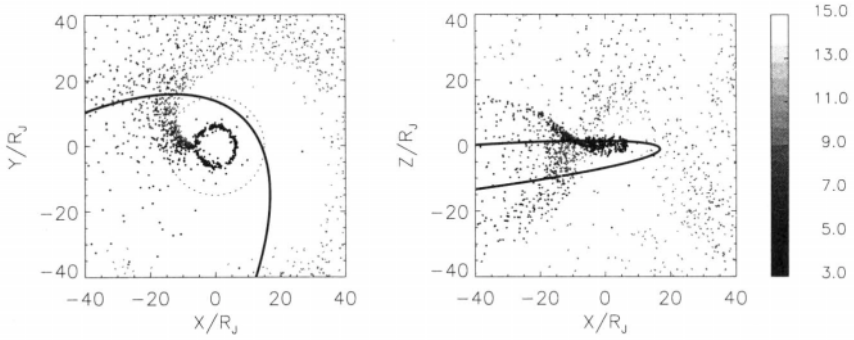


Figure 1. A snapshot of the positions of small grains released at the moon Io ($r = 6R_J$). The left side shows the projection into the equatorial plane and the right side shows the projection perpendicular to the equatorial plane (the Sun is to the right and Jupiter’s orbital motion points into the paper). The dashed circle represent the orbit of moon Ganymede ($r = 15R_J$) and the thick lines show the orbit of the Galileo spacecraft as it cut through to Jovian system moving from South to North, in counter-clockwise direction. The gray scale represents the radius of the dust particles in nano-meters (nm). The ‘ring’ of the smallest grains at $6R_J$ is due to the temporarily trapped grains in the Io plasma torus.

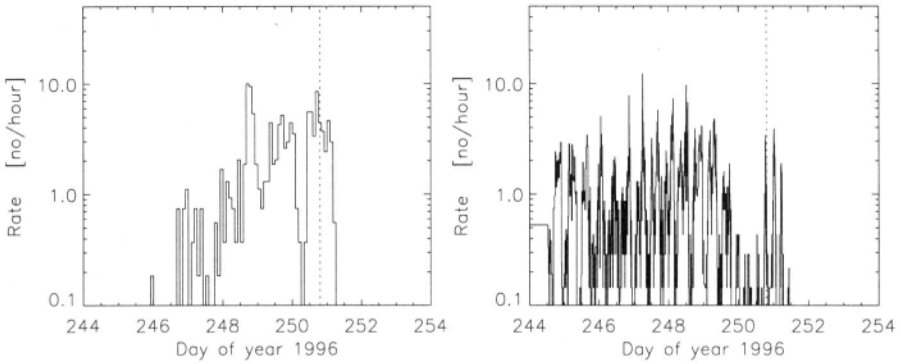


Figure 2. The impact rates from our computer simulations (left panel) and measured rates (right panel) during the second loop of the Galileo spacecraft about Jupiter. The dotted line marks the time of the closest approach to the moon Ganymede.

NUMERICAL RESULTS

The ultimate test of the model is to reproduce the observed impact rates.⁹ For the G2 orbit (the second loop of the spacecraft at Jupiter) we started our simulation 10 days before the closest approach and followed Galileo for 12 days. The initial position of Io and the spacecraft, and the phase of the magnetic field was matched to the real values. We have generated one particle every minute from Io and followed their trajectory and charge to a distance of $1.5 \times R_G$, where R_G is the instantaneous distance of the spacecraft from Jupiter. A snapshot of the evolving dust cloud is shown in Fig. 1. For each grain we noted the time and the relative velocity of the closest approach to Galileo. In the course of a simulation we have generated 17,280 particles randomly selected from the range of $3 \leq a \leq 15$ nm.

Fig. 2 compares our simulation result with the measurements. We capture the gross features of the observations, but did not reproduce the details. The exact timing and the relative intensity of the flux peaks are features that are generally not well reproduced. The grain size distribution, the fields and particles environment close to Io, or the location of the dust sources on Io are not modeled yet, but likely to be important.

In our computer simulations we used a simple description of the Io plasma torus and assumed a constant production rate of dust from Io that was treated as a point source. We captured the gross features of the observations, signaling that the basic physical ideas in this model are correct. The model can and will be further developed by comparing its predictions with later observations during consecutive orbits. Since every tiny dust grain ejected from Io acts as an active probe of the fields and particles environment, matching the observed dust impact rates provides perhaps the most stringent test of our models of Jupiter's magnetosphere.

REFERENCES

- [1] Bagenal, F., 1994, Empirical model of the Io plasma torus: Voyager observations, *J. Geophys. Res.*, *99*, 11,043.
- [2] Connerney, J. E. P., 1993, Magnetic Fields of the Outer Planets, *J. Geophys. Res.*, *98*, 18,659.
- [3] Collins, S. A., 1981, Spatial color variations in the volcanic plume at Loki on Io, *J. Geophys. Res.*, *86*, 8621.
- [4] Grün, E. *et al.*, 1993, Discovery of jovian dust streams and interstellar grains by the Ulysses spacecraft, *Nature*, *363*, 428.
- [5] Grün, E. *et al.*, 1996, Constraints from Galileo observations on the origin of jovian dust streams, *Nature*, *381*, 395.
- [6] Hamilton, D. P., J. A. Burns, 1993, Ejection of dust from Jupiter's gossamer ring, *Nature* *364*, 550.
- [7] Horányi, M., G. Morfill and E. Grün, 1993, The dust skirt of Jupiter, *J. Geophys. Res.*, *98*, 21245, 1993.
- [8] Horányi, M., 1996, Charged dust dynamics in the Solar System, *Annu. Rev. Astron. Astrophys.* *34*, 383.
- [9] Horányi, M., 1997, Modeling the Galileo dust measurements at Jupiter, *Geophys. Res. Lett.* *24*, 2,175.
- [10] Whipple, E. C., 1981, Potential of surfaces in space, *Rep. Prog. Phys.*, *44*, 1197.
- [11] Zook, H. A., *et al.*, 1996 Solar wind magnetic field bending of jovian dust trajectories, *Science*, *274*, 1501.
- [12] Liou and Zook, private communication, 1997.

COLLECTIVE PROCESSES IN STRONGLY COUPLED DUSTY PLASMAS

M. Rosenberg

Department of Electrical and Computer Engineering
University of California, San Diego
La Jolla, CA

INTRODUCTION

Ionized gases laden with fine (charged) dust, loosely referred to as dusty plasmas, occur in several laboratory environments. The dust grains, with radius a ranging from μm to sub- μm , can be highly charged in the plasma. A consequence of grain charging is that the dust can be strongly coupled when¹

$$\Gamma_d = \frac{Z_d^2 e^2}{dT_d} \exp(-d/\lambda_D) = \Gamma \exp(-\kappa) \geq 1 \quad (1)$$

where Z_d is the dust charge state, d is the intergrain spacing ($d \sim n_d^{-1/3}$, where n_d is the dust density), T_d is the dust thermal energy, and λ_D is the plasma screening length. Strongly coupled dusty plasmas in which the grains form highly organized lattice structures, referred to as Coulomb crystals or “plasma crystals,” have recently been produced in the laboratory by a number of experimental groups.²⁻⁵ In addition, strongly coupled dusty plasmas may occur in laboratory rf plasmas used for processing⁶⁻⁹ and have been observed in thermal plasmas.¹⁰

While the grains are charged negatively by the plasma electron and ion collection currents in the recent Coulomb crystal experiments, we have theoretically investigated a different type of Coulomb crystal with positively charged grains when photoelectron emission is the dominant charging current.^{11,12} We discuss this scheme for forming a Coulomb lattice of positively charged dust grains in both moderate and high pressure gases.

It has been shown within the context of standard plasma theory that the presence of highly charged dust grains in a plasma can lead to new low frequency dust acoustic waves and instabilities.¹³⁻¹⁹ When the dust is strongly coupled, with $\Gamma_d > 1$, the strong spatial correlation of the dust grains can affect the dispersion relation of such modes.^{20,21} We discuss the dispersion relation for dust acoustic waves in a strongly coupled dusty plasma, and compare with available experimental results.

COULOMB CRYSTALS WITH POSITIVELY CHARGED DUST

Recently we suggested that the condition for Coulomb crystallization of positively charged dust grains might be achieved in a high-pressure ($P > 1$ Torr) inert gas with dispersed

dust grains in the presence of a flux of ultraviolet (UV) photons.^{11,12} This avoids the need for a background plasma to charge the grains, but requires photons with sufficient energy ($h\nu \gtrsim 6$ eV) to charge the grains positive by the photoelectric emission of electrons, but with energy low enough ($h\nu < 12$ eV) to avoid photoionization of the gas. This driven system would thus be comprised of positively charged dust grains and photoemitted electrons in a background gas which cools the grains; the dust itself then provides the source of ionization and thereby controls the (electron) Debye length. The maximum charge Z_d^{max} on a grain can be estimated from the energetics of the photoemission process; the energy of the incoming photon should be greater than $W + e\phi_s$ (where W is the photoelectric work function of the grain material and ϕ_s is the grain surface potential), giving $Z_d^{max} \sim (h\nu - W)a/e^2$.

The positive equilibrium potential of the grain is maintained by the balance of photoelectron emission and electron re-collection on the grains. The electron photoemission current for $\phi_s > 0$ is²²

$$I_{ph} = e\pi a^2 Q_{abs} Y J \exp(-e\phi_s/T_{pe}) \quad (2)$$

where Q_{abs} is the efficiency of absorption for the UV radiation ($Q_{abs} \sim 1$ for $2\pi a/\lambda > 1$, where λ is the wavelength), J is the UV photon flux, Y is the yield of the photoelectrons, and T_{pe} is their average energy. The expression for the electron collection current to the grain depends on the regime of Knudsen number $Kn = l/a$ (ratio of the mean free path for electron-neutral collisions to the grain radius), as well as the ratio λ_D/a . In the collisionless regime where $Kn \gg 1$, the orbit-limited current to an attracting probe is²³

$$I_e = -(8\pi)^{1/2} e n_e v_e a^2 \left(1 + \frac{e\phi_s}{T_e} \right), \quad (3)$$

where n_e is the electron density and $v_e = (T_e/m_e)^{1/2}$ is the thermal velocity of electrons with temperature T_e . In the collisional regime where $Kn \ll 1$, the electron current to the grain taking into account mean free path effects is smaller²³ by roughly a factor of (l/a) . The equilibrium charge is obtained by balancing the currents $I_{ph} + I_e = 0$, using the condition for charge neutrality $n_e = Z_d n_d$, and estimating the electron temperature by noting that $T_e \sim T_{pe}$ when the electrons are re-collected onto the grains faster than they thermalize with the background gas, while thermalization give $T_e \sim$ the neutral temperature T_n .

We find theoretically that the condition for Coulomb crystallization $\Gamma_d > 170$ can be satisfied for a broad range of dust sizes and interparticle spacings both in the collisionless $Kn > 1$ and collisional $Kn < 1$ regimes (e.g., figs. 1 and 2 in Ref. 12). For example, in the $Kn > 1$ regime ($P \sim 3$ Torr, $T_n \sim .03$ eV), for photon intensity $I \sim 5$ W/cm² ($h\nu \sim 8 - 9$ eV, $J \sim 4 \times 10^{18}$ photons cm⁻² s⁻¹), and with $T_e \sim T_{pe} \sim 1$ eV, and $T_d \sim T_n$, we find that $\Gamma_d > 170$ for a ranging from $\sim 5 - 20$ μm and d ranging from $\sim 30 - 300$ μm . In such systems comprised of two charged components (electrons and positive dust), the dust provides the source of ionization so that both the interparticle spacing and the electron Debye length might be varied. In addition, higher neutral pressure may lead to more efficient cooling of the dust motion, and additional forces on the grains due to the UV flux, such as the photophoretic force, might aid in levitation or confinement.¹²

DUST ACOUSTIC WAVES IN STRONGLY COUPLED DUSTY PLASMAS

The dust acoustic wave is the analog of the ion acoustic wave in very low frequency regimes, where the dust mass m_d provides the inertia and the electrons and ions provide the pressure to sustain the wave.¹³ The wave has frequency $\omega \leq$ the dust plasma frequency $\omega_{pd} = (4\pi n_d Z_d^2 e^2 / m_d)^{1/2}$ and phase speed \ll the ion thermal speed. The dust acoustic wave

has been observed in a laboratory dusty plasma experiment,²⁴ and recently the dispersion of the dust acoustic wave in the strong-coupling regime has been studied experimentally.²⁵

To investigate the effect of strong dust coupling on dust acoustic waves, we consider a model system comprising dust grains that interact with each other via a screened Coulomb (Yukawa) potential

$$\phi(r) = \frac{Z_d^2 e^2}{r} \exp(-r/\lambda_D) \quad (4)$$

with the exponential factor taking into account within the linear approximation the screening of the dust charge by the plasma electrons and ions that are weakly correlated and classical. The strength of the intergrain coupling in this system is characterized by Γ_d as given in Eq. (1) in terms of two parameters: the Coulomb coupling parameter $\Gamma = Z_d^2 e^2 / d T_d$ and the parameter $\kappa = d / \lambda_D$ which is a measure of dust charge screening by the plasma.²⁶ For high coupling values $\Gamma_d \gg 1$, but below the crystallization limit the dust plasma is a “liquid” phase with a strong short-range order. Focusing on this phase,²⁰ we use a Quasi Localized Charge (QLC) approximation which was developed to study waves in strongly coupled plasmas.^{27,28} Based on the main physical feature of strongly coupled Coulomb systems that the charges are quasilocalized when $\Gamma \gtrsim 10$ but smaller than the critical value for solidification, the QLC approximation describes the motion of the system around the average configuration represented through the equilibrium pair correlation function $g(r)$.

The QLC model adapted to the Yukawa system can be used to determine the linear response of the system to a small perturbing external scalar potential.²⁰ This is done by considering the microscopic equations of motion for the rapid oscillations of the dust charges about their slowly drifting equilibrium sites, and then calculating the linear response. The resulting dielectric function $\epsilon(\mathbf{k}\omega)$ of the system, which can be written in terms of a dynamical matrix $\mathcal{D}(k)$ which is a functional of $g(r)$, gives the dispersion of collective modes. In the small- k domain, and for $\kappa \leq 1$, the dispersion can be related to the total correlation energy of the system: this latter can be obtained from the results of numerical simulations of Yukawa systems given in Ref. 26. This results in the following dispersion relation for dust acoustic waves²⁰

$$\frac{\omega^2}{\omega_{pd}^2} = \left[\frac{k^2 d^2}{k^2 d^2 + \kappa^2} + \mathcal{D}(k) \right] \quad (5)$$

where the term arising from strong coupling is given approximately by $\mathcal{D}(k \rightarrow 0) \approx f k^2 d^2$ with $f \approx -(4/45)[0.9 + 0.05\kappa^2]$ when $\kappa \leq 1$ and $\Gamma \gg 1$.

There appear to be three effects of strong dust–dust correlations on the dust acoustic wave dispersion relation. In the regime $kd \ll \kappa$ (i.e., $k\lambda_D \ll 1$), Eq. (5) gives $\omega^2 \approx k^2 c_{sd}^2 [1 + f\kappa^2]$, where $c_{sd} = \omega_{pd} \lambda_D$ is the dust acoustic speed. From here it can be seen that the first effect of strong dust coupling is a softening of the mode dispersion, with the phase speed decreasing (note that $f < 0$). The decrease of the phase speed as κ increases may be related to an increase in the compressibility of the fluid as the range of the repulsive intergrain potential decreases.²⁹ In the regime $kd \gg \kappa$ (i.e., $k\lambda_D \gg 1$), the dispersion relation (5) becomes $\omega^2 \approx \omega_{pd}^2 [1 + f\kappa^2 k^2 \lambda_D^2]$. Here it can be seen that the second effect is a reduction of the effective dust plasma frequency, which may be related to a decrease of the effective dust charge with stronger screening, i.e., with increasing κ .^{29,30} The third effect here is the onset of negative dispersion, that is, $\partial\omega/\partial k < 0$. These properties are analogous to those of ion acoustic waves in strongly coupled electron–ion plasmas analyzed in Ref. 31.

The effects of collisions of charged dust particles with neutrals can be included via an ad hoc collisional damping term in the microscopic equation of motion for the dust, using the hard sphere collision rate $\nu_d \sim \pi a^2 n_n v_n m_n / m_d$ (here n_n , m_n , and v_n are the neutral density, mass, and thermal speed).²⁰ The result is that $\omega^2 \rightarrow \omega(\omega + i\nu_d)$ in Eq. (5). From

this it can be seen that collisional effects can dominate strong coupling effects when roughly $\nu_d \omega / \omega_{pd}^2 > |\mathcal{D}| \sim |f' \kappa^2 k^2 \lambda_D^2|$. This may help explain why a fluid dispersion relation without strong coupling effects apparently fit the experimental results as reported in Ref. 25.

Acknowledgements

This work was supported in part by NSF and AFOSR.

REFERENCES

- [1] H. Ikezi, *Phys. Fluids* 29:1764 (1986).
- [2] H. Thomas, G. E. Morfill, V. Demmel, J. Goree, B. Feuerbacher, and D. Mohlmann, *Phys. Rev. Lett.* 73:652 (1994).
- [3] J. H. Chu and Lin I, *Physica A* 205:183 (1994).
- [4] Y. Hayashi and K. Tachibana, *Jpn. J. Appl. Phys.* 33: L804 (1994).
- [5] A. Melzer, T. Trottenberg, and A. Piel, *Phys. Lett. A* 191: 301 (1994).
- [6] G. S. Selwyn, J. E. Heidenreich, and K. L. Haller, *Appl. Phys. Lett.* 57:1876 (1990).
- [7] G. S. Selwyn, *Jpn. J. Appl. Phys.* 32:3068 (1993).
- [8] R. T. Farouki and S. Hamaguchi, *Appl. Phys. Lett.* 61:2973 (1992).
- [9] D. Winske and M. E. Jones, *IEEE Trans. Plasma Sci.* 22:454 (1994).
- [10] V. E. Fortov, A. P. Nefedov, O. F. Petrov, A. A. Samarian, and A. V. Chernyshev, *Phys. Lett. A* 219:89 (1996).
- [11] M. Rosenberg and D. A. Mendis, *IEEE Trans. Plasma Sci.* 23:177 (1995).
- [12] M. Rosenberg, D. A. Mendis, and D. P. Sheehan, *IEEE Trans. Plasma Sci.* 24:1422 (1996).
- [13] N. N. Rao, P. K. Shukla, and M. Y. Yu, *Planet. Space Sci.* 38:543 (1990).
- [14] N. D'Angelo, *Planet. Space Sci.* 38:1143 (1990).
- [15] M. Rosenberg, *Planet. Space Sci.* 41:229 (1993).
- [16] F. Melandso, T. Aslaksen, and O. Havnes, *J. Geophys. Res.* 98:13315 (1993).
- [17] D. Winske, S. P. Gary, M. E. Jones, M. Rosenberg, V. W. Chow, and D. A. Mendis, *Geophys. Res. Lett.* 22:2069 (1995).
- [18] M. Rosenberg, *J. Vac. Sci. Technol. A* 14:631 (1996).
- [19] N. D'Angelo and R. L. Merlino, *Planet. Space Sci.*, 44:1593 (1996).
- [20] M. Rosenberg and G. Kalman, Dust acoustic waves in strongly coupled dusty plasmas, *Phys. Rev. E* (in press) (1997).
- [21] P. Kaw and A. Sen, Collective modes in strongly coupled dusty plasmas, in this volume.
- [22] C. K. Goertz, *Rev. Geophys* 27:271 (1989).
- [23] J.-S. Chang and J. G. LaFramboise, *Phys. Fluids* 19:25 (1976).
- [24] A. Barkan, R. L. Merlino, and N. D'Angelo, *Phys. Plasmas* 2:3563 (1995).
- [25] J. B. Pieper and J. Goree, *Phys. Rev. Lett.* 77:3137 (1996).
- [26] S. Hamaguchi, R. T. Farouki, and D. H. E. Dubin, *J. Chem. Phys.* 105:7641 (1996).
- [27] G. Kalman and K. I. Golden, *Phys. Rev. A* 41:5516 (1990).
- [28] K. I. Golden, G. Kalman, and P. Wynn, *Phys. Rev. A* 46:3454 (1992).
- [29] J. L. Barrat, J. P. Hansen, and H. Totsuji, *J. Phys. C: Solid State Phys.* 21:4511 (1988).
- [30] F. Melandso, *Phys. Plasmas* 3:3890 (1996).
- [31] K. Golden, *Phys. Rev. A* 35:5278 (1987).

LATTICE WAVES IN PLASMA CRYSTALS

H. M. Thomas,¹ J. R. Jokipii,² G. E. Morfill* and M. Zuzic¹

¹Max-Planck-Institut für extraterrestrische Physik
85740 Garching, Germany

²University of Arizona
Tucson AZ

INTRODUCTION

“Plasma crystals” have rapidly become an established means of investigating certain “solid state” properties. Their possible existence was first suggested by Ikezi¹ on theoretical grounds, experimentally the first announcements came 8 to 9 years later.²⁻⁶ They consist of charged monodisperse microspheres (typical sizes are a few microns) embedded in a plasma, which in most investigations is generated by radio-frequency discharges and recently also in DC glow discharges^{7,8} and combustion plasmas.⁹ The microspheres become self-organized by mutual Coulomb interaction into a regular crystalline structure — which is their minimum energy state — provided the Coulomb coupling parameter and the spatial density exceed certain thresholds [see e.g.,³]. Since the original discovery there have been important fundamental investigations on processes such as the solid/liquid phase transition,¹⁰⁻¹² dislocations^{13,14} and stimulated sublimation.¹⁵ For a review of our work on plasma crystals see [16]. The unique properties of plasma crystals, i.e., their fast response times (seconds), the small damping, the easy experimental control, the wide accessible range of parameters and the detailed imaging, possible even at high time resolution, make them ideal objects for studying dynamical effects of interest in crystal physics, colloidal physics, strongly coupled plasma physics and monolayer physics. Here we report on one such dynamical aspect of crystal physics — the propagation and damping of *lattice waves*.

In a recent paper,¹⁷ Pieper and Goree examined the dispersion of compressional waves propagating through a colloidal (or dusty) plasma in the strong coupling regime. Over a wide range of coupling strengths ($30 \lesssim \Gamma \lesssim 10000$, where $\Gamma = \text{Coulomb potential} / \text{kinetic energy}$) they found that the measured dispersion relation could be fitted rather well to the theory of damped dust acoustic waves (DAW, see [18]) but not dust lattice waves (DLW). Surprisingly, DLW were never seen!

In many ways plasma crystals can be expected to behave much like natural crystals — the heavy, charged, microspheres correspond to the ions and the plasma in the Debye-sphere surrounding the microspheres may be viewed analogous to the electron cloud surrounding the ion. Thus plasma crystals should propagate “acoustic” lattice waves as well as the equivalent of the “optical branch” — the latter occurring at infrared–microwave frequencies, however.¹⁹

In addition, there are of course plasma crystal specific effects, such as the random charge fluctuations and Brownian motion, which introduce a random forcing term,²⁰ the polarization of the microspheres themselves,²¹ and the systematic charge fluctuations associated with compression and rarefaction^{22,23} in these longitudinal lattice waves.

THEORY

In order to calculate the wave propagation through a plasma crystal we have to treat the mutual interaction of three components: the negatively charged microspheres, the Debye clouds of positive charges and the neutral gas background. For present purposes we restrict ourselves to two components only (microspheres and neutral gas) and assume the neutrals to be stationary. In¹⁹ we will consider the Debye ion clouds as well.

Wave propagation in crystals is a well-studied subject [e.g.,²⁴ and references therein]. We adopt the established techniques here and adapt them, where appropriate, to the conditions relevant for plasma crystals. Accordingly we use a screened Coulomb potential to describe the interaction between neighboring particles (microspheres) in the plasma crystal lattice. Using a linear chain model and considering only nearest-neighbor forces, we can derive the force acting on particle n in this chain

$$F_n = \frac{Q^2}{r_-} e^{-\frac{r_-}{\lambda_d}} \left\{ \frac{1}{r_-} + \frac{1}{\lambda_d} \right\} - \frac{Q^2}{r_+} e^{-\frac{r_+}{\lambda_d}} \left\{ \frac{1}{r_+} + \frac{1}{\lambda_d} \right\} \quad (1)$$

where we have assumed that all particles carry the same charge, Q . The separation between n and $n-1$ is r_- , that between n and $n+1$ is r_+ , $\lambda_d \equiv \left(\frac{K}{4\pi n_p e^2} \right)^{\frac{1}{2}} \left(\frac{1}{T_e} + \frac{1}{T_i} \right)^{-\frac{1}{2}}$ is the total Debye length. The undisturbed plasma density is n_p , T_e and T_i are electron and ion temperatures, respectively, K is Boltzmann's constant and e the electronic charge unit.

The neutral gas in the rf-discharge chamber exerts a frictional force on the microspheres. Conditions are such that the mean free path for the gas molecules is substantially larger than the particle size, so that we have to use the Epstein drag law. The validity of this was checked experimentally using single suspended microspheres and was found to be correct to better than 15%.²⁵ The frictional force term is

$$F_{gn} = -2\sqrt{\pi} \rho_g R^2 c_s v_n \quad (2)$$

where ρ_g is the neutral gas density, c_s the thermal speed of the gas atoms, R the radius of the microspheres and v_n the velocity of the n th particle in the chain. Writing (1) and (2) in terms of the mean lattice spacing, a , and defining the particle's deviation, Δ_n , from the ideal lattice site as $x_n \equiv \Delta_n/a$, etc. yields in the limit of $x \ll 1$

$$Ma\ddot{x}_n = \alpha (x_{n-1} - 2x_n + x_{n+1}) - \nu a\dot{x}_n \quad (3)$$

with M the particle's mass and the "coupling constant" defined as

$$\alpha \equiv \frac{Q^2}{a^2} e^{-\xi} [(1 + \xi)^2 + 1] \quad (4)$$

where $\xi \equiv \frac{a}{\lambda_d}$. The constant $\nu \equiv 2\sqrt{\pi} \rho_g R^2 c_s$. Making use of the Bloch condition, i.e., the fact that to zero order we have a regularly spaced array of particles, we get

$$x_l(t) = e^{ik \cdot l} x_o(t) \quad (5)$$

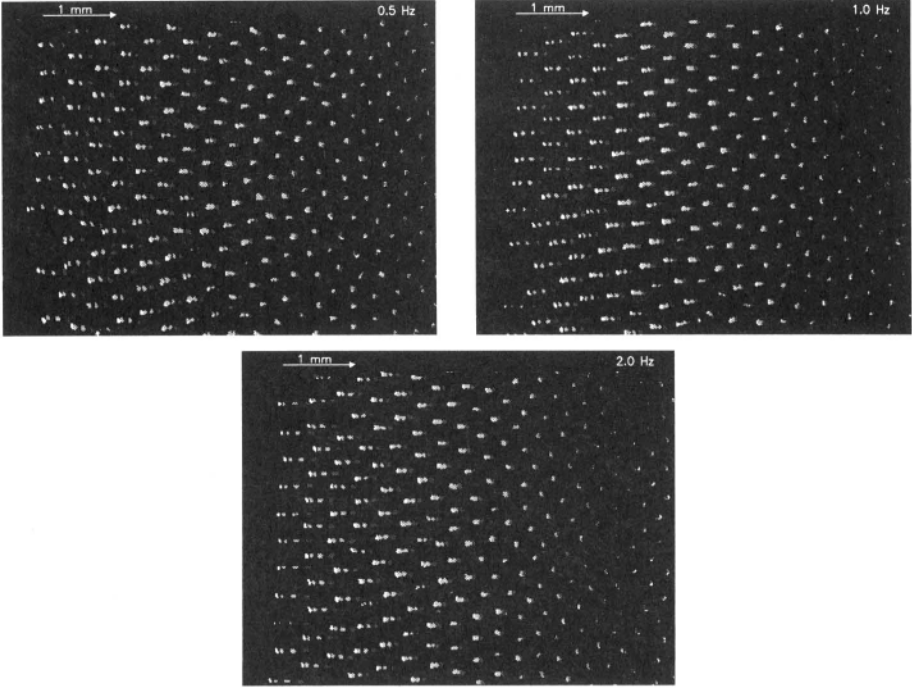


Figure 1. The amplitude variation of microspheres in the plasma crystal, oscillating in an externally applied sinusoidally varying electric field at frequencies 0.5 Hz, 1 Hz and 2 Hz, is shown. The field is applied from a wire located in the crystal plane (=image plane) parallel to the y-axis on the left of the image. Images were recorded at 50 Hz, the particle positions are plotted at each individual recording and gray-scale-coded from white (first image) to dark gray (5th image).

where \underline{k} is a given wave vector, \underline{l} the lattice vector and subscript o denotes our origin. In an infinite periodic lattice the origin position is arbitrary (so we may pick position n). Then we get

$$\begin{aligned}
 x_{n-1} &= x_o e^{-ika} \\
 x_n &= x_o \\
 x_{n+1} &= x_o e^{+ika}
 \end{aligned} \tag{6}$$

and the force equation becomes

$$Ma\ddot{x}_o = -2\alpha x_o (1 - \cos ka) - \nu a \dot{x}_o \tag{7}$$

The dispersion relation is then given as

$$w^2 - \beta^2 \sin^2 \left(\frac{ka}{2} \right) - i w \gamma = 0 \tag{8}$$

where $\beta^2 \equiv \frac{4\alpha}{Ma}$ and $\gamma = \frac{\nu}{M}$. This result is identical to the linear solution obtained by Melandsø²⁶ with the addition of the damping term. As shown in [26] nonlinear corrections do not lead to a significant change, so that (8) is a rather good representation of the dispersion relation for DLW.

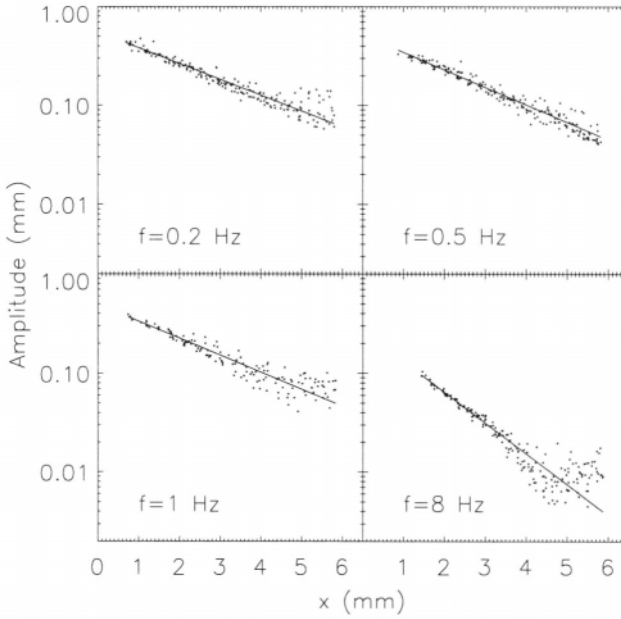


Figure 2. The amplitude variation of the plasma crystal particles is plotted in a log-linear diagram to emphasize the exponential nature of the damping. Representative examples are shown at 0.2 Hz, 0.5 Hz, 1.0 Hz and 8.0 Hz. The solid line represents the least squares fit through the data points.

EXPERIMENTAL RESULTS

In order to measure the propagation and damping of lattice waves, we used the rf-discharge chamber described in [3], modified as discussed in [25]. The plasma was ignited (Krypton at a pressure of 0.42 mbar, neutral gas temperature 300 K) and the microspheres were injected (radius $3.45 \cdot 10^{-4}$ cm, density 1.51 g/cm³). The plasma crystal formed had typically ~ 40 lattice planes in the horizontal and ~ 8 lattice planes in the vertical direction (particle separation ~ 0.25 mm). A sinusoidal electrical signal was applied to a wire located outside the crystal approximately in the crystal plane and the response of the microspheres was monitored with a CCD camera from vertically above. Examples of such observations are shown in Fig. 1. The length of the particle trajectories in the x-direction gives a direct measure of their oscillation amplitudes, A. These amplitudes decrease with distance, x. It is easy, therefore, to measure the decay of the propagating wave by fitting an exponential function to all the amplitudes A(x). Repeating this over a broad range of frequencies (from 0.1 Hz to 10 Hz) we can measure the damping length variation and thus determine k_i directly. To show that the decay really is exponential to a very good approximation, we have compiled several results at different frequencies in Fig. 2.

The real component, k_r , can be obtained directly also — by measuring the signal propagation speed, c_s , as a function of frequency and using $c_s = \frac{\omega}{k_r}$. A second method is the Fourier technique described in [17]. This also yields k_i and k_r , of course, so that in principle we have two ways to determine the dispersion relation, providing an independent check and independent assessments of the uncertainties.

The comparison between theory and measurements is shown in Fig. 3 a and b. The experiment was repeated under the same conditions, showing that the results are reproducible. Regarding the quantitative agreement we point out the following:

- The neutral gas damping is known accurately to a few percent, because the gas pressure

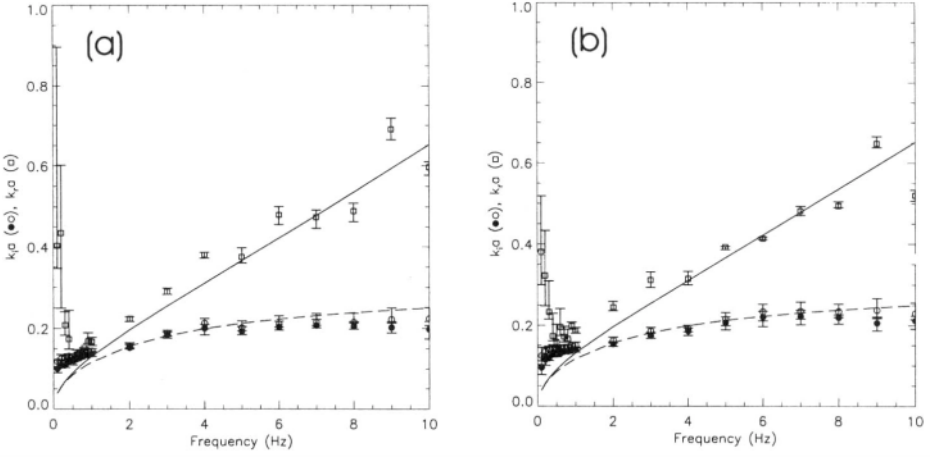


Figure 3. a, b) The normalized wave number and damping length for lattice waves in plasma crystals are defined as $k_r a$ and $(k_i a)^{-1}$ respectively. In this figure we plot $k_r a$ and $k_i a$ as a function of wave frequency, f . Increasing $k_i a$ implies more rapid damping. Measurements of $k_r a$ are given by the open squares, those of $k_i a$ by the open circles and the filled circles. Open symbols were computed using the Fourier analysis method, filled symbols were obtained from fitting exponentials to the amplitude variations (see text). The theoretical results are given by the continuous line for $k_r a$ and the dashed line for $k_i a$. The theoretical values were calculated for Krypton at room temperature for particles of diameter $6.9\mu\text{m}$ and material density $1.51\text{g}/\text{cm}^3$. The lattice distance, a , was set equal to the Debye length, λ_d , and the charge on the microspheres was taken as $1.1 \cdot 10^4 e$. Two experiments are shown, which were performed under similar conditions (a and b), to illustrate repeatability.

is monitored.

- The lattice coupling is not known so well, because the charge on the microspheres is not known to better than a factor 2. In addition the ratio a/λ_d , which enters in the expression for the coupling constant, is $O(1)$ but again the exact value is somewhat uncertain.

Hence the procedure is to vary the parameter β in (8), until a good theoretical fit is obtained for both k_i and k_r as a function of wave frequency. The theoretical fits shown are for $\xi \equiv \frac{a}{\lambda_d} = 1$ and $Q = 1.1 \cdot 10^4 e$.

This allows us now to determine some more plasma crystal properties. The lattice wave speed at high frequencies is measured to be frequency independent, i.e., the waves are nondispersive — as the theory suggests. Its value is $C_L = 2.42 \text{ cm/sec}$ for the particular plasma crystal parameters of our experiment. The Debye frequency (i.e., that frequency where the wavelength is twice the lattice separation) is for the principal direction of a hexagonal lattice structure

$$f_D = \frac{C_L}{\sqrt{3}a} \quad (9)$$

which turns out to be 55.8 Hz for our crystal parameters. Lattice waves with higher frequencies should not be able to propagate through the crystal.

We see from Fig. 3 that the quantitative agreement between measurements and DLW theory is, in general, very good, confirming the identification that we are indeed observing dust lattice waves. There are, however, also some discrepancies.

- There is a weak suggestion in the data that damping at high frequencies may be somewhat lower than predicted.

- at low frequencies $f < 1$ Hz both k_r and k_i as derived from the measurements are significantly larger than the theoretical predictions.

This low frequency result may have an interesting explanation: the plasma crystal had ~ 40 lattice planes. When the wavelength gets larger than the crystal size, the particles still move under the influence of the wave field, but the crystal then works more in the manner of a compressible membrane. For our system this happens when $k_r a \lesssim \frac{2\pi}{40} \simeq 0.157$, i.e., at about 1.5 Hz, just at the “point of departure.” If this explanation is correct, we have an interesting possibility to study signal transfer effects across lossy membranes microscopically for the first time. This requires more research, but it is clear that the near constancy of the signal damping length (with frequency) in this “membrane regime” is an important pointer towards the physics there.

REFERENCES

- [1] H. Ikezi, “Coulomb Solid of Small Particles in Plasmas,” *Phys. Fluids* 29: 1764 (1986).
- [2] H. Thomas, in Formation, Transport and Consequences of Particles in Plasmas (Abstract), NATO Advanced Research Workshop (ed. J. P. Boeuf and G. S. Selwyn), (1993).
- [3] H. Thomas and G. E. Morfill and V. Demmel and J. Goree and B. Feuerbacher and D. Möhlmann, “Plasma crystal: Coulomb crystallization in a dusty plasma,” *Phys. Rev. Lett.* 73: 652 (1994).
- [4] J. H. Chu and L. I., “Direct observation of Coulomb crystals and liquids in rf dusty plasmas,” *Phys. Rev. Lett.* 72: 4009 (1994).
- [5] Y. Hayashi and K. Tachibana, “Observation of Coulomb-crystal formation from carbon particles grown in a methane plasma,” *Jpn. J. Appl. Phys.* 33: 804 (1994).
- [6] A. Melzer, T. Trottenberg and A. Piel, “Experimental determination of the charge on dust particles forming Coulomb lattices,” *Phys. Lett. A* 191: 301 (1994).
- [7] V. E. Fortov and A. P. Nefedov and O. F. Petrov and A. A. Samarian and A. V. Chernyshev, “Emission properties and structural ordering of strongly coupled dust particles in a thermal plasma,” *Phys. Lett. A* 219: 89 (1996).
- [8] V. E. Fortov and A. P. Nefedov and O. F. Petrov and A. A. Samarian and A. V. Chernyshev, “Particle ordered structures in a strongly coupled classical thermal plasma,” *Phys. Rev. E* 54: 2236 (1996).
- [9] V. E. Fortov et al., *Phys. Rev. Lett.*, subm. (1997).
- [10] H. M. Thomas and G. E. Morfill, “Melting dynamics of a plasma crystal,” *Nature* 379: 806 (1996).
- [11] A. Melzer, A. Homann and A. Piel, “Experimental investigation of the melting transition of the plasma crystal,” *Phys. Rev. E* 53: 2757 (1996).
- [12] L. I. and W. T. Juan and C. H. Chiang and J. H. Chu, “Microscopic particle motions in strongly coupled dusty plasmas,” *Science* 272: 1626 (1996).
- [13] G. E. Morfill and H. Thomas, “Plasma crystal,” *J. Vac. Sci. Technol. A* 14: 490, 1996.
- [14] C.-H. Chiang and L. I., “Cooperative particle motions and dynamical behaviors of free dislocations in strongly coupled quasi-2D dusty plasmas,” *Phys. Rev. Lett.* 77: 647 (1996).
- [15] M. Zuzic, H. Thomas and G. E. Morfill, in preparation (1997).
- [16] G. E. Morfill, H. M. Thomas and M. Zuzic, “Plasma Crystals—A Review,” in *Advances in Dusty Plasmas*, edited by P. K. Shukla, D. M. Mendis and T. Desai, World Scientific, Singapore, 1998.
- [17] J. B. Pieper and J. Goree, “Dispersion of plasma dust acoustic waves in the strong-coupling regime,” *Phys. Rev. Lett.* 15: 3137 (1996).
- [18] N. N. Rao, P. K. Shukla and M. Y. Yu, “Dust Acoustic Waves in Dusty Plasmas,” *Planet. Space Sci.* 38: 543 (1989).
- [19] G. E. Morfill et al. (in preparation) (1997).
- [20] J. R. Jokipii et al. (in preparation) (1997).
- [21] S. Hamaguchi and R. T. Farouki, “Polarization Force on a Charged Particulate in a Nonuniform Plasma,” *Phys. Rev. E* 49: 4430 (1994).
- [22] O. Havnes, G. Morfill and C. Goertz, “Plasma Potential and Grain Charges in a Dust Cloud Embedded in a Plasma,” *J. Geophys. Res.* 89: 10999 (1984).
- [23] C. Goertz and W. Ip, *Geophys. Res. Lett.* 15: 84 (1988).
- [24] J. M. Ziman, “Principles of the Theory of Solids,” Cambridge University Press, 2nd Edition (1972).
- [25] M. Zuzic, H. M. Thomas and G. E. Morfill, “Wave propagation and damping in plasma crystals,” *J. Vac. Sci. Technol. A* 14: 496 (1996).
- [26] F. Melandsa, “Lattice waves in dust plasma crystals,” *Physics of Plasmas* 11: 3890 (1996).

STRUCTURAL TRANSITIONS IN CONFINED YUKAWA SYSTEM AS A MODEL OF DUSTY PLASMAS AND CHARGE STABILIZED COLLOIDAL SUSPENSIONS

Hiroo Totsuji, Tokunari Kishimoto, and Chieko Totsuji

Department of Electrical and Electronic Engineering
Okayama University
Tsushimaoka 3-1-1, Okayama 700, Japan

INTRODUCTION

Dusty plasma is a mixture of charged macroscopic dust particles and plasma which is often encountered in semiconductor plasma processes and space physics. The control of dusty plasma is an important issue to improve the quality of semiconductor wafers and the behavior of dust particles is closely related to various astrophysical phenomena. Since dust particles are usually highly charged and can easily be in the state of strong coupling, their collective properties are quite interesting as a subject of basic plasma physics.

The interaction between dust particles is screened by environmental plasma. As the simplest approximation, we assume they interact via the isotropic Yukawa potential:

$$(q^2/r) \exp(-r/\lambda). \quad (1)$$

Due to their large mass, dust particles concentrate around the boundary of the plasma and the sheath where the gravitation and the electrostatic force balance with each other. In other words, they are confined by these forces. Recent experiments have shown that dust crystals of various structures are formed in strongly coupled dusty plasmas.¹⁻⁴

In charge stabilized colloidal suspensions, charged macroscopic particles interact via the DLVO potential. When the radius of core is neglected, the interaction potential reduces to the Yukawa potential. In many cases, these colloidal particles are strongly coupled and are observed to form colloid crystals. When they are confined between parallel glass plates, various layered structures have been observed.⁵

These confined Yukawa systems have the dimensionality between two and three and the Yukawa potential covers both short-ranged and long-ranged interactions. The purpose of this article is to present some results of numerical experiments and theoretical analyses on the strongly coupled confined Yukawa system.⁶⁻⁹

Around the equilibrium plane, the effect of external forces may be expressed by a one-dimensional parabolic potential

$$kz^2/2. \quad (2)$$

The bulk Yukawa system is characterized by two dimensionless parameters. With the introduction of a new parameter k , we have now three independent dimensionless parameters

characterizing our system at the temperature T :

$$\Gamma = q^2/ak_B T, \quad \xi = a/\lambda, \quad \text{and} \quad \eta = k/4\pi q^2 N_s^{3/2}. \quad (3)$$

Here a is the mean distance defined by $1/(\pi N_s)^{1/2}$, N_s being the surface number density.

We have performed molecular dynamics simulations on the confined Yukawa system with a number of sets of characteristic parameters. Periodic boundary conditions in x - and y -directions are imposed and free deformation of magnitudes and directions of fundamental vectors are allowed. The temperature and the surface number density are kept constant for each set of characteristic parameters. Typical number of particles is 10^3 . Details of numerical method are given elsewhere.⁸

STRUCTURES IN THE GROUND STATE

One of the most interesting properties of our system may be the structures at low temperatures. Though the phase diagram of the three-dimensional Yukawa system is well known,¹⁰ our system has an additional parameter related to confinement.

At high temperatures, particles are distributed as a thick cloud with infinite extensions in the xy -plane. When the temperature is slowly decreased, the cloud changes into a collection of almost equally spaced thin layers. The number of layers is a function of characteristic parameters at low temperatures, ξ and η , as shown in Fig. 1 which is a kind of phase diagram for the ground state structure. A competition between the confinement and mutual repulsion determines the structure; we have smaller number of layers for strong confinement (larger η and/or larger ξ), and larger number of layers for strong mutual repulsion (smaller η and/or smaller ξ). The distance between layers repeats systematic changes: When parameters are changed to increase the number of layers, the distance is smallest just after the appearance of a new layer and largest just before the appearance of another new layer. In each layer, particles are organized into two-dimensional lattices and the lattice symmetry changes from square to triangular synchronously with the interlayer distance as shown in Fig. 2.

The structures of confined nonneutral plasmas have been analyzed theoretically from the viewpoint what is essential in the formation of such structures.^{11,12} We extend this method to confined Yukawa systems.⁷⁻⁹ The natural starting point is the continuum model where particles are regarded as a fluid. In the case of nonneutral plasma without screening, the minimum energy state of the fluid model approximately reproduces the profile of particle distribution in z . In our case, this model overestimates the profile by a factor of two.

The next step may be to assume the existence of layers (shells) and compare the ground state of such a shell model with experiments. The ground state, however, has an infinite number of shells and we are forced to return to the continuum model.

When we take the correlation energy in each layer into account, the structures observed in numerical experiments are reproduced to a good accuracy as shown in Fig. 1 by thin lines. This indicates that the effect of correlation in each shell is of essential importance to make layered structures stable against the state with infinite number of layers (continuum).

Some examples of three-dimensional configuration are shown in Fig. 3. We have bcc, fcc, and hcp-like structures according to values of parameters. In experiments, there often (but not always) appears the structure where particles are aligned in z -direction and it has been argued that the alignment is due to an effective attraction between particles resulting from the ion flow in the sheath. In our numerical experiments with isotropic Yukawa potential, particles in adjacent layers are not aligned, seemingly indicating the role of the anisotropic part of interaction potential.

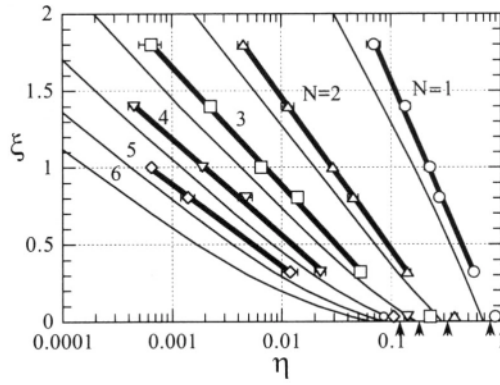


Figure 1. Phase diagram for structure in the ground state. Boundaries determined by our simulation (thick lines with symbols) are compared with our theory (thin lines) and other results for $\xi = 0$ (arrows).

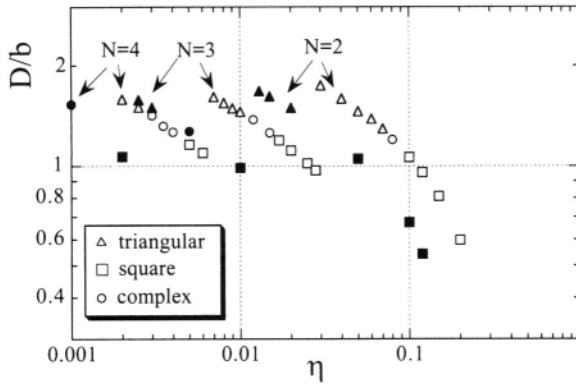


Figure 2. Intralayer symmetry and interlayer distance D for $\xi = 1.0$ (open symbols) and 1.4 (closed symbols), b being mean distance in each layer. Triangles and squares denote triangular and square symmetries, respectively.

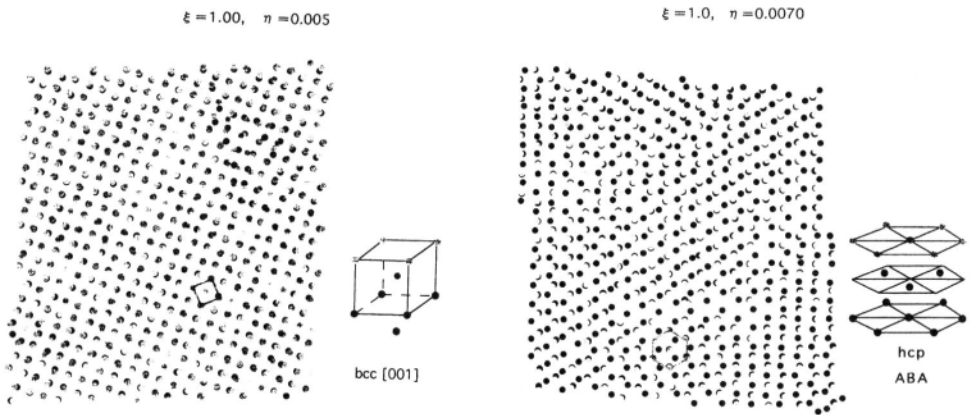


Figure 3. Examples of three-dimensional particle configuration projected onto xy -plane.

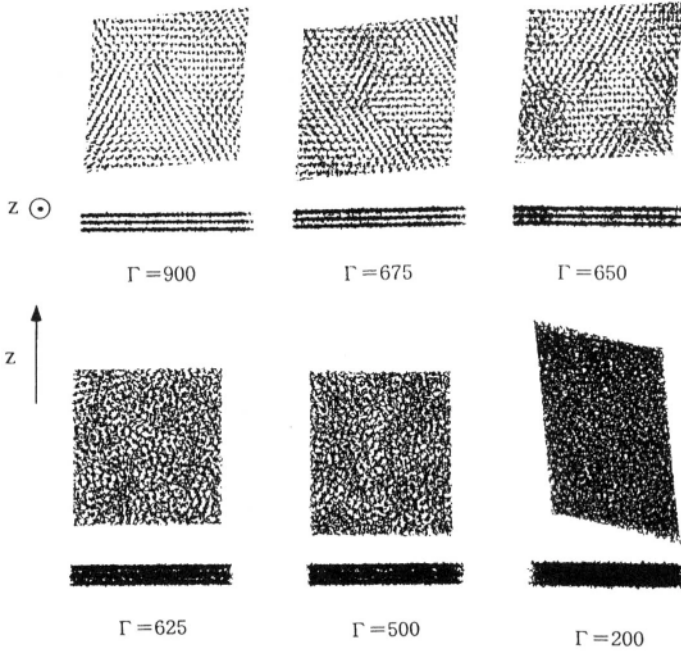


Figure 4. Examples of orbits at various temperatures.

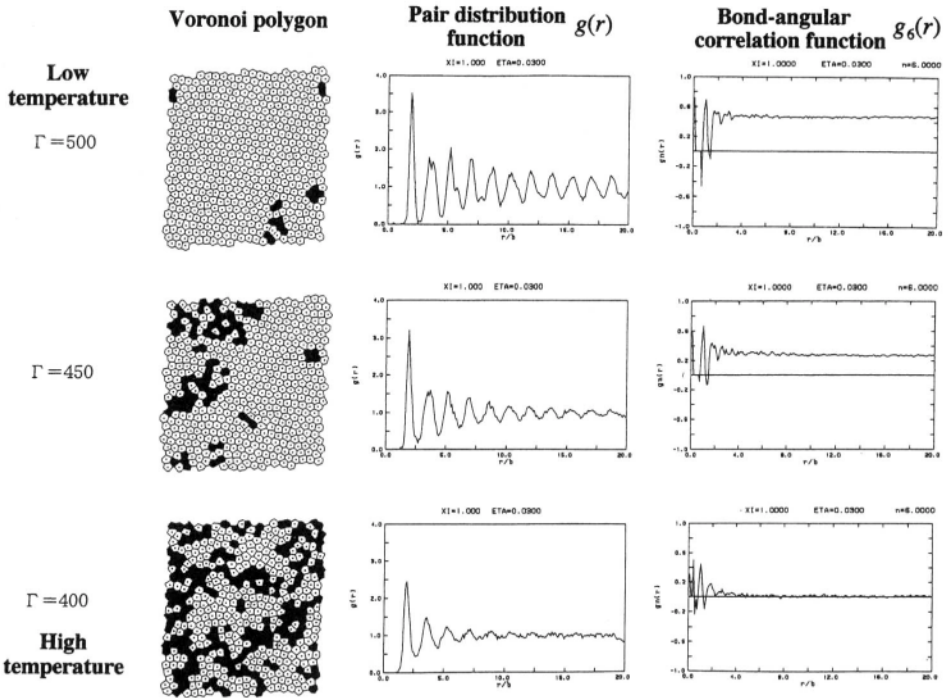


Figure 5. Examples of Voronoi analysis and positional and bond-angular correlation functions. Filled polygons are lattice defects.

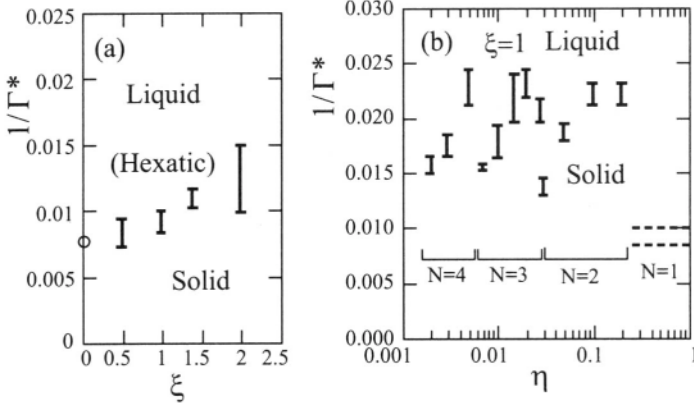


Figure 6. Phase diagram for melting: Two-dimensional Yukawa system (a) and confined Yukawa system with a few layers (b). Ordinate $1/\Gamma^* = 1/\Gamma \exp(-N^{1/2}\xi)$ is proportional to critical temperature and N is number of layers.

MELTING OF CONFINED YUKAWA SYSTEM

With the increase of the temperature, the above structures melt and particles form a thick cloud at high temperatures as shown in Fig. 4. In the ground state, there are two kinds of orders, lattice structures within each layer and layers in z -direction. We observe that these structures are lost in this order: Layered structures survives the melting in each layer and there exists a domain of layered liquid.

Regarding each layer as two-dimensional, we have analyzed the behavior of correlation functions for the positions and bond angles of neighboring particles. Some examples are given in Fig. 5. The melting in two dimensions is characterized by disappearance of quasi-long range positional order and those of long range and quasi-long range bond angle orders. In a theory due to KTHNY, two-dimensional solids melt via two second order transitions.¹³ first, to a phase called hexatic with short-range positional and quasi-long-range orientational orders, and then to liquid where both orders are short-ranged.

We have observed the positional and orientational correlation functions and determined the boundaries of phases by the long-range behavior of the bond angular correlation function: The boundary between solid and hexatic or liquid is drawn at the highest temperature for which the long-range limit of the bond-angular correlation function is finite, and the boundary between liquid and hexatic is drawn at the lowest temperature for which the long-range limit of the bond-angular correlation function is short-ranged. The result is summarized in Figs. 6a and 6b. In the case of one-layer state shown in Fig. 6a, our system is nothing but the two-dimensional Yukawa system. The domains of liquid and solid are determined by the long-range limit of the bond-angular correlation function. In the domain between bars, we may possibly have the hexatic phase. Our phase diagram is also consistent with that of classical electrons in two dimensions shown by a small circle. It is to be noted, however, that the positions of bars could be lower since the long-range limit is taken in our finite system.

For multilayer cases, the phase diagram is shown in Fig. 6b. We observe that, with decreasing η , the critical temperature repeats the changes from higher values just after the appearance of a new layer to lower values just before the appearance of another new layer. These changes are synchronized with those of interlayer distance and we may regard them as the effect of nearby layers: Two-dimensional solid in each layer is stabilized by the existence of neighboring layers and such an effect is stronger when neighboring layers are closer.

CONCLUSION

We have analyzed the Yukawa system confined by external fields. The structure in the ground state is obtained as a phase diagram in the parameter domain and we have reproduced the diagram by taking intralayer correlation energy into account. Ordered structure in each layer melts before the structure in z -direction and critical temperatures of intralayer melting is determined including the case of two-dimensional Yukawa system. It is shown that the critical temperature is enhanced when neighboring layers are closer.

REFERENCES

- [1] H. Thomas, G. E. Morfill, V. Demmel, J. Goree, B. Feuerbacher, and D. Möhlmann, *Phys. Rev. Lett.* **73**, 652(1994).
- [2] J. H. Chu and Lin I, *Physica A* **205**, 183(1994); *Phys. Rev. Lett.* **72**, 4009(1994).
- [3] Y. Hayashi and T. Tachibana, *Jpn. J. Appl. Phys.* **33**, L804(1994).
- [4] A. Melzer, T. Trottenberg, and A. Piel, *Phys. Lett. A* **191**, 301(1994).
- [5] For example, D. H. Van Winkle and C. A. Murray, *Phys. Rev. A* **34**, 562(1986).
- [6] H. Totsuji, T. Kishimoto, Y. Inoue, C. Totsuji, and S. Nara, *Phys. Lett. A* **221**, 215(1996).
- [7] H. Totsuji, T. Kishimoto, and C. Totsuji, *Phys. Rev. Lett.* **78**, 3113(1997).
- [8] H. Totsuji, T. Kishimoto, and C. Totsuji, *Jpn. J. Appl. Phys.* **36**, 4980(1997).
- [9] H. Totsuji, T. Kishimoto, and C. Totsuji, in *Advances in Dusty Plasmas* (eds. P. K. Shukla, D. A. Mendis, and T. Desai, World Scientific, Singapore, 1997).
- [10] For example, M. O. Robbins, K. Kremer, and G. S. Grest, *J. Chem. Phys.* **88**, 3286 (1988) and S. Hamaguchi and R. T. Farouki, *J. Chem. Phys.* **101**, 9876(1994); *ibid.* 9885(1994).
- [11] H. Totsuji and J. -L. Barrat, *Phys. Rev. Lett.* **60**, 2484 (1988).
- [12] H. Totsuji, *Strongly Coupled Plasma Physics* (ed. S. Ichimaru, Elsevier Science Publishers, Amsterdam, 1990), p. 213; *Phys. Rev. E* **47**, 3784(1993).
- [13] For a review, K. J. Strandburg, *Rev. Mod. Phys.* **60**, 161 (1988) and M. A. Glaser and N. A. Clark, *Advances in Chemical Physics LXXXIII* (eds. I. Prigogine and S. A. Rice, John Wiley and Sons, New York 1993), p. 543.

NUMERICAL SIMULATION OF GRAVITOELECTRODYNAMICS IN DUSTY PLASMAS

Lorin Swint Matthews and T. W. Hyde

Space Physics Theory Group
Baylor University
Waco, Texas 76798-7316

INTRODUCTION

Stars, planets, and most other bodies in the universe are presumed to have formed from collections of primordial dust. A necessary part of this formation is the accumulation of microscopic dust into macroscopic bodies. Generally the strongest force acting on dust particles is gravity or radiation pressure; in many cases, however, the dust coexists with a plasma and becomes charged. The magnitude of the electrostatic force between the grains can then exceed the magnitude of the gravitational force for micron-sized dust grains and influence the dynamics of particles up to 1 cm in size. These effects play an important role in many gravitoelectrodynamic phenomena such as the coagulation of grains, the formation of Coulomb lattices, and the perturbation of ring particles from Keplerian orbits.

Several coagulation methods have been investigated recently including studies on coagulation in various astrophysical environments,^{1,2,3} enhanced coagulation due to oppositely charged grains,⁴ and the production of fluffy aggregates during coagulation.⁵ Most of these models fail to incorporate many of the physical parameters important to the coagulation process. In particular, most statistical approaches assume that the result of a collision between two spheres is a spherical particle with mass equal to that of its constituent particles, completely ignoring the three dimensional geometry of the problem. Models that allow fractal aggregates circumvent this, but usually only allow for either particle-cluster aggregation, where a single particle collides with an aggregate, or cluster-cluster aggregation, where two clusters of the same size collide. This is a problem since it is more likely that agglomeration proceeds through the collision of clusters of different size.

The formation of Coulomb lattices in dusty plasmas was first suggested by Ikezi,⁶ predicted in theoretical simulations,⁷ and subsequently observed in laboratory plasmas.⁸ Lattices or “dust crystals” may play a role in the stability of tenuous rings or aid in explaining the contradiction between the observed and theoretical particle sizes in Uranus’ ϵ -ring. This study addresses several of these problems by employing a numerical simulation for the charged dust cloud which allows the consequent coagulation or equilibrium positions of the grains to be explicitly followed. The model also allows for a full treatment of rigid body dynamics, including rotation, enabling cluster trajectories and the orientation of fractal aggregates to be tracked.

EQUILIBRIUM OF CHARGED DUST GRAINS

Dust grains usually exist in a radiative and plasma environment and the grains therefore become charged. For isolated grains, the equilibrium potential on each grain is found by

summing the charging currents to the grains. When the net charging current is zero (considering only the electron and ion flux) the equilibrium potential is $\phi \approx -2.5 (kT/e)$.⁹ The charge is related to the grain potential via the capacitance for isolated, spherical grains, $Q = 4\pi a^2 \epsilon_0 \phi/a$, where a is the radius of the grain. Thus, the majority of the grains in the dust cloud will be negatively charged which may reduce or even prohibit coagulation since the grains must then have relative velocities great enough to overcome the subsequent Coulomb repulsion barrier in order for them to collide and stick. Inclusion of the secondary electron current produces multiple solutions for the potential and grains may become charged either positively or negatively.¹⁰ Additionally, changes in the grain environment, such as temperature fluctuations, can also induce a variation in grain charge. This premise was utilized by Horányi and Goertz⁴ to demonstrate that a dust population with variations in size can produce oppositely charged grains for a plasma temperature that oscillated about 1 eV, which in turn could lead to enhanced coagulation. However, plasma temperatures in this range are unlikely to exist for extended periods in astrophysical environments and differential charging is likely to occur only for transient heating events. Work by Chow et al.¹¹ has shown that secondary electron emission can lead to differentially charged grains due simply to the size distribution of the dust, obviating the need for evolving plasma parameters. In some environments, photoemission also plays a large role in grain charging and may lead to oppositely charged grains for particles with the same size but differing photoemission yields.¹² High densities of charged dust can also lead to interesting equilibrium conditions. When the ratio of the thermal kinetic energy of the particles to the electrostatic interaction energy between the grains, $\Gamma = q^2/bT$, exceeds a critical value, $\Gamma_c \approx 170$, a coulomb lattice is formed. (Here q is the charge on the dust grains, b is the interparticle spacing, and T is the temperature.) The plasma will shield the field of the particles requiring Debye-shielding to be incorporated using a shielded coulomb potential $\Gamma_s = q^2 \exp(-b/\lambda_D)/bT$. Coulomb solidification is expected in a laboratory plasma when $\Gamma_s > \Gamma_c$.

NUMERICAL MODEL

To investigate the effects of coagulation and coulomb coupling in dusty plasmas, a computer model for the collisional behavior and coagulation mechanisms of a large number of micron sized dust grains is needed. The model for this study is a modification of the Box_Tree code developed by Richardson.^{13,14} The Box_Tree model is a hybrid of two computer algorithms: a tree code¹⁵ and a box code.¹⁶ The box code specifies a coordinate system, the linearized equations of motion, and a prescription for handling boundary conditions. The tree code provides the means for a fast calculation of interparticle forces which can then be included as perturbations to the equations of motion. The box code has previously been used to model ring systems by first dividing the ring into self-similar patches or boxes orbiting the planet, where the box size is much greater than the radial mean excursions of the constituent particles. This allows the boxes to be dynamically independent with more distant regions of the ring being represented by copies of the simulated region. Thus a large N system can be modeled by a small N system with boundary conditions being met using ghost boxes. An N-body simulation normally requires CPU time that scales as $O(N^2)$. This rapidly makes direct numerical simulations of systems with large N unreasonable. The tree code is a hierarchical algorithm that reduces the CPU expense to $O(N \log N)$ for sufficiently large N. The idea is to place particles into a tree-like hierarchy of boxes. The force due to particles in a box small enough or far enough away from a test particle may then be calculated by a multipole expansion about the center of mass of the box. In addition to self-gravitational forces, the electrostatic forces between grains must also be calculated. A tree code lends itself to the calculation of the electrostatic forces between particles since the dust cloud in a plasma is charged to a non-zero potential. An option has been added to the code for including electrostatic forces with or without debye shielding.

RESULTS

Initial simulations indicate that fractal agglomeration significantly increases the amount of coagulation in a given system (Figures 1a, c). Oppositely charged particles will produce larger aggregates than gravitational interactions alone (Figure 1b), while like charged particles

reduce the average size of the aggregates. These results require further analysis, however, since this preliminary model does not take into account several of the important physical properties of charged aggregates. Arguably the most important of these is that currently charge is assumed to reside at the center of the aggregate. In a more realistic charging model, charge would migrate toward fractal extremities. The stress on the aggregate due to the resulting electric fields could be sufficient to exceed the tensile strength of the bonds between the individual particles comprising the aggregate and thus cause a disruption of the extremities. However, the resulting fractal “debris” could in turn recombine with the aggregate in such a way as to produce a denser, more compact aggregate with a more stable charge configuration.

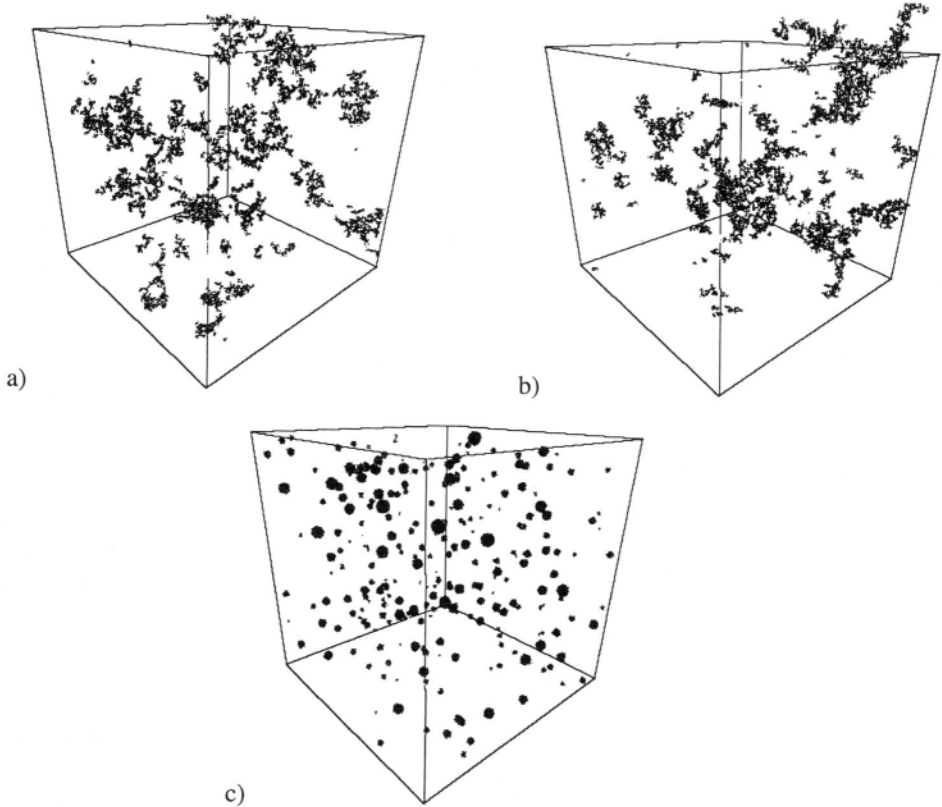


Figure 1. Coagulation of 5600 dust particles in a dusty plasma, showing effects of charged vs. uncharged grains and fractal agglomeration vs. simple collisions after 6500s. The box is 900μ on a side and the grains range in size from 1 to 6μ . a) Particles influenced only by self-gravity undergoing fractal agglomeration. Seventy-one aggregates formed with the largest containing 7.5% of the total mass. b) Fractal agglomeration of oppositely charged particles. Sixty-six aggregates with the largest containing 30% of total mass. c) Coagulation of charged particles allowing only spherical particles as a result of collisions. Total of 314 particles with the largest containing 2.7% of the total mass.

Coulomb solidification was observed in the dust for the parameters used experimentally by Thomas, et al⁸. The “dust crystal” contained 724 particles in a box 7.7 mm on a side. The particles ranged in size from $6.8-7.2 \mu$ and had a density of 1.514 g/cc. The charge on the dust grains was $(1.2 \pm 0.4) \times 10^4 e$, and the debye length $\lambda_d \approx 60\mu\text{m}$. The dust grains were given an initial random distribution and with Brownian velocities and allowed to reach equilibrium. A Voronoi analysis of the dust grain equilibrium positions showed the grains occupying mainly six-sided cells with uniform spacing (Figure 2).

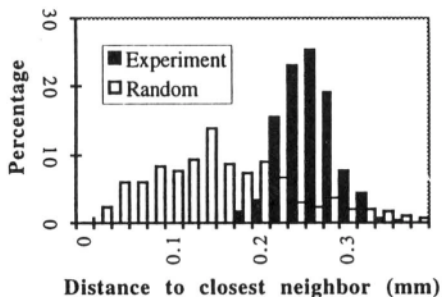
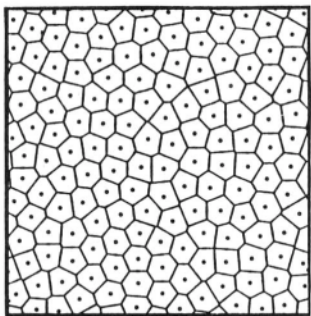


Figure 2. Detail of Voronoi analysis of positions of dust particles. The cells are mostly six-sided with equal spacing between particles. Analysis of nearest neighbor distances shows that the interparticle spacing is peaked at 0.26 mm. Nearest neighbor distances for a random distribution of particles (white columns) is shown for comparison.

CONCLUSIONS

Fractal agglomeration appears to lead to enhanced coagulation over coagulation methods which only allow the participants and products of collisions to be spherical. It also has the added benefit of being a more realistic approach. The consequences of more realistic charging and charge distribution algorithms for the fractal are the topic of ongoing research.

ACKNOWLEDGMENTS

This material is based upon work supported under a National Science Foundation Graduate Research Fellowship, an NSF grant, a NASA/Texas Space Grant Consortium Fellowship, and the Baylor University Research Committee.

REFERENCES

1. H. Mizuno, *Icarus* 80:189 (1989).
2. M.F. Sterzik and G.E. Morfill, *Icarus* 111:536 (1994).
3. S.J. Weidenschilling and T.V. Ruzmaikina, *Ap. J.* 430:713 (1994).
4. M. Horányi and C.K. Goertz, *Ap. J.* 361:155 (1990).
5. V. Ossenkopf, *Astron. Astrophys.* 280(2):617 (1993).
6. H. Ikezi, *Phys. Fluids* 29(6):1764 (1986).
7. T.W. Hyde and W.M. Richter, *Adv. Space Res.* 13:179 (1993).
8. H. Thomas, G.E. Morfill, V. Demmel, J. Goree, B. Feuerbacher, and D. Mohlmann *Phys. Rev. Lett.* 73:652 (1994).
9. L. Spitzer. *Physical Processes in the Interstellar Medium*, John Wiley, New York (1978).
10. N. Meyer-Vernet, *Astron. Astrophys.* 105:98 (1982).
11. V.W. Chow, D.A. Mendis, and M. Rosenberg, *J. Geophys. Res.* 98(A11):19,065 (1993)
12. B. Feuerbacher, R.F. Willis, and B. Fitton, *Ap. J.* 181:102 (1973).
13. D.C. Richardson, *MNRAS* 269:493 (1994).
14. D.C. Richardson, *Icarus* 115:320 (1995).
15. J. Barnes and P. Hut, *Nat.* 324:446 (1986).
16. J. Wisdom, and S. Tremaine, *Astron. J.* 95(3):925 (1988).

RELAXATION OF DUSTY PLASMAS

Yuriy I. Chutov,¹ Olexandr Yu. Kravchenko,¹ Roman D. Smirnov,¹
and Pieter P. J. M. Schram²

¹Faculty of Radio Physics, Taras Shevchenko Kiev University,
Volodymyrs'ka Str. 64, 252017 Kiev, Ukraine

²Department of Physics, Eindhoven University of Technology, The
Netherlands

INTRODUCTION

Relaxation phenomena accompany any change of plasma parameters caused by various plasma processes, for example by strong plasma oscillations or waves. The relaxation phenomena can include various elementary processes, for example an ionization, an excitation, and a deexcitation of atoms and molecules as well as a recombination of electrons and ions. These phenomena can include also various transport processes, for example a diffusion, thermal and electrical conductivity, as well as other collision processes. Relaxations can be caused also by some collisionless evolution of self-consistent electric and magnetic fields. Therefore relaxation phenomena can be very various even in plasmas without dust particles.

However in cases of dusty plasmas, some new relaxation process takes place, namely: a collection of electrons and ions by dust particles. This collection strongly depends from an energy of electrons and ions therefore there is a possibility of new relaxation phenomena, for example due to an possible influence of this collection on electron and ion energy distribution functions¹⁻⁴. Of course, these new relaxation phenomena can be accompanied by other various processes, for example various collisions, which have to be taken into account in general cases. However a relaxation due to a collection of electrons and ions is interesting without other processes especially in cases of a mutual influence of dust particles which takes place in dusty crystals. Therefore the main aim of this work is a study of these relaxation phenomena in some dust crystals where this mutual influence is strong.

MODEL

Some 2D crystal initially consisting of motionless neutral dust particles of the radius R_d and background equilibrium electrons and ions with initial densities n_o and temperatures T_{eo} and T_{io} is considered. Dust particles are divided by some distance d which is counted out centers of these particles. Relaxation phenomena start after a start of an interaction of electrons and ions with dust particles (collection and collisions). Collisions between

electrons and ions are not taking into account, because the relaxation time is less than the electron-ion collision time owing to the choice of plasma parameters.

Of course, there is some square crystal cell around each dust particle. A periodic structure of the crystal gives on boundaries of this cell some periodic boundary conditions which provides an equality of all parameters in corresponding points of these boundaries.

The modified 2D PIC method⁵ is used for a modeling of relaxation phenomena. A crystal cell around some dust particle is divided by square simulation cells where electrons and ions are presented by large macroelectrons and macroions of a corresponding square cross-section. These microparticles are collected by a dust particle if their trajectories cross a surface of this dust particle. Macroparticles are reflected from boundaries that is a result of an influence of neighbour crystal cells. The Poisson's equation is solved using the Fourier transform method with periodic boundary conditions.

RESULTS

Typical results are shown in Fig. 1-4 for a dust crystal with $R_d = 0.2$, $d = 1$, $(T_{eo} / T_{io}) = 10$ where spatial coordinates and all line sizes are divided by an initial Debye length, and a time t is multiplied by a initial ion plasma frequency.

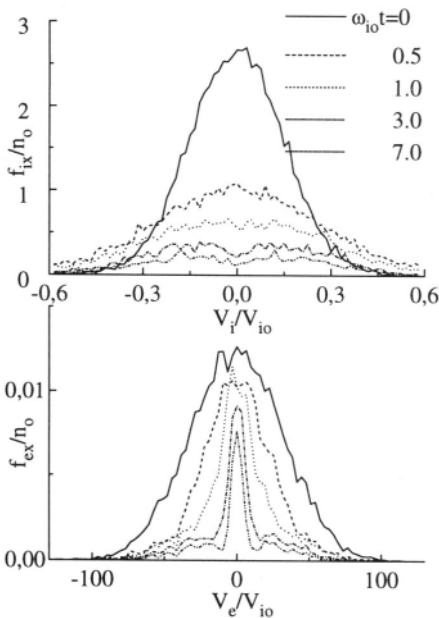


Figure 1. Mean X-components of electron f_{ex} and ion f_{ix} velocity distribution functions for various times t after a relaxation start. Here and then ω_{io} is the initial ion plasma frequency, $V_{io} = (kT_{io} / M)^{1/2}$ is the initial mean ion velocity

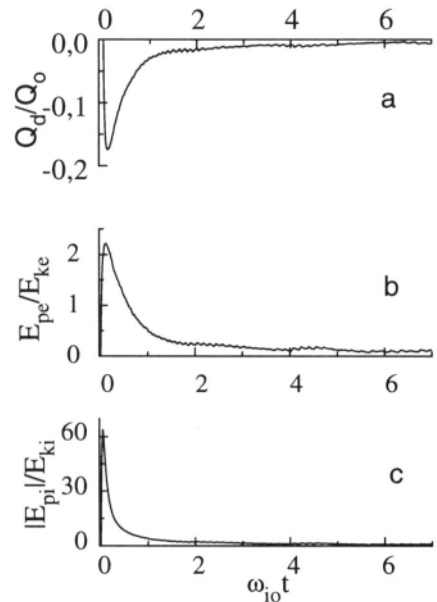


Figure 2. An evolution of a dust particle charge Q_d (a) and relations of mean potential E_p and kinetic E_k energies of electrons (b) and ions (c). Here Q_o is an initial ion charge in the Debye cube.

Of course, obtained results show a monotonous decrease of the total number of electrons and ions in a crystal cell due to their collection by the corresponding dust particle. However this decrease is accompanied by an essential change of electron and ion velocity distribution functions. Mean X-components of these functions are plotted for various times

t after a relaxation start in Fig. 1 where ω_{i0} is the initial ion plasma frequency. Y-components were identical.

As can be seen from Fig. 1, an electron velocity distribution function f_e is impoverished by fast electrons during a relaxation in contra to an ion velocity distribution function f_i which is impoverished by slow ions. This evolution is a result of a collection of electrons and ions by a dust particle with a negative charge Q_d like^{1,2}. An evolution of this charge is shown in Fig. 2a where Q_d is divided by an initial ion charge Q_o in the Debye cube.

The plasma relaxation is accompanied by a change of mean potential E_p and kinetic E_k energies of electrons and ions. A time evolution of relations of these energies E_p / E_k are shown in Fig. 2b and Fig. 2c for electrons and ions, respectively. As can be seen from these figures, these relations grow quickly after the relaxation start and are essentially more one during some time. It means that electrons and ions are non-ideal components of relaxing dusty plasmas during this time although their initial number in the Debye cube is essentially more one and these electrons and ions have to be an ideal gas without dust particles.

This non-ideality of electrons and ions is caused by a change of self-consistent potential ϕ distributions in a crystal cell due to a charging of a dust particle and a corresponding change of spatial distributions of background electrons and ions. Spatial distributions of the potential ϕ and a electric charge $\rho = \rho_i - \rho_e$ are shown in Fig. 3 and Fig. 4 for various times t after a relaxation start, respectively. The potential ϕ and the electric charge $\rho = \rho_i - \rho_e$ are divided by kT_{e0} / e and an initial spatial ion charge ρ_{i0} , respectively.

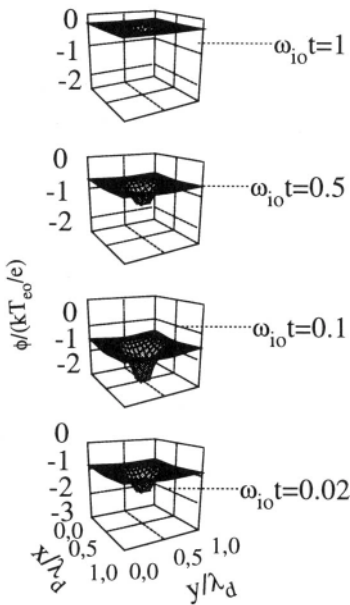


Figure 3. Spatial distributions of the potential ϕ for various times t after a relaxation start. Here a potential ϕ is divided by kT_{e0} / e where T_{e0} is an initial electron temperature.

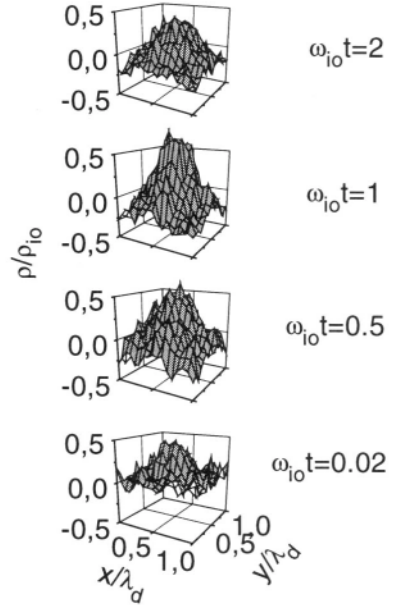


Figure 4. Spatial distributions of a electric charge $\rho = \rho_i - \rho_e$ for various times t after a relaxation start. Here ρ_{i0} is an initial spatial ion charge.

As can be seen from Fig.3, the potential ϕ is negative in all points of this cell including its boundaries due to an influence of neighbour cells during a relaxation. Note that this potential is equal zero in all points before a relaxation due to a plasma quasineutrality and neutral dust particles.

Corresponding spatial distributions of an electric charge $\rho = \rho_i - \rho_e$ (Fig. 4) show a sandwich structure. Slow electrons are concentrated close to boundaries of a crystal cell according to spatial distributions of a self-consistent electric potential. Of course, positive ions are concentrated close to a negative charged dust particle due to a previous reason. These spatial distributions show a non-trivial shielding of an electric potential in relaxing plasmas with dust particles due to a selective collection of electrons and ions by dust particles.

CONCLUSION

Computer modelling of relaxation phenomena in dusty plasmas shows a essential influence of a collection of electrons and ions by dust particles on these phenomena. Electrons and ions are non-ideal components of relaxing dusty plasmas due to a self-consistent electric potential caused by a mutual influence of dust particles even in the case if an initial number of electrons and ions is essentially more one. Besides, electron and ion velocity distribution functions are strongly non-equilibrium in such plasmas due to a selective collection of electrons and ions by dust particles. Spatial distributions of electrons and ions around dust particles are strongly non-uniform so that some sandwich structure of a space electric charge.

ACKNOWLEDGMENT

This work was partially supported by INTAS in the framework of contract No 96-0617 and by a grant from the Ukrainian Committee of Science and Technology.

REFERENCES

1. Yu. I. Chutov, A. Yu. Kravchenko and P. Schram, Expansion of a bounded plasma with dust particles, *J. Plasma Physics*. 55, part 1:87 (1996).
2. Yu. I. Chutov, A. Yu. Kravchenko and P. Schram, Evolution of an expanding plasma with dust particles, *Physica*. B 128:11 (1996).
3. O. G. Sytenko, A. G. Zagorodny, Yu. I. Chutov, P. Schram and V. N. Tsytovich, Statistical properties and relaxation of dusty plasmas, *Plasma Physics and Controlled Fusion*. 38:A 105 (1996).
4. Yu. I. Chutov. Invited talks of the Fifth Symposium on Double Layers - Potential Formation and Related Nonlinear Phenomena in Plasmas, September 17-19, 1996, Sendai, Japan. Abstracts of PFNL'96, p.71
5. C. K. Birdsall and A. B. Langdon. "Plasma Physics via Computer Simulation," McGraw-Hill, New York (1985)

TRANSITION FROM 3-DIMENSIONAL COULOMB CRYSTALS TO A 2-DIMENSIONAL ONE IN A DUSTY PLASMA

Yasuaki Hayashi

Department of Electronics and Information Science,
Kyoto Institute of Technology
Matsugasaki, Kyoto 606, Japan
e-mail: hayashi@dj.kit.ac.jp

INTRODUCTION

The theoretical prediction of the formation of a Coulomb crystal in a dusty plasma¹ has been verified by the experiments in glow discharge plasmas containing carbon particles²⁻⁵, silicon-dioxide particles⁶, and melamine resin particles⁷ of microns in diameter. The structures of the crystals were simple hexagonal, body-centered cubic (BCC), face-centered cubic (FCC), and so on. A simple hexagonal crystal was observed with their (0001) planes parallel to electrodes. Therefore particles are vertically aligned for the crystal, i. e., form a 2-dimensional structure. On the other hand, (110) planes for the BCC-like structure and (111) planes for the FCC structure, parallel to electrodes, were observed. In these crystals, particles are alternately arranged in the vertical direction and form 3-dimensional crystals. We have shown with the help of in-situ monitoring of Mie-scattering ellipsometry^{8,9} that 3-dimensional crystals are formed by smaller particles while the 2-dimensional one by larger particles. In this paper, the transition of structure of Coulomb crystals in relation to the forces acting on particles will be discussed.

EXPERIMENTAL

Coulomb crystals composed of spherical monodisperse carbon particles, which were synthesized by coating of hydrogenated amorphous carbon films on the seeds of ultra-fine particles, were formed in a 20% methane/helium RF plasma generated between two parallel plates set horizontally. The gas was introduced into the reactor under a controlled gas flow so as not to blow away particles trapped in the plasma. The time evolutions of size and density of particles at the sheath-plasma boundary near a lower grounded electrode during the growth were obtained by Mie-scattering ellipsometry. The particle arrangement of top and side views in Coulomb crystals was observed by the scattered light of an argon-ion laser with a CCD video camera.

RESULTS AND DISCUSSIONS

Particle density first increased because growing particles were transferred from the upper sheath-plasma boundary to a measurement position by gravity, and then decreased. The decreasing rate changed by four stages, i. e., fast, slow, fast, and slow in this sequence. The top views of particle arrangement were disordered during the fast decreasing periods, while ordered during the slow periods. Being taken into consideration of cohesive forces in solid, it can be supported that the particle arrangement was in the liquid phase during the first and third periods and in the solid or the hexatic phase during the second and fourth periods.

The crystal structures during the second period were body-centered-cubic-like (BCC-like) or face-centered cubic (FCC). The structure during the fourth period was simple hexagonal. Figure 1(a) shows a top view of particle arrangement in the two lowest layers during the second stage, (110) planes of a BCC-like structure. In the image, particles are alternately arranged in the two layers. The average distance between two adjacent particles in the same layer is laterally $110\ \mu\text{m}$ and lengthwise $69\ \mu\text{m}$. The ratio of the lateral distance to the lengthwise one is not the value for the BCC structure, 1.4 but 1.6. Figure 1(b) shows a top view during the fourth stage, (0001) planes of a simple hexagonal structure. In the latter image particles are piled up in the perpendicular direction to (0001) planes.

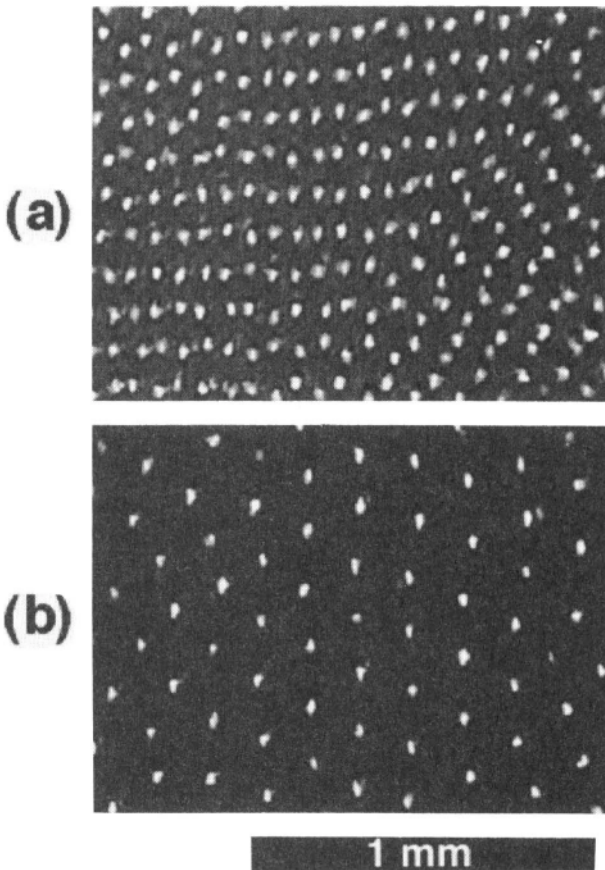


Fig.1 Top views of particle arrangement in the two lowest layers for (a) a 3-dimensional Coulomb crystal and (b) a 2-dimensional Coulomb crystal.

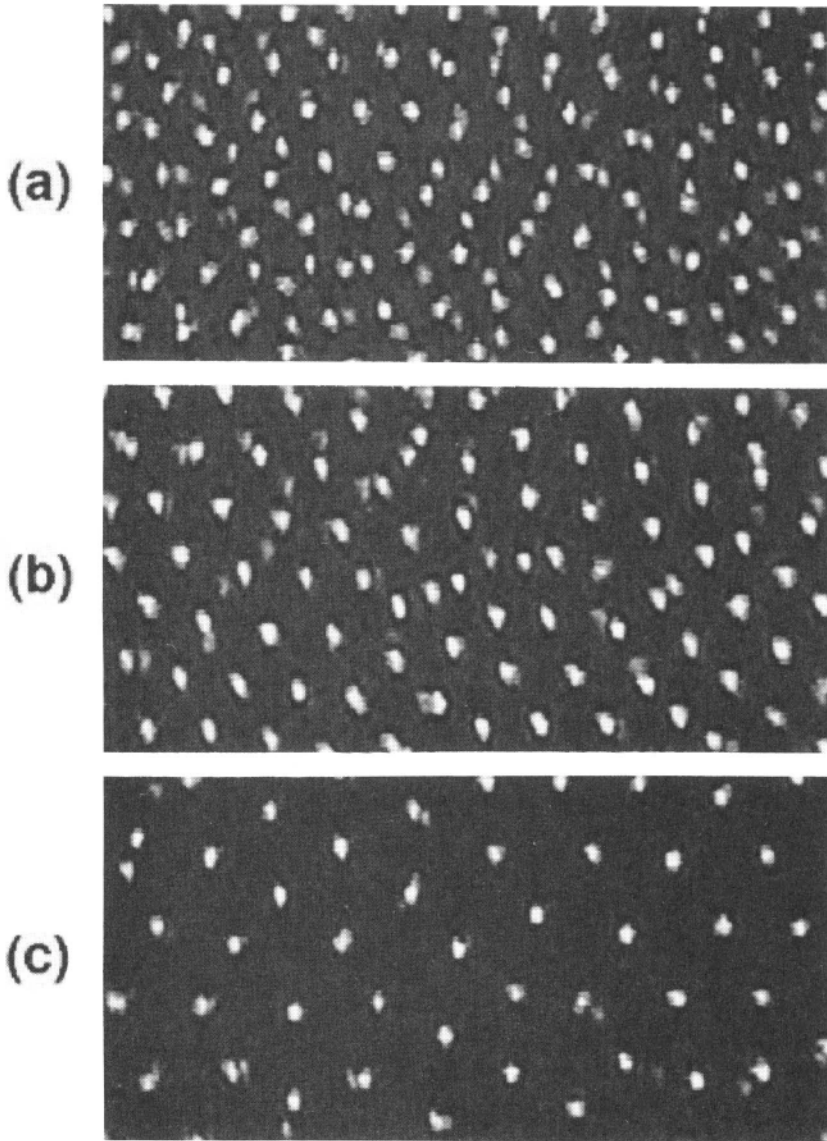


Fig.2 Time evolution of particle arrangement in the two lowest layers. The determined particle diameter was (a) $1.5 \mu\text{m}$, (b) $1.7 \mu\text{m}$, and (c) $1.9 \mu\text{m}$.

Figure 2 shows the time evolution of particle arrangement in the two lowest layers during the third stage when the particle diameter and density determined by the Mie-scattering ellipsometry were $1.5 \mu\text{m}$ and $4 \times 10^5 \text{ cm}^{-3}$ for (a), $1.7 \mu\text{m}$ and $3 \times 10^5 \text{ cm}^{-3}$ for (b), and $1.9 \mu\text{m}$ and $2 \times 10^5 \text{ cm}^{-3}$ for (c). It is seen in the images that the particles in the second lowest layer, which are indicated by dimmed spots, gradually approach the horizontal positions of the particles in the lowest layer, which are indicated by bright spots. Particle charges were estimated, with plasma parameter values measured in a pure helium plasma under the same conditions, to be $3100e$ for (a), $3700e$ for (b), and $4500e$ for (c) in Fig.2.

The gravity for carbon particles of 1.5 μm , 1.7 μm , and 1.9 μm in diameter are $3.9 \times 10^{-14}\text{N}$, $5.7 \times 10^{-14}\text{N}$, and $7.9 \times 10^{-14}\text{N}$ respectively. The estimated strength of an ion-drag or an electrostatic force under the conditions is larger than those values.

It is suggested that the crystals in the second stage were formed mainly by the three-dimensional Coulomb repulsive force, while the crystal formation in the fourth stage was affected by the two-dimensional Coulomb force aligning particles in the perpendicular direction to the electrodes. Forces acting on particles are able to be supposed to be isotropic in a plane parallel to the electrodes but perpendicularly directional due to the electrode arrangement. The directional forces, like an ion-drag or an electrostatic one, affect the formation of layered structure parallel to the electrode¹⁰ not only for a 2-dimensional crystal but also for 3-dimensional crystals. The effect was also observed for 3-dimensional structures in the reconstruction of particle arrangement from FCC to BCC-like: the ratio of the lateral distance to the lengthwise one in the BCC-like structure in Fig.1(a) is close to the value of minimum Coulomb potential energy, 1.6 calculated for the ratio of the Wigner-Seitz radius to the Debye length of 3 and the constant particle density in layers¹¹. In the two-dimensional Coulomb crystal, a force attractive in a far region but repulsive in a close region might exist between particles in the perpendicular direction. It is suggested that the force is caused by the interaction of dipoles, which result from the negatively charged particles and the surrounding positive ions or by the wake potential due to an ion flow to an electrode¹².

REFERENCES

1. H. Ikezi, *Phys. Fluids* **29** (1986) 1764.
2. Y. Hayashi and K. Tachibana, *Japan. J. Appl. Phys.* **33** (1994) L804.
3. Y. Hayashi and K. Tachibana, *J. Vac. Sci. Technol. A* **14** (1996) 506.
4. Y. Hayashi, K. Takahashi, and K. Tachibana, *Advances in Dusty Plasmas* (World Scientific, Singapore, 1997) in press.
5. Y. Hayashi and K. Takahashi, *Japan. J. Appl. Phys.* **36** (1997) 4976.
6. J. H. Chu and Lin I, *Phys. Rev. Lett.* **72** (1994) 4009.
7. H. Thomas, G. E. Morfill, V. Demmel, J. Goree, B. Feuerbacher, and D. Mohlmann, *Phys. Rev. Lett.* **73** (1994) 652.
8. Y. Hayashi and K. Tachibana, *Japan. J. Appl. Phys.* **33** (1994) L476.
9. Y. Hayashi and K. Tachibana, *Japan. J. Appl. Phys.* **33** (1994) 4208.
10. H. Totsuji, T. Kishimoto, and C. Totsuji, *Phys. Rev. Lett.* **78** (1997) 3113.
11. Y. Hayashi, unpublished.
12. M. Nambu, S. V. Vladimirov, and P. K. Shukla, *Phys. Lett. A* **203** (1995) 40.

COLLECTIVE MODES IN STRONGLY COUPLED DUSTY PLASMAS

P. K. Kaw and A. Sen

Institute for Plasma Research
Bhat, Gandhinagar 382 428, India

INTRODUCTION

A dusty plasma is a classical Coulomb system consisting of electrons, ions and highly charged massive dust grains. Such a system can readily go into the strongly coupled regime, because, for the charged dust component the parameter $\Gamma = (Z_d e)^2 / a T_d$ can easily be of order 1 or larger ($Z_d e$ is the charge on the dust grain, a is the intergrain distance and T_d is the dust temperature). This was first pointed out by Ikezi¹ and many recent laboratory experiments²⁻⁴ have vindicated this prediction. It is therefore of considerable interest to investigate the question of collective excitations in such strongly coupled systems and to develop appropriate theoretical descriptions of wave propagation in this regime. In this paper we carry out such an analysis for extremely low frequency modes in a strongly coupled dusty plasma by using the generalized hydrodynamic description. We find that for the longitudinal dust acoustic wave⁵⁻¹³ strong correlations introduce new dispersive corrections, an overall reduction in frequency and the existence of regions where $\partial\omega/\partial k < 0$. We also find that a novel transverse shear like mode can propagate in this regime.

MODEL EQUATIONS AND DISPERSION RELATIONS

We assume the electrons and ions to be in the weakly coupled regime and to have a Boltzman distribution ($\delta n_{e,i} = n_{0e,0i} \exp(\mp e\phi/T_{e,i})$). The weak coupling assumption is justified because when the Γ for dust is large the corresponding coupling parameter for the electrons and ions can still be small due to their higher temperatures and smaller electric charges. For the strongly coupled dust dynamics we adopt the generalized hydrodynamics model which provides a simple physical picture of the effects of strong correlations through the introduction of viscoelastic coefficients.¹⁴⁻¹⁷ This phenomenological model is generally valid over a large range of the coupling parameter Γ , all the way from the weakly coupled gaseous phase ($\Gamma \ll 1$) to the strongly coupled liquid state ($1 \ll \Gamma < \Gamma_c$) and may even be used in the supercooled regime (beyond the critical Γ_c for crystallization) as long as the plasma retains its fluid characteristics. The linearized GH equations are given as [16]

$$\frac{\partial}{\partial t} \delta n_d(\mathbf{r}, t) + n_{0d} \nabla \cdot \delta \mathbf{u}_d(\mathbf{r}, t) = 0 \quad (1)$$

$$M_d n_{0d} \frac{\partial}{\partial t} \delta \mathbf{u}_d(\mathbf{r}, t) = -\nabla \Pi(\mathbf{r}, t) \quad (2)$$

$$(1 + \tau_m \frac{\partial}{\partial t}) [\nabla \Pi(\mathbf{r}, t) - \nabla P(\mathbf{r}, t) + Z_d e n_{0d} \mathbf{E}(\mathbf{r}, t)] = -\eta \nabla \cdot \nabla \delta \mathbf{u}_d(\mathbf{r}, t) - \left(\zeta + \frac{\eta}{3} \right) \nabla (\nabla \cdot \delta \mathbf{u}_d(\mathbf{r}, t)) \quad (3)$$

where $\tau_m = (\frac{4}{3}\eta + \zeta)/(T_{0d}n_{0d}(1 - \gamma_d\mu_d) + \frac{4}{15}u(\Gamma))$ is the viscoelastic relaxation time, η, ζ are the coefficients for the shear viscosity and the bulk viscosity respectively, γ_d is the adiabatic index, $\mu_d = (1/T_{0d})(\partial P/\partial n)_T = 1 + u(\Gamma)$ is the compressibility, $u(\Gamma) = E_c/T_{0d}n_{0d}$ is the so called the excess internal energy, E_c is the correlation energy and other notations are standard. The quantity $u(\Gamma)$ is usually calculated from simulations or statistical schemes and expressed in terms of an analytically fitted formula. Typically, for weakly coupled plasmas ($\Gamma < 1$), $u(\Gamma) \approx -\frac{\sqrt{3}}{15}\Gamma^{3/2}$. In the range of $1 \leq \Gamma \leq 200$, Slattery *et al*¹⁸ have given the relation, $u(\Gamma) = -0.89\Gamma + 0.95\Gamma^{1/4} + 0.19\Gamma^{-1/4} - 0.81$ where we omit a small correction term due to finite N (number of particles). The dependence of the other transport coefficients e.g., η, ζ on Γ are somewhat more complex and are available as tabulated results derived from MD simulations and a variety of statistical schemes.¹⁶ Finally, we note that the plasma equations need to be closed by the full set of Maxwell's equations for the field quantities and the equilibrium charge neutrality condition, $Z_d n_{0d} = n_{0i} - n_{0e}$.

For longitudinal low frequency waves ($\omega \ll kv_{Te}, kv_{Ti}$), the linear dielectric response of the electrons and ions (which obey the Boltzmann law) can be simply expressed in terms of the susceptibilities, $\chi_{i,e} = 1/k^2\lambda_{i,e}^2$, where $\lambda_{i,e}$ denote the Debye lengths for the ion and electron species respectively. The corresponding susceptibility function for the dust component can be obtained by Fourier transforming Eqs. (1)–(3) in time and space. Carrying this out and introducing the dimensionless quantities, $\omega = \omega/\omega_{pd}$, $k = ka$, $\tau_m = \tau_m\omega_{pd}$, $\lambda_{e,i,d} = \lambda_{e,i,d}/a$, $\eta^* = (\frac{4}{3}\eta + \zeta)/(M_{0d}n_{0d}\omega_p a^2)$, $\lambda_p^{-2} = \lambda_e^{-2} + \lambda_i^{-2}$ (where $a = (4\pi n_{0d}/3)^{-1/3}$ is the Wigner–Seitz radius), the low frequency dispersion relation for the correlated dusty plasma can be written down as,

$$1 + \frac{1}{k^2\lambda_p^2} - \frac{1}{\omega^2 - \gamma_d\mu_d k^2\lambda_d^2 + i\omega k^2 \frac{\eta^*}{1 - i\omega\tau_m}} = 0 \quad (4)$$

We solve this dispersion relation in two limits, namely, for $\omega \ll 1/\tau_m$ (hydrodynamic regime) and for $\omega \gg 1/\tau_m$.

For $\omega\tau_m \ll 1$ the dispersion relation (4) simplifies to, $\omega^2 = k^2(\gamma_d\mu_d\lambda_d^2 + \lambda_p^2/(1 + k^2\lambda_p^2)) - i\omega\eta^*k^2$ which can be readily solved to give,

$$\omega_R = \pm \frac{k\lambda_p}{\sqrt{1 + k^2\lambda_p^2}} \left[1 + \frac{\lambda_d^2\gamma_d\mu_d - (k\eta^*/2)^2}{\lambda_p^2} (1 + k^2\lambda_p^2) \right]^{1/2}, \quad \omega_I = -\frac{k^2\eta^*}{2} \quad (5)$$

For ($\eta^* = \mu_d = 0$), Eq. (5) describes the usual undamped dust acoustic mode in a weakly correlated plasma. In the presence of correlations ($\eta^* \neq \mu_d \neq 0$), we see that this mode changes its phase velocity through μ_d terms, gets additional dispersive corrections through η^* terms and also suffers a damping proportional to the viscosity η^* with the damping rate being given by ω_I . In the weak coupling limit ($\Gamma \ll 1$), η^* reduces to the standard Navier–Stokes viscosity coefficient arising from collisional damping of the dust species and is inversely proportional to the dust dust collision frequency. Thus the damping decrement has a $\Gamma^{-3/2}$ dependence in the weakly coupled regime. MD simulations confirm

this behavior of η^* which continues to decrease as a function of Γ and displays a broad minimum in the region of $1 < \Gamma < 10$ after which it begins to rise again.¹⁶ Very close to the crystallization point (near $\Gamma = \Gamma_c$) there is a sharp and very large rise in η^* which is attributed to a change in the momentum transfer mechanism in the presence of short range order.¹⁹ Turning now to the changes in the phase velocity, we note that in the range $1 < \Gamma < 10$, the μ_d corrections can change sign (since $u(\Gamma)$ is a negative quantity that increases with Γ). This has the interesting consequence that the dust acoustic dispersion curve can turn over with the group velocity going to zero and then to negative values. Typically this turnover happens for $\Gamma \sim 3.5$.

In the limit $\omega\tau_m \gg 1$ (sometimes called the kinetic regime) the dispersion relation simplifies to $\omega^2 = k^2(\gamma_d\mu_d\lambda_d^2 + (\eta^*/\tau_m) + \lambda_p^2/(1+k^2\lambda_p^2))$. Substituting for η^* and τ_m this further gives,

$$\omega = \pm k \left[\frac{\lambda_p^2}{1+k^2\lambda_p^2} + \lambda_d^2 \left(1 + \frac{4}{15}u(\Gamma)\right) \right]^{1/2} \quad (6)$$

In the kinetic regime, the dust acoustic mode does not experience the viscous damping of the hydrodynamic regime and dissipation can arise only through Landau damping on the electrons and ions. The existence of these modes is restricted to the weak coupling regime and the very strong coupling regime where the condition $\omega\tau_m \gg 1$ can be satisfied.

We next consider transverse wave propagation. The GH equations show that a dusty plasma with strong correlations acquires significant ‘rigidity’ to transverse motions and may therefore be able to support ‘shear’ modes with $(\mathbf{k} \cdot \delta\mathbf{u}_d = 0)$. This is a novel behavior which is unlike normal fluids and arises only because of the strong correlations. The low frequency transverse motion of the dust fluid will produce transverse currents $\mathbf{J}_d = -n_{0d}eZ_d\delta\mathbf{u}_d$ which couple these shear modes to electromagnetic waves $(\mathbf{k} \times \mathbf{E} \neq 0)$. However the dominant response of electrons and ions $\delta\mathbf{J}_{e,i} = in_{0e,i}e^2\mathbf{E}/(m_{e,i}\omega)$ to such slow perturbations makes the coupling quite weak. Following standard procedure, we use the perpendicular components of the equation of motion and the Maxwell’s equations to get the dispersion relation,

$$\omega \left(1 - \frac{\omega_{pd}^2}{\omega_{pe}^2 + \omega_{pi}^2}\right) = -i \frac{\eta^* k^2}{1 - i\omega\tau_m} \quad (7)$$

As discussed, the electromagnetic contributions represented by the $\omega_{pd}^2/(\omega_{pe}^2 + \omega_{pi}^2)$ term is quite negligible and this shear mode is primarily of a mechanical nature. In the hydrodynamic limit ($\omega\tau_m \ll 1$), the above dispersion relation yields a low frequency damped mode, $\omega \approx -i\eta^*k^2$, which is very reminiscent of a convective cell mode in ordinary plasmas. In the opposite limit, ($\omega\tau_m \gg 1$) one obtains a propagating mode given by,

$$\omega^2 \approx \frac{\eta^* k^2}{\tau_m} \quad (8)$$

Substituting for τ_m , reverting to dimensional variables, and taking the large Γ limit (where the condition $\omega\tau_m \gg 1$ holds) Eq. (8) can be rewritten approximately as,

$$\omega^2 \approx k^2 \frac{\gamma_d E_c}{M_{0d} n_{0d}} \quad (9)$$

This is analogous to elastic wave propagation in solids with the correlation energy E_c playing the role of the elasticity modulus.

SUMMARY

We have studied the propagation of low frequency waves in strongly coupled dusty plasmas. The dust dynamics has been modelled using the generalized hydrodynamics description which accounts for the dust correlation effects by means of generalized viscoelastic coefficients that are functions of the coupling constant Γ . The principal effects on the dust acoustic wave propagation in addition to viscous damping are new dispersive corrections in the strongly correlated regime, an overall reduction of the frequency and phase velocity and the existence of parameter regions where $\partial\omega/\partial k < 0$. These effects are analogous to what has been predicted for ion acoustic waves propagating in strongly coupled electron ion plasmas.^{17, 19-22} A novel result for the strongly coupled dusty plasma regime is the possibility of sustaining a low frequency transverse mode that has no analog in the weakly coupled gaseous regime. This dust shear mode is similar in nature to elastic waves in a solid with the correlation energy playing the role of the elastic bulk modulus. Such modes should be excitable in the dusty plasma as one approaches solidification point or in 'melting' experiments of dust crystals. It should also be possible to look for evidence of these modes in molecular dynamic simulations.

REFERENCES

- [1] H. Ikezi, Phys. Fluids **29** 1764 (1986).
- [2] J. H. Chu and Lin I, Phys. Rev. Lett. **72** 4009 (1994).
- [3] H. Thomas, G. E. Morfill, V. Demmel, J. Goree, B. Feuerbacher and D. Mohlmann, Phys. Rev. Lett. **72** 4520(1991).
- [4] Y. Hayashi and K. Tachibana, Jpn. J. Appl. Phys., **33** L804 (1994)
- [5] N. N. Rao, P. K. Shukla and M. Y. Yu, Planet. Space Sci. **38** 4 (1990).
- [6] M. Rosenberg, Planet. Space Sci. **41** 29 (1993).
- [7] F. Melandso, T. K. Aslaksen, O. Havnes, Planet. Space Sci. **41** 321 (1993).
- [8] A. Barkan, R. L. Merlino and N. D'Angelo, Phys. Plasmas **2** 3563 (1995).
- [9] J. H. Chu, Ji-Bin Du and Lin I, J. Phys. D:Appl. Phys. **27** 296 (1994).
- [10] N. D'Angelo, J. Phys. D: Appl. Phys. **28** 1009 (1995).
- [11] G. Praburam and J. Goree, Phys. Plasmas **3** 1212 (1996).
- [12] F. Melandso, Phys. Plasmas **2** 1212 (1996).
- [13] J. B. Pieper and J. Goree, Phys. Rev. Letts. **77**,3137(1996).
- [14] Y. I. Frenkel, *Kinetic Theory of Liquids* (Clarendon Press, Oxford, 1946).
- [15] J. P. Boon and S. Yip, *Molecular Hydrodynamics* (McGraw-Hill Inc., New York, 1980).
- [16] S. Ichimaru, H. Iyetomi and S. Tanaka, Phys. Rep. **149** 91 (1987).
- [17] M. A. Berkovsky, Phys. Lett. A **166** 365 (1992).
- [18] W. L. Slattery, G. D. Doolen and H. E. DeWitt, Phys. Rev. A **21** 2087 (1980).
- [19] V. M. Atrazhev and I. T. Iakubov, Phys. Plasmas **2**, 2624 (1995).
- [20] P. Carini, G. Kalman and K. I. Golden, Phys. Rev. A **26** 1686 (1982); P. Carini and G. Kalman, Phys. Lett. A **105** 232 (1984).
- [21] F. Postogna and M. P. Tosi, Nuovo Cimento B **55** 399 (1980).
- [22] K. I. Golden, Phys. Rev. A **35** 5278 (1987)

EXPANDING PLASMA LAYERS WITH DUST PARTICLES

Yuriy I. Chutov,¹ Olexandr Yu. Kravchenko,¹ Pieter P. J. M. Schram,²
and Volodymyr S. Yakovetsky¹

¹Faculty of Radio Physics, Taras Shevchenko Kiev University,
Volodymyrs'ka Str. 64, 252017 Kiev, Ukraine

²Department of Physics, Eindhoven University of Technology, The
Netherlands

INTRODUCTION

Expanding plasmas with dust particles have been intensively investigated in recent years¹⁻³ including investigations of relaxation phenomena in such plasmas^{2,3}. However these investigations have been carried out under an assumption of an equilibrium initial state although non-equilibrium plasmas can be realized in many cases, for example, by an interaction of laser radiation with solid state surfaces, in particular in laser fusion.

The aim of this work is the computer modeling of an expansion of bounded plasma layers with dust particles and with two groups of electrons with different temperatures which can be realized by an interaction of laser radiation with solid state surfaces.

MODEL

An uniform quasi-neutral plasma layer with the initial size L and sharp boundaries consist of two groups (cold and hot) of electrons with initial densities n_{eo}^c and n_{eo}^h as well as with different initial temperatures T_{eo}^c and T_{eo}^h , respectively, as well as ions with density n_o and temperature T_o . The quasi-neutrality condition gives the following relation between densities of electrons and ions: $n_o = n_{eo} = n_{eo}^c + n_{eo}^h$.

This plasma layer can expand into a vacuum due to the self-consistent electric field. Non-charged dust particles with radius R_d and density n_d appear in this plasma layer at the initial time. Therefore the plasma relaxation takes place both by this plasma expansion and by the collection of electrons and ions from the plasma on dust particles. The plasma is considered to be collisionless because the plasma relaxation time is much less than the electron-ion collision time due to a choice of plasma parameters and non-charged dust particles.

Various parameters of this relaxing plasma have been numerically simulated using the PIC method and taking into account the dynamics of the dust particle charge in the framework of the orbit-limited-probe theory without the assumption about equilibrium of

electrons and ions. Coulomb collisions of electrons and ions with dust particles are taken into account in the framework of the method of stochastic differential equations. In some cases, the electron and ion collection by dust particles and the Coulomb collisions have been also simulated by the Monte Carlo method.

RESULTS

Typical results of the computer modeling are plotted in Fig. 1 - 6 for different numbers $N_d = n_d L_\delta^3$ of dust particles in the Debye cube at $R_d = 0.32$, $(T_{eo}^h / T_{eo}^c) = 10$, $T_{io} = T_{eo}^c$ and $m_i / m_e = 256$ which last value is taken to obtain higher simulation precision. Here R_d and the spatial coordinates X are divided by the initial Debye length L_δ of the cold electrons, the time t is multiplied by the initial ion plasma frequency ω_{oi} .

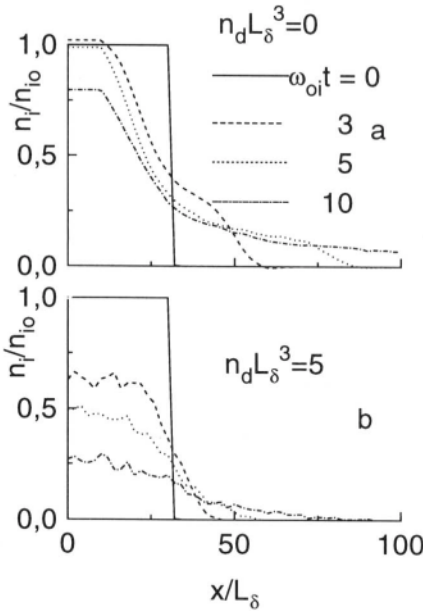


Figure 1. Spatial distributions of an ion density n_i for various times t after the start of the plasma expansion without dust particles (a) and with dust particles (b) where ω_{oi} is an initial ion plasma frequency, n_{io} is the initial ion density.

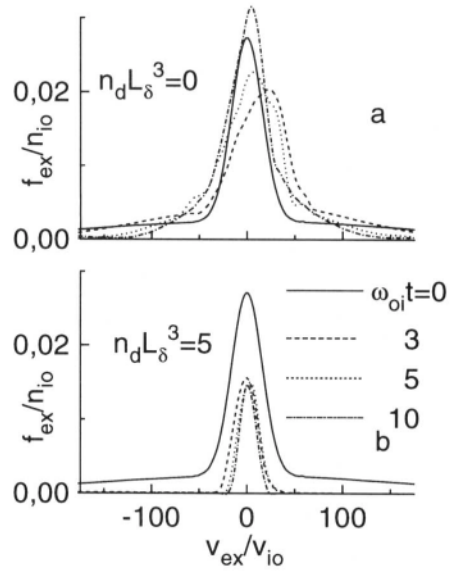


Figure 2. X-components f_{ex} of the mean (for positive values of the spatial X-axis) electron velocity distribution function for various cases corresponding to Fig. 1. Here $v_{io} = (kT_{io} / M)^{1/2}$ is the initial mean ion velocity.

The influence of dust particles on the plasma expansion is clearly seen from Fig. 1 in which the spatial distributions of the ion density n_i divided by the initial ion density n_{io} are shown for various times after the start of the plasma expansion in case of the plasma expansion without dust particles (upper part) and in case of the plasma expansion with dust particles (lower part). In the first case, we have the usual plasma expansion with a rarefaction wave propagating into the central part of the plasma layer. Therefore the decrease of the ion density in the same layer point starts only after this point has been reached by the rarefaction wave. In case of plasma expansion with dust particles (lower part of Fig. 1) the decrease of the ion density starts in all points of the plasma layer

simultaneously due to the ion collection by dust particles. Besides, this decrease is faster than in the case of the plasma expansion without dust particles.

The influence of dust particles on electrons is clearly seen from Fig. 2 in which the X-components of the mean (for positive values of the spatial X-axis) electron velocity distribution function are shown for various cases corresponding to Fig. 1. As can be seen from Fig. 2, this function is non-equilibrium initially because the plasma layers consist of two groups of electrons. In the case of plasma without dust particles, this function evolves due to a transfer of the electron energy to ions by the self consistent electric field during the plasma acceleration. All electrons participate in this energy transfer and therefore the non-equilibrium of this function as well as the special properties of this non-equilibrium are preserved during the plasma expansion without dust particles (Fig. 2a). However in the case of plasma with dust particles, fast electrons can only be collected by dust particles due to their negative electric charge. Therefore these fast electrons vanish just after the start of the plasma expansion and the electron velocity distribution function is like Maxwellian.

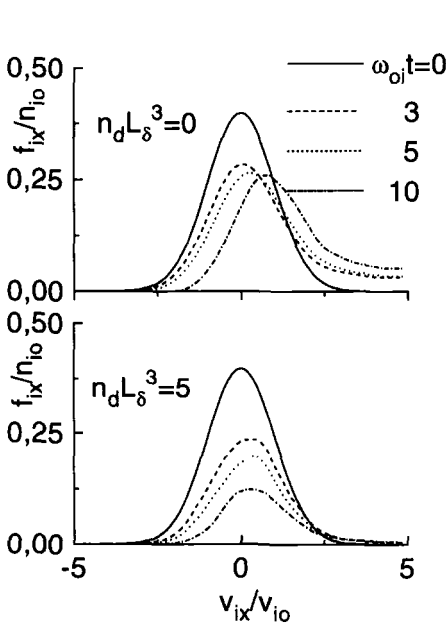


Figure 3. X-components f_{ix} of the mean (for positive values of the spatial X-axis) ion velocity distribution function for various cases corresponding to Fig. 1.

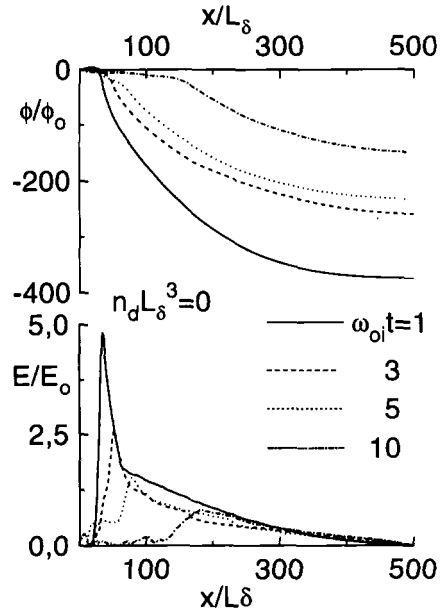


Figure 4. Spatial distributions of electric potential ϕ and field E in an expanding plasma layer without dust particles for various cases corresponding to Fig. 1. Here $\phi_o = kT_{eo}^c / e$, $E_o = kT_{eo}^c / eL_\delta$.

As can be seen from Fig. 3, there is also some difference between the evolution of the mean ion velocity distribution function during the plasma expansion for these two cases. In case without dust particles, the ion acceleration takes place due to the self consistent electric field along the X-axis during the plasma expansion. Therefore there is some shift of the mean (for positive values of the spatial X-axis) ion velocity distribution function to the right. In the case of plasma without dust particles, this shift is smaller because fast electrons are just collected by dust particles and their contribution to the ion acceleration is smaller than in the case of plasma without dust particles.

It is of interest to investigate especially the influence of dust particles on an electric potential ϕ and field E which are created during the plasma layer expansion. Spatial distributions of these parameters are plotted in Fig. 4 in the case of plasma without dust particles as well as in Fig. 5 - 6 for different numbers of dust particles in the Debye cube. Electric fields E and potentials ϕ are divided in these figures by characteristic values $E_o = kT_{eo}^c / eL_\delta$ and $\phi_o = kT_{eo}^c / e$ respectively.

Comparison of these figures shows that dust particles essentially decrease electric fields and electric potentials created by the plasma expansion. This change corresponds to the influence of dust particles on electron and ion velocity distribution functions during plasma expansions.

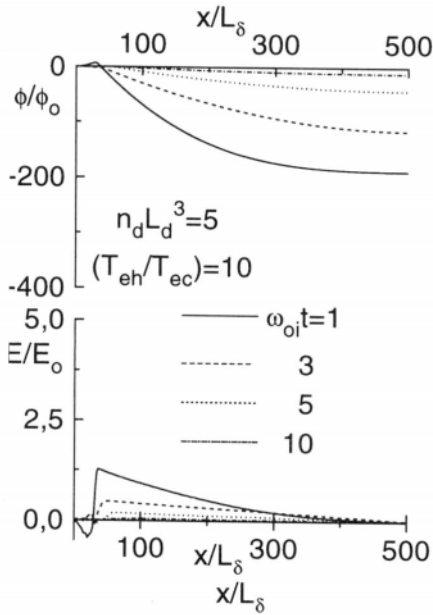


Figure 5. Spatial distributions of electric potential ϕ and field E in an expanding plasma layer with dust particles at $n_d L_d^3 = 5$ and $(T_{eh} / T_{ec}) = 10$ for various cases corresponding to Fig. 4.

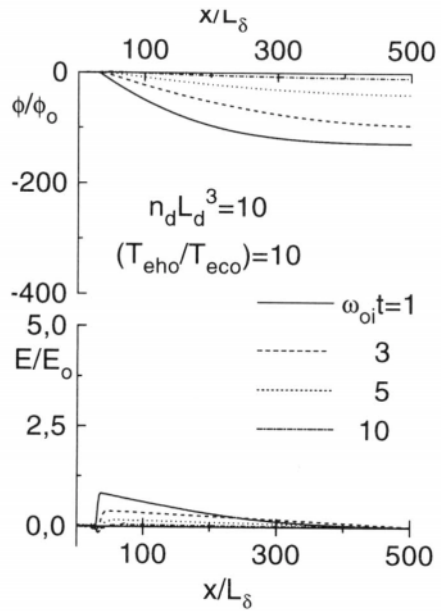


Figure 6. Spatial distributions of electric potential ϕ and field E in an expanding plasma layer with dust particles $n_d L_d^3 = 10$ and $(T_{eho} / T_{eeco}) = 10$ for various cases corresponding to Fig. 4.

CONCLUSION

Computer modeling of expanding non-equilibrium plasma layers with dust particles show that dust particles can strongly influence different phenomena accompanying this expansion. This influence is caused by the selective collection of electrons and ions by dust particles with self-consistent negative electric charge. First of all, these particles can change the initial energy distribution functions of electrons and ions due to the selective collection of electrons and ions.

ACKNOWLEDGMENT

This work was partially supported by INTAS in the framework of contract No 94-2959 and by a grant from the Ukrainian Committee of Science and Technology

REFERENCES

1. M. Y. Yu, H. Luo, Adiabatic self-similar expansion of dust grains in a plasma, *Phys. Plasmas*, 2:591 (1995).
2. Yu. I. Chutov, A. Yu. Kravchenko and P. Schram, Evolution of an expanding plasma with dust particles, *Physica. B* 128:11 (1996).
3. Yu. I. Chutov, A. Yu. Kravchenko and P. Schram, Expansion of a bounded plasma with dust particles, *J. Plasma Physics*. 55, part 1:87 (1996).

This page intentionally left blank

NON-LINEAR SHEATHS WITH DUST PARTICLES

Yuriy I. Chutov, Olexandr Yu. Kravchenko, Volodymyr S. Yakovetsky

Faculty of Radio Physics, Taras Shevchenko Kiev University,
Volodymyrs'ka Str. 64, 252017 Kiev, Ukraine

INTRODUCTION

Non-linear sheaths are existing on all cold walls which the plasma is in a contact. These sheaths determine an interaction of plasmas with wall surfaces including flows of charged particles from plasmas to these walls. In much practical important cases, for example at an interaction of a laser radiation with a pellet, dust particles can be created close to a surface. These particles can strongly influence various plasma properties, including sheaths, due to a selective collection of electrons and ions from plasmas.

The aim of this work is to study non-linear sheaths in plasmas with dust particles in order to investigate an influence of these particles on sheaths.

MODEL

An one-dimensional slab plasma consisting of equilibrium electrons and ions with densities $n_{eo} = n_{io} = n_o$ and temperatures T_e and T_i , creates an equilibrium sheath in front of an electrode to which a large negative potential ϕ_o is applied. According to the Bohm's sheath criterion¹, an drift ion velocity u_o has to satisfy the well known boundary condition $u_o \geq (kT_e / M)^{1/2}$ close to a sheath boundary where M is the ion mass. Dust particles with a density $N_d = N_{do} \exp(-x^2 / x_o^2)$ and a radius R_d appear in this sheath at some initial time and both a collection and scattering starts of electrons and ions by these dust particles here. These processes cause an evolution of a sheath.

The PIC method is used for computer modelling of sheaths, taking into account the dynamics of dust particle charge in plasmas with self-consistent energy distribution functions of electrons and ions²⁻⁴. The Coulomb scattering of electrons and ions are taken into account in the framework of the Monte-Carlo method.

A case of a sheath without dust particles is used as a test of computer programs created according to these methods. In this case, spatial distributions of plasma parameters for a usual steady-state sheath¹ are used as initial conditions for a computer simulation of their evolution. These simulations show that initial equilibrium distributions are conserved during simulation times. In case of some deviations of initial distributions from the equilibrium case, these non-equilibrium distributions evolve to equilibrium one during several ion plasma cycles. These results confirm an adequation of computer programs.

RESULTS

Obtained results show that an influence of dust particles on sheaths strongly depends from relations between some characteristic times, namely: a time τ_p of an ion penetration through a sheath, an ion collection time τ_a , and an ion scattering time τ_s . Of course, this influence is very small in the case of $\tau_p \ll \tau_a, \tau_s$. In the opposite case of $\tau_p \gg \tau_a, \tau_s$, dust particles create some barrier between a plasma and an electrode due to a strong collection and scattering of electrons and ions by dust particles so that electrons and ions can not reach an electrode at all. In this last case, there is not a space electric charge close to an electrode and a sheath vanish.

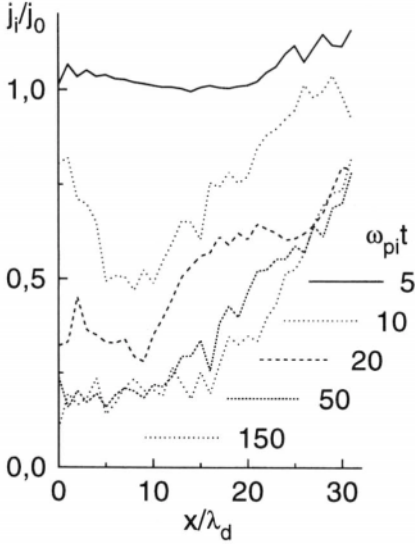


Figure 1. Spatial distributions of an ion flux j_i in a sheath with dust particles for various times t after an appearance of dust particles in a sheath where ω_{pi} is the initial ion plasma frequency, λ_d is an initial Debye length, $j_o = n_o(kT_{eo} / M)^{1/2}$ is the Bohm's flux.

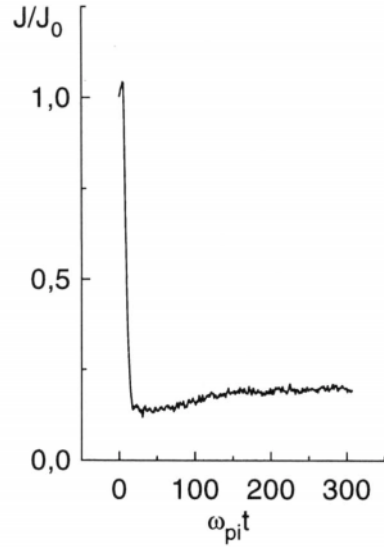


Figure 2. An evolution of an electric current J in an external circuit after an appearance of dust particles in a sheath where J_o is the initial current.

The most interesting phenomena are realized in the case $\tau_p \sim \tau_a + \tau_s$. Typical results of computer simulations are shown for this case in Fig. 1 - 6 for $N_{do} = 1$, $R_d = 0.1$, $x_o = 16\lambda_d$, $\phi_o = 10$. Spatial distributions of various plasma parameters are plotted here for various times t after a start of their evolution from initial equilibrium distributions due to an appearance of dusty particles in a sheath at $\omega_{pi}t = 5$. In these figures, the spatial coordinate x is divided by the initial Debye length $\lambda_d = (kT_e / 4\pi n_o e^2)^{1/2}$, a time t is multiplied by the initial ion plasma frequency $\omega_{pi} = (4\pi n_o e^2 / M)$, a potential ϕ is divided by a characteristic value kT_e / e , N_d is the number of dust particles in the Debye cube, R_d is the radius of a dust particle divided by the initial Debye length λ_d .

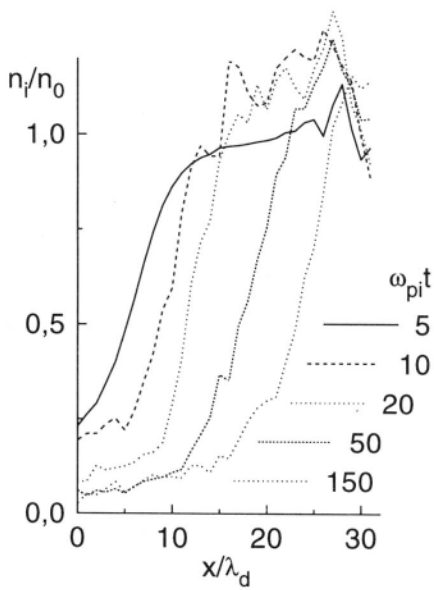


Figure 3. Spatial distributions of an ion density n_i in a sheath with dust particles for various times t after an appearance of dust particles in a sheath where n_o is a plasma density.

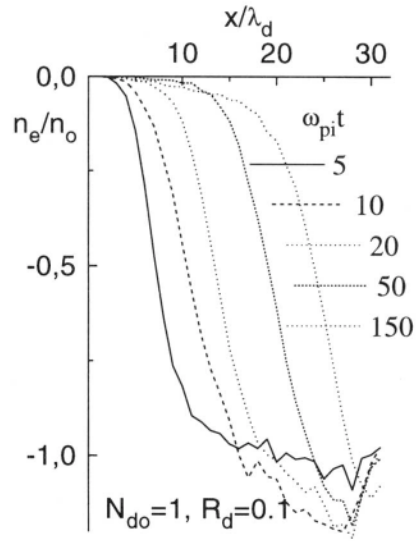


Figure 4. Spatial distributions of an electron n_e in a sheath with dust particles for various times t after an appearance of dust particles in a sheath where n_o is a plasma density,

As can be seen from these figures, all plasma parameters change essentially due to an influence of dust particles in a sheath. This influence is seen especially clear from an evolution of an ion flux j_i , shown in Fig. 1. Initially, this flux is practically uniform because it is a case of steady-state sheaths without dust particles¹. However dust particles decrease this flux and cause its essential heterogeneity due to a different collection and scattering of ions in different places of a sheath. A flux decrease causes corresponding changes of an electric current J in an external circuit (Fig. 2).

A sheath evolution is accompanied by a decrease of ion n_i and electron n_e densities in a sheath (Fig. 3-4) due to their collection and scattering by dust particles. However some increase of these densities takes place close to a boundary of a sheath with a plasma. This increase is caused by a scattering of an ion flux by dust particles close to this boundary. Therefore an ion flux changes here and does not correspond an preliminary ion flux from a non-disturbed plasma¹.

Of course, distributions of an electric potential ϕ (Fig. 5) evolve according to an evolution of electron and ion densities. These distributions can be non-monotonous during their evolution times but a final distribution is monotonous always. Note, the Child-Langmuir law¹ is not valid for sheaths with dust particles because an ion flux does not conserve in a sheath for this case (Fig. 1).

Finally, spatial distributions of a dust particle charge q_d (Fig. 6) show a various sign of these charges in various regions of a sheath according to spatial distributions of electrons and ions. Note that Fig. 6 allows to determine q_d for various cases using a plasma ion charge q_o in a Debye cube.

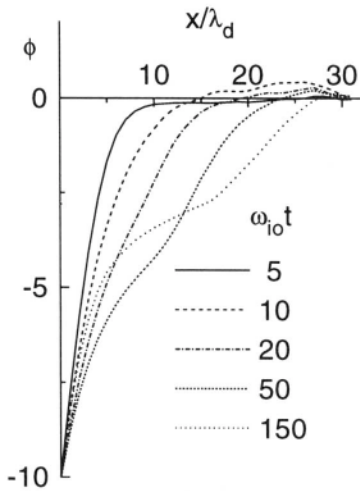


Figure 5. Spatial distributions of an electric potential ϕ in a sheath with dust particles for various times t after an appearance of dust particles in a sheath where n_o is a plasma density.

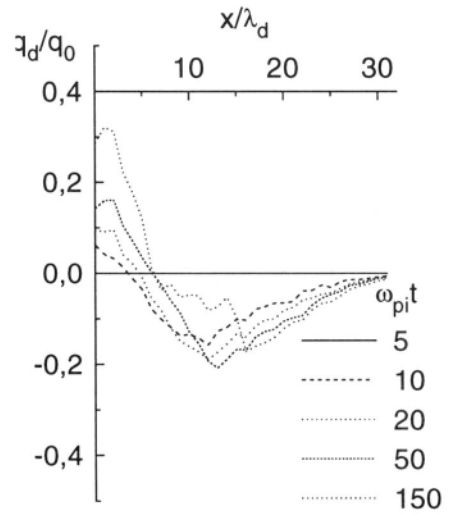


Figure 6. Spatial distributions of a dust particle charge q_d in a sheath with dust particles for various times t after an appearance of dust particles in a sheath where q_o is a plasma ion charge in a Debye cube.

CONCLUSION

Computer modeling of sheaths with dust particles show that dust particles can strongly influence properties of these sheaths. This influence is caused by a collection and a scattering of electrons and ions by dust particles with self-consistent negative electric charge. First of all, these particles can strongly change an ion flux in a sheath that causes other change of sheath parameters.

ACKNOWLEDGMENT

This work was partially supported by INTAS in the framework of contract No 96-0617 and by a grant from the Ukrainian Committee of Science and Technology.

REFERENCES

1. F. F. Chen. "Introduction to plasma physics," Plenum Press, New York and London (1985).
2. Yu. I. Chutov, A. Yu. Kravchenko and P. Schram, Expansion of a bounded plasma with dust particles, *J. Plasma Physics*. 55, part 1:87 (1996).
3. O. G. Sytenko, A. G. Zagorodny, Yu. I. Chutov, P. Schram and V. N. Tsytovich, Statistical properties and relaxation of dusty plasmas, *Plasma Physics and Contrlled Fusion*. 38:A 105 (1996).
4. Yu. I. Chutov, A. Yu. Kravchenko and P. Schram, Evolution of an expanding plasma with dust particles, *Physica*. B 128:11 (1996).

FROM COLD DUSTY PLASMAS TO HOT MICROPLASMAS X-RAY DUST

Yu. K. Kurilenkov,¹ M. Skowronek,² G. Louvet,² and P. Romeas²

¹Institute for High Temperatures (IVTAN), Russian Academy of Sciences,
Moscow 127 412, Russia.

²Laboratoire des Plasmas Denses, Universite P.& M. Curie, F-75252 Paris
Cedex 05, France

INTRODUCTION. BASIC REMARKS

This paper concerns some new aspects of dusty plasmas physics, which have attracted the great interest during few recent years. The features of correlated systems with cold grains immersed into low temperature plasma were studied and discussed intensively [1]. Below, we will pay attention to opposite case: behavior of high temperatures dense plasma “grains” on the background of rather cold dilute plasmas. We consider the creation of a high power density matter (HPDM) configured in a low pressure discharges. Our prime goal is to produce and study a “dusty”-like (erosion) plasma followed by an intense energy deposition into this medium. The anomalous absorbing (stopping) power phenomena related provide to use this media as a working one for high power sources of radiation including hard x-ray. We present below the basic physics used to create HPDM. This is followed by a brief description of the experiments related and results obtained on hard x-ray generation.

The never-ending and exciting physics of pulse electrical discharges in vacuum and at low pressure have allowed to study dense plasma phenomena like cathode micro drops and hot spots [2-4]. The occurrence and physics of anode cations are less investigated [3,5]. Theory is led by the experiment here, and the summing up both the knowledge available for particular processes in discharges and hot dense matter physics itself allows hopefully to formulate the set of conditions for getting a new quality, in particular, for the possible simple ways of HPDM production and use. The present work is concerned by this goal-oriented experimental study of this cross-disciplinary problem.

We are looking for to realize few cumulative (or high local power density) effects for our aim: to transform cold dusty plasmas into hot microplasmas dust, with further collecting HPDM (originated from clusters or dust grains) in the inter electrode space [6]. As a reference system we consider the hollow cathode ns discharge scheme at low pressure which have been modified reasonably [5,6]. Some key points of scenario needed are presented and discussed below.

First, a well known fact is that the initial electronic beams issued from hollow cathode are converging at a near-axis area. This feature together with a variation of the cathode -

anode distance is a way to get a maximum current density j_{\max} at the axis for particular electrode configuration.

Second, the choice of the anode configuration itself may essentially increase the efficiency of its heating by pre-breakdown electron beams. In fact, the anode power density related may be higher than known values $10^8\text{--}10^9 \text{ W/cm}^2$, being effectively close up to laser action of $10^{17}\text{--}10^{19} \text{ W/cm}^2$ [1,2]. For example, it can be realized as a result of “scanning” of anode sharpen edge by avalanche beams with high power density delivered on a small surface ($10^5\text{--}10^6 \text{ J/cm}^3$). Additionally, the special choice of the anode geometry may provide the focusing of explosively evaporated matter on the axis during its expansion into vacuum (this cooling associated partially with the adiabatic one). The expansion process of the anode flare and oversaturation of concentrated anode vapours on the axis will be accompanied by the compact collecting of clusters, nucleated microdrops, accelerated microparticles, etc. at the fixed place beyond the electrodes. The degree of condensation is estimated as high as 0.2-0.5 [2,3]. The analysis of the experiments shows that the dust grains (cluster, microparticles) may typically vary from 0.01 to 1 μm under certain conditions [2,7]. Thus, unique configured medium with combination of advantages both solid density and gas-plasma “targets” may be “prepared” behind of anode flare front before the moment of breakdown.

Just after breakdown., the further anomalous deposition of external energy into this condensed phase obtained in vacuum (beams-clusters interactions and their ns heating by postbreakdown current) may provide a large number of well-collected microplasmas with extreme temperatures and densities inside of each ones ($T = 100 \text{ eV} - 1 \text{ keV}$, $n_e = 10^{19}\text{--}10^{21} \text{ cm}^{-3}$). In fact, low velocity ion stopping and Joule heating j_{\max}^2/σ_{\min} under anomalous low plasma conductivity $\sigma_{\lim} \approx \omega_{pe}/4\pi$ [8] (ω_{pe} is the plasma frequency) due to current- and beams-driven instabilities have to allow the very effective energy deposition, up to $10^7\text{--}10^8 \text{ J/cm}^3$. (The plasma spot conductivity $\sigma_{\lim}(T)$ will decrease at any stage of the hydrodynamic expansion, $\tau_{\text{expand}} \leq 1 \text{ ns}$, supporting the overheating of dense plasma.) Correspondingly, the process of destruction of dusty grains by high density currents ($10^8\text{--}10^9 \text{ A/cm}^2$) have to be accompanied by x-ray radiation during expansion, cooling and recombination of the dense hot microplasmas created. In principal, further manipulation with the effective frequencies of hot grain-grain collisions may provide the different levels of their overlapping. The related goal-oriented experiments and the results obtained are presented and discussed briefly below.

EXPERIMENT

The preparation of hot dense plasmas with extreme parameters in vacuum is a complex task where very different physics are involved. The application of the general scheme described above is performed using a hollow cathode, a cylindrical anode and a low inductance ns discharge at low pressure ($10^{-6}\text{--}10^{-2} \text{ mbar}$). The electrode typical diameter is 5 mm. A Marx generator provides a 70 kV, 50 ns, $I_{\max} \approx 1 \text{ kA}$ pulse and a stored energy of 1 J [5,6]. The spatial distribution of the emitting hot spots has been determined using a sensitive imaging device and a rapid scintillator. The exposure time may be as short as 5 ns. During a single pulse, when the voltage is applied, the “dusty” anode matter is first created and focused in the interelectrode space. After breakdown, this dusty plasma-like medium is transformed into HPDM (on the background of rather dilute post breakdown plasma). The radiation with wavelength $\lambda < 0.1 \text{ nm}$ of this HPDM is registered during 10 to 40 ns, through appropriate attenuators. It may have the shape of a 1 to 4 mm diameter “ball” of collected micro plasmas hot spots. To illustrate it, Fig. 1 shows a typical example of rather

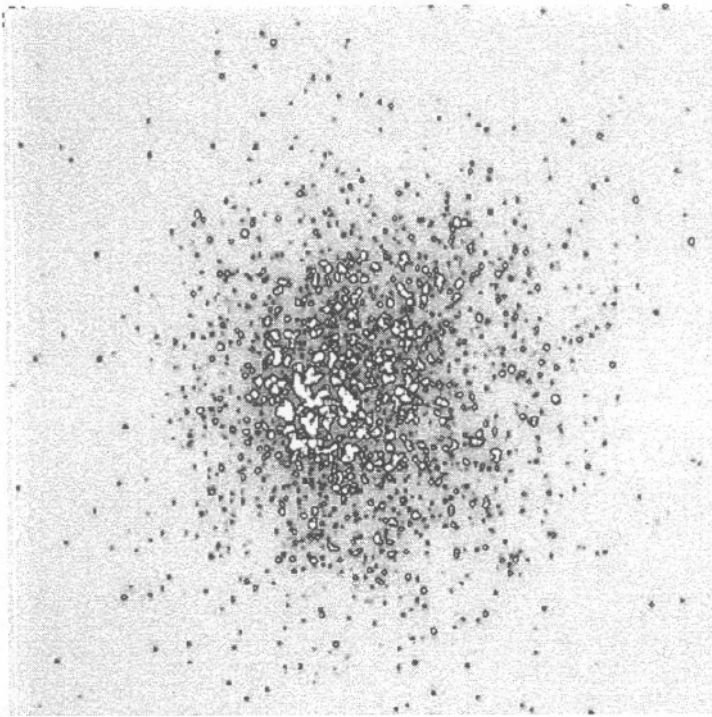


Figure 1. Hard x-ray radiation from hot microplasmas dust cloud

"transparent" x-ray "ball" (inverted solarized intensities). This collection of hot microplasmas may be transformed into cylindrical or disk-like clouds of hot microplasmas dust. Compression of this sort of clouds may be accompanied by partial merging of hot microplasmas. This process started is illustrated by Fig. 2. In a latter case the x-ray intensity and duration are increasing under particular circumstances.

CONCLUSION

We have considered consequently few qualitatively different stages of creation of high power density matter in our simple experiments with hollow cathode discharge: solid target (anode) – electron beam interaction, generation of anode flare with cold grains collected (cold dusty plasma), hot plasmas dust ensemble (with extreme local parameters and anomalous properties of hot spots), and high temperature uniform self-organized plasma. This study have allowed to demonstrate some crucial effects: formation hard x-ray "balls" with power $\sim 10^5\text{--}10^6$ W and total photons number about $10^{11}\text{--}10^{12}$ per shot, self-organization of microplasmas of extreme parameters, certain suprathreshold x-ray output. The experimental data accumulated in this new branch of dusty plasma physics is a broad basis for the formulation of reasonable and adequate theoretical description.

Note that the x-ray production and the energetics related are of similar origin and levels as that due to the volume irradiation of clusters by intense laser pulses [9], but differ of high current z-pinch. The role of possible intracluster processes, inner-shell excitations and anomalous x-ray emission under direct e and i beams deposition have to be discussed also [10], as well as some elements of other cluster ionization mechanism models [11].

A relatively small and low energy device provides the well reproducible generation of high power density matter configured (with maximal energy densities up to $\sim 10^7$ J/cm³) [6].

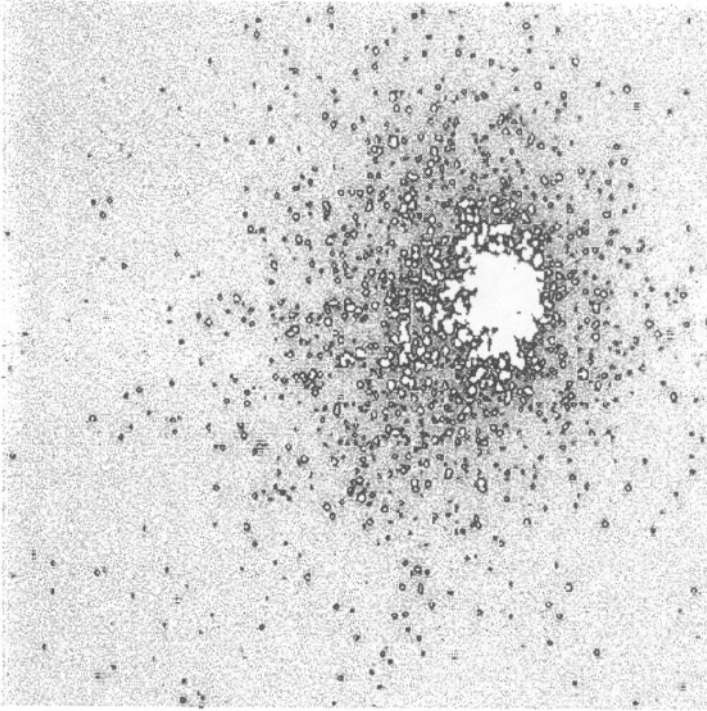


Figure 2. The example of compressed x-ray "ball" consisted of partially merged microplasmas.

Different opportunities related with possible manipulating by hot microplasmas after their creation in pseudospark discharge are studied. In fact, this table top scale experiments give new ultimate opportunities for studies of energy conversion, lasant media, superchemistry, self-organization effects [12] or evolution's of dense astrophysical plasmas.

ACKNOWLEDGMENTS

We acknowledge with thanks the stimulating discussions with V. M. Batenin, A. A. Rukhadze, G. Maynard, J. Dufty, and L. D'yachkov. This work was partially supported by NATO Scientific Programme under Linkage Grant HTECH.LG 960803.

REFERENCES

1. "The Physics of Dusty Plasmas," P. S. Shukle, D. A. Mendes, and W. V. Chow, eds., World Scientific, Singapore (1996).
2. A. Mesyats and D. I. Proskurovsky. "Pulsed Electrical Discharge in Vacuum," Springer-Verlag (1989).
3. A. Mesyats. "Ectons," Nauka, Ekaterinburg (1993).
4. Anders, S. Anders, B. Juttner, and H. Luck, *IEEE Transactions on Plasma Science* 24:69 (1996).
5. Skowronek, A. Ikhlef *et al.*; *Plasma Sources Science and Technology*, 5:70 (1996).
6. Yu. K. Kurilenkov, M. Skowronek, G. Louvet, and P. Romeas, *in*: "XXIII Int Conf. on Phenomena in Ionized gases," Toulouse, France (1997), v. I, p. 186; M. Skowronek, Yu. K. Kurilenkov, G. Louvet, and P. Romeas, *in*: "Int.Conf. on Physics of Dusty Plasmas, Abstracts," Goa, India (1996).

7. Witke, A. Lenk, P. Siemroth, *in*: “XVII Int.Conf. on Physics of Vacuum Discharges and Insulation in Vacuum,” Berkeley, USA (1996).
8. Yu. K. Kurilenkov, M. A. Berkovsky, *in*: “Transport and Optical properties of Nonideal Plasma,” G. A. Kobzev, I. T. Iakubov, and M. M. Popovich, eds., Plenum, New York (1995), p. 215.
9. Ditmire, T. Donnelly, R. W. Falcone, and M. D. Perry, *Phys. Rev. Lett.* 75:3122 (1995).
10. McPherson, T. S. Luk, B. D. Thompson, A. B. Borisov, O. B. Shiryaev, X. Chen, K. Boyer, and C. K. Rhodes, *Phys. Rev. Lett.* 72:1810 (1994).
11. M. Snyder, S. A. Buzza, and A. W. Castleman, Jr., *Phys. Rev. Lett.* 77:3347 (1996).
12. N. Tsytovitch, *Physics–Uspekhi* 40:53 (1997).

This page intentionally left blank

ON THE LOWER LIMIT OF SPOKE PARTICLE RADII

Laura A. Bringol-Barge and Truell W. Hyde

Space Physics Theory Group
Baylor University
Waco, TX 76798-7316

INTRODUCTION

The B-ring of Saturn consists of an admixture of ice flakes and plasma electrons and can be referred to as a “dusty plasma.” Ice grains in Saturn’s rings range in size with the majority of those contributing to the observed opacity lying in the range of centimeter to meter-sized.¹ The presence of radial features of lower optical depth in the B-rings (the “spokes”) strongly suggests localized regions comprised of micron to submicron-sized grains. Electrons present in the B-ring are generally produced by photoemission from the ice and/or injection from the ionosphere of the planet. Under normal circumstances, the electron density in the B-ring is very low and only about 10^{-2} cm^{-3} . As a result, the probability of an ice flake being able to attain even a single electron charge for any significant amount of time is extremely small. Thus the charging processes in the ring proper under “normal conditions” are inefficient and probably not responsible for any macroscopic electrostatic phenomena, such as the spokes.² The best, current theory attempting to explain the spokes assumes a meteoritic impact on the primary ring which vaporizes the source as well as part of the target material, forming a plasma cloud which rapidly expands and thermalizes. It has been shown³ that the expansion of such a plasma cloud ceases at a plasma density of 10^2 cm^{-3} and a plasma temperature of 2 eV and that the cloud corotates with the planet, frozen to the magnetic field lines and moving radially outward. This plasma cloud in the region of the ring increases the probability of ice grains being able to maintain a charge long enough to allow for levitation of the charged grains through electrostatic forces out of the ring plane proper. Thus, as the plasma cloud moves radially away from the planet, the grains that have a normal electric force strong enough to overcome the gravitational attraction to the ring are “levitated” out of the ring plane in the wake of the cloud. The spokes can form anywhere on the ring, but it has been recently suggested⁴ that there is a preference for their creation in the shadow of the planet.

GRAIN CHARGING

The grain’s charge and radius along with the plasma’s shielding properties are the determining factors for the possibility of grain levitation. The charge on a grain is determined through its surface potential which is found by demanding a vanishing current to the grain

surface along with charge conservation in the cloud. The present model considers the primary ion and electron along with the secondary electron current. (The secondary electron current can be nonzero even in low-temperature plasmas, if insulating submicron grains are present.) Since the possibility of spoke formation while in the shadow of the planet is being examined, the model does not consider the photoelectric current. Once the potentials are computed and an appropriate capacitance is assumed, the grain charge is easily found. The resulting electrostatic force normal to the ring must be greater than the gravitational attraction of the grain to the ring for levitation to occur. Using this criterion, the range of grain sizes which can be levitated while in the shadow of the planet are calculated.

Currents to the Grain Cloud

The equations describing the charging currents to a single grain immersed in an ambient Maxwellian plasma are well known and assumed as given in Bringol and Hyde⁵ or Chow et al.:⁶

$$J_j = eZ_j n_j \cdot \pi r^2 \cdot \sqrt{\frac{8kT_j}{\pi m_j}} \cdot \begin{cases} 1 - \frac{eZ_j U}{kT_j}, & Z_j U \leq 0 \\ \exp\left(-\frac{eZ_j U}{kT_j}\right), & Z_j U \geq 0 \end{cases} \quad (1)$$

$$J_{se} = en_e \cdot \pi r^2 \cdot \sqrt{\frac{8kT_e}{\pi m_e}} (kT_e)^{-2} \exp\left(\frac{eU}{kT_e}\right) \cdot \int_0^\infty E \delta(E, r) \exp\left(-\frac{E}{kT_e}\right) dE, \quad U \leq 0 \quad (2a)$$

$$J_{se} = en_e \cdot \pi r^2 \cdot \sqrt{\frac{8kT_e}{\pi m_e}} (kT_e)^{-2} \exp\left(\frac{eU}{kT_e}\right) \cdot \exp\left(-\frac{eU}{kT_s}\right) \left(1 + \frac{eU}{kT_s}\right) \cdot \int_{eU}^\infty E \delta(E, r) \exp\left(-\frac{E}{kT_e}\right) dE, \quad U \geq 0 \quad (2b)$$

J_j being the primary current ($j = i$ for ions, $j = e$ for electrons) and J_{se} being the secondary electron current. The plasma ion species charge is eZ_j , with e the electron charge, r the grain radius, T_j the plasma temperature, n_j the plasma number density, m_j the plasma species mass and U the grain surface potential. The secondary electron yield parameter is $\delta(E, r)$ and kT_s is the thermal energy of the secondary electrons under the assumption that they exhibit a Maxwellian distribution leaving the grain.

To find the currents to a grain cloud immersed in a plasma, the single grain currents must be integrated over the specified distribution of grain sizes, which can be taken as a power-law for grains residing in planetary rings¹ or

$$f(r) = Cr^{-s}. \quad (3)$$

The power-law parameter is given as S with C (a normalization constant) taken to be

$$C = N_d \left[\int_{r_{\min}}^{r_{\max}} r^{-s} \right]^{-1} \quad (4)$$

where N_d is the total number density of the grains in cm^{-3} and r_{\min} and r_{\max} are the minimum and maximum grain radii, respectively. For this model, we assume a very flat spectrum ($S = 0.4$) for the layer of smaller-sized dust in the B-ring as is appropriate for rings having large numbers of micron-sized dust.⁷ Thus, the integrated currents are

$$I_j = \int_{r_{\min}}^{r_{\max}} f(r) J_j(r) dr \quad (5)$$

where the subscript j represents ions (i), electrons (e) or secondary electrons (se). (Integrating over a distribution of grain radii allows for size-dependent effects to be taken into account.) The plasma number density is assumed to be Maxwellian

$$n_j = n_{0j} \exp\left(-\frac{Z_j e V}{k T_j}\right) \quad (6)$$

(where n_{0j} is the number density of species j in the absence of the grains, and V is the average plasma potential) and the condition for current conservation to the grain surface is

$$I_i(U, V) + I_e(U, V) + I_{se}(U, V) = 0. \quad (7)$$

Charge Conservation

Assuming the plasma cloud is of finite extent, plasma particles will be lost from the cloud as the grains charge. Subsequently, the potentials in the dusty plasma must also obey charge conservation. Assuming equal numbers of ions and electrons (in the absence of grains) and that the grains are initially uncharged,

$$Q_{dc} + Q_{pc} = 0 \quad (8)$$

where Q_{dc} is the charge on the grain cloud and Q_{pc} is the charge on the plasma cloud. The charge on a cloud of icy grains of radii r is found by multiplying the surface potential (assumed constant on each grain surface) by the capacitance. (As a first approximation, the capacitance will be taken to be its free-space value.) Employing (3), (5) yields,⁵

$$Z_i e n_{0i} \exp\left(-\frac{Z_i e V}{k T_i}\right) - e n_{0e} \exp\left(\frac{e V}{k T_e}\right) + \bar{U} \int_{r_{\min}}^{r_{\max}} r f(r) dr = 0. \quad (9)$$

Grain Number Density

The B-ring will be assumed to consist of a mixture of micron and submicron grains floating above a layer of larger grains. The density in the B-ring for the smaller grains of mean radius \bar{r} is given by

$$N_d = \frac{\tau}{\pi \bar{r}^2 h} \quad (10)$$

with the normal optical depth of the B-ring τ given as ~ 1.0 and the scale height h approximately equal to 1.0 km.⁸

PARTICLE LEVITATION

Equations (7) and (9) are solved simultaneously for the grain surface potential (U) and the plasma potential (V) and the charges on the grains are then calculated. Once this charge is calculated, the ratio of the electrostatic force to the gravitational force can be found using

$$R = \frac{Q(r)E}{m(r)g} \quad (11)$$

which yields a measure of the grain's probability to be levitated out of the ring proper. In the above, E is the local electric field normal to the plane, $m(r)$ is the mass of a grain of radius r , and g is the local gravitational acceleration normal to the plane. Equations (7) and (9) are solved so that, along with (10), the ratio of forces $R(r_{max})$ can be found. The electric field due to the B-ring is taken to be 3.3×10^{-4} dyne/C, the gravitational acceleration toward the ring is 5.0×10^{-5} cm/s² and the density of the ice grains is 1.0 g/cm³.⁶ Since the upper limit on grain size is not precisely known, it must be specified in the model. Cases of $r_{max} \approx 10$ microns and 100 microns are considered, following a suggestion by Cuzzi et al.¹ Consequently, a range of grain sizes that can be levitated is determined.

DISCUSSION

The model described above takes into consideration charging effects in a dust cloud with a specified power-law size distribution due to the ambient plasma from an impact plasma cloud. Figure 1 shows the levitation ratio R as a function of the grain radius for specific values of the smallest grain size with 10 microns being the largest grain size considered. Figure 2 is a plot of the levitation ratio R as a function of the grain radius with 100 microns being the largest grain size considered. It can be seen that the formation of spokes within the planet's shadow is possible while considering only primary and secondary charging effects. As can be seen in Figure 1, for example, for a B-ring cloud with a range of sizes from 0.05 microns to 10 microns, all dust smaller than 1.0 microns will be levitated. The model presented does not take into effect the deviation from a Maxwellian velocity distribution of the plasma due to ion and electron depletion or the modification of the dust cloud capacitance, which will not be strictly equal to the free-space value, as assumed. Even with these approximations, the model agrees well with previously published results in the field^{2,4} and predicts the minimum grain size that can be levitated off of the B-ring plane.

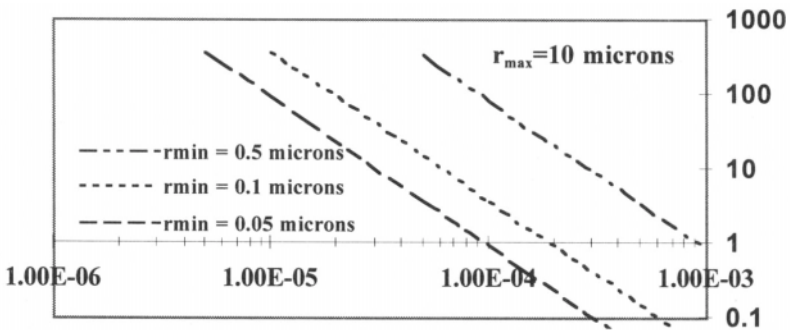


Figure 1. Levitation ratio R as a function of grain size for a maximum cloud grain radius of 10 microns.

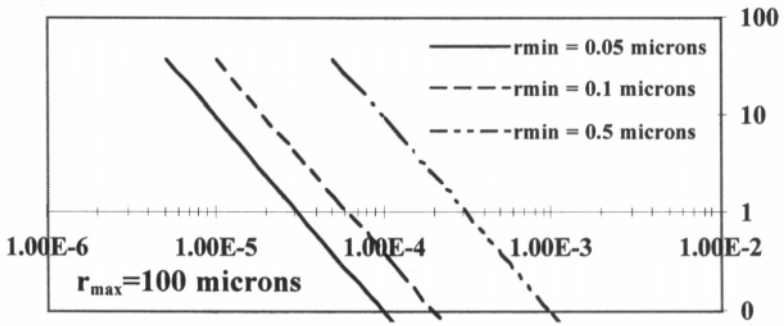


Figure 2. Levitation ratio R as a function of grain size for a maximum cloud grain radius of 100 microns.

ACKNOWLEDGMENTS

The authors wish to acknowledge support from the NASA Texas Space Grant Consortium, the National Science Foundation and the Baylor University Research Committee.

REFERENCES

1. J. N. Cuzzi, J. J. Lissauer, L. W. Esposito, J. B. Holberg, E. A. Marouf, G. L. Tyler and A. Boischof, Saturn's rings: properties and processes, in: *Planetary Rings*, R. Greenberg and A. Brahic, ed., University of Arizona Press, Tuscon (1984).
2. L. -H. Shan, Electromagnetic effects in Saturn's B-ring, Doctoral Thesis, University of Iowa (1990).
3. G. E. Morfill and C. K. Goertz, Plasma clouds in Saturn's rings, *Icarus*, **55**, 111 (1983).
4. E. Grün, C. K. Goertz, G. E. Morfill and O. Havnes, Statistics of Saturn's spokes, *Icarus*, **99**, 191 (1992).
5. L. A. Bringol and T. W. Hyde, Charging in a dusty plasma, Accepted for publication *Adv. Space Res.*, (1997).
6. V. W. Chow, D. A. Mendis, and M. Rosenberg, Role of grain size and particle velocity distribution in secondary electron emission in space plasmas, *J. Geophys. Res.*, **98**, 19065 (1993).
7. E. Grün, G. E. Morfill, G. Schwehm, and T. V. Johnson, A model for the origin of the Jovian Ring, *Icarus*, **44**, 326 (1980).
8. E. Grün, G. E. Morfill, and D. A. Mendis, Dust-magnetosphere interactions, in: *Planetary Rings*, R. Greenberg and A. Brahic, ed., University of Arizona Press, Tuscon (1984).

This page intentionally left blank

MD SIMULATIONS OF DUSTY PLASMA CRYSTAL FORMATION: PRELIMINARY RESULTS

J. E. Hammerberg, B. L. Holian, G. Lapenta, M. S. Murillo, W. R. Shanahan,
and D. Winske

Los Alamos National Laboratory
Los Alamos, NM

INTRODUCTION

In the last few years, a number of laboratory experiments involving dusty plasmas have shown that a crystalline structure can be produced under certain conditions.¹⁻⁴ The experiments involve a weakly ionized rf discharge plasma and take advantage of the fact that the dust grains collect in “electrostatic traps,” i.e., regions of the discharge where the electric, ion drag, and gravitational forces balance. Typically, the dusty plasma crystal is only a few layers thick, but can extend for many (~ 100) lattice spacings in the transverse directions. Because the grains charge negatively to relatively large values, $Q_d > 1000e$, where e is the electron charge, the coupling parameter can be very large, $\Gamma > 1000$.

In this paper we present some preliminary calculations of plasma crystal formation using molecular dynamics (MD) methods. A Yukawa potential is used to model the interaction of the charged grains shielded by the plasma, while an external potential is added to model effects imposed by the discharge. The external potential is based on the forces (electric, ion drag, gravity) experienced by charged grains in the trap region⁵ and is modeled as a (asymmetric) Morse potential in the direction (x) normal to the electrode. This is in contrast to the model of Totsuji *et al.*, who assume a parabolic potential. At present, our calculations do not include the effect of shielding due to ions streaming toward the electrodes. This process has been shown via particle orbit studies² and crystal formation simulations that include ion dynamics³ to be a potentially important effect to explain the observed crystalline structure. Some preliminary studies of this effect are described below.

MD SIMULATIONS

We assume the parameters of a typical rf discharge (plasma density $\sim 10^9 \text{cm}^{-3}$, electron and ion temperatures, $T_e \sim 2 \text{eV}$ and $T_i \sim 0.03 \text{eV}$, and rf voltage $\sim 100 \text{V}$) to calculate profiles for the density, temperature, and electric field across the steady-state discharge. Given these profiles, we then calculate⁵ the profiles of the electric, ion drag, and gravitational forces and the resulting potential $U(x)$ acting on an individual dust grain, assumed to have a radius of $2 \mu\text{m}$ and a (constant) charge of $-2000|e|$. The gravitational and ion drag forces push the dust

grain toward the electrode ($x = 0$), while the electric force pushes the the negatively charge grain away from the electrode, leading to a minimum in the potential near $x \sim 4\mu\text{m}$ from the electrode.

Some idea of the steady state configuration in the trap potential can be gotten from MD simulations neglecting the angular dependence due to ion streaming effects and using pure Yukawa potentials of the form,

$$u(r) = \epsilon \left(\frac{r_0}{r} \right) \exp(-\alpha(r/r_0)), \quad (1)$$

for the pair-wise interaction between charged dust particles. We have taken $\alpha = 1$ corresponding to using the electron Debye screening length. The initial nearest neighbor separation is denoted by r_0 and $\epsilon = Z^2 e^2 / r_0$. Both of these quantities are determined from the temperature and $\Gamma = Z^2 e^2 / k_B T r_{WS}$, where r_{WS} is the Wigner-Seitz radius for the dust particles. In these calculations we have taken $\Gamma = 1000$. The external potential is modeled with a Morse potential of the form:

$$U(x) = 2\epsilon_M \left(1 - e^{-\alpha_M(x/r_0)} \right) - \epsilon_M \left(1 - e^{-2\alpha_M(x/r_0)} \right), \quad (2)$$

with $\epsilon_M = 7\epsilon$ and $\alpha_M = 0.25$. ϵ_M has been adjusted so that the interplanar spacing is ≈ 1 . We have taken a computational volume which is periodic in the transverse directions and started from a (thermodynamically unstable) cubic lattice of 1024 particles at temperature $k_B T / \epsilon = 0.0015$. A Nosé-Hoover thermostat was used to keep the global temperature equal to this value on average. Yukawa systems have a marked tendency toward planar ordering⁷ and we find that after a time of order 100 – 200 t_0 , a planar order appears perpendicular to the x-axis. Here, $t_0 = r_0 \sqrt{m/\epsilon}$ where m is the dust particle mass. The order within the planes is hexagonal but defective with dislocations. The structure of the planes becomes very diffusive as distance increases outward from the minimum of the Morse potential. These effects are shown in Fig. 1 and Fig 2. Consistent with this change from two-dimensional planes to a disordered three-dimensional outer cloud are changes in the local distribution of kinetic energy. We have divided our system into four Lagrangian volumes containing 256 particles each, extending outward from the electrode. The average position $\langle x \rangle$, the out-of-plane temperature $\langle T_{xx} \rangle$, and the in-plane temperature $\langle T_{yy} + T_{zz} \rangle / 2$, as defined by $3Nk_B \langle T_{\alpha\beta} \rangle = \sum m \langle v_\alpha v_\beta \rangle$, are plotted in Fig 3. The out-of-plane temperature is lower than the in-plane temperature, consistent with the defective planar order, and these approach each other linearly with distance from the electrode as the diffuse region is approached.

ION SHIELDING

We have also studied the uniformity of the dust particle charge including ion flow. The charging of a dust particle immersed in an ambient plasma is studied with the CELESTE-2D particle in cell code. The electrons and ions are governed by the Vlasov–Poisson model and interact with the dust surface. To model accurately a dielectric dust particle, the electrons and ions that hit the surface are captured locally on the exact point where they hit; this effect can lead to nonuniform charge distributions over the dust surface.⁸ Figure 4 shows the equilibrium ($\omega_{pit} = 30$) potential around a dust particle. The electrons (ions) are distributed initially according to a nondrifting (drifting) Maxwellian. The plasma parameters are: $T_e/T_i = 5$, $m_i/m_e = 100$, $a/\lambda_D = 0.25$, where λ_D is the linearized Debye length $\lambda_D = \left(\frac{1}{\lambda_{De}^2} + \frac{1}{\lambda_{Di}^2} \right)^{-1/2}$ and a is the dust radius. Note that the nonuniformity of the surface charge and of the surface potential is important.

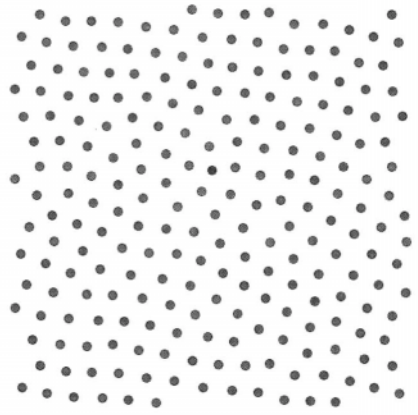
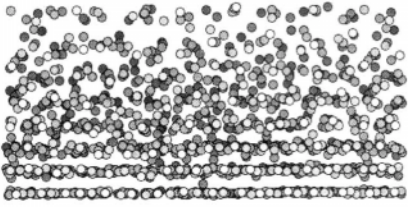


Figure 1. The configuration at $t = 122t_0$: (a) view parallel to the electrode (with the electrode at the bottom), (b) in plane view of one of the hexagonal planes.

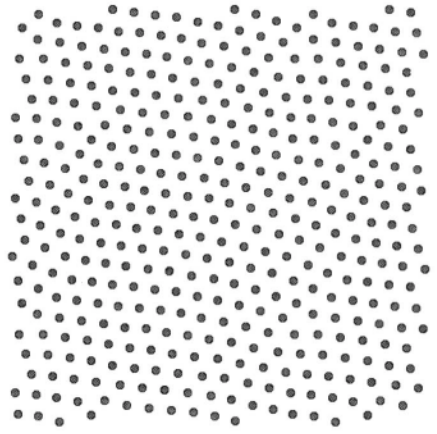
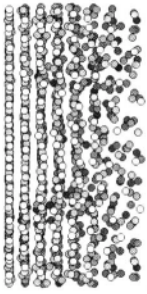


Figure 2. The configuration at $t = 322t_0$: (a) view parallel to the electrode (with the electrode at the bottom), (b) in plane view of one of the hexagonal planes.

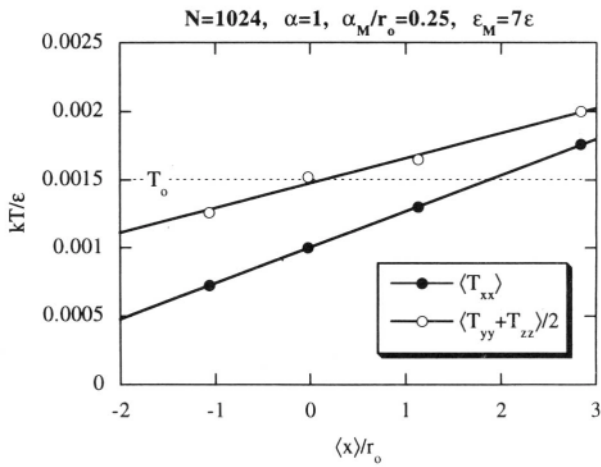


Figure 3. Normal and transverse temperature distribution at $t = 420t_0$.

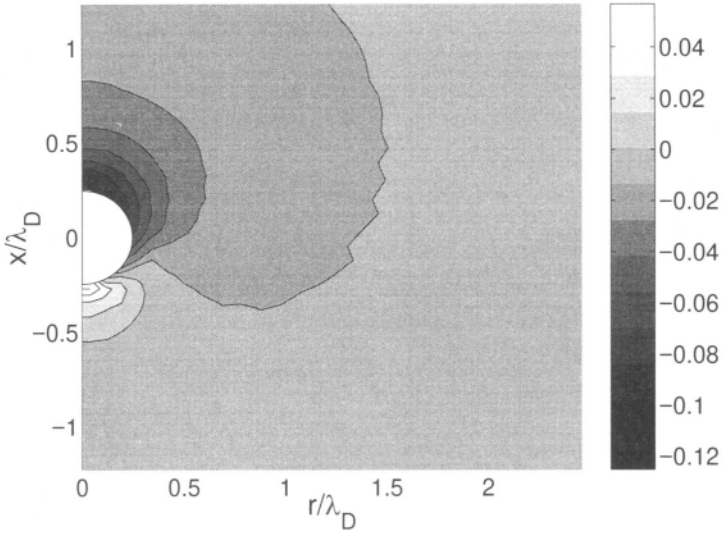


Figure 4. Electrostatic potential around a dust particle at $\omega_{di}t = 30$. The ion drift velocity, toward positive x , is $v_{di} = 3v_b$, where $v_b = (k_B T_e / m_i)^{1/2}$ is the Bohm velocity. The electron drift speed is zero.

Acknowledgements

This work was supported by the Laboratory Directed Research and Development Program.

REFERENCES

- [1] C. H. Chiang and L. I, "Cooperative particle motions and dynamical behaviors of free dislocations in strongly coupled quasi-2D dusty plasmas," *Phys. Rev. Lett.* **77**, 647 (1996).
- [2] A. Melzer, V. A. Schweigert, I. V. Schweigert, A. Homann, S. Peters, and A. Piel, "Structure and stability of the plasma crystal," *Phys. Rev. E* **54**, R46 (1996).
- [3] F. Melandso, "Heating and phase transitions of dusty plasma crystals in a flowing plasma," *Phys. Rev. E* **55**, 7495 (1997).
- [4] G. E. Morfill and H. Thomas, "Plasma crystal," *J. Vac. Sci. Technol. A* **14**, 490 (1996).
- [5] D. Winske and M. E. Jones, "Paniculate dynamics at the plasma-sheath boundary in dc glow discharges," *IEEE Trans. Plasma Sci.* **22**, 454 (1994).
- [6] H. Totsuji, T. Kishimoto, and C. Totsuji, "Structure of confined Yukawa system (dusty plasma)," *Phys. Rev. Lett.* **78**, 3113(1997).
- [7] J. E. Hammerberg, B. L. Holian, and R. Ravelo, "Nucleation of long-range order in quenched Yukawa plasmas," *Phys. Rev. B* **50**, 1372 (1994).
- [8] G. Lapenta, *Phys. Rev. Lett.* **75**, 4409 (1995).

HEATING AND MELTING OF THE DUST CRYSTAL IN RF DISCHARGE: NON-LINEAR ANALYSIS

I. V. Schweigert,¹ V. A. Schweigert,² A. Melzer,³ A. Homann,³ and A. Piel³

¹Institute of Semiconductor Physics

Novosibirsk, Russia

²Institute of Theoretical and Applied Mechanics

Novosibirsk, Russia

³Institut für Experimentalphysik, Christian-Albrechts-Universität

Kiel, 24098 Kiel, Germany

INTRODUCTION

The possibility of the dust crystal formation in plasmas have been predicted by Ukezi¹ in 1986. In the experiments it was observed practically simultaneously in a magnetron² and radio frequency discharges³⁻⁵ only in 1994. It is well known that in a low temperature plasma the microparticles attain the large negative charge $eZ = 10^3 \div 10^4 e$ and arrange the ordered structure. In a radio frequency discharge the crystal of the microparticles locates into the sheath over the bottom electrode, where the gravity acting on the negatively charged particles is balanced by the electrical field. The microparticles arrange the extended crystalline lattice of 100×100 elementary cells in the radial plane. Along the longitude direction the crystal has usually a few layers.

As shown in the first observations the dust crystal behavior exhibits at least two peculiarities which can not be explained in the framework of the classical theory of the Coulomb systems. First, the dust crystal might be close packed, as well as with vertical alignment, where the particles of the lower layer are situated just under the particles of the upper layer. As followed from the experimental study⁶ of the structure composed by growing particles in an ethylene plasma the transition from bcc type of the lattice to the aligned structure happens with increasing the particle size. Note, that the theory of the Coulomb systems and Ukawa ones gives only the energetically preferable close packed structures the type of which changes depending on the interlayer distance. As pointed in the several works⁷⁻¹⁰ the reason of the alignment is the occurrence of the enhanced ion density just behind the upper stream particles. These ion clouds appear due to focusing action of the negatively charged particles on the ion flux and attract the particles of the lower layer.

Another unexpected property of the dust crystal is observed either with lowering the pressure or with increasing the discharge power, when the multi-layer crystal begins to melt. Some parameter G measuring the electrostatic energy of the particle interaction in their thermal energy $G = e^2 Z^2 / a_c T_p$ (where T_p is the particle temperature, $a_c = \sqrt{1/\pi n}$,

$a_c = (3/4\pi n)^{1/3}$ for 2D and 3D cases, respectively, n is the particle density) characterizes the state of the system. As followed from the theory of one component plasma the transition from liquid to solid state takes place at $G = 130 \div 140$ and at $G \approx 170$, for 2D and 3D cases, respectively. Under conditions of the our experiment the crystalline state of the dust structure should be realized,⁴ since $G = 10000 \div 20000$. However, the experimental study¹¹ of the particle motion shows that at the pressure less than some critical magnitude the multi-layer crystal becomes unstable. It has been found that depending on the pressure oscillations of the particles increasing in time can either be stabilized or lead to the melting transition. It is interesting to notice the single layer crystal stability is unaffected by changing of the pressure.

An explanation of the instability of the multi-layer crystal have been given in our works^{9, 10} and concludes in acting of ion clouds. The dust crystal in the sheath is the open system in which the energy of the directed ion flux transforms to the energy of the particle oscillations. In previous works^{9, 10} on the base of the linear analysis we obtained the main characteristics of the unstable two layer crystal such as the critical pressure, the frequency of the oscillations and the phase shift between the particles of the lower and upper layers which agree qualitatively with the experimental data.

In this work we present the results of non- linear analysis of the dust crystal instability obtained with Langevin molecular dynamics method. For the cases of the Coulomb interaction and screened one we revealed the change of the mean particle energy, the velocity distribution function and the velocity autocorrelation function for the different pressures. We studied the solid-liquid phase transition and calculated numerically the particle temperature which is close to the measured one.

MODEL

The infinite in the radial plane two layer crystal is considered. Using the periodical boundary conditions, we simulate a fragment of the crystal (224 particles in each layer). The particles are aligned in the vertical direction. The Newton equations for the particle motion are

$$M \frac{d^2 \vec{\rho}_i}{dt^2} = \vec{F}_i - \lambda \frac{d\vec{\rho}_i}{dt} + F_{lan},$$

where $\vec{\rho}_i$ is the i -particle coordinate. \vec{F}_i is the electrostatic forces acting between the particles, and λ is the friction constant. The seconds term is the force of friction. Third term is the Langevin force. The force F_i includes the particle-particle interaction and particles-positive charge interaction. These effective ion charges are obtained in our works^{9, 10} with using Monte-Carlo simulations of the ions flowing through sheath containing the dust crystal. The interparticle potential U is supposed to be either Coulomb or screened with $\lambda = 2$, $U(\vec{\rho}_i - \vec{\rho}_j) = e^2 Z^2 / |\vec{\rho}_i - \vec{\rho}_j| \exp(-(\vec{\rho}_i - \vec{\rho}_j)\lambda)$.

Under conditions of the experiment $v = 0.29P$, the characteristic dust crystal frequency is $\omega_{pc} = 89s^{-1}$ (below v is normalized with ω_{pc}), the particle charge is $Z = 1300e$, $a = 450\mu km$, the interlayer distance is $d = 0.8a$.

PARTICLE MOTION SIMULATION

Our model allows to follow the motion of all particles in the crystal fragment. The particle trajectories show the increase of the amplitude of oscillations (and, consequently, the kinetic energy) with lowering the pressure. It is possible to separate three different regimes of particle motion depending on the friction constant (pressure). The mean kinetic energy of the particles of the upper and lower layers as a function of friction is plotted in Fig. 1, where

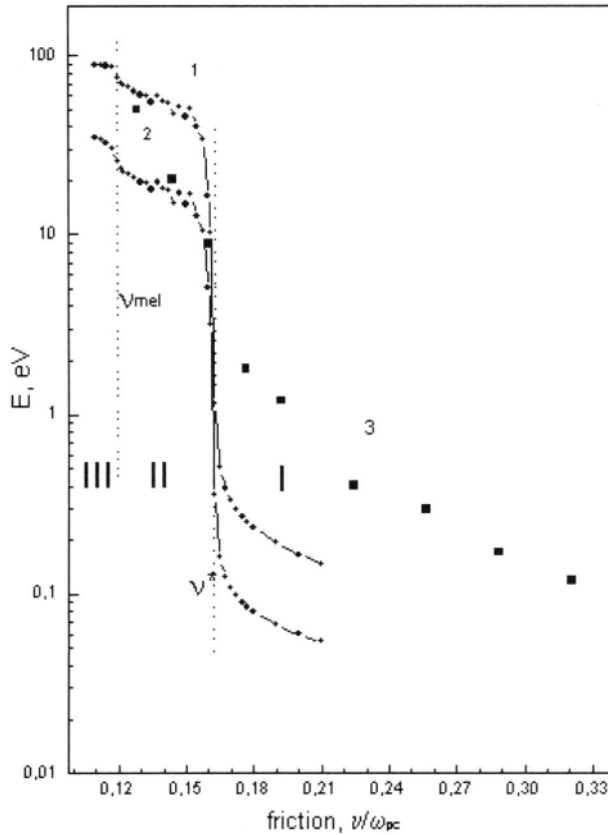


Figure 1. The particle temperature via friction for the screened potential, 1, 2 refer to the lower and upper layers (calculation), 3- for the upper layer (experiment).

all regimes (I,II,III) are pointed. In the regime I, the particles oscillate with small amplitudes and the system remains crystalline with time. This regime is realized at the friction constant larger than some critical value, $\lambda > \lambda^* = 0.16125$ ($P=49$ Pa). With decreasing pressure at $\lambda < \lambda^*$ unstable modes arise in the oscillation spectrum. In the linear analysis^{9, 10} this critical friction λ^* denotes the beginning of an exponential growth of the amplitudes followed by melting. Unlike in the linear analysis, the present non-linear consideration shows the existence of an intermediate regime II. In spite of the presence of the unstable modes, the particle amplitude of oscillations tends to some value which may be rather large, but limited. Then the particle motion is stabilized. Below some friction $\lambda_{mel} = 0.115$ ($P = 36$ Pa) the increase of the amplitude becomes unlimited and the particle motion transforms into a gas like one. It is regime III in which the self- excited oscillations of particles result the melting transition. In the experiment and simulations the oscillation of particles in the lower layer is shown to be more prominent. It should be noted that the agreement between the theoretical and measured temperature of the particles is comparably good in regimes II and III, Fig. 1, but in regime I essentially differs. This fact may be explained by the occurrence of the defects in a real hexagonal lattice in the experiment which enhance the oscillation process.

As seen in Fig. 1 the transition between regimes I and II specifying the crystalline state and the vibration one is accompanied by quick rise of the particle temperature. But the point of the solid state-liquid phase transition λ_{mel} is not marked with some essential temperature change. This point of the phase transition can be defined with using the modified

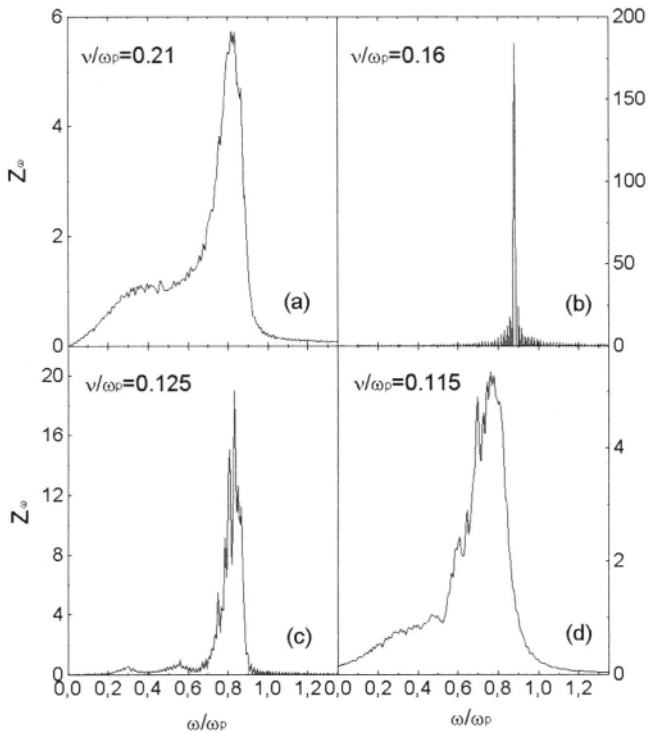


Figure 2. The spectrum of the velocity autocorrelation function at the different friction constants

Lindeman criterion, calculating numerically the parameter L which characterizes the degree of the structure disorder. As seen from numerical results at $\lambda = \lambda_{mel}I$ increases quickly, marking clearly the point melting transition.

The velocity autocorrelation function particles was calculated for the different regimes. Using the Fourier transformation, we have revealed the excitation spectrum of this autocorrelation function, Fig. 2. The system exhibits usual for the hexagonal structure the wide excitation spectrum of the eigen-modes for $\nu > \nu^*$ in the crystalline state, Fig. 2(a). At friction some less than ν^* ($\nu = 0.16$) the spectrum is established to have a sharp and narrow shape referring to the frequency $\omega = 0.88\omega_{pc}$, Fig. 2(b). With lowering the friction constant, the spectrum becomes wider, Fig. 2 (c). It is asymmetrical and restricted with $\omega = 0.88\omega_{pc}$ on the side of the high frequencies. At $\nu < \nu_{mel} = 0.115$ the spectrum demonstrates the presence zero-frequency, and the system behaves like liquid, Fig. 2(d).

In this work on the base of the proposed model we have modeled the development of the instability, the melting transition, and explained the reasons of its arising. The calculated rise of the particle temperature with decreasing the gas pressure agrees with the experimental data. We have established the existence the vibration regime within some range of pressure in which the particle oscillations first develop with time, then achieve some large amplitude and stabilize. The existence of some resonance regime where the particles exhibits the harmonical behavior has been found.

REFERENCES

- [1] H. Ikezi, Phys. Fluids. **29**, 1764 (1986).
- [2] J. H. Chu and Lin. I, Phys. Rev. Lett. **72**, 4009 (1994).

- [3] H. Tomas *et al.*, Phys. Rev. Lett. **73**, 652 (1994).
- [4] Y. Hayashi and K. Tachibana, Jpn. J. Appl. Phys. **33**, L804 (1994).
- [5] A. Melzer, T. Trottenberg, and A. Piel, Phys. Lett. A **195**, 301 (1994)
- [6] Y. Hayashi and K. Tachibana, J. Vac. Sci. Technol. A **14**, 506 (1996).
- [7] S. V. Vladimirov and M. Nambu, Phys. Rev. E, **52**, 2172 (1995).
- [8] F. Melandso, and J. Goree, Phys. Rev. E. **52**, 5312 (1995).
- [9] A. Melzer, V. A. Schweigert, I. V. Schweigert, A. Homann, S. Peters, and A. Piel, Phys. Rev. E **54**, R46 (1996)
- [10] V. A. Schweigert, I. V. Schweigert, A. Melzer, A. Homann, and A. Piel, Phys. Rev. E **54**, 4155 (1996).
- [11] A. Melzer, A. Homann, and A. Piel, Phys. Rev. E **53**, 2757 (1996)

This page intentionally left blank

DETERMINATION OF THE EFFECTIVE AND BARE CHARGES IN DUSTY PLASMAS

E. A. Allahyarova,¹ P. P. J. M. Schram,² and S. A. Trigger¹

¹Institute for High Temperatures
Izhorskaya 13/19, Moscow 127412, Russia

²Eindhoven University of Technology
P. O. Box 513, 5600 MB Eindhoven, The Netherlands

The experimental and theoretical determination of the real (bare) values of the charge-number Z of the macroparticles in dusty plasmas as a function of the plasma parameters, is an important and far from trivial problem. In many interesting situations the Coulomb coupling parameters between electrons, γ_{ee} , ions, γ_{ii} , and between these subsystems, γ_{ei} , are small, whereas all interactions with participation of dust particles are strong. This means that, if we are interested in the equilibrium value of the charge Ze , we can use the generalized integral form of the nonlinear Poisson–Boltzmann equation for the distributions of electrons and ions

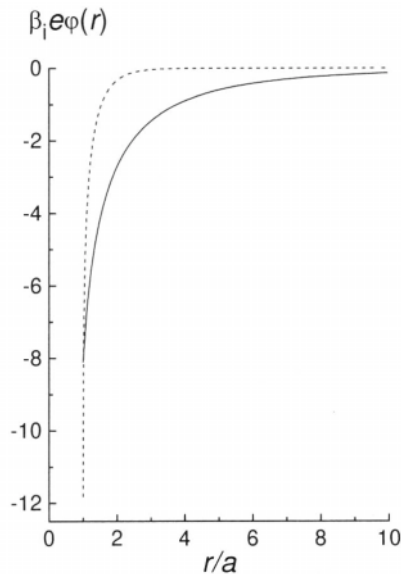


Figure 1. Nonlinear potential $\phi(r)$ versus r/a . Solid line: $Z = 10^4$, $n_{0-} = 5 \cdot 10^5 \text{ cm}^{-3}$. Dashed line: $Z = 10^6$, $n_{0-} = 5 \cdot 10^7 \text{ cm}^{-3}$.

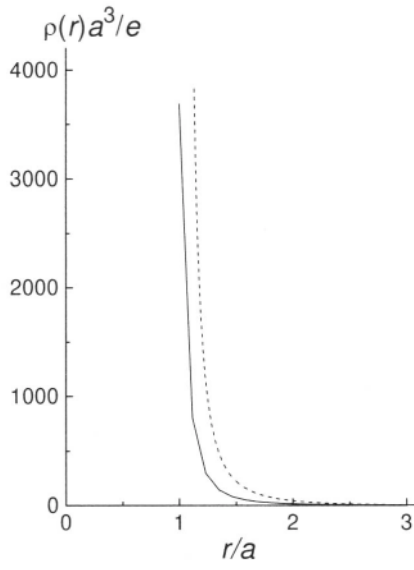


Figure 2. Nonlinear charge distribution $\rho(r)$ versus r/a . Solid line: $Z = 10^4$, $n_{0-} = 5 \cdot 10^5 \text{ cm}^{-3}$. Dashed line: $Z = 10^6$, $n_{0-} = 5 \cdot 10^7 \text{ cm}^{-3}$.

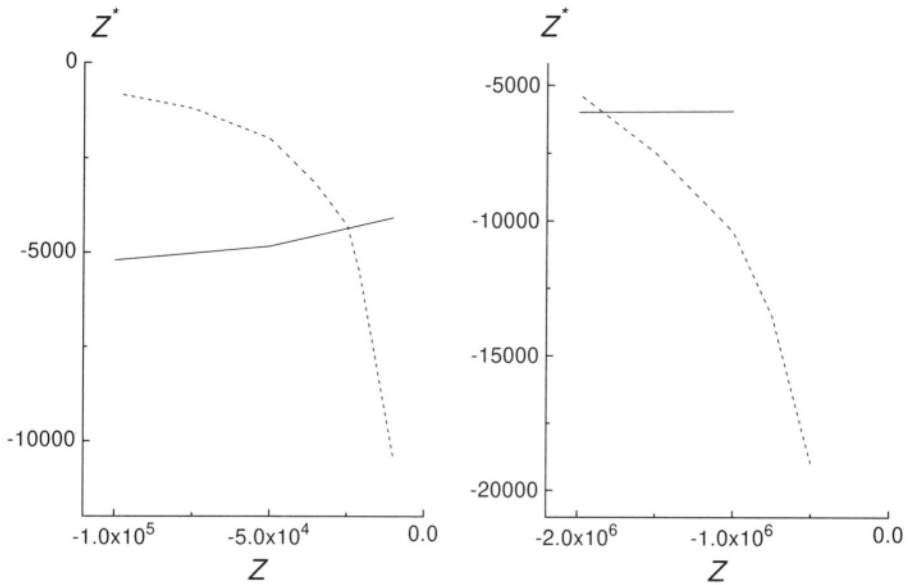


Figure 3. (a) The dependence of $Z^*(Z)$. $n_{0-} = 5 \cdot 10^5 \text{ cm}^{-3}$ (b) The dependence of $Z^*(Z)$. $n_{0-} = 5 \cdot 10^7 \text{ cm}^{-3}$

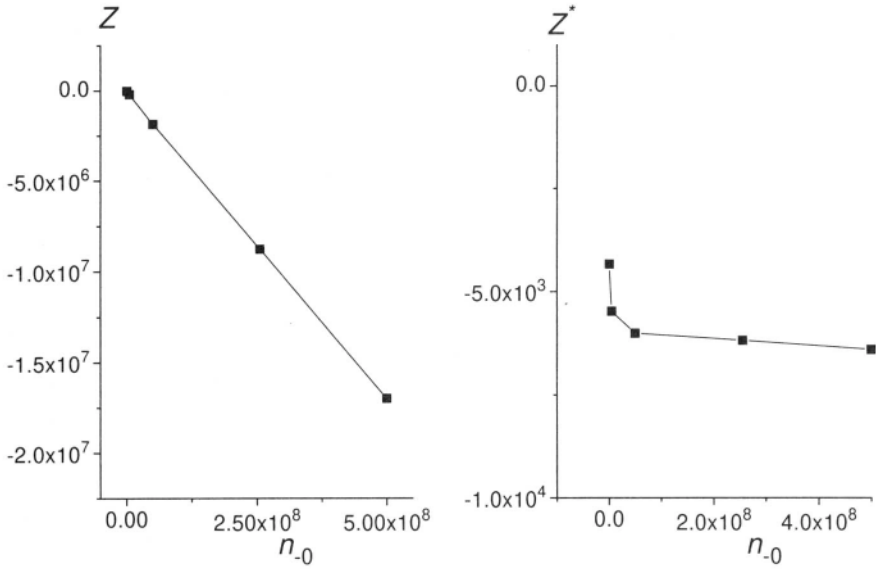


Figure 4. (a) The dependence $Z(n_{0-})$. (b) The dependence $Z^*(n_{0-})$.

around a dust particle with some fixed value of Z :

$$\varphi(r) = eZ/r + 4\pi[1/r \int_a^r dr' r'^2 \rho(r') + \int_r^\infty dr' r' \rho(r')] \quad (1)$$

$$\rho(r) = e[\delta n_+(r) - \delta n_-(r)] \quad (2)$$

$$\delta n_+(r) = n_{0+}[\exp\{-\beta_e \varphi(r)\} - 1] \quad (3)$$

$$\delta n_-(r) = n_{0-}(r)[\exp\{\beta_e \varphi(r)\} - 1] \quad (4)$$

Here a is the radius of the spherical dusty particle, $\beta_e = 1/T_e$, $\beta_i = 1/T_i$ are the inverse temperatures of electrons and ions, e is the magnitude of the electron charge, n_{0+} and n_{0-} are the average densities of ions and electrons, connected by the electroneutrality condition:

$$eZ_+ n_{0+} + eZ_- n_{0-} + eZ n_M = 0. \quad (5)$$

For electrons we have $Z_- = -1$. For simplicity we also take $Z_+ = 1$. The system of nonlinear equations (1)–(4) can be solved iteratively to get the potential $\varphi(r)$ together with the density profiles of electrons and ions around the dust grain. Therefore one can define and calculate the effective charge-number of the dust particle by

$$Z^* = a\varphi(a)/e = Z + 4\pi a/e \int_a^\infty dr' r' \rho(r'). \quad (6)$$

On the other hand the effective charge-number Z^* can also be determined from the equation of balance for the electron and ion currents on the surface of the dust particle. In the stationary case this balance takes the form

$$n_{0-} \exp(\beta_e e^2 Z^* / a) = n_{0i} (\beta_e m_e / \beta_i m_i)^{1/2} (1 - \beta_i Z_i e^2 Z^* / a). \quad (7)$$

Thereby, for the fixed parameters β_e , β_i , n_{0-} and n_{0+} , the set of equations (6),(7) completely determines the bare and effective charges of the dust particle. It is worth noting that the effects of absorption of the electrons and ions were taken into account in Refs. [2–4]. In

case of orbital motion (bound particles) additional terms $n_+(r)$ and $n_-(r)$ should be taken into account on the left hand sides of Eqs. (3), (4). For the limiting case $Zn_M \ll n_{0+}, n_{0-}$ (as proposed in [6]), when $n_{0+} = n_{0-}$ can be assumed, these terms have a $1/r^2$ asymptotic behavior. This leads to a divergence of the integrals in Eqs. (1) and (6). Therefore a more accurate investigation of the physics of absorption is a matter of our future investigations.

In the present work the following set of experimental parameters⁷ is considered: $T_i = 300K$, $T_e = 5 \cdot 10^4 K$, $n_M = 5 \cdot 10^3 cm^{-3}$, $a = 2.8 \cdot 10^{-3}$ and varying on some interval $10^5 cm^{-3} < n_{0-} < 10^9 cm^{-3}$. The results of the calculations are shown in Figures 1–4.

The nonlinear potentials $\varphi(r)$ obtained from Eqs. (1)–(4) by an iteration scheme, are shown in Figure 1. Note that the bigger the bare charge of the dust particle, the stronger the screening of its potential. This also follows from Figure 2, where the corresponding curves of the normalized charge distribution, $a^3 \rho(r)/e$ are presented.

In figures 3a,b the solid curves correspond to $Z^*(Z)$ as solutions to Eq. (6) for fixed n_0 . The dashed lines correspond to $Z^*(Z)$ as solutions to Eq. (7) (balance of currents). The crossing point of these curves determines the real bare charge of the dust particle, $Z(n_0)$. The full dependence of the bare and effective charges on n_{0-} is illustrated in Figures 4a,b.

Further dependences of Z on other plasma parameters (a, T_i, T_e) will be part of our future investigations.

REFERENCES

- [1] T. G. Nothrop, *Phys. Scripta* **45** (1992) 475.
- [2] O. Haynes, G. Mofill and C. Goertz, *J. Geophys. Res.* **89** (1987) 1099.
- [3] J. F. Allen, *Phys. Scripta* **45** (1992) 497.
- [4] F. F. Chen, *Plasma Diagnostic Techniques*, ed. by R. H. Huddlestone and L. S. Leonard, New York Academic Press, 1965, Chapter 4.
- [5] I. Bernstein and I. Rabinovich, *Phys. Fluids* **2** (1959) 112.
- [6] Y. K. Khodataev et al., *Plasma Phys. (Sovj. Phys.)* **11** (1996) 1028.
- [7] V. E. Fortov et al., accepted by *Phys. Letters A* 1997.

CRYSTALLIZING WHITE DWARFS

J. Isern,¹ E. García-Berro,² M. Hemanz,¹ and R. Mochkovitch³

¹Institut d'Estudis Espacials de Catalunya — Unitat del CSIC

²Institut d'Estudis Espacials de Catalunya — Dept Física Aplicada (UPC)
Ed. NEXUS; c/Gran Capità 2-4
08034 Barcelona (Spain)

³Institut d'Astrophysique de Paris (CNRS)
98 bis Bd Arago
75014 Paris (France)

INTRODUCTION

White dwarfs are the final remnants of low and intermediate mass stars. Their evolution is essentially a cooling process that lasts for ~ 10 Gyr. Since the study of white dwarfs allows to obtain information about the age of the Galaxy, it is important to identify all the sources of energy as well as the mechanisms that control its outflow.

The vast majority of white dwarfs are made of a mixture of carbon, oxygen and some impurities coming from the metal content of the parent star. The most important of these impurities is ^{22}Ne , which results from He-burning of the ashes of the CNO cycle, and reaches $\sim 2\%$ by mass in Population I stars, followed by ^{56}Fe which abundance can be as high as $\sim 0.1\%$. Since during the cooling process the star experiences a phase transition, it is natural to wonder if a change of miscibility at the onset of crystallization can provide an extra source of energy.^{2, 6, 7, 11} Although the importance of the mechanical and thermodynamical consequences of the solidification of alloys has been recognized in Geophysics, this is not the case in Astrophysics and very often this phenomenon is either completely ignored or sometimes, misinterpreted. In this paper we examine the role that the redistribution of the chemical elements during the crystallization process can play in the cooling of white dwarfs.

THE PHYSICS OF CRYSTALLIZATION

Crystallization introduces two sources of energy: latent heat release and gravitational energy release related to sedimentation. In the case of Coulomb plasmas, the latent heat is of the order of kT_s per nuclei, where k is the Boltzmann constant and T_s is the temperature of solidification.

During the crystallization process, the equilibrium chemical composition of the solid and liquid plasmas are not equal. Therefore, if the resulting solid is denser than the liquid mixture, it sinks towards the central region. If it is lighter, it rises upwards and melts when

the solidification temperature, which depends on the density, becomes equal to that of the isothermal core. The net effect is a migration of the heavier elements towards the central regions with the subsequent release of gravitational energy. Of course, the efficiency of the process depends on the detailed chemical composition profile.

If there is a change in the chemical composition, the local energy budget of the white dwarf can be written as:

$$\frac{dL_r}{dm} = -\epsilon_\nu - P \frac{dV}{dt} - \frac{dE}{dt} \quad (1)$$

where E is the internal energy per unit mass and $V = 1/\rho$.

Integrating over all the star we obtain:³

$$L + L_\nu = - \int_0^{M_{\text{WD}}} C_v \frac{dT}{dt} dm - \int_0^{M_{\text{WD}}} T \left(\frac{\partial P}{\partial T} \right)_{V, X_0} \frac{dV}{dt} dm + (l_s + e_g) \frac{dM_s}{dt} \quad (2)$$

The first term is the well known contribution of the heat capacity to the total luminosity.⁵ The second term represents the contribution to the luminosity of the change of volume. It is in general small^{4, 10} except when the white dwarf enters into the Debye regime.¹ The third term contains two contributions. One represents the contribution of the latent heat to the total luminosity at freezing, l_s . The other, e_g , represents the energy released by the chemical readjustment of the star.³ This last term is usually negligible in normal stars, since it is much smaller than the energy released by nuclear reactions, but it must be taken into account when all other energy sources are small. It can be written as:

$$\epsilon_g = -(X_0^{\text{sol}} - X_0^{\text{liq}}) \left[\left(\frac{\partial E}{\partial X_0} \right)_{M_s} - \left\langle \frac{\partial E}{\partial X_0} \right\rangle \right] \quad (3)$$

$$\left\langle \frac{\partial E}{\partial X_0} \right\rangle = \frac{1}{\Delta M} \int_{\Delta M} \left(\frac{\partial E}{\partial X_0} \right)_{T, V} dm \quad (4)$$

where ΔM is the mixing region.

CONSEQUENCES ON THE WHITE DWARF COOLING

Ségretain and Chabrier⁸ and Ségretain et al.⁹ computed phase diagrams for arbitrary binary mixtures in terms of the modern density-functional theory of freezing. They showed that the shape of the phase diagram was completely characterized by the charge ratio of the mixture, Z_1/Z_2 . Their diagrams evolve from the spindle form for $0.72 \leq Z_1/Z_2 < 1$, into an azeotropic form for $0.58 \leq Z_1/Z_2 < 0.72$ and finally into an eutectic form for $Z_1/Z_2 < 0.58$. Isern et al² and Ségretain et al.⁹ approximated the ternary mixtures, C/O/Ne and C/O/Fe by effective binary mixtures where N nuclei mimic the behavior of an homogeneous mixture of C/O nuclei.

Table 1 displays the energy released near the center of the white dwarf at the beginning of the solidification process for three binary mixtures. In the case of the C/O mixture it is assumed, for simplicity, that the white dwarf is made of an homogeneous 50:50 (by mass) mixture of carbon and oxygen while in the case of “N”/Ne and “N”/Fe mixtures the abundances were taken as solar. It is important to note that as the process of sedimentation proceeds, the energy released per unit mass decreases. The total energies, ΔE_g , released by these processes are also shown. The limited influence of iron as compared to that of neon is due to its smaller abundance, its larger solidification temperature and its larger number of electrons per barion.

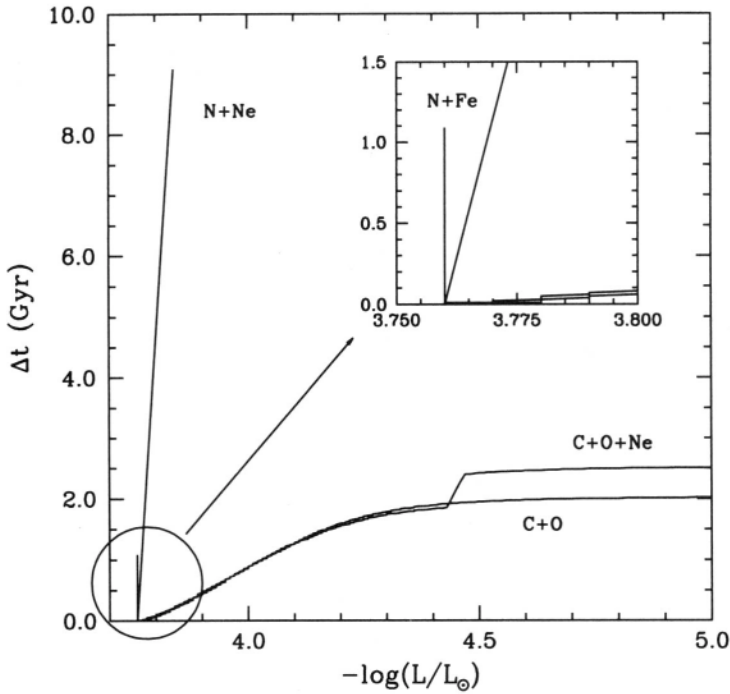


Figure 1. Delay introduced by solidification versus the luminosity of the white dwarf. The C+O curve displays the delay introduced by the sedimentation of a pure carbon–oxygen mixture. The N+Ne and the N+Fe curves display the delay introduced by these impurities if the binary C+O mixture behaves like an average nucleus called N. The C+O+Ne curve displays the delay introduced by sedimentation in the case of a ternary mixture.

Table 1. Energetics and time delay due to chemical differentiation induced by crystallization

Mixture	l_s (erg/g)	e_g (erg/g)	ΔE_g (erg)	Δt (Gyr)
C/O	2.24×10^{13}	3.54×10^{13}	1.95×10^{46}	1.81
N/Ne	2.26×10^{13}	1.46×10^{15}	1.52×10^{47}	9.09
N/Fe	2.25×10^{13}	7.53×10^{15}	2.00×10^{46}	1.09

Since, to a good approximation, the luminosity of a white dwarf can be considered to be a function of the temperature of its nearly isothermal core, T_c , it is possible to estimate the delay introduced by the solidification as:

$$\Delta t = \int_0^{M_{\text{WD}}} \frac{\epsilon_g(T_c)}{L(T_c)} dm \quad (5)$$

where $T_c(m)$ is the core temperature when the crystallization front is located at m . Of course, the total delay essentially depends on the transparency of the envelope. Any change in one sense or another can amplify or damp the influence of solidification in the cooling of white dwarfs and for the moment there are not completely reliable envelope models at low luminosities. Here we have adopted the same envelope as in Ségretain et al.⁹ Table 1 displays the total delays introduced in the cooling by the different cases considered here and Figure 1 the delay as a function of the luminosity.

Although the use of an effective binary mixture is justified in the case of impurities of very high atomic number, it cannot be applied to Ne since C/Ne mixtures display an azeotropic behavior and O/Ne a spindle one.⁸ Recently, Ségretain (1996) has shown that

when the abundance of oxygen is small enough, ^{22}Ne sees the C/O mixture as if it was pure carbon and it displays its azeotropic behavior. Therefore, its influence is very small, $\Delta t = 0.5$ Gyr, as it can be seen in Figure 1.

CONCLUSIONS

Sedimentation of heavy chemical species upon crystallization represents a major source of energy for cool white dwarfs. The delay introduced by the C+O separation amounts 1 to 2 Gyr, depending on the chemical profile. Minor species are the main source of uncertainty since neon can introduce a delay in the range of 0.5 to 9 Gyr, while iron can introduce an additional delay of 1 Gyr. Therefore, it is of the highest importance to understand the behavior of the minor species.

Acknowledgements

This work has been supported by the DGICYT grants PB94-0111, PB94-0827-C02-02, by the CIRIT grant GRQ94-8001 and by the AIHF95-335.

REFERENCES

- [1] D'Antona, F., Mazzitelli, I., 1990, Cooling of white dwarfs, *Ann. Rev. Astron. Astrophys.* 28: 139.
- [2] Isern, J., Mochkovitch, R., García-Berro, E., Hernanz, M., 1991, The role of the minor chemical species in the cooling of white dwarfs, *Astron. Astrophys.* 241: L29
- [3] Isern, J., Mochkovitch, R., García-Berro, E., Hernanz, M., 1997, The physics of crystallizing white dwarfs, *Astrophys. J.* 485: 308.
- [4] Lamb, D. Q., Van Horn, H. M., 1975, Evolution of crystallizing pure ^{12}C white dwarfs, *Astrophys. J.* 200: 306.
- [5] Mestel, L., 1952, On the theory of white dwarf stars. I. The energy sources of white dwarfs, *MNRAS* 112: 583.
- [6] Mochkovitch, R., 1983, Freezing of a carbon-oxygen white dwarf, *Astron. Astrophys.* 122: 212.
- [7] Schatzman, E. 1958, in "Hdb. d. Phys." Vol. 51, S. Flüge editor, (Berlin: SpringerVerlag)
- [8] Ségretain, L., Chabrier, G., 1993, Crystallization of binary ionic mixtures in dense stellar plasmas, *Astron. Astrophys.* 271: L13.
- [9] Ségretain, L., Chabrier, G., Hernanz, M., García-Berro, E., Isern, J., Mochkovitch, R., 1994, Cooling theory of crystallized white dwarfs, *Astrophys. J.* 434: 641.
- [10] Shaviv, G., Kovetz, A., 1976, The cooling of carbon-oxygen white dwarfs, *Astron. Astrophys* 51: 383.
- [11] Stevenson, D. J., 1980, A eutectic in carbon-oxygen white dwarfs, *J. Phys. Suppl.* No 3, 41: C2-53.

THE DYNAMIC EFFECT IN THE SCREENING OF NUCLEAR REACTIONS IN STELLAR PLASMAS

Giora Shaviv¹ and Nir J. Shaviv²

¹Department of Physics & Asher Space Research Institute
Israel Institute of Technology
Haifa, 32000, Israel

²Theoretical Astrophysics
California Institute of Technology
Pasadena, CA

INTRODUCTION AND MOTIVATION

The basic problem arises from the fact that the particles participating in the nuclear reactions in stars are those in the Gamow peak. This peak is usually at energies much higher than the particles mean kinetic energy and hence are in the far tail of the distribution. Slower particles just have a much too small probability to penetrate through the potential barrier while there are too few particles more energetic particles (which do not have the problem of penetration through the potential barrier). The basic problem at hand can be stated as follows: Do these particles have the same properties as the thermal ones vis-a-vis the electrostatic energy that they feel? If the answer to this question is negative then the following question emerges: how to treat these particles. In particular, does the conventional statistical mechanics treatment which handles the *average particles over a long time* hold in this case? As we shall see, the reply to this question affects the treatment of screening as a thermodynamic treatment or kinetic.

IS THERE A DYNAMIC EFFECT IN STATISTICAL EQUILIBRIUM?

The classical treatment of the electrostatic field around a fast moving particle assumes the particle to be a *test* particle that is not in statistical equilibrium with the rest of the particles. On the other hand the particles in the Gamow peak are part of the system and hence are in equilibrium with the system. Consequently, there are claims that the dynamic screening of the test particles does not apply to the particles in the Gamow peak and the properties of the particles in the Gamow peak are identical to the mean properties of the plasma particles. We will try to explain why this is not the case and argue that CSK are correct. Note that the claim is on the electrostatic energy though the terminology used is screening.

The basic claim that the screening is not a function of the kinetic energy of the particle is based on the fact that when the binary interaction potential $\phi(\mathbf{x}_i - \mathbf{x}_j)$ depends only on the

space coordinates, the ensemble average of the potential interaction does not depend on the momentum of the particles. All particles, irrespective of their momentum (energy) have the same *mean* potential energy. Consider the distribution function of the canonical ensemble, namely,

$$f_N = \exp\left(-\sum_i p_i^2/2mkT\right) \exp\left(-\sum_{ij} \phi(\mathbf{x}_i - \mathbf{x}_j)/kT\right) \quad (1)$$

with obvious notation. This distribution function is separable. In other words, averages over the configuration space *at a given time* do not depend on the energies of the particles.

To demonstrate this fact define an operator O as

$$O = \sum_{i,j,\dots}^N O_i(E_i, E_G, \Delta) + O_i O_j + O_i O_j O_k \dots$$

where

$$O_i(E_i, E_G, \Delta) = \theta(E_i - E_G - \Delta)\theta(E_G + \Delta - E_i),$$

is the single particle operator and

$$\theta(x) = \begin{cases} 0 & \text{for } x < 0 \\ 1 & \text{for } x > 0 \end{cases} \quad (2)$$

is the θ function, E_i is the kinetic energy of particle i and E_G and Δ are the Gamow peak energy and the width of the peak respectively. The operators are designed to extract those particles with kinetic energy in the range of the Gamow peak. The first term in the operator O considers the possibility that a single particle is inside the Gamow peak, the second term considers the possibility that two particles are in this state and so on.

According to the statistical mechanics ensemble average, the potential energy U felt by a particle with kinetic energy in the Gamow peak is therefore:

$$\langle U(E_{kin} \in \{E_G\}) \rangle_s = \frac{\int_{-\infty}^{\infty} dp_1^3 dp_2^3 \dots dp_N^3 \int_{-\infty}^{\infty} dr_1^3 dr_2^3 \dots dr_N^3 U O f_N}{\int_{-\infty}^{\infty} dp_1^3 dp_2^3 \dots dp_N^3 \int_{-\infty}^{\infty} dr_1^3 dr_2^3 \dots dr_N^3 O f_N} \quad (3)$$

It is readily seen that according to this definition of the *ensemble average* that:

$$\langle U(E_{kin} \in \{E_G\}) \rangle_s = \langle U \rangle_s, \quad (4)$$

where $\langle U \rangle_s$ is the ensemble average without any condition. Hence the fast particles feel *at time* $t = t_0$ the same potential energy as the thermal ones and hence there should be no dynamic screening. This is so because the operator O depends only on the kinetic energy. Note that in the ensemble average we do not know the identity of the fast particle and hence we do not know who are the fast particles at time t_0 .

There are other ways to find the statistical average of a given quantity. Suppose we are interested in the *long time average* of the potential energy of a *given known particle*. Prescription 3 is not the right one to use since it does not distinguish between particles let alone our chosen one. The proper way is the following: let $U_i(t)$ be the time dependent potential felt by particle i as a function of time. Define *the long time average* of the particle's potential as:

$$\langle U_i(T) \rangle = \frac{1}{T} \int_0^T U_i(t) dt. \quad (5)$$

Here $U_i(t)$ is the potential energy as a function of time as the particle moves through the plasma. According to the *weak ergodic theorem*:⁴

$$\lim_{T \rightarrow \infty} \langle U_i(T) \rangle \equiv \langle U \rangle_\tau = \langle U \rangle_s, \quad (6)$$

where the index τ means the time average and the index s implies the ensemble average. Note that the index i appears on the left but disappears on the right, namely the long time average of all particles is the same. The meaning of this result is that for *long times* the time average of a given property of a particle is likely to be very close to the expectation of this property calculated with the equilibrium probabilities. This is so because *any* particle (including our selected one) goes over all possible states, sometimes it is fast, in other times it is slow and *on the average over a long time* it goes through all states and it experiences the mean equilibrium values. The ergodic theorem does not say that the value of the particular averaged quantity of the particle is *always and at all times* equal to the mean value, nor does it say what the mean value is if additional conditions are imposed.^{4,6}

The nuclear reactions do not take place between thermal particles but between very special fast particles. Consequently, what one is interested in the case of the screening is not what an average ion feels over a long time but what the fast one feels or what a given particle feels only when it happens to be fast. In other words, we are interested in

$$\begin{aligned} \langle U(E_{kin} \in \{E_G\}) \rangle &= \lim_{T \rightarrow \infty} \frac{\int_0^T \theta(E_i - E_G - \Delta) \theta(E_G + \Delta - E_i) U_i(t) dt}{\int_0^T \theta(E_i - E_G - \Delta) \theta(E_G + \Delta - E_i) dt} \\ &= \lim_{T \rightarrow \infty} \sum_{\alpha} \frac{1}{\tau_{\alpha}} \int_{\tau_{\alpha}} U_i(t) dt. \end{aligned} \quad (7)$$

The index i refers to a specific particle, namely the contributions to the integral are added only when the energy of particle i is within the Gamow peak and the periods of time τ_{α} are those periods in which the kinetic energy of the particle is within the Gamow peak. Said differently, the contributions to the long time average are added only over periods in which the kinetic energy of our selected particle is within the Gamow peak. We are interested in time of the order of τ and not in the long time scale which is the thermodynamic one. *There is no ergodic theorem about this conditional limit.* In this case one considers special conditions for contributions to the time average: instead of averaging the potential energy over all the phase space, it is averaged only over a certain small well defined part of it. In other words, for the ensemble average to be equivalent to the time average, each particle has to go through *all* states, not only through a special specified state. The time for going through all states is the time needed to obtain the equivalence between the two methods to obtain the average. Thermodynamics exists only in the limit of times which are sufficiently long to allow each particle to go through many energy states. On shorter times one must use kinetic equations (and not equilibrium thermodynamics).

It is surprising that the electrostatic potential, which does not depend on the velocity, appears to be ‘velocity dependent’ and that the ensemble average fails to ‘see’ it. As for the ensemble average, clearly on the long run, when the particle goes through all possible energy states the average given by the ensemble is velocity independent. More accurately, it is averaged over all possible velocities of the particle This is exactly what Krainov et al.⁷ did. As to the time average, one averages only over selected domains in the phase space namely, only when the particles are fast. There are however, two small differences between the calculation of a fast test particle and fast particles in an ensemble. The first one is that in the calculation of the test particles one *assumes* that it moves at a constant speed (as if it had an infinite mass) for a sufficiently long time to establish an equilibrium distribution around it. On the other hand, the particles in the ensemble are scattered into this energy state and must establish a new charge cloud distribution around them. This process takes time. Also, the particles do not stay forever in the high energy state. We have estimated this time and found that the fast particles do have time to establish a relaxed distribution. The details of the estimates and calculations will be reported elsewhere.

FLUCTUATIONS

As first suggested by Shaviv & Shaviv,⁵ another problem in plasma screening is evident when considering the number of particles within a Debye sphere:

$$N_D = \frac{4\pi}{3} r_D^3 n = \frac{4\pi}{3} \left(\frac{r_D}{\bar{r}} \right)^3 = \frac{1}{4\pi\sqrt{6}\Gamma^{3/2}}. \quad (8)$$

At the center of the Sun for example, we find that $N_D \approx 1 - 3$. Hence, the fluctuation in the potential energy which is proportional to $1/\sqrt{N_D}$ may be non-negligible. *The small number of particles in the Debye sphere casts doubts about the validity of a relaxed particle distribution around any particular ion, yet to estimate the effect we assume that the distribution is relaxed.*

Assume that the screening energies E_{sc} have a Gaussian distribution given by $f(E_{sc}, \Theta) \equiv dN(E_{sc})/E_{sc}$ with a $1-\sigma$ width of ΘkT and a mean value E_{sc}^0 . The formal form will be:

$$f(E_{sc}, \Theta) = \frac{1}{\sqrt{2\pi}\Theta kT} \exp\left(-\frac{(E_{sc} - E_{sc}^0)^2}{2(\Theta kT)^2}\right). \quad (9)$$

For a given screening energy E_{sc} , the reaction rate is increased approximately by a factor (Clayton 1968):

$$R(E_{sc}) = \exp(-E_{sc}/kT). \quad (10)$$

Thus, for our given distribution, the rate of the reaction is enhanced by a factor of:

$$\begin{aligned} \bar{R}(E_{sc}^0, \Theta) &= \int_{-\infty}^{\infty} R(E_{sc}) f(E_{sc}, \Theta) dE_{sc} \\ &= \frac{1}{\sqrt{2\pi}\Theta} \int_{-\infty}^{\infty} \exp(x) \exp\left(-\frac{(x - x_0)^2}{2\Theta^2}\right) dx, \end{aligned} \quad (11)$$

where $x = E_{sc}/kT$ and $x_0 = E_{sc}^0/kT$.

We can now integrate and find:

$$R(E_{sc}^0, \theta) = \exp\left(-\frac{E_{sc}^0}{kT} + \frac{\Theta^2}{2}\right). \quad (12)$$

It is therefore apparent that for $\sigma_{E_{sc}} \sim \sqrt{E_{sc}^0/kT}$, the *average* screening correction is comparable to the correction due to *fluctuations* in the screening energy.

HOW TO CALCULATE THE SCREENING EFFECT

Since the number of particles in the Debye sphere is so small, the close approach of one particle to the another changes significantly the electrostatic field around it and leads to large deviations from the mean field (which is obtained after a long time of averaging). Hence, instead of evaluating the enhancement from the mean field as is usually done, one has to find the field when the two particles are very close to one another. This type of calculations is now under way.

SUMMARY AND CONCLUSIONS

- Ensemble average is not the proper average for the screening problem. The proper average to use is the conditional time average over a single particle time history. The basic ergodic theorem is not applicable in this case.
- There is a dynamic effect on the potential energy of a particle. The effect is to reduce the enhancement of the reaction rate due to the screening.
- As a consequence we conclude that simple thermodynamic arguments cannot be used to infer the *rate* of the nuclear reaction. The Helmholtz free energy formalism when applied to the screening² is a prescription to *approximate* the screening potential *assuming* that the screening potential does not depend on the energy of the reacting ions (among other assumptions). The effect of the plasma on the *rate* of the nuclear reaction must be derived from kinetic arguments.
- The contribution of the fluctuations does not average out to zero due to the non linearity of the screening correction as a function of the screening energy. Moreover, the fluctuation width can be estimated in the weak screening limit and is found to enhance the rates by a factor as large as the screening correction itself and hence plays an important role in various circumstances.

REFERENCES

- [1] Carraro, C., Schafer, A. & Koonin, S.,E. 1988, Ap. J., **331**, 565 (CSK).
- [2] DeWitt, H. E., Graboske, H. C. & Cooper, M. S., Astrophys. J. **181**, 439 (1973).
- [3] Hill, T. L. 1956, *Statistical Mechanics*, McGraw-Hill, p181.
- [4] Penrose, O. *Foundations of Statistical Mechanics* 1970, Pergamon Press, Oxford, p. 90.
- [5] Shaviv, N. J. & Shaviv, G. 1996, Ap. J. 433.
- [6] Thompson, C. J., 1992, *Mathematical Statistical Mechanics*, Princeton Univ. Press.
- [7] V. P. Krainov et al., 1997 (these proceedings).

This page intentionally left blank

EFFECT OF DYNAMICAL SCREENING OF CHARGED PARTICLES IN MAXWELLIAN PLASMAS ON CRITERION OF PLASMA NON-IDEALITY

V.P. Krainov¹, V.A. Rantsev-Kartinov² and E.E. Trofimovich³

¹Physical Technical Institute, Dolgoprudnyi, Moscow region, 141700, Russia;

²INF RRC "Kurchatov Institute", Moscow, 123182, Russia;

³International University for Nature, Society and Man of the Dubna, Universitetskaya 19, Dubna, Moscow region, 141980 Russia

INTRODUCTION

It is most appropriate to represent plasma non-ideality domain in terms of the n_e vs. T_e diagram, where n_e and T_e are electron density and temperature, respectively. The straight line $\gamma = e^2 n_e^{1/3} / kT = 1$ separates two regions in this diagram. Ignoring quantum effects and particle degeneration, one can see that the area above the line corresponds to an ideal plasma, whereas the area below the line corresponds to a non-ideal plasma. Sometimes the value $\xi = 4\pi r_D^3 n_e / 3 = e^2 / 6r_D kT$ is also used as a parameter of the non-ideality. Its value equals to the number of charged particles inside Debye sphere. Formally speaking, the difference between ξ and γ is in the definition of potential energy. For the value of ξ , the later is defined as the energy of the Coulomb interaction at the Debye radius whereas for the value of γ the mean distance between particles, $n_e^{-1/3}$, is used. The line $\xi = 1$ is a straight line in the n_e vs. T_e diagram which is parallel to the line $\gamma = 1$. The density for the curve $\xi = 1$ is three orders of value lower than that corresponding to $\gamma = 1$. In the domain between these two lines the Debye screening approximation is not valid. At the same time, the non-ideal corrections to thermodynamic equation of state are small yet so that the ideal gas approximation still gives reasonable results. Usually plasma is described as a non-ideal one if $\xi > 1$ or $\gamma > 0.1$.

It is shown in this paper that for a wide range of plasma parameters the dynamic descreening increases the screening radius by a factor of about 10, in comparison with the static Debye screening. Hence, if one substitute the dynamic screening radius into parameter ξ instead of using the static screening radius r_D , the value ξ becomes the same order of magnitude as the value of γ . Thus, the line $\xi = 1$ coincides with line $\gamma = 1$ under this condition, and $\gamma = 1$ is the relevant boundary of the plasma non-ideality in the n_e vs. T_e diagram.

THE POTENTIAL OF A MOVING CHARGE IN A PLASMA

As it was shown by Montgomery,¹ if a free charged particle and the polarization cloud it produces moves the lowest-order multipole moment which appears is quadrupole, and it vanishes only when the velocity of the free charge equals zero. Outside of the polarization cloud the potential of the system falls off in inverse proportion to the cube of the distance. The present work is aimed at investigating the behavior of the dynamic screening -- for the non-relativistic motion -- for both the particles of the equilibrium plasma itself and for the free charges moving in it. The most suitable quantity for describing this situation is the effective charge of a particle. Numerical calculations reveal that dynamic screening differs significantly from static ones; this is seen in the transition that takes place at the extremities of the polarization cloud as the velocity of the charge increases, when the Debye potential turns into the Coulomb potential, and also in a change in the sign of the effective charge, whose magnitude can exceed that of the original charge. The present work supplements papers,^{2,3} where there was used the exact dispersion relation for a Maxwellian plasma, and represents a natural continuation of the work.^{4,5} Although the general expressions for the time-independent electric field of a point charge moving in an isotropic plasma with constant velocity are well known,⁶⁻⁸ until recently numerical calculations have been performed only with a model dispersion relation.^{9,10} Here we consider a fully ionized Maxwellian plasma consisting of singly charged ions and electrons (although in fact all the calculations can be extended to other types of plasma after simple modifications). Assume that a unit free charge is moving in the plasma with some velocity \mathbf{u} . According to Refs.[6-8], the electric potential of a moving charge in a plasma $\varphi(\mathbf{k}, \omega)$ has the form

$$\varphi(\mathbf{k}, \omega) = (8\pi^2 / k^2 \epsilon_l) \delta(\omega - \mathbf{k}\mathbf{u}), \quad (1)$$

where the longitudinal part $\epsilon_l(\mathbf{k}, \omega)$ of the permittivity takes the form:¹¹

$$\epsilon_l(\mathbf{k}, \omega) = 1 + (ka)^{-2} \left[1 + F\left(\frac{\omega}{\sqrt{2}kv}\right) \right]. \quad (2)$$

Here a is the Debye radius, the function $F(x)$ is determined from the integral:

$$F(x) = \frac{x}{\pi^{1/2}} \int_{-\infty}^{\infty} \frac{\exp(-z^2) dz}{z-x} + i\pi^{1/2} x \exp(-x^2), \quad (3)$$

where the first term is defined in the sense of principal value. After inverting the Fourier transform one has:⁶⁻⁸

$$\varphi(\mathbf{R}) = \frac{1}{2\pi^2} \int \frac{d\mathbf{k}}{k^2} \frac{\exp(i\mathbf{k}\mathbf{R})}{\epsilon_l(\mathbf{k}, \mathbf{k})}. \quad (4)$$

Here the notation $\mathbf{R}=\mathbf{r}-\mathbf{u}t$ is introduced so that in the coordinate system moving with the charge the electric field distribution is independent of time.

CONDITIONS FOR APPLICABILITY OF THE SOLUTION

The approximation in which the motion of the free charge is prescribed is only valid if we can neglect the feedback between total electric field and the charge. As is well known [6], in an isotropic plasma the longitudinal waves can have such small velocities that they can be

produced by Cherenkov emission when the resonance condition $\omega = \mathbf{k} \cdot \mathbf{u}$ is satisfied. Hence expression (4) is actually valid for times Δt large enough for the polarization clouds to develop but small enough so that their energy losses through Cherenkov radiation can be regarded as small. If we extrapolate the results of Ref.[4] then the first condition becomes $\Delta t \gg 10 (\omega_p)^{-1}$, where ω_p is the plasma frequency. On the other hand, this time must be short enough that the energy losses of the free charge through Cherenkov emission of plasma waves are small in comparison with its kinetic energy. Based on the results of work¹² the second condition becomes $\Delta t \ll \frac{Mu^3}{e^2 \omega_p^2 \ln(1 + 2u^2/v^2)}$, here M is the mass of a free charge and e , is its charge.

NON-EXPONENTIAL DECAY OF THE POTENTIAL AS A FUNCTION OF DISTANCE

The screening of a moving free charge by the plasma differs substantially from the Debye screening of a charge at rest. This is seen in the non-exponential decay of the potential (4) as a function of distance R . Expanding (4) to first order in the velocity u ($\ll v$) of the charge and, assuming that from (3) we have $F(x) = -2x^2 + i\pi^{0.5}x$, $x \ll 1$, and we find the following result:

$$\varphi(R) = R^{-1} \exp(-R/a) + 4(2\pi)^{0.5} a^2 (uR) / v R^4, \quad R \gg a. \quad (5)$$

This was obtained first by Cooper.¹³ Thus, at distances large in comparison with the Debye radius the potential of a moving charge falls off as the inverse cube of distance and has a strong angular dependence. The first term in (5) can be neglected in comparison with the second. Then in the rear hemisphere relative to the direction of particle motion the effective charge of the moving particle is reversed, i.e., a moving electron repels electrons located ahead of it and drags electrons behind it.

SCREENING OF THE FIELD OF THE PLASMA PARTICLES

Thus far we have been talking about an individual free charge moving in a Maxwellian plasma. Here we turn to an aggregate of plasma charges. If we consider the simplest fully ionized hydrogenous plasma, then we are concerned with the motion of the ions and electrons. As regards the ions in the isothermal case, because of their large mass their thermal velocity is much less than the electron thermal velocity, which is responsible for the Debye screening. Hence the potential produced by ions in this case is almost purely Debye-like, since we can treat them as though they were at rest. The situation is different, e.g., for the plasma electrons. In order to demonstrate this fact, let us find the mean potential for an ensemble of particles with thermal velocity v_t . Now we separate the Coulomb contribution in (4) and integrate with respect to one of the angular variables and average the potential found above with a Maxwellian distribution at time $t=0$. The average is carried out over both the velocity u of the ensemble particles and over the angle θ (angles between the direction of the radius vector \mathbf{R} and the direction of the velocity u of the particle), on which the Maxwellian distribution does not depend. It is more convenient to start by averaging expression (1) for the Fourier component of the potential of the moving charge over the Maxwellian distribution. We find

$$\langle \varphi(\mathbf{k}, \omega) \rangle = [2^{2.5} \pi^{1.5} / v_t k^3] \epsilon_i(\mathbf{k}, \omega) \exp(-\omega^2 / 2k^2 v_t^2). \quad (6)$$

Inverting the Fourier transform and integrating over the angles of the vector k we find $\langle \varphi(k, \omega) \rangle = \langle \chi(r) \rangle / r$,

$$\langle \chi(r) \rangle = 2^{0.5} \pi^{-1.5} v_i^{-1} \int_{-\infty}^{\infty} d\omega \int_0^{\infty} dk \frac{\sin(kr)}{k^2 \varepsilon_i(k, \omega)} \exp\left[-\frac{\omega^2}{2k^2 v_i^2}\right] \quad (7)$$

Using expression (2) and making a change of variables, we can perform the integral with respect to k . We finally obtain

$$\langle \chi(\rho) \rangle = 2(\mu / \pi)^{0.5} \int_0^{\infty} dz \cos[S_{\pm}(z)\rho] \exp[-\mu z^2 - S_{\pm}(z)\rho]. \quad (8)$$

Here we have introduced the dimensionless variables $\mu = (v / v_i)^2$, $\rho = r / a$, and the notation $S_{\pm}(z) = 2^{-0.5} \{[(1 + F(z))^2 + (F'(z))^2]^{0.5} \pm (1 + F(z))\}^{0.5}$. The results of the numerical calculation shows that the inclusion of electron motion weakens the Debye screening, as one would expect.. Thus, the dynamic descreening increases the screening radius by a factor of about 10, in comparison with the Debye screening, for a wide range of plasma parameters.

REFERENCES

1. D. Montgomery, G. Joyce, and R. Sughara, *Plasma Phys.* 10:681,(1967)
2. T. Peter, *J. Plasma phys.* 44:269, (1990)
3. C. L. Wang and G. Jouce, *J. plasma Phys.*, 25:225, (1981)
4. E. E. Trofimovich and V. P. Krainov, [*Sov. Phys. JETP*, 75:37, (1992)
5. E. E. Trofimovich and V. P. Krainov, *Sov. Phys. JETP*, 77:910, (1993)
6. V. P. Silin, «Introduction to the Kinetic Theory of Gases» [in Russian], Nauka, Moscow, (1971)
7. W. B. Thompson and J. Hubbard, *Rev. Mod. Phys.*, 32:714, (1960)
8. N. Rostoker, *Nucl. Fusion*, 1:101, (1960)
9. L. Chen, A. B. Langdon, and M. A. Liberman, *J. Plasma Phys.*, 9:311, (1973)
10. T. Peter, *J. Plasma Phys.*, 44:269, (1990)
11. E. M. Lifshitz and L. P. Pitaevskiy, «Physical Kinetics», Pergamon Press, Oxford, (1981)
12. D. Pines and D. Bom, *Phys. Rev.*, 85:338, (1952)
13. G. Cooper, *Phys. Fluids*, 12:2707, (1969)

THE EFFECTS OF EXCHANGE AND CORRELATION FOR ASTROPHYSICAL QUANTITIES

W. Stolzmann^{1,2} and T. Blöcker^{2,3}

¹Astrophysikalisches Institut Potsdam
Potsdam, Germany

²Institut für Astronomie und Astrophysik, Universität Kiel
Germany

³Max-Planck-Institut für Radioastronomie
Bonn, Germany

INTRODUCTION

For astrophysical applications, e.g., stellar evolution or astroseismological investigations, it is necessary to determine a set of thermodynamic functions over a wide range of densities and temperatures. This concerns the pressure P (i.e., the equation of state), the internal energy U , the isothermal compressibility $1/K_T$ (or the density exponent χ_ρ , resp.), the generalized Grüneisen coefficient (or the temperature exponent χ_T , resp.) and the isochoric specific heat C_v (or the isobaric specific heat C_p , resp.). We present for some of these quantities and further relevant parameters for astrophysical applications, as, e.g., the adiabatic gradient ∇_{ad} , a semirelativistically analytical description being valid for $T < 2 \cdot 10^9 K$ and any density. Nonideal effects due to the correlations between electrons and z -charged ions are included by Padé Approximants which cover a wide range of degeneracy and Coulomb coupling. Numerical studies and comparisons are given for fully ionized plasmas consisting of light (He) and heavy (C) elements, respectively.

THERMODYNAMIC RELATIONS

We summarize briefly some standard relations, which are frequently used to provide the thermodynamics for astrophysical applications. We have to determine all the first and second-order quantities which are related by

$$\gamma = \frac{C_p}{C_v} = 1 + \frac{\lambda_p^2}{K_T C_v T}, \quad (1)$$

with the specific heats C_v and C_p . The thermal expansion coefficient λ_p can be expressed by

$$\lambda_p = K_T C_v T \gamma_G = K_T \mathfrak{S}, \quad (2)$$

with the generalized Grüneisen coefficient

$$\gamma_G = \frac{P}{C_V T} \chi_T, \quad (3)$$

the inverse isothermal compressibility and the coefficient of strain \mathfrak{S}

$$\frac{1}{K_T} = P \chi_\rho = -V \left(\frac{\partial P}{\partial V} \right)_T, \quad \mathfrak{S} = P \chi_T = T \left(\frac{\partial P}{\partial T} \right)_V. \quad (4)$$

χ_ρ and χ_T are the “density and temperature exponents” in the equation of state.

The adiabatic temperature gradient defined by $\nabla_{\text{ad}} = (\partial \ln T / \partial \ln P)_S$ (S denotes the entropy) is given by

$$\nabla_{\text{ad}} = \frac{P}{C_p T} \lambda_p. \quad (5)$$

Starting with the Helmholtz free energy and by means of P, K_T, \mathfrak{S} and C_V we are able to calculate ∇_{ad} by Eq. (5).

THEORY AND NUMERICAL STUDIES

The Helmholtz free energy F for a fully ionized plasma is given by

$$F(T, V, N_e, N_i) = F_e^{\text{id}} + F_i^{\text{id}} + F^{\text{coul}}, \quad (6)$$

with F_a^{id} being the ideal free energy of species a and F^{coul} representing the Coulomb interaction contribution. We consider for the Coulomb contribution the following parts:

$$F^{\text{coul}} = F_{\text{ee}}^{\text{x}} + F_{\text{ee}}^{\text{c}} + F_{\text{ii}}^{\text{c}} + F_{\text{ii}}^{\text{cq}} + F_{\text{ie}}^{\text{c}}, \quad (7)$$

where x and c denote the exchange and the correlation term, resp. F_{ee} and F_{ii} correspond to the electron and the ion plasma including gaseous, fluid and solid phases. F_{ie} describes the effect of the screening between interacting ions and electrons and $F_{\text{ii}}^{\text{cq}}$ considers ionic quantum corrections. The electronic idealness and exchange are described by relativistic effects

$$F_e^{\text{id}} = \left(n_e k T \psi - \frac{2kT}{\Lambda_e^3} \left(J_{3/2}(\psi, \lambda) + \frac{5}{4} \lambda J_{5/2}(\psi, \lambda) \right) \right) V \quad (8)$$

$$n_e = \frac{2}{\Lambda_e^3} \left(J_{1/2}(\psi, \lambda) + \frac{3}{2} \lambda J_{3/2}(\psi, \lambda) \right) \quad (9)$$

$$F_{\text{ee}}^{\text{x}} = \frac{V}{(2\pi\hbar)^6} \cdot \int d^3 p_1 d^3 p_2 n_1 n_2 \varepsilon^{\text{x}}(p_1, p_2) \quad (10)$$

$$n_k = \left[\exp \left(\frac{\varepsilon_k}{kT} - \psi - \frac{1}{\lambda} \right) + 1 \right]^{-1}, \quad \varepsilon_k = mc^2 \sqrt{1 + \left(\frac{pk}{mc} \right)^2} \quad (11)$$

Electronic idealness and exchange are considered by the approximations^{1,2}

1. arbitrary degeneracy ($\psi = \mu/kT$) and weak relativity ($\lambda = kT/mc^2 < 1$)
2. strong degeneracy ($\psi > 1$) and arbitrary relativity (λ)

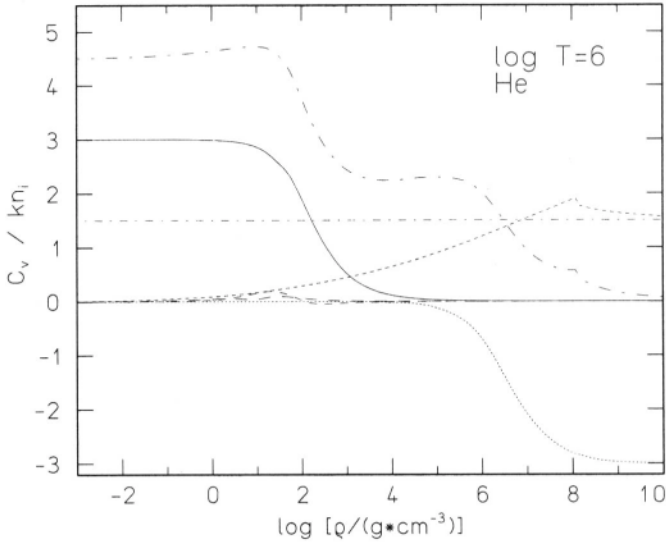


Figure 1. Contributions of the isochoric specific heat in units of $n_i k$ (n_i : ionic density, k : Boltzmann const.) for helium at $\log(T/K) = 6$. The lines refer to the ideal electrons (solid) and ions (short-dashed dotted), the electronic exchange (long-dashed), the electronic correlation (dashed), the ionic correlation (short dashed), the ionic quantum correction (dotted), and the sum of those (long-dashed dotted). The discontinuity in the the ionic correlation is caused on the fluid–solid phase transition⁴ at $\Gamma = 178$.

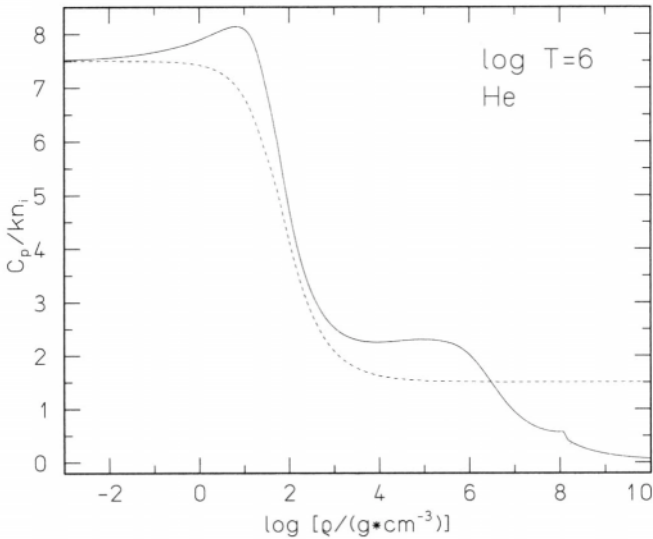


Figure 2. Isobaric specific heat for helium at $\log(T/K) = 6$ compared with the ideal behavior (dashed line).

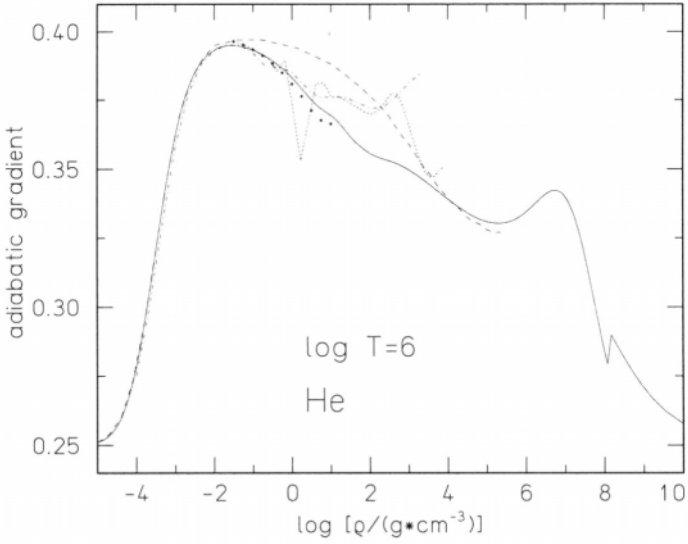


Figure 3. Adiabatic gradient ∇_{ad} for helium at $\log(T/K) = 6$ compared with the results from Rogers et al.⁵(dots), Saumon et al.⁶(dotted line), Straniero⁷(dashed line), and Fontaine et al.⁸(dashed-dotted line). The low-density limiting value $\nabla_{\text{ad}} = 1/4$ refers to the inclusion of the photon contribution in Eq. (6). The discontinuity in our curve (solid) is caused on the fluid–solid phase transition⁴ at $\Gamma = 178$.

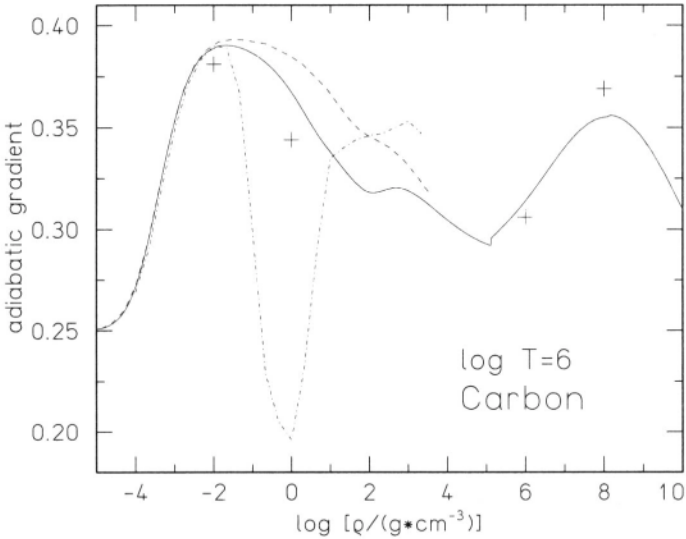


Figure 4. Adiabatic gradient ∇_{ad} for carbon at $\log(T/K) = 6$ compared with the results from Straniero⁷(dashed line), Fontaine et al.⁸(dashed-dotted line), and Lamb⁹(crosses).

The correlations F_{ee}^c , F_{ii}^c , and F_{ie}^c are taken into account by Padé Approximants² which correspond to analytical results of the perturbation theory for the weakly coupled system and to Monte-Carlo (MC) calculations for the strongly coupled plasmas.

$$f_{ee}^c = \frac{F_{ee}^c}{N_e k T} = - \frac{a_0 \Gamma_e^{3/2} - a_2 \Gamma_e^6 [\varepsilon_c(r_s, 0) + \Delta \varepsilon_c(r_s, \tau)] / \tau}{1 + a_1 \Gamma_e^{3/2} + a_2 \Gamma_e^6} \quad (12)$$

$$g_{ee}^c = \frac{\mu_{ee}^c}{k T} - \frac{s_0 \Gamma_e^{3/2} - s_2 \Gamma_e^6 [\mu_c(r_s, 0) + \Delta \mu_c(r_s, \tau)] / \tau}{1 + s_1 \Gamma_e^{3/2} + s_2 \Gamma_e^6}, \quad (13)$$

For the ion-ion correlation F_{ii}^c we construct our Padé formula from the analytical OCP result from Cohen and Murphy³ and the MC-fit from Stringfellow et al.⁴

$$f_{ii}^c = - \frac{b_0 \Gamma_{ion}^{3/2} \left(1 + b_3 \Gamma_{ion}^{3/2} (\ln \Gamma_{ion} + A_0) \right) + b_2 \Gamma_{ion}^{13/2} \varepsilon_{ii}(\Gamma_{ion})}{1 + b_1 \Gamma_{ion}^3 (\ln \Gamma_{ion} + B_0) + b_2 \Gamma_{ion}^{13/2}} \quad (14)$$

$$g_{ii}^c = - \frac{t_0 \Gamma_{ion}^{3/2} \left(1 + t_3 \Gamma_{ion}^{3/2} (\ln \Gamma_{ion} + A_0 + \frac{1}{6}) \right) + t_2 \Gamma_{ion}^{23/4} \mu_{ii}(\Gamma_{ion})}{1 - t_1 \Gamma_{ion}^3 (\ln \Gamma_{ion} + B_0 + \frac{2}{15}) + t_2 \Gamma_{ion}^{23/4}} \quad (15)$$

The ionic quantum effects, which dominates in the dense liquid and solid plasma phases are described by [10]

$$f_{ii}^{cq} = \beta \Theta_i - \frac{2}{3} D_3(\alpha \Theta_i) + 2 \ln \left[1 - e^{-\alpha \Theta_i} \right] + \ln \left[1 - e^{-\gamma \Theta_i} \right] - 3 \ln(\delta \Theta_i), \quad (16)$$

where $D_3(\eta)$ is the Debye integral and $\Theta_i = \hbar \omega_p / k T$ is the ionic quantum parameter, and β , α , γ , and δ are constants. Note, that the last term in Eq. (16) refers to the ideal ionic contribution and to the dominant part of the thermal energy in the solid phase, which is already included in Eq. (6) and Eq. (14). We derived successively the Coulomb interaction contributions as given in Eq. (7) for the first- and second-order thermodynamic quantities listed in Eqs. (1)–(5). Note, all quantities are given by analytical expressions. In Figs. 1–4 are illustrated the specific heats and the adiabatic temperature gradient for astrophysical plasma parameter. The adiabatic temperature gradient ∇_{ad} is a particularly interesting quantity for astrophysical applications since it determines essentially the Schwarzschild criterion for convective instability in stellar objects. The adiabatic gradient is a highly sensitive quantity, because it depends on first and second-order derivatives of the Helmholtz free energy (see Eq. (5)). Saumon et al.⁶ remark that their adiabatic temperature gradient is not smooth in the regime of the fully ionized plasma (see e.g., Fig. 3). Our analytical description generates a behavior without discontinuities. The high-density limit of the adiabatic gradient in this model converges on $\nabla_{ad} = 1/4$, which can be shown in analytical manner¹¹ based on the $\Gamma_{ion} \gg 1$ result from Eq. (14) and the $\Theta_i \gg 1$ expansion from Eq. (16).

REFERENCES

- [1] A. Kovetz, D. Q. Lamb and H. M. Van Horn, *Astrophys. J.* **174** (1972) 109.
- [2] W. Stolzmann and T. Blöcker, *Astron. Astrophys.* **314** (1996) 1024.
- [3] E. G. D. Cohen and T. J. Murphy, *Phys. Fluids* **12** (1969) 1404.
- [4] G. S. Stringfellow, H. E. DeWitt and W. L. Slattery, *Phys. Rev.* **A41** (1990) 1105.
- [5] F. J. Rogers, F. J. Swenson and C. A. Iglesias, *Astrophys. J.* **456** (1996) 902.
- [6] D. Saumon, G. Chabrier and H. M. Van Horn, *Astrophys. J. Suppl.* **99** (1995) 713.
- [7] O. Straniero, *Astron. Astrophys.* **76** (1988) 157.
- [8] G. Fontaine, H. C. Graboske, Jr. and H. M. Van Horn, *Astrophys. J. Suppl.* **35** (1977) 293.
- [9] D. Q. Lamb, *Ph. D. Thesis*, University of Rochester (1974).
- [10] G. Chabrier, N. W. Ashcroft and H. E. DeWitt, *Nature* **360** (1992) 48.
- [11] W. Stolzmann and T. Blöcker, (1997) in preparation.

This page intentionally left blank

DFT CALCULATIONS FOR COMPRESSED ALUMINUM: (I) K-EDGE SPECTRA OF AL FROM SOLID TO LIQUID TO PLASMA; (II) ENERGY RELAXATION IN A TWO-TEMPERATURE Al-PLASMA

M. W. C. Dharma-Wardana

National Research Council
Ottawa, Canada. K1A 0R6
E-mail: chandre@cml.phy.nrc.ca

INTRODUCTION

Short-pulse lasers have extended the study of materials to regimes which were not accessible by shock-wave techniques. The shock technique heats the ions to high temperatures while the electrons remain relatively cool due to the slow transfer of energy from the ions to the electrons. On the other hand, the laser heats the electrons while the ion subsystem remains cool for many electronic time scales. If the laser-pulse rate is slow, the electrons and ions equilibrate (within pico-second time scales) to a hot compressed phase which may be a solid, liquid or plasma depending on the amount of energy dumped into the material from the laser. Thus these experiments can test the theory of both *equilibrium* and *non-equilibrium* (non Eq.) systems.

Density function theory (DFT) provides a first-principles method for equilibrium systems. A computationally convenient form is obtained using the local density approximation(LDA) for constructing the Kohn–Sham potentials that appear in the *coupled equations* for the ions and the electrons.^{1,2} The detailed thermodynamic description of an *equilibrium* system from *first principles* is itself a very formidable problem since the atomic physics for a mixture of ionization states of ions in plasmas has to be carried out self-consistently, determining the bound states, ionization balance, equilibrium correlation functions, etc. We have recently presented such a first-principles study of the equilibrium equation of state (EOS) of Al from relatively low temperature conditions to those of high temperatures and high compressions.² It turns out that those methods can be extended to systems having two temperatures T_e and T_i , providing us a “quasi” equation of state (QEOS) for such non-Eq. systems. These are of course *not* new problems;^{3,4} and the “modern” approaches are given in Martin and Schwinger⁵ and Zubarev.⁶ We have verified our results using the Martin–Schwinger–Keldysh technique, Zubarev technique as well as the Fermi-golden rule applied within a Kohn–Sham basis.

In the experiments studied here, to a very good approximation, there are just two subsystems, i.e., electrons and one kind of ion (Al^{Z+}). Two topics are studied:

1. the shift of the K-edge (i.e, $1s \rightarrow \text{continuum}$ transition) for an Al-target passing from

solid \rightarrow *liquid* \rightarrow *plasma* for the equilibrium case where $T_e = T_i$;

2. the energy relaxation rate of the two-temperature non-equilibrium system, $T_e \neq T_i$.

In discussing the topic (i) we refer to sample calculations for more controlled systems (e.g., from semi-conductor physics and liquid-state physics, where more accurate experiments are possible) as benchmarks of the quality of our calculational methods.

THE K-EDGE OF Al^{3+} AS A FUNCTION OF THE COMPRESSION

If an electron occupying a bound state with energy ϵ_a transits to an energy state ϵ_b , the transition energy $\Delta\epsilon_{ab}$ is measurable. This line position shifts as a function of the density and temperature. Such “chemical shifts” are well known in condensed matter physics, and first-principles calculations of shifts are used to identify atoms in different environments. Thus Ref. [7] discusses the observed $2p$ -core-level spectra of an S atom on a semi-conductor surface and another type of S atom (in a different density environment) just below the top surface. The agreement between experiment and theory is excellent. Another example benchmarking our calculational methods is given in Ref. [8] where the ion-structure factor of liquid Ge is compared with neutron scattering data. Again the agreement is excellent and recovers the Kohn anomaly at $2k_F$ in a liquid structure.

However, the plasma physicists have debated whether energy levels in plasmas are shifted (blue or red), or not shifted at all. Plasma spectral lines have large linewidths which prevent the accurate determination of such shifts. The more popular theoretical efforts have used unacceptably simple models of screening, self-energy corrections, “continuum lowering” (i.e. changes in the electron-chemical potential), etc. The classic “X-ray edge” problem at $T=0$ was treated by Mahan, Nozière, de Dominicis, Combosquet (MNDC) and others.⁹ MNDC addressed the power-law structure of the X-ray edge profile but did not consider the “position” of the edge, and do not include interactions in the particle–particle (or hole–hole) channels.

In our approach we do *NOT* need to evaluate the many-body corrections to the excitation energies. In the K-edge problem the edge position inclusive of many-body effects can be calculated as a difference between the *total energies* of the final state and the initial state. This method was used by us to obtain the chemical shifts of the $2p$ -ionization of the sulphur atoms on $\text{InP}(001)\text{-S}$,⁷ and for the $1s$ -ionization (K-edge) in compressed Al. Figure 1 displays experimental results of Ng et al.,¹² as well as the calculations by Liberman(L), McMahon and Ross(MR) and ourselves (PD). The K-edge shifts to the red from its absolute value at the normal temperature 273K and density 2.7g of Al/cc (NTD). The absolute value of the K-edge at NTD (experiment) is 1560 eV, while our theoretical value is 1560.2 ± 0.5 eV. K-edge spectral profiles calculated using the Fermi golden rule applied between the initial and final Kohn–Sham states of the transition agree with experiment where experimental data are available.¹³

Now we turn to the “Kohn–Sham bonus.” In the K–S method the Hartree term is exactly treated and the continuum is exactly orthogonal to the core. This is not so in most (e.g. diagrammatic) many-body calculations. Even small errors in the Hartree problem and in orthogonality can lead to large errors in energy-shift predictions.

ENERGY RELAXATION IN A TWO-TEMPERATURE Al-PLASMA

Here we assume a two temperature system at T_e and T_i . Using the quasi-equilibrium system parameters as inputs we calculate:

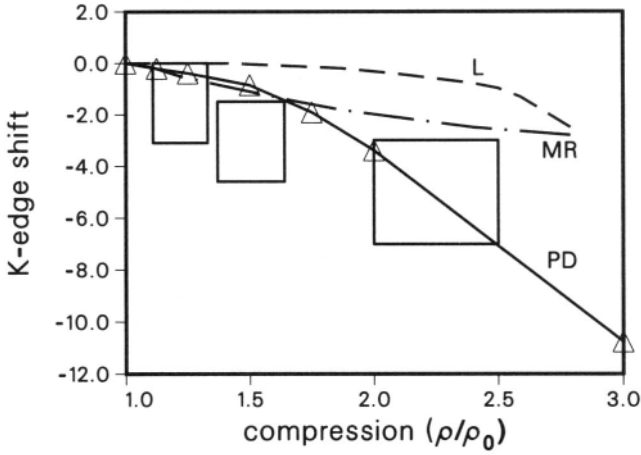


Figure 1. Calculated and experimental¹² K-edge shift from the value at normal density and temperature for Al as a function of compression. The large boxes define the experimental error bars. Our calculation is marked PD and the details are given in Ref. [10].

1. the energy relaxation using Fokker–Planck methods,
2. from the Fermi golden rule approach.

In the latter energy relaxation occurs from the normal modes of the hot subsystem to the normal modes of the cold subsystem, (rather than from encounters between hot and cold particles). Thus the calculation of the dynamic structure factors $S_e(k, \omega, T_e)$, $S_i(k, \omega, T_i)$ of the two subsystems becomes an essential step. We apply DFT to the hot electron system at its temperature T_e to determine the pseudopotentials, scattering cross sections etc., as in normal finite-T equilibrium DFT. The correlation functions of the ion subsystem are obtained from the DFT theory of the ions at its *initial* temperature T_i , since the ion-time scales are too long for these to evolve appreciably. The DFT-theory for the ions reduces to HNC theory of an approximate Kohn–Sham ion-correlation potential, as shown in our publications.²

Fokker–Planck type simplified approaches

In the single particle (non-quantum) approach we consider the kinetic energy w of a test particle, viz., $w = (1/2)mv^2$. Its rate of change, for a “Brownian-like” time scale τ is the mean change $\langle \Delta w \rangle / \tau$ arising from the velocity change $\Delta \mathbf{v}$ during the time interval τ . The velocity changes arise from collisions and can be expressed via the friction coefficient $\mathbf{F}(\mathbf{v})$ and the diffusion coefficient $\mathbf{D}(\mathbf{v})$. Thus,

$$dw/dt = \frac{m}{2} \langle |v + \Delta v(\tau)|^2 - |v|^2 \rangle / \tau \quad (1)$$

$$= m\mathbf{v} \cdot \mathbf{F}(\mathbf{v}) + \frac{m}{2} \text{Tr} \mathbf{D}(\mathbf{v}) \quad (2)$$

The friction coefficient $\mathbf{F}(\mathbf{v})$ and the diffusion-coefficient $\mathbf{D}(\mathbf{v})$ can be expressed in terms of a dielectric tensor.¹⁴ When these expressions are averaged over the particle distributions, they yield an energy relaxation rate for a system of electrons (test particles) and ions (field particles). In the high temperature limit, the result due to Spitzer is recovered.³ Here we give a form inclusive of degeneracy effects:

$$dE_e/dt = -3(m_e/M_i) \frac{2m_e \sqrt{2} \tilde{Z} \tilde{n} \ln(\Lambda)}{3(T_e/m_e + T_i/M_i)^{3/2} [1 + e^{-\mu/T_e}]} F_{1/2}(\mu/T_e) (T_e - T_i) \quad (3)$$

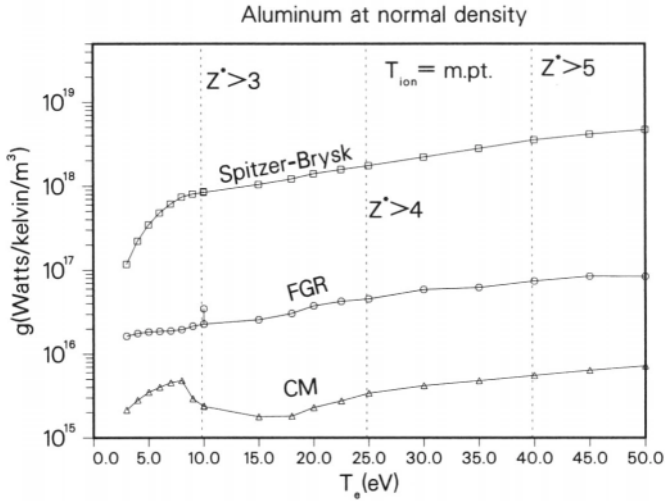


Figure 2. The energy relaxation rate calculated from various models is plotted as a coupling constant g in Watts/Kelvin/cubic meter. The curve labeled FGR is the Fermi Golden rule calculation, Eq. 4. The coupled-mode calculation is labeled CM. The Spitzer–Brysk type curve is based on Eq. 3. The value of the effective ionic charge Z^* applicable to various regimes is also indicated.

In these and other equations, T_i, T_e are in energy units. Z_i, M_i are the ion charge and mass respectively. The Coulomb logarithm $\ln(\Lambda)$ involves the ratio of the average closest distance of approach, i.e., λ_{min} and a Debye-type screening length λ_D and $F_{1/2}$ is the Fermi integral. We shall use the above equations as representative of Spitzer–Brysk type calculation of E_{rlx} .

Fermi Golden Rule Approach

In the classical Fokker–Planck approach (and in quantum self-energy approaches) the damping of a *single* test-particle was calculated first and then an average over the test-particle distribution was used to obtain an estimate of the overall relaxation rate. However, quantum mechanically, the energy relaxation rate of a subsystem with the Hamiltonian H_s is essentially $\langle \dot{H}_s \rangle$ and this is given by the commutator mean value $\langle [H_s, H] \rangle$ where H is the total Hamiltonian. Once quasiequilibrium conditions are assumed the state functions of each subsystem (at its quasiequilibrium density and temperature) are easily calculated. Then the lowest order evaluation of $\langle [H_s, H] \rangle$ reduces to a Fermi Golden Rule (FGR) calculation of the energy exchange rate between the two subsystems. The diagrammatic content and the Keldysh method of the calculation are as in Ref. [17] Here we display only the final result:

$$E_{rlx} = \int_0^\infty \omega \frac{d\omega}{2\pi} \frac{dq^3}{(2\pi)^3} |U_{ie}(\mathbf{q})|^2 [N(\omega/T_e) - N(\omega/T_i)] 4\text{Im}\chi_{ee}(q, \omega, T_e) \text{Im}\chi_{ii}(q, \omega, T_i) \quad (4)$$

Here U_{ie} is the ion–electron pseudopotential, and the spectral functions are related to the response functions χ and the dynamic structure factors in the usual manner. They are calculated as in Ref. [15]. When the electrons are hot, the E_{rlx} is the energy loss rate from electrons, and corresponds to $\langle \dot{H}_e \rangle$. This type of formula is well known in the theory of hot electrons in semiconductors.^{16,17} Thus if the spectral function is restricted to a single mode, e.g. an LO-phonon in a solid, then it describes the energy exchange between electrons and phonon mode of energy ω_q and reduces to Kogan’s formula.¹⁶

Figure 2 displays the energy relaxation rates calculated from these equations as a function of electron temperature T_e , while the ion temperature remains fixed at the m.pt. of liquid

A1. The FGR result is about an order of magnitude smaller than the estimate from the Spitzer–Brysk approach. We have also included a curve marked “cm” (coupled-mode) which goes beyond the simplest Fermi–Golden rule.¹⁷ If the time scales are such that coupled-mode formation could play a role in the energy relaxation, then the relaxation rates are further suppressed by another order of magnitude. Some of the recently available experimental results seem to favor relaxation-rate constants which are about an order of magnitude smaller than those obtained from simple theories.^{18, 19} These new results on slower energy relaxation have great significance in regard to energy relaxation in ICF-targets and other high-energy density systems.

Acknowledgements

François Perrot of the Centre d’Etudes de Limeil–Valenton, France is a principal collaborator in several aspects of this work. It is a pleasure to acknowledge many discussions with Andrew Ng and his colleagues at the University of British Columbia. Finally, we thank Professor Walter Kohn for many discussions and for making this contribution possible.

REFERENCES

- [1] M. W. C. Dharma-wardana and F. Perrot in *Density Functional Theory*, Edited by E. K. U. Gross and R. M. Dreizler (Plenum, New York) 1995 N. D. Mermin, Phys. Rev. **137**, A1441 (1965); P. Hohenberg and W. Kohn, Phys. Rev. **136**, B864 (1964); W. Kohn and L. J. Sham, Phys. Rev. **140**, A1 133 (1965).
- [2] F. Perrot and M. W. C. Dharma-wardana, Phys. Rev E. **52**, 5352 (1995)
- [3] L. Spitzer Jr., *Physics of fully ionized gases* (John Wiley, New York) 1962
- [4] H. Brysk, Plasma Phys. **16**, 927 (1974)
- [5] J. Rammer and H. Smith, Rev. Mod. Phys. **58**, 323 (1986); Landau and Lifshitz, Vol 5.
- [6] D. N. Zubarev, *Non-equilibrium Statistical Thermodynamics*, (1974)
- [7] Z. Tian, M. W. C. Dharma-wardana, Z. H. Lu, Z. H. Lu, R. Cao, and L. W. Lewis, Phys. Rev. B **55**, 5376 (1997)
- [8] F. Perrot and M. W. C. Dharma-wardana, Phys. Rev. Lett. **65**, 76 (1990)
- [9] G. D. Mahan, *Many-Particle Physics* (Plenum, New York) 1981
- [10] F. Perrot and M. W. C. Dharma-wardana, Phys. Rev. Lett. **71**, 797 (1993)
- [11] F. Perrot and M. W. C. Dharma-wardana, Phys. Rev. A **30**, 2619 (1984);
- [12] B. K. Godwal, A. Ng, L. da Silva, Y. T. Lee and D. A. Liberman, Phys. Rev A **40**, 4521 (1989)
- [13] UBC-Livermore experimental collaboration. (A. Ng, private communication).
- [14] S. Ichimaru, *Basic Principles of Plasma Physics* (Benjamin, London) 1973
- [15] F. Nadin, G. Jacucci, and M. W. C. Dharma-wardana, Phys. Rev. A **37**, 1025 (1988)
- [16] Sh. M. Kogan, Soviet Physics. Solid state **4**, 1813 (1963)
- [17] M. W. C. Dharma-wardana, Solid State Communications, **86**, 83 (1993)
- [18] P. B. Corkum, F. Brunel, and N. K. Sherman and T. Srinivasan-Rao Phys. Rev. Lett. **61** 2886 (1988)
- [19] A. Ng, P. Cellier, G. Xu, and A. Forsman, Phys. Rev. E, **52**, 4299 (1995)

This page intentionally left blank

ENSEMBLE DENSITY FUNCTIONAL APPROACH TO INHOMOGENEOUS QUANTUM HALL SYSTEMS

O. Heinonen*

Department of Physics
University of Central Florida
Orlando, FL

The quantum Hall effect (QHE) occurs in a two-dimensional electron gas (2DEG) in a strong magnetic field oriented perpendicular to the plane of the electrons.¹ In a transport measurement it is noted that at certain strengths $B^*(n)$, which depend on the density n of the 2DEG, current can flow without any dissipation. At the same time, the Hall voltage attains a quantized value for a small range of magnetic field. The effect is understood to be the result of an excitation gap in the spectrum of an infinite 2DEG at these magnetic fields. In general, the magnetic field strengths $B^*(n)$ at which the quantum Hall effect is observed are related to the density through the filling factor $\nu = 2\pi\ell_B^2 n$, with $\ell_B = \sqrt{\hbar c/(eB)}$ the magnetic length. The integer QHE² occurs at integer filling factors $\nu = 1, 2, \dots$. Here, disorder dominates the electron–electron interactions, and the energy gap is the kinetic energy gap $\hbar\omega_c = \hbar eB/(m^*c)$. The fractional QHE³ is observed at certain rational filling factors of the form $\nu = p/q$, with p and q relative primes, and q odd. In this case, electron–electron interactions dominate disorder and are the cause of the excitation gap.⁴ Therefore, any computational approach to the fractional QHE must accurately treat the electron correlations.

It is important to note that the energy gaps are only for excitations in the *bulk* of the system. When a system is bounded there *must* be gapless excitations located at the boundaries of the system.⁵ Since all experimental systems are finite and inhomogeneous, the low-energy properties probed by experiments are often determined by the gapless edge excitations. Moreover, advances in semiconductor nanofabrication technologies have led to the possibility of manufacturing systems which are extremely inhomogeneous, and in practice dominated by edges.

The spin–orbit coupling in the GaAs conduction band and the low effective mass conspire to reduce the ratio of Zeeman energy to cyclotron energy to about 0.02. As a consequence, the electron spin becomes an important dynamical variable governed by the electron–electron interactions, rather than by the Zeeman energy. Near some QHE filling factors, this also leads to rather exotic spin-charge textured excitations, called ‘skyrmions’.⁶ According to calculations by Kivelson *et al.*,⁷ charge-spin textures may also appear at the edges of QHE systems.

In order to accurately understand the experiments and inhomogeneous QHE systems in general, we must have a way of accurately calculating their properties, including electron–

*Work done in collaboration with M. I. Lubin, M. D. Johnson, and J. M. Kinaret

electron correlations and the spin degree of freedoms and which can handle inhomogeneous systems with on the order of 10^2 – 10^3 electrons. One such approach which is in principle valid for any interacting electron system is density functional theory (DFT).^{8–10} We have developed for inhomogeneous QHE systems an ensemble DFT^{11–13} scheme within the local density approximation (LDA), and have applied it to circularly symmetric quantum dots. Our calculations show that the exchange and correlation effects of the QHE are very well represented by the LDA and that our approach provides a computational scheme to model large inhomogeneous QHE systems. Recently, we have generalized our DFT approach to include spin degrees of freedom.¹³

In typical DFT calculations of systems of N_{el} electrons, the Kohn–Sham (KS) scheme is implemented, in which the particle density $n(\mathbf{r})$ is expressed in terms of a Slater determinant of $N \geq N_{\text{el}}$ KS orbitals, $\psi_\alpha(\mathbf{r})$. These obey an effective single-particle Schrödinger equation $H_{\text{eff}}\psi_\alpha = \epsilon_\alpha\psi_\alpha$, which is solved self-consistently by occupying the N_{el} KS orbitals with the lowest eigenvalues ϵ_α , and iterating. This scheme works well in practice for systems for which the true electron density can be represented by a single Slater determinant of KS orbitals. However, when the KS orbitals are degenerate at the Fermi energy there is an ambiguity in how to occupy these degenerate orbitals. This is in fact the case for general inhomogeneous QHE systems, so the KS scheme cannot be used. There exists an extension called ensemble DFT which is formally able to deal with this situation.^{9, 10} In it, the density of the system is represented by an ensemble of Slater determinants of KS orbitals. In practical ensemble DFT calculations one introduces as in the KS scheme an auxiliary non-interacting system which has a ground state density identical to the interacting system at hand. A variational principle again yields⁹ the KS equations. However, the density for N electrons is now given by $n(\mathbf{r}) = \sum_\alpha f_\alpha |\psi_\alpha(\mathbf{r})|^2$, $\sum_\alpha f_\alpha = N_{\text{el}}$, with the occupation numbers f_α in the interval $0 \leq f_\alpha \leq 1$. One obtains fractional occupancies f_α only when the corresponding KS eigenvalues ϵ_α are degenerate and equal to the Fermi energy ϵ_F . (If $\epsilon_\alpha < \epsilon_F$, then $f_\alpha = 1$.) However, there has not been available a practical computational scheme for ensemble density functional theory. A significant aspect of our work is that we have developed an ensemble scheme which is practical and useful for the study of inhomogeneous QHE systems.

To construct our LDA, we write the exchange-correlation energy per particle of a uniform electron gas in a constant magnetic field as $\epsilon_{\text{xc}}(\nu) = \epsilon_{\text{xc}}^{\text{s}}(\nu) + \epsilon_{\text{xc}}^{\text{c}}(\nu)$. Here the term $\epsilon_{\text{xc}}^{\text{s}}(\nu)$ is a smooth interpolation of the ground state energy per particle at certain rational fillings of a QHE system^{14, 15} The second one, $\epsilon_{\text{xc}}^{\text{c}}(\nu)$ contains the cusps in the ground state energy which cause the fractional QHE.

As an example, we have self-consistently solved the KS equations

$$\left\{ \frac{1}{2m^*} \left[\mathbf{p} + \frac{e}{c} \mathbf{A}(\mathbf{r}) \right]^2 + V_{\text{ext}}(\mathbf{r}) + V_{\text{H}}(\mathbf{r}) + V_{\text{xc}}(\mathbf{r}, \mathbf{B}) \right\} \psi_\alpha(\mathbf{r}) = \epsilon_\alpha \psi_\alpha(\mathbf{r}), \quad (1)$$

for a spin-polarized quantum dot in a parabolic external potential, $V_{\text{ext}}(r) = \frac{1}{2} m^* \Omega^2 r^2$, by expanding the KS orbitals in the eigenstates of $H_0 = \frac{1}{2m^*} \left(\mathbf{p} + \frac{e}{c} \mathbf{A}(\mathbf{r}) \right)^2$. The use of our LDA-DFT scheme is illustrated by a study of the edge reconstruction of the quantum dot as a function of magnetic field strength. As is known from Hartree–Fock and exact diagonalizations,^{16–19} for strong confinement the quantum dot forms a maximum density droplet in which the density is uniform at $\nu = 1$ in the interior, and falls off rapidly to zero at $r \approx \sqrt{2N} \ell_B = r_0$. As the magnetic field strength increases, a ‘lump’ of density breaks off, leaving a ‘hole’ or deficit at about $r = r_0$. As B is further increased, the correlations will cause incompressible strips with densities $\nu = p/q$ to appear^{19, 20} on the edges, and incompressible droplets to form in the bulk at densities $\nu = p/q$. Figure 1 depicts various stages of edge reconstruction obtained by us as the magnetic field strength is increased.

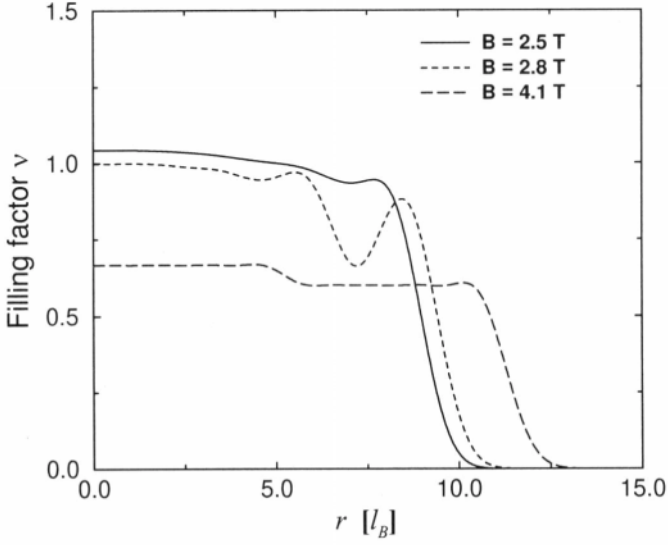


Figure 1. Edge reconstruction of a quantum dot as the magnetic field strength is increased. Plotted here is the local filling factor $\nu(r)$ for a parabolic quantum dot with $\hbar\Omega = 1.6$ meV, $\epsilon_0 = 12.4$, and 40 electrons. For magnetic field strengths $B < 2.5$ T the dot forms a maximum density droplet, and for $B \approx 3.0$ T, an exchange hole is formed. For stronger magnetic fields, incompressible regions form, separated by compressible strips.

We have begun to generalize our ensemble density functional approach to include the spin degree of freedom. In general,²¹ spin density functional theory has to be based on the single-particle density matrix $\rho_{\sigma\sigma'}(\mathbf{r}) = \langle \hat{\psi}_{\sigma}^{\dagger}(\mathbf{r})\hat{\psi}_{\sigma'}(\mathbf{r}) \rangle$, where $\hat{\psi}_{\sigma}(\mathbf{r})$ is the annihilation operator for an electron of spin σ at position \mathbf{r} . However, in the presence of a uniform external magnetic field $\mathbf{B} = B\hat{z}$, the z -component of total electron spin, \hat{S}_z commutes with the Hamiltonian, and it is a reasonable approximation to take $\rho_{\sigma\sigma'}(\mathbf{r})$ to be diagonal in the spin indices, $\rho_{\sigma\sigma'}(\mathbf{r}) = n_{\sigma}(\mathbf{r})$, with $n_{\sigma}(\mathbf{r})$ the up- and down-spin densities. To construct a LDA, the exchange-correlation energy per particle in a homogeneous system with a filling factor ν and polarization ξ now has to be approximated. Except for a few data points obtained by small system numerical diagonalizations,²² this quantity is largely unknown. In order to obtain a useful approximation, we start by considering only the exchange energy $E_x[\nu_{\uparrow}, \nu_{\downarrow}]$. We can correctly interpolate between a fully polarized systems ($\xi = 1$) and a completely un-polarized one ($\xi = 0$) by writing

$$\epsilon_x[\nu, \xi] = \epsilon_x(\nu, \xi = 1) + [\epsilon_x(\nu, \xi = 0) - \epsilon_x(\nu, \xi = 1)]f(\xi), \quad (2)$$

where

$$f(\xi) = \frac{(1 + \xi)^{3/2} + (1 - \xi)^{3/2} - 2\sqrt{2}}{2 - 2\sqrt{2}}, \quad (3)$$

in two dimensions. We then use the *same* interpolation for the correlation energy (excluding here the cusps for simplicity), and write $\epsilon_{xc}^s(\nu, \xi) = \epsilon_{xc}^s(\nu, \xi = 1) + \delta\epsilon_{xc}(\nu)f(\xi)$. The function $\delta\epsilon_{xc}(\nu)$ can be obtained by calculating the energy difference between polarized and un-polarized systems using data obtained from small system numerical diagonalizations.²²

We have applied this spin ensemble DFT to study the phase diagram of a maximum density droplet. For large values of the Landé g -factor, the maximum density droplet is fully polarized, and as the magnetic field is increased, there is an instability to forming a spin-polarized exchange-hole. But for small values of g , the instability is towards forming a spin structure at the edge. The value of g separating the spin-polarized and spin-structured

instabilities, $g/(e^2/(\epsilon_0 l_B)) \approx 0.055$, is consistent with the value found in numerical diagonalizations.²³

Preliminary results using an extension of the spin ensemble DFT which allows for non-collinear spin show that this phase diagram changes when the spin are allowed to rumble. The instability which occurs with decreasing g is now an instability in which the spin quantization axis tumbles gently as the edge is approached from the center of the droplet. This is in qualitative agreement with the results of Karlhede *et al.*⁷ and gives further evidence that the edges of QHE systems are more complicated than thought previously. The QHE continues to surprise and fascinate!

The authors would like to thank M. Ferconi, M. Geller and G. Vignale for helpful discussions, and W. Kohn, K. Burke and E. K. U Gross for useful comments about the DFT. O. H. would like to thank Chalmers Institute of Technology, where part of the work was done. This work was supported by the NSF through grant DMR96-32141.

REFERENCES

- [1] *The quantum Hall effect*, edited R. E. Prange and S. M. Girvin (Springer, New York 1987).
- [2] K. von Klitzing, G. Dorda, and M. Pepper, Phys. Rev. Lett. **45**, 494 (1980).
- [3] D. C. Tsui, H. L. Störmer, and A. C. Gossard, Phys. Rev. Lett. **48**, 1559 (1982).
- [4] R. B. Laughlin, Phys. Rev. Lett. **50**, 1395 (1983).
- [5] See, for example, A. H. MacDonald, in *Quantum Transport in Semiconductor Microstructures*, edited by B. Kramer (Kluwer Academic, 1996).
- [6] S. L. Sondhi, A. Karlhede, S. A. Kivelson, and E. H. Rezayi, Phys. Rev. B **47**, 16 419 (1993).
- [7] A. Karlhede, S. A. Kivelson, K. Lejnell, and S. I. Sondhi, Phys. Rev. Lett. **77**, 2061 (1996).
- [8] W. Kohn and P. Vashista in *Theory of the Inhomogeneous Electron Gas*, edited by S. Lundqvist and N. March (Plenum, New York, 1983).
- [9] *Density Functional Theory: an Approach to the Quantum Many-Body Problem*, by R. M. Dreizler and E. K. U Gross (Springer, Berlin 1990).
- [10] *Density-Functional Theory of Atoms and Molecules*, by R. G. Parr and W. Yang (Oxford University Press, New York, 1989).
- [11] O. Heinonen, M. I. Lubin, and M. D. Johnson, Phys. Rev. Lett. **75**, 4110 (1995).
- [12] O. Heinonen, M. I. Lubin, and M. D. Johnson, Int. J. Quantum Chem. Symp. **30**, 231 (1996).
- [13] M. I. Lubin, O. Heinonen, M. D. Johnson, to be published Phys. Rev. B Oct. 15, 1997.
- [14] D. Levesque, J. J. Weiss and A. H. MacDonald, Phys. Rev. B **30**, 1056 (1984).
- [15] G. Fano and F. Ortolani, Phys. Rev. B **37**, 8179 (1988).
- [16] A. H. MacDonald, S. R. E. Yang and M. D. Johnson. Aust. J. Phys. **46**, 345 (1993).
- [17] C. De C. Chamon and X. G. Wen, Phys. Rev. **B49**, 8227 (1994).
- [18] M. D. Johnson and A. H. MacDonald, Phys. Rev. Lett. **67**, 2060 (1991).
- [19] C. W. J. Beenakker, Phys. Rev. Lett. **64**, 216 (1990).
- [20] D. B. Chklovskii, B. I. Shklovskii, and L. I. Glazman, Phys. Rev. **B46**, 4026 (1992).
- [21] U. von Barth and L. Hedin, J. Phys C **5**, 1629 (1972).
- [22] T. Chakraborty and F. C. Zhang, Phys. Rev. B **29**, 7032 (1984).
- [23] S.-R. Eric Yang, A. H. MacDonald, and M. D. Johnson, Phys. Rev. Lett. **71**, 3194 (1993).

LOCAL AND SEMI-LOCAL DENSITY FUNCTIONAL APPROXIMATIONS FOR EXCHANGE AND CORRELATION: WHY DO THEY WORK, AND DO THEY WORK BEST AT ZERO TEMPERATURE?

John P. Perdew and Stefan Kurth

Department of Physics and Quantum Theory Group
Tulane University
New Orleans, LA

INTRODUCTION

In 1965, Kohn and Sham¹ derived exact self-consistent field equations for the ground-state ($T = 0$) energy E and electron spin densities $n_{\uparrow}(\mathbf{r})$, $n_{\downarrow}(\mathbf{r})$ of N electrons in an external potential $v(\mathbf{r})$:

$$n_{\sigma}(\mathbf{r}) = \sum_{\alpha} f_{\alpha\sigma} |\psi_{\alpha\sigma}(\mathbf{r})|^2 \quad (\sigma = \uparrow \text{ or } \downarrow) , \quad (1)$$

$$f_{\alpha\sigma} = \theta(\mu - \varepsilon_{\alpha\sigma}) , \quad (2)$$

$$\left(-\frac{1}{2}\nabla^2 + v(\mathbf{r}) + \int d^3r' \frac{n(\mathbf{r}')}{|\mathbf{r} - \mathbf{r}'|} + \frac{\delta E_{xc}}{\delta n_{\sigma}(\mathbf{r})} \right) \psi_{\alpha\sigma}(\mathbf{r}) = \varepsilon_{\alpha\sigma} \psi_{\alpha\sigma}(\mathbf{r}) , \quad (3)$$

$$E = \sum_{\alpha\sigma} f_{\alpha\sigma} \langle \psi_{\alpha\sigma} | -\frac{1}{2}\nabla^2 | \psi_{\alpha\sigma} \rangle + \int d^3r n(\mathbf{r})v(\mathbf{r}) + \frac{1}{2} \int d^3r \int d^3r' \frac{n(\mathbf{r})n(\mathbf{r}')}{|\mathbf{r} - \mathbf{r}'|} + E_{xc}[n_{\uparrow}, n_{\downarrow}] . \quad (4)$$

All equations are in atomic units ($\hbar = m = e^2 = 1$). So long as the external potential $v(\mathbf{r})$ is spin-independent, only the total density

$$n(\mathbf{r}) = n_{\uparrow}(\mathbf{r}) + n_{\downarrow}(\mathbf{r}) \quad (5)$$

is formally necessary, but approximations to the exchange-correlation energy functional E_{xc} are more successfully constructed from the separate spin densities. The chemical potential μ of Eq. (2) must be adjusted to make

$$\int d^3r n(\mathbf{r}) = N . \quad (6)$$

Kohn and Sham¹ also proposed the local spin density (LSD) approximation,

$$E_{xc}^{LSD}[n_{\uparrow}, n_{\downarrow}] = \int d^3r n(\mathbf{r}) \epsilon_{xc}(n_{\uparrow}(\mathbf{r}), n_{\downarrow}(\mathbf{r})) , \quad (7)$$

where $\epsilon_{xc}(n_{\uparrow}, n_{\downarrow})$ is the accurately-known exchange-correlation energy per particle of the uniform electron gas.² LSD is exact for densities that vary slowly over space, and is still widely and successfully used in solid state physics.^{3,4} The second-order gradient expansion approximation (GEA),

$$E_{xc}^{GEA} = E_{xc}^{LSD} + \sum_{\sigma, \sigma'} \int d^3r C_{xc}^{\sigma\sigma'} \frac{\nabla n_{\sigma} \cdot \nabla n_{\sigma'}}{n_{\sigma}^{2/3} n_{\sigma'}^{2/3}} , \quad (8)$$

is almost never used, but the generalized gradient approximation (GGA)^{5,6}

$$E_{xc}^{GGA}[n_{\uparrow}, n_{\downarrow}] = \int d^3r n \epsilon_{xc}^{GGA}(n_{\uparrow}, n_{\downarrow}, \nabla n_{\uparrow}, \nabla n_{\downarrow}) . \quad (9)$$

has been enthusiastically adopted in quantum chemistry^{3,4} (and to some extent solid state physics) since 1990. GGA reduces the errors of LSD atomization energies by about a factor of five.

Simple local (Eq. (7)) and semi-local (Eq. (9)) approximations have worked beyond all expectation. This article will summarize some old and new explanations for this success, and suggest that the high accuracy of these approximations at zero temperature may not carry over to non-zero temperature.

EXPLANATION FOR THE SUCCESS OF LOCAL AND SEMI-LOCAL APPROXIMATIONS AT ZERO TEMPERATURE

The LSD approximation of Eq. (7) is exact for densities that vary slowly over space, but the densities of real atoms, molecules, and solids are not slowly varying. If they were, the GEA of Eq. (8) would work better than LSD, but in fact it works less well.

Physical insight into the exchange-correlation energy E_{xc} is provided by the coupling-constant integration.^{7,8} Imagine a Hamiltonian \hat{H}_{λ} depending upon a parameter λ :

$$\hat{H}_{\lambda} = -\frac{1}{2} \sum_i \nabla_i^2 + \sum_i v_{\lambda}(\mathbf{r}_i) + \lambda \frac{1}{2} \sum_i \sum_{j \neq i} \frac{1}{|\mathbf{r}_i - \mathbf{r}_j|} . \quad (10)$$

The external potential v_{λ} is adjusted to keep the ground-state spin densities $n_{\uparrow}(\mathbf{r})$, $n_{\downarrow}(\mathbf{r})$ independent of λ . At $\lambda = 1$, \hat{H}_{λ} describes the real interacting system, while at $\lambda = 0$ it describes the Kohn–Sham non-interacting system.

From the ground-state wavefunction Ψ_{λ} , one can find the pair density $P_{\lambda}(\mathbf{r}, \mathbf{r}')$, defined so that $P_{\lambda}(\mathbf{r}, \mathbf{r}') d^3r d^3r'$ is the joint probability to find an electron in d^3r and another in d^3r' . If these two events were independent (as they typically are not), the pair density would factor as $P_{\lambda}(\mathbf{r}, \mathbf{r}') = n(\mathbf{r})n(\mathbf{r}')$. Instead

$$P_{\lambda}(\mathbf{r}, \mathbf{r}') = n(\mathbf{r})[n(\mathbf{r}') + n_{xc}^{\lambda}(\mathbf{r}, \mathbf{r}')] , \quad (11)$$

where $n_{xc}^{\lambda}(\mathbf{r}, \mathbf{r}')$ is the density at \mathbf{r}' of the exchange-correlation hole about an electron at \mathbf{r} . Then

$$E_{xc} = \frac{1}{2} \int d^3r n(\mathbf{r}) \int d^3r' \frac{n_{xc}(\mathbf{r}, \mathbf{r}')}{|\mathbf{r} - \mathbf{r}'|} , \quad (12)$$

where

$$n_{xc}(\mathbf{r}, \mathbf{r}') = \int_0^1 d\lambda n_{xc}^{\lambda}(\mathbf{r}, \mathbf{r}') = n_x(\mathbf{r}, \mathbf{r}') + n_c(\mathbf{r}, \mathbf{r}') . \quad (13)$$

The coupling-constant average in Eq. (13) is a trick to include the kinetic energy of correlation in a form that “looks like” a potential energy. The exchange hole n_x in Eq. (13) is the integrand in the non-interacting or $\lambda = 0$ limit. Note that electron conservation

$$\int d^3 r' P_\lambda(\mathbf{r}, \mathbf{r}') = n(\mathbf{r})[N - 1] \quad (14)$$

implies the sum rule

$$\int d^3 r' n_{xc}^\lambda(\mathbf{r}, \mathbf{r}') = -1 . \quad (15)$$

The local spin density approximation to the hole is clearly

$$n_{xc}^{LSD}(\mathbf{r}, \mathbf{r}') = n_{xc}^{unif}(n_\uparrow(\mathbf{r}), n_\downarrow(\mathbf{r}); |\mathbf{r}' - \mathbf{r}|) , \quad (16)$$

where $n_{xc}^{unif}(n_\uparrow, n_\downarrow; |\mathbf{r}' - \mathbf{r}|)$ is the hole density in an electron gas with uniform spin densities n_\uparrow, n_\downarrow . Because this is a possible physical system, its hole respects many of the same conditions as the exact hole of the real system:

(a) LSD obeys the sum rules

$$\int d^3 r' n_x(\mathbf{r}, \mathbf{r}') = -1 , \quad (17)$$

$$\int d^3 r' n_c(\mathbf{r}, \mathbf{r}') = -0 , \quad (18)$$

which constrain⁸ the integral of Eq. (12) to reasonable values.

(b) LSD respects⁹ the negativity of the exact exchange hole,

$$n_x(\mathbf{r}, \mathbf{r}') \leq 0 . \quad (19)$$

(c) The LSD “on-top” exchange hole density $n_x(\mathbf{r}, \mathbf{r})$ is exact.¹⁰ This is why accurate approximations for E_{xc} require the spin densities n_\uparrow and n_\downarrow .

(d) The LSD “on-top” correlation hole density $n_c(\mathbf{r}, \mathbf{r})$ is not exact,¹¹ but is still very accurate¹¹ and provides the “missing link” between real systems and the uniform electron gas. Because $n_{xc}(\mathbf{r}, \mathbf{r})$ is accurate in LSD, so is the Coulomb cusp of $n_{xc}(\mathbf{r}, \mathbf{r}')$.

The second-order density-gradient expansion (GEA) for the hole density improves upon LSD for small $|\mathbf{r}' - \mathbf{r}|$, but gives unphysical results for large $|\mathbf{r}' - \mathbf{r}|$.^{5,9} Because the GEA hole is a truncated expansion, and not the hole of any physical system, it violates conditions (a) and (b) above.

A non-empirical derivation of the generalized gradient approximation¹² of Eq. (9) starts from the gradient expansion of the hole density, then cuts off its spurious large- $|\mathbf{r}' - \mathbf{r}|$ contribution to restore conditions (a) and (b). Essentially the same⁴ $\epsilon_{xc}^{GGA}(n_\uparrow, n_\downarrow, \nabla n_\uparrow, \nabla n_\downarrow)$ has been derived more simply⁶ from general constraints on $E_{xc}[n_\uparrow, n_\downarrow]$, without appeal to the hole.

A hierarchy of equations which starts with LSD and proceeds through GGA will probably be completed by some fully-nonlocal approximation of high accuracy. The hole constraints (a) - (d) may find a “last hurrah” in the construction of such an approximation.

In summary, LSD and GGA work well outside their formal domain of validity because they are “conserving approximations” which retain important features of the exact exchange-correlation energy.

NON-ZERO TEMPERATURES AND OPEN SYSTEMS

Formal Kohn–Sham theory¹ was extended to open systems at non-zero temperatures by Mermin.¹³ The basic structure of Eqs. (1) - (10) is preserved, with a few changes:

1. Within the grand-canonical ensemble in the absence of an external magnetic field, $n_{\uparrow}(\mathbf{r}) = n_{\downarrow}(\mathbf{r}) = n(\mathbf{r})/2$ and $\epsilon_{\alpha\uparrow} = \epsilon_{\alpha\downarrow} = \epsilon_{\alpha}$; the exact ensemble or infinite-time average of the spin magnetization is zero even for a spontaneously-magnetized system like iron. For such a system, the LSD or GGA on-top hole density, evaluated in the infinite-time-averaged spin densities will be less accurate for the ensemble than for the pure-state density functional theory.
2. The occupation numbers become Fermi functions

$$f_{\alpha} = \frac{1}{\exp[(\epsilon_{\alpha} - \mu)/kT] + 1} . \quad (20)$$

3. Inputs such as $\epsilon_{xc}(n)$ now depend^{14, 15} upon the temperature T . Interesting applications of this formalism to metallic clusters,¹⁶ liquid metals,¹⁷ and plasmas¹⁷ have been made.

The LSD (Eq. (7)) and GGA (Eq. (9)) approximations should not be expected to work so well at non-zero T as they do at $T = 0$, because of the on-top hole problem mentioned above and because exact constraints like condition (a) of the previous section are no longer satisfied. (Partial compensation for this loss may arise from the fact that the exchange and correlation holes become more short-ranged as the temperature increases - a favorable development for LSD and GGA.)

At non-zero temperature, expectation values are taken not over a single pure state but over an ensemble of states $\Psi_{\nu\lambda}$ with probabilities $w_{\nu\lambda} = \exp[-(E_{\nu\lambda} - \mu N_{\nu})/kT]/Z$. The ensemble pair density is

$$\begin{aligned} P_{\lambda}(\mathbf{r}, \mathbf{r}') &= \sum_{\nu} w_{\nu\lambda} P_{\nu\lambda}(\mathbf{r}, \mathbf{r}') \\ &= \sum_{\nu} w_{\nu\lambda} n_{\nu\lambda}(\mathbf{r}) [n_{\nu\lambda}(\mathbf{r}') + n_{xc}^{\nu\lambda}(\mathbf{r}, \mathbf{r}')] \\ &= n(\mathbf{r}) [n(\mathbf{r}') + n_{xc}^{\lambda}(\mathbf{r}, \mathbf{r}')] , \end{aligned} \quad (21)$$

where $n(\mathbf{r}) = \sum_{\nu} w_{\nu\lambda} n_{\nu\lambda}(\mathbf{r})$. If the exchange-correlation hole density $n_{xc}^{\lambda}(\mathbf{r}, \mathbf{r}')$ for the ensemble were the same as the ensemble average of the hole density

$$\langle n_{xc}^{\lambda}(\mathbf{r}, \mathbf{r}') \rangle = \sum_{\nu} w_{\nu\lambda} n_{xc}^{\nu\lambda}(\mathbf{r}, \mathbf{r}') , \quad (22)$$

then conditions (a) and (b) of the previous section would be respected. But in fact

$$\begin{aligned} n_{xc}^{\lambda}(\mathbf{r}, \mathbf{r}') &= \langle n_{xc}^{\lambda}(\mathbf{r}, \mathbf{r}') \rangle \\ &+ \sum_{\nu} w_{\nu\lambda} \frac{[n_{\nu\lambda}(\mathbf{r}) - n(\mathbf{r})]}{n(\mathbf{r})} [n_{\nu\lambda}(\mathbf{r}') + n_{xc}^{\nu\lambda}(\mathbf{r}, \mathbf{r}')] , \end{aligned} \quad (23)$$

where

$$\int d^3 r' n_{xc}^{\lambda}(\mathbf{r}, \mathbf{r}') = -1 + \sum_{\nu} w_{\nu\lambda} \frac{n_{\nu\lambda}(\mathbf{r})}{n(\mathbf{r})} [N_{\nu} - N] . \quad (24)$$

The sum rule (24) was derived in Ref. 18. The corresponding sum rule for the energetically-important system-averaged hole is

$$\int d^3 r' \left(\frac{1}{N} \int d^3 r n(\mathbf{r}) n_{xc}^{\lambda}(\mathbf{r}, \mathbf{r}') \right) = -1 + \sum_{\nu} w_{\nu\lambda} \frac{(N_{\nu} - N)^2}{N} = -1 + kT \frac{(\partial N / \partial \mu)_{\lambda, T}}{N} . \quad (25)$$

The last term of Eq. (25) is positive for a system with fluctuating electron number, such as an ion in a plasma. The softness $(\partial N / \partial \mu)_{\lambda, T} / N$ depends upon the energy-level structure of \hat{H}_λ , is therefore not predicted exactly by LSD or GGA, and equals $(3\pi^2)^{1/3} n^{-2/3} / \pi^2 = 3 / (2kT_F)$ for a non-interacting uniform electron gas of density n in the limit $T \rightarrow 0$.

Eq. (25) also holds for a classical liquid (see Eqs. (2.28) and (2.29) of Ref. 19), and for a Bose system (see Eqs. (5.76) of Ref. 20).

Acknowledgements

This work was supported in part by the National Science Foundation under Grant No. DMR 95-21353 and in part by the Deutsche Forschungsgemeinschaft.

REFERENCES

- [1] W. Kohn and L. J. Sham, Phys. Rev. **140**, A 1133 (1965).
- [2] D. M. Ceperley and B. J. Alder, Phys. Rev. Lett. **45**, 566 (1980).
- [3] R. M. Dreizler and E. K. U. Gross, *Density Functional Theory* (Springer, Berlin, 1990).
- [4] R. G. Parr and W. Yang, *Density-Functional Theory of Atoms and Molecules* (Oxford University Press, New York, 1989).
- [5] D. C. Langreth and M. J. Mehl, Phys. Rev. B **28**, 1809 (1983).
- [6] J. P. Perdew, K. Burke, and M. Ernzerhof, Phys. Rev. Lett. **77**, 3865 (1996), and references therein. Erratum **78**, 1396(1997).
- [7] D. C. Langreth and J. P. Perdew, Solid State Commun. **17**, 1425 (1975).
- [8] O. Gunnarsson and B. I. Lundqvist, Phys. Rev. B **13**, 4274 (1976).
- [9] J. P. Perdew, Phys. Rev. Lett. **55**, 1665 (1985).
- [10] T. Ziegler, A. Rauk, and E. J. Baerends, Theoret. Chim. Acta **43**, 261 (1977).
- [11] K. Burke, J. P. Perdew, and D. C. Langreth, Phys. Rev. Lett. **73**, 1283 (1994).
- [12] J. P. Perdew, K. Burke, and Y. Wang, Phys. Rev. B **54**, 16533 (1996).
- [13] N. D. Mermin, Phys. Rev. **137**, A 1441 (1965).
- [14] U. Gupta and A. K. Rajagopal, Phys. Rev. A **22**, 2792 (1988).
- [15] U. Gupta and A. K. Rajagopal, Phys. Rep. **87**, 259 (1982).
- [16] M. Brack, O. Genzken, and K. Hansen, Z. Phys. D **21**, 65 (1991).
- [17] C. Dharma-wardana and F. Perrot, in *Density Functional Theory*, Vol. B337 of *NATO ASI Series*, edited by E. K. U. Gross and R. Dreizler (Plenum, New York, 1995), p. 625.
- [18] J. P. Perdew, in *Density Functional Methods in Physics*, Vol. B123 of *NATO ASI Series*, edited by R. M. Dreizler and J. da Providencia (Plenum, New York, 1985), p. 265.
- [19] P. A. Egelstaff, *An Introduction to the Liquid State* (Academic Press, London, 1967).
- [20] A. K. Rajagopal, Adv. in Chem. Phys. **41**, 59 (1980).

This page intentionally left blank

THE AVERAGE ATOM MODEL AND THE DENSITY FUNCTIONAL THEORY USING FUNCTIONAL INTEGRALS

G. Faussurier

Commissariat à l'Energie Atomique
94195 Villeneuve St Georges Cedex
France

INTRODUCTION

Functional integrals (Negele and Orland, 1988) and the notion of Legendre transformation can be used to formulate the average-atom model (Rozsnyai, 1972) and the density functional theory (Dreizler and Gross, 1990) in the same formalism, stressing their common theoretical base. The integral representation is not unique and a large variety of models can be generated like the Hartree, Fock, or Hartree-Fock average-atom models. Particularly, the Kohn and Sham equations are proven to appear naturally by performing a saddle-point evaluation of a specific functional integral.

THE AVERAGE-ATOM MODEL

Using coherent states, the grand canonical partition function Z_G of a nonrelativistic atomic system can be written (with self-explanatory compact notations) as a

functional integral ($V^1(x) = -\frac{Ze^2}{|x|} + v(x)$, $V(x-y) = \frac{e^2}{|x-y|}$):

$$Z_G = \int \mathcal{D}[\phi^*, \phi] e^{-\phi^* \left(\partial_t - \frac{\nabla^2}{2m} + V^1 - \mu \right) \phi - \frac{1}{2} \phi^* \phi \cdot \nabla \phi \phi}$$

m , e , Z , μ , and v are respectively the mass and the charge of the electron, the nuclear number, the chemical potential, and an additional external potential to the electron system.

By introducing an auxiliary bosonic field, $\frac{1}{2} \phi^* \phi \cdot \nabla \phi \phi$ can be eliminated and the integration over the Grassmann variables $[\phi^*, \phi]$ performed:

$Z_G = \int \frac{DU}{N} e^{-S[U]} = \int \frac{DU}{N} e^{\frac{1}{2} UV^{-1}U} Z_G^{ind}[U]$, where $Z_G^{ind}[U]$ is the partition function of an

independent-electron gas in the external potential U and $N = \int DU e^{\frac{1}{2} UV^{-1}U}$. The saddle-

point evaluation of Z_G becomes then possible. By considering only time-independent solutions, the stationary condition on $S[U]$ reduces to the finite-temperature Hartree equations where $f_\alpha = \frac{1}{1 + e^{\beta(\epsilon_\alpha - \mu)}}$ (β is the inverse temperature):

$$\left[-\frac{\nabla^2}{2m} + V^T(\mathbf{x}) + \int dy V(\mathbf{x} - \mathbf{y}) \sum_\alpha f_\alpha |\varphi_\alpha(\mathbf{y})|^2 \right] \varphi_\alpha(\mathbf{x}) = \epsilon_\alpha \varphi_\alpha(\mathbf{x}).$$

These mean-field equations, which have to be solved self-consistently, constitute a generalization of the screened-hydrogenic average-atom equations (Faussurier et al., 1997). The flexibility concerning the choice of the functional-integral representation can be used to generate a large variety of mean-field expansion (Hartree, Fock, Hartree-Fock, ...). The functional-integral technique is equivalent to the operator formalism (Fetter, 1971; Le Bellac, 1996); it offers perhaps a clearer insight of the problem and of the selected approximations.

THE DENSITY FUNCTIONAL THEORY (DFT)

The DFT is one of the most commonly used methods in studying various many-particle systems. In this formalism, the ground-state energy of the system at zero temperature (or the grand canonical potential at finite temperature) is written as a functional of the density. For a N -particle system, the particle density $n(\mathbf{x})$ and its associated calculational scheme is preferred to the complicated wave-function $\Psi(\mathbf{x}_1, \dots, \mathbf{x}_N)$ and the associated Schroedinger-equation. The connection of the DFT with other many-body methods (like the average-atom model) can be stressed by formulating it in terms of Legendre transformation and functional integrals (Fukuda et al., 1994). Only finite temperature case is presented in this paper.

Let us introduce a time-independent source J in the general expression of Z_G :

$$Z_G[J] = e^{-\beta\Omega[J]} = \int D[\phi^*, \phi] e^{-\phi^* \left(\partial_t - \frac{\nabla^2}{2m} + V^T - \mu \right) \phi - \frac{1}{2} \phi^* \phi^* \nabla \phi - J \phi^* \phi}$$

By functionally deriving with respect to J , the particle density n is equal to $n = \frac{\delta\Omega[J]}{\delta J} = n[J]$. Since n appears to be a functional of J , a Legendre transformation is performed in order to express the quantities of interest with respect to n :

$$\Gamma[n] \equiv \Omega[J] - Jn.$$

It is then straightforward to show that the physical density n is solution of the equation

$$\frac{\delta\Gamma[n]}{\delta n} \Big|_{J=0} = 0.$$

An explicit expression of $\Gamma[n]$ can be found by noting that $\Omega[J]$ is more precisely a functional of $J + V^T$. Consequently, $\Omega[J] = \Omega[J + V^T]$ and $n = n[J + V^T]$; $\Gamma[n]$ can thus be rewritten as

$$\begin{cases} \Gamma[\mathbf{n}] = F[\mathbf{n}] + \mathbf{V}^T \mathbf{n} \\ F[\mathbf{n}] \equiv \Omega[\mathbf{J} + \mathbf{V}^T] - (\mathbf{J} + \mathbf{V}^T) \mathbf{n}. \end{cases}$$

$F[\mathbf{n}]$ is a universal functional of \mathbf{n} which does not depend on the external potential \mathbf{V}^T . The key problem is the inversion of the functional relation $\mathbf{J} + \mathbf{V}^T = (\mathbf{J} + \mathbf{V}^T) \mathbf{n}$.

In order to avoid this complicated inversion to extract \mathbf{n} by minimizing $\Gamma[\mathbf{n}]$, the method of auxiliary field and saddle-point method is very convenient (Valiev et al., 1996). Moreover, it allows to clearly connect the aforementioned average-atom model and the DFT. Introducing a bosonic auxiliary field as was done in the previous chapter, $\Omega[\mathbf{J}]$ can be expressed as $\Omega[\mathbf{J}] = W[\mathbf{J}] - \frac{1}{2} \mathbf{J} \mathbf{V}^{-1} \mathbf{J}$ where

$$e^{-\beta W[\mathbf{J}]} = \frac{\int D\sigma e^{\frac{1}{2} \sigma \mathbf{V} \sigma - \sigma \mathbf{J} + \text{Tr} \ln \left[\partial_\tau - \frac{\nabla^2}{2m} + \mathbf{V}^T + \mathbf{V} \sigma - \mu \right]}}{\int D\sigma e^{\frac{1}{2} \sigma \mathbf{V} \sigma}}.$$

As long as the term source is equal to zero, $\Omega[\mathbf{J}]$ and $W[\mathbf{J}]$ describes the same physics.

$$\text{For instance, } \mathbf{n} = \frac{\delta \Omega[\mathbf{J}]}{\delta \mathbf{J}} \Big|_{\mathbf{J}=0} = \frac{\delta W[\mathbf{J}]}{\delta \mathbf{J}} \Big|_{\mathbf{J}=0} = \langle \sigma \rangle.$$

By estimating $e^{-\beta W[\mathbf{J}]}$ with the saddle-point method and keeping only the dominant term, it is easy to get a first approximate expression of the physical particle density \mathbf{n} in terms of the one-electron wave-functions of the Hartree average-atom equations, namely

$$n(\mathbf{x}) \approx \sum_{\alpha} \frac{|\phi_{\alpha}(\mathbf{x})|^2}{1 + e^{\beta(\epsilon_{\alpha} - \mu)}}.$$

The Kohn and Sham equations can be found in the same spirit. By suppressing the source term, performing a translation in order to integrate on the deviation with respect to \mathbf{n} , and rescaling the variable of integration, Z_G reduces to

$$Z_G = e^{\frac{1}{2} n \mathbf{V} n} \frac{\int D\phi e^{\frac{1}{2} \phi \mathbf{V}^{-1} \phi + \phi n + \text{Tr} \ln \left[\partial_\tau - \frac{\nabla^2}{2m} + \mathbf{V}^T + \mathbf{V} n + \phi - \mu \right]}}{\int D\phi e^{\frac{1}{2} \phi \mathbf{V}^{-1} \phi}}.$$

The last step consists in developing the term $\text{Tr} \ln[\dots]$ by choosing a reference potential ϕ_{xc} in order to cancel the linear term ϕn in the functional integral. By introducing G_{xc} , which is the inverse operator of $\left[\partial_\tau - \frac{\nabla^2}{2m} + \mathbf{V}^T + \mathbf{V} n + \phi_{xc} - \mu \right]$, we get an exact expression of the grand canonical potential as a functional of the true particle density \mathbf{n} ($\delta \phi = \phi - \phi_{xc}$):

$$\Omega = -\frac{1}{2} n \mathbf{V} n - \phi_{xc} n - \frac{1}{\beta} \text{Tr} \ln(G_{xc}^{-1}) + \Omega_{xc}$$

with

$$\left\{ \begin{array}{l} S_{xc}[\phi] \equiv -\frac{1}{2} \phi V^{-1} \phi + \sum_{n=2}^{\infty} \frac{(-1)^n}{n} \text{Tr} \ln(G_{xc} \delta \phi) \\ e^{-\beta \Omega_{xc}} \equiv \frac{\int D\phi e^{-S_{xc}[\phi]}}{\int D\phi e^{\frac{1}{2} \phi V^{-1} \phi}} \end{array} \right.$$

and

$$\left\{ \begin{array}{l} \left(-\frac{\nabla^2}{2m} + V^T(\mathbf{x}) + \phi_{xc}(\mathbf{x}) + \int dy V(\mathbf{x}-y) n(y) \right) \varphi_{\alpha}(\mathbf{x}) = \epsilon_{\alpha} \varphi_{\alpha}(\mathbf{x}) \\ n(\mathbf{x}) = \sum_{\alpha} \frac{|\varphi_{\alpha}(\mathbf{x})|^2}{1 + e^{\beta(\epsilon_{\alpha} - \mu)}}, \quad \phi_{xc}(\mathbf{x}) = \frac{\delta \Omega_{xc}[\mathbf{n}]}{\delta n(\mathbf{x})}. \end{array} \right.$$

This shows the deep connection between the density functional theory and the average-atom model. Exact formula for the grand potential at finite temperature (and the ground state energy at zero temperature) can be obtained in terms of the density n without explicitly inverting the functional relation between $J + V^T$ and n . The exchange-correlation potential ϕ_{xc} plays the role of a trial one-body potential to start the saddle-point expansion of Z_G . It has the specific property to express the true density of the interacting many-particle system of interest in terms of the density of a noninteracting particle system.

CONCLUSION

In LTE, the average-atom model and the density functional theory can be expressed in the framework of functional integrals. Both models can be obtained by expanding the grand canonical partition function of the system of interest with the saddle-point method. The next step is to compare this method to a variational principle (Feynman, 1972; Balian et al., 1981) that can also be used to obtain self-consistent mean-field equations. It could be interesting to extend them to treat NLTE situations, as yet to be done by considering a screened-hydrogenic model (Mirone et al., 1997; Daltot et al., 1997).

REFERENCES

1. Negele J. H. and Orland H., 1988, "Quantum Many-Particle Systems", Addison-Wesley, New York.
2. Rozsnyai B. F., 1972, *Phys. Rev.* A5:1137.
3. Dreizler R. M. and Gross E. K. U., 1990, "Density Functional Theory", Springer-Verlag, Berlin.
4. Faussurier G., Blancard C, and A. Decoster, 1997, *Phys. Rev. E* (accepted for publication).
5. Fetter A. L. and Walecka J. D., 1971, "Quantum Theory of Many-Particle Systems". MacGraw Hill, New York.
6. Le Bellac, 1996, "Thermal Field Theory", Cambridge University Press, Cambridge.
7. Fukuda R., Kotani T., Suzuki Y., and Yokojima S., 1994, *Prog. Theor. Phys.* 92:833.
8. Valiev M. and Fernando G. W., 1996, *Phys. Rev.* B54:7765.
9. Feynman R. P., 1972, "Statistical Mechanics: A Set of Lectures", Addison-Wesley, New York.
10. Balian R. and Vénéroni M., 1981, *Phys. Rev. Lett.* 47:1353, 1765(E).

11. Mirone A., Gilleron F., Gauthier J. C., and Faussurier G., 1997, *JQSRT* (submitted for publication).
12. Dallot P., Faussurier G., Decoster A., and Mirone A, 1997, *Phys. Rev. E* (submitted for publication).

This page intentionally left blank

DENSITY FUNCTIONAL THEORY FOR STRICTLY CORRELATED ELECTRONS: AN EXACT FUNCTIONAL FOR SPHERICALLY SYMMETRIC TWO-ELECTRON SYSTEMS

Michael Seidl

Department of Physics and Quantum Theory Group
Tulane University, New Orleans, LA

1. INTRODUCTION

We introduce the concept of strictly correlated electrons to model the limit of infinitely strong interaction. In density functional theory (DFT),¹ this limit provides important information for the ground-state energies of realistic electron systems. Resulting from the Hellman–Feynman theorem,² the coupling-constant integration formula³

$$E_{xc}[\rho] = \int_0^1 d\alpha e_\alpha[\rho], \quad e_\alpha[\rho] = \langle \Psi^\alpha[\rho] | \hat{V}_{ee} | \Psi^\alpha[\rho] \rangle - U[\rho]. \quad (1)$$

is an exact relation for the explicitly unknown functional $E_{xc}[\rho]$ of the exchange-correlation energy.¹ \hat{V}_{ee} is the operator of the realistic electron–electron interaction and

$$U[\rho] = \frac{1}{2} \int d^3r \int d^3r' \rho(\mathbf{r})\rho(\mathbf{r}')/|\mathbf{r} - \mathbf{r}'|$$

is the Hartree–Coulomb energy. $\Psi^\alpha[\rho]$ is the wave function which minimizes the total energy of a fictive electron system with interaction $\alpha\hat{V}_{ee}$ subject to the constraint that it has the ground-state density ρ of the realistic system with coupling-constant $\alpha = 1$. Since exact properties of the integrand function $e_\alpha[\rho]$ are known, Eq. (1) can be utilized to improve an approximate value of $E_{xc}[\rho]$.

Fig. 1 shows a model for $e_\alpha[\rho]$ for the ground-state density ρ of the Helium atom. At $\alpha = 0$, where the interaction is completely turned off, $\Psi^{\alpha=0}[\rho]$ is the ground-state wave function of non-interacting electrons in the external potential of the Kohn–Sham (KS) equations.^{1, 4} Therefore, $e_{\alpha=0}[\rho]$ is the exchange-energy functional of DFT, $e_0[\rho] = E_x[\rho]$, explicitly given by the Fock integral with the KS orbitals. Thus, for any density ρ which has been obtained as a solution of the KS equations, $e_0[\rho]$ is known accurately. According to Görling–Levy perturbation theory,⁶ also the initial slope $e'_0[\rho] = (de_\alpha[\rho]/d\alpha)_{\alpha=0} < 0$ of the function $e_\alpha[\rho]$ can be evaluated in terms of the KS orbitals φ_i and eigenvalues ϵ_i .⁵

The function $e_\alpha[\rho]$, always starting out with a negative slope $e'_0[\rho] < 0$ at $\alpha = 0$, approaches asymptotically a constant value $e_\infty[\rho]$ as $\alpha \rightarrow \infty$,^{7, 8} see Fig. 1. To account for the

resulting curvature of $e_\alpha[\rho]$, we need to know the numerical value of $e_\infty[\rho]$. In section 2, we model the strong-interacting limit $\alpha \rightarrow \infty$ by the concept of strictly correlated electrons (*see*). The resulting functional for $e_\infty[\rho]$ is employed in section 3 to predict by Eq. (1) accurate exchange-correlation energies for realistic two-electron ions. In contrast to earlier work,⁵ the present approach requires information on $e_\alpha[\rho]$ only for the non-interacting ($\alpha = 0$) and the infinitely-strong interaction ($\alpha = \infty$) limits.

2. STRICTLY CORRELATED SPHERICAL TWO-ELECTRON SYSTEMS

In the strong-interaction limit of DFT, electrons are expected to be strongly correlated. We solve here the problem of two strictly correlated electrons with a given spherical density distribution $\rho(r)$. By “strict correlation” we mean that the position \mathbf{r}_2 of the second electron is completely fixed by the position \mathbf{r}_1 of the first one,

$$\mathbf{r}_2 = \mathbf{f}(\mathbf{r}_1) = -\frac{\mathbf{r}_1}{r_1} f(r_1). \quad (2)$$

According to the spherical symmetry, the vector \mathbf{r}_2 in (2) has the opposite direction of \mathbf{r}_1 . Thus, the angle between the electrons is always 180° and $r_2 = |\mathbf{r}_2|$ is a certain function of $r_1 = |\mathbf{r}_1|$: $r_2 = f(r_1)$. Since the electrons are identical particles, we also have $r_1 = f(r_2) = f(f(r_1))$. Therefore, the function f has the property $f(f(r)) = r$ or $f(r) \equiv f^{-1}(r)$. This implies that either $f(r) \equiv r$ or f is monotonically decreasing. We exclude the choice $f(r) \equiv r$ which would allow the strongly interacting electrons to come infinitely close to each other at $r = 0$. The graph of the function $y = f(x)$ is always symmetric with respect to the diagonal line $y=x$.

2.1. The correlation function $f(r)$

We will now show that the “correlation” function $f(r)$ is fixed by the given spherical density $\rho(r)$. Since $f(r)$ is monotonically decreasing, the probability to find electron 1 inside the sphere with radius r is equal to the probability that electron 2 is outside the sphere with radius $f(r)$:

$$\int_0^r du u^2 \rho(u) = \int_{f(r)}^\infty du u^2 \rho(u). \quad (3)$$

If these integrals can be evaluated explicitly, we obtain an analytic equation for $f(r)$. Differentiating (3) with respect to r yields the non-linear first-order differential equation

$$f'(r) = -\frac{r^2 \rho(r)}{f(r)^2 \rho(f(r))} \quad (4)$$

for $f(r)$. The starting condition for numerical integration of (4) is $f(r_0) = r_0$ where, due to (3), r_0 is obtained from

$$\int_0^{r_0} dr r^2 \rho(r) = \int_{r_0}^\infty dr r^2 \rho(r) = \frac{1}{2} \int_0^\infty dr r^2 \rho(r). \quad (5)$$

According to the differential equation (4), in conjunction with the starting condition $f(r_0) = r_0$, the function $f(r)$ is completely determined by the given density $\rho(r)$. Note that $f(r)$ does not depend on the particular form of the electronic repulsion \hat{V}_{ee} . Our results are valid for fermions with any kind of repulsive interaction \hat{V}_{int} .

2.2. The interaction-energy functional

In these strictly correlated systems, the distance $|\mathbf{r}_1 - \mathbf{r}_2|$ between the two electrons is $r + f(r)$, where $r = |\mathbf{r}_1|$. Averaging over the position \mathbf{r}_1 of the first electron with the correctly normalized probability distribution $\frac{1}{2}\rho(\mathbf{r}_1)$, we find

$$V_{ee}^{sce}[\rho] = \int d^3r \frac{\frac{1}{2}\rho(r)}{r+f(r)} = 2\pi \int_0^\infty dr \frac{r^2 \rho(r)}{r+f(r)} \quad (6)$$

for the expectation value $\langle \hat{V}_{ee} \rangle$. Since the function $f(r)$ is fixed by the density $\rho(r)$, Eq. (6) is the exact density functional for the interaction energy of strictly correlated, spherical two-electron systems.

Subtracting the Hartree energy $U[\rho]$, we explicitly obtain the exact density functional

$$e^{sce}[\rho] = V_{ee}^{sce}[\rho] - U[\rho], \quad (7)$$

which is a model for the functional $e_\alpha[\rho]$ in Eq. (1) in the limit $\alpha \rightarrow \infty$ of infinitely strong interaction.

3. APPLICATION TO REALISTIC TWO-ELECTRON SYSTEMS

For an accurate ground-state density ρ_{He} of the He atom,¹⁰ we have solved the differential equation (4) for the correlation function $f(r)$. Evaluating the functional (7) yields the estimate (in hartrees)

$$e_{\alpha \rightarrow \infty}[\rho_{He}] \approx e_{sce}[\rho_{He}] = -1.5000. \quad (8)$$

This asymptotic value is represented by the horizontal dashed line in Fig. 1. For large α , we expect the asymptotic behavior $e_\alpha[\rho] = e_\infty[\rho] + O(\alpha^{-1/2})^9$ for the unknown integrand in Eq. (1). Therefore, we model $e_\alpha[\rho]$ by the interpolation formula

$$e_\alpha^R[\rho] = e_\infty + \frac{e_0 - e_\infty}{\sqrt{1 + 2c\alpha}}, \quad c = \frac{e'_0}{e_\infty - e_0}, \quad (9)$$

using the result (8) for the asymptotic value e_∞ of this function. For the initial value at $\alpha = 0$, we use the exact exchange energy $e_0 = -1.0246^{12}$ of the He atom. For the initial slope, we employ the accurate value $e'_0 = -0.1006$,¹¹ from Görling–Levy perturbation theory for Helium.

The resulting function (9) is plotted as solid curve in Fig. 1. Performing the coupling-constant integration (1) over this function, we easily obtain the accurate approximation $E_{xc}^R = \int_0^1 d\alpha e_\alpha^R[\rho_{He}] = -1.0664$ for the exact xc energy $E_{xc} = -1.066676^{12}$ of the He atom. Ignoring the information (8) on the asymptotic value of $e_\alpha[\rho]$, we find by linear extrapolation the less accurate approximation $E_{xc}^L = \int_0^1 d\alpha (e_0 + \alpha e'_0) = -1.0762$. Table 1 summarizes our results for the He atom and the two-electron ions Be^{2+} and Ne^{8+} . We have employed the accurate Hartree–Fock densities ρ of Ref. [10]. In column 3, $e'_0[\rho] = -0.093326$ is the exact slope¹³ for any exponential two-electron density $\rho \sim \exp(-\lambda r)$. It is a good approximation to the exact densities of heavy two-electron ions, where the Kohn–Sham orbitals are expected to become hydrogen-like wave functions.

Our result for the He atom is very satisfying. For Be^{2+} , which is still similar to He, we expect the exact slope e'_0 to be more negative than the value -0.093326 for an exponential density. For the heavier ion Ne^{8+} , however, this value for the slope appears to be quite a good approximation. A generalization of the present approach to systems with more than two electrons and/or with less than spherical symmetry is under preparation.

Table 1. Exchange energies e_0 ,¹² slopes e'_0 ,^{11,13} and the values $e^{scc}[\rho]$ from Eq. (7) for different two-electron ions. $e^{scc}[\rho]$ is calculated from accurate Hartree–Fock densities.¹⁰ The approximations E_{xc}^L and E_{xc}^R to the exchange–correlation energy are obtained by linear extrapolation and, respectively, by integrating interpolation formula (9). The exact E_{xc} values are taken from Ref. [12]. All energies are in hartrees. (1 hartree = 27.21 eV.)

system	e_0	e'_0	$e^{scc}[\rho] \approx e_\infty$	E_{xc}^L	E_{xc}^R	$E_{xc}(\text{exact})$
He	-1.0246	-0.1006	-1.500	-1.0749	-1.0664	-1.0667
Be ²⁺	-2.2766	-0.093326	-3.324	-2.3233	-2.3195	-2.3209
Ne ⁸⁺	-6.0275	-0.093326	-8.795	-6.0742	-6.0727	-6.0732

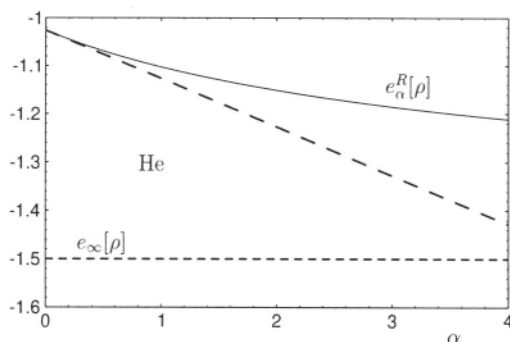


Figure 1. The approximation (9) (solid line) to the integrand $e_\alpha[\rho]$ of Eq. (1) for the ground-state density $\rho = \rho_{He}$ of the Helium atom, plotted (in hartrees) versus the coupling constant α . $e_\alpha^R[\rho]$ approaches the asymptotic value $e_\infty[\rho]$ as $\alpha \rightarrow \infty$, which is modelled here by the value (8) from the theory of strictly correlated electrons.

Acknowledgements

I want to thank Matthias Ernzerhof, Stanislav Ivanov, Mel Levy, and John P. Perdew for interesting discussions. This work was supported by the Deutsche Forschungsgemeinschaft (DFG), and by the National Science Foundation under Grant No. DMR 95-21353.

REFERENCES

- [1] R. G. Parr and W. Yang, *Density-Functional Theory of Atoms and Molecules* (Oxford University Press, New York, 1989)
- [2] For a discussion of the origin of the Hellman–Feynman theorem, see J. I. Musher, *Am. J. Phys.* **34**, 267 (1966)
- [3] D. C. Langreth and J. P. Perdew, *Solid State Commun.* **17**, 1425 (1975)
- [4] W. Kohn and L. J. Sham, *Phys. Rev.* **140**, A1133 (1965)
- [5] M. Ernzerhof, *Chem. Phys. Lett.* **263**, 499 (1996)
- [6] A. Görling and M. Levy, *Phys. Rev. B* **47**, 13 105 (1993)
- [7] E. H. Lieb and S. Oxford, *Int. J. Quantum Chem.* **19**, 427 (1981)
- [8] M. Levy and J. P. Perdew, *Phys. Rev. B* **48**, 11 638 (1993)
- [9] J. P. Perdew, M. Ernzerhof, A. Zupan, and K. Burke, *J. Chem. Phys.*, to appear
- [10] E. Clementi and C. Roetti, *Atomic Data and Nuclear Data Tables* **14**, 177 (1974)
- [11] M. Ernzerhof, *private communication*
- [12] C. J. Umrigar and X. Gonze, *Phys. Rev. A* **50** 3827 (1994)
- [13] S. Ivanov, *private communication*

EQUATION OF STATE OF SHOCK COMPRESSED PLASMA OF METALS

V. E. Fortov¹, V. K. Gryaznov¹, I. L. Iosilevski²,
R. F. Trunin³, M. V. Zhernokletov³, G. Simakov³, L. Trusov³

¹Institute of Chemical Physics in Chernogolovka, 142432, Russia

²Moscow Institute of Physics and Technology, Dolgoprudny 141700, Russia

³All-Russian Research Institute of Experim. Physics, 607200, Sarov, Russia

INTRODUCTION

Thermodynamics and equation of state (EOS) of strongly compressed plasmas are of great interest for understanding of processes in inertial confinement fusion, astrophysics and many other applications. The last of decade shock-wave experiments on metals gave many new results [1]. Now experimental data covers a wide area of phase diagram, which can be quite interesting for theoretical study. For example this area lies in the region where metal-dielectric transition is known to occur. One of well-known approaches to investigation of strongly interacted systems is chemical model [2]. As a rule, this approach is used for gas-like plasma with weak or moderate coupling [3-9]. In this work we will extrapolate chemical model to the region of expanded metals ($T \geq 10^4$ K, $P \geq 10^5$ bar, $\rho = 0.1 \dots 1 \rho_0$), to compare calculated data with shock-wave experiments and to study different plasma effects on EOS of shock-compressed metals. Fig. 1 demonstrates the region of phase diagram under interest, which is covered by shock-wave experiments.

THERMODYNAMIC MODEL

In accordance with the chemical picture [2], we consider multi-component strongly coupled plasmas as a mixture of electrons, atoms and ions of different charges interacting with one another. In terms of chemical model free energy of such a system is splitted into two parts: the ideal-gas contribution of atoms, ions and electrons and term responsible for inter-particle interactions:

$$F \equiv F_i^{(id)} + F_e^{(id)} + F_{ii,ie,ee,\dots}^{(int)} \quad (1)$$

Atoms and ions obey Boltzmann statistics and their contribution takes the well-known form:

$$F_i^{(id)} = \sum_j N_j k_B T \left(\ln \frac{n_j \lambda_j^3}{Q_j} - 1 \right), \quad (2)$$

where k_B - Boltzmann constant, λ_j - thermal de-Broglie wave length and Q_j - internal partition function of atoms and ions. In this work we set all partition functions to be equal to the weight of their ground states.

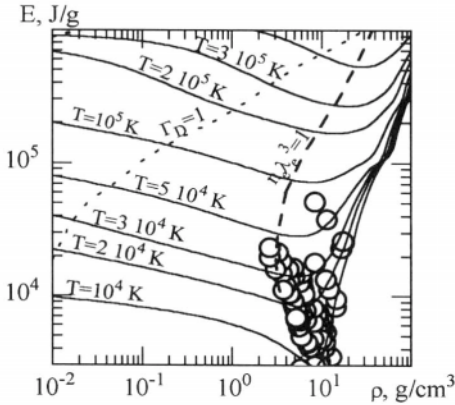


Figure 1. E - ρ diagram of Nickel. Solid lines are isotherms. Dotted line and dashed line are curves where coupling parameter and degeneracy parameter are constant. Circles - experimental results [1].

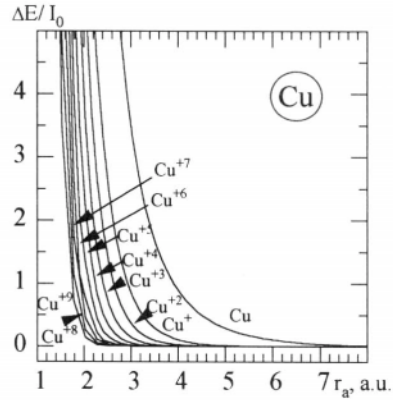


Figure 2. Energy level shifts vs. radius of spherical cell for ground states of Cu atom and ions $\text{Cu}^+ - \text{Cu}^{49}$. Hartree-Fock calculation [8]

ELECTRON DEGENERACY

We consider electrons as a partially degenerated ideal Fermi-gas:

$$F_e^{(id)} = \frac{2Vk_B T}{\pi^{1/2} \lambda_e^3} \left[I_{1/2}(\alpha_e) - \frac{2}{3} I_{3/2}(\alpha_e) \right]; \quad \alpha_e = \frac{\mu_e}{k_B T}, \quad (3)$$

$$P_e^{(id)} / n_e k_B T = (2/3) I_{3/2}(\alpha_e) / I_{1/2}(\alpha_e), \quad (4)$$

where electron density n_e and chemical potential μ_e are connected by relation

$$n_e \lambda_e^3 = 2\pi^{-1/2} I_{1/2}(\alpha_e); \quad I_1(x) = \int_0^\infty \frac{y' dy}{1 + \exp(y-t)} \quad (5)$$

Effects of degeneracy are quite important in this region of the phase diagram because the degeneracy parameter can become large.

COULOMB INTERACTION

Debye approximation in the Grand canonical ensemble [10] for multi-stage ionisation is used for description of Coulomb interaction:

$$\frac{\Omega}{Vk_B T} \equiv \frac{F - \sum N_j \mu_j}{Vk_B T} \equiv \frac{P}{k_B T} = \sum_\alpha n_\alpha - \frac{\tilde{k}_D^3}{24\pi} = \sum_\alpha \left[n_\alpha - \frac{\tilde{\Gamma}_D}{6} \frac{n_\alpha z_\alpha^2}{1 + z_\alpha^2 (\tilde{\Gamma}_D / 2)} \right], \quad (6)$$

with coupling parameter $\tilde{\Gamma}_D$ determined from the equation:

$$\tilde{\Gamma}_D^2 = \left(\frac{e^2}{k_B T \tilde{r}_D} \right)^2 = 4\pi \left(\frac{e^2}{k_B T} \right)^3 \sum_{\alpha} \frac{n_{\alpha} z_{\alpha}^2}{1 + z_{\alpha}^2 (\tilde{\Gamma}_D / 2)}. \quad (7)$$

where \tilde{r}_D is the screening radius. The coupling parameter $\tilde{\Gamma}_D$ differs from the usual Debye parameter $\Gamma_D^2 = 4\pi(e^2/k_B T)^3 \sum n_{\alpha} z_{\alpha}^2$. This approximation is equivalent to the Debye-Hückel value at the limit ($\Gamma_D \Rightarrow 0$) and thermodynamically stable at any coupling (the matrix $\|\partial\mu_i/\partial n_i\|$ is positive definite).

SHORT RANGE ATOM-ATOM, ATOM-ION, ION-ION REPULSION

The effect of overlapping of electron shells of atoms and ions leading to short range repulsion of heavy particles is described in terms of the Mansoori formula [5]:

$$\frac{\Delta F_{HS}}{\sum_i n_i k_B T} \equiv f_{HS}(v) = X \frac{v}{(1-v)^2} + 3Y \frac{v}{1-v} + (X-1) \ln(1-v), \quad (8)$$

$$v \equiv \frac{4\pi}{3} n \bar{r}^3; X = (\bar{r}^2)^3 (\bar{r}^3)^{-2}; Y = \bar{r}^2 \bar{r}^1 (\bar{r}^3)^{-1}; \bar{r}^k = \sum_i n_i r_i^k / \sum n_i; k = 1, 2, 3. \quad (9)$$

This corresponds to contributions in pressure, internal energy and chemical potential:

$$\frac{\Delta P_{HS}}{\sum_i n_i k_B T} = \frac{\partial f_{HS}(v)}{\partial v}; \Delta U_{HS} \equiv 0; \frac{\Delta \mu_i}{k_B T} = f_{HS}(v) + \sum_j n_j \frac{\partial f_{HS}(v)}{\partial n_j} \quad (10)$$

To determine atomic and ionic radii r_j we use two procedures. The first one uses confined atom model [3] in which atom (or ion) is placed in a spherical cell with hard walls; using Hartree-Fock method [8], electron structure is calculated for various cell radii. In Fig.2 calculations of atomic energy shifts as functions of atomic cell radius are represented for ground states of several ions of copper. Determination of particle radii is based on simple formula $\Delta E(r_i) = const \cdot I_i$, where $\Delta E(r_i)$ is ground state energy shift, I_i - ionization potential and r_i - radius of atomic cell. More simple procedure uses the notion that atom (ion) is hydrogen-like structure. In this case radius can be determined from relation

$$r_i \approx r_0 [(z_i + 1) I_0 / I_i] \quad (11)$$

where r_0 , I_0 - radius and ionization potential for atom, r_p , I_i the same for ion and z_i - charge of ion. In reality, procedures considered above are used only to fix the ratio between atomic and ionic radii. Atomic radius is determined from Ashcroft-Leckner's rule [11], in which hard-sphere size at normal density corresponds to fix value of packing fraction $v = 4\pi \sum n_i r_i^3 / 3 = 0.45$. This corresponds to the best coincide of the position of the first maximum of pair correlation function of hard-sphere system with experimentally determined correlation function.

ADDITIONAL ATTRACTION

Calculations in the approximations (1-11) demonstrate reasonable agreement between calculated and experimental data at higher intensities of shock waves. In doing so, short range repulsion is quite important and essentially improves this agreement, but there is

restricted area of phase diagram where none of the r_i set describe experimental data in the approximations (1-11). This is because the relations (1-11) do not contain the mechanism for taking into account for the binding energy, responsible for the existence of the condensed state. We are accounting this effect with an additional attraction that we consider in the form:

$$\Delta F = \Delta U = -A \left(\sum N_i \right)^{1+\delta} \cdot V^{-\delta}; \quad \Delta P = \delta(\Delta U/V),$$

$$\Delta \mu_i = -A(1+\delta)V^{-\delta} \left(\sum N_i \right)^\delta \quad A, \delta = \text{const.} \quad (12)$$

The correction (12) does not depend on temperature. The summing in (12) is over all heavy particles. These corrections don't shift the ionization equilibrium. Notice that $\delta=1$ corresponds to the van der Waals approximation. In accordance with the reference [12], $\delta=1/3$ is appropriate to metallic kinds of binding that, in particular, are valid for expanded metals near critical point. In this approximation, A is determined from a condition that for metal at normal density and $T = 0$ its internal energy coincides with the tabulated value.

RESULTS FOR FOAM NICKEL AND IRON HUGONIOTS

Results of calculations of Hugoniots of foam nickel are represented in Fig.3. On the base of the approximation (1-12) calculations of shock compressed foam iron were carried out. Results of comparison between calculation results and new experimental data [15] are demonstrated in Fig.4.

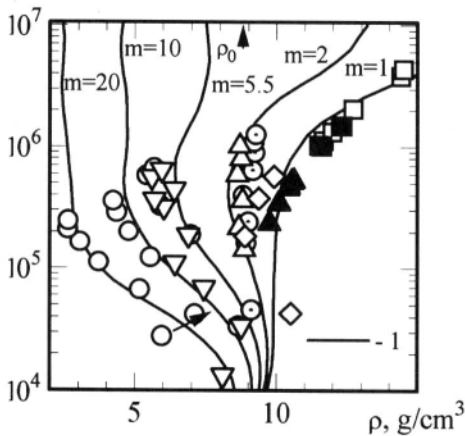


Figure 3. Nickel Hugoniots for different $m = \rho_d / \rho_{\infty}$. 1 - calculation of this work. Squares, triangles and circles - experiment [1] (see [13] and references herein).

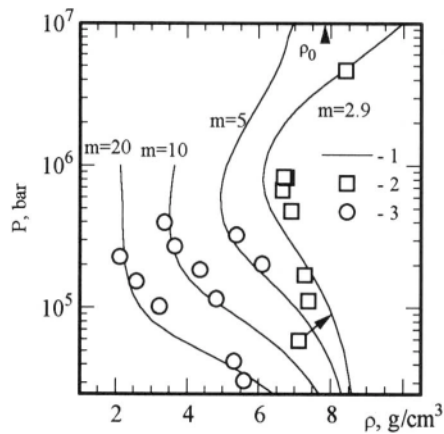


Figure 4. Iron Hugoniots for different $m = \rho_d / \rho_{\infty}$. 1 - calculation of this work; 2 - results of previous experiments (see [1] and references herein); 3 - new experimental data [15].

One can see that the approximations (1-12) being rather simple nevertheless makes it possible to give reasonable agreement between calculations and experiment for all shock-wave compressions and different $m = \rho_d / \rho_{\infty}$ beginning from highest ones up to continuous mater. Fig.4 demonstrates influence of different plasma effects on final thermodynamic results. It is seen that hard-sphere repulsion is very important for position of Hugoniots in P - ρ plane over wide range of pressures, as well as the additional attraction (12) at lower compressions.

CONCLUSIONS

For the example of shock compressed nickel and iron, one can see that the chemical model can provide satisfactory description of strongly coupled plasma of expanded metals. The same agreement with experimental data was achieved for copper and lead [13,14].

ACKNOWLEDGEMENTS

Work was supported by grant N 96-02-18832-a of Russian Foundation for Basic Research.

REFERENCES

1. "Condensed Matter Properties under High pressures and Temperatures" R.F.Trunin, ed. (VNIIEF, 1992); R. F. Trunin, G. V. Simakov, *Sov. Phys. - JETP* 76:1090 (1993).
2. W. Ebeling, *Physica*. 43:293 (1969).
3. V. K. Gryaznov., I. L. Iosilevski *et al.* "Thermophysical Properties of Substances of the Gas-Core Nuclear Engine," V. M. Ievlev, ed., ATOMIZDAT, Moscow (1980).
4. M. Ross, *Phys. Rev.* B21:3140 (1980).
5. T. Kahlbaum, A. Ferster, *Fluid Phase Equilibria*. 76:71 (1992).
6. F. J. Rogers, *Phys. Rev.* A24: 1531 (1981); *Phys. Rev.* A29:868 (1984).
7. N. Daepfen, D. Mihalas, D. G. Hummer, *Astrophys. J.* 332:261 (1988).
8. W. Ebeling, A. Foerster, V. Fortov, V. Gryaznov, A. Polishchuk, "Thermophysical Properties of Hot Dense Plasmas., Teubner, Stuttgart-Leipzig (1991).
9. V. K. Gryaznov, I. L. Iosilevski, V. E. Fortov, *Zh. Prikl. Mat. Tekh. Fiz.* 3:70 (1973).
10. A. A. Likalter, *Sov.Phys. - JETP*. 56:240 (1969).
11. N. W. Ashcroft, J. Lekner, *Phys.Rev.* 145:83 (1966).
12. A. A. Likalter, *Dokl. Akad. Nauk.* 259:96 (1981), *Uspekhi Fiz. Nauk.* 162:119 (1992).
13. V. K. Gryaznov, I. L. Iosilevski, V. E. Fortov, "Physics of Strongly Coupled Plasmas," W. D. Kraeft, M. Schlanges, ed., World Scientific, Singapore-New Jersey-London, p.351-356. (1996).
14. V. K. Gryaznov, I. L. Iosilevski, V. E. Fortov, "Calculation of Porous Metal Hugoniot, in: Physics of Strongly Coupled Plasmas", V. E. Fortov, ed., Moscow, p.31-58. (1995).
15. V. E. Fortov, R. F. Trunin, V. K. Gryaznov, M. V. Zhernokletov, I. L. Iosilevski, G. V. Simakov, Submitted in *Sov. Phys. - JETP*, (1998).

This page intentionally left blank

DISORDERED SYSTEMS WITH A VIRTUAL ATOMIC STRUCTURE

A. A. Likalter

Center of Applied Problems of Electrodynamics
Institute for High Temperatures, Russian Academy of Sciences
Izhorskaya 13/19, Moscow 127412, Russia

INTRODUCTION

Metals with nearly-free valence electrons do not reveal an atomic-like structure. Such a structure appears in the vicinity of the metal-insulator transition where virtual atoms overlap by the classically accessible spheres of partially-free valence electrons. A virtual atomic structure is typical of expanded fluid metals, donors in heavy doped semiconductors, and metals in concentrated ammonia solutions.¹ Similarly, there are virtual molecules in compressed metallic hydrogen. Though the nature of these systems is quite different, the electronic properties behave analogously.

MIXED STATES OF ATOMS

Generally, atoms confine a screening electron charge within a classically accessible radius

$$R_a = e^2 / \epsilon I \quad (1)$$

where e is the electron charge, ϵ is the dielectric constant of a host system, and I is the ionization potential. Since classically accessible spheres overlap in percolation clusters, the atomic screening is partially collective. Otherwise, valence electrons partially move in atomic-like screened potentials, i.e., they are partially free.

According to a quantum-mechanical variational principle, the low bound of the internal energy is the free atom ground level $-I$. Then, a free-motion energy ϵ_p corresponding to the asymptotic momentum p is the excitation. An internal energy of virtual atoms is

$$E_p = -I + \epsilon_p, \quad \epsilon_p = p^2 / 2m \quad (2)$$

where m is the electron mass. A density matrix, which describes admixture of asymptotically free motion to the ground state giving spectrum Eq. 2, is determined by equations

$$a_{pp} + a_{00} = 1, \quad a_{pp} = \frac{\epsilon_p}{I} a_{00}. \quad (3)$$

According to Eq. 3 the higher excitation, the more must be admixture of the free-motion state.

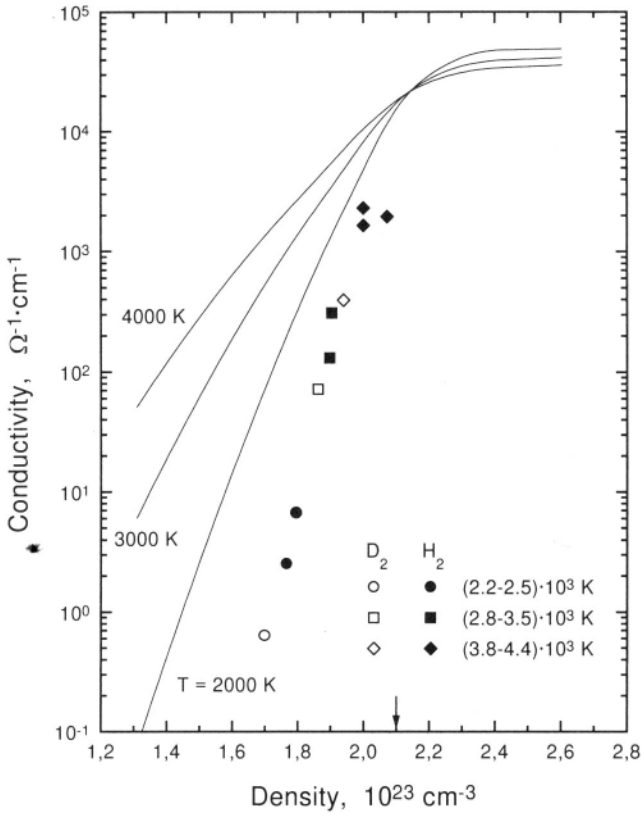


Figure 1. Electric conductivity of dense fluid hydrogen in the insulator–metal transition range. The estimated insulator–metal transition point is shown by arrow.

LOCALIZATION FACTOR

Before the transition to a neighboring ion, an electron can be found in a free-motion sphere around a screened ion with the radius

$$R'_s = v\tau' = R_s/\vartheta \quad (4)$$

where v is the mean free-motion velocity, τ' is a transition time. In second Eq. 4 the free-motion radius R'_s is related to the Wigner–Seitz radius R_s by a localization factor

$$\vartheta = \tau/\tau' \quad (5)$$

with the minimal free-path time

$$\tau = R_s/v. \quad (6)$$

For strong localization the free-motion radius considerably exceeds the Wigner–Seitz radius, i.e., the free-motion spheres in neighboring atoms strongly overlap.

The volume of the free-motion sphere is

$$\Omega = \frac{1}{n_i \vartheta^3} \quad (7)$$

where n_i is the ion number density. The density of mixed atomic states is then

$$\frac{dg}{dp} = g_a \frac{4\pi p^2 \Omega}{(2\pi\hbar)^3} \quad (8)$$

where g_a is the degeneracy of the ground state. Hence, a Fermi momentum of the mixed states

$$p'_F = \hbar \vartheta (6\pi^2 n_i / g_a)^{1/3}. \quad (9)$$

For strong localization the Fermi momentum and energy of mixed states are considerably lower than those of free electrons. Thus, the localization of the mixed electron states strongly extends the limits of Boltzmann statistics.

The localization factor determines the mean electron mobility

$$\mu = \frac{e\tau\vartheta}{m}, \quad (10)$$

which is smaller than a minimal gas-kinetic mobility of free electrons in Boltzmann case. However, for degenerated electrons the localization factor drops out in product $\tau\vartheta$, therefore the minimal gas-kinetic mobility remains in force.

SCALING FUNCTION

We determine the localization factor by a scaling function of the excitation energy

$$\vartheta(\epsilon_p) = \left(\frac{\epsilon_p - \Delta_1}{\Delta_2 - \Delta_1} \right)^\nu, \quad \epsilon_p < \Delta_2 \quad (11)$$

where $\nu \approx 1$ is the critical exponent of the correlation length, Δ_1 is a mobility gap, $\Delta_2 - \Delta_1$ is the width of a soft gap. The Δ_1 and Δ_2 excitations, which enlarge the classically accessible radius up to the percolation radius and the Wigner–Seitz radius, respectively, are

$$\Delta_k = I - \frac{e^2}{\epsilon} \left(\frac{4\pi n_i}{3\zeta_k} \right)^{1/3}, \quad k = 1, 2 \quad (12)$$

where ζ_1 is the volume fraction of the overlapping spheres at the percolation threshold, ζ_2 is the close packing fraction.

The localization factor is

$$\vartheta = \langle \vartheta(\epsilon_p) \rangle \quad (13)$$

where brackets denote the averaging over the energies. On the dielectric side of the transition the localization factor describes an activation temperature dependence

$$\vartheta \approx \frac{2}{\sqrt{\pi}} \frac{(\Delta_1 T)^{1/2}}{\Delta_2 - \Delta_1} \exp\left(-\frac{\Delta_1}{T}\right) \quad (14)$$

where the activation energy goes to zero at the insulator–metal transition point.

On the metallic side of the transition the localization factor describes excitations of electrons within the soft mobility gap

$$\vartheta \approx \frac{3T/2 - \Delta_1}{\Delta_2 - \Delta_1}. \quad (15)$$

As the localization factor goes to unity, one gets a strong scattering regime with a minimal Ioffe–Regel free-path length

$$\ell \sim \hbar / \Delta p \quad (16)$$

where Δp is the momentum uncertainty. Assuming the uncertainty equal to the mean thermal momentum we get

$$\tau = \frac{\ell}{v_F} = \frac{\hbar}{m v_F v_T} \approx \frac{R_s}{v_T}. \quad (17)$$

The last Eq. 17 extrapolates the Boltzmann minimal free-path length into a weak degeneracy range. In case of strong degeneracy Eq. 16 gives a minimal free path equal a few interatomic distances.

INSULATOR–METAL TRANSITION

The theory rather successfully describes metal–insulator transitions in expanded metals,¹ doped semiconductors² and metal–ammonia solutions.³ Here we discuss an insulator–Metal transition in superdense fluid hydrogen. Hydrogen molecules have a nearly ellipsoidal classically accessible domain which is not too far from the sphere. A maximal percolation threshold corresponding to parallel molecular axis coincides with that of the sphere problem. Because of strong intermolecular correlations in a multiple compressed liquid the percolation threshold is close to a random close packing fraction,

$$\zeta_1 = 0.64. \quad (18)$$

This magnitude reasonably agree with the transition point determined experimentally by disappearance of the activation energy.⁴ While data are still lacking, the theory yields the electric conductivity in qualitative agreement with the experiment (Fig. 1).

REFERENCES

- [1] A. A. Likalter, *Sov. Phys. Usp.* 35(7):591 (1992).
- [2] A. A. Likalter, *JETP* 80(6):1105 (1995).
- [3] A. A. Likalter, *JETP* 84(3):516 (1997).
- [4] S. T. Weir, A. C. Mitchell and W. J. Nellis, *Phys. Rev. Lett.* 76:1860 (1996).

DIMENSIONAL CROSS-OVER, CLOSE-PACKED CONFIGURATIONS, SYMMETRY BREAKING, AND FREEZING IN DENSITY FUNCTIONAL THEORY

Yaakov Rosenfeld

Nuclear Research Center Negev
P. O. Box 9001, Beer-Sheva 84190, Israel

The theory of nonuniform classical fluids has made continuous progress in the last two decades, along with the development of important approximations and model Helmholtz free energy functionals, $F[\rho(\mathbf{r})]$, for an inhomogeneous density distribution, $\rho(\mathbf{r})$.¹ The density functional theory should eventually provide a *unified* description of classical systems, including the bulk liquid of uniform density, the bulk solid of narrow density peaks at lattice sites, and the crystallization of a fluid as a strong self-sustained inhomogeneity. The geometrical character of the hard-sphere interactions, which is one of the main reasons for their long standing central role in the microscopic theory of classical fluids,² also simplifies the construction of model functionals.³ Good results for the equation of state of the *fcc* solid and the freezing transition have been obtained by many approaches for the hard spheres with non-local dependence on the density through weight functions.^{1,3} The direct extension of these functionals to continuous (“soft”) potentials brought mixed success and results of sometimes questionable quality.⁴ In turn, standard perturbation expansions around the hard-sphere (HS) reference density functional proved successful for both *bcc* and *fcc* classical solids with simple soft interactions.⁵ In either case, however, elementary properties like the analytic connection of the density functional theory to basic standard models of simple classical solids (notably the free-volume cell model, or the harmonic approximation!) have not been demonstrated, mainly due to the intrinsic limitations of the functionals that were employed. On the other hand, several very recent analyses^{6–10} of the geometrically-based so called fundamental measure functionals (FMFs)^{11–13} revealed that they have many of the basic physical properties expected from the exact (but unknown!) free-energy functional when applied to densely packed hard-spheres. Moreover, these properties are important also for applications to continuous (“soft”) potentials in general, and to charged-particle systems (including plasmas) in particular. These are distinguishing features of the FMF’s, shared by none of the other functionals that were proposed in the literature. In particular, in order to describe correctly densely packed configurations for soft interactions, the hard-sphere functional must feature a *true* divergence of the equation of state at configurations of close packing. The *singularity* which they possess, and their unique geometrically-based structure, enable the FMFs to achieve this as well as other important properties.

Configurations of densely packed hard spheres, confined in different effective dimensions D , provide the ultimate test for model free energy functionals. The exact functional exhibits

correct *dimensional* crossover, namely the description of bulk systems of reduced dimension as strongly inhomogeneous density distributions in a larger dimension, e.g., the functional for $(D - 1)$ should come out from the functional for D when the density profile is a Dirac delta function along one of the coordinates. Solid–solid transitions for confined hard-spheres are dictated by considerations of the close-packed density for each different configuration.¹⁴ The functional must include a mechanism for locating these configurations of close packing, where the equation of state *diverges*. For correct description of densely packed hard-spheres, the solid in particular, when each particle can be viewed as confined in a fluctuating cage of its nearest neighbors, the free energy functional should provide reliable results for the “0D limit” corresponding to a cavity that cannot hold more than one particle.⁶ Correct 0D limit is also required in order to predict the vacancy concentration in the solid.⁶ Finally, the cell-theory free-volume picture is the physically accepted (yet not proven rigorously) behavior of the exact functional near situations of close-packing,^{15–17} with average packing fraction $\bar{\eta} = \bar{\eta}_c$. The free-volume cell-theory result,¹⁵ with the pressure diverging as $P \propto (\bar{\eta}_c - \bar{\eta})^{-1}$, is the exact equation of state for $D = 1$, and numerical simulations indicate^{15–17} that it is correct near *any* configuration of close-packing at $\bar{\eta}_c$ also in $D = 2, 3$.

The free energy functional is composed of two terms, $F[\rho(\mathbf{r})] = F_{id}[\rho(\mathbf{r})] + F_{ex}[\rho(\mathbf{r})]$. The ideal-gas free energy functional is given by the exact relation

$$F_{id}[\rho(\mathbf{r})] = k_B T \int d\mathbf{r} \rho(\mathbf{r}) \{ \ln(\rho(\mathbf{r}) \lambda^D) - 1 \}$$

where $\lambda = (\frac{\hbar^2}{2\pi m k_B T})^{1/2}$ is the de Broglie wave-length, and T is the temperature. For the single component system of hard-spheres of radius R in D -dimensions, the Fundamental-Measure Functionals^{6, 10, 11} have the following form for the excess free energy, $F_{ex}[\rho(\mathbf{r})] = k_B T \int d\mathbf{r} \Phi^{(D)}[\{n_i(\mathbf{r})\}]$ where $\Phi^{(D)}$ is a function of weighted densities, $n_i(\mathbf{r}) = \int \rho(\mathbf{r}') w^{(i)}(\mathbf{r} - \mathbf{r}') d\mathbf{r}'$. The weight functions, $w^{(i)}(\mathbf{r})$, are characteristic functions for the geometry of a sphere, like its volume, $w^{(Volume)}(r) = \theta(R - r)$, or its surface, $w^{(Surface)}(r) = \delta(R - r)$, where $\theta(r)$ and $\delta(r) = -d\theta(r)/dr$ are the Heaviside and Dirac functions, respectively. In particular, $n_{Volume}(\mathbf{r}) \equiv \eta(\mathbf{r})$ is a local packing fraction equal (e.g.,) to $\bar{\eta} = \bar{\rho} \frac{4\pi}{3} R^3$ for the uniform (bulk) 3D fluid of N spheres in a volume V with average density $\bar{\rho} = \frac{N}{V}$. These weighted densities have the property that if the total density is composed of an arbitrary configuration of localized peaks then the FMF excess free energy contributions from each site are completely independent of the others. In particular, if every localized peak is normalized $\int_0^\Delta \rho_\Delta(\mathbf{r}) d\mathbf{r} = \bar{\eta} \leq 1$, then the excess free-energy contribution of every such peak corresponds to the 0D limit, for which the exact result is known: If $\bar{\eta} \leq 1$ is the average occupation (packing fraction) of the cavity, then the *exact* 0D excess (over ideal gas contribution) free energy is given by [6] $\frac{F_{ex}}{k_B T} = \Phi^{(D=0)}(\bar{\eta}) = \varphi_0(\bar{\eta}) = \bar{\eta} + (1 - \bar{\eta}) \ln(1 - \bar{\eta}) \leq 1$, independent of the detailed structure of the cavity. Recent studies revealed^{9, 10} that the correct 0D crossover can be systematically imposed, and the function $\Phi^{(D)}[\{n_i(\mathbf{r})\}]$ depends on $\eta(\mathbf{r})$ by a linear combination of the derivatives, $\varphi_k(\eta) = \frac{\partial \varphi_0(\eta)}{\partial \eta^k}$, $k \leq D$, which are *singular* at $\eta(\mathbf{r}) = 1$. In 1D the FMF is exact¹⁸ and features the logarithmic form, $\ln(1 - \eta(\mathbf{r}))$. In 3D several FMFs were derived,^{6, 11, 12} featuring also the $(1 - \eta(\mathbf{r}))^{-1}$ and $(1 - \eta(\mathbf{r}))^{-2}$ terms, which yield the Percus–Yevick¹⁹ - scaled-particle²⁰ description of the bulk fluid. The most important feature of the FMF’s is their *singularity* at $\eta(\mathbf{r}) = 1$. As detailed in [7, 11] this singularity enables the FMF’s in general to have the mechanism for locating configurations of hard-sphere close packing, and for “symmetry breaking” that separates solid-like and liquid-like solutions for the density profile equation from the free-energy minimization. Improved forms¹⁰ have correct crossover to 0D for almost arbitrary 0D distribution, and yield the *exact* 1D functional for $\rho(\mathbf{r}) = \rho(x)\delta(y)\delta(z)$. With correct 0D forms the FMF’s agree well with simulations for

hard spheres confined in cavities.²¹ FMFs for parallel hard cubes were derived very recently⁹ with completely correct dimensional crossover.

With new forms regularized in the $0D$ limit, the FMFs give⁶ accurate results for the $3D$ fluid–solid transition (predicting for the first time the correct vacancy concentration of the solid), for the equation of state of both the *fcc* and *bcc* crystals all the way from freezing to near close packing, and they become generally reliable in situations of extreme confinements. The FMF excess contribution for configurations of highly localized and densely packed spheres of nearest neighbor distance d , corresponds to the *uncorrelated* cell model, where each cell contribution is equal to the excess free energy in the $0D$ limit of a singly occupied cavity,⁶ which is equal to $F_{ex}/Nk_B T = \Phi^{(D=0)}(\eta = 1) = 1$. What is usually called the configurational free energy¹⁵ is dominated by the *ideal – gas* part of the free energy functional that gives rise to the free-volume pressure, $PV/Nk_B T = (1 - \frac{2R}{d})^{-1}$, while the excess (non-ideal) FMF pressure is zero near close packing, and is relatively very small even near melting. Defining the small parameter $\epsilon = \bar{\eta}_c - \bar{\eta}$, the FMFs give the same free-volume type form for the free energy near *any* configuration of close packing characterized by $\bar{\eta}_c$, namely $F = Nk_B T (-D \ln \epsilon + D \ln(\lambda/R) + \text{const.})$. The corresponding equation of state, with the pressure diverging as $P \propto (\bar{\eta}_c - \bar{\eta})^{-1}$, is in agreement with all the available simulation results^{15–17} for $D = 2, 3$, while the FMF is exact for $D = 1$. Some of the previous functionals²³ exhibit a sharp (but finite!) rise in the region of closest fcc packing, and good agreement with the free-volume equation of state, but they do not contain a *true divergence* at close-packing, they do not feature the *cell picture*, they do not have the mechanisms for *symmetry breaking* and for *dimensional cross-over*, which are *distinguishing features of the FMFs* that are important for soft interactions not less than for the hard-spheres.

The exact thermodynamic perturbation theory divides the interaction potential, $\varphi(\mathbf{r}) = \varphi_{ref}(\mathbf{r}) + \varphi_{pert}(\mathbf{r})$, and free energy, $F[\rho(\mathbf{r})] = F_{ref}[\rho(\mathbf{r})] + F_{pert}[\rho(\mathbf{r})]$, into reference and perturbation parts, where $F_{ref}[\rho(\mathbf{r})]$ is the functional for the reference system.⁵ To first order in the perturbation,⁵ $F_{pert}^{(1)}[\rho(\mathbf{r}')] = \frac{1}{2} N \bar{\rho} \int_0^\infty \bar{g}_{ref}(r; \rho(\mathbf{r})) \varphi_{pert}(r) d\mathbf{r}$, where $\bar{g}_{ref}(r; \rho(\mathbf{r}))$ is obtained by averaging the pair distribution function of the reference system, $\rho_{ref}^{(2)}(\mathbf{r}_1, \mathbf{r}_2; \rho(\mathbf{r}))$. In the fluid, $\rho(\mathbf{r}) = \bar{\rho} \rho^{(2)}(\mathbf{r}_1, \mathbf{r}_2) = \bar{\rho}^2 g(r_{12})$, and the structural information is produced by the pair correlation function $g(r)$. For the solid, when the density is dominated by localized peaks at the lattice sites, previous calculations⁵ assumed, $\rho^{(2)}(\mathbf{r}_1, \mathbf{r}_2) = \rho(\mathbf{r}_1) \rho(\mathbf{r}_2) g(\mathbf{r}_1, \mathbf{r}_2)$, where the product $\rho(\mathbf{r}_1) \rho(\mathbf{r}_2)$ almost exhausts the structural information, and where the main purpose of $g_{HS}(\mathbf{r}_1, \mathbf{r}_2)$ for hard-spheres (*HS*) is to produce the correlation hole of pair exclusion between two spheres of radius R : $g_{HS}(\mathbf{r}_1, \mathbf{r}_2) \cong \theta(r_{12} - 2R)$. This result is obtained *automatically* in the uncorrelated cell model picture, which is the exact limit of the FMFs near any close packing. The reference system parameters are still at our disposal, and we make the variational choice: the optimal (“effective”) hard-sphere radius $R(\rho(\mathbf{r}), T)$ is obtained from the variation equation, $\frac{\partial F[\rho(\mathbf{r})]}{\partial R} = \frac{\partial}{\partial R} (F_{HS}[\rho(\mathbf{r})] + F_p[\rho(\mathbf{r})]) = 0$. The variational method²⁴ proved successful for the fluid and the solid,²⁶ and it can be treated analytically in certain important cases.²⁷

Adopting the Gaussian-peaks picture for a densely packed configuration of hard spheres, and using standard expressions for the uncorrelated cell model²⁴ it was found²⁵ that the first order variational perturbation functional for soft-potential solids, which is based on a FMF for the reference hard-sphere system, features the harmonic potential energy, $\frac{U}{N}(\bar{\rho}, T) = u_M(\bar{\rho}) + \frac{D}{2} k_B T + \dots$, as the leading terms in the asymptotic high density expansion, where $u_M(\bar{\rho})$ is the Static-lattice Madelung energy. This result is general for all D (for $D = 1$ it is exact !) and applies equally well to (e.g.,) the Lennard-Jones potential and to the one component Coulomb plasma. The general quality of this perturbation theory can be

gleaned also from the predominantly harmonic behavior of simple classical solids even near melting. The FMF for the $D = 3$ hard-sphere fluid features the Percus–Yevick¹⁹ pair correlation function and the scaled-particle²⁰ equation of state, so that the present variational perturbation theory belongs to a well studied generic analytic form.^{26, 27} Following that analysis it was found²⁵ that the first order variational perturbation functional for soft-potential fluids yields the following $D = 3$ high density fluid potential energy expansion, $\frac{U}{N}(\bar{\rho}, T) = u_{M, \eta=1}(\bar{\rho}) + (u_{\epsilon, \eta=1}(\bar{\rho}))^{2/5} (k_B T)^{3/5} + \dots$. The temperature independent leading part of the potential energy, $u_{M, \eta=1}(\bar{\rho})$, termed the *fluid Madelung* energy, is evaluated in the bulk $\eta = 1$ limit of the functional (which in $D = 3$ is the $\eta = 1$ limit of the Percus–Yevick equation for hard-spheres²⁷). The leading term for the excess heat capacity behaves like $c_V \sim T^{-2/5}$. The available simulation data for simple fluids is in good agreement²⁶ with the prediction of the variational perturbation theory of which present model is one variant. In particular, for the repulsive inverse power potentials, when $u_{M, \eta=1}(\bar{\rho})$ is subtracted from the simulation energies²⁸ they follow very well the predicted $T^{3/5}$ behavior for temperatures up to many times the melting temperature. It was predicted²⁵ that to within the accuracy of the relative density change upon freezing, which is very small for these potentials ($< 4\%$), the melting densities follow a new universal (independent of potential) *approximate* relation, $\frac{u_M(\bar{\rho}_{melt}) - u_{M, \eta=1}(\bar{\rho}_{melt})}{k_B T} = \text{const.} \cong 0.7$. This relation is obeyed by all available simulation results for repulsive soft interactions. Thus, with a fundamental-measure hard-sphere reference functional we obtain a *unified analytic description* of classical bulk solids and fluids, predicting correctly major features of their equations of state and freezing parameters as obtained by simulations. Moreover, the fundamentally different fluid and solid asymptotic high density expansions for the potential energy, featuring a static-lattice Madelung term and the harmonic $\frac{3}{2} k_B T$ correction, on one hand, and a fluid Madelung energy with a $\sim T^{3/5}$ thermal energy correction, on the other, *both originate from the same singularity in the hard – sphere* free energy functional.

It is possible to improve upon the first order perturbation theory functional.¹¹ The fundamental measure functional provides explicit simple expressions^{11, 29} for the *bridge functional*, which represents the sum of all terms *beyond second order* in the functional Taylor expansion around some reference density. The ansatz of *universality* of the bridge functional,^{11, 29} which is approximated by that for the hard-spheres, enables to apply the hard-sphere functional for fluids with arbitrary interactions. With the bridge functional derived from the FMF's, accurate results were obtained for the bulk pair correlation functions for a large variety of potentials, for both one component systems and mixtures,^{11, 29, 30} including bulk multi-component plasmas.²⁹ The FMF hard-sphere “universal” bridge-functionals has been tested (directly and implicitly) very successfully also for a variety of inhomogeneous systems of particles, in slab geometry, for hard and soft pair interactions and different external potentials.¹¹ Particularly striking tests are provided by strong electrolytes near a charged electrode, and by the plasma of point charges near a wall. This approximation was also used for an accurate solution of the classical “inverse” scattering problem, namely obtaining the pair potential from scattering data for both liquefied rare-gases and liquid metals,³⁰ for one component systems and mixtures. It appears from these many investigations that, by capturing the correct geometrical features, the fundamental-measure hard-sphere functional leads to accurate description of the structure of the inhomogeneous simple fluid under various confinement conditions.

REFERENCES

- [1] See, e.g., the reviews R. Evans in, *Fundamentals of Inhomogeneous Fluids*, edited by D. Henderson (Dekker, 1992); H. Löwen, *Phys. Rep.* **237**, 249(1994).

- [2] J. P. Hansen and I. R. McDonald, "Theory of Simple Liquids," Second Edition, Academic Press, London, (1986).
- [3] P. Tarazona, *Molec. Phys.* **52**, 81 (1984); *Phys. Rev. A* **31**, 2672 (1985).
- [4] A. de Kuijper, W. L. Vos, J. L. Barrat, J. P. Hansen, and J. A. Schouten, *J. Chem. Phys.* **93**, 5187 (1990); B. B. Laird and D. M. Kroll, *Phys. Rev. A* **42**, 4810 (1990); Y. Rosenfeld, *Phys. Rev. A* **43**, 5424 (1991); M. Hasegawa and K. Ohno, *Phys. Rev. E* **54**, 3928 (1996).
- [5] J. F. Lutsko and M. Baus, *J. Phys.:Cond. Matter* **3**, 6547 (1991). C. Rascon, L. Mederos, and G. Nevascues, *Phys. Rev. Lett.* **77**, 2249 (1996); C. Rascon, G. Nevascues, and L. Mederos, *Phys. Rev. E* **53**, 5698 (1996).
- [6] Y. Rosenfeld, M. Schmidt, H. Löwen and P. Tarazona, *J. Phys.: Cond. Matter* **8**, L577 (1996); *Phys. Rev. E* **55**, 4245 (1997).
- [7] Y. Rosenfeld, *J. Phys. Cond. Matter* **8**, L795 (1996).
- [8] A. Gonzalez, J. A. White and R. Evans, *J. Phys.: Cond. Matter* **9**, 2375 (1997).
- [9] J. A. Cuesta and Y. Martinez-Raton, *Phys. Rev. Lett.* **78**, 3681 (1997); *J. Chem. Phys.* **107**, 6379 (1997).
- [10] P. Tarazona and Y. Rosenfeld, *Phys. Rev. E* **55**, R4873 (1997).
- [11] Y. Rosenfeld, *Phys. Rev. Letters* **63**, 980 (1989); *J. Chem. Phys.* **98**, 8126 (1993); *Phys. Rev. E* **50**, R3318 (1994). See also the short review, Y. Rosenfeld, *J. Phys. Cond. Matter* **8**, 9289 (1996).
- [12] E. Kierlik and M. L. Rosinberg, *Phys. Rev. A* **42**, 3382 (1990); **44**, 5025 (1991).
- [13] J. A. Cuesta, *Phys. Rev. Letters* **76**, 3742 (1996).
- [14] B. Pansu, P. Pieranski, and P. Pieranski, *J. Physique* **45**, 331 (1984).
- [15] A. Münster, *Statistical Thermodynamics*, Volume 2, Springer-Verlag, Berlin, 1974, section 16.2, and references therein.
- [16] M. Schmidt and H. Löwen, *Phys. Rev. Lett.* **76**, 4522 (1996).
- [17] M. D. Rintoul and S. Torquato, *Phys. Rev. Lett.* **77**, 4198 (1996).
- [18] J. K. Percus, *J. Stat. Phys.* **15**, 505 (1976).
- [19] J. K. Percus and G. J. Yevick, *Phys. Rev.* **110**, 1 (1958); M. S. Wertheim, *Phys. Rev. Lett.* **10**, 321 (1963).
- [20] H. Reiss, *J. Phys. Chem.* **96**, 4736 (1992).
- [21] A. Gonzalez, J. A. White, F. L. Roman, S. Velasco, and R. Evans, *Phys. Rev. Letters.* **79**, 2466 (1997).
- [22] R. Ohnesorge, H. Löwen, and H. Wagner, *Europhys. Lett.* **22**, 245 (1993).
- [23] Compare the second paragraph of the Discussion on page 69 in A. R. Denton, N. W. Ashcroft, and W. A. Curtin, *Phys. Rev. E* **51**, 65 (1995), with C. F. Texero, M. S. Ripoll, and A. Pérez, *Phys. Rev. E* **52**, 3632 (1995), and with C. F. Tejero, *Phys. Rev. E* **55**, 3720 (1997). See also A. Khein and N. W. Ashcroft, *Phys. Rev. Letters* **78**, 3346 (1997).
- [24] G. A. Mansoori and F. B. Canfield, *J. Chem. Phys.* **51**, 4958, 4967 (1969); H. S. Kang, T. Ree, and F. Ree, *J. Chem. Phys.* **84**, 4547 (1986).
- [25] Y. Rosenfeld and P. Tarazona, *Molec. Phys.*, the John Barker issue, in print.
- [26] Y. Rosenfeld, *Phys. Rev. A* **29**, 2877 (1984); **28**, 3063 (1984); *J. Chem. Phys.* **73**, 5753, 5760 (1980).
- [27] (a) Y. Rosenfeld, *Phys. Rev. A* **32**, 1834 (1985); (b) *ibid* **33**, 2025 (1986).
- [28] See, e.g., W. G. Hoover, S. G. Gray, and K. E. Johnson, *J. Chem. Phys.* **55**, 1128 (1971); G. S. Stringfellow, H. E. DeWitt, and W. L. Slattery, *Phys. Rev. A* **41**, 1105 (1990); E. J. Meijer and D. Frenkel, *J. Chem. Phys.* **94**, 2269 (1991); R. Agrawal and D. Kofke, *Phys. Rev. Lett.* **74**, 122 (1995), and Refs. therein; S. Hamaguchi, R. T. Farouki, and D. H. E. Dubin, *Phys. Rev. E* **56**, 4671 (1997).
- [29] Y. Rosenfeld, *Phys. Rev. E* **54**, 2827 (1996).
- [30] Y. Rosenfeld and G. Kahl, *J. Phys. Cond. Matter* **9**, L89 (1997), and Refs. therein; G. Kahl, B. Bildstein, and Y. Rosenfeld, *Phys. Rev. E* **54**, 5391 (1996).

This page intentionally left blank

ELECTRICAL CONDUCTIVITY OF DENSE COPPER PLASMAS

A. W. DeSilva¹ and J. D. Katsouros²

¹Institute for Plasma Research

²Department of Physics
University of Maryland at College Park
College Park, MD

INTRODUCTION

Measurements are reported of the electrical conductivity of dense copper and aluminum plasmas in the temperature range 10–30 kK, in a density range from about 1/5 solid density down to 0.02 gm/cm³. Plasmas were created by rapid vaporization of metal wires in a water bath. As density decreases from the highest values measured, the conductivity falls roughly as the cube of density, reaches a minimum, and subsequently rises to approach the Spitzer prediction at low density. These results are compared with several theoretical predictions.

In a previous paper,¹ we presented measurements of the electrical conductivity of copper plasmas having densities ranging from about 0.3 to 3 gm/cm³, and temperatures in the range 8,000–30,000 K. Data for that report were obtained by measuring the resistance of plasma created by vaporizing copper wires inside glass capillaries. In the present paper, we have extended these measurements to lower densities. We have departed from the use of glass capillaries to confine the plasma during the measurement period, and have instead utilized water as the confining medium for the vaporized metal wires, a method that offers a significant advantage in interpretation, while restricting somewhat the high density limit of measurement.

In order to make a measurement of the DC electrical conductivity of a metal plasma, we create a cylindrical plasma by vaporizing, with a burst of current, a metal wire embedded in water. The resulting plasma column expands radially, compressing the surrounding water and causing a cylindrical shockwave to move radially outwards in the water. The plasma is observed to remain quite stable during this expansion, and very little diffusion of energy occurs between the plasma and water on the short timescale of the observation.

DATA ANALYSIS

In interpreting the data we assume uniformity of the plasma column. To support this assumption we estimate the thickness Δr of the boundary layer that forms at the interface between water and plasma. A scale length for the thickness Δr of this boundary layer is obtained by equating the heat flow in the temperature gradient across the layer to that

required to raise the temperature of a layer of that thickness in a time Δt . The result is

$$\Delta r^2 = \frac{\lambda \Delta t}{\rho_m C}, \quad (1)$$

where λ is the thermal conductivity, ρ_m is the mass density, and C is the specific heat. Inserting parameters appropriate for water, utilizing the thermal conductivity for compressed heated water,² and taking for the timescale the observation time of about one microsecond, we find the scale length for the boundary layer thickness to be about one micrometer. Applying the same formula to the parameters appropriate to the plasma, utilizing the Wiedemann–Franz relation to deduce the thermal conductivity from our measured electrical conductivity, we find that the scale thickness of the boundary layer is about 2 micrometers. We conclude that boundary layer at the plasma-water interface is thin enough to be ignored in our calculations of the conductivity.

Determination of the resistance $R(t)$ of the column is straightforward, as both the current and voltage across the column may be measured. As the wire vaporizes, the pressure rises rapidly, and the surrounding water is compressed, sending a shock wave radially outwards. The diameter $d(t)$ of the plasma may be determined from measurements of a streak photo of the expanding plasma, and the conductivity then follows simply from

$$\sigma(t) = \frac{1}{R(t)\pi d(t)^2}. \quad (2)$$

The density is now calculated making use of the assumption that the mass of wire initially present now fills the plasma volume uniformly, and ignoring any edge effects.

A satisfactory method to measure the plasma temperature has not been found. Owing to the high plasma density, the optical depth is very small, of order microns, so one would expect that light radiated from the plasma would be Planckian, but representative of the plasma at a depth that lies only in the boundary layer. We are forced, therefore, to use an indirect means of finding the bulk plasma temperature.

To do this, we make use of the LANL SESAME equation of state tables for the metal under study to relate the measured input energy to the changes in temperature and pressure.³ We need, in addition, a model for the growth of the column diameter due to the plasma pressure. A one-dimensional cylindrical fluid code, following the model of Plooster,⁴ is used to describe the compression wave that propagates into the water. It shows the compression of the water by the expanding copper vapor and the shock wave generated by this compression. Equation of state data of water for use in this code are taken from Rice and Walsh.⁵

The plasma column diameter computed as above may be compared with the column diameter observed by streak photography. Figure 1 shows this comparison. The time correspondence for this comparison was made using the spark marker described above, thus there are no adjustable parameters. The close correspondence between calculated and observed diameter gives confidence that the calculations yield a valid picture of the plasma expansion and of the temperature.

As the plasma column expands due to the high internal pressure, the density falls, providing us with a simple means to measure conductivities at a variety of densities. Variation of the charge voltage on the capacitor and of the external series impedance in the circuit allows some control over the temperature vs. density profile. Figure 2 shows time traces of measured current and voltage, and the results of the calculation for pressure, density, temperature, and conductivity.

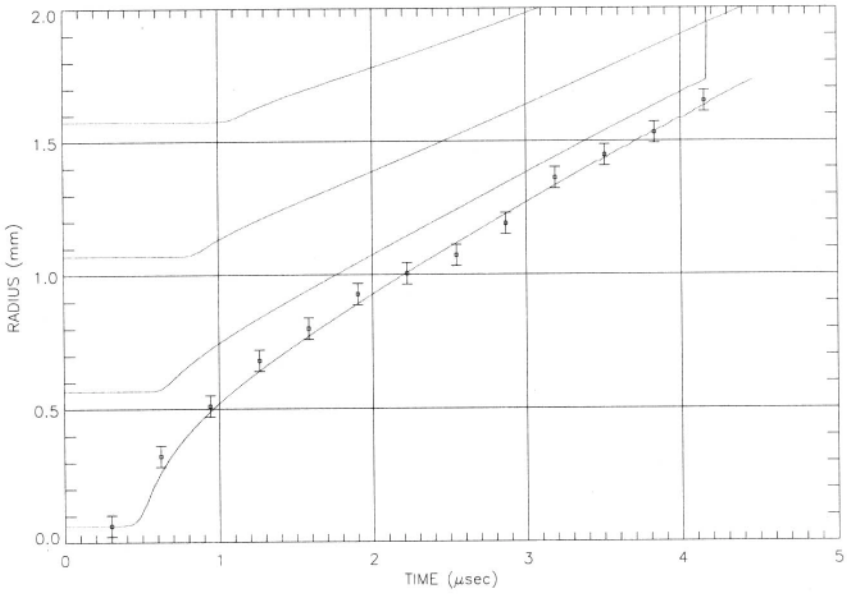


Figure 1. Comparison of computed plasma radius with streak picture. Lines are loci of grid points of calculation. Points are from streak picture.

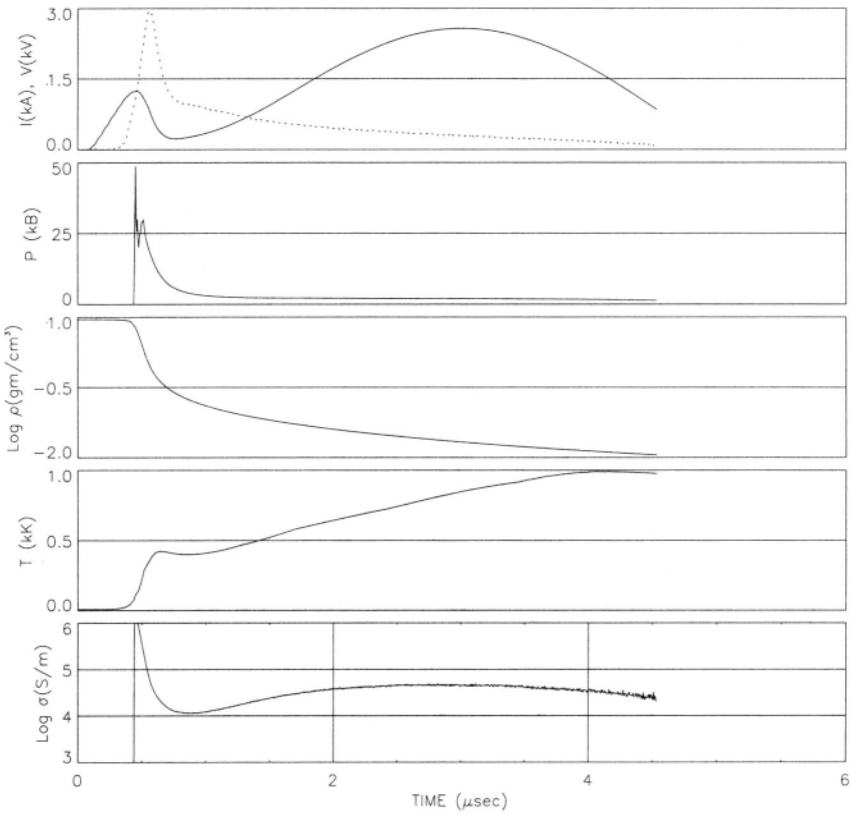


Figure 2. Computed time traces of current (solid line), ohmic voltage (dotted line), pressure, mass density, temperature, and conductivity for the shot of Fig. 1.

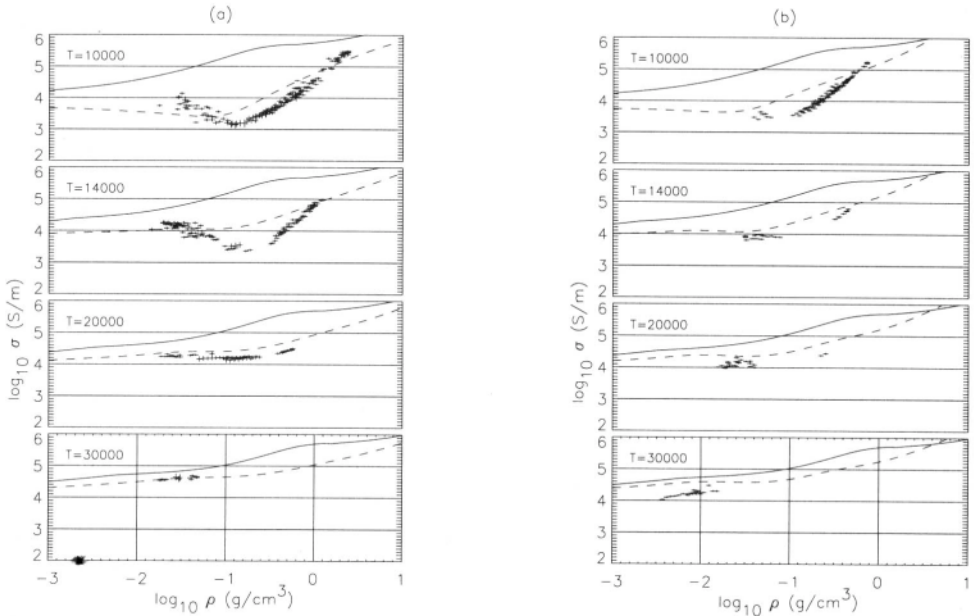


Figure 3. a) Electrical conductivity of copper plasma at four temperatures. The dashed lines are theory from the book by Ebeling et al. and the solid lines are theory of Lee and More. b) Electrical conductivity of aluminum plasma at four temperatures. Theory lines as in Fig. 3a.

RESULTS

Several hundred shots were made, using 99.9% purity 125 micron diameter copper wire as the specimen, and using a variety of charge voltages and external series impedances in the discharge circuit. For each shot, the time history of the measured and calculated parameters were recorded. Data at times when the calculated temperature was within $\pm 3\%$ of selected temperatures (in 2000 K steps) were then extracted for plotting in Fig. 3a.

For a temperature of 10,000 K one sees that as density decreases, the conductivity falls steeply, varying at the highest densities approximately as r^3 with density. At about 0.1 gm/cm^3 , conductivity goes through a minimum, and subsequently rises with falling density. Such behavior has been predicted in dense hydrogen plasmas by Reinholz, Redmer and Nagel,⁶ and has been seen in measurements on mercury plasmas.⁷ The conductivity must rise from the minimum as density falls if it is to connect at very low density with the Spitzer formula. For higher temperatures, the minimum becomes less pronounced.

A similar set of data were taken with 99.9% pure aluminum wires. Resultant conductivity data plotted as a function of mass density are shown in Fig. 3b. In Figs. 4a and 4b, we display the data for both aluminum and copper plotted vs. electron density, for two temperatures. The ionization state for conversion of mass density to electron density was taken from a Thomas–Fermi model of More.⁸

DISCUSSION

The conductivity at fixed temperature seen in the present work falls more steeply with decreasing density than that reported in *I*, which was derived from the glass capillary shots. The two sets of data agree only at the highest densities. We suggest that the data taken in water bath are more reliable, and that the discrepancy is in part due to the finite time required for

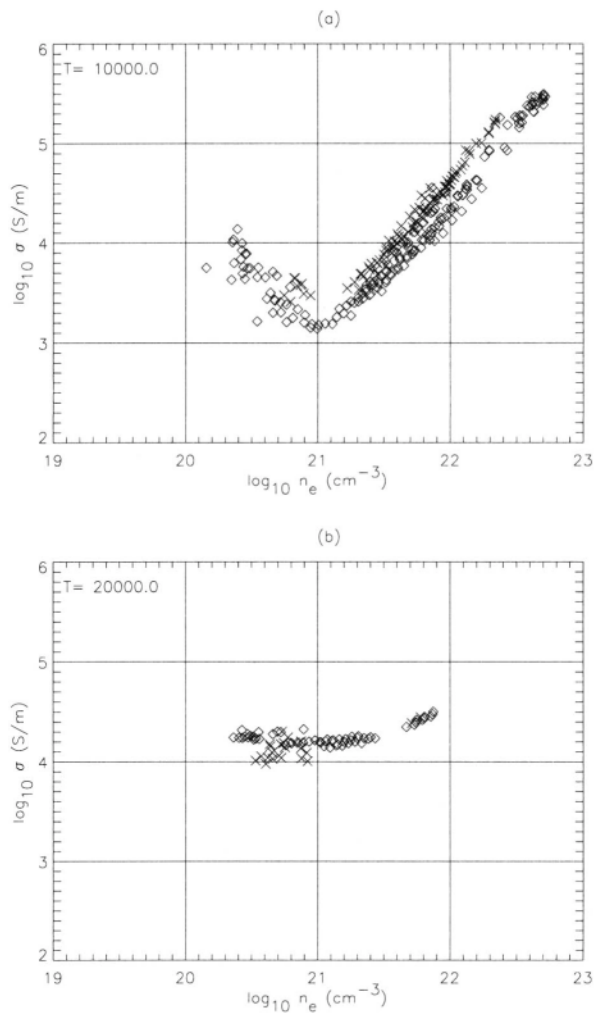


Figure 4. Comparison of copper and aluminum conductivities, plotted versus electron density, at a) $T = 10,000$ K; b) $T = 20,000$ K. Diamonds:copper; X:aluminum.

the metal vapor to fully fill the glass capillary after vaporization begins as pressure is building up. Typically this takes 300 or more nanoseconds. Previous low temperature data were derived from results during this interval, and thus may have been influenced by nonuniform density or even incompletely vaporized material in the plasma volume. In case of the water shots, the plasma is bounded by water from the beginning, and there is no such period of uncertainty about density. A further criticism of glass confinement stems from the less-than-ideal cylindrical boundary formed by the glass. We observed in streak camera pictures in *I* that the glass fractured close behind the cylindrical shock wave. This would have formed fissures in the glass into which plasma could seep, causing the density to depart from that computed with the one dimensional compression model.

Acknowledgements

This work was supported by the National Science Foundation. We thank David Gershon and Jeng-Mei Liu for their able assistance in the early stages of this work. The work would not have been possible without the expert technical help of our now-retired shop supervisor, Kenneth Diller.

REFERENCES

- [1] Desilva, A. W. and Kunze, H.-J., 1994, *Phys. Rev. E* 49:4448 (1994).
- [2] Ebeling, W., Förster, A., Fortov, V. E., Gryaznov V. K. and Polishchuk, A. Ya., 1991, "Thermophysical Properties of Hot Dense Plasmas," B. G. Teubner Verlagsgesellschaft, Stuttgart, pp. 266–275.
- [3] Lee, Y. T. and More, R. M., 1984, *Phys. Fluids* 27:1273.
- [4] Haar, L., Gallagher, John S., and Kell, G. S., 1984, "NBS/NRC Steam Tables, Thermodynamic and Transport Properties and Computer Programs for Vapor and Liquid States of Water in SI Units," Hemisphere Publishing Corp., Washington, p. 269.
- [5] SESAME: The Los Alamos National Laboratory Equation of State Database, Report LA-UR-92-3407, S. P. Lyon and J. D. Johnson, eds., Group T-1.
- [6] Plooster, M. N., 1970, *Phys. Fluids* 13:2665.
- [7] Rice, M. H. and Walsh, J. M., 1957, *J. Chem. Phys.* 26:824.
- [8] Reinholz, H., Redemer, R., and Nagel, S., 1995, *Phys. Rev. E* 52:5368.
- [9] Götzlaff, W., Schönherr, G., and Hensel, F., 1988, *Z. Phys.-Chem.*, NF 156:219.
- [10] More, R. M., 1991, in "Handbook of Plasma Physics," M. N. Rosenbluth and R. Z. Sagdeev, eds.; Vol. 3, A. M. Rubenchik and S. Witkowski, eds., Elsevier Science Publishers B. V., city, p. 70.

MEASURING THE EOS OF A DENSE, STRONGLY COUPLED PLASMA: DESCRIPTION OF THE TECHNIQUE*

John F. Benage, Jr., George Kyrala, Jonathan Workman, and Thomas Tierney
IV

Los Alamos National Lab
Los Alamos, NM

INTRODUCTION

One of the most fundamental properties of materials is the relation between thermodynamic variables as a function of the material state, designated the equation of state (EOS). For most materials under many conditions, this relation is fairly well known, and there has been much experimental work to determine this relation. One region of parameter space that is not well known is the strongly coupled plasma regime. In this regime the EOS physics is quite complicated due to the strong interaction of individual particles with each other. Many theories attempt to calculate the EOS of a dense plasma, from one component plasma models and density functional models to the standard Thomas–Fermi models which are widely used to produce EOS tables. A lack of experimental data prevents a determination of the accuracy of these models in the dense plasma regime.

This paper describes a new experimental design which we believe can produce reasonably accurate data for the EOS of a dense plasma. This design takes advantage of the standard shock technique used for determining the high pressure EOS of solids. It also utilizes recently developed experimental techniques for producing dense, strongly coupled plasmas^{1,2} as well as new diagnostic techniques³ for measuring the properties of these plasmas. The results should be able to distinguish among theoretical models for plasmas at just under solid density and temperatures of 10's of eV.

DESCRIPTION OF THE TECHNIQUE

The standard shock technique for measuring the EOS of a material consists of producing a steady shock in a solid by colliding a flyer plate at high velocity with a solid sample of the material of interest. The flyer plate velocity and the shock velocity are the variables measured in the experiment. If the flyer plate and the sample are the same material, the material velocity behind the shock can be determined using the conservation of momentum. These two measurements along with the equations for conservation of mass, momentum,

*Work performed under the auspices of the Dept. of Energy.

and energy across the shock allow one to determine the pressure, density, and energy of the shocked material. The locus of points produced by a set of such experiments is called the standard Hugoniot, where the variable changed is simply the flyer plate velocity. This technique has been the major source of EOS data in the high energy density regime.

When using the shock technique for determining the EOS of a material, the conservation equations across the shock interface must be utilized. These are written as

$$\rho = 3D\rho_0/(1 - v_p/v_s) \quad (1)$$

$$P = 3DP_0 + \rho_0 v_s v_p \quad (2)$$

$$\varepsilon = 3D\varepsilon_0 + P v_p / (\rho_0 v_s) - v_p^2 / 2 \quad (3)$$

where ρ_0 and ρ are the densities ahead and behind the shock, v_s is the velocity of the shock, v_p is the velocity of the material behind the shock, P_0 and P are the pressures ahead and behind the shock, and ε_0 and ε are the internal energies ahead and behind the shock. These equations are applicable at the shock interface but only apply to the entire sample if the shock produced is planar and steady in time. Here we have three equations and eight unknowns. If the initial pressure and internal energy are very small compared to the final, then approximating them as zero reduces the number of unknowns to six. In the case of solids, the initial density is known. Then one only needs to measure two variables to determine the other three. If the initial density is not known, then three variables must be measured to determine the rest. Such is the case for this experiment and we will measure ρ , ρ_0 , and v_s and use the equations above to determine the pressure and internal energy of the material behind the shock.

Using the shock technique on materials initially in the solid state is not very useful for studying dense plasma effects on EOS. This is because the physics issues that dominate the EOS of materials along the standard Hugoniot are issues of solid state physics, not dense plasma physics. One would therefore like to do experiments in a region of parameter space where the strong coulomb coupling plays a more significant role. This region of parameter space lies in densities less than solid but at temperatures of a few eV. One way to reach these types of conditions is to start off with lower density material not in the solid state. This is what we will attempt to do.

A schematic of our experiment is shown in Fig. 1. In this experiment, we create a uniform dense plasma by electrically heating an aluminum wire to a temperature of ~ 4 eV and allow this plasma to expand into the vacuum through a rectangular slit. The slit is removed from the end of the wire a few wire diameters to allow the expanding plasma flowing through it to be uniform. This should produce a plasma at densities of a few percent solid and temperatures of ~ 1 eV. We will use a high power laser incident on this plasma plume from the side to launch a shock into the plasma. This laser will deposit its energy at the critical surface, producing a hot, high pressure plasma which drives a shock into the plume. By increasing the intensity of the laser and therefore the pressure, we can obtain EOS measurements along a Hugoniot starting from initial conditions much different than the standard Hugoniot. This should provide some of the first EOS measurements of a dense, strongly coupled plasma.

To measure the material conditions, we will use two variations of the same technique. This technique involves using a short pulse laser incident on a solid target to produce a hot plasma source of x-rays. If the intensity of the laser on target is set to the appropriate value, a significant amount of k-shell lines will be produced. By measuring the absorption of these x-rays through the plasma along with the spatial extent of the plasma, we can determine the mass density, assuming we know the absorption cross section. To insure we are confident of this cross section value, we will use a specific high energy line for this absorption measurement. In our case, we plan to use the 4.7 keV line from Tixxi. The production of this line requires an intensity on target of $\sim 10^{15}$ W/cm². Also, the absorption of photons at this energy

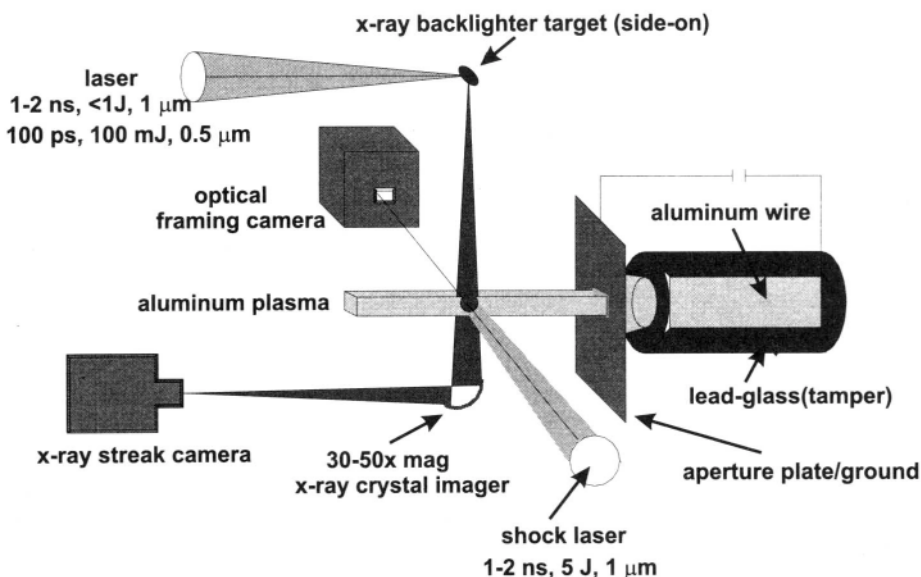


Figure 1. Experimental arrangement for high-density plasma measurements. Included are x-ray and optical diagnostics.

through aluminum should not be affected due to the low ionization state of aluminum at these conditions.

The same x-ray absorption technique can be used to measure the propagation of the shock through the plasma. In this case a longer pulse of x-rays must be used along with a streak camera to obtain a time history of the shock position in the plasma. The line need not be Ti in this case since an absolute absorption number is not required. Thus, we intend to use the 1.3 keV line from MgXII for this measurement. Production of this line only requires an intensity of $\sim 10^{14}\ \text{W/cm}^2$, but since it is needed for a much longer time, the energy in the laser is similar. Both cases require accurate measurements and therefore we need very high spatial resolution when imaging the x-ray absorption through the plasma. To make these measurements, two x-ray microscopes are being constructed. These microscopes will produce a spatial resolution of $\sim 2\ \mu\text{m}$ at the plasma. This spatial resolution should provide sufficient accuracy in our measurements to determine the density within 5% and the energy and pressure within 15%.

The initial conditions we expect to produce in the plasma plume are aluminum densities of $\sim 0.1 - 0.2\ \text{g/cm}^3$ at a temperature of $\sim 1\ \text{eV}$. The laser intensity available to produce a shock in this plasma will be 5×10^{12} to $5 \times 10^{13}\ \text{W/cm}^2$, producing aluminum densities of $\sim 1\ \text{g/cm}^3$ and temperatures of $\sim 25\ \text{eV}$. The Γ for these plasmas, which is the ratio of the average potential energy between ions to their temperature, will be of order 10. At similar conditions for Be the theory of Perrot⁴ differs from the Thomas-Fermi model⁵ by 25% in energy. This difference should be outside the error bars of our experiment, therefore determining which EOS theory is most accurate in this regime.

Presently we are completing work on the pulsed power machine being used for heating the aluminum wires. Soon production of the aluminum plasma plumes will begin with subsequent measurements of their spatial extent, expansion rate, and temperature using a visible framing camera. The construction of the x-ray microscopes for imaging the plume and measuring the density has begun and should be completed shortly. This will be used to measure the density of the plasma plume and determine when the conditions we seek are

produced in this plasma. Subsequently we will complete the construction of the laser for driving the shock in the plasma along with the construction of the second x-ray microscope. This will enable us to begin the EOS measurements in earnest.

REFERENCES

- [1] A. N. Mostovych, K. J. Kearney, J. A. Stamper, and A. J. Schmitt, *Phys. Rev. Lett.* **66**, 612 (1991).
- [2] J. F. Benage, Jr., W. R. Shanahan, M. S. Murillo, *Proceedings of the International Conference on Physics of Strongly Coupled Plasmas*, ed. By W. D. Kraeft and M. Schlanges, World Scientific Publishing, pg. 240 (1996).
- [3] T. A. Pikuz, A. Ya. Faenov, S. A. Pikuz, V. M. Romanova, and T. A. Shelkovenko, *J. X-Ray Sci. & Tech.* **5**, 323 (1995).
- [4] F. Perrot, *Phys. Rev. E.* **47**, 570 (1993).
- [5] J. Barnes, *Phys. Rev.* **153**, 269 (1967).

FISSION-FRAGMENT INDUCED DAMAGE OF SURFACES: A QUASICLASSICAL TRAJECTORY CALCULATION

K. J. LaGattuta

Los Alamos National Laboratory
Los Alamos, NM

INTRODUCTION

The subject of fission-fragment (FF) propagation through solids is rather old. Nevertheless, present understanding is still limited at the microscopic level to a simple picture of peripheral ion-atom inelastic scattering; i.e., ionization induced by long range Coulomb interaction.¹ Even though this picture enables one to compute the range of a FF reliably in a variety of materials, the extent and type of lasting damage induced in materials can hardly be predicted.

A typical FF carries an equilibrium net positive charge of $20 < Z < 25$, and moves with a speed of $3 < v < 5$ a.u. A flux of ionized electrons is emitted along a FF track, exposing a cylindrically shaped volume of positively charged ion (lattice) cores. The initial charge of ions along the track depends on the number of valence (loosely bound) electrons of the material. Heavier elements tend to have more loosely bound electrons than lighter elements, so their charges tend to be greater.

The ion cores experience a large mutual Coulomb repulsion, causing them to move out from the track. As they move, they are subject to electrical neutralization, either through three-body recombination with continuum electrons, or by electron pickup reactions with lattice atoms. The time required to neutralize can be expected to depend strongly on details of continuum electron density and effective temperature, as well as the type of material. However, simple estimates suggest that the time required to neutralize will be of the order of $1psec$ or less, for an ion moving with a few eV of kinetic energy, through a solid material. In this case, one expects ion cores to travel ten or so lattice spacings before neutralizing.

There has been considerable speculation that this highly energetic, albeit utterly microscopic process of rapid ionization followed by ion motion and rapid recombination, can give rise to a shock-wave, which could conceivably propagate over distances of microns.^{2,3} If this shock-wave were to encounter a surface, then reflection at the surface and “unloading” of the wave could result in spall damage to the surface, and ejection of surface material into the vacuum.

Past experiments,^{4,5} have indicated that numbers of atoms can indeed be emitted from a surface, if and when a FF emerges from that surface. There is little agreement, however, on what these numbers are, and published measurements vary over many orders of magnitude.

For these fragments, several mechanisms for producing surface damage have been suggested; e.g., the “displacement spike” theory⁶ for insulators, and “melt motion”⁷ for metals impacted by very low energy ions. The mechanisms relevant to FF’s might well all be grouped under the heading of Coulomb explosion phenomena.

None of these hypotheses have much to recommend them, however, other than an air of plausibility. Therefore, in an attempt to gain heuristic knowledge of the physical mechanisms operating here, we have chosen to embark upon a program of calculations based on a new variation of the classical trajectory method.

THE QUASICLASSICAL METHOD

The classical trajectory method has had much success in elucidating the connection between microscopic and macroscopic behaviors in solids.⁸ However, the classical trajectory method cannot cope with the ionization and recombination of many-electron atoms in any direct way. The reason for this is simply that classical atoms with two or more electrons are dynamically unstable.⁹

Recently, a method has been created for stabilizing multi-electron atoms, within the confines of Hamiltonian mechanics. We refer to this as the quasiclassical method; it has also been called Fermion Molecular Dynamics.¹⁰ In this approach, two momentum dependent potentials are added to the many-particle Hamiltonian: One potential accounts for the effect of the Heisenberg uncertainty principle V_H , and the other potential for the Pauli exclusion principle V_P . Both of these potentials are repulsive and short range; V_H acts between all pairs of oppositely charged particles, while V_P acts between all pairs of electrons with the same “spin.” In this method, electrons are deemed to possess two spin degrees of freedom, and are labelled either spin-up or spin-down.

With the addition of these two types of potential to the many-particle Hamiltonian, a system of a nucleus with charge Z , and Z electrons, half with spin-up and half with spin-down, forms a dynamically stable electrically neutral atom. It is observed that for any $1 \leq Z \leq 94$, this scheme results in stable atoms with reasonably good values of the ionization energy, and possessing a shell structure.¹¹ This is the model that we have adopted for foils of uranium metal by fission fragments, our many-atom calculations.

PRELIMINARY RESULTS

We performed a 2D simulation with a lattice of helium atoms. The initial lattice chosen was square, 6x6 with a lattice spacing $6.6a.u.$ The projectile had a charge $Z_P = 15$, a speed $V_P = 4a.u.$, and passed through the precise center of the lattice, moving in its plane and parallel to one side.

Immediately following the projectile’s exit from the lattice a burst of ionized electrons is emitted from the neighborhood of the track, predominantly into the projectile’s wake. These are so-called convoy electrons.¹² At this time, approximately 3/4 of the atoms along the track are found to be singly ionized. There is no other prompt ionization.

The lattice is left with two parallel lines of He^+ ions in its interior, separated by just one lattice spacing. The two lines of ions then expand outward. Over the duration of the simulation, which was $0.07psec$, no ion neutralization was observed; i.e., due to collisions with lattice atoms. The ions at or near to the center of the lattice are observed to move almost perpendicular to the projectile track; the ions at a lattice edge are observed to move almost parallel to the projectile track. Absent collisions, the actual path traveled by any given ion is determined entirely by its location inside the line of charges. One can estimate the angle

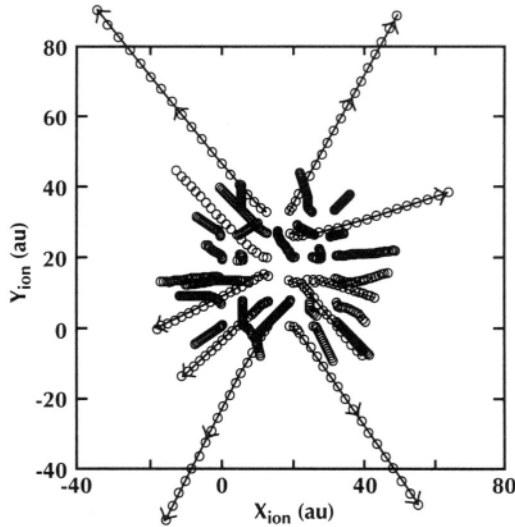


Figure 1. 6x6 (2D) lattice of helium atoms struck by projectile of charge $Z_P = 15$ and speed $V_P = 4a.u.$; projectile traveled from bottom to top, in-plane and along the lattice midline; lattice ion positions (circles) are plotted every $4fsec$.

relative to the projectile track at which a given ion moves by computing the initial value of the electric field at its position, due to all of the other ions; see Fig. 1. Similarly, one can compute the total repulsive potential energy possessed by the ions immediately following their creation. After separation, this potential should translate into $E \approx 9eV$ of kinetic energy, on the average. This value is consistent with the length of the ion tracks recorded.

Although the paths followed by individual electrons are complex, the He^+ paths seem to be simple; i.e., nearly straight. However, this simplicity is somewhat misleading, since for the very small lattice size considered above, no neutralization of a moving ion was observed to occur. This accords with estimates of the mean free path for neutralization under the conditions of our simulation, which is ten or more lattice spacings. Larger lattices are required, therefore, in order to reveal the full complexity of heavy particle motion.

The behavior exhibited in this simulation seems typical of the (hypothetical) response of an electrical insulator, when struck by a fast moving, highly charged projectile (heavy cosmic ray particle). Namely, that response known as the “ion-explosion spike,”⁶ in which a persistent cylindrical volume of rubble (highly disordered lattice material interspersed with voids) is created by the passing projectile.

SUMMARY

We have investigated the dynamics of a small or “minimal” lattice of helium atoms with FMD. The lattice was struck by a fast, highly charged projectile, and a burst of convoy electrons was emitted. The lattice then disassembled due to the mutual Coulomb repulsion of the ion cores. The FMD method has enabled a calculation in which ionization, recombination, and ion kinetic motion could all be followed simultaneously.

An interesting correlated motion of lattice ion cores, following their creation by a rapidly moving projectile, was observed. It is not clear to what extent this correlated motion is affected strongly by the choice of projectile velocity; i.e., its orientation with respect to the lattice principal axes. Recombination of ion cores was not observed, since the lattice employed was

too small. Such motions may also be more nearly typical of behavior in insulators, rather than conductors in which recombination is probably much more rapid.⁶

The code now being proven out, future work will focus on simulating the responses of larger lattices to fast moving, highly charged projectiles. Lattice atoms with more electrons will also be employed. At very slightly higher material densities, when valence shells of adjacent atoms in the initial lattice are allowed to overlap, we expect to be able to see the difference in responses between electrically insulating and conducting materials.

REFERENCES

- [1] N. Bohr and J. Lindhard, Electron capture and loss by heavy ions penetrating through matter, *Det Kgl. Danske Vidensk. Selskab.* 28:7:1 (1954).
- [2] G. Carter, Spike and shock processes in high energy deposition density atomic collision events in solids, *Radiation Effects Letts.* 43:193 (1979).
- [3] M. Guinan, Shock wave interactions arising from near surface displacement cascades, *J. Nucl. Materials* 53:171(1974).
- [4] G. Nilsson, Ejection of uranium atoms from electropolished foils of uranium metal by fission fragments, *J. Nucl. Materials* 20:231 (1966).
- [5] M. Rogers, Mass transport of uranium by fission fragments, *J. Nucl. Materials* 15:65 (1965).
- [6] R. Fleischer, P. Price, and R. Walker, Ion explosion spike mechanism for formation of charged-particle tracks in solids, *J. Appl. Phys.* 36:3645 (1965).
- [7] R. Averback and M. Ghaly, A model for surface damage in ion-irradiated solids, *J. Appl. Phys.* 76:3908 (1994).
- [8] J. R. Beeler, Jr., "Radiation Effects Computer Experiments," North-Holland, New York (1983).
- [9] K. Richter and D. Wintgen, Analysis of classical motion on the Wannier ridge, *J. Phys. B* 23:L197 (1990).
- [10] C. Kirschbaum and L. Wilets, Classical many-body model for atomic collisions incorporating the Heisenberg and Pauli principles, *Phys. Rev. A* 21:834 (1980).
- [11] James S. Cohen, Quasiclassical effective Hamiltonian structure of atoms with $Z = 1$ to 38, *Phys. Rev. A* 51:266(1995).
- [12] G. Xiao, G. Schiwietz, P. Grande, N. Stolterfoht, A. Schmoltdt, M. Grether, R. Kohrbruck, A. Spieler, and U. Stettner, Indications of nuclear-track-guided electrons induced by fast heavy ions in insulators, *Phys. Rev. Lett.* 79:1821(1997).

THE SUN: STRONG CONSTRAINTS ON A WEAKLY-COUPLED PLASMA

Werner Däppen and Alan Nayfonov

Department of Physics and Astronomy
University of Southern California
Los Angeles, CA

INTRODUCTION

The equation of state is one of the three fundamental ingredients used to construct stellar models.⁵ The other two are opacity and nuclear energy reaction rates. One star - the Sun - is very special in two respects. First, the methods of helioseismology allow us to obtain very accurate experimental data of the solar interior (in particular, sound speed and density). Second, in the solar convection zone, helioseismology presents an opportunity to isolate the question of the equation of state from opacity and nuclear reaction rates, since the stratification is essentially adiabatic and thus determined by thermodynamics.³

The plasma of the interiors of “normal” stars, such as the Sun, is only slightly non-ideal. One would therefore think that at least for such stars finding a good equation of state is not too difficult. Indeed, simple models of the equation of state have been quite successful in many aspects of stellar structure and evolution. However, the extraordinary accuracy of the helioseismological data led to the further refinement of the idea what a “good” equation of state for the Sun should be. This has been recognized in the early 80s and models with improved equations of state were used in helioseismic studies (for a review see Ref. [3]).

Several discrepancies between the experimental data and models with simple equations of state have been successfully identified as the signatures of various non-ideal phenomena. The most obvious of these phenomena deal with the Coulomb interaction between charged particles, pressure ionization, and the effects of the internal partition functions of bound systems on the thermodynamical properties of the solar plasma. Though these phenomena are only small corrections in such a weakly coupled system, they clearly surpass the uncertainty of the experimental data.² Helioseismology can therefore be used to test the validity of the different nonideal correction terms implemented in the various equations of state.

Such analyses involving several popular equations of state have shown on the one hand the necessity to include the leading Coulomb correction (expressed by the Debye–Hückel approximation) in order to meet the helioseismological constraints.^{2,4} On the other hand, even those equations of state that do include the leading Coulomb correction differ from the solar data by more than the observational uncertainty. They also differ discernibly among themselves, thus revealing the importance of the treatment of the nonideal effects beyond the leading Coulomb term. Thus, though the solar plasma looks conceptually much simpler

than a strongly coupled many-body system, the necessity to compute the solar plasma so accurately requires a substantial effort, comparable to the studies of more strongly-coupled plasmas. With this, helioseismology can make a contribution to the study of thermodynamic properties of Coulomb systems under conditions unattainable on Earth.

RECENT PROGRESS IN THE EQUATION OF STATE

Equations of state with helioseismic accuracy

There are two basic approaches to realize nonideal equations of state: the so-called *chemical* and *physical* pictures. In the chemical picture one assumes that the notion of atoms and ions still makes sense, and ionization is treated like a chemical reaction. One of the more recent realizations of helioseismic accuracy is the Mihalas–Hummer–Däppen (MHD) equation of state,^{6,8,9} in which modifications of atomic states are expressed in a heuristic and intuitive way, by the probability that the state is occupied as a function of the parameters of the surrounding plasma.

The physical picture provides a systematic method to include nonideal effects (see Ref. [7]). An example used in helioseismology is the OPAL equation of state.^{11,12} OPAL starts out from the grand canonical ensemble of a system of the basic constituents (electrons and nuclei), interacting through the Coulomb potential. Configurations corresponding to bound combinations of electrons and nuclei, such as ions, atoms, and molecules, arise in this ensemble naturally as terms in cluster expansions. Any effects of the plasma environment on the internal states are obtained directly from the statistical-mechanical analysis, rather than by assertion as in the chemical picture.

Bound-state energies and the position of the continuum

Arndt *et al.*¹ have examined the consequence of shifts in bound-state energies and the position of the continuum for thermodynamic quantities. A simple free-energy model was used to examine the thermodynamic consequences of the results of a quantum statistical calculations of two-particle properties in a plasma using Green-function technique.¹³ A comparison with data inferred from helioseismology has shown that such an interdisciplinary procedure works very well for lower-level approximations, such as the static screening in the effective two-particle wave equation. However, in the case of dynamic screening in the wave equation, the resulting thermodynamic quantities became inconsistent with observations.

This might have been due to an inadequacy of our method to compute the thermodynamic quantities, or due to an inappropriate treatment of the ion contribution to the electronic self energy corresponding to the dielectric function used in random-phase approximation (RPA). In any case, such results superbly demonstrate the power of helioseismology to test models of basic plasma physics.

Effect of the internal partition function

A recent study on the effect of different internal partition functions on a complete set of three thermodynamical quantities¹⁰ has revealed interesting features about excited states and their treatment in the equation of state. Fig. 1 shows a typical result, the quantity $\chi_\rho = (\partial \ln p / \partial \ln \rho)_T$ for temperatures and densities corresponding to the hydrogen-ionization zone of the Sun. The figure is for the simplest case, a pure hydrogen mixture. Further figures, for other thermodynamic quantities and for a solar-type hydrogen–helium mixture, can be found in the paper by Nayfonov & Däppen.¹⁰ In Fig. 1, results for five different equations of state (eos) are displayed:

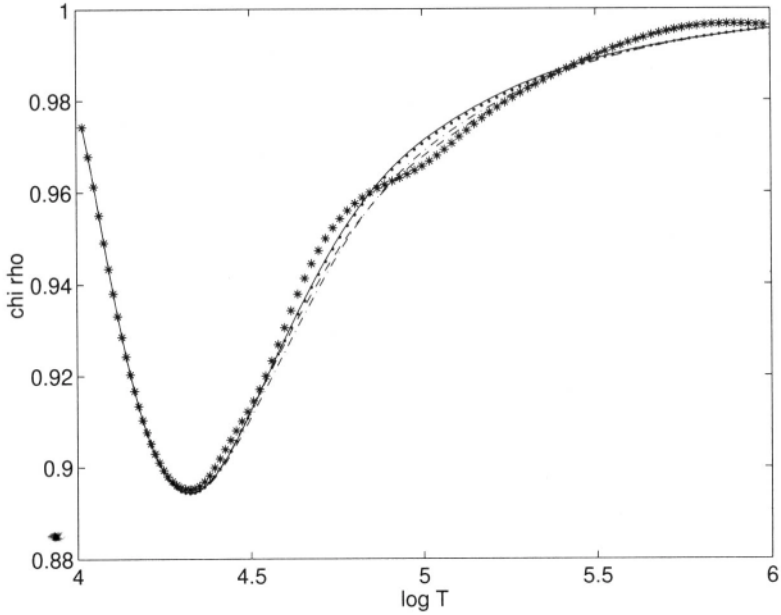


Figure 1. χ_ρ for the temperatures and densities of a typical solar model, for various equations of state with different internal partition functions. See text for line style and further details.

- MHD (asterisks): eos with standard MHD occupation probabilities,
- MHD_{GS} (dashed line): eos with the standard MHD internal partition function of hydrogen truncated to the ground state (GS) term,
- OPAL (solid line): eos of OPAL tables (version of November 1996),
- MHD_{PL} (dotted-dashed line): eos with the standard MHD internal partition function of hydrogen replaced by the Planck–Larkin partition function (see Refs. [7,14]).
- MHD_{PL,GS} (dotted): same as MHD_{PL}, but with partition function truncated to the ground state term.

The MHD equation of state with its specific, density-dependent occupation probabilities⁸ is causing a characteristic wiggle in the thermodynamic quantities. We point out that the presence of excited states is crucial, because MHD_{GS} still has a density-dependent occupation probability of the ground state, but the wiggle does not show up. We also point out that the wiggle, which is a genuine neutral-hydrogen effect, is present despite the fact that most of hydrogen is already ionized. Indeed, in the range of the wiggle ($\log T = 4.7\text{--}5.2$), the fraction of ionized hydrogen increases from 90–97%.

When measured relative to the overall ionization-induced change of a thermodynamic quantity, the signature of the excited states has been found to be most prominent in the quantity $\chi_\rho = (\partial \ln p / \partial \ln \rho)_T$, and less in $\chi_T = (\partial \ln p / \partial \ln T)_\rho$ and $\gamma_1 = (\partial \ln p / \partial \ln \rho)_s$ (s being specific entropy). The opposite could have been expected. After all, χ_T and γ_1 contain, in contrast to χ_ρ , temperature derivatives. One might think that temperature derivatives would cause the highest sensitivity to fine details of the internal partition function because of its Boltzmann factors. However, our results show that the most important effect is coming from the density dependence of the occupation probabilities.

Regarding the helioseismic relevance of the effect of the excited states, we mention that it is also present in γ_1 (and therefore in sound speed), and this with the same magnitude as in $\chi\rho$.¹⁰ Direct helioseismic inversions for γ_1 should therefore be able to reveal the effect of the internal partition function even with present observational data. Recent analyses have demonstrated that the size of the excited-states effect is well within the power of helioseismology.²

CONCLUSIONS

Progress in the solar equation of state serves two purposes. For solar physicists on the one hand, a better equation of state will lead to a smaller uncertainty in solar models, which thus turn into a more reliable astrophysical tool, for instance, to tackle the solar neutrino problem. Plasma physicists on the other hand will recognize that a better equation of state can be found by an astrophysical experiment in a domain where there is not much laboratory competition.

Acknowledgements

This work was supported in part by the grant AST-9618549 of the National Science Foundation and in part by a grant of the Theory Group of Lawrence Livermore National Laboratory.

REFERENCES

- [1] Arndt, A., Däppen, W. & Nayfonov, A. 1997, *Astrophys. J.*, preprint
- [2] Basu, S. & Christensen-Dalsgaard, J. 1997, *Astron. Astrophys.*, 322, L5-L8
- [3] Christensen-Dalsgaard, J. & Däppen, W. 1992, *Astron. Astrophys. Review*, 4, 267
- [4] Christensen-Dalsgaard, J., Däppen, W. & Lebreton, L. 1988, *Nature*, 336, 634
- [5] Christensen-Dalsgaard, J., Däppen, W. & the GONG team 1996, *Science*, 272, 1286–1292
- [6] Däppen, W., Mihalas, D., Hummer, D. G., and Mihalas, B. W. 1988, *Astrophys. J.* 332, 261
- [7] Ebeling, W., Kraeft, W. D. & Kremp, D. 1976, *Theory of Bound States and Ionization Equilibrium in Plasmas and Solids*, Akademie Verlag, Berlin, DDR
- [8] Hummer, D. G. & Mihalas, D. 1988, *Astrophys. J.*, 331, 794
- [9] Mihalas, D., Däppen, W. & Hummer, D. G. 1988, *Astrophys. J.*, 332, 815
- [10] Nayfonov, A. & Däppen, W. 1998, *Astrophys. J.*, preprint
- [11] Rogers, F. J. 1986, *Astrophys. J.*, 310, 723 and references therein
- [12] Rogers, F. J., Swenson, F. J. & Iglesias, C. A. 1996, *Astrophys. J.*, 456, 902
- [13] Seidel, J., Arndt, S. & Kraeft, W.-D. 1995, *Phys. Rev. E* 52, 5387.
- [14] Rogers, F. J., *these proceedings*.

MOLECULAR DYNAMICS MODELING OF DENSE HYDROGEN

J. Kress,¹ L. Collins,¹ T. Lenosky,² I Kwon,³ and N. Troullier⁴

¹Los Alamos National Laboratory
Los Alamos, NM

²Arizona State University
Tempe, AZ

³Seoul National University
Seoul 151-742, South Korea

⁴University of Minnesota
Minneapolis, MN

INTRODUCTION

In order to investigate hydrogen over a wide range of conditions, we have developed two distinct quantum molecular dynamics(QMD) simulation approaches. The more sophisticated¹ relies on explicit diagonalization prescriptions at each time step within a density functional(DF) scheme. The approach compares well to another *ab initio* molecular dynamics(AIMD) method (Car-Parrinello²) and to path integral Monte Carlo(PIMC).³ The computational intensity of these methods limits sample sizes and simulation times to fairly small values. To extend these limits, a more empirical tight-binding(TB)^{4,5} method has evolved. The latter includes direct, exchange, and correlation electronic effects although at a more approximate level than the AIMD; however, these TB models can effectively represent the major mechanisms in a dense fluid: dissociation, ionization, and detachment and their inverse processes. Since we have extensively reviewed these methods elsewhere,^{1,4-6} we shall give only a brief description below.

QUANTUM MOLECULAR DYNAMICS

The basic unit of the molecular dynamics simulation consists of a cubic cell of length L containing equal numbers of electrons and protons [$n_e = n_p = N$]. A periodic replication of this cell throughout space represents the bulk nature of the fluid. We invoke the Born-Oppenheimer approximation and treat the electrons quantum mechanically and the nuclei classically. In this case, a simple two-step procedure suffices to evolve the system in time. First, at a given time step for a fixed configuration of the nuclei, we solve the n_e -electron Schrödinger equation, within a periodically replicated reference cell (supercell) and with a single k-point (the Γ point) sampling of the electronic Brillouin zone, for the quantum mechanical force on each ion. Second, the ions are advanced temporally by solving the

classical equations of motion. Repeating this two-step process evolves the system in time by determining positions, velocities, forces, and electronic properties at each step. From the trajectories, we can determine both static and dynamical properties such as pressure, diffusion coefficients, and electrical conductivities.

Our AIMD approach centers on a finite-temperature DF procedure,⁷ based upon the Mermin functional, which provides a highly accurate determination of the forces. Minimizing this functional with respect to variations of the density leads to a set of equations for the electron orbitals ψ_i of the Kohn–Sham(KS) form. We operate within the local density approximation(LDA) with a free electron gas form for the exchange contribution and the Perdew–Zunger parameterization⁸ for the correlation contribution. In determining the forces, we assume local thermodynamic equilibrium(LTE).

We solve the KS equations for the eigenenergies ϵ_i and associated electron orbitals ψ_i in terms of a plane-wave basis. The truncation of the plane-wave expansion at a fixed energy cut-off produces a matrix of finite size, which we diagonalize by iterative techniques.⁹ Employing the Troullier–Martins pseudopotential¹⁰ with a small cut-off radius, typically of the order less than half the average interatomic separation, considerably reduces the size of the basis and the computational effort at each time step.

We have also developed TB models^{4,5} that accurately represent hydrogen over an extensive range of temperatures and pressures. The total TB energy has the form:

$$E = \sum_i f_i \epsilon_i + \sum_{i<j} \phi_{ij} \quad (1)$$

where f_i is the occupation number based on a Fermi–Dirac(FD) distribution at temperature T , ϕ is an effective pair potential, ϵ_i is an eigenvalue of $\mathbf{H}\psi_i = \epsilon_i \mathbf{S}\psi_i$ with \mathbf{H} and \mathbf{S} , the hamiltonian and overlap matrices respectively. A nonlinear least-squares fit yields the optimal form of the terms in Eq. (1) that best reproduce a set of *ab initio* results. We have developed two complementary tight-binding models: 1) a single s-type nonorthogonal basis(TBs)⁵ for low temperatures($< 3\text{eV}$) and moderate densities($< 1\text{g/cm}^3 \text{H}$) and 2) a double s-type orthogonal basis(TBs')⁴ for higher temperatures and densities.

The frequency-dependent electrical conductivity derived from the Kubo–Greenwood [KG] formulation¹¹ has the form

$$\sigma(\omega) = \frac{2\pi}{\Omega\omega} \sum_{ij} [f_i - f_j] |D_{ij}|^2 \delta(\epsilon_i - \epsilon_j - \omega) \quad (2)$$

where Ω is the atomic volume, ω the frequency, and D_{ij} the velocity dipole matrix element between states i and j . The eigenenergies and eigenstates used to construct $\sigma(\omega)$ come from the KS diagonalization at a given time step.

Since our TB model does not explicitly contain spatial electron orbitals, we cannot calculate the dipole matrix elements required in the KG formulas. However, we can still determine the *dc* electrical conductivity $\sigma(0)$ using approximations to the KG formula due to Mott.¹² These approximations apply mainly at low temperatures at which the difference between the FD distribution functions becomes strongly peaked around the Fermi energy, and the dipole matrix elements depend only weakly on the energy. For these conditions, Eq. (2) becomes:

$$\sigma(0)_{\text{Mott}} = -2\pi a_M \int N(E)^2 \frac{\partial f}{\partial E} dE. \quad (3)$$

with a_M representing an average nearest-neighbor distance within the fluid. The TB model does produce an energy spectrum $[\epsilon_i]$ from the diagonalization, permitting the construction of the density of states $N(E)$. We report a trajectory-averaged electrical conductivity by averaging over the above single time-step formulae.

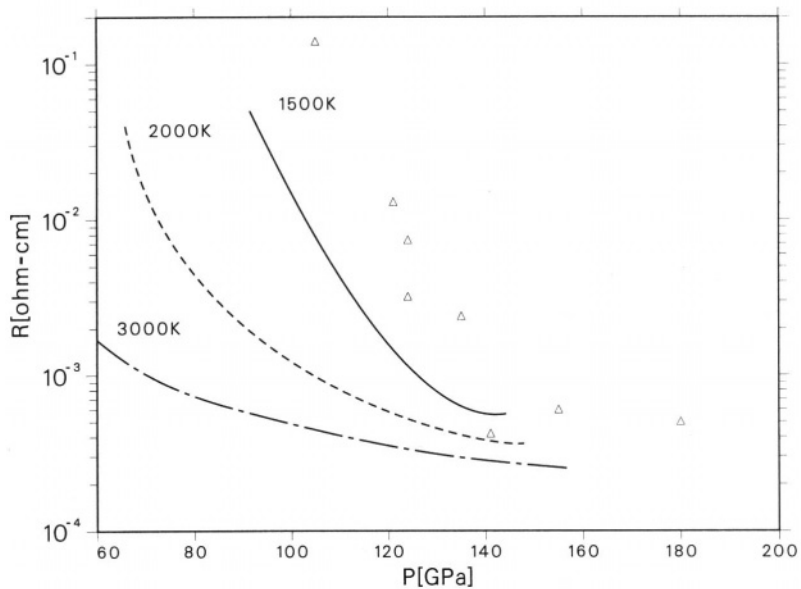


Figure 1. Resistivity as a function of temperature and density for TBs(solid lines); experimental results¹³ (triangles).

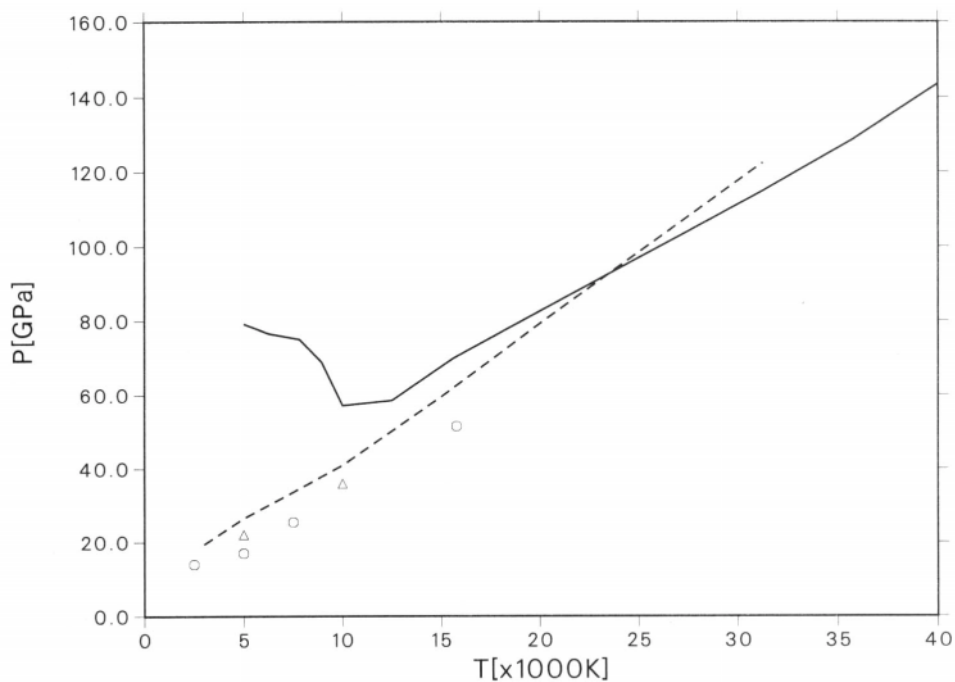


Figure 2. Pressure as a function of temperature at a fixed density [$r_s=2$] for H. TBs MD, 250 atoms (dashed line). AIMD, 54 atoms (open circles). AIMD, 128 atoms (open triangles). PIMC (solid line).

SIMULATIONS

Our applications of the above QMD methods have ranged over a wide variety of systems and physical environments including hydrogen, liquid alkali metals near melt, isotopic hydrogenic mixtures at high densities and elevated temperatures, rare gas solids under high compression, impurities in hydrogen plasmas, and polymers. We describe here several new developments on dense hydrogen at low to moderate temperatures.

Recent gas gun experiments at Livermore,¹³ which compressed cryogenically-cooled deuterium to densities approaching 1g/cm^3 at temperatures of a few thousand K, have shown a marked increase in the electrical conductivity with compression. The peak magnitude ($\sigma \sim 2000/\text{ohm-cm}$) corresponds closely to the liquid alkali metals or semiconductors while the low temperature indicates a predominantly molecular fluid. Our earlier simulations,⁵ using the TBs model for sample sizes ranging up to 1000 atoms, found several interesting trends: 1) the fluid even at the highest densities remained largely molecular ($> 80\%$); 2) the conductivity scaled as the square of the monomer fraction; and 3) the electronic states around the Fermi level had a large monomer component ($> 50\%$). Since at these temperatures, the principal contribution to the conductivity arises from those electronic states near the Fermi level, the third finding indicates that the electron mobility critically depends on the monomer states. Thus, even though the monomers comprise but a small fraction of the sample, they make a substantial contribution to the states that most determine the conductivity. More elaborate AIMD simulations confirm these basic findings. We have performed further calculations with these models to gain a more quantitative comparison with experiment. In Fig. 1, we display the resistivity ($R=1/\sigma$) as a function of pressure (density) for several temperatures. The basic trends consistently match those of the experiment, within the error bounds, for the lower temperatures. In addition, the MD calculations portray a highly transient system with the lifetimes of the molecular bonds on the order of only a few vibrational periods. Therefore, the *dynamical* interplay of the various constituents of the fluid plays an important role in representing the nature of the system.

Recent experiments¹⁴ with the NOVA laser have called into question equation-of-state models for hydrogen by indicating a large swing-out in the shock Hugoniot. Calculations using the TB approaches⁵ described above do not show this excursion and lie closer to the results predicted by older EOS models.¹⁵ To further explore this regime, we have performed additional simulations with the TBs model (250 atoms) as well as with AIMD using sample sizes of 54 and 128 atoms at a representative density. The results appear in Fig. 2 and are compared with the PIMC. Two k-point sampling (not shown) yielded similar pressures compared to the Γ point sampling (Fig. 2) for 54 atoms with AIMD. In neither the TBs or AIMD cases do we observe the rapid pressure rise at low temperatures (negative $\partial P/\partial T$), attributed to a plasma phase transition.³

REFERENCES

- [1] L. Collins, I. Kwon, J. Kress, N. Troullier, and D. Lynch, Phys. Rev. E **52**, 6202 (1995).
- [2] D. Hohl, V. Natoli, D. M. Ceperley, and R. M. Martin, Phys. Rev. Lett. **71**, 541 (1993); J. Kohanoff and J.-P. Hansen, Phys. Rev. E **54**, 768 (1995).
- [3] W. R. Magro, D. M. Ceperley, C. Pierleoni, and B. Bernu, Phys. Rev. Lett. **76**, 1240 (1996).
- [4] I. Kwon, J. D. Kress, and L. A. Collins, Phys. Rev. B **50**, 9118 (1994).
- [5] T. Lenosky, J. D. Kress, L. A. Collins, and I. Kwon, Phys. Rev. B **55**, R11907 (1997); *ibid.* **56**, 5164 (1997).
- [6] I. Kwon, L. Collins, J. Kress, and N. Troullier, Phys. Rev. E **54**, 2844 (1996).
- [7] N. D. Mermin, Phys. Rev. **137A**, 1441 (1965).
- [8] J. P. Perdew and A. Zunger, Phys. Rev. B **23**, 5048 (1981).
- [9] E. R. Davidson, Comp. in Phys. **7**, 521 (1993) and references therein.
- [10] N. Troullier and J. L. Martins, Phys. Rev. B **43**, 1993 (1991).

- [11] W. A. Harrison, *Solid State Theory* (McGraw-Hill, New York, 1970).
- [12] N. F. Mott and E. A. Davis, *Electronic Processes in Non-Crystalline Materials*, (Clarendon Press, Oxford, 1979), chapter 1.
- [13] S. T. Weir, A. C. Mitchell, and W. J. Nellis, *Phys. Rev. Lett.* **76**, 1860 (1996).
- [14] L. B. DaSilva *et. al.* *Phys. Rev, Lett.* **78**, 483 (1997).
- [15] G. I. Kerley, in *Molecular-Based Study of Fluids*, edited by J. M. Habibe and G. A. Mansoori (American Chemical Society, Washington, 1983).

This page intentionally left blank

RESTRICTED PATH INTEGRAL MONTE CARLO CALCULATIONS OF HOT, DENSE HYDROGEN

W. R. Magro,¹ B. Militzer,² D. M. Ceperley,² B. Bernu,³ and C. Pierleoni⁴

¹Dept. of Physics and Theory Center, Cornell University
Ithaca, NY

²Dept. of Physics and NCSA, University of Illinois
Urbana, IL

³LPTL, Université P. et M. Curie
Paris, France

⁴Dipartimento di Fisica, Università dell'Aquila
Aquila, Italy

INTRODUCTION

Hydrogen is the most abundant element in nature and has the simplest composition. Despite considerable research, many aspects of its phases and structure remain unclear. In particular, when dense hydrogen is compressed or heated, it is not obvious whether molecular dissociation proceeds via a first order transition or a continuous transformation. Second, at high density, it is uncertain whether the molecular fluid transforms directly to an ionized plasma or into an intermediate atomic phase.¹ Recent advances have allowed experimentalists to probe the relevant region,^{2,3} but these issues remain unresolved. In this paper, we use a fully interacting quantum many body method, restricted path integral Monte Carlo (PIMC),⁴ to model dense hydrogen at finite temperature and address these issues.

METHOD

We modeled hydrogen and deuterium as a neutral, spin zero system of electrons and nuclei at temperature $T \equiv \beta^{-1}$, interacting with Coulomb potentials in a periodically repeated cube. The quantum statistical mechanics of the system was incorporated via Feynman's path integral formulation,⁵ which expresses the low temperature physics of the system in terms of its high temperature physics, given by the density matrix, ρ_τ :

$$\rho_\beta = e^{-\beta\hat{H}} = \left(e^{-\tau\hat{H}} \right)^M. \quad (1)$$

Once the density matrix is known, operators are computed as

$$\langle \hat{O} \rangle \equiv \frac{\text{Tr} [\hat{O}\rho_\beta]}{\text{Tr} [\rho_\beta]} \quad (2)$$

$$= \frac{\sum_P (-1)^P \int dR dR_1 \cdots dR_{M-1} \langle R | \hat{O} \rho_\tau | R_1 \rangle \langle R_1 | \rho_\tau | R_2 \rangle \cdots \langle R_{M-1} | \rho_\tau | PR \rangle}{\sum_P (-1)^P \int dR dR_1 \cdots dR_{M-1} \langle R | \rho_\tau | R_1 \rangle \langle R_1 | \rho_\tau | R_2 \rangle \cdots \langle R_{M-1} | \rho_\tau | PR \rangle}. \quad (3)$$

The sum is taken over all permutations of spin like electrons* with odd permutations yielding a negative contribution. The negative sign is problematic for Monte Carlo methods and is eliminated using the fixed node approximation.⁶ In this approximate formulation, the domain of integration is limited to the positive domain of a trial density matrix, and permutations are restricted to even exchange cycles. The observable expression then becomes

$$\langle \hat{O} \rangle = \frac{\sum_{P_+} \int_{\Omega_+} dR dR_1 \cdots dR_{M-1} \langle R | \hat{O} \rho_\tau | R_1 \rangle \langle R_1 | \rho_\tau | R_2 \rangle \cdots \langle R_{M-1} | \rho_\tau | PR \rangle}{\sum_{P_+} \int_{\Omega_+} dR dR_1 \cdots dR_{M-1} \langle R | \rho_\tau | R_1 \rangle \langle R_1 | \rho_\tau | R_2 \rangle \cdots \langle R_{M-1} | \rho_\tau | PR \rangle}, \quad (4)$$

with P_+ and Ω_+ denoting all even permutations and the positive domain, respectively.

The Coulomb potential is first broken into long- and short- range pieces using an optimized Ewald breakup. The many-body high-temperature density matrix, ρ_τ , is then constructed from a product of two-body short-range density matrices and a long range many-body correction. The density matrix is constructed to become exact as the time step, τ , vanishes; τ is chosen sufficiently small to provide a reasonable tradeoff between computational effort and accuracy. Simulation temperatures ranged from 5000 K. to 125 000 K with $\tau^{-1} \approx 10^6$ K, yielding the number of ‘time slices,’ $M \equiv \beta/\tau$, in the range of eight to two hundred.

The resulting high-dimensional path integral is evaluated using a generalized Metropolis Monte Carlo method.^{6,7} Many details of the computational techniques employed may be found in Refs. [6,8,9].

MOLECULAR FORMATION AND DISSOCIATION

Figure 1 provides an overview of the simulations at several temperatures and densities. At the lowest density, $r_s = 2.2$, molecules begin to appear near 15 625 K. Molecular formation is essentially complete at 5000 K.¹⁰ It is apparent from the figure that $dP/dT < 0$ for the region separating the plasma from the molecular fluid. This behavior is expected, since dissociation can be separately achieved from any molecular state point by heating or compression. In fact, as reported in Ref. [11], we find a region of $dP/dT < 0$ at constant density for $r_s < 2.2$, which we interpret as coexistence of two phases. This region is the manifestation, at constant volume, of a density discontinuity at constant pressure. Similar results are obtained for deuterium.

While the cooler phase is clearly a molecular fluid, the hotter phase is not a plasma, but rather a partially ionized atomic fluid. This can be seen from Figure 2, which exhibits the ($r_s = 2.0$, $T = 12\,500$ K) electron–proton pair correlation, $r^2 [g_{pe}(r) - 1]$. This function shows the radial redistribution, relative to free particles, of electrons in the presence of protons. The maximum density is achieved near one Bohr radius, as expected for an atomic-like phase. Further, a broad minimum exists near 3 Bohr, indicating the electrons localize near protons long enough to exclude other electrons, even when very few molecules are present. This feature disappears around 30000K, as hydrogen begins to ionize into a plasma.¹⁰

Figure 3 shows the electron exchange probability versus density and temperature. In the plasma phase above 100 000 K, there is very little probability for an electron to be involved in a quantum exchange. As temperature is lowered, however, the exchange probability grows and peaks at the phase line, near 10000K. At constant temperature, exchange increases with density. It is suppressed somewhat as molecules form but remains substantial well into

*Proton exchange is negligible at the conditions we considered and, so, was not considered.

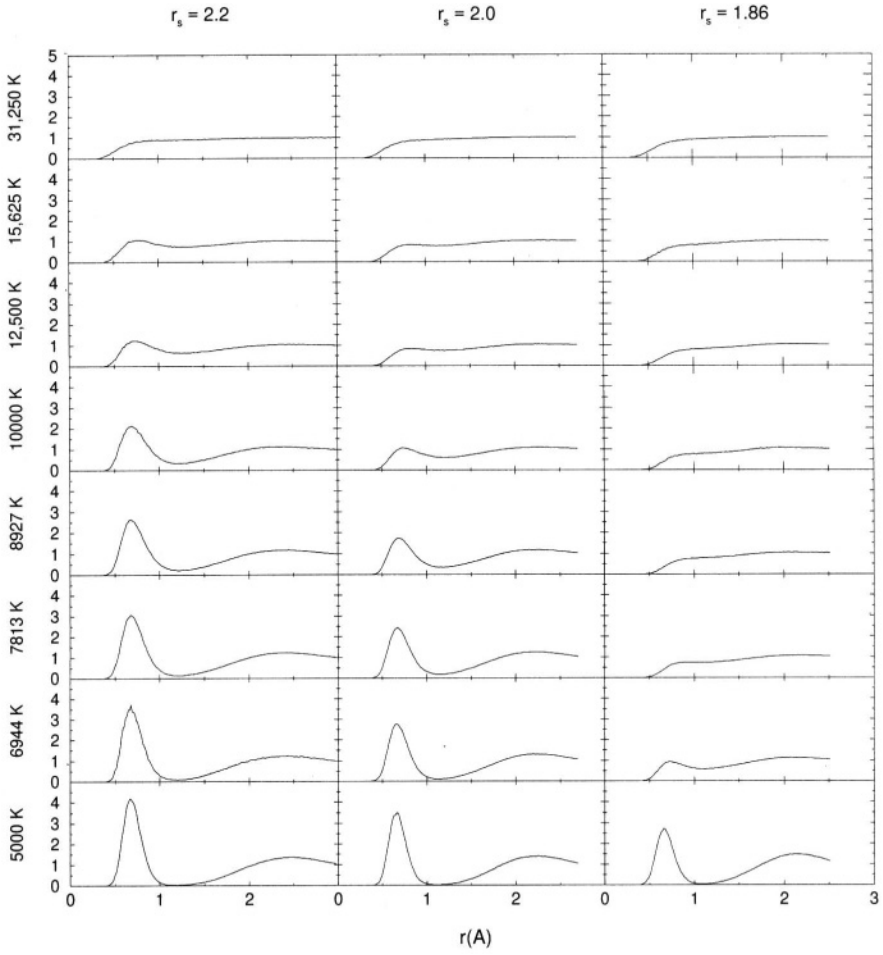


Figure 1. Proton–proton pair correlations, $g_{pp}(r)$.

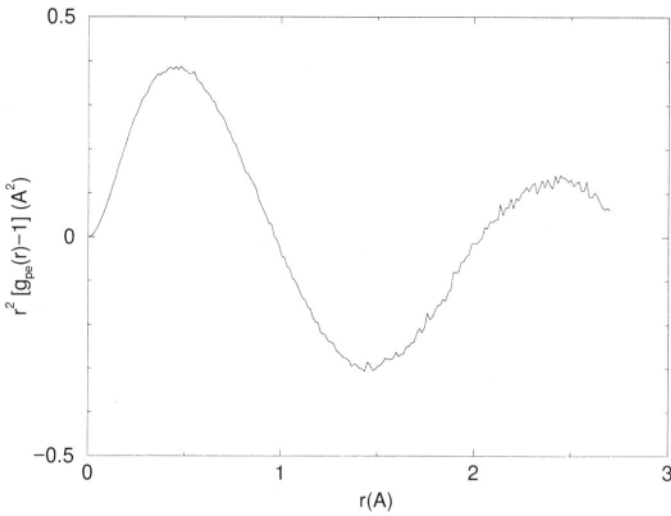


Figure 2. The proton–electron radial correlation function, $r^2 [g_{pe}(r) - 1]$ at $(r_s = 2.0, T \approx 12500 \text{ K})$.

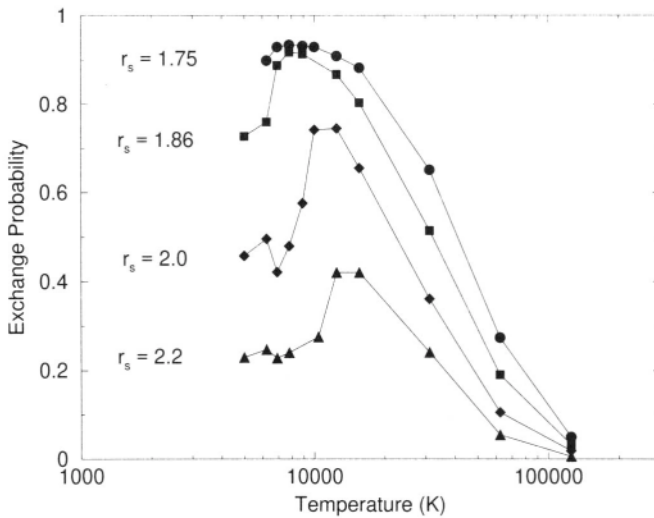


Figure 3. Probability of an electron participating in an exchange.

the molecular phase. Spin-like electrons form long, directed exchange cycles that span the simulation cell. Since electrons of opposite spin occupy each molecular bond, these electron exchanges are *inter*-molecular. In liquid helium, exchange cycles of this type are directly related to superfluidity,⁹ so it seems likely that electronic exchange is related to electrical conductivity. The electrons, then, would be in an unusual state in which they simultaneously provide molecular bonding and contribute to the conductivity. This may explain the recent experimental finding² that shock-compressed hydrogen metallizes before the molecular state is substantially dissociated.

REFERENCES

- [1] D. Saumon and G. Chabrier, *Phys. Rev. A* 46:2054 (1992)
- [2] S. T. Weir, A. C. Mitchell, and W. J. Nellis, *Phys. Rev. Lett.* 76:1860 (1996).
- [3] I. B. Da Silva, P. Celliers, G. W. Collins, K. S. Budil, N. C. Holmes, W. T. Jr. Barbee, B. A. Hammel, J. D. Kilkenny, R. J. Wallace, M. Ross, R. Cauble, A. Ng and G. Chiu, *Phys. Rev. Lett.* 78:483 (1997).
- [4] D. M. Ceperley, Path integral Monte Carlo methods for fermions, in "Monte Carlo and Molecular Dynamics of Condensed Matter Systems," Ed. K. Binder and G. Ciccotti, Bologna, Italy (1996).
- [5] R. P. Feynman, "Statistical Mechanics: A Set of Lectures," W. A. Benjamin, Reading, Massachusetts (1972).
- [6] D. Ceperley, *Phys. Rev. Lett.* 69:331 (1992).
- [7] D. M. Ceperley and E. Pollock, *Phys. Rev. B* 39:2084 (1989)
- [8] W. R. Magro, Ph. D. thesis, University of Illinois, (1994)
- [9] D. M. Ceperley, *Rev. Mod. Phys.* 67:279 (1995).
- [10] B. Militzer, W. Magro, and D. Ceperley, this volume.
- [11] W. R. Magro, D. M. Ceperley, C. Pierleoni, and B. Bernu, *Phys. Rev. Lett.* 76:1240 (1996).

WAVE-PACKET MOLECULAR DYNAMICS SIMULATION OF HYDROGEN

M. Knaup, D. Klakow, P.-G. Reinhard, and C. Toepffer

Institut für Theoretische Physik II
Universität Erlangen, Staudtstr. 7, D-91058 Erlangen, Germany

Hydrogen, being composed of the simplest atom, is a material whose properties have attracted attention since long. It was as early as 1935 that the existence of a metallic phase at high pressures has been postulated.¹ Since then this problem has been intensely studied, not only as a basic challenge in many-body physics but also because of important astrophysical implications.²

Recent experiments with multiple shock waves show a remarked increase of the conductivity by four orders of magnitude for pressures between 93 and 180 GPa.³ In these experiments neither the density nor the temperature have been measured independently. Instead they were calculated by computationally simulating each measurement using a standard equation of state for hydrogen in the molecular fluid phase.⁴ Relating the resistivity to a density-dependent band gap and to the temperature, the data have thus been interpreted in terms of a continuous transition from a semiconducting to a metallic diatomic fluid at 140 GPa and 3000 K.

However, this view does not comply with several theoretical investigations using different advanced many-body methods which all predict a first-order phase transition. A chemical picture has been employed in [5] where hydrogen is described as a mixture of H_2 , H , H^+ and free electrons where the properties of molecules, atoms and ions change with increasing density because of the polarization due to strong coupling. Hierarchical schemes based on the hypernetted chain (HNC) equations allow to account for both long- and short-range correlations in fluids⁶ and these have been applied to the hydrogen problem.⁷ Using the equation of state emerging therefrom and corresponding models for the conductivity,⁸ the results of the multiple shock wave experiments³ have been interpreted as a first-order transition between molecular and metallic phases. This view is supported by path-integral Monte Carlo (PIMC) studies of hydrogen⁹ which show a decreasing pressure $P(T)$ as the temperature is raised between 5000 K and 10000 K at densities around $n = 2 \times 10^{29} \text{ m}^{-3}$. This drop in pressure is due to the decrease in electron kinetic energy density upon the breaking of the molecular bonds during the dissociation of the H_2 molecules. A tight binding calculation¹⁰ shows no such drop in pressure, on the other hand.

Here we investigate the problem of a phase transition in hydrogen at high pressures on the basis of extensive numerical simulations of the equation of state, pair correlation functions and charge transport coefficients. To this end, we employ an efficient quantum mechanical simulation scheme, the wave-packet molecular dynamics (WPMD). The technical simplifications of the scheme allow to use much larger samples which, in turn, help to pin down

the structural changes more precisely. The WPMD was developed for simulations of dense two-component plasmas where quantum effects play a crucial role to guarantee the stability of the system.¹¹ It aims to combine the simplicity of classical MD simulations with the essential quantum features of the dynamics. As usually done in molecular physics, the ions are treated classically while the electrons are described by quantum mechanical wavefunctions. The dynamics of both constituents is carried through simultaneously without recurring to any adiabatic approximation. That is a formidable task. The simplifications consist in describing each electronic wavefunction by a Gaussian wave packet whose position, momentum and (complex) width remain as free dynamical parameters. As a further approximation, antisymmetrization is expanded into a hierarchy of exchanges and the hierarchy is cut at the order of pairwise exchange. Exchange correction remains small for delocalized electron states at temperatures down to one tenth of the Fermi temperature $T_F = \hbar^2(3\pi^2n)^{2/3}/(2k_Bm)$ (where m is the electron mass). The approximation holds to even lower temperatures for localized molecular states. The method has been checked by comparison with density-functional methods¹² and applied successfully to various situations in plasma physics.^{11,13} The ansatz with Gaussian wave packets and the approximative treatment of exchange yield a very efficient scheme which allows to treat large samples. And large samples are particularly important in studying phase transitions.

The actual WPMD-simulations reported here have been done with $N = 256$ or $N = 2048$ electrons and the same number of protons in a periodically continued box. For purposes of comparison we note that the number density n of either protons or electrons is related to the Wigner–Seitz radius a by $n = 3/(4\pi a^3)$. Introducing $r_s = a/a_B$ with the Bohr radius $a_B = 0.529 \times 10^{-10}$ m one obtains $n = 1.613 r_s^{-3} \times 10^{30} \text{ m}^{-3}$ for the number density and the mass density for hydrogen is $\rho = 1.68 n \times 10^{-24}$ g.

An important tool to analyze the structure of a hydrogen system is the proton–proton correlation function g_{pp} . In Figs. 1 and 2 we compare the WPMD result¹⁴ for g_{pp} with $N = 2048$ electrons with the dissociation model⁷ for $n = 2.02 \times 10^{29} \text{ m}^{-3}$. At the lower temperature $T = 2000$ K (Fig. 1), both treatments show a strong molecular peak near the bond length of the H_2 molecule at $1.4a_B$ and a broader peak due to next-neighbor molecules near $4.5a_B$. The sharp minimum around $2a_B$ indicates the low degree of dissociation under these conditions, it is 0.07% in the dissociation model. As shown in Fig. 2 the WPMD and the dissociation model agree also very well at a higher temperature $T = 5000$ K. Here the dissociation model yields 5.9% for the degree of dissociation, and the minimum near $2a_B$ becomes less pronounced. The pair correlation from the tight binding model¹⁰ is even less structured while the PIMC result⁹ with 32 electrons yields an even sharper structure with a shift towards smaller bond lengths. It must be kept in mind in this context, that this PIMC simulation involves a high-temperature approximation, as the nodes of the density matrix are taken from free particles. One may expect that this assumption becomes progressively questionable in a regime dominated by molecules.

In the upper part of Fig. 3 we show for the same density $n = 2.02 \times 10^{29} \text{ m}^{-3}$ the pressure as a function of the temperature. As stated above the free-node approximation⁹ becomes increasingly unreliable for $T \rightarrow 0$, while the WPMD agrees nicely with an earlier PIMC result for the groundstate, obtained by introducing Slater–Jastrow correlations into the trial density,¹⁵ as indicated by the arrow in Fig. 3. Both the PIMC (with 32 electrons) and the WPMD results (with 256 electrons) agree in that they show a drop in pressure around 8500 K which is due to the angular delocalization of the electrons upon the breaking of the molecular bonds. Beyond that temperature drops are forming in the WPMD in which the local density exceeds the limits where the restriction to pairwise exchange is acceptable.

The experimental results suggest that the transition near 8500 K is distinguished by a jump in the conductivity. To that end we have computed the electronic conductivity σ_e which

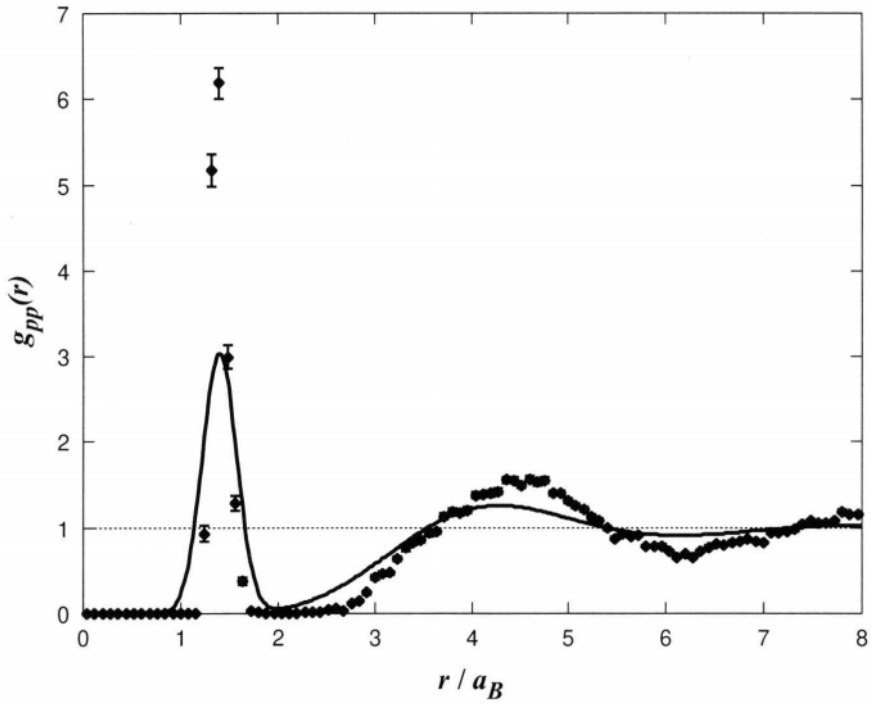


Figure 1. Proton–proton pair distribution at $T = 2000\text{ K}$ and $n = 2.02 \times 10^{29}\text{ m}^{-3}$ ($r_s = 2$). The WPMD result for 2048 electrons (data points) is compared with the dissociation model⁷ (full curve).

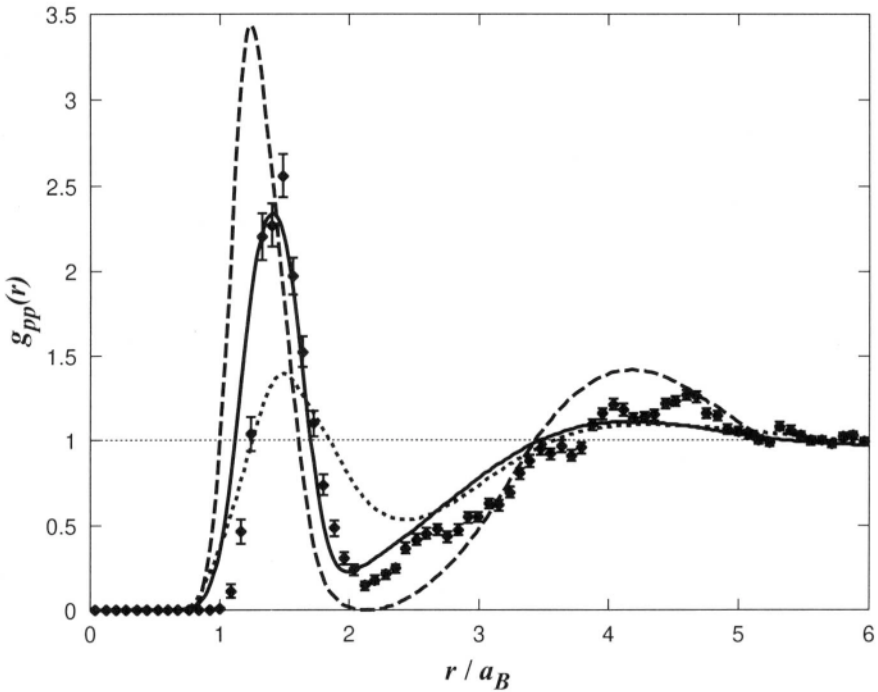


Figure 2. Proton–proton pair distribution at $T = 5000\text{ K}$ and $n = 2.02 \times 10^{29}\text{ m}^{-3}$ ($r_s = 2$). The WPMD result for 2048 electrons (data points) is compared with the dissociation model⁷ (full curve), the PIMC simulation with 32 electrons⁹ (dashed curve) and the tight binding calculation of Ref. [10] (dotted curve).

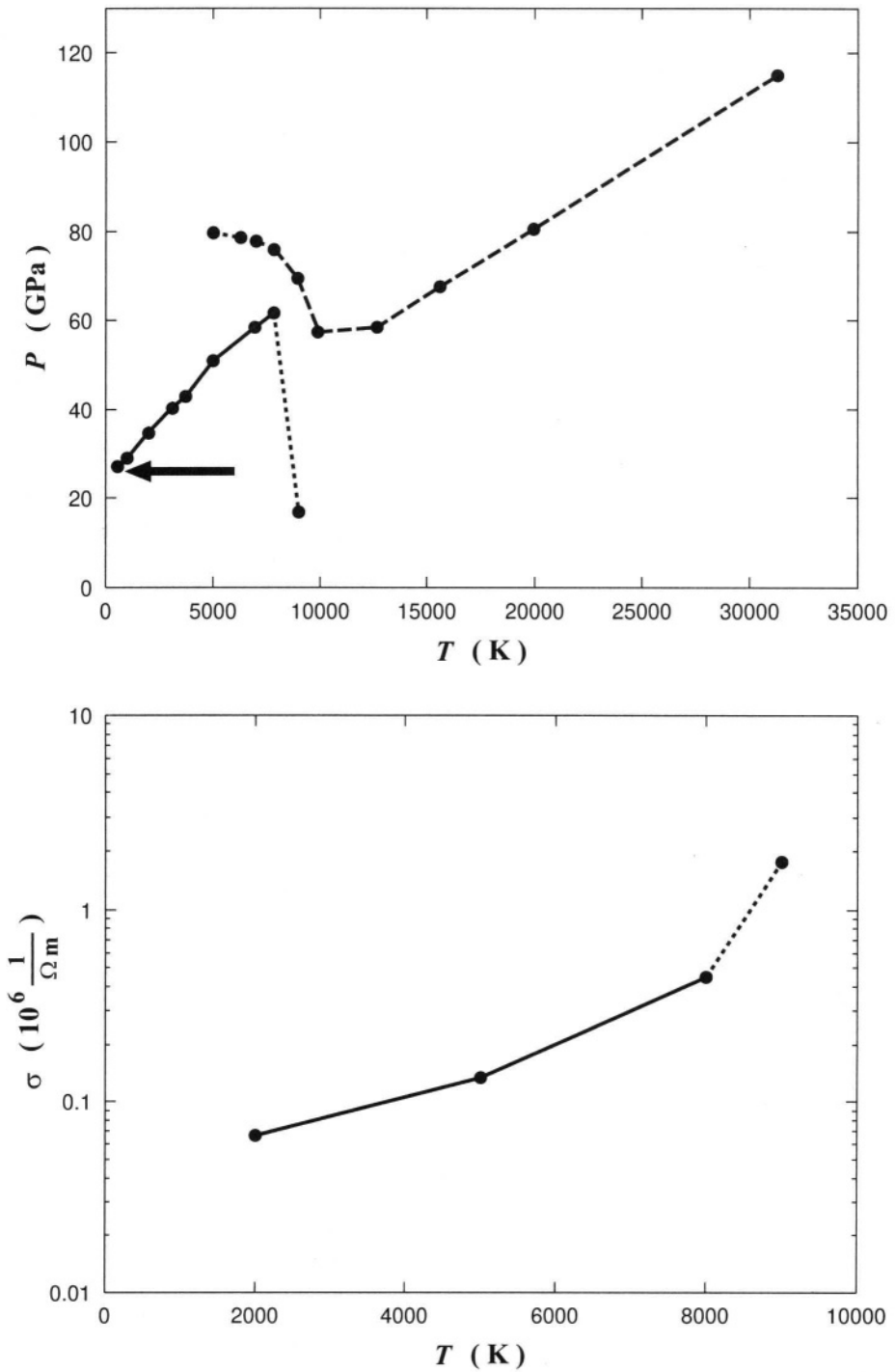


Figure 3. Pressure (upper part) and conductivity (lower part) as a function of temperature at $n = 2.02 \times 10^{29} \text{ m}^{-3}$ ($r_s = 2$). WPMD results for 256 electrons as data points connected by solid curve for $T < 8500 \text{ K}$ and dotted curve for $T > 8500 \text{ K}$. PIMC results⁹ as data points connected by dashed curve for $T > 8500 \text{ K}$ and dotted curve for $T < 8500 \text{ K}$. The arrow in the upper part indicates the ground state pressure from Ref. [15].

carries the dominant fraction of the total conductivity. By virtue of the fluctuation–dissipation theorem $\sigma_e = D_e e^2 n / (k_B T)$ and the diffusivity is obtained from the velocity autocorrelation function (VAF) $Z_e(t)$ as $D_e = k_B T / m \times \int_0^\infty Z_e(t) dt$.¹⁶ The VAF is easily calculated in the true dynamics of the WPMD. The resulting conductivity is shown in the lower part of Fig. 3. We see a distinct rise through two orders of magnitude from low conductivity at lower densities to large conductivity at high densities.

At this stage it appears that the PIMC and the WPMD complement each other in the sense that the PIMC with fixed nodes is better suited to describe delocalized states while the WPMD with only pairwise exchange superiorly describes the localized molecular states. In Fig. 3 we therefore dotted the curves joining the PIMC data for $T < 8500$ K and the WPMD data for $T > 8500$ K.

Our results tend support an interpretation in terms of a first-order phase transition in high-density hydrogen. The calculations at fixed density $n = 2.02 \times 10^{29} \text{ m}^{-3}$ show a sudden drop of the pressure in a temperature interval between 8000 K and 9000 K. These values comply with the experimental results of Weir et al.³ The transition can be interpreted as a transition from molecular hydrogen to a metallic fluid.

The work has been supported by grants from the Bundesministerium für Bildung und Forschung (BMBF, 06 ER 830 2), and the Gesellschaft für Schwerionenforschung (GSI, ER TOT).

REFERENCES

- [1] E. Wigner and H. B. Huntington, *J. Chem. Phys.* **3**, 764 (1935)
- [2] G. Chabrier, D. Saumon, W. B. Hubbard, and J. I. Lunine, *Astrophys. J.* **391**, 817 (1992)
- [3] S. T. Weir, A. C. Mitchell, and W. J. Nellis, *Phys. Rev. Lett.* **76**, 1860 (1996)
- [4] G. I. Kerley, in: “Molecular-Based Study of Fluids,” edited by I. M. Haile and G. A. Mansoori (American Chemical Society, Washington, 1983), pp. 107–138.
- [5] D. Saumon and G. Chabrier, *Phys. Rev. A* **46**, 2084 (1992)
- [6] S. Ichimaru, in: “Statistical Plasma Physics II,” Addison-Wesley, Reading MA 1994, chs. 3,4
- [7] A. Bunker, S. Nagel, R. Redmer, and G. Röpke, *Phys. Rev. B* **56**, 3094 (1997)
- [8] H. Kitamura and S. Ichimaru, *Phys. Rev. E* **51**, 6004 (1995)
- [9] W. R. Magro, D. M. Ceperley, C. Pierleoni, and B. Bernu, *Phys. Rev. Lett.* **76**, 1240 (1996)
- [10] T. J. Lenosky, J. D. Kress, L. A. Collins, and I. Kwon, *Phys. Rev. B* **55**, R 11907 (1997)
- [11] D. Klakow, C. Toepffer, and P.-G. Reinhard, *J. Chem. Phys.* **101**, 1 (1994);
D. Klakow, C. Toepffer, and P.-G. Reinhard, *Phys. Lett. A* **192**, 55 (1994)
- [12] D. Hohl, V. Natoli, D. M. Ceperley, and R. M. Martin, *Phys. Rev. Lett.* **71**, 541 (1993)
- [13] G. Zwicknagel, C. Toepffer, and P.-G. Reinhard, preprint 1997, subm. to *Phys. Rep.*
- [14] S. Nagel, R. Redmer, G. Röpke, M. Knaup, and C. Toepffer, preprint 1997, subm. to *Phys. Rev. E*
- [15] D. M. Ceperley and B. J. Alder, *Phys. Rev. B* **36**, 2092 (1987)
- [16] J. P. Hansen and I. R. McDonald, *Phys. Rev. A* **23**, 2041 (1981)

This page intentionally left blank

SCATTERING CROSS SECTIONS AND CONDUCTIVITY OF STRONGLY COUPLED HYDROGEN PLASMA

Kh. T. Nurekenov,^{1,2} F. B. Baimbetov,² G. L. Gabdullina,² R. Redmer,¹ and G. Röpke³

¹Fachbereich Physik, Universität Rostock
D-18051 Rostock, Germany

²Department of Physics, Al Farabi Kazakh State National University
Tole bi 96, Almaty, 480012, Republic of Kazakhstan

³Arbeitsgruppe "Theoretische Vielteilchensysteme"
Max-Planck-Gesellschaft an der Universität Rostock
D-18051 Rostock, Germany

INTRODUCTION

Due to the long-range character of the Coulomb interaction, many-particle effects play an important role in strongly coupled plasmas. We will study here the effects of screening beyond the Debye–Hückel theory on the transport properties of strongly coupled hydrogen plasma. In previous papers,^{1,2} an effective two-body potential has been derived that takes into account three-particle correlations. This potential was obtained on the basis of a sequential solution of Bogolyubov's chain equations and can be given in analytical form as [1]

$$\Phi(r) = \frac{\gamma}{r} e^{-r} \frac{1 + \gamma f(r)/2}{1 + c(\gamma)}. \quad (1)$$

Here we used the definitions $f(r) = (e^{-\sqrt{\gamma}r} - 1)(1 - e^{-2r})/5$ and $r = r/r_D$, where r_D is the Debye screening length. The potential is expressed in terms of the thermal energy, $\Phi(r) = \Phi(r)/k_B T$, and $\gamma = e^2/(r_D k_B T)$ is a nonideal plasma parameter. $c(\gamma)$ is a correction coefficient for different values of γ .

In the present paper, we present an improved evaluation of the plasma transport quantities and perform quantum mechanical calculation of the scattering cross sections by means of scattering phase shifts δ_l for the effective potential (1) solving Schrödinger equation numerically. For comparison, the analytical expression for the differential cross section in Born approximation is also determined for the effective potential (1). The plasma parameters considered here are $n_e \sim (10^{19} \div 10^{21}) \text{ cm}^{-3}$ and $T \sim (1 \div 10) \times 10^4 \text{ K}$. With the calculated transport cross sections, the electrical conductivity of fully ionized, strongly coupled hydrogen plasma is determined within the frame of the Chapman–Enskog method. Comparison with available experimental data as well as with results of other theoretical approaches is performed.

SCATTERING CROSS SECTIONS

The various cross sections for the scattering between charged particles in a plasma are related to the scattering phase shifts $\delta_l^{4,5}$. In order to calculate scattering phase shifts $\delta_l(k)$, the radial Schrödinger equation for the relevant scattering process is considered,

$$\frac{d^2}{dr^2}u_l(r) + \left[k^2 - \frac{l(l+1)}{r^2} - \frac{2\mu_{ec}}{\hbar^2}\Phi_{ec}(r) \right] u_l(r) = 0, \quad (2)$$

where $\Phi_{ec}(r)$ is the interaction potential between the particles. We solve Eq. (2) by means of the amplitude–phase method.³ The wave function $u_l(r)$ is presented as,

$$u_l(r) = A_l(r) \left[\cos \delta_l(r) \hat{j}_l(kr) - \sin \delta_l(r) \hat{n}_l(kr) \right], \quad (3)$$

where $A_l(r)$ is the amplitude function. After inserting this expression into the Schrödinger equation (2), the so-called Calogero differential equation for the scattering phase shifts $\delta_l(r)$ is derived:³

$$\frac{d}{dr} \delta_l(r) = -\frac{2\mu_{ec}}{k\hbar^2} \Phi_{ec}(r) \left[\cos \delta_l(r) \hat{j}_l(kr) - \sin \delta_l(r) \hat{n}_l(kr) \right]. \quad (4)$$

Here, $\hat{j}_l(x)$ and $\hat{n}_l(x)$ are the Rikkati–Bessel functions which are associated with the Bessel and Neumann functions of fractional order and, therefore, can be given by recurrence relations.^{3,6} The SPS $\delta_l(k)$ are obtained from the phase functions $\delta_l(r)$ for large distances,

$$\delta_l = \lim_{r \rightarrow \infty} \delta_l(r). \quad (5)$$

Therefore, the calculation of the SPS δ_l reduces to the solution of a non-linear differential equation with the initial condition $\delta_l(0) = 0$ (Cauchy problem). In this paper, Eq. (4) is solved numerically by means of the Runge–Kutta method in fourth order, using the effective potential (1). Considering that the Rikkati–Bessel functions $\hat{n}_l(x)$ as well as the effective potential (1) are singular at $r \rightarrow 0$, the integration of Eq. (4) has to start at a finite distance $r = \varepsilon > 0$ with respective boundary condition. With increasing distance r , the SPS $\delta_l(r)$ tends to a constant value which defines the phase shift δ_l via (5). We have determined δ_l at a distance, where the absolute value of the effective potential (1) becomes less than 10^{-6} .

For large orbital quantum numbers $l \gg 1$, the SPS $\delta_l(k)$ can be calculated in the quasi-classical (WKB) approximation,⁴

$$\delta_l^{ec}(k) = \int_{r_0}^{r_c} \sqrt{k^2 - \frac{(l+1/2)^2}{r^2} - \frac{2\mu_{ec}}{\hbar^2} \Phi_{ec}(r)} dr - \int_{r_1}^{r_c} \sqrt{k^2 - \frac{(l+1/2)^2}{r^2}} dr, \quad (6)$$

where r_0 and r_1 are the roots of the first and second integrands, respectively. r_c is the cutoff radius, where $|\Phi_{ec}(r_c)/k_B T| \leq 10^{-6}$. The maximum value of l for the calculations of the cross sections can be obtained from the condition

$$k^2 - \frac{(l+1/2)^2}{r_c} \geq 0, \quad (7)$$

which leads to $l_{max} = \text{Int}(kr_c - 1/2)$; $\text{Int}(x)$ denotes the integer part of x .

The numerical calculation of SPS $\delta_l^{ec}(k)$ by means of the Calogero equation (4) is time consuming. Furthermore, for higher l values, the evaluation of the functions $\hat{j}_l(x)$ and $\hat{n}_l(x)$ becomes complicated. Therefore, we apply the following procedure for the calculation of the

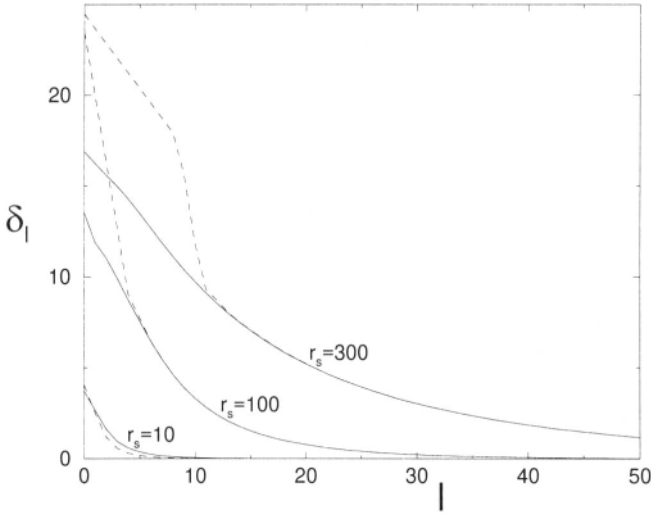


Figure 1. Scattering phase shifts as function of the orbital quantum number l for different $r_s = r_D/a_B$. Dashed line: partial wave expansion; full line: WKB approximation.

cross sections. The SPS for $0 \leq l \leq 20$ are obtained from the Calogero equation (4), whereas the remaining SPS are evaluated within the WKB approximation (6). This procedure is checked by comparing the WKB SPS and the correct numerical ones; if the relative deviation is less than 10^{-3} the higher SPS are calculated by means of the WKB approximation.

In Fig. 1 the numerical results for the SPS solving Eq. (4) and utilizing the WKB approximation are shown for $k = 1/a_B$ and $r_s = 10, 100, 300$ ($r_s = r_D/a_B$, a_B - Bohr radius). For $l \geq 15 \div 20$, the WKB approximation can be used instead of the numerical solution of the Calogero equation (4). In the high-energy region, the scattering potential $\Phi_{ep}(r)$ may be considered as a weak perturbation and the Born approximation becomes valid. Also, we obtain explicit results for the different cross sections in the plasma in the Born approximation.

Fig. 2 show the TCS for electron–proton scattering as function of the wave number for $\gamma = 1$ in comparison with the Born approximation and the TCS for the Debye potential. With increasing nonideal parameter γ , remarkable deviations between the TCS occur at low and moderate energies. At higher energies, the agreement is better.

ELECTRICAL CONDUCTIVITY

We consider now the electrical conductivity of a classical, fully ionized, strongly coupled hydrogen plasma where the electrons are not degenerate, i.e.,

$$\Theta = \frac{k_B T}{E_F} \gg 1. \quad (8)$$

$E_F = \hbar^2/2m_e \cdot (3\pi^2 n_e)^{2/3}$ is the Fermi energy of electrons. For instance, for $r_s = 100$ and $\gamma = 1$ we have $\Theta \sim 113$, whereas for $r_s = 10$ and $\gamma = 1$ a value of $\Theta \sim 11.3$ is derived. The plasma conductivity can be treated within the frame of standard kinetic theory, namely the Chapman–Enskog method.^{9,10} As shown in [11–13], the linear response theory yields identical results for the conductivity in the non-degenerate case and, furthermore, the second-order approximation of the Chapman–Enskog method gives already convergent results.

The expression for the electrical conductivity in second-order approximation within the Chapman–Enskog method accounts for electron–proton and electron–electron scattering and

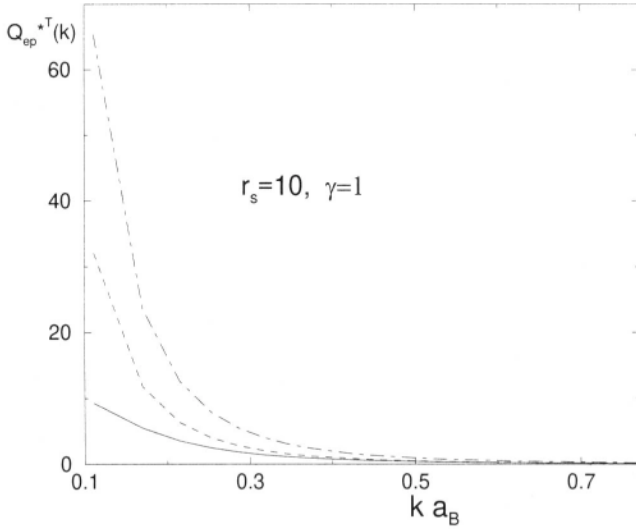


Figure 2. Transport cross sections for electron–proton scattering. $\gamma = 1$, $r_s = 10$. Full line: partial wave expansion; dashed line: Born approximation; dash-pointed line: TCS for the Debye potential.

can be written as [9,10]:

$$\sigma = \frac{3e^2}{16m_e\Omega_{12}^{(1,1)}} \cdot (1 - \Delta)^{-1}, \quad (9)$$

$$\Omega_{ij}^{(l,r)} = \left(\frac{k_B T}{2\pi m_e} \right)^{1/2} \int_0^\infty e^{-g^2} g^{2r+3} Q_{ij}^{(l)} dg,$$

$$Q_{ij}^{(l)} = 2\pi \int_0^\infty [1 - \cos^l \chi_{ij}(b, g)] b db.$$

$\Omega_{12}^{(1,1)}$ is the collision integral in first-order approximation, Δ is the expression for the second-order approximation which consists of various combinations of Ω integrals, b is the impact parameter, and $g = v(m_e/2k_B T)^{1/2}$ the dimensionless relative velocity.

The reduced electrical conductivity can be given as follows:

$$\sigma^* = \sigma \frac{e^2 m_e^{1/2}}{(k_B T)^{3/2}} = \frac{3\sqrt{2}\gamma^2}{8\sqrt{\pi}I_1} \cdot (1 - \Delta)^{-1}, \quad (10)$$

$$\text{where } I_1 = \int_0^\infty e^{-g^2} g^5 Q_{ep}^T(g) dg.$$

In Fig. 3 the reduced electrical conductivity (10) is given as function of the plasma non-ideal parameter γ . Available experimental data,^{14–16} the standard Spitzer curve,¹⁷ and results from other quantum statistical models based on the T matrix approach^{13,18} and the Ziman formula¹⁹ are also given for comparison.

The electrical conductivity obtained within the present approach is in reasonable agreement with the Spitzer theory for $\gamma \ll 1$ and the available experimental data in that region. We consider here the model of a fully ionized plasma, whereas in the experiments a partially ionized plasma is realized so that the Coulomb term of the conductivity has to be extracted.

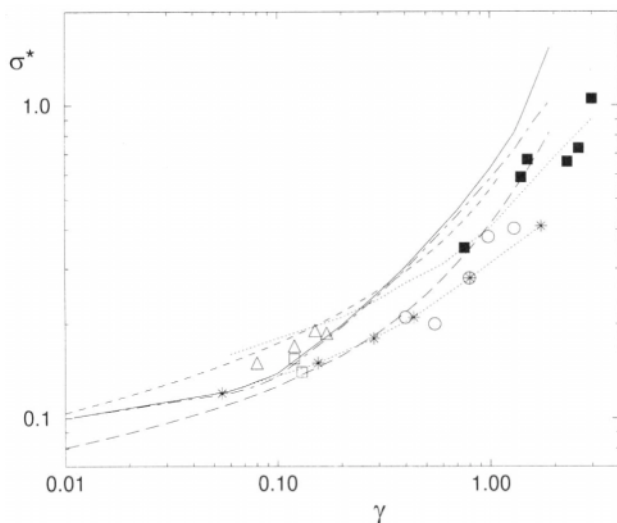


Figure 3. Reduced electrical conductivity σ^* as function of the plasma non-ideal parameter γ , $r_s = 10$. Full line: present two-momentum approximation; dash-pointed line: one-momentum approximation; long dashed line: Born approximation; dashed line: results according to the Spitzer theory;¹⁷ dotted line: T matrix results for the Debye potential;^{13,18} *...*: results of Ichimaru et al.¹⁹ Experiments are shown for comparison: Δ , open box from [14,15]; full box, \circ from [16],

The discrepancies to the other theoretical approaches in that region are probably caused by the utilization of different interaction potentials.

REFERENCES

- [1] F. B. Baïmbetov, Kh. T. Nurekenov, T. S. Ramazanov, Phys. Lett. A 202 (1995) 211.
- [2] F. B. Baïmbetov, Kh. T. Nurekenov, T. S. Ramazanov, Physica A 226 (1996) 181.
- [3] F. Calogero, *Variable Phase Approach to Potential Scattering* (Academic Press, New York, 1967); V. V. Babikov, *The Method of Phase Functions in Quantum Mechanics* (Nauka, Moskva, 1988), in russian.
- [4] L. D. Landau, E. M. Lifshitz, *Lehrbuch der Theoretischen Physik, Band III, Quantenmechanik* (Akademie-Verlag, Berlin, 1985).
- [5] K. Huang, Proc. Phys. Soc, Lond. 60 (1948) 161.
- [6] M. Abramowitz, I. A. Stegun, *Handbook of Mathematical Functions* (U. S. Gov. Printing Office, Washington, 1972).
- [7] D. Bohm, *Quantum theory* (Izdatelstvo Inostrannoi Literatury, Moskva, 1961), in russian.
- [8] B. M. Smirnov, *Atomic Collisions and Elementary Processes in Plasmas* (Atomizdat, Moskva, 1968), in russian.
- [9] S. Chapman, T. G. Cowling, *The Mathematical Theory of Non-Uniform Gases* (Cambridge University Press, Cambridge, 1952).
- [10] J. H. Ferziger, H. G. Kaper, *Mathematical Theory of Transport Processes in Gases* (North-Holland, Amsterdam, 1972).
- [11] W. Ebeling et al., *Transport Properties of Dense Plasmas* (Akademie-Verlag, Berlin, 1984).
- [12] F. E. Höhne, R. Redmer, G. Röpke, H. Wegener, Physica A 128 (1984) 643; C. V. Meister, G. Röpke, Ann. Phys. 39(1982) 133.
- [13] F. Sigeneger, S. Arndt, R. Redmer, M. Luft, D. Tamme, W. D. Kraeft, G. Röpke, T. Meyer, Physica A 152 (1988) 365.
- [14] R. Radtke, K. Günther, J. Phys. D 9 (1976) 1131.
- [15] K. Günther, S. Lang, R. Radtke, J. Phys. D 16 (1983) 1235.
- [16] Yu. L. Ivanov, V. B. Mintsev, V. E. Fortov and A. N. Dremin, Zh. Eksp. Teor. Fiz. 71 (1976) 216; K. Günther, R. Radtke, *Electric Properties of Weakly Nonideal Plasmas* (Akademie-Verlag, Berlin, 1984).
- [17] L. Spitzer, R. Härm, Phys. Rev. 89 977 (1953); L. Spitzer, *The Physics of Fully Ionized Gases* (Interscience, New York, 1960).

- [18] H. Reinholz, R. Redmer, S. Nagel, Phys. Rev. E 52 (1995) 5368.
- [19] S. Ichimaru, S. Tanaka, Phys. Rev. A 32 (1985) 1790.

MONTE CARLO SIMULATION OF THE EQUILIBRIUM PROPERTIES OF A STRONGLY COUPLED HYDROGEN PLASMA

F. B. Baimbetov, M. A. Bekenov, T. S. Ramazanov, and N. N. Iztelevov

Department of Physics, Al Farabi Kazakh State National University
Tole bi 96, Almaty, 480012, Republic of Kazakhstan

INTRODUCTION

The thermodynamical properties of a strongly coupled plasma (SCP) play a important role in the study of astrophysical objects (neutron star crusts, the interiors of white dwarfs, giant planets etc.)

In the statistical physics of many-particle systems the equilibrium properties can be studied within various theoretical methods (Green functions, path integral methods, integral equation, virial expansion methods etc.)

Usually this methods are being used at $\Gamma < 1$ (weakly coupled plasma) and at $\Gamma > 100$ (fully generate plasma). In the intermediate region between these limiting cases the thermodynamical properties of a SCP can be studied within computer simulation methods (Monte Carlo or molecular dynamics calculations). Where Γ is coupling parameter (see below).

In present work the thermodynamical properties (radial distribution functions and equation of state) of a SCP are calculated by Monte Carlo simulation method. We consider a fully ionized, strongly coupled hydrogen plasma. The number density is considered in the range $n = n_e = n_i \sim (10^{21} - 10^{26}) \text{ cm}^{-3}$, and the temperature domain is $T \sim (10^4 - 10^6) \text{ K}$. Dimensionless variables are used. The coupling parameter Γ is defined by

$$\Gamma = \frac{e^2}{ak_B \cdot T}, \quad (1)$$

where k_B is Boltzmann constant; e is the electrical charge; $a = (3/4\pi n)^{1/3}$ is the Wigner–Seitz radius (average distance between the particles). Here the values of Γ are changed in the range between 1 and 10. The dimensionless density parameter $r_s = a/a_B$ is used (where $a_B = \hbar^2/m_e e^2 \simeq 0,53 \cdot 10^{-8} \text{ sm}$ is the Bohr radius). The degeneracy parameter for the electrons is defined by the ratio between the thermal energy $k_B \cdot T$ and the Fermi energy E_F ,

$$\Theta = k_B T/E_F = (2r_s/\Gamma)(4/9\pi)^{2/3} \quad (2)$$

In this case $\Theta < 1$, and we have a fully ionized, strongly coupled hydrogen plasma and electrons are degenerate.

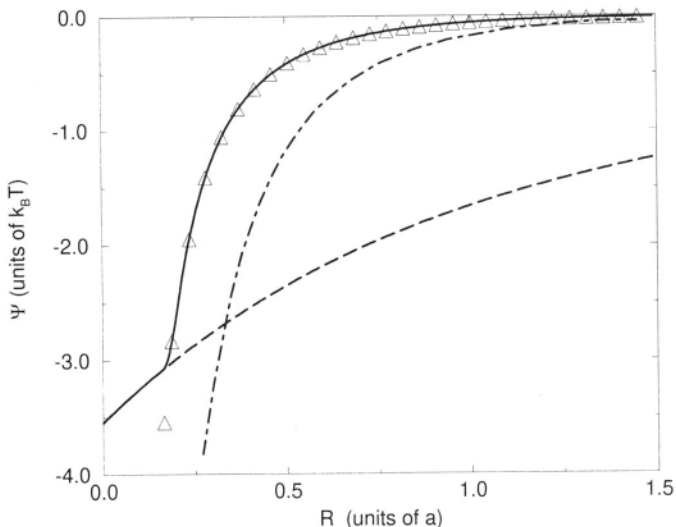


Figure 1. Effective electron–proton potential for dense hydrogen plasma at $r_s = 1$ and $\Gamma = 2$ (solid line). Triangles denote the numerical solution of Eq. (3) for a dense, classical plasma² which accounts for higher-order screening effects. The dashed line denotes potential (5) which shows quantum corrections at short distances. The dot-dashed line: DH potential.

INTERACTION MODEL AND COMPUTATIONAL RESULTS

In present work we utilize a semiclassical effective potential¹ which accounts long-range, many-particle screening effects^{2,8} and short-range, quantum-mechanical diffraction and symmetry effects.^{3,4} The many-particle screening effects have been accounted using the equation for the effective potential:^{5,6}

$$\Delta\Psi - 3\Gamma \cdot \Psi = \pm 3\Gamma \cdot \Psi^2 \quad (3)$$

with the boundary conditions

$$\Psi|_{R \rightarrow 0} = \Gamma/R; \quad \Psi|_{R \rightarrow \infty} = 0 \quad (4)$$

The effective potential (pseudopotential) $\Psi(R)$ is expressed in units of $k_B \cdot T$; $R = r/a$; Δ is the Laplace operator.

The quantum-mechanical diffraction and symmetry effects can be accounted by effective potential.^{3,4}

$$V_{\alpha\beta}(r) = \frac{e^2}{r} \left(1 - \exp\left(-\frac{r}{\lambda_{\alpha\beta}}\right) \right) + \delta_{\alpha\beta} \delta_{ea} \ln(2) k_B T \exp\left(-\frac{r^2}{\pi \ln(2) \lambda_{ee}^2}\right) \quad (5)$$

The effective semiclassical potential was obtained as follows. A spline interpolation between the potential (5) and the numerical solution of equation (3) with the boundary conditions (4) was performed at the intersection point. In figure 1 we can show the effective electron–proton potential for $r_s = 1$ and $\Gamma = 2$.

The Monte Carlo simulation results (for the radial distribution functions) are illustrated in the figure 2. We observe that as the coupling parameter (or density) decreases the electron–electron and proton–proton correlation functions are developed a local extremums (minimums and maximums). For example, electron–electron distribution function have a pronounced peak (see Fig. 2). Similar dependence has been found in [7] by Path Integral Monte Carlo simulation and interpreted as an formation of bound states.

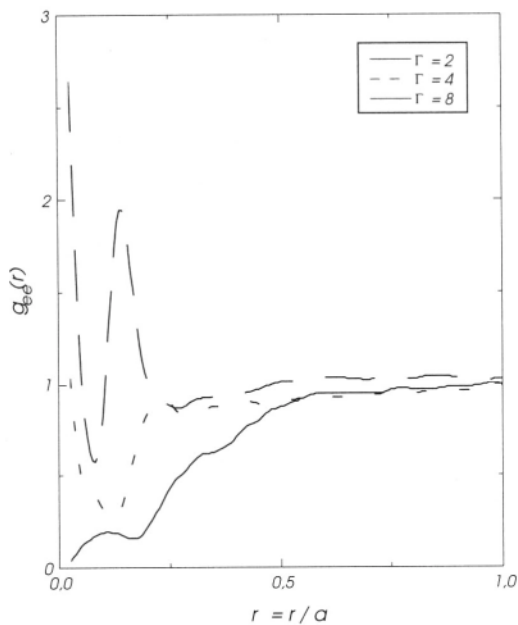


Figure 2. Radial distribution functions between electrons at $r_s = 1$.

This work was supported partially by the Science Foundation of Kazakhstan under Grant No. 74–96 FN.

REFERENCES

- [1] F. B. Baimbetov, M. A. Bekenov, T. S. Ramazanov. Phys. Lett. A **197**, (1995) 157.
- [2] F. B. Baimbetov, Kh. T. Nurekenov, T. S. Ramazanov. Phys. Lett. A **202**, (1995) 211.
- [3] G. Kelbg. Ann. Phys.(Leipzig) **12**, (1963) 219.
- [4] C. Deutsch, M. M. Gombert, H. Mino. Phys. Rev. A **23**, (1981) 924.
- [5] F. B. Baimbetov, T. S. Ramazanov, N. B. Shaltykov, in: *Problems of Statistical Mechanics*. (JINR, Dubna, 1984) (in Russian).
- [6] F. B. Baimbetov, T. S. Ramazanov et al. Teploflz. Vys. Temp. (High Temperature), **28**, (1990) 595 (in Russian).
- [7] C. Pierleoni, D. M. Ceperley et al. Phys. Rev. Lett., **73**, (1994) 2145.
- [8] F. B. Baimbetov, Kh. T. Nurekenov, T. S. Ramazanov. Physica A **226**, (1996) 181.

This page intentionally left blank

FERMIONIC PATH INTEGRAL SIMULATION OF DENSE HYDROGEN

Burkhard Militzer¹, William Magro², and David Ceperley¹

¹Department of Physics, University of Illinois
Urbana, IL

²Department of Physics and Theory Center, Cornell University
Ithaca, NY

INTRODUCTION

Recent laser shock wave experiments by Da Silva et al.¹ have raised new interest in hydrogen and its isotopes at high pressure. Those are the first measurements in a region of pressure where hydrogen has been predicted to undergo a plasma-phase transition. The existence and the properties of this transition are topic of current discussions.^{2,3} In this paper, we report path-integral Monte Carlo (PIMC) simulations⁴ and compare with the experimental results for the equation of state. Further, we identify the number molecules, atoms, and free particles in hydrogen using cluster analysis, which can be compared with chemical models.^{3,5} At high densities, the analysis provides information on the nature of the phase transition.

Path-integral simulations are a powerful tool to determine the static thermodynamic properties of a fully interacting quantum system. It is based on the density matrix, which can be expressed as a product of high temperature density matrices $\rho(\beta) = [\rho(\tau)]^M$ with $M = \beta/\tau$. This becomes a path-integral, which can be evaluated using a multi-stage Metropolis algorithm.⁴ The well-known Fermion sign problem is treated by introducing a nodal restriction on the paths. In the simulation, we use the nodes of the free-particle density matrix.⁶

COMPARISON WITH SHOCK WAVE EXPERIMENTS

The Nova laser shock wave experiments by Da Silva et al.¹ provided the first direct measurements of the equation of state of Deuterium in the pressure region of $0.25 \text{ Mbar} \leq p \leq 2.1 \text{ Mbar}$ at temperatures above 1000K. In these experiments, a shock wave propagates through a sample of precompressed liquid deuterium characterized by its initial state, (E_0, V_0, p_0) . Assuming an ideal shock front, the variables of the shocked material (E, V, p) satisfy the Hugoniot relation⁷

$$H = E - E_0 + \frac{1}{2}(V - V_0)(p + p_0) = 0 \quad (1)$$

The initial conditions in the experiment were $T = 19.6 \text{ K}$ and $\rho = 0.171 \text{ g/cm}^3$. We set $V_0 = 0.102 \text{ \AA}^3$, $E_0 = -1.1676 \text{ Ha}$ per molecule⁸ and $p_0 \approx 0$.

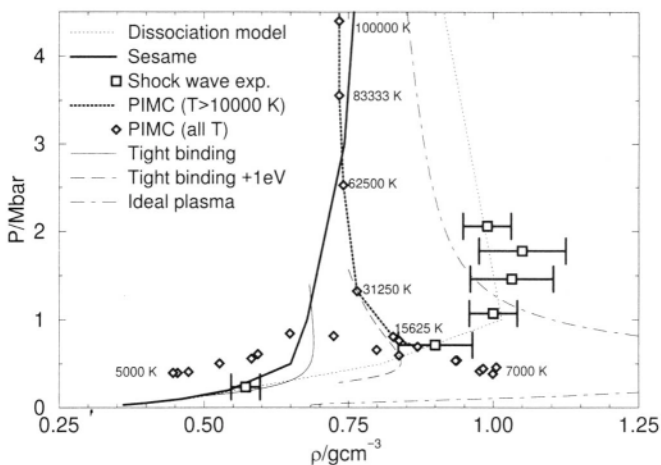


Figure 1. Comparison of Hugoniot from theory and experiment

Theoretical and experimental Hugoniot are shown in Figure 1. Experimentally, one sees a significantly increased compressibility in the range 0.7 Mbar to 2.1 Mbar. This differs substantially from the widely used Sesame data base. Comparing PIMC simulations and the experiment one finds reasonable agreement up to $P=0.7$ Mbar. In the region from 1.0 Mbar to 2.1 Mbar, however, they differ considerably. The PIMC becomes increasingly reliable as temperature increases. Hence, the discrepancy at pressures above 1.0 Mbar is a fundamental problem. According to PIMC, this region is associated with temperatures above 10 000 K as shown. By 15 000 K, almost all molecules are dissociated. At 50 000 K, approximately 60% of the atoms are ionized. These findings cast doubt upon the explanation of the experimental results given in [1], where they were interpreted as effects of dissociation of molecules. Since the ionized phase is not negligible one must also question the explanation in terms of Ross's molecular dissociation model.⁹ We also compare with the tight binding model in Ref. [10]. If 1 eV per atom is added to that model, one finds good agreement with the PIMC above 0.5 Mbar. Finally, we compare with the *ideal* plasma model,⁵ in which one considers a gas of free molecules, atoms, ions, and electrons. We find that some of the measured data points lie at higher densities than predicted by this simple model.

CLUSTER ANALYSIS

Although our calculations describe hydrogen directly as electrons and protons, it is also useful to study the system in the chemical picture,⁵ in which hydrogen is composed of chemical species such as H atoms, H_2 molecules, and the ions H^+ , H_2^+ , etc. In the following cluster analysis, we will identify the concentration of those compound particles from PIMC simulations.

Clusters Defined by Cutoff Radii

In this analysis, we identify clusters by studying the distances between the electrons and protons using the path centroids. We consider two protons as belonging to one cluster if they are less than 1\AA apart. An electron belongs to one particular cluster if it is less than 0.75\AA away from any proton in the cluster. The two cutoff radii were chosen from the molecular and atomic ground state distribution. This approach is adaptable to other systems and can give a cluster of any size. Studying hydrogen in the range of density from $r_s = 4$ and $r_s = 2$

Table 1. Percentages of clusters at $r_s = 3.0$

T/K	e	$H_{(1)}$	H^+	H	H^-	$H_{(2)}$	H_2^{++}	H_2^+	H_2
5000	0	5	2	3	0	95	1	25	69
6944	0	13	7	6	0	87	3	23	61
7812	0	23	8	14	1	76	1	15	60
10,000	0	38	15	23	0	62	2	20	41
15,625	1	55	17	37	1	42	1	12	29
31,250	17	80	26	51	3	18	1	8	9
62,500	40	83	38	43	2	14	1	8	5
125,000	63	88	58	28	2	11	3	6	2
166,667	71	86	63	21	1	12	5	5	1

and temperature from 5000 K to 167 000 K, we found a significant number of many different species including H, H^+ , H^- , H_2^{++} , H_2^+ , H_2 . The numbers of these particles are shown in Table 1 as a function of temperature at $r_s = 3$. $H_{(1)}$ denotes the total clusters with one proton H, H^+ , H^- . $H_{(2)}$ stands for H_2^{++} , H_2^+ and H_2 .

The proposed analysis shows qualitatively the expected temperature behavior of hydrogen. Around 10000 K, many of the H_2 molecules are dissociated. The atoms ionize as the temperature is increased further, yielding an increase in the number of free electrons and protons. This analysis still shows some molecules and atoms at temperatures larger than 100 000 K where no stable compound particles can exist. This effect is caused by instantaneous particle collisions, which cannot be distinguished from bound states by a method based only on distances. Therefore, it leads to a significant overcounting of compound particles. This problem is partially overcome by an improved analysis described in the next section.

Cluster Analysis Based on Pair Correlation Functions

One can improve the analysis by replacing the criterion for a cluster. Instead of using two fixed cutoff radii, one can study the proton–proton and proton–electron pair correlation functions. We consider two limiting cases, the molecular gas at low temperature and ionized plasma at high temperature, and make a fit for any intermediate temperature,

$$g^{(T)}(r) = \alpha g^{(high T)}(r) + (1 - \alpha) g^{(low T)}(r). \quad (2)$$

We determined the degree of dissociation α_D by fitting g_{pp} . Similarly, we calculated the degree of ionization α_I by fitting g_{pe} . We found it advantageous to consider only the nearest neighbor distribution function, because it falls off rapidly within the simulation box and still contains the relevant information.

In our analysis, we use pair correlation functions from our simulations at 5000 K and at 166 667 K as low and high temperature limits. We assume that the first is purely molecular and the latter is completely ionized and that the pair correlation functions for any species have little temperature dependence. We neglect compounds like H_2^+ , H_2^{++} and H^- , which is questionable because of results of our previous analysis. We determine the number of protons, which are bound in molecules $n_{H_2} = \alpha_D$, forming an atom $n_H = 1 - \alpha_D - \alpha_I$ and are free protons $n_H^+ = \alpha_I$. The results are shown in figure 2 for two different densities. At the lower density of $r_s = 4$, one finds a gradual dissociation occurring around $T = 10000$ K and a smooth ionization process with $\alpha_I = 0.5$ at $T = 50000$ K. In the high density case at $r_s = 2$, one finds a rapid change in the number of molecules around $T = 8000$ K, and the resulting atoms can also exist in a small temperature interval before ionization takes place. We interpret these drastic changes as a first order plasma-phase transition described in [2, 11].

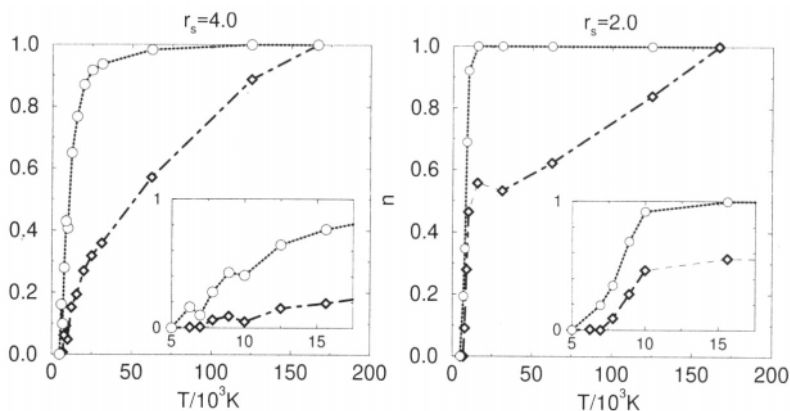


Figure 2. Cumulative plot of proportions of chemical species in the hydrogen plasma: The dash-dot line (\diamond) indicates the number H^+ , the dashed line (\circ) the number of H^+ and H whereas area above gives the number of protons in H_2 .

Acknowledgements

We thank Bernard Bernu and Carlo Pierleoni for useful discussions.

REFERENCES

- [1] I. B. Da Silva, P. Celliers, G. W. Collins, K. S. Budil, N. C. Holmes, W. T. Jr. Barbee, B. A. Hammel, J. D. Kilkenny, R. J. Wallace, M. Ross, R. Cauble, A. Ng and G. Chiu, *Phys. Rev. Lett.* 78:483 (1997).
- [2] W. R. Magro, D. M. Ceperley, C. Pierleoni and B. Bernu, *Phys. Rev. Letts.* 76:1240 (1996).
- [3] D. Saumon and G. Chabrier, *Phys. Rev. A* 46:2054 (1992)
- [4] D. M. Ceperley, *Rev. Mod. Phys.* 67:279 (1995).
- [5] W. Ebeling, W. D. Kraeft and D. Kremp, Theory of bound states and ionisation equilibrium in plasma and solids, in "Ergebnisse der Plasmaphysik und der Gaselektronik," Band 5, Akademie-Verlag, Berlin (1976).
- [6] D. M. Ceperley, Path integral Monte Carlo methods for fermions, in "Monte Carlo and Molecular Dynamics of Condensed Matter Systems," Ed. K. Binder and G. Ciccotti, Bologna, Italy (1996).
- [7] Y. B. Zeldovich and Y. P. Raizer, "Physics of Shock Waves and High-Temperature Hydrodynamic Phenomena," Academic Press, New York (1966).
- [8] W. Kolos and L. Wolniewicz, *J. Chem. Phys.* 41:3674 (1964)
- [9] M. Ross, F. H. Ree and D. A. Young, *J. Chem. Phys.* 79:1487 (1983).
- [10] T. J. Lenosky, J. D. Kress and L. A. Collins, *Phys. Rev. B* 56:5164 (1997).
- [11] W. Magro, B. Militzer, and D. Ceperley, this volume.

CORRELATION FUNCTIONS AND THE EQUATION OF STATE OF A STRONGLY COUPLED HYDROGEN PLASMA IN HNC APPROXIMATION

T. S. Ramazanov,^{1,2} N. F. Baimbetov,² M. A. Bekenov,² R. Redmer,¹ and G. Röpke¹

¹Fachbereich Physik, Universität Rostock
D-18051 Rostock, Germany

²Department of Physics, Al Farabi Kazakh State National University
Tole bi 96, Almaty, 480012, Republic of Kazakhstan

INTRODUCTION

The equation of state for strongly coupled plasmas plays a crucial role in the study of astrophysical objects and inertial confinement fusion plasmas (see, for instance,¹⁻⁶).

The equilibrium properties of dense, strongly coupled plasmas can be studied within various approaches such as Greens functions, path integral methods, computer simulations as Monte Carlo calculations or molecular dynamics, as well as integral equation methods. To investigate high-density effects, we solve the Ornstein-Zernike (OZ) integral equation in hypernetted chain (HNC) approximation.^{7-9,11}

We consider here a fully ionized, strongly coupled hydrogen plasma. The number density considered is in the range $n = n_e = n_i \sim (10^{21} \div 2 \times 10^{25}) \text{ cm}^{-3}$, and the temperature domain is $T \sim (5 \times 10^4 \div 10^6) \text{ K}$. Dimensionless variables are used. The coupling parameter Γ is defined by $\Gamma = e^2/ak_B T$, where k_B is the Boltzmann constant and e is the electrical charge. $a = (3/4\pi n)^{1/3}$ is the average distance between the particles (Wigner-Seitz radius). The dimensionless density parameter $r_s = a/a_B$ is given in terms of the Bohr radius $a_B = \hbar^2/me^2 \approx 0.529 \times 10^{-8} \text{ cm}$. The degeneracy parameter for the electrons is defined by the ratio between the thermal energy $k_B T$ and the Fermi energy E_F : $\Theta = k_B T/E_F = (2r_s/\Gamma)(4/9\pi)^{2/3}$.

We can separate some regions in the temperature-density plane for charged particle systems. For example, at high temperature ($\Theta \gg 1; \Gamma \ll 1$) we have an almost classical plasma. Contrary, for low temperatures ($\Theta \ll 1; \Gamma \gg 1$), we have a fully degenerate, strongly coupled plasma. In the intermediate region between these limiting cases, the system is strongly coupled and the electrons are partially degenerate. In this case $\Gamma \geq 1; \Theta = 0.54 r_s/\Gamma \sim 1; T > 13.6 \text{ eV}$, and we have the fully ionized, strongly coupled hydrogen plasma. This region will be considered in the following.

In this work we utilize a semiclassical effective potential¹² which accounts for the short-range, quantum diffraction and symmetry effects¹³ as well as the long-range, many-particle effects of screening of the charge carriers¹⁴ (for more details, see [19]).

ORNSTEIN–ZERNIKE EQUATION IN HNC APPROXIMATION

In the statistical theory for equilibrium states, the Ornstein–Zernike (OZ) integral equation relates the total correlation function $h_{\alpha\beta}$ to the direct correlation function $c_{\alpha\beta}$ via

$$h_{\alpha\beta}(r) - c_{\alpha\beta}(r) = \sum_{\nu=\alpha,\beta} n_{\nu} \int c_{\alpha\nu}(\vec{r} - \vec{r}') h_{\nu\beta}(\vec{r}') d\vec{r}'. \quad (1)$$

The HNC relation for the direct correlation functions in a two-component system can be written in terms of the interaction potentials $\Phi_{\alpha\beta}(r)$ between the particles,²⁰

$$c_{\alpha\beta}(r) = \exp[-\Phi_{\alpha\beta}(r)/k_B T + \gamma_{\alpha\beta}(r)] - \gamma_{\alpha\beta}(r) - 1, \quad (2)$$

where $\gamma_{\alpha\beta}(r) = h_{\alpha\beta} - c_{\alpha\beta}(r)$, and $\alpha, \beta = e, i$ for electrons and ions. n_{ν} is the particle number density.

The simplest method for solving Eqs. (1) and (2) is their direct iteration: an initial estimate for $\gamma_{\alpha\beta}(r)$ is used in Eq. (2) to calculate $c_{\alpha\beta}(r)$ which is then utilized in Eq. (1) to obtain a new function $\gamma_{\alpha\beta}$ [or $h_{\alpha\beta}(r)$]. Iteration is continued until convergence is achieved. However, for dense systems this simple iteration method may not lead to convergent results in any case. Based on the direct iteration and the Newton method, a very fast and efficient scheme has been proposed by Gillan.^{8, 15} There, the function $\gamma_{\alpha\beta}(r)$ is decomposed into a “coarse” and a “fine” part.

Another rapidly converging method has been derived for simple systems from an expansion of the function $\Gamma(r) = r\gamma(r)$.⁹ A numerical solution of Eqs. (1) and (2) can be obtained via direct iteration with the Fourier transform of the OZ equation.¹⁶ This method is employed in this work.

The Fourier transform of the OZ equation (1) is given by

$$\tilde{h}_{\alpha\beta}(k) = \tilde{c}_{\alpha\beta}(k) + \sum_{\nu=\alpha,\beta} n_{\nu} \tilde{c}_{\alpha\nu}(k) \tilde{h}_{\nu\beta}(k), \quad (3)$$

where

$$\tilde{c}_{\alpha\beta}(k) = 4\pi \int \frac{\sin kr}{kr} c_{\alpha\beta}(r) r^2 dr \quad (4)$$

Again, dimensionless variables are used, i.e., $R = r/a$ and $\Psi_{\alpha\beta}(R) = \Phi_{\alpha\beta}(R)/k_B T$.

For hydrogen plasma, the OZ equations for the different components can be written in dimensionless form, i.e., giving \tilde{h} and \tilde{c} in units of a^3 where $q = ka$ and $b = 3/4\pi$:

$$\begin{aligned} \tilde{\gamma}_{ee} &= \frac{1}{\Omega} [(1/b - \tilde{c}_{ii})\tilde{c}_{ee}^2 + (1/b + \tilde{c}_{ee})\tilde{c}_{ei}^2], \\ \tilde{\gamma}_{ii} &= \frac{1}{\Omega} [(1/b - \tilde{c}_{ee})\tilde{c}_{ii}^2 + (1/b + \tilde{c}_{ii})\tilde{c}_{ei}^2], \\ \tilde{\gamma}_{ei} &= \frac{1}{\Omega} (1/b^2 - \Omega)\tilde{c}_{ei}, \\ \Omega &= (1/b - \tilde{c}_{ii})(1/b - \tilde{c}_{ee}) - \tilde{c}_{ei}^2. \end{aligned} \quad (5)$$

For a numerical solution of the coupled equations (4) and (5), the functions are represented in coordinate space by their values on a set of N mesh points $R_{\alpha\beta}^i = (i-1)\Delta R_{\alpha\beta}$ and in q -space on the N mesh points $q_{\alpha\beta}^i = 2\pi(i-1)/N\Delta R_{\alpha\beta}$. Using the Mayer function as a starting value for the direct correlation function $c_{\alpha\beta}^{(0)}(R) = \exp\{-\Psi_{\alpha\beta}(R)\} - 1$, we calculate $\tilde{\gamma}_{\alpha\beta}^j, j = 1, \dots, N-1$ via Eq. (5). After the inverse Fourier transformation a new estimate for $c_{\alpha\beta}^i$ can be obtained from Eq. (4). Again, the Fourier transform $\tilde{c}_{\alpha\beta}^j$ is inserted in Eq. (5) etc. until convergence of this iteration scheme is achieved. We find that for $\Gamma = (0.05 \div 3.0)$ a good convergence of the computational procedure is obtained within 2–30 iterations.

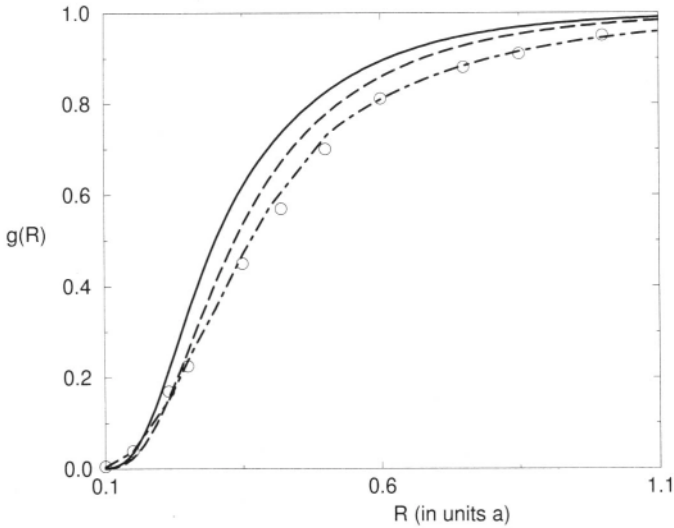


Figure 1. Radial distribution functions between ions at $r_s = 0.4$. Solid line: $\Gamma = 3$; dashed line: $\Gamma = 2$; point-dashed line: $\Gamma = 0.5$. Circles are results from Ref. [16] for $\Gamma = 0.5$.

EQUILIBRIUM PROPERTIES

The resulting ion–ion radial distribution functions $g_{ii}(R) = \gamma_{ii}(R) + c_{ii}(R) + 1$ are shown in Fig. 1 for various parameters of Γ and r_s . Notice, that we have a reasonable agreement between the molecular dynamic data of Hansen and McDonald¹⁰ and our present results for small values of the coupling parameter $\Gamma \leq 0.5$. Fig. 1 also illustrates the fact that the probability of finding a particle at distance R increases as the coupling parameter (or density parameter) increases.

From the radial distribution functions, the equation of state $p = p(\Gamma, r_s)$ can be derived. The corresponding results are shown in Fig. 2 for $r_s = 1$.

We compare our results for the excess pressure with the standard DH theory, with the extended virial expansions of Alastuey *et al.*² and Kraeft *et al.*,⁵ and with the interpolation formula of Ichimaru *et al.*^{11,17} The results of recent path integral Monte Carlo (PIMC) simulations of Pierleoni *et al.*,³ of semiclassical model calculations of Hansen *et al.*,^{10,18} and of density functional molecular dynamic (DFMD) calculations of Penman *et al.*⁴ are also shown.

In the weak coupling limit $\Gamma \ll 1$, we have good agreement with the DH theory. The results of the extended virial expansions agree with our results for $\Gamma \leq 0.3$. Up to $\Gamma \sim 0.6$, we have a good coincidence with the semiclassical model, the interpolation formula of Ichimaru *et al.*, the PIMC and DFMD results. Finally, up to $\Gamma \sim 3$, the present results lie between the data of the DFMD and the semiclassical models for $r_s = 1$ and we have good agreement with the DFMD data for $r_s = 2$.

Our results for the equation of state are thus in reasonable agreement with computer simulations for different regions of the density–temperature domain. This underlines the fact that the effective, semiclassical, screened potential as derived in [12] and utilized here gives an appropriate description of the equilibrium properties of strongly coupled hydrogen plasma.

This work was supported by the German Academic Exchange Service (DAAD) under Grant No. A/96/09574.

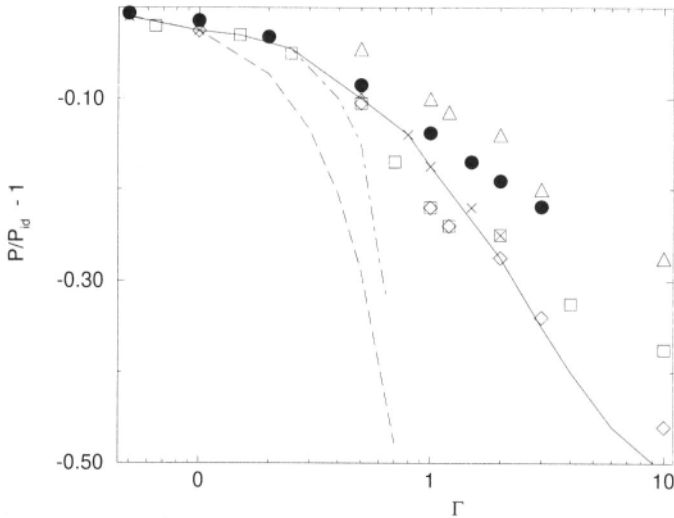


Figure 2. Excess pressure with respect to the ideal quantum system at $r_s = 1$. Filled circles are our numerical results; the dashed line denotes the DH theory; the point-dashed line corresponds to an extended virial expansion;^{2, 5} open squares are results of recent path integral Monte Carlo simulations;³ the solid line is an interpolation formula derived by Ichimaru et al.;^{11, 17} the crosses indicate the results of semiclassical model calculations;^{10, 18} triangles and rhombs are obtained from density functional molecular dynamics calculations.⁴

REFERENCES

- [1] W. Ebeling, W. Richert, Phys. Stat. Sol. B **128** (1985) **467**; Phys. Lett. A **108**, (1985) 80.
- [2] A. Alastuey, A. Perez, Europhys. Lett. **20** (1992) 19.
- [3] C. Pierleoni, D. M. Ceperley, B. Bernu, W. R. Magro, Phys. Rev. Lett. **73**, (1994) 2145.
- [4] J. I. Penman, J. G. Clerouin, P. G. Zerah, Phys. Rev. E **51**, (1995) R5224.
- [5] J. Riemann, M. Schlanges, H. E. DeWitt, W. D. Kraeft, Physica A **219**, (1995) 423.
- [6] H. Reinholz, R. Redmer, S. Nagel, Phys. Rev. E **52**, (1995) 5368.
- [7] J. P. Hansen, I. R. McDonald, *The Theory of Simple Liquids* (Academic Press, New York, 1976).
- [8] G. M. Abernethy, M. J. Gillan, Mol. Phys. **39**, (1980) 839.
- [9] S. Labik, A. Malijevsky, P. Vonka, Mol. Phys. **56**, (1985) 709.
- [10] J. P. Hansen, I. R. McDonald, Phys. Rev. A **23**, (1981) 2041.
- [11] S. Ichimaru, H. Iyetomi, S. Tanaka, Phys. Rep. **149**, (1987) 91.
- [12] F. B. Baimbetov, M. A. Bekenov, T. S. Ramazanov, Phys. Lett. A **197**, (1995) 157.
- [13] C. Deutsch, M. M. Gombert, H. Minoo, Phys. Rev. A **23**, (1981) 924.
- [14] F. B. Baimbetov, Kh. T. Nurekenov, T. S. Ramazanov, Phys. Lett. A **202**, (1995) 211.
- [15] M. J. Gillan, Mol. Phys. **38**, (1979) 1781.
- [16] L. Verlet, Mol. Phys. **41**, (1980) 183.
- [17] X.-Z. Van, S. Tsai, S. Ichimaru, Phys. Rev. A **43**, (1991) 3057.
- [18] B. Bernu, J. P. Hansen, R. Mazighi, Phys. Lett. A **100**, (1984) 28.
- [19] F. B. Baimbetov e.a. Monte Carlo simulation of the equilibrium properties of a strongly coupled hydrogen plasma. Proc. Int. Conference on SCCS. Boston. USA. 1997. (in this book).
- [20] C. A. Croxton. *Liquid State Physics*. (Cambridge University Press, 1974).

EQUATION OF STATE AND METAL–NONMETAL TRANSITION IN DENSE HYDROGEN FLUID

Alex Bunker,¹ Stefan Nagel,² Ronald Redmer,² and Gerd Röpke²

¹University of Georgia, Department of Physics and Astronomy
Athens, GA

²Fachbereich Physik, Universität Rostock
Universitätsplatz 3, D-18051 Rostock, Germany

INTRODUCTION

The first direct evidence for the metallization of fluid hydrogen was obtained recently at 141 GPa and 3000 K.¹ For higher pressures, the electrical conductivity saturates at a value of about 2000/(Ωcm) which is typical for liquid metals. In order to compare with available experimental data for shock-compressed fluid hydrogen, already the strong correlations in the neutral molecular state have to be considered with high precision. First, we take into account pressure dissociation of H_2 molecules via the dissociation equilibrium $\text{H}_2 \rightleftharpoons \text{H} + \text{H}$. The equation of state (EOS) is derived from the pair distribution functions $g_{ab}(r)$ between the different constituents H and H_2 . The proton–proton pair distribution function is extracted and compared with results from computer simulations. Second, also the ionization equilibrium $\text{H} \rightleftharpoons \text{e} + \text{p}$, is treated. Finally, the electrical conductivity of the dense fluid is calculated and a transition from nonmetallic to metallic behavior is found. Comparison with available experiments^{1, 2} is performed.

EQUATION OF STATE

We apply fluid variational theory (FVT),³ the modified hypernetted chain (MHNC) scheme for solving the Ornstein–Zernike equation, and Monte Carlo (MC) simulations to calculate the EOS of fluid hydrogen up to Mbar pressures.^{4,5} We take dense fluid hydrogen to be a mixture of H_2 molecules and H atoms with a dissociation degree $\beta = n_{\text{H}}/(n_{\text{H}} + 2n_{\text{H}_2})$. The molecules and atoms interact via effective two-body potentials which approximate the effects of the real many-body interactions. The exponential-six potential was used to model the interactions between hydrogen molecules (H_2H_2 : $\nu = 1$) in shock-compression experiments,³

$$V_{\nu}(r) = \frac{\varepsilon_{\nu}}{\alpha_{\nu} - 6} \left\{ 6 \exp \left[\alpha_{\nu} \left(1 - \frac{r}{r_{\nu}^*} \right) \right] - \alpha_{\nu} \left(\frac{r_{\nu}^*}{r} \right)^6 \right\}, \quad (1)$$

where $\varepsilon_1/k_B = 36.4$ K, $\alpha_1 = 11.1$, and $r_1^* = 6.482$ a_B . In order to avoid unphysical behavior in the limit of low distances $r \rightarrow 0$, we replace the potential by an exponential function for

$r < 2.95 a_B$, the inflection point, and parameters set to insure continuity. The potential form (1) is also adapted for the other interaction potentials $V_{HH}(r)$ and $V_{HH_2}(r)$. The parameters for the atom–atom interaction (HH: $\nu = 2$) were proposed by Ree:⁶ $\epsilon_2/k_B = 20.0$ K, $\alpha_2 = 13.0$, and $r_2^* = 2.646 a_B$. The parameters for the atom–molecule interaction (HH₂: $\nu = 3$) are derived from the Berthelot mixing rule: $\epsilon_3/k_B = 27.0$ K, $\alpha_3 = 12.0$, and $r_3^* = 4.565 a_B$.

The MC simulations have been performed using these potentials where a finite size box with periodic boundary conditions was initialized with a certain fixed number of H₂ molecules and H atoms at random positions. The degree of dissociation β and the density of particles are thus input variables and fixed for the simulation. A simple Metropolis procedure was used to obtain equilibrium configurations at the desired temperatures from which the pair distribution functions were extracted.

The fraction β of dissociated molecules is determined from the dissociation equilibrium $H_2 \rightleftharpoons H+H$. The correlation contributions to the chemical potentials, derived from FVT, lead to a reduction of the effective dissociation energy with increasing density.⁴ For pressures below 10 GPa, i.e., for conditions reached in the single shock experiments,² the dissociation degree is less than 1%. For the higher pressures reached in the multiple shock experiments,¹ the dissociation degree reaches 19% at 140 GPa. These values are somewhat higher than those derived from an alternative dissociation model^{7,8} which treats dense hydrogen fluid as an ideal mixture of atoms and molecules, and the free energy is minimized with respect to the dissociation degree β . A good agreement with the pressures measured in the shock wave experiments can be stated.⁵

PROTON–PROTON PAIR DISTRIBUTION FUNCTION

The proton–proton pair distribution function is determined from the calculated partial distribution functions $g_{H_2H_2}$, g_{HH_2} , and g_{HH} in order to compare with results of computer simulations. For instance, the formation of molecular hydrogen gas from a neutral system of protons and electrons at a temperature of 5000 K has been described with path-integral Monte Carlo (PIMC) simulations^{9,10} and features of a first-order phase transition were obtained for densities higher than 0.35 g cm^{-3} . Quantum molecular dynamics (QMD)^{11–14} and wave packet molecular dynamics (WPMD) simulations^{15,16} have also been performed for hydrogen in the range $(0.3\text{--}3.0) \text{ g cm}^{-3}$ which indicate that the dense fluid has still a molecular structure but drastic changes in molecular ordering occur with increasing compression.

To calculate the proton–proton pair distribution function g_{pp} , we need the proton distribution $w_{pp}^{H_2}(\mathbf{r})$ in the H₂ molecule for a given temperature. For isolated molecules in the singlet state, this distribution is very well known from the solution of the Schrödinger equation.¹⁷ For simplicity, we neglect in-medium corrections to the molecular structure such as the vibron-shift or a variation of the binding length.

The proton–proton pair distribution function is given by four terms representing the possible cases of finding a neighboring proton:

$$g_{pp}(\mathbf{r}) = \frac{2n_{H_2}}{n_p^2} w_{pp}^{H_2}(\mathbf{r}) + \frac{n_H^2}{n_p^2} g_{HH}(\mathbf{r}) + \frac{4n_H n_{H_2}}{n_p^2} \int d^3s w_{pp}^{H_2}(\mathbf{s}) g_{HH_2}(\mathbf{r} - \mathbf{s}/2) \quad (2)$$

$$+ \frac{4n_{H_2}^2}{n_p^2} \int d^3s_1 \int d^3s_2 w_{pp}^{H_2}(\mathbf{s}_1) w_{pp}^{H_2}(\mathbf{s}_2) g_{H_2H_2}(\mathbf{r} - \mathbf{s}_1/2 - \mathbf{s}_2/2).$$

The total number of protons is $n_p = n_H + 2n_{H_2}$. The first term in (2) describes the internal proton–proton distribution in the H₂ molecule and the second one the proton–proton distribution of the H–H contribution. The third term represents the H–H₂ and the fourth one the H₂–H₂ distribution. Utilizing the calculated distributions for $g_{H_2H_2}$, g_{HH_2} , and g_{HH} , the

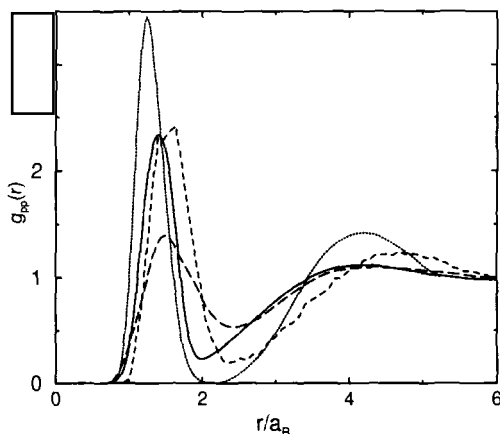


Figure 1. Proton–proton pair distribution function for $T = 5000$ K. and $\rho = 0.33 \text{ g cm}^{-3}$ derived from the present dissociation model (full line) compared with WPMD results of Ref. 16 (dashed line), PIMC simulations of Ref. 10 (dotted line), and QMD simulations of Ref. 14 (long-dashed line).

proton–proton pair distribution function is shown for, e.g., $T = 5000$ K and $\rho = 0.33 \text{ g cm}^{-3}$ ($r_s = 2$) in Fig. 1. The strong first peak at the binding length of the H_2 molecule at $1.4 a_B$ is due to the weak dissociation of 6% at these conditions. The second, broader peak around $4 a_B$ follows from the proton distribution of the H-H_2 and $\text{H}_2\text{-H}_2$ interactions. The H-H interaction gives only a small contribution. A reasonable agreement can be stated with the QMD¹⁴ and WPMD¹⁶ results, whereas the proton–proton pair distribution function derived from the PIMC method¹⁰ is sharper peaked. There, the maximum of the first peak occurs at a smaller value than the proton–proton distance in the isolated H_2 molecule.

ELECTRICAL CONDUCTIVITY

Having obtained a remarkable fraction of monomers in the dense fluid at high pressures due to dissociation, also ionization processes have to be treated in a next step. From the corresponding ionization equilibrium $\text{H} \rightleftharpoons \text{e} + \text{p}$, the ionization degree $\alpha = n_e / (n_e + n_{\text{H}} + 2n_{\text{H}_2})$ is determined taking into account again the correlation contributions to the chemical potentials. Furthermore, the electrical conductivity of such a partially ionized plasma (PIP) consisting of H_2 dimers, H monomers, electrons and protons is calculated within linear response theory.¹⁸ The cross sections for the scattering of electrons at ions and atoms embedded in a polarizable medium of H_2 molecules are derived from a phase shift analysis (t matrix). The proton–proton structure factor is considered. We compare with the available experimental conductivities^{1,2} in Fig. 2.

The present PIP model reproduces the strong increase of the conductivity with the density as observed experimentally. At high densities around $4 \times 10^{23} \text{ cm}^{-3}$, the theoretical EOS shows an instability which produces a jump in the degree of ionization between a branch with low ionization and another one with almost complete ionization — a precursor of the so far hypothetical plasma phase transition. The respective conductivity passes over from a nonmetallic to a metallic behavior, the latter characterized by the Ziman formula. Notice, that the location of the instability region depends strongly on the various correlation contributions to the EOS. More detailed studies of this high-density region are in progress.

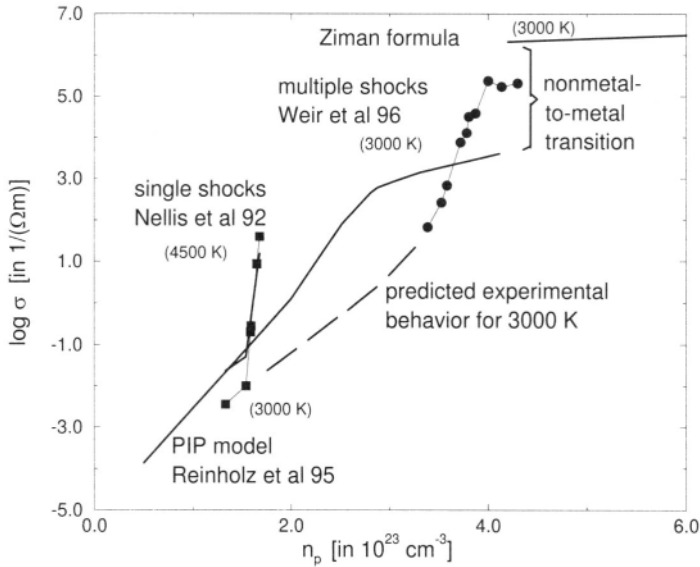


Figure 2. Conductivity of hydrogen fluid for $T = 3000$ K as function of the total proton density n_p calculated within the PIP model of Ref. 18 (solid lines) compared with single (full boxes, Ref. 2) and multiple shock experiments (full circles, Ref. 1). A nonmetal-to-metal transition occurs around $4 \times 10^{23} \text{ cm}^{-3}$ where the conductivity passes over to the Ziman formula valid for the fully ionized fluid.

REFERENCES

- [1] S. T. Weir, A. C. Mitchell, and W. J. Nellis, Phys. Rev. Lett. **76**, 1860 (1996).
- [2] W. J. Nellis, A. C. Mitchell, P. C. McCandless, D. J. Erskine, and S. T. Weir, Phys. Rev. Lett. **68**, 2937 (1992).
- [3] M. Ross, F. H. Ree, and D. A. Young, J. Chem. Phys. **79**, 1487 (1983).
- [4] A. Bunker, S. Nagel, R. Redmer, and G. Röpke, Contrib. Plasma Phys. **37**, 115 (1997).
- [5] A. Bunker, S. Nagel, R. Redmer, and G. Röpke, Phys. Rev. B **56**, 3094 (1997).
- [6] F. H. Ree, in *Shock Waves in Condensed Matter - 1987*, edited by S. C. Schmidt and N. C. Holmes (Elsevier, New York, 1988), p. 125.
- [7] N. C. Holmes, M. Ross, and W. J. Nellis, Phys. Rev. B **52**, 15835 (1995).
- [8] M. Ross, Phys. Rev. B **54**, R9589 (1996).
- [9] C. Pierleoni, D. M. Ceperley, B. Bernu, and W. R. Magro, Phys. Rev. Lett. **73**, 2145 (1994).
- [10] W. R. Magro, D. M. Ceperley, C. Pierleoni, and B. Bernu, Phys. Rev. Lett. **76**, 1240 (1996).
- [11] D. Hohl, V. Natoli, D. M. Ceperley, and R. M. Martin, Phys. Rev. Lett. **71**, 541 (1993).
- [12] J. Kohanoff and J.-P. Hansen, Phys. Rev. Lett. **74**, 626 (1995); Phys. Rev. E **54**, 768 (1996).
- [13] L. Collins, I. Kwon, J. Kress, N. Troullier, and D. Lynch, Phys. Rev. E **52**, 6202 (1995).
- [14] T. L. Lenosky, J. D. Kress, L. A. Collins, and I. Kwon, Phys. Rev. B **55**, R 11 907 (1997).
- [15] D. Klakow, C. Toepffer, and P.-G. Reinhard, Phys. Lett. A **192**, 55 (1994).
- [16] M. Knaup, C. Toepffer, and P.-G. Reinhard, Proceedings of the SCCS 97 (this volume).
- [17] W. Kolos and L. Wolniewicz, J. Chem. Phys. **43**, 2429 (1965).
- [18] H. Reinholz, R. Redmer, and S. Nagel, Phys. Rev. E **52**, 5368 (1995).

THE DENSE HYDROGEN PLASMA: A COMPARISON BETWEEN MODELS

Jean Clerouin

CEA-Centre d'Etudes de Limeil-Valenton
94195 VILLENEUVE-St-GEORGES Cedex
France

INTRODUCTION

Since its inception in 1991,¹ the idea of combining Molecular Dynamics (MD) for the ions with a simplified density functional without orbitals for the electrons, has proven very useful. As usual in density functional theory,² the electronic energy is expressed as sum of several terms: the kinetic energy E_{KE} , the Hartree energy E_{Hart} , the exchange-correlation energy E_{xc} and external energy E_{ext} :

$$E[\rho] = E_{KE}[\rho] + E_{Hart}[\rho] + E_{xc}[\rho] + E_{ext}[\rho] \quad (1)$$

In the Kohn–Sham realization of the HK formalism, the electronic kinetic energy E_{KE} is calculated as the kinetic energy of a non-interacting electron gas, thus introducing a set of n_{occ} occupied electronic orbitals ψ_i :

$$E_{KE}[\rho] = \sum_i \int dr \psi_i(r) \left(-\frac{1}{2} \nabla^2 \right) \psi_i^*(r) \quad \text{where} \quad \rho(r) = \sum_{i=1}^{n_{occ}} \psi_i(r) \psi_i^*(r) \quad (2)$$

In the orbital free approach the electronic kinetic energy must be computed by a functional of the sole electronic density $\rho(r)$. Being the exact kinetic energy for a homogeneous system, the Thomas–Fermi theory (TF) provides a starting point of a whole family of functionals:

$$E_{KE} = c_0 \int \rho(r)^{5/3} dr \quad (3)$$

with $c_0 = \frac{3}{10} (3\pi^2)^{2/3}$. By adding the Dirac exchange term, we obtain the Thomas–Fermi Dirac functional (TFD). To account for the inhomogeneity of the system, this functional can be expanded in terms of gradient of the electronic density, but such an expansion is practically limited to second order in density fluctuations, leading to the von-Weizsäcker correction, which, combined with the Dirac exchange energy, gives the TFDW functional. In order to include the Lindhard response, responsible for the Friedel oscillations in the case of metals, Perrot has proposed a functional which is exact not only in the linear response regime, but for all perturbations in the limit of large q . This functional has been applied successfully to sodium.³ More sophisticated functionals has been devised by Wang⁴ to account for the

shell structure which is missing in the original functional and applied to aluminum.^{5,6} More generally, the orbital free approach have been applied to silicon,^{7,8} metal-salt solutions,⁹ clusters¹⁰ and also hydrogen adsorbed on silicon surfaces.¹¹

Unfortunately, in the case of a hydrogen plasma, such functionals based on a linear response approach are no longer suitable due to the strongly non linear behavior of the electronic density in the vicinity of protons.¹² If we accept to give up binding properties by considering only the very high density regime ($\rho \geq 2 \text{ g.cm}^{-3}$), TF, TFD and TFDW functionals are more appropriate to describe the strong electronic response. It is the goal of this talk (see also [13]) to compare the predictions of this functionals with more sophisticated descriptions such as conventional Car–Parrinello (CP), Tight Binding (TB),¹⁴ or Path Integral Monte Carlo (PIMC).¹⁵

METHOD

The method, Thomas Fermi Molecular Dynamics (TFMD), has been described in details in preceding papers.^{1,16,17} We just mention here that we start from a Lagrangian which includes the ionic and the electronic degrees of freedom:

$$\mathcal{L} = \frac{1}{2} \int \mu \dot{\rho}(r) dr + \frac{1}{2} \sum_{i=1}^N M_i \dot{R}_i^2 - F[\rho(r), R_i] - \Lambda (\sum \rho(r) dr - N) \quad (4)$$

The free energy $F[\rho, R_i]$ is expressed as a sum of the electron kinetic free energy (which in the original method requires orbitals), the exchange free energy, whose finite temperature expression can also be found in [18], and the usual coulombic contributions:

$$F[\rho(r), R_i] = F_e[\rho(r)] + F_{xc}[\rho(r)] + U_{ee} + U_{ie} + U_{ii}.$$

Details on driving the electronic density and preconditioning the fake masses $\mu(q)$ are given in [3]. The external potential is the Coulomb potential, except for small distances ($r < r_c$), where the potential is regularized by an ad-hoc homogeneous smearing of the nucleus leading to a parabolic core for the potential. We have checked¹ that, provided r_c stays smaller than a , this procedure yields no significant differences on collective properties compared with the bare Coulomb potential. Yet, this procedure precludes exact energies calculations and a static correction must to be introduced when calculating the pressure.¹⁷

RESULTS

The pair distribution function $g(r)$ computed from a simulation of a system of 250 ions at $r_s = a_e/a_B = 1$ and different temperatures is compared with CP simulations performed using a Bachelet Hamman Schluter pseudo-potential, and also with PIMC simulations when the temperature was too high to allow for CP simulations. Our CP simulations were checked by comparing our results with low temperature CP simulations of Kohanoff et al. in the same regime.¹⁹ At low temperature $T=3000$ K, the agreement between TFDW and CP simulation is not very satisfactory. Surprisingly, the TFD gives better results, but still indicating a too low screening effect. At $T=7300$ K, the agreement between TFD and CP simulations becomes very good (Fig. 1) and is even excellent at $T=29000$ K when compared to PIMC. The same features are also observed from the comparison of the velocities autocorrelation functions. It is interesting to note that at $T=3000$ K the frequencies of the oscillations of $Z(t)$ are almost the same for CP and TFD, but more pronounced for TFD, leading to a lower diffusion constant. Again at $T=11600$ K the agreement between CP and TFD is excellent (Fig. 2).

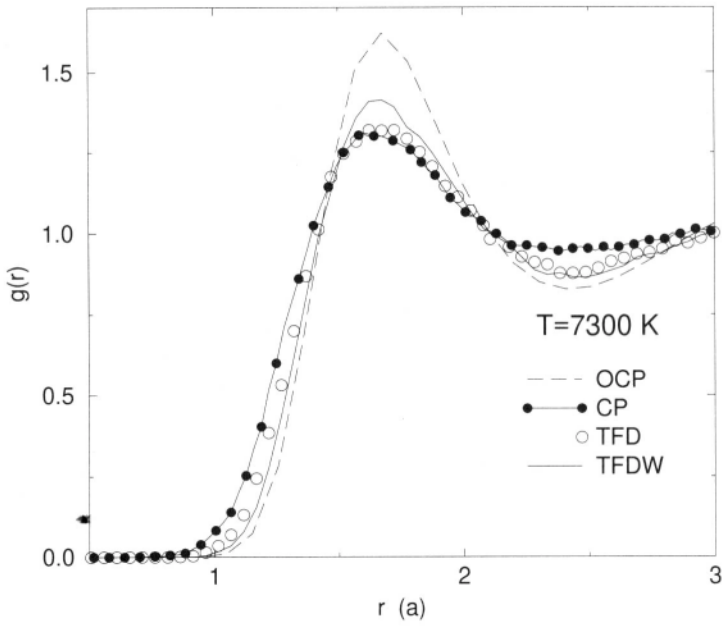


Figure 1. Proton-proton pair distribution function for 7300 K and $r_s = 1$. Long dashed curve is the OCP result, full curve with filled circles: Car-Parrinello simulations (CP); open circles: TFD simulations; full line: TFDW simulations.

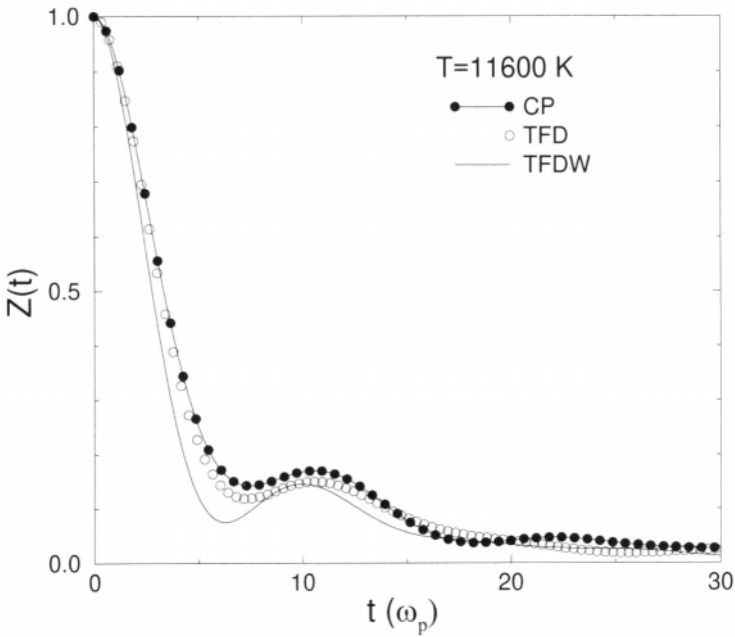


Figure 2. Velocity autocorrelation functions for $T=3000$ K and $r_s = 1$. Full curve with filled circles: Car-Parrinello simulations (CP); open circles: TFD simulations and full line: TFDW simulations.

Table 1. Diffusion coefficients in units $a^2 \omega_p^{-1}$ versus coupling parameter.

Γ	T(eV)	OCP	TFMD		quantum	
			TFDW	TFD	TB	CP
104	0.26	0.006	0.010	0.012	0.013	0.016
50	0.50	0.015	0.025	0.033	0.031	0.030
43	0.63	0.020	0.031	0.037	0.041	0.038
27	1.00	0.038	0.054	0.068	0.065	0.067
10	2.50	0.134	0.164	0.192	0.171	-
5.4	5.00	0.239	0.288	0.360	0.338	-

From the integration of $Z(t)$, we have extracted the diffusion coefficients in order to compare with CP and with recent TB calculations using the non-orthogonal Tight-Binding model²⁰ (the One Component Plasma result is given for comparison). As shown in Table 1, the TFD diffusion coefficients are in fairly agreement with quantum estimations. We have also computed the dynamical structure factor $S(\mathbf{k}, \omega)$, from which we have estimated a sound velocity $c_s \simeq 40$ km/s corresponding to the upper range of pressures encountered in Jupiter.²¹

CONCLUSION

For high density hydrogen ($\rho \geq 2.6 \text{ g.cm}^{-3}$), an orbital free model such as TFMD in the finite temperature version TFD is able to reproduce some features such as the equation of state, screening properties (through the pair distribution function) or diffusion in a very good agreement with results obtained with much more expansive quantum calculations.

REFERENCES

- [1] J. Cl  rouin, E. L. Pollock and P. G. Z  rah, *Phys. Rev. A* **46**:5130(1992).
- [2] P. Hohenberg and W. Kohn, *Phys. Rev. B* **136**:864(1964).
- [3] M. Pearson, E. Smargiassi and P. A. Madden, *J. of Phys.: Condens. Matter* **5**:3221 (1993).
- [4] L. W. Wang, Doctoral Thesis, Cornell University (1991).
- [5] E. Smargiassi and P. A. Madden, *Phys. Rev. B* **49**:5220 (1994).
- [6] M. Foley and P. A. Madden, *Phys. Rev. B* **53**:10589 (1996).
- [7] N. Govind, J. L. Mozos, and H. Guo, *Phys. Rev. B* **51**:7101 (1995).
- [8] L. W. Wang and M. T. Teter, *Phys. Rev. B* **45**:13196 (1992).
- [9] A. Meroni, J. P. Hansen, and P. A. Madden, *J. of Non-Crystalline Solids*, **156–158**:771 (1993).
- [10] V. Shah, D. Nehete, and D. G. Kanhere, *J. of Phys.: Condens. Matter* **6**:10773 (1994).
- [11] N. Govind, J. Wang, and H. Guo, *Phys. Rev. B* **50**:11175 (1995).
- [12] N. Ashcroft in *Strongly Coupled Coulomb Systems conference Boston 1997* proceedings, Plenum Press NY, (1998).
- [13] J. Cl  rouin, and S. Bernard, to appear in *Phys. Rev. E* (1997).
- [14] I. Kwon, L. A. Collins, J. D. Kress, N. Trouiller and D. L. Lynch, *Phys. Rev. E* **49**:R4771 (1994).
- [15] C. Pierleoni, D. M. Ceperley, B. Bernu, and W. R. Magro, *Phys. Rev. Lett.* **73**:2145 (1994).
- [16] P. G. Z  rah, J. Cl  rouin, and E. L. Pollock, *Phys. Rev. Lett.* **69**:446 (1992).
- [17] J. I. Penman, J. G. Cl  rouin, and P. G. Z  rah, *Phys. Rev. E* **51**:R5224 (1994).
- [18] F. Perrot, *Phys. Rev. A* **20**:586 (1979).
- [19] Jorge Kohanoff and J. P. Hansen, *Phys. Rev. E* **54**:768 (1996).
- [20] T. L. Lenovsky, J. D. Kress, L. A. Collins and I. Kwon, *Phys. Rev. B* **55**:R11907 (1997).
- [21] W. B. Hubbard, in *Simple Molecular Systems at Very High Density.*, A. Polian, P. Loubeyre and N. Boccara Editors, Nato ASI series Voll86-Plenum Press NY, (1989).

MD REDISTRIBUTION FUNCTIONS OF RESONANCE RADIATION IN HOT DENSE PLASMAS

A. V. Demura,¹ A. E. Bulyshev,² V. S. Lisitsa,¹ A. N. Starostin,² A. E. Suvorov,² and I.I. Yakunin²

¹Russian Research Center “Kurchatov Institute”
Moscow 123182, Russia

²Troitsk Institute of Innovation and Thermonuclear Research
Troitsk, Moscow Region 142092, Russia

RESCATTERING OF RADIATION IN DENSE PLASMAS WITH MULTIPLY CHARGED IONS

The photon frequency redistribution function $R(\omega, \omega')$ is the joint probability that a photon absorbed at frequency ω' is reemitted at frequency ω . This function enters in the expressions of emission and absorption coefficients in the equations of radiative transfer.

In comparison with the pure collisional redistribution in the astrophysical applications the effects of strong coupling in dense plasmas may appear even at rather low values of electron and ion coupling parameters via a strong interaction of the radiator quantum system with plasma ionic microfields. This strong interaction brings about so called Nonlinear Interference Effects (NIEF), which stem from coupling of population kinetics and various polarizations of the radiating ion in the presence of the plasma microfield.¹ Also the contribution of NIEF is greatly enhanced with increasing the charge of the radiator. These phenomena may be important for plasma conditions with the coupling constant for ionic interaction smaller than unity as well, thus widening the notion of Strongly Coupled Coulomb Systems (SCCS).

For a resonance spectral line, $R(\omega, \omega')$ contains two types of contributions, corresponding to coherent and incoherent photon scattering. When perturbing particles of the medium interact via collisions with the emitting atom (collisional broadening), the ratio of coherent to incoherent rescattering mechanisms contributions is determined by A/Φ , where A is the probability of a radiative decay from the excited state (unaccompanied by frequency redistribution) and Φ is the rate of line-broadening collisions. Thus, coherent scattering, which in the center of rest system of the atom corresponds to a δ -function relation $\delta(\omega - \omega')$ between the frequencies (when the lower level is a ground state), dominates for $A/\Phi \gg 1$. Note that the Doppler effect in the laboratory frame leads to Doppler frequency redistribution as a result of the difference in propagation directions of the absorbed and emitted photons. For $A/\Phi \ll 1$, the scattering becomes completely incoherent, and the photon absorption and emission events turn out to be independent, so that the rescattering function $R(\omega, \omega')$ factors into the product $\phi(\omega)\phi(\omega')$ of independent absorption and emission probabilities described by the line profile

$\phi(\omega)$, which is determined by all broadening mechanisms. This is known as the complete frequency redistribution limit (CR) which is widely used in radiative transfer theory.

The problems of the resonance-radiation transfer have garnered new interest in terms of their relation to hot dense plasma containing multiply charged ions in studies of inertial confinement thermonuclear fusion and x-ray lasers. The peculiarities of line radiation redistribution in a plasma of multiply charged ions relate to the sensitive dependence of A/Φ on ion charge Z . For example, A/Φ is proportional to Z^6/N_e for hydrogenic ions, where N_e is the electron density.

A fundamental aspect of calculations of the function $R(\omega, \omega')$ in a dense plasma is connected with plasma ionic microfield, which leads to Stark broadening of the ionic emission lines. In a dense plasma the photon frequency redistribution in the rest frame of the emitter results from fast “shaking” of the atomic states by electrons and slow shifts of the states by the ions. The action of the electrons can be taken into account through that or another type of collisional integral, whereas numerical evolutionary calculations are required to take into account the effect of the ions. This is because a large number of ions participate simultaneously in the interaction, and this makes the dynamics of the ionic microfield $\mathbf{F}(t)$ complicated. Two classes of problems arise in the calculation of $R(\omega, \omega')$: 1) modeling of the many particle microfield $\mathbf{F}(t)$ of the ions, and 2) calculation of the evolution of the atomic states under the action of this field.

For a static ionic field \mathbf{F} , the problem can be solved analytically for a model three-level system that describes the advent of forbidden components in the emission spectrum of helium-like ions employed for diagnostics of the plasma parameters. In so doing it has been demonstrated that NIEF are important in the formation of the emission spectra and $R(\omega, \omega')$. These effects are due to the interference of the atomic states in an external field, which in a plasma with multiply-charged ions leads to a strongly nonequilibrium distribution of the population over the atomic sublevels. The function $R(\omega, \omega')$ is most sensitive to these effects. Indeed, firstly if NIEF are neglected, $R(\omega, \omega')$ may be not positive definite at least in quasistatic region.¹ Secondly, even for $A/\Phi \ll 1$, when the contribution of the coherent component is negligibly small, $R(\omega, \omega')$ does not reduce to a product of independent profiles (absence of CR). The latter circumstance is not reduced simply to a trivial discrepancy between the microfield averaged product of the profiles and the product of the averages, rather, it reflects the interference of atomic states that results from NIEF.

The next step in the calculation of $R(\omega, \omega')$ is to take into account the nonstationary ionic field generated by the thermal motion of the ions (ion dynamics). In the present work the rescattering function $R(\omega, \omega')$ was calculated for the Ly- α line of hydrogenic ions, taking into account both nonlinear interference effects and the ion dynamics. A fundamental point here is the extent to which the ion dynamics affects the relationship between the coherent and incoherent components of the rescattering function.

Recent calculations of $R(\omega, \omega')$ which consider the ion dynamics in the Model Microfield Method- MMM for helium-like transitions of Al⁺¹¹ in three-level systems and include contributions from NIEF are also presented in this volume.³ The absence of the CR regime also was found, that is important while interpreting measurements of line-radiation yield from impurities added to the compressed thermonuclear target.

REDISTRIBUTION FUNCTION FOR Ly- α LINE IN FLUCTUATING ION MICROFIELD

Results for rescattering of resonance radiation presented are obtained by the compound density matrix method for the system: the “atom (ion) + spontaneous electromagnetic fields” (the fields describe the absorbed photon with frequency ω' and the emitted photon with

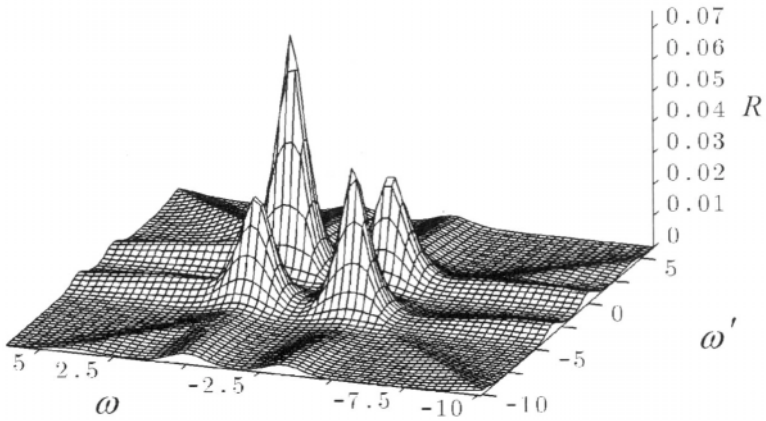


Figure 1. The redistribution function for Ly- α of ArXVIII at a temperature of 1 keV and electron density 10^{24} cm^{-3} in the approximation of a static ionic microfield. The frequencies are given in eV.

frequency ω).¹ These equations are solved in the second order perturbation expansion with respect to the interaction with the incident radiation and in the first order perturbation expansion with respect to the interaction with the scattered radiation,^{1,2} including the interaction with ion microfields in the all orders of the perturbation. The coherent and incoherent contributions are carefully separated by special procedures. The population of the ground state assumed constant while others are put to zero. In this way the rescattering problem equations are solved for each value of the incident frequency ω' individually. The redistribution function is calculated through the general expression for the power $P(\omega, \omega')$ due to the scattered field: $R(\omega, \omega') \propto \text{Re}\langle iG^* e^{i\omega t} \rho_{ij} \rangle$, where ρ_{ij} is the non-diagonal element of the density matrix, G^* defines the complex conjugated amplitude of the scattered radiation, $\langle \dots \rangle$ denotes averaging over the ensemble of perturbing plasma ions. The time dependent solutions of density matrix equations in temporally dependent ion microfields are obtained and averaged with the help of Molecular Dynamics Method (MD) details of which may be found elsewhere.² After the redistribution function is averaged over the angles of the absorbed and emitted photons and the velocity of the radiator.

Figure 1–2 shows results of MD calculations of the redistribution function for the Ly- α line of the Ar XVIII ion in a hydrogen plasma for the electron density $N_e = 10^{24} \text{ cm}^{-3}$ in comparison with results obtained in the quasistatic approximation for the ion microfield. The radical influence of ion dynamics is quite evident. The role of ion dynamics effects is enhanced with the density increasing as well as the role of the incoherent scattering - the ratio of R^{coh} and R^{inc} is highly suppressed by the ion motion. For these conditions the function $R(\omega, \omega')$ obviously differs from the result of the CR approximation because of NIEF, although the influence of ion dynamics usually soften conditions for a practical realization of this approximation.

Thus, in the present work the rescattering function for resonance radiation in the Ly- α spectral line of a multiply-charged ion in hot dense plasma is systematically calculated taking into account nonlinear interference effects and ion dynamics. It differs from CR approximation even at high densities, which may have an important influence on the interpretation of diagnostics involving radiation from impurities in fusion targets. The ion dynamics strongly influences (in contrast to the emission profiles) the ratio of coherent and incoherent components of rescattering, even at comparatively low plasma densities.²

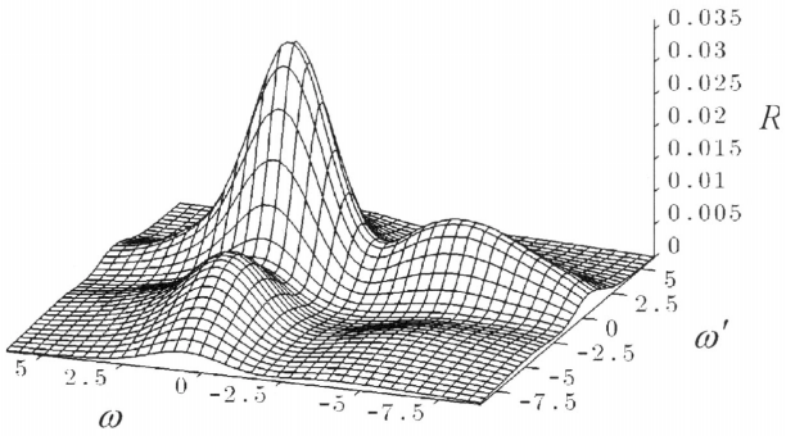


Figure 2. The redistribution function for Ly- α of ArXVIII at temperature 1 keV and electron density 10^{24} cm^{-3} taking ion dynamics into account within Molecular Dynamics Method. The frequencies are given in eV.

REFERENCES

- [1] A. V. Demura, A. V. Anufrienko, A. L. Godunov, Yu. K. Zemtsov, V. S. Lisitsa, A. N. Starostin, M. D. Taran, V. A. Schipakov, *in: SLS v. 6*, L. Frommhold, J. W. Keto, ed., AIP, New York (1990), pp. 227–254.
- [2] A. E. Bulyshev, A. V. Demura, V. S. Lisitsa, A. N. Starostin, A. E. Suvorov, I. I. Yakunin, *Sov. Phys.-JETP* **81**:113(1995).
- [3] A. V. Demura, I. N. Kosarev, N. Feautrier, V. S. Lisitsa, C. Stehlé, this volume (1997).

ON PLASMA STATISTICS OF MICROFIELD GRADIENTS AND LINE ASYMMETRIES

Alexander V. Demura,¹ Dominique Gilles,² and Chantal Stehlé³

¹Hydrogen Energy and Plasma Technologies Institute
Russian Research Center Kurchatov Institute
Moscow 123182, Russia

²C. E. A., Centre d'Etudes de Limeil-Valenton
F-94195, Villeneuve St-Georges Cedex, France

³DARC et UPR 176 du CRNS, Observatoire Paris
5 Place Jules Janssen, F-92190, Meudon, France

INTRODUCTION

In a first approximation, Stark profiles of H-like ions are symmetrical. Eventual asymmetries in optically thin media are attributed to different physical processes. One of them is the effect of the quadrupolar interaction with the spatial gradient of the plasma microfield and the monopolar interaction with its divergence. We investigate here the effects of the microfield gradients on the line asymmetry for highly correlated plasmas using Monte Carlo simulations for the plasma relevant properties and Model Microfield Method for the description of the microfield dynamics. Comparative calculations are performed at various values of the plasma coupling, with alternative choices for the statistics of the plasma microfield (Nearest Neighbor, Holtmark, Baranger–Mozer, APEX formalisms). The results illustrate the high sensitivity of the line asymmetry to the ion dynamic effects and to the plasma statistics.

THEORETICAL BACKGROUND

The interaction potential between the bound electron of the hydrogenic system (dipole \vec{d} , quadrupole \vec{Q} , and distance to the nucleus r) and the plasma is equal to [1]

$$V(\vec{F}) = -\vec{d}\vec{F} + \sum_{ij} Q_{ij}G_{ij} - \frac{1}{6}er^2\vec{\nabla}\cdot\vec{F} \quad (1)$$

In this expression, \vec{F} is the electric microfield, G_{ij} is the component of the traceless non-uniformity tensor \vec{G} (rank 2) and $\vec{\nabla}\cdot\vec{F}$, is the divergence (rank 0), given by

$$G_{ij} = \partial F_i / \partial x_j - \left(\frac{1}{3} \sum_i \partial F_i / \partial x_i\right) \delta_{ij} \quad \text{and} \quad \vec{\nabla}\cdot\vec{F} = \sum_i \partial F_i / \partial x_i \quad (2)$$

They are respectively the sum of all the elementary microfields, gradients and divergencies due to the surrounding plasma ions.

Hereafter we neglect the contribution of the Laplacian of the potential ($\nabla \cdot \vec{F}$), which will be discussed in a following paper. Assuming static electric microfields, the line shape expression is given in terms of the joint distribution function $W(\vec{F}, \vec{G})$ of the field and its non-uniformity tensor by

$$I(\omega) = \int d\vec{F} d\vec{G} W(\vec{F}, \vec{G}) J(\omega, \vec{F}, \vec{G}) \quad (3)$$

Even if the electric microfield is chosen along the quantization axis Oz , this intensity is very difficult to calculate, as it should be averaged over six independent variables (F_z, G_{ij}). This difficulty may be avoided by replacing the field gradient by its conditional average at the fixed value of the microfield \vec{F} ,

$$\left\langle \frac{\partial F_i}{\partial x_j} \right\rangle_{\vec{F}} = \frac{2\pi N_e e}{3} \left\{ B_D(\beta) \left(\frac{3F_i F_j}{F^2} - \delta_{ij} \right) + 2\delta_{ij} B_{DO}(\beta) \right\} \quad (4)$$

where $\beta = Fr_0^2/e$, and r_0 is the mean interelectronic distance.

Like the microfield distribution function $W(\vec{F})$, the functions B_D and B_{DO} (Demura and Stehlé, 1995), introduced in this expression, are a manifestation of the many-body nature of the microfield. (Note that the function B_{DO} enters in the expression of the conditional average of the Laplacian to the value of the field \vec{F}).

Choosing the electric microfield along the z axis, the plasma-radiator interaction potential is written as,

$$V(\vec{F}) = -d_z F_0 \beta + Q_{zz} \frac{\pi N_e e}{3} B_D(\beta) \quad (5)$$

and the expression of the static line intensity (3) reduces to

$$I(\omega) = \int d\vec{F} W(\vec{F}) J(\omega, \vec{F}, \langle \vec{G} \rangle_{\vec{F}}) \quad (6)$$

RESULTS

The line profile calculations have been performed for the Lyman- α line of two species of hydrogen-like ions (He^+ and Ar^{17+}) at various values of the plasma coupling. Doppler and monopolar effects are not included. Ion dynamics effects (Gilles and Stehlé, 1995) are included using the Model Microfield Method (Stehlé, 1994).

The line asymmetry is defined by the ratio

$$\frac{I(h\Delta\nu) - I(-h\Delta\nu)}{I(h\Delta\nu) + I(-h\Delta\nu)} \quad (7)$$

where $\Delta\nu$ (or $\Delta\lambda$) refers to the frequency (wavelength) detuning from the unperturbed transition. The relevant data for this asymmetry are the microfield distribution $P(\beta)$ and the $B_D(\beta)$ functions, obtained either with MC (Monte-Carlo), considered as reference results, APEX (Murillo et al, 1997) or BM (Baranger-Mozer up to second order), the latter having the more restricted validity range for the plasma conditions.

The first case (pure He^+ plasma, electronic density equal to 10^{18} cm^{-3} , $T=10^4 \text{ K}$) corresponds to a relatively low correlated plasma. There is no discrepancy between the results of $P(\beta)$ and $B_D(\beta)$, obtained by the three previous formalisms. As expected for these conditions, ion dynamics effects are important (they reduce the asymmetry by a factor 2) in

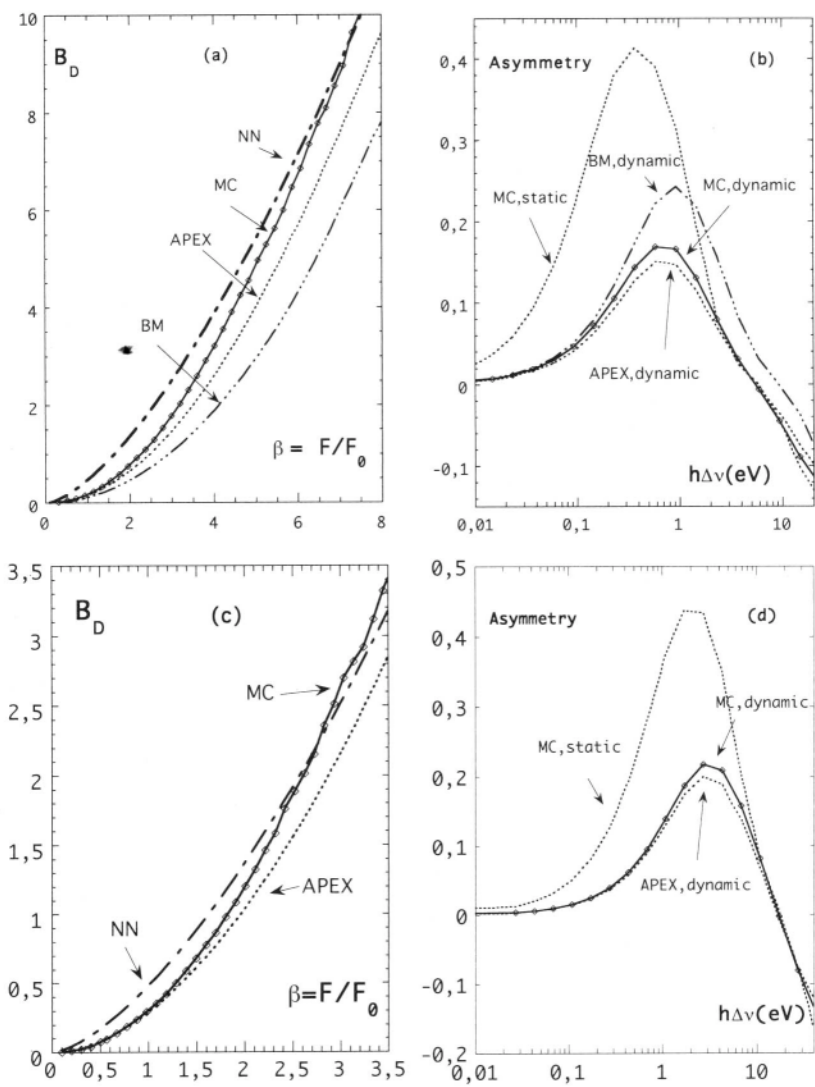


Figure 1. (a) $B_D(\beta)$ and (b) asymmetry of the $\text{Ly}\alpha$ line for a pure Ar^{17+} plasma, $kT = 800 \text{ eV}$, $N_e = 10^{24} \text{ cm}^{-3}$ (c) and (d) same as (a) and (b) at 10^{25} cm^{-3}

the core of the line. The electronic screening affects more the line intensity (factor 2) than the asymmetry, as proved by the difference between Holstmark and BM results (Demura et al., 1996).

For more correlated plasmas and heavier emitters relevant to ICF experiments, the discrepancies between BM, APEX and MC results may be important (Demura et al 1995), specially for the most probable values of the microfield, which give the main contributions to the center and near line wings of the profile. We investigate below the sensitivity of the line asymmetry to the choice of the statistics included in the calculation of P and B_D for a dense plasma of Ar^{17+} ions at 800 eV, and an electronic density between 10^{24} cm^{-3} and 10^{25} cm^{-3} . For these conditions BM is invalid. Nevertheless results have been reported for the less dense case to illustrate the sensitivity of the asymmetry to the data. The very simple two-body Nearest-Neighbor approximation, which is valid only for high field values, is also reported to illustrate the importance of the many-body effects.

The results for the B_D functions and the line asymmetry for the case 10^{24} cm^{-3} are given in figure 1 (a and b). The B_D variations with β have been plotted for values of the reduced field up to 8. For higher values only MC results converge to the OCP-NN limit ($2\beta^{3/2}/17^{1/2}$), but the large discrepancies between the other theoretical results have negligible influence on the asymmetry, due to the rapid decrease of the microfield distribution.

This last conclusion also applies for the densest case 10^{25} cm^{-3} for which B_D functions and the line asymmetry are given on figure 1 (c and d). The APEX and MC results differ slightly in the reported B_D results. Even for this high density and the heavy emitter the ion dynamics effects reduce the asymmetry. The line asymmetry calculated using the OCP-NN approximation for B_D and exact microfield distribution is also reported for comparison.

CONCLUSION

These results illustrate the high sensitivity of the line asymmetry to the ion dynamics effects and to the plasma statistics of the B_D function. Moreover the main contribution of field inhomogeneity to the line asymmetry, comes from the most probable values of the microfield distribution function. This explains the little difference between APEX and MC line asymmetries at high densities. Concerning the B_D functions, the deviation from the Nearest Neighbor results illustrates the influence of the N-body effects. For larger plasma densities than studied in this paper, the electronic correlations are important and the simple Debye-Hückel screening, which was used here for simplicity, becomes questionable (Gilles and Peyrusse, 1995).

REFERENCES

- [1] Demura, A. V. and Stehlé, C., in: "Spectral Line Shapes," Vol 8, AIP Conf. Proc. 328, 177, (1995).
- [2] Demura, A. V., Gilles, D. and Stehlé, C., *J. Quant. Spectrosc. Radiat. Transfer* 54, 123–136, (1995).
- [3] Demura, A. V., Gilles, D. and Stehlé, C., in: "Spectral Line Shapes," Vol 9, AIP Conf. Proc. 386, 119, (1996).
- [4] Gilles, D. and Stehlé, C., *J. Phys. II, France*, 5, 75 (1995).
- [5] Gilles, D. and Peyrusse, O., *J. Quant. Spectrosc. Radiat. Transfer* 53, 647, (1995).
- [6] Stehlé, C., *Astron. and Astrophys.*, 292, 699, (1994).
- [7] Murillo, M. S., Kilkrease, K. L. and Collins, L. A., *Phys. Rev. E*, 55, 6289 (1997).

THE CORRELATION EFFECT IN SPECTRA OF DENSE HYDROGEN PLASMA

T. V. Gavrilova,¹ V. P. Averyanov,¹ Y. Vitel,² C. Le Guen,² L. G. D'yachkov,³
and Yu. K. Kurilenkov³

¹Vavilov State Optical Institute, Birzhevaya 12, 199034 St.-Petersburg, Russia

²Laboratoire des Plasmas Denses, Tour 12E5, Universite P. et M. Curie
4 Place Jussieu, 75252 Paris Cedex, France

³Institute for High Temperature, Russian Academy of Sciences
Izhorskaya 13/19, 127412 Moscow, Russia

INTRODUCTION

A goal-oriented experiment to the quest and research for specific manifestation of inter-particle interactions in optical spectra of non-ideal hydrogen plasma has been realized. The emission and absorption spectra in Balmer region have been studied at temperatures near 20000 K and electron densities about 10^{19} cm^{-3} . This density is the highest one achieved in the labs for pure hydrogen. Spectral distribution may be either conventional¹ according to which a disappearance of spectral series highest members is totally compensated by continuum enlargement in the same spectral region, or with a "clearing-up" effect,² when this compensation does not happen. The effect may be caused by collective modes and plasma microfields action on atoms under strong Coulomb correlations between free charges in a dense plasma.

EXPERIMENT

Plasma clearing-up was revealed previously in air and noble gases,³ but all attempts to get this in hydrogen plasma suffered a reverse.⁴ A main problem was the creation of the pure hydrogen plasma with high density and well-diagnosed parameters. In this work we succeeded in getting it due to use of specially constructed plasma source based on the pulse discharge in closed quartz capillary.⁵ The plasma obtained by this discharge is quasi-stationary and fairly homogeneous in volume. To avoid the wall ablation we reduce pulse duration to 3 μs . Capillaries of square cross section $1 \times 1 \text{ mm}^2$ and length 10 mm are used in experiment. Small transversal size of capillary provided the optical plasma transparency sufficient for direct transmission measurements in visible spectral region. All optical measurements are made at the temperature pulse maximum with time resolution of 0.3 μs . Spectra are recorded by optical multichannel analyzer coupled with a spectrograph giving a spectral resolution of 0.6 nm. For standardization deuterium and tungsten ribbon lamps are used.

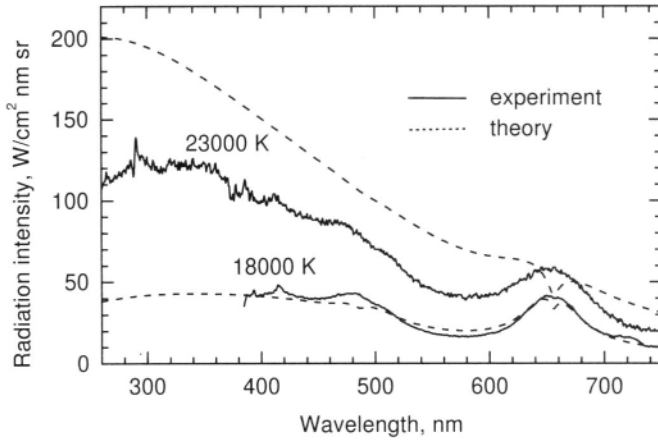


Figure 1. Emission from the two pulse discharges with $T = 18000\text{ K}$, $N_e = 6.6 \cdot 10^{18}\text{ cm}^{-3}$ and $T = 23000\text{ K}$, $N_e = 1.6 \cdot 10^{19}\text{ cm}^{-3}$ in the hot inner area.

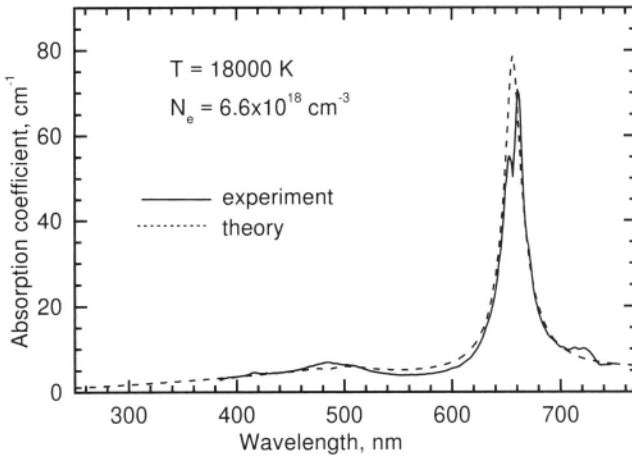


Figure 2. Absorption coefficient for $T = 18000\text{ K}$, $N_e = 6.6 \cdot 10^{18}\text{ cm}^{-3}$ at the capillary axis.

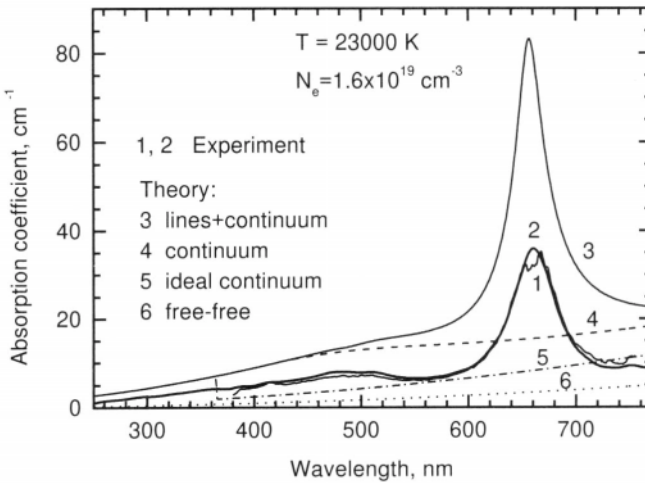


Figure 3. Absorption coefficient for $T = 23000\text{ K}$, $N_e = 1.6 \cdot 10^{19}\text{ cm}^{-3}$ at the capillary axis.

Plasma temperature T is evaluated from independent measurements of brightness b_λ and transparency $t_\lambda = \exp(-k_\lambda l)$ at wavelength $\lambda = 632.8$ nm corresponding to the generation line of He-Ne laser. Transversal profiles of b_λ and t_λ with spatial resolution of 0.1 mm are used to obtain the temperature profile. According to the spatial resolution we divide the capillary volume into five regions from axis to wall (each of 0.1 mm). The temperature is fairly homogeneous within hot near-axis zone having the width of $l_{eff} = 0.75 \pm 0.05$ mm. The relative error in the definition of plasma temperature in this zone is estimated as 3%. The radial distribution of plasma neutral density N is found in the five-region approximation (in each region T , N , and N_e are assumed constant) from the temperature profile and from the conditions⁵ for invariance of the mass and the constancy of the pressure over cross section. The electron concentration N_e is calculated from Saha equation at the known T and N .

METHOD OF CALCULATION

In the spectral range investigated the main contribution to the emission (absorption) comes from the Balmer spectrum. The line intensities are calculated taking into account the dissolution due to destruction of the bound states under the influence of the quasi-static plasma microfields. The probability W that the state is still bound, is defined as the integral of the quasi-static microfield distribution function from zero to the critical value of the field F_c for which the state is found at the top of the potential barrier formed by the microfield and the atomic core Coulomb field. In the calculation we use the distributions for a neutral point by Hooper⁶ and critical values corresponding to the approximation of uniform microfield on the atomic scale. Profiles of H_α and H_β are calculated according to Griem,⁷ while the following Balmer lines are almost completely dissolved and their profiles are not important. The Balmer photoionization cross section is calculated from the exact quantum mechanical equations.⁸ Other photoionization and inverse bremsstrahlung cross sections are calculated in the Kramers approximation with the corresponding Gaunt factors.^{9, 10} The Balmer photoionization cross section is continued over the long-wavelength threshold with the factor $1 - W(\lambda)$, assuming that the total (lines and continuum) density of oscillator strengths is conserved (the loss in the line oscillator strengths is compensated by the continuum extension). For the calculation of the radiation intensity from the capillary we have considered the problem of the radiative transfer in the approximation of five regions.

RESULTS AND DISCUSSION

Spectral emission intensity for two experimental conditions are presented in Fig. 1. Absorption spectra obtained from plasma emission by Kirchhoff-Planck equation are presented in Figs. 2 and 3 in comparison with the absorption coefficient calculated for the inner zone of the capillary. The relative experimental error is about of 7%. In Fig. 3 we present two experimental curves for different discharges under the same conditions. Analysis of the results shows that deviation of experimental data from calculated ones starts for hydrogen plasma at $N_e \approx 10^{19} \text{ cm}^{-3}$ and can be interpreted as the manifestation of essential perturbation of density of oscillator strengths in comparison with isolated atom picture. It is characterized by relative "clearing up" of hydrogen plasma as the density grows. Note, that the data presented in Fig. 3 correspond to maximal value of N_e achieved up to now.^{4, 11} However the five-region approximation may be too crude for exact determination of the density, so this effect may be quantitatively reduced with improvement of the spatial resolution. The effect observed now at first for hydrogen reliably has been discussed during last two decades as well as the "transparency windows" for plasmas of complex elements.^{2, 4, 11}

Acknowledgements

This work is supported by a contract of the 'Club Arc Electrique' of the Electricite de France, by NATO Linkage Grant HTECH. LG 960803, PECO CEI program and RFBR Grant 96-02-18785.

REFERENCES

- [1] L. M. Biberman and G. E. Norman, *Sov. Phys.-Usp.* 10:51 (1967).
- [2] G. A. Kobzev, Yu. K. Kurilenkov, and G. E. Norman, *High Temp.* 15:163 (1977); G. A. Kobzev and Yu. K. Kurilenkov, *High Temp.* 16:385 (1978); G. E. Norman, *High Temp.* 17:382 (1979); Yu. K. Kurilenkov and P. V. Minaev, *Zh. Eksp. Teor. Fiz.* 74:563 (1978).
- [3] T. V. Gavrilova, *Sov. Phys. Tech. Phys.* 24:374 (1979); V. E. Gavrilov, T. V. Gavrilova, and V. E. Fortov, *High Temp.* 28:453 (1990).
- [4] G. A. Kobzev and Yu. K. Kurilenkov, in: "III Int. Workshop on Nonideal Plasmas, Biesenthal, GDR, Proceedings" (1984), p. 42
- [5] S. I. Andreev and T. V. Gavrilova, *High Temp.* 12:1138 (1974).
- [6] C. F. Hooper, Jr., *Phys. Rev.* 165:215 (1968).
- [7] H. Griem. "Spectral Line Broadening by Plasmas," Academic, New York (1974).
- [8] H. A. Bethe and E. E. Salpeter. "Quantum Mechanics of One- and Two-Electron Atoms," Springer, Berlin (1957).
- [9] J. R. Roberts and P. A. Voight, *J. Res. Nat. Bur. Stand.* 75A:291 (1971).
- [10] L. G. D'yachkov, *J. Phys. B* 23:L429 (1990).
- [11] Yu. K. Kurilenkov and M. A. Berkovsky, in: "Transport and Optical properties of Nonideal Plasma," G. A. Kobzev, I. T. Iakubov, and M. M. Popovich, eds., Plenum, New York (1995), p. 215.

PLASMA INDUCED LINE SHIFTS: NEW LIGHT ON AN OLD CONTROVERSY

Charles F. Hooper, Jr.,¹ Gwyneth C. Junkel,¹ Mark A. Gunderson,¹ Donald A. Haynes, Jr.,¹ Roberta C. Mancini,² David Bradley,³ Jacques Deleltrez,³ and Paul Jaanimagi³

¹Department of Physics
University of Florida
Gainesville, Florida

²Department of Physics
University of Nevada
Reno, Nevada

³Laboratory for Laser Energetics
University of Rochester
Rochester, New York

INTRODUCTION

The topic of the magnitude, and even the direction of plasma induced line shifts has been a controversial topic for a number of years.¹⁻⁵ In this paper, we sketch the relevant Stark broadening theory, and compare new calculations with recent experimental data.

STARK BROADENING THEORY

The shapes of the spectral lines emitted by a plasma form a useful, non-interfering probe of the plasma environment.⁶ For a given line, the lineshape can be written

$$I(\omega) = \int d\vec{\mathcal{E}} Q(\vec{\mathcal{E}}) J(\omega; \vec{\mathcal{E}}),$$

where $Q(\vec{\mathcal{E}})$ is the probability distribution function for the electric field at the radiator due to the plasma ions, and $J(\omega; \vec{\mathcal{E}})$ is the plasma–electron perturbed lineshape emitted by radiators experiencing that plasma ion microfield. The form of $J(\omega; \vec{\mathcal{E}})$ is most pedagogical in the approximation that the ions are static during the radiative lifetime of the transition:

$$J(\omega; \vec{\mathcal{E}}) = -\frac{1}{\pi} \text{Im} \text{Tr}_r \vec{d} \cdot [\Delta\omega(\vec{\mathcal{E}}) - H(\omega)]^{-1} \rho_r \vec{d}.$$

In this expression, \vec{d} is the dipole moment operator for the radiator, $\Delta\omega(\vec{\mathcal{E}})$ is the frequency separation from the (ion-perturbed) location of the transition, and $H(\omega)$ is a

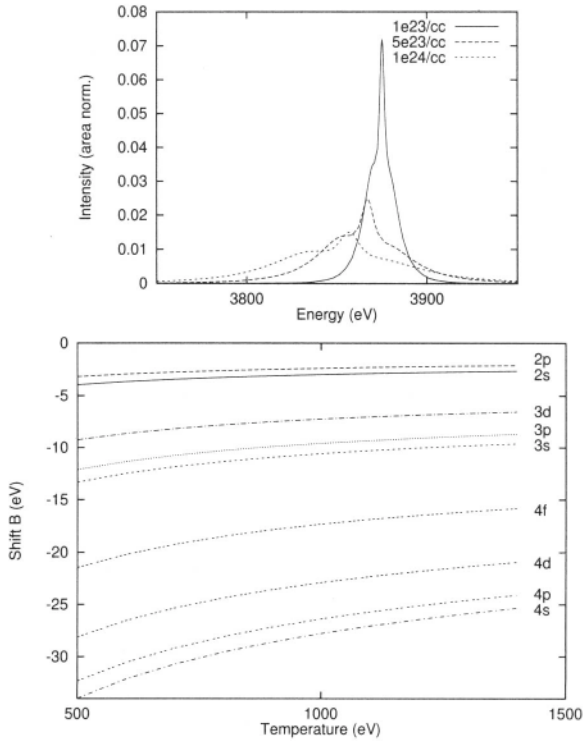


Figure 1. The density dependence of the Ar He- γ line, at a fixed temperature of 1000eV (top), and the temperature dependence of the shifts of the angular momentum components of the Ar He- α , He- β , and He- γ at a fixed density of $1 \times 10^{24} \text{cm}^{-3}$ (bottom).

complex, many-body operator accounting for the effects of the perturbing plasma electrons. The imaginary part of $H(\omega)$ is the electron broadening operator, while the real part is the shift operator with which this article is primarily concerned. In general, this shift operator must be calculated to all orders in the plasma electron-radiator interaction.¹ However, for the transitions, temperatures and densities we consider in the next section, it is sufficient to keep only the terms up to second order in this interaction. For higher densities, lower temperatures, or transitions originating from higher principal quantum numbers, this second order approximation would be suspect, and we are currently implementing an all-order semi-classical approximation. For the highly stripped Ar ions of interest, the dominant term in the shift operator is the first order term, a mean field average of the interaction. We emphasize that the important work of Reference 2 presented an example of shift calculations for neutral radiators, in which this mean field term is zero, and that the results of that paper in no way conflict with the results presented here.

In Figure 1, we display the temperature sensitivity of the shifts of the transitions in the first few members of the Ar He-like Rydberg series at a fixed density, and the density sensitivity of the Ar He- γ line at fixed temperature. As the individual angular momentum components making up the lines shift differently, the lines not only shift, they distort. Note also that the amount of shifting and distortion depends strongly on principal quantum number.

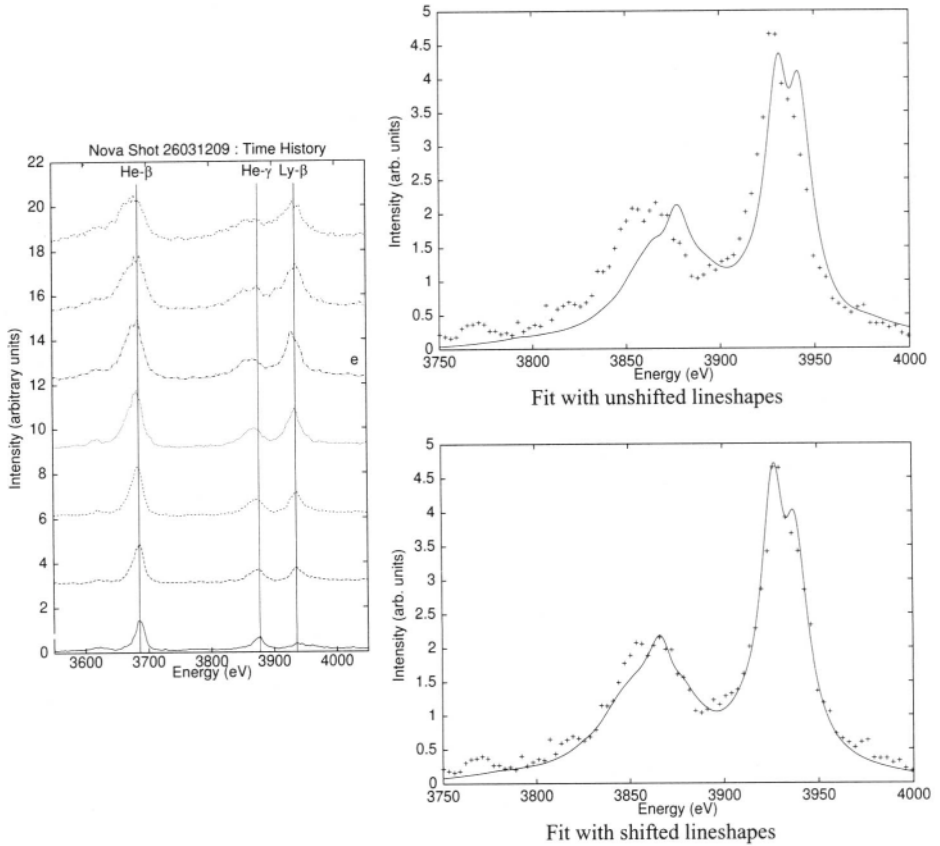


Figure 2. Time history of Nova shot 26031209 as recorded by a streaked survey spectrometer, and fits to a detail of lineout “e” calculated for $n_e = 6 \times 10^{23} \text{cm}^{-3}$, and $kT = 1125 \text{eV}$.

EXPERIMENTS AND ANALYSIS

The strong dependence of the shift on principal and angular-momentum quantum numbers, and a fortunate near coincidence of some spectral lines of highly stripped Ar ions, lead to a spectral region where the shift of several lines is easily observed using spectrometers of moderate resolution ($E/\Delta E \approx 1000$). The unshifted Ar Ly- β line lies at 3936eV, flanked by the Ar He- γ (3877eV) and He- δ (3966eV). The second order shift theory predicts that the average shifts of the Ly- β and He- γ lines at 1000eV and $1 \times 10^{24} \text{cm}^{-3}$ are approximately -7eV, and -19eV, respectively. Thus, the relative shifting of these lines should be easily observable. Unfortunately, the Ar He- δ is so broad at this density that it serves to only slightly modify the blue wing of the Ly- β lines. However, the Ar Ly- β and He- γ lines are prominent, and their narrow spectral range serves as an appropriate region to look for the effects of plasma induced line shifts.

In Figures 2 and 3, we show time resolved spectra from two microballoon implosions, one performed on the Nova laser system using indirect drive, and one performed on the Omega laser system using direct drive, along with detailed fits to the spectral range from 3750eV to 4000eV. The reduction of the data (an image on film of the streaked spectrum) to the form used here (time resolved lineouts) included a correction due to the curvature of isothermal lines inherent in streak cameras. The dispersion relationship was determined by

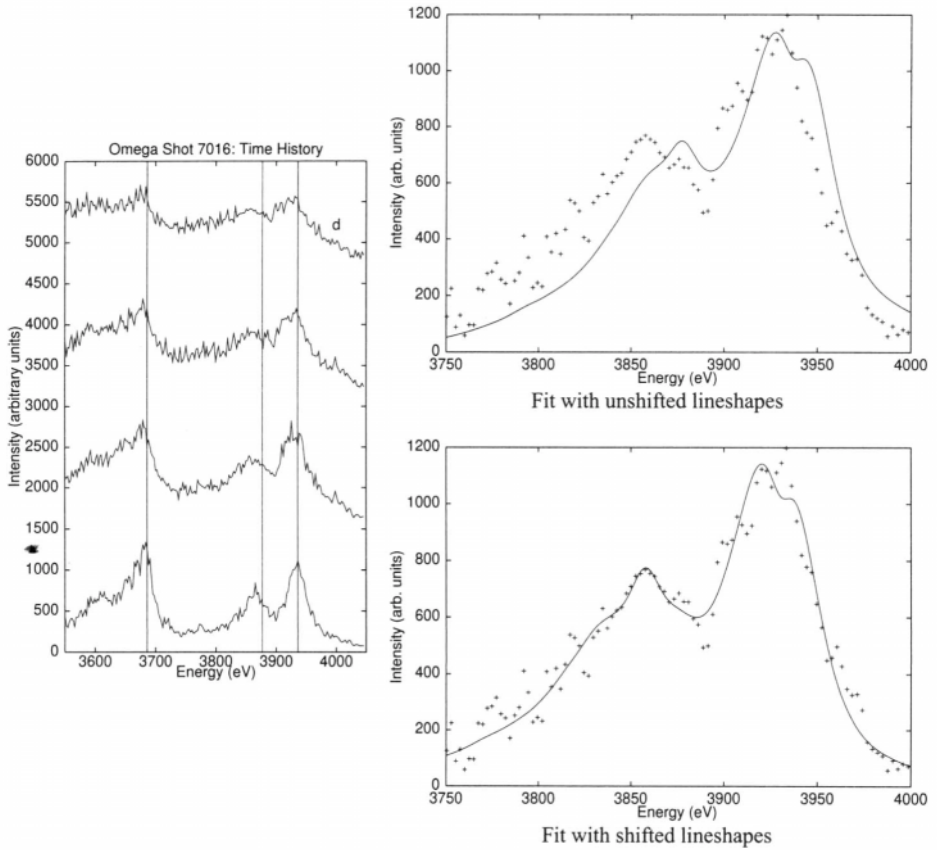


Figure 3. Time history of Omega shot 7016 as recorded by a (different) streaked survey spectrometer, and fits to a detail of lineout “d” calculated for $n_e = 1 \times 10^{24} \text{cm}^{-3}$, and $kT = 1050 \text{eV}$.

identifying the positions of the Ar resonance lines at early times, when the densities were sufficiently low so that any shifts were negligible. One benefit of using the Ar Ly- β and He- γ lines is that their proximity in the image minimizes the effects of the varying magnification across the image.

The calculated spectra include the three resonance lines, and two He-like satellites of the Ly- β and three Li-like satellites of the He- γ . The lineshapes included the effects of ion dynamics, opacity,⁷ and the ion quadrupole effect.⁸ Doppler and appropriate instrumental broadening were also included. The relative intensities of the lines were calculated using a NLTE kinetics model, with the effect of radiative transfer approximated by the use of escape factors.^{7,9}

CONCLUSIONS

It appears that the theoretical lines shifted according to calculations provide substantially better fits than the theoretical line shapes which exclude line shifts. The differing principal quantum numbers associated with the Ly- β and He- γ lead to significantly differing shifts. Thus, the use of unshifted lines, shifted arbitrarily, *en masse*, would not lead to the same quality of fit observed when using the lineshapes shifted according to calculation.

REFERENCES

- [1] J. Cooper, D. E. Kelleher, and R. W. Lee, *On the "plasma polarization shift"*, in Radiative Properties of Hot Dense Matter, eds. J. Davis, C. Hooper, R. Lee, A. Merts, and B. Rozsnyai, World Scientific, Singapore (1985).
- [2] D. B. Boercker and C. A. Iglesias, *Static and dynamic shifts of spectral lines*, Phys. Rev. A **30** 2771, (1984).
- [3] C. A. Iglesias *Shifts of spectral lines in plasmas*, Phys. Rev. A **29** 1366 (1984).
- [4] H. R. Griem, M. Blaha, and P. C. Kepple, *Stark-profile calculations for resonance lines of heliumlike argon in dense plasmas*, Phys. Rev. A **41** 5600 (1990).
- [5] H. Nguyen, M. Koenig, D. Benredjem, M. Caby, and G. Couland, *Atomic structure and polarization line shift in dense and hot plasmas*, Phys. Rev. A **33** 1279 (1986).
- [6] H. R. Griem, *Spectral Line Broadening by Plasmas*, Academic, New York (1974).
- [7] D. A. Haynes, Jr., D. T. Garber, C. F. Hooper, Jr., R. C. Mancini, Y. T. Lee, D. K. Bradley, J. Delettrez, R. Epstein, and P. A. Jaanimagi, *Effects of ion dynamics and opacity on Stark-broadened argon line profiles*, Phys. Rev. E, **53** 1042 (1996).
- [8] R. L. Joyce, L. A. Woltz, and C. F. Hooper, Jr., *Asymmetry of Stark-broadened Lyman lines from laser-produced plasmas*, Phys. Rev. A **35** 2228 (1987).
- [9] R. C. Mancini, R. F. Joyce, and C. F. Hooper, Jr., *Escape factors for Stark-broadened line profiles*, J. Phys. B: At Mol. Phys. **20** 1975 (1987).

This page intentionally left blank

REDISTRIBUTION FUNCTIONS OF HELIUM-LIKE MULTICHARGED IONS IN MODEL MICROFIELD METHOD

A. V. Demura,¹ N. Feautrier,² I. N. Kosarev,³ V. S. Lisitsa,¹ and C. Stehlé⁴

¹Russian Research Center “Kurchatov Institute”
Moscow 123182, Russia

²DAMAP et URA812 du CRNS, Observatoire de Paris
5 Place Jules Janssen, F-92195, Meudon, France

³Institute of Physics & Power Engineering
Obninsk 249020, Russia

⁴DARC et UPR176 du CRNS, Observatoire de Paris
5 Place Jules Janssen, F-92195, Meudon, France

REDISTRIBUTION OF RADIATION AND DENSE PLASMAS ION DYNAMICS IN MMM

Besides the usual plasma correlation effects, described in terms of coupling parameters, the spectral characteristics of Coulomb systems may exhibit strong coupling effects between quantum dynamics and kinetics of the various radiator quantum levels, induced by microfields of perturbing charges.¹ Similar phenomena were called Nonlinear Interference Effects (NIEF) in laser physics and this term was adopted for the study of these effects in the Stark broadening. In the present work the influence of NIEF on the redistribution function of resonance radiation is investigated in the framework of the atomic density matrix formalism with simultaneous account for the ion motion within the Model Microfield Method (MMM).

The redistribution function $R(\omega, \omega')$ is defined as the joint probability of the absorption of a photon with the frequency ω' and the emission of a photon with the frequency ω . Here $R(\omega, \omega')$ is considered in the radiator rest frame thus avoiding the averaging over polarizations and wave vectors of absorbed and emitted photons.

The effects of the ion plasma microfield are essential in the calculation of $R(\omega, \omega')$ for multicharged ions radiation in dense plasmas. The slowly varying ion microfield induces coherences of radiating atomic states (ie the non-diagonal elements of the atomic density matrix become different from zero). This microfield strongly couples kinetics of level populations and coherences in the system of the radiator quantum levels, which makes the essence of NIEF. It should be stressed that the inclusion of NIEF is essential, hence its omission may lead to non physical negative values of $R(\omega, \omega')$.²

The thermal plasma ion motions (ion dynamics) also influences the radiative redistribution in hot dense plasmas, as it is illustrated in [1] for Ly- α -line of a hydrogen-like ion within the Molecular Dynamics Method (MD).

The aim of this paper is to study the influence of both NIEF and ion dynamics on $R(\omega, \omega')$ of the resonance radiation in hot dense Al plasmas ($T \sim 350$ eV, $N_e \sim 10^{20} \div 10^{19}$ cm $^{-3}$) for lines of helium-like multicharged Al $^{+11}$ ions. This study may be of interest for applications to the radiative transfer in the inertial confinement fusion plasmas (ICF or LF) and for X-ray lasers. Line shapes of Al He-like ions have been recently calculated under these conditions. It has been shown that the account of both NIEF and ion dynamics is important in frequency regions near intensity maxima as well as in the nearest wings for low densities.³

The complete redistribution approximation (CR) is often used in the theory of the radiative transfer. Within this approximation, the redistribution function $R(\omega, \omega')$ is equal to $\varphi(\omega)\varphi(\omega')$, where $\varphi(\omega)$ is the normalized line shape calculated according to the standard theory. The results obtained for Ly- α line¹ show that the complete redistribution is not reached. In this paper this question is again studied for the lines of helium-like multicharged ions.

The radiating ion is modelled by the traditional three-level system, relevant for the formulation of the problem of forbidden component of the helium-like ions spectra.³ The radiative decay rate of the excited state 2 is denoted by Γ_2 , while radiative decay rates of the metastable state 3 and the ground state 1 are assumed to be zero. The transition 2–1 is an allowed dipole transition, while the transition 3–1 is a dipole forbidden transition. The levels 3 and 2 are separated by the interval energy $\hbar\omega_{32}$.

The ion dynamics is included by a step-wise stochastic Kangaroo process (MMM).⁴ This approximation models the time statistics of the ion microfield by supposing that the field is constant on time intervals. The jump times follow a Poisson statistics with the jump frequency $\nu(E)$ which depends on the value of the field before the jump. The Fourier transform at ω of the mean evolution operator $\langle U(t, 0) \rangle_{\text{MMM}}$ is expressed in terms of the evolution operators in a static ion field E averaged over the appropriate microfield distribution function $P(E)$ as

$$\langle U(\omega) \rangle_{\text{MMM}} = \langle U_{\text{St}}(\omega + i\nu) \rangle + \langle \nu U_{\text{St}}(\omega + i\nu) \rangle \langle \nu I - \nu^2 U_{\text{St}}(\omega + i\nu) \rangle^{-1} \langle \nu U_{\text{St}}(\omega + i\nu) \rangle, \quad (1)$$

where I is the unit operator, ν is the jump frequency of the MMM Kangaroo process, $U_{\text{St}}(\omega + i\nu)$ is the Laplace transform at $z = -i\omega + \nu$ of the static evolution operator and $\langle \dots \rangle = \int_0^\infty \dots P(E) dE$ denotes the averaged operators.

To apply the formalism to the case of the redistribution, it is necessary to remove from the equations describing the system evolution all the explicit time dependences due to the interaction of an atomic system with the absorbed and scattered radiation. This has been made by separating contributions from a fluorescence and a Rayleigh scattering and expressing the resulting equations through the appropriate Fourier transforms of the evolution operators.

PARTIAL REDISTRIBUTION WITHIN MMM

The formalism of atomic density matrix is used (see [1, 3]). The equations for the radiating atomic states coherences are considered on the same level as those for the diagonal matrix elements defining level populations. The interaction of the radiator with the temporarily varying ion microfield, which mixes both the forbidden and allowed transitions, the electronic and radiative dampings are included in the Hamiltonian in zero order in the amplitudes of the absorbed and scattered radiation in the interaction representation. In the present case the incoherent pumping is put to zero. The initial population of the ground state is equal to unity, while initial populations of other levels are put to zero. The result of the perturbation approach in the first order of the scattered radiation and up to the second order in the incident radiation amplitudes may be expressed within MMM analytically through values defined in the quasistatic approximation for ions. This allows to exhibit $R(\omega, \omega')$ in the form

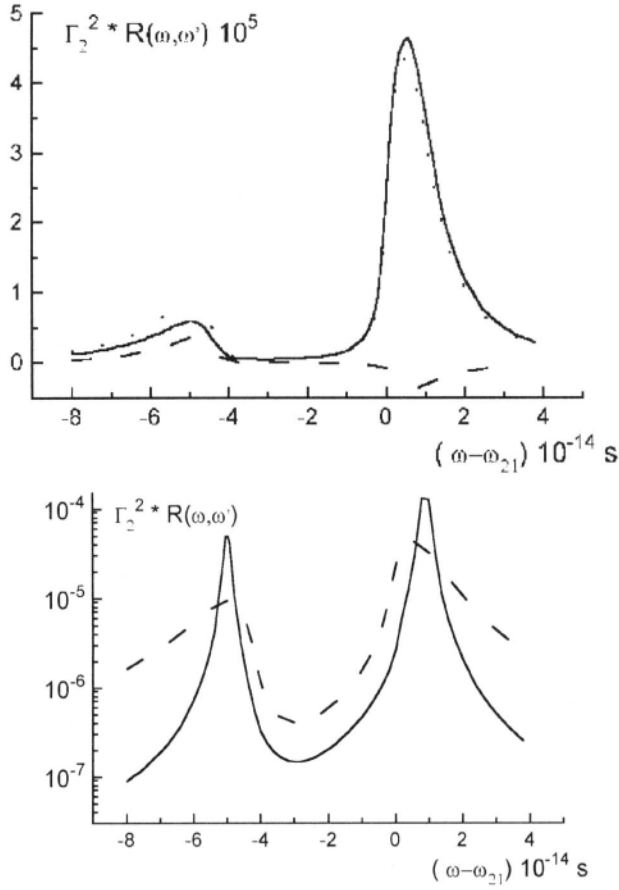


Figure 1. The section of the incoherent part of the redistribution function at the fixed frequency of the absorbed radiation $\omega' - \omega_{21} = -5 \times 10^{14} \text{ s}^{-1}$ of the doublet $2^1S - 4^1P, 2^1S - 4^1D$ of the ion Al^{+11} at $N_e = 10^{20} \text{ cm}^{-3}$, $T = 350 \text{ eV}$: a) without NIEF (full curve), with NIEF (dotted curve), NIEF contribution (dashed curve); b) within the static ion field approximation (full curve), including ion dynamics effects (dashed curve).

$R^{MMM}(\omega, \omega') \propto \text{Re} \langle iG^* e^{i\omega t} \rho_{21}(t) \rangle$, where ρ_{21} is the non-diagonal element of the density matrix, G^* defines the complex conjugated amplitude of the scattered radiation, $\langle \dots \rangle$ denotes averaging over the ensemble of perturbing plasma ions.

The calculations have been performed for the spectral doublet $(1s2s)^1S - (1s4p)^1P$, $(1s2s)^1S - (1s4d)^1D$ of helium-like ion Al^{+11} . The states $4^1P, 4^1D, 2^1S$ correspond respectively to the states 2, 3, 1 of the three level-model system. The radiative decay rate Γ_2 is equal to $4.1 \times 10^{12} \text{ s}^{-1}$. The transition frequency ω_{32} between radiating states 3 and 2 is equal to $-4.1 \times 10^{14} \text{ s}^{-1}$. The electron inelastic collisional decay rate is given by $3.1 \times 10^{-5} N_e (Z_i + 1)^{-2} T^{-1/2}$, (units are $\text{s}^{-1}, \text{cm}^{-3}, \text{eV}$). The results obtained for an electron density $N_e = 10^{20} \text{ cm}^{-3}$ will be briefly reported here.

The ion dynamics have a large influence on the coherent and incoherent parts of the redistribution function. The value of the characteristic frequency of the ion microfield variation $\nu = v_i N_i^{1/3} \cong 25 \times \Gamma_2$ is large compared with the other relevant characteristic frequencies of the problem. The coherent part of the line shape is small in the centers of the allowed and forbidden components and also in the nearest wings. This may be attributed to the large electron relaxation rate compared with the radiative decay rate at these conditions. It follows that the CR approximation is invalid for this case despite the large electron relaxation

rate compared to the radiative decay rate. The contributions from NIEF and ion motions effects are very large. The coherent contribution to the line profile becomes more essential when the plasma density is decreased. In the centers of the allowed and forbidden components, the coherent part is small but as the frequency deviation is increased the coherent contribution to the line shape increases.

The dependence of the incoherent part of $R(\omega, \omega')$ on the frequency of the scattered radiation ω , at a fixed frequency ω' of the absorbed radiation (close to the value of the forbidden transition ω_{31}) is shown in Figs. 1 a and b. One can see from Fig. 1a that the account of NIEF leads to the increase of the intensity of the forbidden component by approximately a factor two, while the influence of NIEF on the allowed component is not essential (approximately 10%). In Fig. 1b one can see that ion dynamics strongly influences the redistribution function, especially in the wings.

REFERENCES

- [1] A. V. Demura, A. E. Bulyshev, V. S. Lisitsa, A. N. Starostin, A. E. Suvorov, I. I. Yakunin, this volume (1997).
- [2] A. V. Demura, A. V. Anufrienko, A. L. Godunov, Yu. K. Zemtsov, V. S. Lisitsa, A. N. Starostin, M. D. Taran, V. A. Schipakov, *in: SLS v. 6*, L. Frommhold, J. W. Keto, ed., AIP, New York (1990), pp. 227–254.
- [3] I. N. Kosarev, C. Stehlé, N. Feautrier, A. V. Demura and V. S. Lisitsa, *J. Phys. B: At. Mol. Opt. Phys.* **30**:215 (1997).
- [4] C. Stehlé, *Astron. Astrophys.* **292**:699 (1994).

STICKY CHARGED SPHERES IN THE MEAN SPHERICAL APPROXIMATION: A MODEL FOR FLEXIBLE POLYELECTROLYTES

O. Bernard¹ and L. Blum²

¹Laboratoire des Propriétés Physico-Chimiques des Electrolytes
URA 430, Université Pierre et Marie Curie
4, Place Jussieu 75252 Paris Cedex 05, France.

²Department of Physics, P. O. Box 23343
University of Puerto Rico
Rio Piedras, PR 00931-3343, USA

INTRODUCTION

Liquid state theories like the MSA and the HNC can be derived as variational problems of the free energy functional, which is written in terms of the Ornstein–Zernike (OZ) direct correlation function and interpolate between the low coupling Mayer and high coupling Onsager limits. This view as recently taken by Rosenfeld and one of us,^{1–3} for systems of charged hard spheres. However, these theories, do not satisfy the high coupling but low density limits. In this limit, ions with charge 1 that form dimers should behave as ions of charge 2, the Debye–Hückel parameter should be twice for the fully dimerized case. This does not happen for theories based on closures of the normal OZ do not give this result. The new Wertheim OZ (WOZ) equation^{4,5} does satisfy this limit for neutral particles, and, as we will show it in this paper, for charged particles in the mean spherical approximation.

In the solution of the MSA of associating spheres given in the present work the Onsager high density limits are satisfied. In the limit of low density and total association the exact asymptotic limits are recovered for dimers, using a two body closure, and for any length chain when three body interactions are included.

One remarkable property of the MSA is that the full solution depends on a single screening parameter Γ ,^{6,7} which also gives the excess full thermodynamics (internal energy and entropy) computed via the Guntelberg charging process. In the case of polymer chains we get

$$\beta\Delta A^{BIM-EXP} = \beta\Delta E^{BIM} - T\Delta S^{MSA} \quad (1)$$

where

$$\Delta S^{MSA} = -k_B \frac{(\Gamma^T)^3}{3\pi} \quad (2)$$

where k_B is Boltzmann's constant and Γ is the MSA screening constant is obtained in every case.

In this communication we discuss the results of previous work, and in particular those of [8] (and references cited therein). We will use also the notation and symbols of that paper.

THE MSA IN THE WERTHEIM ORNSTEIN ZERNIKE FORMALISM

The WOZ formalism was shown to be very successful for ionic systems, both in the HNC approximation and MSA.^{2,9-11} A solution of the restricted linear polymer MSA has been given by Kalyuzhnyi and Stell.¹² A similar and very nice discussion was recently given by Jiang et al.¹³ The full analytical solution of the electrostatic part given in terms of the screening parameter Γ^{T6} of the binding MSA for dimer association was discussed elsewhere (BIMSA)^{8,14,15} In this paper we discuss explicitly the linear polymer case in the BIMSA-EXP approximation, using the results of our earlier work.^{8,15} As in this work, we consider a system with an arbitrary number of components $1 < i \leq n$, with number density ρ_i , charge ez_i , (e is the elementary charge) and hard core diameter σ_i . The solvent is a continuum with dielectric constant ϵ_0 . The temperature of the system is T , Boltzmann's constant is k_B and we use $\beta = 1/k_B T$ throughout. Our system is neutral:

$$\sum_i \rho_i z_i = 0 \quad (3)$$

We get for the screening parameter

$$[\Gamma^T]^2 = \pi \frac{\beta e^2}{\epsilon_0} \sum_k \rho_k [\mathbf{S}_k]^T [\boldsymbol{\alpha}_k] [\mathbf{S}_k]^T \quad (4)$$

There is a second nonlinear equation for the parameter η^T , which in general will depend strongly on the closure approximation for the single density matrix. However, if the binding probabilities are assumed to be uncorrelated, then only the dissociation probabilities α are needed, and the formal result for η^T is model independent.

THE FLEXIBLE FIXED LENGTH LINEAR POLYMER MODEL

Consider the model of a fixed length flexible polymer chain: The individual bead has two different sites, A and B, and we allow only bonds between A and B, and only between particles that have contiguous indices. The interactions are such that only linear chains can be formed.⁸ The density parameters $\sigma_i^{(a)}$ are related to the densities of a -bonded particles $\rho_i^{(a)}$ by

$$\begin{aligned} \hat{\sigma}_i^0 &= \rho_i^0, & \hat{\sigma}_i^A &= \rho_i^0 + \rho_i^A, & \hat{\sigma}_i^B &= \rho_i^0 + \rho_i^B, \\ \hat{\sigma}_i^\Gamma &= \rho_i = \rho_i^0 + \rho_i^A + \rho_i^B + \rho_i^\Gamma \end{aligned} \quad (5)$$

However we shall use the convenient notation

$$\alpha^{(1)} = \frac{\hat{\sigma}_i^B}{\hat{\sigma}_i^\Gamma} \quad \alpha^{(2)} = \frac{\hat{\sigma}_i^A}{\hat{\sigma}_i^\Gamma} \quad \alpha^{(3)} = \frac{\hat{\sigma}_i^0}{\hat{\sigma}_i^\Gamma} \quad (6)$$

for the density parameters. One assumption is to neglect the site-site interactions $t_{ij}^{(a,3)}, t_{ij}^{(3,b)}$ also implies that the probability of both empty sites on a molecule is the product of having site A empty by that of having site B empty:

$$\alpha_i^{(3)} = \alpha_i^{(1)} \alpha_i^{(2)}$$

If only nearest neighbor interactions are allowed then

$$\frac{[1 - \alpha_i^{(a)}]}{2\sigma_{i,i\pm 1}} = \rho_{i\pm 1} \left[\alpha_i^{(a)} t_{ij}^{ab} \alpha_{i\pm 1}^{(b)} \right] \quad (7)$$

The closure relation is obtained from equation (4) as a function of $\alpha_i^{(a)} \chi_i^{(a)}$.

$$(\Gamma^T)^2 = \frac{\pi e^2 \beta}{\varepsilon} \sum_k \rho_k \chi_k^T \hat{\alpha}_k \chi_k \quad (8)$$

$$(\Gamma^T)^2 = \frac{\pi e^2 \beta}{\varepsilon} \sum_k \rho_k \left[\chi_k^0 \sum_{a=0}^2 \alpha_k^{(a)} \chi_k^{(a)} + \alpha_k^1 \chi_k^1 (\chi_k^0 + \alpha_k^2 \chi_k^2) + \alpha_k^2 \chi_k^2 (\chi_k^0 + \alpha_k^1 \chi_k^1) \right] \quad (9)$$

Thermodynamic Properties

From the standard expression for the excess energy per unit volume, is^{6,7} we get^{6,14} as a function of the set of the $\alpha_i^{(a)} \chi_i^{(a)}$:

$$\Delta E = \frac{-e^2}{\varepsilon} \sum_k \rho_k z_k \frac{\Gamma^T z_k + \eta^T \sigma_k}{1 + \Gamma^T \sigma_k} + \frac{e^2}{\varepsilon} \sum_k \rho_k \frac{z_k}{\sigma_k} \sum_{a=1}^2 \alpha_k^{(a)} \chi_k^{(a)} \quad (10)$$

with

$$\eta^T = \frac{\pi}{2\Delta} \sum_k \rho_k \sigma_k \sum_{a=0}^2 \alpha_k^{(a)} \chi_k^{(a)} \quad (11)$$

THE RESTRICTED CASE OF EQUAL DIAMETER MONOMERS

Consider the case where all the diameters and interactions are equal. Then, for arbitrary length polymers with equal charged beads

$$\Delta E = -\frac{e^2}{\sigma \varepsilon} \left\{ \rho_1 z_1 (X_1^o - z_1) \left[n - 2 \frac{x}{(x-1)^2} [x^n + n(1-x) - 1] \right] + \rho_c z_c (X_1^o - z_c) \right\} \quad (12)$$

Two interesting cases can be discussed: The monomers that form the polymer are either of equal or alternating charge. In the first case the chain is neutralized by the counterions c of charge z_c , density ρ_c and the same diameter σ . In the other case unassociated counterions may exist. The general expression derived from Eq. (9) in this case the equation for Γ :

$$vX_1^o = \dots = X_n^o = \frac{z_1 - \eta \sigma^2}{1 + \Gamma \sigma} \quad (13)$$

$$\Gamma^2 = \frac{\pi \beta e^2}{\varepsilon} \rho_1 [X_1^o]^2 \left[n + 2 \sum_{i=1}^n [(i+1)(n-i)] \left[\frac{1 - \alpha}{2(1 + \Gamma \sigma)} \right]^i \right] + \frac{\pi \beta e^2}{\varepsilon} \rho_c [X_c^o]^2 \quad (14)$$

In the case of a fully associated polyelectrolyte $\alpha = 0$ and this equation can be transformed to

$$\Gamma^2 = \frac{\pi \beta e^2}{\varepsilon} \rho_1 [X_1^o]^2 \left[n + 2 \frac{x}{(x-1)^3} (2x^n - 2 + n(1-x)(2-x+x^n)) \right] + \frac{\pi \beta e^2}{\varepsilon} \rho_c [X_c^o]^2 \quad (15)$$

where

$$x = \pm \frac{1}{2(1 + \Gamma \sigma)}$$

where the positive sign corresponds to equal charge monomers, and the minus to the alternating charge case. The infinite dilution limit is obtained when $\Gamma \rightarrow 0$, and $x \rightarrow \pm 1/2$. Then

$$\Gamma^2 \simeq \frac{\pi \beta e^2}{\varepsilon} \rho_1 [(n_{eff} z_c)^2] + \frac{\pi \beta e^2}{\varepsilon} \rho_c [z_c]^2 \quad (16)$$

This equation satisfies the infinite dilution limit for $n=2$ (dimers) exactly, since then $n_{eff} = 2$ or 0. When $n = 3$ then $n_{eff} = 2.91$. As n increases the limiting relation is $n_{eff} \simeq \sqrt{7n}$. For the dimer case this is the only theory that yields the exact association limit.

If the equilibrium equations are modified to include exact 3-body hard core exclusion, then for the case of the chain of equal charges and diameters

$$[\Gamma^T]^2 = \frac{\pi e^2 \beta}{\varepsilon} \left[\rho_p (x_1^0)^2 \left(n + 2 \sum_{i=1}^{n-1} (n-i) \left(\frac{1}{1 + \Gamma^T \sigma_1} \right)^i \right) + \sum_{c=n+1}^m \rho_c (x_c^0)^2 \right]$$

and the low density limit is verified for any length polymer, since $n_{eff} = n$. It is also straightforward to see that the excess entropy is simply

$$\Delta S = -k_B \frac{[\Gamma^T]^3}{3\pi} \quad (17)$$

Acknowledgements

L. B. was supported by NSF programs CHE-95-13558 and OSR-94-52893, and thanks the University P. et M. Curie for their warm hospitality.

REFERENCES

- [1] Y. Rosenfeld and L. Blum, (1986), J. Chem. Phys. **85** 1556 4272.
- [2] M. F. Holovko and Yu. V. Kalyuzhnyi, (1991), Mol. Phys. **73** 1145.
- [3] L. Blum and Y. Rosenfeld, (1991), J. Stat. Phys. **63** 1177.
- [4] M. S. Wertheim, (1984), J. Stat. Phys. **35** 19, 35; (1986), *ibid* **42** 459, 477. **42** 459,477.
- [5] M. S. Wertheim, (1985), J. Chem. Phys. **85** 2929, (1987), *ibid* **87** 7323, (1988), *ibid* **88** 1214.
- [6] L. Blum, (1975), Mol. Phys. **30** 1529.
- [7] L. Blum and J. S. Høye, (1977), J. Phys. Chem. **81** 1311; (1974),
- [8] L. Blum, Yu. V. Kalyuzhnyi, O. Bernard and J. N. Herrera Pacheco (1996), J. Phys. Condens. Matter **8** A143 (1996).
- [9] Yu. V. Kalyuzhnyi and M. F. Holovko, (1993), Mol. Phys. **80** 1165.
- [10] Yu. V. Kalyuzhnyi, M. F. Holovko and A. D. Haymet, (1991), J. Chem. Phys. **95** 9151.
- [11] Yu. V. Kalyuzhnyi and V. Vlachy, (1993), Chem. Phys. Letters, **215** 518.
- [12] Yu. V. Kalyuzhnyi and G. Stell, (1995), Chem. Phys. Lett. **240** 157.
- [13] J. Jiang, H. Liu, Y. Hu and J. M. Prausnitz, (1996), J. Chem. Phys., **104**, 396, and *ibid.*, (in press).
- [14] L. Blum and O. Bernard, (1995), J. Stat. Phys. **79** 569.
- [15] O. Bernard and L. Blum, (1996), J. Chem. Phys. **104** 4746 (1996).
- [16] Yu. V. Kalyuzhnyi and G. Stell, (1993), Mol. Phys. **78** 1247.
- [17] J. K. Percus and G. Yevick, (1966), Phys. Rev. **110** 251.
- [18] J. L. Lebowitz and J. K. Percus, (1966), Phys. Rev. **144** 251.
- [19] E. Waisman and J. L. Lebowitz, (1970), J. Chem. Phys. **52** 4307.

ELECTRONIC PROPERTIES AND MECHANISM OF SUPERIONIC CONDUCTIVITY IN SOLID ELECTROLYTES

Hideaki Kikuchi,¹ Hiroshi Iyetomi,² and Akira Hasegawa²

¹Graduate School of Science and Technology

²Department of Physics

Niigata University

Ikarashi, Niigata 950-21, Japan

INTRODUCTION

Superionic conductors¹ such as AgI, CuI, and silver chalcogenides consist of a stable, ordered lattice of anions and a fluid of cations diffusing through the sublattice. Such fascinating ionic compounds exhibit ionic conductivity comparable to those of electrolyte solutions well below the melting temperatures. Since the moving ions are highly correlated to each other through Coulombic interactions, complex strongly-coupled Coulomb systems are materialized in the superionic conductors.

Silver ions often exhibit particularly fast diffusivity in haloid and chalcogenide matrices. However, steric size of Ag ions used in molecular dynamics (MD) simulations² for the superionic conductors is remarkably small as compared with the representative ionic radius due to Pauling,³ who fruitfully replaced ions by charged hard spheres to discuss structural stability of ionic compounds. Such a fundamental issue as originating from the electronic properties of superionic conductors is out of scope of the MD simulations. Hybridization between Ag 4d states and p states of host atoms forming the sublattices may be a clue to the superionic conduction of Ag ions.⁴

Having such underlying ideas in our mind, we try to shed light on the mechanism of the superionic conductivity through electronic structure calculations in the present paper. The systems studied here are Ag_2Te , Cu_2Te and M_2Te ($\text{M} = \text{Li}, \text{Na}, \text{K}$) with the antifluorite structure as displayed in Fig. 1. Ag_2Te in the α phase ($400 \text{ K} \lesssim T \lesssim 1000 \text{ K}$), a typical superionic conductor, takes basically the antifluorite form as an averaged crystalline structure.⁵ We pay special attention to difference in the closed shells between the noble-metal ions (d-shell) and the alkali ions (sp-shell) embedded in the Te sublattice with valence bands consisting of p states. Comparison of the results for Ag_2Te and Cu_2Te enables us to discuss possible effects of the p-d hybridization on the appearance of the superionic conductivity.

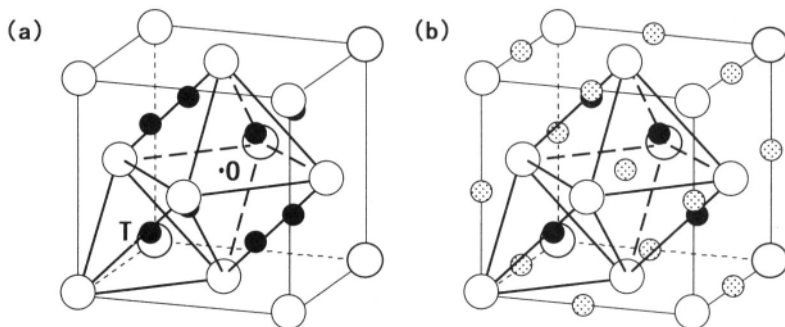


Figure 1. Ag_2Te with the antifluorite structure (a) and the $F\bar{4}3m$ crystal structure (b); the designations T and O in the panel (a) refer to the tetrahedral and octahedral sites in the FCC structure, respectively.

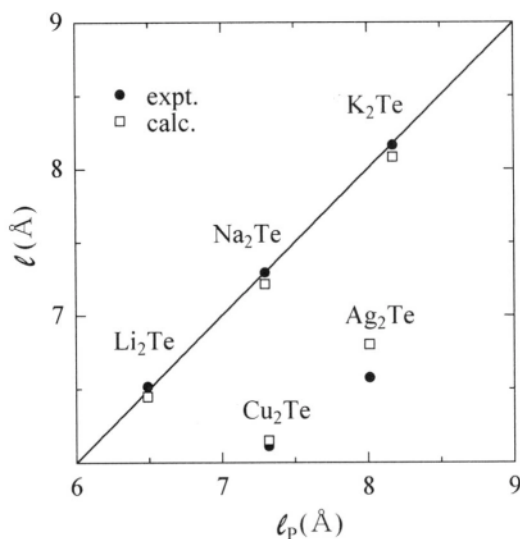


Figure 2. Experimental and theoretical lattice constants ℓ of the tellurides with the antifluorite structure versus those ℓ_p predicted using Pauling's ionic radii.

POLARIZABILITY OF THE D SHELL

We have executed fully self-consistent solutions of the Kohn–Sham equation⁶ with a linearized augmented-plane-wave (APW) method; the exchange–correlation effects of electrons were treated in the local density approximation. For details of the band-structure calculations we refer the readers to Ref. [7]. The lattice constants in equilibrium were thereby obtained through minimization of the total energy. In Fig. 2 those results are successfully compared with the experimental values^{5,8} together with the corresponding lattice constants predicted using Pauling's ionic radii. We observe that Ag_2Te and Cu_2Te shrink substantially in reference to Pauling's predictions, while the lattice constants of the alkali tellurides are explained fairly well by his idea. Such peculiar shrinking of Ag_2Te and Cu_2Te indicates the noble-metal ions with the d shell are remarkably polarizable as compared with the alkali ions with the sp-shell.

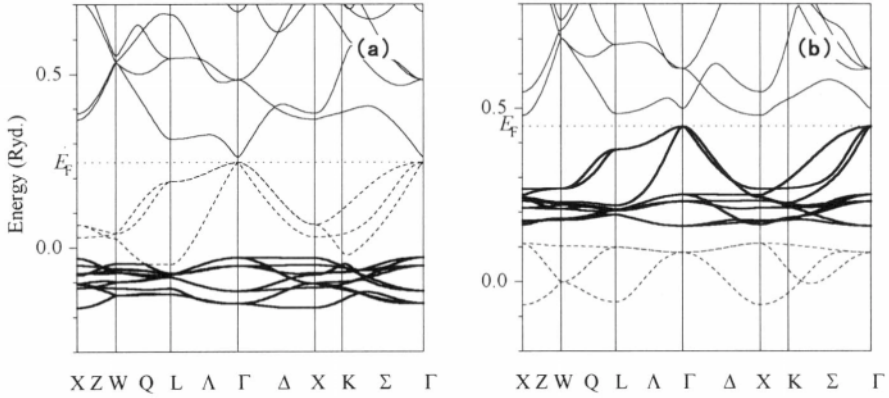


Figure 3. Electronic band structures for Ag_2Te (a) and Cu_2Te (b) with the antifluorite structure in common. The thick curves are bands originating from the d electrons in the noble-metal atoms and the dashed curves, bands from the p electrons in the Te atoms.

THE P-D HYBRIDIZATION

Figure 3 shows the band structures of Ag_2Te and Cu_2Te at the equilibrium lattice constants. We first remark that the relative positions of the d and p bands are interchanged between Ag_2Te and Cu_2Te and the d states in Ag_2Te are significantly localized as compared with those in Cu_2Te . The theoretical calculation correctly reproduces the semiconducting nature of $\alpha\text{-Ag}_2\text{Te}$ with a band gap of 0.2 eV which is in good agreement with the experimental value of around 0.1 eV.⁹ We also confirmed⁷ that the effective masses of electrons and holes near the band gap and the density of states agree well with experimental results. The band-structure calculations for the alkali tellurides show the essential features of the p bands remain unchanged irrespective of the absence of the d bands, indicating the p-d hybridization in Ag_2Te is weak.

The strength of coupling between the Ag d-band and Te p-band is then elucidated by selectively shifting the d-band downward. In Fig. 4 we see that the band characteristics weakly depend on the shift of the d-band and hence those two bands are well separated in Ag_2Te . In sharp contrast, Cu_2Te gives rise to strong p-d hybridization.

ACTIVATION ENERGY FOR IONIC DIFFUSION

To estimate the activation energy for the Ag diffusion in $\alpha\text{-Ag}_2\text{Te}$, we adopted the antifluorite structure as the ground state and a crystal structure with space group $F\bar{4}3m$ (See Fig. 1) as a transition state in the diffusion process. Combination of the diffraction experiments⁵ and the MD simulations¹⁰ justifies this estimation; Ag ions migrate among the adjacent tetrahedral sites via the octahedral sites. We replaced the activation energy by difference of the total energies per Ag ion between the ground and transition states. The activation energies for the other ions were calculated in the same way. The computational results in Table 1 show the activation energy in $\alpha\text{-Ag}_2\text{Te}$ is significantly smaller than the energies in the alkaline counterparts and even smaller than that in the cuprate. This coincides with the experimental facts.^{11,12} Although Cu ions also have d electrons and smaller steric size than Ag ions, Cu ions in Cu_2Te are less mobile than Ag ions in Ag_2Te . This can be traced back to the strong p-d hybridization taking place in Cu_2Te .

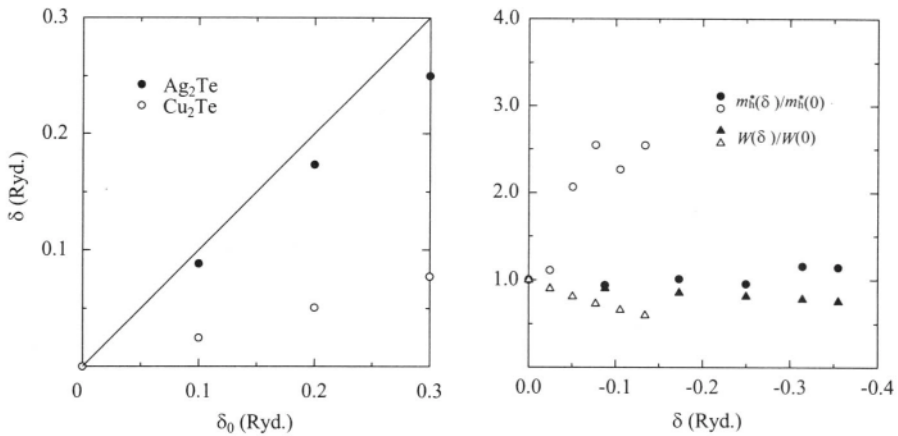


Figure 4. The left panel shows actual shift δ versus given shift δ_0 in the APW resonance condition for the d bands in Ag_2Te or for the p bands in Cu_2Te . The right panel shows the effective hole mass m_h^* (circles) and the band width W (squares) for the p bands in Ag_2Te (filled symbols) or for the d bands in Cu_2Te (open symbols) as functions of δ .

Table 1. Activation Energies in units of eV

	Ag_2Te	Cu_2Te	Li_2Te	Na_2Te	K_2Te
Theor.	0.153	0.197	0.251	0.335	0.357
Expt.	0.141, ^a 0.188 ^a	≈ 0.2 ^b	—	—	—

^aCited from Ref. [11].

^bExtracted from experimental results for a high temperature phase, No. 2, in Ref. [12].

CONCLUDING REMARKS

From the electronic analyses on the tellurides, we infer that interplay of the polarizability of the d shell and the weakness of the p-d hybridization in Ag_2Te plays a primary role in giving rise to the superionic conductivity of Ag ions. The activation energies for the ionic diffusion were estimated in good agreement with the experiments.

Acknowledgements

This work was supported through Grant-in-Aid for Scientific Research, provided by the Japanese Ministry of Education, Science and Culture. One of the authors (HI) appreciates a financial support by the Kumagai Foundation for Science Technology. The numerical calculations were executed in part using the facilities of the Supercomputer Center, Institute for Solid State Physics, University of Tokyo.

REFERENCES

- [1] S. Geller, "Solid Electrolytes," Springer-Verlag, Berlin (1977).
- [2] P. Vashishta, *Solid State Ion.* 18/19:3 (1985).
- [3] L. Pauling, "The Nature of the Chemical Bond," Cornell Univ., Ithaca (1960).
- [4] V. A. Fedorin, *Sov. Phys. Solid State* 30:76 (1988); A. Rakin and M. Kobatashi, *Phys. Rev. B* 53:3088 (1996).
- [5] T. Sakuma and S. Saitoh, *J. Phys. Soc. Jpn.* 54:3647 (1985); J. Schneider and H. Schulz, *Z. Kristallogr.* 203:1 (1993).
- [6] W. Kohn and L. J. Sham, *Phys. Rev.* 140:A1133 (1965).

- [7] H. Kikuchi, H. Iyetomi, and A. Hasegawa, *J. Phys.: Condens. Matter* 9:6131 (1997).
- [8] D. R. Lide (ed.). "CRC Handbook of Chemistry and Physics," 76th ed., CRC Press, New York (1995).
- [9] S. A. Aliev and Z. F. Agaev, *Izv. Akad. Nauk SSSR Neorg. Mater.* 19:2050 (1983).
- [10] F. Tachibana, M. Kobayashi, and H. Okazaki, *Phys. Rev. B* 40:3360 (1989).
- [11] S. Miyatani, *J. Phys. Soc. Jpn.* 50:3451 (1981).
- [12] S. Miyatani, S. Mori, and M. Yanagihara, *J. Phys. Soc. Jpn.* 47:1152 (1979).

This page intentionally left blank

POLARIZATION OF COUNTERIONS IN A STRONGLY COUPLED COULOMBIC SYSTEM: DNA

Udayan Mohanty

Eugene F. Merkert Chemistry Center
Boston College, Chestnut Hill, MA 02158

INTRODUCTION

Stellwagen¹, Elias and Eden² and Diekmann et al.³ have used transient electric birefringence and electric dichroism to analyze the characteristics of DNA fragments as a function of salt concentrations and field strengths. At low field strengths, the Kerr law is satisfied, and for short fragments the polarizability is proportional to the square of the length of DNA.¹ Elias and Eden find the polarizability to scale, instead, as the chain length cubed.² Diekmann *et al.* find that for small numbers of base-pairs, the orientation can be explained by an induced dipole moment mechanism, and in low fields, the polarizability goes as L^2 .³ To describe the orientation data for larger DNA fragments, a constant dipole moment mechanism is needed.³

Experimental data on the polarization of DNA is usually interpreted *via* a classic model due to Mandel.⁴ In this approach, a DNA is viewed as a charged cylinder with counterions bound to it. The charges come from the phosphate groups only. Electrostatic interactions between the counterions and between the counterions and the negative phosphate charges are assumed negligible. The fluctuations of the bound counterions and the phenomenon of counterion condensation have been taken into account by Oosawa⁵ and Manning,⁶ respectively. As a result of the external field, the counterions along the contour length of the DNA are not distributed in a homogeneous way.⁶ This was implemented based on the assumption that the total number of counterions that are bound to the DNA does not change with variations in the electric field. However, the response of the counterions and the DNA due to the Debye atmosphere was ignored. In both models, the dipole moment is proportional to L^3 at low fields.⁵ Fixman-Jagannathan analyzed the effects due to the ion atmosphere and the hydrodynamic interactions on the polarizability of short rods.^{7, 8} The analysis shows that the polarized counterions lead to relaxation of the Debye atmosphere.^{7, 8} By solving a steady state non-linear diffusion equation with an approximate coupling between the Debye atmosphere and the delocalized condensed counterions, Rau and Charney argued that the dipole moment attains a maximum and then decreases with increasing electric field.⁹

POLARIZATION OF DNA

For simplicity of presentation, we model the polyion as an array of N charged sites on a cylinder of total length L , which is immersed in an univalent salt solution. The solvent is described by a uniform dielectric constant ϵ . When an external electric field is applied to the polyion, the counterions vary inhomogeneously along the helical backbone of the DNA. Thus, the average counterion density r depends on the distance being measured along the length of the DNA, x . Consequently, the free-energy $F[r(x)]$ is a functional of the counterions density.^{10,11}

$$F[\rho(x)] = \text{Max}_{u(x)} \left\{ W[u] - \int_L u(x)\rho(x)dx \right\} \quad (1)$$

Here, $u(x)$ is an effective potential

$$u(x) = \beta(V(x) - \mu), \quad (2)$$

and is expressed in terms of the chemical potential μ and an external potential, $V(x)$. The grand-potential is $W[u]$. The maximum in Eq. (1) is over variations of the effective potential by holding the average density fixed.^{10, 11}

We define a quantity $\Delta A([u], [\rho])$, which is such that on minimizing it with respect to variations in the density, one obtains the grand-potential.^{10, 11}

$$W([u]) = \text{Minimum}_{\rho(x)} \Delta A([u], [\rho]) \quad (3)$$

The importance of ΔA is that one can express it in terms of the correlation functions of the polyion-counterion system in the absence of the external field.^{10,11} This leads to an explicit expression for the average density of the counterions.^{10,11}

$$\rho(x) = \rho_o(x) \exp(-U_{\text{effec}}(x)) \quad (4)$$

The effective potential is expressed in terms of the direct correlation function $c(x)$ - a quantity that is either obtained from neutron or x-ray scattering experiments or from polyelectrolyte theories of the liquid state^{10, 11, 12}

$$U_{\text{effec}}(x) = - \int dx_1 [\rho(x_1) - \rho_o(x_1)] c(|x_1 - x|) + V(x), \quad (5)$$

where $\rho_o(x_1)$ is the density of the reference system. For the case at hand, $\rho_o(x_1)$ is independent of x since we have an homogeneous counterion phase in the absence of an electric field. The external potential $V(x)$ is $zqE(x - x_o)$, where z is the valency of the counterion and x_o is a reference point.

The counterion density in low electric fields is expanded as $\rho(x) = \rho_o + m(x - x_o)$, where m is a constant. The dipole moment μ is calculated from the first moment of the counterion density.^{10, 6}

$$\mu - \mu_o = Zq \int_0^L [\rho(x) - \rho(x_o)] (x - x_o) dx \quad (6)$$

However, we can evaluate the slope m directly from the density profile given by Eqs. (4)-(5). On substituting the expression for the density in Eq. (6), one obtains the polarizability p of the polyion in terms of the direct correlation function.¹⁰

$$p = \frac{(Zq)^2 \rho_0 \beta L^3}{12 \left(1 + L \rho_0 \int_0^1 (\lambda' - \lambda_0) \left\{ \frac{dc(\lambda - \lambda')}{d\lambda} \right\}_{\lambda=\lambda_0} d\lambda' \right)} \quad (7)$$

In Eq. (7), $\lambda = x/L$ is a scaled distance. The saturated dipole agrees with Mandel-Manning theories at high fields.^{6, 10}

Let us denote by $L\gamma(L, \dots)$ the quantity in the second term of the denominator in Eq. (7). Clearly, γ is a function of salt concentration, the Manning linear charge density parameter defined as the ratio of the Bjerrum length to the distance between the phosphate charges, and the contour length of the DNA. If the quantity $Lg(L, \dots) \gg 1$, the polarizability scales as L^2 . This is in agreement with experimental data.^{10, 1-3} In this case, either both $g(L, \dots)$ and L are large or L is small with g large. On the other hand, if the quantity $Lg(L, \dots) \ll 1$, the polarizability is proportional to L^3 .¹⁰ Let us recollect at this point that the Mandel-Manning theories predict an L^3 dependence of the polarizability at low fields.^{4, 6} The commencement of saturation behavior is expected to be determined by polyelectrolyte effects through the direct correlation function.¹⁰

DISCUSSION.

The importance of our result is three-fold. First, the polarizability has been reduced to the evaluation of the direct correlation function. Second, the direct correlation function is readily obtained from integral- equation theories of liquids.¹² Third, both attractive and repulsive interactions between the counterions and the polyion have been taken into account.¹⁰

The model can be improved along two lines of thought. First, for oligomers less than thirty base pairs or so, there is a substantial reduction in the surface concentration of the counterions. This must be taken into account since the so-called electrostatic "end effect" has been verified by both grand canonical Monte Carlo simulations and by longitudinal ²³Na NMR.^{13, 14} Secondly, the polarizability of rod-like polyions from the condensed counterions increases as L^2N , while the corresponding contribution from the Debye atmosphere is proportional to the length, provided Lk is larger than ten or so.^{6, 15} Thus, the polarization of the Debye atmosphere must be accounted for in the proposed model.

REFERENCES

- (1) Stellwagen, N. "Electric Birefringence of Restriction Enzyme Fragments of DNA: Optical Factor and Electric Polarizability as a Function of Molecular Weight." *Biopolymers* 1981, 20, 399.
- (2) Elias, J. G.; Eden, D. "Transient Electric Birefringence Study of Persistence Length and Electrical Polarizability of Restriction Fragments of DNA." *Macromolecules* 1981, 14, 410.
- (3) Diekman, S.; Hillen, W.; Jung, M.; Wells, R.; Porschke, D. "Electric Properties and Structure of DNA Restriction Fragments From Measurements of The Electric Dichroism." *Biophys. Chem.* 1982, 15, 157.
- (4) (a) Van der Touw, F.; Mandel, M. "Dielectric Increment and Dielectric Dispersion of Solutions Containing Simple Charged Linear Macromolecules." *Biophys. Chem.* 1974, 2, 218.
(b) Vreugdenhil, Th.; Van der Touw, F.; Mandel, M. " Electric Permittivity and Dielectric Dispersion of Low-Molecular Weight DNA at Low Ionic Strength." *Biophys. Chem.* 1979, 10, 67.
- (5) Oosawa, F. *Polyelectrolytes*, Marcel Dekker: New York, 1971.

- (6) Manning, G. "A Condensed Counterion Theory for Polarization of Polyelectrolyte Solutions in High fields." *J. Chem. Phys.* **1993**, 99, 477.
- (7) Fixman, M.; Jagannathan, S. "Spherical Macroions in Strong Fields." *Macromolecules* **1983**, 16, 685.
- (8) Fixman, M. Jagannathan, "Electrical and Convective Polarization of The Cylindrical Macroions." *J. Chem. Phys.* **1981**, 75, 4048.
- (9) Rau, D. C.; Charney, E. "High-Field Saturation Properties of The Ion Atmosphere Polarization Surrounding a Rigid, Immobile Rod." *Macromolecules* 1983, 16, 1653.
- (10) Mohanty, U.; Zhao, Y. "Polarization of Counterions in Polyelectrolytes." *Biopolymers* **1996** 38, 377-388.
- (11) Jones, G. L.; Mohanty, U. "A Density Functional-Variational Treatment of The Hard-Sphere Transition." *Mol. Phys.* 1985, 54, 1241.
- (12) (a) Hansen, J. P.; McDonald, I. R. *Theory of Simple Liquids* , Academic Press: London, **1976**.
(b) Rowlinson, J. S.; Widom, B. *Molecular Theory of Capilarity* , Clarendon Press: Oxford, **1984**.
- (13) Olmstead, M. C.; Anderson, C. F.; Record, M. T., Jr., "Monte Carlo Description of Oligoelectrolyte Properties of DNA Oligomers: Range of The End Effect and The Approach of Molecular and Thermodynamic Properties to The Polyelectrolyte Limits." *Proc. Nat. Acad. U.S.A.* **1989**, 86, 7766.
- (14) (a) Olmsted, M. C.; Anderson, C. F.; Record, M. T. Jr. "Importance of Oligoelectrolyte End Effects for The Thermodynamic of Conformation Transitions of Nucleic Acid Oligomers: A Grand Canonical Monte Carlo Analysis." *Biopolymers* **1991**, 31, 1593.
(b) Stein, V. M.; Bond, J. P.; Capp, M. W.; Anderson, C. F.; Record, M. T. Jr. "Importance of Coulombic End Effects on Cation Accumulation Near Oligoelectrolyte B-DNA: A Demonstration Using ^{23}Na NMR." *Biophys. J.* **1995**, 68, 1063.
- (15) Bowers, J. S.; Prud'home, R. K. "Low Field Theory of Polymer Transient Electric Birefringence." *J. Chem. Phys.* **1992**, 96, 7135.

THEORY OF COLLOIDAL PLASMAS

P. P. J. M. Schram¹ and S. A. Trigger²

¹Eindhoven University of Technology
P. O. Box 513, 5600 MB Eindhoven, The Netherlands

²Institute for High Temperatures
Izhorskaya 13/19, Moscow 127412, Russia

INTRODUCTION

Charged Colloidal System (CCS) consists of

- macroions with negative charge $-ze$ (z of the order 10^2 to 10^4) and a radius R of 10 up to 300 nm and density n_m of order 10^{12} up to 10^{14} .
- one or more species of counterions, we consider here only one species with positive charge e and radius $r_0 \ll R$. Because of electroneutrality the density is given by $n_c = zn_m$.
- liquid, e.g., water, with relative dielectric constant ϵ .

Peculiarities of CCS:

- strong charge asymmetry, $z \gg 1$.
- possibility of Colloidal Crystal (CC) and crystal waves.

Parameters of Coulomb interactions:

$$\Gamma_{CC} = e^2 n_C^{1/3} / (\epsilon k_B T), \Gamma_{CM} = ze^2 n_C^{1/3} / (\epsilon k_B T), \Gamma_{MM} = z^2 e^2 n_M^{1/3} / (\epsilon k_B T) \quad (1)$$

Usually we have:

$$\Gamma_{CC} \ll 1, \Gamma_{CM} = O(1) \text{ or } \ll 1 \text{ and } \Gamma_{MM} \gg 1 \quad (2)$$

Strong macroion-macroion interaction. Of course we also have a short range (hard sphere) part of $M - M$ interaction. In the case $\Gamma_{CM} \ll 1$ we are able to develop an analytical theory, in the case $\Gamma_{CM} = O(1)$ numerical simulations are required. Even if the Γ 's are all small, the system is not one of only weak interactions because of the hard cores. We try to obtain a quasi one-component system. In general¹ the effective macroion interaction (*EMI*) involves not only pair but also many-particle interactions. This aspect is lost when the *EMI* is defined in terms of the pair distribution function:

$$g_{MM}(r) = \exp[-\beta U_{MM}^{\text{eff}}(r)] \quad (3)$$

Such *EMI* is then determined from the Ornstein–Zernike equations and Percus–Yevick or hypernetted chain approximations.² We adopt here a “microscopic” *EMI* and derive it from first principles.

A usual *EMI* is the Derjaguin–Landau–Verwey–Overbeek (DLVO) one³

$$\begin{aligned} V_{DLVO} &= -(z^*e)2/(\epsilon r)\exp(-r/R_D), \quad r > 2R \text{ with} \\ z^* &= z(1 + R/R_D)^{-1}\exp(R/R_D), \quad R_D^2 = \epsilon k_B T / (4\pi n_C e^2) \end{aligned} \quad (4)$$

This result is found from the solution of the linearized Poisson–Boltzmann equation for the electric potential around a macro-ion with charge number z surrounded by counterions with density $n_C(r)$ and a negative background of density $n_- = z^{-1}n_C(r \rightarrow \infty)$ representing the other macroions. This simple model is only qualitative and needs statistical justification and possibly correction.

THE EFFECTIVE MACROION INTERACTION AND THE MINIMAL CHARGE FOR CRYSTALLIZATION

Partition function of classical CCS:

$$Z = V^{-N} C^{-N} M \int d^3 r_1 \dots d^3 r_{N_C} \int d^3 R_1 \dots d^3 R_{N_M} \exp[-\beta(U_{CC} + U_{CM} + U_{MM})] \quad (5)$$

or

$$Z = V^{-N} M \int d^3 R_1 \dots d^3 R_{N_M} \exp[-\beta U_{MM}] Z_C \quad (6)$$

with

$$Z_C = V^{-N} C \int d^3 r_1 \dots d^3 r_{N_C} \exp[-\beta(U_{CC} + U_{CM})] = \exp[-\beta F_C(\{R\})] \quad (7)$$

The potential energies are:

$$U_{CC} = \sum_{i < j} V_{CC}(r_i - r_j), \quad U_{CM} = \sum_{ij} V_{CM}(r_i - R_j), \quad U_{MM} = \sum_{i < j} V_{MM}(R_i - R_j) \quad (8)$$

with

$$\begin{aligned} V_{CC} &= e^2/(\epsilon r); \\ V_{CM} &= \begin{cases} -ze^2/(\epsilon r), & r > R; \\ \infty, & r < R \end{cases} \\ V_{MM} &= \begin{cases} (ze)^2/(\epsilon r), & r > 2R \\ \infty, & r < 2R \end{cases} \end{aligned} \quad (9)$$

The free energy F_C of (7) is due to indirect interaction.

By means of an expansion in multiplicities of Mayer factors it is possible to find $F_C(R)$. For a system of only two macroions an exact result follows. Numerical calculations have been performed by D’Amico and Loewen⁴ and Allahyarov et al.⁵ by MC and MD resp. The results of [5] for the derivative

$$\partial U_{MM}^{\text{eff}}/\partial R = -(ze)^2/R^2 + \partial U_{MM}^{\text{ind}}/\partial R \quad (10)$$

are presented in Figure 1. The *EMI* is to be distinguished from the energy $E_C(\{R\})$ of counterions in the field of macroions. It is given by

$$E_C(\{R\}) = \partial/\partial\beta(\beta F_C) = \partial/\partial\beta[\beta(C + U_{MM}^{\text{ind}})] \quad (11)$$

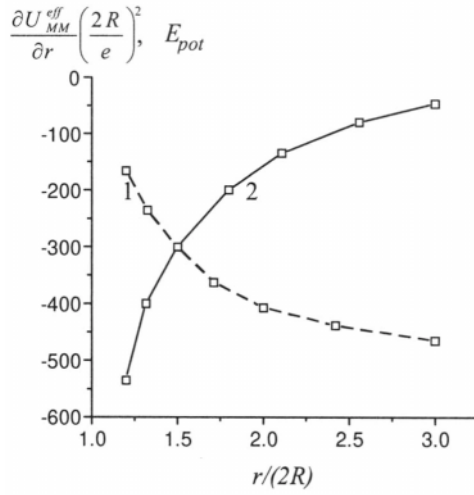


Figure 1. Molecular dynamic simulation for the full energy of a pair $E_{pot} = [(ze)^2/r + E_C(r)]2R/e^2$ -curve 1 and for the derivative of the effective potential, Eq. (10)-curve 2, as a function of the distance $r/(2R)$; $n_M = 3.310^{12} \text{ cm}^{-3}$, macroion radius $R = 5.5410^{-6} \text{ cm}$, $Z = 280$, $T = 293 \text{ K}$.

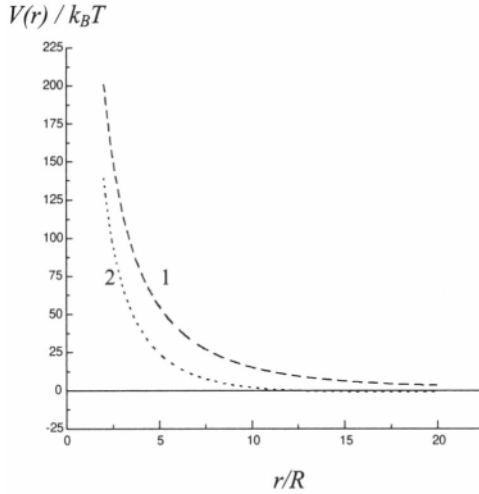


Figure 2. The EMI versus distance r/R , $z = 200$, density, radius and temperature are the same as in Figure 1. The curve 1. is based on [7], the curve 2 on numerical calculation without expansion in V_{CM} .

This is also shown in Figure 1 for the case of 2 macroions. It is necessary to underline that in [4,5] only electrical forces have been included. From our point of view in numerical simulations of pair (and many macroions) interaction the bombarding forces, connected with direct transfer of momentum from counterions to macroions, can play an essential role. Namely these forces can provide the effective attraction of macroions, predicted analytically in [6–8] for small distances and considerable C-M interaction. In the case of many macroions the pair EMI is found by expansion of in degrees of multiplicity of Mayer factors. For low density of counterions this leads to familiar Debye-like results.⁶

If $\Gamma_{CM} \ll 1$ the potential V_{MM}^{eff} has been calculated in [7]. In Figure 2 we see for $z = 200$ curve 1 representing the result of [7] and curve 2 for numerical result without expansion w.r.t. V_{CM} . Figure 3 is similar for $z = 280$. We see the appearance of attraction. The presence of

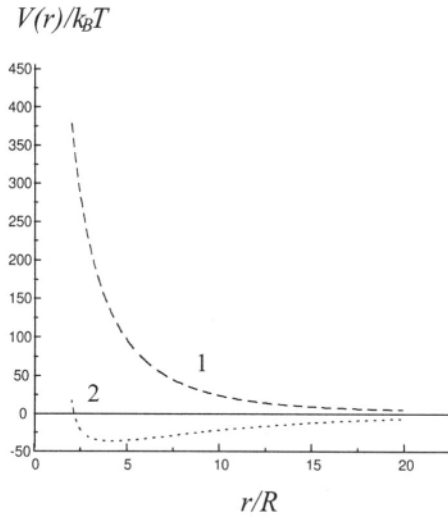


Figure 3. The same as Figure 2, but with charge number $z = 280$.

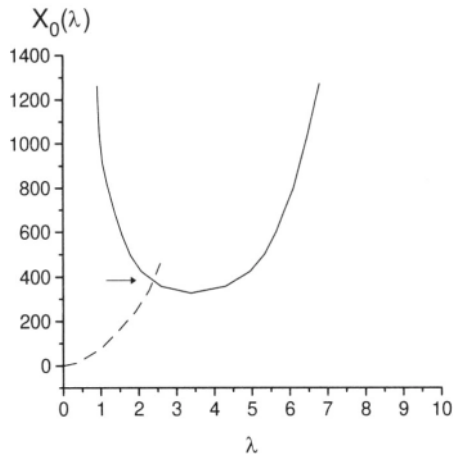


Figure 4. The melting curve $z(\lambda)$. The arrow shows the calculated charge number for the experiment.¹⁰

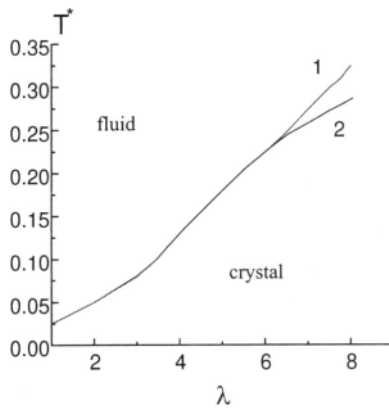


Figure 5. The co-existence curve in the coordinates T^* and λ : 1-numerical calculations,¹¹ 2-Eq. (16).

attraction in the many-, macroion pair EMI has not yet been solved conclusively.

Under some conditions CCS crystallizes to bcc or fcc lattice. Following⁸ we consider here the conditions for melting of a bcc lattice. Lindeman Criterion:

$$(\langle \delta R_i^2 \rangle)^{1/2} / a_0 = \gamma_L, \quad a_0 = n_M^{-1/3} \quad (12)$$

where $\langle \delta R_i^2 \rangle$ is the mean square deviation of the macroion position from the equilibrium position and γ_L is the Lindeman constant, which we take to be equal to 0.19. We use the Einstein model for the frequencies of the macroions with the correction factor $\mu(\lambda)$ from [9] to take account of the more realistic Debye-type model of frequencies in a crystal. Then we have:

$$\begin{aligned} z &= X(\lambda, \phi_0), \\ X(\lambda, \phi_0) &= X_0(\lambda) / \varphi^2(\lambda, \phi_0), \quad X_0(\lambda) = 18\varphi\gamma_L^{-2} f(\lambda)\mu(\lambda), \\ f(\lambda) &= U_0 / (\lambda^4 U_t), \quad U_t = U_0 a_0 / 2 \sum_j R_{ij}^{-1} \exp(-R_{ij}/R_D), \\ U_0 &= (z_{\text{eff}} e)^2 / (\epsilon a_0). \end{aligned} \quad (13)$$

The function $X(\lambda, \phi_0)$ has a deep minimum for each ϕ_0 as a function of λ . This implies the existence of a minimal charge for crystallization. For small volume fractions, $\phi_0 < 0.005$, corresponding to experiments¹⁰ we find the melting curve of Figure 4 and

$$z_{\min} = [X_0(\lambda)]_{\min} = 307. \quad (14)$$

In order to find the bare charge we rewrite (16) as

$$X_0(\lambda) = 47.1 \epsilon T_M n_M^{-1/3} \lambda^2 \quad (15)$$

For the fixed experimental values of [10], $T_M = 293K$ and $n_M = 4.1 \cdot 10^{12} \text{cm}^{-3}$ we find $z = 371$. The experimental value is $z = 360$. It is also seen that for a given $z \leq z_{\min}$ the crystal exists only in a restricted region of λ (or temperature). We present our melting curve in Figure 5 as a plot in terms of the dimensionless variables λ and T^* defined as [11] the thermal energy normalized by the potential energy of two macroions at the average particle distance $n_M^{-1/3}$. It takes the form

$$T^* = 4\pi \exp(\lambda) / (\lambda^2 X_0(\lambda)). \quad (16)$$

The difference between curve 1 of the numerical calculations of [11] and curve 2 of our analytical result is due to the difference in the eigenfrequencies for bcc and fcc.

CONCLUSIONS

A general determination of the effective microscopic macroion–macroion interaction (EMI) has been performed. The Lindeman melting criterion leads to a minimal charge as a necessary condition for crystallization.

REFERENCES

- [1] H. Loewen, *Phys. Reports* **237** (1994) 249.
- [2] D. A. McQuarrie, *Statistical Mechanics* (Harper and Row, New York, 1973); J. K. Percus and G. J. Yevick, *Phys. Rev.* 110(1958)1; L. Belloni, *J. Chem. Phys.* **85** (1986) 519, 88(1988) 5143; O. Gerasimov, P. P. J. M. Schram, A. Sitenko and A. Zagorodny, *Physica* **B228** (1996) 40.

- [3] E. J. W. Verwey and J. Th. G. Overbeek, *Theory of the Stability of Lyophobic Colloids* (Elsevier, Amsterdam, 1948).
- [4] I. D'Amico and H. Loewen, *Physica A*, **237** (1997) 25.
- [5] E. A. Allahyarov et al., to be published.
- [6] S. A. Trigger, L. I. Podloubny and P. P. J. M. Schram, *XIIth ESCAMPIG Abstracts* **18E** (1994) 87.
- [7] E. A. Allahyarov, L. I. Podloubny, P. P. J. M. Schram and S. A. Trigger, *Physica A* **220** (1995) 349.
- [8] P. P. J. M. Schram and S. A. Trigger, *Physica* **B228** (1996) 170.
- [9] M. O. Robbins, K. Kremer and G. S. Grest, *J. Chem. Phys.* **88** (1988) 3286.
- [10] M. Hoppenbrouwers and W. van de Water, *Physica* **B228** (1996) 153.
- [11] E. J. Meijer and D. Frenkel, *J. Chem. Phys.* **94** (1991) 2269.

CRITIQUE OF ELECTROLYTE THEORIES USING THERMODYNAMIC BOUNDS

Michael E. Fisher¹, Daniel M. Zuckerman¹ and Benjamin P. Lee²

¹Institute for Physical Science and Technology,
University of Maryland, College Park, Maryland 20742, U.S.A.

²Polymers Division, National Institute of Standards and Technology
Gaithersburg, Maryland 20899, U.S.A.

INTRODUCTION

Recent experiments concerning the nature of criticality in electrolyte solutions (see, e.g., the reviews [1]) have been puzzling. Consequently, the gas-liquid transition in simple, classical ionic models (which may, here, be identified with the “plasma transition” [2]) has been of current interest [1, 3-7]. The central model — the restricted primitive model (RPM) — consists of $N_+ = N_- = \frac{1}{2}N$ equisized hard spheres of diameter a carrying charges $\pm q$ in a medium of dielectric constant D (to approximate the solvent in real electrolytes). This precise model was, of course, first treated successfully by Debye and Huckel (DH) in 1923 [8]; much later, the mean spherical approximation (MSA) [9] became fashionable for treating the RPM [5,6]. In particular, Ebeling and Grigo [10], following Bjerrum’s ion-pairing proposal (Bj) [11], combined the MSA with a “chemical association picture.” More recently, Stell and coworkers [7] have proposed a rather different set of “pairing mean spherical approximations”: PMSA1, -2, and -3.

On the other hand, Levin and Fisher [3,4] used the *full* (i.e., including the explicit hard core, $a > 0$) DH theory as a basis for introducing ion pairing; however, they supplemented the original Bj approach by (i) including the *dipole-ion salvation free energy* (DI), (ii) using an improved association constant, $K^{Eb}(T)$, due to Ebeling (see [3,4,10]), and (iii) allowing for hard-core excluded volume effects. These DHBjDI theories [1,3,4] have proved significantly more successful in predicting the RPM critical temperature

$$T_c^* \equiv k_B T_c D a / q^2 \simeq 0.05 \quad (1)$$

(see [1]) than theories based on the MSA [4-7,10] despite the encomiums that approximation has received (see, e.g., [12]). Thus the MSA-based theories yield $T_c^* \gtrsim 0.073$ while those based on the DH approach (where the original theory gave $T_c^* = \frac{1}{16}$ [3,4]) yield $T_c^* \lesssim 0.056$. They have also proved effective

in deriving charge *and* density correlation functions [13]. (Incidentally, it should be emphasized that the HNC approximation, also much beloved, *fails entirely* throughout the putative two-phase and expected critical region: see, e.g., [14]).

In these circumstances, it is natural to seek criteria less heuristic than the more-or-less subjective appeal of the various physical and statistical mechanical approximations introduced in the different approaches. Specifically, it would be helpful to distinguish on some uniform grounds between the DH- and MSA-based theories, none of which can, for example, currently claim a variational basis (as may the standard mean-field theories for magnetic transitions in lattice models).

To this end we have [15] called upon (i) Totsuji's lower bound [16] on the internal energy, U_N , which states

$$U^{config} \equiv U_N/N - \frac{3}{2}k_B T \geq -0.960 (q^2/Da), \quad (2)$$

(which improves on Onsager's bound where 0.960 is replaced by unity); (ii) Gillan's upper bound [17] on the Helmholtz free energy, $F_N(V, T)$, which specifically embodies a reduction of the free energy at low temperatures arising from (+, -)-ion pairing; and (iii) the standard thermal stability requirements (see, e.g., [18]) which enforce the positivity of the configurational, constant-volume specific heat, $C_V^{config}(\rho, T)$, where $\rho = N/V$.

COMPARATIVE RESULTS

We may summarize the results found in our study [15] under the following headings:

Energy Bound Violations

The original ("pure") DH and MSA expressions for $U^{config}(\rho, T)/(q^2/Da)$ entail only the variable

$$x = \kappa_D a \quad \text{with} \quad \kappa_D^2 = 4\pi q^2 \rho / D k_B T. \quad (3)$$

Despite contrary claims [12], the original DH theory and versions allowing for excluded volume effects [3,4,15] never violate Totsuji's bound (although, not surprisingly, the *truncated DH limiting law* is in violation for $x \gtrsim 2$). Conversely, again contrary to claims [12], the MSA internal energy violates Totsuji's bound for $x \gtrsim 1200$ (and lies below the bcc crystal value for $x \gtrsim 125$). Even when ion-pairing is included, most of the MSA-based theories still violate Totsuji's bound for $T^* \lesssim 0.015$.

Free Energy Violation of DH and MSA Theories

Both the original DH approximation and the MSA violate Gillan's bound in a region of the (T, ρ) plane of shape roughly mirroring the predicted coexistence curves but lying higher than (with $T_{\max}^* \simeq 0.095$) and enclosing the predicted critical points [15]. The gaseous sides of the coexistence curves are also encompassed while the densities of violation reach to $\rho^* \simeq 0.02$ and 0.09 in the MSA and DH critical regions, respectively. The results are insensitive to the presence and nature of excluded-volume contributions.

Inclusion of Ion-pairing and Free-ion Depletion avoids Violation

The violation of Gillan's free energy bound is totally avoided if, starting with DH theory *or* the MSA, one allows (a) for *ion-pairing* with the density of pairs, ρ_2 , determined via an association constant with sensible behavior as $T \rightarrow 0$ [3, 4, 10, 11] and, correspondingly, (b) one recognizes *depletion* of the residual density,

ρ_1 , of free ions determined via $\rho_1 = \rho - 2\rho_2$ (since each neutral dipolar pair binds two ions). In particular, in expressions for the inverse screening length, κ , [see (3)], the total density, ρ , must be replaced by ρ_1 . The inclusion of dipolar-ionic-fluid solvation (DI) terms in both theories [4] does not change these results (although it serves to remove the unphysical, “banana” coexistence curve of the original pure DHBj theory [3,4]).

Omission of Free-ion Depletion leads to Violations

The PMSA theories advanced more recently by Zhou, Yeh, and Stell [7] explicitly do *not* allow for depletion (retaining ρ in expressions for κ rather than substituting ρ_1). This yields analytically simpler formulations but leads to *violations* of Gillan’s bound on the low-density side of the coexistence curves for $T \leq T_{\max}^* \simeq 0.072 - 0.078$ in all variants of the theory [15]. It is difficult, therefore, to regard the PMSA theories as competitive with the previous DH and MSA pairing theories.

Pairing Theories and Negative Specific Heats

The original DH and MSA theories (with or without excluded volume terms) respect thermal stability requirements so that C_V^{config} is always positive. It transpires, however, that *all* the theories with ion pairing lead to violations of thermal stability by predicting *negative* C_V^{config} in regions of the (ρ, T) plane [15]. At those densities of principal interest for the gas-liquid transition, say $\rho^* \equiv \rho\alpha^3 \lesssim 0.2$ (noting that ρ_c^* lies in the range 0.03-0.08 [1]), these violations arise only above $T_{onset}^* \gtrsim 2T_c^* \simeq 0.1$ (or higher in the PMSA theories) and they disappear at higher temperatures (roughly when $T \gtrsim 2T_{onset}$ [15]). Nevertheless, the behavior is disturbing!

The defect turns out to be a direct consequence of the artificiality of the Bjerrum and Ebeling forms for the association constant, $K(T)$, at temperatures exceeding $T^* \simeq 0.1$ (as already noticed in 1934, in a critique of the Bj theory [19]). Indeed, for many of the theories this also leads to violations of the energy bounds when $T^* \gtrsim 0.5$ [15]. The problem can be repaired in an *ad hoc* way that does not impair accuracy for $T^* \lesssim 0.15$, by replacing the T -dependent cutoff, $R^{Bj}(T)$, in Bjerrum’s definition of $K(T)$, by a fixed cutoff: $R \simeq 3.4a$ proves optimal [15]. However, this and similar remedies lead to serious inaccuracies in the representation of the RPM free energy at higher temperatures. To do better requires a more careful study of the general implications of the “chemical picture” and improved strategies for its implementation [20].

ACKNOWLEDGEMENTS

Interactions with Joel L. Lebowitz and Lesser Blum and support from the National Science Foundation (through Grants CHE 93-11729 and CHE 96-14495) are gratefully acknowledged.

REFERENCES

1. M.E. Fisher, (a) *J. Stat. Phys.* **75**, 1 (1994); (b) *J. Phys. Cond. Matt.* **8**, 9103 (1996).
2. G.É. Norman and A.N. Starostin, *Teplofiz. Vys. Temp.* **6**, 410 (1968); **8**, 40 (1970).
3. M.E. Fisher and Y. Levin, *Phys. Rev. Lett.* **71**, 3826 (1993).

4. Y. Levin and M.E. Fisher, *Physica A*, **225**, 164 (1966). See [15] for errata.
5. R.J.F. Leote de Carvalho and R. Evans, *Molec. Phys.* **83**, 619 (1994).
6. B. Guillot and Y. Guissani, *Molec. Phys.* **87**, 37 (1996).
7. (a) Y. Zhou, S. Yeh, and G. Stell, *J. Chem. Phys.* **102**, 5785 (1995);
(b) S. Yeh, Y. Zhou, and G. Stell, *J. Phys. Chem.* **100**, 1415 (1996).
8. P.W. Debye and E. Hückel, *Phys. Z.* **24**, 185 (1923). For a modern account, see D.A. McQuarrie, *Statistical Mechanics* (Harper Collins, New York, 1976), Chap. 15.
9. E. Waisman and J.L. Lebowitz, (a) *J. Chem. Phys.* **52**, 4307 (1970); *ibid* **56**, 3086 (1972); and (c) *ibid* **56**, 3093 (1972).
10. W. Ebeling and M. Grigo, *Ann. Phys. (Leipzig)* **37**, 21 (1980).
11. N. Bjerrum, *Kgl. Dan. Vidensk. Selsk. Mat.-fys. Medd.* **7**, 1 (1926),
12. L. Blum and O. Bernard, *J. Stat. Phys.* **79**, 569 (1995); L. Blum, M.F. Holvoko, and LA. Protsykevych, *J. Stat. Phys.*, **84**, 191 (1996); and J.-P. Simonin and L. Blum, *J. Chem. Soc. Faraday Trans.* **92**, 1533 (1996).
13. B.P. Lee and M.E. Fisher, *Phys. Rev. Lett.* **76**, 2906 (1996); *Europhys. Lett.* **39**(3)(1997); and to be published. See also: M.E. Fisher, B.P. Lee and S. Bekiranov in these *Proceedings*.
14. L. Belloni, *J. Chem. Phys.* **98**, 8080 (1993).
15. D.M. Zuckerman, M.E. Fisher and B.P. Lee [submitted for publication].
16. H. Totsuji, *Phys. Rev. A* **24**, 1077 (1981).
17. M.J. Gillan, *Molec. Phys.* **41**, 75 (1980)
18. H.B. Callen, *Thermodynamics and an Introduction to Thermostatistics*, 2nd Edn. (Wiley and Sons, New York, 1985) Chap. 8.
19. O. Halpern, *J. Chem. Phys.* **2**, 85 (1934).
20. M.E. Fisher and D.M. Zuckerman [to be published].

INSTABILITY OF FRONT EDGE OF NON-NEWTONIAN SUSPENSION FILM

S. M. Baturin, G. A. Pavlov, A. A. Shiryaev

Institute of Chemical Physics
 Russian Academy of Sciences
 Chernogolovka, Moscow Region, 142432, Russia.
 E-mail: pavlov@icp.ac.ru;
 fax: (096)515-3588.

The investigation of front edge instability during spreading of some suspension over arbitrary surface is interesting both as in view of suspension mechanics science and in practice, because the instability of front edge is a reason of formation of some inhomogenities during forming of any covering. There are the investigations in which the analysis of stability of film surface are made for the case of Newtonian fluid spreading. But in reality the most part of covering is forming by non-Newtonian fluids so that charged suspensions, multicomponent polymer suspensions, polymer solutions, various lacquers and so on. In this work the problem of non-Newtonian fluid edge stability is studied. The fluid is spreading down inclined plane and over rotating disk.

The quasistationary equation for front edge non-Newtonian liquid film which spread down wet inclined surface in lubrication approximation is written as (Baturin, Pavlov, 1996)

$$(1-b^{2+1/n})(y-1)^{-1} - 1 + (1+d^3y/dx^3)^{1/n} y^{2+1/n} = 0 \quad (1)$$

where y is a non-dimensional thickness of film, x - a non-dimensional variable, coincided with the direction of motion, b is a constant characterized the thickness of precursor film. The equation (1) is obtained for rheology law: $\tau=K(\partial v/\partial z)|\partial v/\partial z|^{n-1}$, where τ is shear stress (for Newtonian fluid $n=1$), v is fluid velocity, $z \perp x$. A boundary conditions are:

$$y = 1, x \rightarrow -\infty; y=b, x \rightarrow \infty \quad (2)$$

So that the equation (1) do not keep a variable x immediately the third boundary condition do not necessary and solution of equation (1) is a function of b. Equation (1) may be written in the form:

$$d^3y/dx^3 = F(y) \tag{3}$$

where F(y) is obvious from (1); (3) is third-order nonlinear differential equation. Solution of (3) was reduced to Cauchy problem, instead of boundary problem (1) – (2). With the purpose the probe function

$$y \Rightarrow 1 + a \cdot \exp(qx) \cos(q^{1/2}x)$$

was used, the probe function constants were adapted to give the right boundary condition in (2). The fourth-order Runge-Kutta method for solving (3) was used. So, the problem (1) – (2) was investigated for various values of $n > 1, b > 0$.

As follows from analysis the profile y(x) is characterized by a “hump” in the transition region to precursor film. The hump intensity is determined by precursor film thickness and rheology properties of fluids.

The other aim of the work was the study of instabilities of film surface near the front edge. Used film thickness continuity equation, after substitution profile thickness in the form $y=y_0 + y_1$ (where y_0 is quasistationary front edge form), linearization and some transformations, we have (Baturin, Pavlov, 1996) :

$$\partial y_1 / \partial t = -(\partial / \partial \xi)(\partial / \partial \xi)(y_{1\xi\xi} + y_{1ss})y_0^{n+2}/n + (1+1/n)y_1 + (1-\beta)y_1\beta \tag{4}$$

Equation (4) was obtained for the case, when $b \Rightarrow 0$, must be solved with taking into account the front edge disturbance in the form $\xi_B = A(s)B(t)$, $A(s) = \cos(qs)$ ($-\pi/2 < qs < \pi/2$ is so called “finger” which is growing at $\partial B / \partial t > 0$). Here ξ is dimensionless longitudinal variable, s-dimensionless transverse variable, q - dimensionless wave vector. So y_1 can be defined as:

$$y_1(\xi, s, t) = A(s)G(\xi)\exp(\theta t) \tag{5}$$

The boundary conditions for y_1 are: $y_1, y_1' \Rightarrow 0$ at $\xi \Rightarrow -\infty, \infty$. It is investigated in longwavelength limit the stability of front edge. Substitution (5) in (4) gives only even q power, therefore the following functions G, θ decomposition are used:

$$G = g_0(\xi) + q^2 g_1(\xi) + \dots, \theta = \theta_0 + q^2 \theta_1 + q^4 \theta_2 + \dots$$

After substitution this expression in (5), (4) in zero order q we find:

$$\theta_0 g_0 = - (d/d\xi) (y_0^{n+2} d^3 g_0 / d\xi^3 + k n g_0) / n; k = 2 + 1/n - \beta$$

In the Newtonian fluid case ($\beta=1, n=1$) when $g_0 \sim dy_0/d\xi$ and to take into account (1) (when $b \rightarrow 0$) $\theta_0 = 0$. In the non-Newtonian case ($kn \neq n+1$) θ_0 can be > 0 . So, in the latter case the function $\theta(q) > 0$ at $q \Rightarrow 0$.

Front edge of non-Newtonian suspension film linear instability analysis was carried out for disturbance in (5) form by the following equation:

$$\theta G = -(d/d\xi) \{ [(d/d\xi)(G_{\xi\xi} - q^2 G)] y_0^{n+2}/n + (2+1/n - \beta)G \} \beta$$

The preliminary numerical investigation spectrum of this equation was shown in the typical case that function $\theta(q)$ has maximum, which corresponds the most increased disturbances and $\theta(q)$ profile depends on parameters $\{n, \beta\}$. The most increased disturbances determine the form of film front edge in the early stage instability development.

For experimental checking of our results it is necessary to take into account the nature of film fluid; non-Newtonian liquid can be described by several rheology laws (Bird et al, 1987) and film front edge governing equations may be others than (1), (4).

REFERENCES

1. Baturin S. M., Pavlov G. A., 1996, Pizma v Jurnal Tech. Fiziki, 22, N 10:80.
2. Bird R. B., Curtiss C. F., Armstrong R.C., Hassager O., 1987, "Dynamics of Polymeric Liquids" V. 1,2, John Wiley&Sons, New York.

This page intentionally left blank

ANOMALOUSLY LOW TEMPERATURE IN ELECTRON COOLED HEAVY ION BEAMS

B. Franzke, K. Beckert, F. Nolden, M. Steck, and T. Winkler

GSI — Gesellschaft für Schwerionenforschung
Planckstr. 1, D-64291 Darmstadt, Germany

INTRODUCTION

Crystalline-like order in ion clouds can be generated in ion traps by means of strong laser cooling as has been demonstrated in the last decade.¹ Similar phenomena are expected also in cooled highly-charged ion beams in storage rings.² A first experimental indication of ordering effects in electron cooled proton beams was reported already in 1980.^{3,4}

The Experimental Storage Ring ESR⁵ in combination with the heavy ion linac UNILAC and the 18 Tm-synchrotron SIS is well suited for experimental studies of electron cooled heavy ion beams over a wide range of ion species and specific kinetic energies. After injection to the ESR at a few hundred MeV/u the beams are cooled by means of merging them with a velocity matched, cold electron beam covering approximately 2 % of the ring circumference. After a few seconds an equilibrium state in the ion beam is obtained, which depends on the mass-to-charge ratio of the ion A/Z (or A/q for partially stripped ions), on the number of stored ions N , and on the electron density in the cooler device. Experimental results of systematic investigations of these dependencies are presented together with a brief interpretation.

COOLING AND DIAGNOSIS OF ION BEAMS

Main characteristics of the ESR, a ring of 108.3 m circumference and of maximum bending power $B \times \rho$ of 10 Tm, are large transverse and momentum acceptances, which are used for injection and cooling of "hot" secondary beams (nuclear fragments) and many different beam manipulations. A flexible lattice design in connection with numerous independently controlled power supplies for focusing and orbit correction magnets makes the ring a versatile instrument for many different applications.

The effectively 2 m long electron cooling device^{6,7} is capable to cool ion beams at specific energies between 10 and 450 MeV/u. At the low average vacuum pressure of $\leq 1 \times 10^{-10}$ mbar the beam life is determined by radiative recombination of ions with cooler electrons rather than by collisions with residual gas atoms. But, even for highest ionic charge states q , beam life times of many hours are attained by applying moderate electron beam currents.

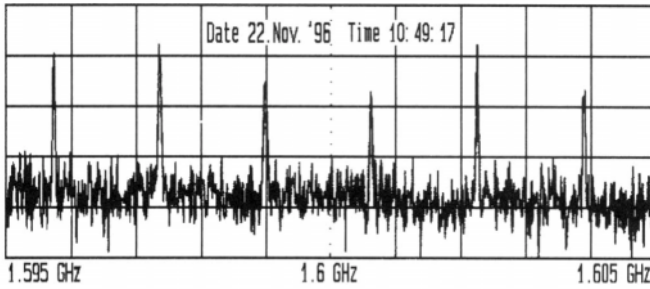


Figure 1. Frequency analyzer spectrum of an electron cooled U^{92+} -beam circulating at 350 MeV/u in the ESR. The Schottky signals were taken from the stochastic cooling pickups installed in the gap of an ESR-dipole. In the case of an uncooled beam, the Schottky bands would be much wider and hardly be visible, nevertheless, useful for generating correction signals for the kicker electrodes of the stochastic cooling system.

Various — mostly non-destructive — techniques of beam observation are applied at the ESR: a DC beam current transformer for beam currents $\geq 1 \mu A$, position and phase monitors for bunched beams, a residual gas ion beam profile monitor, and position sensitive particle detectors for measurements of rates and transverse distributions of ions after radiative recombination (RR) or dielectronic recombination (DR) with cooler electrons. Mechanical beam scrapers around the ring are used to measure beam radii and positions with an accuracy of about 0.1 mm.

Measurement and frequency analysis of beam (Schottky) noise turned out to be the most powerful tool for the diagnosis of cooled, highly-charged ion beams. The beam noise signal picked up by electrode plates near the beam (pickups) comprises all harmonics of the mean revolution frequency f_0 of beam particles up to 120 MHz. The amplified noise is analyzed either directly by means of a frequency analyzer (see Fig. 1) or — after demodulation to the baseband of 100 kHz or 200 kHz — by applying fast Fourier transformation to digitised signals.⁸

The relative width of the Schottky band at an arbitrary harmonic is a measure for the relative spread in longitudinal momenta $\delta p/p$ of beam particles given by the relation $\delta f/f = \eta \cdot \delta p/p$. The frequency dispersion factor $\eta = \gamma^{-2} - \gamma_l^{-2}$ introduces both the influence of the kinetic energy of ions by the Lorentz-factor $\gamma = [1 - \beta^2]^{-1/2}$ (β being the ion velocity in units of the light velocity in vacuum) and that of the special focusing properties of the ring lattice by the transition energy $\gamma_l = \alpha_p^{-1/2}$ (α_p being the momentum compaction factor of the ring).

The sensitivity of the Schottky diagnosis is extremely high especially in the case of highly-charged ions. As the integral Schottky power at a given harmonic of the revolution frequency f_0 increases $\propto Nq^2$, it is applicable — after calibration with current transformer signal at high N — to determine N down to lowest values as seen in figure 2. Even single ions can be detected easily.

RESULTS OF COOLING EXPERIMENTS

The main objective of the experiments reported here was to investigate the dependency of equilibrium ion beam temperatures, i.e., of longitudinal momentum spread and transverse emittances, on N down to lowest N . In order to exclude influences of collective beam oscillations on Schottky spectra, the beam intensity was measured as a function of time, using both the beam transformer at higher N and the Schottky power from highest to lowest N .

In the equilibrium state the ion beam temperatures, represented by longitudinal mo-

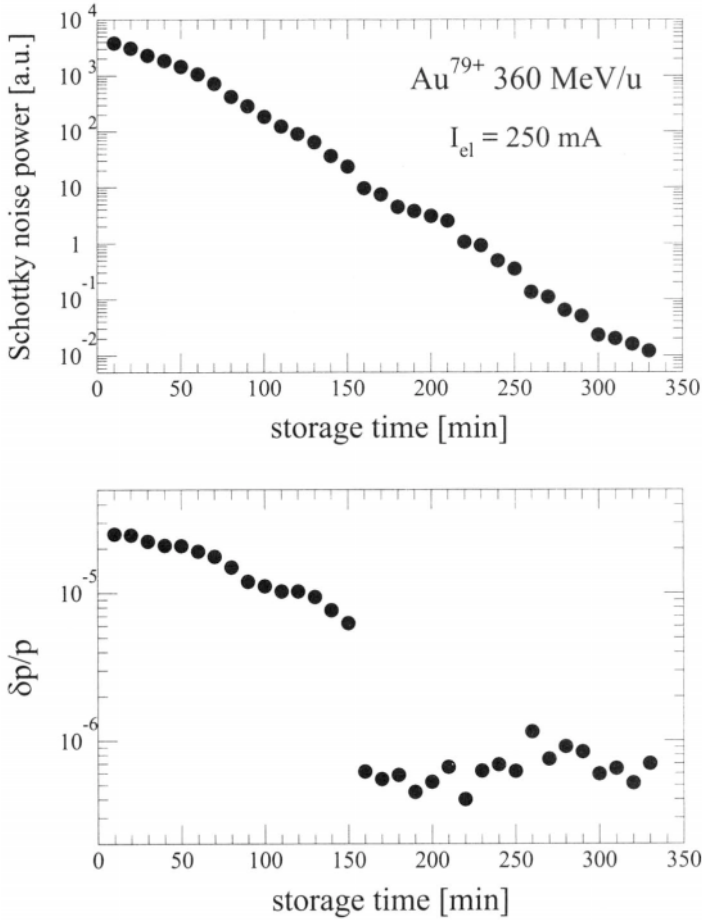


Figure 2. Schottky noise power and momentum spread (FWHM) during decrease of beam intensity due to recombination losses.

momentum spread and transverse emittances, are determined by the balance between electron cooling and heating by intra-beam scattering (IBS). For larger numbers of stored ions, e.g., $N \geq 1 \times 10^4$ the dependence of the ion beam temperatures on N is quite universal for all ion beams. The momentum spread shows a $N^{0.3}$ -dependence, whereas the emittances increase $\propto N^{0.5}$, typically.⁹ In the IBS dominated regime ($N \geq 10^4$) the relative momentum spread in beams of highly-charged ions is in the order of $\delta p/p \simeq 10^{-5} - 10^{-4}$. On the other hand, for some critical N between 10^4 and 10^3 the momentum spread drops below 10^{-6} . If we extrapolate from the IBS dominated regime the observed extremely low momentum spreads would be expected at N as low as 10.

For example, Au^{79+} ions at 360 MeV/u ($\gamma = 1.386$) were injected cooled with an electron current of 0.25 A. corresponding Starting with approximately $N = 10^6$ ions the Schottky noise at the 35th harmonic of the revolution frequency was averaged every 10 minutes over a 30 s time interval. The noise power integral at this harmonic and the derived momentum spread are shown in Fig. 2. The decrease of the Schottky noise power with a time constant $\tau = 1430$ s over the whole intensity range agrees well with that for the beam transformer measurements. The noise power at the end of the measurement ($t = 330$ min) corresponds to 3 ± 1 particles.

First $\delta p/p$ decreases $\propto N^{0.3}$ as expected for the IBS dominated regime. At N of about

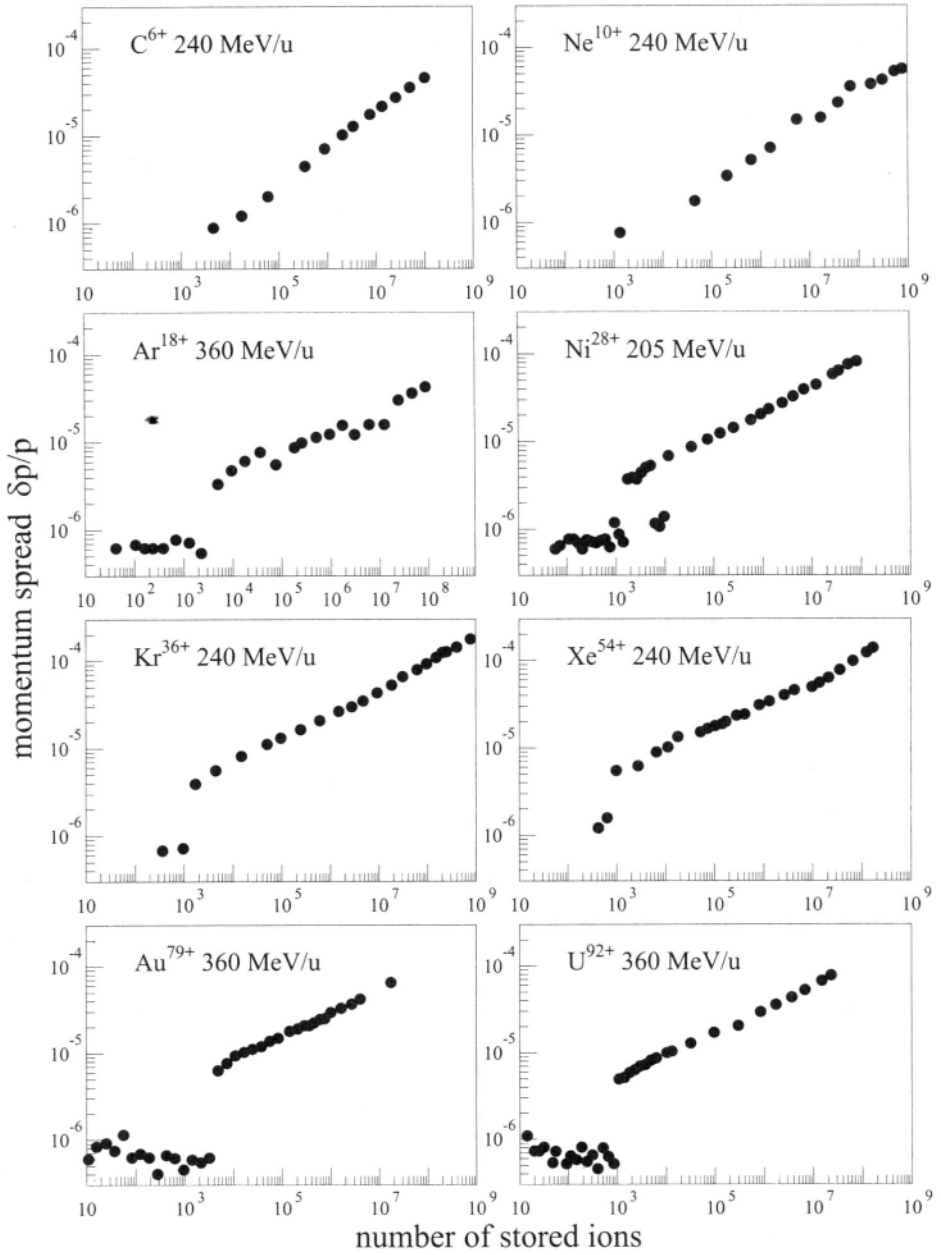


Figure 3. Momentum spread versus number of stored particles for various species of bare ions. All ions were cooled with an electron current of 0.25 A.

4000 a strong discontinuity is observed, where $\delta p/p$ is reduced by a factor of about ten and stays at a constant level of $\delta p/p \simeq 5 \times 10^{-7}$. This minimum value is obviously caused by the variations of the magnet excitation current. Experiments with short averaging times showed that the true momentum spread is considerably smaller, typically $\delta p/p \simeq 2 \times 10^{-7}$. Therefore the spectra measured with record times in the order of minutes give only an upper limit.¹⁰

Similar investigations with several other fully stripped ion species are summarized in Fig. 3. Only for ions with $Z \leq 40$ the described “jump” in $\delta p/p$ is not visible. A systematic dependence on the ion species is not seen, however the reduction factor for $\delta p/p$ is evidently larger for heavier ions. This may be explained by stronger intrabeam scattering above the transition point. Transverse beam emittances of low intensity beams were investigated for a few ion species by the method of mechanical beam scraping. An upper limit of the rms beam radius at the scraper position of $30 \mu\text{m}$ could be evaluated at $N \approx 4000$.

INTERPRETATION OF RESULTS AND CONCLUSION

The measured beam parameters can be interpreted in terms of beam temperatures observed from the reference frame of a particle moving with the ion velocity. The longitudinal beam temperature $kT_{\parallel} = m_i c^2 \beta^2 (\delta p/p)_{rms}^2$ can be determined directly from the measured FWHM momentum spread with $(\delta p/p)_{rms} = (8 \times \ln 2)^{-1/2} \delta p/p$. The transverse beam temperature $kT_{\perp} = 1/2 \times m_i c^2 \beta^4 \gamma^4 (x'_{rms}{}^2 + y'_{rms}{}^2)$ can be calculated from mean transverse beam divergences x'_{rms} and y'_{rms} , $m_i c^2$ being the rest mass of the ion.

For the Au^{19+} -beam case study we deduce longitudinal beam temperatures of $kT_{\parallel} = 0.5 \text{ eV}$ above and $kT_{\parallel} = 4 \times 10^{-3} \text{ eV}$ below the transition point. Some measurements with short average times for the Schottky spectra indicated even a true beam temperature far below 1 meV . The transverse temperature for a rms beam size of $30 \mu\text{m}$ at the scraper is derived by means of the local beam envelope function at the scraper. Taking into account the mean envelope amplitude we get an upper limit of $kT_{\perp} = 1.5 \text{ eV}$. However, from the intensity dependence of emittances mentioned we can extrapolate about 0.3 eV .

The properties of a one-component plasma are usually described by the ratio of potential energy U to thermal energy kT . The plasma parameter $\Gamma = U/kT = q^2 e^2 / 4\pi \epsilon_0 a kT$ with the average particle distance a characterizes the state of the plasma. For a finite one-dimensional plasma a phase transition from gas to liquid is expected for $\Gamma \simeq 1$. We get for the longitudinal potential energy $U_{\parallel} = q^2 e^2 N / 4\pi \epsilon_0 C \gamma$ for N particles equally spaced along the ring circumference C . The transverse potential energy $U_{\perp} = q^2 e^2 / 4\pi \epsilon_0 a_{\perp}$ refers to the potential energy between two ions approaching each other to the average beam radius a_{\perp} . From experimental results for 4000 Au-ions we estimate $U_{\parallel} = 2.4 \times 10^{-4} \text{ eV}$ and $U_{\perp} = 0.3 \text{ eV}$.

In the experiments with electron cooled, highly-charged ions a discontinuous reduction of the longitudinal ion beam temperature by up to two orders of magnitude is observed, when the number of stored ions decreases below 10^4 . This behavior may be interpreted as beginning order. The estimated plasma parameters Γ in the longitudinal and transverse phase planes are close to unity. This might be understood as a phase transition from gaseous to liquid state of the beam.

REFERENCES

- [1] F. Diedrich, E. Peik, J. M. Chen, W. Quint and H. Walther, *Phys. Rev. Lett.*, **59** 2935 (1987)
- [2] J. P. Schiffer and P. Kienle, *Phys. A* **321**, 181 (1985)
- [3] V. V. Parkhomchuk and D. V. Pestrikov, *Sov. Phys. Tech. Phys.*, **25(7)** 818 (1980)

- [4] E. N. Dementev, N. S. Dikansky, A. S. Medvedko, V. V. Parkhomchuk and D. V. Pestrikov, *Sov. Phys. Tech. Phys.* **25(8)**, 1001 (1980)
- [5] B. Franzke, *Nucl. Instr. Methods* **B 24/25**, 18 (1985)
- [6] N. Angert, W. Bourgeois, H. Emig, B. Franzke, B. Langenbeck, K. D. Leible, T. Odenweller, H. Poth, H. Schulte, P. Spädtke, B. Wolf, *Proc. 2nd Europ. Part. Accel. Conf.*, Nice, 1990, P. Marin and P. Mandrillon eds. (Edition Frontieres, Gif-sur-Yvette, France, 1990) p. 1374
- [7] M. Steck, K. Beckert, H. Eickhoff, B. Franzke, F. Nolden and P. Spädtke, *Proc. 1993 Part. Acc. Conf.*, Washington D. C., 1993, (IEEE, Catalogue No. 93CH3279-7, 1993) p. 1738
- [8] K. Beckert, S. Cocher, B. Franzke, U. Schaaf, *Proc. 2nd Europ. Part. Accel. Conf.*, Nice, 1990, P. Marin and P. Mandrillon eds. (Edition Frontieres, Gif-sur-Yvette, France, 1990) p. 777
- [9] M. Steck, K. Beckert, F. Bosch, H. Eickhoff, B. Franzke, O. Klepper, R. Moshhammer, F. Nolden, P. Spädtke and T. Winkler, *Proc. 4th Europ. Part. Acc. Conf.*, London, 1994, V. Suller and Ch. Petit-Jean-Genaz eds. (World Scientific, Singapore, 1994) p. 1197
- [10] M. Steck, K. Beckert, H. Eickhoff, B. Franzke, F. Nolden, H. Reich, B. Schlitt, T. Winkler, *Phys. Rev. Letters* **77**, 3803(1996)

FORMATION AND CONTROL OF COULOMB CRYSTALS IN TRAPPED ION PLASMAS

X.-P. Huang, J. J. Bollinger, W. M. Itano, J. N. Tan,¹ B. Jelenković,²
T. B. Mitchell, and D. J. Wineland

Time & Frequency Division, NIST
Boulder, CO

¹Present address: Frequency & Time Systems, Beverly, MA

²On leave from the Institute of Physics, University of Belgrade, Yugoslavia

INTRODUCTION

Trapped non-neutral plasmas consisting of one charged particle species provide an experimental realization of a classical one-component plasma (OCP).¹ In Penning traps, which use static electric and magnetic fields for confinement, trapped plasmas can relax to a global thermal equilibrium which undergoes a rigid-body rotation about the magnetic field axis.² In a frame rotating with the plasma, there arises an induced electric field which takes the place of the field from the uniform neutralizing background in the OCP model. Active control of the rotation frequency prevents plasmas from spinning down under the ambient drag from static field errors and background neutral molecules, and allows variation of the plasma density and shape.^{2,3}

With Doppler laser cooling, pure ion plasmas with density n_0 greater than 10^8 cm^{-3} and temperature T less than 5 mK can be routinely obtained,² resulting in a Coulomb coupling parameter $\Gamma \equiv (e^2/4\pi\epsilon_0 a_{\text{WS}})(k_{\text{B}}T)^{-1}$ greater than 200. Here, e is the ion charge and a_{WS} is the Wigner-Seitz radius defined by $4\pi a_{\text{WS}}^3/3 \equiv 1/n_0$. A classical, infinite OCP freezes into a bcc lattice at $\Gamma \approx 172$.⁴ However, this result does not strictly apply to the trapped plasmas because of the surface effects associated with their finite size. Both simulations⁵ and experiments⁶ show that a structure of concentric shells forms for nearly spherical plasmas with 10^3 to 10^4 ions. For plasmas with $\gtrsim 2 \times 10^5$ ions or $\gtrsim 30$ shells, time-averaged Bragg scattering patterns are consistent with bcc crystals (presumably located near the plasma center),⁷ in agreement with a theoretical estimate.⁸ But this measurement can not determine whether the Bragg patterns come from single crystals or polycrystals.

In this report, we demonstrate that azimuthally asymmetric electric fields rotating in the same sense as the plasma can phase-lock the rotation of crystallized plasmas without slip, therefore precisely controlling the plasma rotation frequency, density, and surface shape.⁹ We synchronize the detection of Bragg-scattered light either with this active rotation control or using the time dependence of the scattered light itself measured by a fast photomultiplier tube. Time-resolved (stroboscopic) Bragg diffraction patterns are obtained, effectively removing

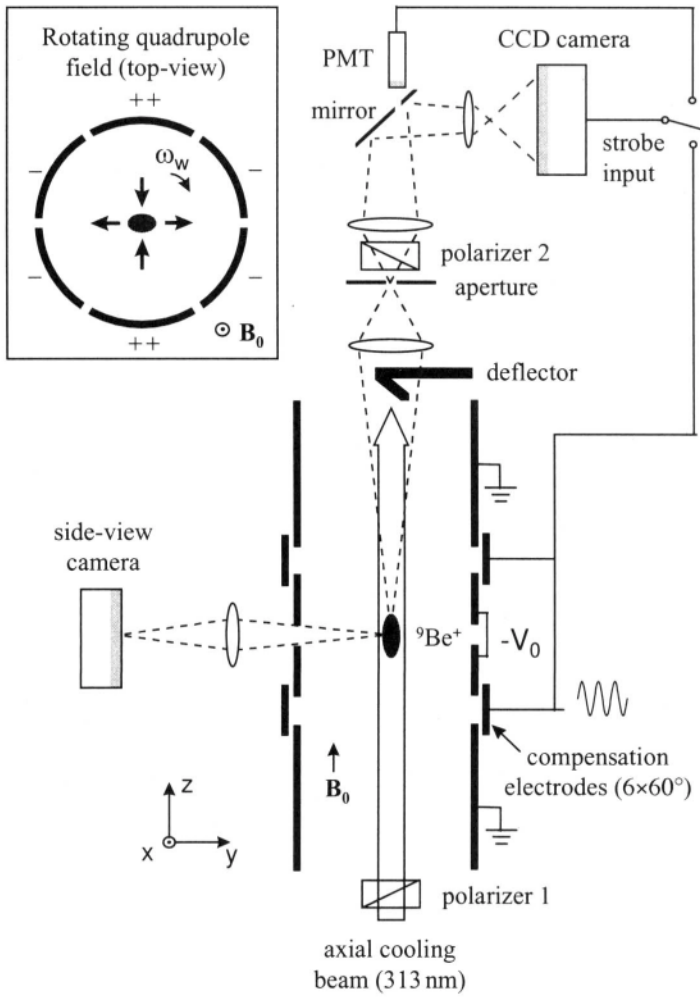


Figure 1. Schematic of the experimental setup.

the plasma rotation.¹⁰ Patterns from single bcc lattices are observed most of the time in these plasmas,¹⁰ in agreement with the theoretically predicted bulk structure of a solid one-component plasma.⁴ In addition, some preferred crystal orientations with respect to the axial laser beam are also seen. With phase-locked rotation, the lattice and its orientation can be stable for longer than 30 min, compared to an observed ~ 1 min lifetime without the active rotation control.

EXPERIMENTAL SETUP

Figure 1 shows the apparatus and the asymmetric rotating field. The trap consists of a 127 mm long stack of cylindrical electrodes at room temperature with an inner diameter of 40.6 mm, enclosed in a 10^{-8} Pa vacuum chamber. An axisymmetric potential $\propto [z^2 - (x^2 + y^2)/2]$ is generated by biasing the central electrodes to $-V_0$, giving axial particle confinement. A uniform magnetic field $B_0 = 4.46$ T from a superconducting magnet is aligned parallel to the trap axis, resulting in global rotation and radial trapping. As shown in the inset, a

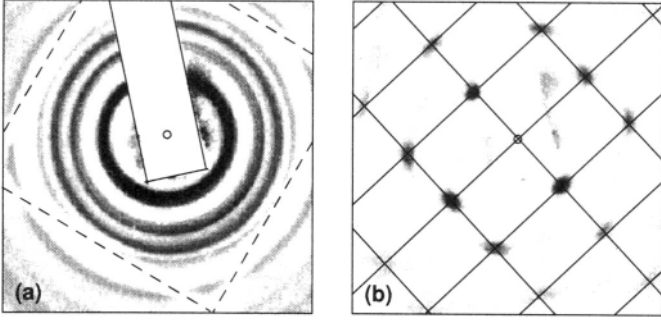


Figure 2. Bragg diffraction from a plasma phase-locked to the rotating field ($\omega_r = \omega_w = 2\pi \times 140$ kHz, $n_0 = 4.26 \times 10^8$ cm $^{-3}$). (a) 1 s time-averaged pattern. The long rectangular shadow is from the beam deflector; four dashed line shadows that form a square are due to a wire mesh, (b) Time-resolved pattern obtained by strobing the camera with the rotating field (integration time ≈ 5 s). For a bcc $\langle 110 \rangle$ crystal, a spot is predicted at each intersection of the rectangular grid lines whose separations are not adjusted.

rotating quadrupole field (rotation frequency ω_w) with a potential $\propto (y^2 - x^2)\cos(2\omega_w t) + 2xy\sin(2\omega_w t)$ is generated by applying properly phased sinusoidal voltages to the 6-fold azimuthal sectors of the compensation electrodes.^{3,9}

We create ${}^9\text{Be}^+$ plasmas by ionizing neutral Be atoms in a separate trap (not shown) and transferring the ions to the main trap for experimentation. This procedure can be repeated several times to accumulate up to 10^6 ions. The trapped ${}^9\text{Be}^+$ ions are then cooled to temperatures T somewhat higher than the limit of 0.5 mK by a laser beam propagating parallel to \mathbf{B}_0 at wavelength $\lambda \approx 313.11$ nm.² In thermal equilibrium, the plasma takes the shape of a spheroid with uniform density and a rigid-body rotation frequency ω_r . The density and aspect ratio of the spheroid are determined by ω_r , for given B_0 and V_0 .² An $f/5$ imaging system detects resonantly scattered photons from the axial cooling beam (diameter ≈ 0.4 mm, power ≈ 50 μW) to produce a side-view image of the plasma, from which we measure ω_r (and n_0) with an uncertainty 5 %. Bragg-scattered light is detected by a CCD camera with a gateable image intensifier near the forward-scattering direction ($< 5.4^\circ$) since $\lambda \ll a_{\text{ws}}$.⁷ Time-resolved Bragg diffraction patterns are obtained by strobing the camera with either one of the two timing signals.¹⁰

RESULTS AND DISCUSSIONS

Figure 2(a) shows a time-averaged diffraction pattern of concentric rings from a nearly spherical plasma with 7.5×10^5 ions. When the pattern is time-averaged, even single crystals produce rings because of the plasma rotation about the axial laser beam.⁷ With the rotating field controlling the plasma rotation, we trigger the intensifier synchronously with the rotating field to open the camera for 50 ns each $2\pi/\omega_w$ period. This enables the camera to record the diffraction pattern in the frame rotating with the quadrupole field. Figure 2(b) shows such a time-resolved pattern taken nearly simultaneously with Fig. 2(a) and accumulated over $\sim 10^6$ plasma rotations. The well-defined rectangular dot pattern demonstrates that the crystal is phase-locked to the rotating field with $\omega_r = \omega_w$.⁹ With this phase-locked rotation, the crystalline lattice and its orientation with respect to the laser beam can last longer than 30 min ($\sim 10^8$ rotations).

The diffraction pattern in Fig. 2 corresponds to a single bcc crystal with a $\langle 110 \rangle$ axis aligned with the laser beam. The theoretically predicted pattern agrees well with the observation within about 1 %. This rectangular grid pattern is essentially a plane of the reciprocal

lattice, as can be seen from the Ewald construction in the forward-scattering limit.¹⁰ From the widths and intensities of the Bragg peaks, we estimate that the crystals consist of at least 10 lattice planes.⁷ Single bcc crystals with many orientations including $\langle 001 \rangle$, $\langle 111 \rangle$, $\langle 012 \rangle$, and $\langle 115 \rangle$, have also been observed,¹⁰ with $\langle 001 \rangle$ and $\langle 110 \rangle$ being the most frequently observed orientations.

In the future, we plan to investigate the experimental reasons for these preferred orientations. We will also attempt to directly image individual ions in crystallized plasmas with phase-locked rotation. Finally, with the improved stability of the crystal lattices obtained by the rotating field, we hope to observe the melting phase transition of the system.

We thank D. Dubin, T. O'Neil, B. King, C. Wood, M. Young, M. Lombardi, and D. Sullivan for discussions and comments. This work is supported by the Office of Naval Research.

REFERENCES

- [1] J. H. Malmberg and T. M. O'Neil, *Phys. Rev. Lett.* **39** (1977) 1333.
- [2] J. J. Bollinger, D. J. Wineland, and D. H. E. Dubin, *Phys. Plasmas* **1** (1994) 1403.
- [3] X.-P. Huang, F. Anderegg, E. M. Hollmann, C. F. Driscoll, and T. M. O'Neil, *Phys. Rev. Lett.* **78** (1997) 875.
- [4] E. L. Pollock and J. P. Hansen, *Phys. Rev. A* **8** (1973) 3110; W. L. Slattery, G. D. Doolen, and H. E. DeWitt, *ibid.* **21** (1980) 2087; **26** (1982) 2255; S. Ogata and S. Ichimaru, *ibid.* **36** (1987) 5451; G. S. Stringfellow and H. E. DeWitt, *ibid.* **41** (1990) 1105; D. H. E. Dubin, *ibid.* **42** (1990) 4972.
- [5] A. Rahman and J. P. Schiffer, *Phys. Rev. Lett.* **57** (1986) 1133; H. Totsuji, in *Strongly Coupled Plasma Physics*, ed. F. J. Rogers and H. E. DeWitt (Plenum, New York, 1987) p. 19; D. H. E. Dubin and T. M. O'Neil, *Phys. Rev. Lett.* **60** (1988) 511; J. P. Schiffer, *Phys. Rev. Lett.* **61** (1988) 1843; R. W. Hasse and V. V. Avilov, *Phys. Rev. A* **44** (1991) 4506; J. P. Schiffer, in *Non-neutral Plasma Physics II*, ed. J. Fajans and D. H. E. Dubin, AIP Conf. Proc. 331 (AIP Press, New York, 1995) p. 191; D. H. E. Dubin and T. M. O'Neil, in *Strongly Coupled Plasma Physics*, ed. S. Ichimaru (Elsevier, 1990) p. 189.
- [6] S. L. Gilbert, J. J. Bollinger, and D. J. Wineland, *Phys. Rev. Lett.* **60** (1988) 2022; G. Birkl, S. Kassner, and H. Walther, *Nature* **375** (1992) 310.
- [7] J. N. Tan, J. J. Bollinger, B. Jelenkovic, and D. J. Wineland, *Phys. Rev. Lett.* **75** (1995) 4198; J. N. Tan, J. J. Bollinger, B. Jelenkovic, W. M. Itano, and D. J. Wineland, in *Physics of Strongly Coupled Plasmas*, ed. W. D. Kraeft and M. Schlanges (World Scientific, Singapore, 1996) p. 387.
- [8] D. H. E. Dubin, *Phys. Rev. A* **40** (1989) 1140.
- [9] X.-P. Huang, J. J. Bollinger, T. B. Mitchell, and W. M. Itano, *Phys. Rev. Lett.* **80** (1998), 73.
- [10] W. M. Itano, J. J. Bollinger, J. N. Tan, B. Jelenkovic, X.-P. Huang, and D. J. Wineland, "Bragg Diffraction from Crystallized Ion Plasmas," *Science* (in press).

QUASI-CLASSICAL THEORY AND SIMULATION OF TWO-COMPONENT PLASMAS

Werner Ebeling¹, Burkhard Militzer², and Friedemann Schautz³

¹Institute of Physics, Humboldt-University
Berlin, Germany

²Department of Physics, University of Illinois
Urbana, IL

³Institute of Physics of Complex Systems, MPG
Dresden, Germany

PLASMA PARAMETER IN THE QUASI-CLASSICAL REGIME

Due to the long-range nature of Coulomb forces, the regime of quasi-classical behavior of plasmas is different from that of van der Waals gases. We consider here a two-component plasma (TCP) consisting of electrons of density n_e and ions of density n_i with the charges $-e$ or $+e$ respectively, in equilibrium at the temperature T . The quasi-classical regime is defined by the conditions

$$d \gg a_0, \quad d \gg \lambda_{ij}, \quad l \gg \lambda_{ij} \quad (1)$$

by using the characteristic length parameters

$$d = (3/4\pi n_e)^{1/3}, \quad l = (e^2/kT), \quad a_0 = (\hbar^2/me^2), \quad \lambda_{ij} = \hbar/(2m_{ij}kT)^{1/2} \quad (2)$$

Under these conditions, the free charges in a plasma may be treated by quasi-classical methods, while the bound states must always be treated quantum-mechanically. This concept was already developed by Planck and Brillouin.¹

QUASI-CLASSICAL PLASMA MODELS

A first description is provided by the Debye–Hückel theory in combination with a mass-action law on the basis of the Planck–Brillouin–Larkin partition function and an appropriate choice of the effective diameter of the charges.^{2,3} The interaction energy per particle reads in this model

$$\epsilon_{int} = -\frac{e^2}{2(r_D + \lambda_{ie}\sqrt{\pi}/4)}, \quad r_D = \frac{kT}{8\pi n_e e^2}. \quad (3)$$

In the quasi-classical regime, this model is consistent with the exact quantum-statistical calculations up to the order $\mathcal{O}(\hbar)$.² A special property of this model is the existence of a

plasma-phase transition, which can be determined analytically.² The critical point is located at $T_c = (e^2/8ka_0)$ and $n_c = a_0^{-3}$.

Another widely used model for quasi-classical plasmas is based on the non-singular potential,⁴⁻⁷

$$V_{ij} = \frac{e_i e_j}{r} \left\{ 1 - \exp\left(-\frac{r}{R_{ij}}\right) \right\}. \quad (4)$$

By generalizing an early work by Kramers, Berlin and Montroll⁸ were able to derive the exact free energy density as a function of $\Gamma = e^2/kTd$ under the assumption that $R_{ij} = O(V^{1/3})$. In our earlier papers,^{9, 10} we used the model of gauss-distributed charges. This relatively simple model can be derived from the method of wave packet dynamics (WPD).¹¹ Under the assumption that the charge e_i is gauss-distributed with radius R_i , we obtain the interaction potential

$$V_{ij} = \frac{e_i e_j}{r} \operatorname{erf}\left(\frac{r}{R_{ij}}\right), \quad R_{ij}^2 = R_i^2 + R_j^2. \quad (5)$$

For this potential, one can find a lower bound for the energy per charge that corresponds to a configuration, in which the Gaussian charges are surrounded by screening clouds of opposite charge concentrated around a common center. This leads to

$$\epsilon_i = -\frac{2e_i^2}{\sqrt{\pi}R_i}. \quad (6)$$

In our quasi classical WPD simulations,^{9, 10} we used the effective radii

$$R_i^2 = r_0^2 = \frac{\hbar^2}{p_0^2} = \frac{3\hbar^2}{2m\epsilon_i^{ideal}} \quad (7)$$

Our results can be approximated by the semi-empirical Debye–Hückel-type equation for the interaction energy per charge

$$\epsilon_{int} = -\frac{e^2}{2r_D + r_0\sqrt{\pi}/2} \quad (8)$$

An even simpler quasi-classical model was treated by Norman et al.¹⁷ on the basis of molecular dynamics.

COMPARISON WITH PATH-INTEGRAL SIMULATIONS

Already in [9], we could show for the OCP that quasi-classical WPD simulations with the potential (5) yield good agreement with the interaction energy obtained in the classical QMC work by Ceperley and Alder.¹² Now we will to compare results of our WPD simulations¹⁰ for mass-symmetrical TCP with new path-integral Monte Carlo calculations (PIMC). PIMC simulations¹³⁻¹⁶ have been proven to be a powerful and accurate technique to study the static properties of quantum systems. The comparison was performed in order to advance a dynamic simulations model, which can reproduce the essential PIMC results with a reasonable accuracy and which then can be used to study dynamic plasma properties. The interaction energies for two densities $n_e = 10^{22}\text{cm}^{-3}$ and $n_e = 10^{23}\text{cm}^{-3}$ and several temperatures are shown in figure 1, in which ϑ denotes the degeneration parameter $\vartheta = T/T_F$. We also included results from analytical approximations by means of Padé formulae¹⁸ and the chemical picture (PACH).^{3, 18} The comparison shows a satisfactory agreement between the PIMC results and the PACH approximations. The WPD simulations shows qualitatively agreement with the other methods but the quantitative agreement is still not sufficing. This is partly caused

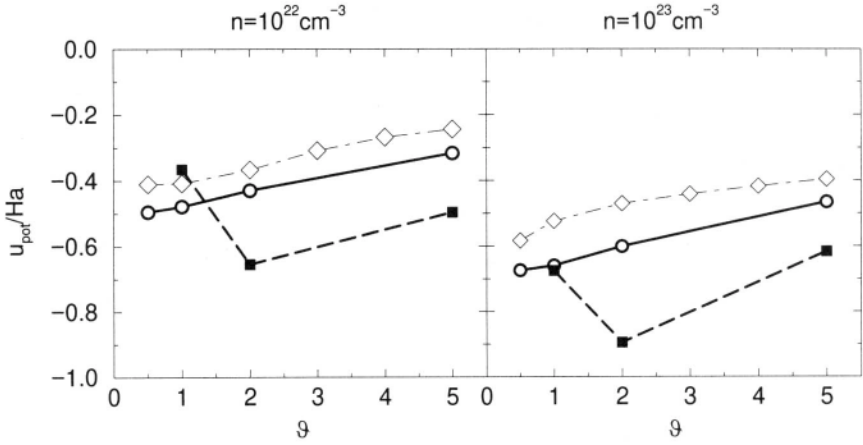


Figure 1. Interaction energy of the electron-positron plasma per pair of particles from wave packet dynamics simulations (dashed line), from path-integral Monte Carlo simulations (solid line) and Padé approximations in the chemical picture (dot-dash line) are compared at the two densities $n = 10^{22} \text{cm}^{-3}$ ($T_F = 19600 \text{K}$) and $n = 10^{23} \text{cm}^{-3}$ ($T_F = 91100 \text{K}$) as a function of $\vartheta = T/T_F$

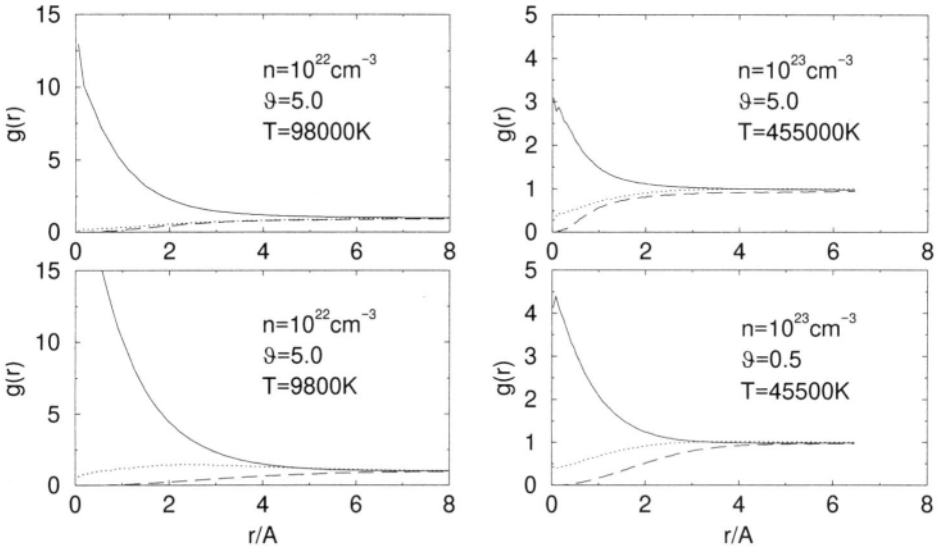


Figure 2. The pair correlation functions $g_{pe}(r)$ (solid line), $g_{ee\uparrow\downarrow}(r)$ (dotted line) and $g_{ee\uparrow\uparrow}(r)$ (dashed line) are shown for two different densities and ϑ values.

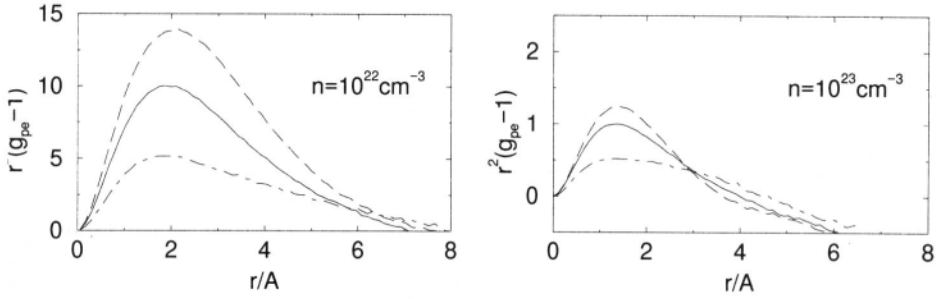


Figure 3. The direct radial electron–positron correlation function $r^2(g_{pe}(r) - 1)$ is shown for two different densities at $\vartheta = 5$ (dashed line), $\vartheta = 2$ (solid line) and $\vartheta = 0.5$ (dot-dash line). The strong peak in the left graphs corresponds to the population of ground state $\psi_0(r) \propto \exp(-r/2a_0)$.

by a too strong interaction potential Eq. (5,7). Hence, the agreement can be improved by adjusting the length parameter R_{pe} . In particular, this is true for the region where $d < \lambda < l$ corresponding to rather low densities and high temperatures. This point however needs a more careful investigation.

The pair correlation function for PIMC simulation are shown in figure 2. Comparing the correlation function for electrons with parallel and anti-parallel spins, one can study the effects of the Pauli exclusion principle, which is realized in PIMC by introducing nodal surfaces.¹⁴ It leads to a stronger repulsion of electrons in the same spin state.

From the peak structure in the electron–positron correlation function in figure 2, one can deduce the existence of bound states.^{15, 16} The population of the ground state can be evaluated by studying the radial direct correlation function $r^2(g_{ep}(r) - 1)$, which is plotted in figure 3. The height of the peak is a direct measure of the number of bound electron–positron pairs. They dominate the structure in the left graph of figure 3 for the lower density, whereas the minor peak in the high density case is caused by the attraction of free electrons and positrons, which leads to Debye screening but not to binding. The effect of thermal ionization can be seen in the left graph of figure 3. The pressure ionization can be studied by comparing the low at high density graph. The reader should keep in mind that we compare at constant ϑ and not at constant temperature.

In conclusion, we state that the symmetrical two-component plasmas are a fairly useful system for testing the accuracy of analytical theories and numerical simulations. On the basis of our comparison, we deduce that the WPD method needs further improvements in order to achieve a level of correctness, which already has been reached for the electron gas.

Acknowledgements

We thank David Ceperley, William Magro, Bernard Bernu and Carlo Pierleoni for developing the PIMC technique and John Shumway for useful discussions.

REFERENCES

- [1] L. Brillouin, *Statistique Quantique*, Paris (1932); Russ. transl. Gostekhisdat Kiev (1934)
- [2] W. Ebeling, W. D. Kraeft, and D. Kremp, *Theory of Bound States and Ionization Equilibrium in Plasmas and in Solids*, Akademie-Verlag Berlin (1976)
- [3] D. Beule, W. Ebeling, A. Förster, *Physica A* (1997), in press
- [4] G. Kelbg, *Ann. Physik* 12:219 (1963); 12:354 (1964); 14:394 (1964)
- [5] C. Deutsch, *Phys. Lett. A* 60:317 (1977)
- [6] C. Deutsch, M. Gombert, and H. Minoos, *Phys. Rev A* 23:924 (1981)
- [7] J.-P. Hansen, and I. R. McDonald, *Phys. Rev A* 23:2041 (1981)

- [8] T. H. Berlin, and E. W. Montroll, *J. Chem. Phys.* 29:75 (1952)
- [9] W. Ebeling, and F. Schautz, *Phys. Rev. E* 56, N0 1 (1997)
- [10] W. Ebeling, B. Militzer, and F. Schautz, *Contr. Plasma. Phys.* 37:137 (1997)
- [11] D. Klakow, C. Toepffer, and P.-G. Reinhardt, *Phys. Lett. A* 192:55 (1994)
- [12] D. M. Ceperley, and B. J. Alder, *Phys. Rev. Lett.* 45:466 (1980)
- [13] D. M. Ceperley, *Rev. Mod. Phys.* 67:279 (1995).
- [14] D. M. Ceperley, Path integral Monte Carlo methods for fermions, *in* "Monte Carlo and Molecular Dynamics of Condensed Matter Systems," Ed. K. Binder and G. Ciccotti, Bologna, Italy (1996).
- [15] W. R. Magro, D. M. Ceperley, C. Pierleoni, and B. Bernu, *Phys. Rev. Letts.* 76:1240 (1996).
- [16] B. Militzer, W. Magro, and D. Ceperley, this volume.
- [17] G. Norman, A. Kaklyugin, and A. Valuev, this volume
- [18] H. Lehmann, and W. Ebeling, *Phys. Rev. E* 54:2451 (1996)

This page intentionally left blank

SCREENED INTERACTION POTENTIAL AND BOUND STATES BETWEEN TWO NEGATIVE CHARGED PARTICLES IN THE THREE- AND TWO-DIMENSIONAL ELECTRON GAS

A. Ghazali¹ and A. Gold²

¹Groupe de Physique des Solides, Universités Paris 7 & 6
2 place Jussieu, 75251 Paris, France

²Laboratoire de Physique des Solides, Université Paul-Sabatier
118 Route de Narbonne, 31062 Toulouse, France

INTRODUCTION

A test charge in a three-dimensional electron gas is screened at large distances.¹ The screened potential exhibits Friedel oscillations.² It was argued that many-body effects, described by the local-field correction (LFC), strongly modify the screening properties of a two-dimensional electron gas at low density and enhance Friedel oscillations.³ The possibility of a Coulomb interaction induced attraction in the electron gas between two equally charged particles was suggested in the literature for a short-range interaction potential.⁴ It was shown that for a negative test charge many-body effects give rise to bound states in the low density range of the two-dimensional⁵⁻⁷ and three-dimensional^{7, 8} electron gas. In this review we restrict our discussion to test charges with charge $q = -|e|$ and no spin. We study the test-charge–test-charge interaction^{5, 6, 8} and the test-charge–electron interaction.⁷

MODEL AND THEORY

The model is a d -dimensional electron gas ($d = 2, 3$) with a parabolic dispersion and density N_d . Distances are expressed in units of the effective Bohr radius $a^* = \epsilon_L/m^*e^2$ with the Planck constant $\hbar = 1$. m^* is the effective mass and ϵ_L is the dielectric constant of the background. Energy values are given in units of the effective Rydberg $Ry^* = m^*e^4/2\epsilon_L^2$. The density parameter r_s is given by $r_s = [3/4\pi N_3 a^{*3}]^{1/3}$ for $d = 3$ and by $r_s = [1/\pi N_2 a^{*2}]^{1/2}$ for $d = 2$. $r_s a^*$ is the Wigner–Seitz radius. $N_3 = k_F^3/3\pi^2$ ($N_2 = k_F^2/2\pi$) is the electron density in $d = 3$ ($d = 2$) and k_F is the Fermi wave number.

The Coulomb interaction potential in the Fourier space between two negative test charges (tt) is repulsive and given by $V_{tt}(q) = V(q)$ with $V(q) = 4\pi e^2/\epsilon_L q^2$ in $d = 3$ and $V(q) = 2\pi e^2/\epsilon_L q$ in $d = 2$. The screened interaction potential $V_{tt,sc}(q)$ is written as $V_{tt,sc}(q) = V_{tt}(q)/\epsilon_{tt}(q)$. The dielectric function $\epsilon_{tt}(q)$, calculated within the RPA and including the LFC, is given⁹ by $1/\epsilon_{tt}(q) = 1 - V(q)\chi_0(q)/[1 + V(q)[1 - G(q)]\chi_0(q)]$. $\chi_0(q)$ is the Lindhard function of the free electron gas.¹

For the interaction between a negatively charged test particle and an electron (*te*) the potential is given by $V_{te}(q) = V(q)$. The screened interaction potential $V_{te,sc}(q)$ is expressed as $V_{te,sc}(q) = V_{te}(q)/\epsilon_{te}(q)$ with $\epsilon_{te}(q) = 1 + V(q)[1 - G(q)]\chi_0(q)$. $\epsilon_{te}(q)$ accounts for the indistinguishability of the electrons in the case of the test-charge–electron interaction potential.⁹

In our calculation we use for the LFC the sum-rule approximation,¹⁰ taking into account the compressibility sum rule,¹¹ of the Singwi, Tosi, Land and Sjölander (STLS) approach.¹² The LFC is parameterized by three coefficients $C_{id}(r_s)$ ($i = 1, 2, 3$) and has a similar form as within the Hubbard approximation,¹ where only exchange effects are taken into account. Finally, we note that the sum-rule approach is in reasonable agreement with recent Monte-Carlo calculations.^{13, 14} As far as exchange and correlation effects are included in the LFC, the specific form used for $G(q)$ in the calculation is not essential for our results.

In order to study bound states we used the matrix diagonalization method of the Schrödinger equation in the momentum space. We also use a variational method. The variational ground-state wave function is given by $\phi_{var}(r) = Ar^{k_1/2} \exp(-r^2/2\alpha^2)$ with the normalization constant A and the variational parameters k_1 and α . The two methods give similar results; however, the binding energies found within the matrix diagonalization method are somewhat larger than those found with the variational method. The differences increase for small binding energies. The bound state energies are classified by a radial quantum number n_r and the angular momentum quantum number l . In this paper we only give results for the ground state with $n_r = 1$ and $l = 0$.

RESULTS

The inverse dielectric functions $1/\epsilon_{tt}(q)$ and $1/\epsilon_{te}(q)$ versus q are shown in Fig. 1 for $r_s = 5$ and $d = 2$. Note that $1/\epsilon_{tt}(q)$ is negative for small wave numbers and this is called overscreening. It is this non trivial q -dependence which leads to the strong attractive parts in $V_{tt,sc}(r)$. Within the RPA and for the test-charge–electron interaction the inverse dielectric function is always positive. It is clear from Fig. 1 that the LFC strongly modifies the screening function compared to the RPA. For $1/\epsilon_{tt}(q)$ in the three-dimensional electron gas and comparison with Monte-Carlo calculations, see Ref. 11.

The screened potential $V_{tt,sc}(r)$ and $V_{te,sc}(r)$ versus interparticle distance r is shown in Fig. 2 for $r_s = 5$ and $d = 2$. Note that the attractive part of the test-charge–test-charge interaction is much larger than for the test-charge–electron interaction. For large interparticle distances one finds Friedel oscillations. At small distances the potential is strongly repulsive. $V_{tt,sc}(r_m)$, $V_{te,sc}(r_m)$ and r_m increase with increasing r_s .^{6,8} The variational wave function shows a maximum at $r^* = (k_1/2)^{1/2}\alpha$. The bound states are very extended in space due to the repulsion at small distances: see the large value of r_m found for the minimum of the screened potential in Fig. 2 and we find $r^* \approx r_m$.

Our results for the binding energy of the ground state in the test-charge–test-charge interaction potential versus r_s are shown in Fig. 3 for $d = 3$ and $d = 2$. For $r_s > r_{sc}$ a finite bound state energy is found and r_{sc} for $d = 2$ is much smaller than for $d = 3$. Many excited bound states have been studied; we refer the interested reader to Refs. 6,7,8.

The results for the binding energy of the ground state in the test-charge–electron interaction potential versus r_s are shown in Fig. 4 for $d = 3$ and $d = 2$. r_{sc} for the test-charge–electron interaction is much larger than for the test-charge–test-charge interaction. We also have studied bound-state energies within the RPA^{6,7} and found much smaller binding energies than for the test-charge–test-charge interaction or the test-charge–electron interaction. We mention that the generally believed argument, namely that in $d = 2$ a bound state always exists if the potential is attractive, is only true for a short-range potential. Our results shown in Fig. 3 and

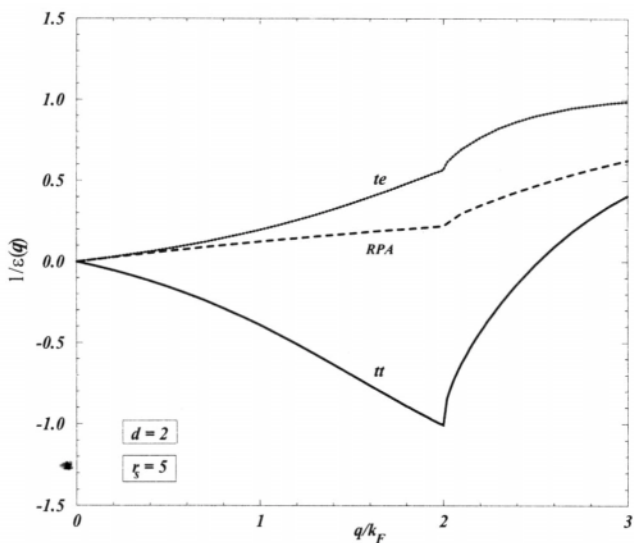


Figure 1. Inverse dielectric function $1/\epsilon_{tt}(q)$ and $1/\epsilon_{te}(q)$ versus wave number q in $d = 2$ for $r_s = 5$. $1/\epsilon_{RPA}(q)$ with $G(q) = 0$ is shown as the dashed line.

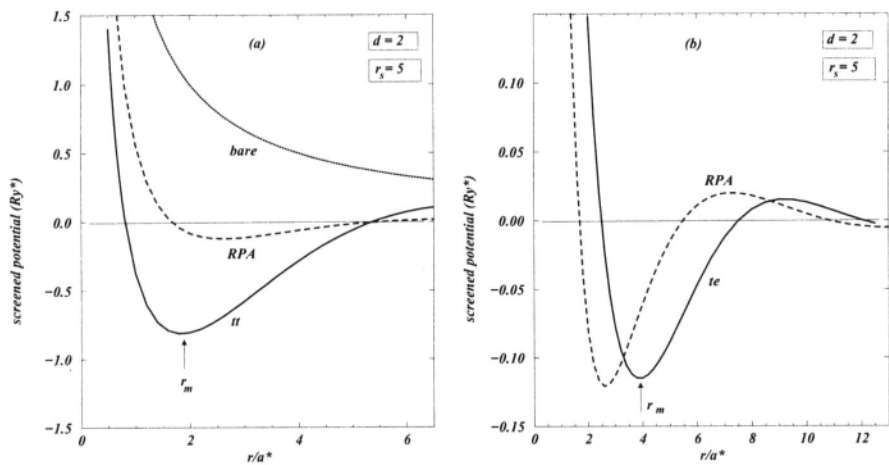


Figure 2. Screened potential $V_{sc,tt}(r)$ (a) and $V_{sc,te}(r)$ (b) versus interparticle distance r for $r_s = 5$ in $d = 2$. The RPA is shown as the dashed line. The unscreened potential $V(r) = 2Ry^*a^*/r$ is also shown. Note the different energy scales for $V_{sc,tt}(r)$ and $V_{sc,te}(r)$.

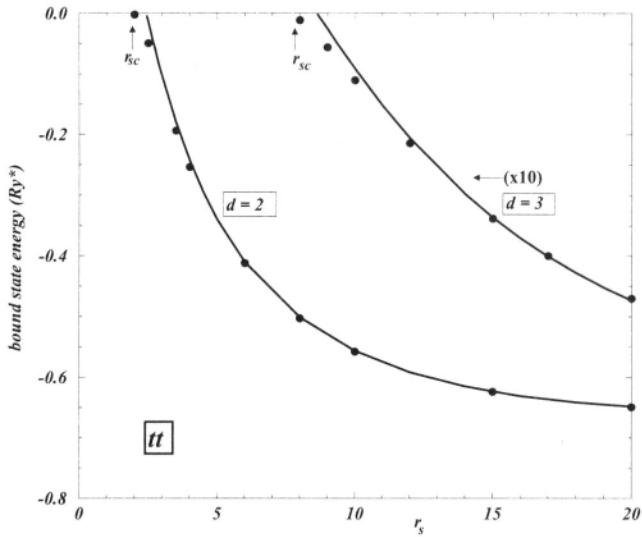


Figure 3. Bound state energies for the screened repulsive test-charge–test-charge interaction found by matrix diagonalization versus r_s for $d = 2$ and $d = 3$ as solid dots. The variational results are shown as solid lines. Note the different energy scales for $d = 3$ and $d = 2$.

Fig. 4 confirm that in $d = 2$ a finite attractive part in the screened potential is present (Friedel oscillations) while no bound states exist for $r_s < r_{sc}$.

DISCUSSION

For the test-charge–electron interaction let us discuss the origin of the attractive part in three dimensions assuming that $\chi_0(q) = \rho_F$, ρ_F is the density of states at the Fermi energy ϵ_F . This approximation represents the Thomas–Fermi (TF) approximation. For the screened potential we find an attractive part because the screened potential in momentum space has the form $1/[q^2 + (1 - G(q))q_{TF}^2]$. The finite $G(q)$ is responsible for the attractive part. With $G(q) = 0$ one obtains for large distances an exponentially screened potential. The strength of the attractive part depends on $G(q)$ and $\chi_0(q)$. For the test-charge–test-charge interaction the attractive part is mainly given by $G(q)$. The attraction is larger in two-dimensional systems. A similar attraction occurs in quasi-one-dimensional systems and the results can be found in Ref. 15. Finally, we would like to indicate that we have also studied bound states between a positive and a negative test charge and we refer the interested reader to the original articles.^{6–8}

For $d = 3$ it was recently argued¹⁶ that Coulomb interaction induced superconductivity should not occur for $r_s < 10$. This is in qualitative agreement with our calculation of the test-charge–test-charge interaction for three dimensions. For a study of the effective electron–electron interaction spin effects have to be taken into account¹⁰ and the LFC for spin-density fluctuations has to be known. For the two-dimensional electron gas the effective electron–electron interaction potential including spin effects has been discussed within the Hartree–Fock approximation.³

CLASSICAL PLASMA

Until now we described the screening due to a quantum liquid. From our discussion above it follows that in a classical one-component plasma, when many-body effects via a

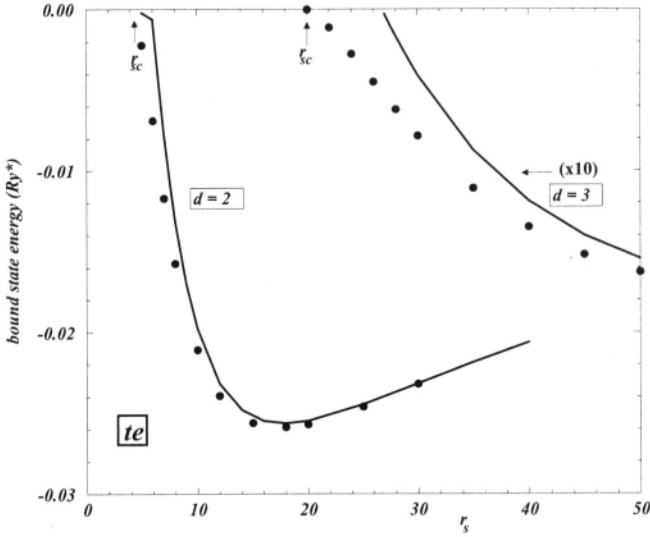


Figure 4. Bound state energies for the screened repulsive test-charge–electron interaction found by matrix diagonalization versus r_s for $d = 2$ and $d = 3$ as solid dots. The variational results are shown as solid lines. Note the different energy scales for $d = 3$ and $d = 2$.

LFC in the screening function are included, attractive parts are also expected in the screened potential between two equally charged particles. The LFC takes into account correlation effects and can be calculated following the STLS-approach.¹⁷ Of course, classical particles are distinguishable and $\epsilon(q) = \epsilon_{cl}(q)$ enters the theory. The Lindhard function for temperature $T = 0$ must be replaced by $\chi_0(q) = N_d/k_B T$ with k_B as Boltzmann's constant. The inverse Debye–Hückel (DH)¹⁸ radius is $\kappa_3 = (4\pi N_3 e^2 / \epsilon_L k_B T)^{1/2}$ in $d = 3$ and $\kappa_2 = 2\pi N_2 e^2 / \epsilon_L k_B T$ in $d = 2$. The dimensionless coupling parameter $\Gamma = e^2 / (\epsilon_L a^* r_s k_B T)$ describes the ratio between the Coulomb energy and the thermal energy. In the classical plasma the degeneracy parameter $\Theta = k_B T / \epsilon_F$ is large, $\Theta > 10$. For $d = 2$ one finds $\kappa_2 a^* = 2\Gamma / r_s = 2/\Theta$. In the DH-theory the dielectric function is given by $\epsilon(q) = 1 + \kappa_3^2 / q^2$ in $d = 3$ and by $\epsilon(q) = 1 + \kappa_2 / q$ in $d = 2$. Within the STLS-approach one gets $\epsilon(q) = 1 + 1/[q^2/\kappa_3^2 - G(q)]$ in $d = 3$ and $\epsilon(q) = 1 + 1/[q/\kappa_2 - G(q)]$ in $d = 2$.

In order to specify the parameter κ_2 we must fix Γ and r_s . Using a simple form of the LFC in $d = 2$,¹⁹ we find an attractive part in the screened potential, but much weaker than for the quantum case. For $\Gamma = 1$ we observe that the attractive part weakens and r_m increases with increasing r_s , corresponding to an increase of Θ and an increase of $1/\kappa_2$. For $\Gamma = 1$ we get $V_{sc}(r_m = 3.3a^*) = -0.076Ry^*$ for $r_s = 5$, $V_{sc}(r_m = 6.2a^*) = -0.039Ry^*$ for $r_s = 10$, and $V_{sc}(r_m = 13.4a^*) = -0.019Ry^*$ for $r_s = 20$. We conclude that the attractive part is strongest in the quantum case and weakens with increasing temperature. In three dimensions and $\Gamma = 1$ we did not find an attractive part in the screened potential. More details concerning classical plasmas will be published elsewhere.¹⁹

CONCLUSION

Our calculations of bound-states between equally charged particles and screened by an electron gas might indicate that paired electrons are possible. We conclude from our results for the binding energy and r_{sc} that in $d = 2$ the attraction between equally charged particles, induced by many-body effects, should occur at higher electron density than in $d = 3$. A finite

temperature weakens the attraction.

REFERENCES

- [1] G. D. Mahan, *Many-Particle Physics*, New York, Plenum (1990).
- [2] J. Friedel, *Adv. Phys.* 3:446 (1953).
- [3] A. Gold, *Phil. Mag. Lett.* 70:141 (1994).
- [4] W. Kohn and J. M. Luttinger, *Phys. Rev. Lett.* 15:525 (1965).
- [5] A. Ghazali and A. Gold, *Phys. Rev.* B52:16634 (1995).
- [6] A. Gold and A. Ghazali, *J. Phys.- Condensed Matter* 9:6885 (1997).
- [7] A. Gold and A. Ghazali, *J. Phys.- Condensed Matter* 9:3749 (1997).
- [8] A. Gold and A. Ghazali, *J. Phys.- Condensed Matter* 8:7393 (1996).
- [9] C. A. Kukkonen and A. W. Overhauser, *Phys. Rev.* B20:550 (1979).
- [10] A. Gold and L. Calmels, *Phys. Rev.* B48: 11622 (1993).
- [11] A. Gold, *Z. Phys.* B103:491 (1997).
- [12] K. S. Singwi and M. P. Tosi, *Solid State Physics* 36:177 (1981).
- [13] S. Moroni, D. M. Ceperley, and G. Senatore, *Phys. Rev. Lett.* 64:303 (1990).
- [14] C. Bowen, G. Sugiyama, and B. J. Alder, *Phys. Rev.* B50:14838 (1994).
- [15] L. Calmels and A. Gold, *Phys. Rev.* B51:11622 (1995).
- [16] C. F. Richardson and N. W. Ashcroft, *Phys. Rev.* B54:R764 (1996).
- [17] K. F. Berggren, *Phys. Rev.* A1:1783 (1970).
- [18] P. Debye and E. Hückel, *Z. Phys.* 24:185 (1923).
- [19] A. Gold, unpublished.

DYNAMIC PROPERTIES OF AN ELECTRON GAS AT $r_s = 3.5$ AND $k \gg k_F$ AND APPLICATION TO DEEP INELASTIC SCATTERING

M. Howard Lee,¹ Jongbae Hong,² and Jangil Kim^{1,3}

¹Department of Physics, University of Georgia,
Athens, Georgia, 30602-2451, U.S.A.

²Department of Physics Education, Seoul National University,
Seoul 151, Korea

³Department of Physics, Pusan National University,
Pusan 609, Korea

INTRODUCTION

For nearly a century the electron gas has been studied as a model for free-electron metals in the ground state. The basic parameter of this model is r_s , whose values have a range of 2-5 for metals. If $r_s \ll 1$, the properties of the electron gas are determined largely by its kinetic energy, i.e., zero-point motion. It is a regime that is applicable to dense matter, e.g., white dwarf stars. If $r_s \gg 10$, the properties of the electron gas are determined largely by the potential or Coulombic interaction energy. It is a regime that is applicable to nonmetallic solids and other novel systems such as electrons confined to the surface of liquid *He*. When the values of r_s are very small or very large, there are perturbative techniques which are known to work very well. When the values of r_s fall in the metallic regime, these approximation techniques are generally not satisfactory. In particular when dynamical properties are calculated by these techniques, one finds notable disagreement between theory and experiment. Perhaps the most notable is in the dynamic structure factor $S(k, \omega)$, where k and ω are respectively the wave vector and frequency. It would thus be significant progress in both technique and understanding if one could find some kind of exact dynamical solution.

The recurrence relations method,¹ developed at the University of Georgia over the past 15 years, has been demonstrated that it can yield exact solutions to frequency dependent problems.² It does not rely on the usual perturbative ideas. It is based on certain geometric notions about Hilbert spaces. When this method is applied to the electron gas, it has been shown that an asymptotically exact solution for the dynamic structure factor can be obtained,³ which is valid at $r_s = 3.5$ approximately and $k \gg k_F$, where k_F is the Fermi wave vector. This solution is summarized in this work. What is interesting is that this solution can be extended in such a way to study the dynamic structure factors of liquids

$He - 3$ and $He - 4$ at very deep inelastic scattering regimes. The experimental studies of very deep inelastic scattering from these quantum fluids have been spurred by the impulse approximation (IA) theory of the many-body problem.⁴ According to this theory, the single-particle momentum distribution can be deduced from deep inelastic scattering data. This idea has not been fully realized owing to scatter in the experimental data. But we shall see that the dynamic structure factors that the recurrence relations method yields for large momentum transfers show very good agreement with these data. Hence the physical idea behind the IA can be put to test by our solutions.

GENERAL THEORY

In the ground state the dynamic structure factor of the density may be used to define the frequency moments,

$$\int_0^{\infty} \omega^{2n-1} S(k, \omega) d\omega = \frac{1}{2} C_n(k), \quad n = 0, 1, 2, \dots, \quad (1)$$

where C_0 and C_1 for example represent the susceptibility and f sum rules, respectively. It should be noted that the above sum rules (1) do not depend on statistics and hence they are applicable to both Fermi and Bose systems. The moments C_n 's are also calculable by the actions of the Liouville operator L on the density ρ_k

$$C_n(k) = (L^n \rho_k, L^n \rho_k), \quad (2)$$

where the inner product means the Kubo scalar product. Since $L\rho = [H, \rho]$ and $H = T + V$, both the kinetic and interaction energies contribute to the moments. One may assume that for some problems these moments can be calculated to any desired order. One may thus ask: Given all the moments, can one obtain $S(k, \omega)$? From the point of view of (1) it becomes then an inverse problem.

The above inverse problem is solvable by Kubo's linear response theory and our recurrence relations method. If $R(t) = (\rho(t), \rho) / (\rho, \rho)$ the relaxation function, where we have suppressed the k index for simplicity, according to Kubo,

$$\tilde{S}(\omega) = -\frac{1}{\pi} \text{Im} \{1 - z\tilde{R}(z)\}_{z=i\omega+\epsilon}, \quad (3)$$

where $\tilde{S} = S / X$, $X = (\rho, \rho)$, and

$$\tilde{R}(z) = T R(t) = 1 / z + \Delta_1 / z + \Delta_2 / z + \dots, \quad (4)$$

where the rhs of (4) means a continued fraction and the deltas are functions of $\lambda_n \equiv C_{n+1} / C_n$, $n = 0, 1, \dots$. Thus given this set of the deltas, known as the *recurrents*, i.e., ratios of the moments, one can solve the inverse problem by going from (4) to (3).

APPLICATION TO THE ELECTRON GAS

For the electron gas at $k \gg k_F$, it is possible to give the ratios of the moments an expansion in powers of k : To order k^0

$$\lambda_n = P + nQ + \alpha_n A + \beta_n B, \quad (5)$$

where the coefficients of A and B have a nonlinear dependence on n , while A and B themselves depend on r_s only. Thus even as the recurrants are known, the inverse problem is not doable owing to the nonlinear coefficients. But if $A = B = 0$ simultaneously at some value of r_s , then the problem is in a sense linear and solvable. At the ideal limit ($r_s = 0$), $A = 0.1$ and $B = 0.36$. Hence it is not necessarily obvious a priori that $A = B = 0$ at some r_s and even if it were so, such a value would be interesting physically. We shall nevertheless take as our ansatz that $A = B = 0$ at a unique value of $r_s = r_s^*$, say, and obtain by (2-5)

$$\tilde{S}(\omega) = \left[\frac{\omega^{2s}}{Q^s \Gamma(s)} \right] e^{-\omega^2/Q}, \quad (6)$$

where $s \equiv P/Q = (3/16x)k^2 + \dots$ and $Q = (16x/3)k^2 + \dots$, and $x \equiv \langle T \rangle$, all of which are at $r_s = r_s^*$ and only the leading orders in k are shown. The dynamic structure factor at this value of r_s and $k \gg k_F$ has a "skewed" Gaussian form. It also has a quadratic maximum at $\omega_r = \sqrt{sQ}$, which is the recoil frequency since it becomes $k^2/2m$ as $k \rightarrow \infty$.

Using (6), together with the kinetic energy sum rules and Kimball's relation, one can now justify the ansatz ex post facto.³ A numerical analysis shows that $r_s^* = 3.5$, which is close to that of $Li(r_s = 3.3)$. The experimental structure factor of Li at $k/k_F = 2.08$ is very accurately reproduced by (6).³

The following static properties of the electron gas at $r_s = 3.5$ are obtained in dimensionless units: $x \equiv \langle T \rangle = .73$, $y \equiv \langle T^2 \rangle = .888$, $g(0) = .08$, $\omega_p = 1.76$, which are to be compared with those for $r_s = 0$, respectively, 0.6, 0.428, 0.5, and 0.

APPLICATION TO DEEP INELASTIC SCATTERING

In recent experiments of inelastic neutron scattering from liquid $He - 3$, k/k_F have attained high values, e.g., greater than 15.⁵ Where the momentum transfers have such high values may be termed very deep inelastic scattering. There is considerable scatter in the measured structure factors, but they have been fitted reasonably well with a simple Gaussian with one parameter--the kinetic energy x . There is of course no theoretical basis for this fitting.

If by deep inelastic scattering we mean $k \rightarrow \infty$, then the dynamic structure factor for it is already given by (6). When $k \rightarrow \infty$, the nonlinear terms drop out as if by the ansatz. There is however a subsidiary condition still retained, i.e., $x^2 = (3/5)y$. Observe that the asymptotically exact structure factor is a "skewed" Gaussian of $x = \langle T \rangle$. This is the reason why the experimental structure factors could be approximately fitted by a simple Gaussian. The best fit of measurements of Sokol et al.⁵ by (6) is obtained for $x = 8.1$ $\cdot k$.

We have similarly examined the measured structure factors for liquid $He - 4$, obtained roughly in the same regime, by Mook et al.⁶ They are remarkably similar to those of liquid $He - 3$ in spite of the different statistics involved. The best fit for the Bose system is given

by $x = 12 \text{ } ^\circ k$, larger than the Fermi value. That the dynamic structure factors show no special statistics dependence bears the idea of asymptotic freedom.

The interest in obtaining very deep inelastic neutron scattering appears to have been kindled by the theoretical predictions based on the IA theory. In particular the single particle momentum function, according to this theory, is relatable to the structure factor obtained in very deep inelastic scattering.⁴ As mentioned, the scatter in the measurements has prevented from realizing this goal. There are however indications that the predicted momentum function may not be observed. Since our theoretical structure factor is asymptotically exact and since it agrees extremely well with the measured ones, it may be used to test the IA ideas. Because of the space limitation, we can make only a few remarks.

The IA theory says that the momentum function $n(p)$ is obtained by the slope of S^{IA} and that if $k \rightarrow \infty$, $S^{IA} = S^{\text{exp}}$, hence $n(p)$ by (6). Since (6) is not symmetric about ω_r , there are two branches of $n(p)$, but similar enough to ignore the differences. They together satisfy the number sum rule. For $He - 3$, $n(p)$ is smooth with no break at $p = \hbar k_F$ and $n(0) = 0.642$. Lam et al.⁷ give a discontinuous $n(p)$ with $n(0) = 0.62$ but with an 8% violation of the sum rule. For $He - 4$, it is also smooth and $n(0) = 0.584$. McMillan⁸ gives a smooth $n(p)$ with $n(0) = 0.75$, but not accurate for $p \rightarrow 0$. Our results indicate that the IA theory fails to yield the expected behavior of the quantum fluids.

ACKNOWLEDGMENTS

This work is dedicated to the memory of the late Professor K. S. Singwi, whose encouragement has been a source of continuing inspiration. The support by NATO (CRG 921268) is gratefully acknowledged. We thank Ms. Sherri H. McElroy for her expert assistance in preparation of this work.

REFERENCES

1. M. H. Lee, *Phys. Rev. B* 26:2547 (1982).
2. M. H. Lee and J. Hong, *Phys. Rev. Lett.* 48:634 (1982).
3. J. Hong and M. H. Lee, *Phys. Rev. Lett.* 70:1972 (1993).
4. G. D. Mahan. "Many Particle Physics," Plenum, NY (1981).
5. P. E. Sokol et al., *Phys. Rev. Lett.* 54:910 (1985).
6. H. A. Mook et al., *Phys. Rev. A* 6:2268 (1972).
7. P. M. Lam et al. *Phys. Lett.* 58A:454 (1976).
8. W. L. McMillan, *Phys. Rev.* 138:A442 (1965).

RIGOROUS BOUNDS TO COULOMB ENERGY FUNCTIONALS I: ATOM-POSITRON BOUND STATES

Rajeev K. Pathak

Department of Physics
University of Pune, Pune-411007
Maharashtra, India

1. INTRODUCTION

In the study of atom-positron interactions, an intriguing question that has hitherto not been conclusively answered is whether a positron forms a (transient) bound state with the atom (or ion) prior to the annihilation of the former with an atomic electron.¹⁻³ Employing an adiabatic like approximation to Coulomb interactions, Gertler, Snodgrass and Spruch¹ derived a necessary condition for the existence of such bound states for a number of systems, including those for an atom and a positron. Gertler, Snodgrass, and Spruch, using Schwinger's^{4,5} criterion for existence of a bound state, concluded that a He and e^+ bound state is impossible, and further conjectured that under purely Coulomb interactions, an $H + e^+$ system will also be unbound, a conclusion in agreement with that of Aronson, Klienman and Spruch² and Golden and Epstein.³ Golden and Epstein, within a different kind of adiabatic approximation, proved that He, N, and Ne in their ground states will be incapable of binding positrons, but also pointed out that binding of positrons to H, O, Ar, and Kr was not precluded within their approximation.

Some very accurate variational(not involving any adiabatic approximation) calculations by Clary⁶ suggest that a neutral atom and a positron bound state indeed exist for the species(in the notation of Ref. [6]) $^1,2S[He, e^+]$ and $^1,2S[Li, e^+]$ but noticeably, the variational wave functions had to incorporate the electron-positron distance to give rise to a bound state. That the atom and e^+ bound state crucially depends on the polarization (i.e., deviation from spherical symmetry) of the electron density was also emphasized by the Patrick and Cade.⁷

It is the purpose of this paper to obtain a rigorous necessary criterion for atom-positron binding and further to demonstrate that for binding of positrons to neutral atoms, it is imperative to have a non-spherical (around the nucleus) joint electron-positron number distribution(see below). The present derivation closely parallels Lieb's⁸ remarkable maximum negative ionicity theorem.⁸⁻¹⁰ We shall examine here atom-positron and *not* ion-positronium states.

2. BINDING CRITERION

We consider a non-relativistic quantum-mechanical system of N negative charges (fermions or bosons or an admixture of both) $-q_j|e|$ ($q_j > 0; j = 1, 2, \dots, N$) in the field of a nucleus of charge $Z|e|$ and an extra, *delocalized* (this is crucial) positive charge $Q|e|$, $Q > 0$. With exclusively the Coulomb interactions, the (spin-free) Hamiltonian H for such a system is given by

$$H = H_0 + H_1, \quad (1)$$

with

$$H_0 = \sum_{j=1}^N (T_j - q_j e^2 V(\vec{r}_j)) + e^2 \sum_i \sum_{j(>i)} \frac{q_i q_j}{|\vec{r}_i - \vec{r}_j|} \quad (2)$$

and

$$H_1 = T_{\vec{R}} + Qe^2 V(\vec{R}) - Qe^2 \sum_{j=1}^N \frac{q_j}{|\vec{R} - \vec{r}_j|} \quad (3)$$

Here, T_j is the j th electron kinetic energy operator, with m_j denoting the masses of the negative charges; $V(\vec{r}) = Z/|\vec{r}|$ and $T_{\vec{R}} = -\hbar^2 \nabla_{\vec{R}}^2 / (2M)$, M being the mass of a delocalized positive charge, in particular, that of a positron. The coordinates $\{\vec{r}_j\}$ refer to those of the electrons while \vec{R} denotes the location of the positron. Evidently, H_0 refers to the atomic Hamiltonian, with the positron absent. Let $\Psi(\vec{r}_1, \vec{r}_2, \dots, \vec{r}_N; \vec{R})$ be the many-particle ground state energy eigenfunction of the system with $H\Psi = E\Psi$; E being the ground state energy of the atom and positron system. (The spin degrees of freedom may also be incorporated in Ψ). For a stable bound state of such a system, one must have $E \geq E_0$, where E_0 is the atomic ground state energy with the positron absent. We also assume that E is below the lowest continuum threshold of the system. The variational principle, as applied to the atomic system, readily gives inequality

$$\int d^3R \left[\int d^{3N}r |\vec{R}|^{1/2} \Psi^* H_0 |\vec{R}|^{1/2} \Psi \right] \geq E_0 \int d^3R \left[\int d^{3N}r |\vec{R}| |\Psi|^2 \right]; \quad (4)$$

with $|\vec{R}|^{1/2} \Psi$ treated as the trial function for the atomic system; the interior integration being carried out for a *fixed* \vec{R} . (This ‘‘fixed \vec{R} ’’ is only for bounding the integral and does not involve any adiabatic approximation.) Thus, one obtains

$$\langle |\vec{R}| \Psi | H_0 | \Psi \rangle \geq E_0 \langle |\vec{R}| \Psi | \Psi \rangle \quad (5)$$

a result analogous to Lieb’s inequality in Ref. [8]. We may take Ψ to be real, in view of the reality of H . Now, we have the following string of arguments:

$$\int d^3R \int d^{3N}r |\vec{R}| \Psi H \Psi = E \int d^3R \int d^{3N}r |\vec{R}| \Psi^2, \quad (6)$$

whence

$$\begin{aligned} & \int d^3R \int d^{3N}r |\vec{R}| \Psi H_0 \Psi + \int d^3R \int d^{3N}r |\vec{R}| \Psi \\ & \times \left\{ T_{\vec{R}} + Qe^2 V(\vec{R}) - Qe^2 \sum_{j=1}^N \frac{q_j}{|\vec{R} - \vec{r}_j|} \right\} \Psi \\ & = E \langle |\vec{R}| \Psi | \Psi \rangle \geq E_0 \langle |\vec{R}| \Psi | \Psi \rangle, \end{aligned} \quad (7)$$

since $\langle |\vec{R}| \Psi | \Psi \rangle > 0$. One thus finds that

$$\int d^3R \int d^{3N}r |\vec{R}| \Psi \left\{ T_{\vec{R}} + Qe^2 V(\vec{R}) - Qe^2 \sum_{j=1}^N \frac{q_j}{|\vec{R} - \vec{r}_j|} \right\} \Psi \leq 0 \quad (8)$$

Noting that $\nabla_{\vec{R}}^2 |\vec{R}|^{-1} = -4\pi \delta^{(3)}(\vec{R})$ [$\delta^{(3)}$ being the three-dimensional Dirac- δ function] along with the identification $g(\vec{R}) = |\vec{R}| \Psi$ with now the electronic coordinates fixed, an appeal to Lieb's proof leads to

$$-\frac{\hbar^2}{2M} \int d^3R g(\vec{R}) \nabla_{\vec{R}}^2 \left(\frac{g(\vec{R})}{|\vec{R}|} \right) = \frac{\hbar^2}{2M} \left[\int d^3R \frac{(\nabla_{\vec{R}} g(\vec{R}))^2}{|\vec{R}|} + 2\pi g^2(0) \right] > 0 \quad (9)$$

for any real $g(R)$ that is not identically zero (such as the present one). Therefore, a strict inequality emerges, viz.:

$$\int d^{3N}r \int d^3R |\vec{R}| \Psi T_R \Psi > 0. \quad (10)$$

Simultaneous validity of the inequalities (8) and (10) demands that

$$Z \int d^3R \int d^{3N}r \Psi^2 - \int d^3r \int d^{3N}r |\vec{R}| \Psi \left[\sum_{j=1}^N \frac{q_j}{|\vec{R} - \vec{r}_j|} \right] \Psi < 0, \quad (11)$$

where we have canceled the common factor $Qe^2 > 0$ without altering the above strict inequality. The inequality (11) gives a rigorous necessary condition for the existence of a bound state, in addition to the square-integrability of Ψ . Further, employing a normalized Ψ and specializing to electrons ($q_i = 1, m_i = m_e; i = 1, 2, \dots, N$), and noting the antisymmetry of Ψ (hence symmetry of Ψ^2) under an interchange of two electron coordinates, the above inequality simplifies to

$$Z \int d^3R |\vec{R}| \int d^3r \frac{D(\vec{r}, \vec{R})}{|\vec{R} - \vec{r}|} = \int d^3R |\vec{R}| \bar{\phi}(\vec{R}) \quad (12)$$

where the *joint* electron-positron ($Q = 1, M = m_e$) number density distribution $D(\vec{r}, \vec{R})$ is identified with

$$N \int |\Psi(\vec{r}_1, \vec{r}_2, \dots, \vec{r}_N; \vec{R})|^2 d^3r_2 \dots d^3r_N \equiv \left\langle \Phi \left| \sum_{i=1}^N \delta^{(3)}(\vec{r} - \vec{r}_i) \right| \Psi \right\rangle \geq 0. \quad (13)$$

Here $\bar{\phi}(\vec{R})$ is the magnitude of the "classical" electron-positron attractive potential at \vec{R} . The inequality (12) thus gives the desired necessary condition, which is a rigorous one and should be contrasted against the "adiabatic approximation" conditions of Refs. [1-3]. This condition may be used as a test for binding: only the electron-positron attractive potential derived from an optimal variational wave function is needed here, bringing out a reduction from a multivariate problem to a three dimensional one.

From the definition of D , the following connections emerge: $N^{-1} \int D(\vec{r}, \vec{R}) d^3r = p(\vec{R})$; and $\int D(\vec{r}, \vec{R}) d^3R = n(\vec{r})$, where p and n are respectively, the positron and electron number densities. The conjecture of Patrick and Cade,⁷ Golden and Epstein³ and such other independent particle models¹² that a neutral S -state atom and an S -state positron will not always bind together may now be escalated to a more rigorous footing. For a zero-angular momentum state of the positron, and *in particular*, when D depends only on the distances of its arguments from the nucleus, it is demonstrable that a neutral atom-positron binding is impossible. Thus if $D(\vec{r}, \vec{R}) \equiv D(r, R)$, then

$$\int d^3r \frac{D(r, R)}{|\vec{R} - \vec{r}|} = \frac{1}{R} \int_0^R D(r, R) 4\pi r^2 dr + \int_0^R D(r, R) 4\pi r dr \leq NR^{-1}P(R), \quad (14)$$

where we have used, in the second integral $1/r \leq 1/R$ (cf. Ref. [13]). Thus from the inequality (12) it follows that binding necessitates $Z < N$, which immediately rules out binding of a

positron to neutral atoms *under the above premise*. The same conclusion is also arrived at through the following:

$$\begin{aligned} \int d^3r \int d^3R \frac{RD(r,R)}{|\vec{R}-\vec{r}|} \\ = \int d^3r \left[\int_0^r dR \frac{4\pi R^3}{D(r,R)_r} + \int_r^\infty dR D(r,R) r \pi R^2 \right] \\ \leq \int d^3r n(r) = N. \end{aligned} \quad (15)$$

Thus, in fact it suffices to have the function D to be spherically symmetric in *either* the positron *or* the electron coordinate. Similar arguments hold good in that case.

It is gratifying that a necessary condition for atom-positron bound state is derivable in terms of the first moment of a one-particle quantity $\phi(\vec{R})$ which has a direct physical interpretation as the magnitude of the electron-positron attractive potential. Further, for a zero-angular momentum atom *or* a positron, neutral atom-positron bound states are impossible.

3. EXACT DIFFERENTIAL EQUATION FOR THE POSITRON DENSITY

To this end, in the spirit of Levy *et al.*,¹⁴ we construct a function Φ with the prescription

$$\Phi_{\vec{R}}(\vec{r}_1, \vec{r}_2, \dots, \vec{r}_N) \equiv \Phi_{\vec{R}}(\{\vec{r}_j\}) = [p(\vec{R})]^{-\frac{1}{2}} \Psi(\{\vec{r}_j\}, \vec{R}).$$

Notice that Φ incorporates a parametric dependence on \vec{R} , the positron coordinate. By construction, $\langle \Phi_{\vec{R}} | \Phi_{\vec{R}} \rangle = 1$, for every \vec{R} , where the integration is performed over the configuration space of the electrons. We now have $(H(\{\vec{r}_j\}, \vec{R}) - E_o) \Psi(\{\vec{r}_j\}, \vec{R}) = (E - E_o) \Psi(\{\vec{r}_j\}, \vec{R}) \equiv \mu \Psi(\{\vec{r}_j\}, \vec{R})$, where E_o is the ground state energy of the N-electron system (with the positron absent). Premultiplying this equation by $\Phi_{\vec{R}}^*(\{\vec{r}_j\})$ throughout and integrating over the electronic degrees of freedom, and simplifying, one arrives at

$$\begin{aligned} \{ \langle \Phi_{\vec{R}} | H_o - E_o | \Phi_{\vec{R}} \rangle - \int d^3r \frac{n^-(\vec{r}, \vec{R})}{|\vec{r} - \vec{R}|} + v_{ext}^{(+)}(\vec{R}) \} [p(\vec{R})]^{\frac{1}{2}} \\ - \frac{1}{2} \int d^{3N}r \Phi_{\vec{R}}^*(\{\vec{r}_j\}) \nabla_{\vec{R}}^2 ([p(\vec{R})]^{\frac{1}{2}} \Phi_{\vec{R}}(\{\vec{r}_j\})) = \mu [p(\vec{R})]^{\frac{1}{2}}. \end{aligned} \quad (16)$$

Here, $n^-(\vec{r}_1, \vec{R})$ is identified with $N \int |\Phi_{\vec{R}}(\{\vec{r}_j\})|^2 d^3r_2 \dots d^3r_N$. In view of the time-reversal-invariance of H ,¹¹ assuming $\Phi_{\vec{R}}(\{\vec{r}_j\})$ to be real, so that invoking $\vec{\nabla}_{\vec{R}} \int \Phi_{\vec{R}}^2 d^{3N}r = \vec{0}$ and $\nabla_{\vec{R}}^2 \int |\Phi_{\vec{R}}|^2 d^{3N}r = 0$, one obtains the desired equation

$$\begin{aligned} \{ -(1/2) \nabla_{\vec{R}}^2 + v_{ext}^{(+)}(\vec{R}) - \int d^3r \frac{n^-(\vec{r}, \vec{R})}{|\vec{r} - \vec{R}|} + \\ \int d^{3N}r \frac{(\vec{\nabla}_{\vec{R}} \Phi_{\vec{R}}(\{\vec{r}_j\}))^2}{2} + \langle \Phi_{\vec{R}} | H_o - E_o | \Phi_{\vec{R}} \rangle \} \sqrt{p(\vec{R})} \\ = \mu \sqrt{p(\vec{R})}, \end{aligned} \quad (17)$$

which is an exact differential equation satisfied by the positron density. Note that the second, fourth and fifth terms bracketed on the left side of Eq. (17) pose a non-negative contribution to the total "effective potential." The asymptotic behavior of the positron density is now

derivable by taking the extreme limit, $R \rightarrow \infty$. In this event, the function $\Phi_{\vec{R}}(\{\vec{r}_j\})$ merges into the N-electron ground state $\Psi_o(\{\vec{r}_j\})$ (or into a degenerate linear combination of ground states with the same energy E_o), so that all the “effective potential” terms of Eq. (17) vanish, leading to

$$\nabla_{\vec{R}}^2 \sqrt{p(\vec{R})} = -2\mu \sqrt{p(\vec{R})} \quad (R \rightarrow \infty) \quad (18)$$

whence, for s-state positrons in an atomic or ionic (single center) situation,

$$p(\vec{R})_{R \rightarrow \infty} \sim \exp(-2\sqrt{-2\mu}R)$$

implying an exponential asymptotic decay. Note that in the foregoing analysis, we have tacitly assumed that the positron has formed a bound state, giving $\mu < 0$.

Acknowledgements

This work was supported by the UGC, New Delhi, India through a research grant[No. F. 10-15/92(RBB-II)].

REFERENCES

- [1] F. H. Gertler, H. B. Snodgrass, and L. Spruch, Phys. Rev. **172**, 110(1968);
- [2] I. Aronson, C. J. Kleinman, and L. Spruch, Phys. Rev. A **4**, 841(1971);
- [3] S. Golden and I. R. Epstein, Phys. Rev. A **10**, 761 (1974);
- [4] J. Schwinger, Proc. Natl. Acad. Sci. U. S. A. **47**, 122(1961); see also E. H. Lieb, Rev. Mod. Phys. **48**, 533(1976);
- [5] V. Bargmann, Proc. Natl. Acad. Sci. U. S. A. **38**, 961(1952);
- [6] D. C. Clary, J. Phys B **9**, 3115(1976);
- [7] A. J. Patrick and P. E. Cade, J. Chem. Phys. **75**, 1903(1981);
- [8] E. H. Lieb, Phys. Rev. Lett. **52**, 315(1984); Phys. Rev. A. **29**, 3018(1984);
- [9] E. H. Lieb, I. M. Sigal, B. Simon, and W. Thirring, Phys. Rev. Lett. **52**, 994(1984);
- [10] R. Benguria and E. H. Lieb, Phys. Rev. Lett. **50**, 1771(1983);
- [11] See, for example, L. I. Schiff, *Quantum Mechanics*, 3rd ed. (McGraw-Hill, New York, 1968), Sec. 29, p. 233;
- [12] J. G. Harrison, J. Chem. Phys. **84**, 1659(1986);
- [13] E. H. Lieb, Phys. Lett. **70A**, 444(1997); see also E. H. Lieb and S. Oxford, Int. J. Quantum Chem. **19**, 427(1981);
- [14] M. Levy, J. P. Perdew, and V. Sahni, Phys. Rev. A **30**, 2745 (1984).

This page intentionally left blank

CROSSOVER FROM THE DEGENERATE TO THE CLASSICAL REGIME OF A STRONGLY INTERACTING 2D HOLE LAYER

S. Shapira,¹ U. Sivan,² P.M. Solomon,³ E. Buchstab,² M. Tischler³ and G. Ben Yoseph²

¹ Cavendish Laboratory, Madingley Road,
Cambridge CB3 0HE, UK. e-mail: ss245@cus.cam.ac.uk

² Solid State Inst. and Physics Dept.,
Technion - Israel Inst. of Technology, Haifa 32000, Israel.

³ IBM, T. J. Watson Research Center,
Yorktown Heights, NY 10598, USA.

A degenerate hole layer in GaAs is a strongly interacting two dimensional fermion system. The large hole mass ($m = 0.4 m_0$) leads to large values, $5 < r_s < 24$ of the ratio $r_s \equiv U/E_F$ ($U \equiv (e^2/4\pi\epsilon) \times \sqrt{\pi p}$ being the average interparticle coulomb energy at density p , and E_F the fermi energy). The low temperature behavior of this system is therefore dominated by interaction induced quantum correlations which are close to the value predicted for wigner crystallization, $r_s = 37$ ¹.

We describe here a measurement of the inverse thermodynamic density of states (ITDOS), $\partial\mu/\partial p$, of a two dimensional hole layer in which the temperature is varied from values lower than the fermi energy up to temperatures higher than the interaction energy (and consequently more than an order of magnitude higher than the degeneracy temperature). The behavior of the system correspondingly crosses over from that of a strongly interacting degenerate system to that of an ideal classical layer and agrees with the theoretical predictions for these two regimes. This work focuses on the crossover between these two limits. While heretofore, no theoretical or experimental studies of this regime have been conducted, we find it to display a rich number of features. At low temperatures the ITDOS is negative and temperature independent. At $T \approx 17$ K temperature dependence commences abruptly for all densities. $\partial\mu/\partial p \approx \partial\mu/\partial p(T=0) + k_B T/p$ turning less negative with a slope similar to that of an ideal gas. The ITDOS reverses sign simultaneously at all densities. We find this behavior similar to that of the specific heat in other strongly correlated systems.²

At temperatures comparable to the interaction energy the slope of $\partial\mu/\partial p$ with respect to p is enhanced as the layer crosses over to an ideal classical gas. A classical gas is attained at temperatures more than an order of magnitude larger than the fermi temperature.

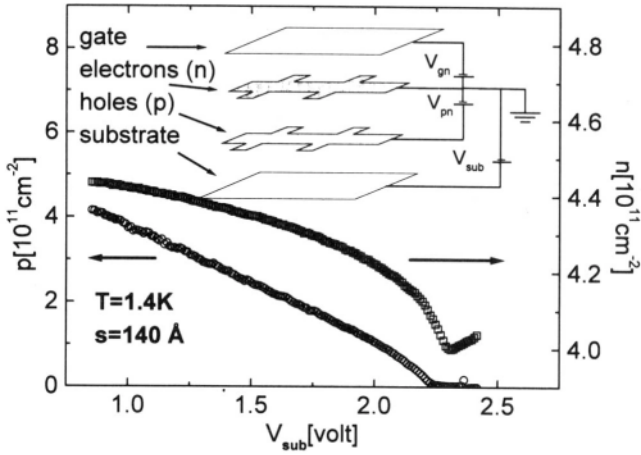


Fig 1: Typical n,p data at low temperatures. Inset: schematic description of the system as a four plate capacitor with the middle plates patterned as hall bars.

The devices we used in this experiment house a two dimensional hole layer adjacent to an electronic one the layers are separated by a $s=140\text{\AA}$ (400\AA in another device) AlGaAs barrier³. The layers are separately contacted and a conducting substrate and a gate allow the variation of the layer densities. The structure, thus, can be effectively described as a four plate capacitor with the electron and hole layers being represented by the middle two plates (fig. 1, inset). The layers are patterned in the form of hall bars, thus the densities and mobilities of both layers are monitored simultaneously.

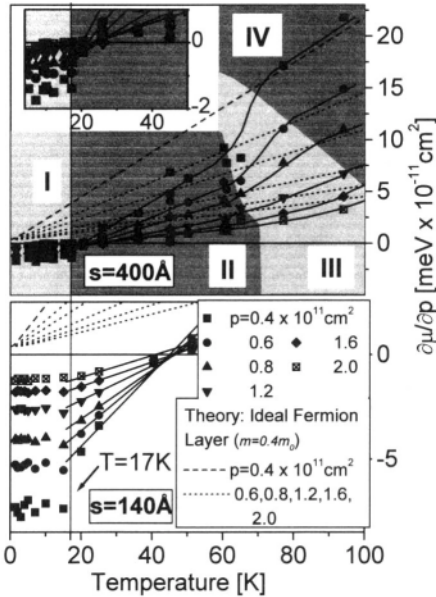


Fig. 2: $\partial\mu/\partial p$ vs. T for various hole concentrations compared to the behavior of an ideal fermion layer. The data from the thin barrier sample is limited to $T < 50\text{K}$ due to leakage through the barrier. The regimes marked I-IV are described in the text. Inset: expanded low temperature data for the $s=400\text{\AA}$ barrier device.

We measure the hole layer ITDOS via a three layer capacitive measurement.⁴ The conducting substrate is utilized as a gate to vary the hole layer density. The ITDOS of the hole layer is then measured in the following manner: an external battery sets a constant electrochemical potential difference, eV_{pn} , between the hole layer and the adjacent “probe” electron layer. Due to this coupling (neglecting interlayer correlations between truly two dimensional layers) the sum of the variation of the chemical potentials in both layers, and the electrostatic interlayer energy, is zero:

$$\delta\mu + \delta\mu_n + (e^2 s/\epsilon) * \delta n = e\delta V_{pn} = 0.$$

The variation in the hole chemical potential is therefore compensated by the variation of the interlayer electrostatic energy, $(e^2 s/\epsilon) * \delta n$, and the electronic layers’ chemical potential. Thus

$$\frac{\delta n}{\delta p} = -\frac{\epsilon e^2}{s + d_n} \frac{\partial \mu}{\partial p}, \text{ where } d_n = \frac{\epsilon}{e^2} \frac{\partial \mu_n}{\partial n}$$

is the two dimensional screening length of the electronic layer, and s the electron hole layers separation.

The Hartree effects due to the finite well width slightly modify this relation. They are accounted for by calculating the total free energy of the system using the Fang Howard variational wavefunctions.⁵ Requiring the total free energy to be a minimum yields equations which link $\partial\mu/\partial p$ to $\partial n/\partial p$ which is derived from the n, p data (fig. 1).

The resulting $\partial\mu/\partial p$ derived from measurement of devices with interlayer separations $s=140,400\text{\AA}$ is presented in fig. 2. The difference in the low temperature values of $\partial\mu/\partial p$ for the different barrier separations suggest the importance of interlayer correlations which should be enhanced for adjacent electron and hole layers.⁶

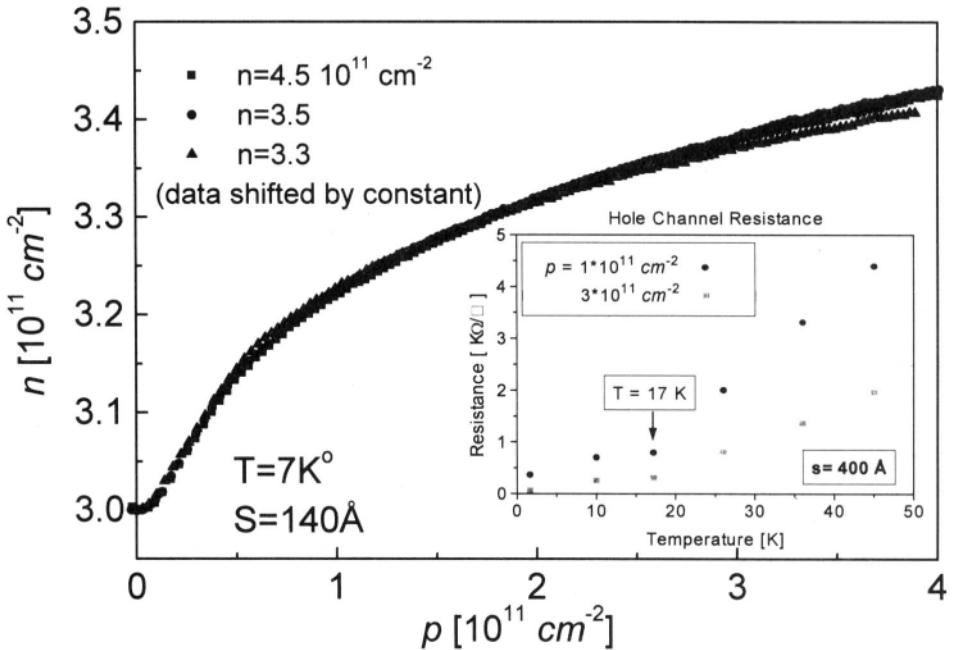


Fig 3: Data taken at different densities of the probing electronic layer, demonstrating the absence of dependence on these densities. Inset: temperature dependence of the hole layer resistance, displaying a sharp change at $T=17\text{K}$ similar to the one displayed by the ITDOS.

Four distinct regimes are observed (fig. 2):

- I. The low temperature regime ($T < 17K$).** The ITDOS, $\partial\mu/\partial p$, is negative^{1,4} and its magnitude diverges as the density diminishes. It is temperature independent throughout although the hole layer turns non degenerate within this region (e.g. the degeneracy temperature for a hole layer density of 10^{11} cm^{-2} is about 6° K). The negative divergence of $\partial\mu/\partial p$ as $p \rightarrow 0$ is theoretically accounted for¹ by exchange and quantum correlations.
- II. “Intermediate” regime ($T > 17K$).** The temperature dependence begins abruptly at $T = 17K$ for all densities. It is accompanied by a similar behavior of the hole channel resistance (fig. 3, inset). The negative value of $\partial\mu/\partial p$ at low temperatures demonstrates that in this regime the layer is interaction dominated. Nevertheless the correlated liquid we observe displays the behavior of a classical ideal gas shifted down by the (negative) low temperature values of an interacting layer, $\partial\mu/\partial p \approx \partial\mu/\partial p(T = 0) + k_B T/p$. When the temperature is raised, the negative sign of $\partial\mu/\partial p$ is reversed as it vanishes almost simultaneously.
- III. The crossover regime.** The variation of $\partial\mu/\partial p$ with temperature is enhanced in this regime as the correlated liquid crosses over from the “intermediate regime” behavior and becomes an ideal classical gas. The regime is bounded within values of the classical plasma parameter $0.65 < \Gamma = U/k_B T < 1.5$ while the temperatures exceed the degeneracy temperature by a factor of ~ 7 .
- IV. Ideal classical gas.** At sufficiently high temperatures a classical ideal gas behavior is observed. The slope of $\partial\mu/\partial p$ with temperature decreases and $\partial\mu/\partial p$ assumes the classical ideal gas values, $\partial\mu/\partial p = k_B T/p$. The transition happens in our system at $\Gamma = 0.7 - 0.9$ ($T = 70 - 94 \text{ K}$ for $p = 1.6 - 0.4 * 10^{11} \text{ cm}^{-2}$). The Fermi energy is about an order of magnitude smaller than the temperature demonstrating that the physics is interaction dominated.

The behavior observed in the low temperature and ideal classical gas complies with theory.³ Regimes II, III have yet to be explored theoretically and their data is therefore due a closer examination.

The temperature dependence of the ITDOS in regime II implies that the contribution of interactions to the ITDOS is temperature independent up to temperatures $k_B T \approx U$ which are almost an order of magnitude higher than the fermi temperature. The linear slope with temperature being due to entropy as in an ideal gas. The ITDOS observed for an electron gas ($1 < r_s < 4$) displays a different behavior crossing over smoothly from the low temperature behavior to an ideal gas at around the degeneracy temperature⁷. While degeneracy effects seem not to play a role⁸ in the strongly interacting hole system they are important in the electronic one, although it is also found in the $1 < r_s$ regime.

The “crossing” point in regime II where the ITDOS almost simultaneously vanishes for all densities may be an fortuitous combination of circumstances, however, we point out that a similar effect has been observed for the temperature and pressure dependence of the specific heat of other strongly correlated systems² and may have a deeper origin.

The ITDOS measured for samples with two different layer separations $s = 140, 400 \text{ \AA}$, qualitatively display the same features. Nevertheless the magnitudes at low temperatures differ by a factor of 3. While interlayer correlations are expected to affect the ITDOS of each layer,⁶ we have tested the dependence of the measured hole ITDOS on the density of the probing electronic layer, and have found no such effect within the range of densities accessible in our experiment (fig. 3). The layer separation, may however enhance the overall value of the measured ITDOS.

In summary, the thermodynamics of a two dimensional hole layer at large r_s numbers was characterized by measuring the inverse thermodynamic density of states.. Four distinct regimes have been identified in the density-temperature plane (fig. 2). At low temperatures $\partial\mu/\partial p$ is negative and qualitatively agrees with theory.^{1,3} They are temperature independent up to $T \approx 17$ K where the temperature dependence appears abruptly for all hole densities. The dependence of $\partial\mu/\partial p$ on temperature is at first very similar to that of an ideal classical gas, $\partial\mu/\partial p = k_B T/p$, shifted down by a constant value. As the temperature is further increased, $\partial\mu/\partial p$ reverses sign almost simultaneously at all hole densities, indicating a metallic screening at finite densities and temperatures. At higher temperatures a crossover is observed to an ideal classical gas which is attained at temperatures higher than the interaction energy and almost an order of magnitude higher than the degeneracy temperature.

REFERENCES

1. B. Tanatar and D.M.Ceperely, Phys. Rev. B **39**, 5005(1989) .
2. Vollhardt, Phys.Rev. Lett. **78** p 1307 (1997)
3. S.Shapira, U. Sivan, P.M. Solomon, E. Buchstab, M. Tischler and G. Ben Yoseph, Phys. Rev. Lett. **77** p 3181 (1996).
4. J. Eisenstein , L. Pfeiffer, K. West, Phys. Rev. Lett. **68**, 674 (1992); (our system is actually four plate but the residual penetration of field to the fourth plate will actually leads to an underestimation of the ITDOS by much less than a percent of its measured value.)
5. F. F. Fang and W. E. Howard, Phys. Rev. Lett. **16**, 797 (1966).
6. L. Swierkowski, J. Szymanski, and Z.W. Gortel, Phys. Rev. Lett. **74**, 3245 (1995).
7. I. Millard, N. Patel private communication
8. The T=17K transition is density independent.

This page intentionally left blank

EXCHANGE-CORRELATION POTENTIALS IN THE ELECTRON GAS

S. Conti, R. Nifosì, and M. P. Tosi

Istituto Nazionale di Fisica della Materia and Scuola Normale Superiore
I-56126 Pisa, Italy

INTRODUCTION

The so-called STLS theory of Singwi *et al.*¹ gave a central role to the local structure of the electron gas and to its consistency with dynamical structure. The accuracy of the STLS predictions for the ground state energy as a function of the coupling strength r_s was verified by the Quantum Monte Carlo (QMC) work of Ceperley and Alder² (see Table 1). With regard to the density-fluctuation spectrum the STLS theory predicted strong renormalization of the plasmon dispersion and of the electron-hole pair continuum from short-range correlations. These predictions have been confirmed by electron-energy-loss³ and inelastic X-ray scattering⁴ experiments.

Recent developments in Density Functional Theory⁵ (DFT) for treating the dynamical properties of inhomogeneous electron systems beyond the adiabatic local density approximation (ALDA) provide motive for a quantitative study of the excitation spectrum of long-wavelength density fluctuations in the electron gas⁶ and for its extension to the spectrum of transverse current fluctuations.⁷ The main excitation process in these spectra at long wavelengths is associated with the creation of two correlated electron-hole pairs.

EXCHANGE-CORRELATION POTENTIALS

In brief, the work of Vignale and Kohn⁵ shows that the evolution of the density $n(\mathbf{r}, t)$ in an inhomogeneous electron system subject to a time-dependent *scalar* external potential can be studied by single-particle equations! in a local approximation for exchange and correlation (xc), provided that these are described through a *vector* potential $\mathbf{a}^{xc}(\mathbf{r}, \omega)$. For slowly varying densities, known symmetries and conservation laws allow one to express $\mathbf{a}^{xc}(\mathbf{r}, \omega)$ exactly in

Table 1. Ground-state energy of the electron gas (Rydbergs/electron).

r_s	1	2	5	10	20
RPA	1.137	-0.030	-0.180	—	—
STLS ¹	1.170	0.002	-0.151	-0.106	-0.062
QMC ²	1.174	0.0041	-0.1512	-0.10675	-0.06329

terms of long-wavelength xc potentials $f_{xc}^{L,T}(\omega)$ for the homogeneous electron gas. These are defined as the $k \rightarrow 0$ limit of

$$f_{xc}^{L,T}(k, \omega) = \frac{\omega^2}{k^2} \left\{ \frac{1}{\chi_{L,T}^0(k, \omega) + \rho/m} - \frac{1}{\chi_{L,T}(k, \omega) + \rho/m} \right\} - v_{L,T}. \quad (1)$$

Here, $\chi_{L(T)}$ is the current–current longitudinal (transverse) response of the electron gas at density $\rho = n_0(\mathbf{r})$, $\chi_{L(T)}^0$ is the equivalent ideal-gas quantity, $v_L = 4\pi e^2/k^2$ and $v_T = 0$. The longitudinal xc potential is related to the frequency-dependent local field factor $G(k, \omega)$ introduced in the STLS theory by $G(k, \omega) = -f_{xc}^L(k, \omega)/v_L$. Terms beyond the ALDA correspond to complex, frequency-dependent viscoelasticity coefficients.⁸

In our calculations of the dynamic xc potentials^{6,7} we use the equation of motion for the current density operator to find the exact relation

$$\ll \mathbf{j}_{\mathbf{k}}^i; \mathbf{j}_{-\mathbf{k}}^j \gg_{\omega} = \frac{1}{\omega^2} \langle [\mathbf{j}_{\mathbf{k}}^i, H], \mathbf{j}_{-\mathbf{k}}^j \rangle - \frac{1}{\omega^2} \ll [\mathbf{j}_{\mathbf{k}}^i, H]; [\mathbf{j}_{-\mathbf{k}}^j, H] \gg_{\omega} \quad (2)$$

for the current–current response function. The first term on the RHS fixes the high frequency limit, which is related to the leading spectral moments. We approximately decouple the four-point response function in Eq. (2) into products of two-point response functions, thus including by construction the processes of excitation of two electron–hole pairs. The result for the longitudinal (transverse) spectrum is:

$$\begin{aligned} \text{Im}f_{xc}^{L,T}(\omega) = & - \int_0^{\omega} \frac{d\omega'}{\pi} \int \frac{d^3q}{(2\pi)^3 \rho^2} v_q^2 \frac{q^2}{(\omega - \omega')^2} \text{Im}\chi_L(q, \omega - \omega') \\ & \times \left[a_{L,T} \frac{q^2}{\omega'^2} \text{Im}\chi_L(q, \omega') + b_{L,T} \frac{q^2}{\omega'^2} \text{Im}\chi_T(q, \omega') \right] \end{aligned} \quad (3)$$

with $a_L = 23/30$, $a_T = 8/15$, $b_L = 8/15$ and $b_T = 2/5$. The real part of f_{xc} is then obtained via the Kramers–Kronig relation. The expression for the longitudinal part in Eq. (3) is equivalent to that obtained by Hasegawa and Watabe⁹ by diagrammatic means. In our calculations the expression (3) was modified by a frequency-dependent factor to enforce the compressibility sum rule and to allow for final-state exchange processes, which in perturbative treatments reduce the total two-pair spectral weight by a factor of 2 at high frequency. The high-frequency form of our final results then agrees with that given by Glick and Long¹⁰ for the longitudinal term.

In our calculations we find that the shapes of the longitudinal and transverse xc spectra are very similar. In fact, the xc transverse spectrum is accurately reproduced at all frequencies by setting $\text{Im}f_{xc}^T(\omega) \simeq 0.72 \text{Im}f_{xc}^L(\omega)$, whereas for the real part there is an additional shift due to the different asymptotic values.⁷

The spectral structure of the xc potentials emerges from Eq. (3) when one uses the RPA for the response functions in the RHS. The RPA longitudinal response contains contributions from the single-pair continuum and from the sharp plasmon excitation. In turn this leads to structure in the xc potentials from a threshold for the two-plasmon channel at twice the plasma frequency. As we are neglecting retardation the transverse response contains only a broad continuum and is dominant at low frequency. The analysis of the longitudinal spectrum into its various channels is shown in Figure 1.

Our curves for $\text{Re}f_{xc}$ exhibit a sharp minimum at 2ϕ , which corresponds to the threshold found in $\text{Im}f_{xc}$. Its physical origin lies in the large spectral strength of the plasmon excitation as compared to single-pair excitations, which accumulates the strength of two-pair processes near 2ϕ . This structure becomes sharper with increasing r_s . When exchange and short-range correlations are included in the response functions in the RHS of Eq. (3), the

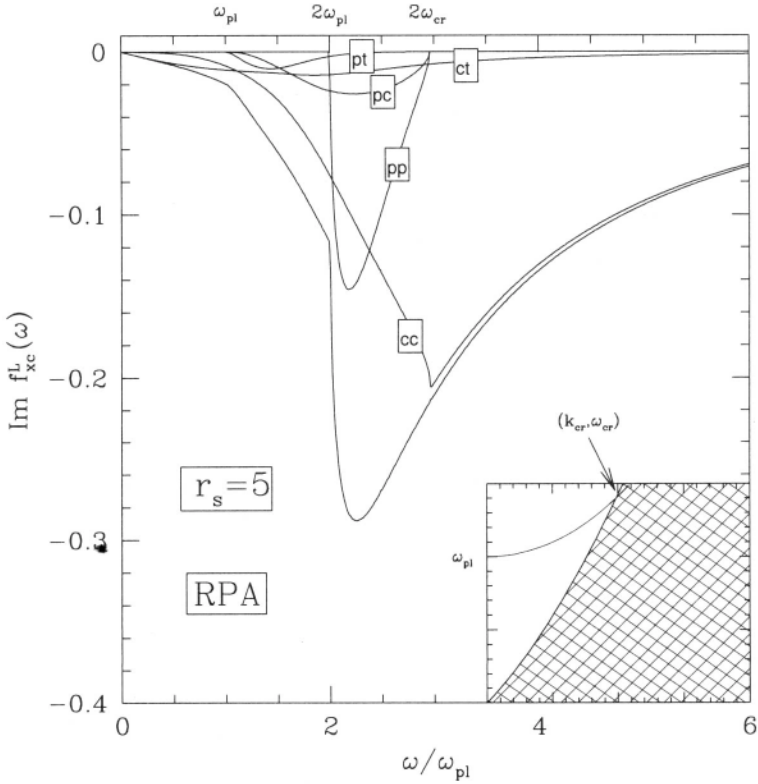


Figure 1. Channels of paired modes (c=single-pair continuum, p=plasmon, t=transverse) contributing to the longitudinal spectrum in an RPA calculation at $r_s = 5$.

structure associated with the two-plasmon contribution becomes much sharper as the plasmon dispersion curve flattens out with increasing r_s . This is seen from Figure 2, comparing $\text{Im}f_{xc}$ and $\text{Re}f_{xc}$ as obtained from RPA and from STLS response functions at $r_s = 5$. The smooth interpolation proposed by Gross and Kohn¹¹ (GK) is also shown in Figure 2.

SUMMARY AND CONCLUDING REMARKS

In summary, we have presented a model for the longitudinal and transverse xc potentials of the homogeneous electron gas. Our results have been fitted⁷ to analytic expressions to facilitate their use as input for DFT calculations in the linearized long-wavelength regime.

Similar calculations of the xc potentials in a two-dimensional electron gas with e^2/r interactions show spectral structure and non-monotonic behavior in $\text{Re}f_{xc}$, even though in 2D the plasma frequency vanishes at long wavelengths.¹² Earlier calculations were done by Holas and Singwi.¹³

Available data on the plasmon dispersion coefficient in alkali metals³ indicate strong deviations from RPA with increasing coupling strength. Although band-structure effects play a significant role in a quantitative comparison, the dynamic correction indicated by our results for $\text{Re}f_{xc}$ improves the agreement with the experimental data. The spectral structure at $2\omega_{pl}$ may possibly be observable in electron-energy-loss experiments on a metal such as Rb, in which the plasmon dispersion curve is almost flat.

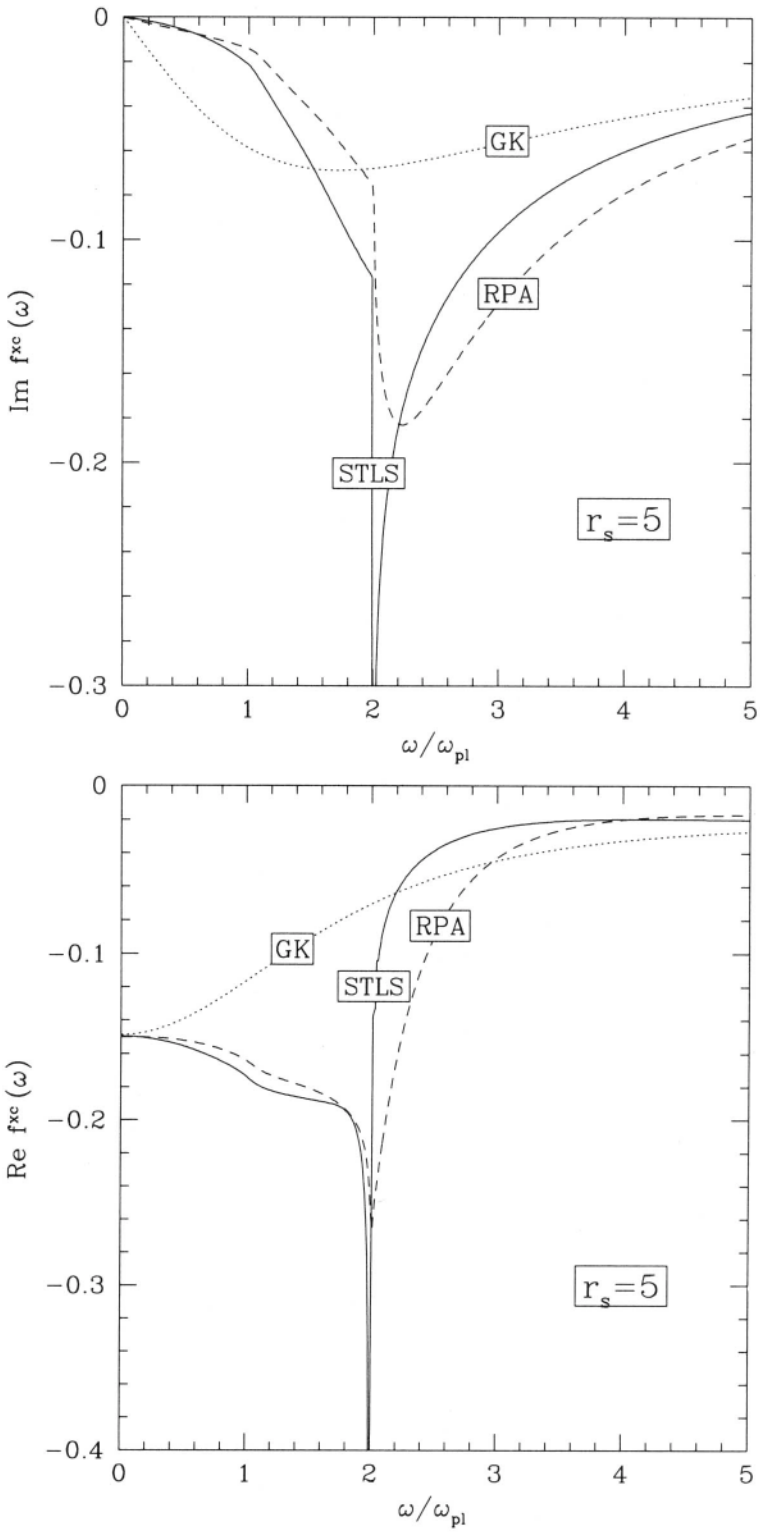


Figure 2. Longitudinal xc potential at $r_s = 5$ from RPA and STLS calculations.

REFERENCES

- [1] K. S. Singwi, M. P. Tosi, R. H. Land and A. Sjölander, Electron correlations at metallic densities, *Phys. Rev.*, 176:598 (1968).
- [2] D. M. Ceperley and B. J. Alder, Ground state of the electron gas by a stochastic method, *Phys. Rev. Lett.*, 45:566 (1980).
- [3] A. vom Felde, J. Sprösser-Prou and J. Fink, Valence-electron excitations in the alkali metals, *Phys. Rev. B*, 40:10181 (1989).
- [4] P. M. Platzman and P. Eisenberger, Presence of an incipient Wigner electron lattice in solid-state electron gases, *Phys. Rev. Lett.*, 33:152 (1974).
- [5] G. Vignale and W. Kohn, Current-dependent exchange-correlation potential for dynamical linear response theory, *Phys. Rev. Lett.*, 77:2037 (1996).
- [6] H. M. Böhm, S. Conti and M. P. Tosi, Plasmon dispersion and dynamic exchange-correlation potential from two-pair excitations in degenerate plasmas, *J. Phys.: Condens. Matter*, 8:781 (1996).
- [7] S. Conti, R. Nifosì and M. P. Tosi, Exchange-correlation potential for Current Density Functional Theory of frequency dependent linear response, *J. Phys.: Condens. Matter*, 9:L475 (1997).
- [8] G. Vignale, C. A. Ullrich and S. Conti, Time-dependent density functional theory beyond the adiabatic local density approximation, preprint cond-mat/9706306 (1997).
- [9] M. Hasegawa and M. Watabe, Theory of plasmon damping in metals, *J. Phys. Soc. Jpn.*, 27:1393 (1969).
- [10] A. J. Glick and W. F. Long, high-frequency damping in a degenerate electron gas, *Phys. Rev. B*, 4:3455 (1971).
- [11] E. K. U. Gross and W. Kohn, Local density-functional theory of frequency-dependent linear response, *Phys. Rev. Lett.*, 55:2850 (1985); *ibid* 57:923 (1986).
- [12] R. Nifosì, S. Conti and M. P. Tosi, Dynamic exchange-correlation potentials for the 2D electron gas, *Physica E*, to appear (1997).
- [13] A. Holas and K. S. Singwi, High-frequency damping of collective excitations in fermion systems, *Phys. Rev. B*, 40:158 (1989).

This page intentionally left blank

WIGNER APPROACH AND GENERALIZATION MOLECULAR DYNAMICS METHOD IN QUANTUM THEORY OF STRONGLY COUPLED SYSTEMS OF PARTICLES

Vladimir Filinov,¹ Yurii Lozovik, Alex Filinov,² and Igor Zacharov³

¹'IVTAN' Association, Russian Academy of Sciences

High Energy Density Research Center

Izhorskaya str. 13/19, Moscow, 127412, Russia

²Institute of Spectroscopy, Russian Academy of Sciences

Troitsk, Moscow region, 142092, Russia

³Silicon Graphics Computer Systems, SGI Europe

Grand Atrium, route des Avouillons 30

1196 Gland, Switzerland

WIGNER REPRESENTATION

Our starting point is a general operator expression for canonical ensemble averaged time correlation function:¹

$$C_{FA}(t) = Z^{-1} \text{Tr} \left(\hat{F} \exp \left(i\hat{H}t_c^*/\hbar \right) \hat{A} \exp \left(-i\hat{H}t_c/\hbar \right) \right)$$

Here \hat{H} is a Hamiltonian of the system, $t_c = t - i\hbar\beta/2$, $\beta = 1/k_B T$, \hat{F} and \hat{A} are quantum operators of considered dynamic quantities, $Z = \text{Tr} \left(\exp \left(-\beta\hat{H} \right) \right)$ is partition function. Wigner representation of the time correlation function can be written as:

$$C_{FA}(t) = \frac{1}{(2\pi\hbar)^{2v}} \int \int dp_1 dq_1 dp_2 dq_2 F(p_1, q_1) A(p_2, q_2) \times \\ \times W(p_1, q_1; p_2, q_2; t; i\hbar\beta)$$

where the spectral density $W(p_1, q_1; p_2, q_2; t; i\hbar\beta)$ is defined by:

$$W(p_1, q_1; p_2, q_2; t; i\hbar\beta) = Z^{-1} \int \int d\xi_1 d\xi_2 \exp \left(i\frac{p_1\xi_1}{\hbar} \right) \exp \left(i\frac{p_2\xi_2}{\hbar} \right) \times \\ \times \left\langle q_1 + \frac{\xi_1}{2} \left| \exp \left(i\hat{H}t_c^*/\hbar \right) \right| q_2 - \frac{\xi_2}{2} \right\rangle \left\langle q_2 + \frac{\xi_2}{2} \left| \exp \left(-i\hat{H}t_c/\hbar \right) \right| q_1 - \frac{\xi_1}{2} \right\rangle$$

and $F(p_1, q_1)$ and $A(p_2, q_2)$ are Weyl's symbols of operators \hat{F} and \hat{A} :²

$$A(p, q) = \int d\xi \exp \left(-i\frac{p\xi}{\hbar} \right) \left\langle q - \frac{\xi}{2} \left| \hat{A} \right| q + \frac{\xi}{2} \right\rangle$$

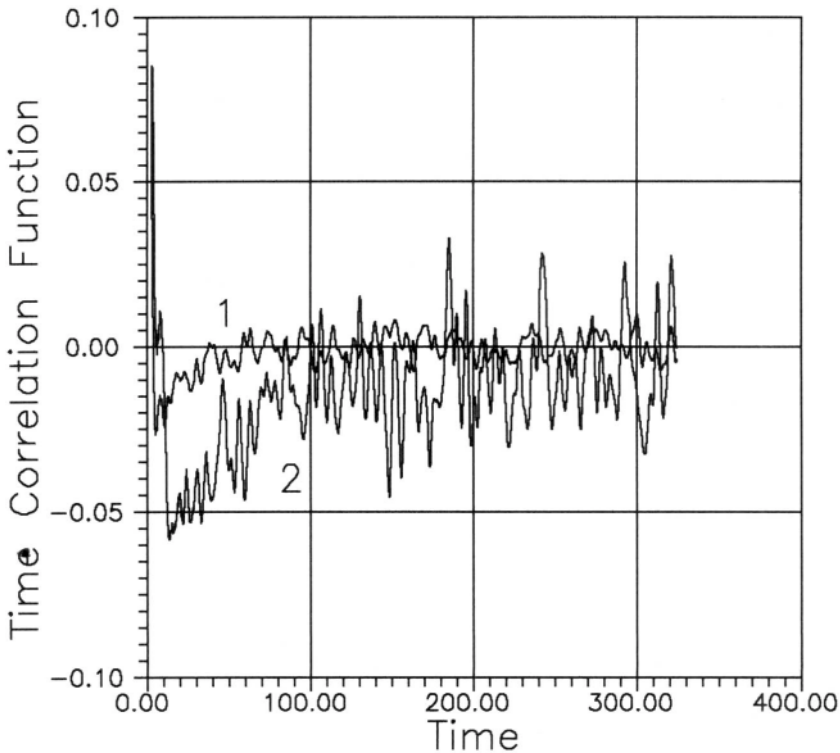


Figure 1. Momentum–momentum time correlation function versus tV_0/\hbar for temperature $kT/V_0 = 0.04$ for 1D case: 1 — approximation of the classical trajectories; 2 — quantum trajectories

where $\langle q' | \hat{A} | q'' \rangle$ are matrix elements and u is the space dimension. So the problem of numerical calculation of the canonically averaged time correlation function can be reduced to the consideration of the evolution of the spectral density satisfying to the following integral equation:

$$W(p_1, q_1; p_2, q_2; t; i\hbar\beta) = \bar{W}(\bar{p}_0, \bar{q}_0; \bar{p}_0, \bar{q}_0; i\hbar\beta) + \int_0^t d\tau \int ds d\eta W(\bar{p}_\tau - s, \bar{q}_\tau; \bar{p}_\tau - \eta, \bar{q}_\tau; \tau; i\hbar\beta) \gamma(s, \bar{q}_\tau; \eta, \bar{q}_\tau) \quad (1)$$

where

$$\gamma(s, \bar{q}_\tau; \eta, \bar{q}_\tau) = \frac{1}{2} \{ \omega(s, \bar{q}_\tau) \delta(\eta) - \omega(\eta, \bar{q}_\tau) \delta(s) \},$$

$\delta(s)$ is the Dirac delta function, $\omega(s, q)$ is defined by the expression:

$$\omega(s, q) = \frac{4}{(2\pi\hbar)^{1/2}} \int dq' V(q - q') \sin\left(\frac{2sq'}{\hbar}\right) + F(q) \frac{d\delta(s)}{ds}$$

while $\{\bar{q}_\tau(\tau; p_1, q_1, t), \bar{p}_\tau(\tau; p_1, q_1, t)\}$ and $\{\bar{q}_\tau(\tau; p_2, q_2, t), \bar{p}_\tau(\tau; p_2, q_2, t)\}$ are pair of dynamic pq -trajectories for 'negative and positive time direction' respectively and initial condition at $\tau = t$:

$$\begin{aligned} d\bar{p}/d\tau &= F(\bar{q}_\tau(\tau))/2; \bar{q}_t(t; p_1, q_1, t) = q_1 \\ d\bar{q}/d\tau &= \bar{p}_\tau(\tau)/2m; \bar{p}_t(t; p_1, q_1, t) = p_1 \\ d\bar{p}/d\tau &= -F(\bar{q}_\tau(\tau))/2; \bar{q}_t(t; p_2, q_2, t) = q_2 \\ d\bar{q}/d\tau &= -\bar{p}_\tau(\tau)/2m; \bar{p}_t(t; p_2, q_2, t) = p_2 \end{aligned}$$

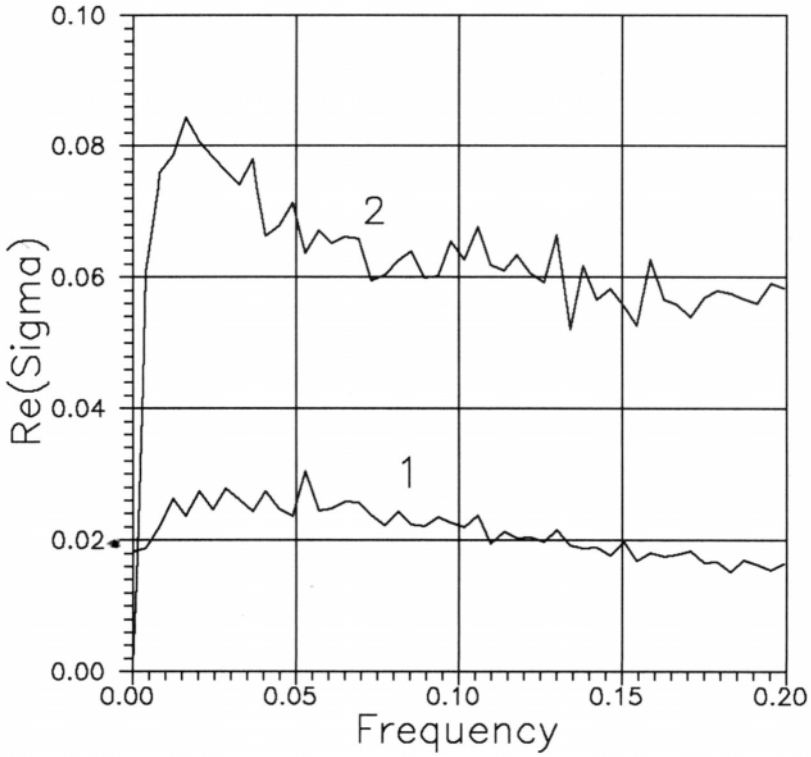


Figure 2. The real part of Fourier transform of the momentum–momentum time correlation function versus $\hbar\omega/V_0$ for temperature $kT/V_0 = 0.04$ for 1D case: 1 — approximation of the classical trajectories; 2 — quantum trajectories

Spectral density initial condition $\bar{W}(p_1, q_1; p_2, q_2; i\hbar\beta) \equiv W(p_1, q_1; p_2, q_2; 0; i\hbar\beta)$ can be written in the form of the finite difference approximation of the path integrals:³

$$\begin{aligned} \bar{W}(p_1, q_1; p_2, q_2; i\hbar\beta) &\approx \\ &\approx \int \int d\tilde{q}_1 \dots d\tilde{q}_M \int \int dq'_1 \dots dq'_M \Psi(p_1, q_1; p_2, q_2; \tilde{q}_1, \dots, \tilde{q}_M; q'_1, \dots, q'_M; i\hbar\beta) \\ &\Psi(p_1, q_1; p_2, q_2; \tilde{q}_1, \dots, \tilde{q}_M; q'_1, \dots, q'_M; i\hbar\beta) = \\ Z^{-1} \langle q_1 | \exp(-\epsilon \hat{K}) | \tilde{q}_1 \rangle \exp(-\epsilon U(\tilde{q}_1)) \langle \tilde{q}_1 | \exp(-\epsilon \hat{K}) | \tilde{q}_2 \rangle \exp(-\epsilon U(\tilde{q}_2)) \times \\ &\dots \exp(-\epsilon U(\tilde{q}_M)) \langle \tilde{q}_M | \exp(-\epsilon \hat{K}) | q_2 \rangle \varphi(p_2; \tilde{q}_M, q'_1) \times \\ &\langle q_2 | \exp(-\epsilon \hat{K}) | q'_1 \rangle \exp(-\epsilon U(q'_1)) \langle q'_1 | \exp(-\epsilon \hat{K}) | q'_2 \rangle \exp(-\epsilon U(q'_2)) \times \\ &y \dots \exp(-\epsilon U(q'_M)) \langle q'_M | \exp(-\epsilon \hat{K}) | q_1 \rangle \varphi(p_1; q'_M, \tilde{q}_1) \end{aligned}$$

where $\hat{H} = \hat{K} + \hat{U}$, \hat{K} is the kinetic energy operator, \hat{U} is the potential energy operator, $\epsilon = \frac{\beta}{2M}$, $M \gg 1$, $\lambda^2 = 2\pi\hbar^2\beta/2mM$ and

$$\varphi(p; q', q'') = (2\lambda^2)^{\nu/2} \exp\left(-\frac{\langle p\lambda/\hbar + i\pi(q' - q'')/\lambda | p\lambda/\hbar + i\pi(q' - q'')/\lambda \rangle}{2\pi}\right)$$

Let us rewrite the integral equation (1) and iteration form of its solution in symbolic form: $W^t = \bar{W}^t + K_r^t W^t$ and

$$W^t = \bar{W}^t + K_{\tau_1}^t \bar{W}^{\tau_1} + K_{\tau_2}^t K_{\tau_1}^{\tau_2} \bar{W}^{\tau_1} + K_{\tau_3}^t K_{\tau_2}^{\tau_3} K_{\tau_1}^{\tau_2} \bar{W}^{\tau_1} + \dots$$

Here \bar{W}^{τ_i} is the quantum initial density evolving classically in interval $[0, \tau_i]$ and $K_{\tau_i}^{\tau_{i+1}}$ is operator, which describes propagation between times τ_i and τ_{i+1} . The time correlation functions are the linear functional of spectral density:

$$C_{FA}(t) = \frac{1}{(2\pi\hbar)^{2v}} \int \int dp_1 dq_1 dp_2 dq_2 F(p_1, q_1) A(p_2, q_2) \times \\ \times W(p_1, q_1; p_2, q_2; t; i\hbar\beta) = \\ (\phi | \bar{W}^t) + (\phi | K_{\tau_1}^t \bar{W}^{\tau_1}) + (\phi | K_{\tau_2}^t K_{\tau_1}^{\tau_2} \bar{W}^{\tau_1}) + (\phi | K_{\tau_3}^t K_{\tau_2}^{\tau_3} K_{\tau_1}^{\tau_2} \bar{W}^{\tau_1}) + \dots \quad (2)$$

where (\cdot) means integration over phase spaces $\{p_1, q_1; p_2, q_2\}$. The possibility to convert series (2) into the form convenient for probabilistic interpretation allow us to develop the Monte Carlo method for its calculation.⁴⁻⁶ To check the basic ideas of the developed approach we have taken the simple Gaussian form of the of electron-scatterer and scatterer-scatterer interaction potentials $U(|r-r'|/\sigma) = V_0 \exp(-|r-r'|^2/\sigma^2)$ with equal to each other all constants of interaction ($V_0^{es} = V_0^{ss} > 0$).

ELECTRICAL CONDUCTIVITY

According to quantum Kubo formulas in one electron approximation the tensor of electrical conductivity may be written in the following form:¹

$$\sigma_{\alpha\gamma}(\omega) = n \int_0^\infty \exp(i\omega t - \epsilon t) \int_0^\beta \langle \hat{J}_\gamma \hat{J}_\alpha(t + i\hbar\lambda) \rangle d\lambda dt$$

where $\epsilon \rightarrow 0$, n is the electron density, $\hat{J}_\alpha = e\dot{x}_\alpha(t) = ep_\alpha/m$ is the electrical current operator, \dot{x}_α is the α component of electron velocity operator. Wigner representation of this tensor may be written in the form:

$$\sigma_{\alpha\gamma}(\omega) = n \int_0^\infty \exp(i\omega t - \epsilon t) \int_0^\beta \phi_{\alpha\gamma}(t, \lambda) d\lambda dt \equiv \\ \equiv nk^{-2} e^2 \bar{\sigma}_{\alpha\gamma}(\omega) / 2E_0 t' \\ \phi_{\alpha\gamma}(t, \lambda) = \langle \hat{J}_\gamma \hat{J}_\alpha(t + i\hbar\lambda) \rangle = \\ = \frac{1}{(2\pi\hbar)^{2v}} \int dp_1 dq_1 dp_2 dq_2 J_\gamma(p_1, q_1) J_\alpha(p_2, q_2) W(p_1, q_1; p_2, q_2; t; i\hbar\beta; i\hbar\lambda) \\ W(p_1, q_1; p_2, q_2; t; i\hbar\beta; i\hbar\lambda) = \int d\xi_1 d\xi_2 \exp\left(i\frac{p_1 \xi_1}{\hbar}\right) \exp\left(i\frac{p_2 \xi_2}{\hbar}\right) \times \\ \left\langle q_1 + \frac{\xi_1}{2} \left| \exp\left(i\frac{\tau_1 H}{\hbar}\right) \right| q_2 - \frac{\xi_2}{2} \right\rangle \left\langle q_2 + \frac{\xi_2}{\hbar} \left| \exp\left(-i\frac{\tau_2 H}{\hbar}\right) \right| q_1 - \frac{\xi_1}{\hbar} \right\rangle$$

where $\tau_1 = t_1 + i\hbar\lambda$, $\tau_2 = t_2 - i\hbar(\beta - \lambda)$, E_0 is the characteristic energy of the considered quantum system, t' is the fixed maximum value of evolution time of the considered system and the reciprocal wave number k^{-1} is determined by the ratio $k^2 = 2mE_0/\hbar^2$.

The Fig. 1 presents results on diagonal elements of momentum–momentum time correlation function. Curve 1 relates to calculations taking into account only one term of iteration series (2) while curve 2 present results allowing for all terms of iteration series (2). So curve 1 have been obtained by using only the classical trajectories without momentum jumps, while curve 2 presents momentum–momentum time correlation function obtained for dynamic trajectories with momentum jumps. The momentum–momentum time correlation functions have the traditional fast decay.

Fig. 2 demonstrates the real part of its Fourier transforms versus the dimensionless frequency $\hbar\omega/V_0$. The real part of Fourier transform characterizes the Ohmic losses of electromagnetic energy and has the physical meaning of electron conductivity. The curve 2 (quantum trajectories) on Fig. 2 is higher than the curve 1 (classical trajectories) but both

curves is going to zero at small frequency pointing out that the static conductivity at zero frequency is equal to zero or is very small, which is the consequence of the Anderson localization of electrons in 1D case.

The authors are very grateful to Professors K. Singer, G. Coccotti, R. Kapral, R. Car and D. Coker for fruitful discussions, invaluable comments and interest in the work. The authors expresses thanks to Russian Fund for Basic Researches for financial support of this work (grant 97-02-16572).

REFERENCES

- [1] D. N. Zubarev. "Non-Equilibrium Thermodynamics," Nauka, Moscow (1971).
- [2] V. I. Tatarskii, The Wigner Representation of Quantum Mechanics, *Usp. Fiz. Nauk*, 139:587 (1983).
- [3] R. P. Feynman and A. R. Hibbs. "Quantum Mechanics and Path Integrals." McGraw-Hill Book Company, New York, 1965.
- [4] V. S. Filinov, Yu. V. Medvedev and V. L. Kamskii, *J. Mol. Phys.* 85:711,(1995).
- [5] V. S. Filinov, *J. Mol. Phys.* 88:1517, (1996).
- [6] V. S. Filinov, *J. Mol. Phys.* 88:1529, (1996).

This page intentionally left blank

EQUILIBRIUM PROPERTIES OF WEAKLY COUPLED MAGNETIZED PLASMAS*

M. Steinberg, J. Ortner, and W. Ebeling

Institut für Physik
Humboldt-Universität zu Berlin
Invalidenstraße 110, D-10115, Germany

INTRODUCTION

Matter in strong magnetic fields gives rise to a wide range of physical problems. The magnetic field strength considered varies from 10^6 G (weak-field regime), as applied to solids, to 10^{12} G (strong-field regime), as can be found on the surface of neutron stars. An overview of laboratory and cosmic plasmas with large magnetic fields is given in Weisheit.¹ In this paper we consider a one component system of point charges in a quantizing magnetic field. The point charges interact via the Coulomb force. Using the method of Green's function, we calculate contributions to the correlation energy of a weakly degenerate electron gas up to the order ($n^2 e^4$).

First, we want to discuss some general properties of a plasma in a magnetic field. A homogeneous magnetic field modifies the energy spectrum of a charged particle according to $E_{N,p_z,\sigma_z} = \hbar\omega_c(N + \frac{1}{2}) + \frac{p_z^2}{2m} + \mu_B B \sigma_z$. The terms describe the Landau quantization, the free motion parallel to the magnetic field and the spin Zeeman energy respectively. The ideal pressure and the particle density are given by a sum of Fermi integrals $f_j(\mu - N\hbar\omega_c) = \frac{1}{\Gamma(j+1)} \int_0^\infty dt t^j / (e^{t-\beta(\mu - N\hbar\omega_c)} + 1)$ over all Landau levels N (the prime indicates the double summation except for $N = 0$ level)

$$p_{id} = \frac{\hbar\omega_c}{\Lambda^3} \sum_{N=0}^{\prime} f_{\frac{1}{2}}(\mu - N\hbar\omega_c); \quad n = \frac{\hbar\omega_c}{kT} \frac{1}{\Lambda^3} \sum_{N=0}^{\prime} f_{-\frac{1}{2}}(\mu - N\hbar\omega_c). \quad (1)$$

For plasmas obeying the Boltzmann distribution, the particle density becomes $n\Lambda^3/2 = z(x/\tanh(x)) = z\Lambda^3/2$ with $x = \hbar\omega_c/2kT$, $\Lambda = h/(2\pi mkT)^{1/2}$ and $z = e^{\beta\mu}$. Thus the magnetic field increases the domain of classical behavior ($z < 1$) towards higher densities. Furthermore, strong magnetic fields enlarge the non-ideal region $\Gamma = E_{pot}/\frac{2}{3}E_{kin} > 1$. This can be verified by the fact that in the weakly degenerate limit for $B \rightarrow \infty$ the kinetic energy reduces monotonically to $kT/2$. On the other hand, at $T = 0$ the ratio of the kinetic energy at a strong field ($\hbar\omega_c > \epsilon_F$) to the kinetic energy at a vanishing magnetic field is $\sim (\epsilon_F/\hbar\omega_c)$. Hence the non-ideal region is enlarged.

*Supported by the Deutsche Forschungsgemeinschaft (DFG, Germany)

GREEN'S FUNCTION FOR THE MAGNETIC FIELD PROBLEM

In this section we consider the uncorrelated one-electron Green's function for the magnetic field problem in a closed form. The Green's function is given by the solution of the equation of motion (using symmetric gauge):

$$\left(\frac{\Delta_{\mathbf{R}}}{2m} - \frac{m\omega_c^2}{8}(X^2 + Y^2) + \frac{\omega_c}{4}L_z - \mu_B B \sigma_3 + i \frac{\partial}{\partial T} \right) G'(\mathbf{R}, T) = \delta(R) \delta(T). \quad (2)$$

$G'(\mathbf{r}, \mathbf{r}', T)$ can be expressed in terms of the correlation functions by

$$G'(\mathbf{r}, \mathbf{r}', T) = \theta(T) G'_>(\mathbf{r}, \mathbf{r}', T) + \theta(-T) G'_<(\mathbf{r}, \mathbf{r}', T).$$

Both $G'_>$ and $G'_<$ satisfy the homogeneous counterpart of Eq. (2). According to Horing,² for arbitrarily chosen gauge they can be written as

$$\begin{aligned} G'_{\{\gtrless\}}(\mathbf{r}, \mathbf{r}', T) &= C(\mathbf{r}, \mathbf{r}') \int \frac{d\omega}{2\pi} \left\{ \begin{array}{l} -i[1 - f_0(\omega)] \\ if_0(\omega) \end{array} \right\} \exp(-i\omega T) \int_{-\infty}^{\infty} dT' \exp(i\omega T') \\ &\times \int \frac{d\mathbf{p}}{(2\pi)^3} \exp(i\mathbf{p}\mathbf{R}) \exp \left[-i \left(\mu_B B \sigma_3 + \frac{p_z^2}{2m} \right) T' \right] \\ &\times \frac{1}{\cos\left(\frac{\omega_c}{2} T'\right)} \exp \left[-i \frac{p_x^2 + p_y^2}{m\omega_c} \tan\left(\frac{\omega_c}{2} T'\right) \right]. \end{aligned} \quad (3)$$

The gauge dependence of the Green's function is explicitly given in the factor $C(\mathbf{r}, \mathbf{r}')$. Noting that $C(\mathbf{r}, \mathbf{r}')$ is only a function of $(\mathbf{r} - \mathbf{r}')$ and that it obeys the relation $C(\mathbf{r}, \mathbf{r}')C(\mathbf{r}', \mathbf{r}) = 1$, this factor can be left aside in the following calculations.

CORRELATION ENERGY OF A WEAKLY DEGENERATE PLASMA

In general, the thermodynamic properties of a many-body system can be calculated by the formula (charging process)

$$p - p_{id} = -\frac{1}{\Omega} \int_0^1 \frac{d\lambda}{\lambda} \langle V \rangle_{\lambda}, \quad (4)$$

which gives the pressure as a function of the fugacities. Here we focus upon the low density and high temperature region ($n\Lambda^3(\tanh(x)/x) < 1$), for which various methods for determining the average value of the potential energy have been developed, e.g., Slater sums, Feynman–Kac formalism etc. The Feynman–Kac formalism was employed in Ref. [3] to calculate the free energy of a magnetized plasma. In this work we use the method of thermodynamic Green's function. Within this framework, a systematic perturbation expansion can be performed and diagrammatically represented.^{4–6} Considering all diagrams up to the order e^4 , one obtains

These diagrams represent the Hartree term, the Montroll-Ward term, the Hartree–Fock term and the exchange e^4 term respectively. The Montroll-Ward graph consists of a screened potential line, which arises from the collective behavior of the Coulomb system. The screened interaction potential V^s is evaluated in the random phase approximation $V^s(\mathbf{q}, \omega) = V(\mathbf{q})/(1 - V(\mathbf{q})\Pi^{RPA}(\mathbf{q}, \omega))$. For the low density region it is sufficient to replace V^s by a statically screened potential $V^s = 4\pi e^2/(q^2 + \kappa^2)$ with $\kappa^2 = 4\pi e^2 \Pi^{RPA}(0, 0) = 4\pi \beta e^2 \bar{z}$. The Hartree–Fock term and the exchange e^4 term are computed using the Coulomb interaction.

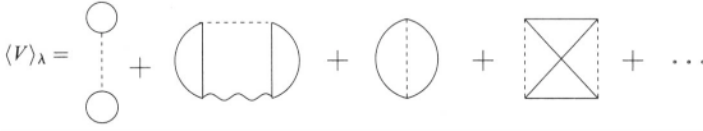


Figure 1.

In order to include the magnetic field, we replace the free particle Green's function by the Green's function for the magnetic field problem (Eq. (3)). Introducing $\lambda = \hbar/(mkT)^{1/2}$, we obtain the fugacity expansion of the pressure within the order $(z^2 e^4)$

$$\beta p = z + \frac{\kappa^3}{12\pi} + z^2 \left(-\frac{\pi^{\frac{3}{2}}}{4} e^4 \beta^2 \lambda f_1(x) + \frac{\pi}{2} \beta e^2 \lambda^2 f_2(x) - \frac{\pi^{\frac{3}{2}}}{4} e^4 \beta^2 \lambda \ln(2) f_3(x) \right). \quad (5)$$

Using the relation $n = z \frac{\partial(\beta p)}{\partial z}$, we obtain the equation of state by iteration

$$\beta p = \beta p_{id} - \frac{\kappa_D^3}{24\pi} - n^2 \left(-\frac{\pi^{\frac{3}{2}}}{4} e^4 \beta^2 \lambda f_1(x) + \frac{\pi}{2} \beta e^2 \lambda^2 f_2(x) - \frac{\pi^{\frac{3}{2}}}{4} e^4 \beta^2 \lambda \ln(2) f_3(x) \right) \quad (6)$$

with the square of the inverse Debye screening length $\kappa_D^2 = 4\pi e^2 \beta n^2$. The first and second contribution refer to the Montroll-Ward graph, the third and fourth term to the Hartree-Fock term and the exchange e^4 term respectively. The first correction to the ideal pressure is the Debye limiting law. This result is in agreement with the Bohr-van-Leeuwen theorem^{7,8} stating that a magnetic field does not affect the thermodynamic properties of a classical plasma. The following terms describe the quantum corrections. Each of these terms may be represented by its corresponding result at zero magnetic field modified by a function $f(x)$ describing the influence of a magnetic field. These functions are found to depend on the ratio of magnetic energy $\hbar\omega_c$ to kT only. A detailed analysis is carried out in [9]. We obtain the analytical result for the Hartree-Fock term

$$f_2(x) = \frac{\cosh(2x) \tanh(x)}{\cosh^2(x)} \frac{\operatorname{arctanh} \sqrt{1 - \frac{\tanh(x)}{x}}}{x \sqrt{1 - \frac{\tanh(x)}{x}}}. \quad (7)$$

Furthermore, we obtain integral representations for $f_1(x)$ and $f_3(x)$, which are explicitly given in [9]. The results of the numerical investigation of these integrals are plotted in Fig. 1.

Moreover, we propose a fit expression for $f_1(x)$ and $f_3(x)$. If we define

$$g(x, a_i, b_i) = \left(\frac{\tanh(b_i x)}{(b_i x)} \right)^{a_i} \times \frac{\operatorname{arctanh} \sqrt{1 - \frac{\tanh(b_i x)}{(b_i x)}}}{\sqrt{1 - \frac{\tanh(b_i x)}{(b_i x)}}}, \quad (8)$$

we find the approximations (within an accuracy of about 1%) $f_1(x) \approx 1/2 + 1/2 \times g(x, a_1 = 1.1247, b_1 = 0.5375)$ and $f_3(x) \approx (\cosh(2x)/\cosh^2(x)) \times g(x, a_3 = 0.9169, b_3 = 0.8349)$, where a_i and b_i are fitted parameters.

In Fig. 2 the pressure of a magnetized OCP using the low density expansion (Eq. (5)) is shown. Generally, this expansion is an inappropriate description of the system at high densities. However, with increasing magnetic field strength the low density expansion becomes valid at even higher densities, as can be concluded from Fig. 2.

The interpolation between the results in the weakly degenerate limit obtained in this work and the partially known results in the degenerate limit will be subject of a forthcoming paper.

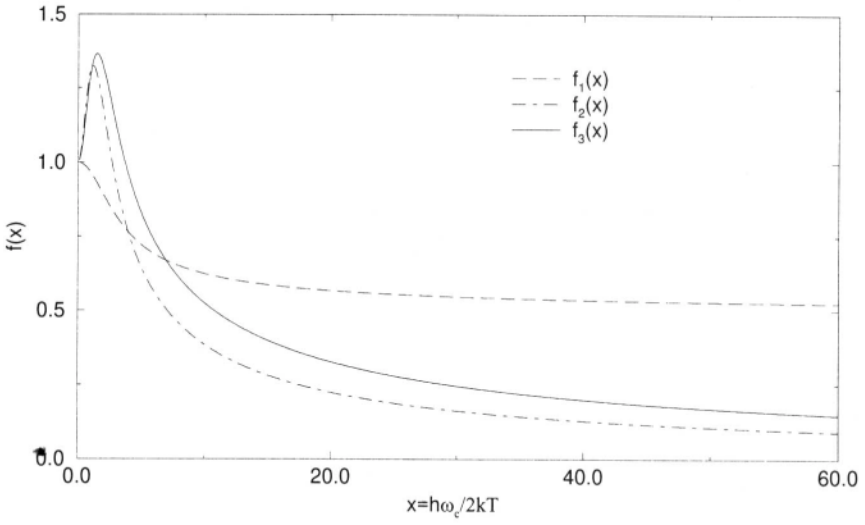


Figure 2. Plot of $f_1(x)$, $f_2(x)$, and $f_3(x)$.

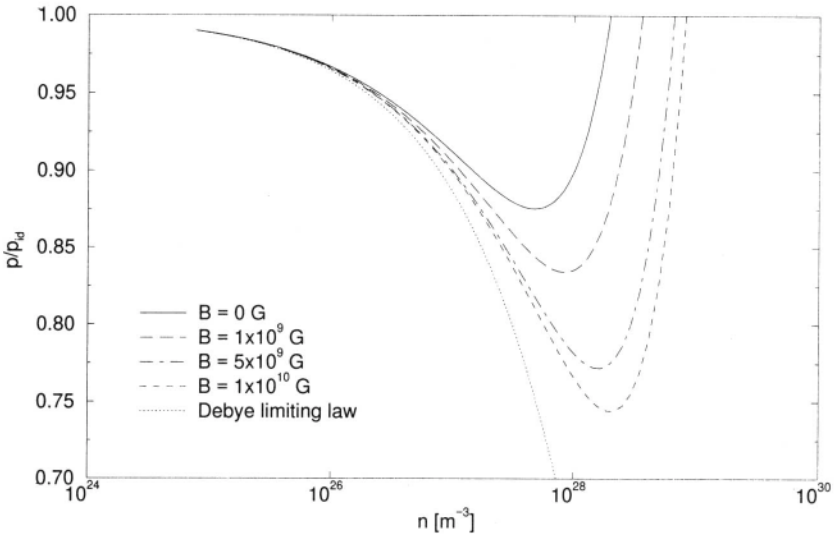


Figure 3. Plot of the pressure for various magnetic fields at $T=50000$ K according to Eq. (5), also included the Debye limiting law.

REFERENCES

- [1] J. C. Weisheit “*Proceedings of the International Conference on Physics of Strongly Coupled Plasmas,*” World Scientific, Singapore (1995).
- [2] N. J. Horing, *Annals of Physics* 31:1 (1965).
- [3] F. Cornu, *Europhys. Lett.* 37:591 (1997),
- [4] A. A. Vedenov, A. I. Larkin, *Zhur. Eksptl. i Teoret. Fiz.* 36:1133 (1959).
- [5] W. Ebeling, W. D. Kraeft, D. Kremp, “*Theory of Bound States and Ionization Equilibrium in Plasmas and Solids,*” Akademie-Verlag, Berlin (1976).
- [6] W. D. Kraeft, D. Kremp, W. Ebeling, and G. Röpke, “*Quantum Statistics of Charged Particle Systems,*” Plenum, New York (1986).
- [7] J. H. van Leeuwen, *J. Physique* 2:361 (1921).
- [8] N. Bohr, “*dissertation,*” Copenhagen (1911).
- [9] M. Steinberg, “*diploma thesis,*” Humboldt-Universität, Berlin (1997).

This page intentionally left blank

MODELING OF THE ELECTRONIC STATIC LOCAL FIELD CORRECTION

I. M. Tkachenko, P. Fernández de Córdoba, and J. M. Belda

Departamento de Matemática Aplicada
 Universidad Politécnica de Valencia
 Aptdo. 22012. E-46071 Valencia, Spain
 E-mail address: imtk@iqn.upv.es

A natural approach to the investigation of static correlations in strongly coupled plasmas, is based on the separation of electronic and ionic components of the system, so that the interionic interactions are assumed to be screened by the electronic static dielectric function $\epsilon_e(k)$. In dense systems the latter should be treated beyond the RPA, i.e., the calculation of $\epsilon_e(k)$ involves the electronic static local field correction (LFC) $G_e(k)$.

There exists a number of various approaches to the computation of the LFC $G_e(k)$ (see, e.g.,¹⁾, but mostly they are applicable in specific realms of the system phase diagram. We present and test a simple alternative model which it is to serve as a basis for future studies of various properties of strongly coupled systems.

The interpolating formula for the electronic LFC suggested in Ref. [2]

$$G_e(z) = (b + a/4z^2)^{-1} \quad z = k/2k_F \quad (1)$$

incorporates both long and short wavelength asymptotic values of $G_e(k)$, $z = k/2k_F$, k_F is the Fermi wave-number.

In particular,

$$b^{-1} = \lim_{k \rightarrow \infty} G_e(k). \quad (2)$$

The short-range behavior of $G_e(k)$ in the low-temperature limit has been studied in the papers of Shaw³ and Kimball⁴ (see also [5]). Namely, it has been shown that if $T \rightarrow 0$ in hydrogen-like systems,

$$b^{-1} = 1 - g_e(0), \quad (3)$$

$g_e(r)$ being the usual electronic radial distribution function. This result is based on the ‘‘cusp’’ condition which can be obtained from the s-solution of the two-particle Schrödinger equation at $r=0$ (see, e.g.,⁴⁾.

On the other hand, since $G_e(k \rightarrow \infty)$ involves only the short-range properties of the system, one expects the asymptotic value of Eq. (3) to be finite and the relation (4) to hold at arbitrary values of temperature T .⁶

One further notices that the long-wavelength behavior of $G_e(k \rightarrow 0) \approx a^{-1}(k/k_F)^2$ is responsible for the screening of a static impurity in the plasma. On the other hand, the

parameter a is determined by the system thermodynamic properties via the compressibility sum rule.

The most recent MC data on the OCP EOS⁷

$$P = \frac{n}{\beta} + \frac{nf(\Gamma)}{3\beta} \quad (4)$$

(P is the system pressure) are utilized here with

$$f_{OCP}(\Gamma) = A\Gamma + B + C\Gamma^{-\frac{1}{3}} + D\Gamma^{\frac{1}{3}} \quad (5)$$

and

$$\begin{aligned} A &= -0.8993749, \\ B &= -0.2244699, \\ C &= -0.0178747, \\ D &= 0.5175753, \\ \Gamma &= \beta e^2 \left(\frac{4\pi n}{3} \right)^{1/3} \end{aligned}$$

β^{-1} is the system temperature in energy units.

The interpolation form (5) valid in a very wide region of values of Γ , $0 \leq \Gamma \leq 200$, brought us to a simple algebraic expression for the a parameter,

$$a = -(12\pi^2)^{-\frac{1}{3}} \left(\frac{A}{9} + \frac{B}{12}\Gamma^{-1} + \frac{2C}{27}\Gamma^{-\frac{4}{3}} + \frac{5D}{54}\Gamma^{-\frac{2}{3}} \right)^{-1}. \quad (6)$$

No quantum effects are included in the EOS (5) and, hence, there is discrepancy between (6) (and, thus, Eq. (2) too) and our desire to apply it to electron liquids under ‘‘quantum’’ thermodynamic conditions.

To diminish the influence of this inconsistency, electronic radial distribution function $g_e(r)$ and its zero separation value $g_e(0)$ (and b of Eq. (2)) were determined by a precise self-consistent procedure. In effect, the value of $g_e(r)$ was computed via a simultaneous solution of two integral equations,

$$S_e(z) = \sum_{l=-l_1}^{l_1} \frac{\mathcal{P}_e(z, l)}{\varepsilon_e(z, l)}, \quad (7)$$

$$g_e(r) = 1 + \frac{6}{rk_F} \int_0^\infty z \sin(2k_F r z) (S_e(z) - 1) dz. \quad (8)$$

In Eq. (7) the summation is over the Matsubara frequencies, $\nu_l = (\pi\Theta l)/(2z)$, and

$$\varepsilon_e(z, l) = 1 + \frac{\Gamma}{(12\pi^2)^{1/3}} \frac{\mathcal{P}_e(z, l)}{z^2}; \quad (9)$$

as usually, $\Theta = 2m/(\beta\hbar^2 k_F^2)$, the l_1 -parameter was determined by the numerical precision.

$\mathcal{P}_e(z, l)$ in Eq. (12) is the dimensionless polarization operator $\Pi_e(k, \omega)$ with the LFC, included,

$$\mathcal{P}_e(z, l) = \mathcal{P}_e^0(z, l) \left(1 - \frac{\Gamma}{(12\pi^2)^{\frac{1}{3}}} \frac{G_e(z)\mathcal{P}_e^0(z, l)}{z^2} \right)^{-1}, \quad (10)$$

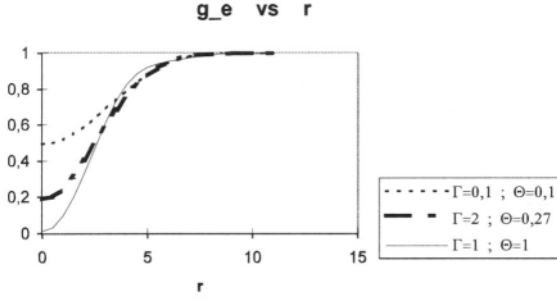


Figure 1. The electronic radial distribution function for different thermodynamic conditions.

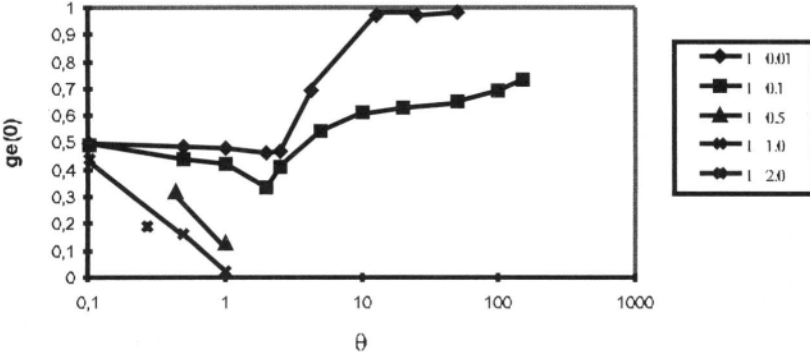


Figure 2. The zero-separation value of the pair correlation function $g_e(r)$ in the electron liquid as a function of the degeneracy parameter Θ and for $\Gamma = 2.0$ (one point), $\Gamma = 1.0$ (long dashes), $\Gamma = 0.5$ (short dashes), $\Gamma = 0.1$ (dots) and $\Gamma = 0.01$ (solid line). Points represent the results of the present model, the lines are drawn to distinguish different values of the coupling parameter Γ .

The RPA dimensionless polarization operator $\mathcal{P}_e^0(z, l)$ can be calculated (for each value of density and temperature, z and l) by simple integration (see, e.g.,¹).

The results for the radial distribution function $g_e(r)$ and its zero-separation value $g_e(0)$ are presented in Figs. 1 and 2 for various values of electronic density and temperature.

Where available, our results coincide with the data of [8], when the electron-ion LFC was set to be zero.

The self-consistency procedure also permitted us to calculate the static structure factor of electrons, these results are provided in Fig. 3 for three characteristic pairs of values of the parameters Γ , Θ and $g_e(0)$.

Using our data for the radial distribution function we calculated the excess Coulomb interaction energy density normalized to $\beta, f(\Gamma)$:

$$f(\Gamma) = \frac{1}{8} \frac{k_D^2}{k_F^2} \int_0^\infty (g_e(r) - 1) r dr \quad (11)$$

with $k_D^2 = 4\pi n_e e^2 \beta$. The results are given in Table 1, where we also provided the corresponding values of $f_{OCP}(\Gamma)$ of Eq. (5). Both estimates are closer in less degenerate electronic liquids.

Table 1. The excess Coulomb interaction energy density (normalized to temperature) $f(\Gamma)$, and the results of the electronic liquid MC-simulation, Eq. (5).

$n_e(10^{24} \text{cm}^{-3})$	$T(10^5 \text{K})$	Γ	Θ	$F(\Gamma)$	$f_{OCP}(\Gamma)$
0.258	1.715	1.00	1.00	-0.54	-0.62
1.610	6.315	0.5	1.09	-0.24	-0.29
1.611	1.579	2.0	0.27	-1.11	-1.38
$2.579 \cdot 10^5$	$1.715 \cdot 10^3$	0.10	0.10	-0.044	-0.11

At certain thermodynamic conditions (below the points provided in Fig. 2), our approach breaks down in the sense that it produces negative, unphysical, values for the $\mathbf{g}_e(\mathbf{0})$ parameter.

We intended to avoid this inconsistency, introducing a correction to Eq. (2). The form of this correction was virtually suggested in [9]: $\hat{G}_e(\mathbf{k})$ is sought as a functional of the RPA electronic polarization operator real part of Eq. (10):

$$\hat{G}_e(z) = \frac{1}{b + a/4z^2} + \frac{2z}{c} h(z) \quad (12)$$

with $h(z) = (4\pi/3\Theta)\mathcal{P}_e^o(z, 0)$

Some preliminary calculations were carried out on the basis of this modified model LFC. It turned out that with $\hat{G}_e(z)$ of Eq. (12) one can (at least for the conditions considered) avoid negative values for $\mathbf{g}_e(\mathbf{0})$.

Particularly, if one takes $c \sim 3$ (for $\Gamma = 0.5$ and $\Theta = 2$ and $\Gamma = 1$ and $\Theta = 1.5$) the zero-separation value of the electronic radial distribution function, $\mathbf{g}_e(\mathbf{0})$, no longer takes negative values, while the data of Table 1 does not change significantly.

Nevertheless, further studies of $\mathbf{g}_e(\mathbf{0})$ should be carried out to include low-temperature and dynamic effects.

In addition, to improve the physical self-consistency of our approach, one needs the quantal EOS, either theoretical or numerical (obtained, e.g., within a quantum-statistical variant of the MC method), see, e.g.,¹⁰

REFERENCES

- [1] S. Ichimaru *Statistical Plasma Physics*. Vol. II: Condensed Plasmas. (Addison-Wesley, 1994).
- [2] I. M. Tkachenko, *Europhys. Lett.* **9**, 351 (1989); Z. Djurić et al., *Phys. Lett. A* **155**, 415 (1991).
- [3] R. W. Shaw, *J. Phys. C* **3**, 1140 (1970).
- [4] J. C. Kimball, *Phys. Rev. A* **7**, 1648 (1973); J. C. Kimball, *Phys. Rev. B* **14**, 2371 (1976).
- [5] S. Ichimaru, *Rev. Mod. Phys.* **54**, 1017 (1982).
- [6] I. M. Tkachenko, P. Fernández de Córdoba, M. Urrea, *J. Phys. A* **29**, 2599 (1996).
- [7] G. S. Stringfellow, H. E. de Witt, W. L. S. Slattery, *Phys. Rev. A* **41**, 1105 (1990)
- [8] S. Tanaka, X.-Z. Yan, S. Ichimaru, *Phys. Rev. A* **41**, 5616 (1990); see also [1].
- [9] K. Utsumi and S. Ichimaru, *Phys. Rev. A* **26**, 603 (1982).
- [10] W. Stolzmann, T. Blöcker, *Phys. Lett., A* **221**, 99 (1996); *Astron. Astrophys.* **314**, 1024 (1996); W. Stolzmann, M. Rösler, *Physics of Strongly Coupled Plasmas*, eds. W. D. Kraeft and M. Schlanges, World Scientific, Singapore, 1996, p. 87; M. Rösler, W. Stolzmann, *ibid.*, p. 91.

QUANTUM MELTING ON A LATTICE AND A DELOCALIZATION TRANSITION

E. V. Tsiper and A. L. Efros

Department of Physics
University of Utah
Salt Lake City, UT

INTRODUCTION

The insulator–metal (IM) transition and the role of electron–electron interaction in this transition is a problem of permanent interest, both theoretical and experimental. It has been shown^{1–3} that in the systems with strong disorder the interaction is in favor of delocalization because electrons may help each other to overcome the random potential. In clean systems the role of the interaction is opposite. It may create the so-called correlated insulator in a system which would be metallic otherwise. The Wigner crystal (WC) is a good example of such insulator.

WC in continuum is not an insulator itself, since it can move as the whole and carry current. However, due to shear modulus it can be pinned by a small disorder. The ground-state energy of the continuum WC and its zero-temperature melting was widely studied in the recent years both with and without magnetic field.⁴

In contrast to the continuum case, the WC on a lattice can be an insulator without any disorder due to the Umklapp processes in a host lattice. The WC on a lattice does not have any sound or soft plasma modes and its excitation spectrum has a gap.

Here we report on the study of the structural and IM transitions for spinless fermions at $\nu = 1/2$ and $1/6$. To detect these transitions we use the ground-state splitting and the flux sensitivity^{5,6} respectively. The purpose of the work is to take advantage of the exact diagonalization technique and to study the modification of the low-energy part of the spectrum in a wide interval of the hopping amplitude J all the way from the classical WC to the free fermion limit.

GENERAL REMARKS

We consider spinless fermions at $T = 0$ on the 2D square lattice described by the following model Hamiltonian

$$H = J \sum_{\mathbf{r}, \mathbf{s}} a_{\mathbf{r}+\mathbf{s}}^\dagger a_{\mathbf{r}} \exp(i\phi \mathbf{s}) + \frac{1}{2} \sum_{\mathbf{r} \neq \mathbf{r}'} n_{\mathbf{r}} n_{\mathbf{r}'} V(|\mathbf{r} - \mathbf{r}'|). \quad (1)$$

Here $n_{\mathbf{r}} = a_{\mathbf{r}}^{\dagger} a_{\mathbf{r}}$, the summation is performed over the lattice sites \mathbf{r}, \mathbf{r}' and over the vectors of translations \mathbf{s} to the nearest-neighbor sites. We consider long-range (LR) Coulomb potential $V(r) = 1/r$ and short-range (SR) strongly screened Coulomb potential $V(r) = \exp(-r/r_s)/r$ with $r_s = 0.25$ in the units of lattice constant. We study rectangular clusters $L_x \times L_y$ with the periodic boundary conditions. The dimensionless vector potential $\phi = (\phi_x, \phi_y)$ in the Hamiltonian is equivalent to the twist of the boundary conditions by the flux $\Phi_i = L_i \phi_i$, $i = x, y$. The energy spectrum is periodic in Φ_x and Φ_y , with the period 2π .

As a basis for computations we use many-electron wave functions at $J = 0$ in the coordinate representation: $\Psi_{\alpha} = \prod_{i=1}^N a_{\mathbf{r}_i}^{\dagger} |\text{VAC}\rangle$. They can be visualized as pictures, which we call *icons*. The total number of icons is C_M^N , where $M = L_x \times L_y$ is the area of a system, and N is the number of particles. The icon with the lowest energy is a fragment of the crystal. The icons with higher energies represent different types of defects in WC.

The Hamiltonian Eq. (1) is translationally invariant. For each icon α there are m_{α} different icons that can be obtained from it by various translations. These icons are combined to get the wave function with total quasimomentum \mathbf{P} :

$$\Psi_{\alpha\mathbf{P}} = \frac{1}{\sqrt{m_{\alpha}}} \sum_{\mathbf{r}} \exp(i\mathbf{P}\mathbf{r}) T_{\mathbf{r}} \Psi_{\alpha}. \quad (2)$$

The summation is performed over m_{α} translations $T_{\mathbf{r}}$.

For the icons with periodic structures the number m_{α} of different functions $\Psi_{\alpha\mathbf{P}}$ is smaller than M . For example, the icon Ψ_0 of the WC with one electron per primitive cell generates $m_0 = 1/\nu$ different values of \mathbf{P} . Note that the total number of allowed values of \mathbf{P} for the WC is the property of the WC and remains finite at infinite cluster size. Contrary, an icon representing a point defect in a WC generates all vectors \mathbf{P} . Their total number is equal to the volume M of the first Brillouin zone of the background lattice.

In the macroscopic system all the states generated by the WC icon form the ground state degenerate at small J . This degeneracy appears because the effective matrix elements which connect translated WC's are zero in the macroscopic limit. The total energy as a function of quasimomentum \mathbf{P} has identical minima at all \mathbf{P} generated by the WC icons. The spectra of excitations in the vicinity of these minima are also identical. The lifting of the ground state degeneracy at some critical value J_c indicates a structural phase transition and restoration of the host lattice symmetry.

The flux sensitivity of a macroscopic system is zero at small J . It becomes non-zero at some finite value of J which might be different from J_c . We associate this transition with the IM transition.⁵

For the finite system the following results can be obtained directly using the perturbation theory with respect to J :

1. the ground state and the lowest excited states have a large common negative shift which is proportional to J^2 and to the total number of particles N . This shift is the same for all low-lying states and does not affect the excitation spectrum of the system;
2. at $\nu = 1/2$ the splitting of the ground state appears in the N -th order and is proportional to J^N . At other filling factors the splitting is proportional to J^K with K being proportional to N ;
3. the flux dependence of the ground state for the flux in x -direction appears in the L_x -th order and is proportional to J^{L_x} in 2D case. In 1D the flux dependence appears in the N -th order and is proportional to J^N .

Thus, we conclude that both lifting of the ground-state degeneracy and appearance of the flux sensitivity occur very sharply and they can be used as convenient criteria for

the structural and the IM transitions respectively. Note that the correlation function is a less sensitive criterion for small clusters^{7,8} since it does not exhibit sharp behavior in the transition region.

THE MECHANISM OF TRANSITION

Our data suggest the following mechanism of the transition. The width of the band of the defect in the WC increases with J such that its lowest edge comes close to the energy of the ground state.^{8,9} Strong mixing between the crystalline and defect states with the same quasimomentum occurs at this point and an avoided crossing appears between the ground state and the states in the defect band.

One can interpret the avoided crossing in terms of the ground state which acquires a large admixture of defect states. This interpretation reminds the idea of zero-point defectons proposed by Andreev and Lifshitz.¹⁰

In principle, one can imagine that the state with a quasimomentum \mathbf{P} different from those generated by the WC icon becomes the ground state via a branch crossing. However, in all cases we have considered, we observe the avoided crossing between the crystalline state and the state in the defect band with the same \mathbf{P} . Assuming that this is the case for larger clusters, we conclude that the phase transition is not of the first order.

The proposed mechanism implies that critical value of J is determined by the energy Δ of the lowest defect at $J = 0$. Our data suggest the following simple empirical rule for J_c :

$$J_c = \beta \Delta \quad (3)$$

where β is some number which is close to 0.5 for all 2D and 1D systems we have studied.

For the exactly soluble 1D problem with nearest-neighbor interaction¹¹⁻¹³ β is exactly equal to 0.5. For the 1D Coulomb problem $\Delta = 2 \ln 2 - 1 = 0.386$. Our computations⁹ show that for the Coulomb interaction J_c is between 0.17 and 0.3, which gives $0.44 < \beta < 0.77$. Note that this result clearly contradicts to the statement by Poilblanc et al.¹⁴ that 1D Coulomb system is metallic at all J .

We have found Eq. (3) to be extremely useful¹⁵ when applied to the 1D problem with the nearest neighbor interaction V_1 and the next-nearest neighbor interaction V_2 . This problem has been studied¹⁶ in connection with the spin version of the Hamiltonian Eq. (1). The IM phase diagram for this model has been studied recently in Ref.¹⁴.

In this case Δ is a function of V_1 and V_2 , so that Eq. (3) gives the IM phase diagram in the (V_1, V_2) -space. We have found that the phase diagram obtained in such a way is consistent with our extensive numerical simulations. It predicts the existence of metallic phase at arbitrarily large values of interaction. The ground state in this phase represents a mixture of two degenerate crystalline phases.

GAP AT NONZERO J

At large enough J , the excitation gap in the spectrum is determined by the confinement quantization. On the other hand, the gap Δ at $J = 0$ is the energy of defect and it has a non-zero limit in macroscopic system. Thus, an important question arises, whether or not the gap has a non-zero limit right after the IM transition. The non-zero gap would mean that the state after the transition is superconducting.¹⁷

We have made a lot of computational efforts to answer this question but the results are still inconclusive. We have found that the gap for the 4×8 cluster is less than for 4×4 cluster but the ratio is significantly larger than 0.5 as would be expected from the confinement quantization solely.

CONCLUSIONS

We have performed a numerical study of the structural and IM phase transitions in 2D fermionic systems with Hamiltonian Eq. (1). We argue that the structural transition on a lattice is not of the first order in all cases considered. We think that the origin of the transition is an avoided crossing of the ground state and the defect states in the Wigner crystal with the same total quasimomentum. This simple picture implies that the critical value of J is determined by the defect with the lowest energy Δ at $J = 0$. To illustrate our point the data for 1D systems with Coulomb interaction and with next-nearest neighbor interactions are also presented. The possibility of the delocalized phase above the transition to be superconducting is discussed.

REFERENCES

- [1] A. L. Efros, F. G. Pikus, *Solid State Commun.* **96**, 183 (1995).
- [2] R. Berkovits, Y. Avishai, *Europhys. Lett.* **29**, 475 (1995).
- [3] D. L. Shepelyansky, *Phys. Rev. Lett.* **73**, 2607 (1994); Y. Imry, *Europhys. Lett.* **30**, 405 (1995);
- [4] X. Zhu, S. G. Louie, *Phys. Rev. B* **52**, 5863 (1995) and early references quoted therein.
- [5] W. Kohn, *Phys. Rev.* **133**, A171 (1964).
- [6] D. J. Scalapino, S. R. White, S. Zhang, *Phys. Rev. B* **47**, 7995 (1993).
- [7] F. G. Pikus, A. L. Efros, *Solid State Commun.* **92**, 485 (1994).
- [8] E. V. Tsiper, F. G. Pikus, and A. L. Efros, unpublished, preprint cond-mat/9512150.
- [9] E. V. Tsiper, A. L. Efros, unpublished, preprint cond-mat/9708150.
- [10] A. F. Andreev and I. M. Lifshitz, *Sov. Physics JETP.* **29**, 1107 (1969).
- [11] C. N. Yang and C. P. Yang, *Phys. Rev.* **147**, 303 (1966); **150**, 327 (1966); **151**, 258 (1966), and earlier references quoted therein.
- [12] J. des Cloizeaux, *J. Math. Phys.* **7**, 2136 (1966).
- [13] B. Sutherland, B. S. Shastry, *Phys. Rev. Lett.* **65**, 1833 (1990).
- [14] D. Poilblanc, S. Yunoki, S. Maekawa, E. Dagotto, *Phys. Rev. B* **56**, R1645 (1997).
- [15] E. V. Tsiper and A. L. Efros, to be published in *J. Phys. C.*, preprint cond-mat/9708167.
- [16] V. J. Emery and C. Noguera, *Phys. Rev. Lett.* **60**, 631 (1988); *Synthetic Metals* **29**, F523 (1989), and earlier references quoted therein.
- [17] E. V. Tsiper and A. L. Efros, submitted to *J. Phys.*

INTERACTING ELECTRONS IN STRONG MAGNETIC FIELDS: A GENUINE EXAMPLE OF A TWO-DIMENSIONAL NON-FERMI-LIQUID

D. V. Khveshchenko

NORDITA

Blegdamsvej 17, Copenhagen DK-2100, Denmark

The quest for possible departures from the conventional Fermi-liquid behavior, exhibited by various kinds of strongly correlated electronic systems, became one of the mainstream topics in the modern microscopic many-body theory.

Among the mostly studied examples are such systems as the high T_c materials in their normal state known as a “strange metal” and heavy fermion compounds close to a ferro- or antiferromagnetic $T = 0$ quantum critical point. Distinct NFL features observed in transport and other measurements are now well-documented experimentally. However, the theoretical analysis of these systems appears to be extremely involved, the reasons being a strong intrinsic coupling between charge and spin degrees of freedom, non-spherical Fermi surface effects (nesting, van Hove singularities), and dimensional ($2D - 3D$) crossovers.

On the other hand, 2DEG in *GaAs/AlGaAs* heterostructures provides an example of a strictly 2D system with a nearly isotropic (bare) Fermi surface, which is governed by strong Coulomb interactions. Moreover, in a strong magnetic field all electronic spins get polarized which effectively decouples spin and charge degrees of freedom by simply freezing out the former ones.

If the interaction parameter r_s is not very large ($r_s \sim 1$), then at zero field, all in all, the 2DEG remains a Fermi liquid. In the strong coupling (or the low density, since $r_s \sim n_e^{-1/2}$ where n_e is the 2DEG density) limit the electrons are expected to eventually form a 2D Wigner crystal at $r_s \approx 40$. There are also indications that in the presence of disorder the Wigner crystal might occur at much lower $r_s \sim 10$, although the possibility of other phases at intermediate values of r_s currently remains open.

One of the conventional Fermi-liquid-like features is a reaction of the 2DEG on applied perpendicular magnetic field B . As long as the field remains classically weak ($\nu = 2\pi n_e/B \gg 1$), the magnetoresistivity $\rho_{xx}(B)$ demonstrates Shubnikov–de Haas oscillations, which are consistent with the single-particle cyclotron motion along the orbits of radius $R_c = k_F/B$.

In increasingly stronger fields, the 2DEG first enters the Integer Quantum Hall (IQH) regime at integer filling factors lying in the interval $1 < \nu < 10$. At $\nu < 1$ the Fractional Quantum Hall (FQH) behavior eventually sets in at odd denominator filling fractions. Both, IQH and FQH regimes are characterized by excitation spectra with gaps, which qualifies them as incompressible (at $T = 0$) states despite the difference in their microscopic origin

(the IQH behavior is believed to be dominated by disorder effects, whereas the FQH one is due to Coulomb interactions).

Either behavior, however, differs drastically from that at EDFs exhibited by the strongly correlated EDF electronic states at $\nu \sim 1/\Phi$ ($\Phi = 2, 4, \dots$).

The features observed at these EDFs in the surface acoustic wave and other experiments¹ imply that despite the strong magnetic field, there are some fermionic quasiparticles which propagate along straight lines until they hit an impurity or each other.

Such a rationalization of the experimental findings motivated the theoretical idea² to describe these states as a new kind of Fermi liquid, which is formed by spinless fermionic quasiparticle named composite fermions (CFs). On the mean field level the CFs, regarded as spin-polarized electrons bound to Φ flux quanta, experience zero net field and occupy all states with momenta $k < k_{F,cf} = \sqrt{2}k_F = (4\pi n_e)^{1/2}$ below the effective CF FS. Formally, the residual interactions of the CFs, as well as their interactions with charged impurities (remote ionized donors sitting on a distance $\xi \sim 10^2 nm$ apart from the 2DEG) turn out to be essentially more singular than the original Coulomb ones. In the framework of the Chern–Simons theory of Ref. [2] these interactions appear as gauge forces, whose strength depends on the Coulomb electron interaction potential $V_{ee}(q) \sim 1/q$. In turn, the Coulomb potential of randomly distributed donors $V_{ei}(q) \sim 1/q e^{-q\xi}$ changes to that of spatially random but static magnetic fluxes (RMF): $V_{ei}(q) \sim i(\mathbf{p} \times \mathbf{q}/q^2) e^{-q\xi}$.

Conceivably, a 2D Fermi system governed by long-ranged gauge interactions of both dynamic (exchange by $\omega \neq 0$ gauge fluctuations) and static (RMF due to impurities and/or $\omega = 0$ gauge fluctuations at $T > 0$) nature, could demonstrate quite unusual properties, and thereby provide an example of a genuine 2D NFL.

Indeed, a naive attempt to proceed beyond the mean field approximation and estimate perturbatively the effects of gauge fluctuations on the CF spectrum reveals (even in a purely academic case of $T = 0$ and no impurities) a singular self-energy, which behaves as $\Sigma_{cf} \sim \epsilon \ln \epsilon$, suggesting a divergent effective mass $m_{cf}^*(\epsilon) \sim \ln \epsilon$. Moreover, in a more realistic situation with impurities present and/or $T > 0$ the perturbative analysis fails to yield any finite self-energy (formally, $\Sigma_{cf} = \infty$).

A non-perturbative eikonal calculation³ shows a super-exponential decay of a CF wave packet moving along its semiclassical trajectory:

$\langle \Psi_{cf}(v_F t, t) \Psi_{cf}^\dagger(0, 0) \rangle \sim \exp(-t \ln t)$ which implies a completely incoherent character of a CF propagation, resulting in a failure of the naive “golden rule”-type estimates of Σ_{cf} and other gauge-non-invariant quantities.

Therefore, an impressive qualitative success of the mean field CF theory² in explaining the experiments,¹ where CFs seem to propagate over distances of a few μm , appears puzzling and urging for a theoretical understanding.

It had been shown in [4] that the electrical current relaxation processes, which correspond to smooth fluctuations of the ostensible CF FS, can be safely described by means of the kinetic equation, where the singular self-energy and the Landau function-type terms largely compensate each other. This implies that at small q and ω the electromagnetic response functions of EDF states $K_{\mu\nu}(\omega, \mathbf{q})$ exhibit no singularities and can be computed within the random phase approximation (RPA).⁵

We arrived at the conclusions similar to those drawn in Ref. [4] by applying to the EDF problem the geometrical method of the 2D bosonization developed in [6]. In contrast to the earlier versions of the 2D bosonization the procedure of Ref. [6] facilitates an account of a finite FS curvature. The latter is crucially important for a bosonic description of $D > 1$ Fermi systems, and in particular, for calculating such physical quantities as Hall conductivity σ_{xy} or diffusion thermopower \mathcal{S}_d , which simply vanish in the particle–hole symmetric limit of zero FS curvature.

The geometrical approach to the $D > 1$ bosonization starts off with a choice of a particular basis of coherent states $\{|g(\mathbf{p}, \mathbf{q})\rangle\} = \hat{g}|0\rangle$, which are generated by operators $\hat{g} = \exp[i\sum_{\mathbf{p}, \mathbf{q}} \mathbf{g}(\mathbf{p}, \mathbf{q}) \hat{n}(\mathbf{p}, \mathbf{q})]$ from the reference state $|0\rangle$ corresponding to the unperturbed circular FS of radius k_F , in order to quantize the algebra of bi-linear spinless fermionic operators $\hat{n}(\mathbf{p}, \mathbf{q}) = \Psi_{\mathbf{p}}^\dagger \Psi_{\mathbf{p}+\mathbf{q}}$ (2D analogue of the 1D algebraic structure known as W_∞). The orbit of the group action $g|0\rangle\langle 0|g^{-1}$ can be parameterized in terms of the phase space “distribution function” $f(\mathbf{r}, \mathbf{p})$, which describes spatial fluctuations of the occupied (“Luttinger”) volume in momentum space. Some additional analysis is required to identify all important kinds of FS fluctuations for a given Hamiltonian H . It turns out that if one deals with small angle scattering with transferred momenta being almost tangential to a FS (which is the case for the Chern–Simons gauge theory of Ref. [2]) the most relevant fluctuations are those of the FS shape, and not of its profile. If only shape fluctuations are present, then $f(\mathbf{r}, \mathbf{p})$ amounts to a support function $\Theta(k_F(\mathbf{r}) - p)$, and a local Fermi momentum $\mathbf{k}_F(\mathbf{r}, \Omega)$ at the FS point Ω can be used as an unconstrained (obviously, bosonic) variable. The local density $\rho(\mathbf{r}) = \oint \frac{d\Omega}{4\pi} \frac{\partial \mathbf{k}_F}{\partial \Omega} \times \mathbf{k}_F$ and current $\mathbf{J}(\mathbf{r}) = e \oint \frac{d\Omega}{4\pi} \mathbf{v}_F \frac{\partial \mathbf{k}_F}{\partial \Omega} \times \mathbf{k}_F$ (\mathbf{v}_F is given by the second functional derivative of H : $\delta H = \epsilon_F \frac{1}{2\pi} \frac{\partial \mathbf{k}_F}{\partial \Omega} \times \mathbf{k}_F$, $\delta \epsilon_F = \mathbf{v}_F \delta \mathbf{k}_F + \oint \frac{d\Omega'}{4\pi} \frac{\partial \mathbf{k}_F}{\partial \Omega'} \times \mathbf{k}_F$) are, in general, non-linear functionals of \mathbf{k}_F . In the presence of an external field ΔB the equation of motion for \mathbf{k}_F reads in the clean limit as

$$\frac{\partial \mathbf{k}_F}{\partial \Omega} \times (\partial_t - \mathbf{v}\nabla + \frac{\Delta B}{m^*} \partial_\Omega) \mathbf{k}_F = 0 \quad (1)$$

and serves as a counterpart of the kinetic equation, where a perturbation of the equilibrium distribution function $f_0 = \Theta(k_F - p)$ is proportional to a local FS displacement: $\delta f(\mathbf{r}, \mathbf{p}) \sim \frac{\partial \mathbf{k}_F}{\partial \Omega} \times \delta \mathbf{k}_F$.

Thus, a construction of a kinetic-type equation describing density (current) relaxation appears to be possible in the absence of well-defined (in the Landau sense) fermionic quasiparticles.

In the framework of the Chern–Simons theory of Ref. [2] our method of the 2D bosonization enables one to obtain closed integral expressions for the irreducible CF polarization $\Pi_{\mu\nu}(\omega, \mathbf{q})$, which is related to the correlator $\langle k_F^i(\mathbf{r}, \Omega, t) k_F^j(\mathbf{0}, \Omega', 0) \rangle$. Thereby we confirm a number of results, which were obtained earlier in the “optical regime” $1/\tau_{lr} \ll \omega \ll E_F$ and $1/l \ll q \ll k_{F,cf}$ ($l = v_{F,cf} \tau_{lr}$ is the CF mean free path) while neglecting impurities.^{5,7} For instance, the irreducible CF density polarization behaves similarly to that of free fermions with a finite mean field mass $m_{cf}^* \sim k_{F,cf}/e^2$, namely: $Re\Pi_{00} \sim m_{cf}^*$, $Im\Pi_{00} \sim m_{cf}^* \omega/k_{F,cf} q$.

The CF polarization still remains to be related to $K_{\mu\nu}$, which requires an analogue of the Silin’s extension of the standard Landau FL theory onto the case of long-ranged interactions. In the problem at hand it yields the physical response functions in the RPA form.^{2,5} Despite of the absence of a small parameter, such as $e^2 m_{cf}^*/k_{F,cf}$, the RPA form of the long wavelength response is dictated by the asymptotic Ward identities, which stem from an approximate particle number conservation at every FS point Ω .

In particular, the dynamic structure factor has a form

$$S(\omega, \mathbf{q}) = \text{Im}K_{00}(\omega, \mathbf{q}) \sim \omega q^3 / (\omega^2 + V_{ee}^2(q) q^6).$$

The corresponding static structure factor $S_{EDF}(q) = \int d\omega S(\omega, \mathbf{q}) \sim q^3$ In q has to be contrasted with the result $S_{FQHE}(q) \sim q^4$ for the incompressible FQHE states.

The response, however, becomes different from the Fermi-liquid-like at large q , and the divergence of m_{cf}^* does show up in processes, which correspond to rough fluctuations of the CF FS.⁴ Such processes are responsible for the SdH-type oscillations of

$$\rho_{xx}(B) = \rho_{xx}(0) + \sum_k \rho_k \cos(4\pi^2 n_e / \Delta B) \quad (2)$$

at $y = \tau_{tr}\Delta B/m_{cf}^* > 1$.

In the semiclassical theory of magnetotransport ρ_k can be related to a gauge field phase factor of a single CF making k laps along its cyclotron orbit of radius $R_{cf} = k_{F,cf}/\Delta B$: $\rho_k \sim \langle \exp(i \oint_k \mathbf{a} d\mathbf{r}) \rangle$.

Accordingly, the experiments⁸ show that the corresponding Dingle plot for $\ln \left(\frac{\Delta \rho_{xx}(B)}{\rho_{xx}(0)} \right)$ exhibits such NFL features as a $\sim (\Delta B)^{-4}$ enveloping function at $T \rightarrow 0$ and a divergent $m_{cf}^*(\Delta B) \sim (\Delta B)^{-4}$ derived from the T -dependent part in the regime $y > 1$.

We also confirmed a strong enhancement of the density response at $q = 2k_{F,cf}$, which is another apparently NFL feature. This behavior gives rise to a strong backscattering of CFs off impurities or other inhomogeneities. Therefore, one might expect to see its manifestations, for instance, in processes when a CF hits an impurity and then scatters off a standing non-uniform local exchange potential caused by the impurity itself $U_{exch}(r) \sim \sin 2k_F r / r^{3/2-\eta}$ where η characterizes the divergence of the density correlator $\langle \rho(\mathbf{q})\rho(-\mathbf{q}) \rangle \sim |q - 2k_F|^{-\eta}$. Similar kind of static Friedel oscillations of the exchange potential develop near the boundaries of the CF system in constrained geometries. These effects can be in principle observed in ballistic nanoscale devices, such as quantum wires, where they could be responsible, for instance, for a reduction of the conductance of an otherwise perfectly transmitting wire with respect to its naively expected value $G = \sigma_{xy}$.

Obviously, disorder effects are, by no means, negligible at small ω and q . In fact, the remote donors, which supply electrons to the 2DEG and provide the dominating mechanism of scattering at low densities $n_e \sim 10^{11} \text{ cm}^{-2}$, should be treated as an intrinsic element of the overall neutral Coulomb system.

Both the method of Ref, [4] and our 2D bosonization are well suited for a systematic account of disorder, which can be introduced into Eq. (1) as a RMF: $\Delta B \rightarrow \Delta B + b(\mathbf{r})$ with a white-noise correlator $\langle b(\mathbf{q})b(-\mathbf{q}) \rangle = 2\pi^2 \Phi^2 n_e e^{-2q\xi}$.

First, we solve Eq. (1) while neglecting the residual gauge interactions among CFs.⁹ At $\Phi > 1$ the RMF problem does not feature a small parameter, which would enable one to apply a customary Born approximation. However, under the condition $k_{F,cf}\xi > \Phi$ one can resort on the eikonal-type solution for $\mathbf{k}_F(\mathbf{r}, \Omega, t)$. In particular, this solution yields the CF conductivity $\sigma_{xx,cf} = \frac{e^2}{h} (k_{F,cf}\xi) \exp(\Phi^2/2) K_1(\Phi^2/2)$ which appears to be more than twice as large as the result of the first Born approximation.²

In the presence of a uniform field ΔB Eq. (1) yields a non-trivial negative magnetoresistance (MR) $\Delta \rho_{xx}(\Delta B)/\rho_{xx}(0) \approx -0.06y^2$. This result implies that one should probably take into account the CF gauge interactions in order to reconcile the theory with experiment, which shows broad minima of $\rho_{xx}(B)$ in the vicinity of the primary EDFs.

At $T > 0.1mK$ it suffices to include just the first order correction to the RMF solution, which results from quantum interference between the RMF scattering and the CF gauge interactions.¹⁰ In the framework of the kinetic equation it stems from corrections to the non-equilibrium CF density of states and the non-local part of the collision integral. Higher order terms can only become relevant at very low T .

Proceeding this way, we obtain the correction to the tensor of the CF conductivity tensor $\hat{\sigma}_{cf}$, which is related to the physical one as $\hat{\sigma}_{cf}^{-1} = \hat{\sigma}^{-1} - (\hbar/e^2\nu) \begin{pmatrix} 0 & 1 \\ -1 & 0 \end{pmatrix}$, at finite $y < 1$ (before the onset of the SdH oscillations):

$$\Delta \sigma_{xx,cf} = (1 - y^2) \Delta \sigma_{cf}, \quad (3)$$

$$\Delta \sigma_{xy,cf} = 2y \Delta \sigma_{cf} \quad (4)$$

where $\Delta \sigma_{cf} = \frac{2e^2}{h} \ln(T\tau_{tr}) \ln(k_{F,cf}l)$ for a short-range V_{ee} , and

$\Delta \sigma_{cf} = \frac{2e^2}{h} \ln(T\tau_{tr}) [\ln(k_{F,cf}l) + \frac{1}{4} \ln(T\tau_{tr})]$ in the Coulomb case. These estimates are in a

qualitative agreement with the experimental data from [11].

Compared to its zero field counterpart for ordinary electrons, the correction (2) is enhanced and non-universal (it is larger in samples of higher mobility). It also yields a positive contribution to the MR, which is greater than the negative RMF term. Therefore, preceding the SdH regime, the overall MR in the vicinity of primary EDFs increases as $\sim (\Delta B)^2$.

Also, the quantum interference corrections manifest themselves in the response of EDF state to an applied thermal gradient. In contrast to the case of zero field, the tensor of thermoelectric coefficients $\hat{\eta}$ receives a $\ln T$ contribution, and so does the low- T diffusion thermopower (TEP) $\hat{S}_d = \hat{\sigma}^{-1} \hat{\eta}$ at EDFs: $\Delta S_d \sim T \ln T$.¹² Observation of this effect should be, in principle, possible with the existing experimental techniques.

Thus, despite the fact that in the ballistic regime ($1/\tau \ll \omega \ll E_F$) the density (current) response of EDF states resembles that of a 2DEG in zero field, yet there will be observable departures in the diffusive regime ($\omega \ll 1/\tau$). These, intrinsically NFL, features result from interference between scattering off the impurities and the residual (gauge) CF interactions.

REFERENCES

- [1] R. L. Willett *et al*, Phys. Rev. Lett.**65**, 112 (1990); H. W. Jiang *et al*, *ibid* **65**, 633 (1990); R. L. Willett *et al*, *ibid* **71**, 3846 (1993); W. Kang *et al*, *ibid* **71**, 3850 (1993); V. J. Goldman *et al*, *ibid* **72**, 2065 (1994).
- [2] B. I. Halperin, P. A. Lee, and N. Read, Phys. Rev.**B47**, 7312 (1993).
- [3] P. A. Lee, E. Mucciolo, and H. Smith, Phys. Rev.**B54**, 8782 (1996); D. V. Khveshchenko and P. C. E. Stamp, *ibid* **B49**, 5227 (1994).
- [4] Y. B. Kim, P. A. Lee, and X.-G. Wen, Phys. Rev.**B52**, 17275 (1995).
- [5] S. H. Simon and B. I. Halperin, Phys. Rev.**48**, 17368 (1993); Y. B. Kim, A. Furusaki, X.-G. Wen, and P. A. Lee, *ibid* **B50**, 17917 (1994); A. Stern and B. I. Halperin, *ibid* **B52**, 5890 (1995); S. H. Simon, A. Stern, and B. I. Halperin, *ibid* **54**, R11114 (1996).
- [6] D. V. Khveshchenko, Phys. Rev.**B52**, 4833 (1995).
- [7] B. L. Altshuler, L. B. Ioffe, and A. Millis, *ibid* **B50**, 14048 (1994).
- [8] H. C. Manoharan, *et al*: Phys. Rev. Lett.**73**, 3270 (1994); R. R. Du *et al*, *ibid* **73**, 3274 (1994); P. T. Coleridge *et al*, Phys. Rev.**B52**, R11603 (1995).
- [9] D. V. Khveshchenko Phys. Rev. Lett.**77**, 1817 (1996).
- [10] D. V. Khveshchenko, Phys. Rev. Lett.**77**, 362 (1996); Phys. Rev.**B55**, 13817 (1997).
- [11] L. P. Rokhinson *et al*, Phys. Rev.**B52**, R11588 (1995); *ibid* **B56**, R1672 (1997).
- [12] D. V. Khveshchenko, Phys. Rev.**B54**, R14317 (1996).

This page intentionally left blank

TRANSPORT THROUGH LOW DENSITY QUANTUM DOTS

Richard Berkovits

The Jack and Pearl Resnick Institute of Advanced Technology
Department of Physics
Bar-Ilan University
Ramat-Gan 52900, Israel

INTRODUCTION

As a result of the great advances in the fabrication of nanostructures and in measurement methods the physical properties of novel quantum dots in which few electrons (of order of 10–1000 electrons) reside are now experimentally accessible. Several recent experiments^{1–5} have measured the transport properties of these dots, weakly coupled to the external world by leads. The conductance through the dot is measured as function of the gate voltage on the dot which controls the number of electrons in the dot. The low temperature conductance shows sharp peaks for values of the gate voltage for which a degeneracy between states of N and $N + 1$ electrons in the dot exists.

One is immediately stricken by two main features of the conductance: an almost constant spacing between the conductance peaks, and a strong variation in the peaks heights. These features are best described by plotting the distributions of the peak spacings and the peak heights. The distribution of the peak spacings is almost Gaussian, where the width of the distribution is between 5%⁵ and 15%³ of the mean spacing value. The peak heights have a broad distribution which peaks at zero when no magnetic field is applied, and peaks at a non-zero value once a magnetic field is present. Moreover, the peak height sensitivity to a change in the magnetic field is also measured.^{1, 2}

These features were customary interpreted in the framework of the constant interaction picture, which neglects all correlations between the electrons. Although this theory captures some of the features of the conductance, it fails to account for others. We show that once short range correlations between the electrons due to electron–electron interactions are taken into account the conductance features are better reproduced.

The importance of the short range correlations in these systems stems from the low density of the electrons within the dot. In the leads the 2DEG (two dimensional electron gas) density is about $2 - 3.5 \times 10^{-11} \text{cm}^{-2}$, and the density in the dot is probably significantly lower. The condition for which the uncorrelated electron approximation fails is $r_s = e^2/v_f < 1$, where v_f is the Fermi velocity. Therefore, for $n < 1/\pi a_B^2$, where n is the electron density in the dot and a_B is the Bohr radius, which in GaAs is $\sim 100 \text{\AA}$, one expects the constant interaction model to fail at densities of $n < 3 \times 10^{-11} \text{cm}^{-2}$.

CONSTANT CHARGING MODEL

Since the discovery of the Coulomb blockade phenomenon, most tunneling experiments through a quantum dot were interpreted within the constant interaction model.^{6,7} In this approximation, the ground state energy of a quantum dot populated by N electrons is expressed as $E_N = \frac{e^2 N^2}{2C} + \sum_{i=1}^N \eta_i$ where C is the dots constant (or slowly varying) capacitance, and η_i are the single particle energies. In this model only the long range part of the interaction is taken into account while the short range correlations are neglected.

Peaks in the conductivity will appear only at values of gate voltage V_g corresponding to $E_N + \gamma V_g = E_{N+1}$ ³ (where γ is the capacitive coupling between the gate and the dot). Thus the spacing between the consecutive conductance peaks denoted by Δ_2 is proportional to

$$\Delta_2 = E_{N+1} - 2E_N - E_{N-1} \sim \frac{e^2}{C} + \eta_{N+1} - \eta_N. \quad (1)$$

Since e^2/C has no significant fluctuations even in the random phase approximation,^{8,9} all the fluctuations arise from the the fluctuations in the single electron level spacing $\Delta = \eta_{N+1} - \eta_N$. The fluctuations in the single electron level spacings are governed by the well known random matrix theory, which result in a non-symmetric Wigner distribution of width proportional to $\sqrt{\delta^2 \Delta_2} \sim \Delta/2$.³ These results do not agree with the experimental findings since the measured distribution is Gaussian (symmetric) and the width for most experimental measurements (excluding perhaps Ref. [5]) is to small considering the fact that $\Delta \sim 0.05 e^2/C$

The distribution of the conductance peak can be calculated from the single electron wave functions resulting in [1, 2]:

$$P_{B=0}(\alpha) = \sqrt{\frac{2}{\pi\alpha}} e^{-2\alpha}, \quad (2)$$

and

$$P_{B \neq 0}(\alpha) = 4\alpha [K_0(2\alpha) + K_1(2\alpha)] e^{-2\alpha}. \quad (3)$$

Here, α is the normalized conductance peak height and K_0, K_1 are the modified Bessel functions. These predictions fit the experimental distributions quite well. On the other hand, the correlation flux, i.e., the change in flux for which the peak height loses correlation with its previous value, is of order $0.2 - 0.3 \Phi_0$ (Φ_0 is a quantum flux), while the experimental value is larger by a factor of 3.

SHORT RANGE CORRELATIONS

As we have seen in the previous section, the constant interaction model fails to explain some of the observed experimental behavior. This is not surprising, since as we have previously argued the dots are in a density regime for which we don't expect this approximation to hold. In order to study this regime we numerically study a system of interacting electrons modeled by a tight-binding Hamiltonian.^{3, 8, 10} We choose a 2D cylindrical geometry of circumference L_x and height L_y . This particular geometry is very convenient for the study of the influence of a magnetic flux ϕ threading the cylinder in the \hat{y} direction. The Hamiltonian is given by:

$$H = \sum_{k,j} \epsilon_{k,j} a_{k,j}^\dagger a_{k,j} - V \sum_{k,j} (\exp(i2\pi(\phi/\Phi_0)s/L_x) a_{k,j+1}^\dagger a_{k,j} + a_{k+1,j}^\dagger a_{k,j} + h.c.) + H_{int}, \quad (4)$$

where $\epsilon_{k,j}$ is the energy of a site (k,j) , chosen randomly between $-W/2$ and $W/2$ with uniform probability, $a_{k,j}^\dagger$ is the fermionic site creation operator, V is a constant hopping

matrix element, and s is the lattice unit. The interaction Hamiltonian is given by.

$$H_{int} = U \sum_{k,j>l,p} \frac{a_{k,j}^\dagger a_{k,j} a_{j,p}^\dagger a_{l,p}}{|\vec{r}_{k,j} - \vec{r}_{l,p}|/s} \quad (5)$$

where $U = e^2/s$. The distance $|\vec{r}_{k,j} - \vec{r}_{l,p}|/s = (\min\{(k-l)^2, (L_x/s - (k-l))^2\} + (j-p)^2)^{1/2}$. The interaction term represents Coulomb interaction between electrons confined to a 2D cylinder embedded in a 3D space.

The Hamiltonian matrix is numerically diagonalized and the N electron ground-state eigenvectors Ψ_N and Eigenvalues E_N are obtained. The conductance spacings can be directly calculated from the eigenvalues (Eq. (1)), while the height g_{max} of a conductance peak is given by [10]

$$g_{max} = \frac{e^2}{h} \left(\frac{\pi}{2k_B T} \right) \frac{\Gamma_L \Gamma_R}{\Gamma_L + \Gamma_R}. \quad (6)$$

The tunneling rates may be formulated in a tight-binding many particle language as

$$\Gamma_{L(R)} \propto \left| \sum_{k,j \in [L(R)]} \langle \Psi_{N+1} | a_{k,j}^\dagger | \Psi_N \rangle \right|^2, \quad (7)$$

where summation is performed on sites $k, j \in [L(R)]$ i.e, sites adjacent to the left (right) lead.

For small values of U (corresponding to high densities) all the results of the constant charging model are reproduced.

For higher values of U (corresponding to low densities) the following results are obtained:

1. Short range correlations between the electrons appear.⁸
2. A Gaussian shaped distribution of the conductance peak spacings appears. The shape of the distribution is quite independent on the value of U (as long as the density is not low enough for the Wigner crystallization to appear).³
3. The width of the spacing distribution is of order of 10%–20% of the average conductance peak spacing.³
4. The distribution of the peak heights for both $B = 0$ and $B \neq 0$ fits rather well Eqs. (2) and (3) over a large range of values of U .¹⁰
5. The correlation flux value increases by a factor of 4 when the value of the interaction strength U is changed by an order of magnitude.¹⁰

COLLISIONS

As can be seen from the results summarized in the previous section, the behavior of the Hamiltonian in the region of strong interactions for which short range correlations exist fits the results of the experiment better than the results in the weak interaction (corresponding to the constant interaction) regime. Especially one should note the shape of the conductance peak spacing and the value of the correlation flux. The strong interaction behavior of these quantum dots is the result of their low density. The fact that these quantum dots are strongly coupled Coulomb systems can be seen from the results of recent transport measurements, which cannot be explained in the weak interaction limit.

Acknowledgements

I would like to thank A. Auerbach, B. L. Altshuler and U. Sivan, with whom I have collaborated on various aspects of the work reported here.

REFERENCES

- [1] J. A. Folk, S. R. Patel, S. F. Godijn, A. G. Huibers, S. M. Cronenwett, C. M. Marcus, K. Campman and G. Gossard, *Phys. Rev. Lett.* **76**, 1699 (1996).
- [2] A. M. Chang, H. U. Baranger, L. N. Pfeiffer, K. W. West and T. Y. Chang, *Phys. Rev. Lett.* **76**, 1695 (1996).
- [3] U. Sivan, R. Berkovits, Y. Aloni, O. Prus, A. Auerbach and G. Ben-Yoseph, *Phys. Rev. Lett.* **77**, 1123 (1996).
- [4] F. Simmel, T. Heinzel and D. A. Wharam, *Europhys. Lett.* **38**, 123 (1997).
- [5] S. R. Patel, S. M. Cronenwett, D. R. Stewart, A. G. Huibers, C. M. Marcus, C. I. Duruoz, J. S. Harris, K. Campman and G. Gossard, /cond-mat 9708090
- [6] M. A. Kastner, *Rev. Mod. Phys.* **64**, 849 (1992).
- [7] U. Meirav and E. B. Foxman, *Semicond. Sci. Technol.* **10**, 255 (1995).
- [8] R. Berkovits and B. L. Altshuler, *Phys. Rev. B* **55**, 5297 (1997).
- [9] Ya. M. Blanter, A. D. Mirlin and B. A. Muzykantskii, *Phys. Rev. Lett.* **78**, 2449 (1997).
- [10] R. Berkovits and U. Sivan /cond-mat 9707138

ELECTRONIC CORRELATIONS IN SEMICONDUCTOR QUANTUM DOTS

Pawel Hawrylak

Institute for Microstructural Sciences
National Research Council of Canada
Ottawa, K1A 0R6, Canada

Recent work toward electronic and opto-electronic devices with sub-micron dimensions has led to Quantum Dot (QD) based single-electron transistors(QSET)¹ and single-exciton lasers (QSXL).² Despite the word “single” in their names these devices are complex many-body systems, with electronic “correlations” playing an important role. The electronic properties of QSET/QSXL can be tuned with the number of free carriers N , much like properties of atoms change drastically across the table of elements.

We review here progress toward the understanding of electronic properties of QDs using exact diagonalization techniques(EDT) applied to electrons and/or excitons in semiconductor quantum dots.

We consider quantum dots produced in quasi-two-dimensional systems by surface gates, and by strain during growth of strained quantum wells.^{1, 3} These physically different systems turn out to be well approximated by a simple model of quantum dots with parabolic confining potential $\frac{1}{2}m^*\omega_0^2(x^2 + y^2)$, and m^* is the effective mass. The confining potential is given by energy ω_0 , which may depend on the number of particles N . Typical values for ω_0 are 1 – 10meV for gated dots and 10 – 100meV for self-assembled dots.

The single particle Hamiltonian can be diagonalized exactly^{4, 5} and corresponds to a pair of harmonic oscillators. The single-particle energies are $\epsilon_{mn} = \Omega_+(n + \frac{1}{2}) + \Omega_-(m + \frac{1}{2})$, where $\Omega_{\pm} = \frac{1}{2}(\sqrt{\omega_c^2 + 4\omega_N^2} \pm \omega_c)$ and $\omega_c = eB/m^*c$ is the cyclotron frequency and B is the magnetic field. The magnetic length is $l_0 = 1/\sqrt{m^*\omega_c}$ and the effective magnetic length in the presence of confinement is $l_{\text{eff}} = l_0/(1 + 4\omega_N^2/\omega_c^2)^{1/4}$. The orbital angular momentum of the state $|m, n\rangle$ is $m - n$.

The parabolic form of the confining potential leads to dynamical symmetries. The symmetries manifest themselves in degeneracies of the spectrum of two harmonic oscillators whenever $\Omega_+/\Omega_- = p$. For example, for $p = 1$ $\epsilon_{mn} = \Omega_+(n + m + 1)$, i.e., there are shells of degenerate levels whenever $n + m = \text{const}$.

The parabolic confinement in QDs leads to important many-particle symmetry associated with the separability of the Center-of-Mass (CM) motion.^{5, 6} Hence QDs poses many properties of translationally invariant Fermi systems. Attempts have been made to incorporate both the CM symmetry and symmetries associated with the invariance of the Hamiltonian due to spin rotation in constructing a convenient set of many-particle wavefunctions.⁷⁻¹²

Our work was based on the harmonic oscillator (HO) representation of the Hamiltonian.^{4, 5} The key to the success of the method was the introduction of generalized Jacobi coordinates consistent with representation of the permutation group S_N of N electrons. The HO representation allowed us to *derive* the explicit form of few electron wavefunctions. The restrictions imposed on bosonic HO states by Fermi statistics led to new statistical quantum numbers.⁵ Exact diagonalization studies of $N = 3$ artificial atom in HO representation have been reported in Ref. [4,5]. An experimental verification of transitions between “magic states” can be found in recent Single Electron Capacitance (SECS)^{13, 14} and tunneling experiments.¹⁵

The generalized Jacobi coordinates provide a significant insight into correlations particular to parabolic QDs in a magnetic field. They are however difficult to implement for larger number of electrons.¹⁶ One therefore resorts to standard EDT in the language of second quantization.^{17–22} This method works well in strong magnetic fields which restrict the single particle basis. Alternative methods of attack on large number of electrons include Hartree–Fock approach,^{21, 23, 24} density functional calculations,^{25–27} and Composite Fermion approach.²⁸ QDs in strong magnetic fields have been studied experimentally using SECS,¹³ tunneling,¹⁵ and transport^{29–31} spectroscopies.

We discuss here two examples of electron correlations in QD in strong magnetic fields: oscillations of total spin in the filling factor regime $1 < \nu < 2$ and chiral Luttinger liquid behavior in the fractional regime.^{6, 12, 21, 22}

The behavior of total spin in the regime $1 < \nu < 2$ has been studied by Wojs et al.²² At low magnetic fields both spin down and up electrons occupy the lowest kinetic energy single particle states. With increasing magnetic field, spin up electrons flip their spin and move to the edge of the droplet. The ground state corresponding to well defined spin up and down electron droplets corresponds to Hartree–Fock configurations^{6, 23} with maximum total spin $S = S_z$. These configurations are surprisingly interrupted by configurations with minimum total spin $S = 0$. The loss of Zeeman and exchange energy is compensated by gain in kinetic and correlation energy. For an insight into the wavefunctions of these spin textures see Oaknin et al.⁶ and references therein.

Wen²¹ predicted that the Hamiltonian describing edge excitations of 2DEG at fractional filling is equivalent to the Hamiltonian describing the chiral Luttinger liquid. Kinaret et al.¹² suggested that the signature of the Luttinger liquid behavior is the suppression of the density of states at the chemical potential. This has been successfully tested through EDT^{22, 33} where it was verified that as the magnetic field increases and the droplet evolves toward fractional occupations, the addition of an extra electron to the edge of the droplet becomes forbidden. The suppression of the GS-GS transitions below $\nu = 1$ is a signature of the non-Fermi-liquid behavior.

Let us now turn to electronic properties of self-assembled quantum dots (SAD). SADs are produced without additional processing, and therefore attracted a lot of attention.^{2, 3, 34–39} The one-electron states in SAD can be described by the HO oscillator model.⁴⁰ These dots are characterized by large kinetic energy quantization $\omega_0 \approx 10 - 100$ meV, and have the potential for useful room temperature devices. The electronic structure of SAD filled with electrons has been investigated by Wojs et al.^{41, 42} using EDT in configuration-interaction basis. The numerical calculations established a simple picture of electronic shells consistent with Hund’s rules. In case of partially filled shells i.e., degenerate states, the configuration with maximum total spin and maximum angular momentum forms the ground state.

Drexler *et al.*⁴³ and Fricke *et al.*⁴⁴ reported FIR absorption measurements of electronic excitations in SADs as a function of the number of electrons and the magnetic field. The SECS and FIR spectra were calculated by Wojs et al.⁴¹ For an infinite parabolic confinement only the center of mass excitations with frequencies Ω_+ and Ω_- (generalized Kohn’s theorem)^{1, 45} can be measured in FIR. In SAD, a finite number of confined FD levels leads to additional

transitions in the IR spectrum related to the magnetic field induced changes in the GS, e.g., spin triplet to spin singlet transition leading to a splitting of the FIR transitions. Experiments by Fricke et al.⁴⁴ indeed showed the predicted splitting, which illustrates the desired sensitivity of the optical transitions to the number of electrons N .

Photoluminescence is the simplest probe of the electronic structure in semiconductors. The interaction of electrons with an exciton in quantum dots^{4, 24, 46, 47} and the recombination spectrum of modulation doped SADs has been studied recently.^{42, 48} The photoluminescence spectrum has been related to the spectral function of the hole (vacancy) created in the correlated electron ground state. Wojs et al.⁴² have shown that there are oscillations and splittings of the photoluminescence spectra, directly related to the number of electrons in the dot. The splitting of the PL line is related to many resonant excited configurations of the interacting system coupled by Coulomb interactions. Recent experiments by Schmidt et al.⁴⁸ on modulation doped SAD appear to be consistent with theoretical predictions.

Inelastic light scattering measures the excitation spectrum of a QD^{49–52} and, in principle, can provide direct evidence of the discrete nature of energy spectrum in zero-dimensional (0D) systems. The electron–electron interactions play a significant role in determining these excitations.⁴⁹ A number of groups^{50–53} have undertaken the inelastic light scattering experiments in quantum dots. Lockwood et al.⁵¹ carried out investigation of electronic excitations in modulation doped quantum dots in a magnetic field. Their result supported the notion of electronic shells even in dots with ≈ 100 electrons.

Recently, Potemski et al.⁵³ carried out resonant inelastic light scattering studies of SAD. The findings were interpreted in terms of correlations between an electron, a valence hole, and a phonon.

To understand the operation of a quantum dot based laser one must understand the effect of exciton–exciton interaction on optical properties of highly excited SAD. Experiments⁵⁴ and calculations^{54, 55} were carried out for SAD which can be filled with up to 30 electrons and holes. For most quantum dots where electrons and holes are confined in the same physical area, the electron and hole interactions are highly symmetrical. For symmetrical interactions in a degenerate shell, the commutator of the Hamiltonian and the interband polarization operator P^+ can be approximated as $[H, P^+] = E_X P^+$, where E_X is an approximate exciton binding energy. This commutation relation is a manifestation of hidden symmetry.⁵⁶ One can construct coherent N exciton states $(P^+)^N |v\rangle$ as eigenstates of P^2 . Due to hidden symmetry these coherent states are also eigenstates of the shell Hamiltonian with energies $E(N) = N E_X$. The energy of these states is the sum of energies of noninteracting excitons.

In a QSXL one needs to add/subtract an exciton to/from a dot already filled with excitons. Numerically calculated energy to add an exciton to N excitons indeed showed the constant value, independent of the number of excitons, in agreement with the “hidden symmetry” argument.

An application of the magnetic field destroys the hidden symmetry responsible for this behavior, as demonstrated by Raymond et al.⁵⁴ The blueshift of the chemical potential was also evident in a SAD red-emitting laser structure studied by Fafard et al.²

REFERENCES

- [1] For reviews and references see R. C. Ashoori, Nature **379**, 413 (1996), M. Kastner, Physics Today, **24**, January 1993; T. Chakraborty, Comments in Cond. Matter Physics **16**, 35 (1992);
- [2] S. Fafard, K. Hinzer, S. Raymond, M. M. Dion, J. P. McCaffrey, Y. Feng, S. Charbonneau, Science **274** 1350 (1996).
- [3] P. M. Petroff and S. P. Denbaars, Superlattices and Microstructures **15**, 15 (1994); Proceedings of International Conference on Modulated Semiconductor Structures, Madrid, 1995, Solid State Electronics, **40** (1996).

- [4] P. Hawrylak and D. Pfannkuche, *Phys. Rev. Lett.* **70**, 485 (1993)
- [5] P. Hawrylak, *Phys. Rev. Lett.* **71**, 3347 (1993).
- [6] J. H. Oaknin, L. Martin–Moreno, and C. Tejedor, *Phys. Rev.* **B54**, 16 850 (1996).
- [7] Yu. A. Bychkov, S. V. Iordanskii, and G. M. Eliashberg, *JETP Lett*33,143(1981) Yu. Bychkov and E. I. Rashba, *JETP* **69**, 430(1989).
- [8] R. B. Laughlin, *Phys. Rev.* **B 27**,3383(1983).
- [9] S. M. Girvin and Terrence Jach, *Phys. Rev.* **B 28**, 4506 (1983).
- [10] S. A. Trugman and S. A. Kivelson, *Phys. Rev.* **B 31**, 5280 (1985).
- [11] R. W. Haase, N. F. Johnson *Phys. Rev.* **B 49** 14409 (1994).
- [12] J. M. Kinaret, Y. Meir, N. S. Wingreen, P. A. Lee, and X.-G. Wen, *Phys. Rev.* **B46**, 4681 (1992).
- [13] R. C. Ashoori, H. L. Stormer, J. S. Weiner, L. N. Pfeiffer, K. W. Baldwin, and K. W. West, *Phys. Rev. Lett.* **71**, 613(1993).
- [14] Bo Su, V. J. Goldman, and J. E. Cunningham, *Science* **255**, 313 (1992).
- [15] S. Tarucha, D. G. Austing, T. Honda, R. J. van der Hage, and L. P. Kouvehoven, *Phys. Rev. Lett* **77**, 3613 (1996).
- [16] A. Wojs and P. Hawrylak, to be published
- [17] P. A. Maksym, *Physica* **B184**, 385 (1993); P. A. Maksym and T. Chakraborty, *Phys. Rev. Lett.* **65**, 108 (1990); P. A. Maksym and T. Chakraborty, *Phys. Rev.* **B45**, 1947 (1992).
- [18] A. H. MacDonald, S. R. Eric Yang, and M. D. Johnson, *Aust. J. Phys.* **46**, 345 (1993).
- [19] E. H. Rezayi, *Phys. Rev.* **B36**, 5454 (1987).
- [20] J. J. Palacios, L. Martin–Moreno, G. Chiappe, E. Louis, and C. Tejedor, *Phys. Rev.* **B50**, 5760 (1994).
- [21] X. G. Wen, *Phys. Rev. B*, **41**, 12 838 (1990); C. de Chamon and X.-G. Wen, *Phys. Rev.* **B49**, 8227 (1994).
- [22] Arkadiusz Wojs and Pawel Hawrylak, *Phys. Rev. B* **56**, 13227 (1997).
- [23] P. Hawrylak, *Phys. Rev.* **B51**, 17 708 (1995).
- [24] P. Hawrylak, A. Wojs, and J. A. Brum, *Solid State Commun.* **98**, 847 (1996); *Phys. Rev. B*, **54**, 11 397 (1996).
- [25] M. W. C. Dharma-wardana, *J. Phys. - Condensed Matter*, **7**, 4095, (1995).
- [26] M. Ferconi and G. Vignale, *Phys. Rev. B* **56**, 12108 (1997).
- [27] M. J. Lubin, O. Heinonen, M. D. Johnson, *Phys. Rev. B* **56**, 10373 (1997).
- [28] J. K. Jain, T. Kawamura *Europhys. Lett.* **29**, 321 (1995); R. K. Kamilla, J. K. Jain *Phys. Rev. B* **52**, 2798 (1995).
- [29] P. L. McEuen, E. B. Foxman, J. M. Kinaret, U. Meirav, M. A. Kastner, N. S. Wingreen, and S. J. Wind, *Phys. Rev.* **B45**, 11 419 (1992).
- [30] A. Sachrajda, R. P. Taylor, C. Dharma-wardana, P. Zawadzki, J. A. Adams, and P. T. Coleridge, *Phys. Rev.* **B47**, 6811 (1993).
- [31] O. Klein, S. de Chamon, D. Tang, D. M. Abusch–Magder, U. Meirav, X.-G. Wen, M. A. Kastner, and S. J. Wind, *Phys. Rev. Lett.* **74**, 785 (1995).
- [32] P. Hawrylak, *Solid State Comm.* **88**, 475 (1993).
- [33] J. J. Palacios and A. H. MacDonald, *Phys. Rev. Lett.* **76**, 118 (1996).
- [34] N. Kirstaedter, N. N. Ledentsov, M. Grundmann, D. Bimberg, V. M. Ustinov, S. S. Ruvimov, M. V. Maximov, P. S. Kop'ev, Zh. I. Alferov, U. Richter, P. Werner, U. Gösele, and J. Heydenreich, *Electronics Letters*, **30**, 1416 (1994); M. Grundmann, J. Christen, N. N. Ledentsov, J. Bohrer, D. Bimberg, S. S. Ruvimov, P. Werner, U. Richter, U. Gosele, J. Heydenreich, V. M. Ustinov, A. Yu. Egorov, A. E. Zhukov, P. S. Kop'ev, and Zh. I. Alferov, *Phys. Rev. Lett.*, **74**, 4043 (1995).
- [35] J.-Y. Marzin, J.-M. Gérard, A. Izraël, D. Barrier, and G. Bastard, *Phys. Rev. Lett.*, **73**, 716 (1994).
- [36] R. Notzel, J. Temmyo, and T. Tamamura, *Nature*, **369**, 131 (1994).
- [37] H. Lipsanen, M. Sopanen, and J. Ahopelto, *Phys. Rev. B*, **51**, 13 868 (1995).
- [38] S. Fafard, et. al, *Appl. Phys. Lett.* **65**, 1388 (1994); R. Leon, et. al, *Appl. Phys. Lett.* **67**, 521 (1995); S. Fafard, et. al, *Phys. Rev. B* **52**, 5752 (1995).
- [39] K. H. Schmidt, G. Medeiros–Ribeiro, M. Oestreich, P. M. Petroff, and G. H. Döhler, *Phys. Rev. B*, **54**, 11 346 (1996).
- [40] A. Wojs, P. Hawrylak, S. Fafard, L. Jacak; *Phys. Rev.* **B54**, 5604 (1996).
- [41] A. Wojs and P. Hawrylak, *Phys. Rev. B* **53**, 10 841 (1996)
- [42] A. Wojs and P. Hawrylak, *Phys. Rev. B* **55**, 13066 (1997).
- [43] H. Drexler, D. Leonard, W. Hansen, J. P. Kotthaus, and P. M. Petroff, *Phys. Rev. Lett.*, **73**, 2252 (1994).
- [44] M. Fricke, A. Lorke, J. P. Kotthaus, G. Medeiros–Ribeiro, and P. M. Petroff, *Europhys. Lett.* **36**, 197 (1996).
- [45] W. Kohn, *Phys. Rev.* **123**, 1242 (1961); L. Brey, N. Johnson, B. Halperin, *Phys. Rev. B* **40**, 10 647 (1989); P. Maksym, T. Chakraborty, *Phys. Rev. Lett.* **65**, 108 (1990).

- [46] S. Patel, A. S. Plaut, P. Hawrylak, H. Lage, P. Grambow, D. Heitmann, K. von Klitzing, J. P. Harbison and L. T. Florez, *Solid State Comm.***101**,865 (1997).
- [47] A. Wojs and P. Hawrylak, *Phys. Rev. B* **51**, 10 880 (1995).
- [48] K. H. Schmidt, G. Medeiros-Ribeiro, P. M. Petroff, *Physica B*, in press
- [49] P. Hawrylak, *Solid State Commun.***93**, 915(1995).
- [50] R. Strentz *et al.*, *Phys. Rev. Lett.* **73**, 3022 (1994).
- [51] D. J. Lockwood, P. Hawrylak, P. D. Wang, C. M. Sotomayor-Torres, A. Pinczuk, and B. S. Dennis, *Phys. Rev. Lett.***77**, 354 (1996).
- [52] C. Schuller, G. Biese, K. Keller, C. Steinebach, D. Heitmann, P. Grambow, K. Eberl, *Phys. Rev.* **B54**, 17304 (1996).
- [53] P. Hawrylak, M. Potemski, H. Labbe, D. J. Lockwood, J. Temmyo, and J. Tamamura, "Inelastic light scattering from self-assembled quantum disks," *Physica B*, in press
- [54] S. Raymond, P. Hawrylak, C. Gould, S. Fafard, A. Sachrajda, M. Potemski, A. Wojs, S. Charbonneau, D. Leonard, P. M. Petroff, and J. L. Merz, *Solid State Comm.***101**,883 (1997); S. Raymond, S. Fafard, P. J. Poole, A. Wojs, P. Hawrylak, S. Charbonneau, D. Leonard, R. Leon, P. M. Petroff, and J. L. Merz, *Phys. Rev. B*, **54**, 11548(1996).
- [55] A. Wojs and P. Hawrylak, *Solid State Comm.***100**, 487 (1996); P. Hawrylak and A. Wojs, *Semic. Sci. Tech.* **11**, 1516(1996).
- [56] I. V. Lerner, Yu. E. Lozovik, *Zh. Eksp. Teor. Fiz.* **80**, 1488 (1981) [*Sov. Phys. JETP* **53**, 763 (1981)]; D. Paquet, T. M. Rice, K. Ueda, *Phys. Rev. B*, **32**, 5208 (1985); A. H. MacDonald, E. H. Rezayi, *Phys. Rev. B* **42**, 3224 (1990); Yu. A. Bychkov and E. I. Rashba, *Phys. Rev. B*, **44**, 6212 (1991).

This page intentionally left blank

COLLECTIVE VS INDIVIDUAL DOT RESPONSE OF QUANTUM DOT ENSEMBLES

P. Bakshi and K. Kempa

Physics Department, Boston College,
Chestnut Hill, MA 02167, USA

Quantum dots are microscopic, essentially zero-dimensional structures, where the confining potential can be tailored through the material parameters and the geometry of confinement. A periodic ensemble of quantum dots is created by periodic etching¹ or periodic gating², with the objective of creating a regular lattice of identical quantum dots. In the case of self assembled quantum dots³, on the other hand, the individual dots may vary in size and the interdot separations are randomly distributed. Primary experimental tools employed to study the response of quantum dot ensembles have been the far infrared (FIR) spectroscopy and single electron charging (capacitance) studies. Theoretical studies are by and large based on model confining potentials (for the individual dots) and model electron-electron interactions.

We examine in this paper the FIR response of an ensemble of quantum dots where the individual dots may have different intrinsic FIR responses and where the interdot distances may be randomly distributed. This is the experimental situation for the self assembled dots. It is intuitively clear that if the interdot distances are large, the dots will respond individually at their specific frequencies, and for an ensemble of dots that span a broad frequency range, one should expect a correspondingly broadened line shape. When the interdot separations are small, and the interdot interactions are strong, the possibility arises that the whole ensemble will respond at a single (or a few) *collective* frequencies, with narrow line widths. We develop here a formalism to determine the transition from the individual to the collective behavior.

RESPONSE OF A SINGLE QUANTUM DOT

The confining potential can be created in many different ways, but in all cases, it will have a minimum where a single electron would rest, classically, or have a localized wave function, quantum mechanically. The curvature at the minimum defines the natural frequency ω_0 for simple harmonic motion around the rest position. If the confinement is due to a uniform sphere of jellium (distributed positive charge), the restoring force at distance r is only due to the charge inside the sphere of radius r , $\mathbf{F} = -\mathbf{k}r$, $\mathbf{k} = 4\pi n_+ e^2 / 3\epsilon$, where $n_+ e$ is the charge density and ϵ the dielectric constant. This leads to the Mie frequency

$$\omega_0^2 = \frac{4pn_+e^2}{3me} = \frac{N_+e^2}{m\epsilon R^3}, \quad (1)$$

for confinement by a spherical jellium. The system is isotropic and the exact parabolic potential continues up to the edge of the sphere. N_+e is the positive charge of the jellium sphere. For a uniform (thin) strip of jellium, a simple symmetry argument shows that the net force on an electron displaced from the center by a distance x is only due to the jellium of length $2x$ at the opposite end of the strip, $F = -kx$, $k = 2n_+e^2/R^2\epsilon$ where R is the half length of the strip and n_+e is the linear charge density. The corresponding frequency for small oscillations is

$$\omega_0^2 = \frac{2n_+e^2}{m\epsilon R^2} = \frac{N_+e^2}{m\epsilon R^3}. \quad (2)$$

For a strip, the parabolic potential is enhanced as one moves away from the center. For a uniform disk of jellium, of radius R , and areal charge density n_+e , while the calculation⁴ is not as elementary as the above two cases, the result for small oscillations is the same (note the identity of the last expression in each case),

$$\omega_0^2 = \frac{\pi n_+e^2}{m\epsilon R} = \frac{N_+e^2}{m\epsilon R^3}. \quad (3)$$

Other modes of confinement will also produce some characteristic ω_0 and a nearly parabolic potential.

A single electron in any such confining potential will absorb FIR at frequency ω_0 by making a transition from the ground state to the first excited state. Several noninteracting electrons would also give a similar result. One might expect a dot filled with several (interacting) electrons to produce a different absorption pattern, and thereby reveal some properties of the many body system, due to inter-electron interactions. It was thus a surprise when an experiment⁵ showed that the absorption frequency did not depend on the electron number ($N_- = 3$ to 20).

This phenomenon was soon understood^{6,7} in terms of the center of mass motion of all electrons in a parabolic potential. FIR radiation, due to its long wavelength, only couples to the total dipole strength $N_+e\vec{R} = \sum e\vec{r}_i$. For a parabolic potential the total Hamiltonian is exactly separable into the center of mass and relative coordinates

$$H = H_{CM} + H_{Rel}, \quad H_{CM} = \frac{P^2}{2M} + \frac{1}{2} M\omega_0^2 R^2. \quad (4)$$

The e-e interactions are in the H_{Rel} , and thus do not affect the FIR absorption. It is as if we are dealing with a single charge (N_-e) of mass $M=N_-m$ in a parabolic well of frequency ω_0 , represented by H_{CM} in Eq. (4).

This picture remains valid even in the presence of a magnetic field^{6,7}. For a quantum disk dot, the FIR response with magnetic field B produces absorption peaks at frequencies $\omega_{\pm} = (\omega_0^2 + \frac{1}{4} \omega_c^2)^{1/2} \pm \frac{1}{2} \omega_c$, $\omega_c = eB/mc$. For the parabolic potential, the separability of H_{CM} and H_{rel} is exact and the response remains independent of the number of electrons in the quantum dot.

RESPONSE OF A QUANTUM DOT ENSEMBLE

How would these results change for an ensemble of quantum dots? The simplest case is that of identical dots in a regular array. The positive charges in the neighboring dots can

now alter the restoring force in a given dot. A square array of identical dots, each with intrinsic frequencies ω_0 , leads to FIR absorption at a lower (collective) frequency⁷,

$$\Omega^2 = \omega_0^2 - \sum \frac{N_+ e^2}{d \cdot 2\epsilon m d^3} , \quad (5)$$

The summation is taken over all d 's, the distances of all positive charges in the other dots measured from the center of the given dot. For a square array of lattice period a , assuming that the size of a dot is much smaller than a , the interdot interaction leads to the lowered (collective) frequency

$$\Omega^2 = \omega_0^2 - \lambda \frac{N_+ e^2}{m \epsilon a^3} \quad (6)$$

with $\lambda \approx 4.517$. The FIR response thus changes from the characteristic individual dot response ω_0 , when $a \gg R$, to the collective response $\Omega < \omega_0$, as a is reduced. This is called mode softening. There is only a single peak response for any a . The electron-electron interactions do not affect this result due to the separability into a total H_{CM} for the whole ensemble, and a H_{rel} , as long as the non-parabolic terms remain small.

There were two assumptions in the discussion above: (a) identical dots and (b) a regular array. What would be the result if these assumptions are relaxed? Consider an array where the individual dots have different intrinsic frequencies ω_j (due to different sizes R_j), and where they are arranged at random. (1) If the dots are far apart, each responds at its harmonic frequency ω_j , and a series of sharp absorption peaks at the set $\{\omega_j\}$ will be seen. With other line broadening mechanisms, and closely spaced ω_j , one can expect an overall broad response, comparable to the spread in $\{\omega_j\}$. This is akin to a broad "single particle" absorption spectrum. (2) If the dots are brought closer, strong interdot interactions may become possible, and may eventually enforce a "collective" response from the whole ensemble at a single frequency, producing a narrow line width. This would be the analog of the typical collective interaction and response of any ensemble of charged particles.

It should be noted that if the spread in individual ω_j is negligible (assumption (a)), the response will be a single peak even at large dot-separations. This is due to the degeneracy of ω_j rather than any collective interaction. It should also be noted that by retaining assumption (a), but relaxing assumption (b), the irregularity of distances d in Eq. (5) can lead to different effective frequencies Ω for different dots, thus suggesting a broadened response from a random ensemble of identical dots.

A SIMPLE MODEL

For a quantitative analysis of these questions, we examine a simple model, which shows the transition from the individual to the collective behavior, and which also illustrates various methods that can be used to tackle the general problem. Consider only two dots, with one electron in each dot. The individual confinement frequencies ω_1 and ω_2 are unequal. Treating the system as quasi-one dimensional, the full Hamiltonian is

$$H = \frac{P_1^2}{2m} + \frac{P_2^2}{2m} + \frac{1}{2} m \omega_1^2 x_1^2 + \frac{1}{2} m \omega_2^2 x_2^2 + V_{ee} + V_{ii} + V_{ei} \quad (7)$$

$$V_{ii} = \frac{e^2}{\epsilon d} , \quad V_{ee} = \frac{e^2}{\epsilon [d+x_2-x_1]} , \quad V_{ei} = \frac{-e^2}{\epsilon [d+x_2]} - \frac{e^2}{\epsilon [d-x_1]}$$

where $d > 0$ is the distance between the centers of the two dots, x_1 and x_2 the displacements of the electrons from their rest positions, and the positive charge spread is considered to be small compared to d . For small displacements, H can be simplified to

$$H = \frac{P_1^2 + P_2^2}{2m} + \frac{1}{2} m (\omega_1^2 x_1^2 + \omega_2^2 x_2^2) - \frac{2e^2}{\epsilon d^3} x_1 x_2. \quad (8)$$

METHOD 1. This quadratic form can be diagonalized and made separable in normal coordinates ξ_1 and ξ_2 by standard methods. The normal mode frequencies are given by

$$\Omega_{1,2}^2 = \frac{1}{2} (\omega_1^2 + \omega_2^2) \pm \left\{ \left[\frac{1}{2} (\omega_1^2 - \omega_2^2) \right]^2 + \left(\frac{2e^2}{\epsilon m d^3} \right)^2 \right\}^{1/2}. \quad (9)$$

For the limiting case $\omega_1 = \omega_2 = \omega_0$, this reduces to $\Omega_{1,2}^2 = \omega_0^2 \pm (2e^2/\epsilon m d^3)$, $\xi_1 = x_1 - x_2$, $\xi_2 = \frac{1}{2}(x_1 + x_2) = X$. Thus Ω_2 , which is the smaller frequency, corresponds to the center of mass motion. FIR radiation only couples to ξ_2 and only one peak will appear, irrespective of the strength of the interdot coupling term. The relative motion, in ξ_1 , is not detected by FIR.

With $\omega_1 \neq \omega_2$, the relevant parameters which govern the transition from individual to collective response are $\Delta\omega^2 = |\omega_1^2 - \omega_2^2|$ and $\omega_{ee}^2 = (2e^2/\epsilon m d^3)$. When $\omega_{ee}^2 \ll \Delta\omega^2$, Eq. (9) shows $\Omega_{1,2}^2 = \omega_{1,2}^2 + 0$ ($\omega_{ee}^2 / \Delta\omega^2$), and the normal coordinates approximate the individual dot displacements, $\xi_1 \approx x_1$, $\xi_2 \approx x_2$. The FIR response consists of two peaks, at the individual dot frequencies ω_1 and ω_2 . In the strong interaction domain $\omega_{ee}^2 \gg \Delta\omega^2$, the lower frequency $\omega_2 \rightarrow \Omega_2$ of Eq. (9), $\xi_2 \rightarrow X$, and the response is highly asymmetric with most of the intensity in the center of mass like mode. The transition is best characterized by this continuous loss of intensity from the response at the higher frequency.

METHOD 2. Rewriting Eq. (7) as $H = H_0 + V$, with

$$H_0 = \frac{P_1^2 + P_2^2}{2m} + \frac{1}{2} m \omega_0^2 (x_1^2 + x_2^2)$$

$$V = \frac{1}{2} m \left\{ \frac{1}{2} (\omega_1^2 - \omega_2^2) \right\} (x_1^2 - x_2^2) - \frac{2e^2 x_1 x_2}{d^3} \quad (10)$$

$$\omega_0^2 = \frac{1}{2} (\omega_1^2 + \omega_2^2)$$

the problem is reduced to degenerate perturbation theory, where V breaks the degeneracy of the first excited state of H_0 . This Hamiltonian is separable in (x_1, x_2) as well as in center of mass or relative coordinates. Standard degenerate perturbation theory applied to the states (1,0) and (0,1) in either representation leads to the same results as method 1. Method 2 has the advantage of explicitly displaying *both* perturbations which break the degeneracy (characterized respectively by the inhomogeneity of frequencies, $\Delta\omega^2$ and the interdot interaction ω_{ee}^2). It is also applicable even when the full Coulomb interaction is retained (Eq. (7)) instead of expanding in x_1 and x_2 (Eq. (8)), or when the confining potential in each dot includes nonquadratic terms. The basic result is *not* dependent on the quadratic nature of H_0 , it is a consequence of symmetry breaking due to any V which destroys the $x_1 \leftrightarrow x_2$ interchange symmetry.

GENERALIZATIONS

Both methods can be generalized to a planar ensemble of dots, and with several electrons per dot. In Method 1, for many dots with one electron in each dot, the Hamiltonian still remains a quadratic form as in Eq. (8) after expansion to leading order in the displacements $\{x_i\}$. This form can be diagonalized to obtain the normal mode frequencies

and the normal coordinates, and the precise coupling of FIR radiation to each mode. Depending on the intrinsic spread of the individual dot frequencies $\{\omega_i\}$, and the randomness of the interdot separations, one obtains a spread in the normal mode frequencies and a broadened response to FIR radiation. Even if the intrinsic frequencies are all the same ($\omega_i = \omega_0$), the randomness of interdot separations can give rise to a variation in the normal mode frequencies and a coupling of many different modes to the FIR field, yielding a broadened spectrum with a width of the order of ω_{ee}^2 / ω_0 . For the special situation where the dots form a regular lattice, the influence of all other dots on any given dot is the same, and then the FIR response occurs at a single frequency, downshifted from ω_0 , as in Eq. (5), due to the influence of positive charges in the other dots.⁷ Separability of the Hamiltonian into the center of mass and relative components is recovered and the generalized Kohn's theorem is then applicable.⁷ This single frequency response remains valid for the case of many electrons per dot as well, provided the intrinsic individual dot frequencies are the same and the dots form a regular lattice.

Method 2 is more general, and does not need to rely on parabolic confinement or quadratic form expansions. Consider first a system of many dots, with one electron in each dot, and identical but nonparabolic confining potentials. Without considering interdot interactions, each dot has the same energy spectrum $\{E_n\}$. The ground state energy for the system of N dots is NE_0 and the first excited state is N -fold degenerate with energy $(E_1 - E_0)$ above the ground state. It can be shown that the total dipole operator $e\mathbf{X} = e\sum \mathbf{x}_i$ induces a transition from the ground state to only the fully symmetric first excited state. The remaining $(N-1)$ states in the subspace spanning the first excited state remain unaffected by FIR radiation. The interdot interactions can be treated as a perturbation in this basis. If the dots form a regular lattice, it can be shown that the interdot interactions do not break the interchange symmetry ($\mathbf{x}_i \leftrightarrow \mathbf{x}_j$) and the total dipole operator still couples the ground state to only the fully symmetric first excited state. The main influence of the interdot interactions is to reduce the response frequency. If the individual dots have differing confining potentials, or if the interdot separations are random, the interchange symmetry is broken. Then an average potential should be constructed, and used for each dot to restore the symmetry, treating the deviations from this average potential as the perturbation in this basis. A detailed application of these ideas will be presented elsewhere. These considerations will be relevant for the FIR response of randomly distributed self assembled dots with non parabolic confinement.⁸

ACKNOWLEDGMENT

This work was supported in part by the U.S. Army Research Office, under Grant Nos. DAAH04-94-G-0052 and DAAG55-97-1-0021.

REFERENCES

1. M. Reed, J.N. Randall, R. Aggarwal, R. Matyi, T. Moore and A. Wetsel, *Phys. Rev. Lett.* **60**, 535 (1988).
2. A. Lorke, J. Kotthaus and K. Ploog, *Phys. Rev. Lett.* **69**, 2559 (1990).
3. J.Y. Marzin et al., *Phys. Rev. Lett.* **73**, 716 (1994); M. Grundmann et al., *Phys. Rev. Lett.* **74**, 4043 (1995); H. Drexler, et al., *Phys. Rev. Lett.* **73**, 2252 (1994).
4. D. Broido, K. Kempa and P. Bakshi, *Phys. Rev. B* **42**, 11400 (1990).
5. C. Sikorski and U. Merkt, *Phys. Rev. Lett.* **62**, 2164 (1989).
6. P. Maksym and T. Chakraborty, *Phys. Rev. Lett.* **65**, 108 (1990).
7. P. Bakshi, D. Broido and K. Kempa, *Phys. Rev. B* **42**, 7416 (1990).
8. M. Fricke, A. Lorke, J. Kotthaus, G. Medeiros-Ribeiro and P. Petroff, *Europhys. Letters* **36**, 197 (1996).

This page intentionally left blank

OPTICAL STUDIES OF INDIVIDUAL INAS QUANTUM DOTS

L. Landin, M. S. Miller*, M.-E. Pistol, C. E. Pryor, and L. Samuelson,

Solid State Physics, Box 118
Lund University, S-22100 Lund, Sweden

INTRODUCTION

InAs has a 7.2 % larger lattice constant than GaAs, and only a thin layer of InAs can be grown on a GaAs surface before the film breaks up into small islands [1]. These islands are shaped like pyramids, having typically a height of about 4 nm and a square base with a side length of about 9 nm. The islands are situated on a quantum well (denoted the wetting layer) having a thickness of about 1 atomic layer. Previous optical investigations of individual InP islands (which are larger than the InAs islands investigated here) have shown a discrete energy levels, which were in good correspondence with calculated single-particle energy levels [2,3]. We here report on similar investigations of individual InAs islands, where we observe emission lines corresponding to multi-particle states.

The sample used in our experiment was grown by chemical beam epitaxy. Nearby regions of this sample were patterned with etched grooves and holes for selective island placement, and most of the islands grew only in patterned features [4,5]. The InAs islands were capped with 20 nm GaAs. Growth and processing details have been reported elsewhere [4,5]. It is the very-low island density region away from the pattern features that has been used for photoluminescence measurements in the present study. The emission energy was about 1.35 eV which is slightly higher than typical values for InAs islands, indicating that our islands are slightly smaller than 4 nm in height.

The sample was mounted in an Oxford Instruments Microstate cryostat. All the experiments were carried out at 7 K. For excitation we used a frequency-doubled YAG-laser emitting at 532 nm. The diameter of the laser spot was kept to about 50 microns and the excitation power density varied between 0.5 and 160 W/cm². The emitted light from the sample was collected by a microscope and either dispersed through a monochromator or analyzed and imaged through a band pass interference filter. In both cases we used a CCD camera for detection. When using the monochromator, the image of the sample was focused through a narrow slit with the slit oriented parallel to the grating rulings. Thus, the CCD image axis parallel to the rulings displayed the spatial position of the individual dots along the slit, while the CCD axis perpendicular to the rulings displayed the dispersed spectrum of each dot. The monochromator spectral resolution was typically 0.1 nm. In this way many dots could be simultaneously measured.

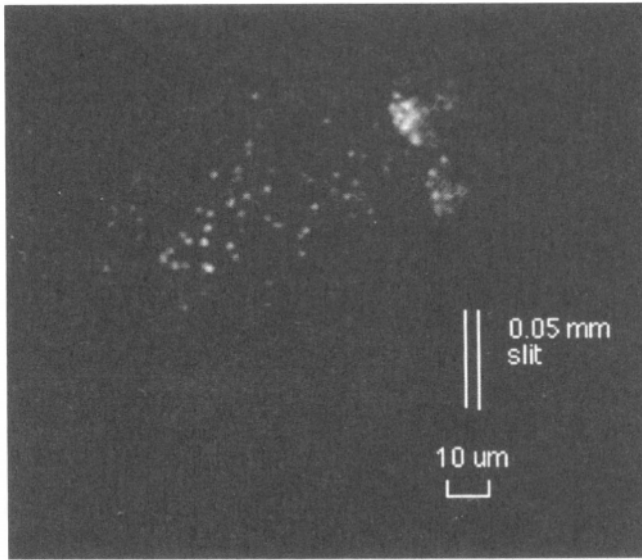


Figure 1. A micrograph of the emission from the sample, showing emission from individual quantum dots. The emission wavelength is 960 nm and the band-pass of the interference filter is 10 nm. In the micrograph we also show size of a 0.05 mm slit in our optical setup.

RESULTS

An image of the photoluminescence at 960 nm (using an interference filter to select the wavelength) is shown in Fig 1. The luminescing area is defined by the laser spot. The 20 micron diameter circular regions above and to the right of the center are concentric circular trenches for which island luminescence energy was found to vary as a function of position around the circles [4]. Away from the patterns, the luminescence from isolated dots can be clearly seen. The 10 nm spectral width of this filter and the 100 meV spread of island energies which is typical for our samples then imply a total luminescing island density of $2 \times 10^7 \text{ cm}^{-2}$. This is the same density measured by atomic force microscopy on an otherwise similar, but uncapped, sample. The emission spectra for four different islands are presented in Fig. 2. At low excitation power the spectra consist of one emission line (line A), which indicates emission from a single quantum dot. At increasing excitation power density, emission lines appear first at higher energy (line B) and then at lower energy than the main line. The energy separation from the main line is about 1 meV. At the highest excitation power density (160 W/cm^2), we observe a continuum-like emission at an energy below the main line. Figure 3 displays high resolution fine-structure spectra from yet two more islands. Four peaks are shown for each island and labeled A to D, where A is the original single peak, B is the same as in Fig. 2, C is the shoulder peak just below B, and D is the low energy peak.

We have calculated the electronic energy levels in these quantum dots, using an eight-band k.p-theory in conjunction with the envelope function approximation. The model includes strain, a realistic shape of the quantum dots, and the piezo-electric potential. Calculations of few-particle effects were included using the Hartree approximation. All of the single-particle states found in the calculation and referred to here are doubly degenerate due to time-reversal. Only one (doubly degenerate) electron level was obtained in the conduction

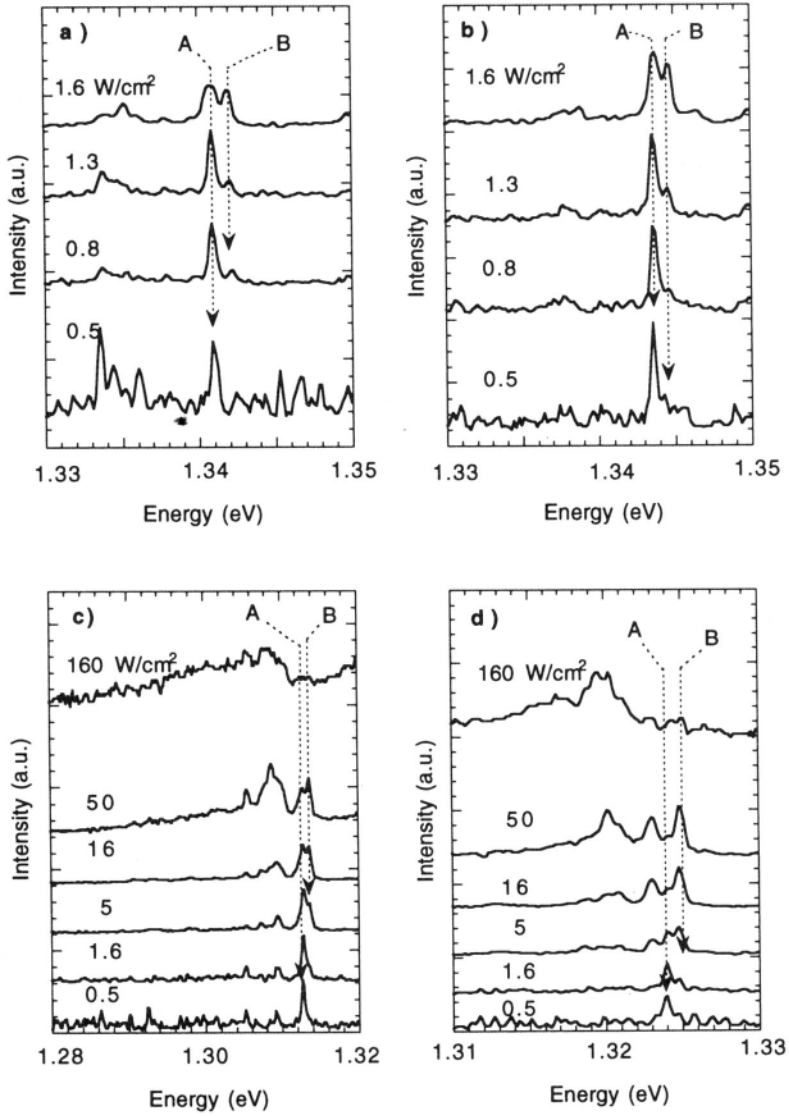


Figure 2. Spectra at different excitation power densities for four different quantum dots, **a)** and **b)** show the evolution of the extra line at higher energy for excitation power densities between 0.5 and 1.6 W/cm^2 . The peak around 1.343 eV in panel a) is due to a different quantum dot. **c)** and **d)** show the evolution of the spectra for excitation power densities between 0.5 and 160 W/cm^2 . Additional emission peaks appear at lower energies and at the highest excitation power density a continuum-like emission is seen.

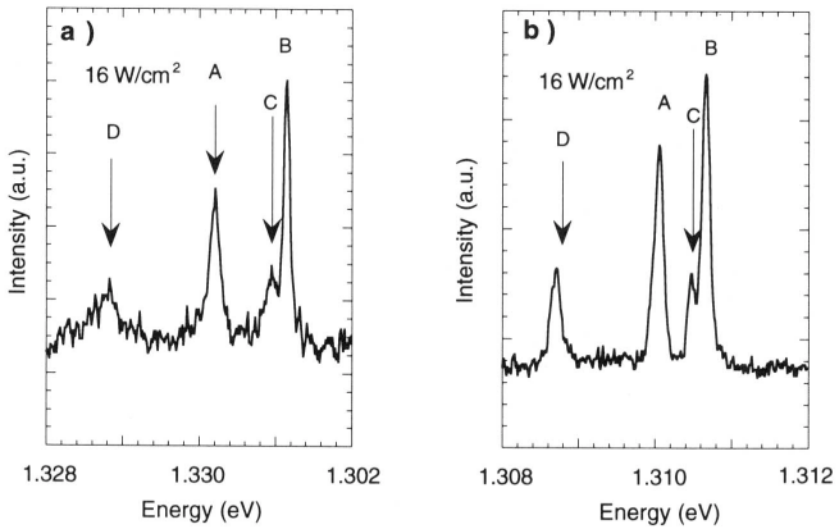


Figure 3. High resolution spectra of quantum dots showing fine-structure, using an intermediate excitation power density. Two different dots have been measured.

band. In the valence band, the hole ground state is separated from the first excited hole state by about 25 meV. Because the lowest excited single-particle state is an order of magnitude higher in energy than the scale of the observed fine-structure splitting, we conclude that the additional peaks that first appear around the main peak are not due to excited hole states and must be due to carrier-carrier interactions when there are more than two carriers in the dot.

We denote electrons by (e) and holes with (h). The calculations show that the recombination energy of four particles, $(e + e + h + h) \rightarrow (e + h)$, is about 2.5 meV higher than the recombination energy of two particles $(e + h)$. The recombination energy of the three particle system, $(e + h + h) \rightarrow (h)$, is 4.3 meV higher than the $(e + h)$ transition energy and

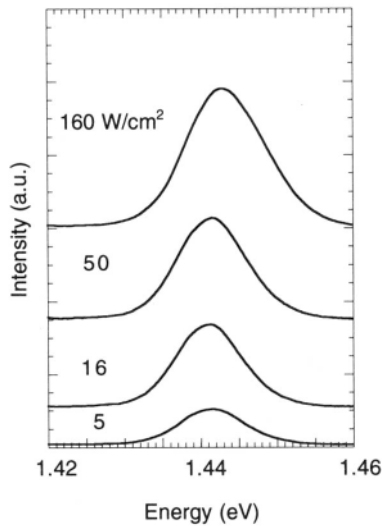


Figure 4. Spectra of the wetting layer emission at different excitation power densities. At the highest excitation power density a blue-shift of the emission occurs.

the recombination energy of the three particle system, $(e + e + h) \rightarrow (e)$, is 1.7 meV higher than the $(e + h)$ transition energy. The $(e + h)$ transition energy is calculated to be about 1.193 eV for a dot height of 4.5 nm, which is slightly smaller than our experimental values.

We conclude from this calculation that few-particle interactions may indeed cause splittings of the observed magnitude. If line A correspond to an $(e + h)$ transition, line B corresponds well with the calculated $(e + e + h + h) \rightarrow (e + h)$ transition energy. From other calculations it has been found that the details of the quantum dot is important even for the sign of certain energy differences [6].

We refrain from a definite assignment of the peaks since we don't have enough knowledge of the sample, e. g. we do not know the position of the Fermi-level in the vicinity of the dots even at thermal equilibrium.

For some systems polariton effects can contribute a splitting to the fine structure because two dots are within a wavelength of light from one another and emitting at the same energy [7]. Polariton effects should be negligible for the present low-density sample because within a given 1 meV range of energy, the dot-to-dot separation is much larger than the wavelength of the emitted light. Other effects such as interference effects and phonon coupling should not depend on excitation power density.

We propose that the continuum-like emission is due to interactions between carriers in the quantum dot and carriers in the wetting layer. In figure 4 we show the emission spectrum of the wetting layer for different excitation power densities. It can be seen that at the highest excitation power density (160 W/cm^2) the wetting layer emission shifts to higher energy, which is typical of state filling. This is the same excitation power density that is needed to observe the continuum-like emission from the quantum dot. This experiment thus supports our idea of the origin of the continuum-like emission from the quantum dots.

ACKNOWLEDGEMENTS

We acknowledge the growth and processing of the sample by Sören Jeppesen, Bernhard Kowalski and Ivan Maximov. We also acknowledge clarifying discussions with Prof. Dave Citrin and Bernhard Kowalski. This work was performed within the Nanometer Structure Consortium in Lund and was supported by grants from the Swedish Natural Science Research Council (NFR), the Swedish National Board for Technical Development (NUTEK), and the Swedish Research Council for Engineering Sciences (TFR).

*present address: Department of Electrical Engineering, University of Virginia, Charlottesville, VA 22903. email: Mark.Miller@virginia.edu

REFERENCES

1. L. Goldstein, F. Glas, J. Y. Marzin, M. N. Charasse and G. L. Roux, *Appl. Phys. Lett.* 47, 1099 (1985).
2. D. Hessman, P. Castrillo, M-E. Pistol, C. Pryor, and L. Samuelson, *Appl. Phys. Lett.* 69, 749 (1996).
3. C. Pryor, M.-E. Pistol and L. Samuelson, cond-mat/9705291
4. M. S. Miller, L. Landin, S. Jeppesen, A. Petersson, I. Maximov, B. Kowalski, and L. Samuelson, *J. Crystal Growth* 175/176, 747 (1997).
5. S. Jeppesen, M. S. Miller, D. Hessman, B. Kowalski, I. Maximov and L. Samuelson, *Appl. Phys. Lett.* 68, 2228 (1996).
6. Ph. Lelong and G. Bastard, *Sol. St. Commun.* 98, 819 (1996).
7. D. S. Citrin, *Optics Letters* 20, 901 (1995).

This page intentionally left blank

ULTRAFAST RELAXATION IN STRONGLY COUPLED COULOMB SYSTEMS

Michael Bonitz, Nai-Hang Kwong, Dirk Semkat, and Dietrich Kremp

FB Physik, Universität Rostock
18051 Rostock, Universitätsplatz 3, FRG

INTRODUCTION: GENERALIZED KINETIC EQUATIONS

With the development of femtosecond lasers, one is now able to create strongly correlated plasmas in extreme nonequilibrium and probe its behavior with high time resolution. During the relaxation, interesting short-time phenomena occur, such as the build-up of correlations, and the formation of bound states and of the screening cloud. As a result of the relaxation, the plasma reaches a correlated equilibrium state.

A complete theoretical description of these processes cannot be given in terms of conventional kinetic equations of the Boltzmann type, since they neglect the correlation dynamics and do not conserve total (kinetic+potential) energy. Furthermore, the equilibrium solution of these collision terms is that of an *ideal* quantum gas, i.e., a Fermi or Bose distribution. All these deficiencies are of particular importance in strongly coupled many-particle systems where the coupling parameter $\Gamma = \langle V \rangle / \langle T \rangle$, the ratio of the mean potential energy and the mean kinetic energy, is of the order of one or even larger. Therefore, a statistical treatment of nonequilibrium processes in these systems requires generalized kinetic equations, see e.g.,¹ where also earlier references are given. In summary, the requirements to these equations are

1. conservation of the sum of kinetic+potential energy,
2. inclusion of correlation buildup and of initial correlations and their damping,
3. relaxation towards the correlated equilibrium state,
4. consistency of the dynamics of one-particle and two-particle properties.

KADANOFF–BAYM APPROACH TO CORRELATED MANY-PARTICLE SYSTEMS

Among the different forms of generalized (non-Markovian) kinetic equations, the Kadanoff–Baym equations (KBE) for the two-time correlation functions have a number of remarkable properties. While non-Markovian kinetic equations for the (one–time) Wigner distribution have problems to fulfill all of the mentioned requirements simultaneously,¹ this is not the case for the KBE. The latter are of high internal consistency because all properties

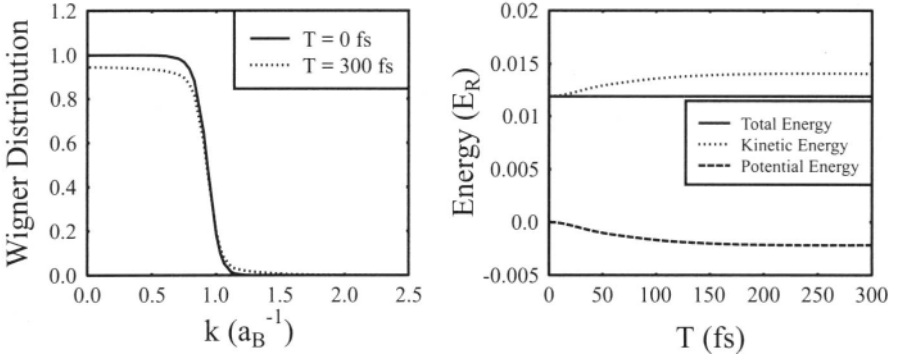


Figure 1. a: Initial uncorrelated and final correlated equilibrium electron distribution, b: Evolution of kinetic, potential and total energy. Parameters are chosen for electrons in a semiconductor (bulk GaAs, $a_B = 132\text{\AA}$, $E_R = 4.2\text{meV}$), $n = 10^{16}\text{cm}^{-3}$, $T = 3\text{K}$

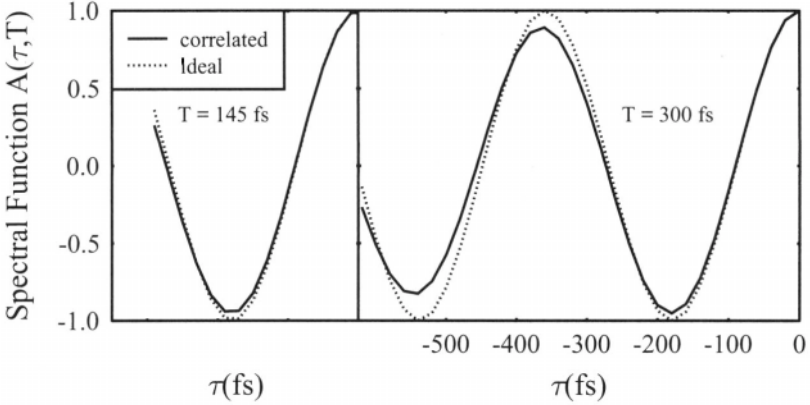


Figure 2. Spectral function corresponding to Fig. 1, for two different times T . The momentum value is $p = 2\hbar/a_B$, $\tau = t - t'$, $A(\tau, T) = A(-\tau, T)$

and approximations are determined by a single function, the self-energy Σ , and they can be generalized to include arbitrary initial correlations.^{2,3}

The KBE are equations of motion for the pair of single-particle correlation functions $g^>(tt')$ and $g^<(tt')$ ⁴ which evolve in the plane $t - t'$ starting from a given initial state. They contain statistical information - on the time diagonal they reduce to the Wigner distribution $g^<(tt) = -i\hbar f(t)$, and also dynamical information which is related to their behavior away from the diagonal. The dynamical properties, and thus the correlations in the system, are contained in the spectral function $A(tt') = i\hbar[g^>(tt') - g^<(tt')]$. To demonstrate the effect of correlations on the femtosecond dynamics, we start with a model case, solving the KBE for an electron gas with self-energies in quasi-static Born approximation. Figs. 1 and 2 show the evolution starting from an uncorrelated equilibrium state (Fermi function). At $t = 0$, the interaction between the carriers is “turned on.” While with conventional Boltzmann-type kinetic equations the system would remain in the initial state, the KBE yield the correct “evolution” towards the *correlated* equilibrium state, Fig. 1a. Due to the buildup of correlations, potential energy increases (it is negative because we assumed a neutralizing background). At the same time kinetic energy rises, while total energy is conserved, Fig. 1b. The saturation of kinetic energy increase marks the end of the correlation buildup and is an appropriate measure for the nonequilibrium correlation time.⁵ Detailed inside into the

correlation dynamics is gained from the spectral function. Fig. 2 shows the evolution of $A(p, \tau, T)$, compared to the free particle case, where $\tau = t - t'$ is the distance from the diagonal and $T = (t + t')/2$ the macroscopic time. While in the free case, A performs harmonic oscillations with the frequency $\hbar\omega = p^2/2m$, correlations between the carriers cause a frequency decrease and damping of the oscillations. Our approach allows to study this effect in its time evolution, i.e., the buildup of correlations, without any additional approximations.

FEMTOSECOND PULSE EXCITED SEMICONDUCTORS

The KB approach is readily applied to systems of practical interest, including nuclear matter² and solids.⁶ In particular, it allows for a self-consistent treatment of the plasma excitation by a short laser pulse and the subsequent relaxation including the buildup of correlations.

As an example, we consider a fs laser pulse which excites an electron–hole plasma in a quasi-two-dimensional (quantum well) semiconductor. The incoming light field $E_L(t) = E_0(t)e^{i\omega t} + c.c.$ is modified by the polarization $P(t)$ of the material giving rise to an effective field E_{eff} , which follows from Maxwell's equations. P depends on the time-dependent response of the semiconductor to the field, on the relaxation processes in the system. In the low-intensity region, this response is due to dipole transitions of electrons between the valence (v) and conduction (c) band. The transition probability P_k^{cv} (the interband polarization) depends on the electron momentum $\hbar k$, which in turn is determined by the laser energy in excess of the energy gap E_{cv} between the two bands and yields the macroscopic polarization according to $P(t) = \sum_k P_k^{cv}(t)$. On a fs scale, the laser is energetically broad, exciting electron–hole pairs within a wide range of energies including their bound states (excitons). This system has a number of remarkable features: it includes the formation of bound states and of the screening cloud around the electrons.

Thus, the microscopic theory needs to compute $P_k^{cv}(t)$. Our approach is to determine this quantity from the solution of the interband generalized KBE, i.e., coupled equations for the band populations f_k^c, f_k^v and P_k^{cv} , which self-consistently includes the effective field $E_{eff}(t)$ as the source of carriers and interband transitions. This allows us to include the carrier generation process into the description leading to a well defined initial state, for details see [7].

Fig. 3 shows results from the interband KBE including all carrier scattering effects in quasi-static second Born approximation. The laser pulse is chosen 50fs long and generates the carrier density (n) in the conduction (electrons) and valence band (holes), see left Fig. part. At the same time, the pulse creates the interband polarization which, after the pulse is gone, decays due to carrier scattering. The oscillations are due to the presence of bound states (excitons) in the system (the frequency arises from beating between the exciton binding energy and the laser energy in excess of the band gap). The right figure part shows the evolution of the different energy contributions. Notice the increase of the total energy which is due to the energy pumped into the system by the external source, i.e., the laser. On the other hand, the division of this energy into various parts depends on the internal properties of the semiconductor. As in the model case above, we see the build up of correlations (causing the correlation energy to increase). In addition, here we took into account the mean field energy (Hartree–Fock energy). Thus, here the potential energy is the sum of correlation and mean field energy. The correlation energy is related to the build up of screening among the laser generated carriers. On the other hand, the mean field energy leads to a modification of the energy of electron–hole pairs. It renormalizes the one-particle energies of free electrons and holes, but also reflects the formation of bound complexes in the laser field, the excitons.

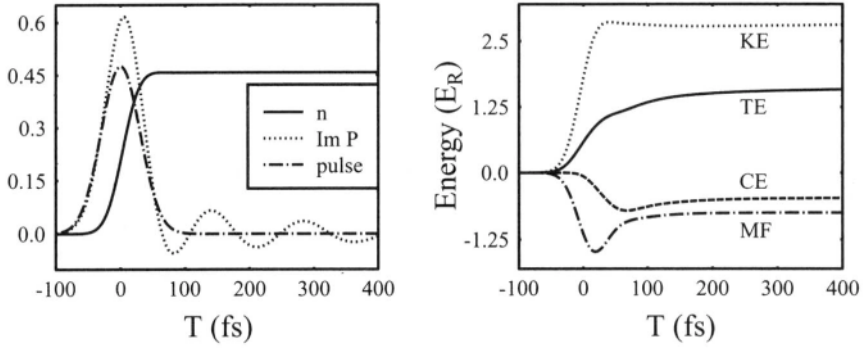


Figure 3. Relaxation of an electron-hole plasma in a GaAs quantum well generated by a 50fs laser pulse, a: Time evolution of density ($n = n_c = n_v$) and envelope of interband polarization P in units of a_B^{-2} , pulse envelope is shown in arbitrary units b: Relaxation of different energy contributions summed over both bands: KE : kinetic energy, MF : mean field (Hartree-Fock) energy, CE : correlation energy and total energy $TE = KE + MF + CE$.

Thus, the Kadanoff-Baym approach is well suited to consistently describe the femtosecond dynamics of correlated many-body systems, including the carrier generation and the formation of screening and bound states.

Acknowledgements

This work is supported by the Deutsche Forschungsgemeinschaft (SFB 198 and Schwerpunkt "Quantenkohärenz in Halbleitern").

REFERENCES

- [1] D. Kremp, M Bonitz, W. D. Kraeft, and M. Schlages, *Annals of Phys. (NY)* 258:320 (1997)
P. Danielewicz,
Ann. Phys. (N. Y.) 152:239(1984)
- [3] M. Bonitz, D. Semkat, and D. Kremp, *Phys. Rev. E* 56:1246 (1997)
- [4] L. P. Kadanoff and G. Baym, "Quantum Statistical Mechanics." Addison-Wesley Publ. Co. Inc., 2nd ed. 1989
- [5] M. Bonitz and D. Kremp, *Phys. Lett. A* 212:83 (1996)
- [6] W. Schäfer, *J. Opt. Soc. Am. B* 13:1291 (1996)
- [7] N. H. Kwong, M. Bonitz, R. Binder, and S. Köhler, *phys. stat. sol. (b)* (accepted)

COULOMB DRAG MEASUREMENTS OF A DOUBLE QUANTUM WELL

J. T. Nicholls, N. P. R. Hill, E. H. Linfield, M. Pepper, and D. A. Ritchie

Cavendish Laboratory, University of Cambridge
Madingley Road, Cambridge, CB3 0HE, United Kingdom

In a Coulomb drag measurement of two closely spaced, electrically isolated two-dimensional electron gases (2DEGs), a voltage V_{drag} is induced in the drag layer when a current I_{drive} is passed through the drive layer. Momentum is not conserved within the individual 2DEGs, and the transresistivity

$$\rho_t = \frac{V_{drag} W}{I_{drive} L} = \frac{m}{n_{drive} e^2 \tau_D}, \quad (1)$$

is a direct measure of the interlayer electron–electron scattering rate τ_D^{-1} , which is determined by the interlayer interaction and the excitations within each layer. In this expression L is the separation of the voltage probes, W is the width of the sample, m is effective mass of the electron, and n_{drive} is the carrier density of the drive layer.

Drag measurements at low temperatures and zero magnetic field show that the interlayer interaction is dominated by a phonon coupling.¹ Here we investigate the interlayer interaction and the single-particle excitations (SPEs) within each layer in two different regimes. Firstly, the collective modes of the double two-dimensional electron gas (2DEG) system are investigated at zero magnetic field and high temperatures, where the drag is enhanced by the plasmon modes.² The measurements are compared to detailed calculations with and without intralayer correlations included in the Hubbard approximation. Secondly, the behavior in the quantum Hall (QH) regime is investigated, and a recent prediction³ for the doubling of the quantum oscillations in the magnetotransresistivity $\rho_t(B)$ is tested.

The plasmon dispersion curves $\omega_p(q)$ for a double 2DEG system consist of two branches. The lower (upper) energy branch is the acoustic (optic) plasmon, where the charge density oscillations in the two layers are in antiphase (phase).⁴ At $\omega_p(q)$ the interlayer dielectric constant $\epsilon(\omega_p, q)$ is at a minimum causing an enhanced interlayer interaction, $W_{12} = V(q)/\epsilon(\omega_p, q)$, where $V(q)$ is the Fourier transform of the interlayer Coulomb interaction. At $T = 0$ K there are no SPEs at $\omega_p(q)$ and the plasmons do not influence the interlayer scattering. However, at temperatures comparable to the Fermi temperature, T_F , the SPE spectrum is sufficiently broadened to allow SPEs at $\omega_p(q)$, and the interlayer scattering is dominated by these SPEs due to the large interaction, W_{12} . Detailed calculations^{5,6} show a plasmon enhancement of the scaled transresistivity $\rho_t T^{-2}$ starting at $0.2 T_F$, and peaking close to $0.5 T_F$. For $T > 0.5 T_F$ the strong coupling between the plasmons and the SPEs causes Landau damping of the two modes, reducing the plasmon enhancement.

Table 1. Sample properties

Sample	t (Å)	layer	n (10^{11}cm^{-2})	μ ($10^5\text{cm}^2\text{V}^{-1}\text{s}^{-1}$)
X	300	upper	3.1	6.5
		lower	2.2	7.6
Y	300	upper	3.3	9.0
		lower	2.3	1.3

The samples consist of two 200 Å wide modulation-doped GaAs quantum wells separated by an $\text{Al}_{0.67}\text{Ga}_{0.33}\text{As}$ barrier of thickness t , with as-grown carrier densities and mobilities as listed in Table 1. Details of the drag measurement are given elsewhere.^{7,8}

Figure 1 shows the scaled transresistivity $\rho_t T^{-2}$ versus T/T_F for sample X at matched carrier densities of $n = 1.37$ to $2.66 \times 10^{11}\text{cm}^{-2}$. The dashed lines in Fig. 1 show $\rho_t T^{-2}$ based on RPA calculations⁵ of the Coulomb coupling between the layers, and do not include the phonon exchange that is measured below $0.1 T_F$. For all densities the transresistivity shows an upturn near $0.2 T_F$, with a maximum close to $0.5 T_F$, in good agreement with the RPA calculations. However, the temperature required to excite the plasmons is lower in the experimental traces, suggesting that the RPA overestimates the plasmon energies. The solid lines in Fig. 1 show calculations where the intralayer exchange interactions are included in the Hubbard approximation. The inclusion of many-body correlations lowers the plasmon energy, thereby lowering the temperature required to excite the acoustic plasmon, and improving the fit to the experimental data. However, differences between the theory and experiment remain. The position of the maximum in ρ_t/T^2 lies at a lower temperature than the model, and the observed decay at higher temperatures is more pronounced. Recent work⁹ on the coupling of the 2DEG to optic phonons shows that the phonon interaction softens the plasmon modes, bringing them closer to the SPE boundary. The resulting traces show a maximum shifted to a lower temperature, with an increased magnitude and a sharper decay. The inclusion of both of these effects may be required to model the drag measurements.

We now investigate the drag in a perpendicular magnetic field B , when the Landau level (LL) structure dominates the properties of the 2DEG. Figure 2(a) shows $\rho_t(B)$ for sample Y at $T = 1.5$ K, together with the magnetoresistivity $\rho_{xx}(B)$ of the upper 2DEG (the lower 2DEG trace is similar). The same LL structure evident in ρ_{xx} is observed in ρ_t because of the modulation of the density of states at the Fermi level, $D(\epsilon_F)$. At even integer filling factors, when ρ_{xx} shows extended minima, transport is via the edges and ρ_t also shows minima. Figure 2 shows the increased sensitivity of ρ_t to the spin-splitting of the LLs; ρ_t is more pronounced minimum at $\nu = 3$, and at higher odd filling factors ρ_t shows clear minima when ρ_{xx} does not. At low filling factors, $1 < \nu < 2$, ρ_{xx} shows a broad minimum resulting from the thermally smeared fractional states; ρ_t is more sensitive to this feature as evidenced by the sharper minimum.

Figure 2(b) shows similar measurements at 8 K, a temperature sufficient to smear both the spin and fractional features seen in ρ_{xx} at lower temperatures. However, the corresponding features in ρ_t persist, further demonstrating its greater sensitivity. Measurements of ρ_{xx} probe predominantly the edge properties of the sample, whereas bulk measurements similar to the drag have also shown an enhanced sensitivity to spin splitting.

Recently Bensager *et al.*³ predicted that $\rho_t(B)$ will show double-peak structures in the QH regime, originating from the interplay between the density of states $D(\epsilon_F)$ and the screening of the interlayer Coulomb interaction. At the center of a LL $D(\epsilon_F)$ is peaked, whereas the interlayer interaction is at a minimum because of the enhanced screening of the half-filled LL. The interplay of these two competing effects may cause ρ_t to be peaked away from the LL center, resulting in a doubling of the structure in ρ_t . However, we observe no doubling in Fig. 2; the structure seen in $\rho_t(B)$ is the same as that which is evident in $\rho_{xx}(B)$

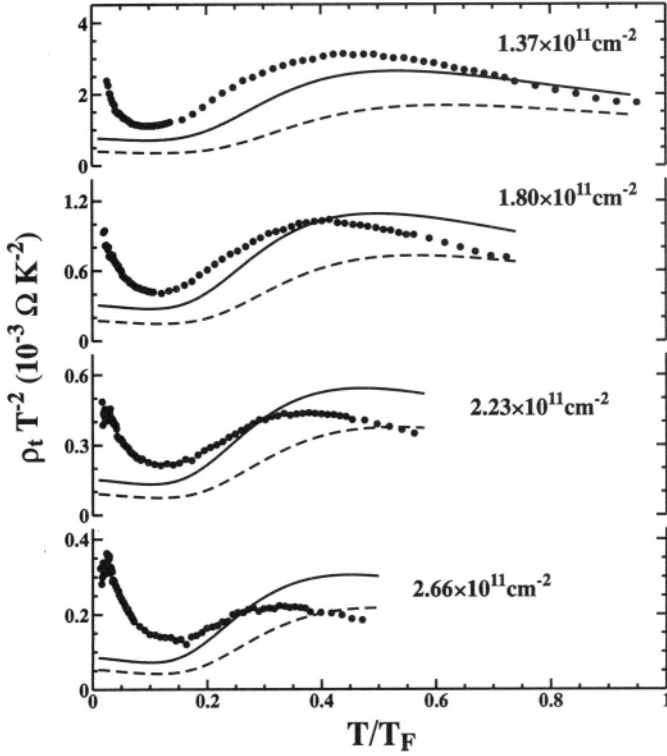


Figure 1. The scaled transresistivity $\rho_t T^{-2}$ versus the reduced temperature T/T_F of sample X, for matched carrier densities $n = 1.37, 1.80, 2.23,$ and $2.66 \times 10^{11} \text{ cm}^{-2}$. The dashed (solid) lines are RPA (Hubbard) calculations. The Hubbard approximation with zero temperature local field corrections improves the agreement between theory and experiment in the low temperature region, but discrepancies remain at elevated temperatures.

at a lower temperatures. Recently Rubel *et al.*¹⁰ have presented experimental results similar to our own,⁵ but have interpreted the enhanced sensitivity to spin splitting as evidence for the predicted doubling of the LL structure.

Bønsager *et al.*³ modelled the LLs as bands of extended states at the LL center; localized states away from the LL center are assumed not to contribute to the interlayer scattering. However, Shimshoni¹¹ has recently shown that the low frequency hopping processes in an Efros-Shklovskii insulator lead to an enhancement of the density fluctuations that contribute to the drag. By analogy, a significant contribution to the interlayer scattering may result from hopping conduction between localized states in the LL tail. Another possible influence of these states is to screen the interlayer interaction as the density of extended states tends to zero. The divergence in W_{12} responsible for the double peaked structure may be removed by the extra screening.

In conclusion, we have measured a plasmon enhancement of the Coulomb drag at high temperatures, in good agreement with the predictions of Flensberg and Hu.⁵ Moreover, we have shown the importance of the many-body corrections that lower the energies of the coupled plasmon modes. In the QH regime the transresistivity shows a greater sensitivity to spin splitting; a theoretical account of this effect is at present lacking.

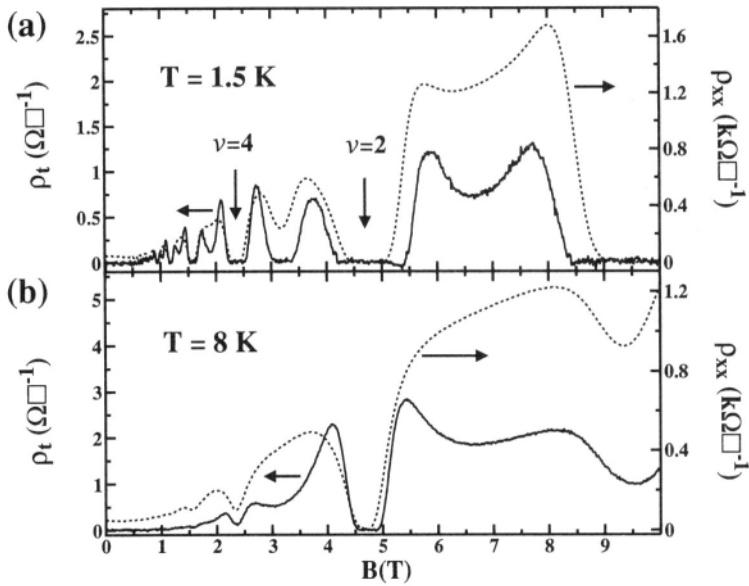


Figure 2. (a) Measurements of $\rho_t(B)$ (solid line) and $\rho_{xx}(B)$ (dotted line) for sample Y at $T = 1.5$ K, at a matched carrier density of $n_{drive} = n_{drag} = 2.2 \times 10^{11} \text{cm}^{-2}$. Filling factors $\nu = 4$ and $\nu = 2$ are indicated with arrows, (b) Similar measurements at $T = 8$ K.

Acknowledgements

We are grateful to Ben Yu-Kuang Hu and Karsten Flensberg for theoretical contributions to this work. We thank the Engineering and Physical Sciences Research Council (U. K.) for supporting this research, and JTN acknowledges an EPSRC Advanced Fellowship.

REFERENCES

- [1] T. J. Gramila *et al.*, Phys. Rev. B **47**, 12957 (1993).
- [2] N. P. R. Hill *et al.*, Phys. Rev. Lett. **78**, 2204 (1997).
- [3] M. C. Bønsager and K. Flensberg and B. Y.-K. Hu and A.-P. Jauho, Phys. Rev. Lett. **77**, 1366 (1996).
- [4] The plasmon modes in similar samples have been investigated with Raman scattering, D. S. Kainth *et al.*, Phys. Rev. B, to be published, (1998).
- [5] K. Flensberg and B. Y.-K. Hu, Phys. Rev. Lett. **73**, 3572 (1994).
- [6] K. Flensberg, B. Y.-K. Hu, A.-P. Jauho, and J. M. Kinaret, Phys. Rev. B **52**, 14796 (1995).
- [7] T. J. Gramila *et al.*, Phys. Rev. Lett. **66**, 1216 (1991).
- [8] N. P. R. Hill *et al.*, J. Phys.: Cond. Matt. **8**, L557 (1996).
- [9] K. Güven and B. Tanatar, Phys. Rev. B **56**, 7535 (1997).
- [10] H. Rubel *et al.*, Phys. Rev. Lett. **78**, 1763 (1997).
- [11] E. Shimshoni, Phys. Rev. B **56**, 13301 (1997).

CLASSICAL ATOMIC BILAYERS

F. M. Peeters,¹ B. Partoens,¹ V. A. Schweigert,² and I. V. Schweigert²

¹Universiteit Antwerpen (UIA), Departement Natuurkunde
B-2610 Antwerpen, Belgium

²Institute of Theoretical and Applied Mechanics
Russian Academy of Sciences, Novosibirsk 630090, Russia

INTRODUCTION

In recent years, there has been considerable theoretical and experimental progress in the study of the properties of systems consisting of a finite number of charged particles.¹ These systems are atomic like structures which have interesting optical properties and may be of interest for single electron devices. In most of the early works the quantum mechanical problem of a small number of electrons was treated. If the number of electrons is increased beyond 6–7 the Coulomb correlation of the electrons has to be treated in an approximate way. In order to fully understand the physics of Coulomb correlations, we made a throughout study of the *classical system*² in which the particles are taken point-like but where no approximation was made on the Coulomb correlation. This approach is valid for quantum dots in high magnetic fields where the kinetic energy of the electrons is quenched or for classical systems like ions in a radio frequency trap,³ two dimensional (2D) Coulomb clusters on the surface of liquid He,⁴ colloidal particles in water drops between glass plates,⁵ etc. In the ground state the charged particles are located on rings and a table of Mendeljev was constructed in Ref. 2. Note that the present system is the 2D equivalent of the Thomson model⁶ which was proposed in 1904 to explain the structure of atoms. These configurations were recovered in a quantum calculation in the limit of large magnetic fields.⁷ A study of the spectral properties of these classical systems such as the energy spectrum, the eigenmodes, and the density of states was made in Ref. 8. Such classical confined systems have been observed in electron dimples on liquid helium,⁴ in drops of colloidal suspensions⁵ and in confined dust particles.⁹

Here we extend our previous work to the case of classical *artificial molecules*¹⁰ which consist of two classical 2D atoms which are laterally separated by a distance d . Intuitively, we expect interesting behavior as function of d which governs the inter atomic interaction. This can be seen as follows (see Fig. 1), for $d = 0$ we have just one 2D atom (e.g., for $2N = 8$, this is a one ring structure with one electron in the center), while for $d \rightarrow \infty$ the system consists of two independent 2D atoms with each half of the total number of particles (e.g., two atoms each having 4 particles on one ring). This implies that as function of d structural transitions (e.g., configurational changes) have to take place. The present molecular systems are the classical analogues of the coupled quantum dot systems which have been studied recently in

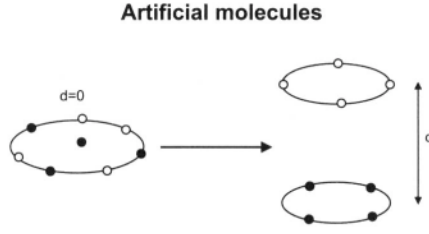


Figure 1. Schematic diagram of a classical artificial molecule consisting of 8 charged particles in the large d limit and for $d = 0$.

Ref. 11.

In the present paper we limit ourselves to the system consisting of an even number, $2N$, of charged particles which are evenly distributed over two layers separated a distance d . In both layers, the confinement potential is centered around the z -axis and this parabolic confinement, which is taken the same for both layers, keeps the system together in the xy -plane. For convenience, we will refer to our charged particles as electrons, keeping in mind that they can also be ions with charge e and mass m . The system is described by the Hamiltonian

$$H = \sum_{i \in I} r_i^2 + \sum_{i < j \in I} \frac{1}{|\vec{r}_i - \vec{r}_j|} + \sum_{i \in II} r_i^2 + \sum_{i < j \in II} \frac{1}{|\vec{r}_i - \vec{r}_j|} + \sum_{i \in I} \sum_{j \in II} \frac{1}{|\vec{r}_i - \vec{r}_j|}. \quad (1)$$

which is expressed in dimensionless form. The coordinates, energy and frequency are in the following units $r' = (e^2/\epsilon)^{1/3} \alpha^{-1/3}$, $E' = (e^2/\epsilon)^{2/3} \alpha^{1/3}$, $\omega' = \omega_0/\sqrt{2}$, respectively, with $\alpha = m\omega_0^2/2$, where m is the mass of the particles, ω_0 the radial confinement frequency, e the particle charge, and ϵ the dielectric constant of the medium the particles are moving in) Note that the groundstate energy is only a function of the number of electrons, $2N$, and the distance d between the layers.

The numerical method used in the present study to obtain the groundstate configuration is based on the Monte Carlo technique supplemented with the Newton Method in order to increase the accuracy of the energy of the groundstate configuration. The latter technique is outlined and compared with the Monte Carlo technique in Ref. 8 and also yields the eigenfrequencies and the eigenmodes of the groundstate configuration.

For $N \rightarrow \infty$ we recover the bilayer system which is composed of two parallel 2D electron gases (2DEG). This system is presently studied extensively experimentally¹² and theoretically.¹³ Here we consider the classical behavior and investigate the melting of the different ordered structures.

ARTIFICIAL MOLECULES

First we consider the case of a molecule consisting of eight electrons distributed over two atoms each with four electrons. For $d = 0$ this is a 2D atom with 8 electrons, of which we know the groundstate configuration,² namely (1,7): 7 electrons on a ring and one electron in the center of the ring. In the opposite limit, $d \rightarrow \infty$, we have two independent 2D atoms, each consisting of four electrons for which the groundstate configuration consists of one ring containing four electrons.² Thus, as function of d , we expect a structural transition. Using the numerical energy minimization technique we examine how and where this transition occurs.

Fig. 2(a) shows the energy per electron of the groundstate (and the energy of the metastable states) and its first derivative with respect to d . At $d = 0.70065$ the first derivative is discontinuous and a structural transition takes place. For $d < 0.70065$ the groundstate

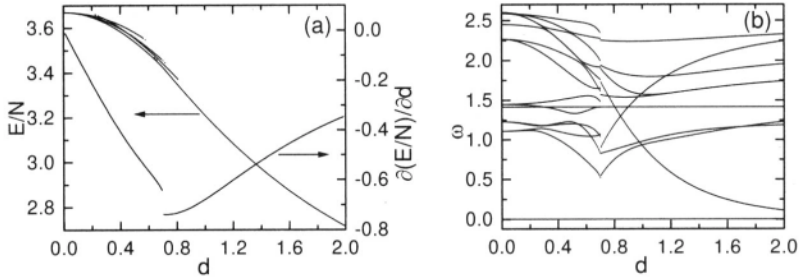


Figure 2. (a) The energy of the ground and metastable states (plotted as dashes) and its first derivative with respect to the lateral distance d between the two atoms constituting the artificial molecule for $2N = 8$. (b) The eigenfrequencies of the normal modes as function of d .

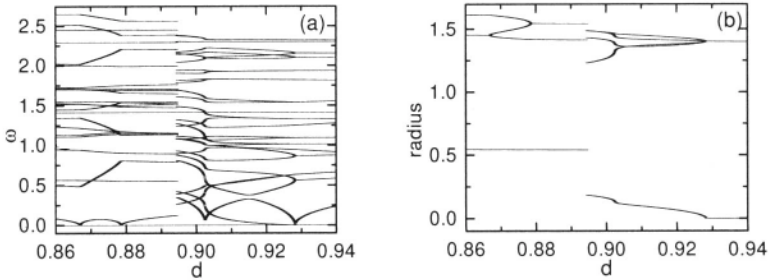


Figure 3. (a) The eigenfrequencies of the groundstate for the artificial molecule with two times eight electrons as a function of d . (b) The radial distance of the different electrons from the center of the confinement potential.

configuration is $(1,3)/(0,4)$: the configuration $(1,3)$ in one layer (indicated by the solid dots in Fig. 1) and $(0,4)$ in the other layer (indicated by the open dots). As viewed from above we have $(1,7)$ which is the configuration of one atom consisting of eight electrons. This implies that the inter-layer correlations are sufficiently strong to impose the one atom configuration to the $2N = 8$ electrons in the molecular structure. For $d > 0.70065$ the configuration is twice $(0,4)$, which is the configuration of two independent atoms each consisting of four electrons.

Given the groundstate configuration we make a normal mode analysis and calculate the eigenfrequencies of the molecule which is shown in Fig. 2(b). Notice that at the first order transition the frequencies exhibit a jump. For $d > 0.70065$ more modes are degenerate in energy and in the limit of $d \rightarrow \infty$ all frequencies are at least twofold degenerate. The latter is a consequence of the fact that the electrons in one layer can vibrate in phase and out-of-phase with respect to the electrons in the other layer. With decreasing d the inter-layer interaction destroys this degeneracy.

As a next example, we consider the artificial molecule consisting of two times eight electrons which is far more complex and exhibits several transitions some of which are qualitatively different. For $d = 0$ this is a 2D atom with 16 electrons and the groundstate configuration is $(1, 5, 10)$ which exists up to $d = 0.205575$ where we have a first order transition from the configuration $(1, 2, 5)/(0, 3, 5)$ to the configuration $(2, 6)/(3, 5)$. For $d > 0.89454$ we have two independent 2D atoms, both with configuration $(1,7)$. In between there is an intermediate configuration $(2, 6)/(2, 6)$ which is the lowest energy configuration in the range $0.47558 < d < 0.89454$.

A closer look reveals that there is another transition region around $d \approx 0.87$. At the transition points $d = 0.86696$ and $d = 0.87862$ there is *no abrupt* change of the configuration, but within this small d -region the radii of the electrons change appreciably, but continuously (Fig. 3(b)). Fig. 3(a) shows that this region is delimited by an eigenfrequency which become

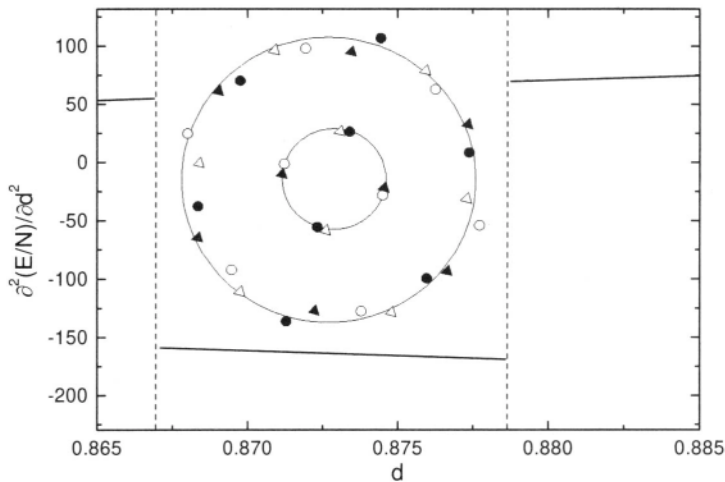


Figure 4. The first and second derivative of the groundstate energy for the system of Fig. 3 in the region of the two second order transitions.

zero and consequently these transitions are induced by the softening of a mode. In Fig. 4 the second derivative of the energy with respect to d is given. There are two discontinuities in the second derivative, namely at $d = 0.86696$ and $d = 0.87862$ while the first derivative is continuous. In the inset of Fig. 4(a) the spatial configuration is shown at $d = 0.865$ (circles) and at $d = 0.880$ (triangles). The open and closed symbols refer to electrons belonging to different layers. Notice that no qualitative changes of the configuration occurs at the second order transitions.

Acknowledgements

B. P. is an Aspirant and F. M. P. a Research Director with the Flemish Science Foundation. This work was supported by the EC-programme: INTAS-93-1495-ext, and the Russian Foundation for Fundamental Investigations 96-023-19134a.

REFERENCES

- [1] See e.g., Proc. of the workshop on *Novel Physics in Low-Dimensional Electron Systems*, Ed. T. Chakraborty, Physica B **212**, N^o 3 (1995).
- [2] V. M. Bedanov and F. M. Peeters, Phys. Rev. B **49**, 2667 (1994).
- [3] P. E. Toschek, in: *New Trend in Atomic Physics*, Vol. 1, eds. G. Grynberg and R. Stora (North-Holland, Amsterdam, 1984), p. 383; B. G. Levi, Phys. Today **41**, 17 (1988); G. Birkl, S. Kassner, and H. Walther, Europhys. News **23**, 143 (1992).
- [4] P. Leiderer, W. Ebner, and V. B. Shikin, Surf. Sci., **113**, 405 (1992).
- [5] J. E. Hug, F. van Swol, and C. F. Zukoski, Langmuir **11**, 111 (1995); S. Nesper, T. Palberg, C. Bechinger, and P. Leiderer, Progr. Colloid Polym. Sci. **104**, 194 (1997); S. Nesper, C. Bechinger, P. Leiderer, and T. Palberg, Phys. Rev. Lett. **79**, 2348 (1997).
- [6] B. Partoens and F. M. Peeters, J. Phys.: Condens. Matter **9**, 5383 (1997).
- [7] P. A. Maksym, Physica B **184**, 385 (1993).
- [8] V. A. Schweigert and F. M. Peeters, Phys. Rev. B **51**, 7700 (1995); F. M. Peeters, V. A. Schweigert, and V. M. Bedanov, Physica B **710**, 237 (1995); V. A. Schweigert and F. M. Peeters, Superl. Microstruct. **16**, 243 (1994).
- [9] C. H. Chiang and L. I, Phys. Rev. Lett. **77**, 647 (1996).
- [10] B. Partoens, V. A. Schweigert, and F. M. Peeters, Phys. Rev. Lett. **79**, 3990 (1997).
- [11] R. Ugajin, Appl. Phys. Lett. **68**, 2657 (1996); H. Imamura, P. A. Maksym, and H. Aoki, Phys. Rev. B **53**, 12613 (1996); S. C. Benjamin and N. F. Johnson, Phys. Rev. B **51**, 14733 (1995).

- [12] See e.g., (and references therein): H. C. Manoharan, Y. W. Suen, M. B. Santos, and M. Shayegan, *Phys. Rev. Lett.* **77**, 1813 (1996).
- [13] L. Świerkowski, D. Nelson, and J. Szymański, *Phys. Rev. Lett.* **67**, 240 (1991); F. Rapisarda and G. Senatore, *Aust. J. Phys.* **49**, 161 (1996); G. Goldoni and F. M. Peeters, *Europhys. Lett.* **37**, 293 (1997).
- [14] G. Goldoni and F. M. Peeters, *Phys. Rev. B* **53**, 4591 (1996).

This page intentionally left blank

RECENT PROGRESS ON THE PHASE DIAGRAM OF COUPLED ELECTRON LAYERS IN ZERO MAGNETIC FIELD

F. Rapisarda¹ and Gaetano Senatore²

¹Institut für Theoretische Physik, Johannes Kepler Universität
Altenberger Strasse 69, A-4040 Linz, Austria

²INFM and Dipartimento di Fisica Teorica dell'Università di Trieste
Strada Costiera 11, I-34014 Trieste, Italy

INTRODUCTION

As is well known, fixed-node diffusion Monte Carlo (fn-DMC) simulations¹ provide to date the most accurate tool to calculate the properties of the electron gas²⁻⁴ and more in general to study electron correlation.⁵ The residual (small) inaccuracy present in the fn-DMC results can be eliminated by allowing for nodal relaxation,² yielding virtually exact results for given number of particles. For extended systems such as the electron gas, a remaining issue is the extrapolation to the thermodynamic limit of results that are actually simulated with a finite number of particles.⁸

The Quantum Monte Carlo method has been used to accurately study the phase diagram of the electron gas both in three² and two^{3,4} dimensions, yielding predictions of magnetic and structural phase transitions. However, without an applied magnetic field, such transitions are predicted only at extremely large values of Coulomb coupling r_s , which are not yet achievable experimentally—even though much progress has been made in two dimensions working with heavy holes in GaAs/AlGaAs heterostructures.^{6,7}

Restricting to two dimensions, in which case the coupling strength r_s is related to the areal density n by $n = 1/\pi r_s^2 a_0^2$ with a_0 the effective Bohr radius, it has been suggested that inter-layer correlations in an electron bilayer should stabilize the crystalline phase at densities up to 3 times larger⁹ than in an isolated layer, facilitating the observation of the thus far elusive Wigner crystal in zero magnetic field.

Motivated by the observation above we have performed extensive simulations¹⁰ of a symmetric electron bilayer using the fn-DMC method. In particular we have evaluated the ground state energy for a number of phases and from these we have extracted the phase diagram that we illustrate below. Here we shall not pause on the technical details of these simulations, referring the interested reader elsewhere.¹⁰

PHASE DIAGRAM OF A SYMMETRIC ELECTRON BILAYER

The systematic study of the symmetric electron bilayer, at zero temperature and magnetic field, involves sampling the two dimensional parameter space (r_s, d) , for each of the phases

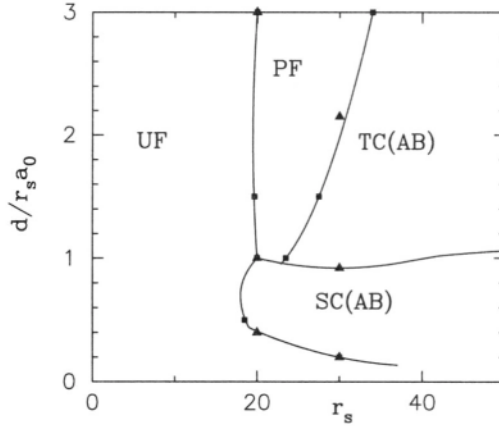


Figure 1. Phase diagram of a symmetric electron bilayer as a function of the density parameter r_s and the interlayer distance d . Four phases are considered: UF denotes the unpolarized fluid, PF the polarized fluid, TC coupled triangular crystals in an AB stacking, SC coupled square crystals in an AB stacking. The triangles (squares) are points calculated by comparing our calculated energies at fixed r_s ($d/r_s a_0$) as a function of $d/r_s a_0$ (r_s). The lines are just a guide to the eye.

considered. To limit the computational burden we have restricted our investigations to four symmetric phases: (i) the spin unpolarized (homogeneous) fluid (UF); (ii) the fully spin polarized (homogeneous) fluid (PF); (iii) coupled triangular crystals (TC) in an AB stacking (in which a particle in the layer above sits right in the center of a triangle in the layer below); (iv) coupled square crystals (SC) in an AB stacking. We have performed actual simulations at $d/r_s a_0 = 0.2, 0.5, 1.0, 1.5$, for $r_s = 10, 20, 30$.

The phase diagram resulting from the phases that we have studied is shown in Fig. 1, in the plane $(r_s, d/r_s a_0)$. We emphasize that the parameter $d/r_s a_0$ should be preferred to d , as it gives a measure of the ratio between the in-layer and the inter-layer couplings. In other words, $d \gtrsim r_s a_0$ corresponds to *weakly interacting* layers and vice-versa $d \lesssim r_s a_0$ corresponds to *strongly interacting* layers, as is evident from Fig. 2, which shows typical fluid correlations in the bilayer. It is evident, in fact that at $d = 1.5 r_s a_0$ inter-layer pair correlations are almost absent in the fluid ($g_{\text{inter}}(r) \simeq 1$), whereas the in-layer correlations are hardly changed from those an isolated layer.¹⁰ On the contrary, $g_{\text{inter}}(r)$ gains a lot of structure for $d = 0.2 r_s a_0$ at the expense of in-layer correlations, which get somewhat *screened* by the inter-layer interactions.

Turning back to the phase diagram, it is clear that at $d = 1.5 r_s a_0$ minor changes are found with respect to the isolated layer situation, which for convenience has been shifted to $d = 3 r_s a_0$ in the figure. One can argue that the crystalline phase gets stabilized with respect to the fluid by the inter-layer interactions, in a situation in which in the fluid inter-layer correlations are negligible. Such a stabilization of the TC phase shifts the crystallization in the bilayer to larger densities with decreasing the distance, as expected.⁹ For $d \lesssim r_s a_0$ the square crystal phase comes into play, being stable over an even larger range of densities, down to $r_s \approx 18$. This value of the in-layer coupling corresponds to a density about three times larger than the crystallization density for the isolated layer, in agreement with earlier estimates based on the dielectric formalism.⁹ The reduction of intra-layer correlation, with the corresponding build up¹⁰ of inter-layer correlation for $d < r_s a_0$, finally leads for small $d/r_s a_0$ to a melting of the crystalline layers, at least for $r_s \leq 34 \times \sqrt{2} \simeq 48$, as shown in Fig. 1.

We stress that the prediction of phase transitions for $r_s \gtrsim 20$ with varying inter-layer distance d is particularly interesting, as this region of parameter space has become accessible in experiments with heavy holes.^{6,7}

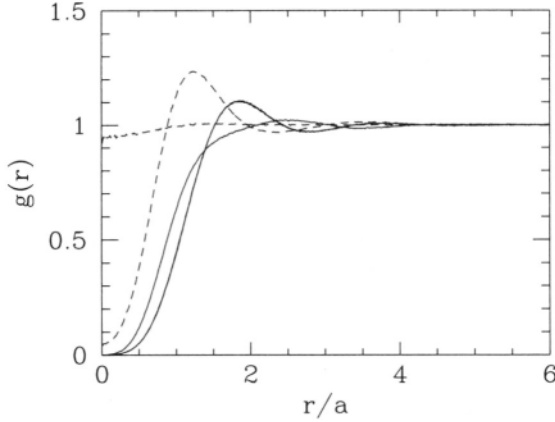


Figure 2. Pair correlation functions for a symmetric electron bilayer in the homogeneous unpolarized fluid phase, at $r_s = 10$. The dashed and full curves give the inter-layer and in-layer correlation function, respectively, for two values of the inter-layer distance, i.e., $d = 1.5r_s a_0$ and $d = 0.2r_s a_0$. For the inter-layer correlations the curve with higher peaks correspond to $d = 0.2r_s a_0$, whereas for the in-layer correlations the curve with higher peaks correspond to $d = 1.5r_s a_0$. Qualitatively similar curves are found at $r_s = 20$ and $r_s = 30$.¹⁰

As already mentioned above, for practical reasons we have only considered two crystalline structures in our investigation. In the classical limit, however, computations are much less demanding and the full zero temperature phase diagram can be mapped out from the comparison of the Madelung energies of the various structures,^{4,11} providing the $r_s \rightarrow \infty$ limit of our phase diagram. In particular it was found that, with varying the inter-layer distance d , five crystalline structures become stable,^{11,12} with the boundary between TC and SC structures lying^{11,12} between $d = 1.1r_s a_0$ and $d = 1.3r_s a_0$. We expect a richer phase diagram also in the quantum regime, if all such phases are included. In fact, four of the five crystalline phases mentioned above have been considered in a study, based on a rather crude *density functional* scheme,¹³ which somewhat overestimates the region of stability of the fluid. No investigation appears to have been made in this study of the reentrant liquid phase present at small distances and moderate values of r_s .

SUMMARY AND CONCLUDING REMARKS

Above, we have presented results of a numerical investigation of a symmetric electron bilayer, the simplest model mimicking the physics of coupled quantum wells to the extent that finite well-width and tunnelling do not play an important role. In fact, very interesting physics should also take place when the carriers are electrons in one well and holes in the other. The attraction between spatially separated Fermi seas, is expected to yield Bose condensation¹⁴ of the electron-hole pairs forming across the two layers or the formation of a BCS like state. We are currently investigating such a system, for which our preliminary results indeed confirm the stability of a BCS like state at $r_s = 10$ and $d = 0.2r_s a_0$.

Our results^{10,15} are also relevant to the recently Hartree-Fock (HF) predicted total charge transfer (TCT) state, whereby all the electron spontaneously jump in one layer.¹⁶ The HF prediction¹⁶ is that TCT takes place in an unpolarized bilayer whenever $r_s \gtrsim 2$. On the contrary, our fn-DMC energies show that the TCT state survives the inclusion of in-layer correlation but is destroyed by the inter-layer correlation. In fact one may exactly show that the TCT state is never stable¹⁵ in an ideal symmetric electron bilayer (with zero layer width and zero tunnelling), in the absence of an applied potential bias.

We conclude by noting that our aim here has been to show that numerical simulations provide an effective tool to study the many-body problem, complementing more traditional techniques as well as experimental investigations.

REFERENCES

- [1] P. J. Reynolds, D. M. Ceperley, B. J. Alder, and W. A. Lester, *J. Chem. Phys.* **77**, 5593 (1982); see, also, C. J. Umrigar, M. P. Nightingale, and K. J. Runge, *J. Chem. Phys.* **99**, 2865 (1993).
- [2] D. M. Ceperley and B. J. Alder, *Phys. Rev. Lett.* **45**, 567 (1980).
- [3] B. Tanatar, and D. M. Ceperley, *Phys. Rev. B* **B 39**, 5005 (1989).
- [4] F. Rapisarda and G. Senatore, *Aust. J. Phys.* **49**, 161 (1996).
- [5] G. Senatore and N. H. March, *Rev. Mod. Phys.* **66**, 445 (1994).
- [6] M. B. Santos, J. Jo, Y. W. Suen, L. W. Engel, and M. Shayegan, *Phys. Rev. B* **46**, 13639 (1992).
- [7] S. Shapira, U. Sivan, P. M. Solomon, E. Buchstab, M. Tischler, and G. Ben Yoseph, *Phys. Rev. Lett.* **77**, 3181 (1996); see, also, S. Shapira *et al* in this volume.
- [8] D. M. Ceperley, *Phys. Rev. B* **18**, 3126 (1978).
- [9] L. Świerkowski, D. Neilson, and J. Szymanski, *Phys. Rev. Lett.* **67**, 240 (1991).
- [10] F. Rapisarda, *Phase Diagram of coupled electron layers*, PhD Thesis, University of Trieste (1996); F. Rapisarda and G. Senatore, to be published.
- [11] G. Goldoni and F. M. Peeters, *Phys. Rev. B* **53**, 4591 (1996); and references therein.
- [12] F. M. Peeters, this volume.
- [13] G. Goldoni and F. M. Peeters, *Europhys. Lett.* **37**, 293 (1997); *ibid.*, **38**, 319 (1997).
- [14] Y. E. Lozovik and V. I. Yudson, *Pis'ma Zh. Eksp. tor. Fiz.* **22** 556 (1995) [*JEPT Lett.* **22**, 274 (1975)].
- [15] S. Conti and G. Senatore, *Europhys. Lett.* **36**, 695 (1996).
- [16] P. P. Ruden and Z. Wu, *Appl. Phys. Lett.* **59**, 2165 (1991).

STRUCTURE AND DYNAMICS OF ELECTRONIC BILAYER LIQUIDS

V. Valtchinov,^{1,2} G. J. Kalman,¹ and K. Golden³

¹Department of Physics, Boston College
Chestnut Hill, MA

²Department of Radiology, Brigham and Women's Hospital
Harvard Medical School, Boston

³Department of Mathematics and Statistics, University of Vermont
Burlington, VT

INTRODUCTION

Electronic bilayers exhibit a rich pattern of behavior, both on the static and on the dynamic level. While at high $r_s (= a/a_B, a = (\pi n)^{-1/2}$ is the Wigner-Seitz radius within a layer, with n being the surface density) values ($r_s > r_s^*$), the bilayer is expected to crystallize (according to [1,2] $r_s^* \geq 20$), and at very low r_s values the RPA description is largely sufficient, the most interesting behavior occurs at $1 < r_s < r_s^*$ domain, where the system is in the liquid state. This is the domain we focus on in this paper.

STRUCTURE

We have calculated the pair correlation functions and other related quantities through the HNC approximation. The calculation is based on the customary model: two 2D electron liquids separated by distance d ; scattering on impurities etc. neglected; no interlayer tunneling; the system is described as a binary liquid with interaction potentials $\varphi_{11}(r) = \varphi_{22}(r) = e^2/r, \varphi_{12}(r) = e^2/\sqrt{r^2 + d^2}$. In addition, the model portrays a classical electron liquid where exchange and other quantum effects are neglected: this approximation is reasonable in the strong coupling domain where the particles are well localized. The coupling is characterized by the parameter $\Gamma = e^2/(aT)$ (where T is the kinetic energy per particle); we note the equivalence $\Gamma \rightarrow 2r_s$. The two two-body functions $g_{11}(\mathbf{r}) = g_{22}(\mathbf{r})$ and $g_{12}(\mathbf{r})$ for different layer separations are given in Fig. 1. There are two remarkable features that can be observed. 1) The peaks of the liquid $g_{11}(\mathbf{r})$ and $g_{12}(\mathbf{r})$ can be brought³ into one-to-one correspondence with the lattice sites of the bilayer solid,⁴ displaying the same series of structural changes as the ones observed in the solid phase, cf. Fig. 2. 2) Up to about $d/a = 0.2$, $g_{11}(\mathbf{r}) = g_{12}(\mathbf{r})$: this indicates a perfect substitutional disorder with respect to the two sublattices in layer 1 and layer 2. This is understandable, since for such layer separations the energy difference between the ordered and the disordered phases is small, while the entropy freed by the disorder is substantial.

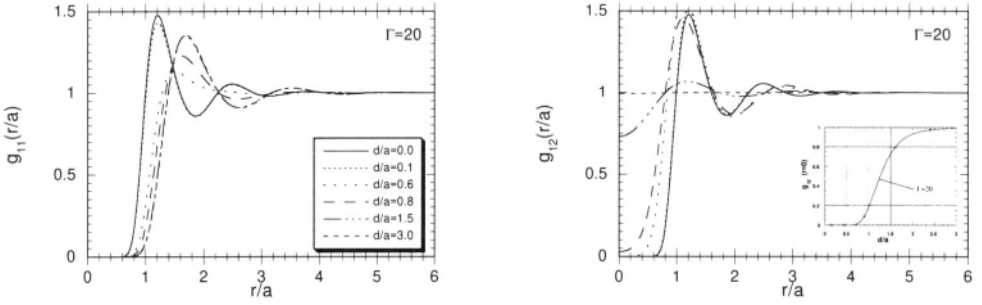


Figure 1. (a) Intralayer and (b) interlayer two-body functions for different layer separations.

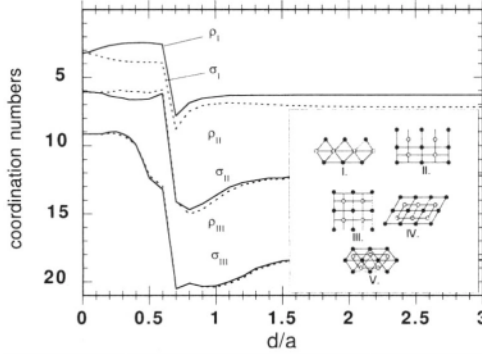


Figure 2. Coordination numbers for shells I, II, and III as a function of layer separations. The inset shows the different underlying structures.

DYNAMICS

The knowledge of the reliable correlation functions makes it possible to analyze the dielectric matrix of the bilayer liquid and determine the characteristics of the collective excitations in the system. Earlier studies of the collective mode structure of bilayers and superlattices were done by Swierkowski *et al.*,⁵ by Gold,⁶ by Zhang and Tzoar,⁷ Golden, Kalman and collaborators⁸⁻¹⁰ and by Pathak.¹¹ Classical bilayer and multilayer structures that form in charged particle traps have also been studied by Dubin.¹² There are two problematic issues that make all the predictions based on these calculations less than reliable.¹³ Most of the works cited^{5-7,11} use methods which violate the 3rd frequency sum-rule, whose satisfaction is well recognized to be an important criterion for providing an acceptable description of the collective mode behavior. Second, no reliable pair correlation function (PCF) data - either for classical or quantum bilayer systems - have been available until fairly recently: thus predictions of the collective mode structure (which turns out to be extremely sensitive to the behavior of the inputted PCF) have been compromised from the outset.

Here consistent calculations of the collective mode spectrum of a strongly coupled electronic bilayer liquid show features which are qualitatively different from the weakly coupled RPA results; they also show that earlier claims concerning the possible emergence of a dynamical instability^{5,6,9,11} cannot be supported by a more consistent treatment of the correlations. The calculation of the dielectric matrix $\epsilon_{ij}(\mathbf{k}\omega)$ is carried out in the Quasi Localized Charge Approximation (QLCA), which has been applied successfully for the description of other strongly coupled Coulomb systems;¹⁴⁻¹⁶ in the QLCA $\epsilon_{ij}(\mathbf{k}\omega)$ becomes a functional of the intralayer and interlayer PCF-s $g_{11}(\mathbf{r})$ and $g_{12}(\mathbf{r})$ or of the corresponding

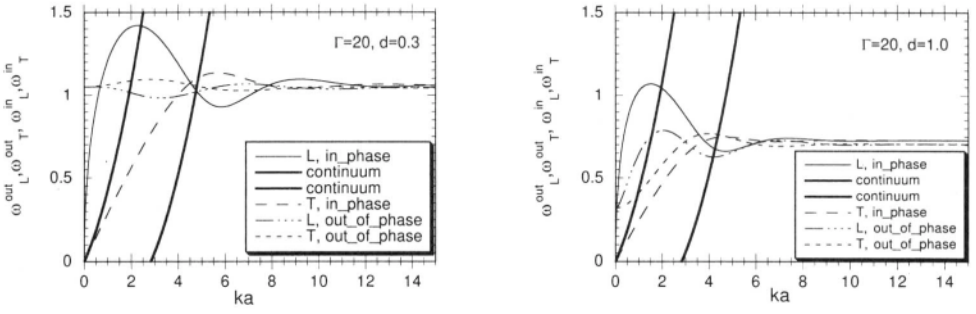


Figure 3. The four principal modes; (a): $d/a = 0.3$, (b): $d/a = 1.0$.

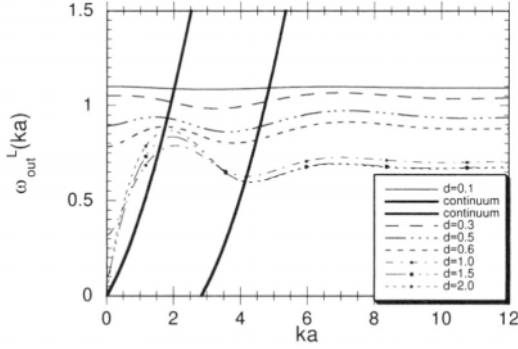


Figure 4. The gapped out-of-phase (*acoustic*) plasmon for different layer separations. Note that the roton minimum never drops below 0.

structure functions $S_{11}(\mathbf{k})$ and $S_{12}(\mathbf{k})$:

$$\varepsilon(\mathbf{k}\omega) = 1 - \omega_0^2(ka) [\omega^2 I - \mathbf{D}(\mathbf{k})]^{-1} \quad (1)$$

($\omega_0 = (\frac{2\pi e^2 n}{ma})^{1/2}$, the nominal plasma frequency of a single 2D layer) with [14]

$$\mathbf{D}_{ij}^{\mu\nu} = \frac{1}{mA} \sum_{\mathbf{q}} k^\mu k^\nu [\varphi_{ij}(q) S_{ij}(|\mathbf{k} - \mathbf{q}|) - \delta_{ij} \sum_l \varphi_{il}(q) S_{il}(q)] \quad (2)$$

In Cartesian space $\varepsilon(\mathbf{k}\omega)$ and similarly $\mathbf{D}(\mathbf{k})$ are reducible to longitudinal $\varepsilon^L(\mathbf{D}^L)$ and transverse $\varepsilon^T(\mathbf{D}^T)$ matrices. The dispersion relation for the longitudinal modes is then obtained from $\|\varepsilon_L^L(\mathbf{k}\omega)\| = 0$ which leads to

$$\omega^2 = \omega_0^2 ka (1 \pm e^{-kd}) + D_{11}^L(k) \pm D_{12}^L(k) \quad (3)$$

With the neglect of retardation effects, the dispersion relation for the transverse modes is derived from $\|\varepsilon^T(\mathbf{k}\omega)^{-1}\| = 0$ which yields

$$\omega^2 = D_{11}^T(k) \pm D_{12}^T(k) \quad (4)$$

The results are portrayed in Figs. 3–4 and the qualitative features of the collective mode dispersion are summarized below.

1. The spectrum of collective modes comprises 4 modes: 2 (longitudinal and transverse) in-phase modes and 2 (longitudinal and transverse) out-of-phase modes (corresponding to the + and - sign in Eqs. 3 and 4, respectively).

2. The in-phase modes (where the two layers oscillate in unison) are not qualitatively different from the similar modes of an isolated 2D layer.¹⁵ In particular, for $k \rightarrow 0$ the longitudinal (plasmon) mode has the typical, quasi-acoustic $\omega \sim \sqrt{k}$ dispersion, while the transverse (shear) mode is acoustic, $\omega \sim k$; both modes are softened by intralayer and interlayer correlations.
3. The out-of-phase modes (where the oscillations of the two layers exhibit a 180° phase difference) are characterized by an $\omega(k=0) > 0$ energy gap. The physical reason for the existence of an energy gap for layered systems has already been discussed elsewhere.⁸ The present calculation clearly shows the marked difference brought about by the strong correlations. Since at $k = 0$ the isotropy of the system is unbroken, the plasmon and the shear modes share a common gap value.
4. From Eqs. 3 and 4 the gap value can be expressed as the integral

$$\omega^2(0, d) = -\frac{\omega_0^2}{2} \int_0^\infty d(qa)(qa)^2 e^{-qd} S_{12}(q).$$

For small layer separation ($d \rightarrow 0$), $\omega(0)$ approaches the $2^{3/4}\omega_0$ value: this is expected since when two out-of-phase uniformly ($k = 0$) oscillating ordered layers are brought together, the resulting pattern is a single, double density, non-uniformly oscillating layer with ka at the quasi-Brillouin zone boundaries and the corresponding 2D $\omega(k)$ frequency is folded back to $k = 0$ and appears as the gap frequency. With increasing d and consequently decreasing interlayer correlations, $\omega(k)$ shows a decreasing tendency and it virtually vanishes for $d > 1.5$ when the separated layers become practically uncorrelated.³ This downward trend is, however, preceded by a slight upturn for $0 < d < 0.22$. Although the details of this behavior are not well understood, it is most likely due to the *substitutional disorder* that prevails in this region:³ the eigenfrequencies of the localized modes in the substitutionally disordered phase are expected to be higher than in the substitutionally ordered phase. Within the domain investigated, the Γ -dependence of $\omega(0)$ is quite mild, but the QLCA being a strong coupling approximation, no inference concerning the behavior of $\omega(0)$ in the moderately coupled ($\Gamma < 10$) domain can be drawn from this observation.

5. For finite k values all the four dispersion curves develop an oscillatory behavior, generated by the similar behavior of the inputted structure functions. This behavior has also been identified for the isolated 2D layer.¹⁵ The structure of the out-of-phase plasmon mode is of special interest here: the first sharp roton-like minimum has attracted attention in earlier studies^{5,9,11} which were based on the neglect or on a highly approximate treatment of the interlayer correlations. It was suggested that the minimum of ω^2 may dip below $\omega^2 = 0^5\text{a},^{9,11}$ or may, at least, reach the close vicinity of $\omega^2 = 0^5\text{b,c}$. The former behavior would indicate a dynamical instability (heralding the onset of CDW-type ground state),⁵ a.;⁹ the latter has been interpreted as the onset of a new high- k , low frequency mode^{5b,c}. Our results show that the roton minimum never drops below the value already reached by the dispersion curve of 2D layer: that both of the above predictions are in fact merely the products of the inconsistent approximations used and do not reflect the actual behavior of the bilayer.
6. At high k -values, for a given d all the dispersion curves approach the same asymptotic frequency value, the frequency of a localized mode, a particle oscillating in the screening environment of the two layers: this result is, probably, only of academic interest, since

it is unlikely that high- k modes would survive the damping mechanism due to decay into multipair excitations.

OUTLOOK

The QLCA is not geared to describe damping processes and therefore our calculation fails to provide information on the damping of the collective modes. However, some qualitative statements can be made. We concentrate on the out-of-phase modes only. Landau damping can be easily assessed from Fig. 4, which shows the pair excitation domain: it is clear that as long as the layer separation is not too large ($d/a < 1.5$) both the out-of-phase plasmon and shear modes are well outside the continuum for small k values and are thus immune to Landau-damping.

The collective mode structure of the strongly coupled bilayer liquid presented in this paper bears a close relationship to the phonon spectrum of the bilayer solid, recently calculated by Goldoni and Peeters.⁴ The four modes in the solid phase can be identified as the transverse acoustic and the longitudinal quasi-acoustic ($\sim \sqrt{k}$) phonons and the transverse and longitudinal optical phonons. The “gaps” exhibited by the latter are, in general, different because of the anisotropy of the lattice. In contrast, in the liquid state, there is only one single isotropic gap, as determined in this paper. This liquid gap value is typically slightly above the arithmetic average of the optical frequencies of the transverse and longitudinal phonons in the solid phase.

Concerning the possible observation of the features predicted in this paper, one can suggest three main areas that should lend themselves to direct experimental verification: 1) the existence and the nonmonotonic d -dependence of the $k = 0$ energy gap; 2) the existence of a transverse shear excitation with a high frequency and expected low damping (this is sharp contrast to the usual scenario for the shear mode in the liquid phase, which vanishes for $k \rightarrow 0$;¹⁶⁻¹⁸ 3) the non-existence of the predicted^{5,6,9,16} instability or low frequency mode in the vicinity of the first roton minimum. We note that the reported Raman scattering experiments¹⁹ are inconclusive because of the low r_s and relatively high k values involved. Recently accomplished advances in fabricating high r_s samples²⁰ and small layer separation should render the suggested experiments feasible.

REFERENCES

- [1] Swierkowski, L., D. Neilson and J. Szymanski, Phys. Rev. Lett. **67**, 240 (1991).
- [2] Rapisada, F. and G. Senatore, in this Volume.
- [3] Valtchinov, V, G. Kalman and K. B. Blagoev, Phys. Rev. **E 56**, 4351 (1997).
- [4] Goldoni, G. and F. M. Peeters, Phys. Rev. **B 53**, 4591 (1996).
- [5] (a). Swierkowski, L., D. Neilson and J. Szymanski, Austr. J. Phys., **46**, 423 (1992); (b) Neilson, D., L. Swierkowski, J. Szymanski and L. Liu, Phys. Rev. Lett. **71**, 4035 (1993), *erratum*, Phys. Rev. Lett. **72**, 2669 (1994); (c) Liu, L., L. Swierkowski, D. Neilson and J. Szymanski, Phys. Rev. **B 53**, 7923 (1996).
- [6] Gold, A., Z. Phys. **B 86**, 193 (1992); **90**, 173 (1993); Phys. Rev. **B 47**, 6762 (1993); Gold, A. and L. Calmels, *ibid*, **48**, 11 622 (1993); Gold, A., Z. Phys. **B 95**, 341 (1994); **97**, 119 (1995).
- [7] C. Zhang, N. Tzoar, Phys. Rev. **A 38**, 5786 (1988); C. Zhang, Phys. Rev. **B 49**, 2939 (1994).
- [8] Golden, K. I. and G. Kalman, *physica status solidi (b)* **180**, 533 (1993); Kalman, G., Y. Ren and K. I. Golden, *Contr. to Plasma Physics* **33**, 449 (1993); Kalman, G. and K. I. Golden, in *Condensed Matter Theories* **8**, edited by L. Blum and B. S. Malik (Plenum Press) (1993); Golden, K. I. in *Modern Perspectives in Many-Body Theory*, edited by M. P. Das and J. Mahanty (World Scientific Press) (1994); Kalman, G., Y. Ren and K. I. Golden, Phys. Rev. Rapid Comm. **B 50**, 2031 (1994).
- [9] D. Lu, K. I. Golden, G. Kalman, Ph. Wyls, L. Miao, X. L. Shi, Phys. Rev. **B 54**, 11457 (1996).
- [10] Golden, K. I., G. Kalman, L. Miao and R. R. Snapp, Phys. Rev. **B 55**, 16349 (1997).
- [11] Moudgil, R. K., P. K. Ahluvalia and K. N. Pathak, Phys. Rev. **B56**, 14776 (1997).

- [12] Dubin, D. H. E., Phys. Rev. Lett. **66**, 2076 (1991); **71**, 2753 (1993); Phys. Fluids **B 5**, 295 (1993).
- [13] Kalman, G. and K. I. Golden, Phys. Rev. **B 57** (in press).
- [14] Kalman, G. and K. I. Golden, Phys. Rev. **A 41**, 5516 (1990).
- [15] Golden, K. I., G. Kalman and Ph. Wyns, Phys. Rev. **A 41**, 6940 (1990).
- [16] Golden, K. I., G. Kalman and Ph. Wyns, Phys. Rev. **A 46**, 3454 (1992).
- [17] Totsuji, H. and H. Takeya, Phys. Rev. **A 22**, 1220 (1980).
- [18] Hansen, J. P., I. R. McDonald and E. L. Pollock, Phys. Rev. **A 11**, 1025 (1975).
- [19] Olego, D., A. Pinczuk, A. C. Gossard and W. Wiegmann, Phys. Rev. **B 25**, 7867 (1982); Fasol, G., N. Mestres, H. P. Hughes, A. Fischer and K. Ploog, Phys. Rev. Lett. **56**, 2517 (1986).
- [20] Shapira, S., U. Sivan, P. M. Solomon, E. Buchstab, M. Tischler and G. B. Yoseph, Phys. Rev. Lett. **77**, 3181 (1996); S. Shapira *et al* in this Volume.

KINETIC APPROACH TO THE STOPPING POWER OF DENSE PLASMAS

D. O. Gericke, M. Schlanges, and W.-D. Kraeft

Institute of Physics
Ernst-Moritz-Arndt University
17487 Greifswald
Germany

INTRODUCTION

The beam-plasma interaction is one of the most important issues in the field of particle driven inertial confinement fusion (ICF). In the scenario of indirect driven fusion, heavy ion beams heat up an absorber layer on the shell of the fusion target which convert the kinetic beam energy into X-rays.¹ In the fast ignitor scheme, a laser produces fast electrons which transfer the energy to the dense core of the fusion pellet.² In both cases, a precise knowledge of the energy loss of the beam particles in dense plasmas is required to optimize the fusion pellet. Due to the high densities in the absorber layer as well as in the core plasma, one has to deal with strongly coupled plasmas. Situations with similar coupling parameters occur in electron cooling devices of ion storage rings, too.³ Here, one has to describe the energy transfer between beam ions and the electrons for low relative velocities.

There exist several approaches to the stopping power. Here, we want to mention the Bethe formula,⁴ the dielectric theory,⁵ the classical binary collision approximation,⁶ and the molecular dynamic simulation technique.⁷ But not all of these treatments are applicable to calculate the stopping power of dense plasmas. In this paper, the stopping power is investigated using the quantum kinetic theory. This allows to include dense plasma effects such as dynamic screening, strong collisions, phase space occupation (Pauli blocking), bound states, and lowering of the ionization energy.

EXPRESSIONS FOR THE STOPPING POWER

According to the definition of the mean value of kinetic energy, the stopping power can be expressed in terms of the beam particle distribution function:

$$\frac{\partial}{\partial t} \langle E \rangle = \frac{1}{n_b} \int \frac{d\mathbf{p}}{(2\pi\hbar)^3} \frac{p^2}{2m_b} \frac{\partial}{\partial t} f_b(\mathbf{p}, t). \quad (1)$$

This distribution function is determined by the kinetic equation; $\partial f_b / \partial t = \sum_c I_{bc}$, where I_{bc} is the 2-particle collision integral. The sum runs over the beam and all species of plasma

particles, i.e., one has to solve a coupled system of equations for the beam and the plasma particles. To reduce the effort, we use a delta function like beam particle distribution function $f_b(\mathbf{p}) \sim \delta(\mathbf{p} - m_b \mathbf{v})$ and assume that the plasma is in equilibrium and the beam density is low that one can neglect correlations between beam particles.

With these assumptions and the collision integral of the Lenard–Balescu equation, the stopping power can be written in terms of the imaginary part of the inverse dielectric function which was taken in the random phase approximation (RPA):⁸

$$\frac{\partial}{\partial t} \langle E \rangle = \frac{2Z_b^2 e^2}{\pi v} \int_0^\infty \frac{dq}{q} \int_{\frac{q^2}{2m} - qv}^{\frac{q^2}{2m} + qv} d\omega \omega \operatorname{Im} \varepsilon^{R-1}(q, \omega) n_B(\omega). \quad (2)$$

In the case of high beam velocities, we get the asymptotic formula:

$$\lim_{v \rightarrow \infty} \frac{\partial}{\partial t} \langle E \rangle = -\frac{Z_b^2 e^2 \omega_{pl}}{v} \ln \left(\frac{2m_b v^2}{\hbar \omega_{pl}} \right); \quad (3)$$

$\omega_{pl} = (\sum_c 4\pi n_c e^2 / m_c)^{1/2}$ is the plasma frequency. This approximation scheme takes into account effects of dynamic screening, e.g., the contribution of the collective excitation (plasmons). But the RPA is valid in the weak coupling limit only.

For dense plasmas, strong correlations have to be included. This can be done using the T-matrix approximation for the collision integral. The T-matrix is closely connected to the scattering cross section,⁹ and therefore, the stopping power in T-matrix approximation can be expressed in terms of the transport cross section:^{8,10}

$$\begin{aligned} \frac{\partial}{\partial t} \langle E \rangle &= \frac{1}{(2\pi)^2 \hbar^3} \sum_c \left(\frac{m_c}{m_{bc}} \right)^3 \frac{n_c \Lambda_c^3 k_B T}{m_b m_c v} \int_0^\infty dp p^3 Q^T(p) \\ &\times \left\{ p_- \exp \left[-\frac{m_c}{2k_B T} v_-^2 \right] - p_+ \exp \left[-\frac{m_c}{2k_B T} v_+^2 \right] \right\}. \end{aligned} \quad (4)$$

Here, the abbreviations $p_\pm = p \pm m_b v + m_b m_{bc} k_B T / m_c p$ and $v_\pm = v \pm p / m_{bc}$ are used, p is the modulus of the momentum of relative motion, $\Lambda_c = (2\pi \hbar^2 / m_c k_B T)^{1/2}$ is the thermal wave length of the plasma electrons, and $m_{bc} = m_b m_c / (m_b + m_c)$ is the reduced mass. The transport cross section was calculated separately using a phase shift analysis: $Q^T(p) = 4\pi \hbar^2 / p^2 \sum_{l=0}^\infty (l+1) \sin(\eta_l - \eta_{l+1})$.⁹ The scattering phase shifts δ_l were computed solving the radial Schrödinger equation with a statically screened Coulomb potential.¹⁰ Additionally, the transport cross section was used in first Born approximation. In the latter case, one gets the stopping power at the level of the quantum Landau equation.

While in the RPA level collective effects are included, the T-matrix level accounts for strong multiple collisions. To combine the effects of both approximation levels, we use a kinetic equation proposed by H. A. Gould and H. E. DeWitt.¹¹ In terms of the collision integrals, it can be written as: $I_{comb} = I_{LB} + I_B - I_L$.¹² On the r.h.s., we have the Lenard-Balescu (RPA) I_{LB} , the Boltzmann (T-matrix level) I_B , and the Landau (statically screened first Born approximation) I_L collision integrals. In this way, one gets a T-matrix which contains a dynamically screened first Born approximation and statically screened higher ladder terms. As the T-matrix and Landau level of the stopping power cancel each other in the case of high beam velocities, the asymptotic behavior is given by formula (3).

In Fig. 1, the stopping power of an electron beam running into a hydrogen plasma is plotted as a function of the beam velocity for the different approximation schemes outlined above. For beam energies smaller than the thermal energy, there is an energy gain of the

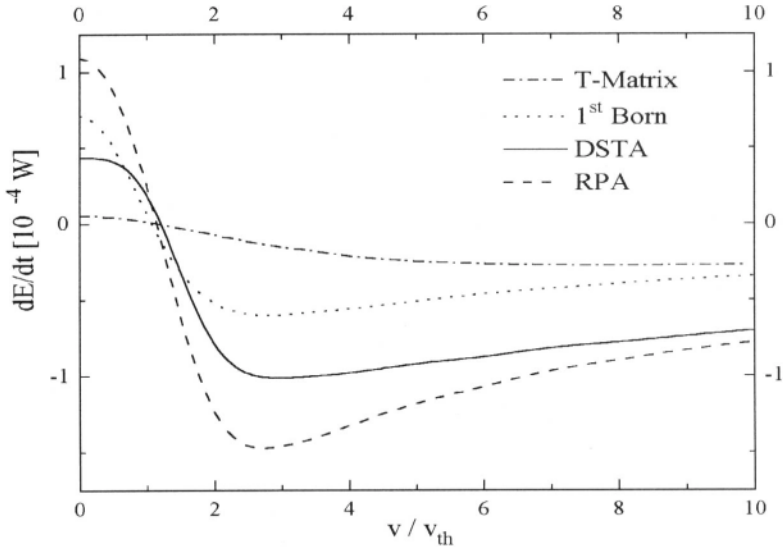


Figure 1. Stopping power of an electron beam in a hydrogen plasma with $n=1.0 \cdot 10^{20} \text{ cm}^{-3}$ and $T=11747 \text{ K}$ versus beam velocity in units of the electron thermal velocity $v_{th} = (2k_B T/m_e)^{1/2}$

beam particles in all approximation schemes. But in the case of ion beams, this energy gain is very small. As already mentioned, the statically screened T-matrix and first Born results coincide for high beam velocities, and therefore, the high velocity behavior is determined by the RPA level. For intermediate velocities, one can observe a deviation of the combined scheme from the pure RPA level as well as from the T-matrix level. Especially, the strong correlations included in the T-matrix reduce the stopping power.

ENERGY DEPOSITION OF HIGHLY CHARGED IONS

The stopping power of highly charged ions depends strongly on the ion charge number Z_b . Theories which account for the beam–plasma interaction in the weak coupling limit only (e.g., dielectric theory, RPA, statically screened first Born approximation) predict an increase of the stopping power according to a Z_b^2 scaling law.

This behavior changes if the beam–plasma correlations become strong, as was shown in molecular dynamic simulation⁷ and calculations dealing with the nonlinearized system of Vlasov and Poisson equations.¹³ Using our kinetic approach, strong collisions are included in the T-matrix approximation. The T-matrix is determined by the Lippmann–Schwinger equation:

$$T_{ab}^R(\omega) = V_{ab}^S + V_{ab}^S G_{ab}^{0R}(\omega) T_{ab}^R(\omega). \quad (5)$$

The Born series shows that the T-matrix is a nonlinear function of the screened ion–electron potential, and therefore, the transport cross section ($\sigma \sim |T|^2$) shows deviations from the Z_b^2 behavior. For weak beam–plasma coupling, the first term of the Born series is sufficient.

Fig. 2 shows the dependence of the stopping power on the ion charge number Z_b in the different approximation schemes discussed above. The weak coupling theories (RPA, first Born approximation) show the known Z_b^2 behavior, whereas the higher correlations included in the T-matrix level reduce the stopping power. This effect becomes stronger with increasing ion charge number, i.e., increasing beam–plasma coupling, and therefore, the T-matrix results show a weaker increase.

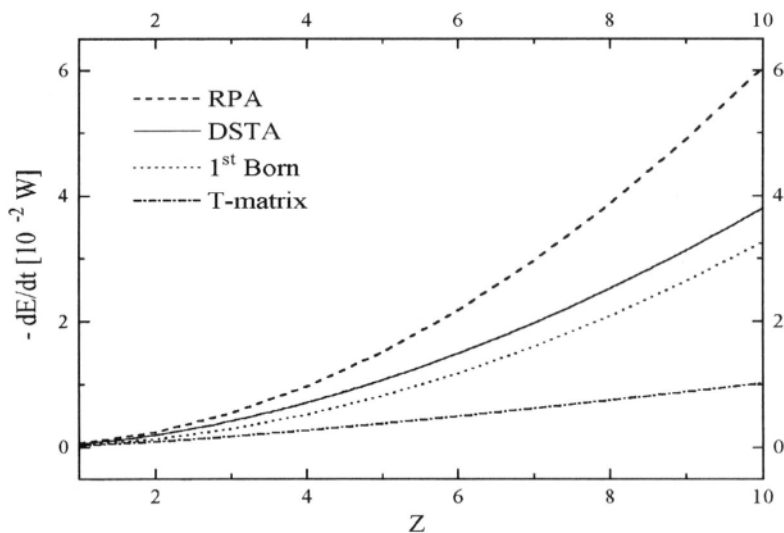


Figure 2. Stopping power of a Cu^{Z_b+} ion beam with a beam velocity of $v=2v_{th}$ in a hydrogen plasma with $n=5.0 \cdot 10^{20} \text{ cm}^{-3}$ and $T=58735 \text{ K}$ versus beam ion charge number Z_b

Acknowledgements

This work was supported by the Sonderforschungsbereich 198 “Kinetik partiell ionisierter Plasmen” of the Deutsche Forschungsgemeinschaft.

REFERENCES

- [1] R. C. Arnold, J. Meyer-ter-Vehn, Rep. Prog. Phys. **50**, 559 (1987)
- [2] M. Tabak et al., Phys. Plasmas **1**, 1626 (1994)
- [3] A. Wolf et al., in J. Bosser(ed.), “Beam Cooling and Related Topics,” CERN, Geneva (1994)
- [4] H. Bethe, Ann. Physik **5**, 325 (1930)
- [5] Th. Peter, J. Meyer-ter-Vehn, Phys. Rev. E **47**, 1998 (1991)
- [6] L. De Ferrariis, N. R. Arista, Phys. Rev. A **45**, 2145 (1984)
- [7] G. Zwicknagel, C. Toepffer, and P.-G. Reinhard, Laser and Particle Beams **13**, 311 (1995)
- [8] W. D. Kraeft, B. Strege, Physica A **149**, 313 (1988)
- [9] J. Joachain “Quantum Collision Theory,” North-Holland, Amsterdam (1979)
- [10] D. O. Gericke, M. Schlanges, and W. D. Kraeft, Laser and Particle Beams **15**, 1 (1997)
- [11] H. A. Gould, H. E. DeWitt, Phys. Rev. **155**, 68 (1967)
- [12] D. O. Gericke, M. Schlanges, and W. D. Kraeft, Phys. Lett. A **222**, 241 (1996)
- [13] O. Boine-Frankenheim, Phys. Plasmas **3**, 1585 (1996)

DISTRIBUTION FUNCTION OF CHARGED PARTICLES IN A PLASMA OF FUSION INTEREST

C. Cereceda,¹ M. de Peretti,² and M. Sabatier²

¹LPGP, Univ. de Paris XI
91405 Orsay Cedex, France

²Centre d'Etudes Limeil-Valenton
94195 Villeneuve-St-Georges Cedex, France

INTRODUCTION

The non-Maxwellian distribution function of charged particles injected into a deuterium–tritium plasma has been found by Cozzani and Horton,¹ and by Liberman and Velikovich,² They use an approximation³ of the collision integral in the Landau form which is valid for charged particle velocities much smaller than the plasma electron thermal velocity and much larger than plasma ion thermal velocity.

If the charged particles are alpha particles generated by deuterium–tritium fusion of a plasma at temperatures in the range from 5 to 30 keV, the previous assumptions are no longer valid. In this work, the Fokker–Planck coefficients are used following the idea suggested by Gus'kov *et al.*,^{4,5} but without neglecting the diffusion coefficient. A second order differential equation for the distribution function is obtained instead of a first order one of previous works. By this way, a general solution of this equation has been found which is valid for all the range of temperatures of fusion interest.

THEORY

The kinetic equation for the unknown distribution function f of charged particles is

$$\frac{\partial f}{\partial t} + v_i \frac{\partial f}{\partial x_i} + \dot{v}_i \frac{\partial f}{\partial v_i} = - \frac{\partial}{\partial v_i} (a_{ij} f - d_{ij} \frac{\partial f}{\partial v_j}) - s + \frac{\dot{n}_\alpha}{4\pi v_\alpha} \delta(v - v_\alpha) \quad (1)$$

where \mathbf{a} is the Fokker–Planck friction vector and \mathbf{d} is the Fokker–Planck diffusion tensor, which can be written as

$$\begin{aligned} a_i &= - \frac{3\sqrt{\pi}\phi(u)u_i}{4\tau b_\beta u^3} \\ d_{ij} &= \frac{3\sqrt{\pi}\phi(u)m_\beta u_i}{8\tau b_\beta^2 m_\alpha u^3 u_j} \end{aligned} \quad (2)$$

with dimensionless velocity $u_i = b_\beta v_i$ and $b_\beta = \sqrt{\frac{m_\beta}{2k_B T_\beta}}$ and

$$\tau = \frac{3m_\alpha k T_e^{\frac{3}{2}}}{4\sqrt{2}\pi m_\beta n_\beta \log \Lambda} \left(\frac{4\pi\epsilon_0}{Z_\alpha Z_\beta e^2} \right)^2$$

$$\phi(u) = \text{erf}(u) - u \frac{\partial \text{erf}(u)}{\partial u} \quad (3)$$

α is the index for the charged particle of interest and β for plasma electrons and ions, and v_α is the injection velocity of these charged particles. Since we are looking for a steady state distribution function of the non thermalized α charged particles, the sink term s is taken to be

$$s(\mathbf{r}, v^2) = 0 \quad (4)$$

for $v > v_c$ with v_c a cut-off velocity greater than the ion thermal velocity.

After summing on i and j and neglecting collisions with plasma ions, a second order differential equation for the distribution function is obtained instead of a first order one of previous works.

$$0 = \frac{d^2 f}{du^2} + \left(\frac{2u}{\eta} + \frac{\phi'}{\phi} - \frac{1}{u} \right) \frac{df}{du} + \frac{2u\phi'}{\eta\phi} f + \frac{2\dot{n}_\alpha \tau b_\beta^3}{3\pi^{\frac{3}{2}} \eta u_\alpha^2} \frac{u^3}{\phi} \delta(u - u_\alpha) \quad (5)$$

with general solution

$$f = B e^{(-\frac{u^2}{\eta})} \int \frac{u}{\phi} e^{(\frac{u^2}{\eta})} du \quad (6)$$

where $\eta = \frac{m_e}{m_\alpha}$. Using a fractional approximation for ϕ

$$\phi = \frac{pu^3}{1 + pu^3} \quad (7)$$

with $p = \frac{4}{3\sqrt{\pi}}$, we obtain the approximate solution

$$f = B \Theta(u_\alpha - u) \left(\frac{\eta}{2} - \frac{1}{pu} + \frac{1}{p} \sqrt{\frac{\pi}{\eta}} e^{(-\frac{u^2}{\eta})} \text{erfi}\left(\frac{u}{\sqrt{\eta}}\right) \right) \quad (8)$$

where B is given by the Dirac delta boundary condition

$$B = \frac{2\dot{n}_\alpha b_e^3 u_\alpha \tau}{3\pi^{\frac{3}{2}} \eta \phi(u_\alpha)} \left[\left(\frac{\phi'(u_\alpha)}{\phi(u_\alpha)} - \frac{1}{u_\alpha} \right) \left(\frac{\eta}{2} - \frac{1}{pu_\alpha} + \frac{1}{p} \sqrt{\frac{\pi}{\eta}} e^{(-\frac{u_\alpha^2}{\eta})} \text{erfi}\left(\frac{u_\alpha}{\sqrt{\eta}}\right) \right) \right]^{-1} \quad (9)$$

RESULTS

By this way, a general solution of this equation has been found which is valid for all the range of temperatures of fusion interest. In figure 1 it is shown the distribution function for the case of non thermal alpha particles produced by the fusion in a deuterium–tritium plasma at a temperature of 5 keV, compared with that obtained in previous works. Both distributions gives approximately the same steady-state density but that of this work predicts a higher accumulation of particles at lower velocities. On the other hand, one can see in figure 2 how the stopping power calculated from the distribution function given by other authors recovers ours only in the limit of velocities much smaller than the electron thermal velocity. We think that this distribution function could be used as a first approximation for the calculation of the distribution function of charged particles isotropically generated in a magnetized plasma like those of the Magnetized Target Fusion approach.

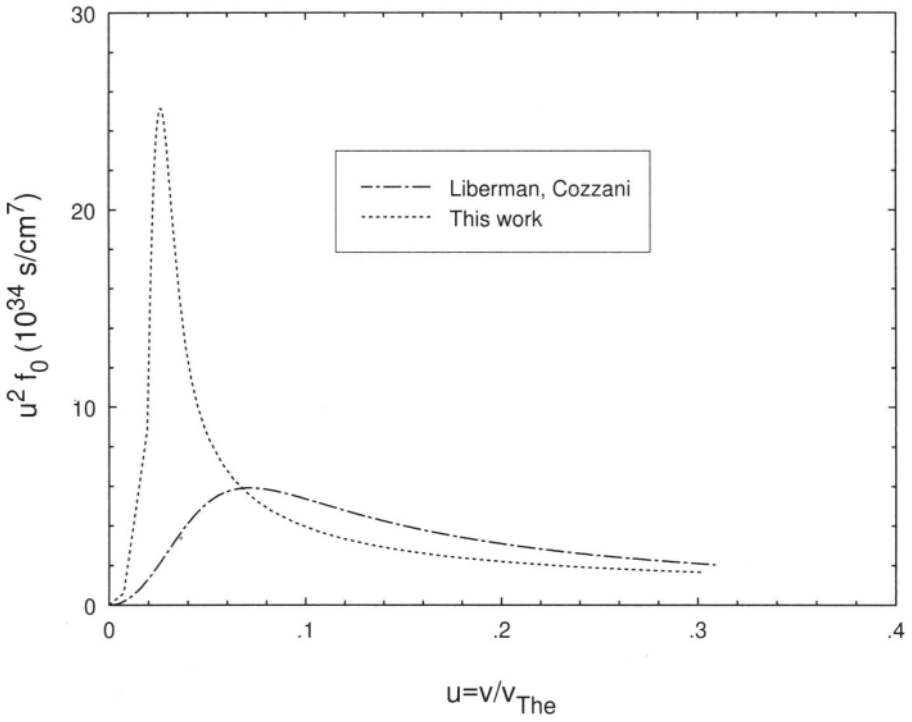


Figure 1. Distribution function for alpha particles in D-T plasma at $kT_e = 5keV$, $n_e = 10^{21}cm^{-3}$ and $f_0 = \frac{f}{n_a}$.

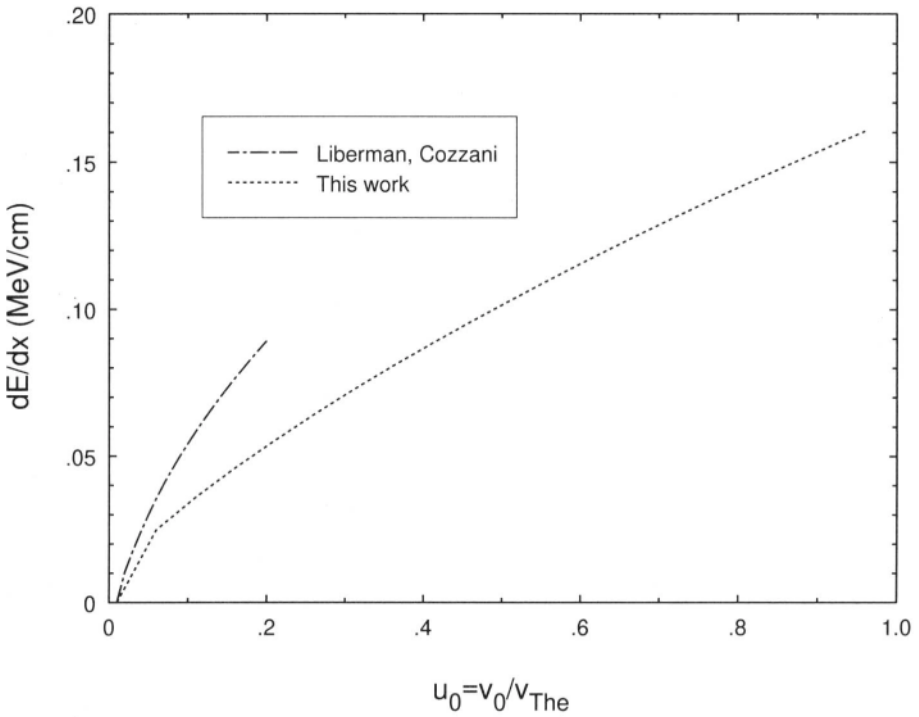


Figure 2. Average stopping power for alpha particles in D-T plasma at $kT_e = 5keV$ and $n_e = 10^{21}cm^{-3}$.

REFERENCES

- [1] F. Cozzani and W. Horton, Collisional transport for a superthermal ion species in magnetized plasma, *J. Plasma Phys.* 36:313 (1986).
- [2] M. A. Liberman and A. L. Velikovich, Distribution function and diffusion of alpha-particles in DT fusion plasma, *J. Plasma Phys.* 31:319(1984).
- [3] S. I. Braginskii, Transport processes in a plasma, *in*:“Reviews of Plasma Physics,” Consultants Bureau, N. Y. (1996).
- [4] S. Yu. Gus’kov, O. N. Krokhin and B. V. Rozanov, Transport of energy by charged particles in a laser plasma, *Sov. J. Quant. Electron.* 4:895 (1975).
- [5] D. V. Sivukhin, Coulomb collisions in a fully ionized plasma, *in*:“Reviews of Plasma Physics,” Consultants Bureau, N. Y. (1996).

ON ABSORBING POWER OF DENSE PLASMAS AT WEAK AND STRONG COUPLING

Yu. K. Kurilenkov¹, G. Maynard,² and J. Dufty³

¹Institute for High Temperature, Russian Academy of Sciences
Izhorskaya 13/19, 127412 Moscow, Russia

²Laboratoire de Physique des gaz et des Plasmas, CNRS-URA73
Universite Paris-Sud, 91405 ORSAY Cedex, France

³University of Florida
Gainesville FL

INTRODUCTION

In this paper we are considering some different aspects of dense and strongly coupled plasmas (SCP) absorbing power for projectile particles (stopping power). The plasma absorption, dynamic transport (optical conductivity), and some stopping phenomena are self-connected, since all of this properties initially have the dynamic (frequency dependent) character. Below we discussed some aspects of this connection, which is not obvious sometimes, in terms of plasma dielectric function and dynamic collision frequency.

All the information on the linear dynamical properties of any media is included into the transverse $\epsilon_{tr}(k, \omega)$ and longitudinal dielectric function $\epsilon_l(k, \omega)$, and the basic optical characteristics may be expressed in terms of these functions correspondingly. For example, propagation of collective modes are characterized by the corresponding dispersion relations¹

$$k_r^2(\omega) = \left(\frac{\omega}{c}\right)^2 \epsilon_{tr}(k, \omega) \quad (1)$$

$$\epsilon_l(k, \omega) = 0. \quad (2)$$

From Eq. 1, the important optical properties of any media are easily defined: the refractive index $n(\omega) = (c/\omega) \text{Re}k_r(\omega)$, the absorption coefficient $\kappa(\omega) = \text{Im}k_r(\omega)$, the depth of electromagnetic wave penetration into plasma (skin depth) $L = 1/\text{Im}k_r(\omega)$, the high frequency conductivity, etc.

In turn, the dielectric function is related with the dynamic electron-ion collision frequency $\nu(\omega)$ by the well-known manner¹

$$\epsilon(\omega) = \epsilon_{tr}(0, \omega) = 1 + \frac{1.96i\omega_p^2}{\omega\nu(\omega)} \quad (3)$$

for $\nu > \omega$, and

$$\epsilon(\omega) = \epsilon_{tr}(0, \omega) = 1 - \frac{\omega_p^2}{\omega(\omega + i\nu(\omega))}. \quad (4)$$

for $\nu < \omega$. Eq. 3 takes into account electron–electron correlations, which are neglected in the high-frequency case 4. Thus, the dynamic collision frequency for classical dense plasmas are playing the key role to calculate in principle the SCP optical properties in wide range of frequencies.

As most of experimental informations on dense plasma dynamical properties is obtained by diagnosing the optical properties of such plasmas, a great amount of theoretical and experimental results have been accumulated on the corresponding quantities $\epsilon_{lr}(k, \omega)$, $n(\omega)$, $\kappa(\omega)$, L and $\nu(\omega)$. Our purpose here is to show that, due to the strong connection between optical properties and stopping phenomena new insight in the latter can be gained from the knowledge of these optical properties. Correspondingly, dense plasma effects in opacity, including the role of collective modes and SCP effects (interparticle correlations) could be included by a natural way, in depending of plasma parameters combination like Γ , θ and ω_{pe} with $\Gamma = Z^2\beta/a$, $\beta = 1/T$ is the inverse temperature, Z is the ionic charge and $a = (3/4\pi n_i)^{1/3}$ is the ion sphere radius, $\theta = T/E_F = 2/\left(\beta(3\pi^2 n_e)^{2/3}\right)$, ω_{pe} = plasma frequency (atomic units are used throughout this paper).

Looking for the ways of optimization of energy deposition, below we are attempt to discuss qualitatively some possible features of stopping power (SP) of dense plasmas at high and low velocity limits, which are followed from known features of SCP opacities, high frequency and static conductivity, and the specifics of SCP collective modes.

HIGH VELOCITY STOPPING

The loss rate of the kinetic energy along the particle trajectory can be put in the form:

$$-\frac{dE}{dx} = S = \left(\frac{Z}{V_0}\right)^2 \frac{\omega_p^2}{2} \int_0^\infty d\omega \int_{\frac{\omega^2}{2V_0^2}}^\infty \frac{dQ}{Q} F(Q, \omega), \quad (5)$$

where V_0 is the projectile velocity, $F(Q, \omega) = \frac{-2\omega}{\pi\omega_p^2} \text{Im} \left(\frac{1}{\epsilon_l(\sqrt{2Q}, \omega)} \right)$ and $Q = \frac{q^2}{2}$, q being the wave number of plasma excitations. For weak coupling plasmas $F(Q, \omega)$ has the simple limits

$$\begin{aligned} \lim_{Q \rightarrow 0} F(Q, \omega) &= \delta(\omega - \omega_p) \\ \lim_{Q \gg T, T_F} F(Q, \omega) &= \delta(\omega - Q), \end{aligned} \quad (6)$$

corresponding to plasma resonance and binary collisions. At high velocity, the integral in 5 can be easily calculated using the f-sum rule:

$$\int_0^\infty \omega d\omega \text{Im} \left(\frac{1}{\epsilon_l(q, \omega)} \right) = -\frac{\pi\omega_p^2}{2}. \quad (7)$$

giving the Bethe SP limit:^{2,3}

$$S = \frac{Z^2\omega_p^2}{V_0^2} \ln \left(\frac{2V_0^2}{\omega_r} \right), \quad (8)$$

with ω_r the mean excitation energy of free electrons defined by the relation

$$\ln \omega_r = \frac{-2}{\pi\omega_p^2} \int \omega d\omega \text{Im} \left(\frac{1}{\epsilon(\omega)} \right) \ln \omega. \quad (9)$$

To derive Eq. 9 we have used the identity $\varepsilon_l(0, \omega) = \varepsilon_{lr}(0, \omega) = \varepsilon(\omega)$. Therefore Eqs. 3,4, 8 and 9 give the general framework for computing high velocity plasma stopping in dense collisional plasma. In the limit of low collision frequency, Eq. 4 and 9 give:⁴

$$\omega_r \approx \omega_p + \frac{\pi}{4} \nu(\omega_p). \quad (10)$$

Whereas for a high collision frequency Eq. 3 provides a large broadening of contributing frequencies in Eq. 9 giving $\omega_r \approx \langle \nu \rangle$, the usual average electron-ion collision frequency. Then a good approximation for the mean excitation energy at any collision frequency could be

$$\omega_r \approx \omega_p + \langle \nu \rangle \quad (11)$$

However classical low density results for $\langle \nu \rangle$ cannot be applied in SCP. In particular small θ and/or large Γ yield a reduction of the collision frequency over the classical result due to quantum diffraction and/or strong screening. In fact it has been shown that long wavelength modes do “survive” in spite of the collision-dominated character of dense plasma.⁶ If precise results are needed, Eqs. 3,4 and 9 has to be solved self consistently. The scheme to be used is exactly the same that was derived for calculating reflectivity and skin depth of dense plasma,⁵ strong electron-ion and electron-electron coupling can be taken into account with the Three Term Approximation (TTA) using a dynamical local field correction for the dielectric constant.

LOW VELOCITY STOPPING

The effect on the stopping power of the redistribution of optical conductivity along the SCP spectrum is limited at high velocity because of the full use in that case of the f-sum rule 7. However as the projectile velocity is decreasing the integration domain in Eq. 5 is reduced ($\frac{\omega^2}{2V_0^2} < Q < 2(V_0^2 + v_{ih}^2)$). Therefore, low velocity limit for SP may be more sensitive to redistribution of SCP absorption coefficient and to coupling and degeneracy effects in principle, as well as conductivity and opacity themselves. In fact, at low velocity, a direct connection can be done between the stopping power and the collision frequency $\nu(\omega)$. Using the Born approximation, $\nu(\omega)$ reads as [5]:

$$\nu_B(\omega) = -\frac{2z_p^2}{3\pi\omega} \int q^2 dq S_{ii}(q) \text{Im} \left(\frac{1}{\varepsilon(q, \omega)} \right), \quad (12)$$

with z_p the charge of plasma ions. Neglecting the ion-ion correlation which generally does not play an important role and taking the low frequency limit of 5 and 12 we get the quite simple result

$$S = \left(\frac{Z}{z_p} \right)^2 V_0 \nu_s, \quad (13)$$

with $\nu_s = \nu(0)$. This result can also be derived writing the low velocity stopping and the collision frequency in term of the force-force correlation function.⁷ Moreover, for $Z = z_p$ Eq. 13 can be applied even at strong coupling. In that case, the non linear stopping expression given in [8] is recovered by calculating ν_s in the TTA approximation. The equation 13 has a simple physical meaning: the dynamic collision frequency characterizes the damping decrement of collective SCP modes, i.e., rate of electron subsystem scattering by ions which are strongly correlated with electrons. Some similarity seems then likely for inverse problem - low velocity ion stopping by electron subsystem at strong coupling. Principally, it means that the knowledge accumulated for decrements of SCP plasma oscillations and their levels for different combinations of Γ and θ may be used to determine the low velocity limits of SP

for different kinds of SCP. In particular, weakly nonideal classical plasmas ($\Gamma \leq 1$, $\theta \gg 1$) and dense degenerate plasmas ($\Gamma > 1$, $\theta < 1$) have rather well defined modes, low values of $\frac{\nu}{\omega_p}$ and, correspondingly, the low stopping values in relative units. Meanwhile, for classical collision-dominated SCP ($\Gamma, \theta > 1$) with poorly defined (damped) modes we may expect the maximum of stopping for low velocity limit. The area of poorly defined modes ($a < k < \omega_p/v_{th}$) will play the dominant role for SP in this case.¹ Probably, the direct comparison of classical SCP plasma wave collisional decrements behavior (Fig 13 in [1]) and available MD results of friction coefficient simulation, $(dE/dx)/V_0$,⁹ for example, under similar plasma parameters may illustrate this analogy additionally. However, this symmetry needs further analysis for different SCP.

Eq. 13 with $Z = z_p = 1$ may be rewritten in terms of static conductivity $\sigma_s = \frac{\omega_p^2}{4\pi\nu_s}$

$$\frac{S}{V_0\omega_p} = \frac{\omega_p}{4\pi\sigma_s} \quad (14)$$

This shows, in particular, that anomalously low transport (for example, anomalous conductivity $\sigma_{lim} = \frac{\omega_p}{4\pi}$ under some instabilities developed even at dense plasma) have to be supplemented by anomalously high stopping at low velocity limit. Anomalously low static SCP conductivity means, in particular, the manifestation of the enhanced scattering of charges by the suprathermal collective and group fields (correspondingly, the effective collision frequency is enhanced, $\nu(\omega) < \omega_p$). For low velocity projectiles it provides the anomalously high values of friction coefficient, i.e., enhanced stopping up to order of magnitude (like the decreasing of static SCP conductivity up to anomalous one). Note that the slope SP as a function of V_0 will be proportional to plasma frequency $\frac{S}{V_0} = \omega_p$.

Acknowledgements

We acknowledge partial support of this work by NATO Linkage Grant HTECH. LG 960803.

REFERENCES

- [1] Yu. K. Kurilenkov and M. A. Bertkowsky, in: "Transport and Optical Properties of Nonideal Plasma," G. A. Kobzev, I. T. Iakubov and M. M. Popovich, eds, Plenum, New York (1995), p. 215
- [2] J. Lindhard and A. Winter, Mat. Fys. Medd 34:4 (1964)
- [3] G. Maynard and C. Deutsch, J. Physique 46: 1113 (1985)
- [4] Yu. S. Sayasov, J. Physique C8:1 (1983)
- [5] M. A. Berkowsky and Yu. K. Kurilenkov, J. Quant. Spectr. Radiat. Transfer. 44:25 (1990)
- [6] M. A. Berkowsky and Yu. K. Kurilenkov, Physica A 197:676 (1993)
- [7] J. W. Dufty and M. A. Berkowsky, Nucl. Instr. Meth. B96:626 (1995)
- [8] G. Maynard, K. Katsonis, S. Mabong; M. Chabot and D. Gardes, Nucl. Instr. Meth. A (1998) in press
- [9] G. Zwicknagel, C. Toepffer and P. G. Reinhard, Hyperfine Interactions 99:285 (1996)

ON THE DEPENDENCE OF CONTINUUM FACTORS ON PLASMA PARAMETERS

Marko M. Popović and Dragutin Djordjević

Institute of Physics
P. O. Box 57, 11001 Beograd, Yugoslavia

INTRODUCTION

Because of the importance of the continuum ξ -factors (Biberman and Norman^{1,2}) for plasma diagnostics, ξ factor dependence on plasma parameters (electron density n_e and temperature T) was discussed in a number of publications. Disagreements between different results were found, especially for high electron densities. In this paper we give the results of our work on the continuum radiation in the high pressure xenon pulsed arc.

In comparison to the stationary plasma sources, certain advantages are characteristic for the quasistationary pulsed arc e.g., simple construction of the pulsed power generators, high specific energy dissipated in the plasma, high ionization degree suitable for the studies of Coulomb interactions etc. The results of our ξ -factor determination in the high pressure xenon pulsed arc of the configuration described elsewhere³ show the similar effect as in the shock tube experiments.^{4,5} Due to its construction this version of the pulsed arc enables a number of advantages for the spectroscopic measurements.

RESULTS AND DISCUSSION

Main plasma diagnostics consist of the plasma dynamic pressure and temperature measurements. Plasma temperature has been determined from the measurements of absorption coefficient k for two different plasma lengths (optically thin $\ll 1$ and thick case $\gg 1$). Conditions of local thermodynamic equilibrium (LTE) are well established in xenon pulsed arc ($T \approx 10000$ K, $n_e \approx 10^{18} \text{ cm}^{-3}$), so that equilibrium relations and Saha equation can be used for the calculations of plasma composition (knowing measured pressure p and temperature T). The temperature has been determined by the method described in [3]. It consists in an absolute measurement of the spectral intensity of a homogeneous plasma layer in dependence of its length d . For this we inserted into the discharge tube a cylindrical auxiliary electrode (TE in figure 1). This electrode can be moved in the tube by means of a magnet from outside without any change of the discharge parameters. Changing the thickness of the radiating layer (optically thin and thick) we estimated the radiation intensities at different wavelengths and calculated from them both the temperature T and absorption coefficient k . The dynamic discharge pressure was ≈ 15 atm.

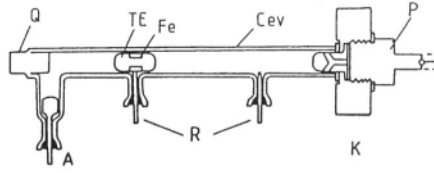


Figure 1. Pulsed arc: A-anode, K-cathode, Q-quartz rod, P-pressure probe, TE-auxiliary electrode.

Table 1. Pulsed arc plasma parameters

λ	525nm	650 nm	725 nm
$k[\text{cm}^{-1}]$	0.19–0.55	0.28–0.45	0.19–0.85
$T[\text{K}]$	10700–12000	10700–13100	10370–13800
$n_e \cdot 10^{-17}[\text{cm}^{-3}]$	4.16–7.74	3.80–10	3.36–12

Another independent diagnostic method for determination of electron density n_e was the use of laser interferometry, where we employed a Mach–Zehnder interferometer. A special care has been paid to the influence of absorption of plasma in the working arm of the interferometer. According to our calculations, it shows up that influence of the plasma optical depth $\tau = k \cdot d$ on the modulation of interference signal can not be neglected already at $\tau \approx 0.4$. For these reasons, we used a method of polar diagram that enables precise determination of the parts of the fringes even in the case of plasma with $\tau \approx 1$. In this method the phase information is derived from the amplitudes of two interference signals which are phase shifted by $\pi/2$. This is accomplished by an auxiliary beam-splitter outside the interferometer and the interference signals phase shifted by $\pi/2$ are recorded by the two monochromatic photo detecting systems. The main plasma parameters are summarized in the Table 1.

The continuum radiation of inert gases was investigated in a number of papers. In some of these publications the ξ -factors dependence on plasma parameters was discussed in detail. Meiners and Weiss⁴ found out in their shock wave experiment that there was a dependence for krypton and xenon whereas for argon ξ did not depend on n_e^2/\sqrt{T} . In another shock wave experiment⁵ ξ -factor decrease with increasing electron density till to the characteristic minimum at $n_e \approx 2 \cdot 10^{19} \text{cm}^{-3}$, which is interpreted by the theoretical prediction of the transparency window.⁶ In our experiment we determine ξ factor dependence on plasma parameters n_e and T , at different wavelengths. The results are presented in terms of dependence of the parameter n_e^2/\sqrt{T} which is characteristic for dependence of the plasma absorption (emission) coefficient on plasma parameters (figure 2). We found ξ factor decrease with increasing value of n_e^2/\sqrt{T} at all relevant wavelengths. As is seen from the figure an overall trend of the decrease of ξ with increasing n_e^2/\sqrt{T} is observed. The measurements at high densities ($> 10^{18} \text{cm}^{-3}$) are necessary for the knowledge of ξ factor dependence on plasma parameters, since only the range of parameters characteristic of weakly non ideal plasma was covered in our experiment. Electron densities higher then approximately $1.2 \cdot 10^{18} \text{cm}^{-3}$ could not be reached in the pulsed arc due to a limitations connected with the value of dynamic pressure attainable.

These results are also compared with our calculations of ξ factor in quasi classical approximation (QCA). Recently in QCA an analytical expression for the continuum absorption coefficient which corresponds to integral accounting of highly excited states has been obtained.^{7,8} Quasi classical approximation is essentially written in the framework of quantum defect method-QDM.⁹ Indeed, the basis of QDM are Coulomb approximation and quantum defect extrapolation to the positive energies. An advantage of this approach compared to the

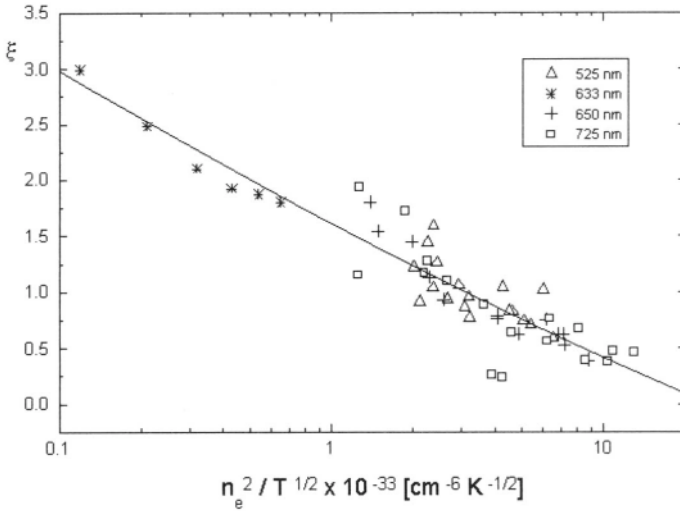


Figure 2. Results in xenon pulsed arc: \triangle 525 nm, $*$ 633 nm, $+$ 650 nm, \square 725 nm.

Table 2. Individually calculated levels

$\text{XeI } ^2P_{3/2}^0$:	6s, 7s, 8s, 9s, 10s; 6p, 7p, 8p, 9p, 10p; 5d, 6d, 7d, 8d, 9d
$\text{XeI } ^2P_{1/2}^0$:	6s', 7s', 8s', 9s', 10s'; 6p', 5d', 6d', 7d', 8d', 9d'
XeII:	6s, 7s; 6p; 5d, 6d

numerical calculations^{1,2, 10-12} is that analytical expressions are obtained without losing the exactness of the results which is important in some applications.

We calculated continuous absorption coefficient of a low temperature xenon plasma ($T \approx 1eV$) in QCA. The data necessary for photoionization cross sections calculations are taken from the Tables.¹³ In the case of small jl -terms splitting, one can use an average value of quantum defects corresponding to the different jl - terms series¹⁴ which considerably simplifies the calculations. In our calculation of the absorption coefficient we take into account a large number of atomic and ionic states. Photoionization was calculated for the xenon excited states shown in Table 2.

In figure 3 we give comparison of QCA calculations with our measurements in pulsed arc at $\lambda = 525, 633, 650, 725 \text{ nm}$ and experimental results¹⁵ in a wall stabilized xenon arc. Quasi classical approximation calculations are for $T=10000 \text{ K}$ both for XeI and XeI+XeII.

CONCLUSION

Satisfactory overall agreement between our QCA calculations and the results by other methods (scaled Thomas-Fermi potential method, including polarization effects — STFP,¹² QDM¹¹) is found, both in the shape and magnitude, except in the region $\lambda < 4000 \text{ \AA}$ where photoionization of XeII begins to play an important role. This is because in STFP and QDM calculations the contribution of XeII photoionization was not taken into account. The agreement between calculations and experimental results is not satisfactory, except in the part of the spectrum. Probable cause of these discrepancies is the influence of different plasma effects (e.g., line broadening, merging of the lines, ionization potential lowering, transparency window), so it is necessary to investigate the dependence of the absorption coefficient on

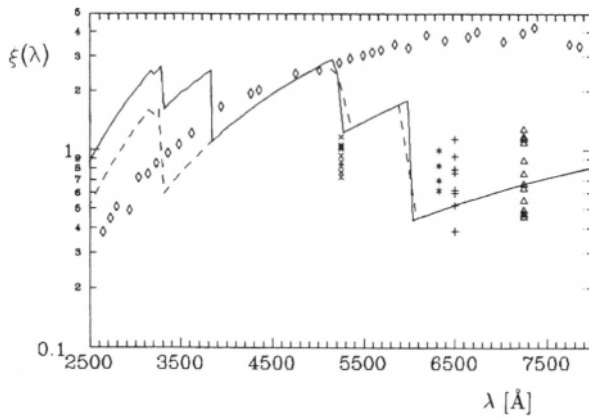


Figure 3. Comparison: QCA-experimental results. — QCA, XeI+XeII; - - - XeI; \diamond Goldbach 12300 K; \times , $*$, $+$, \triangle Xe pulsed arc at $\lambda=5250, 6328, 6500$ and 7250 Å.

electron concentration, especially at higher densities when plasma effects begin to play an important role.

REFERENCES

- [1] Biberman, L. M., and Norman, G. E., *J. Quant. Spectrosc. Radiat. Transfer* 3:221 (1963).
- [2] Biberman, L. M., and Norman, G. E., *Soviet Physics Uspekhi* 10:52 (1967).
- [3] Radtke, R., and Guenther, K., *J. Phys.* D9:1131 (1976).
- [4] Meiners, D., and Weiss, C. O., *J. Quant. Spectrosc. Radiat. Transfer.* 16:273 (1976).
- [5] Sechenov, V. A., *Fizika plazmi* 5:1172 (1981). (in russian)
- [6] Kurilenkov, Yu., and Filinov, V., *Teplofiz. Vys. Temp.* 18:657 (1980). (in russian)
- [7] D'yachkov, L. G., and Pankratov, P. M., *J. Phys. B.* 24:2267 (1991).
- [8] D'yachkov, L. G., and Pankratov, P. M., *J. Phys. B.* 27:461 (1994).
- [9] Burgess, A., and Seaton, M. J., *Mon. Not. R. Astr. Soc.* 120:121 (1960).
- [10] Peach, G., *Mem. R. astr. Soc.*, 73:1 (1970).
- [11] Schlueter, D., *Z. Physik* 210:80 (1968).
- [12] Hofsaess, D., *J. Quant. Spectrosc. Radiat. Transfer* 19:339 (1978).
- [13] Moore, C. E., "Atomic Energy Levels," NBS, Washington (1952).
- [14] Sobelman, I.I., *Atomic Spectra and Radiative Transitions*, Springer-Verlag, Berlin-Heidelberg-New York (1979).
- [15] Goldbach, C., Nollez, G., and Stuck, D., *J. Phys. B: Atom. Mol. Phys.* 7:1191 (1976).

OBSERVATIONS OF THE CHARGED PARTICLE DYNAMIC SCREENING EFFECTS AND THE PLASMA PHASE TRANSITION IN HOT Z-PINCH PLASMA

V. A. Rantsev-Kartinov¹ and E. E. Trofimovich²

¹INF RRC "Kurchatov Institute", 123182, Moscow, Russia

²International University for Nature, Society and Man of the Dubna, Universitetskaya 19, Dubna, Moscow region, 141980 Russia

INTRODUCTION

The scattering of laser radiation in plasmas is known to make transition from incoherent scattering at plasma electrons to the collective scattering (scattering at a dressed particle in plasma). For small values of the Salpeter parameter $\alpha = 1/kl_D \ll 1$, where k is wave number of the scattering vector and l_D is the Debye radius [1], the scattering takes place at individual electrons and the spectrum has Gaussian line shape with the half-width determined by the electron temperature. In opposite limiting case, $\alpha \gg 1$, the scattering is a coherent one and the spectrum contains the narrow central peak, with the half-width determined by the ion temperature, and the symmetric satellites shifted to electron plasma frequency. For intermediate values of Salpeter parameter, $\alpha \sim 1$, the spectrum line shape is very sensitive to the value of α and, thus, to the correlation length of the screening of a charged particle in plasmas. For investigating the dynamic screening effects in dense plasmas it is worth to study the scattering of laser light in Z-pinch plasma in a scattering geometry when $\alpha \sim 1$. The results reveal the importance of allowing for the non-static screening effects in interpreting the experimental spectra and determining major parameters of dense plasmas in a high current gas discharge.

EXPERIMENTAL SET UP

The experimental set-up (Fig. 1) includes discharge tube 60 cm long, 20 cm diameter, with flat copper electrodes on the edges, low inductance capacitor, **60 μ F**, voltage ~ 30 kV. Maximum current, **350+400 kA**, is attained at **4.5 μ s** after discharge breakdown. The diagnostics uses ruby laser of 15 ns pulse duration and energy 5 J. The 10-channel differential diagnostic system (DDS) enables us to extract the signal under conditions of the signal to noise ratio being as small as **0.01+0.005**.

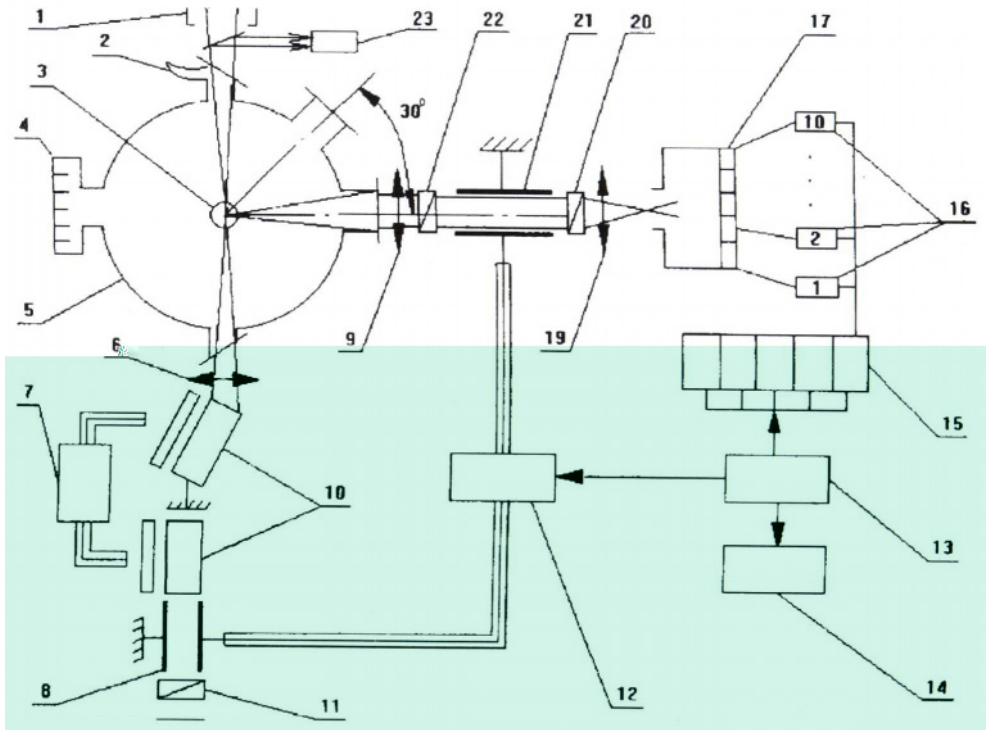


Fig.1. The experimental set-up: 1,2,4 - light traps; 3 - plasma; 5 - vacuum chamber; 6,9,19 • objective lenses; 7 - laser energetic block; 8,21 - Kerr cells; 10 - laser; 11,20,22 - polarization filters; 12 - Kerr cells energetic block; 13 - synchronization block; 14 - capacitor; 15 - oscilloscopes; 16 - photoelectron multipliers; 17 - fiber optics; 18 - polychromator; 23 - coaxial photocell (monitor).

EXPERIMENTAL RESULTS

One of the experimental results for the scattered light spectrum is shown in Fig.2 for scattering angle $\theta = 90^\circ$. Comparison of this experimental curve with various theoretical curves [2] gives an estimation for the value of Salpeter parameter, namely $\alpha \approx 0.1 + 0.2$. This curve is replotted in new special coordinates shown in Fig.3 that allows to determine electron temperature T_e from the slope of the curve. This gives for both components of plasma electrons, namely for background plasma and for electrons captured by the turbulence, the same temperature, namely 36 eV. Here, the accuracy of determining the temperature is about 15%.

The measurements of absolute values of intensity, with the corresponding calibration of the DDS, and of relative intensities of radiation scattered at different angles allow to find electron density and finally to determine value of α which lies in the range of few units. Thus we arrive at a discrepancy. Really, the line shape for these values of α would give much different line shapes than the curve in Fig.2. It appears that we can eliminate such a disagreement if we replace in the definition of Salpeter parameter the conventional Debye radius to the dynamic screening radius which, according to [3,4], is equal to 10-20 Debye radius. The descreening effect can be seen from Fig. 4 for the relative value of the average effective charge for a moving particle in a plasma.

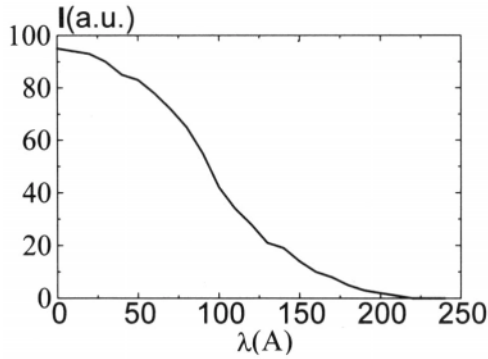


Fig.2. Typical spectrum of scattered radiation (arb.units).

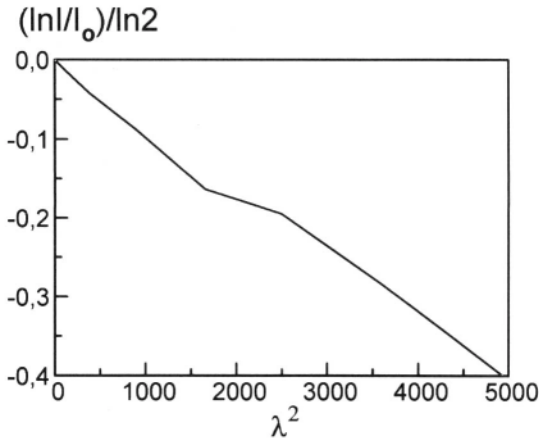


Fig.3. The dependence $(\ln I/I_0)/\ln 2$ vs. λ^2 for conditions of Fig.2.

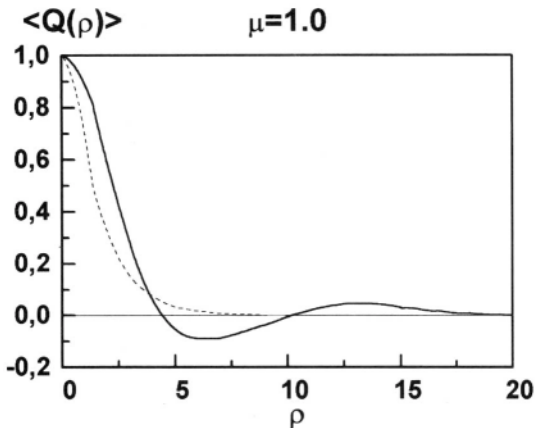


Fig.4. The relative value of the average effective charge $\langle Q(\rho) \rangle$ for a moving particle in a plasma, for a given value of $\mu \equiv (v/v_1)^2$, as a function of distance $\rho = r/l_D$ from the charge, expressed in units of Debye radius (solid curve). The dashed curve corresponds to the Debye screening. Here, v , is the charged particle velocity, and v is thermal velocity of plasma particles.

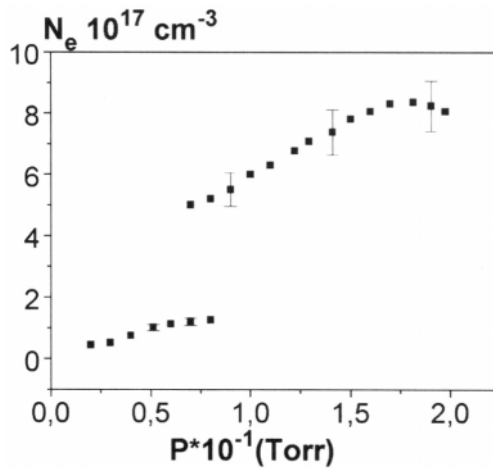


Fig.5. The radially averaged plasma electron density at the moment of maximum plasma compression.

Thus we arrive at a conclusion that the experimentally measured Thomson scattering spectra confirm the qualitative description of the dynamic descreening effects in [3,4].

Figure 5 shows dependence of radially averaged plasma electron density on initial gas pressure at the stage of maximum compression of plasma, which takes place $200 \div 250$ ns before the first singularity of electric current [5] (here the working gas is deuterium).

The value of density N_e was determined from integral intensity of scattered light, with the corresponding calibration, and also from relative measurements of the scattered light intensity at various scattering angles 90° , 60° and 120° . This gives the value of N_e lying in the range $(1 \div 5) \cdot 10^{17} \text{ cm}^{-3}$.

It is seen that there is a bifurcation in the domain (0.065-0.085) Torr. Also the density exhibits stepwise dependence as it makes a jump, by a factor of five, at a certain pressure value, about 0.075 Torr. This can be interpreted as a sort of the phase transition to a dense plasma. Also the saturation of density with growing pressure is seen here.

The next figure, Fig.6, shows radially averaged T_e at the moment of maximum compression. It is seen that the temperature raises monotonously from 30 eV to 130 eV with the

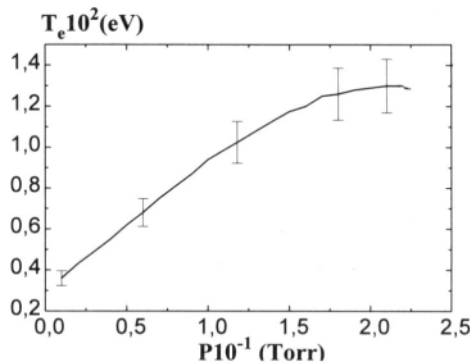


Fig.6. The radially averaged plasma electron temperature at the moment of the maximum plasma compression.

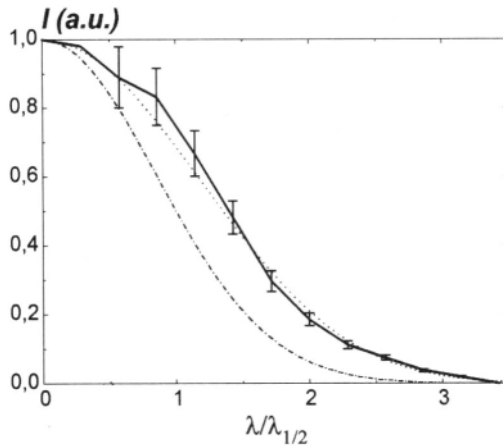


Fig.7 The experimental spectrum for the laser light scattered at the angle $\theta=90^\circ$ (solid line) and computed curves. Here $\lambda_{1/2}$ is the half-width of the spectrum line; dash-dotted, the Gaussian for $T_e = 36 \text{ eV}$; dashed curve stands for the calculation which assumes that 50% of plasma electrons are captured by the turbulence and that both background electrons and captured electrons are Maxwellians and thus they give the Gaussian line shape of scattered radiation.

initial working gas pressure varying from 0.01 Torr to 0.2 Torr, respectively. The temperature attains its limiting value asymptotically with growing pressure. The asymptotic value is determined by the characteristic time of the electron-ion energy exchange, which is equal to 70 ns, at the stage of maximum compression of the pinch which has a duration of about 100 ns.

We have already seen the effect of capturing the electrons by a strong turbulence in the figure for the effective temperatures of scattered spectrum, namely a shift of the spectrum of the radiation scattered at captured electrons. Remind that the Fig.3 shows that the temperature of captured electrons equals to temperature of the 'background' plasma.

CONCLUSIONS

Experimental results, presented on the diagnostics of the Dense Z-pinch plasma from laser scattering spectra, demonstrate the possibility of the phase transition to a dense plasma. It follows from interpreting the spectra of scattered radiation that the formal use of the Salpeter parameter with conventional Debye radius leads to a discrepancy which can be resolved via allowing for the substantial dynamic descreening of a charged particle in hot plasmas. Observations of strong Langmuir turbulence allowed to estimate the fraction of the turbulence-captured electrons.

REFERENCES

1. J.Sheffield «Plasma Scattering of Electromagnetic Radiation», New York, San Francisco, London (1975)
2. L.N. Pyatnitskiy, «Laser Diagnostics of Plasmas», Moscow, Atomizdat (1976)
3. E.E. Trofimovich, and V.P. Krainov, Sov. Phys. *JETP*, **77**:910 (1993).
4. V.P. Krainov, V.A. Rantsev-Kartinov and E.E. Trofimovich, See this volume.
5. V.V. Aleksandrov, A.I. Gorlanov, N.G. Kovalskiy, S.Yu. Lukyanov, V.A. Rantsev-Kartinov, In: Diagnostics of Plasmas (in Russian), v.3, Moscow, Atomizdat (1973).

This page intentionally left blank

ELECTRICAL CONDUCTIVITY OF STRONGLY COUPLED MODEL AND REAL PLASMAS

I. M. Tkachenko and P. Fernández de Córdoba

Department of Applied Mathematics
 Polytechnic University of Valencia
 Valencia E-46071, Spain
 E-mail: imtk@iqn.upv.es

The theory of electrical conductivity of dense cold fully-ionized hydrogen-like plasmas based on the concept of self-consistent field, and the generalized random-phase approximation (RPA) is shown to possess correct low- and high-density limiting properties, and to be in a reasonable agreement with all available experimental data. The basic idea considered in the present approach^{1,2} is: each electron (carrier) moves in a self-consistent field generated by all other free charges in the system. The finite values of the transport coefficients result from the electron's scattering on the self-consistent field fluctuations. This approach was first outlined in [1]. This work was based on the paper³ by S. F. Edwards, which related the Lorentz-model expression for the fully-ionized plasma electrical conductivity to the strict quantum-statistical calculation involving the Green's function formalism with the self-consistent field potential. The starting point for the conductivity calculation is thus the Lorentz formula

$$\sigma = -\frac{4e^2}{3m} \int_0^\infty E dE \frac{d\omega(E)}{dE} \rho(E) \tau(E), \tag{1}$$

where $\rho(E) = (2m^3 E)^{1/2} / (2\pi^2 \hbar^3)$ is the density of one-electron states in the energy space, and $\omega(E)$ is the Fermi–Dirac distribution. Generally speaking, the mean relaxation time $\tau(E)$ of Eq. (1) is determined by the exact pairwise scattering cross-section, and we express it in terms of the self-consistent field correlation function,

$$\tau^{-1}(E) = \frac{me^2}{4\pi(2mE)^{3/2}} \int_0^Q q^3 dq \int_{-\infty}^\infty \langle |\hat{V}(\vec{q}, \omega)|^2 \rangle d\omega. \tag{2}$$

Here $Q = (8mE/\hbar^2)^{1/2}$, momentum $\hbar Q$ being the maximum possible variation of the electronic momentum as a result of the scattering process; and

$$\hat{V}(\vec{q}, \omega) = \frac{4\pi e}{q^2 \varepsilon(q, \omega)} \sum_{a=e,i} Z_a \hat{\rho}_a(\vec{q}, \omega) \tag{3}$$

is the screened field potential operator complete Fourier transform, $\hat{\rho}_a(\vec{q}, \omega)$ being the a -species density operator in the (\vec{q}, ω) -space, and $\varepsilon^{-1}(q, \omega)$ - the plasma dynamic screening

function. The system is presumed to contain electrons (e) and ions (i), characterized by their respective charge numbers $Z_e = -1$ and $Z_i = Z$, so that $n_e = Zn_i$, n_a being the number density of a -species. The field potential correlation function thus equals

$$\langle |\hat{V}(\vec{q}, \omega)|^2 \rangle = \left(\frac{4\pi e}{q^2 \epsilon(q, \omega)} \right)^2 \sum_{a,b} Z_a Z_b S_{ab}(\vec{q}, \omega). \quad (4)$$

The dynamic structure factor of the species a and b , $S_{ab}(\vec{q}, \omega)$ was determined in [2] in terms of the system polarization operators:

$$\tau^{-1}(E) = \frac{4\pi m e^4}{\beta (2mE)^{3/2}} \int_0^Q \frac{dq}{q} \sum_{a,l} \frac{Z_a^2 \Pi_a(q, l)}{\epsilon^3(q, l)}, \quad (5)$$

β^{-1} being the system temperature in energy units. Notice that the corresponding expression of [2] is valid for hydrogen plasmas only. The l -summation in Eq. (5) is spread over the poles $2\pi l / \beta \hbar$, ($l = 0, \pm 1, \pm 2, \dots$) of $\coth(\beta \hbar z / 2)$ on the imaginary z -axis. In our computations we evaluated the real part $\Pi_a(q, l)$ of the a -species polarization operator beyond the standard RPA, using the temperature dependent electronic static local-field correction $G_e(q)$,⁴ parametrized to satisfy both the compressibility sum rule (with the electronic subsystem compressibility determined from the one-component plasma excess interaction energy determined by the Monte Carlo simulation⁵), and the long-wavelength limiting condition of Kimball⁶ with the zero-separation value of the electronic radial distribution function $g_e(0)$ determined by a self-consistent procedure.⁴

Despite the approximations made to obtain our expression for the plasma conductivity, it possesses correct limiting forms corresponding to the cases of dilute gas plasma and metal-density Coulomb systems.⁷ Extensive studies of electrical and thermal conductivities in a wide range of variation of temperature and electronic density in hydrogen-like plasmas (with $n_e = Zn_i$) were carried out in [2,8]. Successful comparison with the results corresponding to model fully-ionized plasmas⁹ were reported in [7,10]. Here we report our results on the conductivities obtained for the conditions corresponding to capillary discharges in polyurethane,¹¹ and copper plasmas obtained by vaporizing copper wire in a water bath.¹²

Dense strongly coupled plasmas were created in a well-diagnosed uniform discharge in polyurethane with density $1.265 \cdot 10^{-2} \text{ g/cc}$ and temperatures in the $25 \div 30 \text{ eV}$ range.¹¹ These results were compared in [11] with several dense plasma theories, showed to be in a significant disagreement. An effective average ionic charge number $Z = 2.3$ was obtained in [11] presuming Saha equilibrium. This permitted us to carry out the calculation of the electrical conductivity of a multiply ionized two-component plasma in the range $n_e = (4.8 \div 5.2) \cdot 10^{21} \text{ cm}^{-3}$ and $T = (2.5 \div 4.0) \cdot 10^5 \text{ K}$. The same (as in [4]) local field correction was employed with $g_e(0) = 0$. The experimental data of [11] (provided graphically for the resistivity) range between $2.0 \cdot 10^5$ and $3.3 \cdot 10^5 (\Omega \cdot m)^{-1}$. Our results varied between $3.3 \cdot 10^5 (\Omega \cdot m)^{-1}$ (for $n_e = 5.2 \cdot 10^{21} \text{ cm}^{-3}$ and $T = 2.5 \cdot 10^5 \text{ K}$) and about $10^6 (\Omega \cdot m)^{-1}$ (for $n_e = 4.8 \cdot 10^{21} \text{ cm}^{-3}$ and $T = 4.0 \cdot 10^5 \text{ K}$), taking the value of $\sigma = 5.0 \cdot 10^5 (\Omega \cdot m)^{-1}$ at about $3 \cdot 10^5 \text{ K}$ and $n_e = 5 \cdot 10^{21} \text{ cm}^{-3}$. This last value is characteristic for the results of “dense plasma theories” referred to in [11]. Notice that the lowest conductivity value reached by these theories is about $4.2 \cdot 10^5 (\Omega \cdot m)^{-1}$.¹¹

We have also carried out a broad comparison with the conductivity data measured by vaporizing copper wires in a water bath.¹² Plasma densities observed ranged from about 2.5 g/cc down to 0.025 g/cc , and temperatures varied between 10 and 30 kK . The ionization state used by A. W. DeSilva and in our computations was taken from the Fermi-Thomas model

Table 1. σ are the results of the present work, the experimental values σ^{exp} were provided by A. W. DeSilva in a private communication, see [12], T, ρ are temperature and mass density of copper, Z_e is its effective ion charge.

$T(kK)$	$\rho(g/cc)$	Z	$\sigma^{exp} 10^{-4} \cdot (S/m)$	$\sigma \cdot 10^{-4} (S/m)$
20	0.7930	1.5	5.1	10.50
10	2.4550	2.3	32.1	21.00
14	1.2036	1.7	9.5	11.95
20	0.1557	1.2	2.2	4.12
26	0.0580	1.4	3.9	3.44
30	0.0400	1.6	4.8	3.42
40	0.0230	2.0	5.8	3.66
10	1.3546	1.7	8.3	11.27
14	0.3500	1.1	1.3	4.90
20	0.0260	1.3	2.0	2.12
10	2.2616	2.2	27.1	19.10
14	0.9704	1.5	6.4	9.86
16	0.1323	1.1	1.2	3.27
20	0.0680	1.2	2.2	2.94
30	0.0270	1.6	4.4	3.03

described by More.¹³ Some results of conductivity computations are provided in the Table. A reasonable 30% agreement is observed in the majority of points, especially at higher densities. A factor of two–three disagreement detected at 14 – 16kK and low densities is attributable to the possible onset at the conductor-dielectric phase transition: the copper plasma begins to undergo a transformation from the fully-ionized state corresponding to our model into the partially ionized state where charge-neutrals interactions are to be taken into account. Notice once more that no adjustable parameters were used in our computations. The only input data were the plasma temperature (T) and density (ρ) (provided by the SESAME code, see [12]) and the precalculated charge number Z (see above). Calculations were carried out for different values of the local-field correction static parameter $g_e(0)$, ranging according to its definition between zero and unity. No appreciable dependence on the value of $g_e(0)$ was detected, further calculations were carried out with $g_e(0)$ set to be zero. Thus, the only “experimental” data our results are based on, is the computer fit to the one-component plasma interaction energy obtained by MC simulations.^{4,5} In conclusion, a theory of electrical conductivity of fully ionized hydrogen-like strongly coupled plasmas, based on the self-consistent field concept and having no adjustable parameters, is presented. The theory is also applicable to multiple-component (non-hydrogen-like, see [7]) plasmas with variable ionization states, and is shown to possess correct low density (Spitzer) and metal density (Ziman) limiting forms.

Acknowledgements

The authors are grateful to A. W. DeSilva for providing his numerical data on conductivity and ionization state, and also to V. M. Adamjan, W. Ebeling, A. A. Mihajlov and J. Ortner for valuable discussions.

REFERENCES

- [1] V. M. Adamyan et al., High Temp. (USA), **18**, 186 (1980).
- [2] Z. Djuric, A. A. Mihajlov, V. A. Nastasyuk, M. Popovic and I. M. Tkachenko, Phys, Lett, **A 155**, 415 (1991).

- [3] S. F. Edwards, *Philos. Mag.*, **3**, 1020 (1958).
- [4] I. M. Tkachenko, *Europhys. Lett.*, **9**, 351 (1989);
I. M. Tkachenko, P. Fernández de Córdoba and M. Urrea, *J. Phys. A*, **29**, 2599 (1996); see also I. M. Tkachenko, P. Fernández de Córdoba and J. M. Belda (present Proceedings).
- [5] G. S. Stringfellow, H. E. de Witt, W. L. S. Slattery, *Phys. Rev. A* **41**, 1105 (1990).
- [6] J. C. Kimball, *Phys. Rev. A* **7**, 1648 (1973);
J. C. Kimball, *Phys. Rev. B* **14**, 2371 (1976).
- [7] I. M. Tkachenko, P. Fernández de Córdoba, *Phys. Rev. E*, 1997 (submitted for publication).
- [8] V. M. Adamyan, Z. Djurić, A. M. Ermolaev, A. A. Mihajlov and I. M. Tkachenko, *J. Phys. D* **27**, 111 (1994); *ibid.*, **27**, 927 (1994).
- [9] J. P. Hansen, I. R. McDonald, *Phys. Rev. A* **23**, 2041 (1981).
- [10] I. M. Tkachenko, P. Fernández de Córdoba, P. Zubía, B. Solís, *Proc. 24th EPS Conference on Controlled Fusion and Plasma Phys.*, Berchtesgaden, Germany, 1997 (to be published).
- [11] J. F. Benage, Jr. et al., *Phys. Rev. E* **49**, 4391 (1994).
- [12] A. W. DeSilva, *Electrical conductivity measurements in copper plasma*, *Proc. Int. Conf. on the Physics of Strongly Coupled Plasmas*, Binz, Germany, 1995. Private communication. **27**, 927 (1994).
- [13] R. M. More, *Atomic Physics of Laser-Produced Plasmas*, Ch. 2 in *Handbook of Plasma Physics*, Eds. M. N. Rosenbluth and R. Z. Sagdeev, Vol. 3, Eds. A. M. Rubenchik and S. Witkowski, Elsevier Sci. Publ. B. V, 1991, p. 70.

PROPERTIES OF STRONGLY COUPLED MICROPLASMAS: EXPERIMENTAL INVESTIGATIONS

Nadja Vogel

University of Technology Chemnitz, Department of Physics, Optical Spectroscopy and Molecule Physics, 09107 Chemnitz, Germany

INTRODUCTION

Physics of plasma formation in cathode spots of vacuum arcs despite of they are the subject of an investigations in many research groups since many decades is not an accomplished manner clear. Electrical arcs in a vacuum burn in a metal-vapor plasma emitted from mobile hot spots at the cathode surface. Because of their smallness ($< 100 \mu\text{m}$) and their non-stationary behavior(nanosecond range), the physical parameters of these cathode spots are difficult to measure. The most important question is one: how the electrode material from the cold cathode surface transforms into the plasma being able to carry out up to some kA current in vacuum. If it is occurs according to a conventional models of gaseous arc when the atoms are evaporated and ionized by electrons that are accelerated in the cathode voltage drop, then it is difficult to explain some experimental facts established at the beginning of vacuum arc physics [1] and not sufficient clarified up to now. Namely, (i) an existence of a directional neutral, as well as (ii) a high energetic ion flows from the cathode surface.

Consistent with a model of microexplosions, which has been confirmed in most resent experiments [2-5], high local power concentration at the electrode surface leads to the formation of a small, dense plasma - strongly coupled microplasma, which transports the electrical current in non-stationary manner.

In this paper we present and discuss an experimental results concerning the properties of non-ideal microplasma in cathode spots of a low current vacuum. In order to examine an optical properties of cathode spot plasma the different experimental techniques: streak camera recording, time-resolved and time-integrated Spectroscopy with a spectral resolution smaller then 0.15 nm was used [6-7]. From spectroscopic measurements in visual spectral range, degeneration of the upper exited atom states is deduced, corresponding to a strong non-ideality of the cathode spot plasma with consequences for the particle density ($N_e > 10^{28} \text{m}^{-3}$). Splitting of the resonance spectral lines of electrode material into three components gives us a confirmation about an existence of self-generated magnetic field of order of 6.8 T in cathode spot fragments [6]. Investigations of a temporal evolution of x-ray radiation from cathode spots of laser-induced discharges by means of picosecond x-ray streak camera shown a presence of an intensive point-like structures of x-ray radiation with life time of

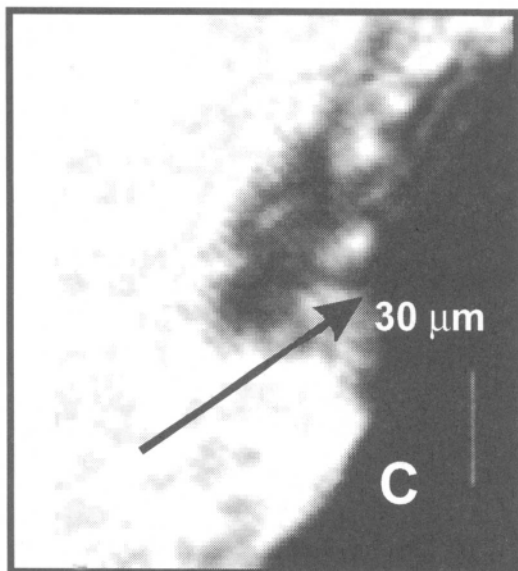


Figure 1: Absorption photograph for a pulse vacuum discharge between Cu-electrodes. Delay time after ignition $t=18$ ns.

a laser pulse was directed onto the cathode surface for spot ignition. The cathode and anode material was copper. The arc spots were ignited at the top of the cathode surface by focusing an IR laser beam of 100 ps duration through a small hole in the anode.

Delaying the probe laser beam at second harmonics (532 nm) relatively to the ignition laser beam by 0.1-20 ns with an accuracy of 50 ps, it was possible to record the breakdown ignition phase for the cathode spots.

One selected absorption image for delay times of 18 ns is shown in Figure 1. We can see for a delay time $t = 18$ ns after ignition some small spots near the cathode surface.

Their diameters can be evaluated from the two-dimensional electron density distribution. They are smaller than $3 \mu\text{m}$. The maximal electron density in a cathode spot fragment is higher than $3 \times 10^{26} \text{ m}^{-3}$, similarly to the plasma channel density in experiments with low dc voltage in air [8]. A momentary arc current for this "frozen" absorption image, was determined from the oscillograms to be 10 A. During 18 ns the spot plasma expanded up to distance of $50 \mu\text{m}$. Small fragments separated from each other connect the boundary of a diffuse plasma in front of the cathode and the cathode surface. They look like a narrow bridge and can clearly be seen in this frame.

ABOUT TEMPERATURE OF CATHODE SPOT PLASMAS

Streak camera recording of the radiation from cathode spot plasma [7] had shown, that in visual spectral range the most intensive emission lasts only 30-40 ns and originates from the small local region of $30 \mu\text{m}$. It indicates a nonstationary character of cathode spot operation. Due to high local power concentration at the cathode surface an explosive evaporation of thin layer of cathode material occurs on the time scale smaller than 1 ns [9]. Therewith an internal energy input per mass unit exceeds value of $W_0 = 8 \text{ kJ/g}$. In result of rapid energy input in small volume on electrode surface high dense microplasma immediately forms and expands into vacuum with following velocity

250-330 ps and temperature above 100 eV, as well as a radiation related to an expanding hot layer, which propagates from cathode surface with a velocity of 1.5 km/s to 5 km/s. From picosecond momentary absorption photography [5] with high spatial ($0.5 \mu\text{m}$) and temporal resolution (100 ps) we evaluated the spatial-temporal density distribution in cathode spot fragments. An absolute density value $> 5 \cdot 10^{26} \text{ m}^{-3}$ in narrow plasma channels with diameter smaller than $5 \mu\text{m}$ was estimated.

ELECTRON DENSITY IN CATHODE SPOT FRAGMENTS

Cathode spots of pulsed and dc discharges were investigated also by laser absorption photography [5]. The cathode consisted of a needle with $300 \mu\text{m}$ diameter, the anode had a large area with a central hole through which

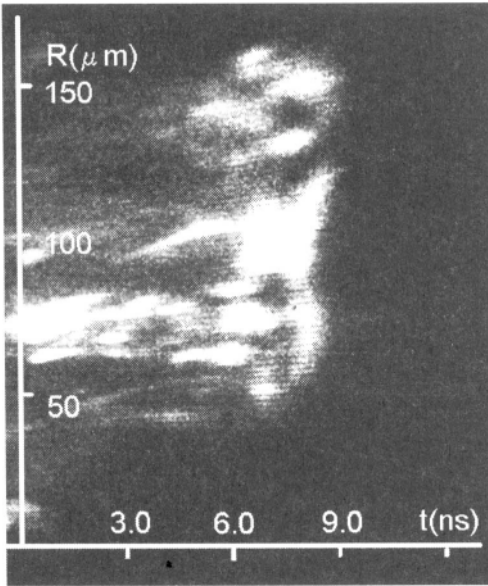


Figure 2: Streak image of x-ray radiation from the laser-induced discharge for delay time $t = 9.63$ ns after ignition by IR laser beam. Discharge voltage $U = 1.7$ kV, current $I = 34$ A.

Obviously, in order to determine the cathode spot fragment temperature in ignition phase the radiation detection in a soft and hard x-ray spectral range with high temporal and spatial resolution is urgent necessary.

X-ray radiation in low-voltage vacuum arcs

Recently, computer simulations on laser-induced low-voltage breakdown (240 V) have shown, that a soft x-ray radiation in result of an overheating instability can be generated in cathode spot plasma [5, 14-15]. For short time of 100 ps the plasma temperature may increase up to some hundreds of eV, as well as in a case of a plasma erosion interruption in small gaps, where the electric potential abruptly raises in some local region of cathode torch to values of some kV or MV [15], the plasma temperature can growth to some keV. Now we demonstrate the first time an experimental results on x-ray radiation from low-voltage vacuum spark.

Time-resolved x-ray emission from cathode spot of pulsed discharges in vacuum was investigated by x-ray streak camera FRF-4 [13]. The cathode consisted of a solid plane target 1 cm growth, the anode had a row form with a central hole through which a laser pulse was directed onto the cathode surface for spot ignition. The cathode and anode material was copper. The arc spots were ignited at the cathode surface by focusing a IR - laser beam of 100 ps duration through a small hole (350 μm diameter) in the anode. The discharges were fed by a 50 Ohm coaxial cable charged up to 150 V, 240 V, 1.7 kV, 2.7 kV.

The radiation from small electrode gap was registered by x-ray streak camera with Au photocathode, which is sensitive in spectral range of order of 0.1 -10 keV. The synchronization of streak camera recording with a discharge initiation was realized by optical signal from a second harmonic radiation of laser pulse and was delayed relative to an ignition

$$V_f = \left(\frac{4\gamma}{\gamma-1} W_0 \right)^{1/2} = 1.4 \cdot 10^6 \text{ (cm/s)}$$

where the ratio of specific heats for plasma γ is of order of 1.2-1.3.

According with [10] the temperature of shock wave front propagating with this velocity can be determined as follows:

$$T_f = 375 \cdot 10^{-8} V_f^2 = 7 \cdot 10^4 \text{ K} \approx 16.5 \text{ eV}$$

Taking into account that the most probable radiation in front of shock wave can be emitted at $\lambda = \frac{hc}{3kT_f} \approx 70 \text{ nm}$ it becomes

clearer why in the streak recording traces in visual spectral range we estimate a dark interval of light emission of order of 30-50 ns. With mentioned above streak camera we can record the radiation from the cathode spot in spectral range of 400-700 nm But at ignition of spot fragment the front temperature can exceed the value of 100 eV.

pulse from - 3 ns with a sweep speed of 3 ns/ screen to 5.7 ns; 9.63 ns; 16.49 ns with a 30 ns/screen sweep speed.

Fig. 2 represents a streak record for the delay time $t = 9.63$ ns after initiation of laser-induced discharge with voltage $U = 1.7$ kV between Cu-electrodes with small gap distance $l = 50 \mu\text{m}$. As it is evident from Fig. 2 two kinds of x-ray radiation on streak images are formed. The first one is a straight line from point-like source with a lifetime of order 250 - 330 ps and size of 3-5 μm . Some similar sources can exist simultaneously and give a traces in form of the straight lines separated from each other in vertical (space on streak record) directions. In addition another kind of traces from x-ray radiation with an linear deflection in vertical direction was estimated. It means that the x-ray source moves relative to streak camera slit with a velocity V corresponding to a ratio of trace deflection from horizontal line (Δr) to time interval Δt - length needed for displacement to this distance ($V = \Delta r/\Delta t$). We receive the velocity of order of $3.7 \cdot 10^5$ cm/s and lifetime of 2.5 ns.

CONCLUSIONS

The theoretical effort that parallels the experimental one has uncovered recently [5, 11-12] many interesting effects of cathode spot plasma: (i) focusing and defocusing of electrical current in dense cathode plasma, which are caused by rapidly changes of electrical conductivity due to phase transition from the metal to a non-ideal plasma with dielectric properties; (ii) generation of "shooting solitons" - non-stationary plasma emissive centers, formed at the moving boundary of the expanding cathode spot plasma with current density of order of 10^6 - 10^{12} A/cm²; (iii) development of an overheating instability and exitation of an intensive heating waves propagating back to the cathode surface. According with these latest results a new mechanism for cathode spot self-sustaining have been proposed. The experimental investigations presented in this paper are in good agreement with this theoretical modelling.

ACKNOWLEDGEMENT

This work was supported by the Deutsche Forschungsgemeinschaft (Vo 527/1-2) and Deutsche Akademie der Naturforscher LEOPOLDINA.

REFERENCES

1. G. Kesaev, Cathode Processes of Electric Arc (Russia, Nauka, 1968)
2. A. Anders et al., IEEE Trans. Plasma Sci., **20**, 466, (1992).
3. B. Jüttner, J. Phys. D: Appl. Phys., **28**, 516, (1995).
4. V. F. Puchkarev and M. B. Bochkarev, J. Phys. D: Appl. Phys., **27**, 1214, (1994).
5. N. Vogel and V. Skvortsov, IEEE Trans. Plasma Sci., (1997)(to be published)
6. N. Vogel and B. Jüttner, J. Phys. D: Appl. Phys., **24**, 922, (1991).
7. N. Vogel, J. Phys. D: Appl. Phys., **26**, 1655, (1993).
8. N. Vogel, J. Heinzinger, F. Cichos, IEEE Trans. Plasma Sci., **23**, 926, (1995).
9. G. A. Mesyats, IEEE Trans. Plasma Sci., **23**, 879, (1995).
10. J. B. Zeldovich and Ju. P. Reizer, Fizika udarnich voln i visokotemp. gidrodin. javlenii, Moscow, Nauka, 1966 (in russian).
11. V. A. Skvortsov and N. Vogel, Physics of Strongly Coupled Plasmas, Ed. W. D. Kraeft and M. Schlanges, Word Scientific, 1996, p.343
12. V. A. Skvortsov and N. Vogel, Proc. 11th Int. Conf. on High Power Particle, BEAMS'96, Prague, 1996, vol. I, p.513
13. S. I. Petrov, V. P. Lazarchuk, V. M. Murugov, A. V. Senik, Proc. 22nd Int. Congress on High-Speed Photography and Photonics, Santa Fe, New Mexico, 27 Oct.-1 Nov., 1996

COMPARISON OF COLLISIONAL AND RADIATIVE PLASMA KINETICS MODEL (CRM) AND AVERAGE ION MODEL (AIM) IN DENSE PLASMA.

P.D.Gasparian, S.A.Belkov, Yu.K.Kochubey, E.T.Mitrofanov, V.I.Roslov

Russian Federal Nuclear Centre - Institute of Experimental Physics,
607190, Sarov, Prospect Mira 37, Nizhny Novgorod Region, Russia.

INTRODUCTION

In many plasma applications there are necessity to describe the complicated plasma flows when the plasma conditions change in a wide range of the parameters: highly ionized heavy elements ($Z > 10$), $T_e \sim 10$ eV...several keV, $N_e \sim 10^{19} \dots 10^{24} \text{ cm}^{-3}$, $\rho \sim 0.001 \dots \rho_{\text{solid}} \text{ g/cm}^3$. In order to study properties of systems under these conditions theoretically and experimentally, atomic physics and gas dynamical codes are being developed based upon the theories of: non-equilibrium population kinetics, radiation transport, radiative gas dynamics etc.

Calculations of radiative emissivity of multicharge non-equilibrium strongly coupled plasma are associated with two problems:

- first, there is no reliable theory of d-d radiation transfer in strongly coupled non-equilibrium plasma. Chemical CRMs are not applicable for describing strongly coupled states near continuous spectrum of ions;
- second, even providing chemical CRMs are applicable, a huge number of states and lines in large-Z-plasma makes the problem of calculating radiative characteristics of such plasma super-labor-consuming in terms of calculation effort.

Approximate solution of these problems is given by Slator's AIM, based on AIM approximation, hydrogen-like SIM and model consideration of strongly coupled plasma. The main goal of this work is to study the dielectron recombination description accuracy in the AIM approximation. These issues are important for creation of economical codes for solution of non-equilibrium gas-dynamical equations using AIM in a multidimensional case.

SLATOR'S HYDROGEN-LIKE MODEL OF MULTICHARGE IONS

Let P_n be whole shell occupation numbers of an ion with the main quantum number n . Ion's state is given by ionic configuration $\{i\} = \{P_1 P_2 \dots\}$. Basic correlation's of hydrogen-like Slater's ion model (SIM) are:

$$U_i = \sum q_n^2 E_n P_n, \quad E_n = -\frac{Ry}{n^2}, \quad q_n = Z - \sum \sigma_{mn} P_m \quad (1)$$

Here: U_i is the total energy of the state; σ_{mn} is screening constants matrix ($m \leq n$); $\epsilon_n^0 = \partial U / \partial P_n$ is ionization potential from the shell n ; q_n is screened charge of a nucleus for n -shell.

Screening constants matrix σ_{mn} was optimized by More¹. One can believe that (1) gives approximate analytical solution of ion structure calculation problem. In the case of zero screening constants matrix $\sigma_{mn} = 0$ we have Bohr's ion model (BIM) in which ion energy linearly depends upon occupation numbers, and ionization potentials of ions from the shell i do not depend on occupation numbers. For BIM was shown² the strict derivation of the kinetic equations of AIM from the RCM. For non-isolated ions in dense plasma, the effect of ion's surroundings upon energy structure takes place as a level shift that is considered for by reduction of ionization potentials. In the ionic sphere model (strongly coupled plasma) level shift of localized electrons is: $\epsilon_n^0 \approx 1.2 R y \cdot Z_c / R_0$, where Z_c is average ion charge, R_0 is average radius of a cell.

In order to describe cross-sections and rates of collisional and radiative processes in SIM and SAIM of multicharge plasma we used quasiclassical expressions of Kramers, Lotz, Regemorter and Tuger-Gould (for ionization, recombination and Auger effect) with oscillator forces correction in order to consider for screening given by More in the paper³.

Dielectron recombination.

One of the reasons for relative success of AIM approximation for averaged description of local plasma kinetics, described by detailed CRMs, is preservation, within AIM approximation, of particles conservation law in reactions between discrete states with single-electron transitions. In autoionization and dielectron recombination reactions (direct and reversed Auger effect) no such conservation law exists. Due to this fact, when they are important for kinetics of strongly non-equilibrium processes, AIM approximation considerably loses its accuracy. In these cases strong dynamic correlation's appear in the system, unsatisfactorily described by AIM.

Let P_{n_1, n_2} be relative concentration of $[n_1, n_2, \dots]$ configurations with n_i bound electrons at the level i , normalized by the number of nuclei in a unit volume: $\sum_{\{i\}} P_{n_1, \dots} = 1$. In the case of configurations consisting of two shells, degeneration degree (statistical weight) of a configuration is $G_{n_1, n_2} = C_{g_1}^{n_1} * C_{g_2}^{n_2}$, where $C_{g_i}^{n_i}$ the number of combinations from g_i by n_i . Let's consider coronal equilibrium limit in Bohr's CRM: $n_e \rightarrow 0$. Solution of steady-state equations in the perturbation theory PT for n_e shows that in zero order ground states (GS) of ions are non-zero: $P_{0n_1}, P_{g_1 n_2}$. Concentrations of excited states (ES), connected with GS by a single-excitation line and any number of decays, are proportional to n_e , twice-excited lines - to- $(n_e)^2$ etc. If ES are not considered P_{n_1, n_2} distribution inside one shell is still binomial, and the single-step GS ionization process is nearly linear. Consideration of radiative (A_{ij}) and Auger (W_{ij}) transitions makes GS ionization kinetics process a non-linear and multistep one. Due to transitions through ES in multilevel CRM, transitions appear between GS connected by a line with decaying ES (cascade transitions). Particularly simple is the case of two-level CRM with preferential occupation of one shell: $f_2 \ll 1$ (at $W_{ij} = 0$ as well). In this case transitions between GS induced by radiative transitions through ES are small perturbations $\sim R_2 / R_1 \ll 1$ (the feature of photo recombination rate at level i R_i) and distribution of P_{0n_1} is close to binomial.

In the case of coronal equilibrium correlator perturbations are zero-order values with respect to n_e . In the case of two-level CRM it is easy to show that, in zero order $(n_1^k n_2)_0 = g_1^k n_2$. However, in a special case, if $R_2 / R_1 \ll 1, I_2 / R_2 \ll 1$ (here I is an ionization rate) and

if $f_2 \ll 1$, when binomial distribution “works”, they yield the average occupation numbers \bar{n}_1 and \bar{n}_2 close to exact values and the number of spontaneous decay acts, despite absolute violation of “statistical” independence of P_{n,n_2} . Consideration of Auger processes even in this case does not permit to describe \bar{n}_1 and \bar{n}_2 satisfactorily by the usual kinetic equations, since cascade processes start playing the important role, which strongly changes correlators in coronal equilibrium limit (up to changing their signs). Due to this reason, AIM approximation, based on correlator uncoupling, is not correct for describing the effect of dielectron recombination upon average plasma characteristics.

In order to study possibility of using the AIM approximation and to evaluate its accuracy for description of Auger processes, we developed a program for calculation of kinetics equations for SCRM, calculations with which can be a “reference” for evaluating AIM approximation accuracy. Ions’ characteristics were calculated using (1). Comparison of basic plasma parameters in coronal limit: average charge (Z_0) and emissivity (J_{tot}) in a wide range of conditions for electronic temperature, density and compositions of plasma has shown that approximation of Slator’s AIM and Slator’s CRM without consideration of Auger processes are in rather good agreement with each other in these parameters - with an accuracy better than $\sim 10\text{--}20\%$ for J_{tot} and $\leq 5\%$ for Z_0 . If Auger processes are considered using average CRM equations the accuracy of these parameters is steeply deteriorated up to ten times for J_{tot} . For multicharge plasma ($Z \gg 10$) this is due to strong role of cascade processes with radiative excitation decay channel, efficiently reducing autoionization processes. Qualitative considerations concerning effective account of cascade processes for AIM are given in the paper of More et al.⁴. In this paper it is suggested to consider for the main channel of cascade process, reducing dielectron recombination rate due to radiative decay to ground states of ions by branching factor:

$$K_{n,l,m} = \frac{A_{nm}}{(1 + \alpha * p_n + \beta * p_m)W_{n,l,m} + A_{nm}}; \quad (2)$$

where A_{nm} is spontaneous decay rate ($n > m$), $W_{n,l,m}$ is Auger process rate ($l > n$), α , β are fitting parameters. Taking into account approximate character of such approximation, in AM approximation we simplified this approach to some extent, preserving AIM equations with reduction of Auger process rate by a factor (2). In this case reversed Auger process rates are preserved, that ensure LTE in equilibrium plasma. This way of consideration for Auger processes considerably improves the initial AIM approximation, “justified” for Bohr’s CRM in the case of weak discrepancy with LTE.

AIM APPROXIMATION IN THE NON-LTE CASE, SOME NUMERICAL CALCULATION RESULTS

AIM approximation and Slator’s AIM of non-equilibrium multicharge plasma kinetics allow quick and easy qualitative evaluation of different effects’ influence in radiative gas dynamics and kinetics of complex systems: - influence of constant values accuracy upon kinetics, of number of levels upon time-progress of processes, role of plasma coupling, relative role of different processes upon emissivity, value of static and dynamic correlation’s, etc. At the same time evaluation of absolute accuracy of the model itself needs comparison to calculations that can be considered as a reference. At present, non-equilibrium theory of weakly coupled plasma is developed rather strictly and is confirmed by agreement with experiments of super-non-equilibrium systems like, for instance, laboratory X-ray lasers. Concerning strongly coupled plasma, things are more complicated, but here also agreement between experiments and theory is rather satisfactory (for instance, in ICF target spectroscopy). The most complete description of weakly coupled plasma kinetics requires

development of complete data bases and weakly coupled plasma kinetics CRM and their implementation in numerical codes. We performed comparison of SAIM calculations to reference calculations with CC-9 code, in which Data Bases are implemented for not very complex ions with average Z ($Z \sim 20 \dots 30$) in applicability area of the reference calculations. Under conditions when complex ions are present in plasma we took as a reference the calculations with Slater's hydrogen-like CRM described above.

Coronal plasma emissivity calculations.

Comparative calculation results for average ionization degree and emissivity of Au plasmas in LTE and coronal equilibrium using SAIM and SCRm codes, with and without Auger processes considered are given in the Tables 1-3. These calculations show high accuracy of AIM approximation in cases of kinetic coefficients close to real values for multicharge plasma.

Table 1. The ratio of averages Au plasma ionization degree calculated due to SAIM and SCRm for different temperatures and densities with Auger process.

T_e	$\beta = \rho \langle Z \rangle / A$			
	5.00E-04	5.00E-03	5.00E-02	5.00E-01
1.50E-01	1.02E+00	1.01E+00	1.03E+00	1.06E+00
2.00E-01	1.02E+00	1.01E+00	1.02E+00	1.07E+00
2.50E-01	1.02E+00	1.02E+00	1.02E+00	1.07E+00
3.00E-01	1.02E+00	1.02E+00	1.02E+00	1.06E+00
4.00E-01	1.00E+00	1.02E+00	1.02E+00	1.04E+00
5.00E-01	9.83E-01	1.01E+00	1.01E+00	1.02E+00
7.50E-01	9.43E-01	9.93E-01	9.79E-01	9.79E-01
1.00E+00	9.20E-01	9.66E-01	9.64E-01	9.65E-01
1.50E+00	9.21E-01	9.45E-01	9.70E-01	9.76E-01
2.00E+00	9.54E-01	9.66E-01	1.19E+00	9.89E-01
2.50E+00	9.77E-01	9.83E-01	1.00E+00	9.99E-01
5.00E+00	1.00E+00	1.01E+00	1.04E+00	1.02E+00

Table 2. The ratio of Au plasma emissivities calculated due to SAIM and SCRm for different temperatures and densities with Auger process.

T_e	$\beta = \rho \langle Z \rangle / A$			
	5.00E-04	5.00E-03	5.00E-02	5.00E-01
1.50E-01	9.76E-01	1.21E+00	2.00E+00	4.03E+00
2.00E-01	9.32E-01	1.14E+00	1.73E+00	3.39E+00
2.50E-01	9.12E-01	1.08E+00	1.57E+00	3.00E+00
3.00E-01	9.08E-01	9.51E-01	1.47E+00	2.71E+00
4.00E-01	9.27E-01	1.00E+00	1.34E+00	2.40E+00
5.00E-01	9.73E-01	1.01E+00	1.33E+00	2.39E+00
7.50E-01	1.15E+00	1.13E+00	1.62E+00	3.04E+00
1.00E+00	1.44E+00	1.45E+00	2.19E+00	2.76E+00
1.50E+00	2.38E+00	2.24E+00	1.97E+00	1.86E+00
2.00E+00	1.73E+00	1.70E+00	1.51E+00	1.57E+00
2.50E+00	1.42E+00	1.33E+00	1.32E+00	1.42E+00
5.00E+00	9.89E-01	9.95E-01	9.82E-01	1.11E+00

Table 3. The ratio of Au plasma emissivities calculated due to SAIM for different temperatures and densities with and without Auger process.

T _e	$\beta = \rho \langle Z \rangle / A$			
	5.00E-04	5.00E-03	5.00E-02	5.00E-01
1.50E-01	2.20E+00	1.59E+00	1.09E+00	1.00E+00
2.00E-01	2.42E+00	1.66E+00	1.14E+00	1.00E+00
2.50E-01	2.67E+00	1.69E+00	1.19E+00	1.01E+00
3.00E-01	2.34E+00	1.60E+00	1.23E+00	1.03E+00
4.00E-01	3.13E+00	1.87E+00	1.30E+00	1.12E+00
5.00E-01	3.40E+00	2.13E+00	1.45E+00	1.27E+00
7.50E-01	3.48E+00	2.52E+00	1.78E+00	1.56E+00
1.00E+00	2.89E+00	2.38E+00	1.92E+00	1.56E+00
1.50E+00	2.36E+00	2.17E+00	1.90E+00	1.58E+00
2.00E+00	2.25E+00	2.23E+00	1.96E+00	1.62E+00
2.50E+00	2.55E+00	2.38E+00	2.18E+00	1.74E+00
5.00E+00	3.98E+00	3.94E+00	3.30E+00	2.09E+00

CONCLUSION

Estimation of accuracy of SIM approximation for model systems (Bohr's and Slatov's CRMs) has shown that in a number of cases SAIM, regarded as an approximation of "exact" CRM, can satisfactorily (with precision up to two times) represent the effect of "dynamic" correlations upon plasma radiation spectrum in conditions of strong non-LTE, including consideration of Auger processes in a wide range of densities, temperatures and compositions of multicharge plasma.

Solution of a number of stationary problems in local and non-local cases using SAIM and more precise calculations with detailed CRM for weakly coupled plasma, where CRM-calculations are reference calculations, has shown that SAIM can describe with sufficient accuracy "averaged" plasma characteristics both in states, close to LTE and coronal equilibrium states, rather far from LTE.

Non-equilibrium generalization of SAM is, at present time, apparently, the only model for universal description of kinetics of strongly coupled non-equilibrium plasma. The largest inaccuracy of SAM is associated with description of Auger processes and d-d radiation transfer in cases of weak line-overlapping. One can expect that in conditions of strong line-overlapping accuracy of SAM will increase.

ACKNOWLEDGEMENTS

The authors are grateful to Prof. A. N. Starostin for fruitful discussion of non-equilibrium kinetics of coupled plasma and permanent interest to this problem.

The work has been done with partial support from ISTC Project #76.

REFERENCES

1. R.More, Radiative properties of hot dense matter, *J.Q.S.R.T. Special issue*, 27:345 (1982).
2. S.A.Belkov, P.D.Gasparian, G.V.Dolgolyova, Yu.K.Kochubey, Comparison of radiative collisional model of plasma kinetics and average ion model in the non-local case, "International Conference Radiative Properties of Hot Dense Matter", Santa-Barbara, November 4 - 7, 1996, *Special issue J.Q.R.S.T.*, to be published (1997).
3. R.More, Plasma processes in non-ideal plasmas, *Preprint UCRL 94360* (1986).
4. R.M.More, G.B.Zimmerman, and Z.Zinamon, Dielectronic recombination in the average-atom model. AIP Conf. Proceeding, #16, "6th Conf. on Atomic Processes in High-temperature Plasmas", Santa Fe, , A.Hauer and A.Merts ed., (1987).

This page intentionally left blank

SELF-ORGANIZATION PHENOMENA IN DENSE PLASMA FOCUS EXPERIMENTS

A.B. Kukushkin, V.A. Rantsev-Kartinov, A.R. Terentiev

Institute for Nuclear Fusion, RRC "Kurchatov Institute",
123182 Moscow, Russia

INTRODUCTION

The formation of a linear dense Z-pinch as an essentially axis-symmetric 2D structure was the major goal of experimental research programs on Dense Z-Pinches, both in cylindrical geometry and non-cylindrical one, like e.g. plasma foci. Here, all the deviations from axial symmetry were considered as a serious threat to concentrating the energy. However, a lot of data is accumulated that exhibit importance of the essentially 3D behavior of the plasma and magnetic field in the case of successful enough driving the load in high-current discharges. In particular, formation of a closed, spheromak-like magnetic configuration, of several cm size, in Filippov-type plasma focus gaseous discharges takes place thanks to (i) strong filamentation of helical electric currents and (ii) enhanced propagation rate of magnetic field (and current sheath) along the anode, due to Hall effect in plasmas (see Ref. [1]). So, the question does exist: to what extent does the 3-D 2-fluid MHD govern the high-current discharges?

Here, we present a number of experimental results which have been accumulated in earlier studies carried out at the Filippov-type plasma focus facility.² Such a presentation is focused at illustrating the coexistence and interaction of complicated structures, both disordered and ordered ones, of various space scale, in plasma focus gaseous discharges at conditions typical for the high current discharges.

SELF-FORMATION AND SELF-COMPRESSION OF A CLOSED, SPHEROMAK-LIKE MAGNETIC CONFIGURATION

The model [3] and the analysis of experimental results obtained from earlier experiments in various high-current gaseous discharges has allowed the identification of the following characteristics of the spheromak-like magnetic configuration (SLMC) formation¹: (1) The self-consistent generation of a poloidal magnetic field (the dynamo effect), solely by the internal dynamics of the magnetic field in the discharge. (2) Strong filamentation of electric currents, which occurs both in the inner region of the SLMC (i.e. in the combined Z- ϑ -pinch) and in its periphery. (3) SLMC formation is stimulated by the enhanced propagation rate of the magnetic field along the anode, due to the Hall effect in plasmas. (4) A magnetic field reconnection process leading to the formation of the SLMC as a closed configuration, appears to occur before the current sheath converges on the axis. (5) In its

final stage, the SLMC takes the form of a squeezed spheromak configuration, confined and driven by the pressure of the residual magnetic field of the plasma focus discharge. (6) Large space scale (vs. "hot spot") determined by the geometry (and capacitance) of the facility. (7) The power density in the combined Z- θ -pinch at the major axis exceeds the peak power density of a force-free flux-conserver-confined spheromak by several orders of magnitude. (8) The SLMC exhibits a cyclical, evolutionary tendency to form, be compressed and eventually repelled away from the anode, and reform repeatedly. (9) Self-organization of the discharge plasma (non-monotonic dependence of input vs. output parameters; "quantization" of the discharge energy).

A great deal of experimental data obtained in earlier neon gas studies carried out at the Filippov-type plasma focus facility² supports the SLMC model.³ Some of the results presented here and in Ref.[1] have not been previously published, as they were not fully understood before. Significantly, the identification of the SLMC formation appears to be available essentially from *combining* the results of the following diagnostics with different (and complementary to each other) spatial and spectroscopic scales: namely, (i) motion picture of the evolution of SLMC formation, taken with the help of a ruby-laser-based interferometer operating in the Bates regime (0.01-J laser pulse energy; 2-ns duration); (ii) visible light photographs taken with the help of an electronic optical converter which is synchronized with the current to an accuracy of <50 ns; (iii) time-integrated SXR spectra from a pinhole camera.

The results are presented for the following discharge conditions: mushroom-shaped anode (11-cm diam.) inside a coaxial metallic chamber 80-cm long and 30-cm high, which acts as the cathode; capacitance, 180 μ F; initial inductance, 55 nG; initial voltage, 16 kV; discharge energy, 20 kJ; maximum current, 530 kA; neon gas pressure, 3 Torr. Time zero ($t=0$) corresponds to the major peak of the time derivative of the current.

SHORT-SCALE MIXING OF THE PLASMA AND MAGNETIC FIELD

The Hall effect in plasmas,⁴ which is caused by the frozenness of the magnetic field into electron plasma and by the resulting transfer of magnetic field with electric current velocity, manifests itself in the enhanced rate, as compared with ordinary diffusion, of magnetic field propagation in plasmas in the case of electric current moving along the gradient of plasma density. The major physical mechanism is the "scattering" of magnetic field, which is transferred by the electric current, at positive gradient of electron density. Such a phenomenon is identified in full in the case of steep electron density gradients at plasma-conductor boundaries. For instance, the current sheath slipping along the anode at initial stage of the discharge in plasma focus facility² has been reproduced in the 2-D 2-fluid numerical modelling⁵ with allowing for the Hall term (see also the database presented in Ref.[1]). Contrary to ideal MHD instabilities, this mechanism gives regular, highly reproducible dynamics that agrees quite well with numerous experimental data. Similar phenomena may take place in plasma interior as well. Here, the enhanced propagation rate leads to penetrating the domain of the lower plasma density and subsequent superseding the plasma by the magnetic field. Such a mechanism leads to a stochastic short-scale (as compared with space scales of the current sheath) mixing of the plasma and magnetic field, being thus an alternate for the snow plough regime of current sheath formation and driving.

The pictures shown in Fig.1 ($t= -90$ ns) and Fig.2 ($t= +174$ ns), for deuterium gaseous discharge of initial pressure 163 Torr, are the shadowgrams taken with the help of a ruby laser (0.01-J laser pulse energy; 15-ns duration; pulse direction perpendicular to the system axis). The anode is at the bottom of the diagnostic window (4 cm diam.), the plasma focus major axis coincides with the vertical axis of the window.

A great deal of experimental database exhibit cell-like structure of the plasma. Such a phenomenon may be interpreted as the formation of a thin volumetric (three-dimensional)

net-like structure of the magnetic field penetrating the plasma. The local values of magnetic field inside this net may substantially exceed its values averaged over several cells, up to the order of magnitude. Therefore this mechanism of plasma-magnetic field interaction doesn't need large spatially averaged values of the parameter $\omega_e \tau_{ei}$, thus suggesting that the criterion for the onset of the 2-fluid effects may be strongly dependent on the local values of density fluctuation level of the appropriate space scale. Such a 2-fluid instability being developed in a certain small volume, can propagate in space and interact with conventional ideal-MHD instabilities, e.g. via triggering the current sheath breakthrough by the Rayleigh-Taylor instability.

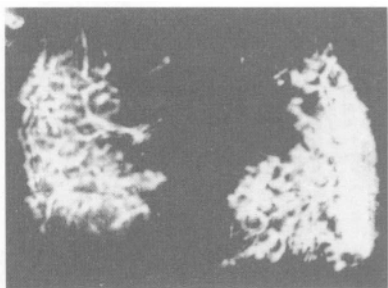


Figure 1

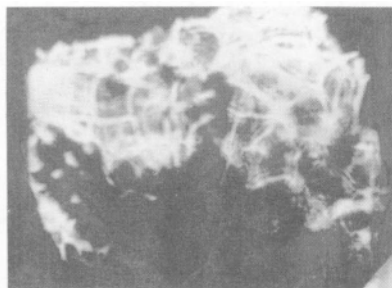


Figure 2

FILAMENTS AND MAGNETIC FLUX ROPES

The complexity of short-scale structure of the magnetic field penetrating the plasma, leads to existence of a rich background for short-scale self-organization processes. This results in forming the strongly inhomogeneous plasma structures, with the filaments of electric current and the magnetic flux tubes (magnetic flux ropes, according to the space plasma language, see e.g. Ref.[6]) being the building blocks of these structures. The filaments are characterised by the enhanced plasma density, due to pinching effect, whereas magnetic flux ropes exhibit substantially lower plasma density, with force free-like configuration of magnetic field. It is combination of these two substructures, under condition of appreciable helicity, that supports long-range, essentially three-dimensional correlations of electric currents and magnetic field.

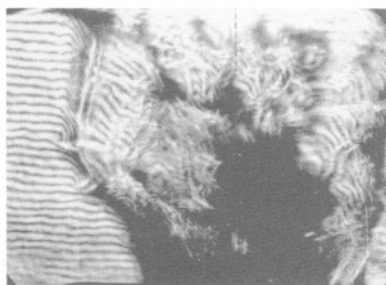


Figure 3.

magnetic configuration of several cm size.¹ Here, filamentation of electric currents is needed for the production of the poloidal magnetic field and the respective 3D large-scale ordering of both the plasma incorporated in a closed configuration and the plasma carrying the current of external circuit. Figure 3 (interferogram, Bates scheme, ruby laser, 2ns pulse duration)

The filamentation of electric current is well known to characterize plasma behavior at initial stage of gaseous discharges. Being driven by the inflated magnetic field toward system's axis, the filaments may form a quasi-uniform current sheath of a cylindrical/linear Z-pinch. However, this may not be the case when filamented structures form essentially 3D plasma structure as it happens, in particular, in a certain type of plasma focus discharge resulted in the formation of a closed, spheromak-like

shows fine structure of the filamented inner, closed magnetic configuration and the current sheath formed by the residual magnetic field (D_2 , 6 Torr, 24 kV, -150 ns; system's axis is indicated, - space scale the same as in Figs. 1,2). The interferogram of Fig. 4 (negative; 20 ns; discharge type similar to that of Fig.3) illustrates the braidedness of the twisted filaments.

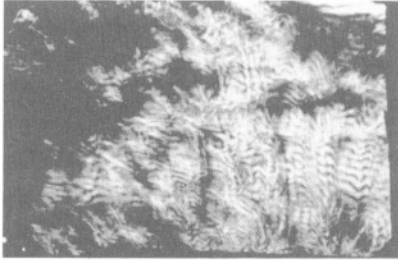


Figure 4

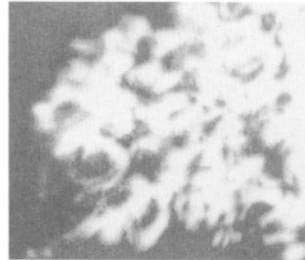


Figure 5

Interaction of filaments and magnetic field lines, via twisting, winding and interweaving, leads to formation of the heterogeneous force free-like magnetic configurations. Such a structure may form a heterogeneous magnetic flux rope. Separate section of the (teared to pieces) rope forms a stick-like, heterogeneous plasma formation embedded into a closed, spheromak-like magnetic configuration. Typical formation of this type is shown in Fig. 5 (see left upper part of the Figure) which is extracted from the right lower part of Fig. 1.

CONCLUSIONS

Experimental results presented illustrate complexity of plasma and magnetic field behavior in high-current discharges. It follows that the 2-fluid effects (the Hall effect in plasmas) may produce more intense (short-scale) mixing of the plasma and magnetic field, as compared with that predicted by the ideal MHD. This, in turn, leads to formation of essentially 3D structures of space scale of the above mixing. Interaction of these processes with electric current filamentation leads to long-range 3D correlations and strong local self-organization. The latter results in formation of closed, strongly inhomogeneous magnetic configurations of various space scale, up to several cm size formations reported in Ref.[1].

The results suggest the necessity to allow for the effects of the 3-D 2-fluid MHD in numerical modelling of plasma radiation sources.

REFERENCES

1. B. Kukushkin, V. A. Rantsev-Kartinov, and A. R. Terentiev, *Fusion Technology*, 32:83 (1997); *Preprint of the RRC "Kurchatov Institute"*, IAE 5737/7, Moscow, January 1994; *Transactions of Fusion Technology* 27:325 (1995).
2. M. Orlov, A. R. Terentiev, and V. A. Khrabrov, *Fizika Plazmy (Sov. J. Plasma Phys.)*, 11:1268,1517 (1985).
3. B. Kukushkin and V. A. Rantsev-Kartinov, *Preprint of the RRC "Kurchatov Institute"*, IAE 5646/6, Moscow, June (1993).
4. I. Morozov and A. P. Shubin, *Zh.Eksp.Teor.Fiz. (Sov.Phys.JETP)* 46:710 (1964).
5. V. Vikhrev, O. Z. Zabaidullin, and A. R. Terentiev, *Plasma Phys. Reports*, 21:20 (1995). *Physics of Magnetic Flux Ropes*, Geophysical Monograph 58 (Eds. C.T.Russel, E.R.Priest, and L.C.Lee), Am. Geophys. Union (1990).

THEORY OF THERMOELECTRIC FIELD IN LTE PLASMAS

V.P.Krainov,¹ V.A. Rantsev-Kartinov,² and E.E.Trofimovich,³

¹Physical Technical Institute, Dolgoprudnyi, Moscow region, 141700, Russia;

²INF RRC "Kurchatov Institute", Moscow, 123182, Russia;

³International University for Nature, Society and Man of the Dubna, Universitetskaya 19, Dubna, Moscow region, 141980 Russia

INTRODUCTION

The problems of calculating the electric field and revealing the mechanism of its formation in a non-equilibrium inhomogeneous plasmas has been widely studied. Here, we restrict ourselves to investigating the case of a quasi-stationary plasma in local thermodynamic equilibrium (LTE). At a quasi-stationary stage of gas discharges in laboratory plasmas the LTE may be sustained by, e.g., strong external magnetic field, and the electron and ion temperatures are inhomogeneous and different.

The electric field can be explained using balance equations. In this approach the electric field is necessary to explain ambipolar diffusion. Calculation of the electric field is very complicated due to difficulties in correct determination of particle flows because of anomalous character of diffusion.

In the present work we use microscopic approach for calculating the electric field, which is based on the generalization of the results.^{1,2} It is shown that the electric field has a thermoelectric origin connected with different screening of particles of inhomogeneous plasmas. Thus the inhomogeneity and deviation from equilibrium play a key role for the screening of the potential, because in a homogeneous and equilibrium plasma the potential is obviously constant and is not connected to the screening. Dynamic character of screening is important because zero value of potential, irrespectively to local deviation from equilibrium, is obtained in the model of static Debye screening, due to quasineutrality condition. The electric field space distribution is explained by competition between the electron and ion contributions.

STATEMENT OF THE PROBLEM AND THE MODEL

We shall consider a completely ionized, two component plasma consisting of ions, of charge $Z_i e$, and electrons. We assume that time and space dependencies of plasma parameters are adiabatically flat. Characteristic space scale L of plasma inhomogeneity is assumed to be large in comparison with electron Debye radius a_e , i.e. $\lambda = L/a_e \gg 1$. For

typical main sequence of stars one has $\lambda \geq 10^2$, and for laboratory plasmas one has $\lambda \sim 10^4 + 10^6$. The condition of quasistationarity means that the rates of processes are determined by ion motion which results in slow change of electrical potential, and electron distribution follows it adiabatically. In this case the plasma can be considered as a quasi-neutral medium.³ However, this does not mean that there is no macroscopic electric field in plasma. This implies only the smallness of uncompensated charge density in comparison with separate electron and ion charge density perturbations. Charge density perturbations are just charge densities in an inhomogeneous plasma. Note that the potential of the electric field can be found from the Poisson equation if uncompensated charge density is known. However, it is a nonmeasurable quantity; and there are no reasons to put it precisely equal to zero. As it will be seen from further calculations of the potential, we have $\phi \sim T_e / \theta$ (T_e is electron temperature), and then $|(Z_i n_i - n_e) / n_e| \sim \lambda^{-2} \ll 1$, when n_i and n_e are ion and electron density. Thus, nonzero macroscopic electric field in a plasma does not contradict to its quasi-neutrality. In contrast, we shall use the quasi-neutrality condition $Z_i n_i \cong n_e$ for obtaining the potential of this field. We assume that the distribution functions of plasma components $f_a(\vec{r}, \vec{v})$, ($a=e, i$) are of Maxwellian type. All space dependencies of these functions arise from dependencies of respective moments ($n_a(\vec{r}), T_a(\vec{r})$) and current velocity $\vec{u}_a(\vec{r})$ of the plasma components. We consider these functions as given (for example, determined from the experiment) and we do not set a problem of their determination. Our results are of general form and do not depend on a particular kind of these functions. The gradients of plasma parameters certainly distort electron and ion distributions, but these corrections give the contribution to potential $\sim \lambda^{-2}$ and do not considered hereinafter.

We shall note that the locally isothermal state is not an equilibrium one. Obviously such a state is never achieved in practice since, as a rule, the plasma cannot be considered as an isolated system. Runaway electrons, auxiliary and Ohmic heating in a plasma result in infringement of local equilibrium and deviation of distribution functions from a Maxwellian. In practice the distribution functions are unobservable quantities, and only some their moments can be measured. Since the distribution functions enter in the expression for the potential in the integrand this suggest an idea of weak dependence of the potential on details of their behavior. Thus when simulating the local non-equilibrium we have selected a phenomenological approach, using corrections to the Maxwellian. We assume that the number of particles in the screening cloud is large. Thus it is possible to consider plasma as a collisionless one and to use the approach of linear response. We consider the plasma as a gas of neutral quasi-particles, plasma particles "dressed" by their polarization clouds. A distinct feature of inhomogeneous plasma quasi-particles is the possible non-identity of quasi-particles produced by particles of one kind, as far as screening can be different at different places. Below we shall see that just difference of the sizes and of the structure of quasi-particles (polarization clouds) results in appearance of the macroscopic electric field. Thus dynamic character of screening plays a key role.

POTENTIAL

Application of similar expression for a weakly inhomogeneous plasma ($\lambda \gg 1$) was justified by work of R.L. Guerncey.⁴ Thus the dependence of plasma polarization on magnetic (gravitational) field in our phenomenological approach is arising from space distribution of plasma parameters which are formed self-consistently in quasi-stationary (stationary) state supported by this field.

Following the approach developed in our paper² we shall calculate the potential of a particle of charge e_a and moving with constant velocity \vec{v} . The expression has the form:⁵

$$\varphi_{a,r(t),v}(\vec{r}) = \frac{e_a}{2\pi^2} \int \frac{d\vec{k}}{k^2} \exp[i\vec{k}(\vec{r} - \vec{r}(t))] \int_{-\infty}^{\infty} \frac{d\omega \delta(\omega - \vec{k}\vec{v})}{\varepsilon_l(\vec{k}, \omega)}, \quad (1)$$

where $\vec{r}(t) = \vec{r}_0 + \vec{v}t$, $\varepsilon_l(k, \omega)$ is the longitudinal part of the permittivity tensor (we assume that the motion is a non-relativistic one). This potential is produced by the charged particle and its polarization cloud. Average potential taking into account electron and ion quasi-particle contributions has the form

$$\langle \varphi(\vec{r}) \rangle = \sum_{a=e/i} \iint d\vec{r}_0 d\vec{v} f_a(\vec{r}_0, \vec{v}) \varphi_{a,r_0,v}(\vec{r}). \quad (2)$$

Substituting $\varepsilon_l(k, \omega)$, according to Eqs.(1) and distribution function in Eq.(3)³, and neglecting the terms of order of $\sim 1/\lambda$, and $\sim m_e/m_i$ as well as neglecting the macroscopic velocities of particles in comparison with thermal velocities of particles, and using the quasi-neutrality condition we arrive at the following results for the potential which has a form typical for thermoelectric potentials:

$$\langle \varphi \rangle = -\alpha T_e(\vec{r}). \quad (3)$$

Here the thermoelectric coefficient α is defined by the expression

$$\alpha = (2/e\sqrt{\pi}) [G_e - G_i(u)], \quad u = ZT_e/T_i. \quad (4)$$

In the LTE the electron contribution does not depend on space variables and is equal to $G_e^{eq} \cong 0.3445$. Ion contribution is represented by a function $G_i^{eq}(u)$ of dimensionless variable u . We are to stress that this result does not depend on the choice of the particular structure of the electron and ion temperature profiles.

The potential is vanished at static Debye screening (with accuracy $\alpha\lambda^{-2}$) irrespectively to specific form of distribution function. The influence of possible local electron non-equilibrium is simulated by the small addition to Maxwellian distribution function also corresponding to a local equilibrium but with the temperature in κ_e times greater and corresponding to a part $\beta_e < 1$ of plasma electrons. Thus the total electron distribution function is described by local Maxwellian distribution, having plateau in the tail. The value of G_e again does not depend on space variables. Dependence of this value on "plateau width" κ_e for a part of non-equilibrium electrons $\beta_e = 0.1$ show that weak non-equilibrium can result, nevertheless, in appreciable electron contribution to thermoelectric coefficient at sufficiently large "plateau width". This situation corresponds to an increase of effective temperature. Thus electron non-equilibrium increases the electron contribution G_e and does not influence the ion contribution G_i (at small values of β_e). Such conclusion does not depend on the electron distribution due to mentioned above integrated dependence of the potential.

The locally equilibrium ion function $G_i^{eq}(u)$ presents the ion contribution in the thermoelectric coefficient. It is comparable with the locally equilibrium electron contribution at value of dimensionless parameter $u = \frac{T_e(\vec{r})Z_i}{T_i(\vec{r})} \cong 1.93$ which corresponds to zero potential.

This result is explained by essential difference of electron and ion masses. In practice we have $T_i \leq T_e$ and $v_i \ll v_e$. Hence the ion contribution to the screening of electron is insignificant. Electron contribution to the screening of ions is a static one since the ions look

as stationary particles compared to the fast electrons. In the presence of impurities we have $Z_i = Z_{\text{eff}}$, where Z_{eff} is effective charge of the ion. Here Z_{eff} is a function of space variables and its value should be taken from the experiment.

RESULTS OF NUMERICAL CALCULATIONS

To verify the results of calculations of electric field strength according to expressions (3) we have chosen experimental works^{6,7} from the extensive list of papers, because in these papers the measured profiles both of electron and ion temperatures are presented. The comparison shows that in the core of tokamak TM-4 plasma both calculated and measured potentials have negative value that corresponds to domination of the electron contribution to thermoelectric coefficient because $T_e > T_i$. The potential goes through zero near the plasma boundary and then acquires positive values. Such a behavior is explained by the domination of the ionic contribution over electronic one. Thus theoretical calculation reproduces characteristics of the potential in the case of local equilibrium of the electron and ion component. In the plasma core the value of potential is found which, unlike neoclassical approach, considerably exceeds ion temperature in absolute values. To achieve the quantitative agreement we took into account local non-equilibrium of the electron component caused by the runaway electrons. Results of calculations of the potential give the value of the electron thermoelectric coefficient $G_e = 0.6$, which corresponds to 10% fraction of electrons which has the temperature $T \approx 10 T_e$. In this way the agreement between theoretical calculation and experimental data is improved for plasma core.

The space distribution of potential for DIII-D was calculated in assumption of local equilibrium and $Z_{\text{eff}} = 1$ with temperature profiles presented in it.⁷ The radial component of the electric field was calculated which is found to be in qualitative agreement with values given in this paper⁷. Here the radial electric field strength is positive in the plasma core. This is explained by prevalence of the ion contribution in this experiment. There is a change of sign of the field strength in the plasma periphery caused by the excess of T_e over T_i . The more detailed information about local non-equilibrium of the electron and ion components is necessary for achieving the quantitative agreement between calculated and experimental values.

The authors would like to thank K.A. Razumova, A.V. Mel'nikov and I.S. Nedsel'skij for presenting the experimental data, and for discussions of and interest to this work.

REFERENCES

1. E.M. Lifshitz and L.P. Pitaevskii, «Physical Kinetics», Pergamon Press, Oxford (1981)
2. E.E. Trofimovich, V.P. Krainov, Sov. Phys. *JETP*, 75:31 (1992)
3. E.E. Trofimovich, V.P. Krainov, Sov. Phys. *JETP*, 77:910 (1992)
4. R.L. Guernsey, «The Kinetic Theory of Fully Ionized Gases», Off Nav. Res. Contract No 1224 (15), July (1960)
5. V.P. Silin, «Introduction to the Kinetic Theory of Gases» [in Russian], Nauka, Moscow (1971)
6. Yu. N. Dnestrovskiy et al., IEEE Transactions on *J. Plasma Science*, 22:310 (1994)
7. K.H. Burrell et al., *Role of the radial electric field in the transition from L- mode to H- mode to VH mode in DIII-D tokamak*, (submitted for publication in *Phys. Fluids*

MODELING OF STRONG DISCHARGES IN WATER

I. M. Tkachenko,¹ A. W. DeSilva,² and J. L. Iserte¹

¹Department of Applied Mathematics, Polytechnic University
Valencia, E-46071, Spain

²Institute for Plasma Research and Department of Physics
University of Maryland College Park, MD
E-mail: imtk@iqn.upv.es

The aim of the work is to analyze and model strong discharges in water.¹ In these measurements a cylindrical strongly coupled plasma is created by vaporizing a copper wire embedded in water with a burst of current. The resulting plasma column expands radially, compressing the surrounding water and causing a cylindrical shockwave to move radially outwards in the water. The plasma is observed to remain quite stable during this expansion. Both the current and voltage across the channel were measured, and reactive contributions to the voltage were accounted for. The column diameter was observed photographically and calculated using the SESAME code, and the conductivity values were deduced.

The new set of data,¹ obtained for the conditions different from those reported earlier,² implies that, at longer times ($t = 1 - 9\mu\text{s}$), for some shots the scaling time dependence is valid for the column radius: $r(t) \propto \sqrt{t}$. In this sense the experiments resemble those reported in [3] for longer timescales.

Current was supplied by a capacitor bank of $C = 3.86\mu\text{F}$ charged to $V = 15\text{kV}$. The bank inductance was about 212nH , to which the load (wire) inductance of typically 20 to 30nH must be added. Some shots were terminated by short currents, and we will focus on four shots with the discharge current across the plasma channel measured over a relatively long time interval of up to $10\mu\text{s}$, with up to three current zeros observed.

The circuit current oscillation equation in this case reads:

$$\ddot{I} + \omega^2 I + \frac{d}{dt}(I\Omega) = 0. \quad (1)$$

Here $\omega = \sqrt{LC}$, L being the circuit net inductance,

$$\Omega = \frac{\ell}{\sigma S(t)L}. \quad (2)$$

The wire length ℓ was 26.5mm . We presume the plasma column conductivity σ to be constant on the timescale when the column cross-section $S(t)$ can be approximated as

$$S(t) = \beta t. \quad (3)$$

Table 1.

<i>discharge</i>	1	2	3	4
$\beta(m^2/s)$	3.98	4.20	2.90	4.51
$t_1(\mu s)$	5.33	4.96	6.12	4.85
ν	2.41	2.06	3.04	2.05

Table 2.

<i>discharge</i>	1	2	3	4
$t_2(\mu s)$	8.50	8.09	9.35	8.02
$\tau_2(\mu s)$	8.47	8.24	9.46	8.12
$t_3(\mu s)$	—	11.15	12.36	11.07
$\tau_3(\mu s)$	—	11.55	12.78	11.40

If we presume that the current remains finite at $t = 0$, the resulting differential equation possesses an exact analytical solution in terms of first kind *Bessel* function with the index ν related to the conductivity value:⁴

$$I(t) = I_0(\omega t)^{1-\nu} J_\nu(\omega t), \quad (4)$$

$$\nu = \frac{1}{2} \left(1 + \frac{\ell}{\sigma \beta L} \right). \quad (5)$$

The latter can be determined from the position of the first current zero, the positions of the second and the third (if any) ones can serve to check the validity of the model. In addition, the value of the effective conductivity to be determined from the index value can be compared with the averaged (over the adequate time interval) experimental conductivity.

The values of the model parameters, β , and the position of the first zero, t_1 , of the current were obtained from the experimental data for the discharges under investigation, the values of $x_1 = \omega t_1$ were used to find those of the Bessel function indices, see Table 1.

On the basis of these data we estimated the positions of the second, τ_2 , and third, τ_3 , (not observed for the first discharge) current zeros of the theoretical curve, Eq. (4), and compared them with the corresponding experimental values, t_2 and t_3 , see Table 2, and Fig. 1, where both experimental (solid line), and theoretical curves (dashed curve, the value of I_0 was adjusted to the first maximum of the experimental curve) are displayed as functions of $x = \omega t$, $\omega = 1.05 \cdot 10^6 s^{-1}$, for the discharge No. 3.

The next table contains the values of effective plasma conductivity calculated according to Eq. (5) compared to those estimated from the experimental data averaged over the time intervals, for which Eq. (3) fulfils with high precision.

The factor of two discrepancy between experimental and theoretical values of strongly coupled plasma electrical conductivity, especially taking into account the simplicity of the theory presented, might be considered as satisfactory, see [5].

The fact that the plasma channel cross-section curves demonstrate, for a well defined column, the validity of Eq. (3) for strong discharges in water, and independently of the discharge initial conditions (at least for the cases considered), requires a theoretical interpretation. One

Table 3.

<i>discharge</i>	1	2	3	4
$\sigma(S/m)$	7600	8532	7800	8100
$\bar{\sigma}(S/m)$	8800	16000	16100	17400

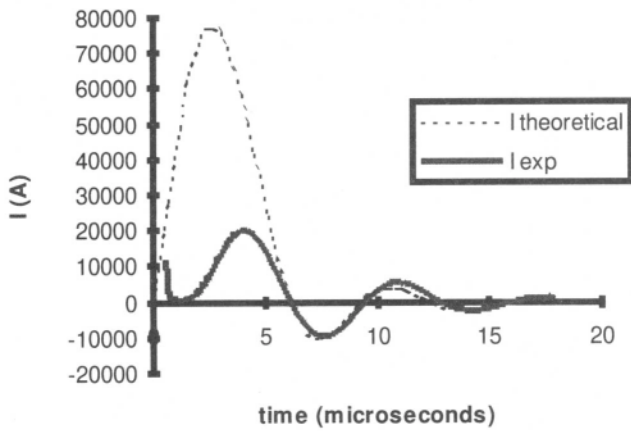


Figure 1. The zeros of the experimental and theoretical current curves coincide.

should keep in mind that these curves were generated by the SESAME code, but were also confirmed by independent streak camera observations.^{1,2} The SESAME code application was based on the kinetic model, which denies any possible mixing of the copper plasma created by the discharge with the surrounding water.

An alternate interpretation of the data, due to one of us (I. M. T.), is that a Mott-type first-order phase transition occurs at the column-water interface. It can be shown⁵ that the interface temperature should be maintained constant and equal to the phase transition temperature while Eq. (3) is verified. The SESAME code 'is increasingly inaccurate with the onset of strong Coulomb interaction',⁶ and cannot include the possible Mott-type phase transition; it predicts a uniform temperature distribution within plasma, and for the discharges we considered the value of the plasma temperature varies quite slowly around $T_{tr} = 20 - 22 kK$ (like in [3]) as long as the column radius is scaled by the square root of time.

The solution of the cylindrical Stefan problem⁴ was used to estimate that within this model the radial distribution of the plasma column temperature differs from the homogeneous one with the temperature equal to T_{tr} by only about 10%.

The justification of the phase-transition model of strong discharges in water requires knowledge, among other things, of the strongly coupled plasma equation of state.

The plasma channel is optically dense, and it complicates its further experimental studies aimed at the construction of a complete energy-conversion model of the discharge.

REFERENCES

- [1] A. W. DeSilva, to be submitted to the Physical Review, E, 1997.
- [2] A. W. DeSilva, Proc. Int. Conf. on the Physics of Strongly Coupled Plasmas, Binz, Germany, 1995.
- [3] I. S. Shvets, High Temp.(USA) **18**, No. 1 (1980).
- [4] P. Fernandez de Cordoba and I. M. Tkachenko, Thermodynamic and kinetic parameters of discharge plasmas, (UPV Press service, Valencia, 1995) (in Spanish).
- [5] I. M. Tkachenko and P. Fernandez de Cordoba, present Proceedings.
- [6] K. S. Trainor, J. Appl. Phys. **54**, 2372 (1983).

This page intentionally left blank

KINETIC EQUATION FOR NONIDEAL SPATIALLY INHOMOGENEOUS PLASMAS

V. V. Belyi,¹ Yu. A. Kukharenko,² and J. Wallenborn³

¹IZMIRAN

Troitsk, Moscow region, 142092, Russia

²UITPRAN

Moscow, Russia

³Physique statistique, Plasma et Optique non linéaire

CP 231, Université Libre de Bruxelles, 1050, Bruxelles, Belgium

We have generalized the Balescu–Lenard kinetic equation to weakly nonideal spatially-uniform polarizable plasma by including non-Markovian effects¹ (see also these proceedings). However, in many problems, nonlocality in space must be considered as well as non-Markovian effects (or nonlocality in time).

For, we extended our previous work to nonuniform systems in such a way that we obtain a nonlinear kinetic equation which shows the local laws of conservation for particle, momentum and total energy densities. This last is, at equilibrium, equal to the Debye–Hückel energy.

Out of equilibrium the evolution of a nonuniform system can be described from the BBGKY-hierarchy. In the so-called plasma approximation (see Ref. [1]), the two first members can be written as:

$$\begin{aligned} \frac{\partial}{\partial t} f_a(\mathbf{p}_1, \mathbf{r}_1, t) + \mathbf{v}_1 \cdot \frac{\partial}{\partial \mathbf{r}_1} f_a(\mathbf{p}_1, \mathbf{r}_1, t) - \sum_b \int d\mathbf{p}_2 d\mathbf{r}_2 \frac{\partial \Phi_{ab}(\mathbf{r}_1 - \mathbf{r}_2)}{\partial \mathbf{r}_1} \cdot \frac{\partial f_a f_b}{\partial \mathbf{p}_1}(\mathbf{p}_2, \mathbf{r}_2, t) \\ = \sum_b \int d\mathbf{p}_2 d\mathbf{r}_2 \frac{\partial \Phi_{ab}(\mathbf{r}_1 - \mathbf{r}_2)}{\partial \mathbf{r}_1} \cdot \frac{\partial}{\partial \mathbf{p}_1} g_{ab}(\mathbf{p}_1, \mathbf{p}_2, \mathbf{r}_1, \mathbf{r}_2, t) = J_a(\mathbf{p}_1, \mathbf{r}_1, t) \end{aligned} \quad (1)$$

where $J_a(\mathbf{p}_1, \mathbf{r}_1, t)$ is the collision integral, $f_a(\mathbf{p}_1, \mathbf{r}_1, t)$ is the one-particle distribution function (df) and $g_{ab}(\mathbf{p}_1, \mathbf{p}_2, \mathbf{r}_1, \mathbf{r}_2, t)$ is the pair correlation function;

$$\begin{aligned} \left\{ \frac{\partial}{\partial t} + \mathbf{v}_1 \cdot \frac{\partial}{\partial \mathbf{r}_1} + \mathbf{v}_2 \cdot \frac{\partial}{\partial \mathbf{r}_2} - \sum_c \int d\mathbf{p}_3 d\mathbf{r}_3 \left[\frac{\partial \Phi_{ac}(\mathbf{r}_1 - \mathbf{r}_3)}{\partial \mathbf{r}_1} \cdot \frac{\partial}{\partial \mathbf{p}_1} \right. \right. \\ \left. \left. + \frac{\partial \Phi_{bc}(\mathbf{r}_2 - \mathbf{r}_3)}{\partial \mathbf{r}_2} \cdot \frac{\partial}{\partial \mathbf{p}_2} \right] f_c(\mathbf{p}_3, \mathbf{r}_3, t) \right\} g_{ab}(\mathbf{p}_1, \mathbf{p}_2, \mathbf{r}_1, \mathbf{r}_2, t) \\ - \sum_c \int d\mathbf{p}_3 d\mathbf{r}_3 \left[\frac{\partial \Phi_{ac}(\mathbf{r}_1 - \mathbf{r}_3)}{\partial \mathbf{r}_1} \cdot \frac{\partial f_a}{\partial \mathbf{p}_1} g_{bc} + \frac{\partial \Phi_{bc}(\mathbf{r}_2 - \mathbf{r}_3)}{\partial \mathbf{r}_2} \cdot \frac{\partial f_b}{\partial \mathbf{p}_2} g_{ac} \right] = A_{ab}(\mathbf{p}_1, \mathbf{p}_2, \mathbf{r}_1, \mathbf{r}_2, t) \end{aligned} \quad (2)$$

with $\Phi_{ab}(\mathbf{r}) = e_a e_b / r$, the Coulomb potential and

$$A_{ab}(\mathbf{p}_1, \mathbf{p}_2, \mathbf{r}_1, \mathbf{r}_2, t) = \frac{\partial \Phi_{ab}(\mathbf{r}_1 - \mathbf{r}_2)}{\partial \mathbf{r}_1} \cdot \left(\frac{\partial}{\partial \mathbf{p}_1} - \frac{\partial}{\partial \mathbf{p}_2} \right) f_a(\mathbf{p}_1, \mathbf{r}_1, t) f_b(\mathbf{p}_2, \mathbf{r}_2, t). \quad (3)$$

The two last terms in the curly bracket in l.h.s. are mean field terms we neglect in a first approach of the problem.

The equation (2) is solved by means of the Green's function method.² In the case of uniform system it was possible to disentangle the collision time from the one-particle df relaxation time. Similarly, in the case of nonuniform system it is possible to separate in the Green's function large length scales from the length scale of effective interaction.

Specifically, we have:

$$g_{ab}(\mathbf{p}_1, \mathbf{p}_2, \mathbf{R}, \mathbf{r}, t) = \sum_{a'b'} \int dt' d\mathbf{p}'_1 d\mathbf{p}'_2 d\mathbf{R}' d\mathbf{r}' \\ \times R_{ab,a'b'}(t-t', \mathbf{R}-\mathbf{R}', \mathbf{r}-\mathbf{r}', \mu t', \mu(\mathbf{R}'+\mathbf{r}'/2), \mu(\mathbf{R}'-\mathbf{r}'/2), \mathbf{p}_1, \mathbf{p}_2, \mathbf{p}'_1, \mathbf{p}'_2) \\ \times A_{a'b'}(\mu t', \mathbf{r}', \mathbf{p}'_1, \mathbf{p}'_2, \mu(\mathbf{R}'+\mathbf{r}'/2), \mu(\mathbf{R}'-\mathbf{r}'/2)) \quad (4)$$

where $R_{ab,a'b'}$ is the Green's function and with $\mathbf{R} = (\mathbf{r}_1 + \mathbf{r}_2)/2$, $\mathbf{r} = \mathbf{r}_1 - \mathbf{r}_2$, $\mathbf{R}' = (\mathbf{r}'_1 + \mathbf{r}'_2)/2$, $\mathbf{r}' = \mathbf{r}'_1 - \mathbf{r}'_2$. As in Ref. [1], μ indicates that the functions varies with respect to variables on the scale of the one-particle df.

We make the change of variables $\mathbf{R}' \rightarrow \mathbf{R} - \mathbf{R}'$, $t - t' \rightarrow \tau$ and expand $R_{ab,a'b'}$ with respect to slow variables; then, after a Laplace transformation with respect to τ and a Fourier transformation with respect to \mathbf{R}' and \mathbf{r} , we obtain

$$g(\mathbf{p}_1, \mathbf{p}_2, \mathbf{R}, \mathbf{k}, t) = \sum_{n=0}^{\infty} \frac{1}{n!} (i \frac{\partial}{\partial z} \frac{\partial}{\partial t})^n \sum_{p=0}^{\infty} \frac{1}{p!} [(i/2 \frac{\partial}{\partial \mathbf{k}} - i \frac{\partial}{\partial \mathbf{K}}) \cdot \frac{\partial}{\partial \mathbf{R}}]^p \\ \times \sum_{q=0}^{\infty} \frac{1}{q!} [(-i \frac{\partial}{\partial \mathbf{K}} - i/2 \frac{\partial}{\partial \mathbf{k}}) \cdot \frac{\partial}{\partial \mathbf{R}}]^q \sum_{a'b'} R_{ab,a'b'}(z, \mathbf{K}, \mathbf{k}, \hat{\mathbf{k}}, \mathbf{R}, \hat{\mathbf{R}}, t, \mathbf{p}_1, \mathbf{p}_2, \mathbf{p}'_1, \mathbf{p}'_2) \\ \times A_{a'b'}(\hat{\mathbf{k}}, \mathbf{R}, \hat{\mathbf{R}}, t, \mathbf{p}'_1, \mathbf{p}'_2) |_{\hat{\mathbf{R}}=\mathbf{R}, \hat{\mathbf{k}}=\mathbf{k}, \mathbf{K}=\mathbf{0}, z=+i0} \quad (5)$$

where we have put $\mu = 1$ since all space and time variables are now on the scale of the one-particle df.

The expression of $R_{ab,a'b'}(z, \mathbf{K}, \mathbf{k}, \hat{\mathbf{k}}, \mathbf{R}, \hat{\mathbf{R}}, t)$ can be obtained as in [1] (see also Ref. [3]). The expression for the pair correlation function is then:

$$g_{ab}(\mathbf{p}_1, \mathbf{p}_2, \mathbf{k}, \mathbf{R}, t) \\ = \sum_{n=0}^{\infty} \frac{1}{n!} (i \frac{\partial}{\partial z} \frac{\partial}{\partial t})^n \sum_{p=0}^{\infty} \frac{1}{p!} [(i/2 \frac{\partial}{\partial \mathbf{k}} - i \frac{\partial}{\partial \mathbf{K}}) \cdot \frac{\partial}{\partial \mathbf{R}}]^p \sum_{q=0}^{\infty} \frac{1}{q!} [(-i \frac{\partial}{\partial \mathbf{K}} - i/2 \frac{\partial}{\partial \mathbf{k}}) \cdot \frac{\partial}{\partial \mathbf{R}}]^q \\ \times H_{ab}(\mathbf{p}_1, \mathbf{p}_2, z, \mathbf{K}, \mathbf{k}, \hat{\mathbf{k}}, \mathbf{R}, \hat{\mathbf{R}}, t) |_{\hat{\mathbf{R}}=\mathbf{R}, \hat{\mathbf{k}}=\mathbf{k}, \mathbf{K}=\mathbf{0}, z=+i0} \quad (6)$$

$$H_{ab}(\mathbf{p}_1, \mathbf{p}_2, z, \mathbf{K}, \mathbf{k}, \hat{\mathbf{k}}, \mathbf{R}, \hat{\mathbf{R}}, t) = - \frac{1}{\omega - \mathbf{k}_2 \cdot \mathbf{v}_2 - \mathbf{k}_1 \cdot \mathbf{v}_1 + i0} \sum_c \int d\mathbf{p}_3 \{ \delta_{bc} \delta(\mathbf{p}_2 - \mathbf{p}_3) \\ - [\frac{1}{\omega - \mathbf{k}_2 \cdot \mathbf{v}_3 - \mathbf{k}_1 \cdot \mathbf{v}_1 + i0} + \frac{1}{\mathbf{k}_2 \cdot \mathbf{v}_3 - \mathbf{k}_2 \cdot \mathbf{v}_2 + i0}] \frac{\Phi_{cc}(\mathbf{k}_2)}{\varepsilon(\mathbf{k}_2, \mathbf{v}_3, \mathbf{k}_2, \hat{\mathbf{R}})} \mathbf{k}_2 \cdot \frac{\partial}{\partial \mathbf{p}_2} f_b(\hat{\mathbf{R}}) \} \\ \{ [f_c(\hat{\mathbf{R}}) - \frac{Q^*(\mathbf{k}_2, \hat{\mathbf{R}}, \mathbf{k}_2, \mathbf{v}_3)}{\varepsilon^*(\mathbf{k}_2, \mathbf{v}_3, \mathbf{k}_2, \hat{\mathbf{R}})} \mathbf{k}_2 \cdot \frac{\partial}{\partial \mathbf{p}_3} f_c(\hat{\mathbf{R}})] \\ \times [\Phi_{ab}(\hat{\mathbf{k}}) \mathbf{k} - \frac{P(\mathbf{k}_1, \hat{\mathbf{k}}, \hat{\mathbf{R}}, \omega - \mathbf{k}_2 \cdot \mathbf{v}_3)}{\varepsilon^*(\omega - \mathbf{k}_2 \cdot \mathbf{v}_3, \hat{\mathbf{R}}, \mathbf{k}_1)} \Phi_{ab}(\mathbf{k}_1) \mathbf{k}_1] \mathbf{k}_1 \cdot \frac{\partial}{\partial \mathbf{p}_1} f_a(\mathbf{R}) \\ - [f_a(\mathbf{R}) - \frac{Q(\mathbf{k}_1, \omega - \mathbf{k}_2 \cdot \mathbf{v}_3, \mathbf{R})}{\varepsilon(\omega - \mathbf{k}_2 \cdot \mathbf{v}_3, \mathbf{k}_1, \mathbf{R})} \mathbf{k}_1 \cdot \frac{\partial}{\partial \mathbf{p}_1} f_a(\mathbf{R})] \\ \times [\Phi_{ab}(\hat{\mathbf{k}}) \hat{\mathbf{k}} - \frac{P^*(\mathbf{k}_2, \hat{\mathbf{k}}, \hat{\mathbf{R}}, \mathbf{k}_2, \mathbf{v}_3)}{\varepsilon^*(\mathbf{k}_2, \mathbf{v}_3, \hat{\mathbf{R}}, \mathbf{k}_2)} \Phi_{ab}(\mathbf{k}_2) \mathbf{k}_2] \cdot \frac{\partial}{\partial \mathbf{p}_3} f_c(\hat{\mathbf{R}}) \} \quad (7)$$

where $\mathbf{k}_1 = \mathbf{K}/2 + \mathbf{k}$, $\mathbf{k}_2 = \mathbf{K}/2 - \mathbf{k}$ and

$$P(\mathbf{k}_1, \hat{\mathbf{k}}, \mathbf{R}, \omega) = \sum_a \Phi_{aa}(\hat{\mathbf{k}}) \int d\mathbf{p}_1 \frac{1}{\omega - \mathbf{k}_1 \cdot \mathbf{v}_1 + i0} \hat{\mathbf{k}} \cdot \frac{\partial}{\partial \mathbf{p}_1} f_a(\mathbf{R}, \mathbf{p}_1, t)$$

$$Q(\mathbf{k}_1, \mathbf{R}, \omega) = \sum_a \Phi_{aa}(\mathbf{k}_1) \int d\mathbf{p}_1 \frac{1}{\omega - \mathbf{k}_1 \cdot \mathbf{v}_1 + i0} f_a(\mathbf{R}, \mathbf{p}_1, t)$$

The collision integral is deduced from Eqs. (1) and (6). It must be pointed out that in Eq. (6) the correlation function is given as a function of \mathbf{R} , the median position between particles 1 and 2, while we need the collision integral at position \mathbf{r}_1 of particle 1. This introduces supplementary derivatives of the form $\sum_{m=0}^{\infty} \frac{1}{m!} [(-i/2 \frac{\partial}{\partial \mathbf{k}} \cdot \frac{\partial}{\partial \mathbf{R}})^m]$ acting on $g_{ab}(\mathbf{p}_1, \mathbf{p}_2, \mathbf{k}, \mathbf{R}, t)$.⁴ With this in mind, we obtain:

$$\begin{aligned} J_a(t, \mathbf{r}_1, \mathbf{p}_1) = & - \sum_b \int \frac{d\mathbf{k}}{(2\pi)^3} d\mathbf{p}_2 \Phi_{ab}(\mathbf{k}) i\mathbf{k} \cdot \frac{\partial}{\partial \mathbf{p}_1} \sum_{m=0}^{\infty} \frac{1}{m!} [(-i/2 \frac{\partial}{\partial \mathbf{k}} \cdot \frac{\partial}{\partial \mathbf{R}})^m \sum_{n=0}^{\infty} \frac{1}{n!} (i \frac{\partial}{\partial z} \frac{\partial}{\partial t})^n] \\ & \times \sum_{p=0}^{\infty} \frac{1}{p!} [(i/2 \frac{\partial}{\partial \mathbf{k}} - i \frac{\partial}{\partial \mathbf{K}}) \cdot \frac{\partial}{\partial \mathbf{R}}]^p \sum_{q=0}^{\infty} \frac{1}{q!} [(-i \frac{\partial}{\partial \mathbf{K}} - i/2 \frac{\partial}{\partial \mathbf{k}}) \cdot \frac{\partial}{\partial \mathbf{R}}]^q \\ & \times \frac{1}{\omega - \mathbf{k}_2 \cdot \mathbf{v}_2 - \mathbf{k}_1 \cdot \mathbf{v}_1 + i0} \frac{1}{\varepsilon(\mathbf{k}_2, \mathbf{v}_2, \mathbf{k}_2)} \{ [f_b(\widehat{\mathbf{R}}) - \frac{Q^*(\mathbf{k}_2, \widehat{\mathbf{R}}, \mathbf{k}_2, \mathbf{v}_2)}{\varepsilon^*(\mathbf{k}_2, \mathbf{v}_2, \mathbf{k}_2, \widehat{\mathbf{R}})} \mathbf{k}_2 \cdot \frac{\partial}{\partial \mathbf{p}_2} f_b(\widehat{\mathbf{R}})] \\ & \times [\Phi_{ab}(\widehat{\mathbf{k}}) \widehat{\mathbf{k}} - \frac{P(\mathbf{k}_1, \widehat{\mathbf{k}}, \mathbf{R}, \omega - \mathbf{k}_2, \mathbf{v}_2)}{\varepsilon(\omega - \mathbf{k}_2, \mathbf{v}_2, \mathbf{k}_1, \widehat{\mathbf{R}})} \Phi_{ab}(\mathbf{k}_1) \mathbf{k}_1] \cdot \frac{\partial}{\partial \mathbf{p}_1} f_a(\mathbf{R}) \\ & - [\Phi_{ab}(\widehat{\mathbf{k}}) \widehat{\mathbf{k}} - \frac{P^*(\mathbf{k}_2, \widehat{\mathbf{k}}, \widehat{\mathbf{R}}, \mathbf{k}_2, \mathbf{v}_2)}{\varepsilon^*(\mathbf{k}_2, \mathbf{v}_2, \widehat{\mathbf{R}}, \mathbf{k}_2)} \Phi_{ab}(\mathbf{k}_2) \mathbf{k}_2] \cdot \frac{\partial}{\partial \mathbf{p}_2} f_b(\widehat{\mathbf{R}}) \\ & [f_a(\mathbf{R}) - \frac{Q(\mathbf{k}_1, \mathbf{R}, \omega - \mathbf{k}_2, \mathbf{v}_2)}{\varepsilon(\omega - \mathbf{k}_2, \mathbf{v}_2, \mathbf{R}, \mathbf{k}_1)} \mathbf{k}_1 \cdot \frac{\partial}{\partial \mathbf{p}_1} f_a(\mathbf{R})] \} \Big|_{\widehat{\mathbf{R}}=\mathbf{R}, \widehat{\mathbf{k}}=\mathbf{k}, \mathbf{k}_1=\mathbf{k}=\mathbf{k}_2, \omega=0} \end{aligned} \quad (8)$$

As a first application we shall restrict the above results to the spatially-uniform Markovian approximation and its first correction in nonlocality in space as well as in time i.e., in Eq. (6) and (8) we only carry terms of order 0 and of order 1 in the derivatives. In this approximation, the balance equations are easily obtained from the kinetic equation (1) with (8). From the equation for the total momentum density,

$$\partial_t \rho \mathbf{u}_i + \frac{\partial}{\partial R_j} (\rho u_i u_j + P_{ij}^{id} + P_{ij}^{cor}) = 0, \quad (9)$$

where \mathbf{u} is the mean velocity field: $\rho \mathbf{u} = \sum_a \int d\mathbf{p}_1 \frac{\mathbf{p}_1}{m_a} f_a$ and

$$P^{id} = \sum_a m_a \int d\mathbf{p}_1 (v_i^j - u^i)(v_j^i - u^j) f_a \quad (10)$$

is the kinetic part of the pressure tensor, we obtain the definition of the potential part of the pressure tensor:

$$P_{ij}^{cor} = -\frac{1}{2} \frac{1}{(2\pi)^3} \sum_{ab} \int d\mathbf{k} d\mathbf{p}_1 d\mathbf{p}_2 \Phi_{ab}(\mathbf{k}) k_i \frac{\partial}{\partial k_j} \text{Re} g_{ab}^0(\mathbf{p}_1, \mathbf{p}_2, \mathbf{k}, \mathbf{R}, t), \quad (11)$$

In the same way, we have the total energy balance equation:

$$\partial_t \left(\frac{\rho \mathbf{u}^2}{2} + E^k + E^p \right) + \frac{\partial}{\partial R_i} [u_i \left(\frac{\rho \mathbf{u}^2}{2} + E^k + E^p \right) + (P_{ij}^{id} + P_{ij}^{cor}) u_j + q_i^k + q_i^{cor}] = 0, \quad (12)$$

where $E^k = \sum_a \int d\mathbf{p}_1 \frac{p_1^2}{2m_a} f_a$ is the kinetic energy density and E^p is the potential energy density.

$$E^p = \frac{1}{2} \frac{1}{(2\pi)^3} \sum_{ab} \int d\mathbf{k} d\mathbf{p}_1 d\mathbf{p}_2 \Phi_{ab}(\mathbf{k}) \text{Re} g_{ab}^0 \quad (13)$$

q_i^k is the kinetic heat flux

$$\mathbf{q}^k = \sum_a \int d\mathbf{p}_1 (\mathbf{v}_1 - \mathbf{u}) \frac{p_1^2}{2m_a} f_a \quad (14)$$

and q_i^{cor} is the potential heat flux

$$q_i^{cor} = \frac{1}{2} \frac{1}{(2\pi)^3} \sum_{ab} \int d\mathbf{p}_1 d\mathbf{p}_2 d\mathbf{k} \Phi_{ab}(\mathbf{k}) [v_1^i - u^i + k_j (v_1^j - u^j) \frac{\partial}{\partial k_i}] \text{Re} g_{ab}^0. \quad (15)$$

Formulas (11)–(15) are of course compatible with those deduced by general arguments from the BBGKY-hierarchy (see for instance Ref. [5]) They show the coherence of our approach. Remind that the approximation used in (11)–(15) is not trivial since g_{ab}^0 takes into account polarization effects and the potential energy (13) becomes at equilibrium the Debye–Hückel one.

REFERENCES

- [1] V. V. Belyi, Yu. A. Kukhareno and J. Wallenborn, *Phys. Rev. Lett.* 76, 3554 (1996); V. V. Belyi, Yu. A. Kukhareno and J. Wallenborn, *submitted to J. Plasma Phys* (see also these proceedings).
- [2] R. Balescu, *Statistical mechanics of charged particles* (Wiley, New York, 1963)
- [3] S. Ichimaru, *Basic principles of plasma physics* (Benjamin, New York, 1973)
- [4] Yu. L. Klimontovich, *Kinetic theory of nonideal gases and nonideal plasmas* (Academic Press, New York, 1975)
- [5] J. H. Ferziger & H. G. Kapper, *Mathematical Theory of Transport Processes in Gases* (North-Holland, Amsterdam, 1972)

VELOCITY-SPACE DRAG AND DIFFUSION IN MODEL, TWO-DIMENSIONAL PLASMA

M. A. Reynolds,¹ B. D. Fried,² and G. J. Morales²

¹National Research Council—NRL Research Associate
Plasma Physics Division, Naval Research Laboratory
Washington, DC
Department of Physics and Astronomy, UCLA
Los Angeles, CA

INTRODUCTION

This investigation consists of a calculation of the Fokker–Planck coefficients for a two-dimensional, isotropic plasma with a low-density component of fast electrons. It sheds light on the role of emission and damping of electrostatic waves in the relaxation of weakly stable plasmas. Two dimensions provides a convenient paradigm because, unlike three dimensions, the transport due to waves dominates collisional effects. No dominant approximation¹ is needed since the Coulomb potential in two dimensions is logarithmic, and, because wave effects are prevalent, there is an enhanced interaction between fast electrons. That is, a fast test electron experiences anomalously large drag and diffusion forces due to the enhanced fluctuations generated by a low-density, fast-electron population. Of course, fast electrons also generate enhanced fluctuations in three dimensions,^{2,3} but for plasmas near equilibrium, their effect on transport is largely masked by collisional processes.^{4,5} The differences between two and three dimensions arise from the fact that both emission and damping of plasma waves are retained to lowest order in two dimensions, while the three-dimensional dominant approximation effectively includes only wave emission by test particles. An understanding of the differences between two and three dimensions is crucial to the interpretation of two-dimensional particle simulations. Some properties of two-dimensional and three-dimensional plasmas are compared in Table 1.

TRANSPORT COEFFICIENTS DUE TO FLUCTUATIONS

The fluctuation integral of Lenard⁶ has been rederived⁷ for application to fewer than three dimensions by considering a quasilinear extension of the Vlasov equation.⁸ The drag and diffusion coefficients of the Fokker–Planck equation, A_{\parallel}^{σ} , D_{\parallel}^{σ} and D_{\perp}^{σ} , represent the drag and diffusion experienced by a test particle due to species σ , and are all proportional to an integral over wave-number $J_{\nu} = \int dk k^{\nu} / |k^2 - \xi^2|^2$, where ν is the spatial dimension (1, 2, or 3) and

Table 1. Comparison between two and three dimensions.

	2D	3D
bare potential	$\ln r$	$1/r$
shielded potential	$K_0(k_D r)$	$e^{-k_D r}/r$
Coulomb core	soft	hard
Fokker–Planck coefficients	integrable	singular
dominant effect	$\epsilon(k, kv) = 0$	$\ln \Lambda$
tail interaction	$\text{Im}\chi_{\text{tail}}$	$\ln \Lambda$

$\xi^2 = \sum_{\sigma} (\omega_{p\sigma}^2 / 2\bar{v}_{\sigma}^2) Z' \left(v \cos \theta / \sqrt{2}\bar{v}_{\sigma} \right)$. In three dimensions \mathcal{J}_3 diverges logarithmically and leads to the dominant¹ approximation: $\mathcal{J}_3 \approx \ln \Lambda$. In two dimensions, because of the soft core of the Coulomb potential, \mathcal{J}_2 retains information about the distribution function and the dispersion relation through ξ

$$\mathcal{J}_2 = -\frac{\pi}{4 \text{Im} \xi}. \quad (1)$$

This result was first obtained by Abraham–Shrauner.⁹

In three dimensions, all the coefficients are proportional to the species density n_{σ} . This makes sense physically because the interaction with a group of particles is expected to be proportional to the quantity of those particles. It is only valid, however, within the dominant approximation, and arises because the kinetic information, which contains the damping of the emitted waves, is neglected. In two dimensions, the parallel diffusion coefficient for a Maxwellian distribution can be written⁷

$$D_{\parallel} = \frac{4\sqrt{2\pi}q^2}{m^2} \left(\frac{q_e^2 n_e}{\bar{v}_e k_{De}} \right) \sum_{\sigma} \overline{D}_{\parallel}^{\sigma}, \quad (2)$$

where

$$\overline{D}_{\parallel}^{\sigma} = k_{De} \left(\frac{q_{\sigma}^2 n_{\sigma}}{\bar{v}_{\sigma}} \right) \left(\frac{\bar{v}_e}{q_e^2 n_e} \right) C_2^{\sigma}, \quad (3)$$

$$C_2^{\sigma} = -\frac{\pi}{4} \int_0^{2\pi} d\theta \frac{\cos^2 \theta e^{-v^2 \cos^2 \theta / 2\bar{v}_{\sigma}^2}}{\text{Im} \xi(\theta)}, \quad (4)$$

with similar expressions for A_{\parallel} and D_{\perp} . At both small and large velocities the Fokker–Planck coefficients behave similarly in two and three dimensions¹⁰ (aside from numerical factors which are geometrical in nature). For nonequilibrium plasmas, however, the weak dynamical shielding of nonthermal particles becomes important, and the interplay between the thermal velocity scales increases in complexity.

Enhanced Large-Velocity Interaction in Two Dimensions

An enhanced large-velocity interaction appears when there is a small, superthermal electron component. If this component is treated as a separate species, then the drag and diffusion due to these hot electrons are only weakly dependent on their density, i.e., even a small population of fast electrons can affect the transport significantly.

We choose a nonequilibrium distribution with three species: ions, bulk electrons, and tail electrons ($\sigma = i, e, t$), each with Maxwellian distributions. Figures 1 and 2 show the coefficients due to the bulk electrons and the tail electrons, respectively, for the parameters $\bar{v}_i^2 / \bar{v}_e^2 = 16$, $n_i / n_e = 0.01$, and an ion-to-electron mass ratio of 64. Because the ions are the slowest species, the ion coefficients are unchanged from the equilibrium case, and are not shown. The coefficients due to the bulk electrons are also virtually unchanged from the

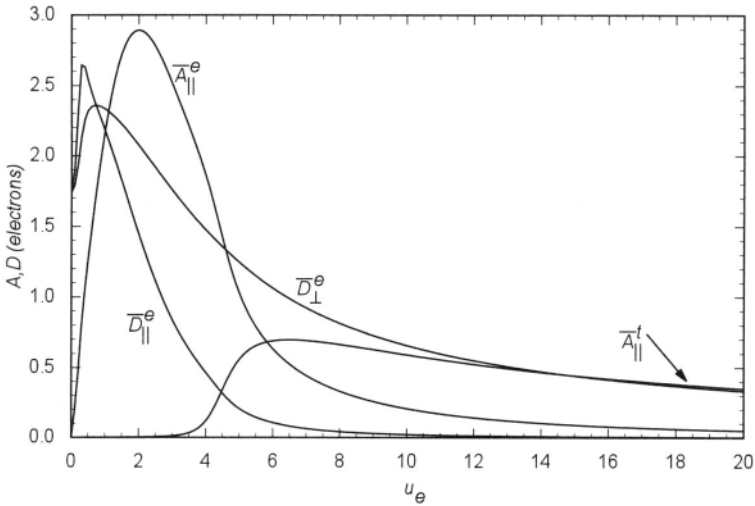


Figure 1. Contribution of the bulk electrons to the Fokker–Planck coefficients of a test electron in a nonequilibrium two-dimensional plasma as a function of $u_e = v/\sqrt{2}\bar{v}_e$. The ion-to-electron mass ratio is 64, $n_i/n_e = 0.01$, and $\bar{v}_i^2/\bar{v}_e^2 = 16$. The contribution of the tail electrons to the parallel drag, A_{\parallel}^t , is shown for comparison.

equilibrium case, but they are shown for comparison with the coefficients due to the tail electrons.

The most striking aspect of Fig. 2 is the strength of the tail interaction at large velocities, $v > \bar{v}_i$. This strength is much larger than the density ratio would predict. The physical reason for this behavior is that because the wave emission and the wave damping are both proportional to the density of the population, and because both are retained in the two-dimensional description, this density dependence cancels out for large velocities.⁷ As v decreases, the damping due to the tail electrons increases more rapidly than the damping due to the bulk electrons (because $\bar{v}_i > \bar{v}_e$, and both are exponential). This continues until the damping due to the tail saturates near $v \approx \bar{v}_i$. In this region, the damping due to the bulk electrons becomes appreciable, and the largest term becomes the electron damping term. For $v \approx \bar{v}_e$, the bulk damping dominates the tail damping and the coefficients due to the tail electrons revert to scaling linearly with density.

The density dependence of the coefficients due to the tail electrons is shown in Fig. 3. This figure shows the strength of the coefficients for $v = 5\sqrt{2}\bar{v}_e$ as a function of the tail density, n_i . It can be seen that on a logarithmic scale, A_{\parallel}^t and D_{\parallel}^t vary only linearly, while D_{\perp}^t exhibits a modicum of exponential behavior, which implies a stronger density dependence.

Comparison with Three Dimensions

Ware² derived a Fokker–Planck equation for the parallel distribution function of fast electrons in a three-dimensional, strongly magnetized plasma ($\omega_{ce} \gg \omega_{pe}$) due to wave emission and damping. He considered only the higher-order terms usually ignored by the dominant approximation in three dimensions, but which are similar in character to the lowest-order term that appears in two dimensions, and obtained the same behavior as in two dimensions. This shows that the enhanced interaction is due to the wave-driven transport, rather than an anomaly of the choice of only two dimensions.

In addition, Tidman and Eviatar³ showed that for large test-particle velocities (i.e., $v > \bar{v}_e$), the correction to $\ln \Lambda$ is exactly equivalent in form (Landau damping in the denominator)

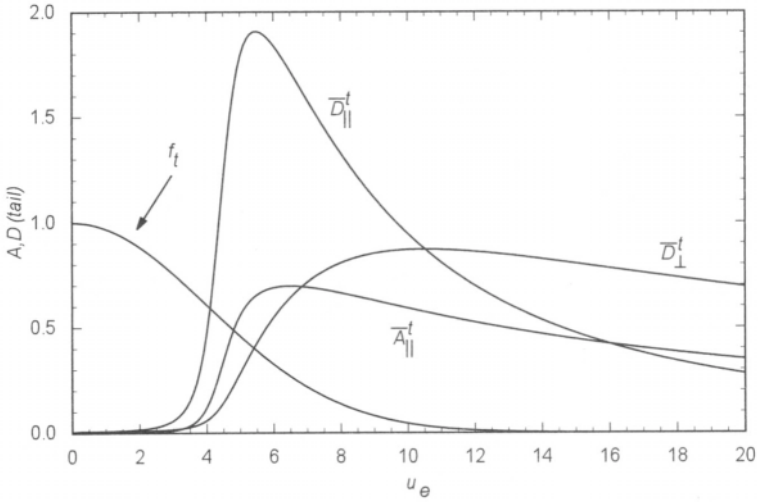


Figure 2. Contribution of the tail electrons to the Fokker–Planck coefficients of a test electron in a nonequilibrium two-dimensional plasma as a function of $u_e = v/\sqrt{2}\bar{v}_e$. The ion-to-electron mass ratio is 64, $n_t/n_e = 0.01$, and $\bar{v}_t^2/\bar{v}_e^2 = 16$. The distribution function of the tail electrons, f_t , is shown for comparison.

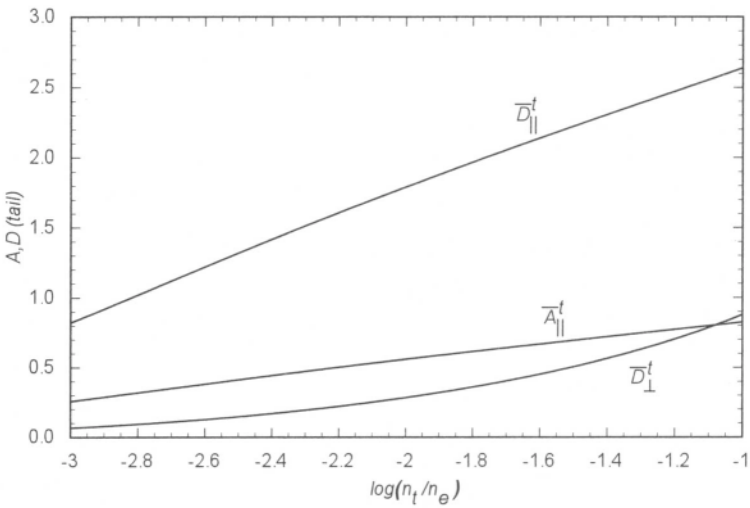


Figure 3. Contribution of the tail electrons to the Fokker–Planck coefficients of a test electron in a nonequilibrium two-dimensional plasma, plotted as functions of the logarithm (base 10) of the tail density. The ion-to-electron mass ratio is 64, $v = 5\sqrt{2}\bar{v}_e$, and $\bar{v}_t^2/\bar{v}_e^2 = 16$.

to that of Ware.² They also showed that for fast electrons, the 90° deflection time is much shorter than the energy loss time, which means that the enhanced fluctuations scatter the fast electrons more quickly than they equilibrate with the bulk electrons. Because this process is the dominant one in two dimensions, this is the probable explanation for the two-dimensional particle simulation results of Decyk *et al.*¹¹

CONCLUSION

We have investigated an effect that is inherent to weakly stable plasmas: an enhanced large-velocity interaction. This behavior is not unique to two dimensions, but is quite similar to the higher-order terms in a three-dimensional dominant approximation expansion, as shown in the studies of Ware² and of Tidman and Eviatar.³ The increased level of fluctuations generated by fast electrons is quite similar in both two and three dimensions. However, because both the emission and absorption of fluctuations by fast electrons is retained by the two-dimensional Fokker–Planck theory to lowest order (no dominant approximation is needed), these electrons interact at a significantly higher level than predicted by an extrapolation based on the usual three-dimensional dominant calculation. Small-angle collisions do not dominate in two dimensions, and the soft core of the logarithmic potential implies that any enhanced fluctuations affect the transport significantly. In three dimensions, a substantial tail would be necessary before a corresponding effect is observed.^{4,5} These results are essential to a complete understanding of two-dimensional particle simulations, especially those of weakly stable plasmas.

REFERENCES

- [1] S. Chandrasekhar, *Rev. Mod. Phys.* **15**, 1 (1943).
- [2] A. A. Ware, *Phys. Fluids B* **5**, 2769 (1993).
- [3] D. A. Tidman and A. Eviatar, *Phys. Fluids* **8**, 2059 (1965).
- [4] F. Perkins and E. E. Salpeter, *Phys. Rev.* **139**, A55 (1965).
- [5] G. Joyce, D. Montgomery and C Roqué, *Phys. Fluids* **10**, 2399 (1967).
- [6] A. Lenard, *Ann. Phys. (N. Y.)* **3**, 390 (1960).
- [7] M. A. Reynolds, B. D. Fried and G. J. Morales, *Phys. Plasmas* **4**, 1286 (1997).
- [8] B. D. Fried, in *Plasma Physics in Theory and Application*, edited by W. B. Kunkel (McGraw-Hill, New York, 1966), Chapter 3.
- [9] B. Abraham–Shrauner, *Physica* **43**, 95 (1969).
- [10] S. Ichimaru, *Basic Principles of Plasma Physics: A Statistical Approach* (W. A. Benjamin, Reading, MA, 1973), Chapter 10.
- [11] V. K. Decyk, G. J. Morales and J. M. Dawson, in *Proc. IAEA Technical Committee Mtg. on Non-inductive Current Drive in Tokamaks, 1983*, edited by D. F. H. Start (Euratom/UKAEA Association, 1983), Vol. I, p. 190.

This page intentionally left blank

PAIR CORRELATION FUNCTION AND NONLINEAR KINETIC EQUATION FOR A SPATIALLY UNIFORM POLARIZABLE NONIDEAL PLASMA

V. V. Belyi,¹ Yu. A. Kukhareno,² and J. Wallenborn³

¹IZMIRAN

Troitsk, Moscow region, 142092, Russia

²UITPRAN

Moscow, Russia

³Physique statistique, Plasma et Optique non linéaire,

CP 231, Université Libre de Bruxelles, 1050, Bruxelles, Belgium

The importance of the polarization effects on plasmas in the kinetic regime has been recognized for a long time. In 1960, Balescu¹ and Lenard² derived their famous kinetic equation valid for weakly coupled polarizable plasmas.

However, Kadanoff and Baym³ and Klimontovich⁴ have noticed that the Balescu–Lenard (BL) equation takes into account the polarization of the system only in the collision integral while the thermodynamics corresponds to the ideal gas: the dissipative and nondissipative phenomena are not treated on an equal footing. They have shown that this discrepancy can be avoided if non-Markovian effects are taken into account. Klimontovich⁵ wrote the system of equations for the one-particle distribution function (*df*) and the pair correlations for the electric field and for the charge density, but he did not succeed in obtaining a closed kinetic equation. On the other hand, Résibois⁶ and Dorfman and Cohen⁷ have formally derived the fully non-Markovian generalization of the BL equation, but their results are not easily tractable in practical case. Still recently, papers on non-Markovian kinetic equations were published. They treat the first density correction to the Uehling–Uhlenbeck equation⁸ and the case of the quantum Landau equation.⁹

We have obtained¹⁰ a nonlinear kinetic equation which generalizes the BL equation for weakly nonideal plasma. This equation includes the dynamical screening of the interaction potential and describes correctly the conservation of the total (kinetic and potential) energy in a nontrivial way.

We have considered a spatially-uniform weakly nonideal multicomponent plasma. Out of equilibrium, its evolution can be described by a kinetic equation which is derived from the BBGKY-hierarchy by making the so-called plasma approximation: triple correlation function as well as interaction between correlated particles are neglected. In this way, the set of equations for the one-particle d.f. $f_a(\mathbf{p}_1, t)$ and for the pair correlation function $g_{ab}(\mathbf{p}_1, \mathbf{p}_2, \mathbf{r}_1, \mathbf{r}_2, t)$ is closed. In Fourier space, they take the form:

$$\frac{\partial}{\partial t} f_a(\mathbf{p}_1, t) = J_a(\mathbf{p}_1, t) = -\frac{i}{8\pi^3} \sum_b \int d\mathbf{k} d\mathbf{p}_2 \Phi_{ab}(\mathbf{k}) \mathbf{k} \cdot \frac{\partial}{\partial \mathbf{p}_1} g_{ab}(\mathbf{p}_1, \mathbf{p}_2, \mathbf{k}, t), \quad (1)$$

where $J_a(\mathbf{p}_1, t)$ is the collision integral and where $g_{ab}(\mathbf{p}_1, \mathbf{p}_2, \mathbf{k}, t)$ is the solution of the equation

$$\begin{aligned} & \left[\frac{\partial}{\partial t} + i\mathbf{k} \cdot (\mathbf{v}_1 - \mathbf{v}_2) \right] g_{ab}(\mathbf{p}_1, \mathbf{p}_2, \mathbf{k}, t) - i\mathbf{k} \cdot \frac{\partial}{\partial \mathbf{p}_1} f_a(\mathbf{p}_1, t) \sum_c \Phi_{ac}(\mathbf{k}) \\ & \times \int d\mathbf{p}_3 g_{bc}(\mathbf{p}_2, \mathbf{p}_3, \mathbf{k}, t) + i\mathbf{k} \cdot \frac{\partial}{\partial \mathbf{p}_2} f_b(\mathbf{p}_2, t) \sum_c \Phi_{bc}(\mathbf{k}) \int d\mathbf{p}_3 g_{ac}(\mathbf{p}_1, \mathbf{p}_3, \mathbf{k}, t) \\ & = i\Phi_{ab}(\mathbf{k}) \mathbf{k} \cdot \left(\frac{\partial}{\partial \mathbf{p}_1} - \frac{\partial}{\partial \mathbf{p}_2} \right) f_a(\mathbf{p}_1, t) f_b(\mathbf{p}_2, t) \end{aligned} \quad (2)$$

$\Phi_{ab}(\mathbf{k}) = \frac{4\pi e_a e_b}{k^2}$ is the Fourier transform of the Coulomb potential and $\mathbf{v}_1 = \frac{\mathbf{p}_1}{m_a}$ is the velocity of particle 1.

By doing the plasma approximation and then solving eqs. (1) and (2), we neglect Markovian contributions of order two in the plasma parameter. These contributions would lead to small quantitative corrections to the relaxation time of one-particle df. If necessary they can be added to our results without qualitative change.

Although eq. (2) is an integro-differential equation with variable coefficients, the so-called Green's function method¹¹ allows to disentangle the time-scales and gives a solution in terms of successive derivatives with respect to time on the scale of the one-particle df.¹⁰ Successive derivatives correspond to successive approximations of the non-Markovian effects.

We considered only the Markovian limit of the solution and its first non-Markovian correction (i.e., the first time-derivative). Let us point out that it is not a trivial approximation since it leads to the total energy conservation.

Specifically we obtain:

$$g_{ab}(\mathbf{p}_1, \mathbf{p}_2, \mathbf{k}, t) = g_{ab}^0(\mathbf{p}_1, \mathbf{p}_2, \mathbf{k}, t) + g_{ab}^1(\mathbf{p}_1, \mathbf{p}_2, \mathbf{k}, t) \quad (3)$$

where $g_{ab}^0(\mathbf{p}_a, \mathbf{p}_b, t)$ is the well known result of Markovian theory:^{11, 13}

$$g_{ab}^0(\mathbf{p}_1, \mathbf{p}_2, \mathbf{k}, t) = i\pi \delta_-(\mathbf{k} \cdot \mathbf{v}_1 - \mathbf{k} \cdot \mathbf{v}_2) G_{ab}(\mathbf{p}_1, \mathbf{p}_2, \mathbf{k}, t) \quad (4)$$

with

$$\begin{aligned} G_{ab}(\mathbf{p}_1, \mathbf{p}_2, \mathbf{k}, t) = & \Phi_{ab}(\mathbf{k}) \left\{ \frac{1}{\varepsilon(\mathbf{k} \cdot \mathbf{v}_2, \mathbf{k})} f_b(\mathbf{p}_2, t) \mathbf{k} \cdot \frac{\partial}{\partial \mathbf{p}_1} f_a(\mathbf{p}_1, t) \right. \\ & - \frac{1}{\varepsilon^*(\mathbf{k} \cdot \mathbf{v}_1, \mathbf{k})} f_a(\mathbf{p}_1, t) \mathbf{k} \cdot \frac{\partial}{\partial \mathbf{p}_2} f_b(\mathbf{p}_2, t) - \sum_c i\pi \int d\mathbf{p}_3 \frac{\Phi_{cc}(\mathbf{k})}{|\varepsilon(\mathbf{k} \cdot \mathbf{v}_3, \mathbf{k})|^2} \\ & \times [\delta_+(\mathbf{k} \cdot \mathbf{v}_3 - \mathbf{k} \cdot \mathbf{v}_1) + \delta_+(\mathbf{k} \cdot \mathbf{v}_2 - \mathbf{k} \cdot \mathbf{v}_3)] f_c(\mathbf{p}_3, t) \\ & \left. \times \mathbf{k} \cdot \frac{\partial}{\partial \mathbf{p}_1} f_a(\mathbf{p}_1, t) \mathbf{k} \cdot \frac{\partial}{\partial \mathbf{p}_2} f_b(\mathbf{p}_2, t) \right\} \end{aligned} \quad (5)$$

and

$$\varepsilon(\mathbf{k} \cdot \mathbf{v}, \mathbf{k}) = 1 - i\pi \sum_a \Phi_{aa}(\mathbf{k}) \int d\mathbf{p} \delta_+(\mathbf{k} \cdot \mathbf{v} - \mathbf{k} \cdot \mathbf{v}_1) \mathbf{k} \cdot \frac{\partial}{\partial \mathbf{p}_1} f_a(\mathbf{p}_1, t) \quad (6)$$

is the dynamical dielectric function. We also used the conventional notations: $i\pi \delta_-(\mathbf{x}) = \frac{1}{x-i0} = i\pi \delta(\mathbf{x}) + \frac{P}{x}$, $-i\pi \delta_+(\mathbf{x}) = \frac{1}{x+i0} = -i\pi \delta(\mathbf{x}) + \frac{P}{x}$, where P means the Cauchy principal part. It can be shown that expression (4) reduces at equilibrium to the Debye-Hückel pair

correlation function. The non-Markovian correction to the pair correlation function is:

$$\begin{aligned}
g_{ab}^1(\mathbf{p}_1, \mathbf{p}_2, \mathbf{k}, t) = & i \frac{\partial}{\partial t} \left\{ i \pi \delta'_-(\mathbf{k} \cdot \mathbf{v}_1 - \mathbf{k} \cdot \mathbf{v}_2) G_{ab}(\mathbf{p}_1, \mathbf{p}_2, \mathbf{k}, t) \right. \\
& + \sum_c \frac{\Phi_{bc}(\mathbf{k})}{\varepsilon^*(\mathbf{k} \cdot \mathbf{v}_1, \mathbf{k})} i \pi \delta_-(\mathbf{k} \cdot \mathbf{v}_1 - \mathbf{k} \cdot \mathbf{v}_2) \mathbf{k} \cdot \frac{\partial}{\partial \mathbf{p}_2} f_b(\mathbf{p}_2, t) \int d\mathbf{p}_3 i \pi \delta'_-(\mathbf{k} \cdot \mathbf{v}_1 - \mathbf{k} \cdot \mathbf{v}_3) \\
& \times G_{ac}(\mathbf{p}_1, \mathbf{p}_3, \mathbf{k}, t) - \sum_c \frac{\Phi_{ac}(\mathbf{k})}{\varepsilon(\mathbf{k} \cdot \mathbf{v}_2, \mathbf{k})} i \pi \delta_-(\mathbf{k} \cdot \mathbf{v}_1 - \mathbf{k} \cdot \mathbf{v}_2) \mathbf{k} \cdot \frac{\partial}{\partial \mathbf{p}_1} f_a(\mathbf{p}_1, t) \\
& \times \int d\mathbf{p}_3 i \pi \delta'_-(\mathbf{k} \cdot \mathbf{v}_3 - \mathbf{k} \cdot \mathbf{v}_2) G_{cb}(\mathbf{p}_3, \mathbf{p}_2, \mathbf{k}, t) + \sum_{cd} i \pi \frac{P}{(\mathbf{k} \cdot \mathbf{v}_1 - \mathbf{k} \cdot \mathbf{v}_2)} \Phi_{ac}(\mathbf{k}) \Phi_{bd}(\mathbf{k}) \\
& \times \int d\mathbf{p}_3 \left[\frac{\delta_-(\mathbf{k} \cdot \mathbf{v}_3 - \mathbf{k} \cdot \mathbf{v}_1)}{|\varepsilon(\mathbf{k} \cdot \mathbf{v}_1, \mathbf{k})|^2} + \frac{\delta_-(\mathbf{k} \cdot \mathbf{v}_3 - \mathbf{k} \cdot \mathbf{v}_2)}{|\varepsilon(\mathbf{k} \cdot \mathbf{v}_2, \mathbf{k})|^2} \right] \mathbf{k} \cdot \frac{\partial}{\partial \mathbf{p}_1} f_a(\mathbf{p}_1, t) \mathbf{k} \cdot \frac{\partial}{\partial \mathbf{p}_2} f_b(\mathbf{p}_2, t) \\
& \left. \times \int d\mathbf{p}_4 i \pi \delta'_-(\mathbf{k} \cdot \mathbf{v}_3 - \mathbf{k} \cdot \mathbf{v}_4) G_{cd}(\mathbf{p}_3, \mathbf{p}_4, \mathbf{k}, t) \right\} \quad (7)
\end{aligned}$$

where $\delta'_-(\mathbf{x})$ is the derivative of $\delta_-(\mathbf{x})$. Finally, the correction to the collision integral is obtained from Eq. (1):

$$J_a^1(\mathbf{p}_1, t) = -\frac{i}{8\pi^3} \sum_b \int d\mathbf{k} d\mathbf{p}_2 \Phi_{ab}(\mathbf{k}) \mathbf{k} \cdot \frac{\partial}{\partial \mathbf{p}_1} g_{ab}^1(\mathbf{p}_1, \mathbf{p}_2, \mathbf{k}, t). \quad (8)$$

The conservation laws are easily verified with the following symmetry property in mind:

$$g_{ab}(\mathbf{p}_1, \mathbf{p}_2, \mathbf{k}, t) = g_{ba}(\mathbf{p}_2, \mathbf{p}_1, -\mathbf{k}, t). \quad (9)$$

The particle conservation is a trivial consequence of expression (1) while the momentum conservation follows directly from eqs. (1) and (9). We know that kinetic energy is conserved by $J_a^0(\mathbf{p}_1, t)$, the Balescu–Lenard collision integral. Therefore, the variation of the kinetic energy is due to the non-Markovian part of the collision integral $J_a^1(\mathbf{p}_1, t)$:

$$\partial_t \sum_a \left\langle \frac{\mathbf{p}_1^2}{2m_a} \right\rangle = -\frac{1}{8\pi^3} \frac{1}{2} \sum_{ab} \int d\mathbf{k} d\mathbf{p}_1 d\mathbf{p}_2 \Phi_{ab}(\mathbf{k}) (\mathbf{k} \cdot \mathbf{v}_1 - \mathbf{k} \cdot \mathbf{v}_2) g_{ab}^1(\mathbf{p}_1, \mathbf{p}_2, \mathbf{k}, t), \quad (10)$$

where we used Eq. (9). The three last terms of r.h.s. of Eq. (7) give no contribution to r.h.s. of Eq. (10) since they are proportional to $\int d\mathbf{p} \frac{\partial}{\partial \mathbf{p}} f_\alpha(\mathbf{p}, t) = 0$. The first term leads to:

$$\partial_t \sum_a \left\langle \frac{\mathbf{p}_1^2}{2m_a} \right\rangle = -\partial_t \frac{1}{8\pi^3} \frac{1}{2} \sum_{ab} \int d\mathbf{k} d\mathbf{p}_1 d\mathbf{p}_2 \Phi_{ab}(\mathbf{k}) g_{ab}^0(\mathbf{p}_1, \mathbf{p}_2, \mathbf{k}, t). \quad (11)$$

The r.h.s. of Eq. (11) is precisely minus the variation of the potential energy at the order of approximation we consider. It is easy to show that this potential energy becomes at equilibrium the Debye–Hückel energy.^{11–13} Equation (11) achieves the consistence of the theory.

REFERENCES

- [1] R. Balescu, Phys. of Fluids **3**, 52 (1960)
- [2] A. Lenard, Ann. Phys.(N. Y.) **10**, 390, (1960)
- [3] L. P. Kadanoff and G. Baym, *Quantum statistical mechanics* (Benjamin, New York, 1964)
- [4] Yu. L. Klimontovich, *Kinetic theory of nonideal gases and nonideal plasmas* (Academic Press, New York, 1975)

- [5] Yu. L. Klimontovich, Sov. Phys. JETP **35**, 920 (1972)
- [6] P. Résibois Phys. of Fluids, **6**, 817 (1963)
- [7] J. R. Dorfman, E. G. D. Cohen, Int. J. Quantum Chem. **16**, 63 (1982)
- [8] K. Morawetz, and G. Roepke, Phys. Rev. E **51**,4246 (1995)
- [9] K. Morawetz, R. Walke, G. Roepke, Phys. Lett. A **190**, 96 (1994); M. Bonitz, D. C. Scott, R. Binder, D. Kremp, W. D. Kraeft, H. S. Köhler in *Proceedings of the International Conference on the Physics of Strongly Coupled Plasmas*, Binz 1995 (World Scientific, Singapore, 1996)
- [10] V. V. Belyi, Yu. A. Kukhareenko and J. Wallenborn, Phys. Rev. Lett. **76**, 3554 (1996); V. V. Belyi, Yu. A. Kukhareenko and J. Wallenborn, *submitted to J. Plasma Physics*.
- [11] R. Balescu, *Statistical mechanics of charged particles* (Wiley, New York, 1963)
- [12] S. Ichimaru, *Basic principles of plasma physics* (Benjamin, New York, 1973)
- [13] G. Kalman, in *Plasma Physics-Les Houches 1972*, edited by C. DeWitt (Gordon and Beach, New York, 1975)

BOUND STATES IN STRONGLY COUPLED PLASMAS

D. Kremp,¹ W.-D. Kraeft,² and M. Schlanges²

¹Department of Physics of the University of Rostock
18051 Rostock, Germany

²Institute of Physics of the University of Greifswald
17487 Greifswald, Germany

INTRODUCTION

The structuring of matter is connected with the formation of bound states and phase transitions. Therefore, the consideration of bound states in strongly correlated many particle systems is an essential task.

In this talk, we want to deal with bound states in a strongly correlated hydrogen plasma. In particular, we want to investigate the influence of bound states on two-particle quantities such as the T matrix, the two-particle Green's function g_{ab} , and the single particle spectrum.

By an elementary theory, the formation of atomic bound states is described by the Schrödinger equation for an isolated electron-proton pair. It is clear that the bound states influence all plasma properties, such as, e.g., the equation of state (EOS). The bound state contribution to the EOS is given by the bound state part of the second virial coefficient¹⁻³

$$B_{ep}^{bound} = 4\pi^{3/2} \lambda_{ep}^3 \sum_{n=1}^{\infty} n^2 e^{-\beta E_n} \quad (1)$$

with $E_n = -Ry/n^2$ and $\lambda_{ep} = \hbar/(2m_{ep}k_B T)^{1/2}$. It is well known that this contribution is divergent. The reason is clear: We neglected completely the influence of the surrounding plasma on the $e-p$ pair. A simple idea to take into account the influence of the medium is to replace the Coulomb potential by a screened one, and, instead of the kinetic energy, we have to take the single particle energy, i.e., we have to add the Debye quasi-particle shift $\Delta_e = \Delta_p = -\kappa e^2/2$ with $\kappa = (8\pi e^2 n_e / (k_B T))^{1/2}$.⁴ In this way we obtained an EOS, which works very well. After a transformation into the chemical picture, the EOS describes the ionization equilibrium and the plasma phase transition.³

BOUND STATES, T-MATRIX ONE PARTICLE EXCITATION SPECTRUM

Let us consider the bound states from a more rigorous point of view. In general, we have to deal with two questions. How do bound states influence the plasma properties?, and how are the bound states modified by the surrounding plasma? For the consideration of this

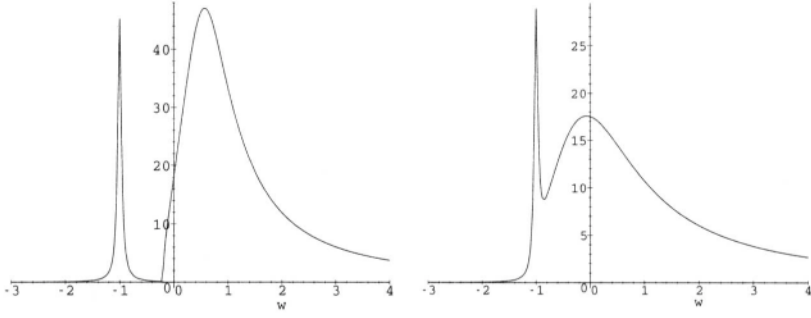


Figure 1. a,b Imaginary part of the off-shell T-matrix for initial and final relative momenta $p = p' = 1$, and $\cos(\vec{p}, \vec{p}') = 0, 7$, $\kappa = 0, 1$ (a) and $\cos(\vec{p}, \vec{p}') = 0, 8$, $\kappa = 0, 5$ (b).

problem, we use the formalism of Green's functions being an appropriate tool. From the point of view of Green's functions, the properties of strongly coupled plasmas are determined by the single particle spectral function

$$a(p\omega) = \frac{\Gamma(p\omega)}{\left(\omega - \frac{p^2}{2m} - \text{Re}\Sigma^R(p\omega)\right)^2 + \frac{\Gamma^2(p\omega)}{4}}, \quad (2)$$

where $\Gamma = 2\text{Im}\Sigma^R$ is the damping of the single particle states which is related to $\text{Re}\Sigma^R$ by a dispersion relation. To include bound states we have to apply Γ in the screened ladder approximation. In this approximation, we find

$$\Gamma(p_1\omega) = \int \frac{dp_2}{(2\pi)^3} 2\text{Im}\langle p_1 p_2 | T^R(\omega + E(p_2)) | p_2 p_1 \rangle \{n_B(\omega + E(p_2)) + f(E(p_2))\}. \quad (3)$$

One can see that Γ and, consequently, the most properties of the strongly coupled plasma are given by the off-shell T -matrix, or, equivalently, by the two particle Green's function according to $T^R(\omega + i\epsilon) = V g_{12}^R(\omega + i\epsilon) V$. On the other hand, the two-particle Green's function and its singularities incorporate the influence of the plasma on the bound states. We determine the two-particle Green's function g_{ep} in the dynamically screened ladder approximation, i.e., from the Bethe Salpeter equation. In momentum representation, we have³

$$\left\{ E_e(p_1) + E_p(p_2) + \Delta_{ep}^R(p_1 p_2 \omega) - \omega \right\} g_{ep}^R(p_1 p_2 p'_1 p'_2 \omega) - N_{ep} \int \frac{dq}{(2\pi)^3} V_{ep}^{eff,R} g_{ep}^R(p_1 - q, p_2 + q, p'_1 p'_2 \omega) = N_{ep} (2\pi)^6 \delta(p_1 - p'_1) \delta(p_2 - p'_2). \quad (4)$$

Here the effective two particle interaction is given by [6]

$$V_{ep}^{eff,R} = V_{ep}^{eff,R}(p_1 p_2 q \omega) = V_{ep}(q) - V_{ep}(q) \int \frac{d\omega'}{2\pi} \text{Im}\epsilon^{-1}(q\omega) \times \left\{ \frac{1 + n_B(\omega')}{\omega - \omega' - E_p(p_2) - E_e(p_1 - q) \pm i\epsilon} + \frac{n_B(\omega')}{\omega + \omega' - E_e(p_1) - E_p(p_2 + q)} \right\}, \quad (5)$$

and the effective two particle self energy shift reads

$$\Delta_{ep}^R(p_1 p_2 \omega) = \int \frac{dq}{(2\pi)^3} \Delta V_{ep}^{eff,R}(p_1 p_2 q \omega) N_{ep}(p_1 - q, p_2 + q). \quad (6)$$

The blocking factor is $N_{ep}(p_1 p_2) = 1 - f_e(p_1) - f_p(p_2)$. So, in Eq. (4) we took into account correlation effects such as dynamical screening, self energy, retardation, and Pauli blocking.

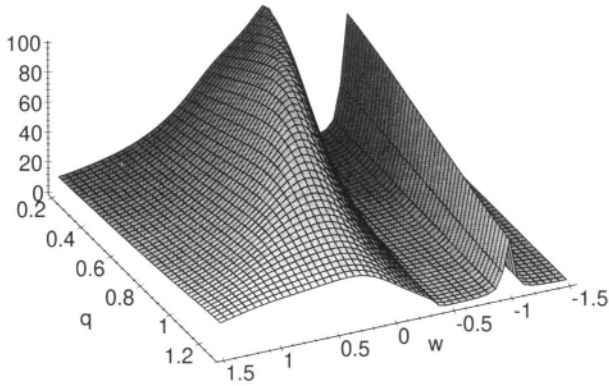


Figure 2. Momentum–energy surface of the imaginary part of the off-shell T-matrix for $p = 0, 8$, $\kappa = 0, 2$, $\cos(\bar{p}, \bar{p}') = 0, 7$

Starting from (4), let us now determine the two particle properties. To this end, we perform a perturbative solution of the Bethe Salpeter equation in the limit of static screening, i.e., instead of the dynamical quantities in (4), we use the statically screened Coulomb potential and the static Debye-shift. On this level, the imaginary part of the off shell T -Matrix $\langle p|T(\omega)|p' \rangle$ was determined for different screening parameters κ , see also [7]. The results for the imaginary part are given in fig. 1a,b.

The bound state manifests itself as a peak separated from the continuum, which is lowered with increasing density. We find that the position of the peak and therefore the bound state energy is weakly density dependent only. The width of the bound state peak broadens, i.e., we have a finite life time. The momentum and energy dependencies of the imaginary part of the T -matrix are demonstrated in fig. 2.

Now we are able to determine the real part of the off-shell T-Matrix $\langle p|T(\omega)|p' \rangle$ from the dispersion relation

$$\text{Re}T(\omega) = V + \int \frac{d\bar{\omega}}{2\pi} \frac{\text{Im}T(\bar{\omega})}{\omega - \bar{\omega}}. \quad (7)$$

The result is shown in fig. 3.

We observe the typical principal value behavior at the peaks of the imaginary part at the bound state positions. Having determined the T -matrix, we obtained Γ from the relation (3) and displayed it in fig. 4.

Again, the bound state peak is separated from the continuum; a lowering of the latter is observed as a function of the screening. Now we come back to the spectral function (2). With Γ and $\text{Re}\Sigma^R$ being calculated from a dispersion relation, the spectral function is determined explicitly. The result is given in fig. 5. Here, the ideal spectral function is indicated for comparative purposes. One sees that the spectral function is strongly modified by correlation effects. The maximum is shifted, and the continuum is broadened, and we have a bound state satellite. Knowing the spectral function, one may determine thermodynamic functions.⁸⁻¹⁰

BOUND STATES IN NONEQUILIBRIUM PLASMAS

The situation is much more complicated in nonequilibrium plasmas with bound states. Again, the most plasma properties are determined by the spectral function which is given now by the two time correlation functions g^{\lessgtr} , i.e., $a(p\omega RT) = g^{\lessgtr}(p\omega RT) - g^{\gtrless}(p\omega RT)$. In nonequilibrium situations, these two functions are independent of each other,¹¹ and both have

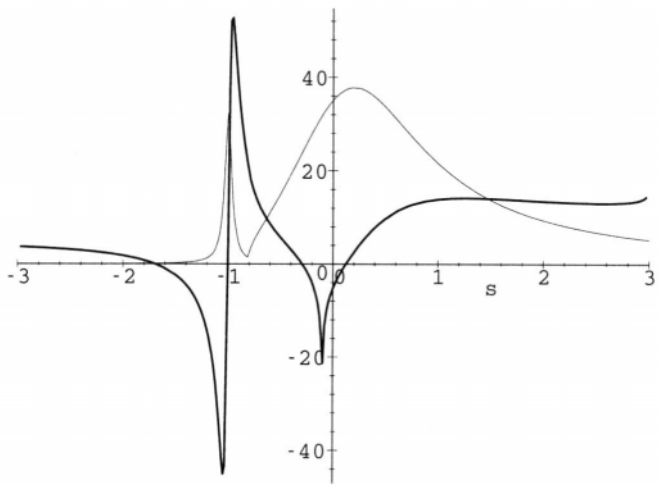


Figure 3. Real and imaginary parts of the off-shell T-matrix for $p = 1$, $p' = 1$, $\cos(\vec{p}, \vec{p}') = 1$, $\kappa = 0,4$

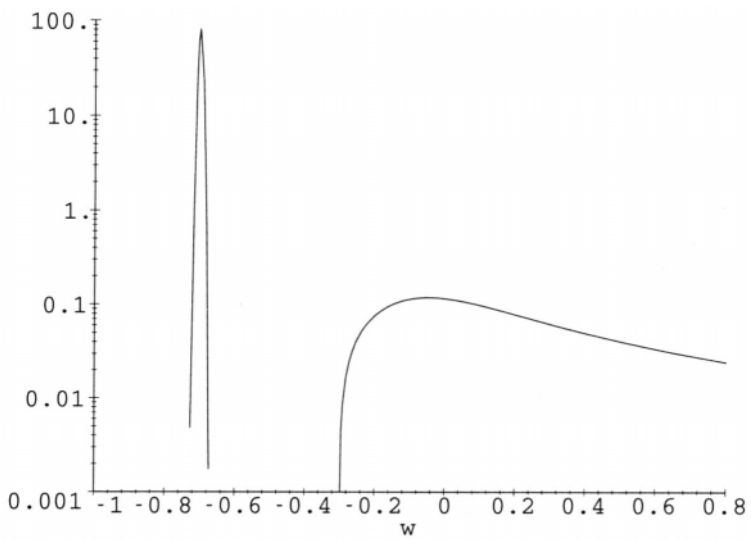


Figure 4. Imaginary part Γ of the self energy for $T = 20000$ K, $p = 0,5$, $\kappa = 0,45$

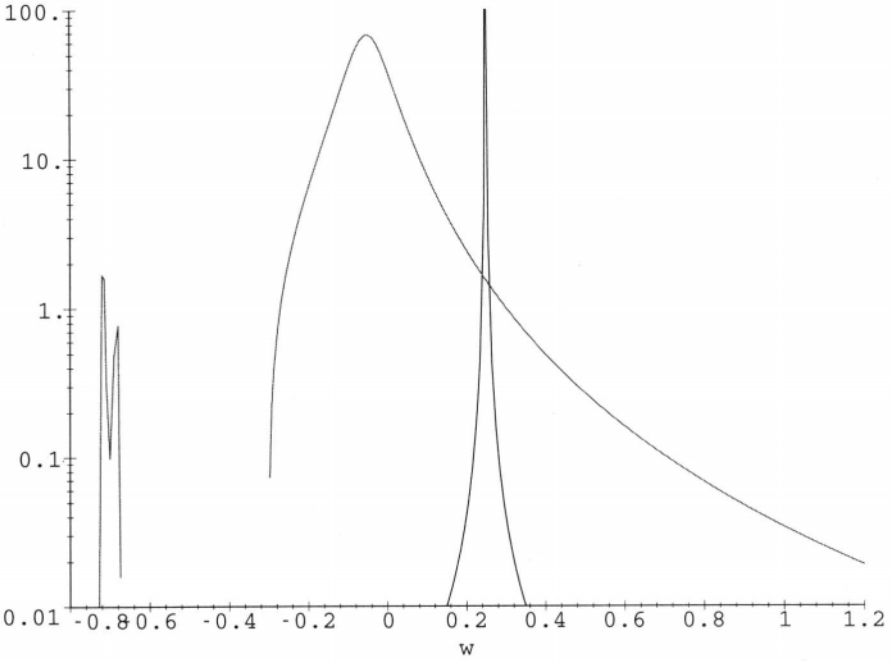


Figure 5. Spectral function for $T = 20000$ $Kp = 0,5$, $\kappa = 0,45$

to be determined from the well known *Kadanoff–Baym equations* which read

$$\left\{i \frac{\partial}{\partial t} + \frac{\nabla_1^2}{2m} + U(1)\right\} g^{\geq}(11') = \int d\bar{1} \Sigma^{HF}(\bar{1}\bar{1}) g^{\geq}(\bar{1}\bar{1}') + \int_{-\infty}^{t_1} d\bar{1} [\Sigma^>(\bar{1}\bar{1}) - \Sigma^<(\bar{1}\bar{1})] g^{\geq}(\bar{1}\bar{1}') - \int_{-\infty}^{t_1} d\bar{1} \Sigma^{\geq}(\bar{1}\bar{1}) [g^>(\bar{1}\bar{1}') - g^<(\bar{1}\bar{1}')], \quad (8)$$

where the self energy and the two-particle Green's functions are related by

$$\int d\bar{1} \Sigma^<(\bar{1}\bar{1}) g^>(\bar{1}\bar{1}') = -i \int d2V(12) g_{12}^<(\bar{1}\bar{1}'2^+). \quad (9)$$

Obviously, again the two particle Green's function is the most important quantity. In order to determine the latter, we have to find a nonequilibrium generalization of the Bethe–Salpeter equation. For this goal, we use an idea of Keldysh. According to this idea, we have to consider the diagram representation of the Bethe–Salpeter equation on the *Keldysh-contour* instead on the physical time axis. In dynamically screened ladder approximation, and using the *Shindo approximation*, we get the following equation (in time representation)

$$\left(i \frac{\partial}{\partial t} - H_{ab}^0\right) g_{ab}(t, t') - \int d\bar{t} \Delta_{ab}(t, \bar{t}) g_{ab}(\bar{t}, t') = -i N_{ab}(t) \delta(t - t') + N_{ab}(t) \int d\bar{t} V_{ab}^{eff}(t, \bar{t}) g_{ab}(\bar{t}, t'). \quad (10)$$

In this equation, $g_{ab}(tt')$ and the other two time quantities are defined at the Keldysh contour. By positioning of the times t, t' at the branches of the contour, one gets the equations for the two-particle correlation functions g_{ab}^{\geq} , and for the causal and anticausal functions. In addition

to Eq. (10), we have to give an expression for the nonequilibrium effective two-particle potential. We found¹²

$$V_{ab}^{eff}(t, t') = V_{ab} \delta(t - t') + i N_{ab}^{-1}(t) \int d\bar{t}_1 d\bar{t}_2 d\bar{t} \left[g_a(t, \bar{t}_1) \delta(t - \bar{t}_2) + g_b(t, \bar{t}_2) \delta(t - \bar{t}_1) \right] \Delta V_{ab}^s(\bar{t}_1, \bar{t}_2) g_a(\bar{t}_1, \bar{t}) g_b(\bar{t}_2, \bar{t}) \mathcal{G}_{ab}^{-1}(\bar{t}, t'). \quad (11)$$

Correspondingly, we have for the nonequilibrium two particle shift¹²

$$\Delta_{ab}(t, t') = \int d\bar{t}_1 d\bar{t}_2 d\bar{t} \left[\bar{\Sigma}_a(t, \bar{t}_1) \delta(t - \bar{t}_2) + \bar{\Sigma}_b(t, \bar{t}_2) \delta(t - \bar{t}_1) \right] g_a(\bar{t}_1, \bar{t}) g_b(\bar{t}_2, \bar{t}) \mathcal{G}_{ab}^{-1}(\bar{t}, t'). \quad (12)$$

Equations (10)–(12) are the basis for the description of strongly correlated nonequilibrium plasmas with bound states. In nonequilibrium, the Bethe–Salpeter equation (10) and the Kadanoff–Baym equations (8) have to be solved self-consistently. Of course, this is an extremely difficult task. First results were achieved in this direction by developing methods for the numerical solution of the Kadanoff–Baym equations; see the contribution of *Bonitz and Kremp* at this conference.

Acknowledgements

This work was supported by the *Deutsche Forschungsgemeinschaft*, Sonderforschungsbereich 198 (Kinetik partiell ionisierter Plasmen).

REFERENCES

- [1] F. J. Rogers; Phys. Rev. **A4**,1145(1971); **A10**,2441(1970)
- [2] F. J. Rogers and H. E. DeWitt; Phys. Rev **A1**,1061(1973)
- [3] W. Ebeling, W. D. Kraeft and D. Kremp; *Theory of Bound States and Ionization Equilibrium in Plasmas and Solids*, Akademie-Verlag Berlin (1976)
- [4] W. Ebeling, W. D. Kraeft and D. Kremp; Invited lecture *Nonideal Plasmas*, held at the *International Conference on the Physics of Ionized Gases (ICPIG)*, Berlin 1977, p. 73
- [5] R. Zimmermann, M. K. Kilimann, W. D. Kraeft, D. Kremp and G. Röpke; phys stat sol (b) **90**,175(1978)
- [6] M. K. Kilimann, W. D. Kraeft and D. Kremp; Phys Letters **A61**,393(1977)
- [7] R. Fehr, PhD thesis, Greifswald 1997 (unpublished)
- [8] W. D. Kraeft, D. Kremp, W. Ebeling, and G. Röpke; *Quantum Statistics of Charged Particle Systems*, Akademie-Verlag Berlin and Plenum, London, New York, 1986
- [9] H. E. DeWitt, M. Schlanges, A. Y. Sakakura and W. D. Kraeft; Phys. Letters **A197**,326(1995)
- [10] J. Riemann, M. Schlanges, H. E. DeWitt and W. D. Kraeft; Physica **A219**,423(1995)
- [11] T. Bornath, D. Kremp, W. D. Kraeft and M. Schlanges; Phys. Rev. **E54**,3274(1996)
- [12] D. Kremp, M. Schlanges and W. D. Kraeft (in preparation)

RELEVANT ION TIME SCALES FOR ELECTRON IMPACT PROCESSES OF ATOMS IN DENSE PLASMAS

Michael S. Murillo

Mail Stop B259, XPA
Applied Theoretical Division
Los Alamos National Laboratory
Los Alamos, NM 87545
E-mail: murillo@lanl.gov

INTRODUCTION

It is now well known that collisional atomic processes in dense plasmas can be considered to arise from density fluctuation perturbations.¹⁻⁵ In particular, it is possible to describe these processes in terms of the dynamic structure factor (DSF) $S(\mathbf{k}, \omega)$, defined by

$$S(\mathbf{k}, \omega) = \int_{-\infty}^{\infty} d\tau e^{i\omega\tau} \langle n(\mathbf{k}, \tau) n(-\mathbf{k}, 0) \rangle, \quad (1)$$

which is a measure of the power spectrum of density fluctuations $n(\mathbf{k}, \tau)$. In the atomic transition problem, the DSF is evaluated at the atomic transition energy $\hbar\omega$ and the plasma density is taken as the plasma charge density which includes all species weighted by their charge. In such a Stochastic Model, interesting dynamic screening behavior arises as a result of different atomic transition energies sampling different frequency regimes, relative to the plasma frequency, of the DSF.

Electron impact processes, characterized by an electron one component plasma DSF, denoted $S_{ee}(\mathbf{k}, \omega)$, may typically be treated within the Born approximation since the electrons, which are light and typically hot, have a high average velocity. Under these conditions the rate can be written directly in terms of $S_{ee}(\mathbf{k}, \omega)$.³

For ion impact processes it is almost always the case that transition frequencies are well above the ion plasma frequency. The dominate behavior then arises from the high frequency limit of $S_{ii}(\mathbf{k}, \omega)$,

$$\lim_{\omega \rightarrow \infty} S_{ii}(\mathbf{k}, \omega) = \lim_{\omega \rightarrow \infty} \int_{-\infty}^{\infty} d\tau e^{i\omega\tau} \langle n_i(\mathbf{k}, \tau) n_i(-\mathbf{k}, 0) \rangle, \quad (2)$$

which has significant contributions only for small values of τ . That is, only *short* times are important in determining $S_{ii}(\mathbf{k}, \omega)$ in the high frequency limit. The treatment of ions is further complicated by the fact that ions can be highly charged. As such, ions cannot be treated in the same perturbative manner as the electrons.

In reality, of course, both electrons and ions simultaneously perturb the atoms so that the criteria governing the slow ions must be taken into account and included when treating electron collisions and vice versa. This prediction is in distinct contrast to previous work which either neglects the surrounding ions entirely or treats them within a thermally averaged potential, which corresponds to a *long*-time average. In summary, it is necessary to construct an electron collision description in which we can account for the following ion features:

- *Ion short-time behavior is important.* This follows directly from Eq. (2) if the transition energies are large. For smaller transition energies ion motion may be important. Here large transition energy $\hbar\omega$ is defined as having frequency ω greater than the ion plasma frequency.
- *Ions are relatively slow.* Due to their large mass, ions, including protons, move with velocity $v_i < v_e/40$ if the electron and ion temperatures are the same. In general, $v_i = v_e\sqrt{T_i m_e/T_e m_i}$.
- *Ions interact strongly.* Ions may be highly charged and move slowly; simple perturbative treatments (e.g., Born approximation) are typically not valid.

A SELF-CONSISTENT MODEL

A model is now presented in which ions are included in a calculation of electron impact processes. Care is taken to treat the ions in the manner discussed above. Estimates are made of the ionization potential depression (IPD) based on this model in the next section.

The atom–plasma Hamiltonian $H = H_0 + V$ can be written as

$$\begin{aligned} H_0 &= H_a + H_i + H_e + H_{ei} \\ V &= H_{ai} + H_{ae}, \end{aligned} \quad (3)$$

where H_a is the atomic Hamiltonian, H_i is the ion Hamiltonian, H_e is the electron Hamiltonian, H_{ei} is the electron–ion interaction Hamiltonian, H_{ai} is the atom–ion interaction Hamiltonian, and H_{ae} is the atom–electron Hamiltonian. The eigenstates of H_0 are defined by

$$H_0|\text{atom}_n\rangle|\text{plasma}_m\rangle = (E_n + E_m)|\text{atom}_n\rangle|\text{plasma}_m\rangle. \quad (4)$$

The probability that there has been a transition from some initial state $|i\rangle = |\text{atom}_n\rangle|\text{plasma}_m\rangle$ to final state $|f\rangle = |\text{atom}_p\rangle|\text{plasma}_q\rangle$ at time t later is

$$P(t) = \left| \langle f | \frac{1}{2\pi i} \oint_c dz e^{-izt} G(z) | i \rangle \right|^2. \quad (5)$$

The contour c encloses the real axis counterclockwise and $G(z) = (z - H)^{-1}$ is the Hamiltonian resolvent. The interesting matrix elements are thus those of $G(z)$.

Fortunately, it is possible to formally obtain the matrix elements $G_{fi}(z) \equiv \langle f | G(z) | i \rangle$ exactly thereby keeping terms to infinite order in the interaction V . The matrix element is written in terms of the level shift operator

$$R(z) = V + V \frac{Q}{Q(z - H)Q} V \quad (6)$$

as

$$G_{fi}(z) = \frac{R_{fi}}{(z - [E_f + R_{ff}])(z - [E_i + R_{ii}]) - R_{if}R_{fi}}, \quad (7)$$

where $Q = 1 - |f\rangle\langle f| - |i\rangle\langle i|$ is the projection onto states other than $|i\rangle$ and $|f\rangle$. This is the central result of this paper which indicates how energy level shifts due to both electrons and ions arise in a self-consistent transition calculation. (Note that the energy level shifts R_{ff} and R_{ii} are generally complex, as is R_{fi} .) This technique also has found wide applicability in quantum optics.⁶ We now estimate the IPDs based on the considerations so far.

PREDICTIONS FOR IONIZATION POTENTIAL DEPRESSION

Consider now a simple model for electron impact ionization of a hydrogenic ion with nuclear charge Z . Note that the matrix element $G_{fi}(z)$ describes transitions arising from both electrons and ions since $V = H_{ai} + H_{ae}$. To isolate the electron impact contribution from the ion impact contribution, only H_{ae} is retained in $R_{fi}(z)$. This describes electron impact transitions in the presence of the electrons and ions which contribute to $R_{ff}(z)$ and $R_{ii}(z)$. (Similarly, we could keep H_{ai} in $R_{fi}(z)$ to describe ion impact processes in the presence of electrons and ions. In either case the $H_{ai} - H_{ae}$ interference term is being ignored, which is a consequence of treating the two processes as distinct.)

A complication arises from the term H_{ei} , which couples the electron and ion subsystems. To obtain simple estimates for the level shifts, we include this coupling approximately by writing

$$\begin{aligned} H_{ae} + H_{ai} &\approx e^2 \int d^3r \frac{\delta n_e(\mathbf{r}')}{|\mathbf{r} - \mathbf{r}'|} - e \sum_i \Phi_i(|\mathbf{r} - \mathbf{r}_i|) \\ &\approx e^2 \int d^3r \frac{\delta n_e(\mathbf{r}')}{|\mathbf{r} - \mathbf{r}'|} - e\Phi(0) - e\mathbf{r} \cdot \nabla\Phi(0) - \frac{e}{2} \sum_{ij} x_i x_j \frac{\partial^2 \Phi(0)}{\partial x_i \partial x_j} + \dots, \end{aligned} \quad (8)$$

where the $\Phi_i(|\mathbf{r} - \mathbf{r}_i|)$ are the potentials arising from statically (electron) screened ions and $\delta n_e(\mathbf{r}')$ represents electron density fluctuations. The first term will be retained in $R_{fi}(z)$ which isolates electron impact processes. The levels are modified by both terms, but mostly the strong interactions of the screened ion terms, and are included in $R_{ff}(z)$ and $R_{ii}(z)$. For very slowly moving ions, H_i can be neglected and the ion configuration is the same for both the initial and final states. Since we don't know the given ion configuration, an average over ion configurations is taken at the end of the calculation. In the second equation, the total potential $\Phi(\mathbf{r}) = \sum_i \Phi_i(|\mathbf{r} - \mathbf{r}_i|)$ due to the screened ions has been expanded in a multipole expansion about small r . This approximate form is useful for *tightly bound* states and allows one to average over the microfield distribution $P(\boldsymbol{\epsilon})$ to account for the various ion configurations.¹ For less localized states, continuum states in particular, the full form of the interaction must be used. It is clear that, in either case, the screened ion microfield is largely responsible for the level shifts whereas the electrons represent a stochastic perturbation; we thus refer to this model as the ‘‘Microfield Stochastic Model’’ (MSM).

Consider now an ionization process from an $n = 2$ level to a plane wave state $|\mathbf{q}\rangle$ in an approximation where $R \approx V$. Ignoring the monopole term $-e\Phi(0)$, the first order energy correction to the bound state arises from the total electric field $\boldsymbol{\epsilon}$ of the perturbing screened ions. Since the $n = 2$ level has angular momentum degeneracy, care must be taken in evaluating the energy level shift. This will, of course, give rise to the well-known Stark shifts⁷ of the bound state levels. Thus we see that the $n = 2$ sublevels *will not be shifted equally*: some levels will move toward the continuum (become less tightly bound) and others move away from the continuum (become more tightly bound). Thus, for the $n = 2$ bound states,

$$E_i + R_{ii} \rightarrow -\frac{Z^2}{2n^2} \pm \frac{3n(n-1)}{2Z} \boldsymbol{\epsilon} \approx -\frac{Z^2}{8} \pm \frac{3}{Z} \left(\frac{4\pi}{3}\right)^{2/3} n_e^{2/3}, \quad (9)$$

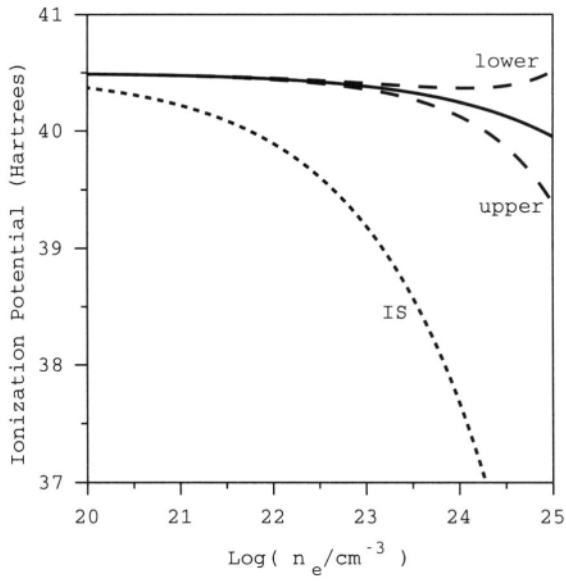


Figure 1. Ionization potential for a hydrogenic argon ion (ICF conditions) from the $n = 2$ level. The curves represent the ionization potentials from the various Stark levels and from a simple ion-sphere model.

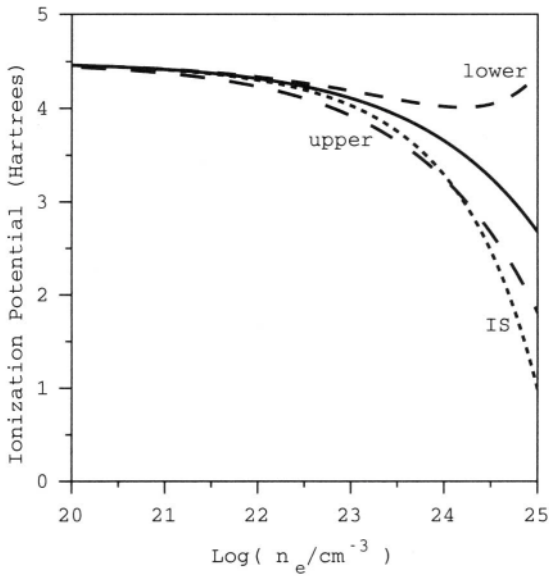


Figure 2. Ionization potential for a hydrogenic carbon ion (short pulse laser conditions) from the $n = 2$ level. The curves represent the ionization potentials from the various Stark levels and from a simple ion-sphere model.

where $\epsilon = -\nabla\Phi(0)$. (Atomic units will now be used.) In the second step a typical field strength of $\epsilon = 1/r_e^2$ has been used (r_e is the electron sphere radius). The \pm energies refer to the upper and lower Stark states, the other two $n = 2$ levels being unshifted. For the final state we have

$$E_f + R_{ff} \approx \frac{q^2}{2} - \langle \mathbf{q} | \sum_i \Phi_i(|\mathbf{r} - \mathbf{r}_i|) | \mathbf{q} \rangle \approx \frac{q^2}{2} - \frac{2\pi}{5} \left(\frac{3\bar{z}}{4\pi} \right)^{2/3} n_e^{1/3}, \quad (10)$$

where ion-sphere potentials have been used as a model screened ion; the multipole expansion has *not* been used for the continuum state. (In general the potentials will also depend on temperature.) From these estimates, we find that the ionization potential I is given by

$$I = E_f(q=0) - E_i \approx -\frac{2\pi}{5} \left(\frac{3\bar{z}}{4\pi} \right)^{2/3} n_e^{1/3} - \left[-\frac{Z^2}{8} \pm \frac{3}{\bar{z}} \left(\frac{4\pi}{3} \right)^{2/3} n_e^{2/3} \right]. \quad (11)$$

Here \bar{z} refers to the mean ion charge surrounding the target atom. This result can now be compared with the shift predicted by simply placing the atom in an ion-sphere cell. This gives an ionization potential I_{IS} , again for $n = 2$, of

$$I_{IS} = \frac{Z^2}{8} - \frac{(Z-1)^{2/3}}{2} \left(\frac{4\pi}{3} \right)^{1/3} n_e^{1/3}. \quad (12)$$

Comparisons of I and I_{IS} are given in Fig. 1 and Fig. 2 for argon in hydrogen and pure carbon, respectively. In the argon calculation $Z = 18$ and $\bar{z} = 1$, which roughly corresponds to ICF conditions. It is clear that the simple ion-sphere screening model predicts a much larger IPD than the MSM model. In particular, note that the lower Stark state is nearly unshifted as a result of a near cancellation of the increased Stark binding and the lowering of the continuum. For such a state, we would not expect a large increase in the ionization rate. In the carbon calculation $Z = 6$ and $\bar{z} = 6$, which roughly corresponds to short-pulse laser experimental conditions. Again we see that the lower Stark state is mostly unshifted, even out to unrealistically large densities. Interestingly, the upper Stark state follows fairly closely to the simple ion-sphere prediction. It is important to note however, that it is only the upper Stark state which follows that prediction, which appears to be fortuitous since the argon case did not show this behavior.

Acknowledgements

I thank Richard Lee, David Kilcrease, and George Csanak for fruitful discussions.

REFERENCES

- [1] E. L. Pollock and J. C. Weisheit, in *Spectral Line Shapes*, Volume 3, ed.F. Rostas, Walter de Gruyter & Co., New York (1985).
- [2] M. Schlanges, Th. Bornath, R. Prenzel, and D. Kremp, in *Atomic Processes in Plasmas* AIP CP 381, AIP Press, 215 (1996).
- [3] M. S. Murillo and J. C. Weisheit, in *Strongly Coupled Plasma Physics*, eds. S. Ichimaru and H. M. Van Horn, Univ. of Rochester Press, 233 (1993).
- [4] M. S. Murillo, in *Atomic Processes in Plasmas*, AIP CP 381, AIP Press, 231 (1996).
- [5] M. S. Murillo and J. C. Weisheit, to appear in *Physics Reports*.
- [6] C. Cohen-Tannoudji, J. Dupont-Roc, and G. Grynberg, *Atom-Photon Interactions*, John Wiley & Sons, Inc., New York (1992).
H. A. Bethe and E. E. Salpeter, *Quantum Mechanics of One- and Two-Electron Atoms*, Plenum, New York (1977).

This page intentionally left blank

STOCHASTIC SIMULATION OF IONIZATION FRONTS IN NONIDEAL PLASMA

D. Beule and A. Förster

Institut für Physik
Humboldt-Universität zu Berlin
Invalidenstraße 110, D-10115 Berlin, Germany

INTRODUCTION

Partially ionized and dense plasma may develop rather complex reaction kinetics. The plasma is usually composed of atoms and ions as well as of free electrons, which undergo mutual transformations by ionization and recombination.^{1,2} The theoretical description of the inhomogeneous kinetic processes in hydrogen plasma can be reduced to coupled reaction–diffusion equations³ for electron, ion and atom densities. Strong Coulomb interaction decreases the reaction energies for ionization and excitation and the corresponding reaction rates depend on the charged-particle densities. This additional non-linearity in the kinetic equations lead not only to an enhancement of ionization and excitation processes and therefore to shifts of stationary states, but also to the appearance of new stable and unstable stationary states. In the area of strong coupling the macroscopic behavior of the plasma may involve collective effects like bistability, nucleation, and front propagation.^{3,4}

MESOSCOPIC DESCRIPTION

We investigate pure hydrogen plasmas using the chemical picture.⁵ The elementary constituents are free electrons e , bare nuclei i , and atoms a . For the stochastic simulation of inhomogeneous kinetic processes⁶ space is divided into M boxes of length h and the number of particles $N_{\nu 1}, \dots, N_{\nu M}$ of species ν in each box $1, \dots, M$ is considered instead of particle densities. The evolution of the number of particles $N_{\nu 1}(t), \dots, N_{\nu M}(t)$ is assumed to be a Markoff process and thus the dynamics are governed by a master equation for the probability distribution P

$$\dot{P} = \hat{A}P, \quad P(N_{\nu 1}, \dots, N_{\nu M}, t). \quad (1)$$

The time-evolution operator \hat{A} consists of a reaction and a diffusion part. The reactions give rise to local particle birth and death processes while the diffusion leads to hopping of particles between neighboring boxes. The probabilities for these events are determined⁶ by considering each box as a homogeneous plasma for sufficiently small box lengths h .

When simulating the master equation for large systems the most time consuming procedure is the probabilistic selection among the large number of possible events. This selection

requires a large summation of event probabilities in each simulation step. The problem can be overcome by collecting events into groups: First the probabilities for all events in a certain cell are summed up. Second cells with probability sums that are similar on a logarithmic scale are collected into classes. Thus the summation of event probabilities can be split into three parts and the selection of the events can be done more efficiently. After selection and performing a change in particle numbers only a few parts of the sum have to be recalculated in order to proceed with the next selection.

MACROSCOPIC MODEL

Neglecting fluctuation and averaging over distribution functions one can derive reaction–diffusion equations for electron, ion and atom density n_e , n_i and n_a . In the macroscopic approach analytical solutions³ and numerical investigations⁴ of inhomogeneous kinetic processes in hydrogen plasma are based on a reaction–diffusion equations for the degree of ionization $\bar{z} = n_e/(n_a + n_i)$. It is derived on the assumption of homogenous mass density ($n = n_a + n_i = \text{const.}$) for the regime of ambipolar diffusion³

$$\dot{\bar{z}}(\mathbf{r}, t) = w(\bar{z}, n, T) + D \Delta \bar{z}(\mathbf{r}, t), \quad w(\bar{z}, n, T) = \alpha n \bar{z} (1 - \bar{z}) - \beta n^2 \bar{z}^3. \quad (2)$$

D denotes the ambipolar-diffusion coefficients while α and β are the rate coefficients for impact ionization $a + e \rightarrow i + e + e$ and three-body recombination $i + e + e \rightarrow a + e$.

The rate coefficient¹ for ionization α_{id} and recombination β_{id} in an ideal thermal plasma are altered by interaction effects that decrease the effective ionization energies $I_{eff} = I - \Delta I$. The ionization coefficients α depend exponentially³ on the lowering of the ionization energy, i.e., $\alpha = \alpha_{id}(T) \exp(\Delta I(\bar{z}, n, T)/k_B T)$. Therefore interaction may change α by orders of magnitudes while recombination coefficients β change only slightly,² $\beta \approx \beta_{id}$. This justifies the approximation $\beta = \beta_{id}$. Rigid shift approximation allows to establish a relation between the lowering of the ionization energy ΔI and the interaction parts of the chemical potential $\mu_{e,i,a}^{int}$ for the constituents: $\Delta I = \mu_a^{int} - \mu_e^{int} - \mu_i^{int}$.

FLUCTUATION EFFECTS ON FRONT PROPAGATION

The general features of equation (2) are determined by the roots of the reaction function $w(\bar{z}, n, T)$, i.e., by its stationary states. For ideal and for most non-ideal plasmas the source function has two roots, corresponding to one stable stationary state and one unstable stationary state. The stable state \bar{z}_s belongs to the ionization equilibrium at given temperature and density of heavy particles, and the unstable state $\bar{z}_u = 0$ corresponds to an atomic gas with no ionization. Small fluctuations will cause transitions from the unstable to the stable state. One scenario is that trigger fronts connecting stable and unstable states propagate in space.

For a plane front, i.e., in a quasi one-dimensional situation it can be shown that all kinds of localized initial condition for Eq. (2) evolve to trigger fronts with fixed shape that propagate with constant velocity⁷ v_0 . Figure 1 compares different stochastic realization that evolved from the same initial conditions with analytical results⁶ for the mean-field equation. Each stochastic simulation has developed a front shape that compares well with the analytical prediction. Furthermore the mean front velocity is also in good agreement with the analytical results.⁶ Nevertheless the front position of different stochastic realization differ significantly. In order to understand this effect one has to check how the mean-field equation (2) is related to the mesoscopic description (1). The relation is usually established by the Ω -expansion.⁸ By using this expansion the master equation for the distribution of particle numbers $P(N_1, \dots, N_M, t)$ is transformed into a differential equation for the densities and a

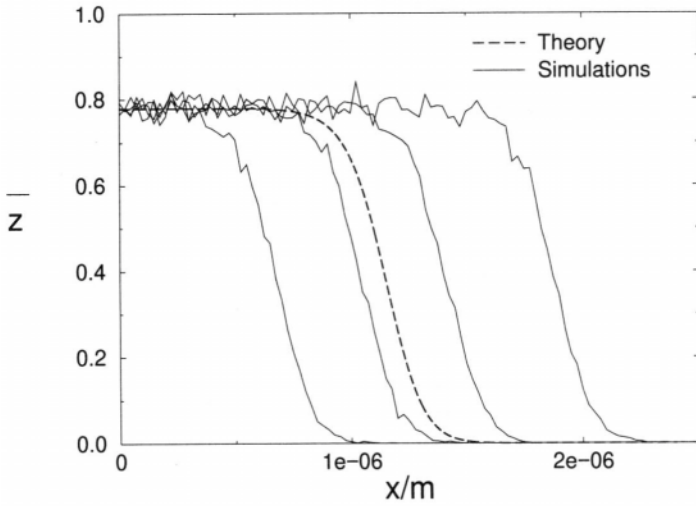


Figure 1. Snapshot of different stochastic realization that evolved from the same initial conditions (rectangular front) with analytical results for the fronts shape of the the mean-field equation (2) at arbitrary position. Density of heavy particles $n = 10^{20}\text{cm}^{-3}$ and temperature $T = 35000\text{K}$.

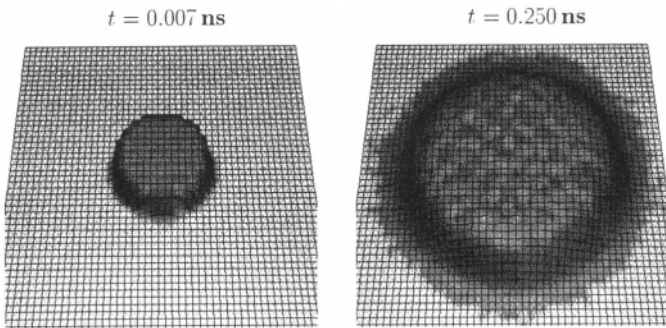


Figure 2. Expansion of an ionization spot into an embedding atomic gas. The height represents the degree of ionization on a linear scale. The initially sharp transition between plasma and atomic gas at $t = 0$ is smeared out and the front propagates into the gas. Both the shape of the spot and the local degree of ionization fluctuate. Density of heavy particles $n = 10^{20}\text{cm}^{-3}$ and temperature $T = 35000\text{K}$.

Fokker–Planck equation for the distribution of the fluctuations. The Ω -expansion requires that fluctuations are always damped in order to keep the distribution of the fluctuations unimodal and narrow. In our model this requirement is violated by fluctuations that correspond to a movement of the whole front relative to a frame moving with the average front velocity \bar{v} . The fact that these modes are not damped reflect the translation invariance of the system and leads to a diffusion-type behavior of the front position. Therefore the position of different stochastic realization of ionization fronts starting from the same initial conditions will drift apart. The fluctuations of the front position show an unusual scaling behavior.⁹

CURVED IONIZATION FRONTS

So far we have considered only quasi one-dimensional situations. The solution of (2) can be generalized for arbitrary dimensions d . The velocity of the front becomes $v(K) = v_0 - (d - 1)DK$, where v_0 denotes the velocity of plane fronts and K is the local curvature of the front.

Figure 2 shows a two dimensional simulation of an ionization spot that grows and expands into the surrounding atomic gas. The initially sharp boundary between plasma and gas is smeared out and the stable front profile starts to build up. The front propagates while its shape and the degree of ionization fluctuate. Due to fluctuations the spot loses its initially spherical symmetry and develops an irregular boundary with different local curvature.

Acknowledgements

We want to thank Thomas Fricke for introducing us to stochastic simulation methods and Werner Ebeling for stimulating discussions.

REFERENCES

- [1] L. M. Biberman, V. S. Vorob'ev, I. T. Yakubov, "Kinetics of Nonequilibrium Low-Temperature Plasmas," Consultants Bureau, New York and London (1987).
- [2] M. Schlanges, this volume.
- [3] W. Ebeling, A. Förster, D. Kremp, M. Schlanges, *Physica A* 159:285 (1989).
- [4] M. Bonitz, Ph. D. Thesis, Universität Rostock (1990).
- [5] W. Ebeling, W.-D. Kraeft, D. Kremp, "Theory of Bound States and Ionization Equilibrium in Plasmas and Solids," Akademie-Verlag, Berlin (1976); Extended Russ. translation: Mir, Moscow (1979).
- [6] D. Beule, A. Förster, T. Fricke, *Z. Phys. Chem.* 193 in press (1997)
- [7] J. D. Murray, "Mathematical Biology," Springer, Berlin (1993).
- [8] N. G. van Kampen, "Stochastic Processes in Physics and Chemistry," North-Holland, Amsterdam (1992).
- [9] H.-P. Breuer, W. Huber, F Petruccione, *Europhys. Lett.* 30:69 (1995).

SPECTRAL PROPERTIES OF DENSE PLASMAS

Roman Fehr and Wolf-Dietrich Kraeft

Institute of Physics
E.-M.-Arndt University Greifswald
Domstraße 10a
D-17489 Greifswald, Germany

INTRODUCTION

The quantum-statistical theory of dense plasmas in the framework of Green's functions needs input quantities like selfenergies, effective potentials, T -matrices and information about few particle properties to set up improved approximations for kinetic equations, stopping power and thermodynamic functions and to go beyond simple approximations like rigid shift, Born approximations and static screening. First showing the essential role of the self energy, we then give an expression for the self energy in the binary collision approximation using off-shell T -matrices.

In kinetic theory, the stopping power

$$\frac{\partial}{\partial t} \langle E \rangle = \frac{1}{n_b} \int \frac{d\mathbf{p}_b}{(2\pi\hbar)^3} \frac{p_b^2}{2m_b} \frac{\partial}{\partial t} f_b(\mathbf{p}_b, t) \quad (1)$$

can be calculated, if the single particle distribution function $f_b(\mathbf{p}_b, t)$ is known. This function can be determined from a general kinetic equation, given in the following shape by Bornath et al.¹

$$\frac{\partial f}{\partial t} = I^0(\mathbf{p}, t) + I^1(\mathbf{p}, t) \quad (2)$$

with the corresponding collision integrals

$$\begin{aligned} I^0(\mathbf{p}, t) &= \int \frac{d\omega}{2\pi} [\Sigma^<(\omega t)g^>(\omega t) - \Sigma^>(\omega t)g^<(\omega t)], \\ I^1(\mathbf{p}, t) &= \frac{\partial}{\partial t} \int \frac{d\omega_1 d\omega_2}{(2\pi)^2} \frac{P'}{\omega_1 - \omega_2} \\ &\quad \times [\Sigma^>(\omega_1 t)g^<(\omega_2 t) - \Sigma^<(\omega_1 t)g^>(\omega_2 t)]. \end{aligned} \quad (3)$$

This kinetic equation is nonlocal in time and conserves the total energy. The self energy correlation functions read

$$\Sigma^>(\mathbf{p}\bar{\omega}t) = \int \frac{d\mathbf{p}_2 d\omega_2}{(2\pi)^4} \langle \mathbf{p}\mathbf{p}_2 | T^>(\bar{\omega} + \omega_2, t) | \mathbf{p}_2 \mathbf{p}_1 \rangle g^<(\mathbf{p}_2 \omega_2 t) \quad (4)$$

with the T -matrices off the energy shell and can be interpreted as scattering rates into and out of a state with momentum \mathbf{p} . It describes the impact of the system on the few particle properties and the effective interaction. The imaginary part Γ of the retarded self energy Σ^R is related to a finite life time of the single particle state due to collisions. We start from an effective wave equation, first given by Röpke et al.²

$$\left(\frac{p_1^2}{2m_a} + \frac{p_2^2}{2m_a} - \hbar z\right) \psi(\mathbf{p}_1, \mathbf{p}_2, z) + \int \frac{d\mathbf{q}}{(2\pi\hbar)^3} V_{ab}(q) \psi(\mathbf{p}_1 - \mathbf{q}, \mathbf{p}_2 + \mathbf{q}, z) = \Delta H_{ab}^{\text{pl}}(\mathbf{p}_1, \mathbf{p}_2, z) \psi(\mathbf{p}_1, \mathbf{p}_2, z), \quad (5)$$

where the plasma hamiltonian can be decomposed as

$$\Delta H_{ab}^{\text{pl}}(\mathbf{p}_1, \mathbf{p}_2, z) \psi(\mathbf{p}_1, \mathbf{p}_2, z) = \Delta H^{\text{Pauli}} \psi + \Delta H^{\text{HF}} \psi + \Delta H^{\text{self}} \psi + \Delta H^{\text{scr}} \psi, \quad (6)$$

describing the phase space occupation (Pauli blocking) and the exchange (HF) self energy as static contributions and the dynamic self energy and the contribution of the dynamically screened potential. So the continuum edge can be written as the sum of the quasiparticle energies of the species

$$E_{\text{cont}} = E_a(p=0) + E_b(p=0), \quad (7)$$

$$E_a(\mathbf{p}) = \frac{p^2}{2m_a} + \text{Re} \Sigma_a^R(\mathbf{p}, E_a(\mathbf{p})), \quad (8)$$

where the quasiparticle energies $E_a(\mathbf{p})$ are determined also more generally by the maxima of the spectral weight function

$$A_a(\mathbf{p}, \omega) = \frac{\hbar \Gamma_a(\mathbf{p}, \omega)}{[\hbar \omega - \frac{p^2}{2m_a} - \text{Re} \Sigma_a^R(\mathbf{p}, \omega)]^2 + [\frac{1}{2} \Gamma_a(\mathbf{p}, \omega)]^2}, \quad (9)$$

the latter having the meaning of a probability function, which gives the energy and momentum distribution of the particle. Again the central role of the self energy is obvious. Thermodynamic properties can be achieved by using the relations for the density or the pressure (the parameter λ may be the charge)

$$n_a(\mu_a, T) = \sum_{\sigma} \int \frac{d\mathbf{p} d\omega}{(2\pi\hbar)^3 2\pi} A_a(\mathbf{p}, \omega) f_F(\omega), \quad (10)$$

$$p(\mu, T) - p^0 = -\frac{1}{4\pi} \sum_{\alpha\sigma} \int_0^1 \frac{d\lambda}{\lambda} \int \int \frac{d\mathbf{p} d\omega}{(2\pi\hbar)^3} \left(\hbar \omega - \frac{p^2}{2m_a} \right) A_a^{(\lambda)}(\mathbf{p}, \omega) f_F(\omega). \quad (11)$$

Results for different approximation schemes are given by Fehr.³

THE BINARY COLLISION APPROXIMATION

In order to include the binary collision and especially the influence of the bound states on the single particle spectrum, it is necessary to deal with the T -matrix approximation of the self energy. In order to discuss the single particle spectral properties one needs the off-shell T -matrices, which depend on momenta and on the complex energy. These quantities can be

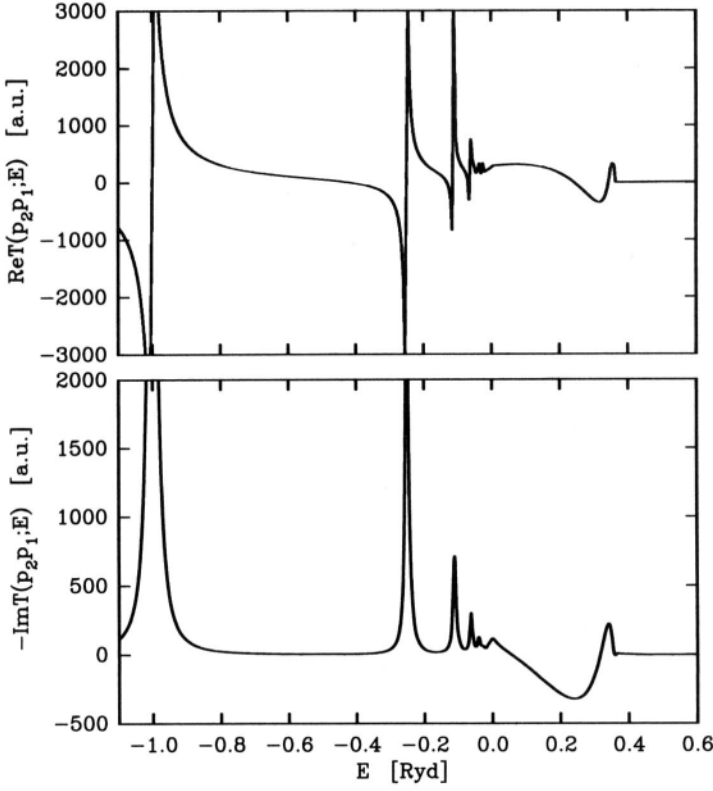


Figure 1. Real and imaginary parts of the T -matrix for an attractive Coulomb potential (hydrogen plasma) $p_2 = 0.6\hbar a_B^{-1}$, $p_1 = 1.0\hbar a_B^{-1}$, $\theta = \hat{\mathbf{p}}_1 \hat{\mathbf{p}}_2 = \pi/3$ as a function of the energy ω . An on-shell singularity can be seen for positive energy.

derived by solving the Lippmann–Schwinger equation for the T -matrix, here written down in c.m. variables

$$\begin{aligned} \langle \mathbf{p} | T_{ab}(\mathbf{P}\omega) | \mathbf{p}' \rangle^\pm &= \langle \mathbf{p} | V_{ab} | \mathbf{p}' \rangle^\pm + \int \frac{d\tilde{\mathbf{p}}}{(2\pi\hbar)^3} \langle \mathbf{p} | V_{ab} | \tilde{\mathbf{p}} \rangle \\ &\times \frac{1 - f_a(\tilde{\mathbf{p}} + \frac{m_a}{M_{ab}}\mathbf{P}) - f_b(\tilde{\mathbf{p}} - \frac{m_b}{M_{ab}}\mathbf{P})}{\hbar\omega - E_a(\tilde{\mathbf{p}} + \frac{m_a}{M_{ab}}\mathbf{P}) - E_b(\tilde{\mathbf{p}} + \frac{m_b}{M_{ab}}\mathbf{P})} \langle \tilde{\mathbf{p}} | T_{cd}(\mathbf{P}\omega) | \mathbf{p}' \rangle^\pm, \end{aligned} \quad (12)$$

the superscript \pm denotes the inclusion of exchange terms. In the case of the Coulomb potential, this Eq. can be solved using Schwinger's⁴ expressions for the Coulomb Green's functions

$$T_{ab}(\mathbf{p}_2 \mathbf{p}_1 E) = V_{ab}(\mathbf{p}_2 - \mathbf{p}_1) \left\{ 1 - \frac{4i\nu}{e^{2\pi\nu} - 1} \int_1^{(0+)} \frac{dt t^{-i\nu}}{\varepsilon(1-t)^2 - 4t} \right\}, \quad (13)$$

with $\nu = \frac{-Ze^2}{4\pi\epsilon_0\epsilon_r} \sqrt{\mu_{ab}/2E}$, $\varepsilon = \frac{(k^2 - p_2^2)(k^2 - p_1^2)}{k^2 |\mathbf{p}_2 - \mathbf{p}_1|^2}$, $\text{Im}E > 0$, $k^2 + i\eta = 2\mu_{ab}E$, and μ_{ab} relative mass. The real part of the T -matrix shows a typical principal value behavior at the bound state energies, and, in the imaginary part, we find delta peak like structures at these energies, see Fig. 1. But this expression shows several singularities, especially on the energy shell, and we have to include an appropriate screening of the potential. The binary collision approximation

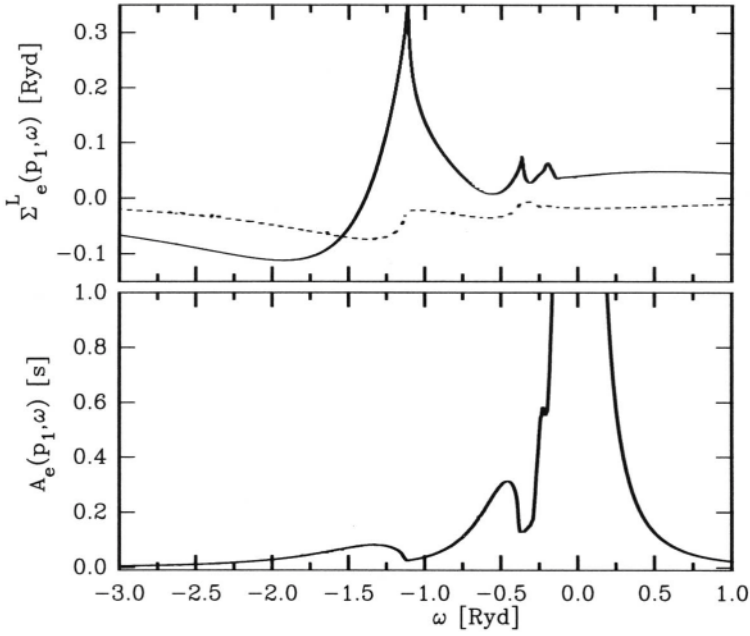


Figure 2. Real and imaginary parts of the selfenergy in binary collision approximation (T -Matrix approximation) and corresponding spectral function for an electron in an electron-hole plasma (equal masses of the species) in atomic units, $T=1\text{Ryd}$ (100K), $\kappa = 0.29a_B^{-1}$ ($n_e = 10^{16}\text{cm}^{-3}$), $p_1 = 0$.

of the self energy reads in c.m. variables

$$\text{Re}\Sigma_a^L(\mathbf{p}_1, \omega) = \sum_{b\sigma} \int \frac{d\tilde{\mathbf{p}}}{(2\pi\hbar)^3} \text{Re}\langle \mathbf{p} | T_{cd}^R(\mathbf{P}, \omega + E_b(\tilde{\mathbf{p}})) | \mathbf{p} \rangle f_b(\tilde{\mathbf{p}}). \quad (14)$$

Since there is no exact solution for the (screened) Debye T -matrix off the energy shell known, we modify the Lippmann-Schwinger equation as proposed by Gorshkov⁵ and get after a summation over all ladder terms

$$T_{ab,\kappa}(\mathbf{p}_2, \mathbf{p}_1; E) = V_{ab}^{\text{Debye}}(\mathbf{p}_2 - \mathbf{p}_1) + V_{ab}(\mathbf{p}_2 - \mathbf{p}_1) \left\{ \frac{2i\nu}{e^{2\pi\nu} - 1} \int_{\infty}^{(1+)} \left(\frac{s-1}{s+1} \right)^{-i\nu} \frac{ds}{s^2 - 1 - \varepsilon + \zeta_{\kappa}(s)} \right\} \quad (15)$$

with κ — inverse Debye screening length and ζ_{κ} — screening function

$$\zeta_{\kappa}(s) = \frac{\kappa^2(k^2 s^2 - p_1^2) - 2i\kappa k s(k^2 - p_1^2)}{k^2 |\mathbf{p}_2 - \mathbf{p}_1|^2}. \quad (16)$$

This corrects the singularities, however the dispersion relation of the T -matrix is violated. The characteristics of the T -matrix as to be seen in Fig. 1 determine the real (full line) and the imaginary parts (dashed) of the selfenergy in binary collision approximation shown in Fig. 2 for an electron together with the corresponding spectral function. The merging of the higher bound states into the continuum is clearly to be seen. More details can be found in Fehr.⁶

SUMMARY

We tried to give a relative simple way for the inclusion of bound states in selfenergy corrections by modifying the Lippmann-Schwinger equation and calculating off-shell T -matrix

elements. This left open questions considering an appropriate screening. For alternatives see the contributions of Kremp and Kraeft and of Schlanges to these proceedings.

Acknowledgements

This work was supported by the Deutsche Forschungsgemeinschaft DFG–SFB 198 *Kinetics of partially ionized gases*.

REFERENCES

- [1] T. Bornath, D. Kremp, W. D. Kraeft, and M. Schlanges, *Phys. Rev.* **E54** (4):3274 (1996).
- [2] G. Röpke et al., *Phys. Stat. Sol.* **B88**:K59 (1978).
- [3] R. Fehr and W. D. Kraeft, *Contrib. Plasma Phys.* **35** (6):463 (1995).
- [4] J. Schwinger, *J. Math. Phys.* **5** (11): 1606 (1964).
- [5] V. G. Gorshkov, *Sov. Phys.-JETP* **20** (1):234 (1965).
- [6] R. Fehr, *Spektrale Eigenschaften in dichten Plasmen*, PhD thesis, Greifswald University, 1997.

This page intentionally left blank

HIGHLY CHARGED IONS IN POLYETHYLENE CAPILLARY DISCHARGE PLASMA

A. Förster,¹ D. Beule,¹ H. Conrads,² and W. Ebeling¹

¹Institut für Physik

Humboldt-Universität zu Berlin

Invalidenstraße 110, D-10115 Berlin, Germany

²Institut für Niedertemperatur-Plasmaphysik e. V.

an der Ernst-Moritz-Arndt-Universität Greifswald

Robert-Blum-Straße 8-10, D-17489 Greifswald, Germany

EXPERIMENT

It is known since the fifties¹ that discharges between two electrodes bridged by an insulator in high vacuum start in flashing over the insulating surface. A so-called sliding spark develops. Bridging the electrodes by a capillary, the same phenomenon was observed.²⁻⁵ The capillaries were typically made of polyethylene in order to observe line-free recombination spectra of C VI. During the discharge the capillary wall material is evaporated and ionized due to Joule heating and a hot dense carbon-hydrogen plasma is formed. In high-vacuum discharges the capillary is filled in much less than 50 ns. Typical plasma parameters are $10^{18} \dots 10^{21} \text{ cm}^{-3}$ for electron density and $10^4 \dots 10^6 \text{ K}$ for electron temperature.

Since the sixties capillary discharge experiments were of interest as highly reproducible light sources. Sparks emitting intense continuum radiation in the visible and ultraviolet spectral region are important for many applications: temperature determination in plasma by means of line-reversal method, for measurement of absorption coefficients in the ultraviolet and soft X-ray domains, especially of the discontinuities at the absorption edges, or for use as radiation standards. Today they are considered as promising x-ray laser sources.⁶

Electron density and temperature in the plasma column (Fig. 1) are determined by measurement of emitted absolute radiation intensity from optical thin and optical thick layers. As the process of ablation continues more and more material is released from the wall of the capillary and transformed into plasma. The increase in plasma density is accompanied by a steady decrease in temperature in the way that the pressure remains almost constant. Radiation from prominent bound-bound transitions allows to record the temporal appearance of ions of different charges. At the temperatures under consideration hydrogen is fully ionized. The carbon ions may be identified by the line radiation from the transitions between the lowest excited states and the ground states, respectively. The experimental data of Fig. 2 suggest that the plasma composition in the first hundreds of nanoseconds is dominated by C VI and C v. The massive appearance of highly charged carbon ions is still not well understood.

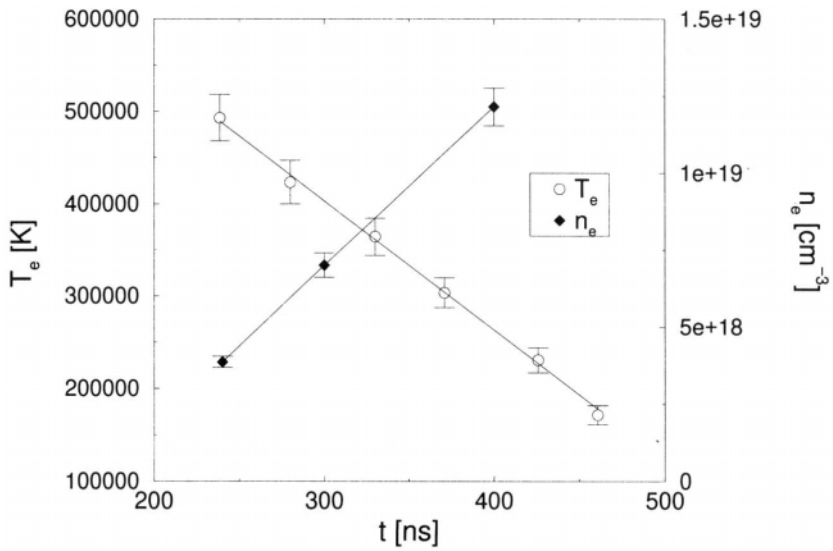


Figure 1. Experimental data for electron temperature T_e and electron density n_e as function of time. A polyethylene capillary of 10 cm length and inner diameter of 2 mm was used.²

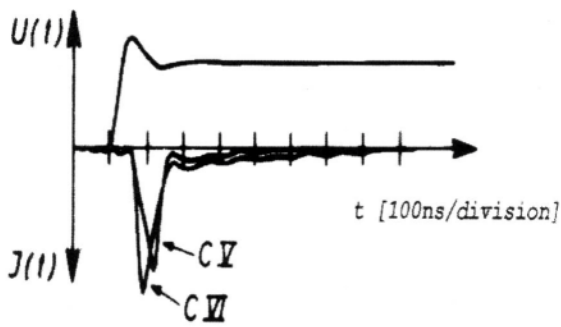


Figure 2. Temporal development of intensity emitted by the C VI line at 3.373 nm and the C V line at 4.027 nm and of discharge current U

THEORETICAL MODEL

The theoretical description aims at a calculation of the plasma composition over time. In the considered state of the discharge process recombination takes place by fast capture of electrons into highly excited levels which are followed by radiative de-excitation processes. Our treatment is based on the assumption that the evolution of the charge-state distribution in the plasma column during the discharge process may be approximately described as a sequence of equilibrium states. The detailed modelling of the excitation and de-excitation processes would need a more sophisticated treatment based on rate equations.⁷

Our model for the equilibrium takes into account several dense plasma effects such as correlation and continuum lowering due to Coulomb interaction, degeneracy, and quantum-mechanical exchange. The basic thermodynamic quantity is the free energy density $F/V = f(\{n_z\}, n_e, T)$ that depends on the densities of the different ions $\{n_z\}$, of the free electrons n_e , and of the temperature T . The construction of free energy density follows the ideas of PACH⁸ and has the structure

$$f = f_i^{id} + f_e^{id} + f_i + f_e + f_{ie} + f_{hs}. \quad (1)$$

The ideal contribution of the ions (indices i, id) and electrons (indices e, id) are computed following the Boltzmann and the Fermi–Dirac statistics. The correlation and exchange contributions of the ionic (index i) and electronic (index e) subsystems as well as of the ion–electron interaction (index ie) are given by Padè approximations which interpolate between the analytically known limit cases for the interaction expressions. The last term in the free energy density models the short-range repulsion between ions due to overlapping electron shells by an neutral hard-sphere system (index hs). The detailed plasma composition for a given total heavy-particle density n and temperature T may be calculated by minimizing the free energy density with respect to the individual ion densities. In Fig. 3 we present a map of the ionization state of carbon as part of a $(CH_2)_n$ plasma in the temperature range of $10^5 \dots 10^6$ K and a mass-density range of $10^{-6} \dots 1 \text{ g cm}^{-3}$. The knowledge of the detailed composition implies naturally also the figures of the free-electron density in any point of the ionization map.

The experimental points of Fig. 1 for the electron density and temperature may be in good approximation interpolated by linear functions of time t :

$$\begin{aligned} n_e(t) &= t \cdot 5.2 \cdot 10^{16} \frac{\text{cm}^{-3}}{\text{ns}} - 8.6 \cdot 10^{18} \text{ cm}^{-3}, \\ T_e(t) &= -t \cdot 1400 \frac{\text{K}}{\text{ns}} + 823000 \text{ K}. \end{aligned} \quad (2)$$

The corresponding path for the evolution of the wall material during the discharge process is indicated by the full line in Fig. 3. The detailed plasma composition along the evolution path of the capillary discharge plasma is given in Fig. 4.

DISCUSSION

The charge state distribution (Fig. 3) is dominated at high temperatures by fully ionized carbon ions (lower right corner), followed by a narrow strip dominated by C VI and a relatively large area of almost pure C V (lower left area) at medium temperatures. The shape of the different areas is mainly determined by temperature ionization and reflects the jump of ionization energies between C I... C IV and C V and C VI, respectively. The effects of density ionization may be studied in the upper part of Fig. 3 but they are relatively small in the area of

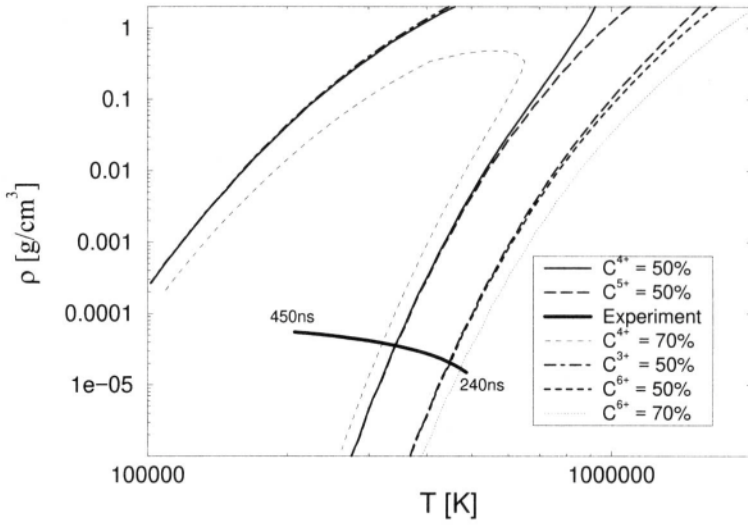


Figure 3. Equilibrium abundances of highly charged ions in the mass density–temperature plane and experimental path (thick black line)

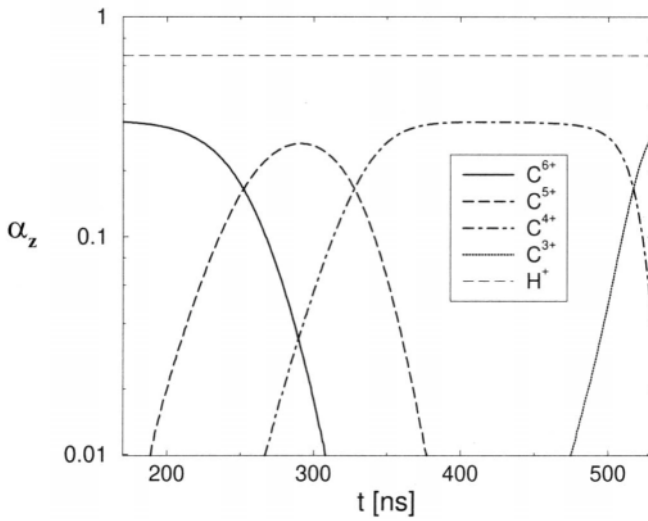


Figure 4. Detailed composition $\alpha_z = n_z/n$ calculated along the experimental path of Eq. 2.

the recorded path of the wall material. Morgan et al.⁹ argue that fully ionized carbon needs a temperature of $\geq 160\text{eV}/k_B$ to appear. The characteristic ionization temperature is naturally a function of the density. According to our calculation the mass density of the discharge plasma is between 10^{-4} and 10^{-5}g cm^{-3} . In this range a temperature of $\geq 30\text{eV}/k_B$ is sufficient to produce a substantial amount of fully ionized carbon. Consequently, our calculation of the detailed composition (Fig. 4) starts in the area with fully ionized carbon and continues over C VI and C V to C IV. This way the model supports the facts of the appearance of highly charged carbon in a transitory discharge regime.

REFERENCES

- [1] P. Gleichauf, *J. Appl. Phys.* 22:766,538 (1951)
- [2] P. Bogen, H. Conrads, D. Rusbüldt, *Z. Phys.* 186:240 (1965)
- [3] P. Bogen, H. Conrads, G. Gatti, W. Kohlhaas, *J. Opt. Soc. Am.* 58:302 (1968)
- [4] H. Shin, D. Kim, T. Lee, *Phys. Rev. E* 50:902 (1994)
- [5] H. J. Kunze, K. N. Koshelev, C. Steden, D. Uskov, H. T. Woeschebrink, *Phys. Lett. A* 193:183 (1994)
- [6] J. J. Roca, V. Shlyaptsev, F. G. Tomasel, O. D. Cortázar, D. Hartshorn, J. L. A. Chilla, *Phys. Rev. Lett.* 73:2192 (1994)
- [7] D. Beule, H. Conrads, W. Ebeling, A. Förster, "Density Effects for Plasmas of Capillary Discharges," INP-Report IX, Institut für Niedertemperatur-Plasmaphysik, Greifswald (1995)
- [8] W. Ebeling, A. Förster, V. E. Fortov, V. K. Gryaznov, A. Ya. Polishchuk, "Thermophysical Properties of Hot Dense Plasmas," Teubner, Stuttgart and Leipzig (1991)
- [9] C. A. Morgan, H. R. Griem, R. C. Elton, *Phys. Rev. E* 49:2282 (1994)

This page intentionally left blank

ADIABATIC EQUATION OF STATE AND IONIZATION EQUILIBRIUM IN STRONGLY COUPLED PLASMA

D. Beule, W. Ebeling, and A. Förster

Institut für Physik
Humboldt-Universität zu Berlin
Invalidenstraße 110, D-10115 Berlin, Germany

INTRODUCTION

Adiabatic processes play an important role in plasma physics. A list of examples includes sound waves, expansion of plasma or gas into vacuum, and shock-wave experiments.¹ Further they play an important role in astrophysics since e.g., the radial structure of the stars as well as of the fluid planets like Jupiter or Saturn follows an adiabat;² further we mention the three adiabatic coefficients used in astrophysics and in particular in planetary and helioseismology.³ Adiabatic processes are characterized by a relatively fast change of state so that the system undergoing the change does not exchange heat with its surroundings. Reversible adiabatic processes are isentropic, since they take place with no change in entropy. Here we consider strongly coupled plasma under isentropic conditions. In difference to an earlier work devoted to moderately coupled isentropic plasma,⁴ we extend here the theory to strong coupling using the full Padé approximant (PACH - approach).

ADIABATIC EOS IN PARTIALLY IONIZED PLASMA

We investigate pure hydrogen plasma using the chemical picture.⁵ The elementary constituents are free electrons e , bare nuclei i , atoms a , and molecules m . n_e , n_i , n_a , and n_m denote the particle densities of these constituents. We do not consider the ionic species H^- and H_2^+ since their concentration are found to be negligible. For a given total density of nuclei $n = n_i + n_a + 2n_m$ the composition can be described by the fraction of atoms $\alpha_0 = n_a/n$ and the fraction of molecules $\beta_m = 2n_m/n$. These quantities are related to the degree of ionization $\alpha = n_i/n$ via the relation $\alpha = 1 - \alpha_0 - \beta_m$. The thermodynamic properties of the plasma model are characterized by the free energy density $f(T, V, n_e, n_i, n_a, n_m)$. Taking electro-neutrality ($n_e = n_i$) into account, one particle density can be eliminated and the free energy can be expressed in terms of the degree of ionization α and the fraction of molecules β_m , i.e., $f(T, V, n, \alpha, \beta_m)$. The characterization of the plasma state involves a minimization procedure with respect to the composition under the constraints of electro-neutrality and given total density n . This constrained minimization can be expressed by: $\delta f / \delta \beta_m = 0$ and $\delta f / \delta \alpha = 0$. Other thermodynamic properties can be obtained by the usual thermodynamic relations. The

adiabatic EOS $p(s, T)$, here called AEOS, can be calculated from the isothermal pressure $p(n, T)$ and the isothermal specific entropy $s(n, T) = SNk_B$ by solving the specific entropy $s(n, T)$ with respect to T and inserting the result into $p(n, T)$. Already in ideal or weakly coupled plasma this leads to a rather complex equation.⁴

AEOS IN STRONGLY COUPLED PLASMA

For many applications of an adiabatic equation of state the model of ideal or weakly coupled plasma is insufficient. Under non-ideal conditions the Coulomb interactions lower the ionization energy, alter the degree of ionization and yield negative contributions to, e.g., the pressure and the entropy. Additionally, electrons may become degenerated and quantum exchange and correlation effects appear. In effect, there is a strong interplay between the Coulomb coupling and quantum effects on one hand and the ionization equilibrium and the AEOS on the other. This interplay is characterized by the following feedback effect: The more the ionization is developed and charged particles dominate the plasma composition the stronger are the Coulomb effects in the plasma. On the other hand the Coulomb interaction shifts the ionization equilibrium to higher ionization states; this effect is also known as pressure ionization.

A quantitative treatment of interaction effects for a broad range of densities and temperatures is given by the so-called PACH model.⁶ In the framework of this model the free energy $f(\alpha, \beta_m, T, V)$ is calculated from an expression with the following structure

$$f = f_e^{id} + f_i^{id} + f_e + f_i + f_{ie} + f_{hs} + f_a^{id} + f_m^{id} \rightarrow \text{Minimum}. \quad (1)$$

This free energy density is to be minimized with respect to the degree of ionization α and the degree of dissociation β_m . The ideal electron contribution f_e^{id} is calculated from Fermi–Dirac statistics, while for the ideal ion contribution f_i^{id} Boltzmann statistics is used. The Coulomb interaction contributions that interpolate analytic results^{6,7} consist of three Padé approximations: the exchange and correlation contribution of the electron gas f_e , the Coulomb contribution of ionic subsystem f_i , and ion–electron screening contribution f_{ie} . The contribution of neutral hard-sphere system f_{hs} is taken in the Carnahan–Starling approximation. The excited states of the atoms are accounted for by a Planck–Larkin partition sum in the atomic contribution F_a^{id} . For the molecules F_m^{id} contains also vibrational and rotational contributions.⁸

The Padé approximation takes advantage of the quantum virial functions.⁵ For efficient numerical treatment we approximate the infinite sums by new interpolation formulas that are improvements of those given in Ref. [11]

$$E_2^*(-x) = \frac{4}{x^2\sqrt{\pi}}E_2(-x) = \frac{\ln 2 - \frac{\pi^{\frac{3}{2}}x}{18} + 0.133x^2 + 0.14x^{5.9}\left(\frac{2}{\sqrt{\pi}x} - \frac{1}{x^2}\right)}{1 + 0.14x^{5.9}}, \quad (2)$$

$$Q_3^*(-x) = \frac{Q_3(-x)}{x^3} = \frac{0.14787 + \frac{\pi^{\frac{5}{2}}x}{192} + \frac{0.17x^{3.8}}{6}\left(\ln|3x| + 2C_E - \frac{11}{6} + \frac{3\sqrt{\pi}}{4x} - \frac{1}{x^2}\right)}{1 + 0.17x^{3.82}}, \quad (3)$$

where $C_E = 0.577216\dots$ denotes the Euler constant.

RESULTS AND DISCUSSION

The essential part of the PACH approach is the minimization with respect to α and β_m . The degree of ionization α and the degree of dissociation β_m have to be determined

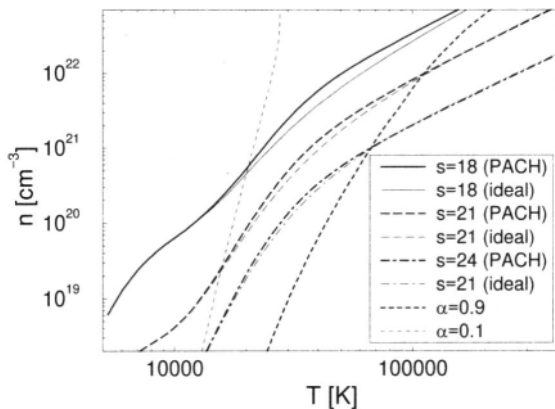


Figure 1. Plasma isentropes as obtained from PACH (solid) and in ideal plasma (dashed). The thin black lines limit the area where ionization raises from weakly ionized $\alpha = 0.1$ to the nearly completely ionized $\alpha = 0.9$.

simultaneously. We achieve the minimization of the free energy density by a simulated annealing procedure⁹ that was originally developed for multi-component systems.¹⁰ After performing this procedure on a dense grid in the density–temperature plane one can calculate different thermodynamic properties by numerical differentiation. An alternative approach is to construct separate Padé approximations for each thermodynamic property. So far this has only been done for completely ionized plasma.¹¹

We calculated the isentropes $s = \text{const.}$ for hydrogen plasma. They are plotted in figure 1 together with lines of constant degree of ionization. In general the difference between ideal and non-ideal isentropes increases as density increases and temperature decreases but the interaction effects vanish when the ions and electrons are bound into atoms and molecules. Therefore the ideal and non-ideal isentropes that nearly coincide at high temperatures merge again after they have crossed the area of partial ionization. Due to the decrease in particle number the adiabats become steeper as atoms and molecule formation takes place for decreasing temperature. Lower values of reduced entropy correspond to higher densities or lower temperatures and therefore to larger non-ideal effects and thus to greater differences in the degree of ionization. There are points where the non-ideal contributions to entropy (cf. figure 1) cancel each other and the ideal and non-ideal isentropes cross. This points are found in the region of highly ionized plasma.

In order to demonstrate how bound-state formation significantly alters the adiabatic EOS we plot adiabatic EOS obtained from PACH and of an ideal system where no ionization processes take place. For such systems the adiabatic EOS can be obtained by integrating

$$\nabla_{ad} = \left(\frac{d \ln T}{d \ln p} \right)_s. \quad (4)$$

For a Boltzmann plasma with fixed degree of ionization one finds $\nabla_{ad} = 0.4$. Therefore the adiabatic EOS for such a system is given by a set of parallel straight lines in a $\log(p)$ over $\log(T)$ plot. One of these lines is shown in figure 2. For high temperatures (i.e., a high degree of ionization) the PACH isentropes fulfil $\nabla_{ad} \approx 0.4$. But in the area where the formation of bound states takes place the adiabatic EOS deviates significantly from this value. For decreasing temperature the pressure is decreasing much faster than in a system with fixed degree of ionization. For $s = 18$ one can even see a second steep decrease in pressure at low temperature where molecule formation starts.

In conclusion we may state that bound-state formation and strong coupling effects alter significantly the AEOS in definite regions of the temperature-density plane.

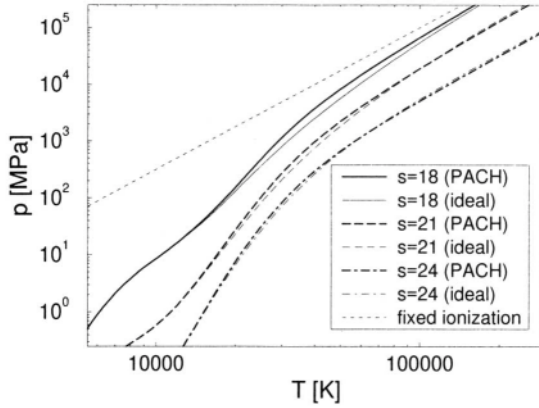


Figure 2. Adiabatic equation of state for reduced entropy $s = 18, 21, 24$ over temperature. We compare the pressure of an ideal plasma (thin lines) with the pressure obtain from PACH (thick lines). For comparison we also plot an adiabatic EOS for a fixed degree of ionization as obtained from Eq. (4) using $\nabla_{ad} = 0.4$ (short dashed line).

REFERENCES

- [1] V. E. Fortov, I. T. Yakubov, “Physics of Nonideal Plasmas,” Hemisphere Publ. Corp., New York (1990).
- [2] R. Kippenhahn, A. Weigert, “Stellar structure and Evolution,” Springer, Berlin (1994).
- [3] J. Christensen-Dalsgaard, W. Däppen, *Astron. Astrophys. Review* 4:267 (1992).
- [4] D. Beule, W. Ebeling, A. Förster, *Physica A*241:719 (1997).
- [5] W. Ebeling, W. D. Kraeft, D. Kremp, “Theory of Bound States and Ionisation Equilibrium in Plasmas and Solids,” Akademie-Verlag, Berlin (1976); Extended Russ. translation Mir, Moscow (1979).
- [6] W. Ebeling, A. Förster, V. E. Fortov, V. K. Gryaznov, A. Ya. Polishchuk, “Thermophysical Properties of Hot Dense Plasmas” Teubner Verlagsgesellschaft, Stuttgart and Leipzig (1991).
- [7] W. Ebeling, *Contrib. Plasma Phys.* 30:553 (1990).
- [8] R. Fowler, E. A. Guggenheim, “Statistical Thermodynamic,” Cambridge University Press, Cambridge (1952).
- [9] S. Kirkpatrick, C. D. Gelatt, M. P. Vecchi, *Science* 220:671 (1983).
- [10] A. Förster, D. Beule, H. Conrads, W. Ebeling, this volume.
- [11] W. Stolzmann, T. Blöcker, *Phys. Lett. A*221:99 (1996); *Astr. & Astrophys.* 314:1024 (1996).

EIKONAL CROSS SECTION FOR ELASTIC ELECTRON-ION SCATTERING IN STRONGLY COUPLED PLASMA

Young-Dae Jung¹ and Jung-Sik Yoon

Department of Physics, Hanyang University, Ansan
Kyunggi-Do 425-791, South Korea

¹E-mail: yjung@bohr.hanyang.ac.kr

1. INTRODUCTION

There are number of collision processes involved in plasma production and diagnostics.¹⁻³ These are elastic scattering, ionization, excitation, dissociative ionization, recombination, electron capture, etc. Among them, the elastic scattering process plays a key role in plasmas. Plasma in laboratory and astrophysical environments can be classified as weakly and strongly coupled plasmas according to the strength of coupling due to Coulomb interaction in plasmas.⁴ Those plasma with values of the plasma coupling parameter $\Gamma [= (e^2/b)/kT]$ much smaller than unity may be called weakly coupled plasmas; those with the plasma coupling parameter around or greater than unity, strongly coupled plasmas, where b and T are the interparticle distance and the temperature. A description of the strongly coupled plasmas is provided by the ion-sphere (or Wigner-Seitz) model.⁵⁻⁷ Astrophysical dense plasmas are those we find in the interiors, surfaces, and outer envelopes of astrophysical objects, such as neutron stars, white dwarfs, the Sun, etc. The ion-sphere model has been widely used to investigate the atomic processes in strongly coupled plasmas, such as excitation⁸ and bremsstrahlung^{9, 10} processes. The ion-sphere model has played an important part in elucidating the properties of the strongly coupled plasmas.^{4, 6, 7} The semiclassical method called the eikonal approximation^{11, 12} has been widely used in many collision processes.³ However, most of the literature has focused on electron collision processes in weakly coupled plasmas.¹³⁻¹⁷ Also, the eikonal method has not been used in elastic electron-ion collisions in strongly coupled plasmas. Thus, in this paper we investigate the elastic electron-ion collisions in strongly coupled plasmas using the ion-sphere model with the eikonal approximation. The eikonal differential elastic scattering (EDES) cross section in dense plasmas is obtained as a function of the impact parameter (b) and ion-sphere radius (Rz). A modified eikonal method called the Wallace correction^{18, 19} is also applied to calculate the cross sections. The results show that the Wallace correction on the EDES cross sections cannot be neglected in the cutoff impact parameter, i.e., the ion-sphere radii. The EDES cross sections substantially decrease as an increase of the energy of the projectile electron and increase as the plasma-screening effect decreases through the ion-sphere radius.

2. EIKONAL AND MODIFIED EIKONAL APPROXIMATIONS

A first-order theory, in the rearrangement sense, arises from the Lippmann–Schwinger equation,²⁰

$$\Psi(\mathbf{r}) = \phi(\mathbf{r}) + \int d^3\mathbf{r}' G_0(\mathbf{r}, \mathbf{r}') U(\mathbf{r}') \Psi(\mathbf{r}'), \quad (1)$$

where $\Psi(\mathbf{r})$ is the solution of the Schrödinger equation,

$$(\nabla^2 + k^2)\Psi(\mathbf{r}) = U(\mathbf{r})\Psi(\mathbf{r}); \quad (2)$$

here k is the wave number, the reduced potential $U(\mathbf{r})$ is given by the potential $V(\mathbf{r})$: $U(\mathbf{r}) = 2mV(\mathbf{r})/\hbar^2$, and $\phi(\mathbf{r})$ is the solution of the homogeneous equation,

$$(\nabla^2 + k^2)\phi(\mathbf{r}) = 0, \quad (3)$$

and $G_0(\mathbf{r}, \mathbf{r}')$ is a Green's function, such that

$$(\nabla^2 + k^2)G_0(\mathbf{r}, \mathbf{r}') = \delta^3(\mathbf{r} - \mathbf{r}'). \quad (4)$$

The free outgoing solution of the above equation is obtained by

$$G_0^{(+)}(\mathbf{r}, \mathbf{r}') = -\frac{1}{4\pi} \frac{e^{ik|\mathbf{r}-\mathbf{r}'|}}{|\mathbf{r}-\mathbf{r}'|}. \quad (5)$$

Then a solution to Eq. (2) can be written in the form

$$\Psi_{\mathbf{k}_i}^{(+)}(\mathbf{r}) = (2\pi)^{-3/2} e^{i\mathbf{k}_i \cdot \mathbf{r}} \Phi(\mathbf{r}), \quad (6)$$

where we have, for convenience, defined

$$\Phi(\mathbf{r}) = 1 + \int d^3\mathbf{r}' e^{-i\mathbf{k}_i \cdot (\mathbf{r}-\mathbf{r}')} G_0^{(+)}(\mathbf{r}, \mathbf{r}') U(\mathbf{r}') \Phi(\mathbf{r}'). \quad (7)$$

If we have chosen the z axis in the direction of the incident wave vector \mathbf{k}_i , the free outgoing Green's function can be written as

$$\begin{aligned} G_0^{(+)}(\mathbf{r}, \mathbf{r}') &= -(2\pi)^{-3} e^{-i\mathbf{k}_i \cdot (\mathbf{r}-\mathbf{r}')} \lim_{\epsilon \rightarrow 0^+} \int d^3\mathbf{p} \frac{e^{i\mathbf{p} \cdot (\mathbf{r}-\mathbf{r}')}}{2k_i p_z + p^2 - i\epsilon}, \\ &\cong G_0^{(1)}(\mathbf{r}, \mathbf{r}') + G_0^{(2)}(\mathbf{r}, \mathbf{r}') + \dots, \end{aligned} \quad (8)$$

where $G_0^{(1)}(\mathbf{r}, \mathbf{r}')$ is given by

$$G_0^{(1)}(\mathbf{r}, \mathbf{r}') = -\frac{i}{2k_i} e^{ik_i(z-z')} \delta^2(\mathbf{b}-\mathbf{b}') \theta(z-z'), \quad (9)$$

with the impact parameters $\mathbf{b}(\equiv \mathbf{r} - z\hat{\mathbf{k}}_i)$, $\mathbf{b}'(\equiv \mathbf{r}' - z'\hat{\mathbf{k}}_i)$, and $\theta(x) (= 1$ for $x \geq 0$; $= 0$ for $x < 0$) is the step function. The eikonal wave function is then

$$\Psi^E(\mathbf{r}) = (2\pi)^{-3/2} \exp\left(i\mathbf{k}_i \cdot \mathbf{r} - \frac{i}{2k_i} \int_{-\infty}^z dz' U(\mathbf{b}, z')\right). \quad (10)$$

If we adopt a cylindrical coordinate system such that $\mathbf{r} = \mathbf{b} + z\hat{\mathbf{n}}$, $\hat{\mathbf{n}}$ being a unite vector perpendicular to the momentum transfer $\Delta(\equiv \mathbf{k}_i - \mathbf{k}_f)$ and the integral over the variable z , the eikonal scattering amplitude f^E becomes

$$f^E = \frac{k_i}{2\pi i} \int d^2\mathbf{b} e^{i\Delta \cdot \mathbf{b}} \exp[i\chi(\mathbf{k}_i, \mathbf{b}) - 1], \quad (11)$$

where $\chi(\mathbf{k}_i, \mathbf{b})$ is the eikonal phase,

$$\chi(\mathbf{k}_i, \mathbf{b}) = \frac{1}{k_i} \chi_0(\mathbf{b}) = -\frac{1}{2k_i} \int_{-\infty}^{\infty} dz U(\mathbf{b}, z). \quad (12)$$

After some manipulation the total elastic scattering cross section in the eikonal approximation is obtained by

$$\sigma_{\text{tot}}^E = \int d\Omega |f^E|^2 = 2\pi \int db b |\exp[i\chi(k, b) - 1]|^2, \quad (13)$$

where the differential solid angle $d\Omega$ was replaced by $d^2\Delta/k^2$ (here, $|\mathbf{k}_i| = |\mathbf{k}_f| = k$). The EDES cross section is then

$$\frac{d\sigma_{\text{tot}}^E}{db} = 2\pi b \left| \exp\left(\frac{i}{k} \chi_0(b)\right) - 1 \right|^2, \quad (14)$$

where

$$\chi_0(b) = -\frac{m}{\hbar^2} \int_{-\infty}^{\infty} dz V(r), \quad (15)$$

for a symmetric potential $V(r)$ with $r = (b^2 + z^2)^{1/2}$. Here the condition of validity of the eikonal approximation is $|V|/E \ll 1$, where E is the energy of the incident electron. A simple modification to the eikonal approximation has been suggested by Wallace.^{18, 19} The modified eikonal scattering amplitude containing the reading correction to the eikonal phase is

$$f^{\text{ME}} = \frac{k_i}{2\pi i} \int d^2\mathbf{b} e^{i\Delta \cdot \mathbf{b}} \exp[i\chi'(\mathbf{k}_i, \mathbf{b}) - 1], \quad (16)$$

where the corrected eikonal phase $\chi'(\mathbf{k}_i, \mathbf{b})$ is given by

$$\chi'(\mathbf{k}_i, \mathbf{b}) = \frac{1}{k_i} \chi_0(\mathbf{b}) + \frac{1}{k_i^3} \chi_1(\mathbf{b}); \quad (17)$$

here Wallace phase $\chi_1(\mathbf{b})$ is obtained by

$$\chi_1(\mathbf{b}) = \frac{1}{2} \int_{-\infty}^{\infty} dz (\nabla \chi_+) \cdot (\nabla \chi_-), \quad (18)$$

with

$$\chi_+(\mathbf{b}, z) = -\frac{1}{2} \int_{-\infty}^z dz' U(\mathbf{b}, z'), \quad (19)$$

$$\chi_-(\mathbf{b}, z) = -\frac{1}{2} \int_z^{\infty} dz' U(\mathbf{b}, z'). \quad (20)$$

The modified EDES cross section with the Wallace correction is found to be

$$\frac{d\sigma_{\text{tot}}^E}{db} = 2\pi b \left| \exp\left[i\left(\frac{1}{k} \chi_0(b) + \frac{1}{k^3} \chi_1(b)\right)\right] - 1 \right|^2, \quad (21)$$

where $\chi_0(b)$ is given by Eq. (16) and the Wallace phase now reduce to

$$\chi_1(b) = -\frac{1}{4} \left(\frac{m}{\hbar^2}\right)^2 \int_{-\infty}^{\infty} dz' V(r) \left(V(r) + r \frac{d}{dr} V(r)\right), \quad (22)$$

for a symmetric potential $V(r)$.

Table 1. Numerical values of the EDES (left columns) and modified EDES (right columns) cross sections in strongly coupled plasmas at the maximum positions with various projectile energies and ion-sphere radii

	$\left(\frac{\sigma_{\text{tot}}^E}{db}\right)_{\text{SCP}} / \pi a_Z^2$		$\left(\frac{\sigma_{\text{tot}}^{ME}}{db}\right)_{\text{SCP}} / \pi a_Z^2$	
	$\bar{R}_Z = 5$	$\bar{R}_Z = 10$	$\bar{R}_Z = 5$	$\bar{R}_Z = 10$
	$\bar{b} = 1$	$\bar{b} = 2$	$\bar{b} = 1$	$\bar{b} = 2$
$\epsilon = 10$	0.772	1.545	0.782	1.555
$\epsilon = 20$	0.393	0.785	0.395	0.787

3. EIKONAL ELASTIC SCATTERING CROSS SECTION IN STRONGLY COUPLED PLASMA

A most typical example of a strongly coupled plasma may be seen in the system of ions inside a highly evolved star. A description of the strongly coupled plasmas is provided by the ion-sphere model.^{5-7, 21} In this model the interaction potential is obtained by

$$V^{\text{IS}} = -\frac{Ze^2}{r} \left[1 - \frac{r}{2R_Z^2} \left(3 - \frac{r^2}{R_Z^2} \right) \right] \theta(R_Z - r), \quad (23)$$

where $R_Z [= (3Z/4\pi n_e)^{1/3}]$ is the ion-sphere radius (or the Wigner-Seitz radius). This ion-sphere potential is designed so that potential and its first derivative vanish at some cutoff distance, which is the so-called ion-sphere radius. Thus, in strongly coupled plasmas, screening is better described by this ion sphere picture, in which the stationary ion of charge Z is surrounded by Z electrons, uniformly distributed throughout the ion-sphere radius. Using this potential, the ordinary eikonal phase is obtained by

$$\chi_0(b) = \frac{2mZe^2}{\hbar^2} \left[\ln \left(\frac{R_Z + \sqrt{R_Z^2 - b^2}}{b} \right) + \frac{\sqrt{R_Z^2 - b^2}}{R_Z} \left(-\frac{4}{3} + \frac{b^2}{3R_Z^2} \right) \right]. \quad (24)$$

After some manipulation the Wallace phase is found to be

$$\begin{aligned} \chi_1(b) = & \frac{3}{4} \left(\frac{mZe^2}{\hbar^2} \right)^2 \frac{1}{R_Z} \left[\left(1 - \frac{b^2}{2R_Z^2} \right) \ln \left(\frac{R_Z + \sqrt{R_Z^2 - b^2}}{b} \right) \right. \\ & \left. + \frac{\sqrt{R_Z^2 - b^2}}{R_Z} \left(-\frac{43}{30} + \frac{6b^2}{5R_Z^2} - \frac{4b^4}{15R_Z^4} \right) \right]. \end{aligned} \quad (25)$$

Then the EDES cross section in a strongly coupled plasma is given by

$$\begin{aligned} \left(\frac{\sigma_{\text{tot}}^E}{db}\right)_{\text{SCP}} / \pi a_Z^2 = & 2\bar{b} \left| \exp \left\{ i \frac{2}{\epsilon^{1/2}} \left[\ln \left(\frac{1 + \sqrt{1 - \bar{b}^2/\bar{R}_Z^2}}{\bar{b}/\bar{R}_Z} \right) \right. \right. \right. \\ & \left. \left. \left. + \sqrt{1 - \frac{\bar{b}^2}{\bar{R}_Z^2}} \left(-\frac{4}{3} + \frac{\bar{b}^2}{3\bar{R}_Z^2} \right) \right] \right\} - 1 \right|^2, \end{aligned} \quad (26)$$

where $\bar{R}_Z (\equiv R_Z/a_Z)$ is the scaled ion-sphere radius, $\bar{b} (\equiv b/a_Z)$ is the scaled impact parameter, and $\epsilon (\equiv E/Z^2 R \gamma)$ is the scaled energy of the projectile electron. Including the Wallace correction the modified EDES cross section is found to be

$$\begin{aligned} \left(\frac{\sigma_{\text{tot}}^{ME}}{db} \right)_{\text{SCP}} / \pi a_Z^2 = & 2\bar{b} \left| \exp \left\{ i \frac{2}{\epsilon^{1/2}} \left[\ln \left(\frac{1 + \sqrt{1 - \bar{b}^2/\bar{R}_Z^2}}{\bar{b}/\bar{R}_Z} \right) \right. \right. \right. \\ & + \left. \left. \sqrt{1 - \frac{\bar{b}^2}{\bar{R}_Z^2}} \left(-\frac{4}{3} + \frac{\bar{b}^2}{3\bar{R}_Z^2} \right) \right] + i \frac{3}{4\epsilon^{3/2}} \frac{1}{\bar{R}_Z} \right. \right. \\ & \times \left. \left. \left[\left(1 - \frac{\bar{b}^2}{2\bar{R}_Z^2} \right) \ln \left(\frac{1 + \sqrt{1 - \bar{b}^2/\bar{R}_Z^2}}{\bar{b}/\bar{R}_Z} \right) \right. \right. \right. \\ & \left. \left. \left. + \sqrt{1 - \frac{\bar{b}^2}{\bar{R}_Z^2}} \left(-\frac{43}{30} + \frac{6\bar{b}^2}{5\bar{R}_Z^2} - \frac{4\bar{b}^4}{15\bar{R}_Z^4} \right) \right] - 1 \right\} \right|^2. \end{aligned} \quad (27)$$

Numerical values of the EDES and modified EDES cross sections at the maximum positions are listed in Table 1. Here we consider two cases of ϵ : $\epsilon = 10$ and 20, and consider two case of the ion-sphere radii: $\bar{R}_Z = 5$ and 10. The cross sections are substantially decreased with an increase of the plasma-screening effect through the ion-sphere radius. The Wallace correction effect is increased as the plasma-screening effect increases for a given projectile energy. However, the Wallace correction effect is decreased as the projectile energy increases. For a given ion-sphere radius, the maximum position of the cross section is almost unchanged with a change of the energy of the projectile electron.

Acknowledgements

This research was supported in part by the Korea Science and Engineering Foundation through Grant No. 961-0205-021 -2 and by the Korea Ministry of Education through the Basic Science Research Institute Program (BSRI-97-2448).

REFERENCES

- [1] V. P. Shevelko and L. A. Vainshtein, *Atomic physics for Hot Plasmas* (Institute of Physics, Bristol, 1993), Ch. 4.
- [2] H. P. Summers, *Adv. Atom. Mol. Phys.* **33**, 275 (1994).
- [3] R. K. Janev, L. P. Presnyakov, and V. P. Shevelko, *Physics of Highly Charged Ions* (Springer-Verlag, Berlin, 1985), Ch. 10.
- [4] S. Ichimaru, *Statistical Plasma Physics, Vol. 1: Basic Principles* (Addison-Wesley, Redwood City, CA, 1992), Ch. 1.
- [5] E. E. Salpeter, *Aust. J. Phys.* **7**, 373 (1954).
- [6] S. Ichimaru, *Rev. Mod. Phys.* **54**, 1017 (1982).
- [7] J. C. Weisheit, *Adv. Atom. Mol. Phys.* **25**, 101 (1988).
- [8] Y.-D. Jung, *Phys. Plasmas* **2**, 1775 (1995).
- [9] Y.-D. Jung, *Phys. Plasmas* **3**, 1741 (1996).
- [10] Y.-D. Jung and H.-D. Jeong, *Phys. Rev. E* **54**, 1912 (1996).
- [11] C. J. Joachain, *Quantum Collision Theory*, 3rd ed. (North Holland, Amsterdam, 1983), Ch. 9.
- [12] P. G. Burke and C. J. Joachain, *Theory of Electron-Atom Collisions, Part 1: Potential Scattering* (Plenum, New York, 1995), Ch. 2.
- [13] G. J. Hatton, N. F. Lane, and J. C. Weisheit, *J. Phys. B Atom. Mol. Phys.* **14**, 4879 (1981).
- [14] Y.-D. Jung, *Phys. Fluids B* **5**, 3432 (1993).
- [15] Y.-D. Jung, *Phys. Plasmas* **2**, 332 (1995).
- [16] Y.-D. Jung and J.-S. Yoon, *J. Phys. B Atom. Mol. Phys.* **29**, 3549 (1996).

- [17] J.-S. Yoon and Y.-D. Jung, *Phys. Plasmas* **3**, 3291 (1996).
- [18] S. J. Wallace, *Ann. Phys.* **78**, 190 (1973).
- [19] S. J. Wallace, *Phys. Rev. D* **8**, 1846, 1934 (1973).
- [20] R. Shankar, *Principles of Quantum Mechanics*, 2nd ed. (Plenum, New York, 1994), Ch. 19.
- [21] J. Weisheit, in *Atomic, Molecular, and Optical Physics Handbook*, edited by G. W. F. Dark (American Institute of Physics, New York, 1996), p. 978.

VANISHING OF HIGHER EXCITED BOUND STATES WITHOUT LOWERING OF IONIZATION POTENTIALS IN PARTIALLY IONIZED STRONGLY COUPLED PLASMAS

A.S.Kaklyugin, G.E.Norman

Moscow Physical Society
 PO Box 110, Moscow 121019, Russia
 e-mail: henry@aha.ru, fax: (095)1357995

INTRODUCTION 1,2

The influence of plasma waves on atomic spectra in electron-ion strongly coupled plasmas (SCP) was studied in [1]. The SCP collective model [1,3,4] allows one to consider plasma Hamiltonian as a set of weakly coupled oscillatory-like terms. The model was completed by excited atomic states also in the form of the oscillatory-like terms. The interaction between two oscillatory modes was taken into consideration as a plasma wave field. Thus it becomes possible to construct a rough representation of a SCP plasma spectrum of free and bound electron states.

The principle idea of [1,2] may be formulated in a following way.

Particle motion in the collective states corresponds to the oscillatory type of charge density variation. It is connected with longitudinal electromagnetic waves for frequencies $\omega \geq \Omega_e = (4\pi n e^2 / m)^{1/2}$. Hence collective states, i.e. the continuous spectrum states, can be identified by frequencies from Ω_e to $\omega(\mathbf{q}_0)$ [1,3,4] where \mathbf{q}_0 is a boundary wave vector [1]. The quantity \mathbf{q}_0 is defined by analogy with Debye wave number in solid state theory.

An atomic electron with principle quantum number t behaves upon the action of a circulating electromagnetic field as an oscillator. Its frequency

$$\omega_t = m e^4 / (\hbar t)^3 \tag{1}$$

corresponds to a transition from t -th level to $(t+1)$ -th. This fact permits one to classify the states of this mode over the frequency scale. It is fairly obvious that the energy of the t -th state decreases when t growth.

The low energy states are sufficiently well defined, the interaction with collective states being weak enough in accordance with the inequality $\omega_t = m e^4 / (\hbar t)^3 \gg \Omega_e$. The mode frequencies draw together with the growth of t . A resonance condition is achieved at some value $t=t^*$

$$\omega_{t^*} = me^4/(\hbar t^*)^3 = \omega(q_0). \quad (2)$$

Interaction is carried out by means of plasma wave fields, as well as by atomic polarization fields. The interaction results in mutual repulsion of the resonance oscillation frequencies. An atomic state spectrum is found to be restricted by some frequency, Eq. (2), and by the corresponding energy

$$\varepsilon(t^*) = me^4/2(\hbar t^*)^2. \quad (3)$$

The repulsion and restriction discussed above were treated as an electron spectrum gap

$$\Delta E \approx \varepsilon(t^*) \quad (4)$$

where discrete spectrum vanishes and density of continuous states remains low. The energy gap results in the decrease of (a) shift and broadening constants of spectral lines, (b) spectral line intensities, and (c) continuum spectrum intensities.

There are two weak points in the above presented idea of^{1,2}. First, the definition (1) is not valid for complex atoms. The hydrogen-like Eqs.(1)-(3) can underestimate the value of ΔE substantially. It will be shown in the next Section.

Second, the classical mechanics treatment was implied in^{1,2}. It is inconsistent since there is no concept of discrete spectrum in classical mechanics. Besides, it does not permit to perform quantitative estimates of the gap influence on lines&continuum spectrum intensities. The preliminary statement of the problem for quantum treatment is presented in the last Section. We involve Fano⁵ approach which was only mentioned in².

Note works which are partially related to^{1,2}. Gutierrez and Girardeau^{6,7} tried to consider an atom as bound states of charge particles interacting by means of Coulomb potential renormalized by collective plasma excitation.

COMPLEX ATOM SCP TREATMENT

The resonance condition

$$\omega_{t^*} = \omega(q_0). \quad (5)$$

remains valid. But the Eq.(1) should be replaced with

$$\omega_t = \Delta E_{t^*} / \hbar, \quad (6)$$

where ΔE_{t^*} is the energy difference between t-th and t'-th terms of complex atom.

Now apply the Eqs. (5) and (6) to the analysis of experimental results obtained by Levina and Pukhov⁸. They have measured spectral line broadening for carbon atom CI 2419Å and ion CII 2837Å for electron concentration range $n_e = 1.5 \cdot 10^{18} + 3.1 \cdot 10^{19} \text{ cm}^{-3}$ and temperature about 30000°E. The observed values of the half-width agreed with data⁹ for $n_e = (1.5+2) \cdot 10^{18}$. The values measured became less then values calculated according to⁹ with increasing of n_e . The discrepancy achieved the value of factor 7 for CI 2479Å and factor 4 for CII 2837A at $n_e = 3.1 \cdot 10^{19}$. The nonidealty parameter $\gamma = e^2(2n_e)^{1/3}/kT$ is about $\gamma \approx 0.3$ for $Z=1$ at these conditions, i.e. the Debye radius is less then interparticle distance.

The CI atomic energy levels related to the spectral line CI 2479A and to its broadening are shown in Fig.1a. Note that the broadening quadratic Stark effect constant C_4 is defined by

$$C_4 \sim \sum_i \lambda_i f_i, \quad (7)$$

where λ_i and f_i are the wavelength and the oscillator strength of the optical transition from the level considered to the i -th level. The sum (7) is extended to all levels connected with the level considered.

The effect that we spoke of consists of the following. If the resonance condition (5) is carried out for the substantial part of the i -th levels in (7), these levels should be cancelled from the sum (7) and the value of C_4 decreases.

It is seen in Fig.1a that at $n_e = 1.5 \cdot 10^{18} \text{ cm}^{-3}$ the plasma wave energy $\hbar\Omega_e$ does not almost disturb the levels which give the main contribution to the sum (7) for the line considered. Consequently the halfwidth values were measured to be close to the values obtained from⁹. And vice versa at $n_e = 3.1 \cdot 10^{19}$ the plasma wave energy $\hbar\Omega_e$ disturbs considerably all the levels which contribute to the sum (7). It reduces C_4 substantially.

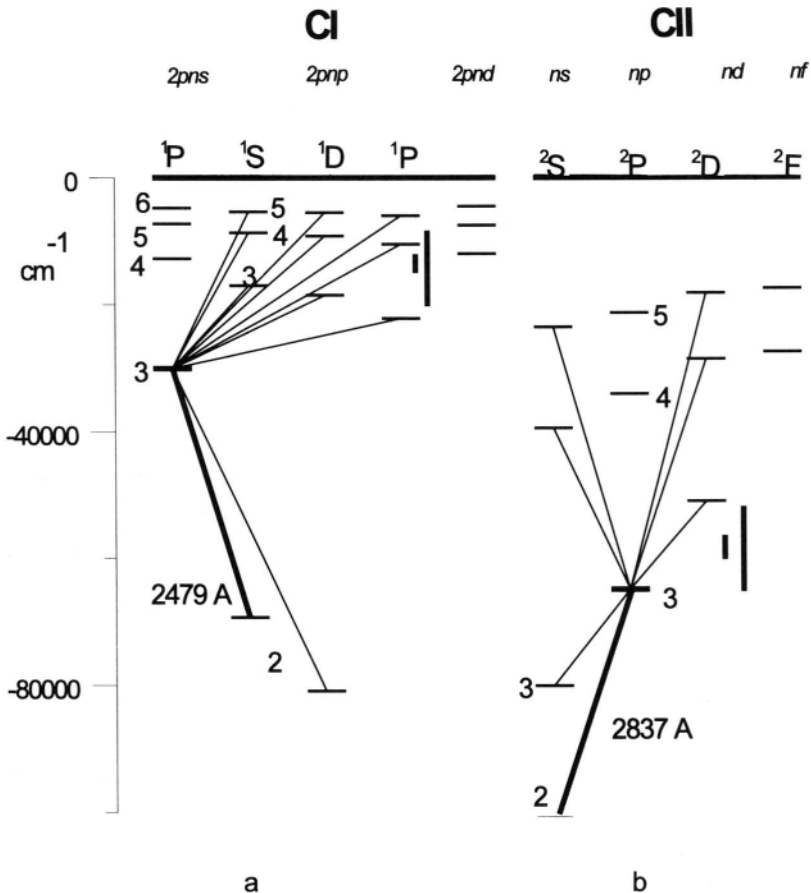


Figure.1. Fragments of energy level diagrams for CI (a) and CII (b) relevant to spectral lines CI 2479Å and CII 2837Å. Vertical thick segments designate energies $\hbar\Omega_e$ for two cases. Thin lines designate terms contributions to the broadening constant (7) (only upper level is considered).

It makes no matter whether we estimate ω_i according to (1) or (6) to treat CI 2479Å. The opposite situation takes place for the spectral line CII2837Å. The estimates according to Eqs.(1)-(4) does not affect at all the sum (7) either at $n_e=1.5 \cdot 10^{18}$ or at $n_e=3.1 \cdot 10^{19}$. If one compares $\hbar\Omega_e$ not with (1) but with (6) (Fig.1b) it is possible to conclude that the plasma wave energy $\hbar\Omega_e$ disturbs considerably all the levels which contribute to the sum (7) for the spectral line CII 2837Å. It is necessary to take into account that the value $\omega(\mathbf{q}_0)$ exceeds by a factor 1.5+2 the value Ω_e for the values γ considered.

Thus, Fig.1b shows that taking into account the atomic energy levels for complex atom may increase the value of ΔE by substantial factor. It results in reducing C_4 value. That was the case in the measurements⁸.

PRELIMINARY STATEMENT OF THE QUANTUM PROBLEM

We treat absorption spectrum in SCP since it is an observable quantity and provides information about energy spectrum.

Approximate Hamiltonian is expected to be constructed from two parts in the following way. The first part accounts for discrete spectrum, the second part accounts for continuous states. The perturbation ΔH is introduced to describe the influence of collective modes which results in mixing of wave functions corresponding to two parts of the Hamiltonian.

It is necessary to emphasize that ΔH is a nonstationary perturbation with frequencies from Ω_e to $\omega(\mathbf{q}_0)$. The perturbation leads to mixing of bound and free states which energies differ by the value $\pm\hbar(\Omega_e+\omega(\mathbf{q}_0))$. This picture agrees with quasiclassical results^{1,2} concerning energy gap value. However this approach opens the way to absorption spectrum calculation.

The effect, which is expected from mixing of the every pair of states, is a Beutler-Fano profile. The effect is entangled by two factors. Nonstationary perturbation results in nonstationary profile. Therefore the time averaging is needed. Moreover treating of mixing of only two states is not a good approximation since all the states interacting with the perturbation are necessary to take into account for photoabsorption calculation. Consequently the final expression should be a double integral from the Beutler-Fano profile over time and energy.

ACKNOWLEDGEMENT

We thank A.M.Pukhov for placing at our disposal the results⁸ before publication.

REFERENCES

1. A.A.Valuev, A.S.Kaklyugin, G.E.Norman, in: *Radiation plasmodynamics*, ed. Yu.S.Protasov (Energoatomizdat, Moscow, 1991) p. 396.
2. A.S.Kaklyugin, G.E.Norman, *Proc. Intern. Conf. Physics of Strongly Coupled Plasmas* (Binz, 1995), eds. W.-D.Kraeft and M.Schlanges (World Scientific, Singapore, 1996) p.278.
3. A.S.Kaklyugin, G.E.Norman, A.A.Valuev, *ibid*, p.435.
4. A.S.Kaklyugin, G.E.Norman, A.A.Valuev, *XXIII ICPIG* (Toulouse, 1997).
5. U.Fano, *Phys. Rev.* **124**, 1866 (1961).
6. F.A.Gutierrez, M.D.Girardeau, *Phys. Rev.* **A42**, 936 (1990).
7. F.A.Gutierrez, *Phys. Rev.* **A42**, 2451 (1990).
8. O.V.Levina, A.M.Pukhov, *Optics and Spectroscopy* **81**, 712 (1996).
9. H.Griem, *Broadening of Spectral Lines in Plasmas*, Moscow, 1978.

IONIZATION KINETICS IN A DENSE CARBON PLASMA

Ralf Prenzel,¹ Thomas Bornath,¹ and Manfred Schlanges²

¹Fachbereich Physik der Universität Rostock
18051 Rostock, Germany

²Institut für Physik, Universität Greifswald
17487 Greifswald, Germany

INTRODUCTION

Recently, hot dense plasmas with electron densities of about 10^{23} cm^{-3} and electron temperatures of about 100 eV were produced by intense laser irradiation of more than 10^{15} W/cm^2 focused on a solid target.¹⁻³ Under such conditions, the plasma becomes nonideal, and correlation induced many-body effects can influence essentially its equilibrium and non-equilibrium properties. An important point in connection with these fascinating developments is, that there is now a unique possibility to confront the theory of strongly coupled plasmas with the obtained experimental results. Of special interest is the recombination and expansion phase. Here, measurements were performed recently to study the temporal evolution of the degree of ionization and of the electron temperature in laser-produced carbon plasmas.¹⁻³

The aim of this paper is to consider the recombination and expansion of such dense plasmas theoretically based on a quantum kinetic approach. In the first part of the paper, the coupled system of equations for the densities and the temperatures is given, including the relevant collision processes as well as the typical plasma density effects. Numerical results are presented which describe the density-temperature relaxation of a dense, hydrogen-like carbon plasma for isoenergetic conditions. Then a simple model is applied to extend the considerations to a adiabatically expanding carbon plasma appearing in the laser-produced experiments.

EQUATIONS FOR DENSITIES AND TEMPERATURES

Rate equations for the population densities of atomic states in a dense plasma can be derived starting from quantum kinetic equations for the Wigner distribution function of free and bound particles.⁴ These equations include many-body effects such as quasiparticle energies, dynamical screening, lowering of ionization energy and Pauli blocking. Integration of the kinetic equations with respect to the momenta leads to hydrodynamic equations for the densities and temperatures. In this section we are interested in the situation, where light and heavy particles have not yet relaxed towards a common temperature. Such plasmas can arise, when a short laser pulse interacts with solid matter.⁵

For a plasma consisting of electrons, fully stripped ions and hydrogen-like ions in different states $|j\rangle$ with number densities n_e, n_Z, n_{Z-1}^j , respectively, we get

$$\frac{\partial n_{Z-1}^j}{\partial t} = n_e^2 n_Z \beta_j - n_e n_{Z-1}^j \alpha_j + \sum_j (n_e n_{Z-1}^j K_{jj} - n_e n_{Z-1}^j K_{jj}), \quad (1)$$

where Z is the nuclear charge number. On the r.h.s. of equation (1), we have the coefficients of impact ionization α_j , three-particle recombination β_j and of excitation/deexcitation K_{jj} . The coefficients account for many-body effects, what leads to a density dependence of these coefficients. Numerical results can be found in Refs.^{6,7}. In order to have analytical formulae for the coefficients, we use here a simple approximation:⁸

$$\alpha_j = \alpha_j^{ideal} e^{-(\Delta_e + \Delta_Z - \Delta_j)/k_B T_e}, \quad \beta_j = \alpha_j (2\pi \hbar^2 / (m_e k_B T_e))^{\frac{3}{2}} e^{I_j^{eff}/k_B T_e}, \quad (2)$$

with α_j^{ideal} being the value for the ideal plasma state. In the following j denotes the principal quantum number only. I_j^{eff} is given by $I_j^{eff} = |E_j| + (\Delta_e + \Delta_Z - \Delta_j)$, where the second term represents the lowering of the ionization energy. The shifts are in the lowest order⁹ $\Delta_a = -\frac{1}{2} z_a^2 e^2 \kappa$. The inverse screening length is given by $\kappa^2 = \kappa_e^2 + \kappa_i^2$; $\kappa_i^2 = \kappa_Z^2 + \kappa_{Z-1}^2$; $\kappa_a^2 = 4\pi z_a^2 e^2 n_a / (k_B T_a)$. The excitation/deexcitation coefficients have been taken from Ref.¹⁰.

In the spatially homogeneous case the balance equations for the electron temperature T_e and the temperature of the ions T_i can be given as

$$\frac{3}{2} n_e k_B \frac{\partial T_e}{\partial t} + \frac{k_B}{32\pi\kappa} \left[\kappa_e^4 \frac{\partial T_e}{\partial t} + \kappa_e^2 \kappa_i^2 \frac{T_e}{T_i} \frac{\partial T_i}{\partial t} \right] \quad (3)$$

$$+ \frac{\partial n_{Z-1}}{\partial t} \left[(2Z - \frac{1}{4}) \kappa e^2 + \frac{k_B T_e}{8\kappa} \kappa_e^2 l \right] = \sum_j \left(\frac{3}{2} k_B T_e - I_j^{eff} \right) \frac{\partial n_{Z-1}^j}{\partial t} + Z_{e,Z} + Z_{e,Z-1}, \quad (4)$$

$$\frac{3}{2} (n_Z + n_{Z-1}) k_B \frac{\partial T_i}{\partial t} + \frac{k_B}{32\pi\kappa} \left[\kappa_i^2 \kappa_e^2 \frac{T_i}{T_e} \frac{\partial T_e}{\partial t} + \kappa_i^4 \frac{\partial T_i}{\partial t} \right] \quad (5)$$

$$+ \frac{\partial n_{Z-1}}{\partial t} \left[(2Z - 1) \frac{\kappa e^2}{4} + \frac{k_B T_i}{8\kappa} \kappa_i^2 l \right] = -Z_{e,Z} - Z_{e,Z-1}, \quad (6)$$

with $l = e^2 / (k_B T_e) + (2Z - 1) e^2 / (k_B T_i)$. The equations describe the temperature relaxation of the light and heavy particles. Many-body effects are included in the terms with the inverse Debye length explicitly, in the source function $\frac{\partial}{\partial t} n_{Z-1} = \sum_j \frac{\partial}{\partial t} n_{Z-1}^j$ and in the terms of energy transfer due to elastic collisions between the electrons and ions $Z_{e,a}$ ($a = Z, Z - 1$). For non-degenerate systems we find in the quasi-hydrodynamic approximation:¹¹

$$Z_{e,a} = \frac{8k_B n_e n_a \mu_{ea}}{m_e + m_a} \sqrt{\frac{2(\phi_e + \phi_a)}{\pi \phi_e \phi_a}} Q_{ea} \cdot (T_a - T_e) \quad (7)$$

with $\phi_a = m_a / (k_B T_a)$ and μ_{ea} is the reduced mass. Q_{ea} is given in terms of the transport cross section.¹¹ The latter is used in first Born approximation.

In the following example, a dense hydrogen-like carbon plasma is investigated. Numerical results following from the solution of the coupled set of equations (1), (3), (4) are presented in Fig. 1. In the initial state, the plasma is chosen to be fully ionized with $n_e^{tot} = 3.5 \cdot 10^{23} \text{ cm}^{-3}$, $T_e(0) = 150 \text{ eV}$, $T_i = 149 \text{ eV}$. In the first stage the screening is so high, that only the ground state and the first excited state ($j = 2$) can be occupied. Due to the recombination, the free electron density is reduced and the electron temperature rises, so that

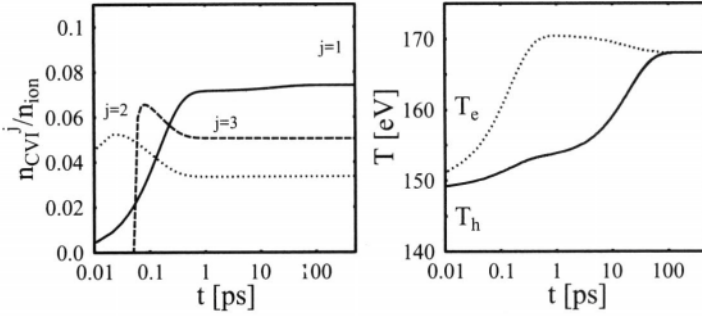


Figure 1. Time evolution of the occupation numbers and the temperatures for a two-temperature carbon plasma: $n_e^{tot} = 3.5 \cdot 10^{23} \text{ cm}^{-3}$, $T_e(0) = 150 \text{ eV}$, $T_i(0) = 149 \text{ eV}$

the screening decreases. After $\approx 0.1 \text{ ps}$ the second excited state ($j = 3$) can exist and appears as a new level (inverse Mott effect). The temperature relaxation is slower than the chemical relaxation by more than one order of magnitude in time. This was discussed also in the case of hydrogen.¹¹ LTE is reached after $\approx 1 \text{ ps}$. Results for the density–temperature relaxation for hydrogen and carbon plasmas based on a stochastic approach are given in Ref. [12].

ADIABATICALLY EXPANDING CARBON PLASMA

In this section we consider the case of an adiabatically expanding plasmas, as produced by high-power, subpicosecond lasers.³ The ionization kinetics of such plasmas is studied using a simple model of adiabatic expansion. For simplicity, a plasma with a common non-equilibrium temperature of the whole plasma is considered. Using the internal energy and the pressure in the approximation of the Debye limiting law,¹³ the equation of the temperature for an adiabatically expanding hydrogen-like plasma can be written as

$$\frac{\partial T}{\partial t} = \sum_j \left\{ \frac{\frac{3}{2} k_B T - \frac{3}{4} \kappa e^2 [1 + Z^2 - (Z-1)^2] + |E_j|}{\frac{3}{2} n_\sigma k_B + \frac{\kappa e^2}{4T} [n_e + Z^2 n_Z + (Z-1)^2 n_{Z-1}]} \right\} \frac{\partial n_{Z-1}^j}{\partial t} \quad (8)$$

$$- \left\{ \frac{p/V}{\frac{3}{2} n_\sigma k_B + \frac{\kappa e^2}{4T} [n_e + Z^2 n_Z + (Z-1)^2 n_{Z-1}]} \right\} \frac{\partial V}{\partial t},$$

with $n_\sigma = n_e + n_Z + n_{Z-1}$. The relaxation of the temperature is determined by the contribution of chemical reactions and by the change of the energy density due to the expansion. Nonideality effects enter this equation via the source term $\frac{\partial}{\partial t} n_{Z-1}^j$, the nonideal pressure p and the inverse Debye length κ .

In the following example, the one-dimensional adiabatic expansion of an laser-produced H-like carbon plasma is examined. Such plasmas were considered by Theobald et al.³ A simple approximation is to set the expanding velocity MO constant and equal to the ion sound velocity $u_{ion} = ((Z_i) T_e(0) k_B / m_i)^{1/2}$. Then $1/V \frac{d}{dt} V = u_0/d$ and $d = d_0 + u_0 t$, (d_0 is the initial thickness of the irradiated foil). In Fig. 2 the time evolution of the plasma is shown. The initial state (fully ionized, $n_e^{tot} = 4 \cdot 10^{23} \text{ cm}^{-3}$, $T(0) = 150 \text{ eV}$, $u_0 = 8.5 \cdot 10^6 \text{ cm/s}$, $d_0 = 70 \text{ nm}$) is similar to the experimental conditions of Ref.¹⁴. In Fig. 2a the time evolution of the plasma temperature in the nonideal case (described model) and ideal case (also without reactions) is plotted. The temperature of the plasma with nonideal corrections is higher than the “ideal” one, because of the reactions and the nonideal pressure. In Fig. 2b the evolution of the free electron density is plotted. From calculations we find, that after $\approx 1 \text{ ps}$ LTE is

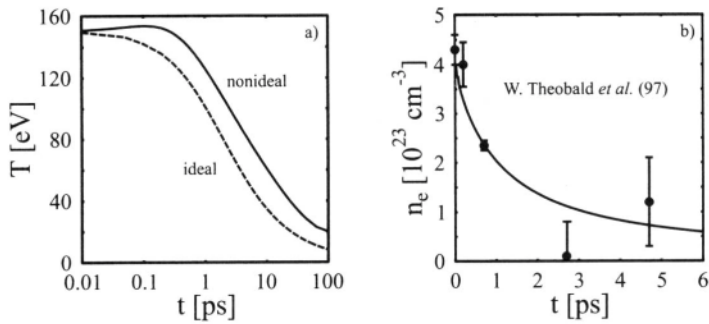


Figure 2. Time evolution of the temperature and the free electron density for an adiabatically expanding, hydrogen-like, carbon plasma: $n_e^{tot} = 4.3 \cdot 10^{23} \text{ cm}^{-3}$, $T(0) = 150 \text{ eV}$, $u_0 = 8.5 \cdot 10^6 \text{ cm/s}$, $d_0 = 70 \text{ nm}$. Points are measurements from Ref. [14].

reached, so that the free electron density can also be calculated by using a nonideal Saha equation with time-dependent temperature. The comparison with measurements¹⁴ shows, that the calculated curve fits the experimental data fairly good.

REFERENCES

- [1] Y. Leng, J. Goldhar, H. R. Griem, R. W. Lee, *Phys. Rev. E* 52: 4328 (1995).
- [2] J.-C. Gauthier, J.-P. Geindre, P. Audebert, A. Rousse, A. Dos Santos, G. Grillon, A. Antonetti, R. C. Mancini, *Phys. Rev. E* 52:2963 (1995).
- [3] W. Theobald, R. Häßner, C. Wülker, R. Sauerbrey, *Phys. Rev. Lett.* 77:298 (1996).
- [4] M. Schlanges, Th. Bornath, *Contrib. Plasma Phys.* 37:239 (1997)
- [5] D. P. Kitcrease, *J. Quant. Spectrosc. Radiat. Transfer* 51:161 (1994).
- [6] Th. Bornath, M. Schlanges, *Physica A* 196:427 (1993).
- [7] R. Prenzel, Th. Bornath, M. Schlanges, *Phys. Lett. A* 223:453 (1996)
- [8] M. Schlanges, T. Bornath, D. Kremp, *Phys. Rev. A* 38:2174 (1988).
- [9] W. D. Kraeft, D. Kremp, W. Ebeling, G. Röpke, "Quantum Statistics of Charged Particle Systems", Plenum, London, New York (1986).
- [10] L. M. Biberman, V. S. Vorob'ev, I. T. Iakubov, "Kinetics of the Nonequilibrium Low-Temperature Plasma", Consultants Bureau, New York (1987).
- [11] T. Ohde, M. Bonitz, T. Bornath, D. Kremp, M. Schlanges, *Phys. Plasmas* 3:1241 (1996).
- [12] D. Beule, W. Ebeling, A. Förster, *Physica B* 228:140 (1996)
- [13] W. Ebeling, W. D. Kraeft, D. Kremp, "Theory of bound states and ionization equilibrium in plasmas and solids", Akademie-Verlag Berlin (1976).
- [14] W. Theobald, R. Häßner, C. Wülker, R. Sauerbrey, private communication.

NONEXPONENTIAL TEMPERATURE DEPENDENCE OF REACTION RATES IN NONIDEAL PLASMAS

A. N. Starostin¹ and N. L. Aleksandrov²

¹Troitsk Institute for Innovation and Fusion Research

²Moscow Institute of Physics and Technology

Time evolution of ionic charge distribution and excited level populations may be density dependent especially under non-ideal plasma conditions.¹⁻⁵ The recent works¹⁻⁵ show a strong increase of ionization and excitation rates mostly due to so-called lowering of ionization potential LIP with increasing density. In the present report we consider another mechanism for increasing reaction rates which turns out to be even more important than the LIP. For nonideal plasmas and dense gases with collisional frequency the adequate description of kinetic phenomena can be done using generalized distribution function over energies and momenta which is defined as

$$f(E, \mathbf{p}) = \int d\tau d\mathbf{r} \cdot e^{iE\tau - i\mathbf{p}\mathbf{r}} \langle \hat{\Psi}^+(x_2) \hat{\Psi}(x_1) \rangle \quad (1)$$

where $\tau = t_1 - t_2$, $\mathbf{r} = \mathbf{r}_1 - \mathbf{r}_2$; $\hat{\Psi}(x)$ - is the particle field operator in Heisenberg representation.⁶ In (1) E and \mathbf{p} are independent Fourier-transform variables and usual distribution functions over energies $f(E)$ or over momenta $f(\mathbf{p})$ can be obtained by integrating $f(E, \mathbf{p})$ over \mathbf{p} or E . Under equilibrium conditions Baym and Kadanoff showed that $f(E, \mathbf{p})$ may be represented in the following way⁶

$$f(E, \mathbf{p}) = \frac{n(E)}{\pi} \frac{\text{Im}\Sigma^R(E, \mathbf{p})}{(E - \varepsilon_p - \text{Re}\Sigma^R)^2 + (\text{Im}\Sigma^R)^2}, \quad (2)$$

where $n(E)$ is a particle population number (for Fermi particles $n(E) = \frac{1}{e^{\frac{E-\mu}{T}} + 1}$), $\varepsilon_p = \frac{p^2}{2M}$ and $\Sigma^R(E, \mathbf{p})$ is the mass operator for one-particle retarded Green's function. The conventional approach¹⁻⁵ neglects $\text{Im}\Sigma^R$ and takes into account only $\text{Re}\Sigma^R$ which for weakly non-ideal plasmas reduces to

$$\text{Re}\Sigma^R \approx -\frac{\Gamma}{2} \cdot T \quad (3)$$

where $\Gamma = \frac{e^2}{r_D T}$ is coupling parameter, and r_D is the Debye radius. This consideration gives an increase in the reaction rates due to the LIP. For low density gases and plasmas we have $\text{Im}\Sigma^R \sim \hbar\nu \sim \hbar N \bar{\sigma} \bar{v}$, where ν is a collisional frequency. For Coulomb scattering we have $\text{Im}\Sigma^R \sim \frac{\lambda}{r_D} \Gamma T$, where λ is the thermal de Broigle wavelength; that is, $\text{Im}\Sigma^R$ is of quantum

nature. Owing to uncertainty principle, for given energy there are particles with any value of momentum. Galitskiy showed that even under equilibrium conditions the non-zero value of $\text{Im}\Sigma^R$ leads in dense gases to the appearance of nonexponential tail for the distribution function over momenta⁷

$$f(\mathbf{p}) = \int dE f(E, \mathbf{p}) = f_M(\mathbf{p}) + \frac{\hbar\nu_p T}{2\pi\varepsilon_p^2} e^{\frac{\mu-E}{T}}, \quad (4)$$

where $f_M(p)$ is the Maxwellian distribution function. The last term in (4) may be many orders of magnitude larger than the first one for large values of momentum. Nevertheless, the distribution over energies is exponential one; e.g., for $\nu_p = \nu = \text{const}$ we have

$$f(E) = e^{\frac{\mu-E}{T}} \text{Re} \sqrt{E + i\nu}. \quad (5)$$

The nonexponential tail in (4) can strongly affect the rates of high-threshold inelastic processes at high densities and low temperatures.

In the general case the rate constant in the Born approximation can be written as follows (compare with [1–5]):

$$\begin{aligned} \overline{N_a n_e k_{i\alpha j\beta}} &= \int \frac{d^4 p d^4 q d^4 p'}{(2\pi)^{12}} |V_{i\alpha j\beta}(q)|^2 \cdot n_e(\omega') \cdot \\ &\cdot \delta_\gamma(\omega' - \varepsilon_{\mathbf{p}'}^e) (1 - n_e(\omega' + \omega)) \delta_\gamma(\omega' + \omega - \omega_{\beta\alpha} - \varepsilon_{\mathbf{p}}^e + \mathbf{q}^e) \\ &\cdot N_a(\omega_p + \omega_i) \delta_\gamma(\omega_p - E_p) (1 - N_a(\omega_p - \omega + \omega_i)) \cdot \\ &\cdot \delta_\gamma(\omega_p - \omega + \omega_{ij} - E_{\mathbf{p}-\mathbf{q}}), \end{aligned} \quad (6)$$

where $n_e(\omega) = \frac{1}{e^{\frac{\omega-\mu_e}{T}+1}}$, $N_a(\omega) = \frac{1}{e^{\frac{\omega-\mu_p}{T}+1}}$ and $V_{i\alpha j\beta}(q)$ is a Fourier transform of matrix element of interaction potential for transition $i(e), \alpha(a) \rightarrow j(e), \beta(a)$.

Here, the usual δ -functions are replaced by the Lorentzian profiles which for electron in nonideal plasmas can be written as

$$\delta_\gamma(\omega - \varepsilon_p) = \frac{\gamma(\omega, p)}{\pi \left[(\omega - \varepsilon_p + \frac{\Gamma T}{2})^2 + \gamma^2(\omega, p) \right]}, \quad (7)$$

where in the gaseous approximation we have $\gamma \sim \text{Im}\Sigma^R \sim N\sigma_p v$.

In (6) the Pauly blocking mechanism is taken into account. More generally, $V(q)$ may be replaced by the two-particle scattering amplitude in media $T(\mathbf{p}, \mathbf{p}', E)$,^{6,7} and in the gaseous approximation one can assume $T \approx f(\mathbf{p}, \mathbf{p}')$, where $f(p, p')$ is the scattering amplitude outside the mass shell ($p \neq p'$). It follows from this consideration that the rate constant is governed mostly by the distribution function over momenta rather than that over energies and that at $\gamma \neq 0$ the nonexponential tails may cause an increase in the rates which is many orders of magnitude higher than that which is due to the LIP. As a model example we can estimate the rate of atom excitation (ionization) using the approximations $f(p, p') \approx \text{const}$ (which is valid near the energy threshold) and $\gamma_p \approx \gamma \approx \text{const}$ (which is reasonable for ionization in dense gases). In this case we obtain

$$k_e = k_0 \left(e^{-\frac{I}{T}} + \frac{\hbar\gamma}{2I} \right) \quad (8)$$

where I is the energy of ionization (including the LIP) or excitation.

The last term in (8) shows the nonexponential behavior of the rates and may be much more important at low temperatures than the first one even if the LIP is taken into account. Figs. 1 and 2 show the normalized rates versus density which were obtained numerically using (6H8).

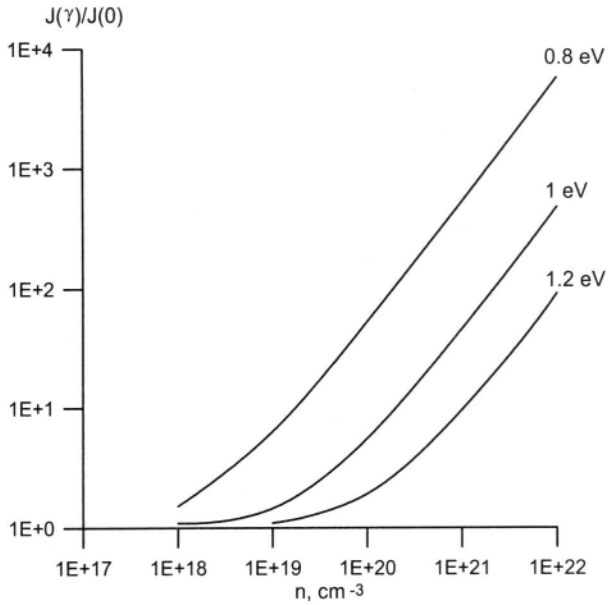


Figure 1. The normalized electron impact ionization rate for model neutral gas with $I=10$ eV and $\gamma=\text{constant}$ versus gas density.

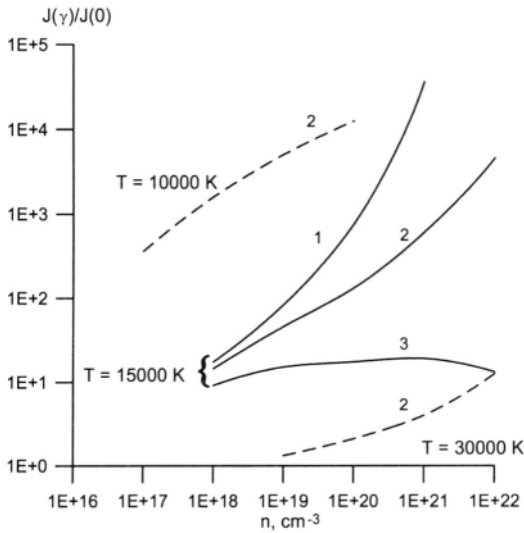


Figure 2. The same magnitudes for model non-ideal plasma versus electron density. Curve 1 is the ratio between our results neglecting the Pauli blocking and that of conventional theory; Curve 2 is the ratio between the same our results and that of the theory¹⁻⁵ and Curve 3 is the same as curve 1 but taking into account the Pauli blocking.

The main conclusions of our calculations are the following:

1. The quantum nonexponential tails in the distribution over momenta⁷ in dense gases and nonideal plasmas lead to nonexponential temperature dependence of rate constants even under equilibrium conditions.

The same exponential acceleration must occur for V-T relaxation rates in dense molecular gases, for ionization rates in dense dielectrics and for chemical reaction. In addition, this can give rise to hard radiation and nuclear fusion reactions at relatively low temperatures and high plasma densities.

2. The ten-fold increase in the rate constants occurs at $\Gamma \leq 1$ while the theories¹⁻⁵ considering the LIP give the same effect only at $\Gamma > 1$, when these theories are not well justified.

3. The degeneracy effect is more pronounced than that which follows from the approach which takes into account only the LIP.

REFERENCES

- [1] Schlages M., Bornath Th., Kremp D., Rate coefficients in reacting strongly coupled plasmas, *Phys. Rev. A*, 38:2174 (1988).
- [2] Bornath Th., Schlages M., Kremp D., Influence of Nonideality Effects on the Ionization and Recombination Coefficients of a Reacting Hydrogen Plasma, *Contrib. Plasma Phys.*, 28:57 (1988).
- [3] Klimontovich Yu., Schlages M., Bornath Th., Kinetic approach to reaction and diffusion in many-particle Systems, *Contrib. Plasma Phys.*, 30:349 (1990).
- [4] Schlages M., Bornath Th., Kremp D., Kinetic theory of ionization processes in dense plasmas, in: "Physics of Nonideal Plasmas," Ed. by W. Ebeling, A. Forster, R. Radtke. Stuttgart–Leipzig: B. G. Teubner Verlagsgesellschaft (1992).
- [5] Kremp D., Morawetz K., Schlages M., Rietz V., Impact ionization in nonideal plasmas in strong electric field, *Phys. Rev. E*, 47:635 (1993).
- [6] Kadanoff L., Baym G., in: "Quantum Statistical Mechanics," W. A. Benjamin. INS, N. Y., (1962).
- [7] Galitskiy V., Relaxion of a particle in the Maxwellian gas, *Zh. Expt. and Theor. Physics*, 51:957(1966).

FORMATION OF BINARY CORRELATIONS IN PLASMA

K. Morawetz,¹ Václav Špička,² and Pavel Lipavský²

¹Fachbereich Physik, Universität Rostock
18051 Rostock, Germany

²Institute of Physics, Academy of Sciences
Cukrovarnická 10, 16200 Praha 6, Czech Republic

INTRODUCTION

Recent lasers allow one to create a high density plasma within few femto seconds and observe its time evolution on a comparable scale.^{1,2} Naturally, this plasma is highly excited at the beginning and relaxes towards equilibrium by various mechanisms. In this paper we discuss the very first time regime, the transient regime, in terms of the energy balance. Let us assume a typically set up of molecular dynamics. One takes N particles, distributes them randomly into a box and let them classically move under Coulomb forces due to their own charges. Those particles which are very close will be expelled from each other. Their first movement thus forms correlations which lower the Coulomb energy $V_C = e^2/r$. This build up of screening stops when the effective Debye potential $V_D = e^2 e^{-kr}/r$ is reached. We will discuss the formation of correlations in terms of correlation energy. It is more convenient to calculate the kinetic energy than the correlation energy because the kinetic one is a single-particle observable.

KINETIC APPROACH

To this end we can use the kinetic equation, of course, such which leads to the total energy conservation. It is immediately obvious that the ordinary Boltzmann equation cannot be appropriate for this purpose because the kinetic energy is an invariant of its collision integral and thus constant in time. We have to consider non-Markovian kinetic equations of Levinson type¹

$$\begin{aligned} \frac{\partial}{\partial t} f_a(t) = & \frac{2}{\hbar^2} \sum_b \int \frac{dpdq}{(2\pi\hbar)^6} V_D^2(q) \int_0^t d\bar{t} \exp\left\{-\frac{t-\bar{t}}{\tau}\right\} \cos\left\{\frac{1}{\hbar}(t-\bar{t})\Delta_E\right\} \\ & \times \{ \tilde{f}'_a \tilde{f}'_b (1-\tilde{f}_a)(1-\tilde{f}_b) - \tilde{f}_a \tilde{f}_b (1-\tilde{f}'_a)(1-\tilde{f}'_b) \}, \end{aligned} \quad (1)$$

where $\Delta_E = \frac{k^2}{2m_a} + \frac{p^2}{2m_b} - \frac{(k-q)^2}{2m_a} - \frac{(p+q)^2}{2m_b}$ denotes the energy difference between initial and final states. The retardation of distributions, $\tilde{f}_a(k, \bar{t})$, $\tilde{f}'_a(k-q, \bar{t})$ etc., is balanced by the

lifetime τ . The total energy conservation for Levinson's equation has been proved in [3]. The full solution of Levinson's equation on the long time scale is a hard problem, however, its solution in the short-time region $t \ll \tau$ can be written down analytically. In this time domain we can neglect the time evolution of distributions, $\tilde{f}_a(t) = f_a(0)$, and the life-time factor, $\exp\left\{-\frac{t-i}{\tau}\right\} = 1$, therefore the deviation of Wigner's distribution from its initial value, $f_a(t) = f_a(0) + \delta f_a(t)$, reads

$$\delta f_a(t) = 2 \sum_b \int \frac{dpdq}{(2\pi\hbar)^6} V_D^2(q) \frac{1 - \cos\left\{\frac{1}{\hbar}t\Delta\tilde{E}\right\}}{\Delta\tilde{E}^2} \{f'_a f'_b (1-f_a)(1-f_b) - f_a f_b (1-f'_a)(1-f'_b)\}. \quad (2)$$

This formula shows how the two-particle and the single-particle concept of the transient behavior meet in the kinetic equation. The right hand side describes how two particles correlate their motion to avoid the strong interaction regions. This very fast formation of the off-shell contribution to Wigner's distribution has been found in numerical treatments of Green's functions.^{4,5}

INCREASE OF KINETIC ENERGY

From Wigner's distribution one can readily evaluate the increase of kinetic energy,

$$\left\langle \frac{k^2}{2m} \right\rangle - \left\langle \frac{k^2}{2m} \right\rangle_0 = \sum_a \int \frac{dk}{(2\pi\hbar)^3} \frac{k^2}{2m_a} \delta f_a. \quad (3)$$

After substitution for δf_a from (2) we symmetrize in k and p and anti-symmetrize in the initial and final states which yields the correlation energy. Of course, starting with a sudden switching approximation we have Coulomb interaction and during the first transient time period the screening is formed. This can be described by the non-Markovian Lenard-Balescu equation⁶ instead of the static screened equation (1) leading to the dynamical expression of the correlation energy [details, see [7]]. To demonstrate its results and limitations, we discuss special cases that allow for analytical treatment. To this end we use equilibrium initial distributions at the high temperature limit, where the distributions are non-degenerated.

COMPARISON WITH SIMULATION

In order to compare the time dependency of the correlation energy with molecular dynamical simulations,⁸ we assume a one component plasma which possess the Maxwellian velocity distribution during this formation time. From (3) we find

$$\begin{aligned} \frac{\partial E_{\text{corr}}^{\text{static}}(t)}{\partial t} &= -\frac{e^2 \kappa T}{2\hbar} \text{Im} \left[(1 + 2z^2) e^{z^2} (1 - \text{erf}(z)) - \frac{2z}{\sqrt{\pi}} \right] \\ \frac{\partial E_{\text{corr}}^{\text{dynam}}(t)}{\partial t} &= -\frac{e^2 \kappa T}{\hbar} \text{Im} \left[e^{z_1^2} (1 - \text{erf}(z_1)) \right] \end{aligned} \quad (4)$$

where we used $z = \omega_p \sqrt{t^2 - it\frac{\hbar}{T}}$ and $z_1 = \omega_p \sqrt{2t^2 - it\frac{\hbar}{T}}$. This is the analytical quantum result of the time derivative of the formation of correlation for statically as well as dynamically screened potentials. For the classical limit we are able to integrate expression (4) with respect to times and arrive at

$$E_{\text{corr}}^{\text{static}}(t) = -\frac{1}{4} e^2 n \kappa \left\{ 1 + \frac{2\omega_p t}{\sqrt{\pi}} - (1 + 2\omega_p^2 t^2) \exp(\omega_p^2 t^2) [1 - \text{erf}(\omega_p t)] \right\}$$

$$E_{\text{corr}}^{\text{dynam}}(t) = -\frac{1}{2}e^2 n \kappa \left\{ 1 - \exp\left(\frac{\omega_p^2}{2} t^2\right) \left[1 - \text{erf}\left(\frac{\omega_p}{\sqrt{2}} t\right) \right] \right\}. \quad (5)$$

In Figs. 1, this formulae are compared with molecular dynamic simulations⁸ for two values of the plasma parameter $\Gamma = 0.1$ and 1. This parameter $\Gamma = \frac{e^2}{a_e T}$, where $a_e = (\frac{3}{4\pi n})^{1/3}$ is the inter-particle distance or Wigner–Seitz radius, measures the strength of the Coulomb coupling. Ideal plasma are found for $\Gamma \ll 1$. In this region the static formula (5) well follows the major trend of the numerical result, see Fig. 1. The agreement is in fact surprising, because the static result underestimates the dynamical long time result of Debye- Hueckel $\sqrt{3}/2\Gamma^{3/2}$ by a factor of two. We have for the longtime and the classical limit $b^2 = (\hbar\kappa)^2 \frac{m_a+m_b}{8m_a m_b T} \rightarrow 0$

$$\begin{aligned} E_{\text{corr}}^{\text{dynam}}(\infty) &= -\frac{e^2 \kappa \sqrt{\pi}}{2} \frac{1}{b} (1 - e^{b^2} \text{erfc}(b)) \rightarrow -\frac{1}{2} e^2 n \kappa \\ E_{\text{corr}}^{\text{static}}(\infty) &= -\frac{e^2 \kappa}{4} (1 - \sqrt{\pi} \text{erfc}(b)) \rightarrow -\frac{1}{4} e^2 n \kappa \end{aligned} \quad (6)$$

where the first result is the Montroll correlation energy.^{9,10} The explanation for this fact is that we can prepare the initial configuration within our kinetic theory such that sudden switching of interaction is fulfilled. However, in the simulation experiment we have initial correlations which are due to the set up within quasiperiodic boundary condition and Ewald summations. For $\Gamma = 1$, see Fig. 1, non-ideal effects become important and the formation time is underestimated within (5). The non-ideal effects were found to be an expression of memory effects¹¹ and lead to a later relaxation.

SUMMARY

The characteristic time of formation of correlations at high temperature limit is given by the inverse plasma frequency $\tau_c \approx \frac{1}{\omega_p} = \frac{\sqrt{2}}{v_{\text{th}} \kappa}$. The inverse plasma frequency indicates that the dominant role play the long range fluctuation. On the other hand, we also see that the correlation time is found to be given by the time a particle needs to travel through the range of the potential with a thermal velocity v_{th} . This confirms the numerical finding of [12] that the correlation or memory time is proportional to the range of interaction. In the low temperature region, i.e., in highly degenerated system $\mu \gg T$, one finds a different picture. From (3) we can calculate the formation of correlations as well.^{13,14} Unlike in the classical case, the equilibrium limit of the degenerated case is rapidly built up and then oscillates around the equilibrium value. We can define the build up time τ_c as the time where the correlation energy reaches its first maximum, $\tau_c \approx 1.0 \frac{\hbar}{\mu}$. Note that τ_c is in agreement with the quasiparticle formation time known as Landau's criterion for μ is the Fermi energy. Indeed, the quasiparticle formation and the build up of correlations are two alternative views of the same phenomena. The formation of binary correlations is very fast on the time scale of dissipative process. Under extremely fast external perturbations, like the massive femto second laser pulses, the dynamics of binary correlations will hopefully become experimentally accessible. Even if related measurement will not reveal any unexpected features, the experimental justification of basic concepts of the non-equilibrium many-body physics is very desirable.

Acknowledgements

We are grateful to G. Zwignagel who was so kind as to provide the data of simulations. Stimulating discussions with G. Röpke are acknowledged. This project was supported by the BMBF (Germany) under contract Nr. 06R0884 and the Max-Planck Society, Grant Agency

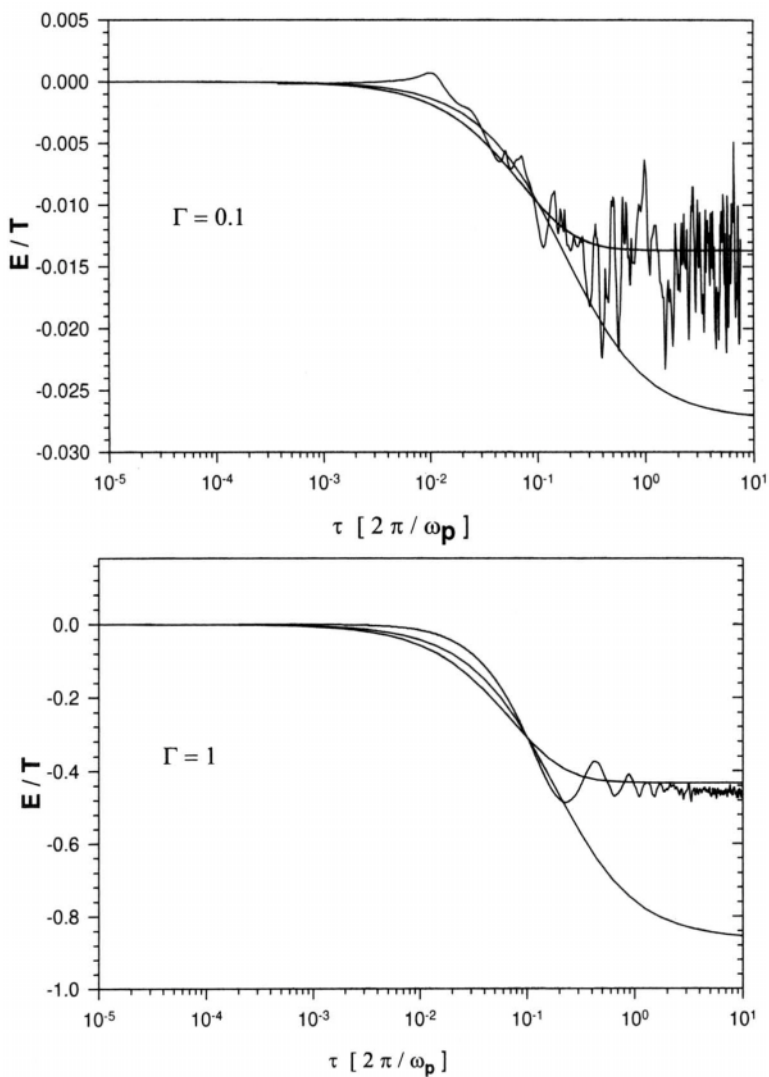


Figure 1. The formation of correlation energy due to molecular dynamic simulations⁸ together with the result of (5) for a plasma parameter $\Gamma = 0.1$ (top) and $\Gamma = 1$ (bottom). The upper curve is the static and the lower the dynamical calculation. The latter one approaches the Debye-Hückel result.

of Czech Republic under contracts Nos. 202960098 and 202960021, and the EC Human Capital and Mobility Programme.

REFERENCES

- [1] H. Haug and A. P. Jauho, *Quantum Kinetics in Transport and Optics of Semiconductors* (Springer, Berlin Heidelberg, 1996).
- [2] W. Theobald, R. Häßner, C. Wülker, and R. Sauerbrey, Phys. Rev. Lett. **77**, 298 (1996).
- [3] K. Morawetz, Phys. Lett. A **199**, 241 (1995).
- [4] P. Danielewicz, Ann. Phys. (NY) **152**, 305 (1984).
- [5] H. S. Köhler, Phys. Rev. C **51**, 3232 (1995).
- [6] K. Morawetz, Phys. Rev. E **50**, 4625 (1994).
K. Morawetz, V. Špička, and P. Lipavský, Phys. Rev. E. in prep.
- [8] G. Zwicknagel, C. Toepffer, and P. G. Reinhard, in *Physics of strongly coupled plasmas*, edited by W. D. Kraeft and M. Schlanges (World Scientific, Singapore, 1995), p. 45.
- [9] W. D. Kraeft, D. Kremp, W. Ebeling, and G. Röpke, *Quantum Statistics of Charged Particle Systems* (Akademie Verlag, Berlin, 1986).
- [10] J. Riemann and et. al., Physica A **219**, 423 (1995).
- [11] K. Morawetz, R. Walke, and G. Röpke, Phys. Lett. A **190**, 96 (1994).
- [12] M. Bonitz and et. al., J. Phys.: Condens. Matter **8**, 6057 (1996).
- [13] K. Morawetz and H. S. Koehler, Phys. Rev. C (1997), sub.
- [14] K. Morawetz, V. Špička, and P. Lipavský, Phys. Lett. A, sub.

This page intentionally left blank

QUADRATIC RESPONSE SOLUTIONS FOR DIFFERENT NONLINEAR APPROACHES OF STATIC SCREENING: A COMPARATIVE STUDY

I. Nagy,¹ A. Bergara,² and P. M. Echenique³

¹Department of Theoretical Physics, Institute of Physics
Technical University of Budapest, H-1521 Budapest, Hungary

²Materia Kondentsatuaren Fisika Saila
Zientzi Falkultatea, Euskal Herriko Unibertsitatea
644 Posta kutxatila, 48080 Bilbo, Basque Country, Spain
E-mail: wmbvejaa@lg.ehu.es

³Materialen Fisika Saila
Kimika Falkultatea, Euskal Herriko Unibertsitatea
1072 Posta kutxatila, 20080 Donostia, Basque Country, Spain

1. INTRODUCTION

The goal of the research to be described here is to compare perturbative solutions of two well-established procedures of nonlinear screening calculations, treating the case of a fixed charged impurity in an ideal, charged-boson gas of density n_0 and particle charge e at $T=0$. The procedures are based on the Euler equation of density-functional theory¹⁻³ and the density-profile relation given by an integral equation.^{4,5}

The perturbative solutions, obtained here up to the quadratic order in the external charge Z for the induced densities and screened potentials, allow a valuable investigation and would extend the validity of the standard linear screening theory.

The systems of charged bosons offers a relatively simple many-body model to the mentioned problem of screening, and thus parallels the system of an electron gas for the same problem.⁶⁻⁸

2. PROCEDURES AND CONSTRAINTS

The ground-state wave-function (ψ_0) of the charged boson system is a unique, non-negative symmetric function and, in our case, it is given by $\psi_0 = \sqrt{n_0}$. We use atomic units ($e^2 = \hbar = m = 1$) throughout this work.

Now, suppose we place a charged test particle in the many-body system. Then, the total boson density depends on the position \mathbf{r} and can be written as:

$$n(\mathbf{r}) = n_0 + \delta n(\mathbf{r}), \quad (1)$$

where the induced density $[\delta n(\mathbf{r})]$ satisfies the screening, i.e., normalization condition

$$\int d^3\mathbf{r} \delta n(\mathbf{r}) = Z. \quad (2)$$

The spherically symmetric, screened potential $[V(r)]$ of the charged impurity is calculated by using the Poisson equation

$$V(r) = -\frac{Z}{r} + \int d^3\mathbf{r}' \frac{\delta n(\mathbf{r}')}{|\mathbf{r} - \mathbf{r}'|}. \quad (3)$$

In the first procedure we consider, according to the Hohenberg–Kohn theorem, the fundamental energy functional for jellium in the presence of a charged test particle. The Euler equation of this variational problem becomes^{1–3}

$$-\frac{1}{2}\nabla^2\omega(r) + V(r)[\psi_0 + \omega(r)] = 0, \quad (4)$$

in which the convenient notation $\sqrt{n(\mathbf{r})} \equiv \psi(r) = \psi_0 + \omega(r)$ is introduced. An investigation of the short-distance limit of Eq. (2.4) results a useful constraint, which is known as the Kato–Kimball nuclear cusp condition⁹

$$\left. \frac{\delta n'(r)}{n(r)} \right|_{r=0} = -2Z. \quad (5)$$

Our quadratic treatment rests on a perturbative expansion, which is defined as follows

$$\psi(r) = \psi_0 + \psi_1(r, Z) + \psi_2(r, Z^2) + \dots, \quad (6)$$

for the ground-state wave function.

For simplicity, from now on, only the indices (1 and 2) will be devoted to first- and second-order expansions. The screened potential is defined as $V(r) = V_1(r) + V_2(r)$ in the quadratic approach, and the corresponding expressions are given by

$$V_1(r) = -\frac{Z}{r} + \int d^3\mathbf{r}' \frac{n_1(\mathbf{r}')}{|\mathbf{r} - \mathbf{r}'|} \quad (7a)$$

$$V_2(r) = \int d^3\mathbf{r}' \frac{n_2(\mathbf{r}')}{|\mathbf{r} - \mathbf{r}'|}. \quad (7b)$$

In Eqs. (7a)–(7b) the solutions $\psi_1(r)$, $[n_1(r, Z) = 2\psi_0\psi_1(r, Z)]$ and $\psi_2(r)$, $[n_2(r, Z^2) = 2\psi_0\psi_2(r, Z^2) + \psi_1^2(r, Z)]$ are the results of coupled equations, obtained by using Eq. (4) up to the relevant order

$$-\frac{1}{2}\nabla^2\psi_1(r) + V_1(r)\psi_0(r) = 0 \quad (8a)$$

$$-\frac{1}{2}\nabla^2\psi_2(r) + V_2(r)\psi_0 + V_1(r)\psi_1(r) = 0. \quad (8b)$$

In the second procedure to be employed, we consider a density-profile relation⁵ given in form of an integral equation, in Fourier-momentum (q) space. This linear integral equation is as follows, for an ideal boson system^{4,5}

$$\delta n(q) = n_1(q) \left[1 + \frac{1}{\pi\omega_p^2} \int_0^\infty dk k^2 f(k, q) \delta n(k) \right], \quad (9)$$

where $\omega_p^2 = 4\pi n_0$ is the classical plasma frequency, and the function $f(k, q)$ has the form

$$f(k, q) = 1 + \frac{q^2 - k^2}{2qk} \ln \left| \frac{q+k}{q-k} \right|. \quad (10)$$

Notice that in Eq. (9) $n_1(q)$ is the linear response solution. This linear-response solution is unique for our procedures and has an asymptotic form (see Sec. 3, below) of $n_1(q) \rightarrow Z(16\pi n_0)/q^4$ for high q -values.

Using this, together with the well-established relation of Kimball⁹

$$\delta n'(r)|_{r=0} = -\frac{1}{8\pi} \lim_{q \rightarrow \infty} [q^4 \delta n(q)], \quad (11)$$

we arrive at [via Eqs. (9)–(10) and the trick of inverse Fourier representation with $r \rightarrow 0$ in the argument of Eq. (9)] the standard Kato–Kimball condition of Eq. (5). Therefore, the nuclear cusp condition is satisfied in the integral-equation procedure.

Our quadratic treatment, for this case, rests on a successive approximation for Eq. (9), by using $n_1(q)$ under the integral-sign in order to define the corresponding second-order solution of this procedure.

3. RESULTS

The present section will be devoted to detailed analytical and numerical results, with relevant comparisons and accompanying analysis. For convenience, we introduce new variables (R and Q) by the $R = r\lambda$ and $Q = q/\lambda$ definitions, where $\lambda = (4\pi n_0)^{1/4}$. In addition, in order to distinguish quadratic solutions, we shall use (beside the index 2) an asterisk for results obtained from the integral-equation (n_2^* and V_2^*).

The linear-response solution, which is unique in both procedures, is defined by Eqs. (7a)–(8a). The linearized, Schrödinger-like Eq. (8a) is solved by standard Fourier-transformation and the results obtained are

$$n_1(Q) = 4Z \frac{1}{Q^4 + 4}, \quad (12)$$

$$V_1(Q) = -\frac{4\pi Z}{\lambda^2} \frac{Q^2}{Q^4 + 4}, \quad (13)$$

in which the above-introduced variables are used.

The real-space equivalents of Eqs. (12) and (13) are calculated by inverse Fourier transformations and have the following forms

$$n_1(R) = \frac{Z\lambda^3}{2\pi} \frac{e^{-R}}{R} \sin R, \quad (14)$$

$$V_1(R) = -Z\lambda \frac{e^{-R}}{R} \cos R. \quad (15)$$

The ratio of $\{n_1(R=0)/n_0\} = 2(Z/\lambda)$ shows that the natural expansion (small) parameter in our treatment is, in fact, Z/λ .

Now, we present our quadratic solutions obtained within the frameworks of applied procedures. Eq. (8b) is solved with the help of Fourier transformation into momentum (q) space and simultaneous application of Eqs. (7b), (14), (15) and $n_1(r)$. The result for the induced density $[n_2(q)]$ is given, in this case, by

$$n_2(Q) = n_1(Q) \frac{Z}{8\lambda} \times \left[Q \ln \frac{4 + (Q+2)^2}{4 + (Q-2)^2} + Q^3 \left(\arctan \frac{Q}{2} + \frac{1}{2} \arctan \frac{2-Q}{2} - \frac{1}{2} \arctan \frac{2+Q}{2} \right) \right], \quad (16)$$

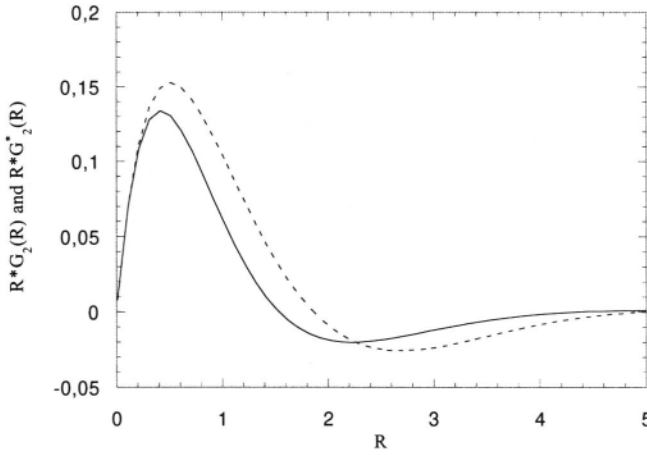


Figure 1. The functions of $R \times G_2$ (solid curve) and $R \times G_2^*$ (dashed curve), introduced in the evaluation of the quadratic induced densities [see Eq. (18)], as a function of the variable $R = r\lambda$.

in which $n_1(Q)$ is given by Eq. (12) and the introduced $Q = q/\lambda$ variable is used. The quadratic, induced potential [see, Eq. (7b)] has a simple form $V_2(q) = (4\pi/q^2)n_2(q)$.

The corresponding result for the integral-equation procedure is as follows

$$n_2^*(Q) = n_1(Q) \frac{Z}{\lambda} \left[1 + \frac{Q}{4} \ln \left| \frac{Q^2 + 2 + 2Q}{Q^2 + 2 - 2Q} \right| + \frac{1}{2Q} \arctan \frac{4Q(Q^2 - 2)}{(Q^2 - 2)^2 - 4Q^2} - \frac{\theta(Q - (\sqrt{3} - 1))\pi}{2Q} - \frac{\theta(Q - (\sqrt{3} + 1))\pi}{2Q} \right]. \quad (17)$$

This equation is obtained by using Eq. (12) in the argument ($q = \lambda Q$) of Eq. (9) and standard application of residue-theorem for integration in the latter. The quadratic, induced potential of this successive approximation is $V_2^*(q) = (4\pi/q^2)n_2^*(q)$.

Now, we perform numerical, inverse Fourier transformations in order to obtain the real-space equivalents of induced quadratic densities and potentials. For convenience, we introduce $G_2(R)$ and $H_2(R)$ functions via definitions of $n_2(R) = (2Z^2\lambda^2)/\pi^2 G_2(R)$ and $V_2(R) = (8Z^2/\pi)H_2(R)$. These functions are as follows

$$G_2(R) = \frac{1}{R} \int_0^\infty dQ Q \sin(QR) \frac{F_2(Q)}{Q^4 + 4}, \quad (18)$$

$$H_2(R) = \frac{1}{R} \int_0^\infty dQ \frac{\sin(QR)}{Q} \frac{F_2(Q)}{Q^4 + 4}. \quad (19)$$

The corresponding functions (G_2^* and H_2^*) for the integral-equation procedure (F_2^*) are denoted by asterisk.

The values of these functions at zero separation, i.e., at $R = 0$, are: $G_2(0) \simeq 0.792$, $H_2(0) \simeq 0.086$ and $G_2^*(0) \simeq 0.771$, $H_2^*(0) \simeq 0.121$, respectively. It is remarkable, that $V_2(R = 0)$ and $V_2^*(R = 0)$ do not depend on the density of the system. The important ratios of densities are determined easily: $[n_2(0)/n_1(0)] \simeq [n_2^*(0)/n_1(0)] \simeq (Z/\lambda)$ by using Eq. (14), also. Perturbative methods for boson system are meaningful for $Z/\lambda < 1$, by our physical guess.

The detailed shapes of $R \times G_2(R)$ and $R \times G_2^*(R)$ are exhibited in Fig. 1, as a function of the R variable. The $R \times H_2(R)$ and $R \times H_2^*(R)$ functions are plotted in Fig. 2.

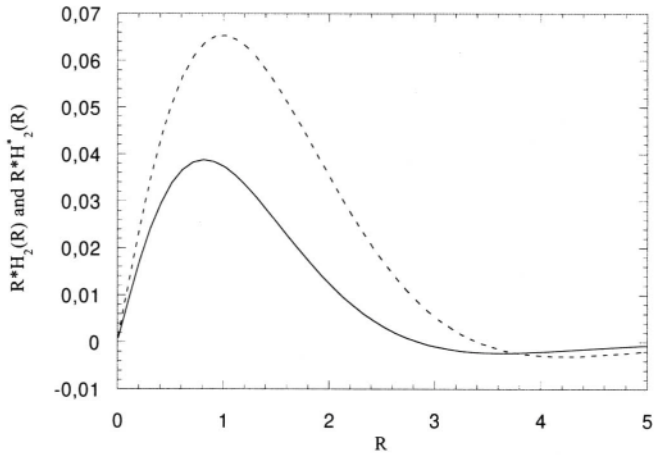


Figure 2. The functions of $R \times H_2$ (solid curve) and $R \times H_2^*$ (dashed curve), introduced in the evaluation of the quadratic induced potentials [see Eq. (19)], as a function of the variable $R = r\lambda$.

REFERENCES

- [1] R. M. Dreizler and E. K. U. Gross. "Density Functional Theory," Springer, Berlin (1993).
- [2] N. H. March, The local potential determining the square root of the ground-state electron density of atoms and molecules from the Schrödinger equation, *Phys. Letters A* 113:476 (1986).
- [3] A. Kallio and J. Piilo, Novel analytic calculation of electron gas properties, *Phys. Rev. Lett.* 77:4237 (1996).
- [4] A. Sjölander and M. J. Stott, Electron distribution around a mobile and fixed point charges in metals, *Phys. Rev. B* 5:2109 (1972).
- [5] A. Krakovsky and J. K. Percus, Hydrodynamic model of an inhomogeneous electron gas, *Phys. Rev. B* 52:7901 (1995).
- [6] C. D. Hu and E. Zaremba, Z^3 correction to the stopping power of ions in an electron gas, *Phys. Rev. B* 37:9268 (1988).
- [7] J. M. Pitarke, R. H. Ritchie and P. M. Echenique, Quadratic response theory of the energy-loss of charged particles in an electron gas, *Phys. Rev. B* 52:13883 (1995).
- [8] A. Bergara, I. Campillo, J. M. Pitarke, and P. M. Echenique, Quadratic induced polarization by an external heavy charge in an electron gas, *Phys. Rev. B*, in press (1997).
- [9] J. C. Kimball, Short range correlations and electron-gas response functions, *Phys. Rev. A* 7, 1648 (1977).

This page intentionally left blank

INVESTIGATION OF THE DYNAMIC PROPERTIES OF THE ELECTRON GAS BY QUASI-CLASSICAL SIMULATIONS*

J. Ortner, F. Schautz, and W. Ebeling

Humboldt Universität zu Berlin, Institut für Physik
Invalidenstr. 110, D-10115 Berlin, Germany

INTRODUCTIONS

The electron gas on a uniform positive background is an important theoretical model. Both the interactions due to Coulomb forces (i.e. the coupling) and quantum statistical effects due to the Fermi character (i.e., the degeneracy) determine the properties of the electron plasma. To characterize the degeneracy of the electron system the dimensionless parameter $\theta = T/E_F$ is introduced, where T is the temperature (in energy units), n the electron density and $E_F = \hbar^2(3\pi^2n)^{2/3}/(2m)$ is the Fermi energy. Further we define the coupling constant as $\Gamma = e^2/aT$, a being the Wigner–Seitz radius.

Important characteristics of the electron gas are the dielectric function and the dynamic structure factor. Knowing these functions the plasma dispersion relation, static correlation functions, and thermodynamic potentials of the electron gas can be obtained. In order to check the validity of the different analytical approaches for the calculation of the dielectric function of a coupled electron gas¹ microscopic simulations of the quantum electron gas could be very useful. Classical simulations of the one component plasma were already performed by Hansen et al.² In this paper the dynamic properties of the quantum electron gas will be investigated on the basis of quasi-classical molecular dynamics simulations.

In order to treat the quantum electron gas by quasi-classical simulations we make use of effective pair potentials. An effective potential depending only on the space coordinates³ leads necessarily to the Maxwell momentum distribution. Since we want to model the momentum distribution of an electron gas governed by Fermi statistics we have to include in our simulations momentum-dependent interaction terms. Our approach follows a line developed by a series of authors as e.g., Wilets and Kirschbaum, Dorso et al.,⁴⁻⁶ We mention here also the wave packet dynamics approach as an alternative possibility to model the electron gas by quasiclassical simulations,⁷⁻⁹

In our model we approximate the real quantum dynamics of the electron system by a phase space dynamics of Hamilton type with certain constraints given by the effective

*Supported by the Deutsche Forschungsgemeinschaft (DFG, Germany)

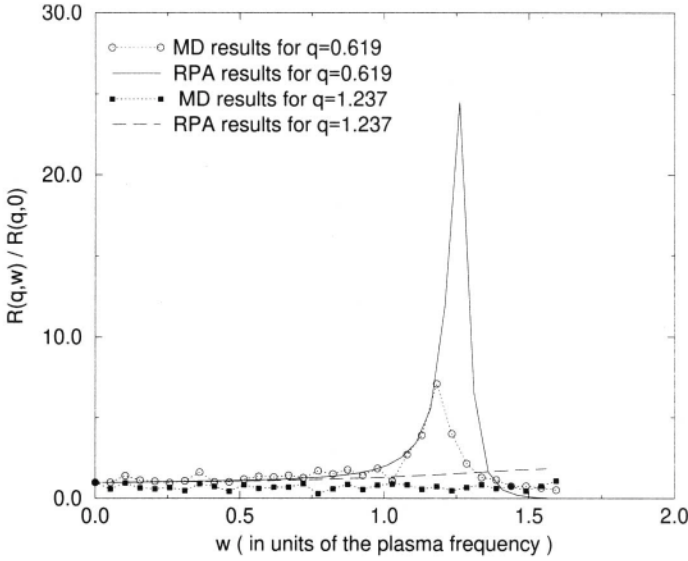


Figure 1. Comparison of the MD and RPA loss function $R(q, \omega)$ versus frequency ω/ω_p for different wavevectors q at $\Gamma = 1$ and $\theta = 1$.

Hamiltonian,^{10,12}

$$H = \sum_{i=1}^N \frac{p_i^2}{2m} + \sum_{i<j}^N V_p\left(\frac{r_{ij}}{r_0}, \frac{p_{ij}}{p_0}\right) + \sum_{i<j}^N e^2 F\left(\frac{r_{ij}}{r_0}, \frac{p_{ij}}{p_0}\right) \quad . \quad (1)$$

Here the first term is the ordinary (classical) kinetic energy of the electrons. The second contribution, the Pauli potential is introduced to model the Pauli exclusion principle, it is chosen in a form suggested by Dorso et al.,⁴

$$V_p(p, r) = V_0 e^{-\Delta^2/2} \quad , \quad (2)$$

where $\Delta^2 = p^2/p_0^2 + r^2/r_0^2$ is the effective phase space distance of two particles with relative momentum p and distance r . The last term in the effective Hamiltonian is the Coulomb interaction averaged with respect to the two particle Gaussian wave packet in order to take into account the Heisenberg uncertainty condition,

$$F(r, p) = \frac{\text{erf}(r/\sqrt{2}r_0)}{r} \quad . \quad (3)$$

The parameters in the Hamiltonian Eq. (1) are chosen to describe the correlation function and the momentum distribution of a free Fermi gas. An appropriate choice is discussed in [10],

$$V_0 = \frac{2}{3} \varepsilon_{kin} \quad , \quad p_0^2 = \frac{2}{3} m \varepsilon_{kin} \quad , \quad r_0^2 = \frac{3\hbar^2}{2m \varepsilon_{kin}} \quad , \quad (4)$$

with ε_{kin} being the kinetic energy per electron of a free Fermi gas. It has been also shown that the mean energy calculated from the simulations based on the Hamiltonian Eq. (1) with the parameters from Eqs. (4) is in good agreement with Quantum Monte Carlo simulations and with Padé approximations.¹⁰ This encourages us to expand our considerations to the investigation of the dynamic properties of the electron gas within the developed approach.¹²

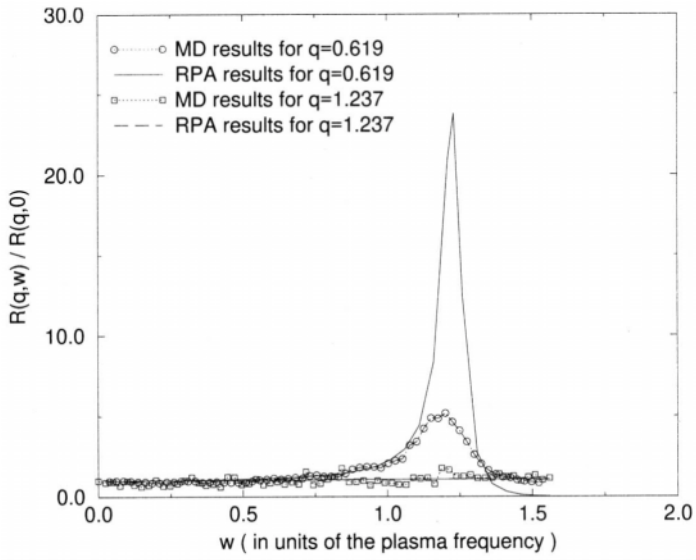


Figure 2. Comparison of the MD and RPA loss function $R(q, \omega)$ versus frequency ω/ω_p for different wavevectors q at $\Gamma = 1$ and $\theta = 50$.

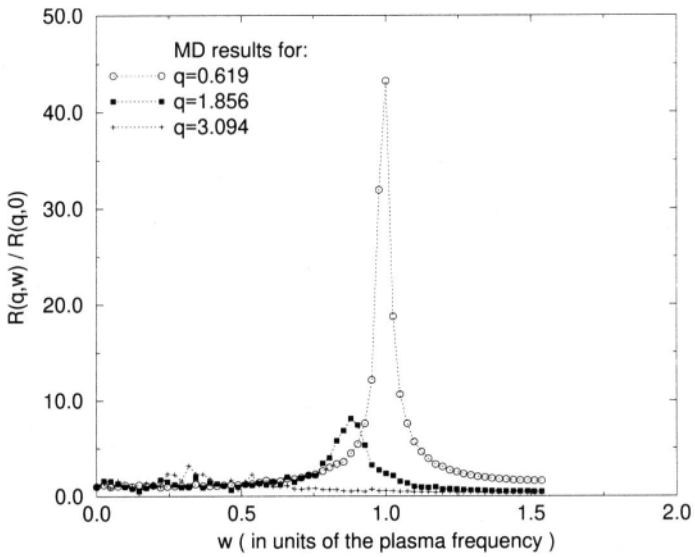


Figure 3. The MD loss function $R(q, \omega)$ versus frequency ω/ω_p for different wavevectors q at $\Gamma = 100$ and $\theta = 50$.

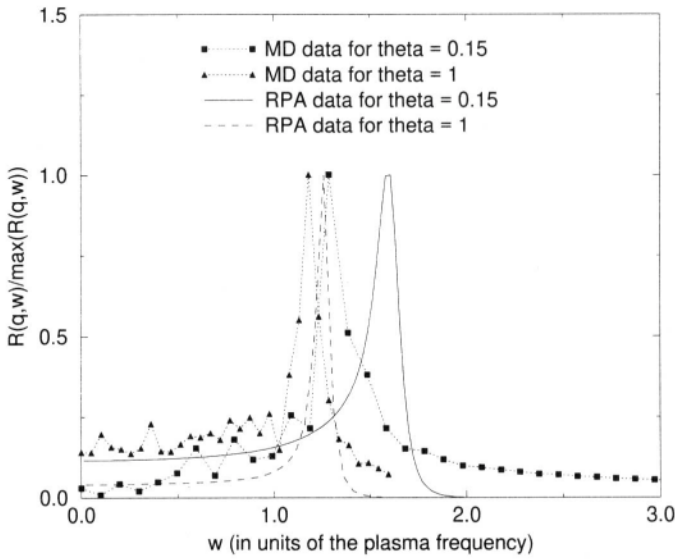


Figure 4. The MD loss function $R(q, \omega)$ versus frequency ω/ω_p for wavevector $q = 0.619$ at fixed $\Gamma = 1$ and different θ .

DYNAMIC PROPERTIES

Consider the dynamic structure factor

$$S(\vec{k}, \omega) = \frac{1}{2\pi N} \int_{-\infty}^{\infty} e^{i\omega t} \langle \rho(\vec{k}, t) \rho(-\vec{k}, 0) \rangle dt, \quad (5)$$

where $\rho(\vec{k}, t) = \sum_i \exp(-i\vec{k}\vec{r}_i)$ is the Fourier component of the microscopic electron density. The dynamic structure factor can be calculated from the MD simulations if one approximates the Heisenberg operator $\vec{r}_i(t)$ by the position of the i -th particle in the simulations. However, the thus obtained quantity (we denote it by $R(\vec{k}, \omega)$) is symmetric with respect to the frequency. It corresponds therefore to a classical fluctuation–dissipation theorem,

$$R(\vec{k}, \omega) = (n\pi\phi(k)\beta\omega)^{-1} \text{Im}\varepsilon^{-1}(\vec{k}, \omega) \quad (6)$$

with the dielectric function $\varepsilon(\vec{k}, \omega)$. From Eq. (6) one concludes that $R(\vec{k}, \omega)$ cannot be regarded as a structure factor, but can be regarded as a normalized loss function. In what follows we will regard the normalized loss function. Note, that in the classical case the loss function and the dynamic structure factor coincide.

In our molecular dynamic simulations we integrated numerically the equations of motions obtained from the effective Hamiltonian of a system of 250 electrons. The typical length of the MD runs were about $10^3\omega_p^{-1}$. The equilibration phase was replaced by a Monte Carlo Simulation. Periodic boundary conditions have been used in order to account for the long range of the Coulomb interaction.

We have studied the collective motion by calculating the loss function.¹² The loss function $R(q, \omega)$ ($q = ka$) is plotted for two q values, at $\Gamma = 1$ and for different parameters of degeneracy $\theta = 1$ (moderate degenerate) and $\theta = 50$ (classical) and for strongly coupled, weakly degenerate electron gas ($\Gamma = 100$ at $\theta = 50$) (Figs. 1–3,¹²). The results of the simulations are compared with the Random Phase approximation (RPA) data. For the case of moderate coupling constants ($\Gamma = 1$) the plasmon peak of the loss function is slightly shifted to the left and has a less height than that predicted by RPA (Figs. 1,2). In both cases the

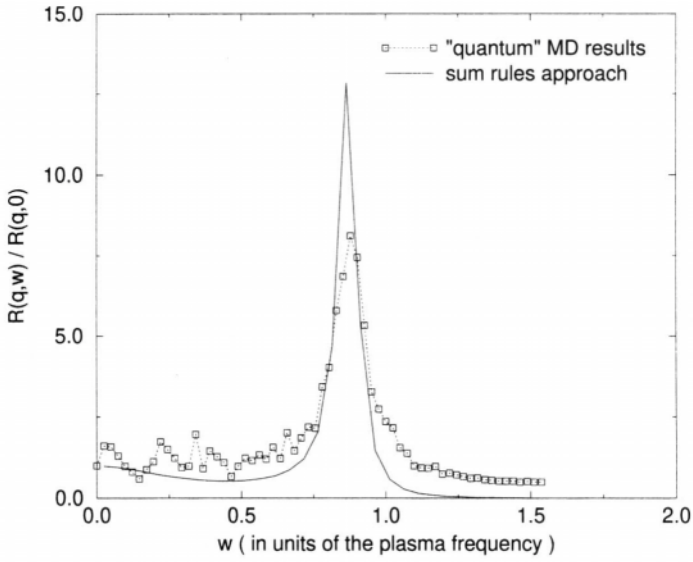


Figure 5. Comparison of the loss function $R(q, \omega)$ from MD simulations and sum rules approach versus frequency ω/ω_p at $\Gamma = 100$ and $\theta = 50$ for wavevector $q = 1.856$.

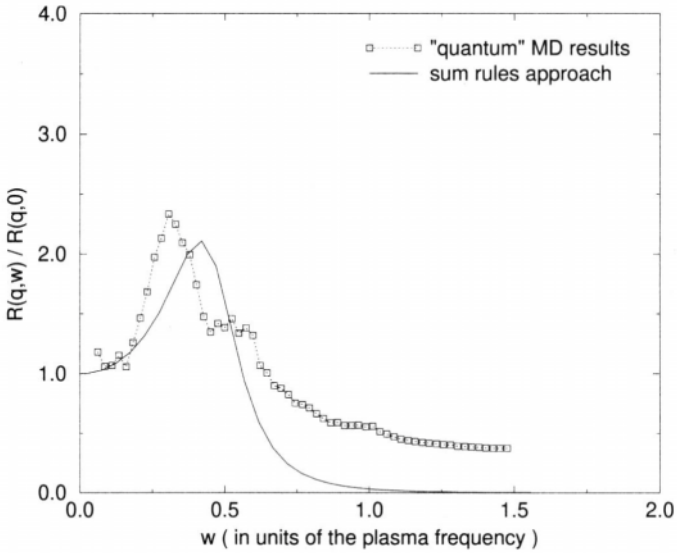


Figure 6. Comparison of the loss function $R(q, \omega)$ from MD simulations and sum rules approach versus frequency ω/ω_p at $\Gamma = 100$ and $\theta = 50$ for wavevector $q = 3.094$.

plasmon peak can be observed only for the smallest q value ($q=0.619$). From Figs. 1 and 2 it can be also seen that the change of the degeneracy parameter θ in the range from 50 to 1 has only a small influence on the results.

However at higher degrees of degeneracy ($\theta = 0.15$) the plasmon peak obtained from the MD datas is shifted towards higher frequencies, but the peak position in this case differs quite significantly from those predicted by the RPA (Fig. 4).

In the strong coupling regime $\Gamma = 100$ a sharp plasmon peak centered near ω_p can be observed at the smallest q value (Fig. 3). A collective plasmon mode has been developed. With increasing wavevector the plasmon peak widens and is shifted more and more to the left. The plasmon peak is present up to $q = 3.1$ and only at still larger q values the plasmon peak vanishes. This behavior contradicts to the RPA predictions where no plasmon peak can be observed due to the strong Landau damping. However, the RPA cannot be applied to the strong coupling regime, where the potential energy is dominant. On the contrary, the results of our simulations for the case of a weakly degenerate plasma are in a good agreement with the results of corresponding MD simulations of Hansen et al. for the classical one component plasma.²

Further we have compared the results of our simulations with the expression of the dynamic structure factor obtained by the application of the classical theory of moments.¹¹ A detailed discussion can be found elsewhere.¹² Here the results for two different q vectors at $\Gamma = 100$ are shown (Figs. 5,6). The agreement with the MD calculations is rather good. The theoretical curves reproduce the varying shape of the dynamic structure factor and describe the plasmon peak position in a good manner. However, the agreement in the height of the peaks is less satisfactory. One of the reasons for this disagreement between the results of simulations with theoretical predictions (both based on RPA and on the sum rules approach) might be the normalization to $S(q,0)$ which is a value rather bad measured in the simulations due to the poor statistics at long times.

Finally we note that due to the quasi-classical character our quantum molecular dynamic simulations describe the dynamic properties of the electron gas only approximately. Our model yields reasonable results at weak and moderate degeneracy, whereas for the case of high degeneracy it seems to break down.

REFERENCES

- [1] S. Ichimaru, *Rev. Mod. Phys.* 54:1017 (1982), and references therein.
- [2] J.-P. Hansen, I. R. McDonald, and E. L. Pollock, *Phys. Rev A* 11: 1025 (1975).
- [3] J. P. Hansen and I. R. McDonald, *Phys. Rev. A* 23:2041 (1981).
- [4] C. Dorso, S. Duarte, and J. Randrup, *Phys. Lett. B* 188:287 (1987).
- [5] C. L. Kirschbaum and L. Wilets, *Phys. Rev. A* 21:834 (1980).
- [6] L. Wilets, E. M. Henley, M. Kraft and A. P. Mackellar, *Nucl. Phys. A* 282:341 (1977).
- [7] H. Feldmaier, K. Bieler, and J. Schnack, *Nucl. Phys. A* 586:493 (1995).
- [8] D. Klakow, Toepffer, and P.-G. Reinhard, *Phys. Lett. A* 192:55 (1994).
- [9] D. Klakow, Toepffer, and P.-G. Reinhard, *J. Chem. Phys.* 101:10766 (1994).
- [10] W. Ebeling and F. Schautz, *Phys. Rev. E* (in press).
- [11] V. M. Adamyan and I. M. Tkachenko, *High Temp. (USA)* 21:307 (1983).
- [12] J. Ortner, F. Schautz, and W. Ebeling, *Phys. Rev. E* (in press).

THE QUADRATIC SUSCEPTIBILITY IN ONE, TWO, AND THREE DIMENSIONS

J. Martin Rommel,¹ Gabor J. Kalman,¹ and Riewa Genga²

¹Department of Physics, Boston College
Chestnut Hill, MA

²Department of Physics
University of Nairobi, Nairobi, Kenya

Linear response theory has been very successful in describing many-body systems. However, in many cases it is not sufficient and one has to take into account higher order contributions. The quadratic contribution to the density change that external scalar potentials induce in an equilibrium system is governed by the quadratic density response function $\chi(\mathbf{k}_1, \omega_1; \mathbf{k}_2, \omega_2)$.

$$\langle \rho(\mathbf{k}, \omega) \rangle^{(2)} = \frac{1}{V} \sum_{\mathbf{q} \notin \{0, \mathbf{k}\}} \int \frac{d\mu}{2\pi} \chi(\mathbf{q}, \mu; \mathbf{k} - \mathbf{q}, \omega - \mu) \Phi(\mathbf{q}, \mu) \Phi(\mathbf{k} - \mathbf{q}, \omega - \mu) \quad (1)$$

For a 3D system it was first derived in the static limit by Lloyd and Sholl¹ in 1968. Twenty years later the dynamical quadratic response function was evaluated, the real part by Cenni and Saracco² and the imaginary part by Hu and Zaremba.³

A closed analytic form of the full dynamical longitudinal quadratic density response of a 2D many-body system was first presented by the first author at the 1997 APS March Meeting. In this contribution we compare the 2D result with the 1D and 3D case and discuss some of their features.

For a free particle system one finds^{3,4} the retarded symmetrized form

$$\begin{aligned} \chi_0(\mathbf{k}_1, \omega_1; \mathbf{k}_2, \omega_2) = \frac{1}{2V} \sum_{\mathbf{p}} n_{\mathbf{p}} \times \quad (2) \\ \left\{ (\omega + \epsilon_{\mathbf{p}} - \epsilon_{\mathbf{p}-\mathbf{k}})^{-1} \left[(\omega_1 + \epsilon_{\mathbf{p}} - \epsilon_{\mathbf{p}-\mathbf{k}_1})^{-1} + (\omega_2 + \epsilon_{\mathbf{p}} - \epsilon_{\mathbf{p}-\mathbf{k}_2})^{-1} \right] \right. \\ + (\omega + \epsilon_{\mathbf{p}+\mathbf{k}} - \epsilon_{\mathbf{p}})^{-1} \left[(\omega_1 + \epsilon_{\mathbf{p}+\mathbf{k}_1} - \epsilon_{\mathbf{p}})^{-1} + (\omega_2 + \epsilon_{\mathbf{p}+\mathbf{k}_2} - \epsilon_{\mathbf{p}})^{-1} \right] \\ - (\omega_1 + \epsilon_{\mathbf{p}+\mathbf{k}_1} - \epsilon_{\mathbf{p}})^{-1} (\omega_2 + \epsilon_{\mathbf{p}} - \epsilon_{\mathbf{p}-\mathbf{k}_2})^{-1} \\ \left. - (\omega_1 + \epsilon_{\mathbf{p}} - \epsilon_{\mathbf{p}-\mathbf{k}_1})^{-1} (\omega_2 + \epsilon_{\mathbf{p}+\mathbf{k}_2} - \epsilon_{\mathbf{p}})^{-1} \right\} \end{aligned}$$

where $\mathbf{k} = \mathbf{k}_1 + \mathbf{k}_2$, $\omega = \omega_1 + \omega_2$, $\epsilon_{\mathbf{p}} = p^2/2m$ and $n_{\mathbf{p}}$ is the Fermi momentum distribution function. It is important to note that each occurrence of an ω_i in (2) is accompanied by an infinitesimal positive imaginary contribution $i0$ that ensures causality.

The RPA for the quadratic response function is obtained from the non-interacting χ_0 by $\chi_{RPA}(\mathbf{k}_1, \omega_1; \mathbf{k}_2, \omega_2) = \chi_0(\mathbf{k}_1, \omega_1; \mathbf{k}_2, \omega_2) / (\varepsilon(\mathbf{k}_1, \omega_1)\varepsilon(\mathbf{k}_2, \omega_2)\varepsilon(\mathbf{k}, \omega))$ with the linear dielectric function $\varepsilon(\mathbf{k}, \omega) = 1 - \chi_0(\mathbf{k}, \omega)\varphi(\mathbf{k})$.

All six terms on the right of (2) have the same analytic structure, namely

$$F(x, \mathbf{k}_x, y, \mathbf{k}_y) = \frac{1}{V} \sum_{\mathbf{p}} \frac{n_p}{(x k_x - \mathbf{p} \cdot \mathbf{k}_x)(y k_y - \mathbf{p} \cdot \mathbf{k}_y)}. \quad (3)$$

In terms of these F -functions the quadratic density response is given by

$$\chi_0(\mathbf{k}_1, \omega_1; \mathbf{k}_2, \omega_2) = \frac{m^2}{2} \left\{ F(A^-, \mathbf{k}, A_1^-, \mathbf{k}_1) + F(A^-, \mathbf{k}, A_2^-, \mathbf{k}_2) + F(A^+, \mathbf{k}, A_1^+, \mathbf{k}_1) \right. \\ \left. + F(A^+, \mathbf{k}, A_2^+, \mathbf{k}_2) - F(A_1^+, \mathbf{k}_1, A_2^-, \mathbf{k}_2) - F(A_1^-, \mathbf{k}_1, A_2^+, \mathbf{k}_2) \right\} \quad (4)$$

where we have introduced the abbreviation $A_l^\pm = m\omega_l/k_l \pm k_l/2$.

The expressions (2) — (4) are valid regardless of the dimensionality of the systems which is only specified by choosing the dimensionality of the \mathbf{p} -integration.

In the low temperature limit n_p becomes a step function $\Theta(k_F - k)$. All wave numbers are in units of the Fermi wave number k_F and energies in units of the Fermi energy $\epsilon_F = k_F^2/2m$.

For a one-dimensional system the integration is a simple matter.

$$F_1(x, \mathbf{k}_x, y, \mathbf{k}_y) = \frac{2}{k_x k_y} \int_{-1}^1 \frac{dp}{2\pi} \frac{1}{(x-p)(y-p)} \quad (5) \\ = \frac{1}{\pi k k_l (x-y)} \left\{ \ln \left| \frac{x-1}{x+1} \right| - \ln \left| \frac{y-1}{y+1} \right| + i\pi [\Theta(1-|x|) - \Theta(1-|y|)] \right\}$$

In the limit $\omega \rightarrow 0^+$ the one-dimensional F_1 obviously becomes singular along the lines $|x| = 1$ and $|y| = 1$. For $|x| < 1$ or $|y| < 1$ F_1 has an imaginary part.

The calculation of F in 2D and 3D is difficult, mostly because we need to integrate over a product of two different angles in the denominator. For F_2 (2D) substituting the variables $z = e^{i\varphi}$ and $b = e^{i\beta_{xy}}$ remedies that problem. The φ -integral becomes a contour integral $\oint dz$ on the unit circle around the origin in the complex z -plane. The integrand has four singularities and we can use the residue theorem.

$$F_2(x, \mathbf{k}_x, y, \mathbf{k}_y) = \frac{2}{4\pi^2 k_x k_y} \int_0^1 dp \int_0^{2\pi} d\varphi \frac{p}{(x-p \cos(\varphi - \beta_{xy}))(y-p \cos(\varphi))} \quad (6) \\ = -\frac{2ib}{\pi^2 k_x k_y} \int_0^1 dp \oint dz \frac{z/p}{(z-z_x^+)(z-z_x^-)(z-z_y^+)(z-z_y^-)}$$

The angle β_{xy} is spanned by \mathbf{k}_x and \mathbf{k}_y . The residues are $z_x^\pm = b(x \pm \sqrt{x^2 - p^2})/p$ and $z_y^\pm = (y \pm \sqrt{y^2 - p^2})/p$. For $x^2 > p^2$ one z_x^\pm -residue always lies within and the other outside the unit circle contour. For the case $x^2 < p^2$ both z_x^\pm -residues appear to lie right on the contour and we have to take the infinitesimal contribution $i0$ into account to see that again one z_x^\pm -residue lies within and one outside the contour. Because z_x^\pm and z_y^\pm differ only by a phase factor $e^{i\beta}$ everything said about the z_x^\pm also holds for the z_y^\pm . The positive $i0$ contained in x and y also determines the sign of square roots as $\sqrt{x^2 - p^2} = i \text{sign}(x) \sqrt{p^2 - x^2}$.

The remaining p -integration can be carried out with some diligence and we find

$$F_2(x, \mathbf{k}_x, y, \mathbf{k}_y) = \frac{1}{\pi \Delta} \left\{ (\pi - \beta_{xy}) + i \ln \left(\frac{\varphi(x, y, \beta_{xy})}{\varphi(y, x, -\beta_{xy})} \right) \right\} \quad (7)$$

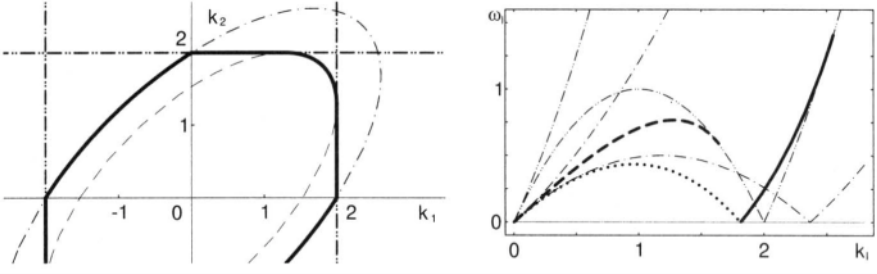


Figure 1. Left: The conditions $\varphi^+ \varphi^- = 0$ (dashed) and $|x| = 1$ in the static limit. The bold region surrounds the area where the static quadratic χ vanishes. The first quadrant depicts $\beta = 130^\circ$, the second quadrant $\beta = 50^\circ$. Right: The conditions $|x| = 1$ and the $\varphi = 0$ singularities (bold) for $k_1 = k_2$ and $\omega_1 = \omega_2$.

where we have used $\Delta = |\mathbf{k}_x \times \mathbf{k}_y| = k_x k_y \sin(\beta_{xy})$ (β_{xy} is positive) and $\varphi(x, y, \beta)$ is defined as $\varphi(x, y, \beta) = x \cos(\beta) - y + \sin(\beta) \sqrt{1 - x^2}$.

We will denote $\varphi(x, y, \beta)$ by φ_x^+ and $\varphi(x, y, -\beta)$ by φ_y^- . As obvious from Eq. (7), the imaginary part of F_2 has a logarithmic singularity if either $\varphi_x^+ = 0$ or $\varphi_y^- = 0$. Concurrently the real part F' shows a discontinuity with a height $1/\Delta$. This feature prevails when the six F_2 are summed up. Where both, φ_x^+ and φ_y^- , vanish the quotient $\varphi_x^+ / \varphi_y^-$ is finite and F_2 no longer singular.

Noting that $\varphi_x^+ \varphi_x^- = \varphi_y^+ \varphi_y^-$ we can write F_2 in a form symmetric in x and y

$$F_2(x, \mathbf{k}_x, y, \mathbf{k}_y) = \frac{1}{\Delta} \left\{ 1 - \frac{\beta_{xy}}{\pi} + \frac{i}{2\pi} \left[\ln \left(\frac{\varphi_x^+}{\varphi_x^-} \right) + \ln \left(\frac{\varphi_y^+}{\varphi_y^-} \right) \right] \right\}. \quad (8)$$

Separating real and imaginary part of the term $i/2 \cdot \ln(\varphi_x^+ / \varphi_x^-)$ gives

$$\begin{aligned} \frac{i}{2} \ln \left(\frac{\varphi_x^+}{\varphi_x^-} \right) &= \Theta(|x| - 1) \text{sign}(x) \arctan \left(\frac{\sin(\beta) \sqrt{x^2 - 1}}{x \cos(\beta) - y} \right) \\ &+ i \Theta(1 - |x|) \text{artanh} \left(\frac{\sin(\beta) \sqrt{1 - x^2}}{x \cos(\beta) - y} \right) \end{aligned} \quad (9)$$

and shows that for $|x| > 1$ and $|y| > 1$ the function $F_2(x, \mathbf{k}_x, y, \mathbf{k}_y)$ is real. For the case $|x| < 1$ and $|y| > 1$ and the case $|x| > 1$ and $|y| < 1$ clearly $F_2(x, \mathbf{k}_x, y, \mathbf{k}_y)$ is complex. Inside the square $|x| < 1$ and $|y| < 1$ the functions φ_x^+ and φ_y^- are real. Accordingly, F_2 is essentially imaginary there (the β/Δ term cancels when the six F_2 are summed), its real part consisting only of multiples of Δ^{-1} .

To discuss F_2 further we switch to the actual arguments, wave numbers and frequencies, and start with the static limit when the density response becomes a real function. In the left of Fig. 1 all $|x| = 1$ boundaries for a fixed total angle β are plotted in the k_2 - k_1 -plane. The angles β_1 and β_2 are determined by the ratio k_2/k_1 . The conditions $|A_1^\pm| < 1$ and $|A_2^\pm| < 1$ simply translate into $|k_1| < 2$ and $|k_2| < 2$ whereas $|A^\pm| < 1$ holds inside the outer ellipse. The inner, dashed ellipse depicts the condition $\varphi^+ \varphi^- = 0$ which, interestingly, for $\omega_l \rightarrow 0$ is identical for all six F_2 . For $\beta = 90^\circ$ the two ellipses become coinciding circles. Since the wave numbers are positive only the first quadrant describes the situation with $\beta = 130^\circ$. The second quadrant corresponds to $\beta = 50^\circ$. The static 2D quadratic density response exhibits two interesting features not seen for $\chi_0(\mathbf{k}_1, 0; \mathbf{k}_2, 0)$ in 3D or for the linear $\chi_0(\mathbf{k}, 0)$ in any dimensionality. For small wave numbers it vanishes and, depending on the angle, the onset of its real part can be discontinuous. The onset is illustrated with a bold line in the left Fig. 1.

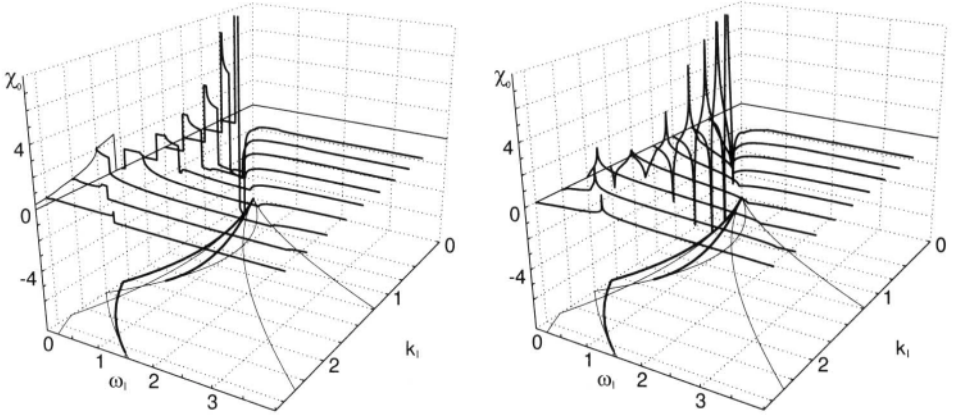


Figure 2. Real and imaginary part of the dynamic quadratic χ_0 for $\beta = 130^\circ$ ($\omega_1 = \omega_2, k_1 = k_2$).

Inside the bold boundary the static 2D quadratic density response is zero. In the upper right where both $\beta_l > |\beta - 90^\circ|$ the onset is a discontinuity caused by the logarithmic singularities $\varphi_x^+ = 0$ or $\varphi_y^- = 0$ on the dashed ellipse.

To simplify the finite frequency discussion we consider only the case $k_1 = k_2$ and $\omega_1 = \omega_2$ where χ_0 consists of only three distinct F_2 . In the right of Fig. 1 the $|x| = 1$ and the three discontinuity conditions (bold) are shown for $\beta = 2\beta_l = 130^\circ$. Note again that the real part of χ_0 vanishes for small k_1 and ω_1 below the lowest parabola.

Figure 2 shows the real and imaginary part of the dynamic $\chi_0(\mathbf{k}_l, \omega_l; \mathbf{k}'_l, \omega'_l)$ for $\beta = 130^\circ$. In the vertical $\omega_l = 0$ plane on the left you find the static χ_0 over k_l . The locations of the discontinuities and other features correspond to right plot in Fig. 1 which is projected onto the bottom of Fig. 2. The large values for small k_l are due to the k_l^{-2} in Δ .

We have solved the three dimensional version of (3) along the same lines as the 2D case. Previous calculations^{5,6} have combined the two angular terms in (3) using the so-called ‘‘Feynman trick’’ $(ab)^{-1} = \int_0^1 du (au + b(1-u))^{-2}$. The resulting F_3 has the form

$$F_3(y, \mathbf{k}, y, \mathbf{k}_l) = \frac{1}{\pi^2 \Delta \sin(\beta_l)} \left\{ \begin{aligned} &(y - x \cos(\beta_l)) \operatorname{arcoth}(x) \\ &+ (x - y \cos(\beta_l)) \operatorname{arcoth}(y) \\ &- \sqrt{\varphi^+ \varphi^-} \operatorname{arcoth}\left(\frac{xy - \cos(\beta_l)}{\sqrt{\varphi^+ \varphi^-}}\right) \end{aligned} \right\} \quad (10)$$

where $\varphi(x, y, \beta)$ is the same as in the 2D calculation.

REFERENCES

- [1] P. Lloyd and C. A. Sholl, *J. Phys. C*, 1:1620–1632, 1968.
- [2] R. Cenni and P. Saracco, *Nucl. Phys. A*, 487:279–300, 1988.
- [3] Z. D. Hu and E. Zaremba, *Phys. Rev. B*, 37(16):9268–9277, 1988.
- [4] Xiao-Yue Gu, PhD thesis, Boston College, 1989.
- [5] Z. C. Tao, PhD thesis, Boston College, 1990.
- [6] C. F. Richardson and N. W. Ashcroft, *Phys. Rev. B*, 50(12):8170–8181, 1995.

THERMODYNAMIC FUNCTIONS OF STRONGLY COUPLED PLASMAS: LOCAL FIELD EFFECTS

W. Stolzmann^{1,2} and M. Rösier³

¹ Astrophysikalisches Institut Potsdam
Potsdam, Germany

² Institut für Astronomie und Astrophysik, Universität Kiel
Germany

³ Hahn-Meitner-Institut
Berlin, Germany

INTRODUCTION

In order to obtain accurate results for the dielectric and thermodynamic functions for strongly coupled plasmas we have to include a local-field correction (LFC) factor $G(q, \omega)$ in the polarization function $\Pi(q, \omega)$. The LFC takes into account exchange and correlation effects between the particles in the polarization potential contribution of the density–density response function. The approximate inclusion of LFC in calculating the dielectric function and thermodynamic properties was done successfully in the classical regime and for the ground-state. Over the past decade considerable effort has been directed towards a generalization of the LFC factor for intermediate degeneracy.^{1,2} One approach is the use of the two standard constraints for the static LFC factor $G(q, \omega = 0)$, the compressibility sum rule and the cusp condition. We apply a generalization of both wavelength constraints to finite temperatures. We adopt for our numerical studies the Vashishta-Singwi (VS) form⁴ for $G(q)$, which has been derived originally for zero-temperature liquid metals. This type of approximation provides the possibility to calculate a dielectric function and the free energy with a static LFC at arbitrary densities and temperatures. Comparisons of thermodynamic functions are presented using different approaches for the LFC factors.

STATIC LOCAL-FIELD FACTOR $G(q)$

In order to improve the dielectric function of an interacting electron system we have to determine $G(q)$, which is defined by

$$\epsilon(q, \omega) = 1 - \frac{v(q)\Pi_0(q, \omega)}{1 + v(q)G(q)\Pi_0(q, \omega)} = 1 + \frac{\epsilon^{\text{RPA}}(q, \omega) - 1}{1 - G(q)[\epsilon^{\text{RPA}}(q, \omega) - 1]}, \quad (1)$$

where $v(q)$ is the Fourier transform of the Coulomb potential and $\Pi_0(q, \omega)$ denotes the ideal fermion part of the polarization function. The dielectric function $\epsilon^{\text{RPA}}(q, \omega)$ in RPA is

related with $\Pi_0(q, \omega)$ given by Eq. (1). We choose for G the static solution from Vashishta and Singwi⁴ expressed by

$$G(q) = A \left[1 - \exp \left(-B \left(\frac{q}{2q_F} \right)^2 \right) \right], \quad (2)$$

which has been derived originally for the metallic density regime. The coefficient A is determined by the cusp condition

$$\lim_{q \rightarrow \infty} G(q) = 1 - g(0) = A, \quad (3)$$

which relates the short-wavelength limit of $G(q)$ with the the (radial) two particle distribution function at zero separation.⁵ Yasuhara⁶ found for $g(0)$

$$g(0) = \frac{1}{8} \left(\frac{2\kappa}{q_F} \right)^2 \left[I_1 \left(\frac{2\kappa}{q_F} \right) \right]^{-2}, \quad (4)$$

where $I_1(z)$ is the modified Bessel function of the first kind.

BA is determined by the compressibility (K^{id} is the isothermal compressibility of the noninteracting electrons)

$$\lim_{q \rightarrow 0} \left(\frac{\kappa}{q} \right)^2 G(q) = 1 - \frac{K^{\text{id}}}{K} = \left(\frac{\kappa}{2q_F} \right)^2 AB \quad (5)$$

It should be noted that both conditions are extended to finite temperatures with (Fermi-Wellenzahl: $q_F = 1/(\bar{\alpha}r_s a_0)$, Brueckner parameter: $r_s = (4\pi n/3)^{-1/3}$, Bohr radius: a_0), $\bar{\alpha} = (9\pi/4)^{-1/3}$, degeneracy parameter: $\Theta = kT/E_F$, Fermi-integrals: $I_\nu(\psi)$)

$$\left(\frac{2q_F}{\kappa} \right)^2 = \frac{\pi}{\bar{\alpha}r_s} \frac{3}{2} \Theta \frac{I_{1/2}(\psi)}{I_{-1/2}(\psi)}. \quad (6)$$

7 9

Finally, we have to calculate the isothermal compressibility $1/K = V(\partial^2 F/\partial V^2)_T$ by means of the free Helmholtz energy F , which we have done explicitly in the RPA - throughout a broad range of densities and temperatures.

NUMERICAL RESULTS

The inverse compressibility normalized to the inverse ideal compressibility are presented at a fixed temperature versus the particle density in Fig. 1. Fig. 2 shows K^{id}/K in dependence of the degeneracy parameter ψ at a fixed (metallic) density. Our LFC corrected RPA results reduce remarkable our RPA calculations for $1/K^c$ in the region of strongly coupling. To determine $G(q)$ with a high accuracy we calculated $G(q)$ given by the compressibility sum rule in a self-consistent manner.¹⁰ Furthermore, we use the LFC factor to calculate the free Helmholtz energy. Fig. 3 shows the correlation contribution of the free Helmholtz energy at a fixed temperature and Fig. 4 at a fixed density over a wide range of the degeneracy. Our comparisons with the self-consistent STLS calculations¹ for the correlation free energy demonstrate that the approximative VS form for modelling of finite temperature static LFC factors is a successful method.² We would like to mention alternatively to the VS form for $G(q)$ we can use a generalized Hubbard form¹⁶ or the form from Moroni et al.¹⁷ for $G(q)$ to study the dielectric and thermodynamic properties.

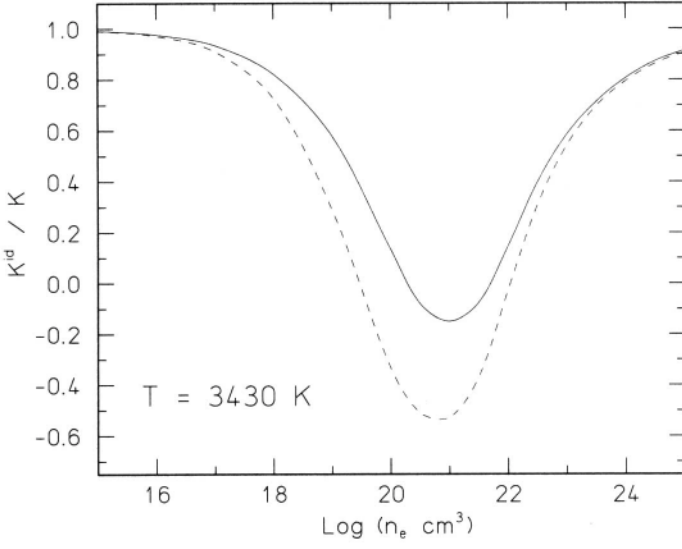


Figure 1. The ratio of the inverse compressibility in RPA^{7,9} (dashed line) compared with the LFC corrected RPA (solid line) vs. the electronic density n_e at $T = 3430K$.

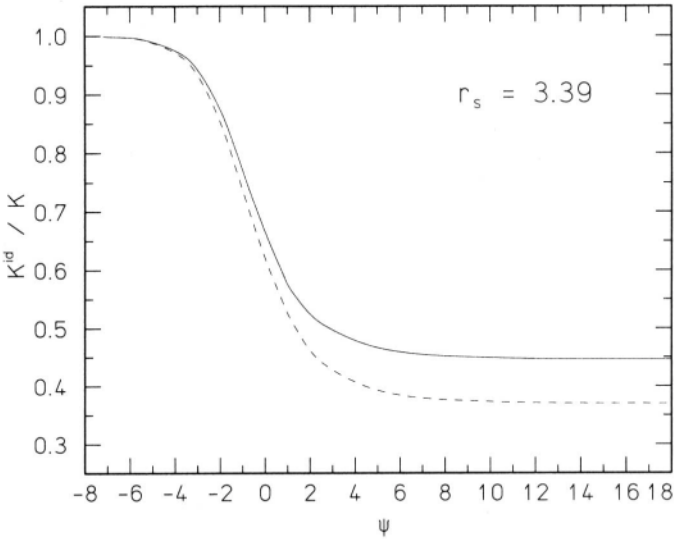


Figure 2. The ratio of the inverse compressibility in RPA^{7,9} (dashed line) compared with the LFC corrected RPA (solid line) vs. the degeneracy parameter ψ at $r_s = 3.39$.

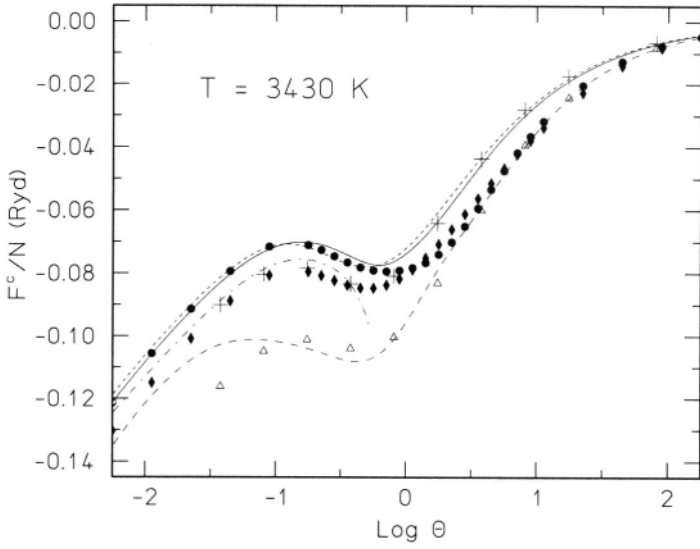


Figure 3. Free Helmholtz correlation energy vs. the degeneracy parameter Θ at $T = 3430\text{K}$. Our LFC corrected RPA approach (+) are compared with the Padé approximant from Stolzmann and Blöcker¹¹ (solid line), Ebeling et al.¹² (dots), Lehmann and Ebeling¹³ (diamonds), and with the parametrizations from Ichimaru et al.¹ (dotted line) and from Dandrea et al.² (dashed-dotted line), which is valid for metallic densities only. The long-dashed line¹⁴ and the triangle (our results for $G(q) = 0$) refer to the RPA.

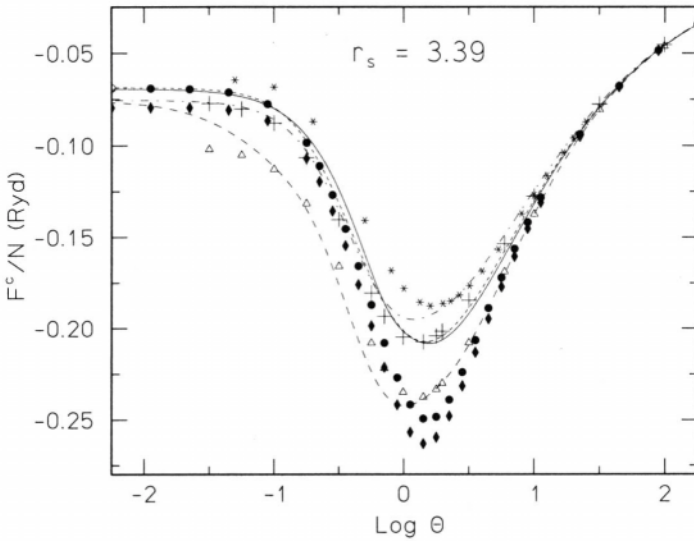


Figure 4. Free Helmholtz correlation energy vs. the degeneracy parameter Θ at $r_s = 3.39$. Our LFC corrected RPA approach (+) are compared with the Padé approximants from Stolzmann and Blöcker¹¹ (solid line), Ebeling et al.¹² (dots), Lehmann and Ebeling¹³ (diamonds), and with the parametrizations from Ichimaru et al.¹ (dotted line) and from Dandrea et al.² (dashed-dotted line). The long-dashed line¹⁴ and the triangle (our results for $G(q) = 0$) refer to the RPA. The stars represent data of the variational calculations from Pokrant.¹⁵

REFERENCES

- [1] S. Ichimaru, H. Iyetomi and S. Tanaka, *Phys. Rep.* **149** (1987) 91.
- [2] R. D. Dandrea, N. W. Ashcroft and A. E. Carlsson, *Phys. Rev.* **B34** (1986) 2097.
- [3] G. D. Mahan, *Many-Particle Physics*, Plenum Press, New York (1990).
- [4] P. Vashishta and K. S. Singwi, *Phys. Rev.* **B6** (1972) 875; Errata **B6**, 4883.
- [5] J. C. Kimball, *Phys. Rev.* **A7** (1973) 1648.
- [6] H. Yasuhara, *Solid State Commun.* **11** (1972) 1481.
- [7] W. Stolzmann and M. Rösier, in *Physics of Strongly Coupled Plasmas*, eds. W. D. Kraeft and M. Schlanges, World Scientific, Singapore (1996) p. 87.
- [8] M. Rösier and W. Stolzmann, *ibid.*, p. 91
- [9] W. Stolzmann, *Thesis II*, Christian-Albrechts-Universität, Kiel (1996).
- [10] W. Stolzmann and M. Rösier, in preparation
- [11] W. Stolzmann and T. Blöcker, *Astron. Astrophys.* **314** (1996) 1024; *Phys. Lett.* **A221** (1996) 99.
- [12] W. Ebeling, A. Förster, V. E. Fortov, V. K. Gryaznov and A. Ya. Polishchuk, *Thermodynamical Properties of Hot Dense Plasmas*, Teubner, Stuttgart (1991) p. 39.
W. Ebeling, *Contrib. Plasma Phys.* **30** (1990) 553.
W. Ebeling and W. Richert, *phys. stat. sol. (b)* **128** (1985) 467.
W. Richert and W. Ebeling, *phys. stat. sol. (b)* **121** (1984) 633.
- [13] H. Lehmann and W. Ebeling, *Phys. Rev.* **E54** (1996) 2451.
W. Ebeling and H. Lehmann, *Ann. Phys. (Leipzig)* **45** (1988) 529.
W. Ebeling, *Physica* **130A** (1985) 587.
- [14] F. Perrot and M. W. C. Dharma-wardana, *Phys. Rev.* **A30** (1984) 2619.
- [15] M. A. Pokrant, *Phys. Rev.* **A16** (1977) 413.
- [16] I. M. Tkachenko, P. Fernández de Córdoba and J. M. Belda, *this volume*.
- [17] S. Moroni, D. M. Ceperley and G. Senatore, *Phys. Rev. Lett.* **75** (1995) 689.

This page intentionally left blank

DIELECTRIC FUNCTION AND TRANSPORT COEFFICIENTS IN STRONGLY COUPLED PLASMAS

Gerd Röpke

Fachbereich Physik, Universität Rostock
Universitätsplatz 3, D-18051 Rostock, Germany

INTRODUCTION

A consistent unified approach to the dielectric function as well as the dc conductivity is presented. A standard approach to the dc electrical conductivity is given by the Chapman-Enskog approach.¹ In dense plasmas, linear response theory has been worked out to relate the dc conductivity to equilibrium correlation functions which can be evaluated using the method of thermodynamic Green functions.^{2,3} The dielectric function can also be expressed in terms of equilibrium correlation functions, but a simple perturbative treatment to include collision effects is not possible near the point $\vec{k} = 0, \omega = 0$, because an essential singularity arises in zeroth order.

Different improvements are known to go beyond the well-known RPA result. In the static limit, local field corrections have been discussed extensively,⁴ and the dynamical behavior of the corrections to the RPA in the long-wavelength limit was investigated in the time-dependent mean field theory neglecting damping effects,⁵ see also Ref. [6] for the strong coupling case. At arbitrary \vec{k} and ω , approximations are made on the basis of sum rules for the lowest moments.⁷ However, these approximations cannot give an unambiguous expression for $\epsilon(\vec{k}, \omega)$ in the entire $\vec{k} - \omega$ space.

Within a generalized linear response theory, the polarization function is related to equilibrium correlation functions for nonideal plasmas. Applying perturbation theory, thermodynamic Green functions⁸ are evaluated in Born approximation. Improvements are possible using diagram techniques and partial summations.² A promising alternative to evaluate equilibrium correlation functions in strongly coupled plasmas is given by molecular dynamics simulations, see the related contributions to this Conference.

GENERALIZED LINEAR RESPONSE THEORY

In homogeneous, isotropic systems the dielectric function $\epsilon(k, \omega)$ is related to the electrical conductivity $\sigma(k, \omega)$ and the polarization function $\Pi(k, \omega)$ according to

$$\epsilon(k, \omega) = 1 + \frac{i}{\epsilon_0 \omega} \sigma(k, \omega) = 1 - \frac{1}{\epsilon_0 k^2} \Pi(k, \omega). \quad (1)$$

In particular, the polarization function was found⁹ as

$$\Pi(k, \omega) = i \frac{k^2}{\omega} \beta \Omega_0 \left| \begin{array}{cc} 0 & M_{0n}(k, \omega) \\ M_{m0}(k, \omega) & M_{mn}(k, \omega) \end{array} \right| / |M_{mn}(k, \omega)|. \quad (2)$$

The matrix elements M_{mn} are equilibrium correlation function. They contain operators B_m and B_n which specify the nonequilibrium state,

$$\begin{aligned} M_{0n}(k, \omega) &= (J_k; B_n), & M_{m0}(k, \omega) &= (B_m; \hat{J}_k), \\ M_{mn}(k, \omega) &= (B_m; [\dot{B}_n - i\omega B_n]) + \langle \dot{B}_m; [\dot{B}_n - i\omega B_n] \rangle_{\omega+i\eta} \\ &\quad - \frac{\langle \dot{B}_m; J_k \rangle_{\omega+i\eta} \langle B_m; [\dot{B}_n - i\omega B_n] \rangle_{\omega+i\eta}}{\langle B_m; J_k \rangle_{\omega+i\eta}}. \end{aligned} \quad (3)$$

The equilibrium correlation functions are defined as

$$\begin{aligned} (A; B) &= (B^+; A^+) = \frac{1}{\beta} \int_0^\beta d\tau \text{Tr} [A(-i\hbar\tau) B^+ \rho_0], \\ \langle A; B \rangle_z &= \int_0^\infty dt e^{izt} (A(t); B), \end{aligned} \quad (4)$$

with $A(t) = \exp(iHt/\hbar) A \exp(-iHt/\hbar)$ and $\dot{A} = \frac{i}{\hbar} [H, A]$. The equilibrium statistical operator is $\rho_0 = \exp(-\beta H + \beta \sum_c \mu_c N_c) / \text{Tr} \exp(-\beta H + \beta \sum_c \mu_c N_c)$.

We will consider a two-component plasma consisting of electrons ($c = e$) and ions ($c = i$). With the single-particle operators

$$n_{p,k}^c = \left(n_{p,-k}^c \right)^+ = c_{p-k/2}^+ c_{p+k/2}, \quad (5)$$

the current density operator is given by

$$J_k = \frac{1}{\Omega_0} \sum_{c,p} \frac{e_c}{m_c} \hbar p_z n_{p,k}^c = \epsilon(k, \omega) \hat{J}_k. \quad (6)$$

MOMENT EXPANSION OF THE POLARIZATION FUNCTION

Up to now, B_n was not specified. It is an advantage of the approach given here that different levels of approximations can be constructed, depending on the use of different sets of B_n . If no finite order perturbation expansion of the correlation functions is performed in evaluating the polarization function (2), all these different approaches are exact and should give identical results. However, evaluating the correlation functions within perturbation theory, different results for the polarization function are expected using different sets of B_n . As has been shown for the electrical conductivity,^{2,3} results from finite order perturbation theory are the better the more relevant observables are considered.

A simple example for a relevant observable B_n characterizing the nonequilibrium state of the system is the current density (6),

$$B_n = J_k. \quad (7)$$

The current density is related to the lowest moment of the distribution function. Possible extensions to more general sets of relevant observables are discussed in Ref. [10].

In the approach given by Eq. (7), we have

$$\Pi(k, \omega) = - \frac{ik^2 \beta \Omega_0}{\omega} \frac{(J_k; J_k) (J_k; \hat{J}_k)}{M_{JJ}}, \quad (8)$$

with

$$M_{JJ} = -i\omega \langle J_k; J_k \rangle + \langle \hat{J}_k; \hat{J}_k \rangle_{\omega+i\eta} - \frac{\langle \hat{J}_k; J_k \rangle_{\omega+i\eta}}{\langle J_k; J_k \rangle_{\omega+i\eta}} \langle J_k; \hat{J}_k \rangle_{\omega+i\eta}. \quad (9)$$

Applying integration by part, the expression (8) can be rewritten as

$$\Pi(k, \omega) = -\frac{ik^2 \beta \Omega_0}{\omega} \frac{\langle J_k; \hat{J}_k \rangle_{\omega+i\eta}}{\langle J_k; J_k \rangle - \eta \langle \hat{J}_k; \hat{J}_k \rangle_{\omega+i\eta}}. \quad (10)$$

Performing the limit $\eta \rightarrow 0$, we obtain the simple result

$$\Pi(k, \omega) = -\frac{ik^2 \beta \Omega_0}{\omega} \langle J_k; \hat{J}_k \rangle_{\omega+i\eta} \quad (11)$$

which is also denoted as the Kubo formula for the polarization function. Different approaches based on different sets of relevant observables \mathbf{B}_n are formally equivalent as long as no approximations in evaluating the correlation functions are performed.

RESULTS FOR TWO-COMPONENT PLASMAS

In the case considered here, the relevant observable J_k (6) is given by a single particle observable. The correlation functions occurring in (8) will contain the operators $n_{p,k}^c = c_{p-k/2}^+ c_{p+k/2}$ and $\hat{n}_{p,k}^c = -(i\hbar p_z k/m_c) n_{p,k}^c + v_{p,k}^c$, with

$$v_{p,k}^c = \frac{i}{\hbar} \sum_{d,p',q} V_{cd}(q) \left[c_{p-k/2-q}^+ d_{p'+q}^+ d_{p'} c_{p+k/2} - c_{p-k/2}^+ d_{p'+q}^+ d_{p'} c_{p+k/2+q} \right]. \quad (12)$$

To evaluate the correlation functions, we perform a perturbation expansion with respect to the interaction V . In addition to the zeroth order terms which reproduce the RPA result, we consider the Born approximation. We obtain in the nondegenerate case for small k , ω

$$\Pi(k, \omega) = -\frac{\beta \sum_c e_c^2 n_c [1 + z_c D(z_c)]}{1 - i \frac{\omega}{k^2} \frac{e_e^2 e_i^2}{(4\pi\epsilon_0)^2} n_e n_i \frac{\mu_{ei}^{1/2}}{(k_B T)^{5/2}} \frac{2(2\pi)^{1/2}}{\sum_c e_c^2 n_c / m_c} \int_0^\infty dp e^{-p^2} \left(\ln \frac{\lambda-1}{\lambda+1} + \frac{2}{\lambda+1} \right) W(p)} \quad (13)$$

with

$$W(p) = \frac{2}{3} p \left(\frac{e_e}{m_e} - \frac{e_i}{m_i} \right)^2 \frac{\sum_c e_c^2 n_c [1 + z_c D(z_c)]}{\sum_c e_c^2 n_c / m_c} - \frac{M_{ei}^{1/2}}{\mu_{ei}^{1/2}} \left(\frac{e_e}{m_e} - \frac{e_i}{m_i} \right) \int_{-1}^1 dc c \left[e_e D(z_{ei} - \sqrt{\frac{m_i}{m_e}} cp) + e_i D(z_{ei} + \sqrt{\frac{m_e}{m_i}} cp) \right]. \quad (14)$$

Here, $z_{ei} = \frac{\omega}{k} \sqrt{\frac{M_{ei}}{2k_B T}}$, $z_c = \frac{\omega}{k} \sqrt{\frac{m_c}{2k_B T}}$, $\lambda(p) = (\hbar^2 \kappa^2) / (4\mu_{ei} k_B T p^2) + 1$, and

$$D(z) = \frac{1}{\sqrt{\pi}} \int_{-\infty}^{\infty} e^{-x^2} \frac{dx}{x - z - i\eta} = i\sqrt{\pi} e^{-z^2} [1 + \text{Erf}(iz)] \quad (15)$$

denotes the Dawson integral. Note that a statically screened potential was used in (12) to obtain a convergent collision integral, the screening parameter is given by $\kappa^2 = \sum_c e_c^2 n_c / (\epsilon_0 k_B T)$. From (13) it is immediately to be seen that the RPA result is obtained in the limit of vanishing interactions, $W(p) = 0$.

Expression (8) allows to include the effect of collisions in the entire $k-\omega$ plane. It fulfills important sum rules as well as the Kramers–Kronig relation.¹⁰ For small k , the conductivity corresponding to the Faber–Ziman formula at finite temperatures is obtained.⁹

OPTICAL LINE SPECTRA

Line shapes can be obtained from the perturbative treatment of the polarization function within a cluster decomposition.¹¹ Pressure broadening in dense plasmas due to the interaction with electrons are treated in a systematic way expanding the two-particle self-energy and vertex function with respect to the density. As a result of nonideality, the shift and width of spectral lines are not proportional to the density.¹² The quantum statistical approach is not only able to explain deviations from linearity observed by experiments but predicts also blue shifts which have been observed afterwards in experiments with dense Cs plasmas.¹³

An interesting point is the treatment of the ionic effects on spectral line shapes. By reason of its large masses, the influence of the ions is usually replaced by a static microfield. For light ions, in particular also for highly ionized radiators, a dynamic microfield has to be considered which is given by a stochastic model process,¹⁴ a systematic cluster expansion,¹⁵ or molecular dynamics simulations of the motion of ions, respectively. A unified systematic treatment of electrons as well as ions with respect to their influence on spectral line shapes is, however, missing until now.

REFERENCES

- [1] Chapman, S., and Cowling, T., 1939, "Mathematical Theory of Non-Uniform Gases," University Press, Cambridge.
- [2] Röpke, G., 1988, *Phys. Rev. A* 38:3001.
- [3] Röpke, G., and Redmer, R., 1989, *Phys. Rev. A* 39:907;
Redmer, R., Röpke, G., Morales, F., and Kilimann, K., 1990, *Phys. Fluids B* 2:390;
Reinholz, H., Redmer, R., and Nagel, S., 1995, *Phys. Rev. A* 52:5368;
Esser, A., and Röpke, G., submitted to *Phys. Rev. E*.
- [4] Singwi, K. S., Tosi, M. P., Land, R. H., and Sjolander, A., 1968, *Phys. Rev.* 176:589;
K. S. Singwi, K. S., A. Sjolander, A., M. P. Tosi, M. P., and R. H. Land, R. H., 1969, *Solid State Commun.* 7:1503;*Phys. Rev. B* 1:1044;
H. Totsuji, H., and S. Ichimaru, S., 1974, *Prog. Theor. Phys.* 50:735; 52:42;
Ichimaru, S., 1982, *Rev. Mod. Phys.* 54:1017.
- [5] Golden, K. I., and Kalman, G., 1979, *Phys. Rev. A* 19:2112.
- [6] Kalman, G., and Golden, K. I., 1990, *Phys. Rev. A* 41:5516.
- [7] Adamyan, V. M., and Tkachenko, I. M., 1983, *Teplofiz. Vys. Temp.* 21:417;
Hong J., and Lee, M. H., 1993, *Phys. Rev. Lett.* 70:1972.
- [8] Kraeft, W. D., Kremp, D., Ebeling, W., and Röpke, G., 1986, "Quantum Statistics of Charged Particle Systems," Plenum, New York.
- [9] Röpke, G., 1997, preprint physics/9709018, 13 Sep97.
- [10] Röpke, G., and Wierling, A., 1997, preprint physics/9709021, 15 Sep97.
- [11] Röpke, G., and Hitzschke, L., 1989, "Spectral Line Shapes," J. Szudy, ed., Vol. 5, p. 49, Ossolineum Publishing House, Wroclaw.
- [12] Günter, S., Hitzschke, L., and Röpke, G., 1991, *Phys. Rev. A* 44:10.
- [13] Hitzschke, L., and Günter, S., 1996, *J. Quant. Spectrosc. Radiat. Transfer* 56:423.
- [14] Brissaud, A., and Frisch, U., 1917, *J. Quant. Spectrosc. Radiat. Transfer* 11:1767;
Seidel, J., 1977, *Z. Naturf.* 32a:195.
- [15] Könies, A., Günter, S., and Röpke, G., 1996, *J. Phys. B: At. Mol. Opt. Phys.* 29:6091.

OPTICAL CHARACTERISTICS OF STRONGLY COUPLED COULOMB SYSTEMS

G.A. Pavlov

Institute of Chemical Physics, RAS
Chernogolovka, 142432, Moscow Region, Russia.
e-mail: pavlov@icp.ac.ru;
fax: (096) 515-3588.

Reflexion (R_ω), absorption (κ_ω) and scattering of electromagnetic irradiation by Coulomb systems are considered. The first two can be analysed provided that transverse dielectric susceptibility ($\epsilon^\perp(\mathbf{0}, \omega)$) of the Coulomb system is known. Practically the latter can be calculated in the limit of long wavelengths in which case it immediately follows from proper time correlation function. The scattering - the power of electromagnetic field scattered by Coulomb system - depends on the dynamical structure factor of electrons $S_c(\mathbf{k}, \omega)$. Direct determination of the transverse dielectric susceptibility and the dynamical structure factor for strongly coupled Coulomb system is hardly possible. For this reason a new technique is proposed to calculate frequency dependence of absorption and reflection coefficients and scattering spectra. The technique is based on proper approximations for the transverse dielectric susceptibility and the dynamical structure factor with a number of fitting parameters and the sum rules (frequency moments) being used. The technique enables one to simplify considerably calculation of dynamical characteristics of nonideal Coulomb systems reducing the problem to calculating moments of these characteristics, i.e. coordinate correlation function. Frequency moments are in fact thermodynamical characteristics of Coulomb systems.

$$\kappa_\omega = \sqrt{2}(\omega/c) \left\{ 4\pi\sigma''(\omega)/\omega - 1 + [(1 - 4\pi\sigma''(\omega)/\omega)^2 + (4\pi\sigma'(\omega)/\omega)^2]^{1/2} \right\}^{1/2} \quad (1)$$

$$R_\omega = \left| \frac{\sqrt{\epsilon(\omega)} - 1}{\sqrt{\epsilon(\omega)} + 1} \right|^2$$

In these formulas c - light velocity; $\sigma'(\omega)$, $\sigma''(\omega)$ - real and imaginary parts of $\sigma(\omega)$.

The scattering electromagnetic irradiation power is proportional to $S_c(\mathbf{k}, \omega)$. The following expression is well known ($\mathbf{h} \rightarrow \mathbf{0}$; N, V - number of particle and volume of the system; β - inverse temperature)

$$\text{Re } \sigma^l(\mathbf{k}, \omega) = (e^2/k^2)\pi\beta\omega^2(N/V) S_{\rho\rho}(\mathbf{k}) \quad (2)$$

$$S_{\rho\rho}(\mathbf{k}, \omega) = (1/2)[S_i(\mathbf{k}, \omega) + S_e(\mathbf{k}, \omega) + 2S_{ei}(\mathbf{k}, \omega)]$$

Thereby it is interesting to consider the frequency moments of dynamical structure factors, ϵ^\pm (σ^\pm), $\hat{\sigma}^l(1/\epsilon^l)$ and connected with these: $\sigma^l(\epsilon^l)$, $\tilde{\sigma}(\omega)$ - Kubo coefficient. $S_e(\mathbf{k}, \omega)$, $S_{\rho\rho}(\mathbf{k}, \omega)$ are even function of ω in the classical limit, therefore it ought to investigate

$$\int_{-\infty}^{\infty} \omega^{2n} S_{\rho\rho}(\mathbf{k}, \omega) d\omega = \frac{(i)^{2n}}{N} \lim_{t \rightarrow 0} \left\langle d^{2n}(\rho_{\mathbf{k}}(t)\rho_{-\mathbf{k}}(0)) / dt^{2n} \right\rangle_0 = \quad (3)$$

$$= \frac{1}{N} \left\langle |d^n \rho_{\mathbf{k}}(t) / dt^n|_{t=0}|^2 \right\rangle_0$$

In this equation $\rho_{\mathbf{k}}(t) = \sum_i z_i \exp(-ikr_i(t))$, z_i - charge number of i -particle, r_i - i -particle coordinate.

From (3) and using the expression

$$\left\langle \frac{\partial U}{\partial x_i} F(r_1, r_2, \dots, r_N) \right\rangle_0 = \beta^{-1} \left\langle \partial F(r_1, \dots, r_N) / \partial x_i \right\rangle_0$$

it is possible to determine frequency moments of four various definitions of conductivity and, hence, other linear response theory characteristics of Coulomb system. Some moments calculations of external longitudinal conductivity real part $\text{Re } \hat{\sigma}^l(\mathbf{k}, \omega)$ are reduce to $(\hat{\omega}_l^{2n} = \int_{-\infty}^{\infty} \omega^{2n} \text{Re } \hat{\sigma}^l(\mathbf{k}, \omega) d\omega)$, other frequency moments of external conductivity are equal to zero) :

$$\hat{\omega}_l^0 = \frac{N \pi e^2}{V} \left(\frac{1}{m_e} + \frac{1}{m_i} \right)$$

$$\hat{\omega}_l^2 = (3/2)\pi e^2 k^2 \frac{N}{V} \left(\frac{1}{\beta m_e^2} + \frac{1}{\beta m_i^2} \right) + \frac{\pi n^2 e^2}{m_e^2} \times$$

$$\times \left(\int (\hat{k} \cdot \nabla)^2 v_{ee}(r) (1 - \cos k \cdot r) g_{ee}(r) dr + \int (\hat{k} \cdot \nabla)^2 v_{ei}(r) g_{ei}(r) dr + \right.$$

$$\left. + \frac{2\pi n^2 e^2}{m_e m_i} \int (\hat{k} \cdot \nabla)^2 v_{ei}(r) \cos k \cdot r g_{ei}(r) dr + \frac{\pi n^2 e^2}{m_i^2} \left(\int (\hat{k} \cdot \nabla)^2 v_{ii}(r) \times \right. \right.$$

$$\left. \left. \times (1 - \cos k \cdot r) g_{ii}(r) dr + \int (\hat{k} \cdot \nabla)^2 v_{ei}(r) g_{ei}(r) dr \right) \right.$$

In these expressions m_e , m_i - electrons and ions masses, $n=N/2V$, $g_{\alpha\beta}$ - binary correlation functions. The following frequency moments connect with triple correlation functions and so on. From (4) it is easy to find dynamic structure factors frequency moments .

Write out even frequency moments of $\text{Re } \sigma^\perp(\mathbf{k}, \omega)$ over frequency moments of external conductivity real part (other frequency moments of $\sigma^\perp(\mathbf{k}, \omega)$ are equal to zero)

$$\omega_i^0 = \hat{\omega}_i^0$$

$$\omega_i^2 = \hat{\omega}_i^2 - 4(\hat{\omega}_i^0)^2 \tag{5}$$

$$\omega_i^4 = \hat{\omega}_i^4 - 8\hat{\omega}_i^0\hat{\omega}_i^2 + 16(\hat{\omega}_i^0)^3$$

and so on. Frequency moments of σ^\perp and Kubo coefficient $\omega_\perp^{2n}, \tilde{\omega}^{2n}$ investigated as well as external conductivity frequency moments .

So, the frequency moments of values, which directly define reflection, absorption and scattering of electromagnetic irradiation by Coulomb systems - $S_e(\mathbf{k}, \omega), \epsilon^\perp(\mathbf{k}, \omega)$, are investigated. Besides that, frequency moments of other connected with previous linear response characteristics of Coulomb systems are considered. Therefore it is interesting to find out the question about commutation different linear response characteristics frequency moments. With this purpose to compare frequency moments of four different Coulomb system conductivity definitions. The comparison in the classical case shows that these moments are different at finite wave vector k . In longwavelength limit $\omega_\perp^{2n}, \tilde{\omega}^{2n}, \hat{\omega}_i^{2n}$ coincide with each other. In that case the moments are defined by the members with $v_e(\mathbf{r})$ and depended on $v_e(\mathbf{r} \rightarrow 0)$ form. In spite of the coincidence the moments in longwavelength limit, $\lim_{\omega \rightarrow 0} \lim_{k \rightarrow 0} \hat{\sigma}^\perp(\mathbf{k}, \omega) = 0$, but σ^\perp and $\tilde{\sigma} \neq 0$ in this case. Longwavelength limit of ω_i^{2n} is not equal to the limits of $\omega_\perp^{2n}, \tilde{\omega}^{2n}, \hat{\omega}_i^{2n}$. Frequency moments are thermodynamical characteristics of Coulomb systems. Some restriction on $g_{\alpha\beta}(\mathbf{r}), g_{\alpha\beta\gamma}(\mathbf{r})$ and inequalities between the moments follow from the fact that the moments are positive. Series of the inequalities define by the well known integral inequalities between response function of Coulomb systems (Pavlov, 1991, 1992).

To describe the Coulomb systems optical characteristics experimental data it is necessary to have the functions - $S_e(\mathbf{k}, \omega), \epsilon^\perp(\mathbf{k}, \omega)$. Frequency behaviour reconstruction of these ω -functions by its known frequency moments (moments problem decision) require, generally speaking, infinite number known frequency moments. It is, in practice, not available, therefore proper approximations for transverse dielectric susceptibility and the dynamical structure factor with a number of fitting parameters are used. The fitting parameters determine by known frequency moments of $S_e(\mathbf{k}, \omega), \epsilon^\perp(\mathbf{k}, \omega)$. This technique is used for frequency behaviour reconstruction dynamic structure factors of electron; comparison reconstruction results shows a good agreement with molecular dynamic simulation data (Pavlov, 1991) .

Reflection and absorption of electromagnetic irradiation in linear response case are described, as well known, by longwavelength limit of transverse dielectric susceptibility. Imaginary part of $\epsilon^\perp(\mathbf{k}, \omega)$ was elected in the following form:

$$\text{Im } \epsilon^\perp(0, \omega) = \alpha \omega^m [e^{-(\omega - \omega_0)^2 / \delta^2} - e^{-(\omega + \omega_0)^2 / \delta^2}] \tag{6}$$

In this formula $\alpha, m, \delta, \omega_0$ - fitting parameters; $\text{Im } \epsilon^\perp(0, \omega)$ is odd ω -function, real part of $\epsilon^\perp(0, \omega)$ defined by Kramers-Kronig relations. Calculation results of R_ω (1), re-

ceived by described method, are presented in (Pavlov, 1991). The comparison Coulomb system κ_{ω} indicates a satisfactory agreement with nonideal plasma inert gases experimental data. These conclusions mean, that Coulomb system is available nonideal plasma model (Pavlov, 1995).

REFERENCES

1. Pavlov G.A., 1991, Jurnal Tech. Fiziki, 61, N 2:6.
2. Pavlov G.A., 1992, Teoreticheskaya i Matematicheskaya Fizika, 90:460.
3. Pavlov G.A., 1995, "Transport Processes in Low Temperature Plasma with Strong Coulomb Interactions", Energoatomizdat, Moscow.

STATISTICS OF QUANTUM-ELECTRODYNAMIC PLASMAS IN EXTERNAL MAGNETIC FIELDS

L. G. Suttorp

Institute of Theoretical Physics, University of Amsterdam
Valckenierstraat 65, 1018 XE Amsterdam, The Netherlands

INTRODUCTION

In the standard statistical description of a one-component quantum plasma the interaction is assumed to be purely Coulombic. Magnetic effects are taken into account only in so far as they are generated by an external field. Hence, induction effects cannot be studied in the context of that model. To determine the relevance of these effects one has to incorporate the quantized radiation field in the theoretical analysis. In this paper we shall study the equilibrium statistical properties of a one-component quantum-electrodynamic plasma in an external magnetic field, with an emphasis on fluctuations. Fluctuations in quantum-electrodynamic plasmas have been discussed before¹⁻³ in the context of specific perturbative approximations like the random-phase approximation. Here, a more general reasoning based on the equations of motion will be followed.

MODEL

The model that we shall discuss is a generalization of the usual one-component plasma consisting of charged particles with charge e and mass m that move in a uniform background of opposite charge in a volume V . Apart from the Coulomb interaction the particles interact through their coupling to the quantized radiation field. Moreover, a static and uniform external magnetic field \mathbf{B} is present. The Hamiltonian is

$$\begin{aligned}
 H = & \frac{\hbar^2}{2mV} \sum_{\mathbf{k}} \psi^\dagger(\mathbf{k}) \left(\mathbf{k} - \frac{ie}{2\hbar c} \mathbf{B} \wedge \nabla_{\mathbf{k}} \right)^2 \psi(\mathbf{k}) \\
 & - \frac{e\hbar}{mcV^2} \sum_{\mathbf{k}, \mathbf{k}'} \psi^\dagger(\mathbf{k}) \left(\mathbf{k} - \frac{ie}{2\hbar c} \mathbf{B} \wedge \nabla_{\mathbf{k}} \right) \cdot \mathbf{a}(\mathbf{k}') \psi(\mathbf{k} - \mathbf{k}') \\
 & + \frac{e^2}{2mc^2V^3} \sum_{\mathbf{k}, \mathbf{k}', \mathbf{k}''} \psi^\dagger(\mathbf{k}) \mathbf{a}(\mathbf{k}') \cdot \mathbf{a}(\mathbf{k}'') \psi(\mathbf{k} - \mathbf{k}' - \mathbf{k}'') \\
 & + \frac{1}{2V^3} \sum_{\mathbf{k}, \mathbf{k}'} \sum_{\mathbf{q} \neq 0} \frac{e^2}{q^2} \psi^\dagger(\mathbf{k} + \mathbf{q}) \psi^\dagger(\mathbf{k}' - \mathbf{q}) \psi(\mathbf{k}') \psi(\mathbf{k}) + \hbar c \sum_{\mathbf{k}, \lambda} k \left(a_{\mathbf{k}, \lambda}^\dagger a_{\mathbf{k}, \lambda} + \frac{1}{2} \right). \quad (1)
 \end{aligned}$$

The matter fields $\psi(\mathbf{k})$ and $\psi^\dagger(\mathbf{k})$ satisfy (anti-)commutation relations. The field operator $\mathbf{a}(\mathbf{k})$ in the Coulomb gauge is a combination of photon annihilation and creation operators, and of polarization vectors $\mathbf{e}_{\mathbf{k},\lambda}$ orthogonal to the wave vector \mathbf{k} .

EQUATIONS OF MOTION

The sources of the quantized radiation field are the charge and current density. The charge density is defined as

$$Q(\mathbf{k}) = \frac{e}{V} \sum_{\mathbf{k}'} \psi^\dagger(\mathbf{k}' - \mathbf{k}) \psi(\mathbf{k}'). \quad (2)$$

The current density is:

$$\mathbf{J}(\mathbf{k}) = \frac{e\hbar}{mV} \sum_{\mathbf{k}'} \psi^\dagger(\mathbf{k}' - \mathbf{k}) \left(\mathbf{k}' - \frac{1}{2}\mathbf{k} - \frac{ie}{2\hbar c} \mathbf{B} \wedge \nabla_{\mathbf{k}'} \right) \psi(\mathbf{k}') - \frac{\omega_p^2}{c} \mathbf{a}(\mathbf{k}) - \frac{e}{mc} [Q\mathbf{a}](\mathbf{k}), \quad (3)$$

with ω_p the plasma frequency. Here we introduced convolution products in Fourier space by writing $[A_1 A_2](\mathbf{k}) = V^{-1} \sum_{\mathbf{q}(\neq 0, \mathbf{k})} A_1(\mathbf{k} - \mathbf{q}) A_2(\mathbf{q})$. The field equations for the radiation field are found to have the usual form:

$$[H, \mathbf{e}(\mathbf{k})] = \hbar c \mathbf{k} \wedge \mathbf{b}(\mathbf{k}) + i\hbar \mathbf{J}_\perp(\mathbf{k}) \quad , \quad [H, \mathbf{b}(\mathbf{k})] = -\hbar c \mathbf{k} \wedge \mathbf{e}(\mathbf{k}), \quad (4)$$

with $\mathbf{J}_\perp(\mathbf{k})$ the transverse part of the current density.

In a one-component plasma the current density is proportional to the momentum density. It turns out to satisfy a balance equation of the form:

$$\begin{aligned} [H, \mathbf{J}(\mathbf{k})] = & -\hbar \omega_p^2 \frac{\mathbf{k}}{k^2} Q(\mathbf{k}) - i\hbar \omega_p^2 \mathbf{e}(\mathbf{k}) - i\hbar \omega_c \mathbf{J}(\mathbf{k}) \wedge \hat{\mathbf{B}} \\ & - \frac{ie\hbar}{m} [Q\mathbf{e}](\mathbf{k}) - \frac{ie\hbar}{mc} [\mathbf{J} \wedge \mathbf{b}](\mathbf{k}) - \frac{e\hbar}{m} \mathbf{k} \cdot \mathbf{T}(\mathbf{k}), \end{aligned} \quad (5)$$

with ω_c the cyclotron frequency and with $\hat{\mathbf{B}}$ a unit vector in the direction of the external magnetic field. The last term is the divergence of the (material) pressure tensor; it is the sum of a kinetic term (depending on the radiation field as well) and a potential term accounting for the Coulomb interaction.

Likewise, one may derive a balance equation for the energy density $E(\mathbf{k})$. It has the general form $[H, E(\mathbf{k})] = -\hbar \mathbf{k} \cdot \mathbf{J}_E(\mathbf{k})$, with an energy flux $\mathbf{J}_E(\mathbf{k})$.

FLUCTUATIONS

Fluctuation formulas are the long-wavelength limits of Green functions in Fourier space:

$$F_{AB}(\tau) = \frac{1}{V} \langle A(\mathbf{k})_\tau B(-\mathbf{k}) \rangle_T, \quad (6)$$

with A and B local operators, with the label τ denoting imaginary time translation (that is, a transform with $e^{\tau H}$), with a subscript T meaning truncation, and with brackets indicating a (grand)canonical averaging.

Kubo-transformed fluctuation formulas (denoted by the symbol \mathcal{K}) follow by integration over all τ between 0 and β :

$$\mathcal{K}F_{AB} = \frac{1}{\beta} \int_0^\beta d\tau F_{AB}(\tau). \quad (7)$$

These Kubo-type fluctuation formulas arise in analyzing the (linear) response of a system to external disturbances. They can be derived from the equations of motion, with the help of an identity that is a direct consequence of the Kubo–Martin–Schwinger-condition:

$$\mathcal{K} \frac{1}{V} \langle \{H, A(\mathbf{k})\}_T B(-\mathbf{k}) \rangle_T = -\beta^{-1} \frac{1}{V} \langle \{A(\mathbf{k}), B(-\mathbf{k})\} \rangle, \quad (8)$$

for arbitrary local operators A and B .

By exploiting the equations of motion in a systematic way one may derive a set of Kubo-type fluctuation formulas for the charge density, the current density, the energy density and the radiation field. A few examples of the results that can be obtained in this way will be given presently. First of all, the charge fluctuations satisfy the formula

$$\mathcal{K} \frac{1}{V} \langle \mathcal{Q}(\mathbf{k}) \mathcal{Q}(-\mathbf{k}) \rangle_T = \beta^{-1} k^2 + \mathcal{O}(k^3). \quad (9)$$

It has the same form as the well-known Stillinger–Lovett relation for the standard one-component plasma. Remarkably enough, its form does not change by incorporating the effects of an external magnetic field and of the radiation field.

The current fluctuations fulfil the relation:

$$\mathcal{K} \frac{1}{V} \langle \mathbf{J}(\mathbf{k}) \mathbf{J}(-\mathbf{k}) \rangle_T = \beta^{-1} \omega_p^2 \mathbf{U} + \mathcal{O}(k^2). \quad (10)$$

It should be noted that the current density contains contributions of the radiation field and of the external field, as we have seen in (3). Nevertheless, the right-hand side has the same form as in the standard one-component plasma without radiation and external fields.

The transverse electric field satisfies the fluctuation formula:

$$\mathcal{K} \frac{1}{V} \langle \mathbf{e}(\mathbf{k}) \mathbf{e}(-\mathbf{k}) \rangle_T = \beta^{-1} (\mathbf{U} - \hat{\mathbf{k}} \hat{\mathbf{k}}), \quad (11)$$

which is valid at all length-scales (for all k). It is an exact relation, that has a similar form as the fluctuation formula for the longitudinal field $\mathbf{e}_L(\mathbf{k}) = -i(\mathbf{k}/k^2)\mathcal{Q}(\mathbf{k})$. Indeed, from (9) one finds $\mathcal{K}(1/V) \langle \mathbf{e}_L(\mathbf{k}) \mathbf{e}_L(-\mathbf{k}) \rangle_T = \beta^{-1} \hat{\mathbf{k}} \hat{\mathbf{k}} + \mathcal{O}(k)$. In contrast to (11) this fluctuation formula is an approximate one, valid for small k only.

As it turns out, the formula (11) does not have an analogous counterpart describing the magnetic-field fluctuations. In fact, the magnetic-field fluctuations are found to be influenced by the pressure tensor in a rather subtle way. A simple result for the magnetic-field fluctuations is obtained only in the trivial case of a free field.

SCALING BEHAVIOR

The pressure occurring in the momentum balance is a tensor that even in equilibrium does not need to be isotropic owing to the presence of the external magnetic field. To determine its anisotropic part one considers the change of the grand potential under a change of volume $V \rightarrow V'$, which is brought about by a change $\delta \mathbf{r}_w = \delta \boldsymbol{\epsilon} \cdot \mathbf{r}_w$ of the position \mathbf{r}_w of the wall enclosing the system. The variation of the grand potential is

$$\delta \Omega = \beta^{-1} \delta \log Z_{gr} = -\frac{1}{Z_{gr}} \sum_N \sum_n \delta E_n e^{-\beta E_n + \beta \mu N}, \quad (12)$$

with μ the chemical potential of the particles with varying number N . The change of the energy levels δE_n is a consequence of the adjustment of the boundary conditions to the new

position of the wall. By a rescaling of the Hamiltonian H one finds $\delta\Omega = -\langle\delta H\rangle$, with δH the variation of H . In performing the rescaling one should be careful to scale both the wave vector and the polarization vectors as:

$$\mathbf{k} \rightarrow \mathbf{k} \cdot (\mathbf{U} - \delta\boldsymbol{\epsilon}) \quad , \quad \mathbf{e}_{\mathbf{k},\lambda} \rightarrow \mathbf{e}_{\mathbf{k},\lambda} + \frac{1}{2}(\delta\boldsymbol{\epsilon} - \delta\tilde{\boldsymbol{\epsilon}}) \cdot \mathbf{e}_{\mathbf{k},\lambda} + \frac{1}{2}\hat{\mathbf{k}} \cdot (\delta\boldsymbol{\epsilon} + \delta\tilde{\boldsymbol{\epsilon}}) \cdot \mathbf{e}_{\mathbf{k},\lambda} \hat{\mathbf{k}}, \quad (13)$$

with $\delta\tilde{\boldsymbol{\epsilon}}$ the transpose of $\delta\boldsymbol{\epsilon}$. Applying these transformations one arrives at the result:

$$\delta\Omega = \delta\boldsymbol{\epsilon} : [\langle\mathbf{T}\rangle + \langle\mathbf{S}\rangle] - \delta\boldsymbol{\epsilon} : [\mathbf{B} \langle\mathbf{M}\rangle - \mathbf{B} \cdot \langle\mathbf{M}\rangle \mathbf{U}]. \quad (14)$$

Here $\langle\mathbf{T}\rangle$ is the averaged material pressure, integrated over the volume, and $\langle\mathbf{S}\rangle$ the averaged integrated Maxwell stress tensor. The presence of an external magnetic field has led to additional terms involving the averaged integrated magnetization $\langle\mathbf{M}\rangle$.

If the grand potential is taken to be independent of the shape of the system the variation $\delta\Omega$ depends on the change of volume only, and hence on the trace of $\delta\boldsymbol{\epsilon}$. This implies that the averaged integrated total pressure tensor $\langle\mathbf{T}\rangle + \langle\mathbf{S}\rangle$ must be anisotropic in such a way that the anisotropy of the terms with $\langle\mathbf{M}\rangle$ in (14) is compensated. The anisotropy found here is similar to that of the pressure tensor in magnetized Coulomb systems.⁴ The difference is that here the Maxwell stress tensor appears as well.

The anisotropy of the pressure tensor plays a role in the fluctuation formulas involving the energy density. While the auto-fluctuation formula of the energy is trivial, the cross-fluctuation formula of the energy density and the charge density is found to depend on the averaged integrated total pressure tensor:

$$\mathcal{K} \frac{1}{V} \langle Q(\mathbf{k}) E(-\mathbf{k}) \rangle = \frac{e}{\beta m \omega_p^2} e_v k^2 + \frac{e}{\beta m \omega_p^2 \cos \theta} \frac{\partial}{\partial \beta} \left[\beta \hat{\mathbf{k}} \cdot \frac{\langle \mathbf{T} + \mathbf{S} \rangle}{V} \cdot \hat{\mathbf{B}} \right] k^2 + \mathcal{O}(k^3). \quad (15)$$

The leading term is of order k^2 , as could be expected for a one-component plasma. Here e_v is the energy density, and θ the angle between the external field and the wave vector. Using our specific knowledge of the anisotropic part of the averaged integrated total pressure tensor we easily find that the cosine in the denominator is compensated by a factor in the numerator, with the result:

$$\mathcal{K} \frac{1}{V} \langle Q(\mathbf{k}) E(-\mathbf{k}) \rangle = \frac{e}{\beta m \omega_p^2} \left[e_v + \frac{\partial}{\partial \beta} (\beta p_{therm}) \right] k^2 + \mathcal{O}(k^3). \quad (16)$$

The thermodynamic pressure p_{therm} is defined in the usual way in terms of the grand potential.

A second example of a fluctuation expression that depends on the averaged integrated total pressure tensor is the cross-fluctuation formula of the energy density and the magnetic part of the radiation field. Once again it turns out that information on the anisotropy of the pressure tensor is essential in understanding the nature of the fluctuations. More details on that example, and on the statistical properties of the quantum-electrodynamic one-component plasma in general can be found in a thesis⁵ by P. John, in collaboration with whom the above research has been carried out.

REFERENCES

- [1] H. D. Sivak, Fluctuations in the relativistic quantum plasma, *Ann. Physics* 159: 351 (1985).
- [2] S. Cable and T. Tajima, Low-frequency fluctuations in plasma magnetic fields, *Phys. Rev. A* 46: 3413 (1992).
- [3] D. Lemoine, Fluctuations in the relativistic plasma and primordial magnetic fields, *Phys. Rev. D* 51: 2677 (1995).
- [4] P. John and L. G. Suttrop, Pressure and compressibility in a quantum one-component plasma, *J. Phys. A* 27: 6053(1994).
- [5] P. John, "On Quantum Plasmas," Ph. D. thesis University of Amsterdam, Amsterdam (1995).

EXTRA LOOP IN PLASMON DISPERSION FOR STRONGLY COUPLED COULOMB LIQUIDS

Dexin Lu

Department for Intensive Instruction
Nanjing University
Nanjing 210093, China

Two-dimensional strongly coupled electron liquid can be treated in the quasilocalized charge (QLC) approximation, initiated by Kalman and Golden.¹ When direct thermal effect is taken into account, we have mean field theory. The resulting dispersion curve is quantitatively similar to RPA dispersion curve. The curve is divided into two branches: the upper branch corresponds to plasmon branch and the lower branch is related to soundlike mode. They form a loop.²

Based on the formalism, we can consider layered electrons, or superlattice. The superlattice model consists of a large stack of N_L equally spaced electron plasma monolayers embedded in a dielectric substrate of dielectric constant ϵ_s ; each monolayer of large area A is parallel to the xy plane; $L = d \cdot N_L$ is the length of the superlattice; the Wigner-Seitz radius $a = 1/(\pi n_s)^{1/2}$, where $n_s = N_e/A$ is the two-dimensional areal electron density. The intralayer coupling strength is characterized by the plasma parameter $\Gamma = \beta e^2/a\epsilon_s$. The collective mode structure of the superlattice has been analyzed in a number of works.³⁻⁵ A strongly correlated superlattice can be treated in a parallel way,⁶ in QLC scheme. The dielectric response function is

$$\epsilon(\vec{k}, q, \omega) = 1 + \frac{F(k, q) \cdot \alpha_0(k, \omega)}{1 + \alpha_0(k, \omega) \cdot D(\vec{k}, q)} \quad (1)$$

where the form factor

$$F(k, q) = \frac{\sinh kd}{\cosh kd - \cos qd} \quad (2)$$

and

$$D(\vec{k}, q) = \frac{1}{N_e N_L} \sum_{\vec{k}'} \sum_{|q'| \leq \pi/d} \frac{(\vec{k} \cdot \vec{k}')^2}{k^3 k'} F(k', q') \times [S(\vec{k} - \vec{k}', q - q') - S(\vec{k}', q')] \quad (3)$$

For weak interlayer correlation case, (say $d/a=10$), we can first neglect interlayer correlation at all and $D(\vec{k}, q)$ reduces to single-layer expression:

$$D(\vec{k}) = \frac{1}{N_e} \sum_{\vec{k}'} \frac{(\vec{k} \cdot \vec{k}')^2}{k^3 k'} [S(\vec{k} - \vec{k}') - S(\vec{k}')] \quad (4)$$

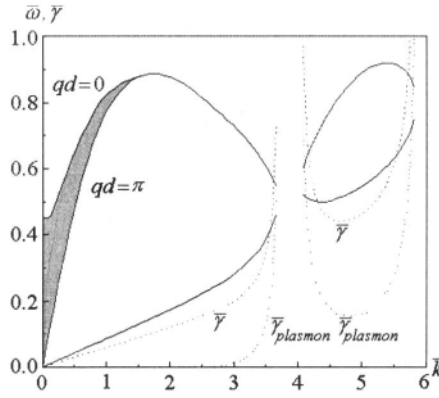


Figure 1. Extra Loop Structure in Dispersion of SCCS

where the intralayer structure function

$$S(\vec{k}) = \frac{1}{N_L} \sum_{|q| \leq \pi/d} S(\vec{k}, q) \quad (5)$$

and the equilibrium pair-correlation function

$$g(r) = \frac{1}{N_e} \sum_{\vec{k}} [S(\vec{k}) - 1] e^{i\vec{k} \cdot \vec{r}} \quad (6)$$

Following standard procedure, we can obtain dispersion from Eq. (1). Resulting curves are of similar structure to two-dimensional system, reported years ago. Data are from Ref. 7, and for $\Gamma = 36$, and 90(MC) $\Gamma = 120$ (HNC) from Ref. 8. In the superlattice case, the upper branch is now a band instead due to values of parameter q . Physically it spreads from 2D shape to a 3D gap structure. Examination for six values of Γ shows that for the largest value of $\Gamma = 120$, there is an extra loop, the only one, at shorter wavelength side. It is necessary to find corresponding damping.

Let $\omega = \omega_p - i\gamma_p$, we can separate the dispersion equation as

$$\varepsilon'(\vec{k}, q, \omega_p) = 0 \quad (7)$$

or

$$1 + \alpha'_0(\vec{k}, \omega_p) \cdot [F(k, q) + D(\vec{k}, q)] = 0 \quad (8)$$

and

$$\gamma_p(k, q, \omega_p) = \frac{\varepsilon''(k, q, \omega_p)}{\left[\frac{\partial \varepsilon'(k, q, \omega_p)}{\partial \omega} \right]_{\omega_p}} \quad (9)$$

where

$$\varepsilon' = \frac{1 + \alpha'_0 \cdot [F + D]}{1 + \alpha'_0 \cdot D} \quad (10)$$

$$\varepsilon'' = \frac{\alpha'_0 \cdot [F + D]}{1 + \alpha'_0 \cdot D} \quad (11)$$

Using Eq. (11), we can find

$$\frac{\partial \varepsilon'}{\partial \omega} = \frac{\frac{\partial \alpha'_0}{\partial \omega} \cdot [F + D]}{1 + \alpha'_0 \cdot D} \quad (12)$$

Eq. (9), (11), and (12) give us

$$\gamma_P(k, q, \omega_P) = \frac{\alpha_0'}{\left[\frac{\partial \alpha_0'}{\partial \omega} \right]_{\omega_P}} \quad (13)$$

So formally the leading term is exact 2D RPA Landau damping. Surely here the argument ω_P is k - and structure dependent. We know that 2D RPA polarizability is

$$\alpha_0^{2D} = \frac{2\Gamma}{k} [1 + i\sqrt{\pi}ZW(Z)] \quad (14)$$

and

$$W(Z) = \frac{i}{\pi} \int_{-\infty}^{\infty} du \frac{e^{-u^2}}{Z - u + i0} \quad (15)$$

$$= e^{-Z^2} \left(1 + \frac{2i}{\sqrt{\pi}} \int_0^Z dt e^{t^2} \right) \quad (16)$$

is the plasma dispersion function. The polarizability can be resolved into real and imaginary parts as follows.

$$\alpha_0' = \frac{2\Gamma}{k} \left[1 - \sqrt{\pi}ZW''(Z) \right] \quad (17)$$

$$= \frac{2\Gamma}{k} [1 - 2ZD] \quad (18)$$

$$\alpha_0'' = 2\sqrt{\pi}\Gamma^{3/2} \frac{\bar{\omega}}{k^2} \exp \left[-\Gamma \frac{\bar{\omega}^2}{k^2} \right] \quad (19)$$

With

$$Z = \sqrt{\Gamma} \frac{\bar{\omega}}{k} \quad \text{and} \quad W'' = \frac{2}{\sqrt{\pi}} D(Z) \quad (20)$$

where D is Dawson integral

$$D(Z) \equiv e^{-Z^2} \int_0^Z e^{t^2} dt \quad (21)$$

The frequency $\bar{\omega}$ are measured in units of $\omega_0 = \left(\frac{2\pi n e^2}{ma} \right)^{1/2}$, and $\bar{k} = ka$. We have

$$\frac{\partial \alpha_0'}{\partial \omega} = 4 \frac{\Gamma^{3/2}}{\omega_0 \bar{k}^2} [Z + D - 2Z^2D] \quad (22)$$

Then

$$\bar{\gamma} = \frac{\sqrt{\pi}}{2} \exp(-Z^2) \left[-\frac{d}{dZ}(Z \cdot D) \right]^{-1} \bar{\omega} \quad (23)$$

$$= \frac{\sqrt{\pi} \exp(-Z^2)}{2(Z + D - 2Z^2D)} \bar{\omega} \quad (24)$$

The damping $\bar{\gamma}$ is also measured in units of ω_0 . Eq. (24) is the fundamental equation for damping calculation. Computation indicates that in both loops soundlike mode is heavily damped. While the plasmon band in the first loop is only damped near maximum k edge, curve in the extra loop is relatively light damped than soundlike mode, see Fig. 1. So plasmon mode can develop to some extent. For weaker coupling (smaller values of Γ), there is no extra loop. We believe the extra loop is substantially due to the strong intralayer coupling, a 2D characteristics. It is definitely related to crystallization, but in this scheme, no example was found for other values of Γ . The possible physical reason why the dispersion band (or curve) is broken is still lack.

REFERENCES

- [1] G. Kalman and K. Golden, Phys. Rev. **A41**,5516(1990).
- [2] K. I. Golden, G. Kalman, and P. Wynn. Phys. Rev. **A41**,6940(1990).
- [3] A. L. Fetter, Ann. Phys.(N. Y.)**88**,1(1974).
- [4] S. Das Sarma and J. J. Quinn, Phys. Rev.**B25**,7603(1982).
- [5] A. Tselis and J. J. Quinn, Phys. Rev. **B29**, 3318(1984).
- [6] D. Lu, K. I. Golden, G. Kalman, P. Wynn, L. Miao, and X. Shi, Phys. Rev. **B54**, 11457(1996).
- [7] H. Totsji, Phys. Rev.**A17**,399(1978).
- [8] R. C. Gann, S. Chakravarty, and G. V. Chester, Phys. **Rev. 20**, 326(1979).

EFFECTIVE TRANSPORT COEFFICIENTS IN LOW TEMPERATURE MULTICOMPONENT PLASMA

G.A. Pavlov

Institute of Chemical Physics, RAS
Chernogolovka, Moscow region , 142432, Russia.
e-mail: pavlov@icp.ac.ru
fax: (096)515-3588.

A modelling approach is proposed, providing full set of transport coefficients, determining currents of pulse, heat, mass and charge in low temperature, multicomponent plasma with strong Coulomb interactions and chemical reactions: coefficients of viscosity, thermoconductivity, multicomponent diffusion and thermodiffusion, electrical conductivity and so on. To do this a detailed analysis has been carried out of experimental data available on transport coefficients of nonideal plasmas of various substances. A number of commonly used techniques of plasma composition calculations were applied in the course of this analysis. A set of kinetic equations was derived with collision integrals written in Boltzmann form. In written out these equations elementary processes, essential in nonideal plasma, plasma composition peculiarities and data on kinetic coefficients in strongly coupled Coulomb systems have been taken into account. This approach made possible separate analysis of contributions to kinetic coefficients resulting from composition of plasma and interparticle interactions, i.e. "nonCoulomb" and Coulomb contributions.

Effective transport coefficients are introduced, relating mass currents of chemical elements and convective heat current to temperature and element concentration gradients and the effective field in plasma. Local thermodynamic equilibrium approximation solution of high temperature gas dynamic problems in the case, when number of components is greater than the number of chemical elements, constituting plasma, is considerably simplified, if made in terms of effective transport coefficients. It is shown that nonideality of thermodynamical forces should be taken into account when calculating effective transport coefficients (Pavlov, 1984).

The scheme of effective transport coefficient calculations is rather complicated. For this reason a number of conditions imposed on the nonlinear, nondiagonal matrix of effective transport coefficients are derived. These conditions can be used as a criterion to control effective transport coefficients numerical values. Properties of this matrix are also important in problems in high temperature gas hydrodynamic, when the full set of transport coefficients is used. Analysis is also carried out of the high derivative coefficients matrix of the set of conservation equations for medium with strong interparticle interactions (Pavlov, 1985,1995).

$$D \bullet \mu^{-1} = (\mu^{-1})^T \bullet D^T \quad (5)$$

Matrix α_{ab} is α , matrix D_{ab} is D and $TD = \alpha \bullet \mu$ (μ consists of μ^a_b), therefore (5) may be received from Onsager relations between α_{ab} . The matrixes $a(u)$, $a'(u)$ are investigated, the latter has the following form:

$$a'(u) = \begin{bmatrix} 1 & & & \\ & 0 & 1 & 0 \\ & \vdots & & \\ & \frac{\tilde{h}_1 - \tilde{h}_e}{\lambda} & \dots & T/T\delta \end{bmatrix} \bullet \begin{bmatrix} \alpha_{11}/T & \dots & T_\delta \alpha_{1q}/T^2 \\ \vdots & & \\ \frac{T_\delta \alpha_{q1}}{\lambda T^2} & \dots & \frac{T_\delta^2 \tilde{\lambda}}{T \lambda^2} \end{bmatrix} \bullet \begin{bmatrix} \mu_1^1 & \dots & 0 \\ \vdots & & \\ 0 & & \lambda \end{bmatrix} \quad (6)$$

Usually matrix $a(u)$ is supposed as parabolic, this property of matrix $a(u)$ is important for system of equations type (1), (2) solutions. Matrix $a'(u)$ is not generally speaking parabolic. The product of two latter matrix in (6) is parabolic matrix. The product of matrixes α , μ and $b'(u)$ (see (7)) is equal to $a(u)$.

$$b'(u) = \begin{bmatrix} \rho_m^{-1} & & & \\ & 0 & \rho_m^{-1} & 0 \\ & \vdots & & \\ \frac{\sum_{a=1}^{N_a-1} (\tilde{h}_a - \tilde{h}_e)'_{c_1} c_a + (\tilde{h}_e)'_{c_1}}{\rho_m c_p T_\delta} & \dots & \frac{T\lambda}{T_\delta^2 \rho_m c_p} \end{bmatrix} \quad (7)$$

Matrix $b'(u)$ is diagonal and, consequently, $a(u)$ is parabolic matrix in "ideal" case, when $\{\tilde{h}_a\}$ is not dependent on $\{c_a\}$. Matrix $b'(u)$ is nondiagonal in the contrary case and $a(u)$ is, generally speaking, nonparabolic matrix. Thus, the corresponding hydrodynamic problem may be noncorrect in the nonideal case.

REFERENCES

1. Pavlov G.A., 1984, Zhurnal Tech. Fiziki, 54:873.
2. Pavlov G.A., 1985, Pizma v Zhurnal Tech. Fiziki, 11, N 18:1141.
3. Pavlov G.A., 1995, "Transport Processes in Low Temperature Plasma with Strong Coulomb Interactions", Energoatomizdat, Moscow.

This page intentionally left blank

ELECTROMAGNETIC MODES IN COLD MAGNETIZED STRONGLY COUPLED PLASMAS*

J. Ortner,¹ V. M. Rylyuk,² and I. M. Tkachenko³

¹Humboldt Universität zu Berlin
D-10115 Berlin, Germany

²University of Odessa, 270100
Odessa, Ukraine

³Polytechnic University of Valencia
E-46071 Valencia, Spain

INTRODUCTION

In Ref. [1] the dielectric tensor of cold nonideal magnetized plasma is constructed applying the classical theory of moments. The aim of this paper is to use the results of Ref. [1] to analyze the spectra of electromagnetic waves propagating in such a system. Hereby we will regard the damping of the modes as negligibly small. The validity of such an assumption can be confirmed obviously only experimentally. We notice that damping can be essential and must be taken into account near the cyclotron resonances. Here the thermal motion of the particles leading to the spatial dispersion must be accounted for also. Thus, the following considerations in which we exclude damping are valid only far from the cyclotron resonances.

In neglect of the thermal motion the dielectric tensor reads

$$\varepsilon_{\mu\nu} = \begin{pmatrix} \varepsilon_{\perp} & ig & 0 \\ -ig & \varepsilon_{\perp} & 0 \\ 0 & 0 & \varepsilon_{\parallel} \end{pmatrix}, \quad (1)$$

where ε_{\perp} and ε_{\parallel} are the transverse and longitudinal (with respect to the external magnetic field) components of the dielectric tensor.

The components of the dielectric tensor of nonideal magnetized fully ionized plasmas consisting of electrons and pointlike ions are obtained using the method of moments,¹ and within the first approximation in the ratio $\sqrt{m/m_i}$ (m and m_i being the electron and the ion masses):

$$\varepsilon_{\perp} = 1 - \omega_p^2 \frac{\omega^2 - \Omega_{\perp}^2}{(\omega^2 - \Omega_{\perp}^2)^2 - \omega^2 \omega_B^2}$$

*Partially supported by the Deutsche Forschungsgemeinschaft (DFG, Germany)

$$\varepsilon_{\parallel} = 1 - \frac{\omega_p^2}{\omega^2 - \Omega_{\parallel}} \quad , \quad g = \omega_p^2 \frac{\omega \omega_B}{(\omega^2 - \Omega_{\perp}^2)^2 - \omega^2 \omega_B^2} \quad , \quad (2)$$

where $\omega_p = (4\pi n e^2 / m)^{1/2}$ is the plasma frequency, $-e$, and n being the charge and the density of the electrons, $\omega_B = eB/mc$ is the electron cyclotron frequency. The positive magnitudes Ω_{\perp} and Ω_{\parallel} take into account the Coulomb correlations between the particles and are expressible via the second frequency moment of the magnetized plasma conductivity tensor,

$$\Omega_{\perp}^2 = \frac{\omega_p^2}{2} \sum_{\vec{q} \neq 0} S_{ei}(\vec{q}) \frac{q_{\perp}^2}{q^2} \quad , \quad \Omega_{\parallel}^2 = \omega_p^2 \sum_{\vec{q} \neq 0} S_{ei}(\vec{q}) \frac{q_{\parallel}^2}{q^2} \quad , \quad (3)$$

$S_{ei}(\vec{q})$ being the partial electron-ion static structure factor, and q_{\perp} (and q_{\parallel}) is the projection of the vector \vec{q} on the direction perpendicular (parallel) to the external magnetic field. A detailed analysis of these magnitudes is beyond the scope of this paper, we mention here only that in the ideal plasma limit both Ω_{\perp} and $\Omega_{\parallel} \rightarrow 0$. We also wish to emphasize that the electron-ion correlations are the factor which guarantees the existence of nonvanishing parameters Ω_{\perp} and Ω_{\parallel} . Notice that the above expression Eqs. (2) for the dielectric tensor coincides (within the first order in the ratio $\sqrt{m/m_i}$) with that of the quasilocalized charges model developed by Kalman and Golden.²

WAVES IN STRONGLY COUPLED MAGNETIZED PLASMAS

The *dispersion equation* of electromagnetic waves propagating in magnetized plasmas reads in the Cartesian system of coordinates with the z-axis parallel to the external magnetic field \vec{B} as follows:

$$AN^4 + BN^2 + C = 0 \quad , \quad (4)$$

where $N = \omega_0/\omega$ is the scalar refraction index, $\omega_0 = |\vec{k}|c$, and

$$\begin{aligned} A &= \varepsilon_{\perp} \sin^2 \theta + \varepsilon_{\parallel} \cos^2 \theta \quad , \\ B &= -\varepsilon_{\perp} \varepsilon_{\parallel} (1 + \cos^2 \theta) - (\varepsilon_{\perp}^2 - g^2) \sin^2 \theta \quad , \\ C &= \varepsilon_{\parallel} (\varepsilon_{\perp}^2 - g^2) \quad , \end{aligned} \quad (5)$$

and θ is the angle between the wavevector \vec{k} and the magnetic field \vec{B} .

Eq. (4) has two different solutions:

$$N_{\pm}^2 = \frac{1}{2A} \left\{ -B \pm (B^2 - 4AC)^{1/2} \right\} \quad , \quad (6)$$

which are associated to the *ordinary* and *extraordinary* waves. In a magnetized plasma there are two different kinds of waves of given frequency and different refraction indices. These waves are generally elliptically polarized, a wave which propagates along the external magnetic field is transverse polarized: the ordinary wave is characterized by the right-handed circular polarization, the extraordinary wave is left-handed polarized.

The frequencies that satisfy the relation $A(\omega, \vec{k}) = 0$ are called the *plasma resonance frequencies*. Note that one of the refraction indices tends to infinity as the frequency approaches the resonance value $N_{\pm}^2 = -B/A$ whereas the second one remains finite, $N_{\pm}^2 = -C/B$. Making use of Eqs. (5) and (2) we obtain a cubic equation with respect to ω^2 . Hence it determines three resonance frequencies in contrast to an ideal magnetized plasma ($\Omega_{\perp} = \Omega_{\parallel} = 0$) where

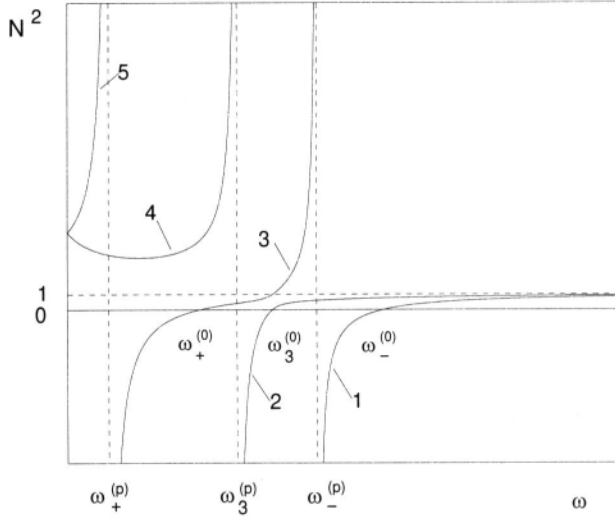


Figure 1. Squares of refractive indices of strongly coupled magnetized plasma vs. frequency (in arbitrary units)

only two resonances exist if one neglects the ion motion. For the case of near longitudinal propagation $\theta \ll 1$ the resonances are

$$\begin{aligned} \omega_{\pm}^{(p)} &= \frac{1}{2} \left\{ \mp \omega_B + [\omega_B^2 + 4\Omega_{\perp}^2]^{1/2} \right\} , \\ \omega_3^{(p)} &= \sqrt{\omega_p^2 + \Omega_{\parallel}^2} \left(1 + \frac{\theta^2}{2} \frac{\omega_p^2 \omega_B^2}{\omega_p^4 - \omega_p^2 \omega_B^2 - \Omega_{\parallel}^2 \omega_B^2} \right) . \end{aligned} \quad (7)$$

For the case of transverse propagation one obtains the following expressions for the poles of the refractive indices:

$$\begin{aligned} (\omega_{\pm}^{(p)})^2 &= \Omega_{\perp}^2 + \frac{1}{2} \left\{ \omega_p^2 + \omega_B^2 \mp [(\omega_p^2 + \omega_B^2)^2 + 4\omega_B^2 \Omega_{\perp}^2]^{1/2} \right\} , \\ \omega_3^{(p)} &= \Omega_{\parallel} . \end{aligned} \quad (8)$$

The zeros of the N_{\pm}^2 determine the boundaries between the domains of propagation for different waves. From Eq. (4) it follows that $N_{\pm}^2 = 0$, if the coefficient C is equal to zero. We find three zeros,

$$\omega_{\pm}^{(0)} = \frac{1}{2} \left\{ \mp \omega_B + [\omega_B^2 + 4(\omega_p^2 + \Omega_{\perp}^2)]^{1/2} \right\} , \quad \omega_3^{(0)} = (\omega_p^2 + \Omega_{\parallel}^2)^{1/2} \quad (9)$$

Once one knows the poles and the zeros and taking into account that $N_{\pm}^2(\omega = 0) = 1 + \omega_p^2/\Omega_{\perp}^2 \equiv N_0^2$, as well as the relation $N_{\pm}^2(\omega \rightarrow \infty) \rightarrow 1$, one easily plots the refractive indices. In Fig. 1 we show the frequency dependence of the refractive indices for an angle $0 < \theta < \pi$.

The branches of propagation ($N^2(\omega) > 0$) are associated with the eigenfrequencies ω_k . The latter are shown in Fig. 2 as functions of the wavevector. The modes ω_k are determined by Eq. (4). Since in neglect of ion motion Eq. (4) is an equation of fifth power with respect to ω^2 , we can find five eigenmodes. This is in contrast to the ideal plasma where only four eigenfrequencies can be found in neglect of ion motion (i.e., neglecting the Alfvén wave).

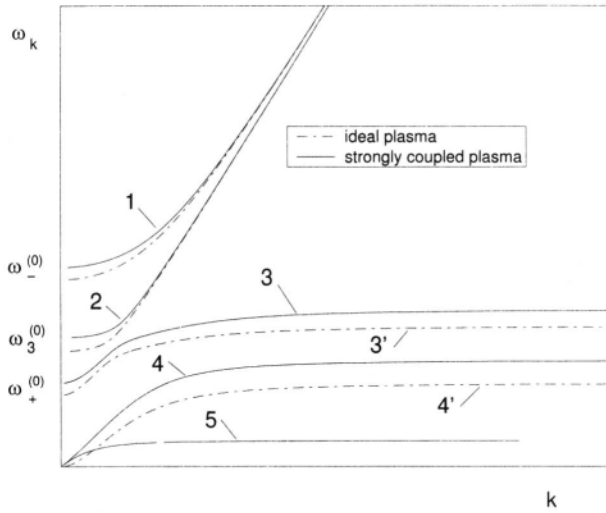


Figure 2. Frequencies of various eigenmodes of strongly coupled and ideal magnetized plasma vs. wavevector (in arbitrary units). 1-fast extraordinary wave; 2- ordinary wave; 3, 3' - slow extraordinary wave; 4,5 - strongly coupled plasma whistling sound waves; 4' - helicon wave of ideal plasmas ($0 < \theta < \pi$)

From Fig. 2 we can see that in the case of a strongly coupled plasma the helicon wave of an ideal plasma splits into two branches, which we call the strongly coupled plasma whistling sound waves.

Thus five eigenmodes occur in strongly coupled magnetized plasma: ordinary and extraordinary whistling sound wave, the slow extraordinary, the ordinary and the fast extraordinary waves.

Consider in more details the low frequency region of the spectra if $\omega \ll \omega_B$, i.e., the dispersion of the whistling sound waves at small wavenumbers. Then the dispersion equation reduces to a quadratic equation with respect to ω^2 . For the case of parallel with respect to the external magnetic field propagation the corresponding solution reads

$$\omega_k^{(4,5)} = \frac{1}{2} \left\{ \pm \frac{\omega_B \omega_0^2}{\omega_p^2 + \Omega_\perp^2 + \omega_0^2} + \left[\frac{\omega_B^2 \omega_0^4}{(\omega_p^2 + \Omega_\perp^2 + \omega_0^2)^2} + 4 \frac{\omega_0^2 \Omega_\perp^2}{\omega_p^2 + \Omega_\perp^2 + \omega_0^2} \right]^{1/2} \right\} . \quad (10)$$

In ideal magnetized plasmas (i.e., $\Omega_\perp = 0$) the solution of Eq. (10) represents then the spiral wave - the *helicon*, or the whistler, the frequency of which is³

$$\omega_k^{(h)} = \frac{\omega_0^2 \omega_B}{(\omega_p^2 + \omega_0^2)} , \quad (11)$$

and tends to zero as $|\vec{B}| \rightarrow 0$.

For the case of strong interaction between the particles and at small wavenumbers, i.e., if $\Omega_\perp > (\omega_B \omega_0) / \omega_p$ the solutions of Eq. (10) describe the ordinary and extraordinary whistling sound waves propagating in strongly coupled plasmas,

$$\omega_k^{(4,5)} = v_s k \pm \frac{1}{2} \frac{\omega_B \omega_0^2 \omega_p^2}{(\omega_p^2 + \Omega_\perp^2)^2} , \quad (12)$$

with the whistling sound velocity

$$v_s = c \frac{\Omega_\perp}{(\omega_p^2 + \Omega_\perp^2)^{1/2}} . \quad (13)$$

CONCLUSIONS

In this paper the dispersion laws for electromagnetic waves in cold magnetized plasmas are analyzed. The basis of our analysis was the expression for the dielectric tensor obtained from the classical theory of moments. The dielectric tensor is constructed without using the perturbation theory. Thus both the case of weak and strong Coulomb coupling can be regarded. A qualitative distinction in the electromagnetic wave propagation for the low-frequency region between systems with weak and strong Coulomb coupling has been established. It has been shown that the helicon branch for the case of a weakly coupled plasma splits into two whistling sound branches in the case of strongly coupled plasmas.

REFERENCES

- [1] Ortner, J., Rylyuk, V. M., and Tkachenko, I. M., 1994, *Phys. Rev. E* 50:4937.
- [2] Kalman, G. and Golden, G., 1990, *Phys. Rev. A* 41:5516.
- [3] Akhiezer, A. I., Akhiezer, I. A., Polovin, R. V., Sitenko, A. G., and Stepanov, K. N., 1975, "Plasma Electrodynamics" Pergamon Press, Oxford.

This page intentionally left blank

ALGEBRAIC SCREENING AND VAN DER WAALS FORCES IN PARTIALLY IONIZED GASES

Angel Alastuey,¹ Françoise Cornu,¹ and Philippe A. Martin²

¹Laboratoire de Physique, Unité de Recherche 1325 associée au CNRS
École normale supérieure de Lyon, 46, allée d'Italie
69 364 Lyon cedex 07, France

²Institut de Physique Théorique
École Polytechnique Fédérale de Lausanne, PHB-Ecublens
CH-1015 Lausanne, Switzerland

INTRODUCTION

The present contribution is about the status of van der Waals forces in a gas at low density and low temperature which is always partially ionized by entropy or thermal excitations. The description of van der Waals forces in the framework of the N -body problem with Coulomb interactions contains many difficulties. For instance, the formation of atoms from the fundamental entities such as nuclei and electrons is to be described by quantum mechanics and not from a chemical approach in which the atoms would be preformed objects. The long range of Coulomb interaction must be handled with in a systematic way that incorporates collective screening effects. At last, the quantum statistics should be taken into account without any approximation.

The standard calculation of van der Waals forces for two atoms in their ground state in the vacuum relies on the fact that at distances R large compared with the Bohr radius, the dipole-dipole-like interaction between the charges that belong to two different atoms is negligible with respect to the ionization energy $|E_H^0|$ of one atom. The averaged electric dipole inside an atom vanishes and, according to the second order perturbation theory, its quantum fluctuations give rise to a squared dipolar effective interaction. When this calculation is generalized in a naive way to the case where the two atoms are in a partially ionized medium, then the bare Coulomb potential between charges in different atoms is to be replaced by some screened interaction. If the latter decayed exponentially at large distances, the effective attractive interaction between two atoms would be short ranged as well. In fact the screening in quantum plasmas is only algebraic,¹⁻³ namely the screened effective interactions between the charges surrounded by their polarization clouds behave as some squared dipolar-like interactions induced by the intrinsic quantum fluctuations of the particles. Thus the decay of the particle correlations in a partially ionized gas should be controlled by the two similar mechanisms that generate algebraic screening and van der Waals forces respectively. This interplay has already been investigated in a simple solvable model.⁴ Here we extend this

analysis to the many-body problem in the framework of the path integral formalism.

ATOMIC LIMIT FOR A GAS OF PROTONS AND ELECTRONS

For the sake of simplicity, we restrict the study to the Hydrogen plasma. We consider the quantum grand partition function of the system at temperature T where the fundamental entities are protons and electrons with chemical potentials μ_p and μ_e respectively. We stress that there is no preformed atom. The Hamiltonian is the sum of the kinetic energies of the particles and of the Coulomb pair interactions. Since all negative charges are fermions, the H -stability requirement is fulfilled.⁵ On the other hand, screening effects ensure that the system does not explode and the thermodynamic limit exists.⁶

Another important result is that, whatever the values of the chemical potentials are, the charge neutrality relation is satisfied by the densities of protons and electrons, ρ_p and ρ_e , in the bulk in the thermodynamic limit, $\rho_e = \rho_p$.⁶ As a consequence, we can set $\mu_p + \mu_e = 2\mu$ and $\mu_p - \mu_e = -(3/2) \ln(m_p/m_e)$ as in Ref. 7. The interest of such a choice is that, when Coulomb interactions are neglected, the densities of protons and electrons in the corresponding ideal gas are compelled to satisfy the charge neutrality.

First, let us consider the zero-temperature limit at fixed negative values of μ . In this limit, the recombination of electrons and protons into complex entities (atoms, molecules, ions) in their ground states competes with ionization favored by entropy effects since the density goes to zero. As rigorously shown by Fefferman,⁸ the pressure of the system then behaves as that of a mixture of ideal gases made with the following simple and/or complex entities: protons and electrons if $\mu < -|E_H^0|$, protons electrons and Hydrogen atoms if $\mu = -|E_H^0|$, only Hydrogen atoms if $-|E_H^0| < \mu < \text{cst}$ where the constant is smaller than $-(|E_{H_2}^0| - |E_H^0|)/2$. We stress that the atomic gas may exist though one Hydrogen molecule has a lower ground state energy than two isolated atoms, $2|E_H^0| < |E_{H_2}^0|$, because the inequality $|E_{H_2}^0| < 3|E_H^0|$ allows entropy to win over energy when the density is sufficiently small. (For instance, on earth Hydrogen molecules are formed, whereas Hydrogen atoms may be found in interstellar clouds that are dilute enough.) In order to control the ionization rate at $\mu = -|E_H^0|$, the previous limit can be replaced by the following scaling limit

$$\mu(T) = -|E_H^0| + k_B T \ln w \quad (1)$$

where the temperature goes to zero and w is a fixed parameter that determines the proportion of atoms and free charges. It has been proved that the corresponding equation of state exactly reduces to the familiar Saha formula.⁷ (The contributions of the interactions between entities become negligible because of infinite dilution.) In the following, we study the quantities of interest in the previous scaling limit.

QUANTUM FLUCTUATIONS AND COULOMB SCREENING

For our purpose it is convenient to use the Feynman-Kac path integral representation. Indeed, contrarily to the standard many-body theory, this formalism is not based on a perturbative treatment of Coulomb interactions, and consequently it is able to describe the recombination of electrons and protons in a simple way. Furthermore, it naturally provides low-density expansions that incorporate both quantum effects and collective screening. Finally, it allows one to investigate the large-distance decay of correlations straightforwardly.

First, we recall the basic outlines of the formalism and we briefly describe the structure of the diagrammatic representations derived in this framework. (For a detailed presentation see

Ref. [2].) By using the Feynman–Kac representation of the matrix elements of the quantum Gibbs factor in position space, the noncommuting quantum operators can be replaced by path integrals of scalar functions in which a Brownian path is associated with each point particle. In the case of Boltzmann statistics, only diagonal matrix-elements appear and one particle corresponds to one closed path. When quantum statistics is taken into account, matrix elements of the Gibbs factor between sets of permuted positions are to be considered. The open paths that are associated with the particles exchanged in a given cyclic permutation can be collected in a bigger closed path. Thus, as first used by Ginibre,⁹ a quantum system of point particles with *Fermi/Bose* statistics is equivalent to a classical system of loops with random shapes and *Maxwell–Boltzmann* statistics. Then standard methods of statistical mechanics for classical fluids can be used. For instance, generalized Mayer graphs for the system of loops can be devised and the divergencies due to the long range of the Coulomb interaction are exactly resummed by a generalization of the method introduced by Meeron.¹⁰ This provides the required diagrammatic representations in terms of various resummed bonds that incorporate the following phenomena. In one of these bonds denoted by F_R , the recombination is taken into account nonperturbatively. (The contributions of Rydberg states, all of which are excited as soon as the temperature is nonzero, are also automatically screened by collective effects.) The large-distance charge–charge and charge–multipole interactions between the loops are exponentially screened. However, the multipole–multipole interactions in F_R are only algebraically screened, because, according to Feynman–Kac formula, a line element of a loop interacts with only one line element of the other loop and not with all line elements of the other loop, as it would be the case for the electrostatic interaction between wires. The fluctuations of the partially screened $1/r^3$ dipolar-like interactions present in F_R ultimately generate the algebraic tails in the particle correlations which decay as $1/r^6$ at large distances.

The previous formalism, or similar versions,¹¹ has been used for computing the low-density expansion of the equation of state at finite non-zero temperature (with [12] or without¹³ external uniform magnetic field). The corresponding forms of the coefficients of the algebraic tails in the particle correlations have also been obtained.³ In the present scaling limit, this formalism is still well-suited if the diagrammatic series are expressed in terms of the fugacities rather than the densities (notice that the relation between the fugacities and the densities is non-linear in the scaling limit). Indeed the inequalities between ground states energies introduced by Fefferman⁸ can be used here for showing that only the first resummed graphs in the fugacity expansions contribute. This allows us to recover immediately the Saha equation of state (and next corrections beyond the ideal gas behavior might be investigated). Similarly, the coefficient A in the large-distance tail $-\beta\rho_p^2 A/r^6$ of the proton–proton correlation can be evaluated exactly at leading order in the considered limit. It appears as the sum of three contributions: a particle–particle contribution, A_{p-p} , a particle–atom one, A_{p-at} , and an atom–atom contribution, A_{at-at} . All the corresponding $1/r^6$ contributions exhibit the following structure,

$$\begin{aligned}
 -\beta\frac{A_{12}}{r^6} \propto & \int_0^1 ds_1 \int_0^{s_1} dt_1 \int_0^1 ds_2 \int_0^{s_2} dt_2 [\delta(s_1 - s_2) - 1] [\delta(t_1 - t_2) - 1] \\
 & \times \langle \Delta \mathbf{x}_1(s_1) \Delta \mathbf{x}_1(t_1) \rangle \langle \Delta \mathbf{x}_2(s_2) \Delta \mathbf{x}_2(t_2) \rangle \left(\frac{\beta e^2}{r^3} \right)^2
 \end{aligned} \tag{2}$$

where the factor involving the delta-distribution $[\delta(s_1 - s_2) - 1]$ is a track of the partial quantum screening of dipole–dipole interactions, (The δ -distribution gives the contribution in the vacuum and the -1 is due to the medium). The $\langle \Delta \mathbf{x}(s) \Delta \mathbf{x}(t) \rangle$ is a symbolic notation for the quantum fluctuations of either the position of a particle alone or of the relative position between the electron and the proton inside a proton. The particle fluctuations behave as the squared de Broglie thermal wave length whereas the fluctuations of the atomic dipole behave

as the squared Bohr radius. At leading order in $1/\beta$, the integration over the imaginary times (in $\beta\hbar$ units) s 's and t 's gives an extra factor $1/(\beta E_0)$ if at least one of the position fluctuations refers to an atom. Thus the dependencies in β of the various contributions are the following: A_{p-p} is proportional to β^3 , A_{p-at} to β and A_{at-at} is independent of β at leading order. A miracle shows up not only at the qualitative level but also at the quantitative level: the effective potential A_{at-at}/r^6 reduces to the van der Waals potential calculated in the vacuum, as if the surrounding medium had no effect. More precisely, the partial screening due to the free charges does not contribute to the leading behavior of A_{at-at} when the temperature goes to zero.

CONCLUSION

As a conclusion from our study, the van der Waals forces between atoms do exist in a partially ionized Hydrogen gas. They cannot be screened by the free charges present in the system, contrarily to the predictions of a naive classical description of screening. Moreover, at sufficiently low temperature and low density, their quantitative form is given by the standard calculation in the vacuum and does not depend on the ionization rate. Our analysis shows that van der Waals-like effective interactions also appear between a free charge and an atom, and between two free charges. All these effective interactions arise from the genuine Coulomb interactions and from quantum fluctuations of positions of a particle which are controlled either by the de Broglie wavelength if the charge is free or by the Bohr radius if the charge is bound in an atom. The $1/r^6$ tails in the particle correlations result from the contributions of these three effective interactions. Their low-temperature form in the scaling regime of interest is exactly evaluated, by discarding exponentially decaying terms (in particular the contributions of excited atomic or molecular states). The present results should remain valid in any partially ionized gas at sufficiently low temperature and low density. The existence of van der Waals forces between neutral entities in an ionized medium, as well as between solids separated by a plasma, can be viewed as an indirect proof of algebraic screening in quantum plasmas.

REFERENCES

- [1] A. Alastuey and Ph. A. Martin, Phys. Rev. A, **40** (1989) 6485.
- [2] F. Cornu, Phys. Rev. E, **53** (1996) 4562; 4595.
- [3] F. Cornu, Phys. Rev. Lett. **78** (1997) 1464.
- [4] Ph. A. Martin, Helv. Phys. Acta, **70** (1997) 80.
- [5] F. J. Dyson and A. Lenard, J. Math. Phys. **8** (1967) 423; A. Lenard and F. J. Dyson, *ibid* **9** (1968) 698.
- [6] E. H. Lieb and J. L. Lebowitz, Adv. Math. **9** (1972) 316.
- [7] N. Macris and Ph. Martin, J. Stat. Phys. **60** (1990) 619.
- [8] Ch. L. Fefferman, Rev. Math. Iberoamericana, **1** (1985) 1.
- [9] J. Ginibre, J. Math. Phys. **6** (1965) 238; **6** (1965) 252; **6** (1965) 1432.
- [10] E. Meeron, J. Chem. Phys. **28** (1958) 630; *Plasmas Physics* (McGraw-Hill, New-York, 1961).
- [11] A. Alastuey, F. Cornu and A. Perez, Phys. Rev. E **49** (1994) 1077; A. Alastuey and A. Perez, Phys. Rev. E **53**(1996)5714.
- [12] F. Cornu, Europhys. Lett. **37** (1997) 591.
- [13] A. Alastuey and A. Perez, Europhys. Lett. **20** (1992)

TWO-DIMENSIONAL LOGARITHMIC INTERACTION ON CURVED SURFACES

Bernard Jancovici

Laboratoire de Physique Théorique et Hautes Energies *
Bâtiment 210, Université de Paris-Sud, 91405 Orsay Cedex, France

INTRODUCTION: TWO-DIMENSIONAL COULOMB SYSTEMS

For mimicking real three-dimensional Coulomb systems in a two-dimensional world (a plane), it is appropriate to write the interaction energy, between two charges q_i and q_j at a distance r from each other, as $-q_i q_j \log(r/L)$, where L is some irrelevant length scale. With such an interaction, the usual equations of electrostatics (Poisson equation, Gauss theorem, etc...) hold in two dimensions. These two-dimensional *models* should not be confused with systems of real charges, such as electrons, confined in a plane, for which the interaction of course remains the usual $q_i q_j / r$ law. A good reason for being interested in these two-dimensional logarithmic models is that exact solutions are obtainable, for classical equilibrium statistical mechanics.

ON A SPHERE

Two-dimensional models living on the surface of a sphere are of interest, especially because they are very appropriate for performing numerical simulations¹ (three-dimensional models on the surface of an hypersphere have also been used²). Here, we review the sphere problem as an introduction to the next section.

Coulomb Potential

In terms of the spherical coordinates (θ, φ) , the two-dimensional Laplacian on a sphere of radius R is

$$\Delta = \frac{1}{R^2} \left[\frac{1}{\sin \theta} \frac{\partial}{\partial \theta} \sin \theta \frac{\partial}{\partial \theta} + \frac{1}{\sin^2 \theta} \frac{\partial^2}{\partial \varphi^2} \right]. \quad (1)$$

One might wish to take for the potential ϕ at an angular distance ψ from a unit point charge a solution of

$$\Delta \phi = -2\pi \delta^{(2)}(R\psi). \quad (2)$$

However, (2) has no solution; this is because the field lines emitted by the +1 point charge will converge into a -1 charge at the antipodal point, and therefore there is no solution for

*Laboratoire associé au Centre National de la Recherche Scientifique — URA D0063

one point charge. One resorts to the choice

$$\phi = -\log \sin \frac{\psi}{2} = -\log \sin \frac{D}{2R} \quad (3)$$

(where $D = R\psi$ is the geodesic distance), which obeys

$$\Delta\phi = -2\pi \left[\delta^{(2)}(D) - \frac{1}{4\pi R^2} \right]. \quad (4)$$

This ϕ is the potential due to a unit point charge and a uniform background of opposite charge.

Solvable Models

For particles of charge q at a temperature T , when $q^2/k_B T = 2$, the one-component plasma³ (OCP), the two-component plasma⁴ (TCP), and the TCP plus a background,⁵ with the interaction (3), are solvable models.

Method of Solution

The model on a sphere can be transformed into a plane model by a stereographic projection, from the North pole of the sphere onto the plane P tangent at the South pole. A point on the sphere, with spherical coordinates (θ, φ) , is projected into a point of P with polar coordinates (r, φ) such that

$$z = r e^{i\varphi} = 2R \operatorname{ctn}(\theta/2) e^{i\varphi}. \quad (5)$$

In terms of (r, φ) , an infinitesimal distance ds on the sphere is such that

$$ds^2 = \frac{dr^2 + r^2 d\varphi^2}{\left(1 + \frac{r^2}{4R^2}\right)^2} \quad (6)$$

while the finite geodesic distance $D = R\psi$ between two points on the sphere can be expressed in terms of the coordinates z, z' of their projections by

$$\sin \frac{D}{2R} = \frac{|z - z'|/2R}{\left(1 + \frac{|z|^2}{4R^2}\right)^{1/2} \left(1 + \frac{|z'|^2}{4R^2}\right)^{1/2}}. \quad (7)$$

For a system of charges on the sphere with the interaction (3), the total potential energy can be reexpressed as the one of a flat model, by using (7).

For instance, in the case of an OCP of N unit charges, one finds a total potential energy

$$V = -\sum_{i < j} \log \frac{|z_i - z_j|}{2R} + \frac{N-1}{2} \sum_i \log \left(1 + \frac{|z_i|^2}{4R^2} \right) + C \quad (8)$$

where C is a constant. Thus, the OCP on a sphere maps onto a flat OCP with an r -dependent background charge density. This flat model is easy to solve, when $q^2/k_B T = 2$. The truncated two-body density, for two particles separated by a geodesic distance D , was found³ to be

$$n_T^{(2)} = -n^2 \left(\cos \frac{D}{2R} \right)^{8\pi n R^2 - 2}. \quad (9)$$

ONE-COMPONENT PLASMA ON A SURFACE OF CONSTANT NEGATIVE CURVATURE

Our interest for this problem was triggered by a recent work by M. B. Hastings.⁶ Admittedly this is essentially a mathematical game, but, in our opinion, an amusing one.

Surface of Constant Negative Curvature

The whole surface cannot be embedded in Euclidean three-dimensional space, but it can be represented by a plane projection, the Poincaré disk, which closely resembles the plane stereographic projection of a sphere. The *whole* surface is represented by the *inside* of a disk of radius $2a$. In terms of polar coordinates (r, φ) , an infinitesimal distance is now given by (6) where the squared curvature radius R^2 is replaced by the negative number $-a^2$. The geodesics are circle arcs normal to the boundary circle. The geodesic distance D between two points of complex coordinates $z = r e^{i\varphi}$ and $z' = r' e^{i\varphi'}$ is given by

$$\sinh \frac{D}{2a} = \frac{|z - z'|/2a}{\left(1 - \frac{|z|^2}{4a^2}\right)^{1/2} \left(1 - \frac{|z'|^2}{4a^2}\right)^{1/2}} \quad (10)$$

instead of (7). D becomes infinite if $r = 2a$ or $r' = 2a$, which means that the circle of radius $2a$ represents surface points at infinity.

Coulomb Potential

The Poisson equation for the potential ϕ at a geodesic distance D from a unit point charge now does have a solution

$$\phi(D) = -\log \tanh \frac{D}{2a} \quad (11)$$

this potential vanishes at $D = \infty$, i.e., on the boundary circle.

One-Component Plasma

The one-component plasma, with a particle number density n and the curved metric, maps onto a flat model in the Poincaré disk with an r -dependent background charge density and ideal conductor walls. When $q^2/k_B T = 2$, one finds a truncated two-body density

$$n_T^{(2)} = -n^2 \left(\cosh \frac{D}{2a} \right)^{-8\pi n a^2 - 2} \quad (12)$$

instead of (9).

An Unusual Equivalence

The ideal conductor walls in fact play no role, because in the flat model mapping the image charges are screened by a density which is infinite at the boundary. Thus, one obtains the same correlations by using for the interaction the analog of (3)

$$\phi(D) = -\log \sinh \frac{D}{2a} \quad (13)$$

which has no image forces.

Thus, two different interactions (11) and (13) generate the same n -body correlation functions (in the thermodynamic limit).

Perfect Screening

Generic perfect screening sum rules are expected to hold. The screening of a particle of the system is expressed as

$$\int n_r^{(2)}(D) dS = -n \quad (14)$$

where dS is the area of a surface element computed with the curved metric. The screening of an infinitesimal external charge (and linear response theory) lead to the Carnie and Chan sum rule

$$\int \langle \rho(0) \phi(D) \rangle dS = k_B T \quad (15)$$

involving the correlation between the charge density ρ and the electric potential ϕ ; this sum rule can be rewritten as

$$\int \langle \rho(0) \rho(D) \rangle 4\pi a^2 \log \cosh \frac{D}{2a} dS = -k_B T \quad (16)$$

na generalization of the second-moment Stillinger–Lovett sum rule.

These sum rules are indeed obeyed by the OCP when $q^2/k_B T = 2$.

REFERENCES

- [1] J. M. Caillol, D. Levesque, J. J. Weis, and J. P. Hansen, A Monte-Carlo study of the classical two-dimensional one-component plasma, *J. Stat. Phys.* 28:325 (1982).
- [2] J. M. Caillol, A Monte-Carlo study of the liquid–vapor coexistence of charged hard spheres, *J. Chem. Phys.* 100:2161 (1994).
- [3] J. M. Caillol, Exact results for a two-dimensional one-component plasma on a sphere, *J. Physique-lettres (Paris)* 42:L–245(1981).
- [4] P. J. Forrester, B. Jancovici, and J. Madore, The two-dimensional Coulomb gas on a sphere: exact results, *J. Stat. Phys.* 69:179(1992).
- [5] P. J. Forrester and B. Jancovici, The two-dimensional two-component plasma plus background on a sphere: exact results, *J. Stat. Phys.* 84:337 (1996).
- [6] M. B. Hastings, Non-Hermitian fermion mapping for one-component plasma, cond-mat/9703006 and *J. Stat. Phys.*, to be published.

A MONTE CARLO FINITE SIZE SCALING STUDY OF CHARGED HARD SPHERE CRITICALITY

J. M. Caillol,¹ D. Levesque,² and J. J. Weis²

¹M. A. P. M. O. Université d'Orléans, BP 6759
45067 Orléans, France

²L. P. T. H. E. Bât. 211, Université Paris-Sud
91405 Orsay, France

INTRODUCTION

A subject of current theoretical and experimental interest is the critical behavior of ionic fluids.¹⁻³ The experimental situation appears for the moment somewhat controversial as both classical and Ising-like behaviors have been observed. Evidence accumulates, though, that the situation might be that of a crossover to Ising-type critical behavior at scales $t_x = |T - T_c|/T_c$ whose values may vary appreciably with nature of the system. A review of theoretical achievements concerning ionic criticality is given by Pr. M. E. Fisher in this volume.^{1,2} However, no firm conclusion concerning the nature of ionic criticality can be drawn from these theoretical works. Hence the present attempt to see whether computer simulations together with a finite size scaling (f.s.s.) analysis can help elucidating the nature of ionic criticality. We have studied the restricted primitive model (RPM) near its critical point. The RPM is an equimolar mixture of positively and negatively charged hard spheres of the same size which captures the main features of realistic ionic fluids. As shown by previous Monte Carlo (MC) simulations the model exhibits a liquid vapor transition with a critical point at unusual low temperature and density.⁴⁻⁷

MODEL AND BOUNDARY CONDITIONS

The RPM of an ionic solution consists of $N/2$ hard spheres of diameter σ and charge $+q$ and $N/2$ hard spheres of the same diameter and charge $-q$. The pair potential between ions i and j is given by

$$v_{ij}(r) = \begin{cases} q_i q_j / r & \text{if } r \geq \sigma \\ \infty & \text{if } r < \sigma \end{cases} \quad (1)$$

A thermodynamic state is characterized by a reduced density $\rho^* = N\sigma^3$ and a reduced temperature $T^* = kT\sigma/q^2$ (k Boltzmann constant). We also introduce a reduced inverse temperature $\beta^* = 1/T^*$.

As well known, numerical simulations of Coulomb fluids need some caution due to the long range of electrostatic interactions. A possible way of handling the problem is to confine the particles at the surface of a 4D sphere, a hypersphere for short. This surface, denoted S_3 , is a 3D non Euclidean, homogeneous, isotropic, albeit finite space well suited for the numerical simulations of fluids. Moreover the Poisson equation can be solved analytically in this geometry which enables simulations of Coulombic fluids.^{6,8} In S_3 the pair potential between ions i and j reads

$$v_{ij}(R\psi) = \begin{cases} q_i q_j \cot \psi & \text{if } R\psi \geq \sigma \\ \infty & \text{if } R\psi < \sigma \end{cases} \quad (2)$$

where $\psi = \arccos(\mathbf{OM}_i \cdot \mathbf{OM}_j / R^2)$ is the angle between the vectors \mathbf{OM}_i and \mathbf{OM}_j of the ions on the hypersphere of center O and radius R . The use of hyperspherical geometries has been checked,^{6,8} to give results for the thermodynamic and structural properties of the RPM similar to those obtained with more conventional Ewald periodical geometries.

ENSEMBLE

We performed our MC simulations of the RPM in S_3 in the grand canonical (GC) ensemble. In this ensemble the volume V , the temperature T and the chemical potential μ are fixed but the number N of ions can vary. The MC sampling of the GC ensemble was made in cycles, each cycle comprising, in a random order, displacement trial moves, as well as attempted insertions and deletions of a neutral pair of ions. Biased schemes were introduced in order to speed up the convergence.^{6,7} The aim of the calculations was to determine the joint distribution $p_L(\rho, u)$ of the density ρ and energy per unit of volume u for a given system of size $L \sim R$. From the knowledge of p_L one can compute all the moments and cross correlations of ρ and u as required in a f.s.s. analysis. Of course the distribution $p_L(\rho, u)$ is wanted for all (continuous) values of ρ and u in the critical region. This was achieved by using (multiple) histogram reweighting of N_s distinct states ($N_s \sim 20$) more or less uniformly sampling the critical region.⁹ Five system sizes corresponding to reduced volumes $V^*(= V/\sigma^3) = 1500, 2500, 3500, 5000$, and 10000 were considered, for each volume about $6.5\text{--}10.0 \times 10^9$ MC sweeps were generated.

FINITE SIZE ANALYSIS

Revised Scaling

The first step to perform a f.s.s. analysis is to identify the scaling operators and variables. This was done in the framework of revised scaling theory by Rehr and Mermin.¹⁰ In this phenomenological theory the critical properties of a liquid are described by two scaling fields h and τ which are supposed to be analytical functions of T and μ . The conjugate operators of h and τ are denoted respectively \mathcal{M} and \mathcal{E} . Therefore in the vicinity of the critical point the scaling fields can be written

$$\begin{aligned} h &= \mu^* - \mu_c^* + r(\beta_c^* - \beta^*) \\ \tau &= \beta_c^* - \beta^* + s(\mu^* - \mu_c^*) \end{aligned} \quad (3)$$

where (r, s) are field mixing parameters, $\mu^* \equiv \beta^* \mu$, and the subscript c denotes values at the critical point. The expressions for the scaling operators are

$$\mathcal{M} = \frac{\rho - su}{1 - sr}$$

$$\varepsilon = \frac{u - r\rho}{1 - sr} \quad (4)$$

In fact the quantities of interest are the deviations $\delta\mathcal{M} = \mathcal{M} - \langle\mathcal{M}\rangle_c$ and $\delta\mathcal{E} = \mathcal{E} - \langle\mathcal{E}\rangle_c$ of the scaling operators from their values at criticality. The linear mapping $(\rho, u) \rightarrow (\delta\mathcal{M}, \delta\mathcal{E})$ amounts to associate to the fluid an hypothetical magnetic system of magnetization $\delta\mathcal{M}$, magnetic energy $\delta\mathcal{E}$, temperature τ in the presence of a magnetic field h . The hamiltonian of this associated system is invariant in the symmetry $\delta\mathcal{M} \rightarrow -\delta\mathcal{M}$ for $h = 0$.

Within this framework the order parameter of the liquid vapor transition is $\delta\mathcal{M}$ and the coexistence line is denned by the condition $h = 0$. Note that obviously one has $p_L(\mathcal{M}, \mathcal{E}) \sim p_L(\rho, u)$. The field mixing parameter $r = \partial\mu^*/\partial\beta^*$, where the derivative must be evaluated along the coexistence line ($h = 0$) at T_c . The parameter s is obtained, for a given T^* , by tuning the values of μ^* and s in such a way that the distribution of the ordering field $p_L(\mathcal{M}) = \int p_L(\mathcal{M}, \mathcal{E}) d\mathcal{E}$ is an even function of $\delta\mathcal{M}$.¹¹ For the RPM we found $r = -0.62$ and $s = -1.46$, values which do not depend appreciably upon system size L .

F.s.s. hypothesis and analysis

It has been postulated by Bruce and Wilding that the scaling behavior of $p_L(\mathcal{M}, \mathcal{E})$ in the critical region and f.s.s. limit is that of a usual magnetic system.¹¹ For instance, at coexistence ($h = 0$) and for sufficiently large systems, one should have

$$p_L(\mathcal{M}) \simeq a_M^{-1} L^{d-y_h} \tilde{p}_M(a_M^{-1} L^{d-y_h} \delta\mathcal{M}, a_E L^{y_\tau} \tau, a_i L^{y_i}) \quad (5)$$

where a_M and a_E are non-universal amplitudes, \tilde{p}_M is a universal function which depends only on the universality class of the model and the type of geometry, and the renormalized exponents are given in terms of the usual exponents β , ν , and θ (Wegner's correction-to-scaling exponent), assuming hyperscaling, by $y_h = d - \beta/\nu$, $y_\tau = 1/\nu$, and $y_i = -\theta/\nu$.

From Eq. (5) one finds that for an apparent critical temperature $T_c(L)$ ¹¹

$$p_L(\mathcal{M}) = a_M^{-1} L^{\beta/\nu} \tilde{p}_M^*(a_M^{-1} L^{\beta/\nu} \delta\mathcal{M}) \quad (6)$$

where $\tilde{p}_M^*(x) \equiv \tilde{p}_M(x, 0, 0)$ is a universal function. Moreover $T_c(L)$ scales with system size as

$$T_c(L) - T_c(\infty) \sim L^{-(\theta+1)/\nu} \quad (7)$$

We have found for the RPM that $p_L(\mathcal{M})$ collapses according to Eq. (6) on the fixed point distribution $\tilde{p}_M^*(x)$ corresponding to the 3D Ising universality class within periodic boundary conditions (this function is known from earlier MC simulations¹²). This point is illustrated by Fig. 1. The scaling law (Eq. (6)) for $T_c(L)$ allows to compute the (true) critical temperature of the 3D RPM: $T_c \equiv T_c(\infty) = 0.0488(2)$. Similar collapse of $p_L(\mathcal{E})$ on the fixed point distribution of the 3D Ising model shows that the data for the joint distribution $p_L(\mathcal{M}, \mathcal{E})$ of the RPM are compatible with an Ising-like behavior.

We also made an attempt to compute directly the critical exponents of the RPM by considering Binder's cumulant $Q_L = \langle\delta\mathcal{M}^2\rangle_L^2 / \langle\delta\mathcal{M}_L^4\rangle$ which should scale as

$$Q_L(\beta^*) = Q^* + q_1(\beta^* - \beta_c^*)L^{y_\tau} + q_2(\beta^* - \beta_c^*)^2 L^{2y_\tau} + \dots + b_1 L^{y_i} + \dots \quad (8)$$

where Q^* is universal while q_1, q_2, \dots and b_1, \dots are non universal constants. We have attempted to determine Q^* , y_τ , and y_i using the values of Q_L calculated for the five volumes along the gas-liquid coexistence curve for 21 temperatures in the range 0.0480–0.050. A fit of our data by Eq. (8) yields: $Q^* = 0.6(1)$, $y_\tau = 1.7(2)$, and $y_i = -0.82(2)$ in fair agreement with recent estimates of 3D Ising values $Q^* = 0.623$, $y_\tau = 1.583$, $y_i = -0.83$.¹³ An analysis similar to that made for Q_L but for $n\langle\delta\mathcal{M}_L^2\rangle$ leads to the value $\beta/\nu = 0.5(1)$, once again in agreement with that of the 3D Ising model.

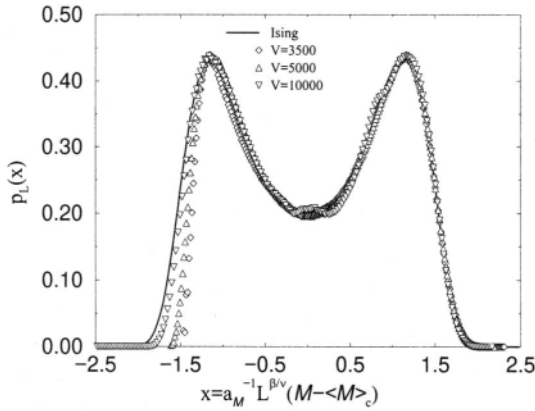


Figure 1. Collapse of the ordering operator distribution $p_L(\mathcal{M})$ on the universal fixed point operator distribution $\tilde{p}_{\mathcal{M}}^*(x)$ for $(V^* = 3500, T_c^*(L) = 0.04959)$, $(V^* = 5000, T_c^*(L) = 0.04928)$, and $(V^* = 10000, T_c^*(L) = 0.04915)$.

CONCLUSION

This work represents a first attempt to determine the criticality of a simple model of Coulomb fluid by means of a f.s.s. analysis of MC data. Despite poor precision in comparison with current lattice MC simulations of Ising and related models our data are clearly in favor of an Ising-like criticality. More details concerning this work may be found in Refs. (14,15).

REFERENCES

- [1] M. E. Fisher, *J. Stat. Phys.*, 75:1 (1994)
- [2] G. Stell, *J. Stat. Phys.*, 78:197 (1995)
- [3] H. Weingärtner, M. Kleemeier, S. Wiegand, and W. Schröer, *J. Stat. Phys.*, 78:169 (1995)
- [4] J. P. Valleau, *J. Chem. Phys.*, 95:584 (1991)
- [5] A. Z. Panagiotopoulos, *Fluid Phase Equilib.*, 95:97 (1992)
- [6] J. M. Caillol, *J. Chem. Phys.*, 100:2161 (1994)
- [7] G. Orkoulas and A. Z. Panagiotopoulos, *J. Chem. Phys.*, 101:1452(1994)
- [8] J. M. Caillol, *J. Chem. Phys.*, 99:8953 (1993)
- [9] A. M. Ferrenberg and S. H. Swendsen, *Phys. Rev. B*, 63:1195 (1989)
- [10] J. J. Rehr and N. M. Mermin, *Phys. Rev. A*, 8:472 (1973)
- [11] A. D. Bruce and N. B. Wilding, *J. Phys.: Condens. Matter*, 4:3087 (1992)
- [12] N. B. Wilding and M. Müller, *J. Chem. Phys.*, 102:2562 (1995)
- [13] H. W. Blöte, E. Luijten, and J. R. Heringa, *J. Phys. A: Math. Gen.*, 28:6289 (1995)
- [14] J. M. Caillol, D. Levesque, J. J. Weis, *Phys. Rev. Lett.*, 77:4039 (1996)
- [15] J. M. Caillol, D. Levesque, J. J. Weis, *J. Chem. Phys.*, 107:1565 (1997)

THERMAL PHOTONIC SCREENING IN A WEAKLY RELATIVISTIC PLASMA

Walter Appel and Angel Alastuey

Laboratoire de Physique, Unité de Recherche 1325 associée au CNRS
École normale supérieure de Lyon
46, allée d'Italie, 69 364 Lyon cedex 07, France

INTRODUCTION

In many physical systems, the description of a plasma as a Coulomb system is sufficient to reproduce most of the properties of interest. If the system is cold enough, the mean velocities of the particles are much smaller than the speed of light, and the charges may be assumed to interact *via* the instantaneous Coulomb potential. However, at sufficiently high temperatures, this approximation is no longer valid, and the contributions of the relativistic effects (which include, apart from the trivial kinetic corrections, the magnetic interactions, and of course all the retardation effects) must be incorporated when studying the equilibrium properties of the system. For a weakly relativistic plasma, the corrections to the Coulomb quantities can be expanded in powers of $1/c$. In the classical (non quantum) case, there exist various approaches based on the so-called Darwin Hamiltonian, which describes the equations of motion of a classical system with electromagnetic interactions up to order $1/c^2$.¹⁻⁷ However, the classical models are not entirely reliable to describe real plasmas, as shown by an analysis within the framework of Quantum Electrodynamics (QED) at finite temperature, the sole theory that provides a complete and coherent treatment of both matter and radiation at equilibrium.⁵⁻⁷

In this paper, the failures of the classical models are illustrated through the QED study of the current correlations. We shall show that the retarded interactions beyond the Coulomb potential, generated by the exchange of thermalized photons, are exponentially screened on the thermal photonic wavelength $\lambda_{\text{photon}} = \beta \hbar c$. This invalidates the large-distances predictions of all the classical Darwin models which equally fail (contrarily to what is claimed in the literature.) However, at distances $\lambda_{\text{dB}} = \sqrt{\beta \hbar^2 / m} < r < \lambda_{\text{photon}}$, the first non-ideal relativistic corrections are indeed given by the Darwin models. In order to avoid the classical collapse between opposite charges due to the Coulomb attraction, we restrict ourselves to the case of a One-Component Plasma.

GENERAL FRAMEWORK

We consider, in the framework of QED at finite temperature,^{8,9} a system composed of

matter: electrons and positrons are described by a bi-spinorfield $\psi(\mathbf{x})$, the free Hamiltonian of which is the Dirac Hamiltonian $\mathcal{H}_{\text{matter}}\{\psi(\mathbf{x})\}$. The chemical potential of the electrons will be denoted $\mu = mc^2 + \mu^*$, where μ^* is the usual chemical potential. The chemical potential of the positrons is then $-\mu$.

radiation: photons are described by a four-vector field $A_\mu(\mathbf{x})$; their chemical potential is identically zero. They are described by a free Hamiltonian $\mathcal{H}_{\text{rad}}\{A_\mu(\mathbf{x})\}$, which depends on the gauge choice.

Matter and radiation are coupled *via* the interaction Hamiltonian

$$\mathcal{H}_{\text{int}} = e \int \bar{\psi}(\mathbf{x}) \gamma^\mu \psi(\mathbf{x}) A_\mu(\mathbf{x}) d\mathbf{x}. \quad (1)$$

In order to investigate the equilibrium statistical mechanics of the system at given temperature $k_B T = 1/\beta$ and chemical potential μ , we introduce the usual imaginary-time evolved operators

$$\psi(\tau, \mathbf{x}) = e^{\tau \mathcal{H}'_{\text{mat}}} \psi(\mathbf{x}) e^{-\tau \mathcal{H}'_{\text{mat}}}, \quad \text{where} \quad \mathcal{H}'_{\text{mat}} = \mathcal{H}_{\text{mat}} - \mu \int \bar{\psi}(\mathbf{x}) \gamma^0 \psi(\mathbf{x}) d\mathbf{x}, \quad (2)$$

and

$$A_\mu(\tau, \mathbf{x}) = e^{\tau \mathcal{H}_{\text{rad}}} A_\mu(\mathbf{x}) e^{-\tau \mathcal{H}_{\text{rad}}}. \quad (3)$$

The familiar Dyson expansion with respect to \mathcal{H}_{int} of the equilibrium quantities leads to Feynman graphs, which can be expressed in terms of free propagators, built with $\psi(\tau, \mathbf{x})$ and $A_\mu(\tau, \mathbf{x})$. Since the imaginary-time free propagators are periodic (or antiperiodic) functions with period β , they can be decomposed in Fourier sums over discrete Matsubara frequencies. For instance, the Fourier components of the free photon propagator read, in the Feynman gauge

$$\mathcal{D}_{\mu\nu}(\omega_n, \mathbf{k}) = \frac{-4\pi}{\omega_n^2 / \hbar^2 c^2 + \mathbf{k}^2} g_{\mu\nu}, \quad (4)$$

where we have set $\omega_n = 2\pi n/\beta$.

In order to study the weakly relativistic and almost classical limit of the system, we take μ^* negative such that

$$k_B T \ll |\mu^*| \ll mc^2. \quad (5)$$


This inequality ensures that *primo* the matter is mainly made of classical electrons (the density of the positrons vanishes then as $e p\{-2\beta mc^2\}$) and *secundo* they are weakly relativistic.

CURRENT CORRELATIONS

For our purpose, it is interesting to introduce the current correlations

$$g^{\mu\nu}(\mathbf{r}) = \langle J^\mu(\mathbf{0}) J^\nu(\mathbf{r}) \rangle \quad \text{with} \quad J^\mu = e \bar{\psi} \gamma^\mu \psi, \quad (6)$$

where $\langle \dots \rangle$ denotes a thermal equilibrium average. The first-order terms in the Dyson expansions are represented by the two following Feynman graphs



$$\text{and} \quad (7)$$

The second one is of purely quantum origin, and has no classical equivalent. Only the first one will be of interest for us.

In order to avoid the quantum effects arising from the overlap of the electrons wavefunctions, we will restrict the analysis to distances $r \gg \lambda_{\text{dB}}$, where $\lambda_{\text{dB}} = \sqrt{\beta \hbar^2 / m}$ is the de Broglie thermal wavelength of the electrons. When we calculate the contribution of the first graph in (7), we observe the emergence of two distinct spatial regimes, separated by the photonic thermal wavelength $\lambda_{\text{photon}} = \beta \hbar c$:

At intermediate distances $\lambda_{\text{dB}} \ll r \ll \beta \hbar c$, and at the lowest orders in e^2 and in $1/c$, the three dimensional current correlation function is an algebraically decreasing function of the distance

$$\langle \mathbf{j}(\mathbf{0}) \cdot \mathbf{j}(\mathbf{r}) \rangle \simeq -\frac{2e^4 \rho^2}{\beta m c^2 r}. \quad (8)$$

At large distances $\lambda_{\text{photon}} \ll r$, on the contrary, the classical part of the correlations $\langle \mathbf{j}(\mathbf{0}) \cdot \mathbf{j}(\mathbf{r}) \rangle$ decays exponentially fast with respect to the distance. Indeed, the photon propagator exhibits a factor $1/(\mathbf{k}^2 + 4\pi^2 n^2 / \lambda_{\text{photon}}^2)$, while the static ($n = 0$) non-vanishing contributions are purely quantum (they depend on \hbar .)

This proves the existence of the thermal photonic screening of the transverse effective interactions between classical charges. We stress that this screening does not result from a collective effect (note that the screening length λ_{photon} does not depend on the density.)

At higher orders in e^2 and $1/c$, the effective interactions between classical charges that appear in each Feynman graph should reduce to a sum of the Coulomb potential and of screened transverse effective interactions.

INTERPRETATION IN TERMS OF CLASSICAL THEORIES

The two different behaviors of the current correlations can be explained in the framework of two different classical approaches. The large-distance behavior can be obtained within Classical Field theory, while the intermediate-distances behavior coincides with the predictions of the Darwin models.

Classical field theory

Let us consider a purely classical and fully relativistic model of a one-component plasma of electrons, interacting *via* a classical electromagnetic field A_μ . This field can be written as the sum of a Coulomb instantaneous field, and a retarded transverse field (in the Coulomb gauge.) Using an appropriate set of canonical variables, the free Hamiltonian of the system can be recast in the following form:

$$\mathcal{H} = \sum_{i=1}^n \sqrt{m^2 c^4 + (\boldsymbol{\pi}_i - \frac{e}{c} \mathbf{A}(\mathbf{r}_i))^2 c^2} + \mathcal{U}_{\text{Coulomb}} + \mathcal{H}_{\text{trans}}, \quad (9)$$

where \mathbf{A} is the vector potential (transverse field), $\boldsymbol{\pi}_i$ is the canonical momentum of particle i , $\mathcal{U}_{\text{Coulomb}}$ is the electrostatic Coulomb energy, and $\mathcal{H}_{\text{trans}}$ is the energy of the transverse field (which can be written as the sum of harmonic oscillators.) The partition function then factorizes into the product of the free transverse-field partition function and the Coulombic-matter partition function. The transverse field is then decoupled from the particles, that behave like a purely Coulomb system. Consequently the current correlations identically vanish. However, the classical statistics of the (free) transverse field involves well-known ultraviolet divergencies, and the present analysis is only valid for the range of momenta $\hbar c |\mathbf{k}| \ll k_B T$ (for larger momenta, the field must be treated quantum mechanically), that is to say, using the Fourier conjugation, at distances $r \gg \beta \hbar c = \lambda_{\text{photon}}$. So, in agreement with the above QED analysis, the current correlations do vanish at these large distances.

Darwin models

Let us consider a model of one-component plasma made of classical point particles with electromagnetic interactions.^{1,2} We assume that all the speeds of the particles are much smaller than the speed of light c . The equations of motion can then be expanded in powers of $1/c$ and, at order $1/c^2$, they can be recast into an Hamiltonian where only the particles degrees of freedom appear (the electromagnetic field is eliminated like in the purely Coulomb description.) This Hamiltonian is the sum of a kinetic term, the Coulomb interaction, and a two-body momentum-dependent term of order $1/c^2$ which reads

$$v_d(i,j) = -\frac{e^2}{2m^2c^2r_{ij}} [\boldsymbol{\pi}_i \cdot \boldsymbol{\pi}_j + (\boldsymbol{\pi}_i \cdot \mathbf{n}_{ij})(\boldsymbol{\pi}_j \cdot \mathbf{n}_{ij})]. \quad (10)$$

We have studied this model⁵⁻⁷ and shown that the Darwin interactions are weakly autoscreened on a scale $\xi^{-1} = \sqrt{mc^2/k_B T} \kappa^{-1}$, where $\kappa^2 = 4\pi\beta\rho e^2$. At distances $r \ll \xi^{-1}$, no screening occurs, and the current correlations, at lowest orders in e^2 and $1/c$, reduce to the contribution of the two-body direct interaction between the two involved particles, *i.e.*,

$$\langle \mathbf{j}(\mathbf{0}) \cdot \mathbf{j}(\mathbf{r}) \rangle = -\frac{2e^4\rho^2}{\beta mc^2 r}. \quad (11)$$

This prediction is therefore in agreement with our previous QED analysis at intermediate distances. We stress that the above autoscreening of the Darwin current correlation has nothing to do with the thermal photonic screening. Consequently, the large-distance behaviors computed in the Darwin models do not make any physical sense. The same considerations apply to the other related models based on the Darwin approach.^{3,4}

CONCLUSION

Our QED analysis of the first-order terms (in e^2 and $1/c$) of the current correlation functions proves that a thermal photonic screening occurs at distances $r > \lambda_{\text{photon}}$. This screening is responsible for the failure of the different Darwin models at large distances, although some predictions of these models, involving only the contributions from the window $\lambda_{\text{dB}} < r < \lambda_{\text{photon}}$, are expected to be relevant pieces of the relativistic corrections for real plasmas. This analysis is confirmed by the study of the excess pressure that appears in [10].

REFERENCES

- [1] J. E. Krizan and P. Havas. Relativistic corrections in the statistical mechanics of interacting particles. *Phys. Rev.*, 128(6):2916–2924, December 1962.
- [2] J. E. Krizan. Relativistic plasmas and long-range effects. *Phys. Rev A*, 10(1):298–301, July 1974.
- [3] V. V. Kosachev and B. A. Trubnikov. Relativistic corrections to the distribution functions of particles in a high-temperature plasma. *Nuclear Fusion*, 9:53–56, 1969.
- [4] B. A. Trubnikov and V. V. Kosachev. Thermodynamics of a weakly relativistic plasma. *Soviet Physics JETP*, 27(3):501–506, 1968.
- [5] A. Alastuey and W. Appel. Weakly relativistic plasmas at equilibrium. In W. D. Kraeft and M. Schlanges, editors, *Physics of Strongly Coupled Plasmas*, pages 59–65. World Scientific, 1996.
- [6] A. Alastuey and W. Appel. A model of relativistic OCP with Darwin interactions. *Physica A*, 238:369–404, 1997.
- [7] W. Appel and A. Alastuey. Relativistic corrections to a classical OCP with Darwin interactions. To be published in *Physica A*.
- [8] J. I. Kapusta. *Finite-Temperature Field Theory*. Cambridge University Press, 1989.
- [9] M. Le Bellac. *Thermal Field Theory*. Cambridge University Press, 1996.
- [10] W. Appel. *Plasma faiblement relativiste à l'équilibre*. Thèse de doctoral, École normale supérieure de Lyon, 14 janvier 1997.

LIST OF PARTICIPANTS

Eric J. Amis	NIST Gaithersburg	USA
Walter Appel	Labo de Physique, Lyon	France
Neil W. Ashcroft	Cornell University	USA
Fazilkhan B. Baimbetow	IETP Almaty	Kazakhstan
Pradip M. Bakshi	Boston College	USA
Uwe Bauder	Technische Universität München	Germany
Kevin Bedell	Boston College	USA
Stefan Bekiranov	University of Maryland	USA
Vyacheslav Belyi	IZMIRAN Troitsk	Russia
John Benage	LANL	USA
Aitor Bergara	University of the Basque Country	Spain
Richard Berkovits	Bar-Ilan University	Israel
Dieter Beule	Humboldt-Universität Berlin	Germany
Krastan B. Blagoev	Boston College	USA
Lesser Blum	University of Puerto Rico	Puerto Rico
Michael Bonitz	University of Rostock	Germany
Thomas Bornath	University of Rostock	Germany
Laura Bringol Barge	Baylor University	USA
Eberhard Burkel	University of Rostock	Germany
Jean-Michel Caillol	Universite d'Orleans	France
Carlo Cereceda	LPGP Orsay	France
Dov Chelst	Rutgers University	USA
Junzo Chihara	Atomic Energy Research Institute	Japan
Yuriy Chutov	Taras Shevchenko University Kiev	Ukraine
Jean Clerouin	CEA Villeneuve St-Georges	France
Francoise Cornu	Ecole Normale Superieure de Lyon	France
Werner Däppen	University of Southern California	USA
Alexander V. Demura	Kurchatov Institute	Russia
Alan DeSilva	University of Maryland	USA
Claude Deutsch	Universite Paris XI	France
Hugh DeWitt	LLNL	USA
Chandre Dharma-wardana	IMS NRC	Canada
Daniel H. E. Dubin	UCSD	USA
James Dufty	University of Florida	USA
Werner Ebeling	Humboldt-Universität Berlin	Germany
Gerald Faussurier	CEA Villeneuve St. Georges	France
Roman Fehr	University of Greifswald	Germany

Vladimir S. Filinov	HEDRC-IVTAN	Russia
Kevin S. Fine	UCSD	USA
Michael E. Fisher	University of Maryland	USA
Andreas Förster	Humboldt-Universität Berlin	Germany
Vladimir E. Fortov	Institute of Chemical Physics	Russia
Bernhard Franzke	GSI Darmstadt	Germany
Petros D. Gasparian	Russian Federal Nuclear Center	Russia
Alice P. Gast	Stanford University	USA
David K. Geller	Rice University	USA
Dirk O. Gericke	University of Greifswald	Germany
Dominique Gilles	CEA Villeneuves St Georges	France
Alfred Gold	Universite Paul-Sabatier, Toulouse	France
Kenneth I. Golden	University of Vermont	USA
Harvey Gould	Clark University	USA
Rudolf Grimm	MPI für Kernphysik Heidelberg	Germany
Satoshi Hamaguchi	IBM Watson Research Center	USA
Jeffrey S. Hangst	Aarhus University	Denmark
Pawel Hawrylak	IMS NRC	Canada
Yasuaki Hayashi	Kyoto Institute of Technology	JAPAN
Olle G. Heinonen	University of Central Florida	USA
Charles F. Hooper	University of Florida	USA
Mihaly Horanyi	University of Colorado	USA
Pei Huang	NIST Boulder	USA
Truell W. Hyde	Baylor University	USA
Igor L. Iosilevski	MIPT Dolgoprudny	Russia
Jordi Isern	Institut for Space Studies	Spain
Hiroshi Iyetomi	Niigata University	Japan
Bernard Jancovici	Universite de Paris XI	France
John R. Jasperse	Phillips Laboratory	USA
Young-Dae Jung	Hanyang University	South Korea
Torsten Kahlbaum	Humboldt-Universität Berlin	Germany
Gabor J. Kalman	Boston College	USA
Hong Seok Kang	Jeonju University	Korea
Christopher J. Keane	DOE	USA
Dmitri Khveshchenko	NORDITA	Denmark
David P. Kilcrease	LANL	USA
Walter Kohn	UCSB	USA
Uwe Konopka	DLR-Institut für Raumsimulation	Germany
Vladimir Kozhevnikov	Moscow Aviation Institute	Russia/USA
Wolf D. Kraeft	University of Greifswald	Germany
Dietrich Kremp	University of Rostock	Germany
Joel Kress	LANL	USA
Yuri Kurilenkov	IVTAN Moscow	Russia
Kenneth J. LaGattuta	LANL	USA
Michel Le Bellac	Institut Non Lineaire de Nice	France
Joel L. Lebowitz	Rutgers University	USA
M. Howard Lee	University of Georgia	USA
Richard W. Lee	LLNL	USA
Alexander Likalter	HEDRC-IVTAN	Russia
Dexin Lu	Nanjing University	China

William R. Magro	Cornell University	USA
Ernesto Marceca	Philipps-Universität Marburg	Germany
Norman March	Oxford University	U.K.
Philippe Martin	Institut de Physique Theorique	Switzerland
Richard Martin	University of Illinois	USA
Lorin Matthews	Baylor University	USA
Burkhard Militzer	NCSA—University of Illinois	USA
Alessandro Mirone	Ecole Polytechnique	France
Udayan Mohanty	Boston College	USA
Michael S. Murillo	LANL	USA
Stefan Nagel	University of Rostock	Germany
William J. Nellis	LLNL	USA
James Nicholls	Cavendish Laboratory	U.K.
Dmitry N. Nikolaev	Institute of Chemical Physics	Russia
Guenri Norman	Moscow Physical Society	Russia
Irwin Oppenheim	MIT	USA
Jens Ortner	Humboldt-Universität Berlin	Germany
Rajeev K. Pathak	University of Pune	India
Georgii A. Pavlov	Institute of Chemical Physics	Russia
Francois Peeters	University of Antwerp	Belgium
John Perdew	Tulane University	USA
Wolf-Christian Pilgrim	Philipps-Universität Marburg	Germany
Mats-Erik Pistol	Lund University	Sweden
Marko M. Popovic	Institute of Physics, Beograd	Yugoslavia
Ralf Prenzel	University of Rostock	Germany
Richard Quinn	University of Iowa	USA
Attipat K. Rajagopal	Naval Research Laboratory	USA
Valentin A. Rantsev-Kartinov	Kurchatov Institute	Russia
Ronald Redmer	University of Rostock	Germany
Anthony Reynolds	Naval Research Laboratory	USA
Peter Reynolds	ONR	USA
Max Roesler	Hahn–Meitner-Institut Berlin	Germany
Forrest J. Rogers	LLNL	USA
J. Martin Rommel	Boston College	USA
Gerd Röpke	University of Rostock	Germany
Marlene Rosenberg	UCSD	USA
Yasha Rosenfeld	Nuclear Research Center — Negev	Israel
Marie-Louise Saboungi	Argonne National Laboratory	USA
Dmitry Samsonov	University of Iowa	USA
John P. Schiffer	ANL	USA
Manfred Schlanges	University of Greifswald	Germany
Pieter P.J.M. Schram	Eindhoven University of Technology	Netherlands
Irina Schweigert	ISP Novosibirsk	Russia
Vitaly Schweigert	ITAM Novosibirsk	Russia
Michael Seidl	Tulane University	USA
Abhijit Sen	Institute for Plasma Research, Bhat	India
Gaetano Senatore	Universite di Trieste	Italy
William R. Shanahan	LANL	USA
Shye Shapira	Cavendish Laboratory	U.K.
Giora Shaviv	Technion	Israel

Andrey N. Starostin	MIPT	Russia
Mario Steinberg	Humboldt-Universität Berlin	Germany
Michael Stetter	GSI Darmstadt	Germany
Werner Stolzmann	Universität Kiel	Germany
Leendert G. Suttoop	University of Amsterdam	Netherlands
Leszek Swierkowski	University of New South Wales	Australia
Vladimir Ya. Ternovoi	Institute of Chemical Physics	Russia
Hubertus Thomas	MPI für extraterrestrische Physik	Germany
Thomas E. Tierney IV	LANL	USA
Igor Tkachenko	Universidad Politecnica Valencia	Spain
Christian Toepffer	Universität Erlangen-Nürnberg	Germany
Mario Tosi	ICTP Trieste	Italy
Chieko Totsuji	Okayama University	Japan
Hiroo Totsuji	Okayama University	Japan
Eugene Tsiper	University of Utah	USA
Vladimir Valtchinov	Boston College	USA
Nadja Vogel	TU Chemnitz Zwickau	Germany
Jean Wallenborn	Universite Libre de Bruxelles	Belgium
Dean C. Wang	Stanford University	USA
Jonathan Workman	LANL	USA

AUTHOR INDEX

- Alastuey, A., 705, 717
Aleksandrov, N. L., 647
Allahyarova, E. A., 247
Appel, W., 717
Ashcroft, N. W., 81
Averyanov, V. P., 381
- Baimbetov, F. B., 347, 353
Baimbetov, N. F., 361
Bakshi, P., 503
Baturin, S. M., 419
Beckert, K., 423
Bekenov, M. A., 353, 361
Bekiranov, S., 33
Belda, J. M., 479
Belkov, S. A., 569
Belyi, V. V., 587, 597
Benage, Jr, J. F., 319
Bergara, A., 657
Beikovits, R., 493
Bernard, O., 395
Bernu, B., 337
Beule, D., 613, 623, 629
Blöcker, T., 265
Blum, L., 395
Bollinger, J. J., 429
Bonitz, M., 515
Bornath, Th., 95, 643
Bradley, D., 385
Bringol-Barge, L. A., 231
Buchstab, E., 455
Bulyshev, A. E., 373
Bunker, A., 365
Burkel, E., 123
- Caillol, J., 713
Ceperley, D. M., 337, 357
Cereceda, C., 543
Chigvintsev, A. Yu., 135
Chihara, J., 129
Chutov, Yu. I., 203, 215, 221
Clerouin, J., 369
Collins, L., 331
Conrads, H., 623
Conti, S., 461
Comu, F., 705
- Däppen, W., 327
Das, S. P., 171
de Cordoba, P. F., 479, 561
Delettrez, J., 385
Demura, A. V., 373, 377, 391
de Peretti, M., 543
DeSilva, A. W., 313, 583
Deutsch, C., 73
DeWitt, H. E., 1
Dharma-Wardana, M. W. C., 271
Djordjevic, D., 551
Dufty, J. W., 171, 547
D'yachkov, L. G., 381
- Ebeling, W. E., 433, 473, 623, 629, 663
Echenique, P. M., 657
Efros, A. L., 483
- Faussurier, G., 159, 287
Feautrier, N., 391
Fehr, R., 617
Filinov, A., 467
Filinov, V., 467
Fisher, M. E., 33, 415
Förster, A., 613, 623, 629
Fortov, V. E., 147, 297
Franzke, B., 423
Fried, B. D., 591
- Gabdullina, G. L., 347
Garcia-Berro, E., 251
Gasparian, P. D., 569
Gauthier, J., 159
Gavrilova, T. V., 381
Geb, O., 73
Genga, R., 669
Gericke, D. O., 539
Ghazali, A., 439
Gilleron, F., 159
Gilles, D., 377
Gold, A., 439
Golden, K., 533
Gryaznov, V. K., 147, 297
Gunderson, M. A., 385

Halcoussis, Ch., 123
 Hamaguchi, S., 175
 Hammerberg, J. E., 237
 Hasegawa, A., 399
 Hawrylak, P., 497
 Hayashi, Y., 207
 Haynes, Jr., D. A., 385
 Heinonen, O., 277
 Hensel, E., 139, 143
 Hernanz, M., 251
 Hill, N. P. R., 519
 Holian, B. L., 237
 Homann, A., 241
 Hong, J., 445
 Hooper, Jr., C. F., 385
 Horanyi, M., 179
 Huang, X.-P., 429
 Hyde, T. W., 199, 231
 Hyland, G. J., 147

 Iosilevski, I. L., 135, 147, 297
 Isem, J., 251
 Iserte, J. L., 583
 Itano, W. M., 429
 Itzeleuov, N. N., 353
 Iyetomi, H., 399

 Jaanimagi, P., 385
 Jancovici, B., 709
 Jelenkovic, B., 429
 Jokipii, J. R., 187
 Jung, Y. D., 633
 Junkel, G. C., 385

 Kahl, G., 129
 Kahlbaum, T., 165
 Kaklyugin, A. S., 639
 Kalman, G. J., 533, 669
 Kang, H. S., 153
 Katsouros, J. D., 313
 Kaw, P. K., 215
 Kempa, K., 503
 Khveshchenko, D. V., 487
 Kikuchi, H., 399
 Kim, J., 445
 Kishimoto, T., 193
 Klakow, D., 341
 Knaup, M., 341
 Kohn, W., 9
 Kosarev, I. N., 391
 Kotchubey, Yu. K., 569
 Kraeft, W.-D., 539, 601, 617
 Krainov, V. P., 261, 579
 Kravchenko, O. Yu., 203, 215, 221
 Kremp, D., 515, 601
 Kress, J., 331
 Kukhareno, Yu. A., 587, 597
 Kukushkin, A. B., 575
 Kurilenkov, Yu. K., 225, 381, 547
 Kurth, S., 281
 Kwon, I., 331

 Kwong, N., 515
 Kyrala, G., 319

 LaGattuta, K. J., 323
 Landin, L., 509
 Lapenta, G., 237
 Le Bellac, M., 65
 Lebowitz, J. L., 117
 Lee, B. P., 33, 415
 Lee, M. H., 445
 Le Guen, C., 381
 Lenosky, T., 331
 Levesque, D., 713
 Likalter, A. A., 303
 Linfield, E. H., 519
 Lipavsky, P., 651
 Lisitsa, V. S., 373, 391
 Louvet, G., 225
 Lozovik, Y., 467
 Lu, D., 691

 Magro, W. R., 337, 357
 Mancini, R. C., 385
 Marceca, E., 139
 Martin, P. A., 705
 Maruhn, J. A., 73
 Matthews, L. S., 199
 Maynard, G., 547
 Melzer, A., 241
 Militzer, B., 337, 357, 433
 Miller, M. S., 509
 Mirone, A., 159
 Mitchell, A. C., 25
 Mitchell, T. B., 429
 Mitrofanov, E. T., 569
 Mochkovitch, R., 251
 Mohanty, U., 405
 Morales, G. J., 591
 Morawetz, K., 651
 Morfill, G. E., 187
 Murillo, M. S., 237, 607

 Nagel, S., 365
 Nagy, I., 657
 Nayfonov, A., 327
 Nellis, W. J., 25
 Nicholls, J. T., 519
 Nifosi, R., 461
 Nolden, F., 423
 Norman, G. E., 103, 639
 Nurekenov, Kh. T., 347

 Ortner, J., 473, 663, 699

Partoens, B., 523
 Pathak, R. K., 449
 Pavlov, G. A., 419, 683, 695
 Peeters, F. M., 523
 Pepper, M., 519
 Perdew, J. P., 281
 Piel, A., 241
 Pierleoni, C., 337
 Pilgrim, W. C., 143
 Pistol, M.-E., 509
 Popovic, M. M., 551
 Prenzel, R., 643
 Pryor, C. E., 509

 Rajagopal, A. K., 49
 Ramazanov, T. S., 353, 361
 Rantsev-Kartinov, V. A., 261, 555, 575, 579
 Rapisarda, F., 529
 Redmer, R., 347, 361, 365
 Ree, F.H., 153
 Reinhard, P.-G., 341
 Reynolds, M. A., 591
 Ritchie, D.A., 519
 Rogers, F.I., 15
 Romeas, P., 225
 Rommel, J. M., 669
 Ronchi, C., 147
 Röpke, G., 347, 361, 365, 679
 Rosenberg, M., 183
 Rosenfeld, Y., 307
 Rösler, M., 673
 Roslov, V. I., 569
 Ross, M., 143
 Rylyuk, V. M., 699

 Sabatier, M., 543
 Samuelson, L., 509
 Schautz, F., 433, 663
 Schiffer, J. P., 43
 Schlanges, M., 539, 601, 643, 95
 Schram, P. P. J. M., 203, 215, 247, 409
 Schweigert, I. V., 241, 523
 Schweigert, V. A., 241, 523
 Seidl, M., 293
 Semkat, D., 515
 Sen, A., 215
 Senatore, G., 529
 Shanahan, W. R., 237
 Shapira, S., 455
 Shaviv, G., 255
 Shaviv, N.J., 255
 Shiryaev, A. A., 419
 Simakov, G., 297
 Sinn, H., 123
 Sivan, U., 455

 Skowronek, M., 225
 Slattery, W. L., 1
 Smimov, R. D., 203
 Solomon, P. M., 455
 Spivcka, V., 651
 Starostin, A. N., 373, 647
 Steck, M., 423
 Stehle, C., 377, 391
 Steinberg, M., 473
 Stolzmann, W., 265, 673
 Suttorp, L. G., 687
 Suvorov, A. E., 373

 Tahir, N. A., 73
 Tan, J. N., 429
 Terentiev, A. R., 575
 Thomas, H. M., 187
 Tierney, IV, T., 319
 Tischler, M., 455
 Tkachenko, I. M., 479, 561, 583, 699
 Toepffer, C., 341
 Tosi, M. P., 461
 Totsuji, C., 193
 Totsuji, H., 193
 Trigger, S. A., 247, 409
 Trofimovich, E. E., 261, 555, 579
 Troullier, N., 331
 Trunin, R. F., 297
 Trusov, L., 297
 Tsiper, E. V., 483

 Valtchinov, V., 533
 Valuev, A. A., 103
 Vitel, Y., 381
 Vogel, N., 565

 Wallenborn, J., 587, 597
 Weir, S. T., 25
 Weis, J.J., 713
 Wineland, D. J., 429
 Winkler, T., 423
 Winske, D., 237
 Workman, J., 319

 Yakovetsky, V. S., 215, 221
 Yakub, E. S., 147
 Yakunin, I. I., 373
 Yang, L. H., 143
 Yoon, J. S., 633
 Yoseph, G. B., 455

 Zacharov, I., 467
 Zhernokletov, M. V., 297
 Zuckerman, D. M., 415
 Zuzic, M., 187

This page intentionally left blank

SUBJECT INDEX

- Absorbing power, 547
- Acoustic waves, 183
- Activity Expansion Method, 3
- Alkali metals, 30
- APEX formalisms, 377
- Artificial molecules, 523, 525
- Atom–positron interactions, 449
- Augmented-plane-waves (APW), 400
- Average ion model (AIM), 569, 571
- Average-atom model, 287

- Balmer lines, 382
- BBGKY, 68, 171, 587, 589
- Bethe–Salpeter equation, 605
- Bilayer liquids, 533
- Bilayers, 523, 530
 - CDW, 537
 - charge transfer state, 531
 - collective modes, 535, 519
 - crystallization, 531
 - dielectric matrix, 535
 - dynamical instability, 535
 - in magnetic field, 520
 - localized modes, 537
 - pair correlation function, 535, 531
 - phase diagrams, 530
 - phase transition, 531
 - rotor minimum, 537
 - substitutional disorder, 533, 537
 - transresistivity, 521
- Binary collision approximation, 618
- Binary correlations, 651
- Binary liquid, 139
- Bogolyubov’s chain equations, 347
- Bohm–Pines, 49
- Bohr–van-Leeuwen theorem, 475
- Born approximation, 347, 517, 542, 549, 607, 617, 644, 648
- Born–Oppenheimer, 331
- Bound states, 601
- Breathing mode, 82
- Broken symmetry, 81
- Brownian Motion, 161

- Car–Parrinello (CP), 331, 370
- Carbon, 623
- Carbon nanotubes, 59
- Carbon plasma, 100
- Chapman–Enskog method, 349
- Charged-boson gas, 657
- Chemical beam epitaxy, 509
- Chemical picture, 613
- Cherenkov radiation, 263
- Chern–Simons theory, 489
- Classical field theory, 719
- Cluster expansion, 166
- Collective excitations, 65, 211, 640
- Collective processes, 183
- Collisional and radiative
 - plasma kinetics model (CRM), 569, 571
- Colloidal particles, 523
- Colloidal suspensions, 195
- Continuum factors, 551
- Correlation functions, 294, 361
- Correlations, 159, 497
 - Coulomb, 381
 - current, 718
 - long range, 119
 - short range, 494
 - static, 479
- Coulomb
 - crystals, 184, 207, 429
 - drag, 519
 - lattices, 183, 199
- Coulomb potential, 337, 591
 - long range, 484
 - screened, 153, 185
 - short range, 484
 - unscreened, 153
- Coulombsystems
 - classical, 43
- Counterions, 405
- Coupled electron layers, 529
- Critical
 - behavior, 40, 713
 - exponents, 33, 138
 - temperature, 714
- Crossover scale, 34
- Crystalline semiconductors, 86

- Crystallization, 251, 411
- Darwin Hamiltonian, 717
- Debye–Hückel Approximation, 15, 33, 148
- Deep-inelastic scattering, 447, 447
- Delocalization transition, 485
- Dense hydrogen plasma, 381
- Density correlation length, 34
- Density functional molecular dynamic, 363
- Density functional theory (DFT), 9, 58, 271, 277, 281, 287, 293, 307, 331, 369, 461, 607, 657
- Density functional theory (HNC), 129, 153
- Deuterium, 337
- Deuterium–tritium plasma, 543
- Diffusion Monte Carlo, 529
- Diffusion process, 161, 591
- Dimensional crossover, 308
- Direct correlation function, 130
- Discharges
 - in water, 583
 - vacuum, 225
- Disorder, 485
- Disordered phase, 533
- Disordered system, 303
- Dispersion relation, 183
- DNA, 405
- Dust crystal, 241
- Dust lattice waves, 187
- Dust particles, 175, 179, 221
- Dynamic screening, 555
- Dynamic structure factor, 447, 607, 684
- Dyson equation, 96
- Effective-potential, 165, 361
- Effective transport coefficients, 695
- Eikonal method, 633
- Electrolytes, 400, 417
- Electromagnetic modes, 699
- Electron gas, 439, 446, 663
- Electron temperature, 556.
- Electronic bilayers, 533
- Equation of state, 15, 314, 319, 327, 328, 361, 365, 368, 601, 629
- Exact diagonalization, 485
- Exchange-correlation, 265, 281, 284, 461
- Fermi golden rule, 272
- Fermi liquid, 49, 487
- Fermi surface, 89
- Fermion sign problem, 357
- Fermionic path integral, 357
- Feynman–Kac path integral, 16, 165, 474, 706
- Filaments, 577
- Fine-structure splitting, 512
- Fission-fragment (FF), 323
- Fluctuations, 117, 160, 258, 674
- Fokker–Planck, 271, 543, 591
- Fractal aggregates, 199
- Fractional approximation, 544
- Freezing, 307
- Friedel oscillations, 369, 439
- Functional integrals, 287
- Fundamental measure functionals, 307
- Fusion, 73
- GaAs quantum wells, 455, 509, 520
- Gamow peak, 255
- Gap, 486
- Georling–Levy perturbation theory, 293
- Ginsburg’s criterion, 37
- Gradient expansion approximation, 282
- Green’s function, 57, 96, 473, 598, 601, 652, 674
- GW approximation, 57
- Hall effect, 576
- Hard sphere, 307, 713
- Hartree approximation, 510
- Hartree–Fock–Slater, 54
- He–Hg mixture, 139
- Heliogeology, 327
- Helium, 295, 324
- Helium-like, 391
- Hellman–Feynman theorem, 293
- Hexagonal lattice, 191
- High power density matter (HPDM), 225
- Hohenberg–Kohn, 9, 658
- Hubbard approximation, 519
- Hydrogen, 623, 706
 - chemical picture, 613
 - dense, 81, 331, 337, 341, 358, 369
 - equation of state, 329
 - experiments, 381
 - metallic, 25, 29, 83
 - strongly coupled plasma, 347, 353, 629, 361
- Hypennetted chain (HNC), 2, 273, 341, 361, 395, 416, 396, 692
 - perturbative (PHNC), 153, 154
 - quantal (QHNC), 129, 130
- Impulse approximation, 447
- InAs, 509
- Ion beam, 423
- Ion traps, 423
- ionization
 - equilibrium, 629
 - fronts, 613
 - kinetics, 643
 - potential, 608, 647
- Jupiter, 26, 93, 179
- Kadanoff–Baym equations, 515, 603, 604
- Kato–Kimball condition, 658
- Kimball relation, 659
- Kinetic equation, 515, 587
- Kohn anomaly, 272
- Kohn–Sham, 271, 278, 281, 287, 293, 332, 400
- Kubo coefficient, 684
- Kubo formulas, 469

- Landau damping, 106, 692
- Landau level, 520
- Langevin force, 242
- Laser fusion, 215
- Laser plasma, 95
- Lattice waves, 187
- Lennard–Balescu equation, 96, 173, 541
- Lindeman criterion, 243
- Lindhard response, 369
- Linear response theory, 669
- Linear screening approximation, 155
- Lippmann–Schwinger, 541, 618, 619, 634
- Liquid helium, 338, 523
- Liquid metal, 129, 144
- Local density approximation (LDA), 10, 271, 278, 461
- Local field correction, 439, 462, 673
 - static, 479, 673
- Local spin density approximation, 281
- Local thermodynamic equilibrium, 579
- Logarithmic potential, 591
- Long range Coulomb potential, 484

- Madelung constant, 3
- Magnetic fields, 523, 673
- Magnetospheric fields, 179
- Marcovian approximation, 589
- Markoff process, 613
- Melting, 197, 241
- Microfield Stochastic Model (MSM), 609
- Microplasmas, 225, 565
- Model Microfield Method (MMM), 391
- Molecular Dynamics (MD), 1, 43, 103, 108, 109, 116, 175, 212, 237, 331, 341, 353, 373, 375, 391, 400, 467, 550, 664
 - fermion, 324
 - quantum, 331, 366
 - Thomas–Fermi, 370
 - wave-packet, 342, 366
- Monomers, 397
- Monte Carlo (MC), 1, 123, 221, 242, 353, 377, 407, 440, 468, 479, 481, 524, 692
 - fixed-node diffusion, 529
 - path-integral, 16, 89, 337, 341, 357, 363, 366, 370
 - Metropolis, 338
 - quantum, 57, 434, 461, 529, 664
- Morse potential, 146, 237
- MOSFET, 59
- Multi-component system, 117

- Neutral-pseudo-atom potential, 124
- Neutron stars, 1, 473, 633
- Nonequilibrium, 215, 515
- Non-Fermi liquid, 487
- Nonlinear interference, 373, 391
- Non-Markovian, 597, 651
- Non-Newtonian fluids, 419
- Nonuniform classical fluids, 307
- Nuclear reactions, 255

- One-component plasma (OCP), 1, 137, 429, 710, 687, 717
- One-dimensional (1D), 485, 615, 669
- Optical characteristics, 683
- Ornstein–Zernike, 362, 395

- Pade approximation, 434, 265, 630
- Pair correlation function, 359, 535, 597
- Pair distribution function, 366, 409
- Partially ionized, 15, 705
- Penning trap, 429
- Perfect screening, 712
- Phase
 - crystal, 171
 - diagram, 529
 - fluid, 171
- Phase separation, 101
- Phase transition, 137, 568
 - first order, 137, 360
 - insulator–metal, 305, 485
 - liquid–liquid, 84
 - metal–insulator, 59
 - metal–nonmetal, 141, 365
 - Mott-type, 585
 - second order, 197
 - structural, 195
- Plasma
 - aluminum, 313
 - approximation, 587
 - carbon, 643
 - classical, 441
 - cold, 225, 699
 - colloidal, 409
 - column conductivity, 583
 - compressed, 297
 - copper, 313
 - coronal, 571
 - crystals, 187, 237
 - dense, 319, 320, 381, 541, 547, 562, 575, 607, 617
 - diagnostics, 551
 - discharge, 623
 - dusty, 183, 195, 199, 203, 207, 211, 225, 231, 247
 - electron–ion, 103
 - frequency, 700
 - germanium, 160
 - hot, 373
 - inhomogeneous, 587
 - layer, 215
 - liquid, 252
 - magnetized, 473, 699
 - multicomponent, 695
 - nonideal, 104, 381, 597, 613, 647, 699
 - non-neutral, 429
 - oscillations, 203
 - particles, 263
 - quark–gluon, 65
 - relativistic, 717
 - solid, 252
 - strongly coupled, 347

- Plasma, *Continued*
 - weakly coupled, 327
 - waves, 639
 - xenon, 553
- Plasmon dispersion curves, 519
- Plasmon modes, 519
- Plasmons, 540
- Polarization function, 673
- Polyelectrolytes, 395
- Positron density, 452

- Quadratic response, 657
- Quadratic susceptibility, 659, 669
 - 2D, 671
 - charged bosons, 657
- Quantum chromodynamics (QCD), 65
- Quantum dots (QD), 493, 497, 503, 509, 39
- Quantum electrodynamics (QED), 65, 718, 720
- Quantum Hall effect (QHE), 53, 487, 519, 277
- Quantum melting, 485
- Quantum well, 519
- Quasiclassical approximation, 348
- Quasilocalized charge (QLC), 691

- Radial distribution function, 129, 132, 156, 479
- Raman shifts, 82
- Random matrices, 120
- Random phase approximation (RPA), 97, 462, 463, 488, 520, 541, 666, 670, 674, 691, 692
 - generalized, 561
- Reaction rates, 97, 647
- Relativistic effects, 53, 266
- Response
 - generalized, 679
 - linear, 103
- Restricted
 - ionic model (RIM), 147
 - primitive model (RPM), 34, 417, 713
- Rubidium, 129, 143

- Saddle-point, 287–289
- Saha equation, 15, 95
- Saturn, 26
- Scaling, 305, 675, 713
- Schottky, 424, 425
- Screening, 98, 658
 - dynamical, 99, 261
 - of nuclear reactions, 255
 - photonic, 717
 - static, 657
- Self-energy, 97
- Self-organization, 575
- Shock-wave, 297, 323
- Short range Coulomb potential, 484
- Spherical approximation, 395
- Spinless fermions, 485
- Square lattice, 485
- Stark broadening, 374, 385
- Stark profiles, 377
- Stark states, 610
- Stellar evolution, 265
- Stellar plasmas, 255
- Stochastic model, 607
- Stochastic simulation, 613
- Stopping power, 541, 547, 548
- Storage ring, 423
- Strictly correlated electrons, 293
- Structural transitions, 195
- Substitutional disorder, 533, 537
- $SU(3)$, 65
- Sun, 327, 633
- Superconductivity, 53
- Superfluidity, 338
- Suspension film, 419
- Symmetry breaking, 307

- T-matrix, 100, 541, 603, 618
- Thermoelectric field, 579
- Thermonuclear fuel, 73
- Thomas–Fermi–Dirac functional, 369
- Thomas–Fermi model, 22, 314
- Thomson scattering, 558
- Transport, 493
- Two-component plasma (TCP), 154, 433, 681, 710
- Two-dimensional (2D), 324, 439, 485, 494, 592, 669, 691
 - atoms, 523
 - configuration, 44
 - crystal, 203
 - electron gas (2DEG), 487, 498, 519, 524
 - hole layer, 455
 - logarithmic interactions, 709
 - solid, 197

- Ultrafast relaxation, 515
- Universality, 33
- Uranium dioxide, 147

- Van der Waals, 12, 705
- Variation equation, 309
- Virial expansions, 165
- Vlasov equation, 66, 591

- Weak ergodic theorem, 257
- White Dwarf, 53, 251, 633
- Wiedemann–Franz relations, 313
- Wigner crystal, 485, 529
- Wigner distribution, 652
- Wigner representation, 467

- X-ray, 125
 - emission, 568
 - radiation, 567
 - scattering, 123
- Xenon plasma, 553

- Yukawa, 6, 154, 175, 195, 237